Chapter 1

Biochemical Reactions

Cells can do lots of wonderful things. Individually they can move, contract, excrete, reproduce, signal or respond to signals, and carry out the energy transactions necessary for this activity. Collectively they perform all of the numerous functions of any living organism necessary to sustain life. Yet, remarkably, all of what cells do can be described in terms of a few basic natural laws. The fascination with cells is that although the rules of behavior are relatively simple, they are applied to an enormously complex network of interacting chemicals and substrates. The effort of many lifetimes has been consumed in unraveling just a few of these reaction schemes, and there are many more mysteries yet to be uncovered.

1.1 The Law of Mass Action

The fundamental "law" of a chemical reaction is the law of mass action. This "law" describes the rate at which chemicals, whether large macromolecules or simple ions, collide and interact to form different chemical combinations. Suppose that two chemicals, say A and B, react upon collision with each other to form product C,

$$\text{A} + \text{B} \xrightarrow{k} \text{C}. \tag{1.1}$$

The rate of this reaction is the rate of accumulation of product, $\frac{d[\text{C}]}{dt}$. This rate is the product of the number of collisions per unit time between the two reactants and the probability that a collision is sufficiently energetic to overcome the free energy of activation of the reaction. The number of collisions per unit time is taken to be proportional to the product of the concentrations of A and B with a factor of proportionality that depends on the geometrical shapes and sizes of the reactant molecules and on the temperature of the mixture. Combining these factors we have

$$\frac{d[\text{C}]}{dt} = k[\text{A}][\text{B}]. \tag{1.2}$$

The identification of (1.2) with the reaction (1.1) is called the *law of mass action*, and the constant k is called the *rate constant* for the reaction. However, the law

of mass action is not a law in the sense that it is inviolable, but rather it is a useful model, much like Ohm's law or Newton's law of cooling. As a model, there are situations where it is not valid. For example, at high concentrations, doubling the concentration of one reactant need not double the overall reaction rate, and at extremely low concentrations, it may not be appropriate to represent concentration as a continuous variable.

For thermodynamic reasons all reactions proceed in both directions. Thus, the reaction scheme for A, B, and C should have been written as

$$A + B \underset{k_-}{\overset{k_+}{\rightleftharpoons}} C, \tag{1.3}$$

with k_+ and k_- denoting, respectively, the forward and reverse rate constants of reaction. If the reverse reaction is slow compared to the forward reaction, it is often ignored, and only the primary direction is displayed. Since the quantity A is consumed by the forward reaction and produced by the reverse reaction, the rate of change of [A] for this bidirectional reaction is

$$\frac{d[A]}{dt} = k_-[C] - k_+[A][B]. \tag{1.4}$$

At equilibrium, concentrations are not changing, so that

$$\frac{k_-}{k_+} \equiv K_{eq} = \frac{[A]_{eq}[B]_{eq}}{[C]_{eq}}. \tag{1.5}$$

The ratio k_-/k_+, denoted by K_{eq}, is called the *equilibrium constant* of the reaction. It describes the relative preference for the chemicals to be in the combined state C compared to the disassociated state. If K_{eq} is small, then at steady state most of A and B are combined to give C.

If there are no other reactions involving A and C, then $[A]+[C] = A_0$ is constant, and

$$[C]_{eq} = A_0 \frac{[B]_{eq}}{K_{eq} + [B]_{eq}}, \qquad [A]_{eq} = A_0 \frac{K_{eq}}{K_{eq} + [B]_{eq}}. \tag{1.6}$$

Thus, when $[B]_{eq} = K_{eq}$, half of A is in the bound state at equilibrium.

There are several other features of the law of mass action that need to be mentioned. Suppose that the reaction involves the dimerization of two monomers of the same species A to produce species C,

$$A + A \underset{k_-}{\overset{k_+}{\rightleftharpoons}} C. \tag{1.7}$$

For every C that is made, two of A are used, and every time C degrades two copies of A are produced. As a result, the rate of reaction for A is

$$\frac{d[A]}{dt} = 2k_-[C] - 2k_+[A]^2. \tag{1.8}$$

However, the rate of production of C is half that of A,

$$\frac{d[C]}{dt} = -\frac{1}{2}\frac{d[A]}{dt}, \tag{1.9}$$

and the quantity [A]+2[C] is conserved (provided there are no other reactions).

In a similar way, with a trimolecular reaction, the rate at which the reaction takes place is proportional to the product of three concentrations, and three molecules are consumed in the process, or released in the degradation of product. In real life, there are probably no truly trimolecular reactions. Nevertheless, there are some situations where a reaction might be effectively modeled as trimolecular (Exercise 2).

Unfortunately, the law of mass action cannot be used in all situations because not all chemical reaction mechanisms are known with sufficient detail. In fact, a vast number of chemical reactions cannot be described by mass action kinetics. Those reactions that follow mass action kinetics are called *elementary reactions* because presumably, they proceed directly from collision of the reactants. Reactions that do not follow mass action kinetics usually proceed by a complex mechanism consisting of several elementary reaction steps. It is often the case with biochemical reactions that the elementary reaction steps are not known or are very complicated to write down.

1.2 Thermodynamics and Rate Constants

There is a close relationship between the rate constants of a reaction and thermodynamics. The fundamental concept is that of *chemical potential*, which is the Gibbs free energy, G, per mole of a substance. Often, the Gibbs free energy per mole is denoted by μ rather than G. However, because μ has many other uses in this text, we retain the notation G for the Gibbs free energy.

For a mixture of ideal gases, X_i, the chemical potential of gas i is a function of temperature, pressure and concentration,

$$G_i = G_i^0(T, P) + RT \ln(x_i), \tag{1.10}$$

where x_i is the mole fraction of X_i, R is the universal gas constant, T is the absolute temperature and P is the pressure of the gas (in atmospheres); values of these constants, and their units, are given in the Appendix. The quantity $G_i^0(T, P)$ is the standard free energy per mole of the pure ideal gas, i.e., when the mole fraction of the gas is 1. Note that, since $x_i \leq 1$, the free energy of an ideal gas in a mixture is always less than that of the pure ideal gas. The total Gibbs free energy of the mixture is

$$G = \sum_i n_i G_i, \tag{1.11}$$

where n_i is the number of moles of gas i.

The theory of Gibbs free energy in ideal gases can be extended to ideal dilute solutions. By redefining the standard Gibbs free energy to be the free energy at a concentration of 1 M (i.e., 1 mole per liter) we obtain

$$G = G^0 + RT \ln(c), \tag{1.12}$$

where the concentration, c, is in units of moles per liter. The standard free energy, G^0, is obtained by measuring the free energy for a dilute solution and then extrapolating to $c = 1$. For biochemical applications, the dependence of free energy on

pressure is ignored and the pressure is assumed to be 1 atm, while the temperature is taken to be 25° C. Derivations of these formulas can be found in physical chemistry textbooks such as Levine (1978) or Castellan (1971).

For non-ideal solutions, such as are typical in cells, the free energy formula (1.12) should use the chemical activity of the solute rather than its concentration. The relationship between chemical activity a and concentration is nontrivial. However, for dilute concentrations, they are approximately equal.

Since the free energy is a potential, it denotes the preference of one state compared to another. Consider, for example, the simple reaction

$$A \longrightarrow B. \tag{1.13}$$

The change in chemical potential ΔG is defined as the difference between the chemical potential for state B (the product), denoted G_B, and the chemical potential for state A (the reactant), denoted G_A,

$$\begin{aligned} \Delta G &= G_B - G_A \\ &= G_B^0 - G_A^0 + RT\ln([\text{B}]) - RT\ln([\text{A}]) \\ &= \Delta G^0 + RT\ln([\text{B}]/[\text{A}]). \end{aligned} \tag{1.14}$$

The sign of ΔG is important, which is why it is defined with only one reaction direction shown even though we know that the back reaction also occurs. In fact, there is a wonderful opportunity for confusion here, since there is no obvious way to decide which is the forward and which is the backward direction for a given reaction. If $\Delta G < 0$ then state B is preferred to state A and the reaction tends to convert A into B, whereas, if $\Delta G > 0$, then state A is preferred to state B and the reaction tends to convert B into A. Equilibrium occurs when neither state is preferred, so that $\Delta G = 0$ in which case

$$\frac{[\text{B}]_{\text{eq}}}{[\text{A}]_{\text{eq}}} = e^{\frac{-\Delta G^0}{RT}}. \tag{1.15}$$

Expressing this reaction in terms of forward and backward reaction rates,

$$A \underset{k_-}{\overset{k_+}{\rightleftarrows}} B, \tag{1.16}$$

we find that in steady state, $k_+[\text{A}]_{\text{eq}} = k_-[\text{B}]_{\text{eq}}$ so that

$$\frac{[\text{A}]_{\text{eq}}}{[\text{B}]_{\text{eq}}} = \frac{k_-}{k_+} = K_{\text{eq}}. \tag{1.17}$$

Combining this with (1.15), we observe that

$$K_{\text{eq}} = e^{\frac{\Delta G^0}{RT}}. \tag{1.18}$$

In other words, the more negative the difference in standard free energy, the greater the propensity for the reaction to proceed from left to right, and the smaller K_{eq}. Notice, however, that this gives only the ratio of rate constants, and not their

individual amplitudes. We learn nothing about whether a reaction is fast or slow from the standard free energy.

Similar relationships hold when there are multiple components in the reaction. Consider, for example, the more complex reaction

$$\alpha A + \beta B \longrightarrow \gamma C + \delta D. \tag{1.19}$$

The change of free energy for this reaction is defined as

$$\begin{aligned}
\Delta G &= \gamma G_C + \delta G_D - \alpha G_A - \beta G_B \\
&= \gamma G_C^0 + \delta G_D^0 - \alpha G_A^0 - \beta G_B^0 + RT \ln \left(\frac{[C]^\gamma [D]^\delta}{[A]^\alpha [B]^\beta} \right) \\
&= \Delta G^0 + RT \ln \left(\frac{[C]^\gamma [D]^\delta}{[A]^\alpha [B]^\beta} \right),
\end{aligned} \tag{1.20}$$

and at equilibrium,

$$\begin{aligned}
\Delta G^0 &= RT \ln \left(\frac{[A]_{eq}^\alpha [B]_{eq}^\beta}{[C]_{eq}^\gamma [D]_{eq}^\delta} \right) \\
&= RT \ln(K_{eq}).
\end{aligned} \tag{1.21}$$

An important example of such a reaction is the hydrolysis of ATP to ADP and inorganic phosphate P_i, represented by the reaction

$$\text{ATP} \longrightarrow \text{ADP} + P_i. \tag{1.22}$$

The standard free energy change for this reaction is

$$\Delta G^0 = G_{\text{ADP}}^0 + G_{P_i}^0 - G_{\text{ATP}}^0 = -31.0 \text{ kJ mol}^{-1}, \tag{1.23}$$

and from this we could calculate the equilibrium constant for this reaction. However, the primary significance of this is not the size of the equilibrium constant, but rather the fact that ATP has free energy that can be used to drive other less favorable reactions. For example, in all living cells ATP is used to pump ions against their concentration gradient, a process called free energy transduction. In fact, if the equilibrium constant of this reaction is achieved then one can confidently assert that the system is dead. In living systems, the ratio of [ATP] to [ADP][P_i] is held well above the equilibrium value.

1.3 Detailed Balance

Suppose that a set of reactions forms a loop, as shown in Fig. 1.1. By applying the law of mass action and setting the derivatives to zero we can find the steady-state concentrations of A, B and C. However, for the system to be in thermodynamic equilibrium a stronger condition must hold. Thermodynamic equilibrium requires that the free energy of each state be the same so that each individual reaction is in equilibrium. In other words, at equilibrium there is not only, say, no net change in
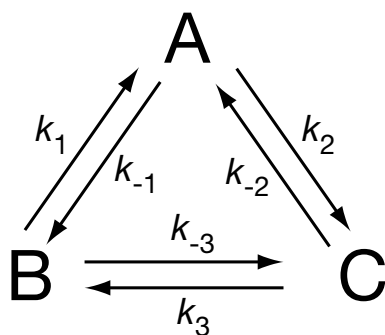
Figure 1.1: Schematic diagram of a reaction loop

[B], there is also no net conversion of B to C or B to A. This condition means that, at equilibrium, $k_1[B] = k_{-1}[A]$, $k_2[A] = k_{-2}[C]$ and $k_3[C] = k_{-3}[B]$. Thus, it must be that

$$k_1 k_2 k_3 = k_{-1} k_{-2} k_{-3}, \qquad (1.24)$$

or

$$K_1 K_2 K_3 = 1, \qquad (1.25)$$

where $K_i = k_{-i}/k_i$. Since this condition does not depend on the concentrations of A, B or C, it must hold in general, not only at equilibrium.

For a more general reaction loop, the principle of detailed balance requires that the product of rates in one direction around the loop must equal the product of rates in the other direction. If any of the rates are dependent on concentrations of other chemicals, those concentrations must also be included.

1.4   Enzyme Kinetics

To see where some of the more complicated reaction schemes come from, we consider a reaction that is catalyzed by an enzyme. Enzymes are catalysts (generally proteins) that help convert other molecules called *substrates* into products, but they themselves are not changed by the reaction. Their most important features are catalytic power, specificity, and regulation. Enzymes accelerate the conversion of substrate into product by lowering the free energy of activation of the reaction. For example, enzymes may aid in overcoming charge repulsions and allowing reacting molecules to come into contact for the formation of new chemical bonds. Or, if the reaction requires breaking of an existing bond, the enzyme may exert a stress on a substrate molecule, rendering a particular bond more easily broken. Enzymes are particularly efficient at speeding up biological reactions, giving increases in speed of up to 10 million times or more. They are also highly specific, usually catalyzing the reaction of only one particular substrate or closely related substrates. Finally, they are typically regulated by an enormously complicated set of positive and negative feedbacks, thus allowing precise control over the rate of reaction. A detailed

presentation of enzyme kinetics, including many different kinds of models, can be found in Dixon and Webb (1979) or the encyclopedic Segel (1975). Here, we present some of the simplest models.

One of the first things one learns about enzyme reactions is that they do not follow the law of mass action directly. For, as the concentration of substrate (S) is increased, the rate of the reaction increases only to a certain extent, reaching a maximal reaction velocity at high substrate concentrations. This is in contrast to the law of mass action, which, when applied directly to the reaction of S with the enzyme E

$$S + E \longrightarrow P + E$$

predicts that the reaction velocity increases linearly as [S] increases.

A model to explain the deviation from the law of mass action was first proposed by Michaelis and Menten (1913). In their reaction scheme, the enzyme E converts the substrate S into the product P through a two-step process. First E combines with S to form a complex C which then breaks down into the product P releasing E in the process. The reaction scheme is represented schematically by

$$S + E \underset{k_{-1}}{\overset{k_1}{\rightleftharpoons}} C \underset{k_{-2}}{\overset{k_2}{\rightleftharpoons}} P + E.$$
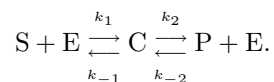
Although all reactions must be reversible, as shown here, reaction rates are typically measured under conditions where P is continually removed, which effectively prevents the reverse reaction from occurring. Thus, it often suffices to assume that no reverse reaction occurs. For this reason, the reaction is usually written as

$$S + E \underset{k_{-1}}{\overset{k_1}{\rightleftharpoons}} C \overset{k_2}{\longrightarrow} P + E.$$
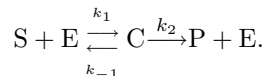
The reversible case is considered in Section 1.4.5.

There are two similar, but not identical, ways to analyze this equation; the equilibrium approximation, and the quasi-steady-state approximation. Because these methods give similar results it is easy to confuse them, so it is important to understand their differences.

We begin by defining $s = [S], c = [C], e = [E]$, and $p = [P]$. The law of mass action applied to this reaction mechanism gives four differential equations for the rates of change of s, c, e, and p,

$$\frac{ds}{dt} = k_{-1}c - k_1 se, \tag{1.26}$$

$$\frac{de}{dt} = (k_{-1} + k_2)c - k_1 se, \tag{1.27}$$

$$\frac{dc}{dt} = k_1 se - (k_2 + k_{-1})c, \tag{1.28}$$

$$\frac{dp}{dt} = k_2 c. \tag{1.29}$$

Note that p can be found by direct integration, and that there is a conserved quantity since $\frac{de}{dt} + \frac{dc}{dt} = 0$, so that $e + c = e_0$, where e_0 is the total amount of available enzyme.

1.4.1 The Equilibrium Approximation

In their original analysis, Michaelis and Menten assumed that the substrate is in instantaneous equilibrium with the complex, and thus

$$k_1 se = k_{-1} c. \tag{1.30}$$

Since $e + c = e_0$, we find that

$$c = \frac{e_0 s}{K_1 + s}, \tag{1.31}$$

where $K_1 = k_{-1}/k_1$. Hence, the velocity, V, of the reaction, i.e., the rate at which the product is formed, is given by

$$V = \frac{dp}{dt} = k_2 c = \frac{k_2 e_0 s}{K_1 + s} = \frac{V_{\max} s}{K_1 + s}, \tag{1.32}$$

where $V_{\max} = k_2 e_0$ is the maximum reaction velocity, attained when all the enzyme is complexed with the substrate.

At small substrate concentrations, the reaction rate is linear, at a rate proportional to the amount of available enzyme e_0. At large concentrations, however, the reaction rate saturates to $V_{\max}$, so that the maximum rate of the reaction is limited by the amount of enzyme present and the dissociation rate constant k_2. For this reason, the dissociation reaction $C \xrightarrow{k_2} P + E$ is said to be *rate limiting* for this reaction. At $s = K_1$, the reaction rate is half that of the maximum.

It is important to note that (1.30) cannot be exactly correct at all times; if it were, then according to (1.26) substrate would not be used up, and product would not be formed. This points out the fact that (1.30) is an approximation. It also illustrates the need for a systematic way to make approximate statements, so that one has an idea of the magnitude and nature of the errors introduced in making such an approximation.

It is a common mistake with the equilibrium approximation to conclude that since (1.30) holds, it must be that $\frac{ds}{dt} = 0$, which if this is true, implies that no substrate is being used up, nor product produced. Furthermore, it appears that if (1.30) holds, then it must be (from (1.28)) that $\frac{dc}{dt} = -k_2 c$, which is also false. Where is the error here?

The answer lies with the fact that the equilibrium approximation is equivalent to the assumption that the reaction (1.26) is a very fast reaction, faster than others, or more precisely, that $k_{-1} \gg k_2$. Adding (1.26) and (1.28), we find that

$$\frac{ds}{dt} + \frac{dc}{dt} = -k_2 c, \tag{1.33}$$

expressing the fact that the total quantity $s + c$ changes on a slower time scale. Now when we use that $c = \frac{e_0 s}{K_s + s}$, we learn that

$$\frac{d}{dt} \left(s + \frac{e_0 s}{K_1 + s} \right) = -k_2 \frac{e_0 s}{K_1 + s}, \tag{1.34}$$

and thus,

$$\frac{ds}{dt} \left(1 + \frac{e_0 K_1}{(K_1 + s)^2} \right) = -k_2 \frac{e_0 s}{K_1 + s}, \tag{1.35}$$

which specifies the rate at which s is consumed.

This way of simplifying reactions by using an equilibrium approximation is used many times throughout this book, and is an extremely important technique, particularly in the analysis of Markov models of ion channels, pumps and exchangers (Chapters 2 and 3). A more mathematically systematic description of this approach is left for Exercise 20.

1.4.2 The Quasi-Steady-State Approximation

An alternative analysis of an enzymatic reaction was proposed by Briggs and Haldane (1925) who assumed that the rates of formation and breakdown of the complex were essentially equal at all times (except perhaps at the beginning of the reaction, as the complex is "filling up"). Thus, dc/dt should be approximately zero.

To give this approximation a systematic mathematical basis, it is useful to introduce dimensionless variables

$$\sigma = \frac{s}{s_0}, \quad x = \frac{c}{e_0}, \quad \tau = k_1 e_0 t, \quad \kappa = \frac{k_{-1} + k_2}{k_1 s_0}, \quad \epsilon = \frac{e_0}{s_0}, \quad \alpha = \frac{k_{-1}}{k_1 s_0}, \quad (1.36)$$

in terms of which we obtain the system of two differential equations

$$\frac{d\sigma}{d\tau} = -\sigma + x(\sigma + \alpha), \tag{1.37}$$

$$\epsilon \frac{dx}{d\tau} = \sigma - x(\sigma + \kappa). \tag{1.38}$$

There are usually a number of ways that a system of differential equations can be nondimensionalized. This nonuniqueness is often a source of great confusion, as it is often not obvious which choice of dimensionless variables and parameters is "best." In Section 1.6 we discuss this difficult problem briefly.

The remarkable effectiveness of enzymes as catalysts of biochemical reactions is reflected by their small concentrations needed compared to the concentrations of the substrates. For this model, this means that ϵ is small, typically in the range of 10^{-2} to 10^{-7}. Therefore, the reaction (1.38) is fast, equilibrates rapidly and remains in near-equilibrium even as the variable σ changes. Thus, we take the *quasi-steady-state approximation* $\epsilon \frac{dx}{d\tau} = 0$. Notice that this is *not* the same as taking $\frac{dx}{d\tau} = 0$. However, because of the different scaling of x and c, it is equivalent to taking $\frac{dc}{dt} = 0$ as suggested in the introductory paragraph.

One useful way of looking at this system is as follows; since

$$\frac{dx}{d\tau} = \frac{\sigma - x(\sigma + \kappa)}{\epsilon}, \tag{1.39}$$

$dx/d\tau$ is large everywhere, except where $\sigma - x(\sigma + \kappa)$ is small, of approximately the same size as ϵ. Now, note that $\sigma - x(\sigma + \kappa) = 0$ defines a curve in the σ, x phase plane, called the *slow manifold* (as illustrated in the right panel of Fig. 1.14). If the solution starts away from the slow manifold, $dx/d\tau$ is initially large, and the solution moves rapidly to the vicinity of the slow manifold. The solution then moves along the slow manifold in the direction defined by the equation for σ; in this case, σ is decreasing, and so the solution moves to the left along the slow manifold.

Another way of looking at this model is to notice that the reaction of x is an exponential process with time constant at least as large as $\frac{\kappa}{\epsilon}$. To see this we write (1.38) as

$$\epsilon \frac{dx}{d\tau} + \kappa x = \sigma(1 - x). \tag{1.40}$$

Thus, the variable x "tracks" the steady state with a short delay.

It follows from the quasi-steady-state approximation that

$$x = \frac{\sigma}{\sigma + \kappa}, \tag{1.41}$$

$$\frac{d\sigma}{d\tau} = -\frac{q\sigma}{\sigma + \kappa}, \tag{1.42}$$

where $q = \kappa - \alpha = \frac{k_2}{k_1 s_0}$. Equation (1.42) describes the rate of uptake of the substrate and is called a *Michaelis–Menten law*. In terms of the original variables, this law is

$$V = \frac{dp}{dt} = -\frac{ds}{dt} = \frac{k_2 e_0 s}{s + K_m} = \frac{V_{\max} s}{s + K_m}, \tag{1.43}$$

where $K_m = \frac{k_{-1} + k_2}{k_1}$. In quasi-steady state, the concentration of the complex satisfies

$$c = \frac{e_0 s}{s + K_m}. \tag{1.44}$$

Note the similarity between (1.32) and (1.43), the only difference being that the equilibrium approximation uses K_1, while the quasi-steady-state approximation uses K_m. Despite this similarity of form, it is important to keep in mind that the two results are based on different approximations. The equilibrium approximation assumes that $k_{-1} \gg k_2$ whereas the quasi-steady state approximation assumes that $\epsilon \ll 1$. Notice, that if $k_{-1} \gg k_2$, then $K_m \approx K_1$, so that the two approximations give similar results.

As with the law of mass action, the Michaelis–Menten law (1.43) is not universally applicable but is a useful approximation. It may be applicable even if $\epsilon = e_0/s_0$ is not small (see, for example, Exercise 14), and in model building it is often invoked without regard to the underlying assumptions.

While the individual rate constants are difficult to measure experimentally, the ratio K_m is relatively easy to measure because of the simple observation that (1.43) can be written in the form

$$\frac{1}{V} = \frac{1}{V_{\max}} + \frac{K_m}{V_{\max}} \frac{1}{s}. \tag{1.45}$$

In other words, $1/V$ is a linear function of $1/s$. Plots of this double reciprocal curve are called *Lineweaver–Burk plots*, and from such (experimentally determined) plots, $V_{\max}$ and K_m can be estimated.

Although a Lineweaver–Burk plot makes it easy to determine $V_{\max}$ and K_m from reaction rate measurements, it is not a simple matter to determine the reaction rate as a function of substrate concentration during the course of a single experiment. Substrate concentrations usually cannot be measured with sufficient accuracy or time resolution to permit the calculation of a reliable derivative. In practice, since

it is more easily measured, the initial reaction rate is determined for a range of different initial substrate concentrations.

An alternative method to determine K_m and $V_{\max}$ from experimental data is the direct linear plot (Eisenthal and Cornish-Bowden, 1974; Cornish-Bowden and Eisenthal, 1974). First we write (1.43) in the form

$$V_{\max} = V + \frac{V}{s}K_m, \tag{1.46}$$

and then treat $V_{\max}$ and K_m as variables for each experimental measurement of V and s. (Recall that typically only the initial substrate concentration and initial velocity are used.) Then a plot of the straight line of $V_{\max}$ against K_m can be made. Repeating this for a number of different initial substrate concentrations and velocities gives a family of straight lines, which, in an ideal world free from experimental error, intersect at the single point $V_{\max}$ and K_m for that reaction. In reality, experimental error precludes an exact intersection, but $V_{\max}$ and K_m can be estimated from the median of the pairwise intersections.

1.4.3 Enzyme Inhibition

An enzyme inhibitor is a substance that inhibits the catalytic action of the enzyme. Enzyme inhibition is a common feature of enzyme reactions, and is an important means by which the activity of enzymes is controlled. Inhibitors come in many different types. For example, *irreversible inhibitors*, or *catalytic poisons*, decrease the activity of the enzyme to zero. This is the method of action of cyanide and many nerve gases. For this discussion, we restrict our attention to *competitive* inhibitors and *allosteric* inhibitors.

To understand the distinction between competitive and allosteric inhibition, it is useful to keep in mind that an enzyme molecule is usually a large protein, considerably larger than the substrate molecule whose reaction is catalyzed. Embedded in the large enzyme protein are one or more *active sites*, to which the substrate can bind to form the complex. In general, an enzyme catalyzes a single reaction of substrates with similar structures. This is believed to be a steric property of the enzyme that results from the three-dimensional shape of the enzyme allowing it to fit in a "lock-and-key" fashion with a corresponding substrate molecule.
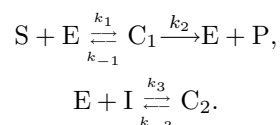
If another molecule has a shape similar enough to that of the substrate molecule, it may also bind to the active site, preventing the binding of a substrate molecule, thus inhibiting the reaction. Because the inhibitor competes with the substrate molecule for the active site, it is called a competitive inhibitor.

However, because the enzyme molecule is large, it often has other binding sites, distinct from the active site, the binding of which affects the activity of the enzyme at the active site. These binding sites are called *allosteric* sites (from the Greek for "another solid") to emphasize that they are structurally different from the catalytic active sites. They are also called *regulatory sites* to emphasize that the catalytic activity of the protein is regulated by binding at this allosteric site. The ligand (any molecule that binds to a specific site on a protein, from Latin *ligare*, to bind) that binds at the allosteric site is called an *effector* or *modifier*, which, if it increases the activity of the enzyme, is called an allosteric activator, while if it decreases

the activity of the enzyme, is called an allosteric inhibitor. The allosteric effect is presumed to arise because of a conformational change of the enzyme, that is, a change in the folding of the polypeptide chain, called an *allosteric transition.*

Competitive Inhibition

In the simplest example of a competitive inhibitor, the reaction is stopped when the inhibitor is bound to the active site of the enzyme. Thus,

$$S + E \underset{k_{-1}}{\overset{k_1}{\rightleftharpoons}} C_1 \overset{k_2}{\longrightarrow} E + P,$$

$$E + I \underset{k_{-3}}{\overset{k_3}{\rightleftharpoons}} C_2.$$

Using the law of mass action we find

$$\frac{ds}{dt} = -k_1 se + k_{-1}c_1, \tag{1.47}$$

$$\frac{di}{dt} = -k_3 ie + k_{-3}c_2, \tag{1.48}$$

$$\frac{dc_1}{dt} = k_1 se - (k_{-1} + k_2)c_1, \tag{1.49}$$

$$\frac{dc_2}{dt} = k_3 ie - k_{-3}c_2. \tag{1.50}$$

where $s = [S]$, $c_1 = [C_1]$, and $c_2 = [C_2]$. We know that $e + c_1 + c_2 = e_0$, so an equation for the dynamics of e is superfluous. As before, it is not necessary to write an equation for the accumulation of the product. To be systematic, the next step is to introduce dimensionless variables, and identify those reactions that are rapid and equilibrate rapidly to their quasi-steady states. However, from our previous experience (or from a calculation on a piece of scratch paper), we know, assuming the enzyme-to-substrate ratios are small, that the fast equations are those for c_1 and c_2. Hence, the quasi-steady states are found by (formally) setting $dc_1/dt = dc_2/dt = 0$ and solving for c_1 and c_2. Recall that this does *not* mean that c_1 and c_2 are unchanging, rather that they are changing in quasi-steady-state fashion, keeping the right-hand sides of these equations nearly zero. This gives

$$c_1 = \frac{K_i e_0 s}{K_m i + K_i s + K_m K_i}, \tag{1.51}$$

$$c_2 = \frac{K_m e_0 i}{K_m i + K_i s + K_m K_i}, \tag{1.52}$$

where $K_m = \frac{k_{-1} + k_2}{k_1}$, $K_i = k_{-3}/k_3$. Thus, the velocity of the reaction is

$$V = k_2 c_1 = \frac{k_2 e_0 s K_i}{K_m i + K_i s + K_m K_i} = \frac{V_{\max} s}{s + K_m(1 + i/K_i)}. \tag{1.53}$$

Notice that the effect of the inhibitor is to increase the effective equilibrium constant of the enzyme by the factor $1 + i/K_i$, from K_m to $K_m(1 + i/K_i)$, thus decreasing the velocity of reaction, while leaving the maximum velocity unchanged.
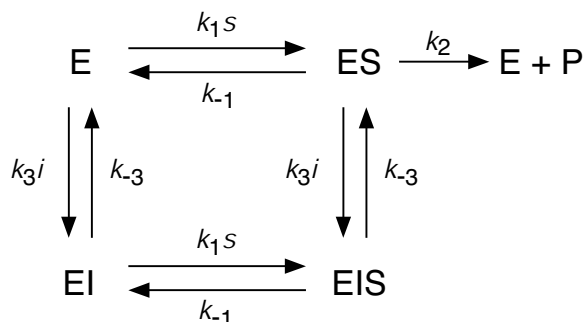
Figure 1.2: Diagram of the possible states of an enzyme with one allosteric and one catalytic binding site.

Allosteric Inhibitors

If the inhibitor can bind at an allosteric site, we have the possibility that the enzyme could bind both the inhibitor and the substrate simultaneously. In this case, there are four possible binding states for the enzyme, and transitions between them, as demonstrated graphically in Fig. 1.2.

The simplest analysis of this reaction scheme is the equilibrium analysis. (The more complicated quasi-steady-state analysis is left for Exercise 6.) We define $K_s = k_{-1}/k_1$, $K_i = k_{-3}/k_3$, and let x, y, and z denote, respectively, the concentrations of ES, EI and EIS. Then, it follows from the law of mass action that at equilibrium (take each of the 4 transitions to be at equilibrium),

$$
\begin{align}
(e_0 - x - y - z)s - K_s x &= 0, \tag{1.54}\\
(e_0 - x - y - z)i - K_i y &= 0, \tag{1.55}\\
ys - K_s z &= 0, \tag{1.56}\\
xi - K_i z &= 0, \tag{1.57}
\end{align}
$$

where $e_0 = e + x + y + z$ is the total amount of enzyme. Notice that this is a linear system of equations for x, y, and z. Although there are four equations, one is a linear combination of the other three (the system is of rank three), so that we can determine x, y, and z as functions of i and s, finding

$$
x = \frac{e_0 K_i}{K_i + i} \frac{s}{K_s + s}. \tag{1.58}
$$

It follows that the reaction rate, $V = k_2 x$, is given by

$$
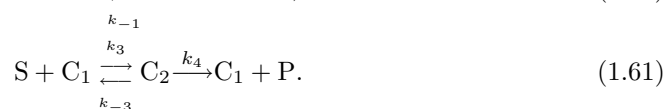V = \frac{V_{\max}}{1 + i/K_i} \frac{s}{K_s + s}, \tag{1.59}
$$

where $V_{\max} = k_2 e_0$. Thus, in contrast to the competitive inhibitor, the allosteric inhibitor decreases the maximum velocity of the reaction, while leaving K_s unchanged. (The situation is more complicated if the quasi-steady-state approximation is used, and no such simple conclusion follows.)

1.4.4 Cooperativity

For many enzymes, the reaction velocity is not a simple hyperbolic curve, as predicted by the Michaelis–Menten model, but often has a sigmoidal character. This can result from cooperative effects, in which the enzyme can bind more than one substrate molecule but the binding of one substrate molecule affects the binding of subsequent ones.

Much of the original theoretical work on cooperative behavior was stimulated by the properties of hemoglobin, and this is often the context in which cooperativity is discussed. A detailed discussion of hemoglobin and oxygen binding is given in Chapter 13, while here cooperativity is discussed in more general terms.

Suppose that an enzyme can bind two substrate molecules, so it can exist in one of three states, namely as a free molecule E, as a complex with one occupied binding site, C_1, and as a complex with two occupied binding sites, C_2. The reaction mechanism is then

$$S + E \underset{k_{-1}}{\overset{k_1}{\rightleftharpoons}} C_1 \overset{k_2}{\longrightarrow} E + P, \qquad (1.60)$$

$$S + C_1 \underset{k_{-3}}{\overset{k_3}{\rightleftharpoons}} C_2 \overset{k_4}{\longrightarrow} C_1 + P. \qquad (1.61)$$

Using the law of mass action, one can write the rate equations for the 5 concentrations $[S], [E], [C_1], [C_2]$, and $[P]$. However, because the amount of product $[P]$ can be determined by quadrature, and because the total amount of enzyme molecule is conserved, we only need three equations for the three quantities $[S], [C_1]$, and $[C_2]$. These are

$$\frac{ds}{dt} = -k_1 se + k_{-1} c_1 - k_3 sc_1 + k_{-3} c_2, \qquad (1.62)$$

$$\frac{dc_1}{dt} = k_1 se - (k_{-1} + k_2) c_1 - k_3 sc_1 + (k_4 + k_{-3}) c_2, \qquad (1.63)$$

$$\frac{dc_2}{dt} = k_3 sc_1 - (k_4 + k_{-3}) c_2, \qquad (1.64)$$

where $s = [S], c_1 = [C_1], c_2 = [C_2]$, and $e + c_1 + c_2 = e_0$.

Proceeding as before, we invoke the quasi-steady-state assumption that $dc_1/dt = dc_2/dt = 0$, and solve for c_1 and c_2 to get

$$c_1 = \frac{K_2 e_0 s}{K_1 K_2 + K_2 s + s^2}, \qquad (1.65)$$

$$c_2 = \frac{e_0 s^2}{K_1 K_2 + K_2 s + s^2}, \qquad (1.66)$$

where $K_1 = \frac{k_{-1} + k_2}{k_1}$ and $K_2 = \frac{k_4 + k_{-3}}{k_3}$. The reaction velocity is thus given by

$$V = k_2 c_1 + k_4 c_2 = \frac{(k_2 K_2 + k_4 s) e_0 s}{K_1 K_2 + K_2 s + s^2}. \qquad (1.67)$$

Use of the equlibrium approximation to simplify this reaction scheme gives, as expected, similar results, in which the formula looks the same, but with different definitions of K_1 and K_2 (Exercise 10).

It is instructive to examine two extreme cases. First, if the binding sites act independently and identically, then $k_1 = 2k_3 = 2k_+$, $2k_{-1} = k_{-3} = 2k_-$ and $2k_2 = k_4$, where k_+ and k_- are the forward and backward reaction rates for the individual binding sites. The factors of 2 occur because two identical binding sites are involved in the reaction, doubling the amount of the reactant. In this case,

$$V = \frac{2k_2 e_0 (K + s)s}{K^2 + 2Ks + s^2} = 2\frac{k_2 e_0 s}{K + s}, \tag{1.68}$$

where $K = \frac{k_- + k_2}{k_+}$ is the K_m of the individual binding site. As expected, the rate of reaction is exactly twice that for the individual binding site.

In the opposite extreme, suppose that the binding of the first substrate molecule is slow, but that with one site bound, binding of the second is fast (this is large positive cooperativity). This can be modeled by letting $k_3 \to \infty$ and $k_1 \to 0$, while keeping $k_1 k_3$ constant, in which case $K_2 \to 0$ and $K_1 \to \infty$ while $K_1 K_2$ is constant. In this limit, the velocity of the reaction is

$$V = \frac{k_4 e_0 s^2}{K_m^2 + s^2} = \frac{V_{\max} s^2}{K_m^2 + s^2}, \tag{1.69}$$

where $K_m^2 = K_1 K_2$, and $V_{\max} = k_4 e_0$.

In general, if n substrate molecules can bind to the enzyme, there are n equilibrium constants, K_1 through K_n. In the limit as $K_n \to 0$ and $K_1 \to \infty$ while keeping $K_1 K_n$ fixed, the rate of reaction is

$$V = \frac{V_{\max} s^n}{K_m^n + s^n}, \tag{1.70}$$

where $K_m^n = \Pi_{i=1}^n K_i$. This rate equation is known as the *Hill equation*. Typically, the Hill equation is used for reactions whose detailed intermediate steps are not known but for which cooperative behavior is suspected. The exponent n and the parameters $V_{\max}$ and K_m are usually determined from experimental data. Observe that

$$n \ln s = n \ln K_m + \ln \left(\frac{V}{V_{\max} - V} \right), \tag{1.71}$$

so that a plot of $\ln(\frac{V}{V_{\max} - V})$ against $\ln s$ (called a *Hill plot*) should be a straight line of slope n. Although the exponent n suggests an n-step process (with n binding sites), in practice it is not unusual for the best fit for n to be noninteger.

An enzyme can also exhibit negative cooperativity (Koshland and Hamadani, 2002), in which the binding of the first substrate molecule *decreases* the rate of subsequent binding. This can be modeled by decreasing k_3. In Fig. 1.3 we plot the reaction velocity against the substrate concentration for the cases of independent binding sites (no cooperativity), extreme positive cooperativity (the Hill equation), and negative cooperativity. From this figure it can be seen that with positive cooperativity, the reaction velocity is a sigmoidal function of the substrate concentration, while negative cooperativity primarily decreases the overall reaction velocity.
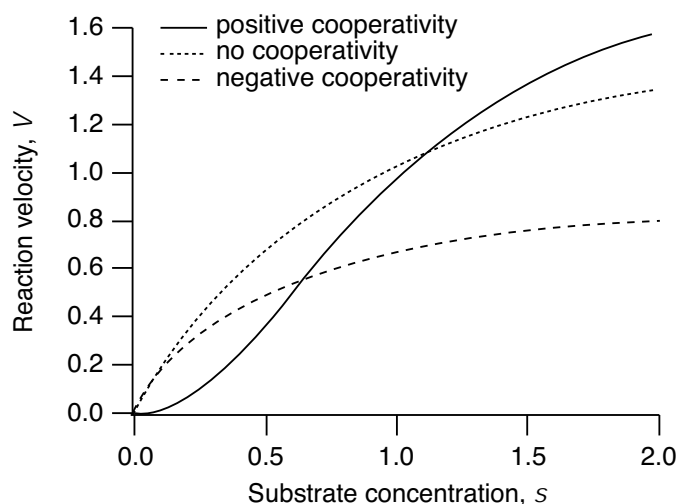
Figure 1.3: Reaction velocity plotted against substrate concentration, for three different cases. Positive cooperativity, $K_1 = 1000$, $K_2 = 0.001$; independent binding sites, $K_1 = 0.5$, $K_2 = 2$; and negative cooperativity, $K_1 = 0.5$, $K_2 = 100$. The other parameters were chosen as $e_0 = 1$, $k_2 = 1$, $k_4 = 2$. Concentration and time units are arbitrary.

The Monod–Wyman–Changeux Model

Cooperative effects occur when the binding of one substrate molecule alters the rate of binding of subsequent ones. However, the above models give no explanation of how such alterations in the binding rate occur. The earliest model proposed to account for cooperative effects in terms of the enzyme's conformation was that of Monod, Wyman, and Changeux (1965). Their model is based on the following assumptions about the structure and behavior of enzymes.

1. Cooperative proteins are composed of several identical reacting units, called *protomers*, or subunits, each containing one binding site, that occupy equivalent positions within the protein.

2. The protein has two conformational states, usually denoted by R and T, which differ in their ability to bind ligands.

3. If the binding of a ligand to one protomer induces a conformational change in that protomer, an identical conformational change is induced in all protomers. Because of this assumption, Monod-Wyman-Changeux (MWC) models are often called *concerted* models, as each subunit acts in concert with the others.

To illustrate how these assumptions can be quantified, we consider a protein with only two binding sites. Thus, the protein can exist in one of six states: $R_i, i = 0, 1, 2$, or $T_i, i = 0, 1, 2$, where the subscript i is the number of bound ligands. (In the
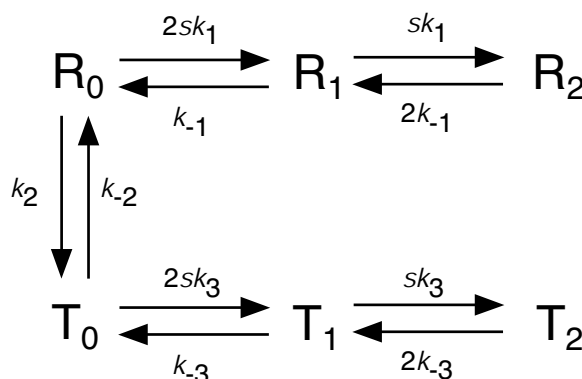
Figure 1.4: Diagram of the states of the protein, and the possible transitions, in a six-state Monod–Wyman–Changeux model.

original model of Monod, Wyman and Changeux, R denoted a *relaxed* state, while T denoted a *tense* state.) For simplicity, we also assume that R_1 cannot convert directly to T_1, or vice versa, and similarly for R_2 and T_2. The general case is left for Exercise 7. The states of the protein and the allowable transitions are illustrated in Fig. 1.4. As with other enzyme models, we assume that the production rate of product is proportional to the amount of substrate that is bound to the enzyme.

We now assume that all the reactions are in equilibrium. We let a lowercase letter denote a concentration, and thus r_i and t_i denote the concentrations of chemical species R_i and T_i respectively. Also, as before, we let s denote the concentration of the substrate. Then, the fraction Y of occupied sites (also called the *saturation function*) is

$$Y = \frac{r_1 + 2r_2 + t_1 + 2t_2}{2(r_0 + r_1 + r_2 + t_0 + t_1 + t_2)}. \tag{1.72}$$

(This is also proportional to the production rate of product.) Furthermore, with $K_i = k_{-i}/k_i$, for $i = 1, 2, 3$, we find that

$$r_1 = 2sK_1^{-1}r_0, \qquad r_2 = s^2K_1^{-2}r_0, \tag{1.73}$$
$$t_1 = 2sK_3^{-1}t_0, \qquad t_2 = s^2K_3^{-2}t_0. \tag{1.74}$$

Substituting these into (1.72) gives

$$Y = \frac{sK_1^{-1}(1 + sK_1^{-1}) + K_2^{-1}[sK_3^{-1}(1 + sK_3^{-1})]}{(1 + sK_1^{-1})^2 + K_2^{-1}(1 + sK_3^{-1})^2}, \tag{1.75}$$

where we have used that $r_0/t_0 = K_2$. More generally, if there are n binding sites, then

$$Y = \frac{sK_1^{-1}(1 + sK_1^{-1})^{n-1} + K_2^{-1}[sK_3^{-1}(1 + sK_3^{-1})^{n-1}]}{(1 + sK_1^{-1})^n + K_2^{-1}(1 + sK_3^{-1})^n}. \tag{1.76}$$

In general, Y is a sigmoidal function of s.

It is not immediately apparent how cooperative binding kinetics arises from this model. After all, each binding site in the R conformation is identical, as is each binding site in the T conformation. In order to get cooperativity it is necessary that the binding affinity of the R conformation be different from that of the T conformation. In the special case that the binding affinities of the R and T conformations are equal (i.e., $K_1 = K_3 = K$, say) the binding curve (1.76) reduces to

$$Y = \frac{s}{K + s},\qquad\qquad(1.77)$$

which is simply non-cooperative Michaelis-Menten kinetics.

Suppose that one conformation, T say, binds the substrate with a higher affinity than does R. Then, when the substrate concentration increases, T_0 is pushed through to T_1 faster than R_0 is pushed to R_1, resulting in an increase in the amount of substrate bound to the T state, and thus increased overall binding of substrate. Hence the cooperative behavior of the model.

If $K_2 = \infty$, so that only one conformation exists, then once again the saturation curve reduces to the Michaelis-Menten equation, $Y = s/(s + K_1)$. Hence each conformation, by itself, has non-cooperative Michaelis-Menten binding kinetics. It is only when the overall substrate binding can be biased to one conformation or the other that cooperativity appears.

Interestingly, MWC models cannot exhibit negative cooperativity. No matter whether $K_1 > K_3$ or *vice versa*, the binding curve always exhibits positive cooperativity.

**The Koshland-Nemethy-Filmer model**

One alternative to the MWC model is that proposed by Koshland, Nemethy and Filmer in 1966 (the KNF model). Instead of requiring that all subunit transitions occur in concert, as in the MWC model, the KNF model assumes that substrate binding to one subunit causes a conformational change in that subunit only, and that this conformational change causes a change in the binding affinity of the neighboring subunits. Thus, in the KNF model, each subunit can be in a different conformational state, and transitions from one state to the other occur sequentially as more substrate is bound. For this reason KNF models are often called *sequential* models. The increased generality of the KNF model allows for the possibility of negative cooperativity, as the binding to one subunit can *decrease* the binding affinity of its neighbors.

When binding shows positive cooperativity, it has proven difficult to distinguish between the MWC and KNF models on the basis of experimental data. In one of the most intensely studied cooperative mechanisms, that of oxygen binding to hemoglobin, there is experimental evidence for both models, and the actual mechanism is probably a combination of both.

There are many other models of enzyme cooperativity, and the interested reader is referred to Dixon and Webb (1979) for a comprehensive discussion and comparison of other models in the literature.

1.4.5 Reversible Enzyme Reactions

Since all enzyme reactions are reversible, a general understanding of enzyme kinetics must take this reversibility into account. In this case, the reaction scheme is

$$S + E \underset{k_{-1}}{\overset{k_1}{\rightleftarrows}} C \underset{k_{-2}}{\overset{k_2}{\rightleftarrows}} P + E.$$
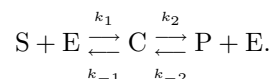
Proceeding as usual, we let $e + c = e_0$ and make the quasi-steady state assumption

$$0 = \frac{dc}{dt} = k_1 s(e_0 - c) - (k_{-1} + k_2)c + k_{-2}p(e_0 - c), \tag{1.78}$$

from which it follows that

$$c = \frac{e_0(k_1 s + k_{-2}p)}{k_1 s + k_{-2}p + k_{-1} + k_2}. \tag{1.79}$$

The reaction velocity, $V = \frac{dP}{dt} = k_2 c - k_{-2}pe$, can then be calculated to be

$$V = e_0 \cdot \frac{k_1 k_2 s - k_{-1}k_{-2}p}{k_1 s + k_{-2}p + k_{-1} + k_2}. \tag{1.80}$$

When p is small (e.g., if product is continually removed), the reverse reaction is negligible and we get the previous answer (1.43).

Unlike the irreversible case, the equilibrium and quasi-steady-state assumptions for reversible enzyme kinetics give qualitatively different answers. If we assume that S, E and C are in fast equilibrium (instead of assuming that C is at quasi-steady state) we get

$$k_1 s(e_0 - c) = k_{-1}c, \tag{1.81}$$

from which it follows that

$$V = k_2 c - k_{-2}p(e_0 - c) = e_0 \frac{k_1 k_2 s - k_{-1}k_{-2}p}{k_1 s + k_{-1}}. \tag{1.82}$$
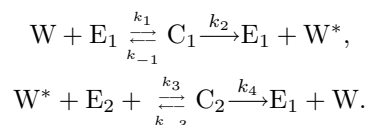
Comparing this to (1.80) we see that the quasi-steady-state assumption gives additional terms in the denominator involving the product, p. These differences result from the assumption underlying the fast equilibrium assumption, that k_{-1} and k_1 are both substantially larger than k_{-2} and k_2, respectively. Which of these approximations is best depends, of course, on the details of the reaction.

Calculation of the equations for a reversible enzyme reaction in which the enzyme has multiple binding sites is left for the exercises (Exercise 11).

1.4.6 The Goldbeter-Koshland function

As is seen in many ways in this book, cooperativity is an important ingredient in the construction of biochemical switches. However, highly sensitive switching behavior requires large Hill coefficients, which would seem to require multiple interacting enzymes or binding sites, making these unlikely to occur. An alternate mechanism by which highly sensitive switching behavior is possible was suggested

by Goldbeter and Koshland (1981), and uses only two enzymatic transitions. In this model reaction, a substrate can be in one of two forms, say W and W^*, and transferred from state W to W^* by one enzyme, say E_1, and transferred from state W^* to W by another enzyme, say E_2. For example, W^* could be a phosphorylated state of some enzyme, E_1 could be the kinase that phosphorylates W, and E_2 could be the phosphatase that dephosphorylates W^*. Numerous reactions of this type are described in Chapter 10, where W is itself an enzyme whose activity is determined by its phosphorylation state. Thus, the reaction scheme is

$$W + E_1 \underset{k_{-1}}{\overset{k_1}{\rightleftharpoons}} C_1 \overset{k_2}{\longrightarrow} E_1 + W^*,$$

$$W^* + E_2 + \underset{k_{-3}}{\overset{k_3}{\rightleftharpoons}} C_2 \overset{k_4}{\longrightarrow} E_1 + W.$$

The full analysis of this reaction scheme is not particularly difficult, however, a simplified analysis quickly shows the salient features. If we suppose that the enzyme reactions take place at Michaelis-Menten rates, the reaction simplifies to

$$W \underset{r_{-1}}{\overset{r_1}{\rightleftharpoons}} W^*, \tag{1.83}$$

where

$$r_1 = \frac{V_1 E_1}{K_1 + W}, \qquad r_{-1} = \frac{V_2 E_2}{K_2 + W^*}, \tag{1.84}$$

and the concentration of W is governed by the differential equation

$$\frac{dW}{dt} = r_{-1}(W_t - W) - r_1 W, \tag{1.85}$$

where $W + W^* = W_t$. In steady state, the forward and backward reaction rates are the same, leading to the equation

$$\frac{V_1 E_1}{V_2 E_2} = \frac{W^*(K_1 + W)}{W(K_2 + W^*)}. \tag{1.86}$$

After rescaling, one finds

$$\frac{v_1}{v2} = \frac{(1 - y)(\hat{K}_1 + y)}{y(\hat{K}_2 + 1 - y)}. \tag{1.87}$$

where $y = \frac{W}{W_t}$. Plots of y as a function of the ratio $\frac{v_1}{v_2}$ are easy to draw. One simply plots $\frac{v_1}{v_2}$ as a function of y and then reverses the axes. Examples of these are shown in Fig. 1.5. As is seen in this figure, the ratio $\frac{v_1}{v_2}$ controls the relative abundance of w in a switch-like fashion. In particular, the switch becomes quite sharp when the equilibrium constants $\hat{K}_1$ and $\hat{K}_2$ are small compared to 1. In other words, if the enzyme reactions are running at highly saturated levels, then there is very sensitive switch-like dependence on the enzyme velocity ratio $\frac{v_1}{v_2}$.

The equation (1.87) can be viewed as a quadratic polynomial in y, and therefore its explicit solution can easily be determined to be

$$y = \frac{\beta - \sqrt{\beta^2 - 4\alpha\gamma}}{2\alpha} \tag{1.88}$$

Figure 1.5: Plots of y as a function of the ratio $\frac{v_1}{v_2}$. **James, It should take you no more than 5 minutes to make this plot.**

where

$$\alpha = \frac{v_1}{v_2} - 1 \tag{1.89}$$

$$\beta = (1 - \hat{K}_1) - \frac{v_1}{v_2}(\hat{K}_2 + 1) \tag{1.90}$$

$$\gamma = \hat{K}_1. \tag{1.91}$$

The function

$$G(v_1, v_2, \hat{K}_1, \hat{K}_2) = \frac{\beta - \sqrt{\beta^2 - 4\alpha\gamma}}{2\alpha} \tag{1.92}$$

is called the *Goldbeter-Koshland function*. Because it represents the relative amount of the enzyme W, this function can be used much as is a Hill function to quantify the velocity of an enzymatic reaction. The Goldbeter-Koshland function is often used in descriptions of biochemical networks, as is described in Chapter 10.

1.5 Glycolysis and Glycolytic Oscillations

Metabolism is the process of extracting useful energy from chemical bonds. A metabolic pathway is the sequence of enzymatic reactions that take place in order to transfer chemical energy from one form to another. The common carrier of energy in the cell is the chemical *adenosine triphosphate* (ATP). ATP is formed by the addition of an inorganic phosphate group (HPO_4^{2-}) to *adenosine diphosphate* (ADP), or by the addition of two inorganic phosphate groups to *adenosine monophosphate* (AMP). The process of adding an inorganic phosphate group to a molecule is called *phosphorylation*. Since the three phosphate groups on ATP carry negative charges, considerable energy is required to overcome the natural repulsion of like-charged phosphates as additional groups are added to AMP. Thus, the hydrolysis (the cleavage of a bond by water) of ATP to ADP releases large amounts of energy.

Energy to perform chemical work is made available to the cell by the oxidation of glucose to carbon dioxide and water, with a net release of energy. The overall chemical reaction for the oxidation of glucose can be written as

$$C_6H_{12}O_6 + 6O_2 \longrightarrow 6CO_2 + 6H_2O + \text{energy}, \tag{1.93}$$
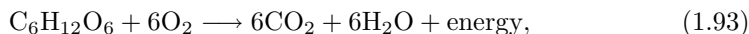
but of course, this is not an elementary reaction. Instead, this reaction takes place in a series of enzymatic reactions, with three major reaction stages, *glycolysis*, the *Krebs cycle*, and the *electron transport* (or *cytochrome) system*.

The oxidation of glucose is associated with a large negative free energy, $\Delta G^0 = -2878.41$ kJ/mol, some of which is dissipated as heat. However, in living cells much of this free energy in stored in ATP, with one molecule of glucose resulting in 38 molecules of ATP.
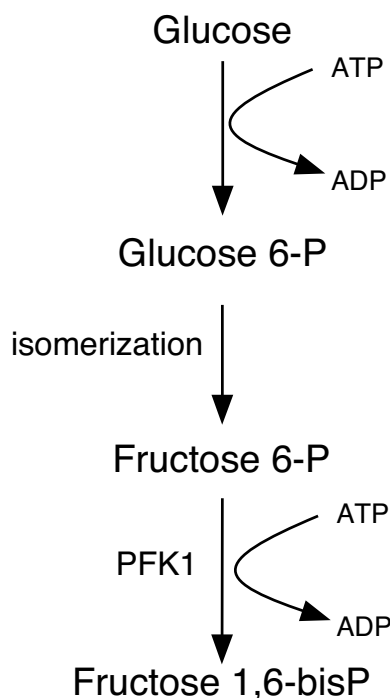
Figure 1.6: The first three reactions in the glycolytic pathway.

Glycolysis involves 11 elementary reaction steps, each of which is an enzymatic reaction. Here we consider a simplified model of the initial steps. (To understand more of the labyrinthine complexity of glycolysis, interested readers are encouraged to consult a specialized book on biochemistry, such as Stryer, 1988.) The first three steps of glycolysis are (Fig. 1.6)

1. the phosphorylation of glucose to glucose 6-phosphate;

2. the isomerization of glucose 6-phosphate to fructose 6-phosphate; and

3. the phosphorylation of fructose 6-phosphate to fructose 1,6-bisphosphate.

The direct reaction of glucose with phosphate to form glucose 6-phosphate has a relatively large positive standard free energy change ($\Delta G^0 = 14.3$ kJ/mol) and so does not occur significantly under physiological conditions. However, the first step of metabolism is coupled with the hydrolysis of ATP to ADP (catalyzed by the enzyme hexokinase), giving this step a net negative standard free energy change and making the reaction strongly spontaneous. This feature turns out to be important for the efficient operation of glucose membrane transporters, which we discuss in the next chapter.

The second step of glycolysis has a relatively small positive standard free energy change ($\Delta G^0 = 1.7$ kJ/mol), with an equilibrium constant of 0.5. This means that

significant amounts of product are formed under normal conditions.

The third step is, like the first step, energetically unfavorable, were it not coupled with the hydrolysis of ATP. However, the net standard free energy change ($\Delta G^0 = -14.2$ kJ/mol) means that not only is this reaction strongly favored, but also that it augments the reaction in the second step by depleting the product of the second step.

This third reaction is catalyzed by the enzyme phosphofructokinase (PFK1). PFK1 is an example of an allosteric enzyme as it is allosterically inhibited by ATP. Note that ATP is both a substrate of PFK1, binding at a catalytic site, and an allosteric inhibitor, binding at a regulatory site. The inhibition due to ATP is removed by AMP, and thus the activity of PFK1 increases as the ratio of ATP to AMP decreases. This feedback enables PFK1 to regulate the rate of glycolysis based on the availability of ATP. If ATP levels fall, PFK1 activity increases thereby increasing the rate of production of ATP, whereas, if ATP levels become high, PFK1 activity drops shutting down the production of ATP.

As PFK1 phosphorylates fructose 6-P, ATP is converted to ADP. ADP, in turn, is converted back to ATP and AMP by the reaction

$$2\text{ADP} \rightleftharpoons \text{ATP} + \text{AMP},$$

which is catalyzed by the enzyme adenylate kinase. Since there is normally little AMP in cells, the conversion of ADP to ATP and AMP serves to significantly decrease the ATP/AMP ratio, thus activating PFK1. This is an example of a positive feedback loop; the greater the activity of PFK1, the lower the ATP/AMP ratio, thus further increasing PFK1 activity.

It was discovered in 1980 that in some cell types, another important allosteric activator of PFK1 is fructose 2,6-bisphosphate (Stryer, 1988), which is formed from fructose 6-phosphate in a reaction catalyzed by phosphofructokinase 2 (PFK2), a different enzyme from phosphofructokinase (PFK1) (you were given fair warning about the labyrinthine nature of this process!). Of particular significance is that an abundance of fructose 6-phosphate leads to a corresponding abundance of fructose 2,6-bisphosphate, and thus a corresponding increase in the activity of PFK1. This is an example of a negative feedback loop, where an increase in the substrate concentration leads to a greater rate of substrate reaction and consumption. Clearly, PFK1 activity is controlled by an intricate system of reactions, the collective behavior of which is not obvious *a priori*.

Feedback on PFK is not the only mechanism that has been proposed as causing glycolytic oscillations. For example, hexose transport kinetics and autocatalysis of ATP have both been proposed as possible mechanisms (Madsen et al., 2005), while some authors have claimed that the oscillations arise as part of the entire network of reactions, with no single feedback being of paramount importance (Bier et al., 1996; Reijenga et al., 2002). Here we focus only on PFK regulation as the oscillatory mechanism.

Under certain conditions the rate of glycolysis is known to be oscillatory, or even chaotic (Nielsen et al., 1997). This biochemical oscillator has been known and studied experimentally for some time. For example, Hess and Boiteux (1973)
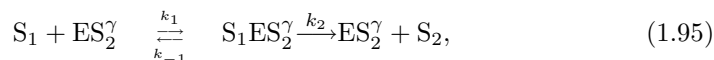
devised a flow reactor containing yeast cells into which a controlled amount of substrate (either glucose or fructose) was continuously added. They measured the pH and fluorescence of the reactants, thereby monitoring the glycolytic activity, and they found ranges of continuous input under which glycolysis was periodic.

Interestingly, the oscillatory behavior is different in intact yeast cells and in yeast extracts. In intact cells the oscillations are sinusoidal in shape, and there is strong evidence that they occur close to a Hopf bifurcation (Danøet al., 1999). In yeast extract the oscillations are of relaxation type, with widely differing time scales (Madsen et al., 2005).

A mathematical model describing glycolytic oscillations was proposed by Sel'kov (1968) and later modified by Goldbeter and Lefever (1972). It is designed to capture only the positive feedback of ADP on PFK1 activity. In the Sel'kov model, PFK1 is inactive in its unbound state but is activated by binding with several ADP molecules. Note that, for simplicity, the model does not take into account the conversion of ADP to AMP and ATP, but assumes that ADP activates PFK1 directly, since the overall effect is similar. In the active state, the enzyme catalyzes the production of ADP from ATP as fructose-6-P is phosphorylated. Sel'kov's reaction scheme for this process is as follows: PFK1 (denoted by E) is activated or deactivated by binding or unbinding with γ molecules of ADP (denoted by S_2)

$$\gamma S_2 + E \underset{k_{-3}}{\overset{k_3}{\rightleftharpoons}} ES_2^\gamma,$$
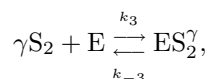
and ATP (denoted S_1) can bind with the activated form of enzyme to produce a product molecule of ADP. In addition, there is assumed to be a steady supply rate of S_1, while product S_2 is irreversibly removed. Thus,

$$\xrightarrow{v_1} \quad S_1, \tag{1.94}$$

$$S_1 + ES_2^\gamma \quad \underset{k_{-1}}{\overset{k_1}{\rightleftharpoons}} \quad S_1 ES_2^\gamma \xrightarrow{k_2} ES_2^\gamma + S_2, \tag{1.95}$$

$$S_2 \quad \xrightarrow{v_2}. \tag{1.96}$$

Note that (1.95) is an enzymatic reaction of exactly Michaelis-Menten form so we should expect a similar reduction of the governing equations.

Applying the law of mass action to the Sel'kov kinetic scheme, we find five differential equations for the production of the five species $s_1 = [S_1], s_2 = [S_2], e = [E], x_1 = [ES_2^\gamma], x_2 = [S_1 ES_2^\gamma]$:

$$\frac{ds_1}{dt} = v_1 - k_1 s_1 x_1 + k_{-1} x_2, \tag{1.97}$$

$$\frac{ds_2}{dt} = k_2 x_2 - \gamma k_3 s_2^\gamma e + \gamma k_{-3} x_1 - v_2 s_2, \tag{1.98}$$

$$\frac{dx_1}{dt} = -k_1 s_1 x_1 + (k_{-1} + k_2) x_2 + k_3 s_2^\gamma e - k_{-3} x_1, \tag{1.99}$$

$$\frac{dx_2}{dt} = k_1 s_1 x_1 - (k_{-1} + k_2) x_2. \tag{1.100}$$

The fifth differential equation is not necessary, because the total available enzyme is conserved, $e + x_1 + x_2 = e_0$. Now we introduce dimensionless variables $\sigma_1 =$

$\frac{k_1 s_1}{k_2 + k_{-1}}, \sigma_2 = (\frac{k_3}{k_{-3}})^{1/\gamma} s_2, u_1 = x_1/e_0, u_2 = x_2/e_0, t = \frac{k_2 + k_{-1}}{e_0 k_1 k_2} \tau$ and find

$$\frac{d\sigma_1}{d\tau} = \nu - \frac{k_2 + k_{-1}}{k_2} u_1 \sigma_1 + \frac{k_{-1}}{k_2} u_2, \tag{1.101}$$

$$\frac{d\sigma_2}{d\tau} = \alpha \left[u_2 - \frac{\gamma k_{-3}}{k_2} \sigma_2^\gamma (1 - u_1 - u_2) + \frac{\gamma k_{-3}}{k_2} u_1 \right] - \eta \sigma_2, \tag{1.102}$$

$$\epsilon \frac{du_1}{d\tau} = u_2 - \sigma_1 u_1 + \frac{k_{-3}}{k_2 + k_{-1}} \left[\sigma_2^\gamma (1 - u_1 - u_2) - u_1 \right], \tag{1.103}$$

$$\epsilon \frac{du_2}{d\tau} = \sigma_1 u_1 - u_2, \tag{1.104}$$

where $\epsilon = \frac{e_0 k_1 k_2}{(k_2 + k_{-1})^2}, \nu = \frac{v_1}{k_2 e_0}, \eta = \frac{v_2 (k_2 + k_{-1})}{k_1 k_2 e_0}, \alpha = \frac{k_2 + k_{-1}}{k_1} (\frac{k_3}{k_{-3}})^{1/\gamma}$. If we assume that ϵ is a small number, then both u_1 and u_2 are fast variables and can be set to their quasi-steady values,

$$u_1 = \frac{\sigma_2^\gamma}{\sigma_2^\gamma \sigma_1 + \sigma_2^\gamma + 1}, \tag{1.105}$$

$$u_2 = \frac{\sigma_1 \sigma_2^\gamma}{\sigma_2^\gamma \sigma_1 + \sigma_2^\gamma + 1} = f(\sigma_1, \sigma_2), \tag{1.106}$$

and with these quasi-steady values, the evolution of σ_1 and σ_2 is governed by

$$\frac{d\sigma_1}{d\tau} = \nu - f(\sigma_1, \sigma_2), \tag{1.107}$$

$$\frac{d\sigma_2}{d\tau} = \alpha f(\sigma_1, \sigma_2) - \eta \sigma_2. \tag{1.108}$$

The goal of the following analysis is to demonstrate that this system of equations has oscillatory solutions for some range of the supply rate ν. First observe that because of saturation, the function $f(\sigma_1, \sigma_2)$ is bounded by 1. Thus, if $\nu > 1$, the solutions of the differential equations are not bounded. For this reason we consider only $0 < \nu < 1$. The nullclines of the flow are given by the equations

$$\sigma_1 = \frac{\nu}{1 - \nu} \frac{1 + \sigma_2^\gamma}{\sigma_2^\gamma} \qquad \left(\frac{d\sigma_1}{d\tau} = 0 \right), \tag{1.109}$$

$$\sigma_1 = \frac{1 + \sigma_2^\gamma}{\sigma_2^{\gamma - 1} (p - \sigma_2)} \qquad \left(\frac{d\sigma_2}{d\tau} = 0 \right), \tag{1.110}$$

where $p = \alpha/\eta$. These two nullclines are shown plotted as dotted and dashed curves respectively in Fig. 1.7.

The steady-state solution is unique and satisfies

$$\sigma_2 = p\nu, \tag{1.111}$$

$$\sigma_1 = \frac{\nu(1 + \sigma_2^\gamma)}{(1 - \nu)\sigma_2^\gamma}. \tag{1.112}$$

The stability of the steady solution is found by linearizing the differential equations about the steady-state solution and examining the eigenvalues of the linearized
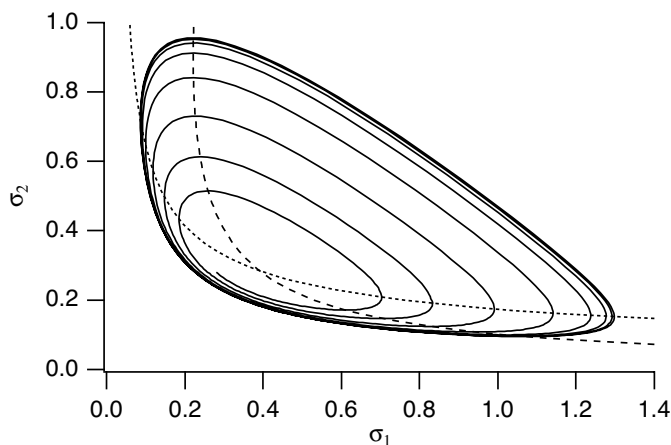
Figure 1.7: Phase portrait of the Sel'kov glycolysis system with $\nu = 0.0285, \eta = 0.1, \alpha = 1.0$, and $\gamma = 2$. Dotted curve: $\frac{d\sigma_1}{d\tau} = 0$. Dashed curve: $\frac{d\sigma_2}{d\tau} = 0$.

system. The linearized system has the form

$$\frac{d\tilde{\sigma}_1}{d\tau} = -f_1\tilde{\sigma}_1 - f_2\tilde{\sigma}_2, \tag{1.113}$$

$$\frac{d\tilde{\sigma}_2}{d\tau} = \alpha f_1\tilde{\sigma}_1 + (\alpha f_2 - \eta)\tilde{\sigma}_2, \tag{1.114}$$

where $f_j = \frac{\partial f}{\partial \sigma_j}, j = 1, 2$, evaluated at the steady-state solution, and where $\tilde{\sigma}_i$ denotes the deviation from the steady-state value of σ_i. The characteristic equation for the eigenvalues λ of the linear system (1.113)–(1.114) is

$$\lambda^2 - (\alpha f_2 - \eta - f_1)\lambda + f_1\eta = 0. \tag{1.115}$$

Since f_1 is always positive, the stability of the linear system is determined by the sign of $H = \alpha f_2 - \eta - f_1$, being stable if $H < 0$ and unstable if $H > 0$. Changes of stability, if they exist, occur at $H = 0$, and are Hopf bifurcations to periodic solutions with approximate frequency $\omega = \sqrt{f_1\eta}$.

The function $H(\nu)$ is given by

$$H(\nu) = \frac{(1 - \nu)}{(1 + y)}(\eta\gamma + (\nu - 1)y) - \eta, \tag{1.116}$$

$$y = (p\nu)^\gamma. \tag{1.117}$$

Clearly, $H(0) = \eta(\gamma - 1), H(1) = -\eta$, so for $\gamma > 1$, there must be at least one Hopf bifurcation point, below which the steady solution is unstable. Additional computations show that this Hopf bifurcation is supercritical, so that for ν slightly below the bifurcation point, there is a stable periodic orbit.

An example of this periodic orbit is shown in Fig. 1.7 with coefficients $\nu = 0.0285, \eta = 0.1, \alpha = 1.0$, and $\gamma = 2$. The evolution of σ_1 and σ_2 are shown plotted as functions of time in Fig. 1.8.
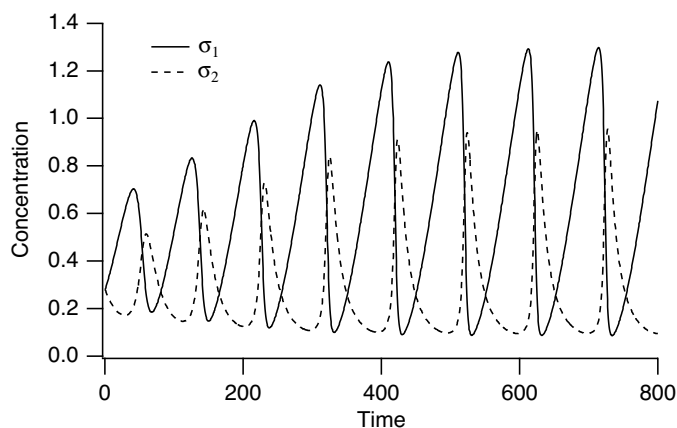
Figure 1.8: Evolution of σ_1 and σ_2 for the Sel'kov glycolysis system toward a periodic solution. Parameters are the same as in Fig. 1.7.

A periodic orbit exists only in a very small region of parameter space, rapidly expanding until it becomes infinitely large in amplitude as ν decreases. For still smaller values of ν, there are no stable trajectories. This information is summarized in a plot (Fig. 1.9), called a bifurcation diagram.

While the Sel'kov model has certain features that are qualitatively correct, it fails to agree with the experimental results at a number of points. Hess and Boiteux (1973) report that for high and low substrate injection rates, there is a stable steady-state solution. There are two Hopf bifurcation points, one at the flow rate of 20 mM/hr and another at 160 mM/hr. The period of oscillation at the low flow rate is about 8 minutes and decreases as a function of flow rate to about 3 minutes at the upper Hopf bifurcation point. In contrast, the Sel'kov model has but one Hopf bifurcation point.

To reproduce these additional experimental features we consider a more detailed model of the reaction. In 1972, Goldbeter and Lefever proposed a model of Monod–Wyman–Changeux type that provided a more accurate description of the oscillations. More recently, by fitting a simpler model to experimental data on PFK1 kinetics in skeletal muscle, Smolen (1995) has shown that this level of complexity is not necessary; his model assumes that PFK1 consists of four independent, identical subunits, and reproduces the observed oscillations well. Despite this, we describe only the Goldbeter–Lefever model in detail, as it provides an excellent example of the use of Monod–Wyman–Changeux models.

In the Goldbeter–Lefever model of the phosphorylation of fructose-6-P, the enzyme PFK1 is assumed to be a dimer that exists in two states, an active state R and an inactive state T. The substrate, S_1, can bind to both forms, but the product, S_2, which is an activator, or positive effector, of the enzyme, binds only to the active form. The enzymatic forms of R carrying substrate decompose irreversibly to yield the product ADP. In addition, substrate is supplied to the system at a constant rate, while product is removed at a rate proportional to its concentration. The
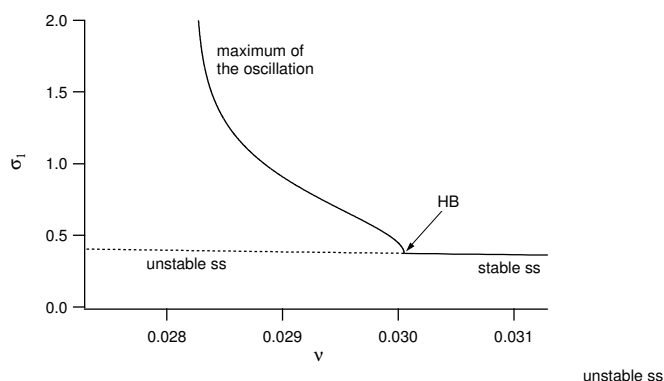
Figure 1.9: Bifurcation diagram for the Selkov glycolysis reaction. **James, there is an extraneous label (unstable ss) on this figure.**

reaction scheme for this is as follows: let T_j represent the inactive T form of the enzyme bound to j molecules of substrate and let R_{ij} represent the active form R of the enzyme bound to i substrate molecules and j product molecules. This gives the reaction diagram shown in Fig. 1.10. In this system, the substrate S_1 holds the enzyme in the inactive state by binding with T_0 to produce T_1 and T_2, while product S_2 holds enzyme in the active state by binding with R_{00} to produce R_{01} and binding with R_{01} to produce R_{02}. There is a factor of two in the rates of reaction because a dimer with two available binding sites reacts like twice the same amount of monomer.

In addition to the reactions shown in Fig. 1.10, the enzyme complex can disassociate to produce product via the reaction

$$R_{ij}\overset{k}{\longrightarrow}R_{i-1,j} + S_2 \tag{1.118}$$

provided $i \geq 1$.

The analysis of this reaction scheme is substantially more complicated than that of the Sel'kov scheme, although the idea is the same. We use the law of mass action to write differential equations for the fourteen chemical species. For example, the equation for $s_1 = [S_1]$ is

$$\frac{ds_1}{dt} = v_1 - F, \tag{1.119}$$

where

$$\begin{aligned} F = \quad & k_{-2}(r_{10} + r_{11} + r_{12}) + 2k_{-2}(r_{20} + r_{21} + r_{22}) \\ & -2k_2s_1(r_{00} + r_{01} + r_{02}) - k_2s_1(r_{10} + r_{11} + r_{12}) \\ & -2k_3s_1t_0 - k_3s_1t_1 + k_{-3}t_1 + 2k_{-3}t_2, \end{aligned} \tag{1.120}$$

and the equation for $r_{00} = [R_{00}]$ is

$$\frac{dr_{00}}{dt} = -(k_1 + 2k_2s_1 + 2k_2s_2)r_{00} + (k_{-2} + k)r_{10} + k_{-2}r_{01} + k_{-1}t_0. \tag{1.121}$$
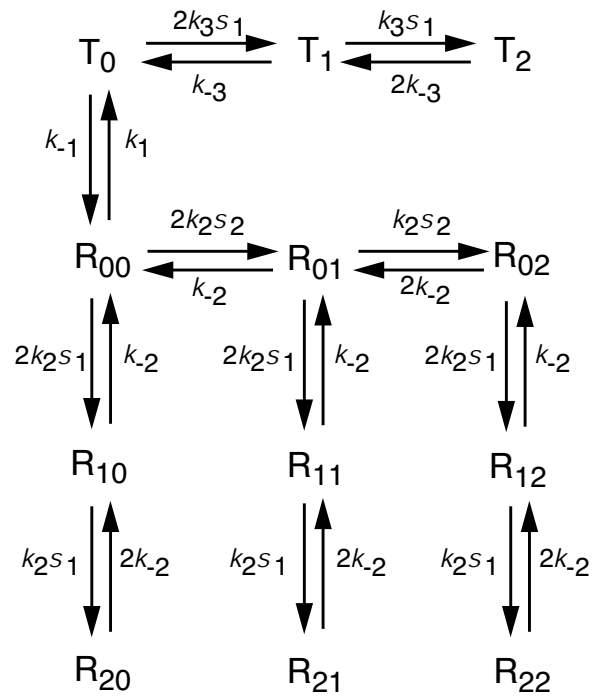
Figure 1.10: Possible receptor states for the enzyme PFK1 in the Goldbeter–Lefever model for glycolytic oscillations.

We then assume that all twelve of the intermediates are in quasi-steady state. This leads to a 12 by 12 linear system of equations, which, if we take the total amount of enzyme to be e_0, can be solved. We substitute this solution into the differential equations for s_1 and s_2 with the result that

$$\frac{ds_1}{dt} = v_1 - F(s_1, s_2), \tag{1.122}$$

$$\frac{ds_2}{dt} = F(s_1, s_2) - v_2 s_2, \tag{1.123}$$

where

$$F(s_1, s_2) = \left(\frac{2k_2 k_{-1} k e_0}{k + k_{-2}} \right) \left(\frac{s_1 (1 + \frac{k_2}{k+k_{-2}} s_1)(s_2 + K_2)^2}{K_2^2 k_1 (\frac{k_3}{k_{-3}} s_1 + 1)^2 + k_{-1}(1 + \frac{k_2}{k+k_{-2}} s_1)^2 (K_2 + s_2)^2} \right), \tag{1.124}$$

where $K_2 = \frac{k_{-2}}{k_2}$. Now we introduce dimensionless variables $\sigma_1 = \frac{s_1}{K_2}, \sigma_2 = \frac{s_2}{K_2}, t = \frac{\tau}{\tau_c}$ and parameters $\nu = \frac{k_2 v_1}{k_{-2} \tau_c}, \eta = \frac{v_2}{\tau_c}$, where $\tau_c = \frac{2k_2 k_{-1} k e_0}{k_1(k+k_{-2})}$, and arrive at the system (1.107)–(1.108), but with a different function $f(\sigma_1, \sigma_2)$, and with $\alpha = 1$. If, in addition, we assume that

1. the substrate does not bind to the T form ($k_3 = 0$, T is completely inactive),

2. T_0 is preferred over R_{00} ($k_1 \gg k_{-1}$), and

3. if the substrate S_1 binds to the R form, then formation of product S_2 is preferred to dissociation ($k \gg k_{-2}$),

then we can simplify the equations substantially to obtain

$$f(\sigma_1, \sigma_2) = \sigma_1 (1 + \sigma_2)^2. \tag{1.125}$$

The nullclines for this system of equations are somewhat different from the Sel'kov system, being

$$\sigma_1 = \frac{\nu}{(1 + \sigma_2)^2} \qquad \left(\frac{d\sigma_1}{d\tau} = 0 \right), \tag{1.126}$$

$$\sigma_1 = \frac{\eta \sigma_2}{(1 + \sigma_2)^2} \qquad \left(\frac{d\sigma_2}{d\tau} = 0 \right), \tag{1.127}$$

and the unique steady-state solution is given by

$$\sigma_1 = \frac{\nu}{(1 + \sigma_2)^2}, \tag{1.128}$$

$$\sigma_2 = \frac{\nu}{\eta}. \tag{1.129}$$

The stability of the steady-state solution is again determined by the characteristic equation (1.115), and the sign of the real part of the eigenvalues is the same as the sign of

$$H = f_2 - f_1 - \eta = 2\sigma_1(1 + \sigma_2) - (1 + \sigma_2)^2 - \eta, \tag{1.130}$$

evaluated at the steady state (1.126)–(1.127). Equation (1.130) can be written as the cubic polynomial

$$\frac{1}{\eta}y^3 - y + 2 = 0, \qquad y = 1 + \frac{\nu}{\eta}. \qquad (1.131)$$

For η sufficiently large, the polynomial (1.131) has two roots greater than 2, say, y_1 and y_2. Recall that ν is the nondimensional flow rate of substrate ATP. To make some correspondence with the experimental data, we assume that the flow rate ν is proportional to the experimental supply rate of glucose. This is not strictly correct, although ATP is produced at about the same rate that glucose is supplied. Accepting this caveat, we see that to match experimental data, we require

$$\frac{y_2 - 1}{y_1 - 1} = \frac{\nu_2}{\nu_1} = \frac{160}{20} = 8. \qquad (1.132)$$

Requiring (1.131) to hold at y_1 and y_2 and requiring (1.132) to hold as well, we find numerical values

$$y_1 = 2.08, y_2 = 9.61, \eta = 116.7, \qquad (1.133)$$

corresponding to $\nu_1 = 126$ and $\nu_2 = 1005$.

At the Hopf bifurcation point, the period of oscillation is

$$T_i = \frac{2\pi}{\omega_i} = \frac{2\pi}{\sqrt{\eta}(1 + \sigma_2)} = \frac{2\pi}{\sqrt{\eta}y_i}. \qquad (1.134)$$

For the numbers (1.133), we obtain a ratio of periods $T_1/T_2 = 4.6$, which is acceptably close to the experimentally observed ratio $T_1/T_2 = 2.7$.

The behavior of the solution as a function of the parameter ν is summarized in the bifurcation diagram, Fig. 1.11, shown here for $\eta = 120$. The steady state solution is stable below $\eta = 129$ and above $\eta = 1052$. Between these values of η, the steady state solution is unstable, but there is a branch of stable periodic solutions, which terminates and collapses into the steady state solution at the two points where the stability changes, the Hopf bifurcation points.

A typical phase portrait for the periodic solution that exists between the Hopf bifurcation points is shown in Fig. 1.12, and the concentrations of the two species are shown as functions of time in Fig. 1.13.

1.6 Appendix: Math Background

It is certain that some of the mathematical concepts and tools that we routinely invoke here are not familiar to all of our readers. In this first chapter alone, we have used nondimensionalization, phase-plane analysis, linear stability analysis, bifurcation theory, and asymptotic analysis, all the while assuming that these are familiar to the reader.

The purpose of this appendix is to give a brief guide to those techniques that are a basic part of the applied mathematician's toolbox but that may not be familiar to all our readers.
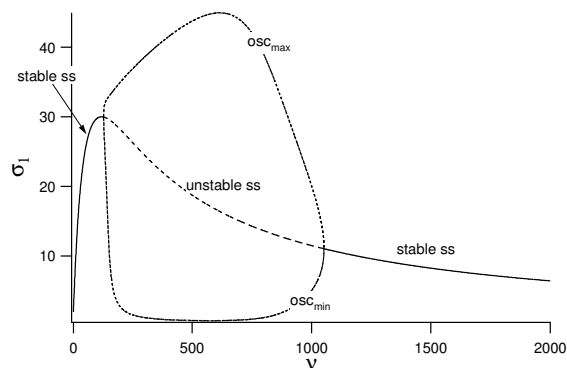
Figure 1.11: Bifurcation diagram for the reduced Goldbeter-Lefever glycolysis reaction, with $\eta = 120$.
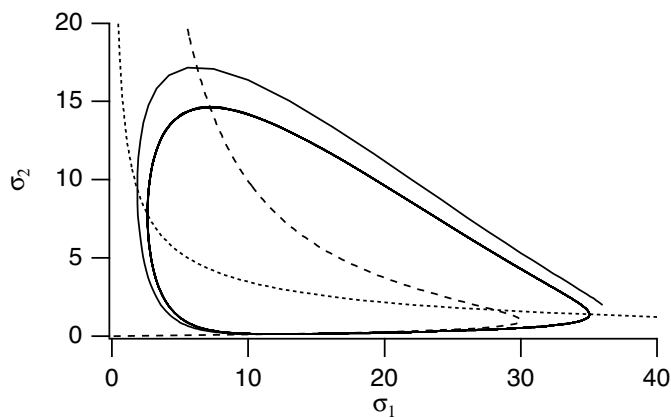

Figure 1.12: Phase portrait of the Goldbeter–Lefever model with $\nu = 200$, $\eta = 120$. Dotted curve: $\frac{d\sigma_1}{d\tau} = 0$. Dashed curve: $\frac{d\sigma_2}{d\tau} = 0$.
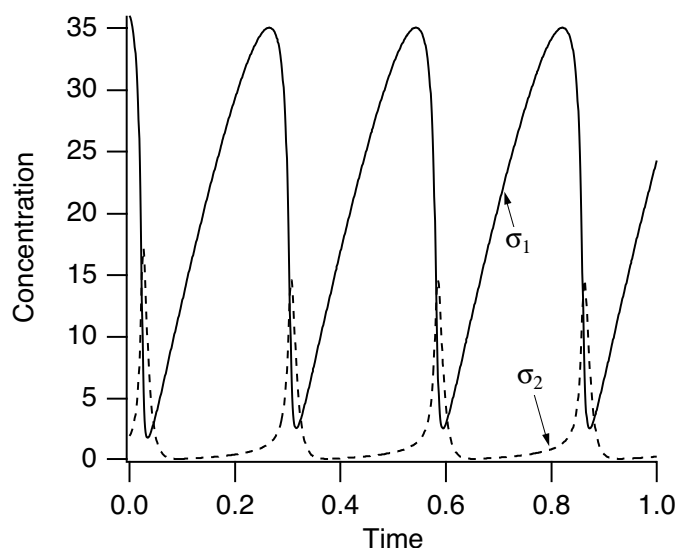
Figure 1.13: Solution of the Goldbeter–Lefever model with $\nu = 200$, $\eta = 120$.

1.6.1 Basic Techniques

In any problem, there are a number of parameters that are dictated by the problem. However, it often happens that not all parameter variations are *independent*; that is, different variations in different parameters may lead to identical changes in the behavior of the model. Second, there may be parameters whose influence on a behavior is negligible and can be safely ignored for a given context.

The way to identify independent parameters and to determine their relative magnitudes is to nondimensionalize the problem. Unfortunately, there is not a unique algorithm for nondimensionalization; nondimensionalization is as much art as it is science.

There are, however, rules of thumb to apply. In any system of equations, there are a number of independent variables (time, space, etc.), dependent variables (concentrations, etc.) and parameters (rates of reaction, sizes of containers, etc.). Nondimensionalization begins by rescaling the independent and dependent variables by "typical" units, rendering them thereby dimensionless. One goal may be to ensure that the dimensionless variables remain of a fixed order of magnitude, not becoming too large or negligibly small. This usually requires some a priori knowledge about the solution, as it can be difficult to choose typical scales unless something is already known about typical solutions. Time and space scales can be vastly different depending on the context.

Once this selection of scales has been made, the governing equations are written in terms of the rescaled variables and dimensionless combinations of the remaining parameters are identified. The number of remaining free dimensionless parameters is usually less than the original number of physical parameters. The primary diffi-

culty (at least to understand and apply the process) is that there is not necessarily a single way to scale and nondimensionalize the equations. Some scalings may highlight certain features of the solution, while other scalings may emphasize others. Nonetheless, nondimensionalization often (but not always) provides a good starting point for the analysis of a model system.

An excellent discussion of scaling and nondimensionalization can be found in Lin and Segel (1988, Chapter 6). A great deal of more advanced work has also been done on this subject, particularly its application to the quasi-steady-state approximation, by Segel and his collaborators (Segel, 1988; Segel and Slemrod, 1989; Segel and Perelson, 1992; Segel and Goldbeter, 1994; Borghans et al., 1996; see also Frenzen and Maini, 1988).

Phase-plane analysis and linear stability analysis are standard fare in introductory courses on differential equations. A nice introduction to these topics for the biologically inclined can be found in Edelstein-Keshet (1988, Chapter 5) or Braun (1993, Chapter 4). A large number of books discuss the qualitative theory of differential equations, for example, Boyce and Diprima (1997), or at a more advanced level, Hale and Koçak (1991), or Hirsch and Smale (1974).

Bifurcation theory is a topic that is gradually finding its way into introductory literature. The most important terms to understand are those of *steady-state* bifurcations, *Hopf* bifurcations, *homoclinic* bifurcations, and *saddle-node* bifurcations, all of which appear in this book. An excellent introduction to these concepts is found in Strogatz (1994, Chapters 3, 6, 7, 8). More advanced treatments include those in Guckenheimer and Holmes (1983), Arnold (1983), or Kuznetzov (1998).

One way to summarize the behavior of the model is with a bifurcation diagram (examples of which are shown in Figs. 1.9 and 1.11), which shows how certain features of the model, such as steady states or limit cycles, vary as a parameter is varied. When models have many parameters there is a wide choice for which parameter to vary. Often, however, there are compelling physiological or experimental reasons for the choice of parameter. Bifurcation diagrams are important in a number of chapters of this book, and are widely used in the analysis of nonlinear systems. Thus, it is worth the time to get familiar with their properties and how they are constructed. Nowadays, all bifurcation diagrams of realistic models are constructed numerically, the most popular choice of software being AUTO (Doedel et al., 2000), which has a number of implementations that are easy to install and use. The bifurcation diagrams in this book were all prepared with XPPAUT (ref???).

In this text, the bifurcation that is seen most often is the Hopf Bifurcation. The Hopf Bifurcation Theorem describes conditions for the appearance of small periodic solutions of a differential equation, say

$$\frac{du}{dt} = f(u, \lambda), \tag{1.135}$$

as a function of the parameter λ. Suppose that there is a steady state solution, $u = u_0(\lambda)$, and that the system linearized about u_0,

$$\frac{dU}{dt} = \frac{\partial f(u_0(\lambda), \lambda)}{\partial u} U, \tag{1.136}$$

has a pair of complex eigenvalues $\mu(\lambda) = \alpha(\lambda) \pm i\beta(\lambda)$. Suppose further that $\alpha(\lambda_0) =$

0, $\alpha'(\lambda_0) \neq 0$, and $\beta(\lambda_0) \neq 0$, and that at $\lambda = \lambda_0$ no other eigenvalues of the system have zero real part. Then λ_0 is a Hopf Bifurcation point, and there is a branch of periodic solutions emanating from the point $\lambda = \lambda_0$. The periodic solutions could exist (locally) for $\lambda > \lambda_0$, for $\lambda < \lambda_0$, or in the degenerate (nongeneric) case, for $\lambda = \lambda_0$. If the periodic solutions occur in the region of λ for which $\alpha(\lambda) > 0$, then the periodic solutions are stable (provided all other eigenvalues of the system have negative real part), and this branch of solutions is said to be supercritical. On the other hand, if the periodic solutions occur in the region of λ for which $\alpha(\lambda) < 0$, then the periodic solutions are unstable, and this branch of solutions is said to be subcritical.

The Hopf Bifurcation Theorem applies to ordinary differential equations and delay differential equations. For partial differential equations, there are some technical issues having to do with the nature of the spectrum of the linearized operator that complicate matters, but we do not concern ourselves with these here. Instead, rather than checking all the conditions of the theorem, we find periodic solutions by looking only for a change of the sign of the real part of an eigenvalue, using numerical computations to verify the existence of periodic solutions, and calling it good.

1.6.2 Asymptotic Analysis

Applied mathematicians love small parameters, because of the hope that the solution of a problem with a small parameter might be approximated by an *asymptotic representation*. A commonplace notation has emerged in which ϵ is often the small parameter. An asymptotic representation has a precise mathematical meaning. Suppose that $G(\epsilon)$ is claimed to be an asymptotic representation of $g(\epsilon)$, expressed as

$$g(\epsilon) = G(\epsilon) + O(\phi(\epsilon)). \tag{1.137}$$

The precise meaning of this statement is that there is a constant A such that

$$\left| \frac{g(\epsilon) - G(\epsilon)}{\phi(\epsilon)} \right| \leq A \tag{1.138}$$

for all ϵ with $|\epsilon| \leq \epsilon_0$ and $\epsilon > 0$. The function $\phi(\epsilon)$ is called a *gauge function*, a typical example of which is a power of ϵ.

Perturbation Expansions

It is often the case that an asymptotic representation can be found as a power series in powers of the small parameter ϵ. Such representations are called *perturbation expansions*. Usually, a few terms of this power series representation suffice to give a good approximation to the solution. It should be kept in mind that under no circumstances does this power series development imply that a complete power series (with an infinite number of terms) exists or is convergent. Terminating the series at one or two terms is deliberate.

However, there are times when a full power series could be found and would be convergent in some nontrivial ϵ domain. Such problems are called *regular pertur-*

bation problems because their solutions are regular, or analytic, in the parameter ϵ.

There are numerous examples of regular perturbation problems, including all of those related to bifurcation theory. These problems are regular because their solutions can be developed in a convergent power series of some parameter.

There are, however, many problems with small parameters whose solutions are not regular, called *singular perturbation problems*. Singular perturbation problems are characterized by the fact that their dependence on the small parameter is not regular, but *singular*, and their convergence as a function of ϵ is not uniform.

Singular problems come in two basic varieties. Characteristic of the first type is a small region of width ϵ somewhere in the domain of interest (either space or time) in which the solution changes rapidly. For example, the solution of the boundary value problem

$$\epsilon u'' + u' + u = 0 \qquad (1.139)$$

subject to boundary conditions $u(0) = u(1) = 1$ is approximated by the asymptotic representation

$$u(x; \epsilon) = (1 - e)e^{-x/\epsilon} + e^{1-x} + O(\epsilon). \qquad (1.140)$$

Notice the nonuniform nature of this solution, as

$$e = \lim_{x \to 0^+} (\lim_{\epsilon \to 0^+} u(x; \epsilon)) \neq \lim_{\epsilon \to 0^+} (\lim_{x \to 0^+} u(x; \epsilon)) = 1. \qquad (1.141)$$

Here the term $e^{-x/\epsilon}$ is a *boundary layer correction*, as it is important only in a small region near the boundary at $x = 0$.

Other terms that are typical in singular perturbation problems are *interior layers* or *transition layers*, typified by expressions of the form $\tan(\frac{x-x_0}{\epsilon})$, and *corner layers*, locations where the derivative changes rapidly but the solution itself changes little. Transition layers are of great significance in the study of excitable systems (Chapter 5). While corner layers show up in this book, we do not study or use them in any detail.

Singular problems of this type can often be identified by the fact that the order of the system decreases if ϵ is set to zero. An example that we have already seen is the quasi-steady-state analysis used to simplify reaction schemes in which some reactions are significantly faster than others. Setting ϵ to zero in these examples reduces the order of the system of equations, signaling a possible problem. Indeed, solutions of these equations typically have *initial layers* near time $t = 0$. We take a closer look at this example below.

The second class of singular perturbation problems is that in which there are two scales in operation everywhere in the domain of interest. Problems of this type show up throughout this book. For example, action potential propagation in cardiac tissue is through a cellular medium whose detailed structure varies rapidly compared to the length scale of the action potential wave front. Physical properties of the cochlear membrane in the inner ear vary slowly compared to the wavelength of waves that propagate along it. For problems of this type, one must make explicit the dependence on multiple scales, and so solutions are often expressed as functions of two variables, say x and x/ϵ, which are treated as independent variables. Solution

techniques that exploit the multiple-scale nature of the solution are called *multiscale methods* or *averaging methods.*

Detailed discussions of these asymptotic methods may be found in Murray (1984), Kevorkian and Cole (1996), and Holmes (1995).

1.6.3 Enzyme Kinetics and Singular Perturbation Theory

In most of the examples of enzyme kinetics discussed in this chapter, extensive use was made of the quasi-steady-state approximation (1.44), according to which the concentration of the complex remains constant during the course of the reaction. Although this assumption gives the right answers (which, some might argue, is justification enough), mathematicians have sought for ways to justify this approximation rigorously. Bowen et al. (1963) and Heineken et al. (1967) were the first to show that the quasi-steady-state approximation can be derived as the lowest-order term in an asymptotic expansion of the solution. This has since become one of the standard examples of the application of singular perturbation theory to biological systems, and it is discussed in detail by Rubinow (1973), Lin and Segel (1988), and Murray (1989), among others.

Starting with (1.37) and (1.38),

$$\frac{d\sigma}{d\tau} = -\sigma + x(\sigma + \alpha), \tag{1.142}$$

$$\epsilon\frac{dx}{d\tau} = \sigma - x(\sigma + \kappa), \tag{1.143}$$

with initial conditions

$$\sigma(0) = 1, \tag{1.144}$$

$$x(0) = 0, \tag{1.145}$$

we begin by looking for solutions of the form

$$\sigma = \sigma_0 + \epsilon\sigma_1 + \epsilon^2\sigma_2 + \cdots, \tag{1.146}$$

$$x = x_0 + \epsilon x_1 + \epsilon^2 x_2 + \cdots. \tag{1.147}$$

We substitute these solutions into the differential equations and equate coefficients of powers of ϵ. To lowest order (i.e., equating all those terms with no ϵ) we get

$$\frac{d\sigma_0}{d\tau} = -\sigma_0 + x_0(\sigma_0 + \alpha), \tag{1.148}$$

$$0 = \sigma_0 - x_0(\sigma_0 + \kappa). \tag{1.149}$$

Note that, because we are matching powers of ϵ, the differential equation for x has been converted into an algebraic equation for x_0, which can be solved to give

$$x_0 = \frac{\sigma_0}{\sigma_0 + \kappa}. \tag{1.150}$$

It follows that

$$\frac{d\sigma_0}{d\tau} = -\sigma_0 + x_0(\sigma_0 + \alpha) = -\sigma_0 \left(\frac{\kappa - \alpha}{\sigma_0 + \kappa} \right). \tag{1.151}$$

These solutions for x_0 and σ_0 (i.e., for the lowest order terms in the power series expansion) are the quasi-steady-state approximation of Section 1.4.2. We could carry on and solve for σ_1 and x_1, but since the calculations rapidly become quite tedious, with little to no benefit, the lowest order solution suffices.

However, it is important to notice that this lowest order solution cannot be correct for all times. For, clearly, the initial conditions $\sigma(0) = 1$, $x(0) = 0$ are inconsistent with (1.150). In fact, by setting ϵ to be zero, we have decreased the order of the differential equations system, making it impossible to satisfy the initial conditions.

There must therefore be a brief period of time at the start of the reaction during which the quasi-steady-state approximation does not hold. It is not that ϵ is not small, but rather that $\epsilon\frac{dx}{dt}$ is not small during this initial period, since dx/dt is large. Indeed, it is during this initial time period that the enzyme is "filling up" with substrate, until the concentration of complexed enzyme reaches the value given by the quasi-steady-state approximation. Since there is little enzyme compared to the total amount of substrate, the concentration of substrate remains essentially constant during this period.

For most biochemical reactions this transition to the quasi-steady-state happens so fast that it is not physiologically important, but for mathematical reasons, it is interesting to understand these kinetics for early times as well. To see how the reaction behaves for early times, we make a change of time scale, $\eta = \tau/\epsilon$. This change of variables expands the time scale on which we look at the reaction and allows us to study events that happen on a fast time scale. To be more precise, we also denote the solution on this fast time scale by a tilde. In the new time scale, the equations are (1.37)–(1.38) become

$$\frac{d\tilde{\sigma}}{d\eta} = \epsilon(-\tilde{\sigma} + \tilde{x}(\tilde{\sigma} + \alpha)), \tag{1.152}$$

$$\frac{d\tilde{x}}{d\eta} = \tilde{\sigma} - \tilde{x}(\tilde{\sigma} + \kappa). \tag{1.153}$$

The initial conditions are $\tilde{\sigma}(0) = 1$, $\tilde{x}(0) = 0$.

As before, we expand $\tilde{\sigma}$ and $\tilde{x}$ in a power series in ϵ, substitute into the differential equations, and equate coefficients of powers of ϵ. To lowest order in ϵ this gives

$$\frac{d\tilde{\sigma}_0}{d\eta} = 0, \tag{1.154}$$

$$\frac{d\tilde{x}_0}{d\eta} = \tilde{\sigma}_0 - \tilde{x}_0(\tilde{\sigma}_0 + \kappa). \tag{1.155}$$

Simply stated, this means that on this time scale $\tilde{\sigma}_0$ does not change, so that $\tilde{\sigma}_0 = 1$. Furthermore, we can solve for $\tilde{x}_0$ as

$$\tilde{x}_0 = \frac{1}{1 + \kappa}(1 - e^{-(1+\kappa)\eta}), \tag{1.156}$$

where we have used the initial condition $\tilde{x}_0(0) = 0$.

Once again, we could go on to solve for $\tilde{\sigma}_1$ and $\tilde{x}_1$, but such calculations, being long and of little use, are rarely done. Thus, from now on, we omit the subscript 0, as it plays no essential role.

One important thing to notice about this solution for $\tilde{\sigma}$ and $\tilde{x}$ is that it cannot be valid at large times. After all, σ cannot possibly be a constant for all times. Thus, $\tilde{\sigma}$ and $\tilde{x}$ are valid for small times (as they satisfy the initial conditions), but not for large times.

At first sight, it looks as if we are at an impasse. We have a solution, σ and x that works for large times but not for small times, and we have another solution $\tilde{\sigma}$ and $\tilde{x}$ that works for small times, but not for large ones. The goal now is to match them to obtain a single solution that is valid for all times. Fortunately, this is relatively simple to do for this example.

In terms of the original time variable τ, the solution for $\tilde{x}$ is

$$\tilde{x}(\tau) = \frac{\tilde{\sigma}}{\tilde{\sigma} + \kappa}(1 - e^{-(1+\kappa)\frac{\tau}{\epsilon}}). \tag{1.157}$$

As τ gets larger than order ϵ, the exponential term disappears, leaving only

$$\tilde{x}(\tau) = \frac{\tilde{\sigma}}{\tilde{\sigma} + \kappa}, \tag{1.158}$$

which has the same form as (1.150). It thus follows that the solution

$$x(\tau) = \frac{\sigma}{\sigma + \kappa}(1 - e^{-(1+\kappa)\frac{\tau}{\epsilon}}) \tag{1.159}$$

is valid for all times.

The solution for σ is obtained by direct solution of (1.151), which gives

$$\sigma + \kappa \log \sigma = (\alpha - \kappa)t + 1, \tag{1.160}$$

where we have used the initial condition $\sigma(0) = 1$. Since σ does not change on the short time scale, this solution is valid for both small and large times.

This simple analysis shows that there is first a time span during which the enzyme products rapidly equilibrate, consuming little substrate, and after this initial "layer" the reaction proceeds according to Michaelis–Menten kinetics along the quasi-steady-state curve. This is shown in Fig. 1.14. In the phase plane one can see clearly how the solution moves quickly until it reaches the quasi-steady-state curve (the slow manifold) and then moves slowly along that curve towards the steady state. Note that the movement to the quasi-steady-state curve is almost vertical, as during that time σ remains approximately unchanged from its initial value. A similar procedure can be followed for the equilibrium approximation (Exercise 20). In this case the fast movement to the slow manifold is not along lines of constant σ, but along lines of constant $\sigma + \alpha x$, where $\alpha = e_0/s_0$.

In this problem the analysis of the initial layer is relatively easy and not particularly revealing. However, this type of analysis is of much greater importance later in this book when we discuss the behavior of excitable systems.
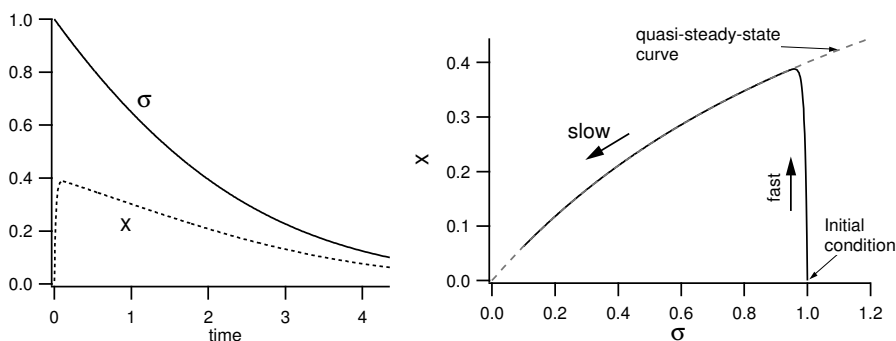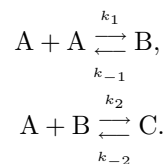
Figure 1.14: The solution to the quasi-state-state approximation, plotted as functions of time (left panel) and in the phase plane (right panel). Calculated using $\kappa = 1.5$, $\alpha = 0.5$, $\epsilon = 0.05$.

Exercises

1. Consider the simple chemical reaction in which two monomers of A combine to form a dimer B, according to
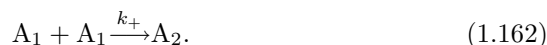
$$\text{A} + \text{A} \underset{k_-}{\overset{k_+}{\rightleftharpoons}} \text{B}. \tag{1.161}$$

   (a) Use the law of mass action to find the differential equations governing the rates of production of A and B.

   (b) What quantity is conserved? Use this conserved quantity to find an equation governing the rate of production of A that depends only on the concentration of A.

   (c) Non-dimensionalize this equation and show that these dynamics depend on only one dimensionless parameter.

2. In the real world trimolecular reactions are rare, although trimerizations are not. Consider the following trimerization reaction in which three monomers of A combine to form the trimer C,

$$\text{A} + \text{A} \underset{k_{-1}}{\overset{k_1}{\rightleftharpoons}} \text{B},$$

$$\text{A} + \text{B} \underset{k_{-2}}{\overset{k_2}{\rightleftharpoons}} \text{C}.$$

   (a) Use the law of mass action to find the rate of production of the trimer C.

(b) Suppose $k_{-1} \gg k_{-2}, k_2 A$. Use the appropriate quasi-steady state approximation to find the rates of production of A and C, and show that the rate of production of C is proportional to $[A]^3$. Explain in words why this is so.

3. The length of microtubules changes by a process called treadmilling, in which monomer is added to one end of the microtubule and taken off at the other end. To model this process, suppose that monomer A_1 is self-polymerizing in that it can form dimer A_2 via

$$A_1 + A_1 \xrightarrow{k_+} A_2. \tag{1.162}$$

Furthermore, suppose A_1 can polymerize an n-polymer A_n at one end making an $n + 1$-polymer A_{n+1}

$$A_1 + A_n \xrightarrow{k_+} A_{n+1}. \tag{1.163}$$

Finally, degradation can occur one monomer at a time from the opposite end at rate k_-. Find the steady state distribution of polymer lengths after an initial amount of monomer A_0 has fully polymerized.

4. Suppose that the reaction rates for the three reactant loop of Fig. 1.1 do not satisfy detailed balance. What is the net rate of conversion of A into B when the reaction is at steady state?

5. Consider an enzymatic reaction in which an enzyme can be activated or inactivated by the same chemical substance, as follows:

$$E + X \underset{k_{-1}}{\overset{k_1}{\rightleftharpoons}} E_1, \tag{1.164}$$

$$E_1 + X \underset{k_{-2}}{\overset{k_2}{\rightleftharpoons}} E_2, \tag{1.165}$$

$$E_1 + S \xrightarrow{k_3} P + Q + E. \tag{1.166}$$

Suppose further that X is supplied at a constant rate and removed at a rate proportional to its concentration. Use quasi-steady-state analysis to find the nondimensional equation describing the degradation of X,

$$\frac{dx}{dt} = \gamma - x - \frac{\beta x y}{1 + x + y + \frac{\alpha}{\delta} x^2}. \tag{1.167}$$

Identify all the parameters and variables, and the conditions under which the quasi-steady state approximation is valid.

6. Using the quasi-steady-state approximation, show that the velocity of the reaction for an enzyme with an allosteric inhibitor (Section 1.4.3) is given by

$$V = \left(\frac{V_{\max} K_3}{i + K_3} \right) \left(\frac{s(k_{-1} + k_3 i + k_1 s + k_{-3})}{k_1 (s + K_1)^2 + (s + K_1)(k_3 i + k_{-3} + k_2) + k_2 k_{-3}/k_1} \right), \tag{1.168}$$

Identify all parameters. Under what conditions on the rate constants is this a valid approximation? Show that this reduces to (1.59) in the case $K_1 = \kappa_1$.

Table 1.1: Data for Problem 8.

Substrate Concentration (mM)	Reaction Velocity (mM/s)
0.1	0.04
0.2	0.08
0.5	0.17
1.0	0.24
2.0	0.32
3.5	0.39
5.0	0.42

7. (a) Derive the expression (1.76) for the fraction of occupied sites in a Monod–Wyman–Changeux model with n binding sites.

   (b) Modify the Monod–Wyman–Changeux model shown in Fig.1.4 to include transitions between states R_1 and T_1, and between states R_2 and T_2. Use the principle of detailed balance to derive an expression for the equilibrium constant of each of these transitions. Find the expression for Y, the fraction of occupied sites, and compare it to (1.72).

8. An enzyme-substrate system is believed to proceed at a Michaelis-Menten rate. Data for the (initial) rate of reaction at different concentrations is shown in Table 20.1.

   (a) Plot the data V vs. s. Is there evidence that this is a Michaelis-Menten type reaction?

   (b) Plot V vs. V/s. Is this data well approximated by a straight line?

   (c) Use linear regression and (1.46) to estimate K_m and V_{max}. Compare the data to the Michaelis-Menten rate function using these parameters. Does this provide a reasonable fit to the data?

9. Suppose the maximum velocity of a chemical reaction is known to be 1 mM/s, and the measured velocity V of the reaction at different concentrations s is shown in Table 20.2.

   (a) Plot the data V vs. s. Is there evidence that this is a Hill type reaction?

   (b) Plot $\ln(\frac{V}{V_{max}-V})$ vs. $\ln(s)$. Is this approximately a straight line, and if so, what is its slope?

   (c) Use linear regression and (1.71) to estimate K_m and the Hill exponent n. Compare the data to the Hill rate function with these parameters. Does this provide a reasonable fit to the data?

10. Use the equilibrium approximation to derive an expression for the reaction velocity of the scheme (1.60)-(1.61).

Table 1.2: Data for Problem 9.

Substrate Concentration (mM)	Reaction Velocity (mM/s)
0.2	0.01
0.5	0.06
1.0	0.27
1.5	0.50
2.0	0.67
2.5	0.78
3.5	0.89
4.0	0.92
4.5	0.94
5.0	0.95

Answer:

$$V = \frac{(k_2 K_3 + k_4 s)e_0 s}{K_1 K_3 + K_3 s + s^2}, \tag{1.169}$$

where $K_1 = k_{-1}/k_1$ and $K_3 = k_{-3}/k_3$.

11. (a) Find the velocity of reaction for an enzyme with three active sites.

   (b) Under what conditions does the velocity reduce to a Hill function with exponent three? Identify all parameters.

   (c) What is the relationship between rate constants when the three sites are independent? What is the velocity when the three sites are independent?

12. The Goldbeter-Koshland function (1.92) is defined using the solution of the quadratic equation with a negative square root. Why?

13. Suppose that a substrate can be broken down by two different enzymes with different kinetics. (This happens, for example, in the case of cAMP or cGMP, which can be hydrolyzed by two different forms of phosphodiesterase—see Chapter 19).

   (a) Write the reaction scheme and differential equations, and nondimensionalize, to get the system of equations

   $$\frac{d\sigma}{dt} = -\sigma + \alpha_1(\mu_1 + \sigma)x + \alpha_2(\mu_2 + \sigma)y, \tag{1.170}$$

   $$\epsilon_1 \frac{dx}{dt} = \frac{1}{\lambda_1}\sigma(1 - x) - x, \tag{1.171}$$

   $$\epsilon_2 \frac{dy}{dt} = \frac{1}{\lambda_2}\sigma(1 - y) - y. \tag{1.172}$$

   where x and y are the nondimensional concentrations of the two complexes. Identify all parameters.

(b) Apply the quasi-steady-state approximation to find the equation governing the dynamics of substrate σ. Under what conditions is the quasi-steady state approximation valid?

(c) Solve the differential equation governing σ.

(d) For this system of equations, show that the solution can never leave the positive octant $\sigma, x, y \geq 0$. By showing that $\sigma + \epsilon_1 x + \epsilon_2 y$ is decreasing everywhere in the positive octant, show that the solution approaches the origin for large time.

14. For some enzyme reactions (for example, the hydrolysis of cAMP by phosphodiesterase in vertebrate retinal cones) the enzyme is present in large quantities, so that e_0/s_0 is not a small number. Fortunately, there is an alternate derivation of the Michaelis-Menten rate equation that does not require that $\epsilon = \frac{e_0}{s_0}$ be small. Instead, if one or both of k_{-1} and k_2 are much larger than $k_1 e_0$, then the formation of complex c is a rapid exponential process, and can be taken to be in quasi-steady state. Make this argument systematic by introducing appropriate non-dimensional variables and then find the resulting quasi-steady state dynamics. (Segel, 1988; Frenzen and Maini, 1988; Segel and Slemrod, 1989; Sneyd and Tranchina, 1989).

15. ATP is known to inhibit its own dephosphorylation. One possible way for this to occur is if ATP binds with the enzyme, holding it in an inactive state, via

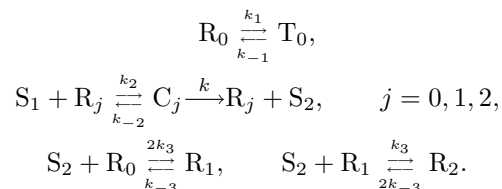$$S_1 + E \underset{k_{-4}}{\overset{k_4}{\rightleftharpoons}} S_1E.$$
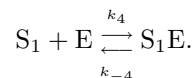
Add this reaction to the Sel'kov model for glycolysis and derive the equations governing glycolysis of the form (1.107)–(1.108). Explain from the model why this additional reaction is inhibitory.

16. In the case of noncompetitive inhibition, the inhibitor combines with the enzyme-substrate complex to give an inactive enzyme-substrate-inhibitor complex which cannot undergo further reaction, but the inhibitor does not combine directly with free enzyme or affect its reaction with substrate. Use the quasi-steady-state approximation to determine that the velocity of this reaction is

$$V = V_{\max} \frac{s}{K_m + s + \frac{i}{K_i}s}. \tag{1.173}$$

Identify all parameters. Compare this velocity with the velocity for other types of inhibition discussed in the text.

17. The following reaction scheme is a simplified version of the Goldbeter–Lefever reaction scheme for glycolytic oscillations:

$$R_0 \underset{k_{-1}}{\overset{k_1}{\rightleftharpoons}} T_0,$$

$$S_1 + R_j \underset{k_{-2}}{\overset{k_2}{\rightleftharpoons}} C_j \overset{k}{\longrightarrow} R_j + S_2, \qquad j = 0, 1, 2,$$

$$S_2 + R_0 \underset{k_{-3}}{\overset{2k_3}{\rightleftharpoons}} R_1, \qquad S_2 + R_1 \underset{2k_{-3}}{\overset{k_3}{\rightleftharpoons}} R_2.$$

Show that, under appropriate assumptions about the ratios k_1/k_{-1} and $\frac{k_{-2}+k_3}{k_2}$ the equations describing this reaction are of the form (1.107)–(1.108) with $f(\sigma_1, \sigma_2)$ given by (1.125).

18. Use the law of mass action and the quasi-steady-state assumption for the enzymatic reactions to derive a system of equations of the form (1.107)–(1.108) for the Goldbeter–Lefever model of glycolytic oscillations. Verify (1.124).

19. When much of the ATP is depleted in a cell, a considerable amount of cAMP is formed as a product of ATP degradation. This cAMP activates an enzyme phosphorylase that splits glycogen, releasing glucose that is rapidly metabolized, replenishing the ATP supply.

    Devise a model for this control loop and determine conditions under which the production of ATP is oscillatory.

20. (a) Nondimensionalize (1.26) to (1.29) in a way appropriate for the equilibrium approximation (rather than the quasi-steady-state approximation of Section 1.4.2). Hint: Recall that for the equilibrium approximation, the assumption is that $k_1 e_0$ and k_{-1} are large compared to k_2. You should end up with equations that look something like

$$\epsilon \frac{d\sigma}{d\tau} = \alpha x - \beta \alpha \sigma (1 - x), \qquad (1.174)$$

$$\epsilon \frac{dx}{d\tau} = \beta \sigma (1 - x) - x - \epsilon x, \qquad (1.175)$$

   where $\epsilon = k_2/k_{-1}$, $\alpha = e_0/s_0$ and $\beta = s_0/K_1$.

   (b) Find the behavior, to lowest order in ϵ for this system. (Notice that the slow variable is $\sigma + \alpha x$.)

   (c) To lowest order in ϵ, what is the differential equation for σ on this time scale?

   (d) Rescale time to find equations valid for small times.

   (e) Show that, to lowest order in ϵ, $\sigma + \alpha x = $ constant for small times.

   (f) Without calculating the exact solution, sketch the solution in the phase plane, showing the initial fast movement to the slow manifold, and then the movement along the slow manifold.

Chapter 2

Cellular Homeostasis

2.1   The Cell Membrane

The cell membrane provides a boundary separating the internal workings of the cell from its external environment. More importantly, it is selectively permeable, permitting the free passage of some materials and restricting the passage of others, thus regulating the passage of materials into and out of the cell. It consists of a double layer (a *bilayer*) of phospholipid molecules about 7.5 nm (75 angstroms) thick (Fig. 2.1). The term *lipid* is used to specify a category of water-insoluble, energy rich macromolecules, typical of fats, waxes, and oils. Irregularly dispersed throughout the phospholipid bilayer are aggregates of globular proteins, which are apparently free to move within the layer, giving the membrane a fluid-like appearance. The membrane also contains water-filled pores with diameters of about 0.8 nm, as well as protein-lined pores, called *channels*, which allow passage of specific molecules. Both the intracellular and extracellular environments consist of, among many other things, a dilute aqueous solution of dissolved salts, primarily NaCl and KCl, which dissociate into Na^+, K^+, and Cl^- ions. The cell membrane acts as a barrier to the free flow of these ions and maintains concentration differences of these ions. In addition, the cell membrane acts as a barrier to the flow of water.

Molecules can be transported across the cell membrane by passive or active processes. An active process is one that requires the expenditure of energy, while a passive process results solely from the inherent, random movement of molecules. There are three passive transport mechanisms to transport molecules through the cell membrane. *Osmosis*, i.e., the diffusion of water down its concentration gradient, is the most important process by which water moves through the cell membrane. Simple diffusion accounts for the passage of small molecules through pores and of lipid-soluble molecules through the lipid bilayer. For example, water, urea (a nitrogenous waste product of metabolism), and hydrated Cl^- ions diffuse through membrane pores. Oxygen and carbon dioxide diffuse through the membrane readily because they are soluble in lipids. Sodium and K^+ ions pass through ion-specific channels, driven by diffusion and electrical forces. Some other mechanism must account for the transport of larger sugar molecules such as galactose, glucose, and
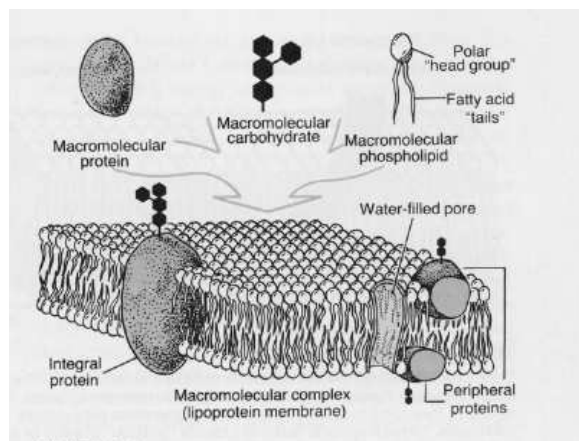
Figure 2.1: Schematic diagram of the cell membrane. (Davis et al., 1985, Fig. 3-1, p. 41.)

sucrose, as they are too large to pass through membrane pores *Carrier-mediated diffusion* occurs when a molecule is bound to a carrier molecule that moves readily through the membrane. For example, the transport of glucose and amino acids across the cell membrane is believed to be by a carrier-mediated process.

Concentration differences are set up and maintained by active mechanisms that use energy to pump ions against their concentration gradient. One of the most important of these pumps is the Na,K-ATPase, which uses the energy stored in ATP molecules to pump Na^+ out of the cell and K^+ in. Another pump, the Ca^{2+}-ATPase, pumps Ca^{2+} out of the cell or into the endoplasmic reticulum. There are also a variety of exchange pumps that use the energy inherent in the concentration gradient of one ion type to pump another ion type against its concentration gradient. For example, the Na^+–Ca^{2+} exchanger removes Ca^{2+} from the cell at the expense of Na^+ entry, and similarly for the Na^+–H^+ exchanger. Typical values for intracellular and extracellular ionic concentrations are given in Table 2.1.

Differences in ionic concentrations create a potential difference across the cell membrane that drives ionic currents. Water is also absorbed into the cell because of concentration differences of these ions and also because of other large molecules contained in the cell, whose presence provides an osmotic pressure for the absorption of water. It is the balance of these forces that regulates both the cell volume and the membrane potential.

2.2   Diffusion

To keep track of a chemical concentration or any other measurable entity, we must track where it comes from and where it goes; that is, we must write a *conservation law*. If U is some chemical species in some region, then the appropriate conservation law takes the following form (in words):

Table 2.1: Typical values for intracellular and extracellular ionic concentrations, Nernst potentials and resting potentials, from three different cell types. Concentrations are given in units of mM, and potentials are in units of mV. Extracellular concentrations for the squid giant axon are for seawater, while those for frog muscle and red blood cells are for plasma. (Adapted from Mountcastle, 1974, Table 1-1.)

	Squid Giant Axon	Frog Sartorius Muscle	Human Red Blood Cell
Intracellular concentrations			
Na^+	50	13	19
K^+	397	138	136
Cl^-	40	3	78
Mg^{2+}	80	14	5.5
Extracellular concentrations			
Na^+	437	110	155
K^+	20	2.5	5
Cl^-	556	90	112
Mg^{2+}	53	1	2.2
Nernst potentials			
V_{Na}	+56	+55	+55
V_K	−77	−101	−86
V_{Cl}	−68	−86	−9
Resting potentials	−65	−99	−6 to −10

rate of change of U=rate of production of U + accumulation of U due to transport.

If Ω is a region of space, this conservation law can be written symbolically as

$$\frac{d}{dt} \int_\Omega u \, dV = \int_\Omega f \, dV - \int_{\partial\Omega} \mathbf{J} \cdot \mathbf{n} \, dA, \tag{2.1}$$

where u is the concentration of the chemical species U, $\partial\Omega$ is the boundary of the region Ω, $\mathbf{n}$ is the outward unit normal to the boundary of Ω, f represents the local production density of U per unit volume, and $\mathbf{J}$ is the flux density of U. According to the divergence theorem, if $\mathbf{J}$ is sufficiently smooth, then

$$\int_{\partial\Omega} \mathbf{J} \cdot \mathbf{n} \, dA = \int_\Omega \nabla \cdot \mathbf{J} \, dV, \tag{2.2}$$

so that if the volume in which u is being measured is fixed but arbitrary, the integrals can be dropped, with the result that

$$\frac{\partial u}{\partial t} = f - \nabla \cdot \mathbf{J}. \tag{2.3}$$

This, being a conservation law, is inviolable. However, there are many ways in which the production term f and the flux $\mathbf{J}$ can vary. Indeed, much of our study in this book is involved in determining appropriate models for production and flux.

2.2.1   Fick's Law

Suppose that u is a function of a single spatial variable, x, and consider the two situations shown in Fig. 2.2, one where u has a steep gradient, the other with a shallow gradient. It is intuitively reasonable that the flux of u should be greater in magnitude in the first case than in the second, and this is indeed what is found experimentally, provided u is not too large. Thus

$$J = -D\frac{du}{dx}. \tag{2.4}$$

Note the sign of J. By definition, a flux of u from left to right is identified as a positive flux, and thus the flux is opposite in sign to the gradient.

In higher dimensions,

$$\mathbf{J} = -D\nabla u. \tag{2.5}$$

Equation (2.5) is called a *constitutive relationship*, and for chemical species it is called *Fick's law*. The scalar D is the *diffusion coefficient* and is characteristic of the solute and the fluid in which it is dissolved. If u represents the heat content of the volume, (2.5) is called *Newton's law of cooling*. Fick's law is not really a law, but is a reasonable approximation to reality if the concentration of the chemical species is not too high. When Fick's law applies, the conservation equation becomes the reaction–diffusion equation

$$\frac{\partial u}{\partial t} = \nabla \cdot (D\nabla u) + f, \tag{2.6}$$

or, if D is a constant,

$$\frac{\partial u}{\partial t} = D\nabla^2 u + f. \tag{2.7}$$

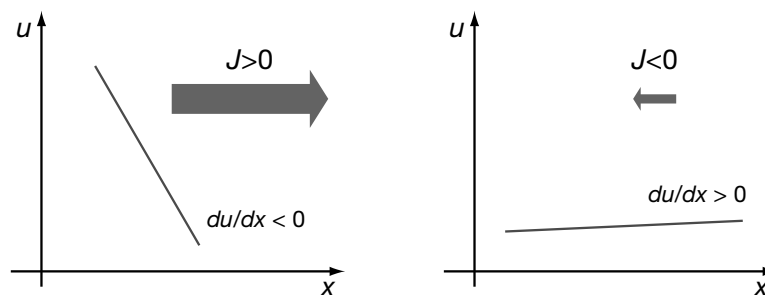The diffusion equation can also be derived from a random walk (Section 2.9.1).

Figure 2.2: Fick's Law. The flux is proportional to the gradient, and opposite in sign.

2.2.2 Diffusion Coefficients

A quantitative understanding of diffusion was given by Einstein (1906) in his theory of Brownian motion. He showed that if a spherical solute molecule is large compared to the solvent molecule, then

$$D = \frac{kT}{6\pi\mu a}, \tag{2.8}$$

where $k = \frac{R}{N_A}$ is Boltzmann's constant, N_A is Avogadro's number, T is the absolute temperature of the solution, μ is the coefficient of viscosity for the solute, and a is the radius of the solute molecule. For nonspherical molecules, Einstein's formula generalizes to

$$D = \frac{kT}{f}, \tag{2.9}$$

where f is the Stokes frictional coefficient of the particle and $f = 6\pi\mu a$ for a sphere. The molecular weight of a spherical molecule is

$$M = \frac{4}{3}\pi a^3 \rho, \tag{2.10}$$

where ρ is the molecular density, so that in terms of molecular weight,

$$D = \frac{kT}{3\mu}\left(\frac{\rho}{6\pi^2 M}\right)^{1/3}. \tag{2.11}$$

The density of most large protein molecules is nearly constant (about $1.3 - 1.4$ g/cm^3), so that $DM^{1/3}$ is nearly the same for spherical molecules at a fixed temperature. The diffusion of small molecules, such as the respiratory gases, is different, being proportional to $M^{-1/2}$.

Table 2.2: Molecular weight and diffusion coefficients of some biochemical substances in dilute aqueous solution.

Substance	Molecular Weight	$D(\text{cm}^2/\text{s})$
hydrogen	1	4.5×10^{-5}
oxygen	32	2.1×10^{-5}
carbon dioxide	48	1.92×10^{-5}
glucose	192	6.60×10^{-6}
insulin	5,734	2.10×10^{-6}
Cytochrome c	13,370	1.14×10^{-6}
Myoglobin	16,900	5.1×10^{-7}
Serum albumin	66,500	6.03×10^{-7}
hemoglobin	64,500	6.9×10^{-7}
Catalase	247,500	4.1×10^{-7}
Urease	482,700	3.46×10^{-7}
Fibrinogen	330,000	1.97×10^{-7}
Myosin	524,800	1.05×10^{-7}
Tobacco mosaic virus	40,590,000	5.3×10^{-8}

2.2.3   Diffusion and Free Energy

It is interesting to note that Fick's law can be interpreted as a gradient flow. Recall from Chapter 1 that the free energy or chemical potential of a dilute chemical species is related to its concentration through

$$G = G^0 + RT \ln u. \tag{2.12}$$

Since this has units of energy per mole, the Gibbs free energy of a single molecule (assuming such a quantity makes sense) is $(G^0 + RT \ln u)/N_A$.

On average, a molecule moves down its Gibbs free energy gradient, and thus down its concentration gradient. Although equilibrium thermodynamics gives no information about the speed at which a molecule moves, it turns out that the speed of movement is linearly proportional to the gradient of the Gibbs free energy. (In a loose sense, the Gibbs free energy is a potential field, and thus its gradient has the units of force. If inertia can be ignored, which it can for molecules, velocity is proportional to force, and thus proportional to ∇G). It follows that

$$\text{velocity} = \frac{RT}{N_A f} \frac{\nabla u}{u} = \frac{kT}{f} \frac{\nabla u}{u}, \tag{2.13}$$

where the constant of proportionality is the frictional coefficient, f.

Finally, since flux is the product of velocity and concentration, we obtain Fick's law,

$$J = u \times \text{velocity} = \frac{kT}{f} \nabla u, \tag{2.14}$$

which confirms Einstein's formula (2.9). Of course, this is not meant to imply that each particle moves with this particular velocity, only that there is an average

velocity with which the bulk moves. We also emphasize that the above is not a rigorous derivation of Fick's Law, but is rather an interpretation thereof, and is meant only to be suggestive of the underlying physical principles.

2.2.4   Diffusion Through a Membrane: Ohm's Law

We can use Fick's law to derive the chemical analogue of Ohm's law for a membrane of thickness L. Suppose that a membrane separates two large reservoirs of a dilute chemical, with concentration c_l on the left (at $x = 0$), and concentration c_r on the right (at $x = L$). According to the diffusion equation, in the membrane (assuming that the only gradients are transverse to the membrane)

$$\frac{\partial c}{\partial t} = D\frac{\partial^2 c}{\partial x^2}, \tag{2.15}$$

subject to boundary conditions $c(0, t) = c_l, c(L, t) = c_r$.

The full time-dependent solution can be found using separation of variables, but for our purposes here, the steady-state solution is sufficient. At steady state, $\frac{\partial c}{\partial t} = 0$, so that $\frac{\partial J}{\partial x} = -D\frac{\partial^2 c}{\partial x^2} = 0$, from which it follows that $J = -D\frac{\partial c}{\partial x} = $ constant, or that $c(x) = ax + b$, for some constants a and b. Applying the boundary conditions, we find

$$c(x) = c_l + (c_r - c_l)\frac{x}{L}. \tag{2.16}$$

From Fick's law it follows that the flux of chemical is constant, independent of x, and is given by

$$J = \frac{D}{L}(c_l - c_r). \tag{2.17}$$

The ratio L/D is the effective "resistance" of the membrane, and so D/L is called the *conductance*, or *permeability*, per unit area.

2.2.5   Diffusion into a capillary

Suppose that a long capillary, open at one end, with uniform cross-sectional area A and filled with water, is inserted into a solution of known chemical concentration C_0, and the chemical species is free to diffuse into the capillary through the open end. Since the concentration of the chemical species depends only on the distance along the tube and time, it is governed by the diffusion equation

$$\frac{\partial c}{\partial t} = D\frac{\partial^2 c}{\partial x^2} \qquad 0 < x < \infty, \qquad t > 0, \tag{2.18}$$

where for convenience we assume that the capillary is infinitely long. Because the solute bath in which the capillary sits is large, it is reasonable to assume that the chemical concentration at the tip is fixed at $C(0, t) = C_0$, and since the tube is initially filled with pure water, $C(x, 0) = 0$.

The solution of this problem is given by

$$C(x, t) = 2C_0\left(1 - \frac{1}{\sqrt{2\pi}}\int_{-\infty}^{z} \exp\left(-\frac{s^2}{2}\right) ds\right), \qquad z = \frac{x}{\sqrt{2Dt}}. \tag{2.19}$$

Table 2.3: Estimates of diffusion times for cellular structures of typical dimensions, computed from the relation $t = x^2/D$ using $D = 10^{-5}$cm^2/s (typical for molecules the size of oxygen or carbon dioxide).

x	t	Example
10 nm	100 ns	Thickness of cell membrane
1 μm	1 ms	size of mitochondrion
10 μm	100 ms	Radius of small mammalian cell
100 μm	10s	Diameter of a large muscle fiber
250 μm	60 s	Radius of squid giant axon
1 mm	16.7 min	Half-thickness of frog sartorius muscle
2 mm	1.1 h	Half-thickness of lens in the eye
5 mm	6.9 h	Radius of mature ovarian follicle
2 cm	2.6 d	Thickness of ventricular myocardium
1 m	31.7 yrs	Length of a (long!) nerve axon

From this, one can easily calculate that the total number of molecules that enter the capillary in a fixed time T is

$$N = A \int_0^\infty C(x,T)dx = 2C_0 A \sqrt{\frac{TD}{\pi}}. \qquad (2.20)$$

From this equation it is possible to determine the diffusion coefficient by solving (2.20) for D, yielding

$$D = \frac{\pi N^2}{4C_0^2 A^2 T}. \qquad (2.21)$$

A second useful piece of information is found from (2.19) by observing that $C(x,t)/C_0$ is constant on any curve for which z is constant. Thus, the curve $t = x^2/D$ is a level curve for the concentration, and gives a measure of how fast the substance is moving into the capillary. The time $t = x^2/D$ is called the *diffusion time* for the process. To give some idea of the effectiveness of diffusion in various cellular contexts, in Table 2.3 is shown typical diffusion times for a variety of cellular structures. Clearly, diffusion is effective for transport when distances are short, but totally inadequate for longer distances, such as along a nerve axon. Obviously, biological systems must employ other transport mechanisms in these situations in order to survive.

2.2.6 Buffered Diffusion

It is often the case that reactants in an enzymatic reaction (as in Chapter 1) are free to diffuse, so that one must keep track of the effects of both diffusion and reaction. Such problems, called *reaction–diffusion systems*, are of fundamental significance in physiology and are also important and difficult mathematically.

An important situation in which reaction and diffusion interact to modify the behavior is when a diffusing species is buffered by a larger diffusing molecule. This occurs, for example, with oxygen in muscle (which we discuss below), or Ca^{2+}, or

hydrogen ions. The earliest studies of the buffered diffusion equation were those of Irving et al. (1990) and Wagner and Keizer (1994), while Neher and his colleagues (Zhou and Neher, 1993; Naraghi and Neher, 1997; Naraghi et al. 1998), have done a great deal of work on Ca^{2+} buffering. More theoretical analyses have been performed by Sneyd et al. (1998), Smith et al. (2001) and Tsai and Sneyd (2006).

Consider a "one-dimensional" cell is which there are hydrogen ions (for example) and buffer. We assume the buffering reaction follows

$$H + B \underset{k_-}{\overset{k_+}{\rightleftharpoons}} HB. \tag{2.22}$$

Conservation implies

$$\frac{\partial u}{\partial t} = D_h \frac{\partial^2 u}{\partial x^2} + k_- w - k_+ uv + f(t, x, u), \tag{2.23}$$

$$\frac{\partial v}{\partial t} = D_b \frac{\partial^2 v}{\partial x^2} + k_- w - k_+ uv, \tag{2.24}$$

$$\frac{\partial w}{\partial t} = D_b \frac{\partial^2 w}{\partial x^2} - k_- w + k_+ uv, \tag{2.25}$$

where $u = [H^+]$, $v = [B]$, and $w = [HB]$. Since the buffer is a large molecule we assume that the diffusion of B and HB is the same. We impose no-flux boundary conditions at the ends of the cell and assume that v and w are initially uniform (for example, if w is initially zero, and the buffer is uniformly distributed). The reaction term $f(t, x, u)$ denotes all the other reactions of u apart from the buffering.

Adding (2.24) and (2.25) we find

$$\frac{\partial(v + w)}{\partial t} = D_b \frac{\partial^2(v + w)}{\partial x^2}. \tag{2.26}$$

Since $v + w$ is initially uniform, it remains uniform for all time, so that $v + w = w_0$, where w_0 is the total amount of buffer.

If the buffering reaction is fast compared to the other reactions (i.e., those described by $f(t, x, u)$) then we can assume u and v to be in quasi-equilibrium, so that

$$k_-(w_0 - v) - k_+ uv = 0, \tag{2.27}$$

which implies that

$$v = \frac{K_{eq} w_0}{K_{eq} + u}, \qquad \text{where} \quad K_{eq} = \frac{k_-}{k_+}. \tag{2.28}$$

Subtracting (2.24) from (2.23) yields

$$\frac{\partial(u - v)}{\partial t} = D_h \frac{\partial^2 u}{\partial x^2} - D_b \frac{\partial^2 v}{\partial x^2} + f(t, x, u). \tag{2.29}$$

However, since we know v as a function of u, we can eliminate v to find a nonlinear reaction diffusion equation for u alone,

$$\frac{\partial}{\partial t} \left(u - \frac{K_{eq} w_0}{K_{eq} + u} \right) = D_h \frac{\partial^2 u}{\partial x^2} - D_b \frac{\partial^2}{\partial x^2} \left(\frac{K_{eq} w_0}{K_{eq} + u} \right) + f(t, x, u). \tag{2.30}$$

We expand some of the derivatives and find

$$\left(1 + \frac{K_{\text{eq}}w_0}{(K_{\text{eq}} + u)^2}\right)u_t = D_h\frac{\partial^2 u}{\partial x^2} + D_b\frac{\partial}{\partial x}\left(\frac{K_{\text{eq}}w_0}{(K_{\text{eq}} + u)^2}u_x\right) + f(t, x, u). \quad (2.31)$$

Letting

$$\theta(u) = \frac{K_{\text{eq}}w_0}{(K_{\text{eq}} + u)^2} \quad (2.32)$$

then gives

$$u_t = \frac{D_h + \theta(u)D_b}{1 + \theta(u)}u_{xx} + \frac{D_b\theta'(u)}{1 + \theta(u)}(u_x)^2 + \frac{f(t, x, u)}{1 + \theta(u)}. \quad (2.33)$$

Thus, buffering gives rise to a nonlinear transport equation with a diffusion coefficient that is a nonlinear function of u.

In some cases it is reasonable to assume that $u \ll K_{\text{eq}}$. In this limit we find that u has an effective diffusion coefficient

$$D_{\text{eff}} = \frac{D_h + D_b\frac{w_0}{K_{\text{eq}}}}{1 + \frac{w_0}{K_{\text{eq}}}}, \quad (2.34)$$

a convex linear combination of the two diffusion coefficients, D_h and D_b. In addition, the reaction terms are scaled by the constant factor $1 + w_0/K_{\text{eq}}$. If, additionally, $D_b = 0$, we recover the usual diffusion equation, but one for which both the diffusion coefficient and the reaction terms are scaled by the same constant factor.

2.3 Facilitated Diffusion

A second important example in which both diffusion and reaction play a role is known as *facilitated diffusion*. Facilitated diffusion occurs when the flux of a chemical is amplified by a reaction that takes place in the diffusing medium. An example of facilitated diffusion occurs with the flux of oxygen in muscle fibers. In muscle fibers, oxygen is bound to myoglobin and is transported as oxymyoglobin, and this transport is greatly enhanced above the flow of oxygen in the absence of myoglobin (Wyman, 1966; Murray, 1971; Murray and Wyman, 1971; Rubinow and Dembo, 1977).

This well-documented observation needs further explanation, because at first glance it seems counterintuitive. Myoglobin molecules are much larger (molecular weight M=16,890) than oxygen molecules (molecular weight M=32) and therefore have a much smaller diffusion coefficient ($D = 4.4 \times 10^{-7}$ and $D = 1.2 \times 10^{-5}\text{cm}^2/\text{s}$ for myoglobin and oxygen, respectively). The diffusion of oxymyoglobin would therefore seem to be much slower than the diffusion of free oxygen. Further, from the calculation in the last section, the diffusion of free oxygen is much slower when it is buffered by myoglobin since the effective diffusion coefficient of oxygen is lowered substantially by diffusion.

To anticipate slightly, the answer is that, at steady state, the total transport of oxygen is the sum of the free oxygen transport and additional oxygen that is transported by the diffusing buffer. If there is a lot of buffer, with a lot of oxygen bound, this additional transport due to the buffer can be substantial.

A simple model of this phenomenon is as follows. Suppose we have a slab reactor containing diffusing myoglobin. On the left (at $x = 0$) the oxygen concentration is held fixed at s_0, and on the right (at $x = L$) it is held fixed at s_L, which is assumed to be less than s_0.

If f is the rate of uptake of oxygen into oxymyoglobin, then equations governing the concentrations of $s = [O_2], e = [Mb], c = [MbO_2]$ are

$$\frac{\partial s}{\partial t} = D_s \frac{\partial^2 s}{\partial x^2} - f, \tag{2.35}$$

$$\frac{\partial e}{\partial t} = D_e \frac{\partial^2 e}{\partial x^2} - f, \tag{2.36}$$

$$\frac{\partial c}{\partial t} = D_c \frac{\partial^2 c}{\partial x^2} + f. \tag{2.37}$$

It is reasonable to take $D_e = D_c$, since myoglobin and oxymyoglobin are nearly identical in molecular weight and structure. Since myoglobin and oxymyoglobin remain inside the slab, it is also reasonable to specify the boundary conditions $\partial e/\partial x = \partial c/\partial x = 0$ at $x = 0$ and $x = L$. Because it reproduces the oxygen saturation curve (discussed in Chapter 13), we assume that the reaction of oxygen with myoglobin is governed by the elementary reaction

$$O_2 + Mb \underset{k_-}{\overset{k_+}{\rightleftharpoons}} MbO_2,$$
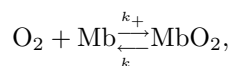
so that (from the law of mass action) $f = -k_- c + k_+ se$. The total amount of myoglobin is conserved by the reaction, so that at steady state $e + c = e_0$ and (2.36) is superfluous.

At steady state,

$$0 = s_t + c_t = D_s s_{xx} + D_c c_{xx}, \tag{2.38}$$

and thus there is a second conserved quantity, namely

$$D_s \frac{ds}{dx} + D_c \frac{dc}{dx} = -J, \tag{2.39}$$

which follows by integrating (2.38) once with respect to x. The constant J (which is yet to be determined) is the sum of the flux of free oxygen and the flux of oxygen in the complex oxymyoglobin, and therefore represents the total flux of oxygen. Integrating (2.39) with respect to x between $x = 0$ and $x = L$, we can express the total flux J in terms of boundary values of the two concentrations as

$$J = \frac{D_s}{L}(s_0 - s_L) + \frac{D_c}{L}(c_0 - c_L), \tag{2.40}$$

although the values c_0 and c_L are as yet unknown.

To further understand this system of equations, we introduce dimensionless variables, $\sigma = \frac{k_+}{k_-} s$, $u = c/e_0$, and $x = Ly$, in terms of which (2.35) and (2.37) become

$$\epsilon_1 \sigma_{yy} = \sigma(1 - u) - u = -\epsilon_2 u_{yy}, \tag{2.41}$$

where $\epsilon_1 = \frac{D_s}{e_0 k_+ L^2}, \epsilon_2 = \frac{D_c}{k_- L^2}$.

Reasonable numbers for the uptake of oxygen by myoglobin (Wittenberg, 1966) are $k_+ = 1.4 \times 10^{10} \text{cm}^3 \, \text{M}^{-1} \text{s}^{-1}$, $k_- = 11 \text{ s}^{-1}$, and $L = 0.022$ cm in a solution with $e_0 = 1.2 \times 10^{-5}$ M/cm^3. (These numbers are for an experimental setup in which the concentration of myoglobin was substantially higher than what naturally occurs in living tissue.) With these numbers we estimate that $\epsilon_1 = 1.5 \times 10^{-7}$, and $\epsilon_2 = 8.2 \times 10^{-5}$. Clearly, both of these numbers are small, suggesting that oxygen and myoglobin are at quasi-steady state throughout the medium, with

$$c = e_0 \frac{s}{K + s}, \tag{2.42}$$

where $K = k_-/k_+$. Now we substitute (2.42) into (2.40) to find the flux

$$
\begin{aligned}
J &= \frac{D_s}{L}(s_0 - s_L) + \frac{D_c}{L} e_0 \left(\frac{s_0}{K + s_0} - \frac{s_L}{K + s_L} \right) \\
&= \frac{D_s}{L}(s_0 - s_L) \left(1 + \frac{D_c}{D_s} \frac{e_0 K}{(s_0 + K)(s_L + K)} \right) \\
&= \frac{D_s}{L}(1 + \mu\rho)(s_0 - s_L), \tag{2.43}
\end{aligned}
$$

where $\rho = \frac{D_c}{D_s} \frac{e_0}{K}, \mu = \frac{K^2}{(s_0+K)(s_L+K)}$.

In terms of dimensionless variables the full solution is given by

$$\sigma(y) + \rho u(y) = y[\sigma(1) + \rho u(1)] + (1 - y)[\sigma(0) + \rho u(0)], \tag{2.44}$$

$$u(y) = \frac{\sigma(y)}{1 + \sigma(y)}. \tag{2.45}$$

Now we see how diffusion can be facilitated by an enzymatic reaction. In the absence of a diffusing carrier, $\rho = 0$ and the flux is purely Fickian, as in (2.17). However, in the presence of carrier, diffusion is enhanced by the factor $\mu\rho$. The maximum enhancement possible is at zero concentration, when $\mu = 1$. With the above numbers for myoglobin, this maximum enhancement is substantial, being $\rho = 560$. If the oxygen supply is sufficiently high on the left side (near $x = 0$), then oxygen is stored as oxymyoglobin. Moving to the right, as the total oxygen content drops, oxygen is released by the myoglobin. Thus, even though the bound oxygen diffuses slowly compared to free oxygen, the quantity of bound oxygen is high (provided that e_0 is large compared to the half saturation level K), so that lots of oxygen is transported. We can also understand that to take advantage of the myoglobin-bound oxygen, the concentration of oxygen must drop to sufficiently low levels so that myoglobin releases its stored oxygen.

To explain it another way, note from (2.43) that J is the sum of two terms, the usual ohmic flux term and an additional term that depends on the diffusion coefficient of MbO$_2$. The total oxygen flux is the sum of the flux of free oxygen and the flux of oxygen bound to myoglobin. Clearly, if oxymyoglobin is free to diffuse, the total flux is thereby increased. But since oxymyoglobin can only diffuse down its gradient, the concentration of oxymyoglobin must be higher on one side than the other.
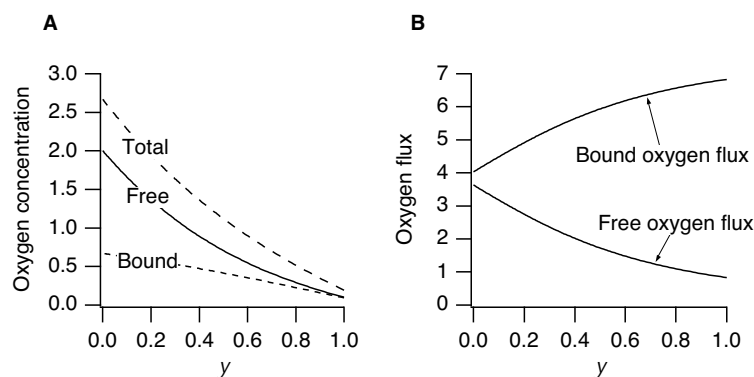
Figure 2.3: A: Free oxygen content $\sigma(y)$ and bound oxygen content $u(y)$ as functions of y. B: Free oxygen flux $-\sigma'(y)$ and bound oxygen flux $-\rho u'(y)$ plotted as functions of y.

In Fig. 2.3A are shown the dimensionless free oxygen concentration σ and the dimensionless bound oxygen concentration u plotted as functions of position. Notice that the free oxygen content falls at first, indicating higher free oxygen flux, and the bound oxygen decreases more rapidly at larger y. Perhaps easier to interpret is Fig. 2.3B, where the dimensionless flux of free oxygen and the dimensionless flux of bound oxygen are shown as functions of position. Here we can see that as the free oxygen concentration drops, the flux of free oxygen also drops, but the flux of bound oxygen increases. For large y, most of the flux is due to the bound oxygen. For these figures, $\rho = 10, \sigma(0) = 2.0, \sigma(1) = 0.1$.

One mathematical detail that was ignored in this discussion is the validity of the quasi-steady-state solution (2.42) as an approximation of (2.41). Usually, when one makes an approximation to boundary value problems in which the order of the system is reduced (as here where the order is four, and drops by two when ϵ_1 and ϵ_2 are ignored), there are difficulties with the solution at the boundary, because the boundary conditions cannot, in general, be met. Such problems, discussed briefly in Chapter 1 in the context of enzyme kinetics, are called *singular perturbation problems*, because the behavior of the solutions as functions of the small parameters is not regular, but singular (certain derivatives become infinitely large as the parameters approach zero). In this problem, however, there are no boundary layers, and the quasi-steady-state solution is a uniformly valid approximation to the solution. This occurs because the boundary conditions on c are of no-flux (Neumann) type, rather than of fixed (Dirichlet) type. That is, since the value of c is not specified by the boundary conditions, c is readily adjusted so that there are no boundary layers. Only a slight correction to the quasi-steady-state solution is needed to meet the no-flux boundary conditions, but this correction affects only the derivative, not the value, of c in a small region near the boundaries.

2.3.1   Facilitated Diffusion in Muscle Respiration

Even at rest, muscle fibers consume oxygen. This is because ATP is constantly consumed to maintain a nonzero membrane potential across a muscle cell wall, and this consumption of energy requires constant metabolizing of sugar, which consumes oxygen. Although sugar can be metabolized anaerobically, the waste product of this reaction is lactic acid, which is toxic to the cell. In humans, the oxygen consumption of live muscle tissue at rest is about 5×10^{-8} mol/cm^{3}s, and the concentration of myoglobin is about 2.8×10^{-7} mol/cm^3. Thus, when myoglobin is fully saturated, it contains only about a 5 s supply of oxygen. Further, the oxygen at the exterior of the muscle cell must penetrate to the center of the cell to prevent the oxygen concentration at the center falling to zero, a condition called *oxygen debt*.

To explain how myoglobin aids in providing oxygen to a muscle cell and helps to prevent oxygen debt, we examine a model of oxygen consumption that includes the effects of diffusion of oxygen and myoglobin. We suppose that a muscle fiber is a long circular cylinder (radius $a = 2.5 \times 10^{-3}$ cm) and that diffusion takes place only in the radial direction. We suppose that the oxygen concentration at the boundary of the fiber is a fixed constant and that the distribution of chemical species is radially symmetric. With these assumptions, the steady-state equations governing the diffusion of oxygen and oxymyoglobin are

$$D_s \frac{1}{r}\frac{d}{dr}\left(r\frac{ds}{dr} \right) - f - g = 0, \tag{2.46}$$

$$D_c \frac{1}{r}\frac{d}{dr}\left(r\frac{dc}{dr} \right) + f = 0, \tag{2.47}$$

where, as before, $s = [O_2]$, $c = [MbO_2]$, and $f = -k_-c + k_+se$. The coordinate r is in the radial direction. The new term in these equations is the constant g, corresponding to the constant consumption of oxygen. The boundary conditions are $s = s_a, dc/dr = 0$ at $r = a$, and $ds/dr = dc/dr = 0$ at $r = 0$. For muscle, s_a is typically 3.5×10^{-8} mol/cm^3 (corresponding to the partial pressure 20 mm Hg). Numerical values for the parameters in this model are difficult to obtain, but reasonable numbers are $D_s = 10^{-5}$ cm^2/s, $D_c = 5 \times 10^{-7}$ cm^2/s, $k_+ = 2.4 \times 10^{10}$ cm^3/mol$\cdot$s, and $k_- = 65$/s (Wyman, 1966).

Introducing nondimensional variables $\sigma = \frac{k_+}{k_-}s$, $u = c/e_0$, and $r = ay$, we obtain the differential equations

$$\epsilon_1 \frac{1}{y}\frac{d}{dy}\left(y\frac{d\sigma}{dy} \right) - \gamma = \sigma(1-u) - u = -\epsilon_2 \frac{1}{y}\frac{d}{dy}\left(y\frac{du}{dy} \right), \tag{2.48}$$

where $\epsilon_1 = \frac{D_s}{e_0 k_+ a^2}, \epsilon_2 = \frac{D_c}{k_- a^2}, \gamma = g/k_-$. Using the parameters appropriate for muscle, we estimate that $\epsilon_1 = 2.3 \times 10^{-4}, \epsilon_2 = 1.2 \times 10^{-3}, \gamma = 3.3 \times 10^{-3}$. While these numbers are not as small as for the experimental slab described earlier, they are small enough to warrant the assumption that the quasi-steady state approximation (2.42) holds in the interior of the muscle fiber.

It also follows from (2.48) that

$$\epsilon_1 \frac{1}{y}\frac{d}{dy}\left(y\frac{d\sigma}{dy} \right) + \epsilon_2 \frac{1}{y}\frac{d}{dy}\left(y\frac{du}{dy} \right) = \gamma. \tag{2.49}$$

We integrate (2.49) twice with respect to y to find

$$\epsilon_1 \sigma + \epsilon_2 u = A \ln y + B + \frac{\gamma}{4} y^2. \tag{2.50}$$

The constants A and B are determined by boundary conditions. Since we want the solution to be bounded at the origin, $A = 0$, and B is related to the concentration at the origin.

Now suppose that there is just enough oxygen at the boundary to prevent oxygen debt. In this model, oxygen debt occurs if σ falls to zero. Marginal oxygen debt occurs if $\sigma = u = 0$ at $y = 0$. For this boundary condition, we take $A = B = 0$. Then the concentration at the boundary must be at least as large as σ_0, where, using the quasi-steady state $\sigma(1 - u) = u$,

$$\sigma_0 + \rho \frac{\sigma_0}{\sigma_0 + 1} = \frac{\gamma}{4\epsilon_1}, \tag{2.51}$$

and where $\rho = \epsilon_2/\epsilon_1$. Otherwise, the center of the muscle is in oxygen debt. Note also that σ_0 is a decreasing function of ρ, indicating a reduced need for external oxygen because of facilitated diffusion.

A plot of this critical concentration σ_0 as a function of the scaled consumption $\frac{\gamma}{4\epsilon_1}$ is shown in Fig. 2.4. For this plot $\rho = 5$, which is a reasonable estimate for muscle. The dashed curve is the critical concentration when there is no facilitated diffusion ($\rho = 0$). The easy lesson from this plot is that facilitated diffusion decreases the likelihood of oxygen debt, since the external oxygen concentration necessary to prevent oxygen debt is smaller in the presence of myoglobin than without.

A similar lesson comes from Fig. 2.5, where the internal free oxygen content σ is shown, plotted as a function of radius y. The solid curves show the internal free oxygen with facilitated diffusion, and the dashed curve is without. The smaller of the two solid curves and the dashed curve have exactly the critical external oxygen concentration, showing clearly that in the presence of myoglobin, oxygen debt is less likely at a given external oxygen concentration. The larger of the two solid curves has the same external oxygen concentration as the dashed curve, showing again the contribution of facilitation toward preventing oxygen debt. For this figure, $\rho = 5$, $\gamma/\epsilon_1 = 14$.

2.4 Carrier-Mediated Transport

Some substances are insoluble in the cell membrane and yet pass through by a process called *carrier-mediated transport*. It is also called *facilitated diffusion* in many physiology books, although we prefer to reserve this expression for the process described in the previous section. Carrier-mediated transport is the means by which some sugars cross the cell membrane to provide an energy source for the cell. For example, glucose, the most important of the sugars, combines with a carrier protein at the outer boundary of the membrane, and by means of a conformational change is released from the inner boundary of the membrane.

There are three types of carrier-mediated transport. Carrier proteins that transport a single solute from one side of the membrane to the other are called *uniports*.
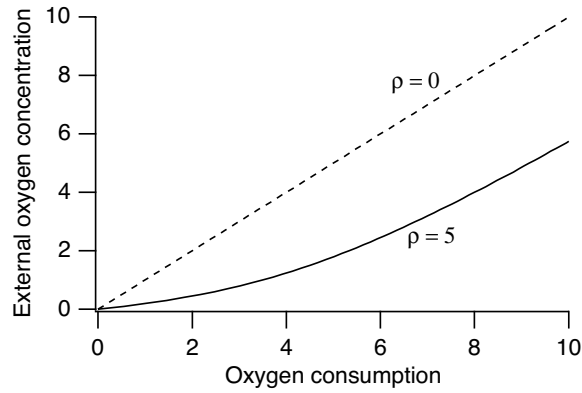
Figure 2.4: Critical concentration σ_0 plotted as a function of oxygen consumption $\frac{\gamma}{4\epsilon_1}$. The dashed curve is the critical concentration with no facilitated diffusion.
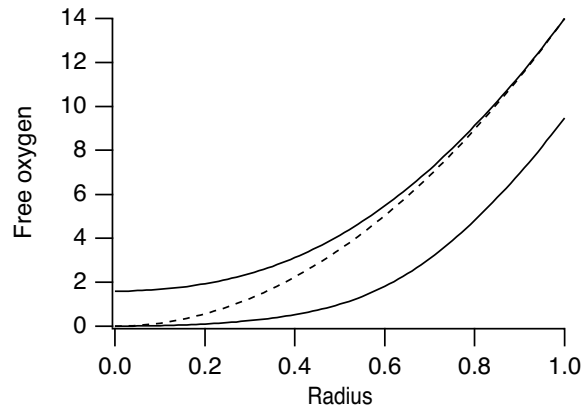

Figure 2.5: Free oxygen σ as a function of radius y. Solid curves show oxygen concentration in the presence of myoglobin ($\rho = 5$), the lower of the two having the critical external oxygen concentration. The dashed curve shows the oxygen concentration without facilitation at the critical external concentration level.
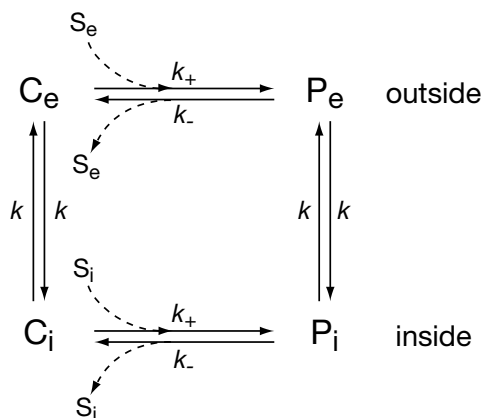
Figure 2.6: Schematic diagram of the glucose transporter described by (2.52-2.55).

Other proteins function as coupled transporters by which the simultaneous transport of two solute molecules is accomplished, either in the same direction (called a *symport*) or in the opposite direction (called an *antiport*).

2.4.1 Glucose Transport

Although the details are not certain, the transport of glucose across the lipid bilayer of the cell membrane is thought to occur when the carrier molecule alternately exposes the solute binding site first on one side and then on the other side of the membrane. It is considered highly unlikely that the carrier molecule actually diffuses back and forth through the membrane.

We can model the process of glucose transport as follows: We suppose that the population of enzymatic carrier proteins C has two conformational states, C_i and C_e, with its glucose binding site exposed on the cell interior (subscript i) or exterior (subscript e) of the membrane, respectively. The glucose substrate on the interior S_i can bind with C_i and the glucose substrate on the exterior can bind with enzyme C_e to form the complex P_i or P_e, respectively. Finally, a conformational change transforms P_i into P_e and vice versa. These statements are summarized in Fig. 2.6.

The equations describing this model are

$$\frac{dp_i}{dt} = kp_e - kp_i + k_+s_ic_i - k_-p_i, \tag{2.52}$$

$$\frac{dp_e}{dt} = kp_i - kp_e + k_+s_ec_e - k_-p_e, \tag{2.53}$$

$$\frac{dc_i}{dt} = kc_e - kc_i + k_-p_i - k_+s_ic_i, \tag{2.54}$$

$$\frac{dc_e}{dt} = kc_i - kc_e + k_-p_e - k_+s_ec_e. \tag{2.55}$$

where $s_i = [S_i]$, $p_i = [P_i]$, etc. Since the total amount of receptor is conserved,
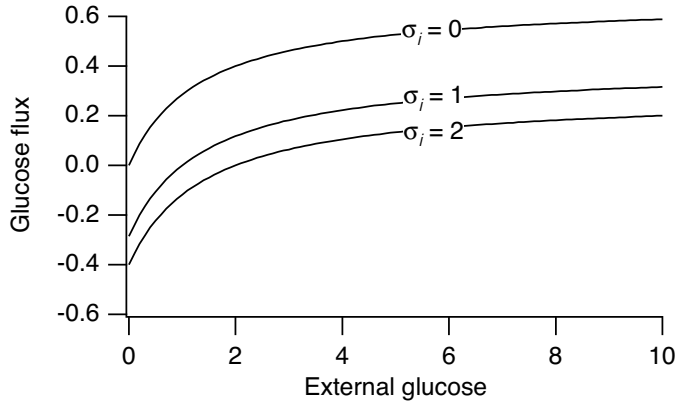
Figure 2.7: Plot of the (nondimensional) flux of glucose as a function of extracellular glucose, for fixed intracellular glucose, with $\kappa = K_d/K = 0.5$.

we have $p_i + p_e + c_i + c_e = C_0$, where C_0 is a constant (the total transporter concentration). Hence there are only three independent equations, not four. The flux, J, is

$$J = k_- p_i - k_+ s_i c_i = k_+ s_e c_e - k_- p_e. \tag{2.56}$$

We find the steady-state flux by setting all derivatives to zero and solving the resulting algebraic system. It follows that

$$J = \frac{1}{2} K_d K k_+ C_0 \frac{s_e - s_i}{(s_i + K + K_d)(s_e + K + K_d) - K_d^2}, \tag{2.57}$$

where $K = k_-/k_+$ and $K_d = k/k_+$. Since k is the rate at which conformational change takes place, it acts like a diffusion coefficient in that it reflects the effect of random thermal activity at the molecular level.

The nondimensional flux is

$$j = \frac{\sigma_e - \sigma_i}{(\sigma_i + 1 + \kappa)(\sigma_e + 1 + \kappa) - \kappa^2}, \tag{2.58}$$

where $\sigma_i = s_i/K, \sigma_e = s_e/K, \kappa = K_d/K$. A plot of this nondimensional flux is shown in Fig. 2.7, plotted as a function of extracellular glucose σ_e, with fixed intracellular glucose and fixed κ. We can see that the rate of transport is limited by saturation of the enzyme kinetics (this saturation is observed experimentally) and thermal conformational change is crucial to the transport process, as transport J drops to zero if $K_d = 0$. The binding affinity of the carrier protein for glucose (k_+), and hence the flux of glucose, is controlled by insulin.

It is important to recognize that the above expression for J is for the steady-state flux only. If the system is not at steady state, then then the flux from the outside onto the transporter, $J_{\text{on}} = k_+ s_e c_e - k_- p_e$, need not be the same as the flux off the transporter to the inside, $J_{\text{off}} = k_- p_i - k_+ s_i c_i$. Obviously, in this case the differential equations must be solved to obtain J_{on} and J_{off}.
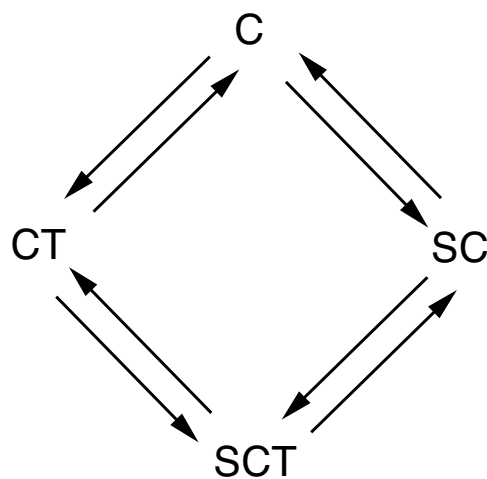
Figure 2.8: States and possible transitions of a transporter with two substrates, S and T, and one binding site for each.

2.4.2 Symports and Antiports

Models for symport and antiport transporters follow in similar fashion. For a symport the protein carrier has multiple binding sites, which can be exposed to the intracellular or extracellular space. A change of conformation exchanges the location of all of the participating binding sites, from inside to outside, or vice versa. An example of a symport is the sodium-driven glucose symport that transports glucose and sodium from the lumen of the gut to the intestinal epithelium. A similar process occurs in epithelial cells lining the proximal tubules in the kidney, to remove glucose and amino acids from the filtrate (discussed in Chapter 17). Five different amino acid cotransporters have been identified.

If there are k binding sites that participate in the exchange, then there are 2^k possible combinations of bound and unbound sites. The key assumption that makes this model of transport work is that only the completely unbound or completely bound carrier participates in a conformational change. Thus, there is a carrier molecule, say C, with two conformations, C_i and C_e, and a fully bound complex P, also with two conformations, P_i and P_e, and possible transformation between the two conformations,

$$C_i \underset{k_{-c}}{\overset{k_c}{\rightleftharpoons}} C_e, \qquad P_i \underset{k_{-p}}{\overset{k_p}{\rightleftharpoons}} P_e. \tag{2.59}$$
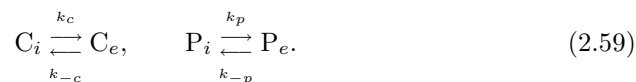
In addition, there are 2^k possible combinations of binding and unbinding in each of the two conformations. For example, with two substrates S and T, and one binding site for each, we have the complexes C, SC, CT, and SCT = P. The possible reactions are summarized in Fig. 2.8.

Unfortunately, the analysis of this fully general reaction scheme is quite compli-

cated. However, it simplifies significantly if we assume that the intermediates can be safely ignored and postulate the multi-molecular reaction scheme

$$m\text{S} + n\text{T} + \text{C} \underset{k_-}{\overset{k_+}{\rightleftharpoons}} \text{P}. \tag{2.60}$$

Now the result for a symport is strikingly similar to the uniport flux, with

$$J = \frac{1}{2} K_d K k_+ C_0 \frac{s_e^m t_e^n - s_i^m t_i^n}{(s_i^m t_i^n + K + K_d)(s_e^m t_e^n + K + K_d) - K_d^2}, \tag{2.61}$$

where the flux of s is mJ and the flux of t is nJ. Here we have set $k_c = k_{-c} = k_p = k_{-p} = k$ and then $K = k_-/k_+$ and $K_d = k/k_+$.

For an antiport, the subscripts on one of the substances must be exchanged, to give

$$J = \frac{1}{2} K_d K k_+ C_0 \frac{s_e^m t_i^n - s_i^m t_e^n}{(s_i^m t_e^n + K + K_d)(s_e^m t_i^n + K + K_d) - K_d^2}. \tag{2.62}$$

The effectiveness of this type of exchanger is determined by the coefficients m and n. For this antiport, flux is positive (S flows inward and T flows outward) if

$$\left(\frac{s_e}{s_i}\right)^m > \left(\frac{t_e}{t_i}\right)^n. \tag{2.63}$$

For example, for the $\text{Na}^+ - \text{Ca}^{2+}$ exchanger (which is discussed in more detail in the next section) for which $m = 1$ and $n = 3$, a ratio of extracellular to intracellular Na^+ of about 8 can be used to effectively pump Ca^{2+} out of a cell even when the ratio of extracellular to intracellular Ca^{2+} is 500.

2.4.3   Sodium-Calcium Exchange

For the glucose transporter described above, membrane flux is driven by a concentration difference of glucose across the membrane, and if glucose concentrations equilibrate, the transmembrane flux becomes zero. However, because it relies on two concentration differences, an antiport transporter such as the Na^+–Ca^{2+} exchanger, can act as a pump. Although this transporter is a passive pump (because it consumes no chemical energy directly) it is often described as a secondarily active pump; it uses the Na^+ gradient to pump Ca^{2+} out of the cell against its concentration gradient, but energy is required to establish and maintain the Na^+ gradient. Na^+–Ca^{2+} exchange is an important mechanism for Ca^{2+} removal in a number of cell types, particularly cardiac ventricular cells, in which much of the Ca^{2+} that enters the cell during an action potential is removed from the cell by the Na^+–Ca^{2+} exchanger (Chapter 12). It has therefore been studied extensively, and a number of highly detailed models have been constructed (Hilgemann, 2004; Kang and Hilgemann, 2004). Here we describe a simple model of this important transporter.

In our model (see Fig. 2.9), E_i is the exchanger protein in the conformation for which the binding sites are exposed to the interior of the cell, and E_e is the conformation for which the binding sites are exposed to the exterior. Starting at state X_1 in the top left of the figure, the exchanger can bind Ca^{2+} inside the cell,
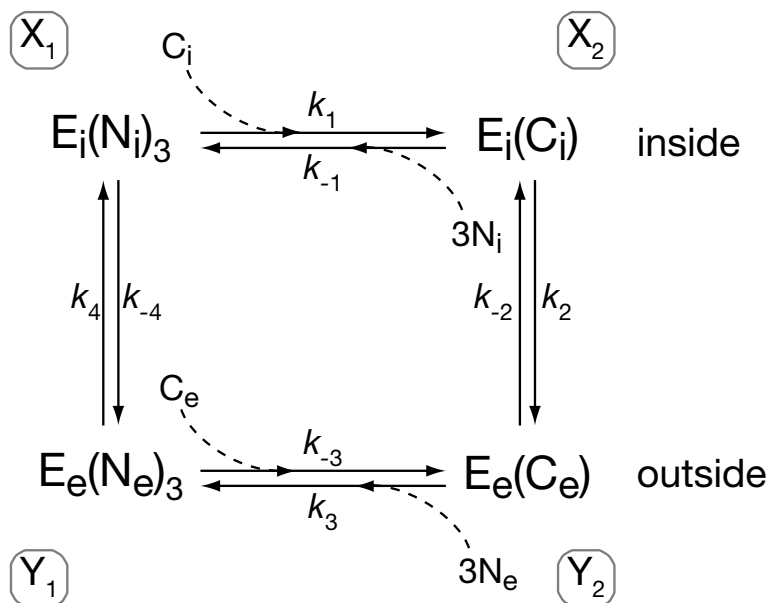
Figure 2.9: Schematic diagram of a simple model of the Na^+-Ca^{2+} exchanger.

simultaneously releasing 3 Na^+ ions to the interior. A change of conformation to E_e then allows the exchanger to release the Ca^{2+} to the outside and bind three external Na^+. A return to the E_i conformation completes the cycle. Of course, it is a crude approximation to assume that one Ca^{2+} and 3 Na^+ ions bind or unbind the exchanger simultaneously.

It is now straightforward to calculate the steady flux for this model. As with the previous transporter models, we first solve for the steady-state values of x_1, x_2, y_1 and y_2, the fraction of exchangers in the state X_1, X_2, Y_1 and Y_2, respectively. There are four equations; three differential equations for exchanger states and one conservation equation. These are

$$\frac{dx_1}{dt} = k_{-1}n_i^3 x_2 + k_4 y_1 - (k_1 c_i + k_{-4})x_1, \tag{2.64}$$

$$\frac{dx_2}{dt} = k_{-2}y_2 + k_1 c_i x_1 - (k_2 + k_{-1}n_i^3)x_2, \tag{2.65}$$

$$\frac{dy_1}{dt} = k_{-4}x_1 + k_3 n_e^3 y_2 - (k_4 + k_{-3}c_e)y_1, \tag{2.66}$$

$$1 = x_1 + x_2 + y_1 + y_2. \tag{2.67}$$

Here, c and n denote, respectively, Ca^{2+} and Na^+ concentration, and the subscripts e or i represent external or internal concentrations.

Note that by taking $x_1 + x_2 + y_1 + y_2 = 1$, we have made a subtle but significant shift of notation, which can be interpreted in two equivalent ways. First, we can interpret the model as referring to a population of exchangers, in which case each variable refers to the fraction of exchangers in the relevant state, and the model

describes the mean behavior of the population. Alternately, we can interpret this model as referring to the behavior of a single exchanger, in which case the variables are probabilities of being in a given state, and the exchanger is modeled as a Markov process (see the Appendix to this chapter).

Using a symbolic package such as Maple, the steady-state solution of these equations is easily calculated. The flux, J, is found to be

$$
\begin{aligned}
J &= k_4 y_1 - k_{-4} x_1 \\
&= \frac{k_1 k_2 k_3 k_4 (c_i n_e^3 - K_1 K_2 K_3 K_4 c_e n_i^3)}{16 \text{ positive terms}},
\end{aligned}
\tag{2.68}
$$

where, as usual, $K_i = k_{-i}/k_i$.

Notice that the units of the flux J here (1/time) are different than in the previous examples (concentration/time), because here the variables x_i and y_i are fractions of exchangers in a particular state (or probabilities) rather than concentrations of exchangers in a particular state. Hence, the flux in this model is a turnover rate, i.e., how many times the exchanger goes around the cycle per unit time. This can easily be converted to a concentration per time if the concentration of the exchangers is known.

An electrogenic exchanger

An important difference between the $Na^+ - Ca^{2+}$ exchange process and the transport processes discussed previously is that Na^+ and Ca^{2+} are ions. Since each cycle of the Na^+-Ca^{2+} exchanger transports two positive charges out and three positive charges in, it generates an electric current. Such exchangers are said to be *electrogenic.*

As is discussed in Section 2.6, most cells have an electrical potential difference across their membranes. Clearly, additional work is necessary for the exchanger to move electric current against a potential difference. To take this into account, consider a ligand, L, with a charge z, and suppose that there is a process that moves L from the cell interior with potential V_i to the cell exterior with potential V_e, i.e.,

$$
L_i \to L_e.
\tag{2.69}
$$

The change in chemical potential for this reaction is

$$
\begin{aligned}
\Delta G &= G_{L_e}^0 + RT \ln([L_e]) + zFV_e - G_{L_i}^0 - RT \ln([L_i]) - zFV_i, \\
&= RT \ln \left(\frac{[L_e]}{[L_i]} \right) - zFV,
\end{aligned}
\tag{2.70}
$$

where $V = V_i - V_e$ is the transmembrane potential. The standard free energy for L is the same on both sides of the membrane, so $G_{L_e}^0 = G_{L_i}^0$. At equilibrium, $\Delta G = 0$, so that

$$
K = \frac{[L_i]_{eq}}{[L_e]_{eq}} = \exp \left(\frac{-zFV}{RT} \right),
\tag{2.71}
$$

where K is the equilibrium constant for the reaction.

For the Na^+–Ca^{2+} exchanger, the overall reaction begins with 3 Na^+ outside the cell and 1 Ca^{2+} inside the cell, and ends with 3 Na^+ inside the cell and 1 Ca^{2+} outside. We can write this as

$$3Na_e^+ + Ca_i^{2+} \longrightarrow 3Na_i^+ + Ca_e^{2+}. \tag{2.72}$$

The change in chemical potential for this reaction is

$$\Delta G = RT \ln\left(\frac{n_i^3 c_e}{n_e^3 c_i}\right) + FV. \tag{2.73}$$

At equilibrium, we must have $\Delta G = 0$ in which case

$$\frac{n_{i,\mathrm{eq}}^3 c_{e,\mathrm{eq}}}{n_{e,\mathrm{eq}}^3 c_{i,\mathrm{eq}}} = \exp\left(-\frac{FV}{RT}\right). \tag{2.74}$$

Recall that detailed balance requires that, around any closed reaction loop the product of the forward rates must be the same as the product of the reverse rates. It follows that

$$k_1 c_{i,\mathrm{eq}} k_2 k_3 n_{e,\mathrm{eq}}^3 k_4 = n_{i,\mathrm{eq}}^3 k_{-1} k_{-4} c_{e,\mathrm{eq}} k_{-3} k_{-2}, \tag{2.75}$$

and thus

$$K_1 K_2 K_3 K_4 = \frac{c_{i,\mathrm{eq}}}{c_{e,\mathrm{eq}}} \frac{n_{e,\mathrm{eq}}^3}{n_{i,\mathrm{eq}}^3}. \tag{2.76}$$

Combining (2.75) and (2.76), we get

$$K_1 K_2 K_3 K_4 = \exp\left(\frac{FV}{RT}\right), \tag{2.77}$$

which, being independent of the concentrations, must hold in general.

It follows from (2.68) that the flux is given by

$$J = \frac{k_1 k_2 k_3 k_4 (c_i n_e^3 - e^{\frac{FV}{RT}} c_e n_i^3)}{16 \text{ positive terms}}. \tag{2.78}$$

All of the terms in the denominator are cubic products of rate constants, so that the flux J has units of inverse time. In general, the denominator of this expression also contains terms that depend on the membrane potential difference.

In writing (2.77), no assumption was made about where the charge transfer takes place. From Fig. 2.9 it might appear that the charge transfer takes place during the transitions $Y_1 \to X_1$ and $X_2 \to Y_2$. However, this is not necessarily the case. It could be that those conformational changes are accompanied by no charge transfer, but that the charge transfer occurs during other transitions. However, if we assume that one Ca^{2+} ion is transferred from inside to outside during the $X_2 \to Y_2$ transition, and three Na^+ ions are transferred during the $Y_1 \to X_1$ transition, free energy arguments yield the additional constraints.

$$\frac{k_{-2}}{k_2} = \tilde{K}_2 \exp\left(\frac{-2FV}{RT}\right), \qquad \frac{k_4}{k_{-4}} = \tilde{K}_4^{-1} \exp\left(\frac{-3FV}{RT}\right), \tag{2.79}$$

where $\tilde{K}_2$ and $\tilde{K}_4$ are independent of voltage, and where $K_1\tilde{K}_2K_3\tilde{K}_4 = 1$.

The most important observation is that for given n_i and n_e (set by other mechanisms such as the Na,K-ATPase discussed in the next section), a negative V enhances the rate at which the Na^+-Ca^{2+} exchanger removes Ca^{2+} from the cell. This makes sense; if V is negative, the potential inside the cell is negative compared to the outside and thus it is easier for the exchanger to move one positive charge into the cell. Since cells typically have a negative resting potential (Section 2.6), the electrogenic nature of the exchanger increases its ability to remove Ca^{2+} in resting conditions. To be specific, if the ratio of extracellular to intracellular Na^+ is 8, and the potential difference $V = -85$ mV (which is typical), Ca^{2+} is removed provided

$$\frac{c_i}{c_e} > \frac{n_i^3}{n_e^3}e^{\frac{FV}{RT}} = 7 \times 10^{-5}. \tag{2.80}$$

Notice that the difference in potential gives an improvement in the capability of the pump by a factor of 27 over a pump that is not electrogenic.

2.5   Active Transport

The carrier-mediated transport described above is always down electrochemical gradients, and so is identified with diffusion. Any process that works against gradients requires the expenditure of energy.

There are three primary means by which cells use energy to pump chemical species. The first is to keep the concentration of the cargo in the downstream domain small by binding or modifying it in some way. A binding protein in one compartment could sequester the transported cargo, or the cargo could be covalently modified in one compartment so that it no longer interacts with the transporter. For example, the flux of glucose is inward because intracellular glucose is quickly phosphorylated, thereby keeping the concentration of intracellular glucose low. However, phosphorylation of intracellular glucose requires the hydrolysis of an ATP molecule, from which the needed energy is extracted.

The second means is to use the gradient of one species to pump another species against its gradient. This is the mechanism of the $Na^+ - Ca^{2+}$ exchanger as well as numerous other exchangers that use to advantage the energy stored in the Na^+ gradient.

The third means is to regulate the binding of the cargo to the transporter in such a way that binding to the transporter is favored in one compartment and unbinding is favored in the other compartment. This change in affinity is driven by the hydrolysis of ATP or GTP. One important example of such an active (energy-consuming) exchanger is the sodium–potassium ATPase pump (Na,K-ATPase). This pump acts as an antiport, actively pumping Na^+ ions out of the cell and pumping K^+ ions in, each against a steep electrochemical gradient. It accomplishes this by using the energy released by the hydrolysis of ATP, and thus is called an ATPase. As is described later in this chapter, the Na,K-ATPase is important for regulating the cell volume and maintaining a membrane potential. Indeed, almost a third of the energy requirement of a typical animal cell is consumed in fueling this pump; in electrically active nerve cells, this figure approaches two-thirds of the cell's energy requirement.
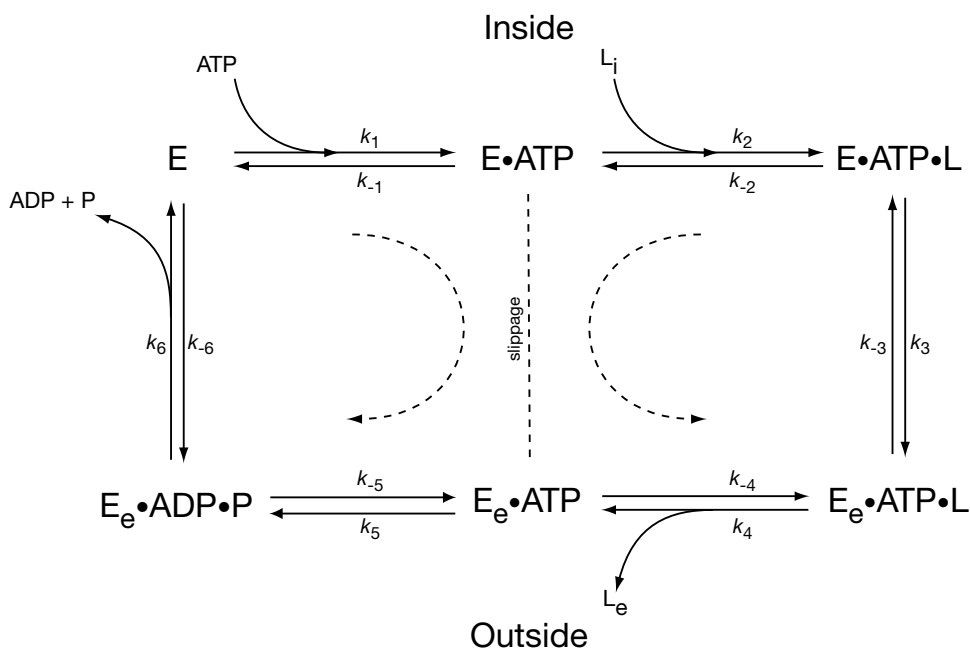
Figure 2.10: Schematic diagram of an ATPase pump that transports one ligand, L, from the inside to the outside against its concentration gradient. For each L transported, one molecule of ATP is hydrolyzed. A subscript e denotes the ATPase conformation in which the L binding sites are exposed to the exterior of the cell.

Other important ATPases are the Sarco/Endoplasmic Reticulum Calcium ATPase pumps (SERCA pumps) that pump Ca^{2+} into the endoplasmic or sarcoplasmic reticulum, or the plasma membrane Ca^{2+} ATPases, which pump Ca^{2+} out of the cell.

2.5.1 A Simple ATPase

We begin by considering a model of an ATPase that pumps a ligand, L, up its concentration gradient (Fig. 2.10). This hypothetical ATPase exists in six states. E is the base state; ATP can bind to E, followed by binding of the ligand L, to form the top line of states in Fig. 2.10. In each of these states the L binding site is exposed to the inside of the cell. Once ATP and L are bound, the ATPase changes conformation, exposing the L binding site to the outside, and at the same time decreasing the affinity of L for its binding site. Thus, L leaves the ATPase, followed by the hydrolysis of ATP, and eventual return of the ATPase to its base state to complete the cycle. The overall cycle results in the transport of one L molecule from inside to outside. Although a realistic ATPase cycle is considerably more complicated than this one, this simple model serves to illustrate the basic

principles.

If there is also a transition from E·ATP to E_e·ATP, as shown by the dashed line, then the overall cycle can break into two separate sub-cycles as indicated. This is called *slippage*, as each of the sub-cycles accomplishes nothing toward the goal of pumping L. The sub-cycle on the left goes naturally in a clockwise direction and hydrolyzes ATP to ADP and inorganic phosphate, P_i, without using this energy to pump L. Similarly, the sub-cycle on the right goes naturally in the direction that allows L to flow down its concentration gradient. The energy of the ATP is used to pump L against its gradient only when the ATPase proceeds around the entire cycle.

We use the law of mass action to write the differential equations for the six ATPase states. For example,

$$\frac{d[\text{E}]}{dt} = k_{-1}[\text{E} \cdot \text{ATP}] + k_6[\text{E}_e \cdot \text{ADP} \cdot \text{P}_i] - (k_1[\text{ATP}] + k_{-6}[\text{P}_i][\text{ADP}])[\text{E}], \quad (2.81)$$

with similar equations for each of the other states. The steady-state flux, J, is given by

$$J = k_1[\text{ATP}][\text{E}] - k_{-1}[\text{E} \cdot \text{ATP}]. \quad (2.82)$$

Even a relatively simple model of six states gives a long expression for the steady-state flux. In this case, (with no slippage)

$$J = \frac{\frac{[\text{ATP}][\text{L}_i]}{[\text{ADP}][\text{P}_i][\text{L}_e]} - K_1 K_2 K_3 K_4 K_5 K_6}{\phi}, \quad (2.83)$$

where $\phi > 0$ is a complicated function of rate constants and concentrations, and where, as usual, $K_i = k_{-i}/k_i$. (Even though it is not obvious from the way it is written, the flux J has, as before, units of inverse time.)

Since detailed balance requires

$$\prod_{i=1}^{6} K_i = \frac{[\text{L}_i]_{\text{eq}}}{[\text{L}_e]_{\text{eq}}} \frac{[\text{ATP}]_{\text{eq}}}{[\text{ADP}]_{\text{eq}}[\text{P}_i]_{\text{eq}}}, \quad (2.84)$$

it follows that

$$J = \frac{\frac{[\text{L}_i]}{[\text{L}_e]} \frac{[\text{ATP}]}{[\text{ADP}][\text{P}_i]} - \frac{[\text{L}_i]_{\text{eq}}}{[\text{L}_e]_{\text{eq}}} \frac{[\text{ATP}]_{\text{eq}}}{[\text{ADP}]_{\text{eq}}[\text{P}_i]_{\text{eq}}}}{\phi}. \quad (2.85)$$

We see from the numerator that the flux is either positive or negative depending on how far the concentrations of L, ATP, ADP and P_i are from their equilibrium concentrations. In general, [ATP] is much higher than its equilibrium concentration (due to other processes in the cell that are continually generating ATP) and it is this that causes a positive pump flux, pumping L against its gradient. However, if $[\text{L}_e]$ is high enough it can force the pump to work in reverse, allowing L to move from the outside to the inside of the cell, generating ATP in the process.

To relate the rate constants to the change in free energy we use that the overall reaction is

$$\text{L}_i + \text{ATP} \longrightarrow \text{L}_e + \text{ADP} + \text{P}_i. \quad (2.86)$$
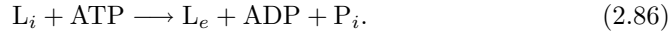
The change in free energy is given by

$$
\begin{aligned}
\Delta G &= G_{\text{ADP}} + G_{\text{P}_i} + G_{\text{L}_e} - G_{\text{ATP}} - G_{\text{L}_i} & (2.87) \\
&= G_{\text{ADP}}^0 + G_{\text{P}_i}^0 - G_{\text{ATP}}^0 - RT \ln\left(\frac{[\text{ATP}][\text{L}_i]}{[\text{ADP}][\text{P}_i][\text{L}_e]}\right) & (2.88) \\
&= \Delta G_{\text{ATP}}^0 - RT \ln\left(\frac{[\text{ATP}][\text{L}_i]}{[\text{ADP}][\text{P}_i][\text{L}_e]}\right). & (2.89)
\end{aligned}
$$

Note that the standard free energy of L is the same inside and outside the cell. At equilibrium $\Delta G = 0$ and thus

$$
\Delta G_{\text{ATP}}^0 = RT \ln\left(\frac{[\text{L}_i]_{\text{eq}}}{[\text{L}_e]_{\text{eq}}} \frac{[\text{ATP}]_{\text{eq}}}{[\text{ADP}]_{\text{eq}}[\text{P}_i]_{\text{eq}}}\right). \tag{2.90}
$$

Combining this with (2.84) gives

$$
\prod_{i=1}^{6} K_i = e^{\frac{\Delta G_{\text{ATP}}^0}{RT}} \text{M}^{-1}, \tag{2.91}
$$

which, because it is independent of concentrations, must hold in general. Notice from (2.90) that both sides of (2.91) must have units of liters per mole, or M^{-1}. In fact, since the free energy released by the hydrolysis of ATP is well known to be -31 kJ mole^{-1},

$$
e^{\frac{\Delta G_{\text{ATP}}^0}{RT}} = 3.73 \times 10^{-6}. \tag{2.92}
$$

Now, from (2.83) it follows that

$$
J = \frac{\frac{[\text{L}_i]}{[\text{L}_e]} \frac{[\text{ATP}]}{[\text{ADP}][\text{P}_i]} - e^{\frac{\Delta G_{\text{ATP}}^0}{RT}} \text{M}^{-1}}{\phi}. \tag{2.93}
$$

2.5.2   Active Transport of Charged Ions

Suppose that the interior of the cell has an electric potential of V_i while the exterior has a potential of V_e, and suppose further that L has a charge z. Then the change in potential of the ATPase cycle (2.86) is

$$
\Delta G = \Delta G_{\text{ATP}}^0 - RT \ln\left(\frac{[\text{ATP}][\text{L}_i]}{[\text{ADP}][\text{P}_i][\text{L}_e]}\right) - zFV, \tag{2.94}
$$

where $V = V_i - V_e$ is, as usual, the transmembrane membrane potential.

An identical argument to before shows that

$$
\prod_{i=1}^{6} K_i = e^{\frac{\Delta^0 G_{\text{ATP}}}{RT}} e^{\frac{-zFV}{RT}} \text{l mole}^{-1}, \tag{2.95}
$$

and thus

$$
J = \frac{\frac{[\text{L}_i]}{[\text{L}_e]} \frac{[\text{ATP}]}{[\text{ADP}][\text{P}_i]} - e^{\frac{\Delta^0 G_{\text{ATP}}}{RT}} e^{\frac{-zFV}{RT}} \text{M}^{-1}}{\phi(V)}. \tag{2.96}
$$

From this we see that, if $z > 0$, a positive V enhances the flow (i.e., increases J), while $V < 0$ decreases J by making it more difficult to move positive ions from inside to outside.

Although this thermodynamic argument shows that there must be some voltage-dependence in the rate constants, it does not tell us in which step (or steps) the voltage-dependence occurs. For example, in this model, the transition from E $\cdot$ ATP $\cdot$ L to $E_e \cdot$ ATP $\cdot$ L involves the net movement of the charge across the cell membrane, so that $\frac{k_{-3}}{k_3} = e^{\frac{-zFV}{RT}}$. (The argument here is identical to the argument used for the voltage dependence of the Na^+-Ca^{2+} exchanger.) However, there are other possibilities. Although each different model must have the same solution when $J = 0$, and their expressions for J must have the same sign, they can have significantly different expressions for $\phi(V)$.

2.5.3 A Model of the Na,K-ATPase

One of the best-known ATPases is the Na,K-ATPase, which pumps K^+ into the cell and Na^+ out of the cell through the overall reaction scheme

$$\text{ATP} + 3\text{Na}_i^+ + 2\text{K}_e^+ \longrightarrow \text{ADP} + \text{P} + 3\text{Na}_e^+ + 2\text{K}_i^+. \tag{2.97}$$
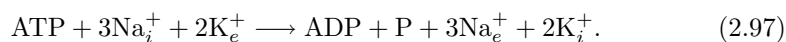
It is an electrogenic pump (each pump cycle transfers one positive charge from inside to out) and a member of the family of P-type active cation transporters which includes the SERCA ATPases that is discussed at length in Chapter 7. A great deal of work has been done to determine the mechanisms that underlie Na^+ and K^+ transport by this ATPase; the most widely accepted model is the Post-Albers model that was developed by two independent groups in the 1960s (Albers et al., 1963; Charnock and Post, 1963). More recent reviews are Apell (2004) or Taniguchi and Kaya (2000), while a history of investigations into the Na,K-ATPase is given by Glynn (2002). An excellent mathematical implementation of the Post-Albers scheme is that of Smith and Crampin (2004).

In the Post-Albers scheme phosphorylation of the pump (i.e., exchange of ATP for ADP) is associated with Na^+ efflux, while hydrolysis (i.e., loss of the additional phosphate group) is associated with K^+ influx. During the transition across the membrane each ion type is occluded, i.e., bound to the pump in a conformation in which it is accessible from neither side of the membrane. Occlusion prevents slippage, thus increasing the efficiency of the pump.

This scenario is illustrated in Fig. 2.11. Starting at the top left of the figure (state X_1), the ATPase begins in the conformation E_i, in which the binding sites for Na^+ and K^+ are exposed to the inside of the cell. The ATPase then loses two K^+ ions (which is assumed to occur in a single step), and gains three Na^+ ions, again in a single step, to move through states X_2 and X_3. ATP remains bound to the pump in each of the states X_1, X_2 and X_3, although this is not shown explicitly in the diagram. Loss of ADP then drives the ATPase to the occluded state Z_2, in which the three Na^+ ions are inaccessible to both the inside and outside of the cell. After another conformational change to the E_e state, in which the Na^+ and K^+ binding sites are exposed to the outside of the cell, the ATPase loses its three Na^+ to the outside, picks up another two K^+, and loses its extra phosphate to move
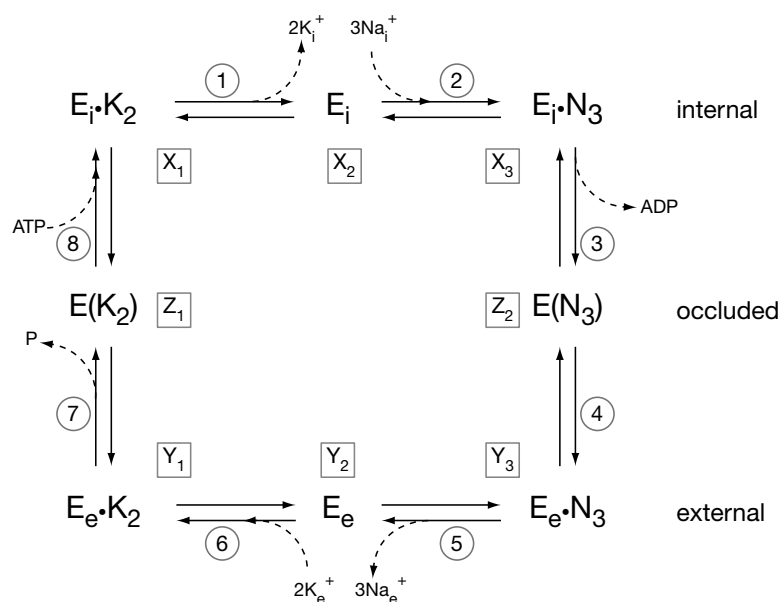
Figure 2.11: Model of the Na,K-ATPase based on the Post-Albers scheme.

through to the occluded state Z_1, in which the K^+ ions are shielded. Binding of ATP then returns the ATPase to the E_i conformation to complete the cycle. The rate constants are not shown explicitly, but each transition between states is labeled by a circled number. For each $i = 1 \ldots 8$, transition i has two rate constants, k_i in the clockwise direction and k_{-i} in the anti-clockwise direction.

From this diagram we can easily write the differential equations for each of the ATPase states. For example, letting a lower case letter denote the fraction of the ATPase in that state, we have

$$\frac{dx_1}{dt} = k_{-1}[K_i^+]^2 x_2 + k_8[\text{ATP}]z_1 - (k_{-8} + k_1)x_1, \tag{2.98}$$

and so on, subject to the constraint $x_1 + x_2 + x_3 + y_1 + y_2 + y_3 + z_1 + z_2 = 1$. The resultant expression for the flux is long and unwieldy of the form

$$J = \frac{[\text{ATP}]n_i^3 \kappa_e^2 - [\text{ADP}][\text{P}_i]\kappa_i^2 n_e^3 (\prod_{i=1}^8 K_i)}{\phi}, \tag{2.99}$$

where ϕ is the sum of a large number of terms involving products of the rate constants and concentrations. Here, n denotes the Na^+ concentration, and κ denotes the K^+ concentration. This expression for the flux is similar to that derived in the simpler model of Section 2.5.1. The same thermodynamic constraints apply, and so some of the rate constants are functions of the membrane potential. Smith and Crampin (2004), following the ideas of Apell (1989), incorporate voltage dependence into the rate constants for Na^+ binding and unbinding, i.e., K_2 and K_5 in this model.

A simplified version of this model is discussed in Exercise 14.

2.5.4 Nuclear Transport

The transport of proteins from the cytoplasm to the nucleus (or the reverse) is accomplished by means that combines features of the each of the above transport mechanisms. The nuclear membrane contains protein structures called nuclear pore complexes (NPCs) which allow free diffusion of soluble carrier proteins. However, these carrier proteins can pass through the pore complex only when they are bound. These carrier proteins (called importins) recognize and readily bind cargo destined for translocation. The energy to transport cargo against its gradient is provided by the hydrolysis of GTP via a GTPase enzyme called Ran. Ran-GTP has a very high binding affinity for the carrier protein ($\Delta G^0 = -51$ kJ mol^{-1}), effectively excluding the cargo from binding. The transportin/Ran-GTP complex is disassembled by the hydrolysis of Ran-GTP ($\Delta G^0 = -33$ kJ mol^{-1}) to Ran-GDP, which has a binding affinity for the carrier protein that is 10,000-fold lower than that of Ran-GTP. The endogenous GTPase activity rate is extremely slow ($k_{\text{cat}} = 1.5 \times 10^{-5} \text{s}^{-1}$). However, the hydrolysis of GTP to GDP on Ran is catalyzed by a cytoplasmic GTPase-activating protein called RanGAP which accelerates this rate by as much as 500,000-fold.

One cycle of transport works as follows. Cargo in the cytoplasm that is targeted for transport binds to the carrier molecule and moves via diffusion through the NPC. In the nucleus, when the cargo unbinds, Ran-GTP quickly binds to the carrier preventing the cargo from rebinding. Ran-GTP is kept at high concentration in the nucleus by another mechanism, so the Ran-GTP carrier complex diffuses into the cytoplasm through the NPC. On the cytoplasmic side of the membrane, Ran-GTP is quickly hydrolyzed to Ran-GDP, which because of its much lower binding affinity, unbinds from the carrier molecule, completing the cycle. Although all the reactions are reversible, the directionality is maintained by the free energy of GTP hydrolysis and the high concentration of GTP in the nucleus.

We defer the development of a model of this transport mechanism to the interested reader. In the absence of RanGAP, the model is similar to that of the Na$^+$-Ca^{2+} transporter described above. On the other hand, if the hydrolysis of Ran-GTP to RanGDP is assumed to be so fast that there is no unbinding of RanGTP in the cytoplasm, then the model is similar to that of the simple ATPase described above.

2.6   The Membrane Potential

The principal function of the active ATPase transport processes described above is to regulate the intracellular ionic composition of the cell. For example, the operation of the Na,K-ATPase results in high intracellular K$^+$ concentrations and low intracellular Na$^+$ concentrations. This is necessary for a cell's survival, as without such regulation, cells swell and burst. However, before we consider models for cell volume regulation, we consider the effects of ionic separation.
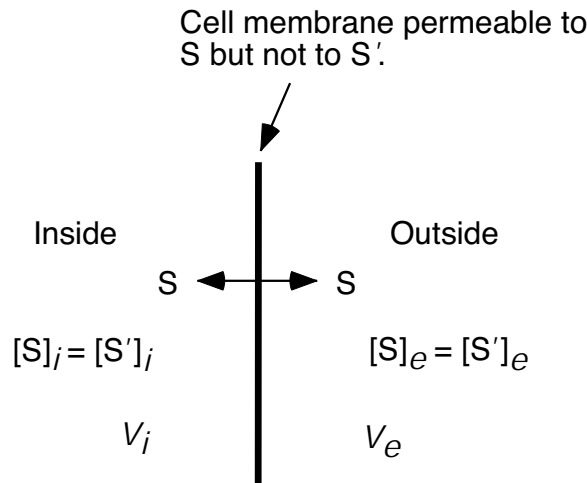
Cell membrane permeable to
S but not to S′.

Inside   Outside

S ⟷ S

$[S]_i = [S']_i$ $[S]_e = [S']_e$

V_i V_e

Figure 2.12: Schematic diagram of a membrane separating two solutions with different ionic concentrations. By convention, the potential difference, V, across the membrane is defined to be $V = V_i - V_e$.

2.6.1 The Nernst Equilibrium Potential

One of the most important equations in electrophysiology is the Nernst equation, which describes how a difference in ionic concentration can result in a potential difference across the membrane separating the two concentrations.

Suppose there are two reservoirs containing the same ion S, but at different concentrations, as shown schematically in Fig. 2.12. The reservoirs are separated by a semipermeable membrane. The solutions on each side of the membrane are assumed to be electrically neutral (at least initially), and thus each ion S is balanced by another ion, S′, with opposite charge. For example, S could be Na$^+$, while S′ could be Cl$^-$. Because we ultimately wish to apply the Nernst equation to cellular membranes, we call the left of the membrane the inside and the right the outside of the cell.

If the membrane is permeable to S but not to S′, the concentration difference across the membrane results in a net flow of S from one side to another, down its concentration gradient. However, because S′ cannot diffuse through the membrane, the diffusion of S causes a buildup of charge across the membrane. This charge imbalance, in turn, sets up an electric field that opposes the further net movement of S through the membrane. Equilibrium is reached when the electric field exactly balances the diffusion of S. Note that at steady state there are more S ions than S′ ions on one side and fewer S ions than S′ ions on the other, and thus neither side of the membrane is exactly electrically neutral. However, because the force from the charge buildup is so strong, only a small amount of S moves across the membrane. To a good approximation, the concentrations of S on either side of the membrane remain unchanged, the solutions on either side of the membrane remain electrically

neutral, and the small excess charge accumulates near the interface. The region in which there is a charge imbalance is called the Debye layer, and is on the order of a few nanometers thick.

The chemical potential of S on the inside of the membrane is

$$G_{\mathrm{S},i} = G_{\mathrm{S}}^0 + RT \ln([\mathrm{S}]_i) + zFV_i, \tag{2.100}$$

while on the outside it is

$$G_{\mathrm{S},e} = G_{\mathrm{S}}^0 + RT \ln([\mathrm{S}]_e) + zFV_e. \tag{2.101}$$

The chemical potential difference is

$$\Delta G_{\mathrm{S}} = G_{\mathrm{S},i} - G_{\mathrm{S},e} = RT \ln\left(\frac{[\mathrm{S}]_i}{[\mathrm{S}]_e}\right) + zFV. \tag{2.102}$$

At equilibrium, it must be that $\Delta G_{\mathrm{S}} = 0$, and thus the equilibrium potential difference, V_{S}, across the membrane must be

$$V_{\mathrm{S}} = \frac{RT}{zF} \ln\left(\frac{[\mathrm{S}]_e}{[\mathrm{S}]_i}\right) = \frac{kT}{zq} \ln\left(\frac{[\mathrm{S}]_e}{[\mathrm{S}]_i}\right), \tag{2.103}$$

called the *Nernst potential*. Here k is Boltzmann's constant $k = \frac{R}{N_A}$, N_A is Avogadro's number, q is the charge on a proton, and z is the charge on the ion S. When $V = V_{\mathrm{S}}$, there is no net current of S across the membrane, as the tendency of ions to move down their gradient is exactly balanced by the electric potential difference.

Throughout this book we follow the usual convention and define the potential difference, V, across the membrane to be

$$V = V_i - V_e, \tag{2.104}$$

i.e., the intracellular potential minus the extracellular potential.

Typical concentrations (in this case, for squid axon) are 397, 50, and 40 mM for K^+, Na^+, and Cl^-, respectively, in the intracellular space, and 20, 437, and 556 mM in the extracellular space. With these concentrations, the Nernst potentials for squid nerve axon are $V_{\mathrm{Na}} = 56$ mV, $V_{\mathrm{K}} = -77$ mV, $V_{\mathrm{Cl}} = -68$ mV (using $RT/F = 25.8$ mV at $27°C$. See Table 2.1).

The Nernst equation is independent of how the ions move through the membrane and depends only on the ratio of concentrations. In this sense, it is a "universal" law (although because it was derived from an "ideal" yet approximate, law, it too is approximate). Any equation that expresses the transmembrane current of S in terms of the membrane potential, no matter what its form, must have the reversal potential of V_{S}; i.e., the current must be zero at the Nernst potential $V = V_{\mathrm{S}}$. However, although this is true when a single ion species crosses the membrane, the situation is considerably more complicated when more than one type of ion can cross the membrane. In this case, the membrane potential that generates zero total current does not necessarily have zero current for each individual ion. For example, a current of S in one direction might be balanced by a current of S′ in the same direction. Hence, when multiple ion types can diffuse through the

membrane, the concentrations are not, in general, at equilibrium, even when there is no total current. Therefore, the arguments of chemical equilibrium used to derive the Nernst equation cannot be used, and there is no universal expression for the reversal potential in the multiple ion case. In this case, the reversal potential depends on the model used to describe the individual transmembrane ionic flows (see Chapter 3).

2.6.2   Gibbs-Donnan Equilibrium

Suppose one side of the membrane contains large charged macromolecules that cannot cross the membrane, but that both of the ion species S and S′ freely diffuse across the membrane. To be specific, suppose that the macromolecules are negatively charged with valence $-z_x$, S is positively charged with valence z, and S′ is negatively charged with valence $-z$. Note that both z and z_x are defined to be positive.

Outside the cell, S and S′ must have the same concentration, to maintain charge neutrality. Inside, charge neutrality requires more S than S′, in order to balance the negative charge on the macromolecules. At equilibrium, the membrane potential must be the Nernst potential for both S and S′, namely

$$V_S = \frac{RT}{zF} \ln \left(\frac{[S]_e}{[S]_i} \right) = -\frac{RT}{zF} \ln \left(\frac{[S']_e}{[S']_i} \right), \tag{2.105}$$

where

$$z_x[X] + z[S']_i = z[S]_i \quad \text{and} \quad [S']_e = [S]_e. \tag{2.106}$$

It follows that

$$[S']_e[S]_e = [S']_i[S]_i, \tag{2.107}$$

and thus

$$[S]_i \left([S]_i - \frac{z_x}{z}[X] \right) - ([S]_e)^2 = 0. \tag{2.108}$$

Now, we assume that the external concentration is fixed, and treat $[S]_e$ as a known parameter. In this case, (2.108) can be solved to find a unique positive value for $[S]_i$

$$[S]_i = \sigma[S]_e, \qquad \sigma = \frac{1}{2}(Z + \sqrt{Z^2 + 4}), \tag{2.109}$$

where $Z = \frac{z_x[X]}{z[S]_e}$, and from this the transmembrane potential can be determined using (2.105).

If, instead, we have a fixed volume and a fixed total amount of S, say, then we use the constraint

$$v_i[S]_i + v_e[S]_e = [S]_{\text{tot}}, \tag{2.110}$$

where $[S]_{\text{tot}}$ is a constant, and v_i and v_e are the internal and external volumes, respectively. We can now solve (2.108) subject to this constraint to find $[S]_i$ and the transmembrane potential. Note, however, that a physical solution is not always possible in this case, as there may be insufficient S or S′ to reach equilibrium.

This equilibrium is called the *Gibbs-Donnan equilibrium* (Exercise 17). The potential difference generated in this way is known to occur across cell membranes

and also across the edge of a gel in aqueous solution. This potential drop occurs across the edge of a gel if the charged macromolecules are immobilized in the gel, and therefore unable to diffuse out of the gel.

2.6.3 Electrodiffusion: The Goldman–Hodgkin–Katz Equations

In general, the flow of ions through the membrane is driven by concentration gradients and also by the electric field. The contribution to the flow from the electric field is given by *Planck's equation*

$$\mathbf{J} = -u\frac{z}{|z|}c\nabla\phi, \tag{2.111}$$

where u is the *mobility* of the ion, defined as the velocity of the ion under a constant unit electric field; z is the valence of the ion, so that $z/|z|$ is the sign of the force on the ion; c is the concentration of S; and ϕ is the electrical potential, so that $-\nabla\phi$ is the electrical field.

There is a relationship, determined by Einstein, between the ionic mobility u and Fick's diffusion constant:

$$D = \frac{uRT}{|z|F}. \tag{2.112}$$

When the effects of concentration gradients and electrical gradients are combined, we obtain the *Nernst–Planck equation*

$$\mathbf{J} = -D\left(\nabla c + \frac{zF}{RT}c\nabla\phi\right). \tag{2.113}$$

If the flow of ions and the electric field are transverse to the membrane, (2.113) can be viewed as the one-dimensional relation

$$J = -D\left(\frac{dc}{dx} + \frac{zF}{RT}c\frac{d\phi}{dx}\right). \tag{2.114}$$

The Nernst equation

The Nernst equation can also be derived from the Nernst–Planck equation (2.114). When the flux J is zero, we find

$$-D\left(\frac{dc}{dx} + \frac{zF}{RT}c\frac{d\phi}{dx}\right) = 0, \tag{2.115}$$

so that

$$\frac{1}{c}\frac{dc}{dx} + \frac{zF}{RT}\frac{d\phi}{dx} = 0. \tag{2.116}$$

Now suppose that the cell membrane extends from $x = 0$ (the inside) to $x = L$ (the outside), and let subscripts i and e denote internal and external quantities respectively. Then, integrating (2.116) from $x = 0$ to $x = L$ we get

$$\ln(c)\big|_{c_i}^{c_e} = \frac{zF}{RT}(\phi_i - \phi_e), \tag{2.117}$$

and thus the potential difference across the membrane, $V = \phi_i - \phi_e$, is given by

$$V = \frac{RT}{zF} \ln\left(\frac{c_e}{c_i}\right), \tag{2.118}$$

which is the Nernst equation.

The constant field approximation

In general, the electric potential ϕ is determined by the local charge density, and so, if it is not zero, J must be found by solving a coupled system of equations (discussed in detail in Chapter 3). However, a useful result is obtained by assuming that the electric field in the membrane is constant, and thus decoupled from the effects of charges moving through the membrane. Suppose two reservoirs are separated by a semipermeable membrane of thickness L, such that the potential difference across the membrane is V. On the left of the membrane (the inside) $[S] = c_i$, and on the right (the outside) $[S] = c_e$. If the electric field is constant through the membrane, $\partial\phi/\partial x = -V/L$, where $V = \phi(0) - \phi(L)$ is the membrane potential.

At steady state and with no production of ions, the flux must be constant. In this case, the Nernst–Planck equation (2.113) is an ordinary differential equation for the concentration c,

$$\frac{dc}{dx} - \frac{zFV}{RTL}c + \frac{J}{D} = 0, \tag{2.119}$$

whose solution is

$$\exp\left(\frac{-zVFx}{RTL}\right)c(x) = \frac{JRTL}{DzVF}\left[\exp\left(\frac{-zVFx}{RTL}\right) - 1\right] + c_i, \tag{2.120}$$

where we have used the left boundary condition $c(0) = c_i$. To satisfy the boundary condition $c(L) = c_e$, it must be that

$$J = \frac{D}{L}\frac{zFV}{RT}\frac{c_i - c_e \exp\left(\frac{-zVF}{RT}\right)}{1 - \exp\left(\frac{-zVF}{RT}\right)}, \tag{2.121}$$

where J is the flux density with units (typically) of moles per area per unit time. Note that these units are equivalent to units of concentration $\times$ speed. This flux density becomes an electrical current density (current per unit area) when multiplied by zF, the amount of charge carried per mole, and thus

$$I_S = P_S\frac{z^2F^2}{RT}V\frac{c_i - c_e \exp\left(\frac{-zFV}{RT}\right)}{1 - \exp\left(\frac{-zFV}{RT}\right)}, \tag{2.122}$$

where $P_S = D/L$ is the permeability of the membrane to S. This is the famous Goldman–Hodgkin–Katz (GHK) current equation, and plays an important role in models of cellular electrical activity. Notice that the GHK flux (2.121) reduces to Fick's law (2.17) in the limit $V \to 0$.

The current is zero if the diffusively driven flow and the electrically driven flow are in balance, which occurs, provided that $z \neq 0$, if

$$V = V_S = \frac{RT}{zF} \ln\left(\frac{c_e}{c_i}\right), \tag{2.123}$$

which is, as expected, the Nernst potential.

If there are several ions that are separated by the same membrane, then the flow of each of these is governed separately by its own current–voltage relationship. In general there is no potential at which these currents are all individually zero. However, the potential at which the net electrical current is zero is called the Goldman–Hodgkin–Katz potential. For a collection of ions all with valence $z = \pm 1$, we can calculate the GHK potential directly. For zero net electrical current, it must be that

$$0 = \sum_{z=1} P_j \frac{c_i^j - c_e^j \exp\left(\frac{-VF}{RT}\right)}{1 - \exp\left(\frac{-VF}{RT}\right)} + \sum_{z=-1} P_j \frac{c_i^j - c_e^j \exp\left(\frac{VF}{RT}\right)}{1 - \exp\left(\frac{VF}{RT}\right)}, \tag{2.124}$$

where $P_j = D_j/L$. This expression can be solved for V, to get

$$V = -\frac{RT}{F} \ln\left(\frac{\sum_{z=-1} P_j c_e^j + \sum_{z=1} P_j c_i^j}{\sum_{z=-1} P_j c_i^j + \sum_{z=1} P_j c_e^j} \right). \tag{2.125}$$

For example, if the membrane separates sodium ($Na^+, z = 1$), potassium ($K^+, z = 1$), and chloride ($Cl^-, z = -1$) ions, then the GHK potential is

$$V_r = -\frac{RT}{F} \ln\left(\frac{P_{Na}[Na^+]_i + P_K[K^+]_i + P_{Cl}[Cl^-]_e}{P_{Na}[Na^+]_e + P_K[K^+]_e + P_{Cl}[Cl^-]_i} \right). \tag{2.126}$$

It is important to emphasize that neither the GHK potential nor the GHK current equation are universal expressions like the Nernst equation. Both depend on the assumption of a constant electric field, and other models give different expressions for the transmembrane current and reversal potential. In Chapter 3 we discuss other models of ionic current, and compare them to the GHK equations. However, the importance of the GHK equations is so great, and their use so widespread, that their separate presentation here is justified.

2.6.4   Electrical Circuit Model of the Cell Membrane

Since the cell membrane separates charge, it can be viewed as a capacitor. The capacitance of any insulator is defined as the ratio of the charge across the capacitor to the voltage potential necessary to hold that charge, and is denoted by

$$C_m = \frac{Q}{V}. \tag{2.127}$$

From standard electrostatics (Coulomb's law), one can derive the fact that for two parallel conducting plates separated by an insulator of thickness d, the capacitance is

$$C_m = \frac{k\epsilon_0}{d}, \tag{2.128}$$

where k is the dielectric constant for the insulator and ϵ_0 is the permittivity of free space. The capacitance of cell membrane is typically $1.0\ \mu F/cm^2$. Using that
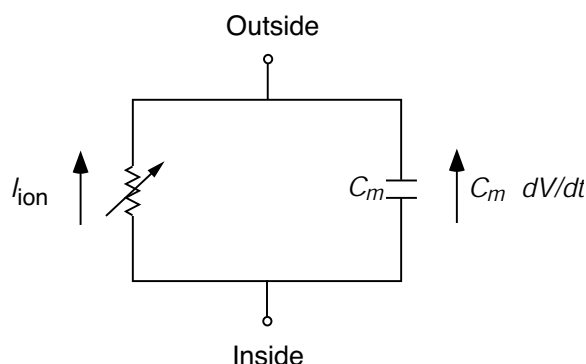
Figure 2.13: Electrical circuit model of the cell membrane.

$\epsilon_0 = (10^{-9}/(36\pi))$F/m, we calculate that the dielectric constant for cell membrane is about 8.5, compared to $k = 3$ for oil.

A simple electrical circuit model of the cell membrane is shown in Fig. 2.13. It is assumed that the membrane acts like a capacitor in parallel with a resistor (although not necessarily ohmic). Since the current is dQ/dt, it follows from (2.127) that the capacitive current is $C_m dV/dt$, provided that C_m is constant. Since there can be no net buildup of charge on either side of the membrane, the sum of the ionic and capacitive currents must be zero, and so

$$C_m \frac{dV}{dt} + I_{\text{ion}} = 0, \tag{2.129}$$

where $V = V_i - V_e$.

This equation appears many times in this book, as it is the basis for much of theoretical electrophysiology. A significant challenge is to determine the form of I_{ion}. We have already derived one possible choice, the GHK current equation (2.122), and others are discussed in Chapter 3.

Another common model describes I_{ion} as a linear function of the membrane potential. In Chapter 3 we show how a linear I–V curve can be derived from more realistic models; however, because it is used so widely, we present a brief, heuristic, derivation here. Consider the movement of an ion S across a membrane. We assume that the potential drop across the membrane has two components. First, the potential drop due to concentration differences is given by the Nernst equation

$$V_{\text{S}} = \frac{RT}{zF} \ln \left(\frac{[\text{S}]_e}{[\text{S}]_i} \right), \tag{2.130}$$

and, second, if the channel is ohmic, the potential drop due to an electrical current is rI_{S}, where r is the channel resistance and I_{S} is the transmembrane current (positive outward) of S. Summing these two contributions we find

$$V = rI_{\text{S}} + V_{\text{S}}, \tag{2.131}$$

and solving for the current, we get the current–voltage relationship

$$I_S = g(V - V_S), \tag{2.132}$$

where $g = 1/r$ is the *membrane conductance*. The current I_S and conductance g are usually specified per unit area of membrane, being the product of the single channel conductance times the number of channels per unit area of membrane.

Notice that this current-voltage relationship also has zero current when $V = V_S$, as it must.

2.7   Osmosis

Suppose two chambers of water are separated by a rigid porous membrane. Because it is porous, water can flow between the two chambers. If the two chambers are topped by pistons, then water can be driven between the two chambers by applying different pressures to the two pistons. In general there is a linear relationship between the pressure difference and the flux of water through the membrane, given by

$$rQ = P_1 - P_2, \tag{2.133}$$

where Q is the flux (volume per unit time) of water from chamber one to chamber two, P_1 and P_2 are the applied pressures for chambers one and two, respectively, and r is the flow resistance of the membrane (not the same as the resistance to flow of ions). The expression (2.133) is actually a definition of the flow resistance r, and this linear relationship is analogous to Ohm's law relating current and voltage in a conductor. It is useful but not universally correct.

Suppose that a solute is added to chamber one, and that the membrane is impermeable to the solute. The difference in free energy per mole (or chemical potential) of solvent (i.e., water) between the two chambers is

$$\Delta G = RT \ln \frac{S_1}{S_2}, \tag{2.134}$$

where S_i is the mole fraction of solvent in the ith chamber. Note that because this expression involves the ratio of S_1 to S_2, we can use whatever units are most convenient. Hence we use mole fraction rather than concentration, which is standard. Because it dilutes the solvent $(S_1 < S_2)$, the presence of a solute lowers the chemical potential of the solvent and induces a flow of solvent from chamber two to chamber one. In other words, the solvent diffuses from a region of higher concentration to one of lower concentration.

At constant temperature, equilibrium can be attained either by diluting the solution until it is pure solvent, or by increasing the pressure on the solution. The *osmotic pressure* π_s is defined to be the pressure that must be applied to chamber 1 to bring the free energy back to the free energy of the pure solvent. It follows that

$$RT \ln \frac{S_1}{S_2} + \pi_s v_s = 0, \tag{2.135}$$

where v_s is the molar volume (liters per mole) of the solvent. Note that, from the ideal gas law $PV = nRT$, we see that $\pi_s v_s$ has the same units as RT.

Since $S_2 = 1$ it now follows that

$$\pi_s = -\frac{RT}{v_s}\ln(S_1) = -\frac{RT}{v_s}\ln(1 - N) \approx \frac{RT}{v_s}N, \qquad (2.136)$$

where N is the mole fraction of solvent. Also, since $N = \frac{n}{n+n_s} \approx \frac{n}{n_s}$, where n and n_s are the number of moles of solute and solvent, respectively, we have that

$$\pi_s = \frac{RT}{v_s}\frac{n}{n_s} \approx RcT, \qquad (2.137)$$

since $n_s v_s$ is quite close to the volume, v, of solution. Here c is the concentration of solvent in units of moles per liter. Using that $c = n/v$, (2.137) becomes

$$\pi_s v = nRT, \qquad (2.138)$$

which is the same as the ideal gas law. Equation (2.137) was first found empirically by van't Hoff.

If n has the units of numbers of molecules per liter, rather than moles per liter, as above, then (2.138) becomes

$$\pi_s v = nkT. \qquad (2.139)$$

As with all things derived from ideal properties, the expression (2.138) is an approximation, and for real solutions at physiological concentrations, the deviation can be significant. The formula

$$\pi_s v = \phi nRT, \qquad (2.140)$$

works much better, where ϕ is a concentration-dependent correction factor found experimentally. For all solutes, ϕ approaches one for sufficiently small concentrations. At concentrations typical of extracellular fluids in mammals, $\phi = 1.01$ for glucose and lactose, whereas for NaCl and KCl, $\phi = 0.93$ and 0.92, respectively. Deviation from ideality is even more significant for proteins, and is typically more concentration dependent as well. In spite of this, in the remainder of this book we use van't Hoff's law (2.137) to calculate osmotic pressure.

Notice that π_s is not the pressure of the solute but rather the pressure that must be applied to the solution to prevent solvent from flowing in through the semipermeable membrane. Thus, the flow rate of solvent is modified by osmotic pressure to be

$$rQ = P_1 - \pi_s - P_2, \qquad (2.141)$$

The flux of water due to osmotic pressure is called *osmosis*. The effect of the osmotic pressure is to draw water into chamber one, causing an increase in its volume and thereby to decrease the concentration of solute.

Osmotic pressure is determined by the number of particles per unit volume of fluid, and not the mass of the particles. The unit that expresses the concentration in terms of number of particles is called the *osmole*. One osmole is 1 gram molecular

weight (that is, one mole) of an undissociated solute. Thus, 180 grams of glucose (1 gram molecular weight) is 1 osmole of glucose, since glucose does not dissociate in water. On the other hand, 1 gram molecular weight of sodium chloride, 58.5 grams, is 2 osmoles, since it dissociates into 2 moles of osmotically active ions in water.

A solution with 1 osmole of solute dissolved in a kilogram of water is said to have osmolality of 1 osmole per kilogram. Since it is difficult to measure the amount of water in a solution, a more common unit of measure is osmolarity, which is the osmoles per liter of aqueous solution. In dilute conditions, such as in the human body, osmolarity and osmolality differ by less than one percent. At body temperature, $37°$ C, a concentration of 1 osmole per liter of water has an osmotic pressure of 19,300 mm Hg, which corresponds to a column of water over 250 meters high. Clearly, osmotic pressures can be very large. It is for this reason that red blood cells burst when the blood serum is diluted with pure water, and this is known to have been the cause of death in hospital patients when pure water was accidentally injected into the veins.

Suppose two columns (of equal cross-section) of water are separated at the bottom by a rigid porous membrane. If n molecules of sugar are dissolved in column one, what will be the height difference between the two columns after they achieve steady state? At steady state there is no flux between the two columns, so at the level of the membrane, $P_1 - \pi_s = P_2$. Since P_1 and P_2 are related to the height of the column of water through $P = \rho g h$, where ρ is the density of the fluid, g is the gravitational constant, and h is the height of the column. We suppose that the density of the two columns is the same, unaffected by the presence of the dissolved molecule, so we have

$$\rho g h_2 = \rho g h_1 - \frac{nkT}{h_1 A}, \tag{2.142}$$

where A is the cross-sectional area of the columns. Since fluid is conserved, $h_1 + h_2 = 2h_0$, where h_0 is the height of the two columns of water before the sugar was added. From these, we find a single quadratic equation for h_1:

$$h_1^2 - h_0 h_1 - \frac{nkT}{2\rho g A} = 0. \tag{2.143}$$

The positive root of this equation is $h_1 = h_0/2 + \frac{1}{2}\sqrt{h_0^2 + \frac{2nkT}{\rho g A}}$, so that

$$h_1 - h_2 = \sqrt{h_0^2 + \frac{2nkT}{\rho g A}} - h_0. \tag{2.144}$$

When the solute is at a high enough concentration, physical solutions of (2.144) are not possible. Specifically, if the solute is too concentrated with $\frac{nkT}{\rho g A} > 4h_0^2$, the weight of a column of water of height $2h_0$ is insufficient to balance the osmotic pressure, in which case there is not enough water to reach equilibrium.

2.8   Control of Cell Volume

The principal function of the ionic pumps is to set up and maintain concentration differences across the cell membrane, concentration differences that are necessary

for the cell to control its volume. In this section we describe how this works by means of a simple model in which the volume of the cell is regulated by the balance between ionic pumping and ionic flow down concentration gradients (Tosteson and Hoffman, 1960; Jakobsson, 1980; Hoppensteadt and Peskin, 1992).

Because the cell membrane is a thin lipid bilayer, it is incapable of withstanding any hydrostatic pressure differences. This is a potentially fatal weakness. For a cell to survive, it must contain a large number of intracellular proteins and ions, but if their concentrations become too large, osmosis causes the entry of water into the cell, causing it to swell and burst (this is what happens to many cells when their pumping machinery is disabled). Thus, for cells to survive, they must regulate their intracellular ionic composition (Macknight, 1988; Reuss, 1988).

An even more difficult problem for some cells is to transport large quantities of water, ions, or other molecules while maintaining a steady volume. For example, Na^+-transporting epithelial cells, found (among other places) in the bladder, the colon, and nephrons of the kidney, are designed to transport large quantities of Na^+ from the lumen of the gut or the nephron to the blood. Indeed, these cells can transport an amount of Na^+ equal to their entire intracellular contents in one minute. However, the rate of transport varies widely, depending on the concentration of Na^+ on the mucosal side. Thus, these cells must regulate their volume and ionic composition under a wide variety of conditions and transport rates (Schultz, 1981).

2.8.1 A Pump–Leak Model

We begin by modeling the active and passive transport of ionic species across the cell membrane. We have already derived two equations for ionic current as a function of membrane potential: the GHK current equation (2.122) and the linear relationship (2.132). For our present purposes it is convenient to use the linear expression for ionic currents. Active transport of Na^+ and K^+ is performed primarily by the Na,K-ATPase (see Section 2.5.3).

Combining the expressions for active and passive ion transport, we find that the Na^+, K^+, and Cl^- currents are given by

$$I_{Na} = g_{Na}\left[V - \frac{RT}{F}\ln\left(\frac{[Na^+]_e}{[Na^+]_i}\right)\right] + 3pq, \tag{2.145}$$

$$I_K = g_K\left[V - \frac{RT}{F}\ln\left(\frac{[K^+]_e}{[K^+]_i}\right)\right] - 2pq, \tag{2.146}$$

$$I_{Cl} = g_{Cl}\left[V + \frac{RT}{F}\ln\left(\frac{[Cl^-]_e}{[Cl^-]_i}\right)\right], \tag{2.147}$$

where p is the rate at which the ion exchange pump works and q is the charge of a single ion.

We can express these current–voltage equations as differential equations by noting that an outward ionic current of ion A^{z+} affects the intracellular concentration of that ion through

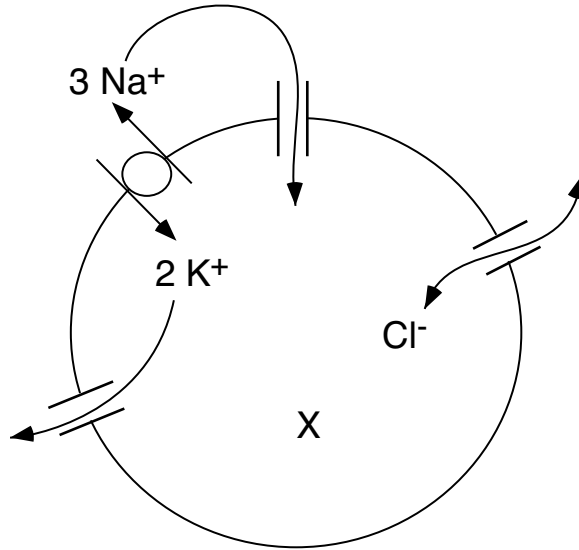$$I_A = -\frac{d}{dt}(zFw[A^{z+}]), \tag{2.148}$$

Figure 2.14: Schematic diagram of the pump–leak model.

with w denoting the cell volume. (We use w rather than v to denote the cell volume to prevent confusion with V, the membrane potential.) Thus we have

$$-\frac{d}{dt}(Fw[\text{Na}^+]_i) = g_{\text{Na}}\left[V - \frac{RT}{F}\ln\left(\frac{[\text{Na}^+]_e}{[\text{Na}^+]_i}\right)\right] + 3pq, \qquad (2.149)$$

$$-\frac{d}{dt}(Fw[\text{K}^+]_i) = g_{\text{K}}\left[V - \frac{RT}{F}\ln\left(\frac{[\text{K}^+]_e}{[\text{K}^+]_i}\right)\right] - 2pq, \qquad (2.150)$$

$$\frac{d}{dt}(Fw[\text{Cl}^-]_i) = g_{\text{Cl}}\left[V + \frac{RT}{F}\ln\left(\frac{[\text{Cl}^-]_e}{[\text{Cl}^-]_i}\right)\right]. \qquad (2.151)$$

Next, we let X denote the number of moles of large negatively charged molecules (with valence $z_x \leq -1$) that are trapped inside the cell. The flow of water across the membrane is driven by osmotic pressure, so that the change of cell volume is given by

$$r\frac{dw}{dt} = RT\left([\text{Na}^+]_i - [\text{Na}^+]_e + [\text{K}^+]_i - [\text{K}^+]_e + [\text{Cl}^-]_i - [\text{Cl}^-]_e + \frac{X}{w}\right). \quad (2.152)$$

Here we have assumed that the mechanical (hydrostatic) pressure difference across the membrane is zero, and we have also assumed that the elastic restoring force for the membrane is negligible.

Now to determine the membrane potential, we could use the electrical circuit model of the cell membrane, and write

$$C_m\frac{dV}{dt} + I_{\text{Na}} + I_{\text{K}} + I_{\text{Cl}} = 0. \qquad (2.153)$$

However, the system of equations (2.149)–(2.153) has an infinite number of steady states. Since the solution is determined by the choice of initial condition, it is better to use the integrated form of (2.153), i.e.,

$$C_m V = Q_i - Q_e, \tag{2.154}$$

where Q_i and Q_e are the total positive charge in the intracellular and extracellular spaces, respectively. (Note that here C_m refers to the total cell capacitance, assumed to be independent of cell volume. In other chapters of this book, C_m refers to membrane capacitance per unit area.) Since total charge is the difference between total number of positive and negative charges, we take

$$Q_i = qw([\text{Na}^+]_i + [\text{K}^+]_i - [\text{Cl}^-]_i) + z_x qX, \qquad Q_e = qw_e([\text{Na}^+]_e + [\text{K}^+]_e - [\text{Cl}^-]_e). \tag{2.155}$$

This expression would be correct if the concentration of an ion was defined as the total number of ions in a region divided by the volume of that region, or if the distribution of ions was spatially homogeneous. But such is not the case here. This is because excess charge always accumulates in a thin region at the boundary of the domain (the Debye layer). However, this excess charge is quite small. To see this, consider a cylindrical piece of squid axon of typical radius 500 μm. With a capacitance of 1 μF/cm^2 and a typical membrane potential of 100 mV, the total charge is $Q = C_m V = \pi \times 10^{-8}$ C/cm. In comparison, the charge associated with intracellular K$^+$ ions at 400 mM is about 0.1 π C/cm, showing a relative charge deflection of about 10^{-7}.

Thus, since Q_i and Q_e are so small compared to the charges of each ion, it is a excellent approximation to assume that both the extracellular and intracellular media are electroneutral. Thus, Na$^+$, K$^+$, and Cl$^-$ are assumed to be in electriacal balance in the extracellular space. In view of the numbers for squid axon, this assumption is not quite correct, indicating that there must be other ions around to maintain electrical balance. In the intracellular region, Na$^+$, K$^+$, and Cl$^-$ are not even close to being in electrical balance, but here, electroneutrality is maintained by the large negatively charged proteins trapped within the cell's interior.

The assumption of electroneutrality gives the two equations

$$[\text{Na}^+]_e + [\text{K}^+]_e - [\text{Cl}^-]_e \ = \ 0, \tag{2.156}$$

$$[\text{Na}^+]_i + [\text{K}^+]_i - [\text{Cl}^-]_i + z_x \frac{X}{w} \ = \ 0. \tag{2.157}$$

It is convenient to assume that the cell is in an infinite bath, so that ionic currents do not change the external concentrations, which are thus assumed to be fixed and known, and to satisfy (2.156).

The differential equations (2.149), (2.150), (2.151), and (2.152) together with the requirement of intracellular electroneutrality (2.157) describe the changes of cell volume and membrane potential as functions of time. Note that we have 4 differential equations and one algebraic equation for the five unknowns ($[\text{Na}^+]_i$, $[\text{K}^+]_i$, $[\text{Cl}^-]_i$, w and V).

Even though we formulated this model as a system of differential equations, we are interested, for the moment, only in their steady-state solution. Time-dependent

currents and potentials become important in Chapter 5 for the discussion of excitability.

To understand these equations, we introduce the nondimensional variables $v = \frac{FV}{RT}$, $P = \frac{pFq}{RTg_{Na}}$, $\mu = \frac{w}{X}[Cl^-]_e$ and set $y = e^{-v}$. Then, the equation of intracellular electroneutrality becomes

$$\alpha y - \frac{1}{y} + \frac{z_x}{\mu} = 0, \qquad (2.158)$$

and the equation of osmotic pressure balance becomes

$$\alpha y + \frac{1}{y} + \frac{1}{\mu} - 2 = 0, \qquad (2.159)$$

where $\alpha = \frac{[Na^+]_e e^{-3P} + [K^+]_e e^{2P\gamma}}{[Na^+]_e + [K^+]_e}$ and $\gamma = g_{Na}/g_K$. In terms of these nondimensional variables, the ion concentrations are

$$\frac{[Na^+]_i}{[Na^+]_e} = e^{-3P}y, \qquad (2.160)$$

$$\frac{[K^+]_i}{[K^+]_e} = e^{2P\gamma}y, \qquad (2.161)$$

$$\frac{[Cl^-]_i}{[Cl^-]_e} = \frac{1}{y}. \qquad (2.162)$$

Solving (2.158) for its unique positive root, we obtain

$$y = \frac{-z_x + \sqrt{z_x^2 + 4\alpha\mu^2}}{2\alpha\mu}, \qquad (2.163)$$

and when we substitute for y back into (2.159), we find the quadratic equation for μ:

$$4(1 - \alpha)\mu^2 - 4\mu + 1 - z_x^2 = 0. \qquad (2.164)$$

For $z_x \leq -1$, this quadratic equation has one positive root if and only if $\alpha < 1$. Expressed in terms of concentrations, the condition $\alpha < 1$ is

$$\rho(P) = \frac{[Na^+]_e e^{-3P} + [K^+]_e e^{2P\gamma}}{[Na^+]_e + [K^+]_e} < 1. \qquad (2.165)$$

One can easily see that $\rho(0) = 1$ and that for large P, $\rho(P)$ is exponentially large and positive. Thus, the only hope for $\rho(P)$ to be less than one is if $\rho'(0) < 0$. This occurs if and only if

$$\frac{3[Na^+]_e}{g_{Na}} > \frac{2[K^+]_e}{g_K}, \qquad (2.166)$$

in which case there is a range of values of P for which a finite, positive cell volume is possible and for which there is a corresponding nontrivial membrane potential.

To decide if this condition is ever satisfied we must determine "typical" values for g_{Na} and g_K. This is difficult to do, because, as is described in Chapter 5, excitability of nerve tissue depends strongly on the fact that conductances are voltage dependent
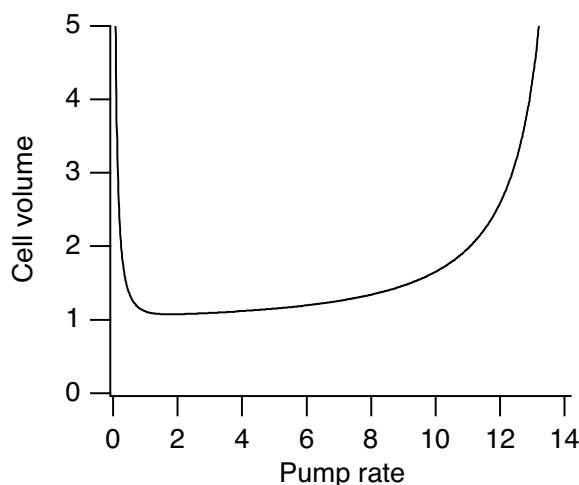
Figure 2.15: Cell volume as a function of the pump rate.

and can vary rapidly over a large range of values. However, at rest, in squid axon, reasonable values are $g_K = 0.367$ mS/cm^2 and $g_{Na} = 0.01$ mS/cm^2. For these values, and at the extracellular concentrations of 437 and 20 mM for Na$^+$ and K$^+$, respectively, the condition (2.166) is readily met.

One important property of the model is that the resting value of V is equal to the Nernst potential of Cl$^-$, as can be seen from (2.151) or (2.162). Thus, the membrane potential is set by the activity of the Na,K-ATPase, and the intracellular Cl$^-$ concentration is set by the membrane potential.

In Figs. 2.15 and 2.16 the nondimensional volume μ and the potential V (assuming RT/F=25.8 mV) are plotted as functions of the pump rate P. In addition, in Fig. 2.16 are shown the Na$^+$ and K$^+$ equilibrium potentials. For these plots, γ was chosen to be 0.11, and $z_x = -1$. Then, at $P = 1.6$, the Na$^+$ and K$^+$ equilibrium potentials and the membrane potentials are close to their observed values for squid axon, of 56, -77 and -68 mV, respectively.

From these plots we can see the effect of changing pump rate on cell volume and membrane potential. At zero pump rate, the membrane potential is zero and the cell volume is infinite (dead cells swell). As the pump rate increases from zero, the cell volume and membrane potential rapidly decrease to their minimal values and then gradually increase until at some upper limit for pump rate, the volume and potential become infinite. The K$^+$ equilibrium potential is seen to decrease rapidly as a function of pump rate until it reaches a plateau at a minimum value. The Na$^+$ equilibrium potential increases monotonically.

Physically realistic values of the membrane potential are achieved fairly close to the local minimum. Clearly, there is little advantage for a higher pump rate, and since the pump rate is proportional to energy expenditure, it would seem that the pump rate is chosen approximately to minimize cell volume, membrane potential, and energy expenditure. However, no mechanism for the regulation of energy
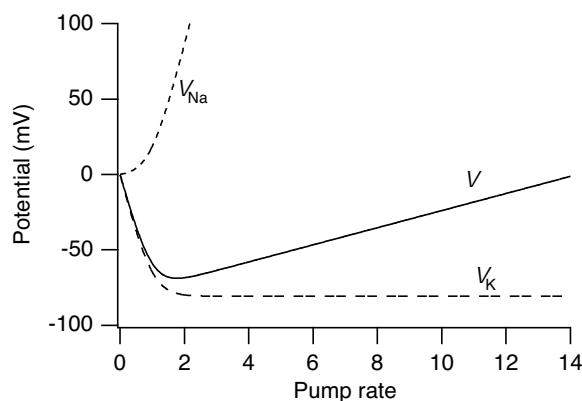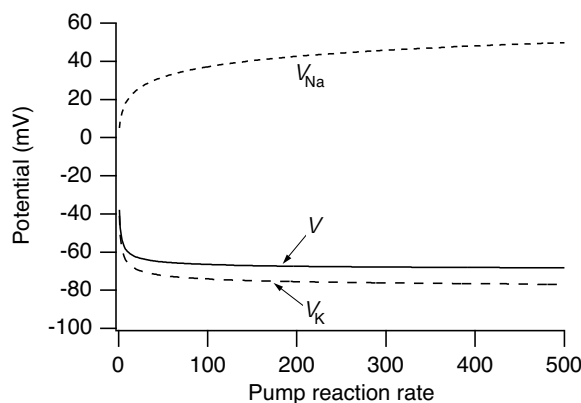
Figure 2.16: Membrane potential, Na^+ equilibrium potential, and K^+ equilibrium potential as functions of the pump rate.

Table 2.4: Resting potentials in some typical excitable cells.

Cell Type	Resting Potential (mV)
Neuron	-70
Skeletal muscle (mammalian)	-80
Skeletal muscle (frog)	-90
Cardiac muscle (atrial and ventricular)	-80
Cardiac Purkinje fiber	-90
Atrioventricular nodal cell	-65
Sinoatrial nodal cell	-55
Smooth muscle cell	-55

expenditure is suggested.

Generalizations

While the above model for control of volume and membrane potential is useful and gives some insight into the control mechanisms, as with most models there are important features that have been ignored but that might lead to substantially different behavior.

There are (at least) two significant simplifications in the model presented here. First, the conductances g_{Na} and g_K are treated as constants. In Chapter 5 we show that the ability of cells to generate an electrical signal results from voltage and time dependence of the conductances. In fact, the discovery that ion channels have differing properties of voltage sensitivity was of fundamental importance to the understanding of neurons. The second simplification relates to the operation of the ion exchange pump. Figure 2.16 suggests that the minimal membrane potential is achieved at a particular pump rate and suggests the need for a tight control of pump rate that maintains the potential near this minimum. If indeed, such a tight

Figure 2.17: Membrane potential, Na^+ equilibrium potential, and K^+ equilibrium potential as functions of the pump rate, for the modified pump rate (2.167).

control is required, it is natural to ask what that control mechanism might be. There is also the difficulty that in this simple model there is nothing preventing the complete depletion of Na^+ ions.

A different model of the pump activity might be beneficial. Recall from (2.97) that with each "stroke" of the ion exchange pump, three intracellular Na^+ ions are exchanged for two extracellular K^+ ions. Our previous analysis of the Na,K-ATPase (see (2.99)) suggests that at low internal Na^+ concentrations, the pump rate can be represented in nondimensional variables as

$$P = \rho u^3, \tag{2.167}$$

where $u = [Na^+]_i/[Na^+]_e$. This representation is appropriate at high pump rates, where effects of saturation are of no concern. Notice that P is proportional to the rate of ATP hydrolysis, and hence to energy consumption. Thus, as u decreases, so also does the rate of energy consumption. With this change, the equation for the Na^+ concentration becomes

$$u \exp(3\rho u^3) = y, \tag{2.168}$$

and this must be solved together with the quadratic polynomials (2.158) and (2.159), with (2.168) replacing (2.160).

In Fig. 2.17 are shown the membrane potential, and the Na^+ and K^+ equilibrium potentials, plotted as functions of the nondimensional reaction rate ρ. Here we see something qualitatively different from what is depicted in Fig. 2.16. There the membrane potential had a noticeable local minimum and was sensitive to changes in pump rate. In this modified model, the membrane potential is insensitive to changes in the pump rate. The reason for this difference is clear. Since the effectiveness of the pump depends on the internal Na^+ concentration, increasing the speed of the pumping rate has little effect when the internal Na^+ is depleted, because of the diminished number of Na^+ ions available to be pumped.
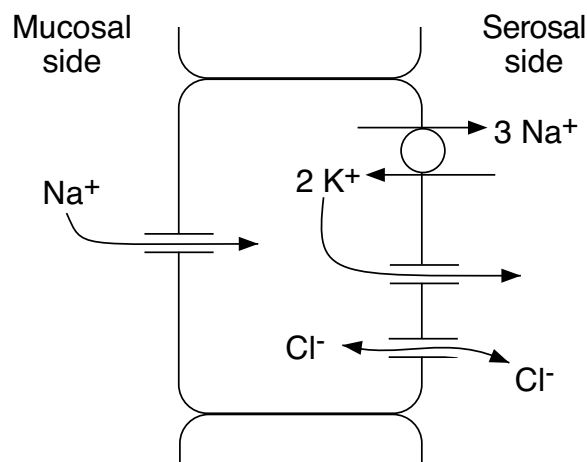
Figure 2.18: Schematic diagram of the model of a Na^+-transporting epithelial cell, based on the model of Koefoed-Johnsen and Ussing (1958).

While the pump rate is certainly ATP dependent, there are a number of drugs and hormones that are known to affect the pump rate. Catecholamines rapidly increase the activity of the pump in skeletal muscle, thereby preserving proper K^+ during strenuous exercise. Within minutes, insulin stimulates pump activity in the liver, muscle, and fat tissues, whereas over a period of hours, aldosterone and corticosterones increase activity in the intestine.

On the other hand, digitalis (clinically known as digoxin) is known to suppress pump activity. Digitalis is an important drug used in the treatment of congestive heart failure and during the 1980s was the fourth most widely prescribed drug in the United States. At therapeutic concentrations, digitalis inhibits a moderate fraction (say, 30–40%) of the Na,K-ATPase, by binding with the Na^+ binding site on the extracellular side. This causes an increase in internal Na^+, which has an inhibitory effect on the Na^+–Ca^{2+} antiport exchanger, slowing the rate by which Ca^{2+} exits the cells. Increased levels of Ca^{2+} result in increased myocardial contractility, a positive and useful effect. However, it is also clear that at higher levels, the effect of digitalis is toxic.

2.8.2   Volume Regulation and Ionic Transport

Many cells have a more difficult problem to solve, that of maintaining their cell volume in widely varying conditions, while transporting large quantities of ions through the cell. Here we present a simplified model for transport and volume regulation in a Na^+-transporting epithelial cell.

As are virtually all models of transporting epithelia, the model is based on that of

Koefoed-Johnsen and Ussing (1958), the so-called KJU model. In the KJU model, an epithelial cell is modeled as a single cell layer separating a mucosal solution from the serosal solution (Fig. 2.18). (The mucosal side of an epithelial cell is that side on which mucus is secreted and from which various chemicals are withdrawn, for example, from the stomach. The serosal side is the side of the epithelial cell facing the interstitium, wherein lie capillaries, etc.) Na^+ transport is achieved by separating the Na^+ pumping machinery from the channels that allow Na^+ entry into the cell. Thus, the mucosal membrane contains Na^+ channels that allow Na^+ to diffuse down its concentration gradient into the cell, while the serosal membrane contains the Na-K-ATPases which remove Na^+ from the cell. The overall result is the transport of Na^+ from the mucosal side of the cell to the serosal side. The important question is whether the cell can maintain a steady volume under widely varying concentrations of Na^+ on the mucosal side.

We begin by letting N, K, and C denote Na^+, K^+, and Cl^- concentrations respectively, and letting subscripts m, i, and s denote mucosal, intracellular and serosal concentrations. Thus, for example, N_i is the intracellular Na^+ concentration, and N_m is the mucosal Na^+ concentration. We now write the conservation equations for Na^+, K^+, and Cl^- at steady state. The conservation equations are the same as those of the pump–leak model with some minor exceptions. First, instead of the linear I–V curve used in the pump–leak model, we use the GHK formulation to represent the ionic currents. This makes little qualitative change to the results but is more convenient because it simplifies the analysis that follows. Second, we assume that the rate of the Na,K-ATPase is proportional to the intracellular Na^+ concentration, N_i, rather than N_i^3, as was assumed in the generalized version of the pump–leak model. Thus,

$$P_{\text{Na}}v\frac{N_i - N_m e^{-v}}{1 - e^{-v}} + 3qpN_i = 0, \qquad (2.169)$$

$$P_{\text{K}}v\frac{K_i - K_s e^{-v}}{1 - e^{-v}} - 2qpN_i = 0, \qquad (2.170)$$

$$P_{\text{Cl}}v\frac{C_i - C_s e^{v}}{1 - e^{v}} = 0. \qquad (2.171)$$

Note that the voltage, v, is non-dimensional, having been scaled by $\frac{F}{RT}$, and that the rate of the Na,K-ATPase is pN_i. Also note that the inward Na^+ current is assumed to enter from the mucosal side, and thus N_m appears in the GHK current expression, but that no other ions enter from the mucosa. Here the membrane potential is assumed to be the same across the lumenal membrane and across the basal membrane. This is not quite correct, as the potential across the lumenal membrane is typically -67 mV while across the basal membrane it is about -70 mV.

There are two further equations to describe the electroneutrality of the intracellular space and the osmotic balance. In steady state, these are, respectively,

$$w(N_i + K_i - C_i) + z_x X = 0, \qquad (2.172)$$

$$N_i + K_i + C_i + \frac{X}{w} = N_s + K_s + C_s, \qquad (2.173)$$

where X is the number of moles of protein, each with a charge of $z_x \leq -1$, that are trapped inside the cell, and w is the cell volume. Finally, the serosal solution is assumed to be electrically neutral, and so in specifying N_s, K_s, and C_s we must ensure that

$$N_s + K_s = C_s. \tag{2.174}$$

Since the mucosal and serosal concentrations are assumed to be known, we now have a system of 5 equations to solve for the 5 unknowns, N_i, K_i, C_i, v, and $\mu = w/X$. First, notice that (2.169), (2.170), and (2.171) can be solved for N_i, K_i, and C_i, respectively, to get

$$N_i(v) = \frac{vN_m e^{-v}}{v + 3\rho_n(1 - e^{-v})}, \tag{2.175}$$

$$K_i(v) = 2\rho_k N_i(v)\frac{1 - e^{-v}}{v} + K_s e^{-v}, \tag{2.176}$$

$$C_i(v) = C_s e^v, \tag{2.177}$$

where $\rho_n = pq/P_{\text{Na}}$ and $\rho_k = pq/P_{\text{K}}$.

Next, eliminating $N_i + K_i$ between (2.172) and (2.173), we find that

$$2\mu(C_i - C_s) = z_x - 1. \tag{2.178}$$

We now use (2.177) to find that

$$z_x - 1 = 2\mu C_s(e^v - 1), \tag{2.179}$$

and thus, using (2.179) to eliminate μ from (2.172), we get

$$N_i(v) + K_i(v) = \frac{C_s}{1 - z_x}[-2z_x + e^v(1 + z_x)] \equiv \phi(v). \tag{2.180}$$

Since $z_x - 1 < 0$, it must be (from (2.179)) that $v < 0$, and as $v \to 0$, the cell volume $w = \mu X$ becomes infinite. Thus, we wish to find a negative solution of (2.180), with $N_i(v)$ and $K_i(v)$ specified by (2.175) and (2.176).

It is instructive to consider when solutions for v (with $v < 0$) exist. First, notice that $\phi(0) = C_s$. Further, since $z_x \leq -1$, ϕ is a decreasing function of v, bounded above, with decreasing slope (i.e., concave down), as sketched in Fig. 2.19. Next, from (2.175) and (2.176) we determine that $N_i(v) + K_i(v)$ is a decreasing function of v that approaches ∞ as $v \to -\infty$ and approaches zero as $v \to \infty$. It follows that a negative solution for v exists if $N_i(0) + K_i(0) < C_s$, i.e., if

$$\frac{N_m}{1 + 3\rho_n} + \frac{2\rho_k N_m}{1 + 3\rho_n} + K_s < C_s. \tag{2.181}$$

Since $K_s + N_s = C_s$, this becomes

$$\frac{N_m}{N_s} < \frac{1 + 3\rho_n}{1 + 2\rho_k}. \tag{2.182}$$

This condition is sufficient for the existence of a solution, but not necessary. That is, if this condition is satisfied, we are assured that a solution exists, but if this
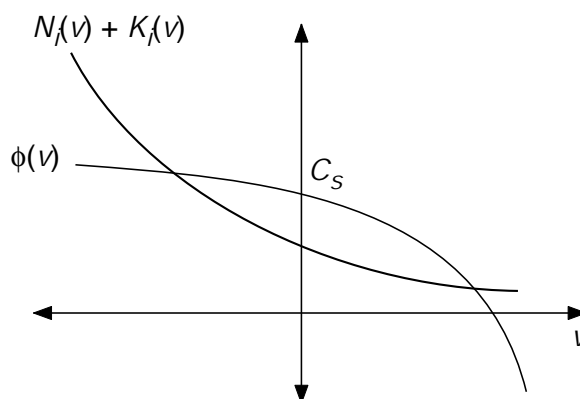
Figure 2.19: Sketch (not to scale) of the function $\phi(v)$, defined as the right-hand side of (2.180), and of $N_i(v) + K_i(v)$, where N_i and K_i are defined by (2.175) and (2.176). $\phi(v)$ is sketched for $z_x < -1$.

condition fails to hold, it is not certain that a solution fails to exist. The problem, of course, is that negative solutions are not necessarily unique, nor is it guaranteed that increasing N_m through $N_s \frac{1+3\rho_n}{1+2\rho_k}$ causes a negative solution to disappear. It is apparent from (2.175) and (2.176) that $N_i(v)$ and $K_i(v)$ are monotone increasing functions of the parameter N_m, so that no negative solutions exist for N_m sufficiently large. However, for $N_m = N_s \frac{1+3\rho_n}{1+2\rho_k}$ to be the value at which the cell bursts by *increasing* N_m, it must also be true that

$$N_i'(0) + K_i'(0) < \phi'(0), \tag{2.183}$$

or that

$$4(1 + 3\rho_n)C_s + N_s(1 - z_x)\frac{3\rho_n - 2\rho_k}{1 + 2\rho_k} > 0. \tag{2.184}$$

For the remainder of this discussion we assume that this condition holds, so that the failure of (2.182) also implies that the cell bursts.

According to (2.182), a transporting epithelial cell can maintain its cell volume, provided the ratio of mucosal to serosal concentrations is not too large. When N_m/N_s becomes too large, μ becomes unbounded, and the cell bursts. Typical solutions for the cell volume and membrane potential, as functions of the mucosal Na^+ concentration, are shown in Fig. 2.20.

Obviously, this state of affairs is unsatisfactory. In fact, some epithelial cells, such as those in the loop of Henle in the nephron (Chapter 17), must work in environments with extremely high mucosal Na^+ concentrations. To do so, these Na^+-transporting epithelial cells have mechanisms to allow operation over a much wider range of mucosal Na^+ concentrations than suggested by this simple model.

From (2.182) we can suggest some mechanisms by which a cell might avoid bursting at high mucosal concentrations. For example, the possibility of bursting is decreased if ρ_n is increased or if ρ_k is decreased. The reasons for this are apparent
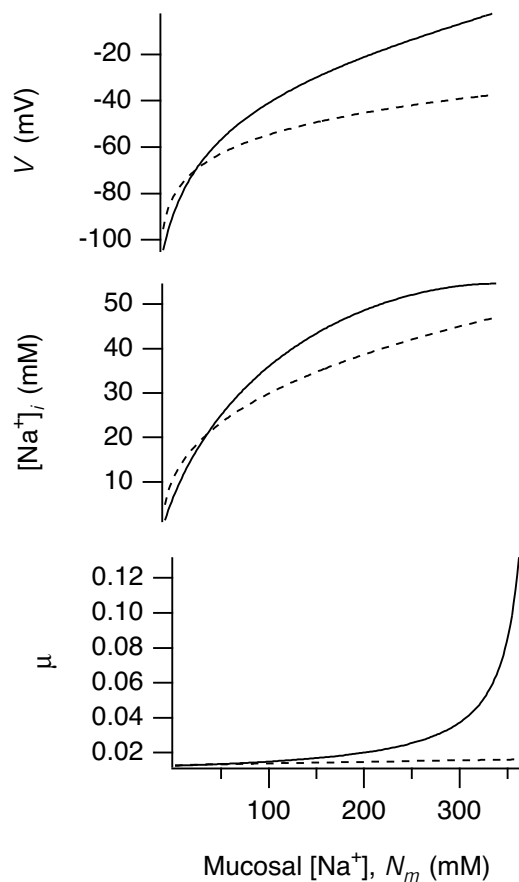
Figure 2.20: Numerical solutions of the model for epithelial cell volume regulation and Na^+ transport. The membrane potential V, the scaled cell volume μ, and the intracellular Na^+ concentration $[Na^+]_i$ are plotted as functions of the mucosal Na^+ concentration. The solid lines are the solutions of the simpler version of the model, where P_{Na} and P_K are assumed to be constant. The dashed lines are the solutions of the model when P_{Na} is assumed to be a decreasing function of N_i, and P_K is assumed to be an increasing function of w, as described in the text. Parameter values are $K_s = 2.5$, $N_s = 120$, $C_s = 122.5$, $P = 2$, $\gamma = 0.3$, $z_x = -2$. All concentrations are in mM.

from (2.175) and (2.176), since $N_i(v) + K_i(v)$ is a decreasing function of ρ_n and an increasing function of ρ_k. From a physical perspective, increasing N_m causes an increase in N_i, which increases the osmotic pressure, inducing swelling. Decreasing the conductance of Na^+ ions from the mucosal side helps to control this swelling. Similarly, increasing the conductance of K^+ ions allows more K^+ ions to flow out of the cell, thereby decreasing the osmotic pressure from K^+ ions and counteracting the tendency to swell.

It has been conjectured for some time that epithelial cells use both of these mechanisms to control their volume (Schultz, 1981; Dawson and Richards, 1990; Beck et al., 1994). There is evidence that as N_i increases, epithelial cells decrease the Na^+ conductance on the mucosal side of the cell, thus restricting Na^+ entry. There is also evidence that as the cell swells, the K^+ conductance is increased, possibly by means of stretch-activated K^+ channels (Ussing, 1982. This assumption was used in the modeling work of Strieter et al., 1990).

To investigate the effects of these mechanisms in our simple model, we replace P_{Na} by $P_{Na}20/N_i$ (20 is a scale factor, so that when $N_i = 20$ mM, P_{Na} has the same value as in the original version of the model) and replace P_K by $P_K w/w_0$, where w_0 is the volume of the cell when $N_m = 100$ mM. As before, we can solve for v and μ as functions of N_m, and the results are shown in Fig. 2.20. Clearly the incorporation of these mechanisms decreases the variation of cell volume and allows the cell to survive over a much wider range of mucosal Na^+ concentrations.

The model for control of ion conductance used here is extremely simplistic, as for example, there is no parametric control of sensitivity, and the model is heuristic, not mechanistic. More realistic and mechanistic models have been constructed and analyzed in detail (Lew et al., 1979; Civan and Bookman, 1982; Strieter et al., 1990; Weinstein, 1992, 1994, 1996; Tang and Stephenson, 1996).

2.9 Appendix - Stochastic Processes

Although all of the models that have been presented so far in this text have been deterministic, the reality is that biological processes are fundamentally noisy. Furthermore, many of the assumptions underlying deterministic models are questionable, largely because of significant stochastic effects.

The purpose of this appendix is to outline some of the basic ideas of stochastic processes that play an important role in mathematical modeling of biological phenomena. Furthermore, there are a number of sections in the remainder of this book where stochastic models are crucial, and hopefully this appendix provides the necessary background for these. Of course, this is not a detailed treatment of these topics; for that one needs to consult texts on stochastic processes such as Gardiner (1985) or van Kampen (1992).

2.9.1 Markov Processes

A *Markov process* is any stochastic process that has no memory. More precisely, if the value of the state variable x is known at two times, say $t_1 < t_2$ to be x_1 and x_2,

respectively, then

$$p(x, t | x_1, t_1, x_2, t_2) = p(x, t | x_2, t_2). \tag{2.185}$$

In words, the conditional probability for the value of the state variable depends only on the most recent condition and not on any previous conditions.

A simple example of a Markov process is radioactive decay. For example, an atom of carbon-14 may lose an electron and decay to nitrogen-14. This is assumed to be a Markov process, because the probability of decay does not depend on how old the carbon-14 atom is. A newly formed carbon-14 atom has exactly the same probability of decay in the next second as a very old carbon-14 atom.

To model this process, we suppose that the state variable has two possible values, say C (for carbon) and N (for nitrogen), and we denote the probability that the molecule is in state S at time t by $P(\text{S}, t)$. Now suppose that the probability of radioactive decay in a small interval of time dt is λdt. (Note that λ need not be independent of time for this to be a Markov process.) Then,

$$P(\text{N}, t + \Delta t) = P(\text{N}, t) + P(\text{C}, t)\lambda \Delta t. \tag{2.186}$$

For this problem we assume that $P(\text{C}, t) + P(\text{N}, t) = 1$. It follows that in the limit $\Delta t \to 0$,

$$\frac{dP(\text{N}, t)}{dt} = \lambda(1 - P(\text{N}, t)). \tag{2.187}$$

By similar arguments, many of the differential equations in this chapter describing concentrations or fractions of molecules in a given state can be reinterpreted as equations for the probability that a single molecule is in a particular state. For example, for a transporter molecule that has two states, say,

$$\text{C}_i \underset{k}{\overset{k}{\rightleftharpoons}} \text{C}_e, \tag{2.188}$$

under the assumption that transitions between states do not depend on how long the molecule has been in a given state, the probability P of being in state C_i at time t, $P(C_i, t)$, is given by

$$\frac{dP(\text{C}_i, t)}{dt} = k(1 - P(\text{C}_e, t)) - kP(\text{C}_i, t), \tag{2.189}$$

Similarly, for the chemical reaction

$$\text{A} \underset{k_-}{\overset{k_+}{\rightleftharpoons}} \text{B}, \tag{2.190}$$

the probability $P(\text{A}, t)$ of a molecule being in state A at time t is determined by

$$\frac{dP(\text{A}, t)}{dt} = k_- P(\text{B}, t) - k_+ P(\text{A}, t). \tag{2.191}$$

Of course, this is the same as the equation found using the law of mass action for the conversion of A to B, namely,

$$\frac{da}{dt} = k_- b - k_+ a. \tag{2.192}$$

Even though these equations are identical, their interpretations are quite different. For example, at steady state, $\frac{a}{b} = \frac{k_-}{k_+}$ implies that the ratio of the number of molecules in state A to the number of those in state B is $\frac{k_-}{k_+}$. However, this cannot be the probabilistic interpretation, since there is no fractional state. Instead, the probabilistic interpretation is that the ratio of time a single molecule spends in state A to the amount of time it spends in state B is $\frac{k_-}{k_+}$.

2.9.2   Discrete-state Markov processes

Often the state space of a Markov process is discrete; for example, the model of the Na,K-ATPase (Fig. 2.11) assumes that the ATPase can be in only a small number of different states. The simple chemical reaction in the previous section is also a model of this type, as the molecule can exist in only two states, A or B. Since time is a continuous variable, such models are called *discrete-space continuous-time Markov processes*. Such Markov processes play an enormously important role in modeling; indeed, a large fraction of the models of chemical reactions, exchangers, pumps, and ion channels we discuss in this book are discrete-space continuous-time Markov processes. As is described in Chapter 3, one of the most important applications of such models is the analysis of data from single ion channels.

To describe the stochastic behavior of a discrete-space continuous-time Markov process with n possible states (open, closed, inactivated, etc.), we introduce a discrete random variable $S(t) \in 1, 2, \ldots, n$ defined so that $S(t) = i$ if the model is in state i at time t. Further, we suppose that the probability that the model changes from state i to state j in the time interval $(t, t + dt)$ is $k_{ij}dt$. In more condensed notation,

$$P[S(t + dt) = j | S(t) = i] = k_{ij}dt, \tag{2.193}$$

where $P[x|y]$ denotes the conditional probability of x given y. Note that (2.193) is valid only in the limit of small dt, since for sufficiently large dt and k_{ij} nonzero, this probability exceeds 1. Also, the probability that the model does not change state in the time interval $(t, t + dt)$ is given by

$$P[S(t + dt) = i | S(t) = i] = 1 - K_i dt, \tag{2.194}$$

where $K_i = \sum_{j \neq i} k_{ij}$.

Now we let $\Phi_j(t) = P[S(t) = j]$, i.e., $\Phi_j(t)$ is the probability that the model is in state j at time t. In words, the probability that the model is in state j at time $t + dt$ is the probability that it was in state j at time t and did not leave state j between times t and $t + dt$ plus the probability that at time t it was in another state and switched into state j in the time interval t to $t + dt$. In mathematical language,

$$
\begin{aligned}
\Phi_j(t + dt) &= \Phi_j(t)P[S(t + dt) = i | S(t) = i] + \sum_{l \neq j} P[S(t + dt) = j | S(t) = l]\Phi_l(t) \\
&= \Phi_j(t)\left(1 - K_j dt\right) + \sum_{l \neq j} k_{lj}\Phi_l(t)dt, \tag{2.195}
\end{aligned}
$$

and thus, taking the limit $dt \to 0$,

$$\frac{d\Phi_j}{dt} = -K_j\Phi_j(t) + \sum_{l \neq j} k_{lj}\Phi_l(t). \tag{2.196}$$

In vector notation, with Φ the vector having elements Φ_j, we have

$$\frac{d\Phi}{dt} = A^T\Phi(t), \tag{2.197}$$

where A is the matrix

$$A = \begin{pmatrix} -K_1 & k_{12} & \cdots & k_{1n} \\ k_{21} & -K_2 & \cdots & k_{2n} \\ \vdots & \vdots & \vdots & \vdots \end{pmatrix}. \tag{2.198}$$

Of course, this is exactly the system of differential equations we would have written down for a system of first order chemical reactions with reaction rates between species k_{ij}. Here, however, the variables Φ_j are probabilities and so must sum to one. In the terminology of stochastic processes, (2.197) is called the *master equation* for this Markov process.

The waiting time

One important question is how long a Markov model stays in a particular state before switching. This is called the waiting time problem. To solve this we let T_i be the random time at which the model switches from state i to some other state, and we let $P_i(t) = P[T_i < t]$, that is, $P_i(t)$ is the probability that by time t the switch has occurred. In words, the probability that the switch has occurred by time $t + dt$ is the probability that it has occurred by time t plus the probability that the switch has not occurred by time t and occurs in the time interval between t and $t + dt$. In mathematical language,

$$P_i(t + dt) = P_i(t) + (1 - P_i)K_i dt. \tag{2.199}$$

Taking the limit $dt \to 0$ we find the differential equation for the waiting time probability

$$\frac{dP_i}{dt} = K_i(1 - P_i), \tag{2.200}$$

which, since $P_i(0) = 0$ (assuming the switch has not occurred at time $t = 0$), and if K_i is independent of time, yields

$$P_i(t) = 1 - \exp(-K_i t). \tag{2.201}$$

The function $P_i(t)$ is a cumulative probability distribution function, with probability density function

$$p_i(t) = \frac{dP_i}{dt} = K_i \exp(-K_i t). \tag{2.202}$$

The probability that the switch occurs between two specified times, t_1 and t_2, is

$$P[t_1 < T_i < t_2] = \int_{t_1}^{t_2} p_i(s) \, ds = P_i(t_2) - P_i(t_1), \qquad (2.203)$$

and the expected switching time is

$$E(T_i) = \int_0^\infty t p_i(t) dt. \qquad (2.204)$$

If K_i is time independent,

$$E(T_i) = \frac{1}{K_i}. \qquad (2.205)$$

The transition time

The waiting time problem can be generalized to calculate the probability density function, ϕ_{ij}, for the time it takes to move from state i to state j.

To do this we make state j an absorbing state and then solve the master equations starting in state i. That is, we set $k_{jl} = 0$ for every l, and then solve for $\Phi_j(t)$, with the initial condition $\Phi_i(0) = 1$, $\Phi_l(0) = 0$ for $l \neq i$. Then, $\Phi_j(t)$ is the probability that the process is in state j at time t, given that it started in state i at time 0. Hence, $\Phi_j(t)$ is the cumulative probability that the transition to state j occurred at some time previous to t. The probability density function for the transition time is the derivative of the cumulative probability. Hence,

$$\phi_{ij}(t) = \frac{d\Phi_j}{dt} = \sum_{l \neq j} k_{lj} \Phi_l. \qquad (2.206)$$

2.9.3 Numerical Simulation of Discrete Markov Processes

It is becoming increasingly important and valuable to do numerical simulations of discrete stochastic processes. The definition (2.193) provides a natural numerical algorithm for such a simulation. For a fixed small time step of size dt, divide the unit interval into $n-1$ regions of length $k_{ij} dt$ and one remaining region of length $1 - K_i dt$. Then, at each time step, pick a random number that is uniformly distributed on the unit interval and determine the next state by the subinterval in which the random number falls.

While this method of numerical simulation is simple and direct, it is not particularly efficient. Furthermore, it converges (i.e., gives the correct statistics) only in the limit that $dt \to 0$.

A method that is much more efficient is known as Gillespie's method (Gillespie, 1977). The idea of this method is to calculate the sequence of random switching times. For example, suppose that at time $t = 0$, the state variable is $S(0) = i$. We know that the probability that the first transition out of state i occurs in the interval $(t, t + dt)$ is $\int_t^{t+dt} K_i \exp(-K_i s) \, ds$. From this, we want to calculate the time to the next transition. We do this by selecting a random number x uniformly distributed on the unit interval, and transforming that number via some transformation $t = f(x)$

to get the time at which the transition occurs. The transformation we use should preserve probabilities,

$$p_i(t)dt = q(x)dx, \qquad (2.207)$$

where $p_i(t)$ is the exponential waiting time distribution, and $q(x) = 1$ is the uniform distribution. Integrating gives $x = \int_0^t p_i(s)\, ds = 1 - \exp(-K_i y) = P_i(t)$, and solving for t, we get

$$t = -\frac{1}{K_i} \ln(1 - x). \qquad (2.208)$$

However, since x is uniformly distributed on the unit interval, it is equivalent to replace $1 - x$ by x to get

$$t = -\frac{1}{K_i} \ln(x). \qquad (2.209)$$

Therefore, to calculate the next switching time, pick a random number that is uniformly distributed on the unit interval, say ξ, and then pick the time interval to the next switch to be

$$T_n = -\frac{1}{K_i} \ln(\xi). \qquad (2.210)$$

To determine the state into which to switch, divide the unit interval into segments of length $\frac{k_{ij}}{K_i}$, and select the next interval to be the subinterval in which another uniformly distributed random number η resides. The reasoning for this is that if a switch is to occur, then the probability that the switch is into state j is $\frac{k_{ij}}{K_i}$.

There are numerous advantages to Gillespie's method. First, it is maximally efficient and it is exact. That is, since there is no time discretization step dt, accuracy does not require taking a limit $dt \to 0$. However, other nice features of the method are that it is easier to collect statistics such as closed time and open time distributions, because these quantities are directly, not indirectly, calculated.

A word of caution, however, is that while this method works well for time-independent processes (which we assumed in this discussion), for time dependent processes, or processes where the transition rates depend on other time varying variables, determination of the next transition time requires a more sophisticated calculation (Alfonsi et al., 2005).

Further difficulties with stochastic simulations occur when there are reactions with vastly different time scales. Then, it is often the case that the rapid reactions achieve quasi-equilibrium but most of the computational time for a stochastic simulation is taken in calculating the many fast transitions of the fast reactions. It is beyond the scope of this text to describe what to do in these situations.

Gillespie's method is the method of choice in many situations. It has been implemented by Adalsteinsson, Elston and McMillen in a useful software package that is readily available (Adalsteinsson et al., 2004).

2.9.4   Diffusion

The diffusion equation (2.7) was derived to describe the evolution of a chemical concentration, under the assumption that the concentration is a continuous variable, even though the number of molecules involved is necessarily an integer. Einstein recognized that the solution of the diffusion equation could also be interpreted as

the probability distribution function for the location of a single particle undergoing some kind of a random walk. That is, if $p(x,t)$ is the solution of the diffusion equation

$$\frac{\partial p}{\partial t} = D\nabla^2 p, \tag{2.211}$$

then $\int_\Omega p(x,t)dx$ could be identified as the probability that a particle is in the region Ω at time t. More specifically, if $p(x,t|x_0,t_0)$ is the probability distribution function for the particle to be at position x at time t, given that it was at position x_0 at time t_0, then

$$p(x,t_0|x_0,t_0) = \delta(x-x_0), \tag{2.212}$$

and solving the diffusion equation (in one spatial dimension) gives

$$p(x,t|x_0,t_0) = \frac{1}{2\sqrt{\pi D(t-t_0)}}\exp\left(-\frac{(x-x_0)^2}{4D(t-t_0)}\right), \tag{2.213}$$

provided $t > t_0$. It follows immediately that the mean and variance of this distribution are

$$\langle x \rangle = \int_{-\infty}^{\infty} xp(x,t|0,0)dx = 0, \tag{2.214}$$

and

$$\langle x^2 \rangle = \int_{-\infty}^{\infty} x^2 p(x,t|0,0)dx = 2Dt. \tag{2.215}$$

The conditional probability $p(x,t|x_0,t_0)$ is the Green's function of the diffusion equation on an infinite domain (where we require, for physical reasons, that the solution and all its derivatives vanish at infinity). As a side issue (but a particularly interesting one), note that, from the transitive nature of Green's functions, it follows that

$$p(x_1,t_1|x_3,t_3) = \int_{x_2} p(x_1,t_1|x_2,t_2)p(x_2,t_2|x_3,t_3)dx_2, \quad t_3 < t_2 < t_1, \tag{2.216}$$

which is known as the Chapman-Kolmogorov equation. From the point of view of conditional probabilities, the Chapman-Kolmogorov equation makes intuitive sense; for Markov processes, the probability of x_1 given x_3 is the sum of the probabilities of each path by which one can get from x_3 to x_1.

Now suppose we let $X(t)$ represent the position as a function of time of a sample path. We can readily calculate that $X(t)$ is continuous, since for any $\epsilon > 0$, the probability of escaping from a region of size ϵ in time Δt is

$$\begin{aligned}
\int_{|x-z|>\epsilon} p(x,t+\Delta t|z,t)dx &= 2\int_{\epsilon}^{\infty} \frac{1}{2\sqrt{\pi D\Delta t}}\exp\left(-\frac{x^2}{4D\Delta t}\right)dx \\
&= \int_{\frac{\epsilon}{2\sqrt{D\Delta t}}}^{\infty} \exp\left(-x^2\right)dx,
\end{aligned}$$

which in the limit $\Delta t \to 0$ approaches zero. On the other hand, the velocity of the particle is likely to be extremely large since

$$
\begin{aligned}
\text{Prob}\left(\frac{1}{\Delta t}(X(t+\Delta t) - X(t)) > k\right) &= \int_{k\Delta t}^{\infty} \frac{1}{2\sqrt{\pi D\Delta t}} \exp\left(-\frac{x^2}{4D\Delta t}\right) dx \\
&= \int_{\frac{k}{2}\sqrt{\frac{\Delta t}{\pi D}}}^{\infty} \exp\left(-x^2\right) dx \to \frac{1}{2}, \quad (2.217)
\end{aligned}
$$

in the limit that $\Delta t \to 0$. In other words, with probability 1 the absolute value of the velocity is larger than any number k, hence infinite.

If $D = 1$, the stochastic process $X(t)$ is known as a *Wiener process*, is usually denoted as $W(t)$, and is a model for Brownian motion.

Diffusion as a Markov process

A popular derivation of the diffusion equation is based on a Markovian random walk on a grid, as follows. We suppose that a particle moves along a one-dimensional line in discrete steps of length Δx at discrete times with time step Δt. At each step, however, the direction of motion is random, with probability $\frac{1}{2}$ of going to the left and probability $\frac{1}{2}$ of going to the right. If $p(x,t)$ is the probability of being at position x at time t, then

$$
p(x, t+\Delta t) = \frac{1}{2}p(x+\Delta x, t) + \frac{1}{2}p(x-\Delta x, t). \tag{2.218}
$$

Now we make the assumption that $p(x,t)$ is a smooth function of both x and t and find the Taylor series expansion of (2.218),

$$
\Delta t\frac{\partial p}{\partial t} + O(\Delta t^2) = \frac{\Delta x^2}{2}\frac{\partial^2 p}{\partial x^2} + O(\Delta x^4). \tag{2.219}
$$

In the limit that Δt and Δx both approach zero, keeping $\frac{\Delta x^2}{\Delta t} = 1$, we find the diffusion equation with diffusion coefficient $\frac{1}{2}$.

2.9.5   Sample Paths; the Langevin equation

The diffusion equation describes the probability distribution that a particle is at a particular place at some time, but does not describe how the particle actually moves. The challenge, of course, is to write (and solve) an equation for motion that is random and continuous, but nowhere differentiable. Obviously, one cannot use a standard differential equation to describe the motion of such a particle. So, instead of writing $\frac{dx}{dt} = $ something (which does not make sense since the velocity $\frac{dx}{dt}$ of a Brownian particle is not finite), it is typical to write

$$
dx = \sqrt{2D}dW. \tag{2.220}
$$

To make careful mathematical sense of this expression requires a discussion of the Ito or Stratonovich calculus, topics which are beyond the scope of this text. However,

a reasonable verbal description of what this means in practical terms is as follows. The term dW is intended to represent the fact that the displacement of a particle after a very short time interval, say dt, is a random variable having three properties, namely, it is uncorrelated with previous displacements (it has no memory and is therefore Markovian), it has zero mean, and it has variance dt, in the limit $dt \to 0$. This is also referred to as uncorrelated *Gaussian white noise*. In fact, this definition is rigged so that the probability distribution for this particle is described by the diffusion equation.

For this text, it is important to know how to numerically calculate representative sample paths, and to this end we write

$$dx = \sqrt{2Ddt}N(0,1), \tag{2.221}$$

where $N(0,1)$ represents the Gaussian (normal) distribution with zero mean and variance 1. The interpretation of this is that at any given time one randomly chooses a number n from a normal distribution, takes a step of size $dx = \sqrt{2Ddt}n$, and then increments time by dt. It can be shown that in the limit that $dt \to 0$, this converges to the Wiener process (2.220).

Equation (2.220) is an example of a stochastic differential equation, also called a Langevin equation. More generally, Langevin equations are of the form

$$dx = a(x,t)dt + \sqrt{2b(x,t)}dW, \tag{2.222}$$

or, in a form that suggests a numerical algorithm,

$$dx = a(x,t)dt + \sqrt{2b(x,t)dt}N(0,1). \tag{2.223}$$

Here $a(x,t)$ represents the deterministic part of the velocity, since if there were no noise ($b(x,t) = 0$), this would be the same as the deterministic equation

$$\frac{dx}{dt} = a(x,t). \tag{2.224}$$

Thus, the displacement dx is a random variable, with mean value $a(x,t)dt$ and variance $2b(x,t)dt$, in the limit $dt \to 0$.

The special case $a(x,t) = -x$, $b(x,t) = 1$, called an *Ornstein-Uhlenbeck* process, is important in the study of molecular motors, described in Chapter 15.

2.9.6 The Fokker-Planck equation and the Mean First Exit Time

The diffusion equation is the simplest example of an equation describing the evolution of the probability distribution function for the position of a particle. More generally, if we suppose that the position of the particle is continuous in time (no finite jumps are possible), that the Chapman-Kolmogorov equation (2.216) holds, and that the displacement of the particle in time dt has mean $a(x,t)dt$ and variance $2b(x,t)dt$, then one can derive that the probability distribution $p(x,t)$ for the position, x, of the particle at time t, is governed by

$$\frac{\partial p}{\partial t} = -\frac{\partial}{\partial x}(a(x,t)p) + \frac{\partial^2}{\partial x^2}(b(x,t)p), \tag{2.225}$$

called the *Fokker-Planck* equation. Note that, since this equation models the motion of a particle, which must be at a single position y at the starting time, t_0, the initial condition must therefore be $p(x, t_0|y, t_0) = \delta(x - y)$. Thus, the probability distribution for the position of the particle is the Green's function of (2.225).

More generally, it is possible to start with the Chapman-Kolmogorov equation (2.216) and derive a general version of the Fokker-Planck equation that includes discrete jump processes. This is the point of view usually taken in the stochastic processes literature, which treats the Chapman-Kolmogorov equation as a fundamental requirement of a Markov process.

An extremely important problem is the so-called *mean first exit time problem*, in which we wish to determine how long a particle stays in a particular region of space. Before we can solve this problem we must first determine the equation for the conditional probability, $p(x, t|y, \tau)$, as a function of y and $\tau < t$, with x and t fixed. That is, we want to know the probability distribution function for a particle with known position x at time t to have been at the location y at time $\tau < t$.

The equation governing this conditional probability is most easily derived by using the fact that $p(x, t|y, \tau)$ is the Green's function of the Fokker-Planck equation. It follows from the properties of Green's functions (Keener, 1998) that

$$p(x, t|y, \tau) = p^*(y, \tau|x, t), \qquad (2.226)$$

where p^* is the Green's function of the adjoint equation. The adjoint equation is easily calculated using integration by parts, and assuming that p and all its derivatives vanish at infinity. It follows that p, considered as a function of y and τ, satisfies the adjoint equation

$$\frac{\partial p}{\partial \tau} = -a(y, \tau)\frac{\partial p}{\partial y} - b(y, \tau)\frac{\partial^2 p}{\partial y^2}, \qquad (2.227)$$

subject to the condition $p(x, t|y, t) = \delta(x - y)$. This equation for the backward conditional probability is called the *backward Fokker-Planck equation*. Notice that this is a *backward* diffusion equation, which in forward time is ill-posed. However, it is well posed when solved for backwards times $\tau < t$.

Armed with the backward Fokker-Planck equation, we now turn our attention to the mean first exit time problem. Suppose a particle is initially at position y, inside a one-dimensional region $\alpha < y < \beta$, and that the wall at $y = \alpha$ is impermeable, but the particle can leave the region freely at $y = \beta$. If we let $\tau(y)$ represent the time at which the particle first leaves the region having started from position y, then

$$P(\tau(y) > t) = G(y, t) = \int_\alpha^\beta p(x, t|y, 0)dx, \qquad (2.228)$$

which is the probability that the particle is inside the region at time t. Notice that since $p(x, 0|y, 0) = \delta(x - y)$, $G(y, 0) = 1$.

Since

$$P(\tau(y) > t) = G(y, t) = -\int_t^\infty G_t(y, s)ds, \qquad (2.229)$$

it follows that $G_t(y, t)$ is the probability density function for the random variable $\tau(y)$. Thus, the expected value of $\tau(y)$ is

$$T(y) = E(\tau(y)) = -\int_0^\infty tG_t(y, t)dt = \int_0^\infty G(y, t)dt, \qquad (2.230)$$

where we have integrated by parts to get the final expression. Note that $T(y)$ is the mean time at which a particle leaves the domain, given that it starts at y at time $t = 0$.

For a time independent process, (i.e., $a(y, t) = a(y)$, $b(y, t) = b(y)$), $p(x, t|y, 0) = p(x, 0|y, -t)$. Hence, substituting $-t$ for t in (2.227), and writing $q(y, t|x) = p(x, t|y, 0)$, it follows that q satisfies the negative backward Fokker-Planck equation

$$\frac{\partial q}{\partial t} = a(y)\frac{\partial q}{\partial y} + b(y)\frac{\partial^2 q}{\partial y^2}, \qquad (2.231)$$

with $q(y, 0|x) = \delta(x - y)$. Integrating with respect to x from $x = \alpha$ to $x = \beta$ (since $G(y, t) = \int_\alpha^\beta p(x, t|y, 0)dx$), then gives

$$\frac{\partial G}{\partial t} = a(y)\frac{\partial G}{\partial y} + b(y)\frac{\partial^2 G}{\partial y^2}, \qquad (2.232)$$

with $G(y, 0) = 1$. Finally, we can determine the equation for the expected value of $\tau(y)$ by integrating (2.232) in time to find

$$-1 = a(y)\frac{\partial T}{\partial y} + b(y)\frac{\partial^2 T}{\partial y^2}. \qquad (2.233)$$

To completely specify the problem we must specify boundary conditions. At impermeable boundaries, we require $\frac{\partial T}{\partial y} = 0$, while at absorbing boundaries (boundaries through which exit is allowed but reentry is not permitted) $T = 0$.

As an example, consider a pure diffusion process on a domain of length L with a reflecting boundary at $x = 0$ and an absorbing boundary at $x = L$. The mean first exit time satisfies the differential equation

$$DT_{xx} = -1, \qquad (2.234)$$

subject to boundary conditions $T_x(0) = 0$, $T(L) = 0$. This has solution

$$T(x) = \frac{-x^2 + L^2}{2D}. \qquad (2.235)$$

We readily calculate that $T(0) = \frac{L^2}{2D}$, as might be expected from (2.215). In addition, as x increases, $T(x)$ decreases, which again makes intuitive sense. The closer the particle starts to the absorbing boundary, the shorter is the mean first exit time.

2.9.7 Diffusion and Fick's Law

The Fokker-Planck equation describes the evolution of the probability distribution function for single particle diffusion. However, it also applies to the concentration of

a dilute chemical species under the assumption that the chemical particles have no self-interaction. If the diffusion coefficient is homogeneous in space, then the Fokker-Planck equation and the diffusion equation are the same. However, if diffusion is not homogeneous in space, then the diffusion equation, derived using Fick's law, and the Fokker-Planck equation are not the same. With Fick's law, the diffusion equation is

$$\frac{\partial c}{\partial t} = \frac{\partial}{\partial x}\left(D\frac{\partial c}{\partial x}\right) \tag{2.236}$$

and the Fokker-Planck equation is

$$\frac{\partial c}{\partial t} = \frac{\partial^2(Dc)}{\partial x^2}. \tag{2.237}$$

Which of these is correct?

There is a simple observation that can help answer this question. If Fick's law is correct, then at steady state the flux in a closed container is zero, so that

$$D\frac{\partial c}{\partial x} = 0, \tag{2.238}$$

implying that $c(x)$ is a uniform constant. On the other hand, if the Fokker-Planck equation is correct, then at steady state

$$D(x)c(x) = \text{constant}. \tag{2.239}$$

Notice that in this solution, the concentration varies inversely with D. That is, if D is low then c should be high, and vice versa. Further, if c is initially uniform, Fick's law predicts no change in the solution as a function of time, whereas, the Fokker-Planck equation predicts transient behavior leading to a nonuniform distribution of c.

Van Milligen et al. (2006) reported a simple experimental test of this observation. They added green food coloring to water and then added differing amounts of gelatin to small quantities of the colored water. They then created gel bilayers consisting of two layers of the colored gelatin with differing gelatin concentrations under the assumption that diffusion of food coloring varies inversely with the amount of gelatin. They recorded the color intensity at several later times and compared these recordings with the solution of the partial differential equations.

The first observation is that the initially uniform concentration of food coloring did not remain uniform, but increased in regions where the gelatin density was highest. Even more striking, they were able to find very good fits of the data to the numerical solution of the Fokker-Planck equation. These observations lead to the conclusion that Fick's law is not the correct description of chemical diffusion in media where the diffusion coefficient is not constant. The more appropriate description, coming from the Fokker-Planck equation, is that

$$J = -\nabla(Dc). \tag{2.240}$$

Exercises

1. A rule of thumb (derived by Einstein) is that the diffusion coefficient for a globular molecule satisfies $D \sim M^{-1/3}$ where M is the molecular weight. Determine how well this relationship holds for the substances listed in Table 2.2 by plotting D and M on a log-log plot.

2. A fluorescent dye with a diffusion coefficient of $D = 10^{-7}$ cm^2/s and binding equilibrium of $K_{\text{eq}} = 30$ mM is used to track the spread of hydrogen ($D_h = 4.4 \times 10^{-5}$cm^2/s). Under these conditions the measured diffusion coefficient is 8×10^{-6}cm^2/s. How much dye is present? (Assume that the dye is a fast buffer of hydrogen and that the amount of hydrogen is much less that K_{eq}.)

3. Segel, Chet and Henis (1977) used (2.21) to estimate the diffusion coefficient for bacteria. With the external concentration C_0 at 7×10^7ml^{-1}, at times t = 2, 5, 10, 12.5, 15, and 20 minutes, they counted N of 1,800, 3,700, 4,800, 5,500, 6,700, and 8,000 bacteria, respectively, in a capillary of length 32 mm with 1 μl total capacity. In addition, with external concentrations C_0 of 2.5, 4.6, 5.0, and 12.0 $\times 10^7$ bacteria per milliliter, counts of 1,350, 2,300, 3,400, and 6,200 were found at $t = 10$ minutes. Estimate D.

4. Calculate the effective diffusion coefficient of oxygen in a solution containing 1.2×10^{-5} M/cm^3 myoglobin. Assume that the rate constants for the uptake of oxygen by myoglobin are $k_+ = 1.4 \times 10^{10}$cm^3 M^{-1}s^{-1}, and $k_- = 11$ s^{-1}.

5. Find the maximal enhancement for diffusive transport of carbon dioxide via binding with myoglobin using $D_s = 1.92 \times 10^{-5}$ cm^2/s, $k_+ = 2 \times 10^8$ cm^3/M·s, $k_- = 1.7 \times 10^{-2}/s$. Compare the amount of facilitation of carbon dioxide transport with that of oxygen at similar concentration levels.

6. Devise a model to determine the rate of production of product for a "one-dimensional" enzyme capsule of length L in a bath of substrate at concentration S_0. Assume that the enzyme is confined to the domain $0 \le x \le L$ and there is no flux through the boundary at $x = 0$. Assume that the enzyme cannot diffuse within the capsule but that the substrate and product can freely diffuse into, within, and out of the capsule. Show that the steady state production per unit volume of enzyme is less than the production rate of a reactor of the same size in which substrate is homogeneously mixed (infinite diffusion).

7. Devise a model to determine the rate of production of product for a spherical enzyme capsule of radius R_0 in a bath of substrate at concentration S_0. Assume that the enzyme cannot diffuse within the capsule but that the substrate and product can freely diffuse into, within, and out of the capsule. Show that spheres of small radius have a larger rate of production than spheres of large radius.

   Hint: Reduce the problem to the nondimensional boundary value problem

$$\frac{1}{y^2}(y^2\sigma')' - \alpha^2 \frac{\sigma}{\sigma + 1} = 0, \tag{2.241}$$
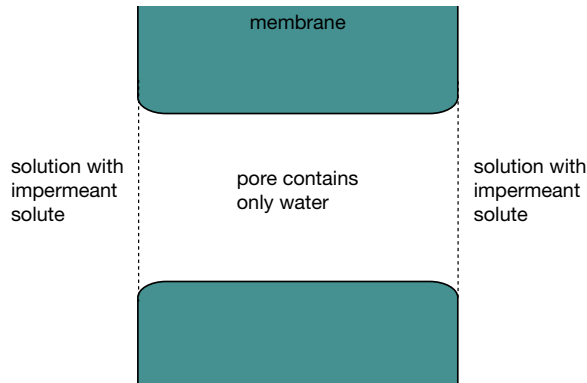
Figure 2.21: Sketch of a pore in a membrane, with an impermeant solute on both sides of the membrane.

$$\sigma'(0) \quad = \quad 0, \qquad\qquad (2.242)$$
$$\sigma(1) \quad = \quad \sigma_0, \qquad\qquad (2.243)$$

and solve numerically as a function of α. How does the radius of the sphere enter the parameter α?

8. **James, every time I try to work through this problem I run into problems that I can't resolve. I also don't think that the chapter defines things well enough for students to do this problem either. I have a list of questions, see below. JK** Suppose a membrane that contains water-filled pores separates two solutions, as sketched in Fig. 2.21.

   (a) Suppose that the solution on either side of the membrane contains an impermeant solute. Show that at steady-state the hydrostatic pressure of the water within the pores must be less than the hydrostatic pressure of the solutions on either side of the membrane. **we have nowhere defined hydrostatic pressure. Are we assuming that the flow across the end of the pore is linearly proportional to the total pressure drop? If so, this is nowhere stated. The text describes flow across a resisting membrane. Here the pore is an opening in a membrane but this is a much different model than the one discussed in the text.** Hint: note that the solute cannot get inside the pore, but water can. What would happen if the hydrostatic pressure of water was the same inside the pore as out? **This requires that there is some mechanism by which a hydrostatic pressure drop can be maintained. In the discussion in the chapter, hydrostatic pressure drops were maintained by a mechanical membrane barrier.**

Here there is no mechanical barrier across which a jump in hydrostatic pressure can be maintained.

(b) If the impermeant solute occurs at the same concentration, c, on both sides of the membrane, what is the steady-state hydrostatic pressure drop between the external solution and the water inside the pore?

(c) Show that if the solute can permeate the pore freely (assuming that different concentrations are maintained on either side of the membrane), osmosis can drive a flow of water in the absence of any hydrostatic pressure gradient. **does water "diffuse" up a concentration gradient of solute? Of course, this would correspond to diffusion down a concentration gradient of solvent, but we have nowhere discussed this possibility. What law governs the flow or diffusion of solvent down its concentration gradient? We have not described this. I suppose that free energy arguments could be used to argue that solute molecules and solvent molecules actually diffuse in opposite directions in a one-for-one manner, but this is a subtlety that is nowhere discussed in the text.**

(d) Now suppose that the impermeant solute occurs at different concentrations on either side of the membrane. We expect there to be flow of water across the membrane, from the region of low solute concentration to the region of high solute concentration. How can this happen, since there cannot be any gradient of solute concentration inside the pore? **what governs the flow of water in the pore? Darcy's law? so that velocity is proportional to the pressure gradient? or is there an osmotic driving force as well? What law sets the hydrostatic pressure?**

(e) If the impermeant solute occurs at different concentrations on either side of the membrane what is the steady-state pressure gradient within the pore? What are the steady-state pressure drops at the ends of the pore? (Assume that the velocity of water flow is proportional to the pressure gradient).

(f) Show that if the solution on one side of the membrane contains both permeant and impermeant solutes, while the solution on the other side contains only the permeant solute, it is possible for water to flow against its chemical potential gradient (at least temporarily). This problem of wrong-way water flow has been observed experimentally, and is discussed in detail by Dawson (1992). Hint: consider the case where the left side of the membrane has a much higher concentration of the permeable solute, while the right side contains a smaller concentration of the impermeant solute. Keep the pressure the same on both sides of the membrane. What hydrostatic pressure gradient is established inside the pore? What effect does this have on the bulk flow of water? Can this overwhelm the diffusion of water from right to left? **all of these questions beg for a quantitative model, but we have not provided enough information for such a model. I find the verbal description of**

possibilities unsatisfactory. How can one distinguish between the diffusion of water and the bulk flow of water? I've never seen a model that distinguishes between the two. Maybe the bulk flow of water is driven by hydrostatic pressure gradient and the diffusion of water by osmotic pressure gradient. But then how does solute move? It surely diffuses, but is it also convected? and with what velocity? So here is my challenge: write down a quantitative model for the flow of water in the pore that exhibits all the features described here. That way all of the underlying assumptions and models will be clarified.

9. Red blood cells have a passive exchanger that exchanges a single Cl^- ion for a bicarbonate (HCO_3^-) ion. Develop a model for this exchanger and find the flux.

10. Almost immediately upon entering a cell, glucose is phosphorylated in the first reaction step of glycolysis. How does this rapid and nearly unidirectional reaction affect the transmembrane flux of glucose as represented by (2.57)? How is this reaction affected by the concentration of ATP?

11. In the model for the glucose transporter (Fig. 2.6) the reaction diagram was simplified by assuming that each conformation of the transporter is equally likely, and that the affinity of the glucose binding site is unaffected by a change in conformation.

    (a) Construct a more detailed model in which these assumptions are relaxed, and calculate the flux through the model.

    (b) What is the total change in chemical potential after one cycle of the exchanger? What is the equilibrium condition?

    (c) Apply detailed balance to obtain a relationship between the rate constants.

12. Consider the model of a non-electrogenic (3 for 1) Na^+-Ca^{2+} exchanger. At equilibrium, the concentrations on either side of the membrane are related by the equation

$$\frac{n_e^3 c_i}{n_i^3 c_e} = 1. \tag{2.244}$$

    Assume that the membrane separates two equal volumes. For a given set of initial concentrations and assuming there are no other exchange processes, what three additional conservation equations must be used to determine the equilibrium concentrations? Prove that there is a unique equilibrium solution. Hint: Give a graphical proof.

13. Simplify the model of the Na^+-Ca^{2+} exchanger (Fig. 2.9) by assuming that the binding and unbinding of Na^+ and Ca^{2+} are fast compared to the exchange processes between the inside and the outside of the cell. Write the new model

equations and calculate the steady-state flux. Hint: The assumption of fast equilibrium gives

$$k_1 c_i x_1 = k_{-1} n_i^3 x_2, \tag{2.245}$$

$$k_3 n_e^3 y_2 = k_{-3} c_e y_1. \tag{2.246}$$

Then introduce the new variables $X = X_1 + X_2$ and $Y = Y_1 + Y_2$ and derive the equations for X and Y.

14. Simplify the model of Fig. 2.11 by assuming fast binding of Na^+ and K^+, and draw the reaction diagram of the simplified model. Calculate the expression for the steady-state flux. Hint: combine the states X_1, X_2 and X_3 into a single state, X, and similarly for Y_1, Y_2 and Y_3. Then use the equilibrium conditions

$$x_1 = K_1 x_2 \kappa_i^2, \tag{2.247}$$

$$n_i^3 x_2 = K_2 x_3, \tag{2.248}$$

$$y_3 = K_5 n_e^3 y_2, \tag{2.249}$$

$$\kappa_e^2 y_2 = K_6 y_1, \tag{2.250}$$

where $K_i = k_{-i}/k_i$, n denotes $[Na^+]$, and κ denotes $[K^+]$, to derive the differential equations for X and Y.

15. The process by which Ca^{2+} is taken up into the sarcoplasmic reticulum (SR) in muscle and cardiac cells is similar to the Na,K-ATPase, but simpler. Two intracellular Ca^{2+} ions bind with a carrier protein with high affinity for Ca^{2+}. ATP is dephosphorylated, with the phosphate bound to the carrier. There is a conformational change of the carrier protein that exposes the Ca^{2+} to the interior of the SR and reduces the affinity of the binding sites, thereby releasing the two ions of Ca^{2+}. The phosphate is released and the conformation changed so that the Ca^{2+} binding sites are once again exposed to the intracellular space.

Formalize this reaction and find the rate of Ca^{2+} uptake by this pump.

16. Calculate the flux of the Ran-GTP nuclear transporter. Use the information given in the text to estimate the concentrating ability of this transporter, assuming there is no difference in potential across the nuclear membrane.

17. Suppose that two compartments, each of one liter in volume, are connected by a membrane that is permeable to both K^+ and Cl^-, but not to water or protein (X). Suppose further that, as illustrated in Fig. 20.28, the extracellular compartment initially contains 300 mM K^+ and 300 mM Cl^-, while the intracellular compartment initially contains 200 mM protein, with valence -2, and 400 mM K^+.

  (a) Is the starting configuration electrically and osmotically balanced?
  (b) Find the concentrations at equilibrium.

Figure 2.22: The initial configuration for Exercise 17.

(c) Why is $[K^+]_i$ at equilibrium greater than its starting value, even though $[K^+]_i > [K^+]_e$ initially? Why does K^+ not diffuse from right to left to equalize the concentrations?

(d) What is the equilibrium potential difference?

(e) What would happen if the connecting membrane were suddenly made permeable to water? How large is the osmotic pressure developed?

18. Suppose the intracellular macromolecule X can bind b molecules of the ion S via $X + bS \rightleftharpoons XS_b$. What is the effect of this buffering on the Gibbs-Donnan equilibrium potential?

19. A 1.5 oz bag of potato chips (a typical single serving) contains about 200 mg of Na^+. When eaten and absorbed into the body, how many osmoles does this bag of potato chips represent?

20. (a) Confirm that π_s in (2.137) has units of pressure.

(b) Confirm the statement that a pressure of 25 atm corresponds to a column of water over 250 meters high.

(c) Consider a vertical tube with a cross-sectional area of $1\ cm^2$. The bottom of the tube is closed with a semi-permeable membrane and 1 gram of sugar is placed in the tube. The membrane-closed end of the tube is then put into an inexhaustible supply of pure water at $T = 300K$. What will be the height of the water in the tube at equilibrium? (The weight of a sugar molecule is 3×10^{-22} gm, and the density of water is $1\ gm/cm^3$).

(d) Two columns with cross-sectional area $1\ cm^2$ are initially filled to a height of one meter with water at $T = 300°\,K$. Suppose 0.001 gm of sugar is dissolved in one of the two columns. How high will the sugary column be when equilibrium is reached?.

(e) Suppose in the previous question 1 gm of sugar is dissolved in one of the two columns. What is the equilibrium height of the two columns?

21. Suppose an otherwise normal cell is placed in a bath of high extracellular K^+. What happens to the cell volume and resting potentials?

22. Based on what you know about glycolysis from Chapter 1, how would you expect anoxia (insufficient oxygen) to affect the volume of the cell? How might you incorporate this into a model of cell volume? Hint: Lactic acid does not diffuse out of a cell as does carbon dioxide.

23. Suppose 90% of the Na^+ in the bath of a squid axon is replaced by inert choline, preserving electroneutrality. What happens to the equilibrium potentials and membrane potentials?

24. Determine the effect of temperature (through the Nernst equation) on cell volume and membrane potential.

25. Simulate the time-dependent differential equations governing cell volume and ionic concentrations. What happens if the extracellular ionic concentrations are suddenly increased or decreased?

26. Ouabain is known to compete with K^+ for external K^+ binding sites of the Na,K-ATPase. Many animal cells swell and burst when treated with the drug ouabain. Why? Hint: How would you include this effect in a model of cell volume control?

27. Since the Na,K-ATPase is electrogenic, the pump rate P in the pump-leak model must also include effects from the membrane potential. What effect does membrane potential have on the expression (2.167) and how does this modification affect the solution?

28. Use (2.221) to simulate a diffusion process, and verify that the mean and variance of the process are 0 and $2Dt$, respectively, as expected.

29. Find the steady state probability distribution for the Ornstein-Uhlenbeck process.

30. A small particle (with diffusion constant D and viscosity ν) experiences a constant load F directed to the left but is not permitted to move into the region with $x < 0$. Suppose that the particle is initially at $x = 0$. What is the expected time to first reach location $x = \delta$?

31. Suppose that a molecule enters a spherical cell of radius 5 μm at its boundary. How long will it take for the molecule to move by diffusion to find a binding target of radius 0.5 nm located at the center of the cell? Use a diffusion coefficient of 10^{-6}cm^2/s. (Hint: In higher dimensions the differential equation for the mean first exit time is $\nabla^2 T = -1$.)

Chapter 3

Membrane Ion Channels

Every cell membrane contains ion channels, macromolecular pores that allow specific ions to travel through the channels by a passive process, driven by their concentration gradient and the membrane potential. One of the most extensively studied problems in physiology is the regulation of such ionic currents. Indeed, in practically every chapter of this book there are examples of how the control of ionic current is vital for cellular function. Already we have seen how the cell membrane uses ion channels and pumps to maintain an intracellular environment that is different from the extracellular environment, and we have seen how such ionic separation results in a membrane potential. In subsequent chapters we will see that modulation of the membrane potential is one of the most important ways in which cells control their behavior or communicate with other cells. However, to understand the role played by ion channels in the control of membrane potential, it is first necessary to understand how membrane ionic currents depend on the voltage and ionic concentrations.

There is a vast literature, both theoretical and experimental, on the properties of ion channels. One of the best books on the subject is that of Hille (2001), to which the reader is referred for a more detailed presentation than that given here. The bibliography provided there also serves as a starting point for more detailed studies.

3.1   Current–Voltage Relations

Before we discuss specific models for ion channels, we emphasize an important fact that can be a source of confusion. Although the Nernst equation (2.103) for the equilibrium voltage generated by ionic separation can be derived from thermodynamic considerations and is thus universally applicable, there is no universal expression for the ionic current. An expression for, say, the Na^+ current cannot be derived from thermodynamic first principles and depends on the particular model used to describe the Na^+ channels. Already we have seen two different models for ionic currents. In the previous chapter we described two common models for Na^+ current as a function of the membrane potential and the internal and external Na^+

concentrations. In the simpler model, we assumed that the Na^+ current across the cell membrane was a linear function of the membrane potential, with a driving force given by the Na^+ Nernst potential. Thus,

$$I_{Na} = g_{Na}(V - V_{Na}), \tag{3.1}$$

where $V_{Na} = (RT/F)\ln([Na^+]_e/[Na^+]_i)$ is the Nernst potential of Na^+, and where $V = V_i - V_e$. (As usual, a subscript e denotes the external concentration, while a subscript i denotes the internal concentration.) Note that the Na^+ current is zero when V is the Nernst potential, as it must be. However, we also discussed an alternative model, where integration of the Nernst–Planck equation (2.113), assuming a constant electric field, gave the Goldman–Hodgkin–Katz (GHK), or constant-field, current equation:

$$I_{Na} = P_{Na}\frac{F^2}{RT}V\left[\frac{[Na^+]_i - [Na^+]_e \exp\left(\frac{-VF}{RT}\right)}{1 - \exp\left(\frac{-VF}{RT}\right)}\right]. \tag{3.2}$$

As before, the Na^+ current is zero when V equals the Nernst potential, but here the current is a nonlinear function of the voltage and linear in the ionic concentrations. In Fig. 3.1A we compare the linear and GHK I–V curves when there is only a single ion present.

There is no one "correct" expression for the Na^+ current, or any other ionic current for that matter. Different cells have different types of ion channels, each of which may have different current–voltage relations. The challenge is to determine the current–voltage, or I–V, curve for a given ion channel and relate it to underlying biophysical mechanisms.

Our choice of these two models as examples was not coincidental, as they are the two most commonly used in theoretical models of cellular electrical activity. Not only are they relatively simple (at least compared to some of the other models we discuss later in this chapter), they also provide good quantitative descriptions of many ion channels. For example, the I–V curves of open Na^+ and K^+ channels in the squid giant axon are approximately linear, and thus the linear model was used by Hodgkin and Huxley in their classic model of the squid giant axon (discussed in detail in Chapter 5). However, the I–V curves of open Na^+ and K^+ channels in vertebrate axons are better described by the GHK equation, and so nonlinear I–V curves are often used for vertebrate models (Frankenhaeuser, 1960a,b, 1963; Campbell and Hille, 1976).

Because of the importance of these two models, we illustrate another way in which they differ. This also serves to illustrate the fact that although the Nernst potential is universal when there is only one ion present, the situation is more complicated when two or more species of ion can pass through the membrane. If both Na^+ and K^+ ions are present and both obey the GHK current equation, we showed in (2.126) that the reversal potential V_r at which there is no net current flow is

$$V_r = \frac{RT}{F}\ln\left(\frac{P_{Na}[Na^+]_e + P_K[K^+]_e}{P_{Na}[Na^+]_i + P_K[K^+]_i}\right). \tag{3.3}$$
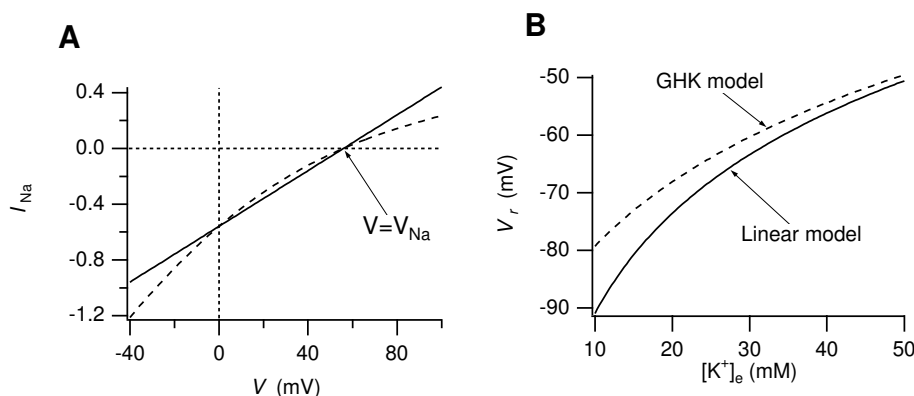
A

B

Figure 3.1: A: I–V curves of the linear and GHK models for Na^+ flux through a membrane. Both curves have the same reversal potential as expected, but the GHK model (dashed curve) gives a nonlinear I–V curve. Typical concentrations and conductances of the squid axon were used: $[Na^+]_i = 50\,mM$, $[Na^+]_e = 437\,mM$, and $g_{Na} = 0.01\,mS/cm^2$. P_{Na} was chosen so that the GHK I–V curve intersects the linear I–V curve at $V = 0$. B: Reversal potentials of the linear and GHK models as functions of $[K^+]_e$. The membrane is permeable to both Na^+ and K^+. The same parameters as A, with $[K^+]_i = 397\,mM$ and $g_K = 0.367\,mS/cm^2$. P_K was chosen so that the GHK I–V curve for K^+, with $[K^+]_e = 20\,mM$, intersects the linear I–V curve for K^+ at $V = 0$.

However, if we assume instead that the I–V curves for Na^+ and K^+ are linear, then the reversal potential is

$$V_r = \frac{g_{Na}V_{Na} + g_K V_K}{g_{Na} + g_K}, \qquad (3.4)$$

where V_K is the Nernst potential of K^+. Clearly, the reversal potential is model-dependent. This is due to the fact that at the reversal potential the net current flow is zero, but the individual Na^+ and K^+ currents are not. Thus, the equilibrium arguments used to derive the Nernst equation do not apply, and a universal form for the reversal potential does not exist. As an illustration of this, in Fig. 3.1B we plot the reversal potentials V_r from (3.3) and (3.4) as functions of $[K^+]_e$. Although the linear and GHK I–V curves predict different reversal potentials, the overall qualitative behavior is similar, making it difficult to distinguish between a linear and a GHK I–V curve on the basis of reversal potential measurements alone.

3.1.1 Steady-State and Instantaneous Current–Voltage Relations

Measurement of I–V curves is complicated by the fact that ion channels can open or close in response to changes in the membrane potential. Suppose that in a population of ion channels, I increases as V increases. This increase could be the result of two different factors. One possibility is that more channels open as V

increases while the current through an individual channel remains unchanged. It is also possible that the same number of channels remain open but the current through each one increases. To understand how each channel operates, it is necessary to separate these two factors to determine the I–V curve of a single open channel. This has motivated the definition of *steady-state* and *instantaneous I–V* curves.

If channels open or close in response to a change in voltage, but this response is slower than the change in current in a channel that is already open, it should be possible to measure the I–V curve of a single open channel by changing the voltage quickly and measuring the channel current soon after the change. Presumably, if the measurement is performed fast enough, no channels in the population have time to open or close in response to the voltage change, and thus the observed current change reflects the current change through the open channels. Of course, this relies on the assumption that the current through each open channel changes instantaneously. The I–V curve measured in this way (at least in principle) is called the instantaneous I–V curve and reflects properties of the individual open channels. If the current measurement is performed after channels have had time to open or close, then the current change reflects the I–V curve of a single channel as well as the proportion of open channels. In this way one obtains a steady-state I–V curve.

There are two basic types of model that are used to describe ion flow through open channels, and we discuss simple versions of each. In the first type of model, the channel is described as a continuous medium, and the ionic current is determined by the Nernst–Planck electrodiffusion equation, coupled to the electric field by means of the Poisson equation. In more complex models of this type, channel geometry and the effects of induced charge on the channel wall are incorporated. In the second type of model the channel is modeled as a sequence of binding sites, separated by barriers that impede the ion's progress: the passage of an ion through the channel is described as a process of "hopping" over barriers from one binding site to another. The height of each barrier is determined by the properties of the channel, as well as by the membrane potential. Thus, the rate at which an ion traverses the channel is a function both of the membrane potential and of the channel type. An excellent summary of the advantages and disadvantages of the two model types is given by Dani and Levitt (1990).

Finally, we discuss simple models for the kinetics of channel gating. These models are of fundamental importance in Chapter 5, where we use an early model for the voltage-dependent gating of ion channels proposed by Hodgkin and Huxley as part of their model for the action potential in the squid giant axon. More detailed recent models for channel gating are not discussed at any length. The interested reader is referred to Hille (2001), Armstrong (1981), Armstrong and Bezanilla (1973, 1974, 1977), Aldrich et al. (1983), and Finkelstein and Peskin (1984) for a selection of models of how channels can open and close in response to changes in membrane potential. An important question that we do not consider here is how channels can discriminate between different ions. Detailed discussions of this and related issues are in Hille (2001) and the references therein.

3.2 Independence, Saturation, and the Ussing Flux Ratio

One of the most fundamental questions to be answered about an ion channel is whether the passage of an ion through the channel is independent of other ions. If so, the channel is said to obey the *independence principle.*

Suppose a membrane separates two solutions containing an ion species S with external concentration c_e and internal concentration c_i. If the independence principle is satisfied, the flow of S is proportional to its local concentration, independent of the concentration on the opposite side of the membrane, and thus the flux from outside to inside, J_{in}, is

$$J_{\mathrm{in}} = k_e c_e, \tag{3.5}$$

for some constant k_e. Similarly, the outward flux is given by

$$J_{\mathrm{out}} = k_i c_i, \tag{3.6}$$

where in general, $k_e \neq k_i$. We let V_S denote the Nernst potential of the ion S, and let V denote the potential difference across the membrane. Now we let c_e^* be the external concentration for which V is the Nernst potential. Thus,

$$\frac{c_e}{c_i} = \exp\left(\frac{zV_S F}{RT}\right), \tag{3.7}$$

and

$$\frac{c_e^*}{c_i} = \exp\left(\frac{zVF}{RT}\right). \tag{3.8}$$

If the external concentration were c_e^* with internal concentration c_i, then there would be no net flux across the membrane; i.e., the outward flux equals the inward flux, and so

$$k_e c_e^* = k_i c_i. \tag{3.9}$$

It follows that the flux ratio is given by

$$
\begin{aligned}
\frac{J_{\mathrm{in}}}{J_{\mathrm{out}}} &= \frac{k_e c_e}{k_i c_i} = \frac{k_e c_e}{k_e c_e^*} = \frac{c_e}{c_e^*} \\
&= \frac{\exp\left(\frac{zV_S F}{RT}\right)}{\exp\left(\frac{zVF}{RT}\right)} \\
&= \exp\left[\frac{z(V_S - V)F}{RT}\right].
\end{aligned}
\tag{3.10}
$$

This expression for the ratio of the inward to the outward flux is usually called the *Ussing flux ratio.* It was first derived by Ussing (1949), although the derivation given here is due to Hodgkin and Huxley (1952a). Alternatively, the Ussing flux ratio can be written as

$$\frac{J_{\mathrm{in}}}{J_{\mathrm{out}}} = \frac{c_e}{c_i} \exp\left(\frac{-zVF}{RT}\right). \tag{3.11}$$

Note that when $V = 0$, the ratio of the fluxes is equal to the ratio of the concentrations, as might be expected intuitively.

Although many ion channels follow the independence principle approximately over a range of ionic concentrations, most show deviations from independence when the ionic concentrations are sufficiently large. This has motivated the development of models that show saturation at high ionic concentrations. For example, one could assume that ion flow through the channel can be described by a barrier-type model, in which the ion jumps from one binding site to another as it moves through the channel. If there are only a limited number of binding sites available for ion passage through the channel, and each binding site can bind only one ion, then as the ionic concentration increases there are fewer binding sites available, and so the flux is not proportional to the concentration. Equivalently, one could say that each channel has a single binding site for ion transfer, but there are only a limited number of channels. However, in many of these models the Ussing flux ratio is obeyed, even though independence is not. Hence, although any ion channel obeying the independence principle must also satisfy the Ussing flux ratio, the converse is not true. We discuss saturating models later in this chapter.

Another way in which channels show deviations from independence is in flux-coupling. If ions can interact within a channel so that, for example, a group of ions must move through the channel together, then the Ussing flux ratio is not satisfied. The most common type of model used to describe such behavior is the so-called *multi-ion model*, in which it is assumed that there are a number of binding sites within a single channel and that the channel can bind multiple ions at the same time. The consequent interactions between the ions in the channel can result in deviations from the Ussing flux ratio. A more detailed consideration of multi-ion models is given later in this chapter. However, it is instructive to consider how the Ussing flux ratio is modified by a simple multi-ion channel mechanism in which the ions progress through the channel in single file (Hodgkin and Keynes, 1955).

Suppose a membrane separates two solutions, the external one (on the right) containing an ion S at concentration c_e, and the internal one (on the left) at concentration c_i. To keep track of where each S ion has come from, all the S ions on the left are labeled A, while those on the right are labeled B. Suppose also that the membrane contains n binding sites and that S ions traverse the membrane by binding sequentially to the binding sites and moving across in single file. For simplicity we assume that there are no vacancies in the chain of binding sites. It follows that the possible configurations of the chain of binding sites are $[A_r, B_{n-r}]$, for $r = 0, \ldots, n$, where $[A_r, B_{n-r}]$ denotes the configuration such that the r leftmost sites are occupied by A ions, while the rightmost $n-r$ sites are occupied by B ions. Notice that the only configuration that can result in the transfer of an A ion to the right-hand side is $[A_n B_0]$, i.e., if the chain of binding sites is completely filled with A ions.

Now we let α denote the total rate at which S ions are transferred from left to right. Since α denotes the total rate, irrespective of labeling, it does not take into account whether an A ion or a B ion is moved out of the channel from left to right. For this reason, α is not the same as the flux of labeled ions. Similarly, let β denote the total flux of S ions, irrespective of labeling, from right to left. It follows that the

rate at which $[A_rB_{n-r}]$ is converted to $[A_{r+1}B_{n-r-1}]$ is $\alpha[A_rB_{n-r}]$, and the rate of the reverse conversion is $\beta[A_{r+1}B_{n-r-1}]$. According to Hodgkin and Keynes, it is reasonable to assume that if there is a potential difference V across the membrane, then the total flux ratio obeys the Ussing flux ratio,

$$\frac{\alpha}{\beta} = \frac{c_e}{c_i} \exp\left(\frac{-VF}{RT}\right). \tag{3.12}$$

This assumption is justified by the fact that a flux of one ion involves the movement of a single charge (assuming $z = 1$) through the membrane (as in the independent case treated above) and thus should have the same voltage dependence. We emphasize that α/β is not the flux ratio of labeled ions, but the total flux ratio.

To obtain the flux ratio of labeled ions, notice that the rate at which A ions are transferred to the right-hand side is $\alpha[A_nB_0]$, and the rate at which B ions are transferred to the left hand side is $\beta[A_0B_n]$. Thus, the flux ratio of labeled ions is

$$\frac{J_{\text{in}}}{J_{\text{out}}} = \frac{\alpha}{\beta} \frac{[A_nB_0]}{[A_0B_n]}. \tag{3.13}$$

At steady state there can be no net change in the distribution of configurations, so that

$$\frac{[A_{r+1}B_{n-r-1}]}{[A_rB_{n-r}]} = \frac{\alpha}{\beta}. \tag{3.14}$$

Thus,

$$\frac{J_{\text{in}}}{J_{\text{out}}} = \frac{\alpha}{\beta} \frac{[A_nB_0]}{[A_0B_n]} = \left(\frac{\alpha}{\beta}\right)^2 \frac{[A_{n-1}B_1]}{[A_0B_n]} = \cdots = \left(\frac{\alpha}{\beta}\right)^{n+1}, \tag{3.15}$$

so that

$$\frac{J_{\text{in}}}{J_{\text{out}}} = \left[\frac{c_e}{c_i} \exp\left(\frac{-VF}{RT}\right)\right]^{n+1}. \tag{3.16}$$

A similar argument, taking into account the fact that occasional vacancies in the chain arise when ions at the two ends dissociate and that these vacancies propagate through the chain, gives

$$\frac{J_{\text{in}}}{J_{\text{out}}} = \left[\frac{c_e}{c_i} \exp\left(\frac{-VF}{RT}\right)\right]^{n}. \tag{3.17}$$

Experimental data confirm this theoretical prediction (although historically, the theory was motivated by the experimental result, as is often the case). Hodgkin and Keynes (1955) showed that flux ratios in the K^+ channel of the *Sepia* giant axon could be described by the Ussing flux ratio raised to the power 2.5. Their result, as presented in modified form by Hille (2001), is shown in Fig. 3.2. Unidirectional K^+ fluxes were measured with radioactive K^+, and the ratio of the outward to the inward flux was plotted as a function of $V - V_K$. The best-fit line on a semilogarithmic plot has a slope of 2.5, which suggests that at least 2 K^+ ions traverse the K^+ channel simultaneously.
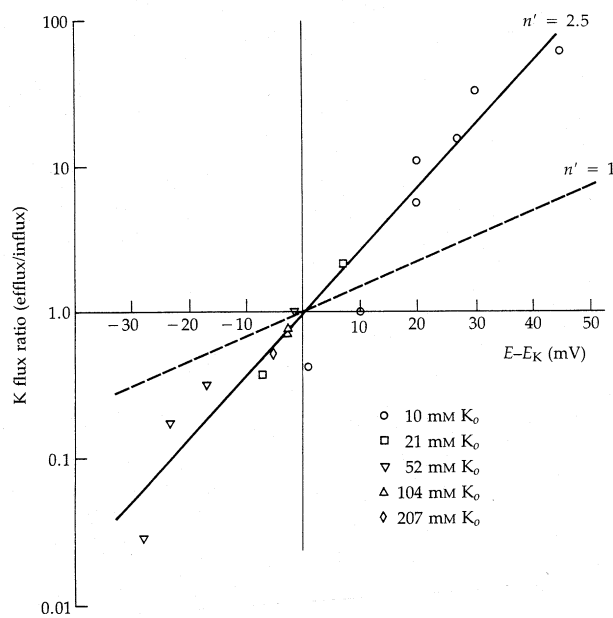
Figure 3.2: K^+ flux ratios as measured by Hodgkin and Keynes (1955), Fig. 7. Slightly modified into modern conventions by Hille (2001), page ? **Check this page number**. K_o is the external K^+ concentration, and n' is the flux-ratio exponent, denoted by n in (3.17). (Hille, 2001, Fig. ?, p. ?.) **Check these**
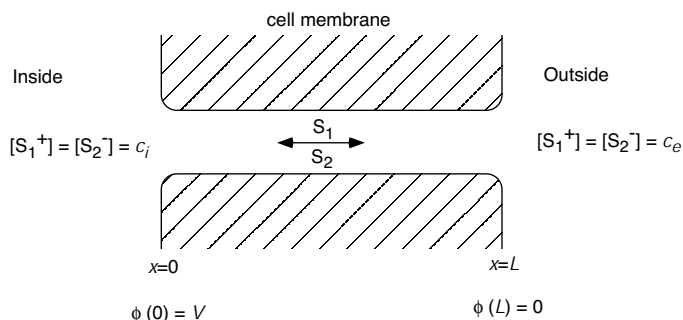
Figure 3.3: Schematic diagram of the electrodiffusion model for current through an ionic channel. Each side of the channel is electrically neutral, and both ion types can diffuse through the channel.

3.3 Electrodiffusion Models

Most early work on ion channels was based on the theory of electrodiffusion. Recall from Chapter 2 that the movement of ions in response to a concentration gradient and an electric field is described by the Nernst–Planck equation,

$$J = -D \left(\frac{dc}{dx} + \frac{zF}{RT} c \frac{d\phi}{dx} \right), \tag{3.18}$$

where J denotes the flux density, c is the concentration of the ion under consideration, and ϕ is the electrical potential. If we make the simplifying assumption that the field $d\phi/dx$ is constant through the membrane, then (3.18) can be solved to give the Goldman–Hodgkin–Katz current and voltage equations (2.122) and (2.125). However, in general there is no reason to believe that the potential has a constant gradient in the membrane. Ions moving through the channel affect the local electric field, and this local field in turn affects ionic fluxes. Thus, to determine the electric field and consequent ionic fluxes, one must solve a coupled problem.

3.3.1 Multi-ion Flux: The Poisson–Nernst–Planck Equations

Suppose we have two types of ions, S_1 and S_2, with concentrations c_1 and c_2, passing through an ion channel, as shown schematically in Fig. 3.3.

For convenience, we assume that the valence of the first ion is $z > 0$ and that of the second is $-z$. Then, the potential in the channel $\phi(x)$ must satisfy Poisson's equation,

$$\frac{d^2\phi}{dx^2} = -\frac{zq}{\epsilon} N_a (c_1 - c_2), \tag{3.19}$$

where q is the unit electric charge and ϵ is the dielectric constant of the channel medium (usually assumed to be an aqueous solution), and N_a is Avogadro's number, necessary to convert units of concentration in moles per liter into number of molecules per liter. The flux densities J_1 and J_2 of S_1 and S_2 satisfy the Nernst–Planck equation, and at steady state dJ_1/dx and dJ_2/dx must both be zero to

prevent charge buildup within the channel. Hence, the steady-state flux through the channel is described by (3.19) coupled with

$$J_1 = -D_1 \left(\frac{dc_1}{dx} + \frac{zF}{RT} c_1 \frac{d\phi}{dx} \right), \tag{3.20}$$

$$J_2 = -D_2 \left(\frac{dc_2}{dx} - \frac{zF}{RT} c_2 \frac{d\phi}{dx} \right), \tag{3.21}$$

where J_1 and J_2 are constants. To complete the specification of the problem, it is necessary to specify boundary conditions for c_1, c_2, and ϕ. We assume that the channel has length L, and that $x = 0$ denotes the left border, or inside, of the membrane. Then,

$$\begin{aligned}
c_1(0) &= c_i, & c_1(L) &= c_e, \\
c_2(0) &= c_i, & c_2(L) &= c_e, \\
\phi(0) &= V, & \phi(L) &= 0.
\end{aligned} \tag{3.22}$$

Note that we have specified that the solutions on both sides of the membrane are electrically neutral. V is the potential difference across the membrane, defined, as usual, as the internal potential minus the external potential. While at first glance it might appear that there are too many boundary conditions for the differential equations, this is in fact not so, as the constants J_1 and J_2 are additional unknowns to be determined.

In general, it is not possible to obtain an exact solution to the Poisson–Nernst–Planck (PNP) equations (3.19)–(3.22). However, some simplified cases can be solved approximately. A great deal of work on the PNP equations has been done by Eisenberg and his colleagues (Chen, Barcilon, and Eisenberg, 1992; Barcilon, 1992; Barcilon, Chen, and Eisenberg, 1992; Chen and Eisenberg, 1993). Here we present simplified versions of their models, ignoring, for example, the charge induced on the channel wall by the presence of ions in the channel, and considering only the movement of two ion types through the channel. Similar models have also been discussed by Peskin (1991).

It is convenient first to nondimensionalize the PNP equations. We let $y = x/L$, $\psi = \phi zF/RT$, $v = VF/RT$, $u_k = c_k/\tilde{c}$, for $k = 1, 2, i$ and e, where $\tilde{c} = c_e + c_i$. Substituting into (3.19)–(3.21), we find

$$-j_1 = \frac{du_1}{dy} + u_1 \frac{d\psi}{dy}, \tag{3.23}$$

$$-j_2 = \frac{du_2}{dy} - u_2 \frac{d\psi}{dy}, \tag{3.24}$$

$$\frac{d^2\psi}{dy^2} = -\lambda^2 (u_1 - u_2), \tag{3.25}$$

where $\lambda^2 = L^2 qFN_a\tilde{c}/(\epsilon RT)$, $j_1 = J_1 L/(\tilde{c}D_1)$, and $j_2 = J_2 L/(\tilde{c}D_1)$. The boundary conditions are

$$\begin{aligned}
u_1(0) &= u_i, & u_1(1) &= u_e, \\
u_2(0) &= u_i, & u_2(1) &= u_e, \\
\psi(0) &= v, & \psi(1) &= 0.
\end{aligned}$$

The short-channel or low concentration limit

If the channel is short or the ionic concentrations on either side of the membrane are small, so that $\lambda \ll 1$, we can find an approximate solution to the PNP equations by setting $\lambda = 0$. This gives

$$\frac{d^2\psi}{dy^2} = 0, \tag{3.26}$$

and thus

$$\frac{d\psi}{dy} = -v. \tag{3.27}$$

Hence, $\lambda \approx 0$ implies that the electric potential has a constant gradient in the membrane, which is exactly the constant field assumption that was made in the derivation of the GHK equations (Chapter 2). The equation for u_1 is then

$$\frac{du_1}{dy} - vu_1 = -j_1, \tag{3.28}$$

and thus

$$u_1 = \frac{j_1}{v} + K_1 e^{vy}. \tag{3.29}$$

From the boundary conditions $u_1(0) = u_i$, $u_1(1) = u_e$ it follows that

$$j_1 = v \cdot \frac{u_i - u_e e^{-v}}{1 - e^{-v}}. \tag{3.30}$$

In dimensional form, this is

$$I_1 = FJ_1 = \frac{D_1}{L}\frac{F^2}{RT} \cdot V \cdot \left(\frac{c_i - c_e \exp(\frac{-zVF}{RT})}{1 - \exp(\frac{-zVF}{RT})} \right), \tag{3.31}$$

which is, as expected, the GHK current equation. Graphs of the concentration and voltage profiles through the membrane are shown in Fig. 3.4. It is reassuring that the widely used GHK equation for the ionic flux can be derived as a limiting case of a more general model.

The long-channel limit

Another interesting limit is obtained by letting the length of the channel go to infinity. If we let $\eta = 1/\lambda$ denote a small parameter, the model equations are

$$-j_1 = \frac{du_1}{dy} + u_1\frac{d\psi}{dy}, \tag{3.32}$$

$$-j_2 = \frac{du_2}{dy} - u_2\frac{d\psi}{dy}, \tag{3.33}$$

$$-\eta^2\frac{d^2\psi}{dy^2} = (u_1 - u_2). \tag{3.34}$$

Since there is a small parameter multiplying the highest derivative, this is a singular perturbation problem. The solution obtained by setting $\eta = 0$ does not, in general,
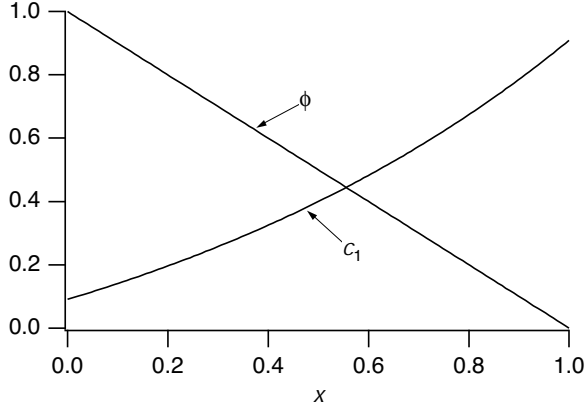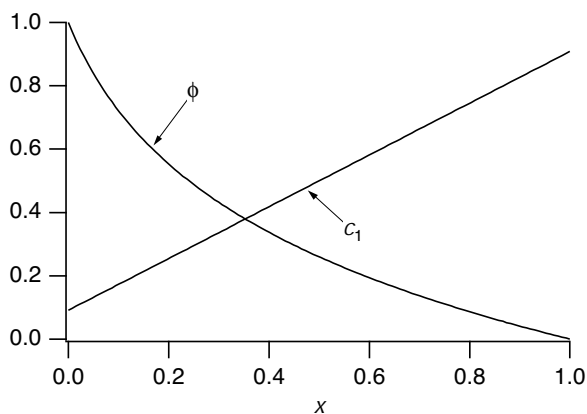
Figure 3.4: Graphs of the concentration and potential profiles for the short-channel limit of the Poisson–Nernst–Planck equations. Dimensionless parameters were set arbitrarily at $u_i = 50/550 = 0.091$, $u_e = 500/550 = 0.909$, $v = 1$. In this limit the electric field is constant through the channel (the potential has a constant slope), the concentration profile is nonlinear, and the GHK I–V curve is obtained.

satisfy all the boundary conditions, as the degree of the differential equation has been reduced, resulting in an overdetermined system. In the present case, however, this reduction of order is not a problem.

Setting $\eta = 0$ in (3.34) gives $u_1 = u_2$, which happens to satisfy both the left and right boundary conditions. Thus, u_1 and u_2 are identical throughout the channel. From (3.32) and (3.33) it follows that

$$\frac{d}{dy}(u_1 + u_2) = -j_1 - j_2. \tag{3.35}$$

Since both j_1 and j_2 are constants, it follows that du_1/dy is a constant, and hence, from the boundary conditions,

$$u_1 = u_2 = u_i + (u_e - u_i)y. \tag{3.36}$$

We are now able to solve for ψ. Subtracting (3.34) from (3.33) gives

$$2u_1 \frac{d\psi}{dy} = 2j, \tag{3.37}$$

where $2j = j_2 - j_1$, and hence

$$\psi = \frac{j}{u_e - u_i} \ln[u_i + (u_e - u_i)y] + K, \tag{3.38}$$

for some other constant K. Applying the boundary conditions $\psi(0) = v$, $\psi(1) = 0$ we determine j and K, with the result that

$$\psi = -\frac{v}{v_1} \ln\left[\frac{u_i}{u_e} + \left(1 - \frac{u_i}{u_e}\right)y\right], \tag{3.39}$$

Figure 3.5: Graphs of the concentration and potential profiles for the long-channel limit of the Poisson–Nernst–Planck equations. Dimensionless parameters were set arbitrarily at $u_i = 50/550 = 0.091$, $u_e = 500/550 = 0.909$, $v = 1$. In this limit the concentration profile has a constant slope, the potential profile is nonlinear, and the linear I–V curve is obtained.

where $v_1 = \ln(u_e/u_i)$ is the dimensionless Nernst potential of ion S_1. The flux density of one of the ions, say S_1, is obtained by substituting the expressions for u_1 and ψ into (3.32) to get

$$j_1 = \frac{u_e - u_i}{v_1}(v - v_1), \tag{3.40}$$

or in dimensional form,

$$J_1 = \frac{D_1}{L}\frac{zF}{RT}\frac{c_e - c_i}{\ln\frac{c_e}{c_i}}(V - \frac{RT}{zF}\ln\frac{c_e}{c_i}), \tag{3.41}$$

which is the linear I–V curve that we met previously. Graphs of the corresponding concentration and voltage profiles through the channel are shown in Fig. 3.5.

In summary, by taking two different limits of the PNP equations we obtain either the GHK I–V curve or a linear I–V curve. In the short-channel limit, ψ has a constant gradient through the membrane, but the concentration does not. In the long-channel limit the reverse is true, with a constant gradient for the concentration through the channel, but not for the potential. It is left as an exercise to prove that although the GHK equation obeys the independence principle and the Ussing flux ratio, the linear I–V curve obeys neither. Given the above derivation of the linear I–V curve, this is not surprising. A linear I–V curve is obtained when either the channel is very long or the ionic concentrations on either side of the channel are very high. In either case, one should not expect the movement of an ion through the channel to be independent of other ions, and so that the independence principle is likely to fail. Conversely, the GHK equation is obtained in the limit of low ionic concentrations or short channels, in which case the independent movement of ions is not surprising.
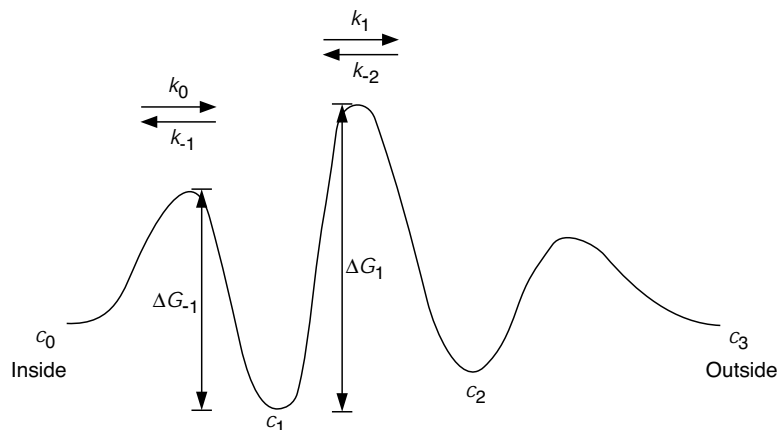
Figure 3.6: General potential energy profile for barrier models. The local minima correspond to binding sites within the channel, and the local maxima are barriers that impede the ion flow. An ion progresses through the channel by hopping over the barriers from one binding site to another.

3.4   Barrier Models

The second type of model that has been widely used to describe ion channels is based on the assumption that the movement of an ion through the channel can be modeled as the jumping of an ion over a discrete number of free-energy barriers (Eyring et al., 1949; Woodbury, 1971; Läuger, 1973). It is assumed that the potential energy of an ion passing through a channel is described by a potential energy profile of the general form shown in Fig. 3.6. The peaks of the potential energy profile correspond to barriers that impede the ion flow, while the local minima correspond to binding sites within the channel.

To traverse the channel the ion must hop from one binding site to another. According to the theory of chemical reaction rates, the rate at which an ion jumps from one binding site to the next is an exponential function of the height of the potential energy barrier that it must cross. Thus, in the notation of the diagram,

$$k_j = \kappa \exp\left(\frac{-\Delta G_j}{RT}\right), \tag{3.42}$$

for some factor κ with units of 1/time. One of the most difficult questions in the use of this expression is deciding the precise form of the factor κ. According to Eyring rate theory (as used in this context by Hille (2001), for example), $\kappa = kT/h$, where k is Boltzmann's constant, T is the temperature, and h is Planck's constant. The derivation of this expression for κ relies on the quantization of the energy levels of the ion in some transition state as it binds to the channel binding sites. However, it is not clear that at biologically relevant temperatures energy quantization has an important effect on ionic flows. Using methods from nonequilibrium statistical thermodynamics, an alternative form of the factor has been derived by Kramers

(1940), and discussions of this, and other, alternatives may be found in McQuarrie (1967) and Laidler (1969). In the Appendix to this chapter, we give a derivation of the Kramers' formula, but we do not enter into the debate of which answer is best. Instead, in what follows, we assume that κ is known, and independent of ΔG_j, even though for the Kramers' formula, such is not the case.

For simplicity, we assume that each local maximum occurs halfway between the local minima on each side. Barriers with this property are called *symmetrical*. An electric field in the channel also affects the rate constants. If the potential difference across the cell membrane is positive (so that the inside is more positive than the outside), it is easier for positive ions to cross the barriers in the outward direction but more difficult for positive ions to enter the cell. Thus, the heights of the barriers in the outward direction are reduced, while the heights in the inward direction are increased. If there is a potential difference of ΔV_j over the jth barrier, then

$$k_j = \kappa \exp\left[\frac{1}{RT}(-\Delta G_j + zF\Delta V_{j+1}/2)\right], \qquad (3.43)$$

$$k_{-j} = \kappa \exp\left[\frac{1}{RT}(-\Delta G_{-j} - zF\Delta V_j/2)\right]. \qquad (3.44)$$

The factor 2 appears because the barriers are assumed to be symmetrical, so that the maxima are lowered by $zF\Delta V_j/2$. A simple illustration of this is given in Fig. 3.7A and B and is discussed in detail in the next section.

In addition to symmetry, the barriers are assumed to have another important property, namely, that in the absence of an electric field the ends of the energy profile are at the same height, and thus

$$\sum_{j=0}^{n-1} \Delta G_j - \sum_{j=1}^{n} \Delta G_{-j} = 0. \qquad (3.45)$$

If this were not so, then in the absence of an electric field and with equal concentrations on either side of the membrane, there would be a nonzero flux through the membrane, a situation that is clearly unphysiological.

A number of different models have been constructed along these general lines. First, we consider the simplest type of barrier model, in which the ionic concentration in the channel can become arbitrarily large, i.e., the channel does not saturate. This is similar to the continuous models discussed above and can be thought of as a discrete approximation to the constant field model. Because of this, nonsaturating models give the GHK I–V curve in the limit of a homogeneous membrane. We then discuss saturating barrier models and multi-ion models. Before we do so, however, it is important to note that although barrier models can provide good quantitative descriptions of some experimental data, they are phenomenological. In other words, apart from the agreement between theory and experiment, there is often no reason to suppose that the potential energy barrier used to describe the channel corresponds in any way to physical properties of the channel. Thus, although their relative simplicity has led to their widespread use, mechanistic interpretations of the models should be made only with considerable caution. Of course, this does not imply that barrier models are inferior to continuous models such as the constant

field model or the Poisson–Nernst–Planck equations, which suffer from their own disadvantages (Dani and Levitt, 1990).

3.4.1   Nonsaturating Barrier Models

In the simplest barrier model (Eyring et al., 1949; Woodbury, 1971), the potential energy barrier has the general form shown in Fig. 3.7A, and it is assumed that the movement of an ion S over a barrier is independent of the ionic concentrations at the neighboring barriers. This is equivalent to assuming that the concentration of S at any particular binding site can be arbitrarily large.

The internal concentration of S is denoted by c_0, while the external concentration is denoted by c_n. There are $n-1$ binding sites (and thus n barriers) in the membrane, and the concentration of S at the jth binding site is denoted by c_j. Note the slight change in notation from above. Instead of using c_e and c_i to denote the external and internal concentrations of S, we use c_n and c_0. This allows the labeling of the concentrations on either side of the membrane to be consistent with the labeling of the concentrations at the binding sites. There is an equal voltage drop across each barrier, and thus the electrical distance between each binding site, denoted by λ, is the same. For convenience, we assume the stronger condition, that the physical distance between the binding sites is the same also, which is equivalent to assuming a constant electric field in the membrane. In the absence of an electric field, we assume that the heights of the energy barriers decrease linearly through the membrane, as in Fig. 3.7, with

$$\Delta G_j = \Delta G_0 - j\delta G, \tag{3.46}$$

for some constant increment δG. Finally, it is assumed that the flux from left to right, say, across the jth barrier, is proportional to c_{j-1}, and similarly for the flux in the opposite direction. Thus, the flux over the jth barrier, J, is given by

$$J = \lambda(k_{j-1}c_{j-1} - k_{-j}c_j). \tag{3.47}$$

Note that the units of J are concentration $\times$ distance/time, or moles per unit area per time, so J is a flux density. As usual, a flux from inside to outside (i.e., left to right) is defined as a positive flux.

At steady state the flux over each barrier must be the same, in which case we get a system of linear equations,

$$k_0c_0 - k_{-1}c_1 = k_1c_1 - k_{-2}c_2 = \cdots = k_{n-1}c_{n-1} - k_{-n}c_n = M, \tag{3.48}$$

where $M = J/\lambda$ is a constant. Hence

$$k_0c_0 = (k_1 + k_{-1})c_1 - k_{-2}c_2, \tag{3.49}$$

$$k_1c_1 = (k_2 + k_{-2})c_2 - k_{-3}c_3, \tag{3.50}$$

$$k_2c_2 = (k_3 + k_{-3})c_3 - k_{-4}c_4, \tag{3.51}$$

$$\vdots$$
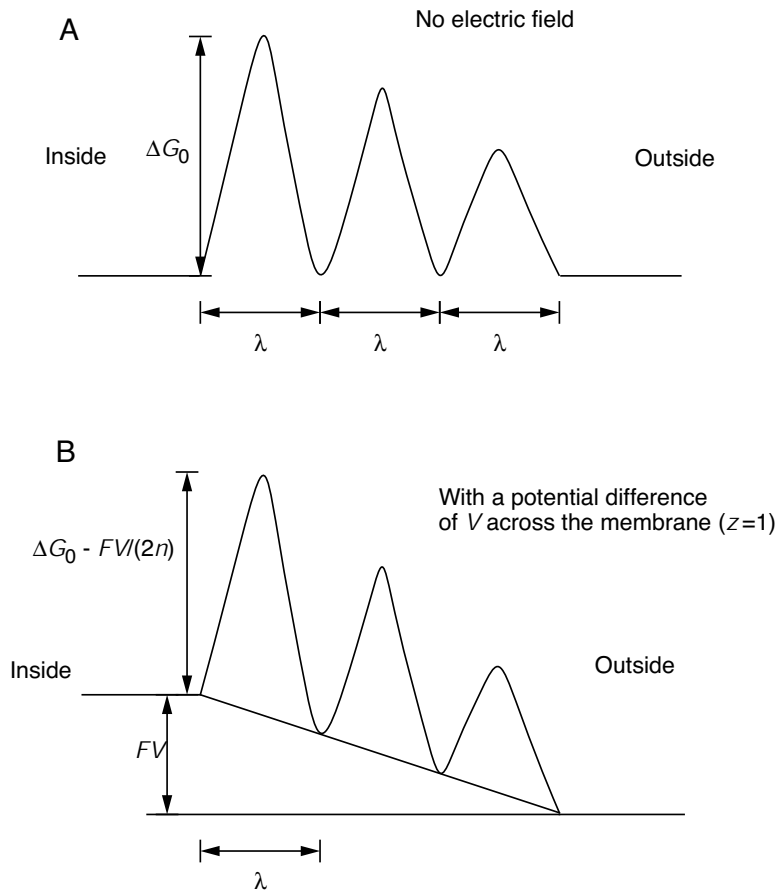
Figure 3.7: The potential energy diagram used in the nonsaturating model of Wood-bury (1971). There is an equal distance between the binding sites, and the barriers are symmetrical. A. In the absence of an electric field the barrier height decreases linearly through the membrane. B. The presence of a constant electric field skews the energy profile, bringing the outside end down relative to the inside. This increases the rate at which positive ions traverse the channel from inside to out and decreases their rate of entry.

We need to determine J in terms of the concentrations on either side of the membrane, c_0 and c_n. Solving (3.50) for c_1 and substituting into (3.49) gives

$$k_0 c_0 = c_2 k_2 \left(1 + \frac{k_{-1}}{k_1} + \frac{k_{-1} k_{-2}}{k_1 k_2} \right) - c_3 k_{-3} \left(1 + \frac{k_{-1}}{k_1} \right), \qquad (3.52)$$

and then solving (3.51) for c_2 and substituting into (3.52) gives

$$k_0 c_0 = c_3 k_3 \left(1 + \frac{k_{-1}}{k_1} + \frac{k_{-1} k_{-2}}{k_1 k_2} + \frac{k_{-1} k_{-2} k_{-3}}{k_1 k_2 k_3} \right) - c_4 k_{-4} \left(1 + \frac{k_{-1}}{k_1} + \frac{k_{-1} k_{-2}}{k_1 k_2} \right). \qquad (3.53)$$

Repeating this process of sequential substitutions, and letting

$$\phi_n = 1 + \frac{k_{-1}}{k_1} + \frac{k_{-1} k_{-2}}{k_1 k_2} + \cdots + \frac{k_{-1} \cdots k_{-n}}{k_1 \cdots k_n}, \qquad (3.54)$$

we find that

$$k_0 c_0 = k_{n-1} c_{n-1} \phi_{n-1} - c_n k_{-n} \phi_{n-2}. \qquad (3.55)$$

Since

$$c_{n-1} = \frac{M + k_{-n} c_n}{k_{n-1}}, \qquad (3.56)$$

it follows that

$$k_0 c_0 = \phi_{n-1}(M + k_{-n} c_n) - c_n k_{-n} \phi_{n-2}, \qquad (3.57)$$

and hence

$$J = \lambda M = \frac{\lambda k_0 \left(c_0 - c_n \frac{k_{-1} \cdots k_{-n}}{k_0 \cdots k_{n-1}} \right)}{1 + \frac{k_{-1}}{k_1} + \frac{k_{-1} k_{-2}}{k_1 k_2} + \cdots + \frac{k_{-1} \cdots k_{-(n-1)}}{k_1 \cdots k_{n-1}}}. \qquad (3.58)$$

It remains to express the rate constants in terms of the membrane potential. If there is a potential difference V across the membrane (as shown in Fig. 3.7B), the constant electric field adds $FzV/(2n)$ to the barrier when moving from right to left, and $-FzV/(2n)$ when moving in the opposite direction. Hence

$$\Delta G_j = \Delta G_0 - j\delta G - \frac{FzV}{2n}, \qquad (3.59)$$

$$\Delta G_{-j} = \Delta G_0 - (j-1)\delta G + \frac{FzV}{2n}. \qquad (3.60)$$

Now we use (3.42) to get

$$\frac{k_{-j}}{k_{j-1}} = \exp(-v/n), \qquad \frac{k_{-j}}{k_j} = \exp(-g - v/n), \qquad (3.61)$$

where $g = \delta G/(RT)$ and $v = FzV/(RT)$. Hence

$$
\begin{aligned}
J &= \frac{k_0 \lambda (c_0 - c_n e^{-v})}{1 + e^{-(g+v/n)} + e^{-2(g+v/n)} + \cdots + e^{-(n-1)(g+v/n)}}, \\
&= k_0 \lambda (c_0 - c_n e^{-v}) \frac{e^{-(g+v/n)} - 1}{e^{-n(g+v/n)} - 1}. \qquad (3.62)
\end{aligned}
$$

As expected, (3.62) satisfies both the independence principle and the Ussing flux ratio. Also, the flux is zero when v is the Nernst potential of the ion.

The homogeneous membrane simplification

One useful simplification of the nonsaturating barrier model is obtained if it is assumed that the membrane is homogeneous. We model a homogeneous membrane by setting $g = \delta G/(RT) = 0$ and letting $n \to \infty$. Thus, there is no increase in barrier height through the membrane, and the number of barriers approaches infinity. In this limit, keeping $n\lambda = L$ fixed,

$$J = \frac{k_{00}\lambda^2}{L} \cdot v \cdot \frac{c_0 - c_n e^{-v}}{1 - e^{-v}}, \tag{3.63}$$

where k_{00} is the value of k_0 at $V = 0$, L is the width of the membrane, and $k_{00}\lambda^2$ is the diffusion coefficient of the ion over the first barrier in the absence of an electric field. Notice that for this to make sense it must be that k_{00} scales like λ^{-2} for small λ. In Section 3.7.3 we show that this is indeed the case.

It follows that in the homogeneous membrane case,

$$\begin{aligned} J &= \frac{D_{\mathrm{S}}}{L} \cdot v \cdot \frac{c_0 - c_n e^{-v}}{1 - e^{-v}}, \\ &= P_{\mathrm{S}} \cdot v \cdot \frac{c_0 - c_n e^{-v}}{1 - e^{-v}}, \end{aligned} \tag{3.64}$$

which is exactly the GHK current equation (2.121) derived previously.

3.4.2 Saturating Barrier Models: One-Ion Pores

If an ion channel satisfies the independence principle, the flux of S is proportional to [S], even when [S] gets large. However, this is not usually found to be true experimentally. It is more common for the flux to saturate as [S] increases, reaching some maximum value as [S] gets large. This has motivated the development of models in which the flux is not proportional to [S] but is a nonlinear, saturating, function of [S]. As one might expect, equations for such models are similar to those of enzyme kinetics.

The basic assumptions behind saturating barrier models are that to pass through the channel, ions must bind to binding sites in the channel, but that each binding site can hold only a single ion (Läuger, 1973; Hille, 2001). Hence, if all the binding sites are full, an increase in ionic concentration does not increase the ionic flux— the channel is saturated. Saturating barrier models can be further subdivided into one-ion pore models, in which each channel can bind only a single ion at any one time, and multi-ion pore models, in which each channel can bind multiple ions simultaneously. The theory of one-ion pores is considerably simpler than that of multi-ion pores, and so we discuss those models first.

The simplest one-ion saturating model

We begin by considering the simplest one-ion pore model, with a single binding site. If we let S_e denote the ion outside, S_i the ion inside, and X the binding site, the

passage of an ion through the channel can be described by the kinetic scheme

$$X + S_i \underset{k_{-1}}{\overset{k_0}{\rightleftharpoons}} XS \underset{k_{-2}}{\overset{k_1}{\rightleftharpoons}} X + S_e. \tag{3.65}$$

Essentially, the binding site acts like an enzyme that transfers the ion from one side of the membrane to the other, such as was encountered in Chapter 2 for the transport of glucose across a membrane. Following the notation of the previous section, we let c_0 denote $[S_i]$ and c_2 denote $[S_e]$. However, instead of using c_1 to denote the concentration of S at the binding site, it is more convenient to let c_1 denote the probability that the binding site is occupied. (In a population of channels, c_1 denotes the proportion of channels that have an occupied binding site.) Then, at steady state,

$$k_0 c_0 x - k_{-1} c_1 = k_1 c_1 - k_{-2} c_2 x, \tag{3.66}$$

where x denotes the probability that the binding site is empty. Note that (3.66) is similar to the corresponding equation for the nonsaturating pore, (3.48), with the only difference that x appears in the saturating model. In addition, we have a conservation equation for x,

$$x + c_1 = 1. \tag{3.67}$$

Solution of (3.66) and (3.67) gives the flux J as

$$J = k_0 c_0 x - k_{-1} c_1 = \frac{k_0 k_1 c_0 - k_{-1} k_{-2} c_2}{k_0 c_0 + k_{-2} c_2 + k_{-1} + k_1}. \tag{3.68}$$

It is important to note that J, as defined by (3.68), does not have the same units (concentration $\times$ distance/time) as in the previous model, but here has units of number of ions crossing the membrane per unit time. The corresponding trans-membrane current, I, is given by $I = zqJ$, where q is the unit charge, and has the usual units of number of charges crossing the membrane per unit time. A plot of J as a function of c_0 is shown in Fig. 3.8. When c_0 is small, J is approximately a linear function of c_0, but as c_0 increases, J saturates at the maximum value k_1.

We now use (3.42) to express the rate constants in terms of the membrane potential. As before, we assume that the local maxima of the energy profile occur midway between the local minima; i.e., we assume that the barriers are symmetrical. However, we no longer assume that the barriers are equally spaced through the channel. If the local minimum occurs at an electrical distance δ from the left-hand side, it follows that

$$k_0 = \kappa \exp\left[\frac{1}{RT}\left(-\Delta G_0 + \delta z F V/2\right)\right], \tag{3.69}$$

$$k_1 = \kappa \exp\left[\frac{1}{RT}\left(-\Delta G_1 + (1-\delta) z F V/2\right)\right], \tag{3.70}$$

$$k_{-1} = \kappa \exp\left[\frac{1}{RT}\left(-\Delta G_{-1} - \delta z F V/2\right)\right], \tag{3.71}$$

$$k_{-2} = \kappa \exp\left[\frac{1}{RT}\left(-\Delta G_{-2} - (1-\delta) z F V/2\right)\right]. \tag{3.72}$$
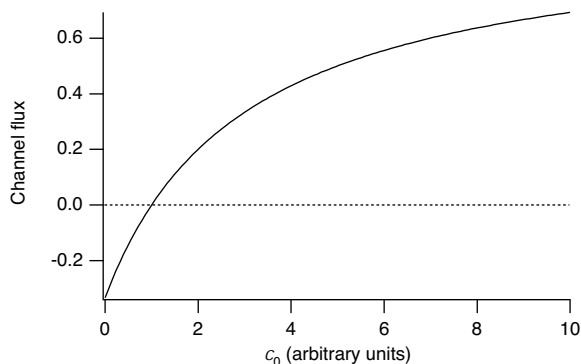
Figure 3.8: Plot of J against c_0 for the simplest saturating model with one binding site. When c_0 is small, the flux is approximately a linear function of c_0, but as c_0 increases, the flux saturates to a maximum value.

Because δ denotes an electrical, not a physical, distance, it is not necessary to assume that the electric field in the membrane is constant, only that there is a drop of δV over the first barrier and $(1 - \delta)V$ over the second. In general, the energy profile of any particular channel is unknown. However, the number and positions of the binding sites and the values of the local maxima and minima can, in principle at least, be determined by fitting to experimental data. We consider an example of this procedure (for a slightly more complicated model) below.

The Ussing flux ratio

Earlier in this chapter we stated that it is possible for a model to obey the Ussing flux ratio but not the independence principle. Single-ion saturating models provide a simple example of this. First, note that they cannot obey the independence principle, since the flux is not linearly proportional to the ionic concentration. This nonlinear saturation effect is illustrated in Fig. 3.8.

To see that the model obeys the Ussing flux ratio, it is necessary to set up the model in a slightly different form. Suppose we have two isotopes, S and $\bar{\text{S}}$, similar enough so that they have identical energy profiles in the channel. Then, we suppose that a channel has only S on the left-hand side and only $\bar{\text{S}}$ on the right. We let c denote [S] and $\bar{c}$ denote [$\bar{\text{S}}$]. Since S and $\bar{\text{S}}$ have identical energy profiles in the channel, the rate constants for the passage of $\bar{\text{S}}$ through the channel are the same as those for S. From the kinetic schemes for S and $\bar{\text{S}}$ we get

$$k_0 c_0 x - k_{-1} c_1 \quad = \quad k_1 c_1 - k_{-2} c_2 x = J_{\text{S}}, \tag{3.73}$$

$$k_0 \bar{c}_0 x - k_{-1} \bar{c}_1 \quad = \quad k_1 \bar{c}_1 - k_{-2} \bar{c}_2 x = J_{\bar{\text{S}}}, \tag{3.74}$$

but here the conservation equation for x is

$$x + \bar{c}_1 + c_1 = 1. \tag{3.75}$$

To calculate the individual fluxes of S and $\bar{\text{S}}$ it is necessary to eliminate x from (3.73) and (3.74) using the conservation equation (3.75). However, to calculate the

flux ratio this is not necessary. Solving (3.73) for J_S in terms of x, c_0, and c_2, we find

$$J_S = x \left(\frac{k_0 c_0 - \dfrac{k_{-1} k_{-2}}{k_1} c_2}{1 + k_{-1}/k_1} \right), \tag{3.76}$$

and similarly,

$$J_{\bar{S}} = x \left(\frac{k_0 \bar{c}_0 - \dfrac{k_{-1} k_{-2}}{k_1} \bar{c}_2}{1 + k_{-1}/k_1} \right). \tag{3.77}$$

The variable x cancels when we calculate the flux ratio, and so we do not need to use the conservation equation. If S is present only on the left-hand side and $\bar{S}$ only on the right, we then have $c_2 = 0$ and $\bar{c}_0 = 0$, in which case

$$\frac{J_S}{J_{\bar{S}}} = -\frac{k_0 k_1}{k_{-1} k_{-2}} \cdot \frac{c_0}{\bar{c}_2}. \tag{3.78}$$

The minus sign on the right-hand side appears because the fluxes are in different directions. Now we substitute for the rate constants, (3.69) to (3.72), and use the fact that the ends of the energy profile are at the same height (and thus $\Delta G_0 + \Delta G_1 - \Delta G_{-1} - \Delta G_{-2} = 0$) to find

$$\left| \frac{J_S}{J_{\bar{S}}} \right| = \exp\left(\frac{zVF}{RT} \right) \cdot \frac{c_0}{\bar{c}_2}, \tag{3.79}$$

which is the Ussing flux ratio, as proposed.

Multiple binding sites

When there are multiple binding sites within the channel, the analysis is essentially the same as the simpler case discussed above, but the details are more complicated. When there are n barriers in the membrane (and thus $n-1$ binding sites), the steady-state equations are

$$k_0 c_0 x - k_{-1} c_1 = k_1 c_1 - k_{-2} c_2 = \cdots = k_{n-1} c_{n-1} - k_{-n} c_n x = J, \tag{3.80}$$

where x is the probability that all of the binding sites are empty and c_j is the probability that the ion is bound to the jth binding site. Because the channel must be in either state x or one of the states $c_1, \ldots, c_{n-1}$ (since there is only one ion in the channel at a time), it follows that

$$x = 1 - \sum_{i=1}^{n-1} c_i. \tag{3.81}$$

For convenience we define

$$\pi_j = \frac{k_{-1} \cdots k_{-j}}{k_1 \cdots k_j}, \qquad \pi_0 = 1, \tag{3.82}$$

$$\phi_j = \sum_{i=0}^{j} \pi_i. \tag{3.83}$$

Note that this definition for ϕ_j is the same as that given in (3.54). It is left as an exercise to show that

$$J = \frac{k_0 c_0 - k_{-n} c_n \pi_{n-1}}{\phi_{n-1} + \beta k_0 c_0 + k_{-n} c_n (\alpha \phi_{n-1} - \beta \phi_{n-2})}, \tag{3.84}$$

where

$$\alpha = \sum_{j=1}^{n-1} \frac{\phi_{n-2} - \phi_{j-1}}{k_j \pi_j}, \tag{3.85}$$

$$\beta = \sum_{j=1}^{n-1} \frac{\phi_{n-1} - \phi_{j-1}}{k_j \pi_j}. \tag{3.86}$$

Equation (3.84) does not satisfy the independence principle, but it does satisfy the Ussing flux ratio. However, the details are left as an exercise (Exercise 5).

3.4.3 Saturating Barrier Models: Multi-Ion Pores

We showed above that single-ion models obey the Ussing flux ratio, even though they do not obey the independence principle. This means that to model the type of channel described in Fig. 3.2 it is necessary to use models that show flux coupling as predicted by Hodgkin and Keynes (1955). Such flux coupling arises in models in which more than one ion can be in the channel at any one time. Although the equations for such multi-ion models are essentially the same as the equations for the single-ion models described in the previous section, the analysis is complicated considerably by the fact that there are many more possible channel states. Hence, numerical techniques are the most efficient for studying such models. A great deal has been written about multi-ion models (e.g., Hille and Schwartz, 1978; Begenisich and Cahalan, 1980; Schumaker and MacKinnon, 1990; Urban and Hladky, 1979; Kohler and Heckmann, 1979). Space does not allow for a detailed discussion of the properties of these models, but so we present only a brief discussion of the simplest model. Hille and Schwartz (1978) and Hille (2001) give more detailed discussions.

Multi-ion models are based on assumptions similar to one-ion models. It is assumed that the passage of an ion through the channel can be described as the jumping of an ion over energy barriers, from one binding site to another. In one-ion models each binding site can either have an ion bound or not, and thus a channel with n binding sites can be in one of n independent states (i.e., the ion can be bound to any one of the binding sites). Hence, the steady-state ion distribution is found by solving a system of n linear equations, treating the concentrations on either side of the membrane as known. If more than one ion can be present simultaneously in the channel, the situation is more complicated. Each binding site can be in one of two states: binding an ion or empty. Therefore, a channel with n binding sites can be in any of 2^n states (at least; more states are possible if there is more than one ion type passing through the channel), and the steady-state probability distribution must be found by solving a large system of linear equations.

The simplest possible multi-ion model has three barriers and two binding sites, and so the channel can be in one of 4 possible states (Fig. 3.9). Arbitrary movements
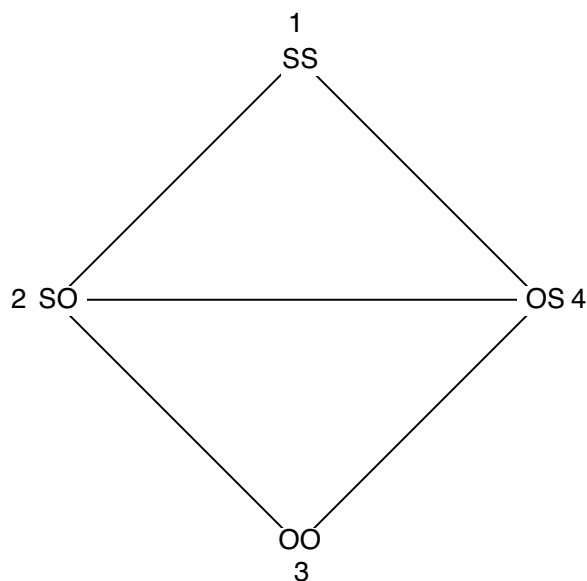
Figure 3.9: State diagram for a multi-ion barrier model with two binding sites and a single ion.

from one state to another are not possible. For example, the state OO (where both binding sites are empty) can change to OS or SO but cannot change to SS in a single step, as this would require two ions entering the channel simultaneously. We number the states as in Fig. 3.9 and let k_{ij} denote the rate of conversion of state i to state j. Also, let P_j denote the probability that the channel is in the jth state, and let c_e and c_i denote the external and internal ion concentrations, respectively. Then, the equations for the probabilities follow from the law of mass action; they are

$$\frac{dP_1}{dt} = -(k_{12} + k_{14})P_1 + k_{21}c_e P_2 + k_{41}c_i P_4, \tag{3.87}$$

$$\frac{dP_2}{dt} = -(k_{21}c_e + k_{23} + k_{24})P_2 + k_{12}P_1 + c_i k_{32}P_3 + k_{42}P_4, \tag{3.88}$$

$$\frac{dP_3}{dt} = -(c_i k_{32} + c_e k_{34})P_3 + k_{43}P_4 + k_{23}P_2, \tag{3.89}$$

$$\frac{dP_4}{dt} = -(k_{41}c_i + k_{42} + k_{43})P_4 + k_{14}P_1 + k_{24}P_2 + c_e k_{34}P_3. \tag{3.90}$$

The probabilities must also satisfy the conservation equation

$$\sum_{i=1}^{4} P_i = 1. \tag{3.91}$$

Using the conservation equation in place of the equation for P_4, the steady-state

probability distribution is given by the linear system

$$
\begin{pmatrix}
-k_{12} - k_{14} & k_{21} & 0 & k_{41} \\
k_{12} & -k_{21} - k_{23} - k_{24} & c_e k_{32} & k_{42} \\
0 & k_{23} & -c_e k_{32} - c_i k_{34} & k_{43} \\
1 & 1 & 1 & 1
\end{pmatrix}
\begin{pmatrix}
P_1 \\ P_2 \\ P_3 \\ P_4
\end{pmatrix}
=
\begin{pmatrix}
0 \\ 0 \\ 0 \\ 1
\end{pmatrix}.
$$
$$(3.92)$$

Since each rate constant is determined as a function of the voltage in the same way as one-ion models (as in, for example, (3.69)–(3.72)), solution of (3.92) gives each P as a function of voltage and the ionic concentrations on each side of the membrane. Finally, the membrane fluxes are calculated as the net rate of ions crossing any one barrier, and so, choosing the middle barrier arbitrarily, we have

$$ J = P_2 k_{24} - P_4 k_{42}. \tag{3.93} $$

Although it is possible to solve such linear systems exactly (particularly with the help of symbolic manipulators such as Maple or Mathematica), it is often as useful to solve the equations numerically for a given energy profile. It is left as an exercise to show that the Ussing flux ratio is not obeyed by a multi-ion model with two binding sites and to compare the I–V curves of multi-ion and one-ion models.

3.4.4 Electrogenic pumps and exchangers

Recall from Chapter 2 that detailed balance required that rate constants in models for electrogenic exchangers and pumps be dependent on the membrane potential. See, for example, (2.77) or (2.95). However, although the arguments from chemical equilibrium show that voltage-dependency must exist, they do not tell us exactly which rate constants depend on the voltage, or what the functional dependency is. As we have come to expect, it is much more difficult to answer these questions. Just as there are many ways to model ionic current flow, so there are many ways to model how rate constants depend on the membrane potential. In addition, depending on the exact assumptions, any of the steps in the model could depend on membrane potential. In other words, not only are there a number of ways to model the voltage-dependence when it occurs, there are also many places where it could occur. It is, in general, a very difficult task to determine the precise place and nature of the voltage-dependence.

One simple approach is to assume that the conformational change of the carrier protein is the step that moves the charge across the membrane, and thus requires the crossing of a free energy barrier. Consider the diagram shown in Fig. 2.9. If we assume that the transition from state X_2 to Y_2 involves the movement of 2 positive ions across an energy barrier and a potential difference V, then we can model the rate constants as

$$ k_2 = \kappa \exp\left[\frac{1}{RT}(-\Delta G_+ + 2FV/2) \right] \tag{3.94} $$

$$ = \bar{k}_2 \exp\left(\frac{FV}{RT} \right), \tag{3.95} $$

$$k_{-2} = \kappa \exp\left[\frac{1}{RT}(-\Delta G_- - 2FV/2)\right] \qquad (3.96)$$

$$= \bar{k}_{-2} \exp\left(\frac{-FV}{RT}\right), \qquad (3.97)$$

where $\bar{k}_2 = \kappa \exp[-\Delta G_+/(RT)]$ and similarly for $\bar{k}_{-2}$. In (3.94) and (3.96) $2FV$ is divided by 2 as we assume, for simplicity, that the energy barrier occurs halfway through the membrane.

If we make similar assumptions for k_4 and k_{-4}, i.e., that these transitions involve the reverse movement of 3 positive charges across an energy barrier and a potential difference, we get similar equations for those rate constants. Then

$$\frac{k_{-2}}{k_2}\frac{k_{-4}}{k_4} = \frac{\bar{k}_{-2}}{\bar{k}_2}\frac{\bar{k}_{-4}}{\bar{k}_4} \exp\left(\frac{-2FV}{RT}\right)\exp\left(\frac{3FV}{RT}\right)$$

$$= \frac{\bar{k}_{-2}}{\bar{k}_2}\frac{\bar{k}_{-4}}{\bar{k}_4} \exp\left(\frac{FV}{RT}\right), \qquad (3.98)$$

from which follows the necessary equilibrium condition, $K_1 K_2 K_3 K_4 = \exp\left(\frac{FV}{RT}\right)$ (cf. (2.77)).

3.5   Channel Gating

So far in this chapter we have discussed how the current through a single open channel depends on the membrane potential and the ionic concentrations on either side of the membrane. However, it is of equal interest to determine how ionic channels open and close in response to voltage. As described in Chapter 5, the opening and closing of ionic channels in response to changes in the membrane potential is the basis for electrical excitability and is thus of fundamental significance in neurophysiology.

Recall that there is an important difference between the instantaneous and steady-state I–V curves. In general, the current through a population of channels is the product of three terms,

$$I = Ng(V,t)\phi(V), \qquad (3.99)$$

where $\phi(V)$ is the I–V curve of a single open channel, and $g(V,t)$ is the proportion of open channels in the population of N channels. In the previous sections we discussed electrodiffusion and barrier models for $\phi(V)$; in this section we discuss models for the dependence of g on voltage and time.

Consider, for example, the curves in Fig. 3.10, which show typical responses of populations of Na^+ and K^+ channels. When the voltage is stepped from -65 mV to -9 mV, and held fixed at the new level, the K^+ conductance (g_K) slowly increases to a new level, while the Na^+ conductance (g_{Na}) first increases and then decreases. From this data we can draw several conclusions. First, as the voltage increases, the proportion of open K^+ channels increases. Second, although the proportion of open Na^+ channels initially increases, a second process is significant at longer times, as the Na^+ channel is inactivated. Thus, Na^+ channels first activate and then inactivate.
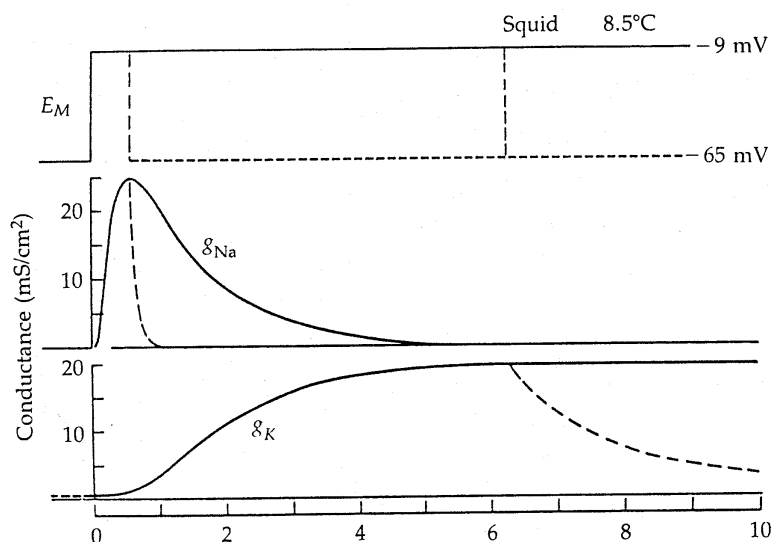
Figure 3.10: Na^+ and K^+ conductances as a function of time after a step change in voltage from -65 mV to -9 mV. The dashed line shows that after repolarization g_{Na} recovers quickly, and g_K recovers more slowly. (Hille, 2001, Fig. ?, p. ?.) **Check these**

3.5.1 A Two-State K^+ Channel

The simplest model for the K^+ channel assumes that the channel can exist in either a closed state, C, or an open state, O, and that the rate of conversion from one state to another is dependent on the voltage. Thus,

$$C \underset{\beta(V)}{\overset{\alpha(V)}{\rightleftarrows}} O. \tag{3.100}$$
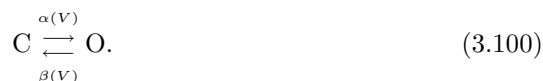
If g denotes the proportion of channels in the open state (so $1 - g$ is the proportion of closed channels), the differential equation for the rate of change of g is

$$\frac{dg}{dt} = \alpha(V)(1 - g) - \beta(V)g. \tag{3.101}$$

Under voltage-clamp conditions (i.e., where the voltage is held fixed, as in Fig. 3.10), α and β are constants, and thus one can readily solve for g as a function of time. Equation (3.101) is often written as

$$\tau_g(V)\frac{dg}{dt} = g_\infty(V) - g, \tag{3.102}$$

where $g_\infty(V) = \alpha/(\alpha + \beta)$ is the steady-state value of g, and $\tau_g(V) = 1/(\alpha + \beta)$ is the time constant of approach to the steady state. From experimental data, such as that shown in Fig. 3.10, one can obtain values for g_∞ and τ_g, and thus α and β can be unambiguously determined.

The form of $g_\infty(V)$ can be determined from free energy arguments. The reason for voltage dependence must be that the subunit is charged and that to change from one conformation to another charges must move in the potential field. This movement of charge is a current, called the gating current. Now the difference in free energy between the two conformations is of the form

$$\Delta G = \Delta G^0 + aFV, \tag{3.103}$$

where ΔG^0 is the free energy difference between the two states in the absence of a potential, and a is a constant related to the number of charges that move and the relative distance they move during a change of conformation. It follows that the equilibrium constant for the subunit must be of the form

$$\frac{\beta}{\alpha} = k_0 \exp\left(\frac{aFV}{RT}\right), \tag{3.104}$$

in which case

$$g_\infty(V) = \frac{\alpha}{\alpha + \beta} = \frac{1}{1 + k_0 \exp(\frac{aFV}{RT})}, \tag{3.105}$$

which can also be expressed in the form

$$g_\infty(V) = \frac{1}{2} + \frac{1}{2}\tanh(b(V - V_0)). \tag{3.106}$$

3.5.2 Multiple Subunits

An important generalization of the two-state model occurs when the channel is assumed to consist of multiple identical subunits, each of which can be in either the closed or open state. For example, suppose that the channel consists of two identical subunits, each of which can be closed or open. Then, the channel can take any of four possible states, S_{00}, S_{10}, S_{01}, or S_{11}, where the subscripts denote the different subunits, with 1 and 0 denoting open and closed subunits, respectively. A general model for this channel involves three differential equations (although there is a differential equation for each of the four variables, one equation is superfluous because of the conservation equation $S_{00} + S_{10} + S_{01} + S_{11} = 1$), but we can simplify the model by grouping the channel states with the same number of closed and open subunits. Because the subunits are identical, there should be no difference between S_{10} and S_{01}, and thus they are amalgamated into a single variable.

So, we let S_i denote the group of channels with exactly i open subunits. Then, conversions between channel groups are governed by the reaction scheme

$$S_0 \underset{\beta}{\overset{2\alpha}{\rightleftarrows}} S_1 \underset{2\beta}{\overset{\alpha}{\rightleftarrows}} S_2. \tag{3.107}$$

The corresponding differential equations are

$$\frac{dx_0}{dt} = \beta x_1 - 2\alpha x_0, \tag{3.108}$$

$$\frac{dx_2}{dt} = \alpha x_1 - 2\beta x_2, \tag{3.109}$$

where x_i denotes the proportion of channels in state S_i, and $x_0 + x_1 + x_2 = 1$. We now make the change of variables $x_2 = n^2$, where n satisfies the differential equation

$$\frac{dn}{dt} = \alpha(1 - n) - \beta n. \tag{3.110}$$

A simple substitution shows that (3.108) and (3.109) are satisfied by $x_0 = (1 - n)^2$ and $x_1 = 2n(1 - n)$.

In fact, we can derive a stronger result. We let

$$x_0 = (1 - n)^2 + y_0, \tag{3.111}$$
$$x_2 = n^2 + y_2, \tag{3.112}$$

so that, of necessity, $x_1 = 2n(1 - n) - y_0 - y_2$. It follows that

$$\frac{dy_0}{dt} = -2\alpha y_0 - \beta(y_0 + y_2), \tag{3.113}$$

$$\frac{dy_2}{dt} = -\alpha(y_0 + y_2) - 2\beta y_2. \tag{3.114}$$

This is a linear system of equations with eigenvalues $-(\alpha + \beta), -2(\alpha + \beta)$, and so y_0, y_2 go exponentially to zero. This means that $x_0 = (1 - n)^2, x_2 = n^2$ is an invariant stable manifold for the original system of equations; the solutions cannot leave this manifold, and with arbitrary initial data, the flow approaches this manifold exponentially. Notice that this is a stable invariant manifold even if α and β are functions of time (so they can depend on voltage or other concentrations).

This argument generalizes to the case of k identical independent binding sites where the invariant manifold for the flow is the binomial distribution with probability n satisfying (3.110) (see Exercise 14). Thus, the channel conductance is proportional to n^k, where n satisfies the simple equation (3.110). This multiple subunit model for channel gating provides the basis for the model of excitability that is examined in the next chapter.

3.5.3 The Sodium Channel

A more complex model is needed to explain the behavior of the Na^+ channel, which both activates and inactivates. The simplest approach is to extend the above analysis to the case of multiple subunits of two different types, m and h, say, where each subunit can be either closed or open, and the channel is open, or conducting, only when all subunits are open. To illustrate, we assume that the channel has one h subunit and two m subunits. The reaction diagram of such a channel is shown in Fig. 3.11. We let S_{ij} denote the channel with i open m subunits and j open h subunits, and we let x_{ij} denote the fraction of channels in state S_{ij}. The dynamics of x_{ij} are described by a system of six differential equations. However, as above, direct substitution shows that this system of equations has an invariant manifold $x_{00} = (1 - m)^2(1 - h)$, $x_{10} = 2m(1 - m)(1 - h)$, $x_{20} = m^2(1 - h)$, $x_{01} = (1 - m)^2 h$, $x_{11} = 2m(1 - m)h$, and $x_{21} = m^2 h$, provided

$$\frac{dm}{dt} = \alpha(1 - m) - \beta m, \tag{3.115}$$

$$S_{00} \underset{\beta}{\overset{2\alpha}{\rightleftarrows}} S_{10} \underset{2\beta}{\overset{\alpha}{\rightleftarrows}} S_{20}$$

$$\gamma \downarrow \uparrow \delta \qquad \gamma \downarrow \uparrow \delta \qquad \gamma \downarrow \uparrow \delta$$

$$S_{01} \underset{\beta}{\overset{2\alpha}{\rightleftarrows}} S_{11} \underset{2\beta}{\overset{\alpha}{\rightleftarrows}} S_{21}$$
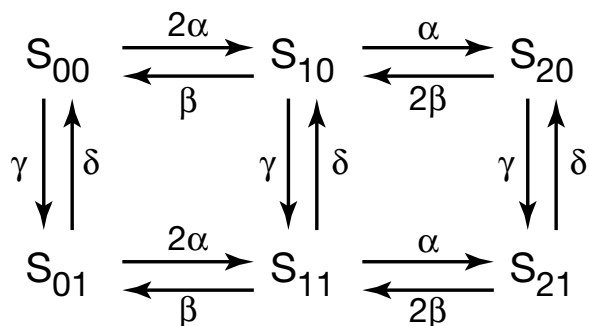
Figure 3.11: Diagram of the possible states in a model of the Na$^+$ channel.

$$C \underset{\beta}{\overset{\alpha}{\rightleftarrows}} O$$

with γ downward from O to I, and δ from C to I.
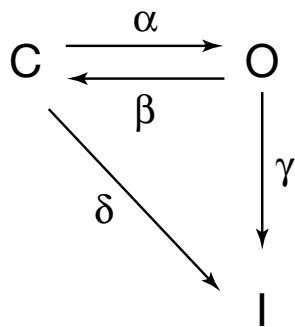
Figure 3.12: A: Schematic diagram of the states of the Na$^+$ channel. C, O, and I denote the closed, open, and inactivated states, respectively.

$$\frac{dh}{dt} = \gamma(1-h) - \delta h. \tag{3.116}$$

Furthermore, the invariant manifold is stable. A model of this type was used by Hodgkin and Huxley in their model of the nerve axon, which is discussed in detail in Chapter 5.

In an alternate model of the Na$^+$ channel (Aldrich et al., 1983; Peskin, 1991), it is assumed that the Na$^+$ channel can exist in three states, closed (C), open (O), or inactivated (I), and that once the channel is inactivated, it cannot return to either the closed or the open state (Fig. 3.12). Thus, the state I is absorbing. While this is clearly not true in general, it is a reasonable approximation at high voltages.

As before, we let g denote the proportion of open channels and let c denote the proportion of closed channels. Then,

$$\frac{dc}{dt} = -(\alpha+\delta)c + \beta g, \tag{3.117}$$
$$\frac{dg}{dt} = \alpha c - (\beta+\gamma)g, \tag{3.118}$$

where the proportion of channels in the inactivated state is $i = 1 - c - g$. Initial

conditions are $c(0) = 1$, $g(0) = 0$, i.e., all the channels are initially in the closed state. This system of first order differential equations can be solved directly to give

$$g(t) = a(e^{\lambda_1 t} - e^{\lambda_2 t}), \tag{3.119}$$

where $\lambda_2 < \lambda_1 < 0$ are the roots of the characteristic polynomial

$$\lambda^2 + (\alpha + \beta + \gamma + \delta)\lambda + (\alpha + \delta)(\beta + \gamma) - \alpha\beta = 0, \tag{3.120}$$

and where

$$g'(0) = \alpha = a(\lambda_1 - \lambda_2) > 0. \tag{3.121}$$

As in the simple two-state model, the function g can be fit to data to determine the parameters a, λ_1, and λ_2. However, unlike the two-state model, the rate constants cannot be determined uniquely from these parameters. For, since λ_1 and λ_2 are the roots of (3.120), it follows that

$$\alpha + \beta + \gamma + \delta \ = \ -\lambda_1 - \lambda_2, \tag{3.122}$$
$$(\alpha + \delta)(\beta + \gamma) - \alpha\beta \ = \ \lambda_1 \lambda_2. \tag{3.123}$$

Thus, there are only three equations for the four unknowns, α, β, γ, and δ, so the system is underdetermined (see Exercise 16). This problem cannot be resolved using the macroscopic data that has been discussed so far, but requires data collected from a single channel, as described in Section 3.6.

3.5.4 Agonist-Controlled Ion Channels

Many ion channels are controlled by agonists, rather than by voltage. For example, the opening of ion channels in the post-synaptic membrane of the neuromuscular junction (Chapter 8) is controlled by the neurotransmitter acetylcholine, while in the central nervous system a host of neurotransmitters such as glutamate, dopamine, γ-aminobutyric acid (GABA), and serotonin have a similar role. The inositol trisphosphate receptor and ryanodine receptor are other important agonist-controlled ion channels (Chapter 7).

Early theories of agonist-controlled ion channels (Clark, 1933) assumed that the channel was opened simply by the binding of the agonist. Thus,

$$A + T \underset{k_{-1}}{\overset{k_1}{\rightleftharpoons}} AT, \tag{3.124}$$

where the state AT is open. However, this simple theory is unable to account for a number of experimental observations. For example, it can happen that only a fraction of channels are open at any given time, even at high agonist concentrations, a result that cannot be explained by this simple model.

In 1957, del Castillo and Katz proposed a model that explicitly separated the agonist binding step from the gating step;

$$
\begin{array}{ccccccc}
A & + & T & \underset{k_{-1}}{\overset{k_1}{\rightleftharpoons}} & AT & \underset{\alpha}{\overset{\beta}{\rightleftharpoons}} & AR. \\
& & \text{state 3} & & \text{state 2} & & \text{state 1} \\
& & \text{closed} & & \text{closed} & & \text{open} \\
& & \text{unoccupied} & & \text{occupied} & & \text{occupied}
\end{array}
\tag{3.125}
$$
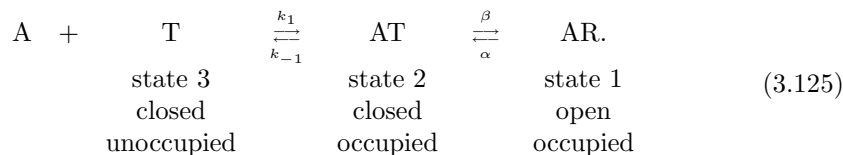
Note that the only open state is AR (state 1; the slightly unusual numbering of the states follows Colquhoun and Hawkes, 1981). Thus, in this model, binding of the agonist places the channel into an occupied state that allows, but does not require, opening. The agonist-binding step is controlled by the *affinity* of the channel for the agonist, while the gating is determined by the *efficacy* of the channel. This separation of affinity and efficacy has proven to be an extremely powerful way of understanding agonist-controlled channels, and is at the heart of practically all modern approaches (Colquhoun, 2006).

The conductance of a population of agonist-controlled channels is determined as the solution of the system of differential equations

$$\frac{d\Phi_1}{dt} = \beta\Phi_2 - \alpha\Phi_1, \tag{3.126}$$

$$\frac{d\Phi_2}{dt} = \alpha\Phi_1 + k_1 a(1 - \Phi_2 - \Phi_1) - (\beta + k_{-1})\Phi_2, \tag{3.127}$$

where Φ_1, Φ_2 and $1 - \Phi_1 - \Phi_2$ represent the percentage of channels in states 1, 2, and 3, respectively, and a is the concentration of agonist, A. The solution of this system of differential equations is easy to determine, provided a is constant. However, the practical usefulness of this exact solution is extremely limited, since in any realistic situation a is changing in time.

The steady state solution is also readily found to be

$$\Phi_1 = \frac{1}{1 + \frac{\beta}{\alpha} + \frac{\beta k_{-1}}{\alpha k_1 a}}, \tag{3.128}$$

and this can be fit to data to find the equilibrium constants $\frac{\beta}{\alpha}$ and $\frac{k_{-1}}{k_1}$. However, complete determination of the four kinetic parameters is much more challenging. One could imagine a "concentration clamp" experiment, in which the concentration of a is suddenly switched from one level to another and the conductance of the channels monitored. From this data one could then determine the two eigenvalues of the system (3.126)–(3.127). However, usually such experiments are very difficult to perform. In Section 3.6 we show that there is more information contained in single-channel recordings and how this additional information can be used to determine the kinetic parameters of channel models.

3.5.5   Drugs and Toxins

Many drugs act by blocking a specific ion channel. There are numerous specific channel blockers, such as Na^+ channel blockers, K^+ channel blockers, Ca^{2+} channel blockers, and so on. In fact, the discovery of site-specific and channel-specific blockers has been of tremendous benefit to the experimental study of ion channels. Examples of important channel blockers include verapamil (Ca^{2+}-channel blocker), quinidine, sotolol, nicotine, DDT, various barbiturates (K^+-channel blockers), tetrodotoxin (TTX, the primary ingredient of puffer fish toxin), and scorpion toxins (Na^+-channel blockers).

To include the effects of a drug or toxin like TTX in a model of a Na^+ channel is a relatively simple matter. We assume that a population P of Na^+ channels is

available for ionic conduction and that a population B is blocked because they are bound by the toxin. Thus,

$$P + D \underset{k_-}{\overset{k_+}{\rightleftharpoons}} B, \tag{3.129}$$

where D represents the concentration of the drug. Clearly, $P + B = P_0$, so that

$$\frac{dP}{dt} = k_-(P_0 - P) - k_+ DP, \tag{3.130}$$

and the original channel conductance must be modified by multiplying by the percentage of unbound channels, P/P_0.

In steady state, we have

$$\frac{P}{P_0} = \frac{K_d}{K_d + D}. \tag{3.131}$$

The remarkable potency of TTX is reflected by its small equilibrium constant K_d, as $K_d \approx 1$–5 nM for Na$^+$ channels in nerve cells, and $K_d \approx 1$–10 μM for Na$^+$ channels in cardiac cells. By contrast, verapamil has $K_d \approx$140–940 μM.

Other important drugs, such as lidocaine, flecainide, and encainide are so-called *use-dependent* Na$^+$-channel blockers, in that they interfere with the Na$^+$ channel only when it is open. Thus, the more the channel is used, the more likely that it is blocked. Lidocaine is an important drug used in the treatment of cardiac arrhythmias. The folklore explanation of why it is useful is that because it is use-dependent, it helps prevent high-frequency firing of cardiac cells, which is commonly associated with cardiac arrhythmias. In fact, lidocaine, flecainide, and encainide are officially classified as antiarrhythmic drugs, even though it is now known that flecainide and encainide are proarrhythmic in certain postinfarction (after a heart attack) patients. A full explanation of this behavior is not known.

To keep track of the effect of a use-dependent drug on a two-state channel, we suppose that there are four classes of channels, those that are closed but unbound by the drug (C), those that are open and unbound by the drug (O), those that are closed and bound by the drug (CB), and those that are open and bound by the drug (OB) (but unable to pass a current). For this four-state model a reasonable reaction mechanism is

$$C \underset{\beta}{\overset{\alpha}{\rightleftharpoons}} O, \qquad CB \underset{\beta}{\overset{\alpha}{\rightleftharpoons}} OB \tag{3.132}$$

$$CB \xrightarrow{k_+} C + D, \qquad O + D \underset{k_-}{\overset{k_+}{\rightleftharpoons}} OB. \tag{3.133}$$
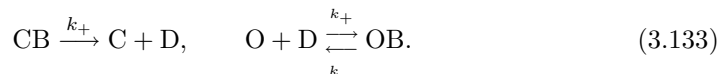
Notice that we have assumed that the drug does not interfere with the process of opening and closing, only with the flow of ionic current, and that the drug can bind the channel only when it is open. It is now a straightforward matter to find the differential equations governing these four states, and we leave this as an exercise.

This is not the only way that drugs might interfere with a channel. For example, for a channel with multiple subunits, the drug may bind only when certain of the subunits are in specific states. Indeed, the binding of drugs with channels can occur in many ways, and there are numerous unresolved questions concerning this complicated process.

3.6   Single-Channel Analysis

Since the late 1970s, the development of patch-clamp recording techniques has allowed the measurement of ionic current through a small piece of cell membrane, containing only a few, or even a single, ionic channel (Hamill et al., 1981; Sakmann and Neher, 1995; Neher and Sakmann received the 1991 Nobel Prize in physiology for their development of the patch-clamp technique).

Much of the mathematical theory of how to analyze single-channel recordings was worked out in a series of papers by Colquhoun and Hawkes (1977, 1981, 1982). As is true of most things written by Colquhoun, these are eminently readable. However, newcomers to the field should first read the two chapters in the Plymouth Workshop Handbook on Microelectrode Techniques (Colquhoun, 1994; Colquhoun and Hawkes, 1994), as these are an excellent introduction. The chapter by Colquhoun and Hawkes in the book by Sakmann and Neher (1995) is also a valuable reference.

An example of an experimental record for Na^+ channels is given in Fig. 3.13. The current through an individual channel is stochastic (panel A) and cannot be described by a deterministic process. Nevertheless, the ensemble average over many experiments (panel B) is deterministic and reproduces the same properties that are seen in the macroscopic measurements of Fig. 3.10. However, the single-channel recordings contain more information than does the ensemble average.

What information is available from single-channel recordings that is not available from ensemble averages? First of all, one can measure how long a channel is open on average, or more generally, the distribution of open times. Similarly, one can measure the distribution of times the channel is in the closed state. If there are additional dynamical processes underlying the opening and closing of channels, as there are with Na^+ channels, one can measure (for example) how many times a channel opens (and closes) before it is inactivated (permanently closed) or how many channels fail to open even once.

The most common models of ion channels are discrete-space continuous-time Markov processes, the basic theory of which was described in Chapter 2, Section 2.9.2. Since it is this theory that lies at the heart of the analysis of single-channel data, the reader is encouraged to review the relevant sections of Chapter 2 before continuing.

3.6.1   Single-Channel Analysis of a Sodium Channel

Consider the Na^+ channel model shown in Fig. 3.12. For this model there are two obvious waiting time problems. The probability that the amount of time spent in the closed state before opening is less than t is governed by the differential equation

$$\frac{dP}{dt} = \alpha(1 - P), \qquad (3.134)$$

with $P(0) = 1$, and therefore is

$$P(t) = 1 - \exp(-\alpha t). \qquad (3.135)$$

so that the closed time distribution is $\alpha \exp(-\alpha t)$.
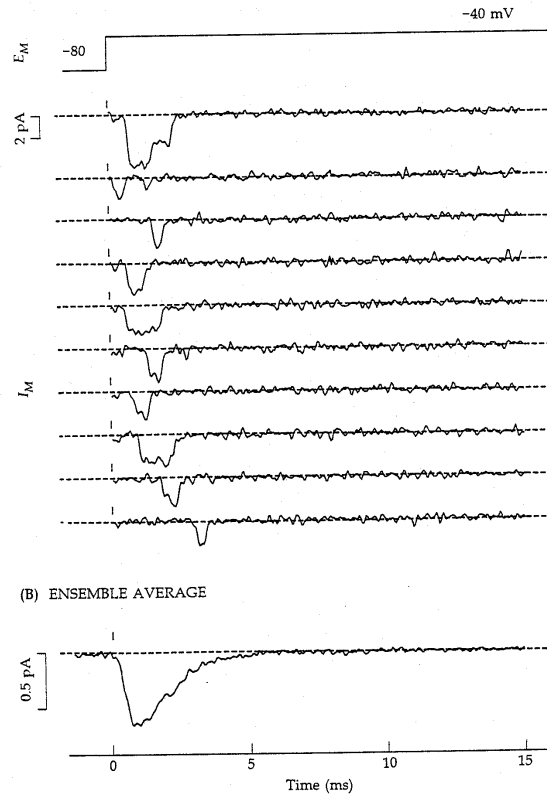
Figure 3.13: A: Na^+ currents from a single channel (or possibly two in the first trace) following a voltage step from -80 mV to -40 mV. B: Average open probability of the Na^+ channel, obtained by averaging over many traces of the type shown in A. (Hille, 2001, Fig. ?, p. ?.) **Check these**

Similarly, the probability that the amount of time spent in the open state is less than t is $1 - \exp(-(\beta + \gamma)t)$, so that the open time distribution is $(\beta + \gamma) \exp(-(\beta + \gamma)t)$.

According to this model, the channel can inactivate from the closed state at rate δ or from the open state at rate γ. At the beginning of the experiment, the channel is in the closed state and from there it can either open or inactivate. The probability that the first transition is to the open state is $A = \frac{\alpha}{\alpha + \delta}$ and the probability that the first transition is to the inactivated state is $1 - A$. Thus, $1 - A$ can be estimated by the proportion of experimental records in which no current is observed, even after the depolarizing stimulus was maintained for a long time.

A channel may open and close several times before it finally inactivates. To understand this, we let N be the number of times the channel opens before it finally inactivates and calculate the probability distribution for N. Clearly, $P[N = 0] = 1 - A$. Furthermore,

$$
\begin{aligned}
P[N = k] &= P[N = k \text{ and channel enters I from O}] \\
&\quad + P[N = k \text{ and channel enters I from C}] \\
&= A^k B^{k-1}(1 - B) + A^k B^k (1 - A) \\
&= (AB)^k \left(\frac{1 - AB}{B} \right).
\end{aligned}
\tag{3.136}
$$

where $B = \frac{\beta}{\beta + \gamma}$.

We now have enough information to estimate the four channel rate constants. Since A can be determined from the proportion of channels that never open, B can be determined from a plot of the experimental data for $P[N = k]$ vs. k. Then, $\beta + \gamma$ can be determined from the open time distribution of the channel and α can be determined from the closed time distribution.

Since the work of Hodgkin and Huxley (described in Chapter 5), the traditional view of a Na^+ channel has been that it activates quickly and inactivates slowly. According to this view, the decreasing portion of the g_{Na} curve in Fig. 3.10 is due entirely to inactivation of the channel. However, single-channel analysis has shown that this interpretation of macroscopic data is not always correct. It turns out that the rate of inactivation of some mammalian Na^+ channels is faster than the rate of activation. For example, Aldrich et al. (1983) found $\alpha = 1/\text{ms}$, $\beta = 0.4/\text{ms}$, $\gamma = 1.6/\text{ms}$ and $\delta = 1/\text{ms}$ at $V = 0$ for channels in a neuroblastoma cell line and a pituitary cell line. Although this reversal of activation and inactivation rates is not correct for all Na^+ channels in all species, the result does overturn some traditional ideas of how Na^+ channels work.

More modern models of the Na^+ channel are based on a wide range of experimental data, including single-channel recordings and macroscopic ionic and gating currents. It is a very difficult matter to decide, on the basis of this data, which is the best model of the channel. One of the most rigorous attempts is that of Vandenberg and Bezanilla (1991), who concluded that a sequential Markov model with three closed states, one open state, and one inactivated state was the best at reproducing
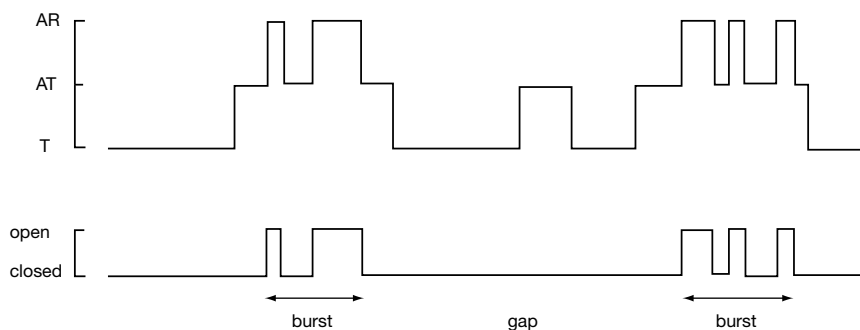
Figure 3.14: Schematic diagram of a possible single-channel recording in the model described by (3.125). The openings occur in bursts as the channel flickers between states AR and AT. However, the transitions between states T and AT cannot be observed. (Adapted from Colquhoun and Hawkes (1981), Fig. 1.)

the widest array of data. However, because of the ill-posed nature of this inverse problem, it is impossible to rule out the existence of multiple other states.

3.6.2 Single-Channel Analysis of an Agonist-Controlled Ion Channel

The single-channel analysis of the agonist-controlled ion channel is more subtle than that of the Na^+ channel. This is because there are states that cannot be directly observed, but can only be inferred from the data. If the state AR is the only open state, then a typical single-channel recording might look (at least, in an ideal situation) like that shown in Fig. 3.14. The openings occur in bursts as the channel flicks between the AR and AT states, with longer interburst periods occurring when the channel escapes from AT into the closed state, T, because of agonist unbinding. However, because the binding and unbinding transitions are not directly observable, this process is called a *hidden Markov process*.

There are two distributions that are readily determined from the data. These are the open time and closed time distributions. Since the open state, AR, can close only by a single pathway to AT, the open time distribution is the exponential distribution $\alpha e^{-\alpha t}$, with mean $1/\alpha$.

The closed time distribution

Every period during which the channel is closed must begin with the channel in state AT, and end with the channel in state AR. However, during this time the channel can be in either of states AT or T. Thus, the closed time distribution is the transition time from state AT to state AR (see Section 2.9.2).

To calculate the closed time probability we set state AR to be an absorbing state (i.e., set $\alpha = 0$), and impose the initial condition that the receptor starts in state

AT. Hence,

$$\frac{d\Phi_1}{dt} = \beta\Phi_2, \tag{3.137}$$

$$\frac{d\Phi_2}{dt} = -(\beta + k_{-1})\Phi_2 + ak_1\Phi_3, \tag{3.138}$$

$$\frac{d\Phi_3}{dt} = k_{-1}\Phi_2 - ak_1\Phi_3, \tag{3.139}$$

with initial data $\Phi_1(0) = 0$, $\Phi_2(0) = 1$, $\Phi_3(0) = 0$.

We can readily solve this system of differential equations to determine that the transition time from state 2 to state 1 has the probability density

$$\phi_{21}(t) = \frac{d\Phi_1}{dt} = \beta x_2 = \frac{\beta}{\lambda_1 - \lambda_2}[(\lambda_1 + ak_1)e^{\lambda_1 t} - (\lambda_2 + ak_1)e^{\lambda_2 t}], \tag{3.140}$$

where the eigenvalues λ_1 and λ_2 are the roots (both negative) of $\lambda^2 + \lambda(\beta + k_{-1} + k_1 a) + ak_1\beta = 0$.

Since the closed time distribution is the sum of two exponentials, the open and closed time distributions along with the steady state open probability (3.128) theoretically provide enough information to determine uniquely the four kinetic parameters of the model.

Other distributions

There are other distributions that can be calculated but obtaining the data for these is somewhat subjective. These are the distribution of closed times during a burst, the number of openings in a burst, and the distribution of gap closed times.

The distribution of closed times during a burst is the easiest to calculate, being simply $\beta \exp(-\beta t)$.

Each time the channel is in state AT a choice is made to go to state AR (with probability $\beta/(\beta + k_{-1})$) or to go to state T (with probability $k_{-1}/(\beta + k_{-1})$). Thus, for there to be N openings in a burst, the channel must reopen by going from state AT to state AR $N - 1$ times, and then end the burst by going from state AT to state T. Hence,

$$P(N \text{ openings}) = \left(\frac{\beta}{\beta + k_{-1}}\right)^{N-1}\left(\frac{k_{-1}}{\beta + k_{-1}}\right), \tag{3.141}$$

where $N \geq 1$, which has mean $1 + \beta/k_{-1}$.

To determine the closed time distribution for gaps, we observe that a gap begins in state AT and then moves back and forth between states T and AT before finally exiting into state AR. The waiting time distribution for leaving state AT into state T is

$$\phi_{23}(t) = k_{-1}e^{-k_{-1}t}. \tag{3.142}$$

The transition time from state T to state AR is $\phi_{31} = \frac{d\Phi_1}{dt}$, determined as the solution of the system (3.137)-(3.139), subject to initial conditions $\Phi_1(0) = 0$, $\Phi_2(0) = 0$,

and $\Phi_3(0) = 1$. One readily determines that

$$\phi_{31} = \beta \frac{(\lambda_2 + ak_1)(\lambda_1 + ak_1)}{k_{-1}(\lambda_2 - \lambda_1)}(e^{\lambda_1 t} - e^{\lambda_2 t}). \tag{3.143}$$

Now, to calculate the gap time distribution, we observe that the time in a gap is the sum of two times, namely the time in state AT before going to state T and the time to go from state T to state AR. Here we invoke a standard result from probability theory regarding the distribution for the sum of two random variables. That is, if $p_1(t_1)$ and $p_2(t_2)$ are the probability densities for random variables t_1 and t_2, then the probability density for the sum of these is the convolution

$$p_{\text{sum}}(t) = \int_0^t p_1(s)p_2(t-s)ds. \tag{3.144}$$

Thus, in this problem, the probability density for the gap time is

$$\phi_{\text{gap}}(t) = \int_0^t \phi_{23}(s)\phi_{31}(t-s)ds. \tag{3.145}$$

It is again straightforward to determine (use Laplace transforms and the Convolution Theorem) that

$$\phi_{\text{gap}}(t) = \beta \frac{(\lambda_2 + ak_1)(\lambda_1 + ak_1)}{(\lambda_2 - \lambda_1)} \left(\frac{e^{\lambda_1 t}}{\lambda_1 + k_{-1}} - \frac{e^{\lambda_2 t}}{\lambda_2 + k_{-1}} + \frac{(\lambda_1 - \lambda_2)e^{-k_{-1}t}}{(\lambda_1 + k_{-1})(\lambda_2 + k_{-1})} \right),$$

a sum of three exponentials.

Making use of these distributions is tricky, because it is not clear how to distinguish between a short gap and a long closed interval during a burst. In fact, if a is large enough and k_{-1} is not too small, then mean gap length is shorter than the mean burst closed time, so that errors of classification are likely.

3.6.3   Comparing to experimental data

Experimental data typically come in lists of open and closed times. They are then displayed in a histogram, where the area under each histogram bar corresponds to the number of events in that interval.

However, it can be very difficult to determine from a histogram how many exponential components are in the distributions; an exponential distribution with three exponentials can look very similar to one with two exponentials, even when the time constants are widely separated.

This problem is sometimes avoided by first taking the log of the times, and plotting a histogram of the log(time) distributions. Since the log function is monotone increasing, we know that

$$P[t < t_1] = P[\log(t) < \log(t_1)], \tag{3.146}$$

and thus the cumulative distributions are the same, whether functions of the log or the linear times. However, the functions that are of interest to us are the probability
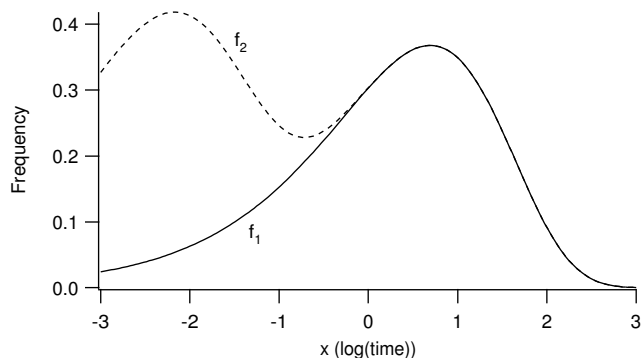
Figure 3.15: Two exponential distributions, transformed according to (3.147), and plotted against log(time). Solid line: $f_1(t) = 0.5e^{-0.5t}$. Dotted line: $f_2(t) = 0.5e^{-0.5t} + 10e^{-10t}$.

density functions, which are the derivatives of the cumulative distribution functions. Suppose $\Phi(t)$ is a cumulative distribution function with corresponding probability density function $\phi(t) = \frac{d\Phi}{dt}$. For any monotone increasing function $g(x)$, $\Phi(g(x))$ is also a cumulative distribution function in x. However, the corresponding probability density function is

$$\frac{d\Phi(g(x))}{dx} = g'(x)\phi(g(x)). \tag{3.147}$$

Thus, to use a log(time) transformation, $x = \ln(t)$, for a given probability density function, $\phi(t)$, we plot $e^x\phi(e^x)$ and fit this to the histogram of the log(time).

There are significant advantages to this scaling of time, especially for exponential distributions, illustrated in Fig. 3.15. The solid line in Fig. 3.15 corresponds to the distribution $\phi_1(t) = 0.5e^{-0.5t}$, transformed according to (3.147). In other words, this is the plot of the function $0.5e^x e^{-0.5e^x}$ against x. Notice that the maximum of the curve occurs at the mean of the distribution, $t = 2$ ($x = \log 2 = 0.69$) (see Exercise 21). The dotted line is the distribution $f_2(t) = 0.5e^{-0.5t} + 10e^{-10t}$, again transformed according to (3.147). (This is not a true probability density function since the area under the curve is 2, rather than 1). The two peaks occur at the means of the individual component exponential distributions, i.e., at $t = 2$ and $t = 0.1$ ($x = 0.69$ and $x = -2.3$ respectively).

Modern methods of fitting models to single-channel data are considerably more sophisticated than merely fitting histograms, as described above. Fitting directly to the set of open and closed times using the log likelihood is a common approach, but, more recently, methods to fit the model directly to the single-channel time course raw data (not simply to a list of open and closed times), using Markov Chain Monte Carlo and Bayesian inference, have been developed (Fredkin and Rice, 1992; Ball et al., 1999; Hodgson and Green, 1999).
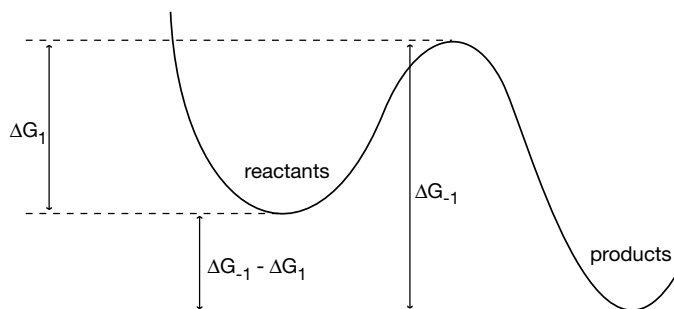
Figure 3.16: Schematic diagram of a potential energy profile of a hypothetical reaction.

3.7 Appendix

In Section 3.4 we made extensive use of the formula (3.42), i.e.,

$$k_i = \kappa \exp\left(\frac{-\Delta G_i}{RT}\right),\qquad(3.148)$$

which states that the rate, k_i, at which a molecule leaves a binding site is proportional to the exponential of the height of the energy barrier ΔG_i which must be crossed to exit. This is called the *Arrhenius* equation, after Svante Arrhenius who first discovered it experimentally in the late 1800s (Arrhenius received the 1903 Nobel Prize in Chemistry). Arrhenius determined, not the dependence of k_i on ΔG_i, but its dependence on temperature T. He showed experimentally that the rate of reaction is proportional to $\exp(-B/T)$, for some positive constant B. He then used the Boltzmann distribution to argue that $B = \Delta G_i/R$, as discussed below.

As was described in Section 1.2, the equilibrium constant, K_{eq}, for a reaction is related to the change in free energy between reactants, ΔG^0, by

$$K_{\mathrm{eq}} = e^{\frac{\Delta G^0}{RT}}.\qquad(3.149)$$

Note that, if κ is independent of ΔG_i, then (3.148) is consistent with (3.149). Given the potential energy profile in Fig. 3.16, it is clear that if $k_1 = \kappa \exp\left(\frac{-\Delta G_1}{RT}\right)$ and $k_{-1} = \kappa \exp\left(\frac{-\Delta G_{-1}}{RT}\right)$, then $K_{\mathrm{eq}} = k_{-1}/k_1 = \exp\left(\frac{\Delta G_1 - \Delta G_{-1}}{RT}\right) = \exp\left(\frac{\Delta G^0}{RT}\right)$, where $\Delta G^0 = \Delta G_1 - \Delta G_{-1}$.

However, despite this consistency, (3.148) does not follow from (3.149); the equilibrium relationship tells us nothing about how each rate constant might depend on T or ΔG_i. Although the derivation of the equilibrium condition depends only on fundamental thermodynamical principles, derivation of a rate expression is much more difficult, and the exact rate expression depends, in general, on the choice of model. There is still enormous controversy over exactly how to derive rate equations, and which is most suitable in any given situation. Here we give only a brief discussion of this important problem, enough to give a plausible derivation of the general form of (3.148). The exponential dependence occurs in every rate equation;

it is the pre-factor, κ, and its possible functional dependences, that is the source of so much discussion.

3.7.1   The Boltzmann Distribution

To show that $B = \Delta G/R$ (or $\Delta G/k$, depending on whether ΔG has units of per mole or per molecule; we have dropped the subscript i for this discussion), Arrhenius assumed that the rate of reaction was proportional to the fraction of molecules with energy greater than some minimum amount. Given this assumption, the Arrhenius equation follows from the Boltzmann distribution, which we now derive.

   We begin with a brief digression. It is intuitively clear that, were we to toss a fair coin 10^{20} times, the chance of obtaining any distribution of heads and tails significantly different from 50:50 is insignificant. We might, of course, get $\frac{10^{20}}{2} - 100$ heads and $\frac{10^{20}}{2} + 100$ tails, but the relative deviation from 50:50 is inconsequential.

   To express this mathematically, suppose that we toss a fair coin n times to get a sequence of heads and tails. Of all the possible sequences, the total number that have h heads and $n - h$ tails (in any order) is $\frac{n!}{h!(n-h)!}$, and thus, since there are 2^n possible sequences, the probability of getting h heads and $n - h$ tails is given by

$$\text{Prob}[n \text{ heads}, n - h \text{ tails}] = \frac{n!}{2^n h!(n-h)!}. \tag{3.150}$$

As n gets very large, the graph of (3.150) becomes sharply peaked, with a maximum of 1 at $h = n/2$. (This can be shown easily using Stirling's formula, $\ln(n!) \approx n \ln(n) - n$ for n large). In other words, the probability of obtaining any sequence that does not contain an equal number of heads and tails is vanishingly small in the limit of large n.

   An identical argument underlies the Boltzmann distribution. Suppose we have n particles each of which can be in one of k states, where state i has energy U_i. Let n_i denote the number of particles in state i. We assume that the total energy, U_{tot}, is fixed, so that

$$\sum_{i=1}^{k} n_i = n, \tag{3.151}$$

$$\sum_{i=1}^{k} U_i n_i = U_{\text{tot}}. \tag{3.152}$$

   The number of ways, W, that these n particles can be partitioned into k states, with n_i particles in the state i, is given by the multinomial factor

$$W = \frac{n!}{\Pi_{i=1}^{k} n_i!}. \tag{3.153}$$

Now, similarly to the probability of heads and tails for a coin toss, the function W is sharply peaked when n is large, and it is the distribution that gives the peak that is most likely to occur. Furthermore, the likelihood of distributions other than at the peak is vanishingly small when n is large. Thus, to find this overwhelmingly most

likely distribution we maximize W subject to the constraints (3.151) and (3.152). That is, we seek to maximize (using Lagrange multipliers)

$$F = \ln W - \lambda \left(\sum_{i=1}^{k} n_i - n \right) - \beta \left(\sum_{i=1}^{k} U_i n_i - U_{\text{tot}} \right). \tag{3.154}$$

(It is equivalent, and much more convenient, to use $\ln W$ rather than W.) According to (3.153)

$$
\begin{aligned}
\ln W &= \ln(n!) - \sum_{i=1}^{k} \ln(n_i!) \\
&\approx n \ln(n) - n + \sum_{i=1}^{k} n_i - \sum_{i=1}^{k} n_i \ln(n_i) \\
&= n \ln(n) - \sum_{i=1}^{k} n_i \ln(n_i), \tag{3.155}
\end{aligned}
$$

where we have used Stirling's formula, assuming all the n_is are large. Thus,

$$\frac{\partial F}{\partial n_i} = -\ln(n_i) - 1 - \lambda - \beta U_i, \tag{3.156}$$

which is zero when

$$n_i = \alpha e^{-\beta U_i}, \tag{3.157}$$

for positive constants α and β, which are independent of i. This most likely distribution of n_i is the *Boltzmann distribution*.

How does this relate to reaction rates? Suppose that we have a population of particles with two energy levels, a ground energy level of U_0, and a reactive energy level $U_r > U_0$. If the particles are at statistical equilibrium, i.e., the Boltzmann distribution, then the proportion of particles in the reactive state is

$$e^{\beta(U_0 - U_r)} = e^{-\beta \Delta U}. \tag{3.158}$$

Since this is also assumed to be the rate at which the reaction takes place, we have that

$$k \propto e^{\beta(U_0 - U_r)} = e^{-\beta \Delta U}. \tag{3.159}$$

To obtain the Arrhenius rate equation it remains to show that $\beta = \frac{1}{RT}$. To do so rigorously is beyond the scope of this text, but a simple dimensional argument can at least demonstrate plausibility. Recall that it is known from experiment that

$$k \propto e^{-B/T}, \tag{3.160}$$

for some constant $B > 0$. Thus, from (3.159), β must be proportional to $1/T$, and to get the correct units, $\beta \propto 1/(RT)$ or $1/(kT)$, depending on whether the units of U are per mole or per molecule. Unfortunately, the proportionality factor cannot be determined by this argument.

3.7.2 A Fokker-Planck equation approach

The above derivation relies on the assumption that there are a large number of particles, each of which can be in one of a number of different states. It is less obvious how such a derivation can be applied to the behavior of a small number of molecules, or a single molecule. To do this, we need to use the methods developed in the appendix to Chapter 2, and turn to a Fokker-Planck description of molecular motion.

Suppose that a molecule moves via Brownian motion, but also experiences a force generated by some potential, $U(x)$, and is subject to friction. If $x(t)$ denotes the position of the molecule, the Langevin equation for the molecular motion (Section 2.9.5) is

$$m\frac{d^2x}{dt^2} + \nu\frac{dx}{dt} + U'(x) = \sqrt{2\nu kT}W(t), \tag{3.161}$$

where W is a Wiener process. Here, ν is the friction coefficient, and is analogous to friction acting on a mass-spring system. If inertial effects can be neglected, which they can in most physiological situations, this simplifies to

$$\nu\frac{dx}{dt} = -U'(x) + \sqrt{2\nu kT}W(t). \tag{3.162}$$

Hence, the probability distribution that the particle is at position x at time t is given by $p(x,t)$, the solution of the Fokker-Planck equation

$$\nu\frac{\partial p}{\partial t} = \frac{\partial}{\partial x}(U'(x)p) + kT\frac{\partial^2 p}{\partial x^2}. \tag{3.163}$$

At steady state, i.e., when $\frac{\partial p}{\partial t} = 0$, (3.163) can be readily solved to give

$$p(x) = \frac{1}{A}\exp\left(-\frac{U(x)}{kT}\right), \tag{3.164}$$

where $A = \int_{-\infty}^{\infty} \exp(-\frac{U(x)}{kT})dx$ is chosen so that $\int_{-\infty}^{\infty} p(x)dx = 1$. We have thus regained a continuous version of the Boltzmann distribution; if $U(x)$ is a quadratic potential well ($U(x) = Ax^2$), then $p(x)$ is a Gaussian distribution.

If $U(x)$ is a double well potential with its maximum at $x = 0$ separating the two wells, then the ratio of the probability of finding the particle on the left to the probability of finding the particle on the right is

$$K_{\text{eq}} = \frac{\int_{-\infty}^{0} p(x)dx}{\int_{0}^{\infty} p(x)dx}. \tag{3.165}$$

Since it is difficult to calculate K_{eq} for general functions $U(x)$, it is useful to discretize the state space into a finite number of states $j = 1, 2, \cdots, n$ with energies U_j. For this, we know that the Boltzmann distribution is

$$p_j = \frac{1}{A}\exp\left(-\frac{U_j}{kT}\right), \tag{3.166}$$

where

$$A = \sum_{j}^{n} \exp\left(-\frac{U_j}{kT}\right). \tag{3.167}$$

We can make the association between the discrete case and the continuous case precise if we determine U_j by requiring

$$\exp\left(-\frac{U_j}{kT}\right) = \int_{x_{j-1}}^{x_j} \exp\left(-\frac{U(x)}{kT}\right) dx, \tag{3.168}$$

where x_j separates the $j-1^{st}$ from the jth potential well. Furthermore, if there are only two energy wells, the ratio of the probability of finding the particle in state one to the probability of finding the particle in state two is

$$K_{\text{eq}} = \frac{p_1}{p_2} = \exp\left(\frac{\Delta U}{kT}\right) = \exp\left(\frac{\Delta G^0}{RT}\right), \tag{3.169}$$

where $\Delta U = U_2 - U_1$ is the change in energy per molecule, so that ΔG^0 is the change in energy per mole. Here we have recovered (3.149) for the equilibrium distribution of a reaction in terms of the difference of standard free energy. However, one should note that with this identification, U_j is approximately, but not exactly, the value of U at the bottom of the jth potential well.

3.7.3 Reaction rates and Kramers' result

As noted in Chapter 1, equilibrium relationships give information only about the ratio of rate constants, not their individual values. To derive an expression for a rate constant, one must construct a model for how the reaction occurs. The consequent expression for the rate constant is only as good as the assumptions underlying the model.

One common model of a reaction rate is based on the mean first exit time of the time-dependent Fokker-Planck equation (3.163). (Mean first exit times are discussed in Chapter 2, Section 2.9.6). This model assumes that a reactant particle can be modelled as a damped oscillator driven by a stochastic force, and that the reaction occurs once the particle reaches the peak of the energy profile between the reactant and product states. Although this model is based on a number of crude assumptions, it gives reasonably good results for a range of potential energy profiles, particularly those for which the energy wells are deep.

The mean first exit time is found from the solution of the ordinary differential equation

$$-U'(x)\frac{d\tau}{dx} + kT\frac{d^2\tau}{dx^2} = -\nu, \tag{3.170}$$

subject to $\tau(x_0) = 0$ at any boundary point x_0 where escape is allowed, or $\tau'(x_1) = 0$ at any boundary point where escape is not allowed, but instead there is reflection. The off-rate, or unbinding rate, is defined as the inverse of the mean first exit time from the bottom of the potential well.

To be specific, consider a potential $U(x)$ such as shown in Fig. 3.17A. Here $U(x)$ is a cubic polynomial, with a minimum at $x = 0$ and a maximum at $x = 1$, with
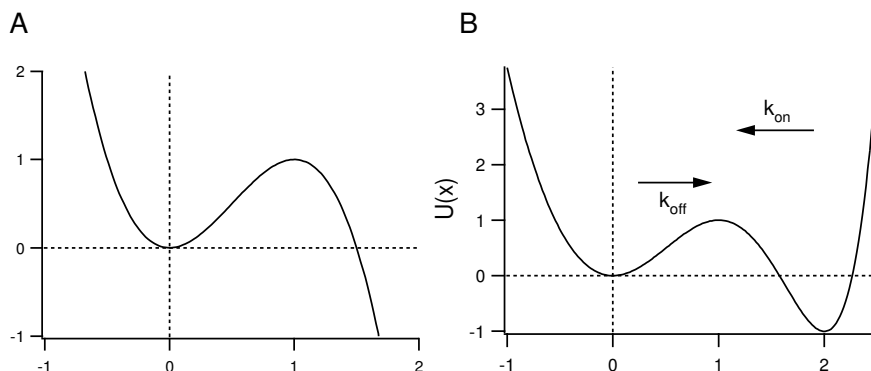
Figure 3.17: Potential energy profiles. A: a cubic profile, $U(x) = \Delta G(2x^2(3/2 - x))$, plotted for $\Delta G = 1$. B: a double well potential, $U(x) = \Delta G^0(\frac{19}{144}x^6 - \frac{1}{24}x^5 - \frac{77}{144}x^4 - \frac{4}{3}x^3 + \frac{25}{9}x^2)$, plotted for $\Delta G^0 = 1$.

$U(1) = \Delta G$. We expect the particle to spend most of its time near $x = 0$. However, if the particle gets to $x = 1$ it can escape to $x = \infty$, and is assumed to have reacted. Thus, the time to react (the inverse of the reaction rate) is approximated by the mean first passage time from $x = 0$ to $x = 1$.

More generally, suppose $U(x) = \Delta G u(\frac{x}{L})$ where $u'(0) = u'(1) = u(0) = 0$ and $u(1) = 1$, so that $x = 0$ is a local minimum and $x = L$ is a local maximum, and the height of the energy barrier is ΔG. The mean first passage time is the solution of (3.170) together with the boundary conditions $\tau(-\infty) = 0$ and $\tau(1) = 0$.

To find the solution it is useful to nondimensionalize (3.170). We set $y = \frac{x}{L}$ and $\sigma = \alpha\tau$ and find

$$-au'(y)\frac{d\sigma}{dy} + \frac{d^2\sigma}{dy^2} = -1, \tag{3.171}$$

where $a = \frac{\Delta G}{kT}$, and $\alpha = \frac{\nu L^2}{kT}$. Now, using an integrating factor, it is easily shown that

$$\sigma(y) = \int_x^1 e^{au(s')} \left(\int_{-\infty}^{s'} e^{-au(s)}\, ds \right) ds', \tag{3.172}$$

and thus the time to react is $\tau(0) = \frac{\nu L^2}{kT}\sigma(0)$, where

$$\sigma(0) = \int_0^1 e^{au(s')} \left(\int_{-\infty}^{s'} e^{-au(s)}\, ds \right) ds'. \tag{3.173}$$

As we demonstrate below, this formula does not agree with the Arrhenius rate law for all parameter values. However, when the potential well at $x = 0$ is deep (i.e., when $a = \Delta G/(kT) \gg 1$), the two are in agreement. Here we provide a demonstration of this agreement.

Notice first that

$$\sigma(0) = \int_0^1 e^{au(s')} \left(\int_{-\infty}^1 e^{-au(s)} \, ds - \int_{s'}^1 e^{-au(s)} \, ds \right) ds'. \tag{3.174}$$

Clearly,

$$\int_0^1 e^{au(s')} \left(\int_{s'}^1 e^{-au(s)} \, ds \right) ds' = \int_0^1 \left(\int_{s'}^1 e^{a(u(s')-u(s))} \, ds \right) ds'$$

$$< \int_0^1 \left(\int_{s'}^1 ds \right) ds' = \frac{1}{2}. \tag{3.175}$$

In fact, with a bit of work one can show that this integral approaches zero as $a \to \infty$. Thus,

$$\sigma(0) \approx \left(\int_0^1 e^{au(s')} \, ds' \right) \left(\int_{-\infty}^1 e^{-au(s)} \, ds \right). \tag{3.176}$$

We now use the fact that $y = 0$ and $y = 1$ are extremal values of $u(y)$ to approximate these integrals. When a is large, the integrands are well approximated by Gaussians, which decay to zero rapidly. Thus, near $y = 0$, $u(y) \approx \frac{1}{2}u''(0)y^2$ so that

$$\int_{-\infty}^1 e^{-au(s)} \, ds \approx \int_{-\infty}^1 e^{-\frac{1}{2}au''(0)s^2} \, ds$$

$$\approx \int_{-\infty}^\infty e^{-\frac{1}{2}au''(0)s^2} \, ds$$

$$= \sqrt{\frac{2\pi}{au''(0)}} \tag{3.177}$$

Similarly, near $y = 1$, $u(y) \approx 1 - \frac{1}{2}|u''(1)|(y-1)^2$, so that

$$\int_0^1 e^{au(s)} \, ds \approx e^a \int_0^1 e^{-\frac{1}{2}|u''(1)|(s-1)^2} \, ds$$

$$\approx e^a \int_{-\infty}^0 e^{-\frac{1}{2}|u''(1)|s^2} \, ds$$

$$= \frac{1}{2} e^a \sqrt{\frac{2\pi}{a|u''(1)|}}. \tag{3.178}$$

Combining (3.176), (3.177) and (3.178) gives

$$\tau(0) \approx \frac{\pi\nu L^2}{\Delta G \sqrt{u''(0)|u''(1)|}} e^{\frac{\Delta G}{kT}}. \tag{3.179}$$

Since the reaction rate is the inverse of the mean first passage time, this gives the Arrhenius rate expression with

$$\kappa = \frac{\Delta G \sqrt{u''(0)|u''(1)|}}{\pi\nu L^2}, \tag{3.180}$$

which is independent of T, but not ΔG. This formula was first derived by Kramers (1940).
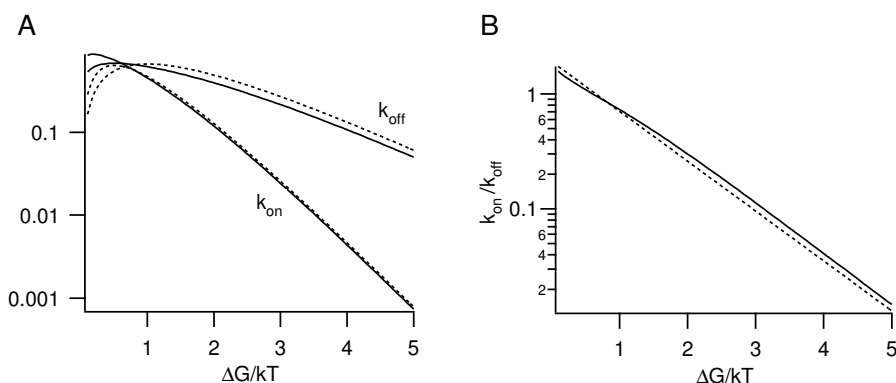
Figure 3.18: Reaction rates for the potential profile shown in Fig. 3.17B. A: exact (solid lines) and approximate (dashed lines) solutions for k_1 and k_{-1}, plotted as functions of $\Delta G^0/kT$. The exact solutions are calculated from (3.173), while the approximations are calculated from (3.179). For simplicity, we set $\nu L^2/kT = 1$. B: exact and approximate calculations of k_{-1}/k_1. As in A, the exact solution is plotted as a solid line.

A double well potential profile

Now suppose that $U(x)$ is a double well potential, such as that shown in Fig. 3.17B. In particular, suppose that $U(x) = \Delta G^0 u(\frac{x}{L})$, where $u(x)$ has two local minima at $x = 0$ and $x = b > 1$, with a local maximum at $x = 1$. For the example in Fig. 3.17B, $\Delta G^0 = L = 1$ and $b = 2$. Note also that the potential profile is such that $\Delta G_{-1} = 2\Delta G^0$, $\Delta G_1 = \Delta G^0$.

According to Kramers' rate theory,

$$k_1 = \frac{\Delta G_1 \sqrt{u''(0)|u''(1)|}}{\pi \nu L^2} e^{-\frac{\Delta G_1}{kT}}, \tag{3.181}$$

$$k_{-1} = \frac{\Delta G_{-1} \sqrt{u''(b)|u''(1)|}}{\pi \nu L^2 (b-1)^2} e^{-\frac{\Delta G_{-1}}{kT}}, \tag{3.182}$$

To compare these with the exact solutions, in Fig. 3.18 we plot k_{-1} and k_1 for the double well potential shown Fig. 3.17B, calculated by numerical integration of (3.173), and using the approximation (3.181) and (3.182). Note that the reaction rates (both exact and approximate) are not exactly exponential functions of ΔG_i, and thus the curves in Fig. 3.18A are not straight lines (on a log scale). For the approximate rate constants this is because the prefactor is proportional to ΔG_i. Interestingly, the approximate solutions agree exactly with the Arrhenius rate law, when viewed as functions of T, while the exact solutions do not.

Next, we observe that using Kramers' formula, the equilibrium constant is

$$K_{eq} = \frac{k_{-1}}{k_1} = \frac{1}{(b-1)^2} \frac{u(1) - u(b)}{u(1) - u(0)} \sqrt{\frac{u''(b)}{u''(0)}} e^{-\frac{\Delta G^0}{kT}}. \tag{3.183}$$

In Fig. 3.18 we plot $\frac{k_{-1}}{k_1}$ for the double well potential shown in Fig. 3.17B, with the exact ratio shown as a solid curve and the approximate ratio from (3.183) shown as a dashed curve. As before, the exact ratio k_{-1}/k_1 (solid line, Fig. 3.17B) is not an exact exponential function of ΔG^0, and thus does not give the correct equilibrium behavior. This results from the fact that, for small ΔG^0, the mean first exit time of the Fokker-Planck equation is not a good model for the reaction rate.

However, the ratio of the approximate expressions for the rate constants (3.183) is a true exponential function of ΔG^0, as the dependence of ΔG^0 in the prefactors cancels out in the ratio. Hence, the dashed line in Fig. 3.18B is straight. Thus, paradoxically, the approximate solution gives better agreement to the correct equilibrium behavior than does the exact solution. However, one must be somewhat cautious with this statement, since there is a factor multiplying the exponential that is not equal to one (as it should be for correct equilibrium behavior), but depends on the details of the shape of the energy function. Thus, if the shape of the potential energy function is modified by, for example, an external voltage potential, this factor is modified as well, in a voltage dependent way.

Exercises

1. Show that the GHK equation (3.2) satisfies both the independence principle and the Ussing flux ratio, but that the linear I–V curve (3.1) satisfies neither.

2. Using concentrations typical of Na^+, determine whether the long channel limit or the short channel limit for (3.25) is the most appropriate approximation for Na^+ channels. (Estimate λ where $\lambda^2 = L^2 q F N_a \tilde{c}/(\epsilon R T)$, for Na^+ ions.)

3. In Section 3.3.1 the PNP equations were used to derive I–V curves when two ions with opposite valence are allowed to move through a channel. Extend this analysis by assuming that two types of ions with positive valence and one type of ion with negative valence are allowed to move through the channel. Show that in the high concentration limit, although the negative ion obeys a linear I–V curve, the two positive ions do not. Details can be found in Chen, Barcilon, and Eisenberg (1992), equations (43)–(45).

4. (a) Show that (3.62) satisfies the independence principle and the Ussing flux ratio.

   (b) Show that (3.62) can be made approximately linear by choosing g such that

$$ng = \ln\left(\frac{c_n}{c_0}\right). \qquad (3.184)$$

   Although a linear I–V curve does not satisfy the independence principle, why does this result not contradict part (a)?

5. Show that (3.84) does not satisfy the independence principle, but does obey the Ussing flux ratio.

6. Derive (3.84) by solving the steady-state equations (3.80) and (3.81). First show that

$$J = x \cdot \frac{k_0 c_0 - k_{-n} c_n \pi_{n-1}}{\phi_{n-1}}. \qquad (3.185)$$

Then show that

$$k_0 c_0 x = k_{n-1} c_{n-1} \phi_{n-1} - x k_{-n} c_n \phi_{n-2}, \qquad (3.186)$$

$$k_j c_j = \frac{k_{n-1} c_{n-1}}{\pi_j} \cdot (\phi_{n-1} - \phi_{j-1}) - \frac{k_{-n} c_n x}{\pi_j} \cdot (\phi_{n-2} - \phi_{j-1}) \qquad (3.187)$$

for $j = 1, \ldots, n-1$. Substitute these expressions into the conservation equation and solve for x.

7. Draw the state diagrams showing the channel states and the allowed transitions for a multi-ion model with two binding sites when the membrane is bathed with a solution containing:

   (a) Only ion S on the left and only ion S' on the right.

   (b) Ion S on both sides and ion S' only on the right.

   (c) Ions S and S' on both the left and right.

   In each case write the corresponding system of linear equations that determine the steady-state ionic concentrations at the channel binding sites.

8. By using an arbitrary symmetric energy profile with two binding sites, show numerically that the Ussing flux ratio is not obeyed by a multi-ion model with two binding sites. (Note that since unidirectional fluxes must be calculated, it is necessary to treat the ions on each side of the membrane differently. Thus, an 8-state channel diagram must be used.) Hodgkin and predicted that the flux ratio is the Ussing ratio raised to the $(n+1)$st power (cf. (3.16)). How does n depend on the ionic concentrations on either side of the membrane, and on the energy profile?

9. Choose an arbitrary symmetric energy profile with two binding sites, and compare the I–V curves of the one-ion and multi-ion models. Assume that the same ionic species is present on both sides of the membrane, so that only a 4-state multi-ion model is needed.

10. Suppose the Na^+ Nernst potential of a cell is 56 mV, its resting potential is -70 mV, and the extracellular Ca^{2+} concentration is 1 mM. At what intracellular Ca^{2+} concentration is the flux of a three-for-one Na^+–Ca^{2+} exchanger zero? (Use that $RT/F = 25.8$ mV at $27°C$.)

11. Modify the pump–leak model of Chapter 2 to include a Ca^{2+} current and the 3-for-1 Na^+–calcium exchanger. What effect does this modification have on the relationship between pump rate and membrane potential?

12. Because there is a net current, the Na^+–K^+ pump current must be voltage dependent. Determine this dependence by including voltage dependence in the rates of conformational change in expression (2.99). How does voltage dependence affect the pump–leak model of Chapter 2?

13. Intestinal epithelial cells have a glucose–Na^+ symport that transports one Na^+ ion and one glucose molecule from the intestine into the cell. Model this transport process. Is the transport of glucose aided or hindered by the cell's negative membrane potential?

14. Suppose that a channel consists of k identical, independent subunits, each of which can be open or closed, and that a current can pass through the channel only if all units are open.

    (a) Let S_j denote the state in which j subunits are open. Show that the conversions between states are governed by the reaction scheme

    $$S_0 \underset{\beta}{\overset{k\alpha}{\rightleftarrows}} S_1 \ldots S_{k-1} \underset{k\beta}{\overset{\alpha}{\rightleftarrows}} S_k. \qquad (3.188)$$

    (b) Derive the differential equation for x_j, the proportion of channels in state j.

    (c) By direct substitution, show that $x_j = \binom{k}{j} n^j (1-n)^{k-j}$, where $\binom{k}{j} = \frac{k!}{j!(k-j)!}$ is the *binomial coefficient*, is an invariant manifold for the system of differential equations, provided that

    $$\frac{dn}{dt} = \alpha(1-n) - \beta n. \qquad (3.189)$$

15. Consider the model of the Na^+ channel shown in Fig. 3.11. Show that if α and β are large compared to γ and δ, then x_{21} is given (approximately) by

    $$x_{21} = \left(\frac{\alpha}{\alpha+\beta}\right)^2 h, \qquad (3.190)$$

    $$\frac{dh}{dt} = \gamma(1-h) - \delta h, \qquad (3.191)$$

    while conversely, if γ and δ are large compared to α and β, then (approximately)

    $$x_{21} = m^2 \left(\frac{\gamma}{\gamma+\delta}\right), \qquad (3.192)$$

    $$\frac{dm}{dt} = \alpha(1-m) - \beta m. \qquad (3.193)$$

16. Show that (3.120) has two negative real roots. Show that when $\beta = 0$ and $a \leq \frac{-\lambda_1}{\lambda_1-\lambda_2}$, then (3.121)–(3.123) have two possible solutions, one with $\alpha+\delta = -\lambda_1$, $\gamma = -\lambda_2$, the other with $\alpha + \delta = -\lambda_2$, $\gamma = -\lambda_1$. In the first solution inactivation is faster than activation, while the reverse is true for the second solution.
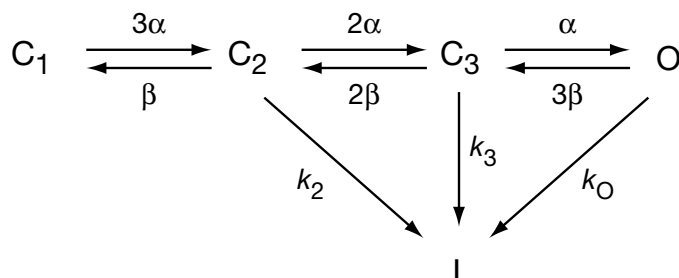
Figure 3.19: The Na$^+$ channel model of Exercise 18. Parameter values are $k_2 = 0.24$ ms^{-1}, $k_3 = 0.4$ ms^{-1}, $k_O = 1.5$ ms^{-1}, $\alpha = 1$ ms^{-1} and $\beta = 0.4$ ms^{-1}.

17. Write a computer program to simulate the behavior of the stochastic three-state Na$^+$ channel shown in Fig. 3.12, assuming it starts in the closed state. Use $\alpha = 1/$ms, $\beta = 0.4/$ms, $\gamma = 1.6/$ms and $\delta = 1/$ms. Take the ensemble average of many runs to reproduce its macroscopic behavior. Using the data from simulations, reconstruct the open-time distribution, the latency distribution, and the distribution of N, the number of times the channel opens. From these distributions estimate the rate constants of the simulation and compare with the known values.

18. Consider the Markov model of a Na$^+$ channel (Patlak, 1991) shown in Fig. 3.19. Write a computer program to simulate the behavior of this stochastic channel assuming it starts in state C$_1$. Take the ensemble average of many runs to reproduce its macroscopic behavior. Using the data generated by these simulations, determine the open-time distribution, the latency distribution, and the distribution of N, the number of times the channel opens. Compare these with the analytically calculated distributions.

19. Construct a set of differential equations that models the interaction of a two-state channel with a use-dependent blocker.

20. Write a computer program to simulate the behavior of the stochastic three-state agonist-binding channel of (3.125) Use $\alpha = 1/$ms, $\beta = 0.4/$ms, $k_{-1} = 0.5/$ms and $ak_1 = 0.2/$ms. Using the data from simulations, plot the open-time distribution and the closed time distribution and estimate the parameters of the model. Is the closed time distribution obviously a double exponential distribution? Repeat this experiment for several different values of ak_1.

21. Show that for an exponential distribution $\phi(t) = \alpha \exp(-\alpha t)$ the plot of the corresponding distribution function on the $\ln(t)$ scale has a maximum at the expected value of the distribution, $t = -\frac{1}{a}$.

22. Find the distribution for the length of a burst in the model of (3.125).

    Hint: the apparent length of the burst is the time taken to get from AR to T, minus the length of one sojourn in AT. Use the Laplace transform and the convolution theorem.

23. Find the mean first exit time from the piecewise linear potential

$$U(x) = \begin{cases} -\frac{\Delta G x}{L}, & -L < x < 0, \\ \frac{\Delta G x}{L}, & 0 < x < L, \end{cases} \tag{3.194}$$

with a reflecting boundary at $x = -L$ and absorbing boundary at $x = L$.

24. Find the most likely event for the binomial distribution

$$P(h) = \frac{n!}{h!(n-h)!} p^h (1-p)^{(n-h)} \tag{3.195}$$

when n is large. Show that the probability of this event approaches 1 in the limit $n \to \infty$.

Chapter 4

Passive Electrical Flow in Neurons

Neurons are among the most important and interesting cells in the body. They are the fundamental building blocks of the central nervous system and hence responsible for motor control, cognition, perception, and memory, among other things. Although our understanding of how networks of neurons interact to form an intelligent system is extremely limited, one prerequisite for an understanding of the nervous system is an understanding of how individual nerve cells behave.

A typical neuron consists of three principal parts: the *dendrites*; the cell body, or *soma*; and the *axon*. The structure of some typical neurons is shown in Fig. 4.1. Dendrites are the input stage of a neuron and receive synaptic input from other neurons. The soma contains the necessary cellular machinery such as a nucleus and mitochondria, and the axon is the output stage. At the end of the axon (which may also be branched, as are the dendrites) are synapses, which are cellular junctions specialized for the transmission of an electrical signal (Chapter 7). Thus, a single neuron may receive input along its dendrites from a large number of other neurons, which is called *convergence*, and may similarly transmit a signal along its axon to many other neurons, called *divergence*.

The behaviors of the dendrites, axon, and synapses are all quite different. The spread of electrical current in a dendritic network is (mostly) a passive process that can be well described by the diffusion of electricity along a leaky cable. The axon, on the other hand, has an excitable membrane of the type described in Chapter 5, and thus can propagate an electrical signal actively. At the synapse (Chapter 8), the membrane is specialized for the release or reception of chemical neurotransmitters. In this chapter we discuss how to model the behavior of a cable, and then focus on the passive spread of current in a dendritic network; in the following chapter we show how an excitable membrane can actively propagate an electrical impulse, or action potential.

Although we discuss neurons in a number of chapters throughout this book, we cover them only in relatively little depth. For more comprehensive treatments of neurons and theoretical neuroscience the reader is referred to the excellent books
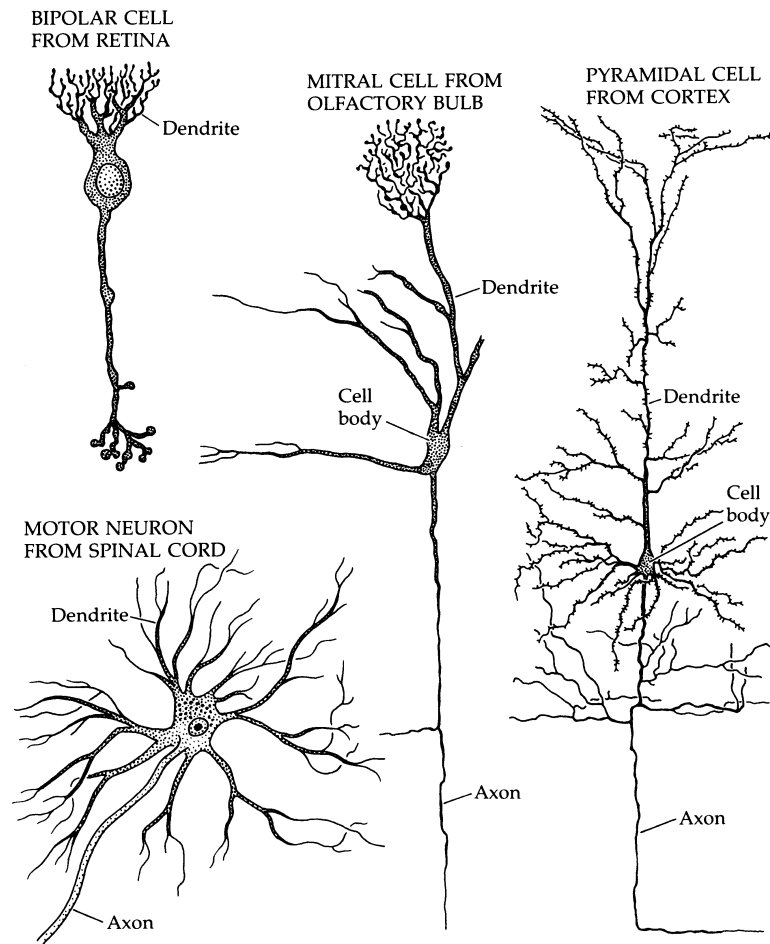
Figure 4.1: Structure of typical neurons. The motor neuron is from a mammalian spinal cord and was drawn by Dieters in 1869. The other cells were drawn by Ramón y Cajal. The pyramidal cell is from mouse cortex, and the mitral cell from the olfactory bulb of a cat. (Kuffler et al., 1984, Fig. 1, p. 10.)
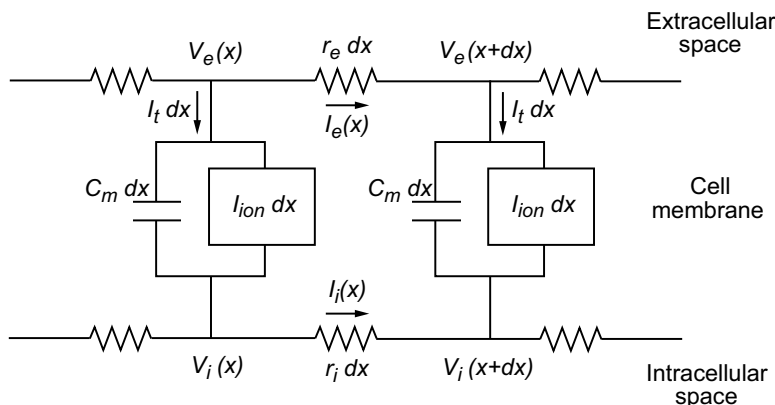
Figure 4.2: Schematic diagram of a discretized cable, with isopotential circuit elements of length dx.

by Koch and Segev (1998), Koch (1999), Dayan and Abbott (2001) and de Schutter (2000).

4.1 The Cable Equation

One of the first things to realize from the pictures in Fig. 4.1 is that it is unlikely that the membrane potential is the same at each point. In some cases spatial uniformity can be achieved experimentally (for instance, by threading a silver wire along the axon, as did Hodgkin and Huxley), but *in vivo*, the intricate branched structure of the neuron can create spatial gradients in the membrane potential. Although this seems clear to us now, it was not until the pioneering work of Wilfrid Rall in the 1950s and 1960s that the importance of spatial effects gained widespread acceptance.

To understand something of how spatial distribution affects the behavior of a cable, we derive the *cable equation*. The theory of the flow of electricity in a leaky cable dates back to the work of Lord Kelvin in 1855, who derived the equations to study the transatlantic telegraph cable then under construction. However, the application of the cable equation to neuronal behavior is mainly due to Hodgkin and Rushton (1946), and then a series of classic papers by Rall (1957, 1959, 1960, 1969; an excellent summary of much of Rall's work on electrical flow in neurons is given in Segev et al., 1995.)

We view the cell as a long cylindrical piece of membrane surrounding an interior of cytoplasm (called a cable). We suppose that everywhere along its length, the potential depends only on the length variable and not on radial or angular variables, so that the cable can be viewed as one-dimensional. This assumption is called the *core conductor assumption* (Rall, 1977). We now divide the cable into a number of short pieces of isopotential membrane each of length dx. In any cable section, all currents must balance, and there are only two types of current, namely, transmembrane current and axial current (Fig. 4.2). The axial current has intracellular

and extracellular components, both of which ared assume to be ohmic, i.e., linear functions of the voltage. Hence,

$$V_i(x + dx) - V_i(x) \;=\; -I_i(x)r_i dx, \tag{4.1}$$
$$V_e(x + dx) - V_e(x) \;=\; -I_e(x)r_e dx, \tag{4.2}$$

where I_i and I_e are the intracellular and extracellular axial currents respectively. The minus sign on the right-hand side appears because of the convention that positive current is a flow of positive charges from left to right (i.e., in the direction of increasing x). If $V_i(x + dx) > V_i(x)$, then positive charges flow in the direction of decreasing x, giving a negative current. In the limit $dx \to 0$,

$$I_i \;=\; -\frac{1}{r_i}\frac{\partial V_i}{\partial x}, \tag{4.3}$$

$$I_e \;=\; -\frac{1}{r_e}\frac{\partial V_e}{\partial x}. \tag{4.4}$$

The numbers r_i and r_e are the resistances per unit length of the intracellular and extracellular media, respectively. In general,

$$r_i = \frac{R_c}{A_i}, \tag{4.5}$$

where R_c is the *cytoplasmic resistivity*, measured in units of Ohms-length, and A_i is the cross-sectional area of the cylindrical cable. A similar expression holds for the extracellular space, so if the cable is in a bath with large (effectively infinite) cross-sectional area, the extracellular resistance r_e is nearly zero.

Next, from Kirchhoff's laws, any change in extracellular or intracellular axial current must be due to a transmembrane current, and thus

$$I_i(x) - I_i(x + dx) = I_t dx = I_e(x + dx) - I_e(x), \tag{4.6}$$

where I_t is the total transmembrane current (positive outward) per unit length of membrane. In the limit as $dx \to 0$, this becomes

$$I_t = -\frac{\partial I_i}{\partial x} = \frac{\partial I_e}{\partial x}. \tag{4.7}$$

In a cable with no additional current sources, the total axial current is $I_T = I_i + I_e$, so using that $V = V_i - V_e$, we find

$$-I_T = \frac{r_i + r_e}{r_i r_e}\frac{\partial V_i}{\partial x} - \frac{1}{r_e}\frac{\partial V}{\partial x}, \tag{4.8}$$

from which it follows that

$$\frac{1}{r_i}\frac{\partial V_i}{\partial x} = \frac{1}{r_i + r_e}\frac{\partial V}{\partial x} - \frac{r_e}{r_i + r_e}I_T. \tag{4.9}$$

On substituting (4.9) into (4.7), we obtain

$$I_t = \frac{\partial}{\partial x}\left(\frac{1}{r_i + r_e}\frac{\partial V}{\partial x}\right), \tag{4.10}$$

where we have used (4.3) and the fact that I_T is constant. Finally, recall that the transmembrane current I_t is a sum of the capacitive and ionic currents, and thus

$$I_t = p\left(C_m \frac{\partial V}{\partial t} + I_{\text{ion}}\right) = \frac{\partial}{\partial x}\left(\frac{1}{r_i + r_e} \frac{\partial V}{\partial x}\right), \tag{4.11}$$

where p is the perimeter of the axon. Equation (4.11) is usually referred to as the cable equation. Note that C_m has units of capacitance per unit area of membrane, and I_{ion} has units of current per unit area of membrane. If a current I_{applied}, with units of current per unit area, is applied across the membrane (as before, taken positive in the outward direction), then the cable equation becomes

$$I_t = p\left(C_m \frac{\partial V}{\partial t} + I_{\text{ion}} + I_{\text{applied}}\right) = \frac{\partial}{\partial x}\left(\frac{1}{r_i + r_e} \frac{\partial V}{\partial x}\right). \tag{4.12}$$

It is useful to nondimensionalize the cable equation. To do so we define the *membrane resistivity* R_m as the resistance of a unit square area of membrane, having units of $\Omega\,\text{cm}^2$. For any fixed V_0, R_m is determined by measuring the change in membrane current when V is perturbed slightly from V_0. In mathematical terms,

$$\frac{1}{R_m} = \left.\frac{dI_{\text{ion}}}{dV}\right|_{V=V_0}. \tag{4.13}$$

Although the value of R_m depends on the chosen value of V_0, it is typical to take V_0 to be the resting membrane potential to define R_m. Note that if the membrane is an ohmic resistor, then $I_{\text{ion}} = V/R_m$, in which case R_m is independent of V_0.

Assuming that r_i and r_e are constant, the cable equation (4.11) can now be written in the form

$$\tau_m \frac{\partial V}{\partial t} + R_m I_{\text{ion}} = \lambda_m^2 \frac{\partial^2 V}{\partial x^2}, \tag{4.14}$$

where

$$\lambda_m = \sqrt{\frac{R_m}{p(r_i + r_e)}} \tag{4.15}$$

has units of distance and is called the cable *space constant*, and where

$$\tau_m = R_m C_m \tag{4.16}$$

has units of time and is called the membrane *time constant*. If we ignore the extracellular resistance, then

$$\lambda_m = \sqrt{\frac{R_m d}{4R_c}}, \tag{4.17}$$

where d is the diameter of the axon (assuming circular cross-section). Finally, we rescale the ionic current by defining $I_{\text{ion}} = -f(V,t)/R_m$ for some f, which, in general, is a function of both voltage and time and has units of voltage, and nondimensionalize space and time by defining new variables $X = x/\lambda_m$ and $T = t/\tau_m$. In the new variables the cable equation is

$$\frac{\partial V}{\partial T} = \frac{\partial^2 V}{\partial X^2} + f(V,T). \tag{4.18}$$

parameter	d	R_c	R_m	C_m	τ_m	λ_m
units	$10^{-4}\,\mathrm{cm}$	$\Omega\,\mathrm{cm}$	$10^3\,\Omega\,\mathrm{cm}^2$	$\mu\mathrm{F}/\mathrm{cm}^2$	ms	cm
squid giant axon	500	30	1	1	1	0.65
lobster giant axon	75	60	2	1	2	0.25
crab giant axon	30	90	7	1	7	0.24
earthworm giant axon	105	200	12	0.3	3.6	0.4
marine worm giant axon	560	57	1.2	0.75	0.9	0.54
mammalian cardiac cell	20	150	7	1.2	8.4	0.15
barnacle muscle fiber	400	30	0.23	20	4.6	0.28

Table 4.1: Typical parameter values for a variety of excitable cells.

Although f is written as a function of voltage and time, in many of the simpler versions of the cable equation, f is a function of V only (for example, (4.19) below). Typical parameter values for a variety of cells are shown in Table 4.1.

4.2   Dendritic Conduction

To complete the description of a spatially distributed cable, we must specify how the ionic current depends on voltage and time. In the squid giant axon, $f(V,t)$ is a function of m, n, h, and V as described in Chapter 5. This choice for f allows waves that propagate along the axon at constant speed and with a fixed profile. They require the input of energy from the axon, which must expend energy to maintain the necessary ionic concentrations, and thus they are often called *active waves*.

Any electrical activity for which the approximation $f = -V$ is valid (i.e., if the membrane is an Ohmic resistor) is said to be *passive* activity. There are some cables, primarily in neuronal dendritic networks, for which this is a good approximation in the range of normal activity. For other cells, activity is passive only if the membrane potential is sufficiently small. For simplicity in a passive cable, we shift V so that the resting potential is at $V = 0$. Thus,

$$\frac{\partial V}{\partial T} = \frac{\partial^2 V}{\partial X^2} - V, \tag{4.19}$$

which is called the *linear cable equation*. In the linear cable equation, current flows along the cable in a passive manner, leaking to the outside at a linear rate.

There is a vast literature on the application of the linear cable equation to dendritic networks. In particular, the books by Jack et al. (1975) and Tuckwell (1988) are largely devoted to this problem, and provide detailed discussions of the theory. Koch and Segev (1998) and Koch (1999) also provide excellent introductions.

4.2.1 Boundary Conditions

To determine the behavior of a single dendrite, we must first specify initial and boundary conditions. Usually, it is assumed that at time $T = 0$, the dendritic cable is in its resting state, $V = 0$, and so

$$V(X, 0) = 0. \tag{4.20}$$

Boundary conditions can be specified in a number of ways. Suppose that $X = X_b$ is a boundary point.

1. Voltage-clamp boundary conditions: If the voltage is fixed (i.e., clamped) at $X = X_b$, then the boundary condition is of Dirichlet type,

$$V(X_b, T) = V_b, \tag{4.21}$$

   where V_b is the specified voltage level.

2. Short circuit: If the ends of the cable are short-circuited, so that the extracellular and intracellular potentials are the same at $X = X_b$, then

$$V(X_b, T) = 0. \tag{4.22}$$

   This is a special case of the voltage clamp condition in which $V_b = 0$.

3. Current injection: Suppose a current $I(T)$ is injected at one end of the cable. Since

$$I_i = -\frac{1}{r_i} \frac{\partial V_i}{\partial x} = -\frac{1}{r_i \lambda_m} \frac{\partial V_i}{\partial X}, \tag{4.23}$$

   the boundary condition (ignoring extracellular resistance, so that the extracellular potential is uniform) is

$$\frac{\partial V(X_b, T)}{\partial X} = -r_i \lambda_m I(T). \tag{4.24}$$

   If X_b is at the left end, this corresponds to an inward current, while if it is on the right end, this is an outward current, if $I(T)$ is positive.

4. Sealed ends: If the end at $X = X_b$ is sealed to ensure that there is no current across the endpoint, then the boundary condition is the homogeneous Neumann condition,

$$\frac{\partial V(X_b, T)}{\partial X} = 0, \tag{4.25}$$

   a special case of an injected current for which $I(T) = 0$.

4.2.2 Input Resistance

One of the most important simple solutions of the cable equation corresponds to the situation in which a steady current is injected at one end of a semi-infinite cable. This is a common experimental protocol (although never with a truly semi-infinite

cable) that can be used to determine the cable parameters R_m and R_c. Suppose the cable extends from $X = 0$ to $X = \infty$ and that a steady current I_0 is injected at $X = 0$. Then, the boundary condition at $X = 0$ is

$$\frac{dV(0)}{dX} = -r_i \lambda_m I_0. \tag{4.26}$$

Setting $\partial V / \partial T = 0$ and solving (4.19) subject to the boundary condition (4.19) gives

$$V(X) = \lambda_m r_i I_0 e^{-X} = V(0)e^{-X} = V(0)e^{-x/\lambda_m}. \tag{4.27}$$

Clearly, by measuring the rate at which the voltage decays along the cable, λ_m can be determined from experimental data. The *input resistance* R_{in} of the cable is defined to be the ratio $V(0)/I_0 = \lambda_m r_i$. Recall that when the extracellular resistance is ignored,

$$\lambda_m = \sqrt{\frac{R_m d}{4R_c}}. \tag{4.28}$$

Combining this with (4.5) gives

$$R_{\text{in}} = \lambda_m r_i = \sqrt{\frac{4R_m R_c}{\pi^2}} \frac{1}{d^{\frac{3}{2}}}. \tag{4.29}$$

Hence, the input resistance of the cable varies with the $-3/2$ power of the cable diameter, a fact that is of importance for the behavior of the cable equation in a branching structure. Since both the input resistance and the space constant of the cable can be measured experimentally, R_m and R_c can be calculated from experimental data.

Some solutions to the cable equation for various types of cable and boundary conditions are discussed in the exercises. Tuckwell (1988) gives a detailed discussion of the various types of solutions and how they are obtained.

4.2.3   Branching Structures

The property of neurons that is most obvious from Fig. 4.1 is that they are extensively branched. While the procedure to find solutions on a branched cable network is straightforward in concept, it can be quite messy in application. Thus, in what follows, we emphasize the procedure for obtaining the solution on branching structures, without calculating specific formulae.

The steady-state solution

It is useful first to consider the simplest branched cable, depicted in Fig. 4.3. The cable has a single branch point, or *node*, at $X = L_1$, and the two offspring branches extend to L_{21} and L_{22}, respectively. For convenience we express all lengths in nondimensional form, with the reminder that nondimensional length does not correspond to physical length, as the distance variable x along each branch of the cable is scaled by the length constant λ_m appropriate for that branch, and each branch may have a different length constant.
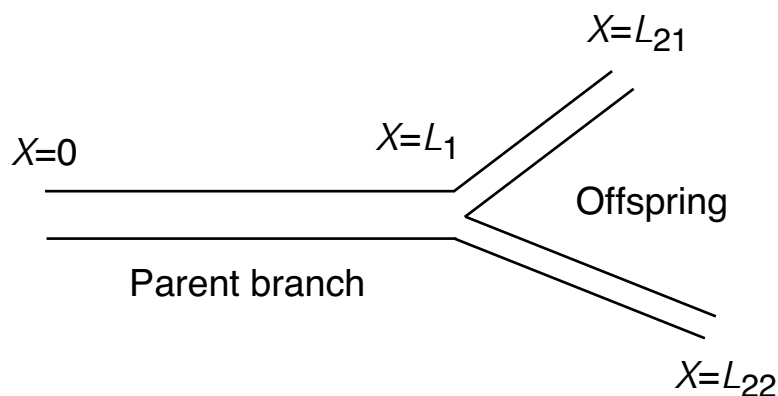
Figure 4.3: Diagram of the simplest possible branched cable.

We construct the solution in three parts: V_1 on cylinder 1, and V_{21} and V_{22} on the two offspring cylinders. At steady state each V satisfies the differential equation $V'' = V$, and so we can immediately write the general solution as

$$
\begin{align}
V_1 &= A_1 e^{-X} + B_1 e^X, \tag{4.30} \\
V_{21} &= A_{21} e^{-X} + B_{21} e^X, \tag{4.31} \\
V_{22} &= A_{22} e^{-X} + B_{22} e^X, \tag{4.32}
\end{align}
$$

where the A's and B's are unknown constants. To determine the 6 unknown constants, we need 6 constraints, which come from the boundary and nodal conditions. For boundary conditions, we assume that a current I_0 is injected at $X = 0$ and that the terminal ends (at $X = L_{21}$ and $X = L_{22}$) are held fixed at $V = 0$. Thus,

$$
\begin{align}
\frac{dV_1(0)}{dX} &= -r_i \lambda_m I_0, \tag{4.33} \\
V_{21}(L_{21}) &= V_{22}(L_{22}) = 0. \tag{4.34}
\end{align}
$$

The remaining three constraints come from conditions at the node. We require that V be a continuous function and that current be conserved at the node. It follows that

$$
V_1(L_1) = V_{21}(L_1) = V_{22}(L_1), \tag{4.35}
$$

and

$$
d_1^{3/2} \sqrt{\frac{\pi^2}{4 R_m R_c}} \frac{dV_1(L_1)}{dX} = d_{21}^{3/2} \sqrt{\frac{\pi^2}{4 R_m R_c}} \frac{dV_{21}(L_1)}{dX} + d_{22}^{3/2} \sqrt{\frac{\pi^2}{4 R_m R_c}} \frac{dV_{22}(L_1)}{dX}. \tag{4.36}
$$

If we make the natural assumption that each branch of the cable has the same physical properties (and thus have the same R_m and R_c), although possibly differing in diameter, the final condition for conservation of current at the node becomes

$$
d_1^{3/2} \frac{dV_1(L_1)}{dX} = d_{21}^{3/2} \frac{dV_{21}(L_1)}{dX} + d_{22}^{3/2} \frac{dV_{22}(L_1)}{dX}. \tag{4.37}
$$

We thus have six linear equations for the six unknown constants; explicit solution of this linear system is left for Exercise 6.

More general branching structures

For this method to work for more general branching networks, there must be enough constraints to solve for the unknown constants. The following argument shows that this is the case. First, we know that each branch of the tree contributes two unknown constants, and thus, if there are N nodes, there are $1 + 2N$ individual cables with a total of $2 + 4N$ unknown constants. Each node contributes three constraints, and there are $2 + N$ terminal ends (including that at $X = 0$), each of which contributes one constraint, thus giving a grand total of $2 + 4N$ constraints. Thus, the resulting linear system is well-posed. Of course, a unique solution is guaranteed only if this system is invertible, which is not known a priori.

Equivalent cylinders

One of the most important results in the theory of dendritic trees is due to Rall (1959), who showed that under certain conditions, the equations for passive electrical flow over a branching structure reduce to a single equation for electrical flow in a single cylinder, the so-called *equivalent cylinder*.

To see this reduction in a simple setting, consider again the branching structure of Fig. 4.3. To reduce this to an equivalent cylinder we need some additional assumptions. We assume, first, that the two offspring branches have the same dimensionless lengths, $L_{21} = L_{22}$, and that their terminals have the same boundary conditions. Since V_{21} and V_{22} obey the same differential equation on the same domain, obey the same boundary conditions at the terminals, and are equal at the node, it follows that they must be equal. That is,

$$\frac{dV_{21}(L_1)}{dX} = \frac{dV_{22}(L_1)}{dX}. \tag{4.38}$$

Substituting (4.38) into (4.37) we then get

$$d_1^{3/2} \frac{dV_1(L_1)}{dX} = (d_{21}^{3/2} + d_{22}^{3/2}) \frac{dV_{21}(L_1)}{dX}. \tag{4.39}$$

Finally (and this is the crucial assumption), if we assume that

$$d_{21}^{3/2} + d_{22}^{3/2} = d_1^{3/2}, \tag{4.40}$$

then

$$\frac{dV_1(L_1)}{dX} = \frac{dV_{21}(L_1)}{dX}. \tag{4.41}$$

Thus V_1 and V_{21} have the same value and derivative at L_1 and obey the same differential equation. It follows that the composite function

$$V = \begin{cases} V_1(X), & 0 \le X \le L_1, \\ V_{21}(X), & L_1 \le X \le L_{21}, \end{cases} \tag{4.42}$$

is continuous with a continuous derivative on $0 < X < L_{21}$ and obeys the cable equation on that same interval. Thus, the simple branching structure is equivalent to a cable of length L_{21} and diameter d_1.

More generally, if the branching structure satisfies the following conditions:

1. R_m and R_c are the same for each branch of the cable;

2. At every node the cable diameters satisfy an equation analogous to (4.40). That is, if d_0 is the diameter of the parent branch, and $d_1, d_2, \ldots$ are the diameters of the offspring, then

$$d_0^{3/2} = d_1^{3/2} + d_2^{3/2} + \cdots;$$ (4.43)

3. The boundary conditions at the terminal ends are all the same;

4. Each terminal is the same dimensionless distance L from the origin of the tree (at $X = 0$);

then the entire tree is equivalent to a cylinder of length L and diameter d_1, where d_1 is the diameter of the cable at $X = 0$.

Using an inductive argument, it is not difficult to show that this is so (although a rigorous proof is complicated by the notation). Working from the terminal ends, one can condense the outermost branches into equivalent cylinders, then work progressively inwards, condensing the equivalent cylinders into other equivalent cylinders, and so on, until only a single cylinder remains. It is left as an exercise (Exercise 7) to show that during this process the requirements for condensing branches into an equivalent cylinder are never violated.

4.2.4 A Dendrite with Synaptic Input

Suppose we have a dendrite with a time dependent synaptic input a some point along the dendrite. Then the potential along the cable satisfies the equation

$$\frac{\partial V}{\partial T} = \frac{\partial^2 V}{\partial X^2} - V + g(T)\delta(X - X_s)(V_e - V),$$ (4.44)

with $V_x = 0$ at both ends of the cable $x = 0, L$ (assuming the ends of the cable are sealed). (For a derivation of the form of the synaptic input, see Chapter 8.)

There are two questions one might ask. First, one might want to know the voltage at the end of the cable with a given input function $g(t)$. However, it is more likely that the voltage at the ends of the cable can be measured so it is the input function $g(t)$ and its location X_s that one would like to determine. This latter is the question we address here.

We suppose that $V(0, t) = V_0(t)$ and $V(L, t) = V_1(t)$ are known. Notice that we can integrate the governing equation with respect to time and find that

$$V_{0xx} - V_0 = 0,$$ (4.45)

provided $X \neq X_s$, where $V_0(x) = \int_{-\infty}^{\infty} V(X,T)dX$, and V_0 must satisfy boundary conditions $V_0(0) = V_0^0$, $V_0(L) = V_0^1$, where $V_0^j = \int_{-\infty}^{\infty} V_j(T)dT$, $j = 0, 1$. It follows that

$$V_0(X) = \begin{cases} V_0^0 \cosh(x), & X < X_s, \\ V_0^1 \cosh(L-x), & X > X_s \end{cases}.$$ (4.46)

Since $V_0(X)$ must be continuous at $X = X_s$, it must be that

$$\frac{V_0^0}{V_0^1} = \frac{\cosh(L-X_s)}{\cosh(X_s)} = F(X_s).$$ (4.47)

The function $F(X_s)$ is a monotone decreasing function of X_s, so there is at most one value of X_s which satisfies (4.47).

Next, notice that integrating (4.44) across $X = X_s$ gives the jump condition

$$V_X|_{X_s^-}^{X_s^+} = g(T)(V(X_s) - V_e),$$ (4.48)

so that $g(T)$ is determined from

$$g(T) = \frac{V_X(X_s^+) - V_X(X_s^-)}{V(X_s) - V_e}.$$ (4.49)

Now, the Fourier transform of V is

$$\hat{V}(x,\omega) = \int_{-\infty}^{\infty} V(X,T)e^{-i\omega T}dT,$$ (4.50)

and the Fourier transformed equation is

$$\hat{V}_{XX} - (1 - i\omega)\hat{V} = 0,$$ (4.51)

for $X \neq X_s$. It follows that

$$\hat{V}(X) = \begin{cases} \hat{V}_0(\omega)\cosh(\mu(\omega)x), & X < X_s, \\ \hat{V}_0(\omega)\cosh(\mu(\omega)(L-x)), & X > X_s \end{cases},$$ (4.52)

where $\mu^2(\omega) = 1 - i\omega$. We now calculate $V(x)$ using the inverse Fourier transform and find

$$V(X_s) = \frac{1}{2\pi}\int_{-\infty}^{\infty} \hat{V}_0(\omega)\cosh(\mu(\omega)X_s)e^{i\omega T}d\omega,$$ (4.53)

$$V_X(X_s^-) = \frac{1}{2\pi}\int_{-\infty}^{\infty} \hat{V}_0(\omega)\mu(\omega)\sinh(\mu(\omega)X_s)e^{i\omega T}d\omega,$$ (4.54)

and

$$V(X_s^+) = \frac{1}{2\pi}\int_{-\infty}^{\infty} \hat{V}_0(\omega)\mu(\omega)\sinh(\mu(\omega)(X_s - L))e^{i\omega T}d\omega.$$ (4.55)

These combined with (4.49), uniquely determine $g(T)$.

This calculation and its extension to multiple synaptic inputs is due to S. Cox: Estimating the Location and Time Course of Synaptic Input From Multi-Site Potential Recordings, J. of Computational Neuroscience, 17(2), pp. 225-243, 2004.
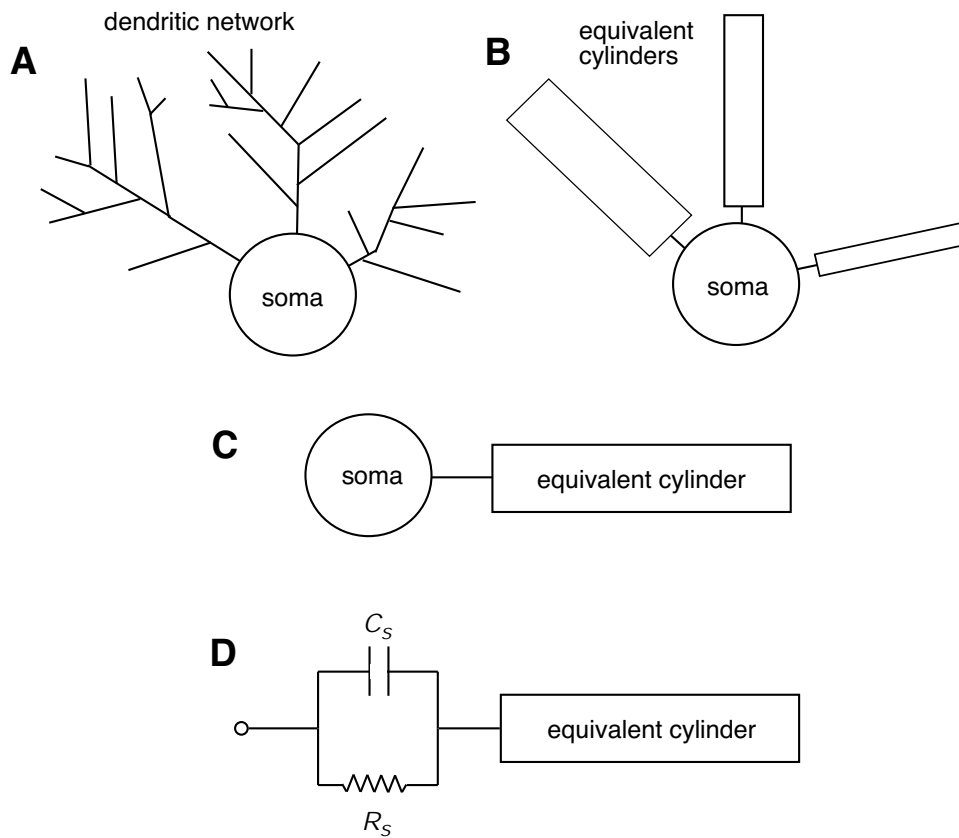
Figure 4.4: Schematic diagram of the Rall lumped-soma model of the neuron. First, it is assumed that the dendritic network pictured in A is equivalent to the equivalent cylinders shown in B, and that these cylinders are themselves equivalent to a single cylinder as in C. The soma is assumed to be isopotential and to behave like a resistance and capacitance in parallel, as in D.

4.3 The Rall Model of a Neuron

When studying a model of a neuron, the item of greatest interest is often the voltage at the cell body, or soma. This is primarily because the voltage at the cell body can be measured experimentally with greater ease than can the voltage in the dendritic network, and further, it is the voltage at the soma that determines whether or not the neuron fires an action potential. Therefore, it is important to determine the solution of the cable equation on a dendritic network when one end of the network is connected to a soma. The most common approach to incorporating a soma into the model is due to Rall (1960), and is called the *Rall lumped-soma model.*

The three basic assumptions of the Rall model are, first, that the soma is isopotential (i.e., that the soma membrane potential is the same at all points), second, that the soma acts like a resistance (R_s) and a capacitance (C_s) in parallel, and,

third, that the dendritic network can be collapsed into a single equivalent cylinder. This is illustrated in Fig. 4.4.

The potential V satisfies the cable equation on the equivalent cylinder. The boundary condition must account for current flow within the soma and into the cable. Thus, if I_0 denotes an applied current at $X = 0$, then the boundary condition is

$$I_0 = -\frac{1}{r_i}\frac{\partial V(0,t)}{\partial x} + C_s\frac{\partial V(0,t)}{\partial t} + \frac{V(0,t)}{R_s}, \tag{4.56}$$

so that

$$R_s I_0 = -\gamma\frac{\partial V(0,T)}{\partial X} + \sigma\frac{\partial V(0,T)}{\partial T} + V(0,T), \tag{4.57}$$

where $\sigma = C_s R_s/\tau_m = \tau_s/\tau_m$ and $\gamma = R_s/(r_i\lambda_m)$. For convenience we assume that the time constant of the soma is the same as the membrane time constant, so that $\sigma = 1$.

4.3.1   A Semi-Infinite Neuron with a Soma

We first calculate the steady response of a semi-infinite neuron to a current I_0 injected at $X = 0$, as in Section 4.2.2. As before, we set the time derivative to zero to get

$$\frac{d^2V}{dX^2} = V, \tag{4.58}$$

$$V(0) - \gamma\frac{dV(0)}{dX} = R_s I_0, \tag{4.59}$$

which can easily be solved to give

$$V(X) = \frac{R_s}{r_i\lambda_m + R_s}r_i\lambda_m I_0 e^{-X}. \tag{4.60}$$

This solution is nearly the same as the steady response of the equivalent cylinder without a soma to an injected current, except that V is decreased by the constant factor $R_s/(R_s + r_i\lambda_m) < 1$. As $R_s \to \infty$, in which limit the soma carries no current, the solution to the lumped-soma model approaches the solution to the simple cable.

The input resistance R_{in} of the lumped-soma model is

$$R_{\text{in}} = \frac{V(0)}{I_0} = \frac{r_i\lambda_m R_s}{r_i\lambda_m + R_s}, \tag{4.61}$$

and thus

$$\frac{1}{R_{\text{in}}} = \frac{1}{r_i\lambda_m} + \frac{1}{R_s}. \tag{4.62}$$

Since $r_i\lambda_m$ is the input resistance of the cylinder, the input conductance of the lumped-soma model is the sum of the input conductance of the soma and the input conductance of the cylinder. This is as expected, since the equivalent cylinder and the soma are in parallel.

4.3.2   A Finite Neuron and Soma

We now calculate the time-dependent response of a finite cable and lumped soma to a delta function current input at the soma, as this is readily observed experimentally.

We assume that the equivalent cylinder has finite length L. Then the potential satisfies

$$\frac{\partial V}{\partial T} = \frac{\partial^2 V}{\partial X^2} - V, \qquad 0 < X < L, T > 0, \tag{4.63}$$

$$V(X, 0) = 0, \tag{4.64}$$

with boundary conditions

$$\frac{\partial V(L, T)}{\partial X} = 0, \tag{4.65}$$

$$\frac{\partial V(0, T)}{\partial T} + V(0, T) - \gamma \frac{\partial V(0, T)}{\partial X} = R_s \delta(T). \tag{4.66}$$

Note that the boundary condition (4.66) is equivalent to

$$\frac{\partial V(0, T)}{\partial T} + V(0, T) - \gamma \frac{\partial V(0, T)}{\partial X} = 0, \qquad T > 0, \tag{4.67}$$

together with the initial condition

$$V(0, 0) = R_s. \tag{4.68}$$

We begin by seeking a generalized Fourier series expansion of the solution. Using separation of variables, we find solutions of the form

$$V(X, T) = \phi(X) e^{-\mu^2 T}, \tag{4.69}$$

where ϕ satisfies the differential equation

$$\phi'' - (1 - \mu^2)\phi = 0, \tag{4.70}$$

with boundary conditions (when $T > 0$)

$$\phi'(L) = 0, \tag{4.71}$$

$$\phi'(0) = \phi(0)\frac{1 - \mu^2}{\gamma}. \tag{4.72}$$

The solution of (4.70) is

$$\phi = A\cos(\lambda X) + B\sin(\lambda X), \tag{4.73}$$

for some constants A and B and $\lambda^2 = \mu^2 - 1$, and applying the boundary conditions, we find

$$B = \frac{-\lambda A}{\gamma} \tag{4.74}$$
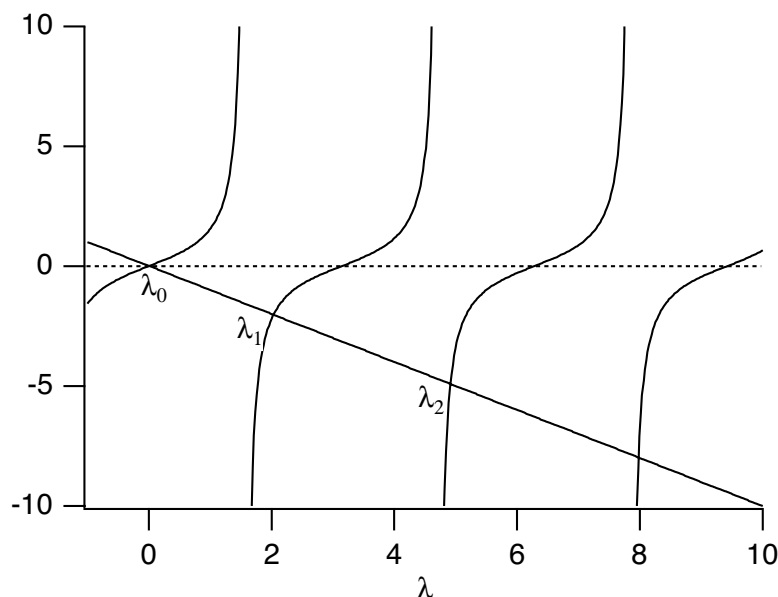
Figure 4.5: The eigenvalues of (4.63)–(4.66) are determined by the intersections of the curves $\tan(\lambda L)$ and $-\lambda/\gamma$. In this figure, $L = \gamma = 1$.

and

$$\tan(\lambda L) = -\frac{\lambda}{\gamma}. \tag{4.75}$$

The roots of (4.75) determine the eigenvalues. Although the eigenvalues cannot be found analytically, they can be determined numerically. A graph of the left and right hand sides of (4.75), showing the location of the eigenvalues as intersections of these curves, is given in Fig. 4.5. There is an infinite number of discrete eigenvalues, labelled λ_n, with $\lambda_0 = 0$. Expecting the full solution to be a linear combination of the eigenfunctions, we write

$$V(X,T) = \sum_{n=0}^{\infty} A_n \phi_n(X) \exp(-(1 + \lambda_n^2)T), \tag{4.76}$$

where

$$\phi_n(X) = \cos(\lambda_n X) - \frac{\lambda_n}{\gamma} \sin(\lambda_n X). \tag{4.77}$$

Note that if λ_n is an eigenvalue, so also is $-\lambda_n$, but the eigenfunction $\phi_n(X) = \cos(\lambda_n X) - \frac{\lambda_n}{\gamma} \sin(\lambda_n X)$ is an even function of λ_n, so it suffices to include only positive eigenvalues in the expansion.

We now strike a problem. The standard procedure is to expand the initial condition in terms of the eigenfunctions and thereby determine the coefficients A_n. However, the eigenfunctions are not mutually orthogonal in the usual way, so the standard approach fails. One way around this is to construct a nonorthogonal

expansion of the initial condition, an approach used by Durand (1984). A different approach (Bluman and Tuckwell, 1987; Tuckwell, 1988) is to calculate the Laplace transform of the solution, and then, by matching the two forms of the solution, obtain expressions for the unknown coefficients.

Here we present a different approach. The standard Fouirier series approach can be rescued by introducing a slightly different operator and inner product (Keener, 1988). Suppose we consider a Hilbert space of vectors of the form

$$U = \left(\begin{array}{c} u(x) \\ \alpha \end{array} \right), \tag{4.78}$$

where α is a real scalar, with the inner product

$$\langle U, V \rangle = \int_0^L u(x)v(x)dx + \gamma\alpha\beta, \tag{4.79}$$

where $V = \left(\begin{array}{c} v(x) \\ \beta \end{array} \right)$. The differential operator L on this space is defined by

$$LU = \left(\begin{array}{c} u''(x) \\ u'(0) \end{array} \right), \tag{4.80}$$

with the boundary conditions $u'(L) = 0$ and $u(0) = \gamma\alpha$. Now, the usual calculation shows that the operator L is a self-adjoint operator with the inner product defined by (4.79). Furthermore, the eigenfunctions of L, $L\Phi = \kappa\Phi$ satisfy the two equations $\phi''(x) = \kappa\phi(x)$ and $\gamma\phi'(0) = \kappa\phi(0)$, which are exactly the equations (4.70) and (4.72) with $\kappa = 1 - \mu^2$. It follows immediately that the eigenfunctions of the operator L are orthogonal and complete on this Hilbert space and are given by

$$\Phi_n(X) = \left(\begin{array}{c} \phi_n(X) \\ \frac{\phi_n(0)}{\gamma} \end{array} \right). \tag{4.81}$$

Furthermore, the solution of the full problem can be written in this Hilbert Space as

$$\left(\begin{array}{c} V(X,T) \\ \frac{1}{\gamma}V(0,T) \end{array} \right) = \sum_{n=0}^{\infty} A_n \Phi_n(X) \exp(-(1 + \lambda_n^2)T), \tag{4.82}$$

and the coefficients are found by requiring

$$\left(\begin{array}{c} V(X,0) \\ \frac{1}{\gamma}V(0,0) \end{array} \right) = \sum_{n=0}^{\infty} A_n \Phi_n(X) = \left(\begin{array}{c} 0 \\ \frac{R_s}{\gamma} \end{array} \right). \tag{4.83}$$

The coefficients A_n are now found by taking the inner product of (4.83) with $\Phi_n(X)$ with the result

$$A_n = \frac{R_s}{\gamma\langle\Phi_n, \Phi_n\rangle}, \tag{4.84}$$

where

$$\gamma\langle\Phi_n, \Phi_n\rangle = \gamma \int_0^L \left(\cos(\lambda_n X) - \frac{\lambda_n}{\gamma} \sin(\lambda_n X) \right)^2 dX + 1 \tag{4.85}$$

$$= \frac{1}{2} + \frac{L}{2\gamma}(\gamma^2 + \mu_n^2). \tag{4.86}$$

4.3.3   Other Compartmental Models

The methods presented above give some idea of the difficulty of calculating analytical solutions to the cable equation on branching structures, with or without a soma termination. Since modern experimental techniques can determine the detailed structure of a neuron (for example, by staining with horseradish peroxidase), it is clear that more experimental information can be obtained than can be incorporated into an analytical model (as is nearly always the case). Thus, one common approach is to construct a large computational model of a neuron and then determine the solution by a numerical method.

In a numerical approach, a neuron is divided into a large number of small pieces, or compartments, each of which is assumed to be isopotential. Within each compartment the properties of the neuronal membrane are specified, and thus some compartments may have excitable kinetics, while others are purely passive. The compartments are then connected by an axial resistance, resulting in a large system of coupled ordinary differential equations, with the voltage specified at discrete places along the neuron.

Compartmental models, numerical methods for their solution, and software packages used for these kinds of models are discussed in detail in Koch and Segev (1998) and de Schutter (2000), to which the interested reader is referred.

4.4   Appendix: Transform Methods

To follow all of the calculations and complete all the exercises in this chapter, you will need to know about Fourier and Laplace transforms, generalized functions and the delta function, Green's functions, as well as some aspects of complex variable theory, including contour integration and the residue theorem. If you have made it this far into this book, then you are probably familiar with these classic techniques. However, should you need a reference for these techniques, there are many books with the generic title "Advanced Engineering Mathematics," from which to choose (see, for example, Kreyszig (1994), O'Neill (1983), or Kaplan (1981)). At an intermediate level one might consider Strang (1986) or Boyce and DiPrima (1997). Keener (1988) provides a more advanced coverage of this material.

Exercises

1. Calculate the input resistance of a cable with a sealed end at $X = L$. Determine how the length of the cable, and the boundary condition at $X = L$, affects the input resistance, and compare to the result for a semi-infinite cable.

2. (a) Find the fundamental solution K of the linear cable equation satisfying

$$-\frac{d^2 K}{dX^2} + K = \delta(X - \xi), \quad -\infty < X < \infty, \qquad (4.87)$$

where $\delta(X - \xi)$ denotes an *inward* flow of positive current at the point $X = \xi$.

(b) Use the fundamental solution to construct a solution of the cable equation with inhomogeneous current input

$$-\frac{d^2V}{dX^2} + V = I(X).$$

(4.88)

3. Solve

$$-\frac{d^2G(X)}{dx^2} + G(X) = \delta(X - \xi), \quad 0 < X, \xi < L,$$

(4.89)

subject to (i) sealed end, and (ii) short circuit, boundary conditions. .

4. (a) Use Laplace transforms to find the solution of the semi-infinite (time-dependent) cable equation with clamped voltage

$$V(X, 0) = 0$$

(4.90)

and current input

$$\frac{\partial V(0, T)}{\partial X} = -r_i \lambda_m I_0 H(T),$$

(4.91)

where H is the Heaviside function.

Hint: Use the identity

$$\frac{2}{s\sqrt{s+1}} = \frac{1}{s+1-\sqrt{s+1}} - \frac{1}{s+1+\sqrt{s+1}},$$

(4.92)

and then use

$$\mathcal{L}^{-1}\left\{\frac{e^{-a\sqrt{s}}}{s + b\sqrt{s}}\right\} = e^{b^2 T + ab}\text{erfc}\left(\frac{a}{2\sqrt{T}} + b\sqrt{T}\right),$$

(4.93)

where $\mathcal{L}^{-1}$ denotes the inverse Laplace transform.

(b) Show that

$$V(X, T) \to r_i \lambda_m I_0 e^{-X}$$

(4.94)

as $T \to \infty$.

5. Calculate the time-dependent Green's function for a finite cylinder of length L for (i) sealed end, and (ii) short circuit, boundary conditions. These may be calculated in two different ways, either using Fourier series or by constructing sums of fundamental solutions.

6. By solving for the unknown constants, calculate the solution of the cable equation on the simple branching structure of Fig. 4.3. Show explicitly that this solution is the same as the equivalent cylinder solution, provided the necessary conditions are satisfied.

7. Show that if the conditions in Section 4.2.3 are satisfied, a branching structure can be condensed into a single equivalent cylinder.

8. Show that

$$\frac{\partial V}{\partial T} = \frac{\partial^2 V}{\partial X^2} - V + \delta(X)\delta(T), \qquad T \geq 0, \tag{4.95}$$

with $V(X,T) = 0$ for $T < 0$, is equivalent to

$$\frac{\partial V}{\partial T} = \frac{\partial^2 V}{\partial X^2} - V, \qquad T > 0, \tag{4.96}$$

with initial condition

$$V(X,0) = \delta(X). \tag{4.97}$$

9. neurex11 Find the numerical solution of (4.44) with $g(T) = Te^{-aT}$. From this determine $V_0(T)$ and $V_1(T)$ and use (4.47) to determine X_s. How does the computed value of X_s compare with the original value?

10. Show that as $n \to \infty$, the eigenvalues λ_n of (4.75) are approximately $(2n-1)\pi/(2L)$.

11. Using the method of Section 4.3.2, find the Green's function for the finite cylinder and lumped soma; i.e., solve

$$\frac{\partial V}{\partial T} = \frac{\partial^2 V}{\partial X^2} - V + \delta(X - \xi)\delta(T), \tag{4.98}$$

$$V(X,0) = 0, \tag{4.99}$$

with boundary conditions

$$\frac{\partial V(L,T)}{\partial X} = 0, \tag{4.100}$$

$$\frac{\partial V(0,T)}{\partial T} + V(0,T) - \gamma\frac{\partial V(0,T)}{\partial X} = 0. \tag{4.101}$$

Show that as $\xi \to 0$ the solution approaches that found in Section 4.3.2, scaled by the factor γ/R_s.

Chapter 5

Excitability

We have seen in previous chapters that the control of cell volume results in a potential difference across the cell membrane, and that this potential difference causes ionic currents to flow through channels in the cell membrane. Regulation of this membrane potential by control of the ionic channels is one of the most important cellular functions. Many cells, such as neurons and muscle cells, use the membrane potential as a signal, and thus the operation of the nervous system and muscle contraction (to name but two examples) are both dependent on the generation and propagation of electrical signals.

To understand electrical signaling in cells, it is helpful (and not too inaccurate) to divide all cells into two groups: excitable cells and nonexcitable cells. Many cells maintain a stable equilibrium potential. For some, if currents are applied to the cell for a short period of time, the potential returns directly to its equilibrium value after the applied current is removed. Such cells are nonexcitable, typical examples of which are the epithelial cells that line the walls of the gut. Photoreceptors (Chapter 19) are also nonexcitable, although in their case, membrane potential plays an extremely important signaling role nonetheless.

However, there are cells for which, if the applied current is sufficiently strong, the membrane potential goes through a large excursion, called an *action potential*, before eventually returning to rest. Such cells are called *excitable*. Excitable cells include cardiac cells, smooth and skeletal muscle cells, some secretory cells, and most neurons. The most obvious advantage of excitability is that an excitable cell either responds in full to a stimulus or not at all, and thus a stimulus of sufficient amplitude may be reliably distinguished from background noise. In this way, noise is filtered out, and a signal is reliably transmitted.

There are many examples of excitability that occur in nature. A simple example of an excitable system is a household match. The chemical components of the match head are stable to small fluctuations in temperature, but a sufficiently large temperature fluctuation, caused, for example, by friction between the head and a rough surface, triggers the abrupt oxidation of these chemicals with a dramatic release of heat and light. The fuse of a stick of dynamite is a one-dimensional continuous version of an excitable medium, and a field of dry grass is its two-dimensional version. Both of these spatially extended systems admit the possibility

193

of wave propagation. The field of grass has one additional feature that the match and dynamite fuse fail to have, and that is recovery. While it is not very rapid by physiological standards, given a few months of growth, a burned-over field of grass will regrow enough fuel so that another fire may spread across it.

Although the generation and propagation of signals have been extensively studied by physiologists for at least the past 100 years, the most important landmark in these studies is the work of Alan Hodgkin and Andrew Huxley, who developed the first quantitative model of the propagation of an electrical signal along a squid giant axon (deemed "giant" because of the size of the axon, *not* the size of the squid). Their model was originally used to explain the action potential in the long giant axon of a squid nerve cell, but the ideas have since been extended and applied to a wide variety of excitable cells. Hodgkin–Huxley theory is remarkable, not only for its influence on electrophysiology, but also for its influence, after some filtering, on applied mathematics. FitzHugh (in particular) showed how the essentials of the excitable process could be distilled into a simpler model upon which mathematical analysis could make some progress. Because this simplified model turned out to be of such great theoretical interest, it contributed enormously to the formation of a new field of applied mathematics, the study of excitable systems, a field that continues to stimulate a vast amount of research.

Because of the central importance of cellular electrical activity in physiology, because of the importance of the Hodgkin–Huxley model in the study of electrical activity, and because it forms the basis for the study of excitability, it is no exaggeration to say that the Hodgkin–Huxley model is the most important model in all of the physiological literature.

5.1   The Hodgkin–Huxley Model

In Chapter 2 we described how the cell membrane can be modeled as a capacitor in parallel with an ionic current, resulting in the equation

$$C_m \frac{dV}{dt} + I_{\text{ion}}(V, t) = 0, \tag{5.1}$$

where V, as usual, denotes the internal minus the external potential ($V = V_i - V_e$). In the squid giant axon, as in many neural cells, the principal ionic currents are the Na^+ current and the K^+ current. Although there are other ionic currents, primarily the Cl^- current, in the Hodgkin–Huxley theory they are small and lumped together into one current called the *leakage current*. Since the instantaneous *I–V* curves of open Na^+ and K^+ channels in the squid giant axon are approximately linear, (5.1) becomes

$$C_m \frac{dV}{dt} = -g_{\text{Na}}(V - V_{\text{Na}}) - g_{\text{K}}(V - V_{\text{K}}) - g_{\text{L}}(V - V_{\text{L}}) + I_{\text{app}}, \tag{5.2}$$

where I_{app} is the applied current. During an action potential there is a measured influx of 3.7 pmoles/cm^2 of Na^+ and a subsequent efflux of 4.3 pmoles/cm^2 of K^+. These amounts are so small that it is realistic to assume that the ionic concentrations, and hence the equilibrium potentials, are constant and unaffected by an
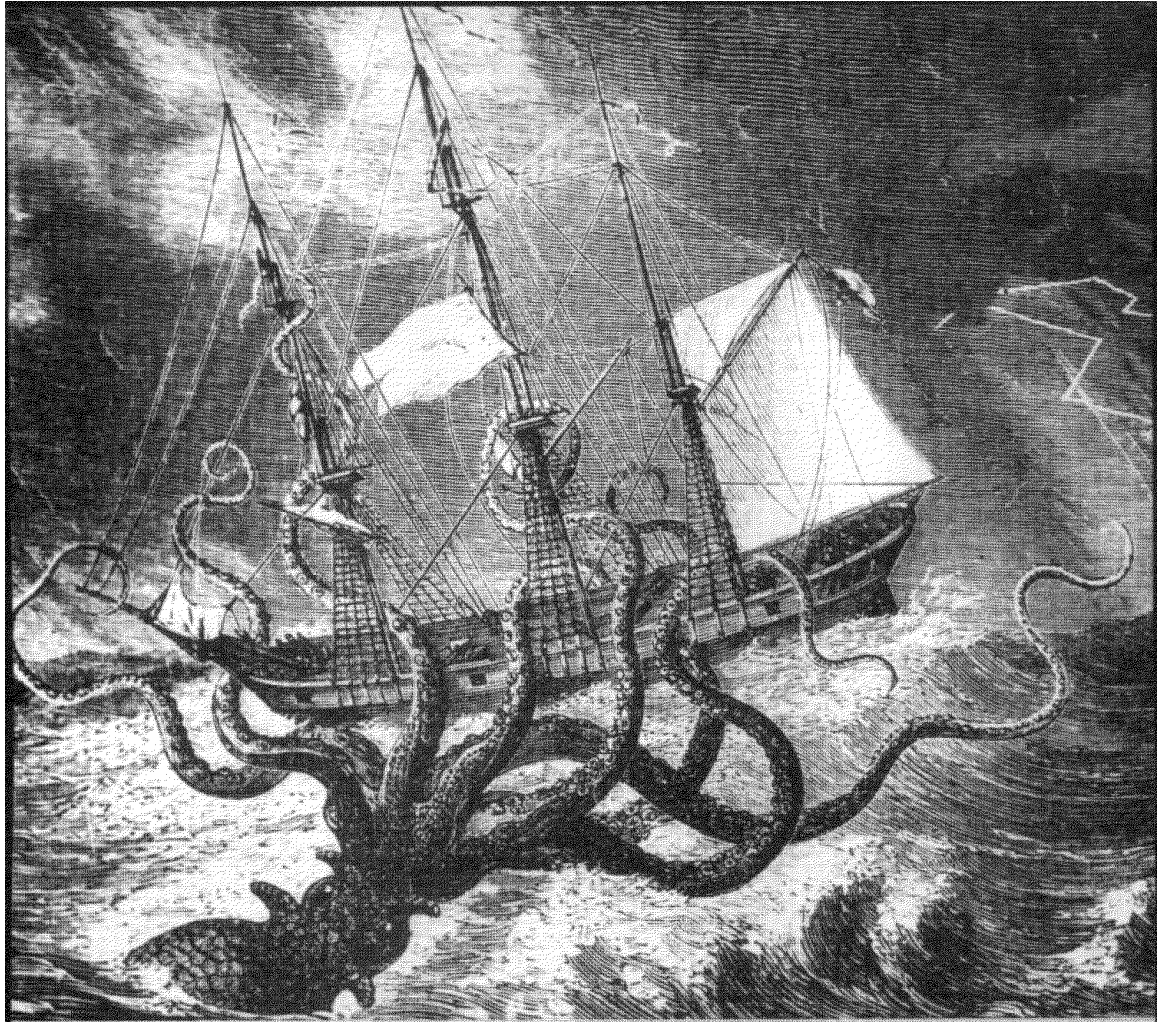
Figure 5.1: The infamous giant squid, having nothing to do with the work of Hodgkin and Huxley on squid giant axon. From *Dangerous Sea Creatures*, © 1976, 1977 Time-Life Films, Inc.

action potential. It is important to emphasize that the choice of linear I–V curves for the three different channel types is dictated largely by experimental data. Axons in other species (such as vertebrates) have ionic channels that are better described by other I–V curves, such as the GHK current equation (2.122). However, the qualitative nature of the results remains largely unaffected, and so the discussion in this chapter, which is mostly of a qualitative nature, remains correct for models that use more complex I–V curves to describe the ionic currents.

Equation (5.2) is a first-order ordinary differential equation and can be rewritten in the form

$$C_m \frac{dV}{dt} = -g_{\text{eff}}(V - V_{\text{eq}}) + I_{\text{app}}, \tag{5.3}$$

where $g_{\text{eff}} = g_{\text{Na}} + g_{\text{K}} + g_{\text{L}}$ and $V_{\text{eq}} = (g_{\text{Na}}V_{\text{Na}} + g_{\text{K}}V_{\text{K}} + g_{\text{L}}V_{\text{L}})/g_{\text{eff}}$. V_{eq} is the membrane resting potential and is a balance between the reversal potentials for the three ionic currents. In fact, at rest, the Na^+ and leakage conductances are small compared to the K^+ conductance, so that the resting potential is close to the K^+ equilibrium potential.

The quantity $R_m = 1/g_{\text{eff}}$, the passive membrane resistance, is on the order of $1000 \ \Omega\text{cm}^2$. The time constant for this equation is

$$\tau_m = C_m R_m, \tag{5.4}$$

on the order of 1 msec. It follows that with a steady applied current, the membrane potential should equilibrate quickly to

$$V = V_{\text{eq}} + R_m I_{\text{app}}. \tag{5.5}$$

For sufficiently small applied currents, this is indeed what happens. However, for larger applied currents, the response is quite different. Assuming that the model (5.2) is correct, the only possible explanation for these differences is that the conductances are not constant but depend in some way on the voltage. Historically, the key step to determining the conductances was being able to measure the individual ionic currents and from this to deduce the changes in conductances. This was brilliantly accomplished by Hodgkin and Huxley in 1952.

5.1.1   History of the Hodgkin–Huxley Equations

(This section is adapted from Rinzel, 1990.) In a series of five articles that appeared in the *Journal of Physiology* in 1952, Alan Lloyd Hodgkin and Andrew Fielding Huxley, along with Bernard Katz, who was a coauthor of the lead paper and a collaborator in several related studies, unraveled the dynamic ionic conductances that generate the nerve action potential (Hodgkin et al., 1952; Hodgkin and Huxley, 1952a,b,c,d). They were awarded the 1963 Nobel Prize in physiology and medicine (shared with John C. Eccles, for his work on potentials and conductances at motorneuron synapses).

Before about 1939, the membrane potential was believed to play an important role in the membrane's state, but there was no way to measure it. It was known that a cell's membrane separated different ionic concentrations inside and outside the cell. Applying the Nernst equation, Bernstein (1902) was led to suggest that

the resting membrane was semipermeable to K^+, implying that at rest, V should be around -70 mV. He believed that during activity there was a breakdown in the membrane's resistance to all ionic fluxes, and potential differences would disappear, i.e., V would approach zero.

In 1940, Cole and Curtis, using careful electrode placement coupled with biophysical and mathematical analysis, obtained the first convincing evidence for a substantial transient increase in membrane conductivity during passage of the action potential. While they estimated a large conductance increase, it was not infinite, so without a direct measurement of membrane potential it was not possible to confirm or nullify Bernstein's hypothesis. During a postdoctoral year in the U.S. in 1937–1938, Hodgkin established connections with Cole's group at Columbia and worked with them at Woods Hole in the summer. He and Curtis nearly succeeded in measuring V directly by tunneling along the giant axon with a glass micropipette. When each succeeded later (separately, with other collaborators), they found, surprisingly, that V rose transiently toward zero, but with a substantial overshoot. This finding brought into serious question the hypothesis of Bernstein and provided much food for thought during World War II, when Hodgkin, Huxley, and many other scientists were involved in the war effort.

By the time postwar experimental work was resuming in England, Cole and Marmont had developed the *space clamp technique*. This method allowed one to measure directly the total transmembrane current, uniform through a known area, rather than spatially nonuniform as generated by a capillary electrode. To achieve current control with space clamping, the axon was threaded with a metallic conductor (like a thin silver wire) to provide low axial resistance and thereby eliminate voltage gradients along the length of the axon. Under these conditions the membrane potential is no longer a function of distance along the axon, only of time. In addition, during the 1947 squid season, Cole and company made substantial progress toward controlling the membrane potential as well.

In 1948, Hodgkin went to visit Cole (then at Chicago) to learn directly of their methods. With some further developments of their own, Hodgkin, Huxley, and Katz applied the techniques with great success to record transient ionic fluxes over the physiological ranges of voltages. Working diligently, they collected most of the data for their papers in the summer of 1949. Next came the step of identifying the individual contributions of the different ion species. Explicit evidence that both Na^+ and K^+ were important came from the work of Hodgkin and Katz (1949). This also explained the earlier puzzling observations that V overshoots zero during an action potential, opposing the suggestion of Bernstein. Instead of supposing that there was a transient increase in permeability identical for all ions, Hodgkin and Katz realized that different changes in permeabilities for different ions could account for the V time course, as V would approach the Nernst potential for the ion to which the membrane was predominantly permeable, and this dominance could change with time. For example, at rest the membrane is most permeable to K^+, so that V is close to V_K. However, if g_K were to decrease and g_{Na} were to increase, then V would be pushed toward V_{Na}, which is positive, thus depolarizing the cell.

The question of how the changes in permeability were dynamically linked to V was not completely stated until the papers of 1952. In fact, the substantial delay

from data collection in 1949 until final publication in 1952 can be attributed to the considerable time devoted to data analysis, model formulation, and testing. Computer downtime was also a factor, as some of the solutions of the Hodgkin–Huxley equations were computed on a desktop, hand-cranked calculator. As Hodgkin notes, "The propagated action potential took about three weeks to complete and must have been an enormous labour for Andrew [Huxley]" (Hodgkin, 1976, p. 19).

The final paper of the 1952 series is a masterpiece of the scientific art. Therein they present their elegant experimental data, a comprehensive theoretical hypothesis, a fit of the model to the experimental data (obtained for fixed values of the membrane potential), and then, presto, a prediction (from their numerical computations) of the time course of the propagated action potential. In biology, where quantitatively predictive theories are rare, this work stands out as one of the most successful combinations of experiment and theory.

5.1.2   Voltage and Time Dependence of Conductances

The key step to sorting out the dynamics of the conductances came from the development of the *voltage clamp*. A voltage clamp fixes the membrane potential, usually by a rapid step from one voltage to another, and then measures the current that must be supplied in order to hold the voltage constant. Since the supplied current must equal the transmembrane current, the voltage clamp provides a way to measure the transient transmembrane current that results. The crucial point is that the voltage can be stepped from one constant level to another, and so the ionic currents can be measured at a constant, known, voltage. Thus, even when the conductances are functions of the voltage (as is actually the case), a voltage clamp eliminates any voltage changes and permits measurement of the conductances as functions of time only.

Hodgkin and Huxley found that when the voltage was stepped up and held fixed at a higher level, the total ionic current was initially inward, but at later times an outward current developed (Fig. 5.2). For a number of reasons, not discussed here, they argued that the initial inward current is carried almost entirely by Na^+, while the outward current that develops later is carried largely by K^+. With these assumptions, Hodgkin and Huxley were able to use a clever trick to separate the total ionic current into its constituent ionic parts. They replaced 90% of the extracellular Na^+ in the normal seawater bath with choline (a viscous liquid vitamin B complex found in many animal and vegetable tissues), which rendered the axon nonexcitable but changed the resting potential only slightly. Since it is assumed that immediately after the voltage has been stepped up, the ionic current is all carried by Na^+, it is possible to measure the initial Na^+ currents in response to a voltage step. Note that although the Na^+ currents can be measured directly immediately after the voltage step, they cannot be measured directly over a longer time period, as the total ionic current begins to include a contribution from the K^+ current. If we denote the Na^+ currents for the two cases of normal extracellular Na^+ and zero extracellular Na^+ by I_{Na}^1 and I_{Na}^2 respectively, then the ratio of the two currents,

$$I_{Na}^1/I_{Na}^2 = K, \tag{5.6}$$

say, can be measured directly from the experimental data.
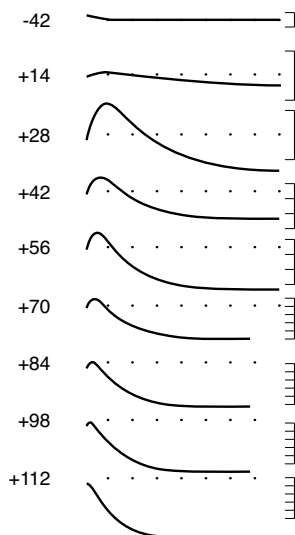
Figure 5.2: Experimental results describing the total membrane current in response to a step depolarization. The numbers on the left give the final value of the membrane potential, in mV. The interval between dots on the horizontal scale is 1 ms, while one division on the vertical scale represents 0.5 mA/cm^2. (Hodgkin and Huxley, 1952a, Fig. 2a.)

Next, Hodgkin and Huxley made two further assumptions. First, they assumed that the Na$^+$ current ratio K is independent of time and is thus constant over the course of each voltage clamp experiment. In other words, the amplitude and direction of the Na$^+$ current may be affected by the low extracellular Na$^+$ solution, but its time course is not. Second, they assumed that the K$^+$ channels are unaffected by the change in extracellular Na$^+$ concentration. There is considerable evidence that the Na$^+$ and K$^+$ channels are independent. Tetrodotoxin (TTX) is known to block Na$^+$ currents while leaving the K$^+$ currents almost unaffected, while tetraethylammonium (TEA) has the opposite effect of blocking the K$^+$ current but not the Na$^+$ current. To complete the argument, since $I_{ion} = I_{Na} + I_K$, and $I_K^1 = I_K^2$, it follows that $I_{ion}^1 - I_{Na}^1 = I_{ion}^2 - I_{Na}^2$, and thus

$$I_{Na}^1 = \frac{K}{K-1}(I_{ion}^1 - I_{ion}^2), \tag{5.7}$$

$$I_K = \frac{I_{ion}^1 - K I_{ion}^2}{1 - K}. \tag{5.8}$$

Hence, given measurements of the total ionic currents in the two cases, and given the ratio K of the Na$^+$ currents, it is possible to determine the complete time courses of both the Na$^+$ and K$^+$ currents.

Finally, from knowledge of the individual currents, one obtains the conductances as

$$g_{Na} = \frac{I_{Na}}{V - V_{Na}}, \qquad g_K = \frac{I_K}{V - V_K}. \tag{5.9}$$

Note that this result relies on the specific (linear) model used to describe the I–V curve of the Na^+ and K^+ channels, but, as stated above, we assume throughout that the instantaneous I–V curves of the Na^+ and K^+ channels are linear.

Samples of Hodgkin and Huxley's data are shown in Fig. 5.3. The plots show ionic conductances as functions of time following a step increase or decrease in the membrane potential. The important observation is that with voltages fixed, the conductances are time dependent. For example, when V is stepped up and held fixed at a higher level, g_K does not increase instantaneously, but instead increases over time to a final steady level. Both the time constant of the increase and the final value of g_K are dependent on the value to which the voltage is stepped. Further, g_K increases in a sigmoidal fashion, with a slope that first increases and then decreases (Fig. 5.3A and B). Following a step decrease in the voltage, g_K falls in a simple exponential fashion (Fig. 5.3A). This particular feature of g_K — a sigmoidal increase coupled with an exponential decrease — is important in what follows when we model g_K. The behavior of g_{Na} is more complex. Following a step increase in voltage, g_{Na} first increases, but then decreases again, *all at the same fixed voltage* (Fig. 5.3C). Hence, the time dependence of g_{Na} requires a more complex model than for that of g_K.

The potassium conductance

From the experimental data shown in Fig. 5.3A and B, it is reasonable to expect that g_K obeys some differential equation,

$$\frac{dg_K}{dt} = f(v, t), \tag{5.10}$$

say, where $v = V - V_{eq}$; i.e., v is the difference between the membrane potential and the resting potential. (Of course, since V_{eq} is a constant, $dv/dt = dV/dt$.) However, for g_K to have the required sigmoidal increase and exponential decrease, Hodgkin and Huxley realized that it would be easier to write g_K as some power of a different variable, n say, where n satisfies a first-order differential equation. Thus, they wrote

$$g_K = \bar{g}_K n^4, \tag{5.11}$$

for some constant $\bar{g}_K$. The fourth power was chosen not for physiological reasons, but because it was the smallest exponent that gave acceptable agreement with the experimental data. The secondary variable n obeys the differential equation

$$\tau_n(v)\frac{dn}{dt} = n_\infty(v) - n, \tag{5.12}$$

for some functions $\tau_n(v)$ and $n_\infty(v)$ that must be determined from the experimental data in a manner that we describe soon. Equation (5.12) is often written in the form

$$\frac{dn}{dt} = \alpha_n(v)(1 - n) - \beta_n(v)n, \tag{5.13}$$

where

$$n_\infty(v) \quad = \quad \frac{\alpha_n(v)}{\alpha_n(v) + \beta_n(v)}, \tag{5.14}$$
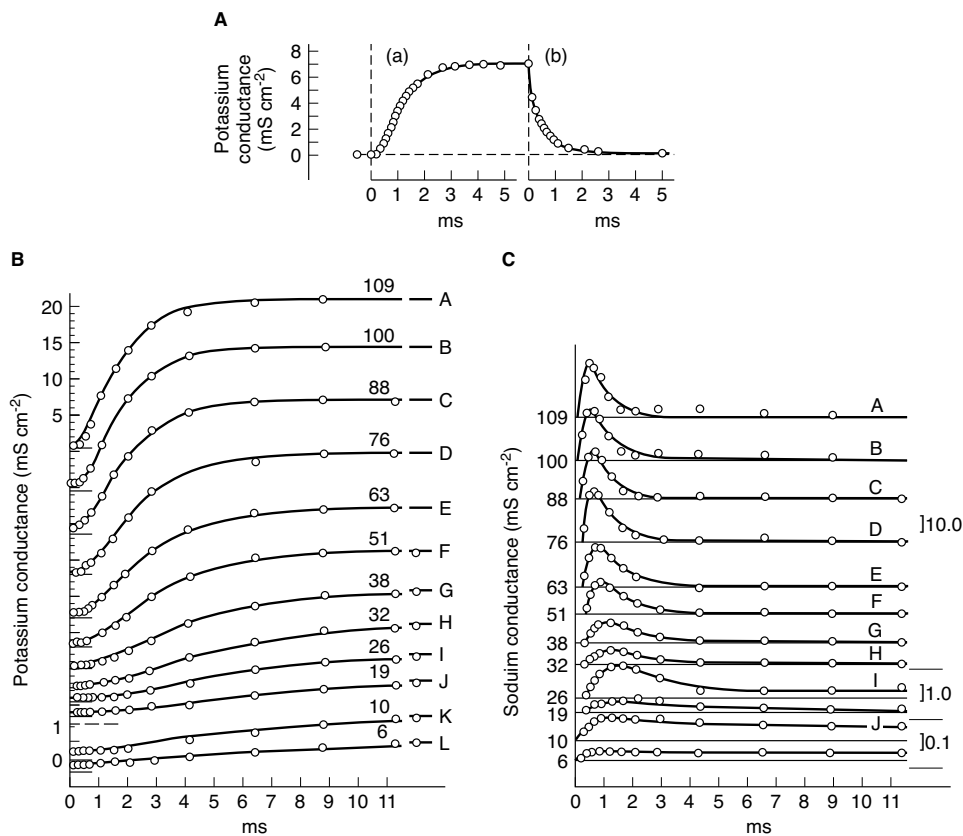
Figure 5.3: Conductance changes as a function of time at different voltage clamps. A: The response of g_K to a step increase in V and then a step decrease. B: Responses of g_K to step increases in V of varying magnitudes. The number on each curve gives the depolarization in mV, and the smooth curves are calculated from solution of (5.11) and (5.12), with the initial condition $g_K(t = 0) = 0.24$ mS/cm^2. The vertical scale is the same in curves A–J, but is increased by a factor of four in the lower two curves. For clarity, the baseline of each curve has been shifted up. C: Responses of g_{Na} to step increases in V of magnitudes given by the numbers on the left, in mV. The smooth curves are the model solutions. The vertical scales on the right are in units of mS/cm^2. (Hodgkin and Huxley, 1952d, Figs. 2, 3, and 6.)

$$\tau_n(v) \quad = \quad \frac{1}{\alpha_n(v) + \beta_n(v)}. \tag{5.15}$$

At elevated potentials $n(t)$ increases monotonically and exponentially toward its resting value, thereby turning on, or *activating*, the K^+ current. Since the Nernst potential is below the resting potential, the K^+ current is an outward current at potentials greater than rest. The function $n(t)$ is called the K^+ *activation*.

It is instructive to consider in detail how such a formulation for g_K results in the required sigmoidal increase and exponential decrease. Suppose that at time $t = 0$, v is increased from 0 to v_0 and then held constant, and suppose further that $n(0) = 0$. Solving (5.12) then gives

$$n(t) = n_\infty(v_0) \left[1 - \exp\left(\frac{-t}{\tau_n(v_0)} \right) \right], \tag{5.16}$$

which is an increasing curve (with monotonically decreasing slope) that approaches its maximum at $n_\infty(v_0)$. Raising n to the fourth power gives a sigmoidally increasing curve as required. Higher powers of n result in curves with a greater maximum slope at the point of inflection. In response to a step decrease in v, from v_0 to 0 say, the solution for n is

$$n(t) = n_\infty(v_0) \exp\left(\frac{-t}{\tau_n(0)} \right), \tag{5.17}$$

in which case n^4 is exponentially decreasing, with no inflection point.

It remains to describe how the functions n_∞ and τ_n are determined from the experimental data. For any given voltage step, the time constant τ_n, and the final value of n, namely n_∞, can be determined by fitting (5.16) to the experimental data. By this procedure one can determine τ_n and n_∞ at a discrete set of values for v, i.e., those values used experimentally. Typical data points for n_∞ are shown in Fig. 5.4 as symbols. To obtain a complete description of g_K, valid for all voltages and not only those used in the experiments, Hodgkin and Huxley fitted a smooth curve through the data points. The functional form of the smooth curve has no physiological significance, but is a convenient way of providing a continuous description of n_∞. A similar procedure is followed for τ_n. The continuous descriptions of n_∞ and τ_n (expressed in terms of α_n and β_n) are given in (5.28) and (5.29) below.

The sodium conductance

The time dependence for the Na^+ conductance is more difficult to unravel. From the experimental data it is suggested that there are two processes at work, one that turns on the Na^+ current and one that turns it off. Hodgkin and Huxley proposed that the Na^+ conductance is of the form

$$g_{Na}(v) = \bar{g}_{Na} m^3 h, \tag{5.18}$$

and they fit the time-dependent behavior of m and h to exponentials with dynamics

$$\frac{dw}{dt} = \alpha_w(1 - w) - \beta_w w, \tag{5.19}$$
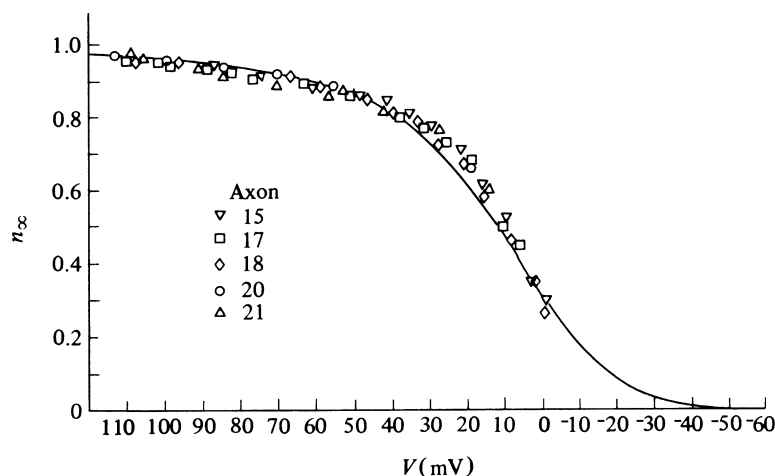
Figure 5.4: Data points (symbols) of n_∞, determined by fitting (5.16) to the experimental time courses. The smooth curve through the symbols provides a continuous description of n_∞, and its functional form has no physiological significance. In the original plot (Hodgkin and Huxley, 1952d, Fig. 5) V was calculated with a reverse sign, which has here been changed to agree with modern conventions. Thus, the horizontal axis appears reversed.

where $w = m$ or h. Because m is small at rest and first increases, it is called the *sodium activation*, and because h shuts down, or inactivates, the Na^+ current, it is called the *sodium inactivation*. When $h = 0$, the Na^+ current is completely inactivated. The overall procedure is similar to that used in the specification of g_K. For any fixed voltage step, the unknown functions α_w and β_w are determined by fitting to the experimental curves (Fig. 5.3C), and then smooth curves, with arbitrary functional forms, are fitted through the data points for α_w and β_w.

Summary of the equations

In summary, the Hodgkin–Huxley equations for the space clamped axon are

$$C_m \frac{dv}{dt} = -\bar{g}_K n^4(v - v_K) - \bar{g}_{Na} m^3 h(v - v_{Na}) - \bar{g}_L(v - v_L) + I_{app}, \quad (5.20)$$

$$\frac{dm}{dt} = \alpha_m(1 - m) - \beta_m m, \quad (5.21)$$

$$\frac{dn}{dt} = \alpha_n(1 - n) - \beta_n n, \quad (5.22)$$

$$\frac{dh}{dt} = \alpha_h(1 - h) - \beta_h h. \quad (5.23)$$

The specific functions α and β proposed by Hodgkin and Huxley are, in units of $(\text{ms})^{-1}$,

$$\alpha_m = 0.1 \frac{25 - v}{\exp\left(\frac{25-v}{10}\right) - 1}, \tag{5.24}$$

$$\beta_m = 4 \exp\left(\frac{-v}{18}\right), \tag{5.25}$$

$$\alpha_h = 0.07 \exp\left(\frac{-v}{20}\right), \tag{5.26}$$

$$\beta_h = \frac{1}{\exp(\frac{30-v}{10}) + 1}, \tag{5.27}$$

$$\alpha_n = 0.01 \frac{10 - v}{\exp(\frac{10-v}{10}) - 1}, \tag{5.28}$$

$$\beta_n = 0.125 \exp\left(\frac{-v}{80}\right). \tag{5.29}$$

For these expressions, the potential v is the deviation from rest $(V = V_{\text{eq}} + v)$, measured in units of mV, current density is in units of $\mu\text{A/cm}^2$, conductances are in units of mS/cm^2, and capacitance is in units of $\mu\text{F/cm}^2$. The remaining parameters are

$$\bar{g}_{\text{Na}} = 120, \qquad \bar{g}_{\text{K}} = 36, \qquad \bar{g}_{\text{L}} = 0.3, \qquad C_m = 1, \tag{5.30}$$

with (shifted) equilibrium potentials $v_{\text{Na}} = 115, v_{\text{K}} = -12$, and $v_{\text{L}} = 10.6$. (The astute reader will notice immediately that these values are not quite consistent with the values given in Table 2.1. Instead, these correspond to $V_{\text{Na}} = 50$ mV, $V_{\text{K}} = -77$ mV, $V_{\text{L}} = -54.4$ mV, with an equilibrium membrane potential of $V_{\text{eq}} = -65$ mV. These values are close enough to those of Table 2.1 to be of no concern.) In Fig. 5.5 are shown the steady-state functions and the time constants.

In Chapter 3 we discussed simple models for the gating of Na^+ and K^+ channels and showed how the rate constants in simple kinetic schemes could be determined from whole-cell or single-channel data. We also showed how models of the form (5.20)–(5.23) can be derived by modeling the ionic channels as consisting of multiple subunits, each of which obeys a simple two-state model. For example, for the Hodgkin–Huxley sodium gating equations can be derived from the assumption that the Na^+ channel consists of three "m" gates and one "h" gate, each of which can be either closed or open. If the gates operate independently, then the fraction of open Na^+ channels is $m^3 h$, where m and h obey the equation of the two-state channel model. Similarly, if there are four "n" gates per K^+ channel, all of which must be open for K^+ to flow, then the fraction of open K^+ channels is n^4.

Now comes the most interesting challenge facing these equations. Having incorporated the measurements of conductance found from voltage-clamp experiments, one wonders whether these equations reproduce a realistic action potential, and if so, by what mechanism is the action potential produced? We can describe in qualitative terms how the Hodgkin–Huxley equations should work. If small currents are applied to a cell for a short period of time, the potential returns rapidly to its
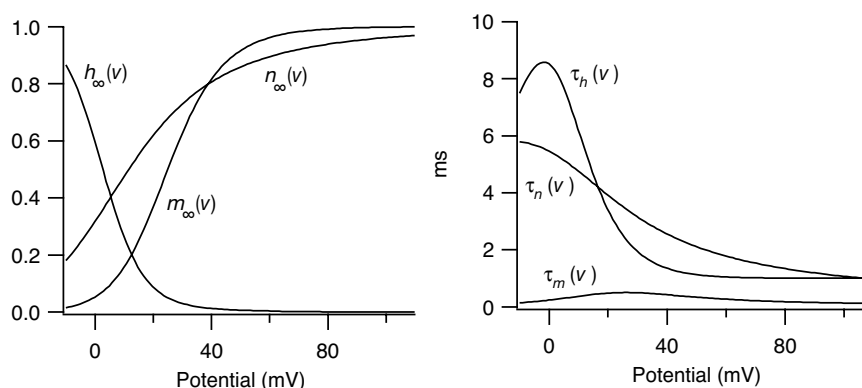
Figure 5.5: In the left panel are the steady-state functions, and in the right panel are the time constants of the Hodgkin–Huxley model (5.20)–(5.23).

equilibrium $v = 0$ after the applied current is removed. The equilibrium potential is close to the K^+ Nernst potential $v_K = -12$, because at rest, the Na^+ and leakage conductances are small. There is always competition among the three ionic currents to drive the potential to the corresponding resting potential. For example, if the K^+ and leakage currents could be blocked or the Na^+ conductance dramatically increased, then the term $g_{Na}(V - V_{Na})$ should dominate (5.2), and as long as v is below v_{Na}, an inward Na^+ current would drive the potential toward v_{Na}. Similarly, while v is above v_K, the K^+ current is outward in an attempt to drive v toward v_K. Notice that since $v_K < v_L < v_{Na}$, v is necessarily restricted to lie in the range $v_K < v < v_{Na}$.

If g_{Na} and g_K were constant, that would be the end of the story. The equilibrium at $v = 0$ would be a stable equilibrium, and following any stimulus, the potential would return exponentially to rest. But since g_{Na} and g_K can change, the different currents can exert their respective influences. The actual sequence of events is determined by the dynamics of $m, n,$ and h. The most important observation for the moment is that $\tau_m(v)$ is much smaller than either $\tau_n(v)$ or $\tau_h(v)$, so that $m(t)$ responds much more quickly to changes in v than either n or h. We can now understand why the Hodgkin–Huxley system is an excitable system. As noted before, if the potential v is raised slightly by a small stimulating current, the system returns to its stable equilibrium. However, during the period of time that the potential v is elevated, the Na^+ activation m tracks $m_\infty(v)$. If the stimulating current is large enough to raise the potential and therefore $m_\infty(v)$ to a high enough level (above its *threshold*), then before the system can return to rest, m will increase sufficiently to change the sign of the net current, resulting in an autocatalytic inward Na^+ current. Now, as the potential rises, m continues to rise, and the inward Na^+ current is increased, further adding to the rise of the potential.

If nothing further were to happen, the potential would be driven to a new equilibrium at v_{Na}. However, here is where the difference in time constants plays an important role. When the potential is at rest, the Na^+ inactivation h is positive, about
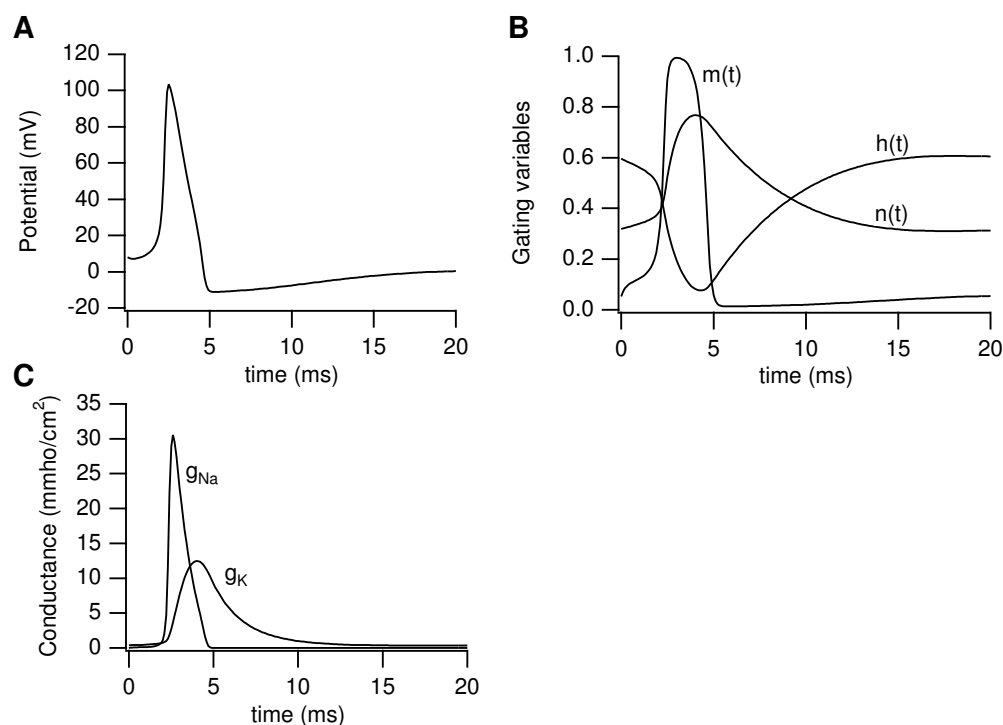
Figure 5.6: An action potential in the Hodgkin–Huxley equations. A: The action potential; B: the gating variables during an action potential, and C: the conductances during an action potential.

0.6. As the potential increases, h_∞ decreases toward zero, and as h approaches zero, the Na$^+$ current is inactivated because g_{Na} approaches zero. However, because the time constant $\tau_h(v)$ is much larger than $\tau_m(v)$, there is a considerable delay between turning on the Na$^+$ current when m increases and turning off the Na$^+$ current when h decreases. The net effect of the two different time scales on m and h is that the Na$^+$ current is at first turned on and later turned off, and this is seen as an initial increase of the potential, followed by a decrease toward rest.

At about the same time that the Na$^+$ current is inactivated, the outward K$^+$ current is activated. This is because of the similarity of the time constants $\tau_n(v)$ and $\tau_h(v)$. Activation of the K$^+$ current drives the potential below rest toward v_K. When v is negative, n declines, and the potential eventually returns to rest, and the whole process can start again. In Fig. 5.6A is shown a plot of the potential $v(t)$ during an action potential following a superthreshold stimulus. In Fig. 5.6B, $m(t)$, $n(t)$, and $h(t)$ during the same action potential are shown.

There are four recognizable phases of an action potential: the *upstroke, excited, refractory,* and *recovery* phases. The refractory period is the period following the excited phase when additional stimuli evoke no substantial response, even though the potential is below or close to its resting value. There can be no response, since

the Na^+ channels are inactivated because h is small. As h gradually returns to its resting value, further responses once again become possible.

Oscillations in the Hodgkin–Huxley equations

There are two ways that the Hodgkin–Huxley system can be made into an autonomous oscillator. The first is to inject a steady current of sufficient strength, i.e., by increasing I_{app}. Such a current raises the resting potential above the threshold for an action potential, so that after the axon has recovered from an action potential, the potential rises to a superthreshold level at which another action potential is evoked.

In Fig. 5.7A we plot the steady state v (i.e., $V - V_{eq}$) as a function of the applied current, I_{app}. The stable steady state is plotted as a solid line, and an unstable steady state is plotted with a dashed line. As I_{app} increases, so does v, and the steady state is stable for $I_{app} < 9.78$, at which value it loses stability in a subcritical Hopf bifurcation. This bifurcation gives rises to a branch of unstable limit cycle oscillations which bend backwards initially. Unstable limit cycles are drawn with a dashed line, and stable ones with a solid line.

In Fig. 5.7A we also plot the minimum and maximum of the oscillations (i.e., osc min and osc max) as functions of I_{app}. The branch of unstable limit cycles terminates at a limit point (a saddle-node of periodics, or SNP, bifurcation) where it coalesces with a branch of stable limit cycles. The stable periodic solutions are observed by direct numerical simulation of the differential equations. At larger values of I_{app}, the limit cycles disappear in another Hopf bifurcation, this time a supercritical one, leaving only a branch of stable steady state solutions for higher values of I_{app}.

Hence, for an intermediate range of values of I_{app}, stable oscillations exist. Two examples are shown in Fig. 5.7B. When I_{app} is too high, the model exhibits only a raised steady state. Furthermore, for a narrow range of values of I_{app}, slightly below the lower Hopf bifurcation, a stable steady state, an unstable periodic orbit, and a stable periodic orbit co-exist.

Immersing the axon in a bath of high extracellular K^+ has the same effect through a slightly different mechanism. Increased extracellular K^+ has the effect of increasing the K^+ Nernst potential, raising the rest potential (since the rest potential is close to the K^+ Nernst potential). If this increase of the K^+ Nernst potential is sufficiently large, the resting potential becomes superthreshold, and autonomous oscillations result. This mechanism of creating an autonomous oscillator out of normally excitable but nonoscillatory cells is important for certain cardiac arrhythmias.

5.1.3 Qualitative Analysis

FitzHugh (1960, 1961, 1969) provided a particularly elegant qualitative description of the Hodgkin–Huxley equations that allows a better understanding of the model's behavior. More detailed analyses have also been given by Rinzel (1978), Troy (1978), Cole et al. (1955), and Sabah and Spangler (1970). FitzHugh's approach is based on the fact that some of the model variables have fast kinetics,

A

B
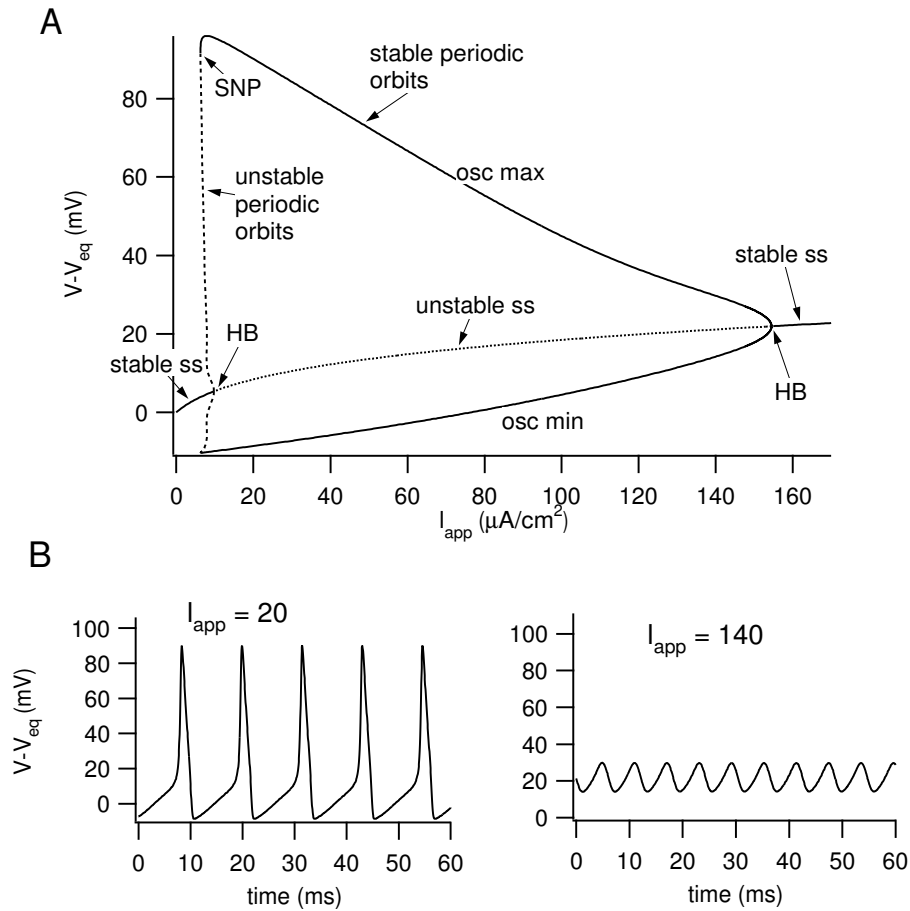
Figure 5.7: A: Bifurcation diagram of the Hodgkin–Huxley equations, with the applied current, I_{app} as the bifurcation parameter. HB denotes a Hopf bifurcation, SNP denotes a saddle-node of periodics bifurcation, osc max and osc min denote, respectively, the maximum and minimum of an oscillation, and ss denotes a steady state solution. Solid lines denote stable branches, dashed or dotted lines denote unstable branches. B: Sample oscillations at two different values of I_{app}.

while others are much slower. In particular, m and v are fast variables (i.e., the Na^+ channel activates quickly, and the membrane potential changes quickly), while n and h are slow variables (i.e., Na^+ channels are inactivated slowly, and the K^+ channels are activated slowly). Thus, during the initial stages of the action potential, n and h remain essentially constant while m and v vary. This allows the full 4-dimensional phase space to be broken into smaller pieces by fixing the slow variables and considering the behavior of the model as a function only of the two fast variables. Although this description is accurate only for the initial stages of the action potential, it provides a useful way to study the process of excitation.

The fast phase plane

Thus motivated, we fix the slow variables n and h at their respective resting states, which we call n_0 and h_0, and consider how m and v behave in response to stimulation. The differential equations for the fast phase plane are

$$C_m\frac{dv}{dt} \;=\; -\bar{g}_\text{K}n_0^4(v - v_\text{K}) - \bar{g}_\text{Na}m^3h_0(v - v_\text{Na}) - \bar{g}_\text{L}(v - v_\text{L}), \qquad (5.31)$$

$$\frac{dm}{dt} \;=\; \alpha_m(1 - m) - \beta_m m, \qquad (5.32)$$

or, equivalently,

$$\tau_m\frac{dm}{dt} = m_\infty - m. \qquad (5.33)$$

This is a two-dimensional system and can be studied in the (m, v) phase plane, a plot of which is given in Fig. 5.8. The curves defined by $dv/dt = 0$ and $dm/dt = 0$ are the v and m nullclines, respectively. The m nullcline is the curve $m = m_\infty(v)$, which we have seen before (in Fig. 5.5), while the v nullcline is the curve

$$v = \frac{\bar{g}_\text{Na}m^3h_0v_\text{Na} + \bar{g}_\text{K}n_0^4v_\text{K} + \bar{g}_\text{L}v_\text{L}}{\bar{g}_\text{Na}m^3h_0 + \bar{g}_\text{K}n_0^4 + \bar{g}_\text{L}}. \qquad (5.34)$$

For the parameters of the Hodgkin–Huxley model, the m and v nullclines intersect in three places, corresponding to three steady states of the fast equations. Note that these three intersections are not steady states of the full model, only of the fast subsystem, and, to be precise, should be called pseudo-steady states. However, in the context of the fast phase plane we continue to call them steady states. We label the three steady states v_r, v_s, and v_e (for resting, saddle, and excited).

It is left as an exercise to show that v_r and v_e are stable steady states of the fast subsystem, while v_s is a saddle point. Since v_s is a saddle point, it has a one-dimensional stable manifold, shown as a dot-dash line in Fig. 5.8. This stable manifold divides the (m, v) plane into two regions: any trajectory starting to the left of the stable manifold is prevented from reaching v_e and must eventually return to the resting state, v_r. However, any trajectory starting to the right of the stable manifold is prevented from returning to the resting state and must eventually end up at the excited state, v_e. Hence, the stable manifold, in combination with the two stable steady states, gives rise to a threshold phenomenon. Any perturbation from the resting state that is not large enough to cross the stable manifold eventually
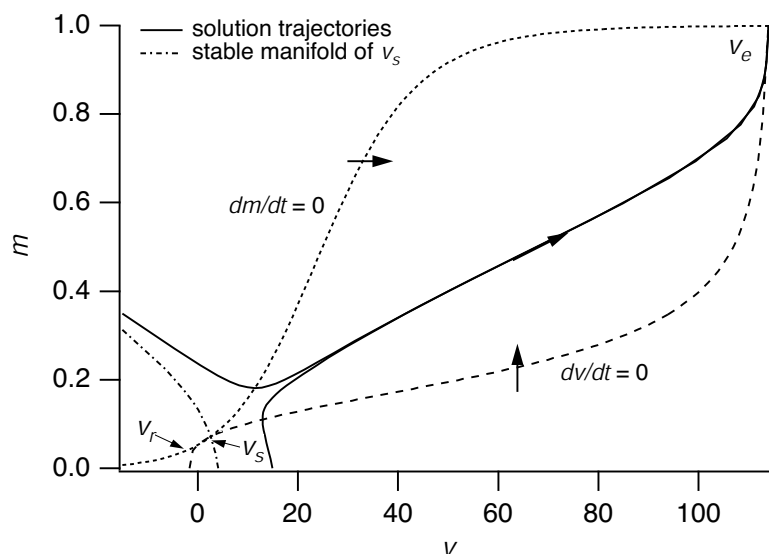
Figure 5.8: The Hodgkin–Huxley fast phase plane, showing the nullclines $dv/dt = 0$ and $dm/dt = 0$ (with $h_0 = 0.596$, $n_0 = 0.3176$), two sample trajectories and the stable manifold of the saddle point v_s.

dies away, but a perturbation that crosses the stable manifold results in a large excursion in the voltage to the excited state. Sample trajectories are sketched in Fig. 5.8.

If m and v were the only variables in the model, then v would stay at v_e indefinitely. However, as pointed out before, v_e is not a steady state of the full model. Thus, to see what happens on a longer time scale, we must consider how slow variations in n and h affect the fast phase plane. First note that since $v_e > v_r$, it follows that $h_\infty(v_e) < h_\infty(v_r)$ and $n_\infty(v_e) > n_\infty(v_r)$. Hence, while v is at the excited state, h begins to decrease, thus inactivating the Na$^+$ conductance, and n starts to increase thus activating the K$^+$ conductance. Next note that although the m nullcline in the fast phase plane is independent of n and h, the v nullcline is not. In Fig. 5.8 the nullclines were drawn using the steady-state values for n and h: different values of n and h change the shape of the v nullcline. As n increases and h decreases, the v nullcline moves to the left and up, as illustrated in Fig. 5.9. As the v nullcline moves up and to the left, v_e and v_s move towards each other, while v_r moves to the left. During this phase the voltage is at v_e and thus decreases slowly. Eventually, v_e and v_s coalesce and disappear in a saddle-node bifurcation. When this happens v_r is the only remaining steady state, and so the solution must return to the resting state. Note that since the v nullcline has moved up and to the left, v_r is not a steady state of the full system. However, when v decreases to v_r, n and h both return to their steady states and as they do so, v_r slowly increases until the steady state of the full system is reached and the action potential is complete. A schematic diagram of a complete action potential is shown in Fig. 5.10.
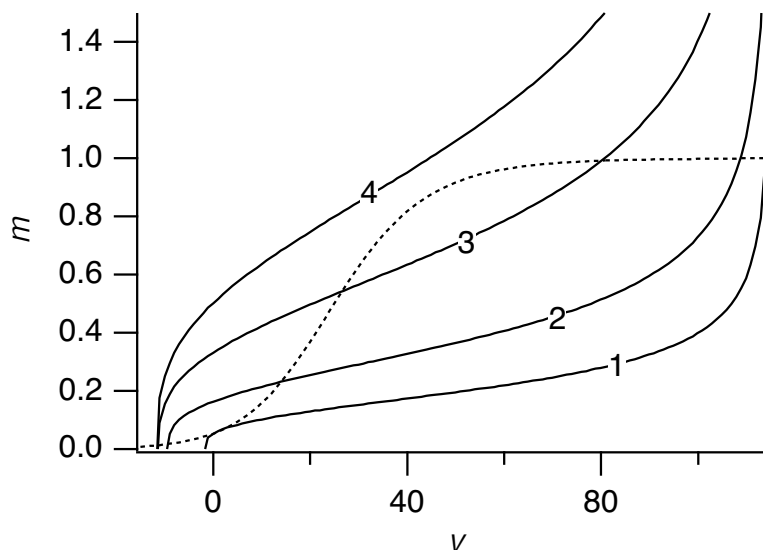
Figure 5.9: The Hodgkin–Huxley fast phase plane as a function of the slow variables, showing the m nullcline (dashed) and the movement of the v nullcline (solid) and the disappearance of the steady states. For these curves, parameter values are (1) $h_0 = 0.596$, $n_0 = 0.3176$; (2) $h_0 = 0.4$, $n_0 = 0.5$; (3) $h_0 = 0.2$, $n_0 = 0.7$; and (4) $h_0 = 0.1$, $n_0 = 0.8$.

The fast–slow phase plane

In the above analysis, the four-dimensional phase space was simplified by taking a series of two-dimensional cross-sections, those with various fixed values of n and h. However, by taking a different cross-section other aspects of the action potential can be highlighted. In particular, by taking a cross-section involving one fast variable and one slow variable we obtain a description of the Hodgkin–Huxley model that has proven to be extraordinarily useful.

We extract a single fast variable by assuming that m is always in instantaneous equilibrium, and thus $m = m_\infty(v)$. This is corresponds to assuming that activation of the Na$^+$ conductance is on a time scale faster than that of the voltage. Next, FitzHugh noticed that during the course of an action potential, $h + n \approx 0.8$ (notice the approximate symmetry of $n(t)$ and $h(t)$ in Fig. 5.6), and thus h can be eliminated by setting $h = 0.8 - n$. With these simplifications, the Hodgkin–Huxley model contains one fast variable v and one slow variable n, and can be written as

$$-C_m \frac{dv}{dt} = \bar{g}_K n^4 (v - v_K) + \bar{g}_{Na} m_\infty^3 (v)(0.8 - n)(v - v_{Na}) + \bar{g}_L(v - v_L) \quad (5.35)$$

$$\frac{dn}{dt} = \alpha_n(1 - n) - \beta_n n. \quad (5.36)$$

For convenience we let $f(v, n)$ denote the right-hand side of (5.35), i.e.,

$$-f(v, n) = \bar{g}_K n^4 (v - v_K) + \bar{g}_{Na} m_\infty^3 (v)(0.8 - n)(v - v_{Na}) + \bar{g}_L(v - v_L). \quad (5.37)$$
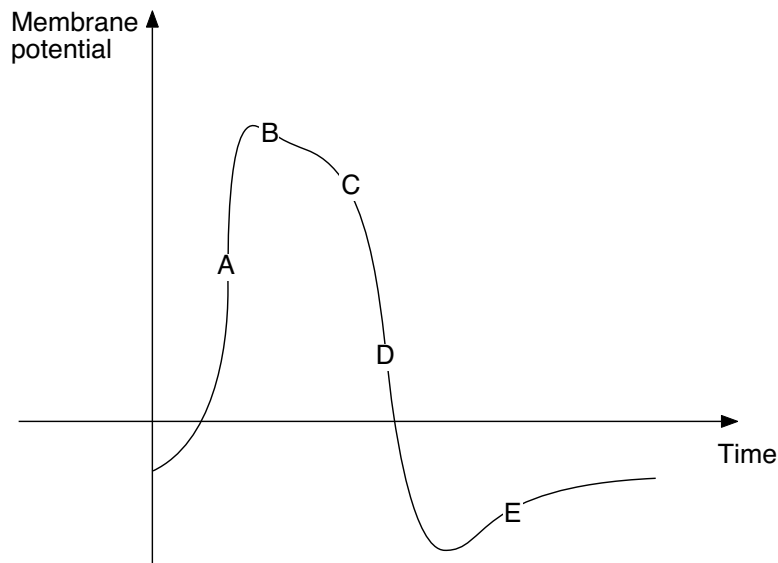
Figure 5.10: Schematic diagram of a complete action potential. A: Superthreshold stimulus causes a fast increase of v to the excited state. B: v is sitting at the excited state, v_e, decreasing slowly as n increases and h decreases, i.e., as v_e moves toward v_s. C: v_e and v_s disappear at a saddle-node bifurcation, and so, D: The solution must return to the resting state v_r. E: n and h slowly return to their resting states, and as they do so, v_r slowly increases until the steady state of the full four-dimensional system is reached.
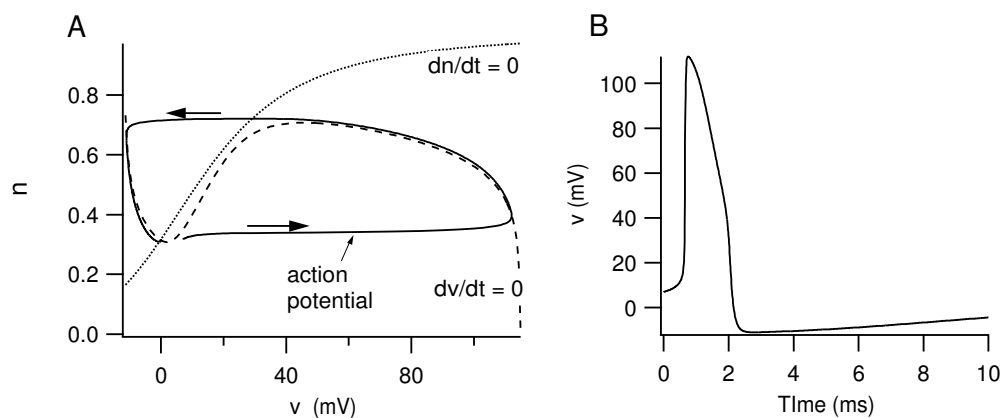
Figure 5.11: A: Fast–slow phase plane of the Hodgkin–Huxley model (with $I_{\mathrm{app}} = 0$), showing the nullclines and an action potential. B: Action potential of panel A, plotted as a function of time.

A plot of the nullclines of the fast–slow subsystem is given in Fig. 5.11A. The v nullcline is defined by $f(v, n) = 0$ and has a cubic shape, while the n nullcline is $n_\infty(v)$ and is monotonically increasing. There is a single intersection (at least for the given parameter values) and thus a single steady state. Because v is a fast variable and n is a slow one, the solution trajectories are almost horizontal except where $f(v, n) \approx 0$. The curve $f(v, n) = 0$ is called the *slow manifold*. Along the slow manifold the solution moves slowly in the direction determined by the sign of dn/dt, but away from the slow manifold the solution moves quickly in a horizontal direction. From the sign of dv/dt it follows that the solution trajectories move away from the middle branch of the slow manifold and toward the left and right branches. Thus, the middle branch is termed the unstable branch of the slow manifold. This unstable branch acts as a threshold. Suppose a perturbation from the steady state is small enough so that v does not cross the unstable manifold. Then, the trajectory moves horizontally towards the left and returns to the steady state. However, if the perturbation is large enough so that v crosses the unstable manifold, then the trajectory moves to the right until it reaches the right branch of the slow manifold, which corresponds to the excited state. On this right branch $dn/dt > 0$, and so the solution moves slowly up the slow manifold until the turning point is reached. At the turning point, n cannot increase any further, as the right branch of the slow manifold ceases to exist, and so the solution moves over to the left branch of the slow manifold. On this left branch $dn/dt < 0$, and so the solution moves down the left branch until the steady state is reached, completing the action potential (Fig. 5.11A). A plot of the potential as a function of time is shown in Fig. 5.11B.

The variables v and n are usually called the excitation and recovery variables, respectively: excitation because v governs the rise to the excited state, and recovery because n causes the return to the steady state. In the absence of n the solution would stay at the excited state indefinitely.
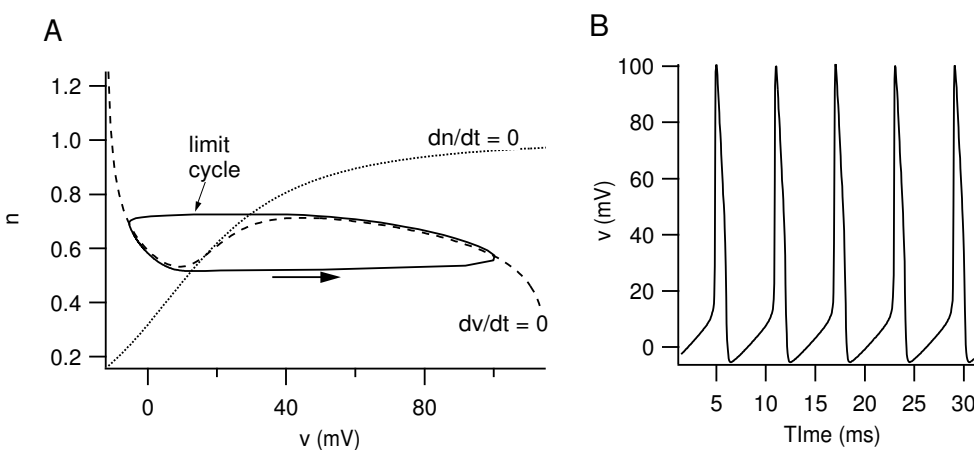
Figure 5.12: A: Fast–slow phase plane of the Hodgkin–Huxley model, with $I_{\mathrm{app}} = 50$, showing the nullclines and an oscillation. B: The oscillations of panel A, plotted as a function of time.

There is a close relationship between the fast phase plane and the fast–slow phase plane. Recall that in the fast phase plane, the v and m nullclines have three intersection points when $n = n_0$ and $h = h_0$. These three intersections correspond to the three branches of the curve $f(v, n_0) = 0$. In other words, when n is fixed at n_0, the equation $f(v, n_0) = 0$ has three possible solutions, corresponding to v_r, v_s and v_e in the fast phase plane. However, consideration of Fig. 5.11 shows that, as n increases, the two rightmost branches of the slow manifold coalesce and disappear. This is analogous to the merging and disappearance of v_e and v_s seen in the fast phase plane. The fast–slow phase plane is a convenient way of summarizing how v_r, v_s, and v_e depend on the slow variables.

This representation of the Hodgkin–Huxley model in terms of two variables, one fast and one slow, is the basis of the FitzHugh–Nagumo model for excitability, and models of this generic type are discussed in some detail throughout this book.

Oscillations in the fast-slow phase plane

As was true for the full Hodgkin–Huxley model, the addition of an applied current to the fast-slow phase plane gives rise to oscillations. Why this is so can be seen in Fig. 5.12. As I_{app} increases, the cubic nullcline moves across and up, until the two nullclines intersect on the middle branch of the cubic. The trajectory can never approach this steady state, always falling off each of the branches of the cubic, and alternating periodically between the two stable branches in what is called a relaxation limit cycle.
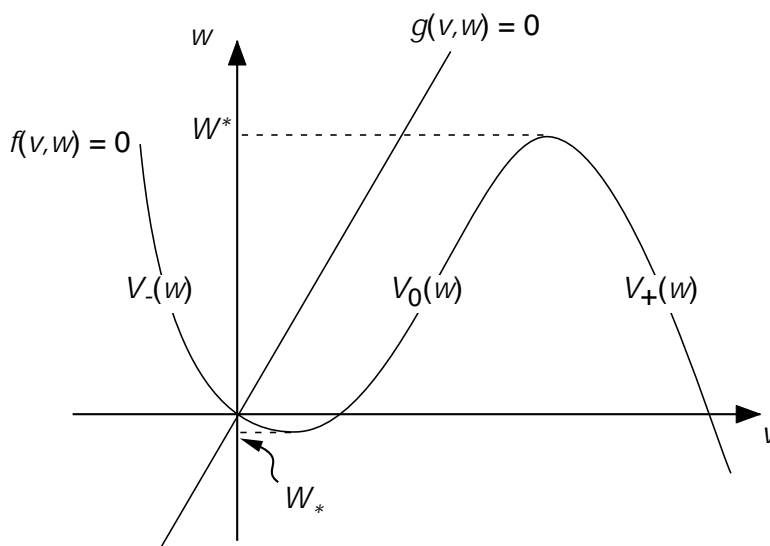
Figure 5.13: Schematic diagram of the generalized FitzHugh–Nagumo phase plane.

5.2 The FitzHugh-Nagumo Equations

There is considerable value in studying systems of equations that are simpler than the Hodgkin–Huxley equations but that retain many of their qualitative features. This is the motivation for the FitzHugh–Nagumo equations and their variants. Basically, the FitzHugh–Nagumo model extracts the essential behavior of the Hodgkin–Huxley fast–slow phase plane and presents it in a simplified form. Thus, the FitzHugh–Nagumo model has two variables, one fast (v) and one slow (w). The fast variable has a cubic nullcline and is called the excitation variable, while the slow variable is called the recovery variable and has a nullcline that is monotonically increasing. The nullclines have a single intersection point, which, without loss of generality, is assumed to be at the origin. A schematic diagram of the phase plane is given in Fig. 5.13, where we introduce some of the notation used later in this section.

The traditional FitzHugh-Nagumo model is obtained by assuming a cubic nullcline for v and a linear nullcline for w. Thus,

$$\epsilon \frac{dv}{dt} = f(v) - w + I_{\text{app}}, \tag{5.38}$$

$$\frac{dw}{dt} = v - \gamma w, \tag{5.39}$$

where

$$f(v) = v(1-v)(v-\alpha), \qquad \text{for } 0 < \alpha < 1, \epsilon \ll 1. \tag{5.40}$$

I_{app} is the applied current. Typical values would be $\alpha = 0.1$, $\gamma = 0.5$ and $\epsilon = 0.01$. Other choices for $f(v)$ include the McKean model (McKean, 1970), for which

$$f(v) = H(v - \alpha) - v, \tag{5.41}$$
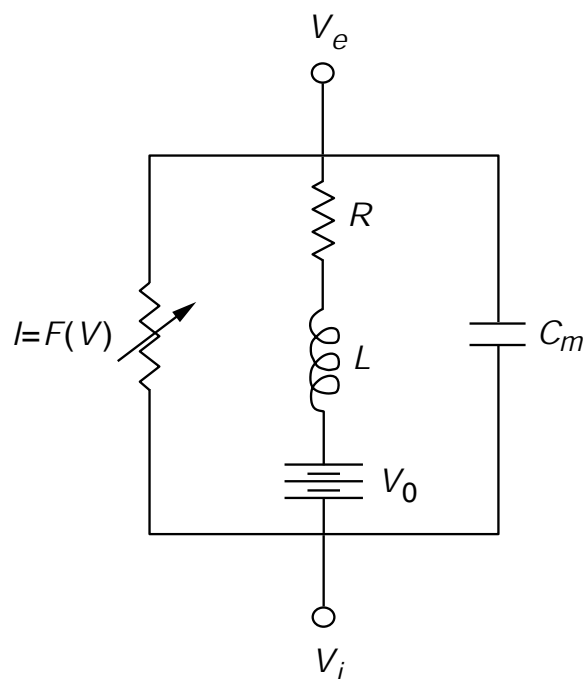
Figure 5.14: Circuit diagram for the FitzHugh–Nagumo equations.

where H is the Heaviside function. This choice recommends itself because then the model is piecewise linear, allowing explicit solutions of many interesting problems. Another piecewise linear model (also proposed by McKean, 1970) has

$$f(v) = \begin{cases} -v, & \text{for } v < \alpha/2, \\ v - \alpha, & \text{for } \frac{\alpha}{2} < v < \frac{1+\alpha}{2}, \\ 1 - v, & \text{for } v > \frac{1+\alpha}{2}. \end{cases} \qquad (5.42)$$

A third piecewise linear model that has found widespread usage is the *Pushchino* model, so named because of its development in Pushchino (about 70 miles south of Moscow), by Krinksy, Panfilov, Pertsov, Zykov, and their coworkers. The details of the Pushchino model are described in Exercise 13.

The FitzHugh–Nagumo model can be derived from a simplified model of the cell membrane (Fig. 5.14). Here the cell (or membrane patch) consists of three components, a capacitor representing the membrane capacitance, a nonlinear current–voltage device for the fast current, and a resistor, inductor, and battery in series for the recovery current. In the 1960s Nagumo, a Japanese electrical engineer, built this circuit using a tunnel diode as the nonlinear element (Nagumo et al., 1964), thereby attaching his name to this system.

Using Kirchhoff's laws, we can write down equations for the behavior of this membrane circuit diagram. We find

$$C_m \frac{dV}{d\tau} + F(V) + i = -I_0, \qquad (5.43)$$

$$L\frac{di}{d\tau} + Ri \;=\; V - V_0, \tag{5.44}$$

where I_0 is the applied external current, i is the current through the resistor–inductor, $V = V_i - V_e$ is the membrane potential, and V_0 is the potential gain across the battery. Here τ is used to represent dimensional time because we shortly introduce t as a dimensionless time variable. The function $F(V)$ is assumed to be of cubic shape, having three zeros, of which the smallest $V = 0$ and largest $V = V_1$ are stable solutions of the differential equation $dV/d\tau = -F(V)$. We take R_1 to be the passive resistance of the nonlinear element, $R_1 = 1/F'(0)$. Now we introduce the dimensionless variables $v = V/V_1, w = R_1 i/V_1, f(v) = -R_1 F(V_1 v)/V_1$, and $t = L\tau/R_1$. Then (5.43) and (5.44) become

$$\epsilon\frac{dv}{dt} \;=\; f(v) - w - w_0, \tag{5.45}$$

$$\frac{dw}{dt} \;=\; v - \gamma w - v_0, \tag{5.46}$$

where $\epsilon = R_1^2 C_m/L, w_0 = R_1 I_0/V_1, v_0 = V_0/V_1$, and $\gamma = R/R_1$.

An important variant of the FitzHugh–Nagumo equations is the *van der Pol oscillator*. An electrical engineer, van der Pol built the circuit using triodes because it exhibits stable oscillations. As there was little interest in oscillatory circuits at the time, he proposed his circuit as a model of an oscillatory cardiac pacemaker (van der Pol and van der Mark, 1928). Since then it has become a classic example of a system with limit cycle behavior and relaxation oscillations, included in almost every textbook on oscillations (see, for example, Stoker, 1950, or Minorsky, 1962).

If we eliminate the resistor R from the circuit (Fig. 5.14), differentiate (5.43), and eliminate the current i, we get the second-order differential equation

$$C_m\frac{d^2 V}{d\tau^2} + F'(V)\frac{dV}{d\tau} + \frac{V}{L} = \frac{V_0}{L}. \tag{5.47}$$

Following rescaling, and setting $F(v) = A(v^3/3 - v)$, we arrive at the *van der Pol equation*

$$v'' + a(v^2 - 1)v' + v = 0. \tag{5.48}$$

From now on, by the *generalized FitzHugh–Nagumo equations* we mean the system of equations

$$\epsilon\frac{dv}{dt} \;=\; f(v, w), \tag{5.49}$$

$$\frac{dw}{dt} \;=\; g(v, w), \tag{5.50}$$

where the nullcline $f(v, w) = 0$ is of "cubic" shape. By this we mean that for a finite range of values of w, there are three solutions $v = v(w)$ of the equation $f(v, w) = 0$. These we denote by $v = V_-(w), v = V_0(w)$, and $v = V_+(w)$, and where comparison is possible (since these functions need not all exist for the same range of w),

$$V_-(w) \leq V_0(w) \leq V_+(w). \tag{5.51}$$

We denote the minimal value of w for which $V_-(w)$ exists by W_*, and the maximal value of w for which $V_+(w)$ exists by W^*. For values of w above the nullcline $f(v, w) = 0$, $f(v, w) < 0$, and below the nullcline, $f(v, w) > 0$ (in other words, $f_w(v, w) < 0$).

The nullcline $g(v, w) = 0$ is assumed to have precisely one intersection with the curve $f(v, w) = 0$. Increasing v beyond the curve $g(v, w) = 0$ makes $g(v, w)$ positive (i.e., $g_v(v, w) > 0$), and decreasing w below the curve $g(v, w) = 0$ increases $g(v, w)$ (hence $g_w(v, w) < 0$). The nullclines f and g are illustrated in Fig. 5.13.

5.2.1   Phase-Plane Behavior

One attractive feature of the FitzHugh–Nagumo model is that because it is a two-variable system, it can be studied using phase-plane techniques. (For an example of a different approach, see Troy, 1976.) There are two characteristic phase portraits possible (shown in Figs. 5.15 and 5.16). By assumption, there is only one steady state, at $v = v^*$, $w = w^*$, with $f(v^*, w^*) = g(v^*, w^*) = 0$. Without loss of generality, we assume that this steady state occurs at the origin, as this involves only a shift of the variables. Furthermore, it is typical that the parameter ϵ is a small number. For small ϵ, if the steady state lies on either the left or right solution branch of $f(v, w) = 0$, i.e., the curves $v = V_\pm(w)$, it is linearly stable. Somewhere on the middle solution branch $v = V_0(w)$, near the extremal values of the curve $f(v, w) = 0$, there is a Hopf bifurcation point. If parameters are varied so that the steady state solution passes through this point, a periodic orbit arises as a continuous solution branch and bifurcates into a stable limit cycle oscillation.

When the steady state is on the leftmost branch, but close to the minimum (Fig. 5.15), the system is excitable. This is because even though the steady state is linearly stable, a sufficiently large perturbation from the steady state sends the state variable on a trajectory that runs away from the steady state before eventually returning to rest. Such a trajectory goes rapidly to the rightmost branch, which it hugs as it gradually creeps upward, where upon reaching the maximum, it goes rapidly to the leftmost branch and then gradually returns to rest, staying close to this branch as it does. Plots of the variables v and w are shown as functions of time in Fig. 5.15.

The mathematical description of these events follows from singular perturbation theory. With $\epsilon \ll 1$, the variable v is a fast variable and the variable w is a slow variable. This means that if possible, v is adjusted rapidly to maintain a pseudo-equilibrium at $f(v, w) = 0$. In other words, if possible, v clings to the stable branches of $f(v, w) = 0$, namely $v = V_\pm(w)$. Along these branches the dynamics of w are governed by the reduced dynamics

$$\frac{dw}{dt} = g(V_\pm(w), w) = G_\pm(w). \tag{5.52}$$

When it is not possible for v to be in quasi-equilibrium, the motion is governed approximately by the differential equations,

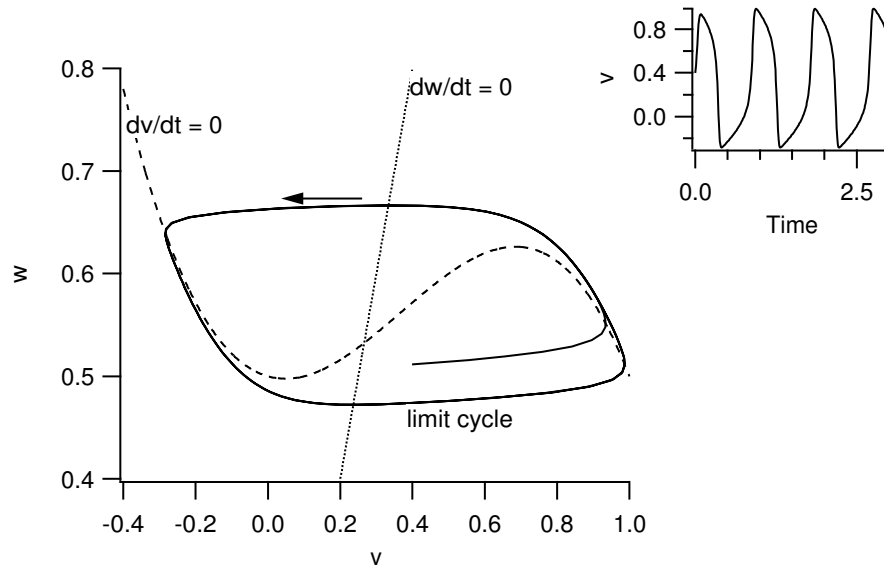$$\frac{dv}{d\tau} = f(v, w), \qquad \frac{dw}{d\tau} = 0, \tag{5.53}$$
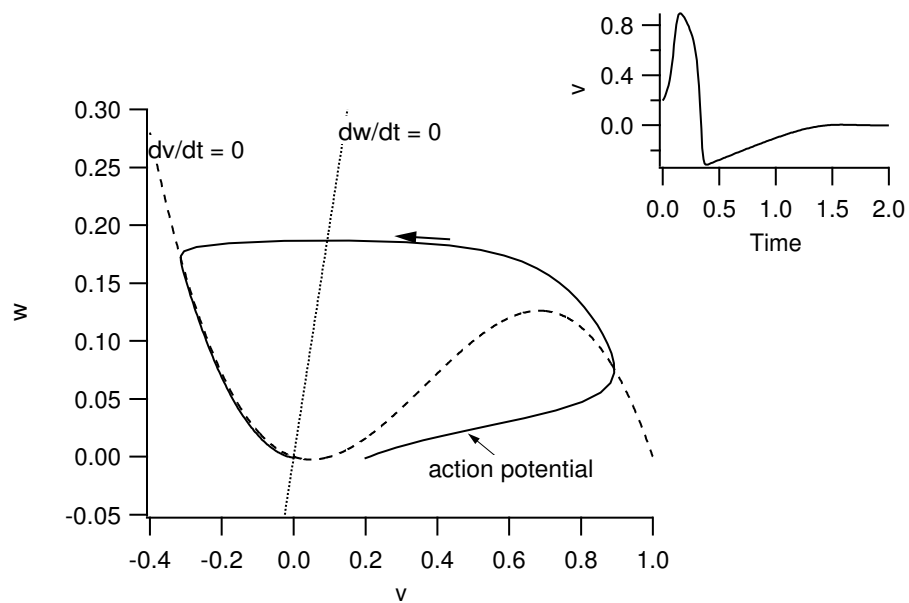
Figure 5.15: Phase portrait for the FitzHugh–Nagumo equations, (5.38)-(5.40), with $\alpha = 0.1$, $\gamma = 0.5$, $\epsilon = 0.01$ and zero applied current. For these parameter values the system has a unique globally stable rest point, but is excitable. The inset at top right shows the action potential as a function of time.

found by making the change of variables to the fast time scale $t = \epsilon\tau$, and then setting $\epsilon = 0$. On this time scale, w is constant, while v equilibrates to a stable solution of $f(v, w) = 0$.

The evolution of v and w starting from specified initial conditions v_0 and w_0 can now be described. Suppose v_0 is greater than the rest value v^*. If $v_0 < V_0(w)$, then v returns directly to the steady state. If $v_0 > V_0(w)$, then v goes rapidly to the upper branch $V_+(w)$ with w remaining nearly constant at w_0. The curve $v = V_0(w)$ is a *threshold curve*. While v remains on the upper branch, w increases according to

$$\frac{dw}{dt} = G_+(w), \tag{5.54}$$

as long as possible. However, in the finite time

$$T_e = \int_{w_0}^{W^*} \frac{dw}{G_+(w)}, \tag{5.55}$$

w reaches the "knee" of the nullcline $f(v, w) = 0$. This period of time constitutes the *excited phase* of the action potential.

When w reaches W^* it is no longer possible for v to stay on the excited branch, so it must return to the lower branch $V_-(w)$. Once on this branch, w decreases following the dynamics

$$\frac{dw}{dt} = G_-(w). \tag{5.56}$$

If the rest point lies on the lower branch, then $G_-(w^*) = 0$, and w gradually returns to rest on the lower branch.

Applied current and oscillations

When a current is applied to the generalized FitzHugh-Nagumo equations, they become

$$\epsilon\frac{dv}{dt} = f(v, w) + I_{\text{app}}, \tag{5.57}$$

$$\frac{dw}{dt} = g(v, w). \tag{5.58}$$

As with the fast-slow phase plane of the Hodgkin–Huxley equations, the cubic null-cline moves up as I_{app} increases. Thus, when I_{app} takes values in some intermediate range, the steady state lies on the middle branch, $V_0(w)$, and is unstable. Instead of returning to rest after one excursion on the excited branch, the trajectory alternates periodically between the upper and lower branches, with w varying between W_* and W^* (Fig. 5.16). This limit cycle behavior, where there are fast jumps between regions in which the solution moves more slowly, is called a *relaxation oscillation*. In this figure, the relaxation nature of the oscillations is not very pronounced; however, as ϵ decreases, the jumps become steeper, and less time consuming. For small ϵ, the period of the oscillation is approximately

$$T = \int_{W_*}^{W^*} \left(\frac{1}{G_+(w)} - \frac{1}{G_-(w)} \right) dw. \tag{5.59}$$

Figure 5.16: Phase portrait for the FitzHugh–Nagumo equations, (5.38)-(5.40), with $\alpha = 0.1$, $\gamma = 0.5$, $\epsilon = 0.01$ and $I_{\mathrm{app}} = 0.5$. For these parameter values, the unique rest point is unstable and there is a globally stable periodic orbit. The inset at top right shows the periodic orbit plotted against time.
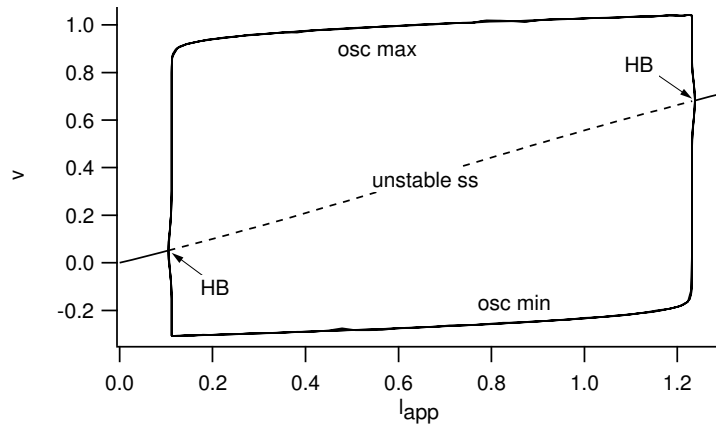
Figure 5.17: Bifurcation diagram of the FitzHugh–Nagumo equations, (5.38)-(5.40), with $\alpha = 0.1$, $\gamma = 0.5$, $\epsilon = 0.01$, with the applied current as the bifurcation parameter. ss denotes a steady state solution, while osc max and osc min denote, respectively, the maximum and minimum of v over an oscillation. HB denotes a Hopf bifurcation point.

This number is finite because $G_+(w) > 0$, and $G_-(w) < 0$ for all appropriate w.

As with the Hodgkin–Huxley equations, the behavior of the periodic orbits as I_{app} varies can be summarized in a bifurcation diagram. For each value of I_{app} we plot the value of v at the steady state, and (where appropriate) the maximum and minimum values of v over a periodic orbit. As I_{app} increases, a branch of periodic orbits appears in a Hopf bifurcation at $I_{\text{app}} = 0.1$ and disappears again in another Hopf bifurcation at $I_{\text{app}} = 1.24$. Between these two points there is a branch of stable periodic orbits. The bifurcation diagram is shown in Fig. 5.17.

Exercises

1. Show that, if $k > 1$, then $(1 - e^{-x})^k$ has an inflection point, but $(e^{-x})^k$ does not.

2. Explain why replacing the extracellular Na^+ with choline has little effect on the resting potential of an axon. Calculate the new resting potential with 90% of the extracellular Na^+ removed. Why is the same not true if K^+ is replaced? (Assume the conductances are constant.)

3. Plot the nullclines of the Hodgkin–Huxley fast subsystem. Show that v_r and v_e in the Hodgkin–Huxley fast subsystem are stable steady states, while v_s is a saddle point. Compute the stable manifold of the saddle point and compute sample trajectories in the fast phase plane, demonstrating the threshold effect.

4. Show how the Hodgkin–Huxley fast subsystem depends on the slow variables; i.e., show how the v nullcline moves as n and h are changed, and demonstrate the saddle-node bifurcation in which v_e and v_s disappear.

5. Plot the nullclines of the fast–slow Hodgkin–Huxley phase plane and compute a complete action potential.

6. How does the phase plane of the fast-slow Hodgkin–Huxley equations change with applied current? How much applied current in the fast-slow Hodgkin–Huxley equations is needed to generate oscillations? Plot a typical oscillation in the phase plane. Plot the maximum of the oscillation against the applied current to construct a bifurcation diagram.

7. Suppose that in the Hodgkin–Huxley fast–slow phase plane, v is slowly decreased to $v^* < v_0$ (where v_0 is the steady state), held there for a considerable time, and then released. Describe what happens in qualitative terms, i.e., without actually computing the solution. This is called *anode break excitation* (Hodgkin and Huxley, 1952d. Also see Peskin, 1991). What happens if v is instantaneously decreased to v^* and then released immediately? Why do these two solutions differ?

8. In the text, the Hodgkin–Huxley equations are written in terms of $v = V - V_{\text{eq}}$. Show that in terms of V the equations are

$$C_m \frac{dV}{dt} \;=\; -\bar{g}_K n^4 (V - V_K) - \bar{g}_{Na} m^3 h (V - V_{Na})$$

$$-\bar{g}_{\mathrm{L}}(V - V_{\mathrm{L}}) + I_{\mathrm{app}}, \tag{5.60}$$

$$\frac{dm}{dt} = \alpha_m(1 - m) - \beta_m m, \tag{5.61}$$

$$\frac{dn}{dt} = \alpha_n(1 - n) - \beta_n n, \tag{5.62}$$

$$\frac{dh}{dt} = \alpha_h(1 - h) - \beta_h h, \tag{5.63}$$

where (in units of $(\mathrm{ms})^{-1}$),

$$\alpha_m = 0.1 \frac{-40 - V}{\exp\left(\frac{-40 - V}{10}\right) - 1}, \tag{5.64}$$

$$\beta_m = 4 \exp\left(\frac{-V - 65}{18}\right), \tag{5.65}$$

$$\alpha_h = 0.07 \exp\left(\frac{-V - 65}{20}\right), \tag{5.66}$$

$$\beta_h = \frac{1}{\exp(\frac{-35 - V}{10}) + 1}, \tag{5.67}$$

$$\alpha_n = 0.01 \frac{-55 - V}{\exp(\frac{-55 - V}{10}) - 1}, \tag{5.68}$$

$$\beta_n = 0.125 \exp\left(\frac{-V - 65}{80}\right), \tag{5.69}$$

and

$$\bar{g}_{\mathrm{Na}} = 120, \qquad \bar{g}_{\mathrm{K}} = 36, \qquad \bar{g}_{\mathrm{L}} = 0.3, \tag{5.70}$$

$$V_{Na} = 55, \qquad V_K = -77, \qquad V_L = -54.4, \qquad V_{\mathrm{eq}} = -65. \tag{5.71}$$

9. Solve the full Hodgkin–Huxley system numerically with a variety of constant current inputs. For what range of inputs are there self-sustained oscillations? Construct the bifurcation diagram as in Exercise 6.

10. The Hodgkin–Huxley equations are for the squid axon at 6.3°C. Using that the absolute temperature enters the equations through the Nernst equation, determine how changes in temperature affect the behavior of the equations. In particular, simulate the equations at 0°C and 30°C to determine whether the equations become more or less excitable with an increase in temperature.

11. Show that a Hopf bifurcation occurs in the generalized FitzHugh–Nagumo model when $f_v(v^*, w^*) = -\epsilon g_w(v^*, w^*)$, assuming that

$$f_v(v^*, w^*)g_w(v^*, w^*) - g_v(v^*, w^*)f_w(v^*, w^*) > 0.$$

On which side of the minimum of the v nullcline can this condition be satisfied?

C_m = 20 μF/cm^2	I_{app} = 0.06 mA/cm^2
g_{Ca} = 4.4 mS/cm^2	g_{K} = 8 mS/cm^2
g_{L} = 2 mS/cm^2	ϕ = 0.04 (ms)$^{-1}$
V_1 = -1.2 mV	V_2 = 18 mV
V_3 = 2	V_4 = 30 mV
V_{Ca}^0 = 120 mV	V_{K}^0 = -84 mV
V_{L} = -60 mV	

Table 5.1: Typical parameter values for the Morris–Lecar model.

12. Morris and Lecar (1981) proposed the following two-variable model of membrane potential for a barnacle muscle fiber:

$$C_m \frac{dV}{dT} + I_{\text{ion}}(V, W) = I_{\text{app}}, \tag{5.72}$$

$$\frac{dW}{dT} = \phi \Lambda(V)[W_\infty(V) - W], \tag{5.73}$$

where V = membrane potential, W = fraction of open K$^+$ channels, T = time, C_m = membrane capacitance, I_{app} = externally applied current, ϕ = maximum rate for closing K$^+$ channels, and

$$I_{\text{ion}}(V, W) = g_{\text{Ca}} M_\infty(V)(V - V_{\text{Ca}}^0) + g_{\text{K}} W (V - V_{\text{K}}^0) + g_{\text{L}}(V - V_{\text{L}}^0) \tag{5.74}$$

$$M_\infty(V) = \frac{1}{2}\left(1 + \tanh\left(\frac{V - V_1}{V_2}\right)\right), \tag{5.75}$$

$$W_\infty(V) = \frac{1}{2}\left(1 + \tanh\left(\frac{V - V_3}{V_4}\right)\right), \tag{5.76}$$

$$\Lambda(V) = \cosh\left(\frac{V - V_3}{2V_4}\right). \tag{5.77}$$

Typical rate constants in these equations are shown in Table 5.1.

(a) Make a phase portrait for the Morris–Lecar equations. Plot the nullclines and show some typical trajectories, demonstrating that the model is excitable.

(b) Does the Morris–Lecar model exhibit anode break excitation (see Exercise 7)? If not, why not?

13. The Pushchino model is a piecewise linear model of FitzHugh–Nagumo type proposed as a model for the ventricular action potential. The model has

$$f(v, w) = F(v) - w, \tag{5.78}$$

$$g(v, w) = \frac{1}{\tau(v)}(v - w), \tag{5.79}$$
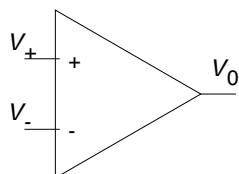
Figure 5.18: Diagram for an operational amplifier (op-amp).

where

$$F(v) = \begin{cases} -30v, & \text{for } v < v_1, \\ \gamma v - 0.12, & \text{for } v_1 < v < v_2, \\ -30(v-1), & \text{for } v > v_2, \end{cases} \tag{5.80}$$

$$\tau(v) = \begin{cases} 2, & \text{for } v < v_1, \\ 16.6, & \text{for } v > v_1, \end{cases} \tag{5.81}$$

with $v_1 = 0.12/(30+\gamma)$ and $v_2 = 30.12/(30+\gamma)$.

Simulate the action potential for this model. What is the effect on the action potential of changing $\tau(v)$?

14. Perhaps the most important example of a nonphysiological excitable system is the Belousov–Zhabotinsky reaction. This reaction denotes the oxidation of malonic acid by bromate in acidic solution in the presence of a transition metal ion catalyst. Kinetic equations describing this reaction are (Tyson and Fife, 1980)

$$\epsilon \frac{du}{dt} = -fv\frac{u-q}{u+q} + u - u^2, \tag{5.82}$$

$$\frac{dv}{dt} = u - v, \tag{5.83}$$

where u denotes the concentration of bromous acid and v denotes the concentration of the oxidized catalyst metal. Typical values for parameters are $\epsilon \approx 0.01, f = 1, q \approx 10^{-4}$. Describe the phase portrait for this system of equations.

15. It is not particularly difficult to build an electrical analogue of the FitzHugh–Nagumo equations with inexpensive and easily obtained electronic components. The parts list for one "cell" (shown in Fig. 5.20) includes two op-amps (operational amplifiers), two power supplies, a few resistors, and two capacitors, all readily available from any consumer electronics store (Keener, 1983).

The key component is an operational amplifier (Fig. 5.18). An op-amp is denoted in a circuit diagram by a triangle with two inputs on the left and a single output from the vertex on the right. Only three circuit connections are shown on a diagram, but two more are assumed, being necessary to connect
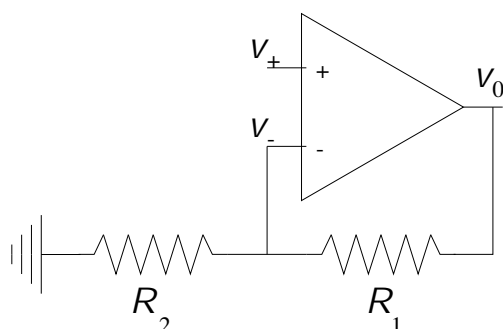
Figure 5.19: Linear amplifier using an op-amp.

with the power supply to operate the op-amp. Corresponding to the supply voltages V_{s-} and V_{s+}, there are voltages V_{r-} and V_{r+}, called the *rail voltages*, which determine the operational range for the output of an op-amp. The job of an op-amp is to compare the two input voltages v_+ and v_-, and if $v_+ > v_-$, to set (if possible) the output voltage v_0 to the high rail voltage V_{r+}, whereas if $v_+ < v_-$, then v_0 is set to V_{r-}. With reliable electronic components it is a good first approximation to assume that the input draws no current, while the output v_0 can supply whatever current is necessary to maintain the required voltage level.

The response of an op-amp to changes in input is not instantaneous, but is described reasonably well by the differential equation

$$\epsilon_s \frac{dv_0}{dt} = g(v_+ - v_-) - v_0. \tag{5.84}$$

The function $g(v)$ is continuous, but quite close to the piecewise constant function

$$g(v) = V_{r+}H(v) + V_{r-}H(-v), \tag{5.85}$$

with $H(v)$ the Heaviside function. The number ϵ_s is small, and is the inverse of the *slew-rate*, which is typically on the order of 10^6–10^7 V/sec. For all of the following circuit analysis, take $\epsilon_s \to 0$.

(a) Show that the simple circuit shown in Fig. 5.19 is a linear amplifier, with

$$v_0 = \frac{R_1 + R_2}{R_2}v_+, \tag{5.86}$$

provided that v_0 is within the range of the rail voltages.

(b) Show that if $R_1 = 0, R_2 = \infty$, then the device in Fig. 5.19 becomes a *voltage follower* with $v_0 = v_+$.

(c) Find the governing equations for the circuit in Fig. 5.20, assuming that the rail voltages for op-amp 2 are well within the range of the rail voltages for op-amp 1.
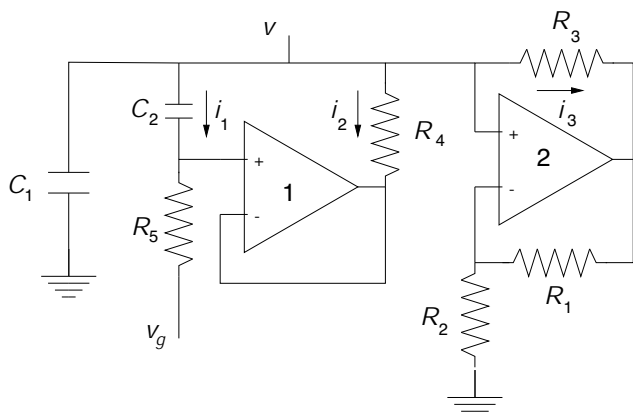
Figure 5.20: FitzHugh–Nagumo circuit using op-amps.

Table 5.2: Parts list for the FitzHugh–Nagumo analog circuit.

2 LM 741 op-amps (National Semiconductor)	
$R_1 = R_2 = 100\text{k}\Omega$	$R_3 = 2.4\Omega$
$R_4 = 1\text{k}\Omega$	$R_5 = 10\text{k}\Omega$
$C_1 = 0.01\mu\text{F}$	$C_2 = 0.5\mu\text{F}$
Power supplies:	
$\pm 15\text{V}$ for op-amp #1	$\pm 12\text{V}$ for op-amp #2

Show that

$$C_1 \frac{dv}{dt} + i_2\left(1 - \frac{R_4}{R_5}\right) + \frac{F(v)}{R_3} + \frac{v - v_g}{R_5} = 0, \qquad (5.87)$$

$$C_2 R_5 \frac{di_2}{dt} + R_4 i_2 = v - v_g, \qquad (5.88)$$

where $F(v)$ is the piecewise linear function

$$F(v) = \begin{cases} v - V_{r_+}, & \text{for } v > \alpha V_{r_+}, \\ -\frac{R_1}{R_2}v, & \text{for } \alpha V_{r_-} \le v \le \alpha V_{r_+}, \\ v - V_{r_-}, & \text{for } v < \alpha V_{r_-}, \end{cases} \qquad (5.89)$$

and $\alpha = \frac{R_2}{R_1 + R_2}$.

(d) Sketch the phase portrait for these circuit equations. Show that this is a piecewise linear FitzHugh–Nagumo system.

(e) Use the singular perturbation approximation (5.59) to estimate the period of oscillation for the piecewise linear analog FitzHugh–Nagumo circuit in Fig. 5.20.

Chapter 6

Wave Propagation in Excitable Systems

The problem of current flow in the axon of a nerve is much more complicated than that of flow in dendritic networks (Chapter 4). Recall from Chapter 5 that the voltage dependence of the ionic currents can lead to excitability and action potentials. In this chapter we show that when an excitable membrane is incorporated into a *nonlinear* cable equation, it can give rise to traveling waves of electrical excitation. Indeed, this property is one of the reasons that the Hodgkin–Huxley model is so important. In addition to producing a realistic description of a space-clamped action potential, Hodgkin and Huxley showed that this action potential propagates along an axon with a fixed speed, which could be calculated.

However, the nerve axon is but one of many examples of a spatially extended excitable system in which there is propagated activity. For example, propagated waves of electrical or chemical activity are known to occur in skeletal and cardiac tissue, in the retina, and in the cortex of the brain. In this chapter we describe this wave activity, beginning with a discussion of propagated electrical activity along one dimensional cables, then concluding with a brief discussion of waves in higher dimensional excitable systems.

6.1   Brief Overview of Wave Propagation

There is a vast literature on wave propagation in biological systems. In addition to the books by Murray (2002), Britton (1986), and Grindrod (1991), there are numerous articles in journals and books, many of which are cited in this chapter.

There are many different kinds of waves in biological systems. For example, there are waves in excitable systems that arise from the underlying excitability of the cell. An excitable wave acts as a model for, among other things, the propagation of an action potential along the axon of a nerve or the propagation of a grass fire on a prairie. However, if the underlying kinetics are oscillatory but not excitable, and a large number of individual oscillatory units are coupled by diffusion, the resulting behavior is oscillatory waves and periodic wave trains. In this chapter we focus

A   **B**
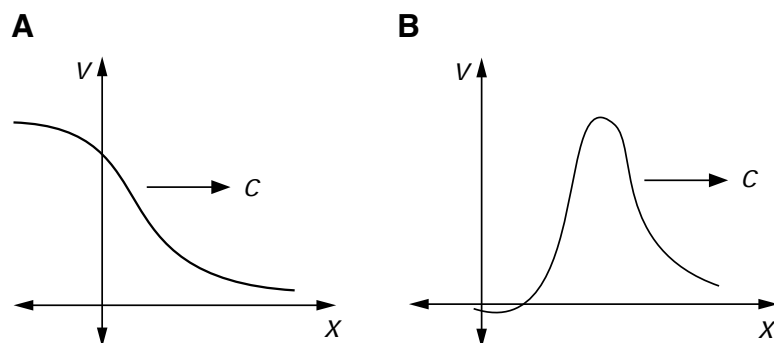
Figure 6.1: Schematic diagram of A: Traveling front, B: Traveling pulse.

our attention on waves in excitable media, and defer consideration of the theory of coupled oscillators to Chapters 12 and 18.

We emphasize at the outset that by a *traveling wave* we mean a solution of a partial differential equation on an infinite domain (a fictional object, of course) that travels at constant velocity with fixed shape. It is also helpful to make a distinction between the two most important types of traveling waves in excitable systems. First, there is the wave that looks like a moving plateau, or transition between different levels. If v denotes the wave variable, then ahead of the wave, v is steady at some low value, and behind the wave, v is steady at a higher value (Fig. 6.1A). Such waves are called *traveling fronts*. The second type of wave begins and ends at the same value of v (Fig. 6.1B) and resembles a moving bump. This type of wave is called a *traveling pulse*.

These two wave types can be interpreted in the terminology of the Hodgkin–Huxley fast–slow phase plane discussed in Chapter 5. When the recovery variable is fixed at the steady state, the fast–slow phase plane has two stable steady states, $v = v_r$ and $v = v_e$ (i.e., it is bistable). Under appropriate conditions there exists a traveling front with $v = v_r$ ahead of the wave and $v = v_e$ behind the wave. Thus, the traveling front acts like a zipper, switching the domain from the resting to the excited state. However, if the recovery variable n is allowed to vary, the solution is eventually forced to return to the resting state and the traveling solution becomes a traveling pulse. The primary difference between the traveling front and the traveling pulse is that in the former case there is no recovery (or recovery is static), while in the latter case there is.

One of the simplest models for biological wave propagation is Fisher's equation. Although this equation is used extensively in population biology and ecology, it is much less relevant in a physiological context, and so is not discussed here (see Exercises 14 and Fife, 1979).

The next level of complexity is the *bistable equation*. The bistable equation is so named because it has two stable rest points, and it is related to the FitzHugh–Nagumo model without recovery. For the bistable equation, one expects to find traveling fronts but not traveling pulses. Inclusion of the recovery variable leads to a more complex model, the spatially distributed FitzHugh–Nagumo model, for

which one expects to find traveling pulses (among other types of waves). Wave propagation in the FitzHugh–Nagumo model is still not completely understood, especially in higher-dimensional domains. At the highest level of complexity are the spatially distributed models of Hodgkin–Huxley type, systems of equations that are resistant to analytical approaches.

6.2 Traveling Fronts

6.2.1 The Bistable Equation

The bistable equation is a specific version of the cable equation (4.18), namely

$$\frac{\partial V}{\partial t} = \frac{\partial^2 V}{\partial x^2} + f(V), \tag{6.1}$$

where $f(V)$ has three zeros at $0, \alpha$, and 1, where $0 < \alpha < 1$. The values $V = 0$ and $V = 1$ are stable steady solutions of the ordinary differential equation $dV/dt = f(V)$. Notice that the variable V has been scaled so that 0 and 1 are zeros of $f(V)$. In the standard nondimensional form, $f'(0) = -1$. (Recall from (4.13) that the passive cable resistance was defined so that the ionic current has slope 1 at rest.) However, this restriction on $f(V)$ is often ignored.

An example of such a function can be found in the Hodgkin–Huxley fast–slow phase plane. When the recovery variable n is held fixed at its steady state, the Hodgkin–Huxley fast–slow model is bistable. Two other examples of functions that are often used in this context are the cubic polynomial

$$f(V) = aV(V - 1)(\alpha - V), \qquad 0 < \alpha < 1, \tag{6.2}$$

and the piecewise-linear function

$$f(V) = -V + H(V - \alpha), \qquad 0 < \alpha < 1. \tag{6.3}$$

where $H(V)$ is the Heaviside function (Mckean, 1970). This piecewise-linear function is not continuous, nor does it have three zeros, yet it is useful in the study of traveling wave solutions of the bistable equation because it is an analytically tractable model that retains many important qualitative features.

By a traveling wave solution, we mean a translation-invariant solution of (6.1) that provides a transition between the two stable rest states (zeros of the nonlinear function $f(V)$) and travels with constant speed. That is, we seek a solution of (6.1) of the form

$$V(x, t) = U(x + ct) = U(\xi) \tag{6.4}$$

for some (yet to be determined) value of c. The new variable ξ, called the traveling wave coordinate, has the property that fixed values move in space–time with fixed speed c. When written as a function of ξ, the wave appears stationary. Note that, because we use $\xi = x + ct$ as the traveling wave coordinate, a solution with c positive corresponds to a wave moving from right to left. We could equally well have used $x - ct$ as the traveling wave coordinate, to obtain waves moving from left to right (for positive c).

By substituting (6.4) into (6.1) it can be seen that any traveling wave solution must satisfy

$$U_{\xi\xi} - cU_\xi + f(U) = 0, \tag{6.5}$$

and this, being an ordinary differential equation, should be easier to analyze than the original partial differential equation. For $U(\xi)$ to provide a transition between rest points, it must be that $f(U(\xi)) \to 0$ as $\xi \to \pm\infty$.

To study (6.5) it is convenient to write it as two first order equations,

$$U_\xi = W, \tag{6.6}$$
$$W_\xi = cW - f(U). \tag{6.7}$$

To find traveling front solutions for the bistable equation, we look for a solution of (6.6) and (6.7) that connects the rest points $(U, W) = (0, 0)$ and $(U, W) = (1, 0)$ in the (U, W) phase plane. Such a trajectory, connecting two different steady states, is called a heteroclinic trajectory, and in this case is parameterized by ξ; the trajectory approaches $(0, 0)$ as $\xi \to -\infty$ and approaches $(1, 0)$ as $\xi \to +\infty$ (see the dashed line in Fig. 6.2A). The steady states at $U = 0$ and $U = 1$ are both saddle points, while for the steady state $U = \alpha$, the real part of both eigenvalues have the same sign, negative if c is positive and positive if c is negative, so that this is a node or a spiral point. Since the points at $U = 0$ and $U = 1$ are saddle points, the goal is to determine whether the parameter c can be chosen so that the trajectory that leaves $U = 0$ at $\xi = -\infty$ connects with the saddle point $U = 1$ at $\xi = +\infty$. This mathematical procedure is called *shooting*, and some sample trajectories are shown in Fig. 6.2A.

First, we can determine the sign of c. Supposing a monotone increasing $(U_\xi > 0)$ connecting trajectory exists, we multiply (6.5) by U_ξ and integrate from $\xi = -\infty$ to $\xi = \infty$ with the result that

$$c \int_{-\infty}^{\infty} W^2 d\xi = \int_0^1 f(u)du. \tag{6.8}$$

In other words, if a traveling wave solution exists, then the sign of c is the same as the sign of the area under the curve $f(u)$ between $u = 0$ and $u = 1$. If this area is positive, then the traveling solutions move the state variable U from $U = 0$ to $U = 1$, and the state at $U = 1$ is said to be *dominant*. In both of the special cases (6.2) and (6.3), the state $U = 1$ is dominant if $\alpha < 1/2$.

Suppose $\int_0^1 f(u)du > 0$. We want to determine what happens to the unstable trajectory that leaves the saddle point $U = 0, U_\xi = 0$ for different values of c. With $c = 0$, an explicit expression for this trajectory is found by multiplying (6.5) by U_ξ and integrating to get

$$\frac{W^2}{2} + \int_0^U f(u)du = 0. \tag{6.9}$$

If this trajectory were to reach $U = 1$ for some value of W, then

$$\frac{W^2}{2} + \int_0^1 f(u)du = 0, \tag{6.10}$$
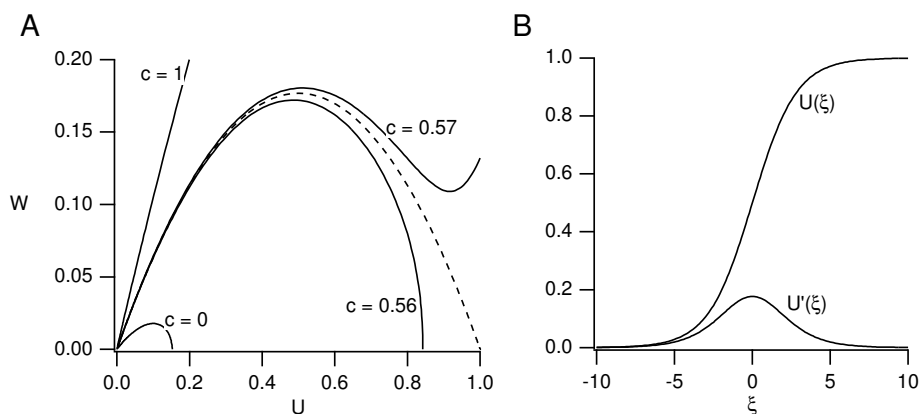
Figure 6.2: A: Trajectories in the (U, W) phase plane leaving the rest point $U = 0$, $W = 0$ for the equation $U_{\xi\xi} - cU_\xi + U(U - 0.1)(1 - U) = 0$, with $c = 0.0$, 0.56, 0.57, and 1.0. Dashed curve shows the connecting heteroclinic trajectory. B: Profile of the traveling wave solution of panel A. In the original coordinates, this front moves to the left with speed c.

which can occur only if $\int_0^1 f(u)du \le 0$. Since this contradicts our assumption that $\int_0^1 f(u)du \ge 0$, we conclude that this trajectory cannot reach $U = 1$. Neither can this trajectory remain in the first quadrant, as $W > 0$ implies that U is increasing. Thus, this trajectory must intersect the $W = 0$ axis at some value of $U < 1$ (Fig. 6.2A). It cannot be the connecting trajectory.

Next, suppose c is large. In the (U, W) phase plane, the slope of the unstable trajectory leaving the rest point at $U = 0$ is the positive root of $\lambda^2 - c\lambda + f'(0) = 0$, which is always larger than c (Exercise 1). Let K be the smallest positive number for which $f(u)/u \le K$ for all u on the interval $0 < u \le 1$ (Exercise: How do we know K exists?), and let σ be any fixed positive number. On the line $W = \sigma U$ the slope of trajectories satisfies

$$\frac{dW}{dU} = c - \frac{f(U)}{W} = c - \frac{f(U)}{\sigma U} \ge c - \frac{K}{\sigma}. \tag{6.11}$$

By picking c large enough, we are assured that $c - K/\sigma > \sigma$, so that once trajectories are above the line $W = \sigma U$, they stay above it. We know that for large enough c, the trajectory leaving the saddle point $U = 0$ starts out above this curve. Thus, this trajectory always stays above the line $W = \sigma U$, and therefore passes above the rest point at $(U, W) = (1, 0)$.

Now we have two trajectories, one with $c = 0$, which misses the rest point at $U = 1$ by crossing the $W = 0$ axis at some point $U < 1$, and one with c large, which misses this rest point by staying above it at $U = 1$. Since trajectories depend continuously on the parameters of the problem, there is a continuous family of trajectories depending on the parameter c between these two special trajectories, and therefore there is at least one trajectory that hits the point $U = 1, W = 0$ exactly.

The value of c for which this heteroclinic connection occurs is unique. To verify this, notice from (6.11) that the slope dW/dU of trajectories in the (U, W) plane is a monotone increasing function of the parameter c. Suppose at some value of $c = c_0$ there is known to be a connecting trajectory. For any value of c that is larger than c_0, the trajectory leaving the saddle point at $U = 0$ must lie above the connecting curve for c_0. For the same reason, with $c > c_0$, the trajectory approaching the saddle point at $U = 1$ as $\xi \to \infty$ must lie below the connecting curve with $c = c_0$. A single curve cannot simultaneously lie above and below another curve, so there cannot be a connecting trajectory for $c > c_0$. By a similar argument, there cannot be a connecting trajectory for a smaller value of c, so the value c_0, and hence the connecting trajectory, is unique.

For most functions $f(V)$, it is necessary to calculate the speed of propagation of the traveling front solution numerically. However, in the two special cases (6.2) and (6.3) the speed of propagation can be calculated explicitly. In the piecewise linear case (6.3) one calculates directly that

$$c = \frac{1 - 2\alpha}{\sqrt{\alpha - \alpha^2}} \tag{6.12}$$

(see Exercise 4).

Suppose $f(u)$ is the cubic polynomial

$$f(u) = -A^2(u - u_0)(u - u_1)(u - u_2), \tag{6.13}$$

where the zeros of the cubic are ordered $u_0 < u_1 < u_2$. We want to find a heteroclinic connection between the smallest zero u_0, and the largest zero u_2, so we guess that

$$W = -B(U - u_0)(U - u_2). \tag{6.14}$$

We substitute this guess into the governing equation (6.5), and find that we must have

$$B^2(2U - u_0 - u_2) - cB - A^2(U - u_1) = 0. \tag{6.15}$$

This is a linear function of U that can be made identically zero only if we choose $B = A/\sqrt{2}$ and

$$c = \frac{A}{\sqrt{2}}(u_2 - 2u_1 + u_0). \tag{6.16}$$

It follows from (6.14) that

$$U(\xi) = \frac{u_0 + u_2}{2} + \frac{u_2 - u_0}{2} \tanh\left(\frac{A}{\sqrt{2}} \frac{u_2 - u_0}{2} \xi\right), \tag{6.17}$$

which is independent of u_1. In the case that $u_0 = 0, u_1 = \alpha$, and $u_2 = 1$, the speed reduces to

$$c = \frac{A}{\sqrt{2}}(1 - 2\alpha), \tag{6.18}$$

showing that the speed is a decreasing function of α and the direction of propagation changes at $\alpha = 1/2$. The profile of the traveling wave in this case is

$$U(\xi) = \frac{1}{2}\left[1 + \tanh\left(\frac{A}{2\sqrt{2}}\xi\right)\right]. \tag{6.19}$$

A plot of this traveling wave profile is shown in Fig. 6.2B.

Once the solution of the nondimensional cable equation (6.1) is known, it is a simple matter to express the solution in terms of physical parameters as

$$V(x,t) = U\left(\frac{x}{\lambda_m} + c\frac{t}{\tau_m}\right), \tag{6.20}$$

where λ_m and τ_m are, respectively, the space and time constants of the cable, as described in Chapter 4. The speed of the traveling wave is

$$s = \frac{c\lambda_m}{\tau_m} = \frac{c}{2C_m}\sqrt{\frac{d}{R_m R_c}}, \tag{6.21}$$

which shows how the wave speed depends on capacitance, membrane resistance, cytoplasmic resistance, and axonal diameter. The dependence of the speed on ionic channel conductances is contained (but hidden) in c. According to empirical measurements, a good estimate of the speed for an axon is given by

$$s = \sqrt{\frac{d}{10^{-6}\mathrm{m}}} \ \mathrm{m/sec}. \tag{6.22}$$

Using $d = 500$ μm for squid axon, this estimate gives $s = 22.4$ mm/ms, which compares favorably to the measured value of $s = 21.2$ mm/ms.

Scaling arguments can also be used to find the dependence of speed on certain other parameters. Suppose, for example, that a drug is applied to the membrane that blocks a percentage of all ion channels, irrespective of type. If ρ is the fraction of remaining operational channels, then the speed of propagation is reduced by the factor $\sqrt{\rho}$. This follows directly by noting that the bistable equation with reduced ion channels

$$V'' - sV' + \rho f(V) = 0 \tag{6.23}$$

can be related to the original bistable equation (6.5) by taking $V(\xi) = U(\sqrt{\rho}\xi)$, $s = c\sqrt{\rho}$.

Thresholds and stability

There are many other features of the bistable equation, the details of which are beyond the scope of this book. Perhaps the most important of these features is that solutions of the bistable equation satisfy a comparison property: any two solutions of the bistable equation, say $u_1(x,t)$ and $u_2(x,t)$, that are ordered with $u_1(x,t_0) \leq u_2(x,t_0)$ at some time $t = t_0$ remain ordered for all subsequent times, i.e., $u_1(x,t) \leq u_2(x,t)$ for $t \geq t_0$.

With comparison arguments it is possible to prove a number of additional facts (Aronson and Weinberger, 1975). For example, the bistable equation exhibits threshold behavior. Specifically, if initial data are sufficiently small, then the solution of the bistable equation approaches zero in the limit $t \to \infty$. However, there are initial functions with compact support lying between 0 and 1 for which the solution approaches 1 in the limit $t \to \infty$. Because of the comparison theorem any

Tissue	Channel density (channels/μm^2)
Mammalian	
Vagus nerve (nonmyelinated)	110
Node of Ranvier	2100
Skeletal muscle	205–560
Other animals	
Squid giant axon	166–533
Frog sartorius muscle	280
Electric eel electroplax	550
Garfish olfactory nerve	35
Lobster walking leg nerve	90

Table 6.1: Sodium channel densities in selected excitable tissues.

larger initial function also initiates a solution that approaches 1 in the limit $t \to \infty$. Such initial data are said to be *superthreshold*.

Furthermore, the traveling wave solution of the bistable equation is stable in a very strong way (Fife, 1979; Fife and McLeod, 1977), as follows. Starting from any initial data that lie between 0 and α in the limit $x \to -\infty$ and between α and 1 in the limit $x \to \infty$, the solution approaches some phase shift of the traveling wave solution in the limit of large time.

6.2.2   Myelination

Most nerve fibers are coated with a lipid material called *myelin* with periodic gaps of exposure called *nodes of Ranvier*. The myelin sheath consists of a single cell, called a *Schwann cell*, which is wrapped many times (roughly 100 times) around the axonal membrane. This wrapping of the axon increases the effective membrane resistance by a factor of about 100 and decreases the membrane capacitance by a factor of about 100. Indeed, rough data are that R_m is 10^3 Ω cm^2 for cell membrane and 10^5 Ω cm^2 for myelin sheath, and that C_m is 10^{-6} μF/cm^2 for cell membrane and 10^{-8} μF/cm^2 for a myelinated fiber. The length of myelin sheath is typically 1 to 2 mm (close to 100 d, where d is the fiber diameter), and the width of the gap is about 1 μm.

Propagation along myelinated fiber is faster than along nonmyelinated fiber. This is presumably caused by the fact that there is little transmembrane ionic current and little capacitive current in the myelinated section, allowing the axon to act as a simple resistor. An action potential does not propagate along the myelinated fiber but rather jumps from node-to-node. This node-to-node propagation is said to be *saltatory* (from the Latin word *saltare*, to leap or dance).
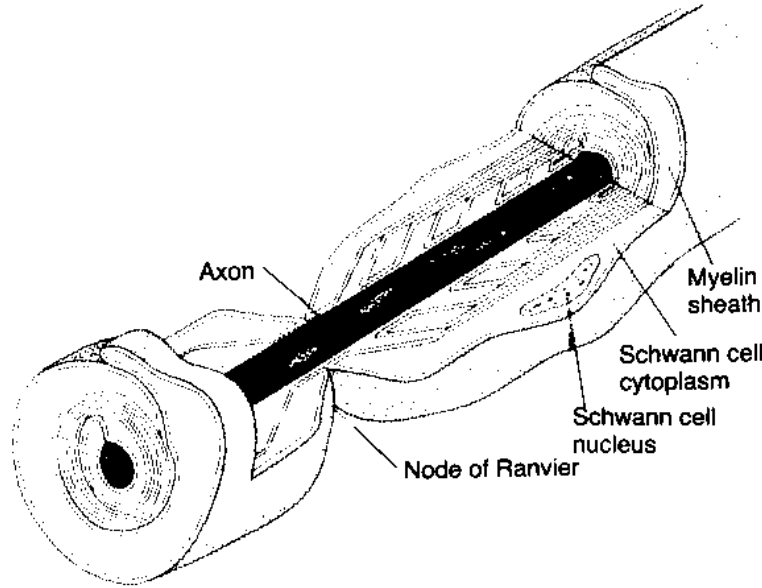
Figure 6.3: Schematic diagram of the myelin sheath. (Guyton and Hall, 1996, Fig. 5-16, p. 69.)

The pathophysiological condition of nerve cells in which damage of the myelin sheath impairs nerve impulse transmission in the central nervous system is called *multiple sclerosis* (MS). MS is an autoimmune disease that usually affects young adults between the ages of 18 and 40, occurring slightly more often in females than males. With MS, there is an immune response to the white matter of the brain and spinal cord, causing demyelination of nerve fibers at various locations throughout the central nervous system, although the underlying nerve axons and cell bodies are not usually damaged. The loss of myelin slows or stops the transmission of action potentials, with the resultant symptoms of muscle fatigue and weakness or extreme "heaviness."

To model the electrical activity in a myelinated fiber we assume that the capacitive and transmembrane ionic currents are negligible, so that along the myelin sheath the axial currents

$$I_e = -\frac{1}{r_e}\frac{\partial V_e}{\partial x}, \qquad I_i = -\frac{1}{r_i}\frac{\partial V_i}{\partial x} \tag{6.24}$$

are constant (using the same notation as in Chapter 4). We also assume that V does not vary within each node of Ranvier (i.e., that the nodes are isopotential), and that V_n is the voltage at the nth node. Then the axial currents between node n and node $n + 1$ are

$$I_e = -\frac{1}{Lr_e}(V_{e,n+1} - V_{e,n}), \qquad I_i = -\frac{1}{Lr_i}(V_{i,n+1} - V_{i,n}), \tag{6.25}$$

where L is the length of the myelin sheath between nodes. The total transmembrane current at a node is given by

$$\mu p \left(C_m \frac{\partial V_n}{\partial t} + I_{\text{ion}} \right) = I_{i,n} - I_{i,n+1}$$

$$= \frac{1}{L(r_i + r_e)}(V_{n+1} - 2V_n + V_{n-1}), \qquad (6.26)$$

where μ is the length of the node.

We can introduce dimensionless time $\tau = \frac{t}{C_m R_m} = t/\tau_m$ (but not dimensionless space), to rewrite (6.26) as

$$\frac{dV_n}{d\tau} = f(V_n) + D(V_{n+1} - 2V_n + V_{n-1}), \qquad (6.27)$$

where $D = \frac{R_m}{\mu L p(r_i + r_e)}$ is the coupling coefficient. We call this equation the *discrete cable equation.*

6.2.3   The Discrete Bistable Equation

The discrete bistable equation is the system of equations (6.27) where $f(V)$ has typical bistable form, as, for example, (6.2) or (6.3). The study of the discrete bistable equation is substantially more difficult than that of the continuous version (6.1). While the discrete bistable equation looks like a finite difference approximation of the continuous bistable equation, solutions of the two have significantly different behavior.

It is a highly nontrivial matter to prove that traveling wave solutions of the discrete system exist (Zinner, 1992). However, a traveling wave solution, if it exists, satisfies the special relationship $V_{n+1}(\tau) = V_n(\tau - \tau_d)$. In other words, the $(n+1)$st node experiences exactly the same time course as the nth node, with time delay τ_d. Furthermore, if $V_n(\tau) = V(\tau)$, it follows from (6.27) that $V(\tau)$ must satisfy the delay differential equation

$$\frac{dV}{d\tau} = D(V(\tau + \tau_d) - 2V(\tau) + V(\tau - \tau_d)) + f(V(\tau)). \qquad (6.28)$$

If the function $V(\tau)$ is sufficiently smooth and if τ_d is sufficiently small, then we can approximate $V(\tau + \tau_d)$ with its Taylor series $V(\tau + \tau_d) = \sum_{n=0} \frac{1}{n!} V^{(n)}(\tau)\tau_d^n$, so that (6.28) is approximated by the differential equation

$$D \left(\tau_d^2 V_{\tau\tau} + \frac{\tau_d^4}{12} V_{\tau\tau\tau\tau} \right) - V_\tau + f(V) = 0, \qquad (6.29)$$

ignoring terms of order τ_d^6 and higher.

Now we suppose that τ_d is small. The leading-order equation is

$$D\tau_d^2 V_{\tau\tau} - V_\tau + f(V) = 0, \qquad (6.30)$$

which has solution $V_0(\tau) = U(c\tau)$, provided that $D\tau_d^2 = 1/c^2$, where U is the traveling front solution of the bistable equation (6.5) and c is the dimensionless

wave speed for the continuous equation. The wave speed s is the internodal distance $L + \mu$ divided by the time delay $\tau_m \tau_d$, so that

$$s = \frac{L + \mu}{\tau_m \tau_d} = (L + \mu)c\frac{\sqrt{D}}{\tau_m}. \tag{6.31}$$

For myelinated nerve fiber we know that $D = \frac{R_m}{\mu L p(r_i + r_e)}$. If we ignore extracellular resistance, we find a leading order approximation for the velocity of

$$s = \frac{L + \mu}{\sqrt{\mu L}} \frac{c}{2C_m} \sqrt{\frac{d}{R_m R_c}}, \tag{6.32}$$

giving a change in velocity compared to nonmyelinated fiber by the factor $\frac{L+\mu}{\sqrt{\mu L}}$. With the estimates $L = 100 \, d$ and $\mu = 1 \, \mu$m, this increase in velocity is by a factor of $10\sqrt{\frac{d}{10^{-6}\text{m}}}$, which is quite substantial. Empirically it is known that the improvement of velocity for myelinated fiber compared to nonmyelinated fiber is by a factor of about $6\sqrt{\frac{d}{10^{-6}\text{m}}}$.

Higher-order approximation

We can find a higher-order approximation to the speed of propagation by using a standard regular perturbation argument. We set $\epsilon = 1/D$ and seek a solution of (6.29) of the form

$$V(\tau) = V_0(\tau) + \epsilon V_1(\tau) + \cdots, \tag{6.33}$$
$$\tau_d^2 = \frac{\epsilon}{c^2} + \epsilon^2 \tau_1 + \cdots. \tag{6.34}$$

We expand (6.29) into its powers of ϵ and set the coefficients of ϵ to zero. The first equation we obtain from this procedure is (6.30), and the second equation is

$$L[V_1] = \frac{1}{c^2}V_1'' - V_1' + f'(V_0)V_1 = -\frac{V_0''''}{12c^4} - \tau_1 V_0''. \tag{6.35}$$

Note that here we are using $L[\cdot]$ to denote a linear differential operator. The goal is to find solutions of (6.35) that are square integrable on the infinite domain, so that the solution is "close" to V_0. The linear operator $L[\cdot]$ is not an invertible operator in this space by virtue of the fact that $L[V_0'(\tau)] = 0$. (This follows by differentiating (6.30) once with respect to τ.) Thus, it follows from the Fredholm alternative theorem (Keener, 1988) that a solution of (6.35) exists if and only if the right-hand side of the equation is orthogonal to the null space of the adjoint operator L^*. Here the adjoint differential operator is

$$L^*[V] = \frac{1}{c^2}V'' + V' + f'(V_0)V, \tag{6.36}$$

and the one element of the null space (a solution of $L^*[V] = 0$) is

$$V^*(\tau) = \exp\left(-c^2\tau\right)V_0'(\tau). \tag{6.37}$$

This leads to the solvability condition

$$\tau_1 \int_{-\infty}^{\infty} \exp\left(-c^2\tau\right) V_0'(\tau)V_0''(\tau)d\tau = -\frac{1}{12c^4} \int_{-\infty}^{\infty} \exp\left(-c^2\tau\right) V_0'(\tau)V_0''''(\tau)d\tau.$$

(6.38)

As a result, τ_1 can be calculated (either analytically or numerically) by evaluating two integrals, and the speed of propagation is determined as

$$s = (L + \mu)\frac{c}{\tau_m}\sqrt{D}\left(1 - \frac{\tau_1 c^2}{2D} + O\left(\frac{c^2}{D}\right)^2\right).$$

(6.39)

This exercise is interesting from the point of view of numerical analysis, as it shows the effect of numerical discretization on the speed of propagation. This method can be applied to other numerical schemes for an equation with traveling wave solutions (Exercise 20).

Propagation failure

The most significant difference between the discrete and continuous equations is that the discrete system has a coupling threshold for propagation, while the continuous model allows for propagation at all coupling strengths. It is readily seen from (6.21) that for the continuous cable equation, continuous changes in the physical parameters lead to continuous changes in the speed of propagation, and the speed cannot be driven to zero unless the diameter is zero or the resistances or capacitance are infinite. Such is not the case for the discrete system, and propagation may fail if the coupling coefficient is too small. This is easy to understand when we realize that if the coupling strength is very weak, so that the effective internodal resistance is large, the current flow from an excited node to an unexcited node may be so small that the threshold of the unexcited node is not exceeded, and propagation cannot continue.

To study propagation failure, we seek standing (time-independent, i.e., $dV_n/d\tau = 0$) solutions of the discrete equation (6.27). The motivation for this comes from the maximum principle and comparison arguments. One can show that if two sets of initial data for the discrete bistable equation are initially ordered, the corresponding solutions remain ordered for all time. It follows that if the discrete bistable equation has a monotone increasing stationary front solution, then there cannot be a traveling wave front solution.

A standing front solution of the discrete bistable equation is a sequence $\{V_n\}$ satisfying the finite difference equation

$$0 = D(V_{n+1} - 2V_n + V_{n-1}) + f(V_n)$$

(6.40)

for all integers n, for which $V_n \to 1$ as $n \to \infty$ and $V_n \to 0$ as $n \to -\infty$.

One can show (Keener, 1987) that for any bistable function f, there is a number $D^* > 0$ such that for $D \leq D^*$, the discrete bistable equation has a standing solution, that is, propagation fails. To get a simple understanding of the behavior of this coupling threshold, we solve (6.40) in the special case of piecewise-linear dynamics

(6.3). Since the discrete equation with dynamics (6.3) is linear, the homogeneous solution can be expressed as a linear combination of powers of some number λ as

$$V_n = A\lambda^n + B\lambda^{-n}, \tag{6.41}$$

where λ is a solution of the characteristic polynomial equation

$$\lambda^2 - \left(2 + \frac{1}{D}\right)\lambda + 1 = 0. \tag{6.42}$$

Note that this implies that

$$D = \frac{\lambda}{(\lambda - 1)^2}. \tag{6.43}$$

The characteristic equation has two positive roots, one larger and one smaller than 1. Let λ be the root that is smaller than one. Then, taking the conditions at $\pm\infty$ into account, we write the solution as

$$V_n = \begin{cases} 1 + A\lambda^n, & \text{for } n \geq 0, \\ B\lambda^{-n}, & \text{for } n < 0. \end{cases} \tag{6.44}$$

This expression for V_n must also satisfy the piecewise-linear discrete bistable equation for $n = -1, 0$. Thus,

$$D(V_1 - 2V_0 + V_{-1}) = V_0 - 1, \tag{6.45}$$
$$D(V_0 - 2V_{-1} + V_{-2}) = V_{-1}, \tag{6.46}$$

where we have assumed that $V_n \geq \alpha$ for all $n \geq 0$, and $V_n < \alpha$ for all $n < 0$. Substituting in (6.43) for D, and solving for A and B, then gives $B = A + 1 = \frac{1}{1+\lambda}$.

Finally, this is a solution for all n, provided that $V_0 \geq \alpha$. Since $V_0 = B = \frac{1}{1+\lambda}$, we need $\frac{1}{1+\lambda} \geq \alpha$, or $\lambda \leq \frac{1-\alpha}{\alpha}$. However, when $\lambda < 1$, D is an increasing function of λ, and thus $\lambda \leq \frac{1-\alpha}{\alpha}$ whenever

$$D \leq D\left(\frac{1-\alpha}{\alpha}\right) = \frac{\alpha(1-\alpha)}{(2\alpha - 1)^2} = D^*. \tag{6.47}$$

In other words, there is a standing wave, precluding propagation, whenever the coupling is small, with $D \leq D^*$. Since α is a measure of the excitability of this medium, we see that when the medium is weakly excitable (α is near $1/2$), then D^* is large and very little resistance is needed to halt propagation. On the other hand, when α is small, so that the medium is highly excitable, the resistance threshold is large, and propagation is relatively difficult to stop.

6.3 Traveling Pulses

A traveling pulse (often called a *solitary pulse*) is a traveling wave solution that starts and ends at the same steady state of the governing equations. Recall that a traveling front solution corresponds to a heteroclinic trajectory in the (U, W) phase

plane, i.e., a trajectory, parameterized by ξ, that connects two different steady states of the system. A traveling pulse solution is similar, corresponding to a trajectory that begins and ends at the *same* steady state in the traveling wave coordinate system. Such trajectories are called *homoclinic orbits.*

There are three main approaches to finding traveling pulses for excitable systems. First, one can approximate the nonlinear functions with piecewise-linear functions, and then find traveling pulse solutions as exact solutions of transcendental equations. Second, one can use perturbation methods exploiting the different time scales to find approximate analytical expressions. Finally, one can use numerical simulations to solve the governing differential equations. We illustrate each of these techniques in turn.

6.3.1   The FitzHugh–Nagumo Equations

To understand the structure of a traveling pulse it is helpful first to study traveling pulse solutions in the FitzHugh–Nagumo equations

$$\epsilon\frac{\partial v}{\partial t} = \epsilon^2\frac{\partial^2 v}{\partial x^2} + f(v, w), \tag{6.48}$$

$$\frac{\partial w}{\partial t} = g(v, w), \tag{6.49}$$

where ϵ is assumed to be a small positive number. Without any loss of generality, space has been scaled so that the diffusion coefficient is ϵ^2. It is important to realize that this does not imply anything about the magnitude of the physical diffusion coefficient. This is simply a scaling of the space variable so that in the new coordinate system, the wave front appears steep, a procedure that facilitates the study of the wave as a whole. The variable v is spatially coupled with diffusion, but the variable w is not, owing to the fact that v represents the membrane potential, while w represents a slow ionic current or gating variable.

To study traveling waves, we place the system of equations (6.48)–(6.49) in a traveling coordinate frame of reference. We define the traveling wave coordinate $\xi = x - ct$, where $c > 0$ is the wave speed, yet to be determined. Note that the traveling wave variable, $\xi = x - ct$, is different from the one previously used in this chapter, $x + ct$. Hence, $c > 0$ here corresponds to a wave moving from left to right.

The partial differential equations (6.48)–(6.49) become the ordinary differential equations

$$\epsilon^2 v_{\xi\xi} + c\epsilon v_\xi + f(v, w) = 0, \tag{6.50}$$

$$cw_\xi + g(v, w) = 0. \tag{6.51}$$

A piecewise-linear model

We begin by examining the simplest case, the piecewise-linear dynamics (Rinzel and Keller, 1973)

$$f(v, w) = H(v - \alpha) - v - w, \tag{6.52}$$

$$g(v, w) = v. \tag{6.53}$$
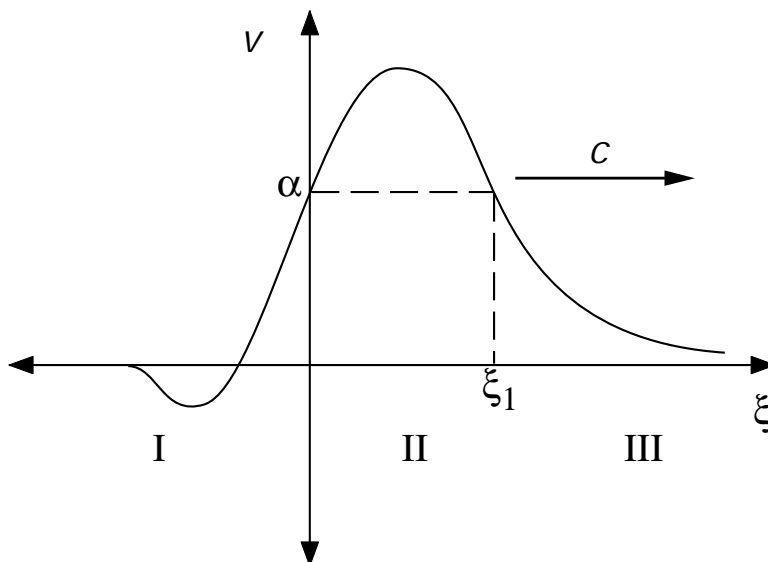
Figure 6.4: Schematic diagram of the traveling pulse.

Because the dynamics are piecewise linear, the exact solution can be constructed in a piecewise manner. We look for solutions of the form sketched in Fig. 6.4. The position of the wave along the ξ axis is specified by fixing $v(0) = v(\xi_1) = \alpha$. As yet, ξ_1 is unknown, and is to be determined as part of the solution process. Note that the places where $v = \alpha$ are those where the dynamics change (since α is the point of discontinuity of f). Let I, II, and III denote, respectively, the regions $\xi < 0$, $0 < \xi < \xi_1$, and $\xi_1 < \xi$. In each region, the differential equation is linear and so can be solved exactly. The three regional solutions are then joined at $\xi = 0$ and $\xi = \xi_1$ by stipulating that v and w be continuous at the boundaries and that v have a continuous derivative there. These constraints are sufficient to determine the solution unambiguously.

In regions I and III, $v < \alpha$, and so the differential equation is

$$\epsilon^2 v_{\xi\xi} + c\epsilon v_\xi - v - w \;=\; 0, \tag{6.54}$$

$$c w_\xi + v \;=\; 0. \tag{6.55}$$

Looking for solutions of the form $v = A \exp(\lambda\xi)$, $w = B \exp(\lambda\xi)$, we find that A and B must satisfy

$$\begin{pmatrix} \lambda^2 \epsilon^2 + c\epsilon\lambda - 1 & -1 \\ 1 & c\lambda \end{pmatrix} \begin{pmatrix} A \\ B \end{pmatrix} = \begin{pmatrix} 0 \\ 0 \end{pmatrix}, \tag{6.56}$$

which has a nontrivial solution if and only if

$$\begin{vmatrix} \lambda^2 \epsilon^2 + c\epsilon\lambda - 1 & -1 \\ 1 & c\lambda \end{vmatrix} = 0. \tag{6.57}$$

Hence, λ must be a root of the characteristic polynomial

$$\epsilon^2 p(\lambda) = \epsilon^2 \lambda^3 + \epsilon c \lambda^2 - \lambda + 1/c = 0. \tag{6.58}$$

There is exactly one negative root, call it λ_1, and the real parts of the other two roots, λ_2 and λ_3, are positive.

In region II, the differential equation is

$$\epsilon^2 v_{\xi\xi} + c\epsilon v_\xi + 1 - v - w = 0, \tag{6.59}$$
$$cw_\xi + v = 0. \tag{6.60}$$

The inhomogeneous solution is $w = 1, v = 0$, and the homogeneous solution is a sum of exponentials of the form $e^{\lambda_i \xi}$.

Since we want the solution to approach zero in the limit $\xi \to \pm\infty$, the traveling pulse can be represented as the exponential $e^{\lambda_1 \xi}$ for large positive ξ, the sum of the two exponentials $e^{\lambda_2 \xi}$ and $e^{\lambda_3 \xi}$ for large negative ξ, and the sum of all three exponentials for the intermediate range of ξ for which $v(\xi) > \alpha$. We take

$$w(\xi) = \begin{cases} Ae^{\lambda_1 \xi} & \text{for } \xi \geq \xi_1, \\ 1 + \sum_{i=1}^{3} B_i e^{\lambda_i \xi} & \text{for } 0 \leq \xi \leq \xi_1, \\ \sum_{i=2}^{3} C_i e^{\lambda_i \xi} & \text{for } \xi \leq 0, \end{cases} \tag{6.61}$$

with $v = -cw_\xi$. Now we require that $w(\xi), v(\xi)$, and $v_\xi(\xi)$ be continuous at $\xi = 0, \xi_1$, and that $v(0) = v(\xi_1) = \alpha$.

There are six unknown constants and two unknown parameters c and ξ_1 that must be determined from the six continuity conditions and the two constraints. Following some calculation, we eliminate the coefficients A, B_i, and C_i, leaving the two constraints

$$e^{\lambda_1 \xi_1} + \epsilon^2 p'(\lambda_1)\alpha - 1 = 0, \tag{6.62}$$

$$\frac{e^{-\lambda_2 \xi_1}}{p'(\lambda_2)} + \frac{e^{-\lambda_3 \xi_1}}{p'(\lambda_3)} + \frac{1}{p'(\lambda_1)} + \epsilon^2 \alpha = 0. \tag{6.63}$$

There are now two unknowns, c and ξ_1, and two equations. In general, (6.62) could be solved for ξ_1, and (6.63) could then be used to determine c for each fixed α and ϵ. However, it is more convenient to treat c as known and α as unknown, and then find α as a function of c. So, we set $s = e^{\lambda_1 \xi_1}$, in which case (6.63) becomes

$$h(s) = 2 - s + \frac{p'(\lambda_1)}{p'(\lambda_2)}e^{-\lambda_2 \ln(s)/\lambda_1} + \frac{p'(\lambda_1)}{p'(\lambda_3)}e^{-\lambda_3 \ln(s)/\lambda_1} = 0, \tag{6.64}$$

where α has been eliminated using (6.62). We seek a solution of $h(s) = 0$ with $0 < s < 1$.

We begin by noting that $h(0) = 2, h(1) = 0, h'(1) = 0$, and $h''(1) = p'(\lambda_1)/\lambda_1^2 - 2$. The first of these relationships follows from the fact that the real parts of λ_2 and λ_3 are of different sign from λ_1, and therefore, in the limit as $s \to 0$, the exponential terms disappear as the real parts of the exponents approach $-\infty$. The second relationship, $h(1) = 0$, follows from the fact that $1/p'(\lambda_1) + 1/p'(\lambda_2) + 1/p'(\lambda_3) =$

0 (Exercise 9). The final two relationships are similar and are left as exercises (Exercises 9, 10).

If $h''(1) < 0$, then the value $s = 1$ is a local maximum of $h(s)$, so for s slightly less than 1, $h(s) < 0$. Since $h(0) > 0$, a root of $h(s) = 0$ in the interval $0 < s < 1$ is assured.

When λ_2 and λ_3 are real, $h(s)$ can have at most one inflection point in the interval $0 < s < 1$. This follows because the equation $h''(s) = 0$ can be written in the form $e^{(\lambda_2 - \lambda_3)\xi_1} = c$, which can have at most one root. Thus, if $h''(1) < 0$, there is precisely one root, while if $h''(1) > 0$ there can be no roots. If the roots λ_2 and λ_3 are complex, uniqueness is not assured, although the condition $h''(1) < 0$ guarantees that there is at least one root.

Differentiating the defining polynomial (6.58) with respect to λ, we observe that the condition $h''(1) < 0$ is equivalent to requiring $\epsilon^2\lambda_1^2 + 2c\epsilon\lambda_1 - 1 < 0$. Furthermore, from the defining characteristic polynomial, we know that $\epsilon^2\lambda_1^2 - 1 = -c\epsilon\lambda_1 + \epsilon^2/(\lambda_1 c)$, and thus it follows that $h''(1) < 0$ if $\lambda_1 < -\frac{1}{c\sqrt{\epsilon}}$. Since the polynomial $p(\lambda)$ is increasing at λ_1, we are assured that $\lambda_1 < -\frac{1}{c\sqrt{\epsilon}}$ if $p(-\frac{1}{c\sqrt{\epsilon}}) > 0$, i.e., if

$$c^2 > \epsilon. \tag{6.65}$$

Thus, whenever $c > \sqrt{\epsilon}$, a root of $h(s) = 0$ with $0 < s < 1$ is guaranteed to exist.

Once s is known, α can be found from the relationship (6.62) whereby

$$\alpha = \frac{1 - s}{\epsilon^2 p'(\lambda_1)}. \tag{6.66}$$

In Fig. 6.5, we show the results of solving (6.64) numerically. Shown plotted is the speed c against α for a sampling of values of ϵ. The dashed curve is the asymptotic limit (6.12) for the curves in the limit $\epsilon \to 0$. The important feature to notice is that for each value of α and ϵ small enough there are two traveling pulses, while for large α there are no traveling pulses. In Fig. 6.6A is shown the fast traveling pulse, and in Fig. 6.6B is shown the slow traveling pulse, both for $\alpha = 0.1, \epsilon = 0.1$, and with $v(\xi)$ shown solid and $w(\xi)$ shown dashed.

Note that the amplitude of the slow pulse in Fig. 6.6B is substantially smaller than that of the fast pulse in Fig. 6.6A. Generally speaking, the fast pulse is stable (Jones, 1984; Yanagida, 1985), and the slow pulse is unstable (Maginu, 1985). Also note that there is nothing in the construction of these wave solutions requiring ϵ to be small.

Singular perturbation theory

The next way to extract information about the traveling pulse solution of (6.48)–(6.49) is to exploit the smallness of the parameter ϵ (Keener, 1980; for a different approach, see Rauch and Smoller, 1978). One reason we expect this to be fruitful is because of similarities with the phase portrait of the FitzHugh–Nagumo equations without diffusion, shown in Fig. 5.15. By analogy, we expect the solution to stay close to the nullcline $f(v, w) = 0$ wherever possible, with rapid transitions between the two outer branches.
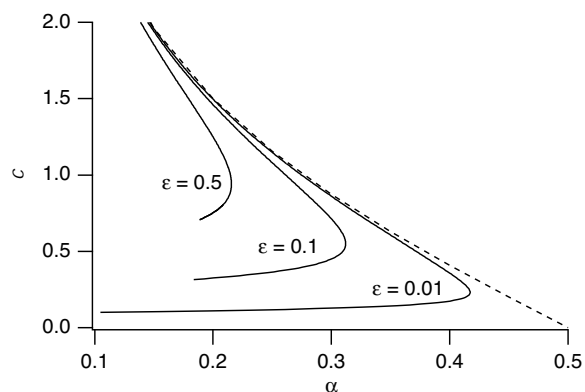
Figure 6.5: Speed c as a function of α for the traveling pulse solution of the piecewise-linear FitzHugh–Nagumo system, shown for $\epsilon = 0.5, 0.1, 0.01$. The dashed curve shows the asymptotic limit as $\epsilon \to 0$, found by singular perturbation arguments.
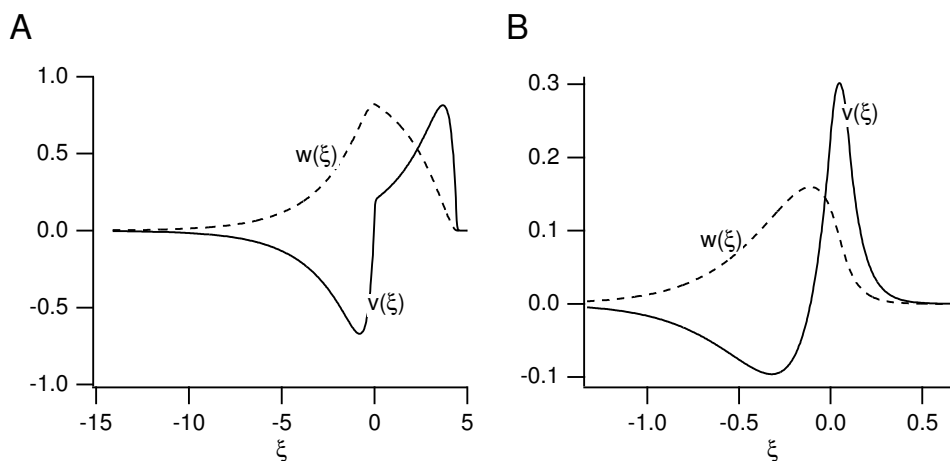
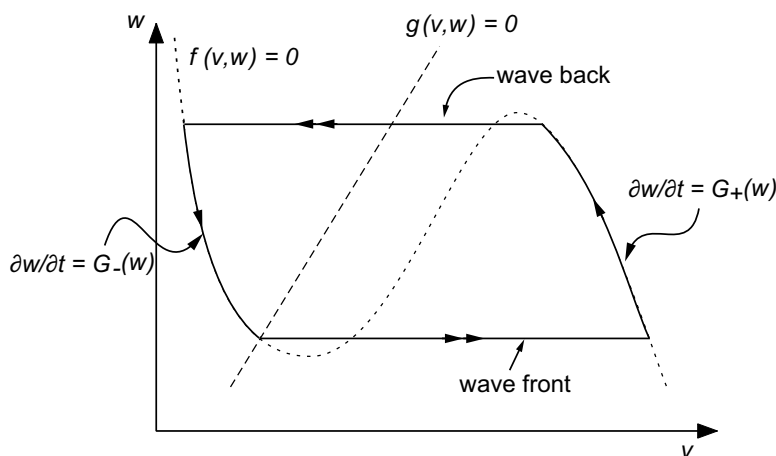Figure 6.6: A: Plots of $v(\xi)$ and $w(\xi)$ for the fast traveling pulse ($c = 2.66$) for the piecewise linear FitzHugh–Nagumo system with $\alpha = 0.1, \epsilon = 0.1$. B: Plots of $v(\xi)$ and $w(\xi)$ for the slow traveling pulse ($c = 0.34$) for the same piecewise linear FitzHugh–Nagumo system as in panel A.

Figure 6.7: Sketch of the phase portrait of the fast traveling solitary pulse for FitzHugh–Nagumo dynamics in the singular limit $\epsilon \to 0$.

The details of this behavior follow from singular perturbation analysis. (This analysis was first given for a simplified FitzHugh–Nagumo system by Casten, Cohen, and Lagerstrom, 1975.) The first observation follows simply from setting ϵ to zero in (9.48). Doing so, we obtain the *outer equations*

$$w_t = g(v, w), \qquad f(v, w) = 0. \tag{6.67}$$

Because the equation $f(v, w) = 0$ is assumed to have three solutions for v as a function of w, and only two of these solutions, the upper and lower solution branches, are stable (cf. Fig. 5.13 and the discussion in Section 5.2), the outer equations (6.67) reduce to

$$\frac{\partial w}{\partial t} = G_{\pm}(w). \tag{6.68}$$

A region of space in which $v = V_+(w)$ is called an *excited region*, and a region in which $v = V_-(w)$ is called a *recovering region*. The outer equation is valid whenever diffusion is not large. However, we anticipate that there are regions of space (*interfaces*) where diffusion is large and in which (6.68) cannot be correct.

To find out what happens when diffusion is large we rescale space and time. Letting $y(t)$ denote the position of the wave front, we set $\tau = t$ and $\xi = \frac{x - y(t)}{\epsilon}$, after which the original system of equations (6.48)–(6.49) becomes

$$v_{\xi\xi} + y'(\tau)v_{\xi} + f(v, w) \;=\; \epsilon \frac{\partial v}{\partial \tau}, \tag{6.69}$$

$$-y'(\tau)w_{\xi} \;=\; \epsilon \left(g(v, w) - \frac{\partial w}{\partial \tau} \right). \tag{6.70}$$

Upon setting $\epsilon = 0$, we find the reduced *inner equations*

$$v_{\xi\xi} + y'(\tau)v_{\xi} + f(v, w) = 0, \tag{6.71}$$

$$y'(\tau)w_{\xi} = 0. \tag{6.72}$$

Even though the inner equations (6.71)–(6.72) are partial differential equations, the variable τ occurs only as a parameter, and so (6.71)–(6.72) can be solved as if they were ordinary differential equations. This is because the traveling wave is stationary in the moving coordinate system ξ, τ. It follows that w is independent of ξ (but not necessarily τ). Finally, since the inner equation is supposed to provide a transition layer between regions where outer dynamics hold, we require the *matching condition* that $f(v, w) \to 0$ as $\xi \to \pm\infty$. Note that here we use $y(t)$ to locate the wave front, rather than ct as before, and then $y'(\tau)$ is the instantaneous wave velocity.

We recognize (6.71) as a bistable equation for which there are heteroclinic orbits. That is, for fixed w, if the equation $f(v, w) = 0$ has three roots, two of which are stable as solutions of the equation $dv/dt = f(v, w)$, then there is a number $c = c(w)$ for which the equation

$$v'' + c(w)v' + f(v, w) = 0 \tag{6.73}$$

has a heteroclinic orbit connecting the two stable roots of $f(v, w) = 0$. This heteroclinic orbit corresponds to a moving transition layer, traveling with speed c. It is important to note that since the roots of $f(v, w) = 0$ are functions of w, c is also a function of w. To be specific, we define $c(w)$ to be the unique parameter value for which (6.73) has a solution with $v \to V_-(w)$ as $\xi \to \infty$, and $v \to V_+(w)$ as $\xi \to -\infty$. In the case that $c(w) > 0$, we describe this transition as an "upjump" moving to the right. If $c(w) < 0$, then the transition is a "downjump" moving to the left.

We are now able to describe a general picture of wave propagation. In most of space, outer dynamics (6.68) are satisfied. At any transition between the two types of outer dynamics, continuity of w is maintained by a sharp transition in v that travels at the speed $y'(t) = c(w)$ if $v = V_-(w)$ on the right and $v = V_+(w)$ on the left, or at speed $y'(t) = -c(w)$ if $v = V_+(w)$ on the right and $v = V_-(w)$ on the left, where w is the value of the recovery variable in the interior of the transition layer. As a transition layer passes any particular point in space, there is a switch of outer dynamics from one to the other of the possible outer solution branches.

This singular perturbation description of wave propagation allows us to examine in more detail the specific case of a traveling pulse. The phase portrait for a solitary pulse is sketched in Fig. 6.7. A traveling pulse consists of a single excitation front followed by a single recovery back. We suppose that far to the right, the medium is at rest, and that a wave front of excitation has been initiated and is moving from left to right. Of course, for the medium to be at rest there must be a rest point of the dynamics on the lower branch, say $G_-(w_+) = 0$. Then, a wave that is moving from left to right has $v = V_-(w_+)$ on its right and $v = V_+(w_+)$ on its left, traveling at speed $y'(t) = c(w_+)$. Necessarily, it must be that $c(w_+) > 0$. Following the same procedure used to derive (6.8), one can show that

$$c(w) = \frac{\int_{V_-(w)}^{V_+(w)} f(v, w)\, dv}{\int_{-\infty}^{\infty} v_\xi^2\, d\xi}, \tag{6.74}$$

and thus $c(w_+) > 0$ if and only if

$$\int_{V_-(w_+)}^{V_+(w_+)} f(v, w_+)\, dv > 0. \tag{6.75}$$

If (6.75) fails to hold, then the medium is not sufficiently excitable to sustain a propagating pulse. It is important also to note that if $f(v, w)$ is of generalized FitzHugh–Nagumo form, then $c(w)$ has a unique zero in the interval (W_*, W^*), where W_* and W^* are defined in Section 5.2.

Immediately to the left of the excitation front, the medium is excited and satisfies the outer dynamics on the upper branch $v = V_+(w)$. Because (by assumption) $G_+(w) > 0$, this can hold for at most a finite amount of time before the outer dynamics force another transition layer to appear. This second transition layer provides a transition between the excited region on the right and a recovering region on the left and travels with speed $y'(t) = -c(w)$, where w is the value of the recovery variable in the transition layer. The minus sign here is because the second transition layer must be a downjump. For this to be a steadily propagating traveling pulse, the speeds of the upjump and downjump must be identical. Thus, the value of w at the downjump, say w_-, must be such that $c(w_-) = -c(w_+)$.

It may be that the equation $c(w_-) = -c(w_+)$ has no solution. In this case, the downjump must occur at the knee, and then the wave is called a *phase wave* since the timing of the downjump is determined solely by the timing, or phase, of the outer dynamics, and not by any diffusive processes. That such a wave can travel at any speed greater than some minimal speed can be shown using standard arguments. The dynamics for phase waves are different from those for the bistable equation because the downjump must be a heteroclinic connection between a saddle point and a saddle-node. That is, at the knee, two of the three steady solutions of the bistable equation are merged into one. The demonstration of the existence of traveling waves in this situation is similar to the case of Fisher's equation, where the nonlinearity $f(v, w)$ in (6.73) has two simple zeros, rather than three in the bistable case. In the phase wave problem, however, one of the zeros of $f(v, w)$ is not simple, but quadratic in nature, a canonical example of which is $f(v, w) = v^2(1 - v)$. We do not pursue this further except to say that such waves exist (see Exercise 16).

In summary, from singular perturbation theory we learn that the value of w ahead of the traveling pulse is given by the steady-state value w_+, and the speed of the rising wave front is then determined from the bistable equation (6.73) with $w = w_+$. The wave front switches the value of v from $v = V_-(w_+)$ (ahead of the wave) to $v = V_+(w_+)$ (behind the wave front). A wave back then occurs at $w = w_-$, where w_- is determined from $c(w_-) = -c(w_+)$. The wave back switches the value of v from $v = V_+(w_-)$ to $v = V_-(w_-)$. The duration of the excited phase of the traveling pulse is

$$T_e = \int_{w_+}^{w_-} \frac{dw}{G^+(w)}. \tag{6.76}$$

The duration of the absolute refractory period is

$$T_{\mathrm{ar}} = \int_{w_-}^{w_0} \frac{dw}{G_-(w)}, \tag{6.77}$$

where w_0 is that value of w for which $c(w) = 0$ (Exercise 11). This approximate solution is said to be a singular solution, because derivatives of the solution become infinite (are singular) in the limit $\epsilon \to 0$.

6.3.2   The Hodgkin–Huxley Equations

The traveling pulse for the Hodgkin–Huxley equations must be computed numerically. The most direct way to do this is to simulate the partial differential equation on a long one-dimensional spatial domain. Alternately, one can use the technique of shooting. In fact, shooting was used by Hodgkin and Huxley in their 1952 paper to demonstrate that the Hodgkin–Huxley equations support a traveling wave solution. Shooting is also the method by which a rigorous proof of the existence of traveling waves has been given (Hastings, 1975; Carpenter, 1977).

The shooting argument is as follows. We write the Hodgkin–Huxley equations in the form

$$\tau_m \frac{\partial v}{\partial t} = \lambda_m^2 \frac{\partial^2 v}{\partial x^2} + f(v, m, n, h), \tag{6.78}$$

$$\frac{dw}{dt} = \alpha_w(v)(1 - w) - \beta_w(v)w, \text{ for } w = n, m, \text{ and } h. \tag{6.79}$$

Now we look for solutions in x, t that are functions of the translating variable $\xi = x/c + t$, and find the system of ordinary differential equations

$$\frac{\lambda_m^2}{c^2} \frac{d^2 v}{d\xi^2} + f(v, m, n, h) - \tau_m \frac{dv}{d\xi} = 0, \tag{6.80}$$

$$\frac{dw}{d\xi} = \alpha_w(v)(1 - w) - \beta_w(v)w, \text{ for } w = n, m, \text{ and } h. \tag{6.81}$$

Linearizing the system (6.80) and (6.81) about the resting solution at $v = 0$, one finds that there are four negative eigenvalues and one positive eigenvalue. A reasonable approximation to the unstable manifold is found by neglecting variations in g_K and g_{Na}, from which

$$v(t) = v_0 e^{\mu t}, \tag{6.82}$$

where

$$\frac{\lambda_m^2}{c^2} \mu^2 - \tau_m \mu - 1 = 0$$

or

$$\mu = \frac{1}{2} \left(\tau_m \frac{c^2}{\lambda_m^2} + \frac{c}{\lambda_m} \sqrt{\tau_m^2 \frac{c^2}{\lambda_m^2} + 4} \right).$$

To implement shooting, one chooses a value of c, and initial data close to the rest point but on the unstable manifold (6.82), and then integrates numerically until (in all likelihood) the potential becomes very large. It could be that the potential becomes large positive or large negative. In fact, once values of c are found that do both, one uses bisection to home in on the homoclinic orbit that returns to the rest point in the limit $\xi \to \infty$.

For the Hodgkin–Huxley equations one finds a traveling pulse for $c = 3.24 \, \lambda_m \, \text{ms}^{-1}$. Using typical values for squid axon (from Table 4.1, $\lambda_m = 0.65 \, \text{cm}$), we find $c = 21 \, \text{mm/ms}$, which is close to the value of 21.2 mm/ms found experimentally by Hodgkin and Huxley. Hodgkin and Huxley estimated the space constant for squid axon as $\lambda_m = 0.58$ cm, from which they calculated that $c = 18.8$ mm/ms. Their

Excitable Tissue	velocity (m/sec)
Myelinated nerve fibers	
Large diameter (16–20 μm)	100–120
Mid-diameter (10–12 μm)	60–70
Small diameter (4–6 μm)	30-50
Nonmyelinated nerve fibers	
Mid-diameter (3–5 μm)	15-20
Skeletal muscle fibers	6
Heart	
Purkinje fibers	1.0
Cardiac muscle	0.5
Smooth muscle	0.05

Table 6.2: Propagation velocities in nerve and muscle.

calculated speeds agreed very well with experimental data and thus their model, which was based only on measurements of ionic conductance, was used to predict accurately macroscopic behavior of the axon. It is rare that quantitative models can be applied so successfully. Propagation velocities for several types of excitable tissue are listed in Table 6.2.

6.4 Periodic Wave Trains

Excitable systems are characterized by both excitability and refractoriness. That is, after the system has responded to a superthreshold stimulus with a large excursion from rest, there is a refractory period during which no subsequent responses can be evoked, followed by a recovery period during which excitability is gradually restored. Once excitability is restored, another wave of excitation can be evoked. However, the speed at which subsequent waves of excitation travel depends strongly on the time allowed for recovery of excitability following the last excitation wave. Generally (but not always), the longer the period of recovery, the faster the new wave of excitation can travel.

One might guess that a nerve axon supports, in addition to a traveling pulse, periodic wave trains of action potentials. With a periodic wave train, if recovery is a monotonic process, one expects propagation to be slower than for a traveling pulse, because subsequent action potentials occur before the medium is fully recovered, so that the sodium upstroke is slower than for a traveling pulse. The relationship between the speed and period is called the *dispersion curve.*

There are at least two ways to numerically calculate the dispersion curve for the
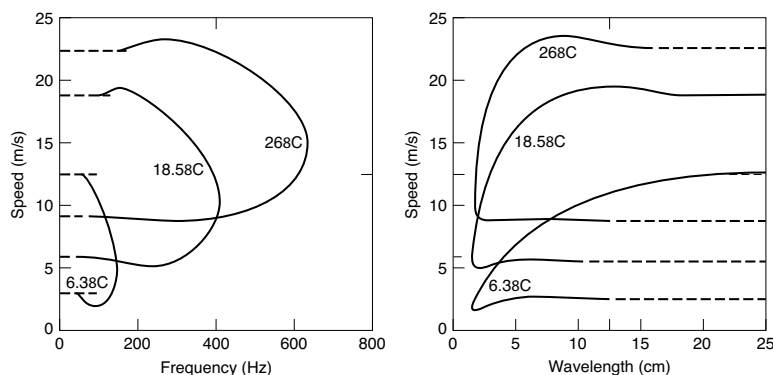
Figure 6.8: Numerically computed dispersion curve (speed vs. frequency and speed vs. wavelength for various temperatures) for the Hodgkin–Huxley equations. (Miller and Rinzel, 1981, Figs. 1 and 2.)

Hodgkin–Huxley equations. The most direct method is to construct a ring, that is, a one-dimensional domain with periodic boundary conditions, initiate a pulse that travels in one direction on the ring, and solve the equations numerically until the solution becomes periodic in time. One can then use this waveform as initial data for a ring of slightly different length, and do the calculation again. While this method is relatively easy, its principal disadvantage is that it requires the periodic solution to be stable. Dispersion curves often have regions whose periodic solutions are unstable, and this method cannot find those. Of course, only the stable solutions are physically realizable, so this disadvantage may not be so serious to the realist.

The second method is to look for periodic solutions of the equations in their traveling wave coordinates (6.80)–(6.81), using a numerical continuation method (an automatic continuation program such as AUTO recommends itself here). With this method, periodic solutions are found without reference to their stability, so that the entire dispersion curve can be calculated.

Dispersion curves for excitable systems have a typical shape, depicted in Figs. 6.8 and 6.9. Here we see a dispersion curve having two branches, one denoting fast waves, the other slow. The two branches meet at a knee or corner at the *absolute refractory period*, and for shorter periods no periodic solutions exist. The solutions on the fast branch are typical of action potentials and are usually (but not always) stable. The solutions on the slow branch are small amplitude oscillations and are unstable.

6.4.1   Piecewise-Linear FitzHugh–Nagumo Equations

The dispersion curve in Fig. 6.9 was found for the FitzHugh–Nagumo system (6.48)–(6.49) with piecewise-linear functions (6.52) and (6.53). The calculation is similar to that for the traveling pulse (Rinzel and Keller, 1973). Since this system is piecewise

linear, we can express its solution as the sum of three exponentials,

$$w(\xi) = \sum_{i=1}^{3} A_i e^{\lambda_i \xi}, \tag{6.83}$$

on the interval $0 \leq \xi < \xi_1$, and as

$$w(\xi) = 1 + \sum_{i=1}^{3} B_i e^{\lambda_i \xi} \tag{6.84}$$

on the interval $\xi_1 \leq \xi \leq \xi_2$, where $v = -cw_\xi$. We also assume that $v > \alpha$ on the interval $\xi_1 \leq \xi \leq \xi_2$. The numbers $\lambda_i, i = 1, 2, 3$, are roots of the characteristic polynomial (6.58).

We require that $w(\xi), v(\xi)$, and $v'(\xi)$ be continuous at $\xi = \xi_1$, and that $w(0) = w(\xi_2), v(0) = v(\xi_2)$, and $v'(0) = v'(\xi_2)$ for periodicity. Finally, we require that $v(0) = v(\xi_1) = \alpha$. This gives a total of eight equations in nine unknowns, $A_1, \ldots, A_3$, $B_1, \ldots, B_3$, ξ_1, ξ_2, and c. After some calculation we find two equations for the three unknowns ξ_1, ξ_2, and c given by

$$\frac{e^{\lambda_1(P-\xi_1)} - 1}{p'(\lambda_1)(e^{\lambda_1 P} - 1)} + \frac{e^{\lambda_2(P-\xi_1)} - 1}{p'(\lambda_2)(e^{\lambda_2 P} - 1)} + \frac{e^{\lambda_3(P-\xi_1)} - 1}{p'(\lambda_3)(e^{\lambda_3 P} - 1)} + \epsilon^2 \alpha = 0, \tag{6.85}$$

$$\frac{e^{\lambda_1 P} - e^{\lambda_1 \xi_1}}{p'(\lambda_1)(e^{\lambda_1 P} - 1)} + \frac{e^{\lambda_2 P} - e^{\lambda_2 \xi_1}}{p'(\lambda_2)(e^{\lambda_2 P} - 1)} + \frac{e^{\lambda_3 P} - e^{\lambda_3 \xi_1}}{p'(\lambda_3)(e^{\lambda_3 P} - 1)} + \epsilon^2 \alpha = 0, \tag{6.86}$$

where $P = \xi_2/c$. It is important to note that since there are only two equations for the three unknowns, (6.85) and (6.86) define a family of periodic waves, parameterized by either the period or the wave speed. The relationship between the period and the speed of this wave family is the dispersion curve. In Fig. 6.9 are shown examples of the dispersion curve for a sampling of values of ϵ with $\alpha = 0.1$. Changing α has little qualitative effect on this plot. The dashed curve shows the limiting behavior of the upper branch (the fast waves) in the limit $\epsilon \to 0$. Of significance in this plot is the fact that there are fast and slow waves, and in the limit of large wavelength, the periodic waves approach the solitary traveling pulses represented by Fig. 6.5 (Exercise 12). In fact, periodic solutions look much like evenly spaced periodic repeats of (truncated) solitary pulses.

The dispersion curve for the piecewise-linear FitzHugh–Nagumo system is typical of dispersion curves for excitable media, with a fast and slow branch meeting at a corner. In general, the location of the corner depends on the excitability of the medium (in this case, the parameter α) and on the ratio of time scales ϵ.

6.4.2 Singular Perturbation Theory

The fast branch of the dispersion curve can be found for a general FitzHugh–Nagumo system in the limit $\epsilon \to 0$ using singular perturbation theory. A periodic wave consists of an alternating series of upjumps and downjumps, separated by regions of outer dynamics. The phase portrait for a periodic wave train is sketched in Fig. 6.10. To be periodic, if w_+ is the value of the recovery variable in the
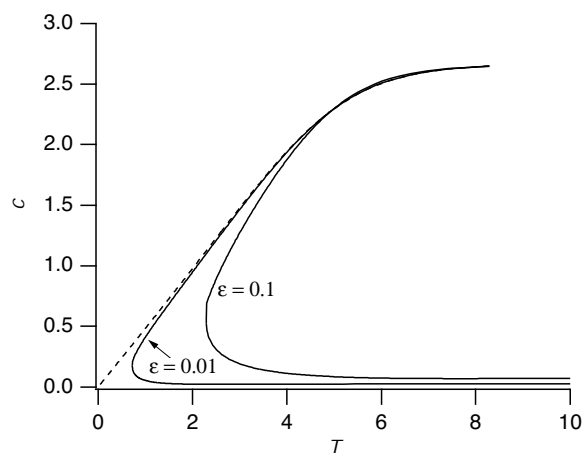
Figure 6.9: Dispersion curves for the piecewise-linear FitzHugh–Nagumo equations shown for $\epsilon = 0.1$ and 0.01. The dashed curve shows the singular perturbation approximation to the dispersion curve.

upjump, traveling with speed $c(w_+)$, then the value of w in the downjump must be w_-, where $c(w_+) = -c(w_-)$. The amount of time spent on the excited branch is

$$T_e = \int_{w_+}^{w_-} \frac{dw}{G_+(w)}, \tag{6.87}$$

and the amount of time spent on the recovery branch is

$$T_r = \int_{w_-}^{w_+} \frac{dw}{G_-(w)}. \tag{6.88}$$

The dispersion curve is then the relationship between speed $c(w_+)$ and period

$$T = T_e + T_r, \tag{6.89}$$

parameterized by w_+. This approximate dispersion curve (calculated numerically) is shown in Fig. 6.9 as a dashed curve.

The slow branch of the dispersion curve can also be found using perturbation methods, although in this case since the speed is small of order ϵ, a regular perturbation expansion is appropriate. The details of this expansion are beyond the scope of this book, although the interested reader is referred to Dockery and Keener (1989). In general, the slow periodic solutions are unstable (Maginu, 1985) and therefore are of less physical interest than the fast solutions. Again, stability theory for the traveling wave solutions is beyond the scope of this book.

6.4.3   Kinematics

Not all waves are periodic. There can be wave trains with action potentials that are irregularly spaced and that travel with different velocities. A *kinematic theory*
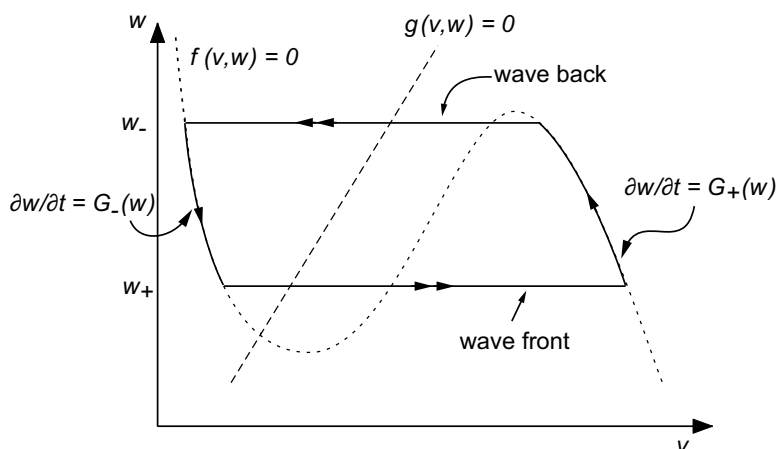
Figure 6.10: Sketch of the phase portrait for the fast traveling periodic wave train for FitzHugh–Nagumo dynamics in the singular limit $\epsilon \to 0$.

of wave propagation is one that attempts to follow the progress of individual action potentials without tracking the details of the structure of the pulse (Rinzel and Maginu, 1984). The simplest kinematic theory is to interpret the dispersion curve in a local way. That is, suppose we know the speed as a function of period for the stable periodic wave trains, $c = C(T)$. We suppose that the wave train consists of action potentials, and that the nth action potential reaches position x at time $t_n(x)$. To keep track of time of arrival at position x we note that

$$\frac{dt_n}{dx} = \frac{1}{c}. \tag{6.90}$$

We complete the description by taking $c = C(t_n(x) - t_{n-1}(x))$, realizing that $t_n(x) - t_{n-1}(x)$ is the instantaneous period of the wave train that is felt by the medium at position x.

A more sophisticated kinematic theory can be derived from the singular solution of the FitzHugh–Nagumo equations. For this derivation we assume that recovery is always via a phase wave, occurring with recovery value W^*. Suppose that the front of the nth action potential has speed $c(w_n)$, corresponding to the recovery value w_n in the transition layer. Keeping track of the time until the next action potential, we find

$$
\begin{aligned}
t_{n+1}(x) - t_n(x) &= T_e(x) + T_r(x) \tag{6.91} \\
&= \int_{w_n}^{W^*} \frac{dw}{G_+(w)} + \int_{W^*}^{w_{n+1}} \frac{dw}{G_-(w)}. \tag{6.92}
\end{aligned}
$$

Differentiating (6.92) with respect to x, we find the differential equation for $w_{n+1}(x)$:

$$\frac{1}{G_-(w_{n+1})} \frac{dw_{n+1}}{dx} = \frac{1}{G_+(w_n)} \frac{dw_n}{dx} + \frac{1}{c(w_{n+1})} - \frac{1}{c(w_n)}. \tag{6.93}$$

With this equation one can track the variable w_{n+1} as a function of x given $w_n(x)$ and from it reconstruct the speed and time of arrival of the $(n+1)$st action potential wave front.

While this formulation is useful for FitzHugh–Nagumo models, it can be given a more general usefulness as follows. Since there is a one-to-one relationship between the speed of a front and the value of the recovery variable w in that front, we can represent these functions in terms of the speeds of the fronts as

$$t_{n+1}(x) - t_n(x) = A(c_n) + t_r(c_{n+1}), \qquad (6.94)$$

where $A(c_n) = T_e$ is the *action potential duration* (APD) since the nth upstroke, and $t_r(c_{n+1}) = T_r$ is the recovery time preceding the $(n+1)$st upstroke. When we differentiate this conservation law with respect to x, we find a differential equation for the speed of the $(n+1)$st wave front as a function of the speed of the nth wave front, given by

$$t_r'(c_{n+1})\frac{dc_{n+1}}{dx} = \frac{1}{c_{n+1}} - \frac{1}{c_n} - A'(c_n)\frac{dc_n}{dx}. \qquad (6.95)$$

The advantage of this formulation is that the functions A and t_r may be known for other reasons, perhaps from experimental data. It is generally recognized that the action potential duration is functionally related to the speed of the previous action potential, and it is also reasonable that the speed of a subsequent action potential can be related functionally to the time of recovery since the end of the last action potential. Thus, the model (6.95) has applicability that goes beyond the FitzHugh–Nagumo context. For an example of how this idea has been used for the Beeler–Reuter dynamics, see Courtemanche et al. (1996).

6.5   Wave Propagation in Higher Dimensions

Not all excitable media can be viewed as one-dimensional cables, neither is all propagated activity one-dimensional. Tissues for which one-dimensional descriptions of cellular communication are inadequate include skeletal and cardiac tissue, the retina, and the cortex of the brain. To understand communication and signaling in these tissues requires more complicated mathematical analysis than for one-dimensional cables.

When beginning a study of two- or three-dimensional wave propagation, it is tempting to extend the cable equation to higher dimensions by replacing first derivatives in space with spatial gradients, and second spatial derivatives with the Laplacian operator. Indeed, all the models discussed here are of this type. However, this replacement is not always appropriate.

Some cells, such as *Xenopus* oocytes (frog eggs), are large enough so that waves of chemical activity can be sustained within a single cell. This is unusual, however, as most waves in normal physiological situations serve the purpose of communication between cells. For chemical waves in single cells, a reasonable first guess is that spatial coupling is by chemical diffusion. In that case, if the local chemical dynamics are described by the differential equation $\frac{\partial u}{\partial t} = kf$, then with spatial coupling the

dynamics are represented by

$$\frac{\partial u}{\partial t} = \nabla \cdot (D\nabla u) + kf, \tag{6.96}$$

where D is the (scalar) diffusion coefficient of the chemical species and ∇ is the three-dimensional gradient operator. Here we have included the time constant k (with units time^{-1}), so that f has the same dimensional units as u.

For many cell types, however, intercellular communication is through gap junctions between immediate neighbors, so that diffusion is not spatially uniform. In this case, the first guess (or hope) is that the length constant of the phenomenon to be described is much larger than the typical cell size, and homogenization can be used to find an effective diffusion coefficient, D_e, as described in Chapter 8. Then (6.96) with the effective diffusion coefficient is a reasonable model. Note that there is no a priori reason to believe that cellular coupling is isotropic or that D_e is a scalar quantity.

If this assumption, that the space constant of the signaling phenomenon is larger than the size of the cell, and hence that homogenization gives a valid approximation, is not justified, then we are stuck with the unpleasant business of studying communication between discretely coupled cells. Descriptions of such studies are included in Chapter 7.

For electrically active cells, such as cardiac or muscle cells, the situation is further complicated by the fact that the signal is the transmembrane potential, and to determine this one needs to know both the intracellular and extracellular potentials. Consequently, spatial coupling cannot be represented by the Laplacian of the transmembrane potential. We address this problem in Chapter 12, where we discuss waves in myocardial tissue.

Even more complicated are neural networks, where axons may extend long distances and cells may be connected to many other cells, far more than their nearest neighbors, so that spatial coupling is non-local.

Suffice it to say, while (6.96) is an interesting place to start the study of waves in higher dimensions, it is by no means obvious that all the results of this study are applicable to cellular media.

6.5.1 Propagating Fronts

Plane Waves

The simplest wave to look for in a higher dimensional medium is a plane wave. Suppose that the canonical problem

$$U'' + c_0 U' + f(U) = 0 \tag{6.97}$$

(with dimensionless independent variable) is bistable and has a wave front solution $U(\xi)$ for some unique value of c_0, the value of which depends on f.

To find plane wave solutions of (6.96), we suppose that u is a function of the single variable $\xi = \mathbf{n} \cdot \mathbf{x} - ct$, where $\mathbf{n}$ is a unit vector pointing in the forward direction of wave front propagation. In the traveling wave coordinate ξ, the time

derivative $\frac{d}{dt}$ is replaced by $-c\frac{d}{d\xi}$, and the spatial gradient operator ∇ is replaced by $\mathbf{n}\frac{d}{d\xi}$, so that the governing equation reduces to the ordinary differential equation

$$(\mathbf{n} \cdot D\mathbf{n})u'' + cu' + kf(u) = 0. \tag{6.98}$$

We compare (6.98) with the canonical equation (6.97) and note that the solution of (6.98) can be found by a simple rescaling to be

$$u(\mathbf{x}, t) = U\left(\frac{\mathbf{n} \cdot \mathbf{x} - ct}{\Lambda(\mathbf{n})}\right), \tag{6.99}$$

where $c = c_0 k\Lambda(\mathbf{n})$ is the (directionally dependent) speed and $\Lambda(\mathbf{n}) = \sqrt{\frac{\mathbf{n} \cdot D\mathbf{n}}{k}}$ is the directionally dependent space constant.

Waves with Curvature

Wave fronts in two- or three-dimensional media are not expected to be plane waves. They are typically initiated at a specific location, and so might be circular in shape. Additionally, the medium may be structurally inhomogeneous or have a nonsimple geometry, all of which introduce curvature into the wave front.

It is known that curvature plays an important role in the propagation of a wave front in an excitable medium. A physical explanation makes this clear. Suppose that a circular wave front is moving inward, so that the circle is collapsing. Because different parts of the front are working to excite the same points, we expect the region directly in front of the wave front to be excited more quickly than if the wave were planar. Similarly, an expanding circular wave front should move more slowly than a plane wave because the efforts of the wave to excite its neighbors are more spread out, and excitation should be slower than for a plane wave.

While these curvature effects are well known in many contexts, we are interested here in a quantitative description of this effect. In this section we derive an equation for action-potential spread called the *eikonal-curvature equation*, the purpose of which is to show the contribution of curvature to wave-front velocity. Eikonal-curvature equations have been used in a number of biological contexts, including the study of wave-front propagation in the excitable Belousov–Zhabotinsky reagent (Foerster et al., 1989; Keener, 1986; Keener and Tyson, 1986; Tyson and Keener, 1988; Ohta et al., 1989), calcium waves in *Xenopus* oocytes (Lechleiter et al., 1991b; Sneyd and Atri, 1993; Jafri and Keizer, 1995) and in studies of myocardial tissue (Keener, 1991a; Colli-Franzone et al., 1990, 1993; also see Chapter 12). Eikonal-curvature equations have a long history in other scientific fields as well, including crystal growth (Burton et al., 1951) and flame front propagation (Frankel and Sivashinsky, 1987, 1988).

The derivation of the eikonal-curvature equation uses standard mathematical arguments of singular perturbation theory, which we summarize here. The key observation is that hidden inside (6.96) is the bistable equation (6.97), and the idea to be explored is that in some moving coordinate system that is yet to be determined, (6.96) is well approximated by the bistable equation (6.97).

Our goal is to rewrite (6.96) in terms of a moving coordinate system chosen so that it takes the form of (6.97). In three dimensions, we must have three spatial coordinates, one of which is locally orthogonal to the wave front, while the other two are coordinates describing the wave-front surface. By assumption, the function u is approximately independent of the wave-front coordinates. We introduce a scaling of the variables such that the derivatives with respect to the first variable are of most importance, and all other derivatives are less so. From this computation, we learn how the coordinate system must move in order to maintain itself as a wave-front coordinate system, and this law of coordinate system motion is the eikonal-curvature equation.

To begin, we introduce a general (as yet unknown) moving coordinate system

$$\mathbf{x} = \mathbf{X}(\xi, \tau), \qquad t = \tau. \tag{6.100}$$

According to the chain rule,

$$\frac{\partial}{\partial \xi_i} = \frac{\partial X_j}{\partial \xi_i} \frac{\partial}{\partial x_j}, \qquad \frac{\partial}{\partial \tau} = \frac{\partial}{\partial t} + \frac{\partial X_j}{\partial \tau} \frac{\partial}{\partial x_j}. \tag{6.101}$$

Here and in what follows, the summation convention is followed (i.e., unless otherwise noted, repeated indices are summed from 1 to 3). It follows that

$$\frac{\partial}{\partial x_i} = \alpha_{ij} \frac{\partial}{\partial \xi_j}, \qquad \frac{\partial}{\partial t} = \frac{\partial}{\partial \tau} - \frac{\partial X_j}{\partial \tau} \alpha_{jk} \frac{\partial}{\partial \xi_k}, \tag{6.102}$$

where the matrix with entries α_{ij} is the inverse of the matrix with entries $\frac{\partial X_j}{\partial \xi_i}$ (the Jacobian of the coordinate transformation (6.100)).

We identify the variable ξ_1 as the coordinate normal to level surfaces of u, so ξ_2 and ξ_3 are the coordinates of the moving level surfaces. Then, we define the tangent vectors $\mathbf{r}_i = \frac{\partial X_j}{\partial \xi_i}, i = 1, 2, 3$, and the normal vectors $\mathbf{n}_i = \mathbf{r}_j \times \mathbf{r}_k$, where $i \neq j, k$, and $j < k$. Without loss of generality we take $\mathbf{r}_1 = \sigma(\mathbf{r}_2 \times \mathbf{r}_3)$, so that $\mathbf{r}_1$ is always normal to the level surfaces of u. Here σ is an arbitrary (unspecified) scale factor. The vectors $\mathbf{r}_2$ and $\mathbf{r}_3$ are tangent to the moving level surface, although they are not necessarily orthogonal. While one can force the vectors $\mathbf{r}_2$ and $\mathbf{r}_3$ to be orthogonal, the actual construction of such a coordinate description on a moving surface is generally quite difficult. Furthermore, it is preferred to have an equation of motion that does not have additional restrictions, since the motion should be independent of the coordinate system by which the surface is described.

We can calculate the entries α_{ij} explicitly. It follows from Cramer's rule (Exercise 23) that

$$\alpha_{ij} = \frac{(\mathbf{n}_j)_i}{\mathbf{r}_j \cdot \mathbf{n}_j} (\text{no summation}), \tag{6.103}$$

where by $(\mathbf{n}_j)_i$ we mean the ith component of the jth normal vector $\mathbf{n}_j$.

Now we can write out the full change of variables. We calculate that (treating the coefficients α_{ij} as functions of $\mathbf{x}$)

$$\frac{\partial u}{\partial t} = \frac{\partial u}{\partial \tau} - \frac{\partial X_j}{\partial \tau} \alpha_{jk} \frac{\partial u}{\partial \xi_k}, \tag{6.104}$$

$$\nabla^2 u \quad = \quad \alpha_{ip}\alpha_{ik}\frac{\partial^2 u}{\partial\xi_p\partial\xi_k} + \frac{\partial\alpha_{ip}}{\partial x_i}\frac{\partial u}{\partial\xi_p}, \tag{6.105}$$

and rewrite (6.96) in terms of these new variables, finding (in the case that D is a constant scalar) that

$$0 = D\alpha_{ip}\alpha_{iq}\frac{\partial^2 u}{\partial\xi_p\partial\xi_q} + D\frac{\partial\alpha_{ip}}{\partial x_i}\frac{\partial u}{\partial\xi_p} - \left(u_\tau - \frac{\partial X_j}{\partial\tau}\alpha_{jk}\frac{\partial u}{\partial\xi_k}\right) + kf(u). \tag{6.106}$$

There are two important assumptions that are now invoked, namely that the spatial scale of variation in ξ_1 is much shorter than the spatial scale for variations in the variables ξ_2 and ξ_3. We quantify this by supposing that there is a small parameter ϵ and that $\alpha_{j1} = O(1)$, while $\alpha_{jk} = O(\epsilon)$ for all j and $k \neq 1$. In addition, we assume that to leading order in ϵ, u is independent of ξ_2, ξ_3, and τ. Consequently, not all of the terms in (6.106) are of equal importance. If we take into account the ϵ dependence of α_{ij}, then (6.106) simplifies to

$$D|\alpha|^2\frac{\partial^2 u}{\partial\xi_1^2} + \left(D\nabla\cdot\alpha + \frac{\partial\mathbf{X}}{\partial\tau}\cdot\alpha\right)\frac{\partial u}{\partial\xi_1} + kf(u) = O(\epsilon), \tag{6.107}$$

where α is the vector with components α_{j1}, and hence, from (6.103), proportional to the normal vector $\mathbf{n}_1$. All of the terms on the left-hand side of (6.107) are large compared to ϵ.

Here we see an equation that resembles the bistable equation (6.97). If the coefficients of (6.107) are constant, we can identify (6.107) with (6.97) by setting

$$\frac{\partial\mathbf{X}}{\partial\tau}\cdot\alpha + D\nabla\cdot\alpha = kc_0, \tag{6.108}$$

while requiring $D|\alpha|^2 = k$.

Equation (6.108) tells us how the coordinate system should move, and since α is proportional to $\mathbf{n}_1$, setting $D|\alpha|^2 = k$ determines the scale of the coordinate normal to the wave front, i.e., the thickness of the wave front. In reality, the coefficients of (6.107) are not constants, and these two requirements overdetermine the full coordinate transformation $\mathbf{X}(\xi, \tau)$. To overcome this difficulty, we assume that since the wave front and the coordinate system are slowly varying in space, we interpret (6.108) as determining the motion of only the midline of the coordinate system, at the location of the largest gradient of the front, rather than the entire coordinate system.

Equation (6.108) is the equation we seek that describes the motion of an action potential front, called the *eikonal-curvature equation*. However, for numerical simulations it is essentially useless. Numerical algorithms to simulate this equation reliably are extremely hard to construct. Instead, it is useful to introduce a function $S(x, t)$ that acts as an indicator function for the fronts (think of S as determining the "shock" location). That is, if $S(x, t) > 0$, the medium is activated, while if $S(x, t) < 0$, the medium is in the resting state. Taking α to be in the direction of forward wave-front motion means that $\alpha = -\sqrt{\frac{k}{D}}\frac{\nabla S}{|\nabla S|}$, where we have used the fact

that $|\alpha| = \sqrt{k/D}$. Since the zero level surface of $S(x,t)$ denotes the wave-front location, and thus S is constant along the wave front, it follows that $0 = \nabla S \cdot X_t + S_t$, so that $X_t \cdot \alpha = \sqrt{\frac{k}{D}} \frac{S_t}{|\nabla S|}$. Hence,

$$S_t = |\nabla S| c_0 \sqrt{Dk} + D|\nabla S| \nabla \cdot \left(\frac{\nabla S}{|\nabla S|} \right). \tag{6.109}$$

The use of an indicator function $S(x,t)$ to determine the motion of an interface is called the *level set method* (Osher and Sethian, 1988), and is both powerful and easy to implement.

Equation (6.109) is called the eikonal-curvature equation because of the physical interpretation of each of its terms. If we ignore the diffusive term, then we have the eikonal equation

$$\frac{\partial S}{\partial t} = |\nabla S| c_0 \sqrt{Dk}. \tag{6.110}$$

If $\mathbf{R}$ is a level surface of the function $S(x,t)$ and if $\mathbf{n}$ is the unit normal vector to that surface at some point, then (6.110) implies that the normal velocity of the surface $\mathbf{R}$, denoted by $\mathbf{R}_t \cdot \mathbf{n}$, satisfies

$$\mathbf{R}_t \cdot \mathbf{n} = c_0 \sqrt{Dk}. \tag{6.111}$$

In other words, the front moves in the normal direction $\mathbf{n}$ with speed $c = c_0 \sqrt{Dk}$.

Equation (6.111) is the basis of a geometrical "Huygens" construction for front propagation, but the numerical integration of either (6.110) or (6.111) is fraught with difficulties. In particular, cusp singularities develop, and the indicator function $S(x,t)$ becomes ill-defined in finite time (usually very quickly). The second term of the right-hand side of (6.109) is a curvature correction, appropriately named because the term $\nabla \cdot \left(\frac{\nabla S}{|\nabla S|} \right)$ is twice the mean curvature (in three-dimensional space) or the curvature (in two-dimensional space) of the level surfaces of S (see Exercise 24). In fact, the eikonal-curvature equation can be written as

$$\mathbf{R}_t \cdot \mathbf{n} = c_0 \sqrt{Dk} - D\kappa, \tag{6.112}$$

or

$$\tau \mathbf{R}_t \cdot \mathbf{n} = c_0 \Lambda - \Lambda^2 \kappa, \tag{6.113}$$

where κ is the curvature (in two dimensions) or twice the mean curvature (in three dimensions) of the front, $\Lambda = \sqrt{D/k}$ is the space constant, and $\tau = 1/k$ is the time constant. Even though it usually represents only a small correction to the normal velocity of fronts, the curvature correction is important for physical and stability reasons, to prevent singularity formation. The sign of the curvature correction is such that a front with ripples is gradually smoothed into a plane wave.

Experiments on the Belousov–Zhabotinsky reagent have verified this relationship between speed and curvature of propagating fronts. For example, Foerster et al. (1988) measured the speed and curvature at different positions of a rotating spiral wave and at intersections of two spiral waves (thus obtaining curvatures of different signs) and found that the relationship between normal velocity and curvature was well approximated by a straight line with slope that was the diffusion coefficient of the rapidly reacting species.

6.5.2   Spatial Patterns and Spiral Waves

Now that we have some idea of how wave fronts propagate in an excitable medium, we next wish to determine the spatial patterns that may result. The most common pattern is created by, and spreads outward from, a single source. If the medium is sufficiently large so that more than one wave front can exist at the same time, then these are referred to as *target patterns*. Target patterns require a periodic source and so cannot exist in a homogeneous nonoscillatory medium.

A second type of spatial pattern is a spiral wave. Spiral waves do not require a periodic source for their existence, as they are typically self-sustained. Because they are self-sustained, spirals usually occur only in pathophysiological situations. That is, it is usually not a good thing for a system that relies on faithful propagation of a signal to be taken over by a self-sustained pattern. Thus, spirals on the heart are fatal, spirals in the cortex may lead to epileptic seizures, and spirals on the retina or visual cortex may cause hallucinations. The most famous example of spiral waves in an excitable medium is in the Belousov–Zhabotinsky reaction (Winfree, 1972, 1974), which we do not discuss here.

The mathematical discussion of spiral waves centers on the nature of periodic solutions of a system of differential equations with excitable dynamics spatially coupled by diffusion. A specific example is the FitzHugh–Nagumo equations with diffusive coupling in two spatial dimensions,

$$\epsilon \frac{\partial v}{\partial t} = \epsilon^2 \nabla^2 v + f(v, w), \tag{6.114}$$

$$\frac{\partial w}{\partial t} = g(v, w). \tag{6.115}$$

The leading-order singular perturbation analysis (i.e., with $\epsilon = 0$) suggests that the domain be separated into two, in which outer dynamics

$$\frac{\partial w}{\partial t} = G_{\pm}(w) \tag{6.116}$$

hold (using the notation of Section 6.3.1). The region in which $\frac{\partial w}{\partial t} = G_+(w)$ is identified as the excited region, and the region in which $\frac{\partial w}{\partial t} = G_-(w)$ is called the recovering region. Separating these are moving interfaces in which v changes rapidly (with space and time constant ϵ), so that diffusion is important, while w remains essentially constant. At any point in space the solution should be periodic in time, so at large radii, where the wave fronts are nearly planar, the solution should lie on the dispersion curve.

The first guess as to how the interface should move is to assume that the interface is nearly planar and therefore has the same velocity as a plane wave, namely

$$\mathbf{R}_t = c(w)\mathbf{n}, \tag{6.117}$$

where $\mathbf{R}$ is the position vector for the interface, $\mathbf{n}$ is the unit normal vector of $\mathbf{R}$, and $c(w)$ is the plane-wave velocity as a function of w.

To see the implications of the eikonal equation, we suppose that the spiral interface is a curve $\mathbf{R}$ given by

$$X(r, t) = r\cos(\theta(r) - \omega t), \qquad Y(r, t) = r\sin(\theta(r) - \omega t). \tag{6.118}$$

Note that the interface is a curve parametrized by r, and so the tangent is (X_r, Y_r). We then calculate that

$$\mathbf{R}_t = \left(\begin{array}{c} -\omega r \sin(\theta - \omega t) \\ \omega r \cos(\theta - \omega t) \end{array} \right) \tag{6.119}$$

and

$$\sqrt{1 + r^2 \theta'^2} \mathbf{n} = \left(\begin{array}{c} -\sin(\theta - \omega t) - r\theta' \cos(\theta - \omega t) \\ \cos(\theta - \omega t) - r\theta' \sin(\theta - \omega t) \end{array} \right), \tag{6.120}$$

so that the eikonal equation becomes

$$c(w)\sqrt{1 + r^2 \theta'^2} = \omega r. \tag{6.121}$$

An integration then gives

$$\theta(r) = \rho(r) - \tan(\rho(r)), \qquad \rho(r) = \sqrt{\frac{r^2}{r_0^2} - 1}, \tag{6.122}$$

where $r_0 = c/\omega$, so that the interface is given by

$$X = r_0 \cos(s) + r_0 \rho(r) \sin(s), \qquad Y = r_0 \sin(s) - r_0 \rho(r) \cos(s), \tag{6.123}$$

where $s = \rho(r) - \omega t$. This interface is the involute of a circle of radius r_0. (The involute of a circle is the locus of points at the end of a string that is unwrapped from a circle.)

There are significant difficulties with this as a spiral solution, the most significant of which is that it exists only for $r \geq r_0$. The parameter r_0 is arbitrary, but positive, so that this spiral is rotating about some hole of finite size. The frequency of rotation is determined by requiring consistency with the dispersion curve. Note that the spiral has wavelength $2\pi r_0$, and period $\frac{2\pi}{\omega}$, and so $c = r_0 \omega$. However, since the dispersion curve generally has a knee, and thus periodic waves do not exist for small enough wavelength, there is a lower bound on the radii for which this can be satisfied. Numerical studies of spirals suggest no such lower bound on the inner core radius and also suggest that there is a unique spiral frequency for a medium without a hole at the center. Unfortunately, the use of the eikonal equation gives no hint of the way a unique frequency is selected, so a different approach, using the eikonal-curvature equation, is required.

To apply the eikonal-curvature equation to find rotating spiral waves, we assume that the wave front is expressed in the form (6.118), so that the curvature is

$$\kappa = \frac{X'Y'' - Y'X''}{(X'^2 + Y'^2)^{3/2}} = \frac{\psi'}{(1 + \psi^2)^{3/2}} + \frac{\psi}{r(1 + \psi^2)^{1/2}}, \tag{6.124}$$

where $\psi = r\theta'(r)$ is called the shape function. Thus the eikonal-curvature equation (6.113) becomes

$$r\frac{d\psi}{dr} = (1 + \psi^2)\left[\frac{rc(w)}{\epsilon}(1 + \psi^2)^{1/2} - \frac{\omega r^2}{\epsilon} - \psi\right]. \tag{6.125}$$

If we suppose that w is constant along the spiral front, then (6.125) can be solved numerically by "shooting" from $r = \infty$. A portrait of sample trajectories in the
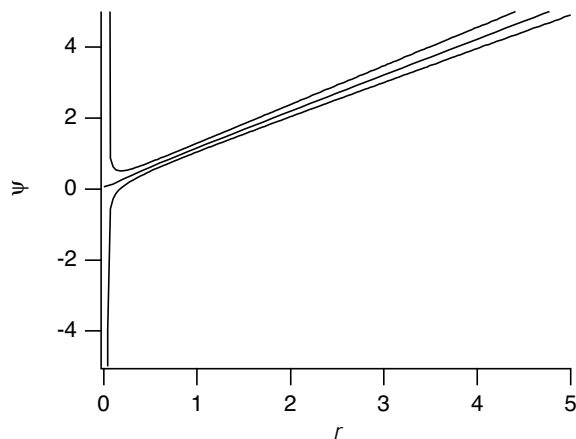
Figure 6.11: Trajectories of (6.125) with $\omega/\epsilon = 2.8, 9m^*$, and 3.2, and $c/\epsilon = 3.0$.

(r, ψ) plane is shown in Fig. 6.11. The trajectories of (6.125) are "stiff," meaning that for large r, the trajectory $c(1 + \psi^2)^{1/2} - \omega r = 0$ is a strong attractor. This stiffness can be readily observed when (6.125) is written in terms of the variable $\phi = \frac{r\psi}{\sqrt{1+\psi^2}}$ as

$$\frac{\epsilon}{r}\frac{d\phi}{dr} = c - \omega\sqrt{r^2 - \phi^2}, \tag{6.126}$$

since ϵ multiplies the derivative term in (6.126).

Integrating from $r = \infty$, trajectories of (6.125) approach the origin by either blowing up or down near the origin $r = 0$. Since the origin is a saddle point, if parameters are chosen exactly right, the trajectory approaches $\psi = 0$. Thus, there is a unique relationship between ω and c of the form $\omega/\epsilon = F(c/\epsilon)$ that yields trajectories that go all the way to the origin $r = 0, \psi = 0$.

Notice that the rescaling of variables $r \to \alpha r, c \to c/\alpha, \omega \to \omega/\alpha^2$ leaves (6.125) invariant, so that the relationship between ω and c for which a trajectory approaches the saddle point at the origin must be of the form

$$\frac{\omega}{\epsilon\alpha^2} = F\left(\frac{c}{\epsilon\alpha}\right). \tag{6.127}$$

It follows that $F(c/\alpha) = \frac{1}{\alpha^2}F(c)$ and thus $F(x) = m^*x^2$, for some constant m^*, so that

$$\omega = \frac{c^2m^*}{\epsilon}. \tag{6.128}$$

Numerically, one determines that $m^* = 0.330958$.

An example of this spiral front is shown in Fig. 6.12, compared with the comparable involute spiral (6.123), shown dashed. For this figure $c/\epsilon = 3.0$.

At this point we have a family of possible spiral trajectories that have correct asymptotic (large r) behavior and approach $\psi = 0$ as $r \to 0$. This family is parametrized by the speed c. To determine which particular member of this family
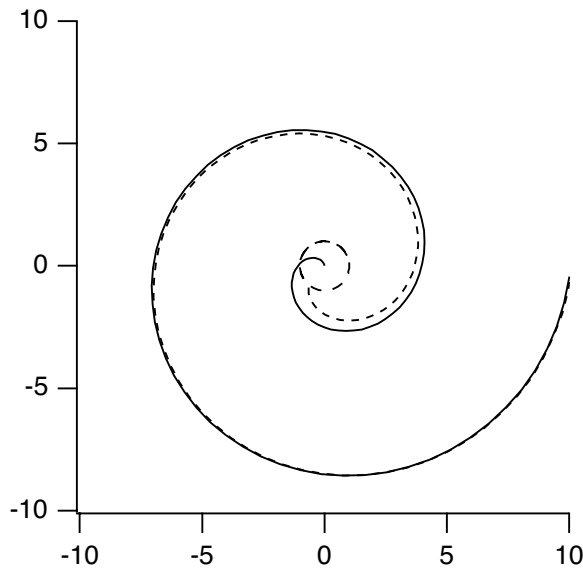
Figure 6.12: Spiral arm corresponding to the trajectory of (6.125) that approaches the origin (shown solid), compared with the involute spiral (shown dashed) with the same parameter values. For this plot, $c/\epsilon = 3.0$.

is the correct spiral front, we also require that the spirals be periodic waves; that is, they must satisfy the dispersion relationship. These two requirements uniquely determine the spiral properties. To see that this is so, in Fig. 6.13 are plotted the critical curve (6.128) and the approximate dispersion curve (6.89). For this plot we used piecewise linear dynamics, $f(v, w) = H(v - \alpha) - v - w$, $g(v, w) = v - \gamma w$ with $\alpha = 0.1$, $\gamma = 0$, $\epsilon = 0.05$.

More About Spirals

This discussion of higher-dimensional waves is merely the tip of the iceberg (or tip of the spiral), and there are many interesting unresolved questions.

While the spirals that are observed in physiological systems share certain qualitative similarities, their details are certainly different. The FitzHugh–Nagumo model discussed here shows only the qualitative behavior for generic excitable systems and so has little quantitative relevance. Other physiological systems are likely governed by other dynamics. For example, a model for spreading cortical depression in the cortex has been proposed by Tuckwell and Miura (1978; Miura, 1981), and numerical simulations have shown rotating spirals. However, a detailed mathematical study of these equations has not been given.

This analytical calculation for the FitzHugh–Nagumo system is based on singular perturbation theory and therefore is not mathematically rigorous. In fact, as yet there is not a rigorous proof of the existence of spiral waves in an excitable medium. While the approximate solution presented here is known to be asymptotically valid,
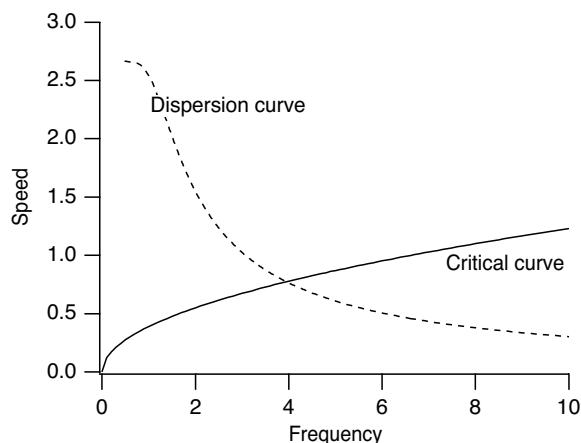
Figure 6.13: Critical curve (6.128) and the approximate dispersion curve (6.89) using piecewise linear dynamics $f(v, w) = H(v - \alpha) - v - w$, $g(v, w) = v - \gamma w$ with $\alpha = 0.1$, $\gamma = 0$, $\epsilon = 0.05$.

the structure of the core of the spiral is not correct. This problem has been addressed by Pelce and Sun (1991) and Keener (1992) for FitzHugh–Nagumo models with a single diffusing variable, and by Keener (1994) and Kessler and Kupferman (1996) for FitzHugh–Nagumo models with two diffusing variables, relevant for chemical reaction systems.

A second issue of concern is the stability of spirals. This also is a large topic, which is not addressed here. The interested reader should consult the work of Winfree (1991), Jahnke and Winfree (1991), Barkley (1994), Karma (1993, 1994), Panfilov and Hogeweg (1995), Kessler and Kupferman (1996).

Because the analytical study of excitable media is so difficult, simpler models have been sought, with the result that finite-state automata are quite popular. A finite-state automaton divides the state space into a few discrete values (for example $v = 0$ or 1), divides the spatial domain into discrete cells, and discretizes time into discrete steps. Then, rules are devised for how the states of the cells change in time. Finite-state automata are extremely easy to program and visualize. They give some useful insight into the behavior of excitable media, but they are also beguiling and can give "wrong" answers that are not easily detected. The literature on finite-state automata is vast (see, for instance, Moe et al., 1964; Smith and Cohen, 1984; and Gerhardt et al., 1990).

The obvious generalization of a spiral wave in a two-dimensional region to three dimensions is called a *scroll wave* (Winfree, 1973, 1991; Keener and Tyson, 1992). Scroll waves have been observed numerically (Jahnke et al., 1988; Lugosi and Winfree, 1988), in three-dimensional BZ reagent (Gomatam and Grindrod, 1987), and in cardiac tissue (Chen et al., 1988), although in experimental settings they are extremely difficult to visualize. In numerical simulations it is possible to initiate scroll waves with interesting topology, including closed scroll rings, knotted scrolls, or linked pairs of scroll rings.

The mathematical theory of scroll waves is also in its infancy. Attributes of the topology of closed scrolls were worked out by Winfree and Strogatz (1983a,b,c; 1984), and a general asymptotic theory for their evolution has been suggested (Keener, 1988b) and tested against numerical experiments on circular scroll rings and helical scrolls. There is not sufficient space here to discuss the theory of scroll waves. However, scroll waves are mentioned again briefly in later chapters on cardiac waves and rhythmicity.

Exercises

1. Show that the (U, W) phase plane of the bistable equation, (6.6) and (6.7), has three steady states, two of which are saddle points. What is the nature of the third steady state? Show that the slope of the unstable manifold at the origin is given by the positive root of $\lambda^2 - c\lambda + f'(0) = 0$ and is always larger than c. What is the slope of the stable manifold at $(U, W) = (1, 0)$? Show that the slopes of both these manifolds are increasing functions of c.

2. Use cable theory to find the speed of propagation for each of the axons listed in Table 4.1, assuming that the ionic currents are identical and the speed of propagation for the squid giant axon is 21 mm/ms.

3. Find the space constant for a myelinated fiber.

4. Construct a traveling wave solution to the piecewise-linear bistable equation, (6.1) and (6.3). Show that the wave travels with speed $\frac{1-2\alpha}{\sqrt{\alpha - \alpha^2}}$.

5. Find the shape of the traveling wave profile for (6.1) in the case that the function $f(V)$ is

$$f(v) = \begin{cases} -v, & \text{for } v < \alpha/2, \\ v - \alpha, & \text{for } \alpha/2 < v < \frac{1+\alpha}{2}, \\ 1 - v, & \text{for } v > \frac{1+\alpha}{2}. \end{cases} \tag{6.129}$$

6. (a) Solve the bistable equation

$$v_t = v_{xx} + v(0.1 - v)(v - 1) \tag{6.130}$$

   numerically and plot a traveling wave.

   (b) Solve the FitzHugh-Nagumo equations

$$\begin{aligned} v_t &= v_{xx} + v(0.1 - v)(v - 1) - w \tag{6.131} \\ w_t &= 0.1(v - w) \tag{6.132} \end{aligned}$$

   numerically and plot a traveling wave.

7. Find the speed of traveling fronts for barnacle muscle fiber using the Morris–Lecar model (Chapter 5, (5.72)–(5.73)).

   Answer: About 6 cm/s .

8. Write a program to numerically calculate the speed of propagation for the bistable equation. Use the program to determine the effect of sodium channel density (Table 6.1) on the speed of propagation in various axons, assuming that all other currents are the same as for the Hodgkin–Huxley model.

9. Show that $1/p'(\lambda_1) + 1/p'(\lambda_2) + 1/p'(\lambda_3) = 0$, where p is defined by (6.58). Hence, show that $h(1) = 0$, where h is defined by (6.64). Show also that $\lambda_1/p'(\lambda_1) + \lambda_2/p'(\lambda_2) + \lambda_3/p'(\lambda_3) = 0$ and thus $h'(1) = 0$. Finally, show that $h''(1) = p'(\lambda_1)/\lambda_1^2 - 2$.

10. The results of Exercise 9 can be generalized. Use contour integration in the complex plane to show that for an nth order polynomial $p(z) = z^n + \cdots$ with simple roots $z_k, k = 1, \ldots, n$,

$$\sum_{k=1}^{n} \frac{z_k^j}{p'(z_k)} = 0, \tag{6.133}$$

provided that $n > j + 1$. In addition, show that

$$\sum_{k=1}^{n} \frac{z_k^{n-1}}{p'(z_k)} = 1. \tag{6.134}$$

11. Show that the duration of the absolute refractory period of the traveling pulse for the generalized FitzHugh–Nagumo model is (approximately)

$$T_{\mathrm{ar}} = \int_{w_-}^{w_0} \frac{dw}{G_-(w)}, \tag{6.135}$$

where w_0 is that value of w for which $c(w) = 0$.

12. Show that in the limit as the period approaches infinity, (6.85) and (6.86) reduce to the equations for a solitary pulse (6.62) and (6.63).

13. Suppose a nearly singular (ϵ small) FitzHugh–Nagumo system has a stable periodic oscillatory solution when there is no diffusive coupling. How do the phase portraits for the spatially independent solutions and the periodic traveling waves differ? How are these differences reflected in the temporal behavior of the solutions?

14. (Fisher's equation.) The goal of this exercise is to find traveling wave solutions of the equation

$$u_t = u_{xx} + f(u), \tag{6.136}$$

where $f(u) = u(1-u)$. This equation, sometimes known as Fisher's equation, is commonly used in mathematical ecology and population biology to model traveling waves. In this context u corresponds to a population density or a gene density.

(a) Convert to the traveling wave coordinate $\xi = x + ct$, where $c \geq 0$ is the wave speed, and show that the PDE converts to the system of ODEs

$$u' = w \qquad\qquad\qquad (6.137)$$
$$w' = cw - u(1 - u). \qquad\qquad (6.138)$$

(b) What are the steady states of the ODE system? Determine the stability of the steady states and sketch the phase plane, including the directions of the eigenvectors at the saddle point.

(c) Show that a biologically relevant traveling wave cannot exist when $c < 2$.

(d) Starting at the saddle point $(1, 0)$, follow the stable manifold backwards in time. Show that while doing so, this stable manifold cannot leave the first quadrant across the u axis.

(e) Show that if $c \geq 2$ there exists a line, $u = mw$, such that the stable manifold of the saddle point cannot be above this line.

(f) Use this to draw a conclusion about the existence of traveling wave solutions to Fisher's equation.

15. Here we examine Fisher's equation (20.515) again in a more general form. Suppose $f(0) = f(1) = 0, f'(0) > 0, f'(1) < 0$, and $f(u) > 0$ for $0 < u < 1$.

(a) Show that when $c = 0$ there are no trajectories with $u \geq 0$ connecting the two rest points $u = 0$ and $u = 1$.

(b) Show that if there is a value of c for which there is no heteroclinic connection with $u \geq 0$, then there is no such connecting trajectory for any smaller value of c.

(c) Show that if there is a value of c for which there is a connecting trajectory with $u \geq 0$, then there is a connecting trajectory for every larger value of c.

(d) Let μ be the smallest positive number for which $f(u) \leq \mu u$ for $0 \leq u \leq 1$. Show that a heteroclinic connection exists for all $c \geq 2\sqrt{\mu}$.

16. (Phase waves.) Suppose $f(0) = f(1) = f'(0) = 0, f'(1) < 0$ and $f(v) > 0$ for $0 < v < 1$. Show that all the statements of Exercise 14 hold.

(a) Show that there are values of c for which there are no trajectories connecting critical points for the equation $V'' + cV' + f(V) = 0$, with $f(0) = f'(0) = f(1) = 0$, and $f(v) > 0$ for $0 < v < 1$. Hint: What is the behavior of trajectories for $c = 0$?

(b) Show that if a connecting trajectory exists for one value of $c < 0$, then it exists for all smaller (larger in absolute value) values of c. Hint: What happens to trajectories when c is decreased (increased in absolute value) slightly? How do trajectories for different values of c compare?

17. Construct a traveling wave solution for the equation $v_t = v_{xx} + f(v)$ with $v(-\infty, t) = 0$ and $v(+\infty, t) = 1$ where $f(v) = 0$ for $0 < v < q$, $f(v) = 1 - v$ for $q < v < 1$. What is the speed of propagation? For what values of q does the wave exist? Plot the traveling waveform on the same graph as the traveling waveform for the piecewise-linear bistable equation for values of q and α for which the speeds are the same.

18. Show that the equation $v_t = v_{xx} + f(v)$, where $f(0) = f(1) = 0$, has a monotone traveling wave solution connecting $v = 0$ to $v = 1$ only if $\int_0^1 f(v)\, dv > 0$. Interpret the results of Exercises 4 and 17 in light of this result.

19. Given a dispersion curve $c = C(T)$, use the simple kinetic theory

$$\frac{dt_n(x)}{dx} = \frac{1}{C(t_n(x) - t_{n-1}(x))} \tag{6.139}$$

to determine the stability of periodic waves on a ring of length L.

Hint: On a ring of length L, $t_n(x) = t_{n-1}(x - L)$. Suppose that $T^* C(T^*) = L$. Perform linear stability analysis for the solution $t_n(x) = \frac{x}{C(T^*)}$.

20. Use perturbation arguments to estimate the error in the calculated speed of propagation when Euler's method (forward differencing in time) with second-order centered differencing in space is used to approximate the solution of the bistable equation.

21. Generalize the kinematic theory (6.93)–(6.95) to the case in which wave backs are not phase waves, by tracking both fronts and backs and the corresponding recovery value. **add reference, E. Cytrynbaum and J. P. Keener, Stability conditions for the Traveling Pulse - Modifying the restitution hypothesis, Chaos, 12, 788-799 (2002).**

22. What is the eikonal-curvature equation for (6.96) when the medium is anisotropic and D is a symmetric matrix, slowly varying in space?

Answer: $S_t = \sqrt{\nabla S \cdot D \nabla S} \left(c_0 \sqrt{k} + \nabla \cdot \left(\frac{D \nabla S}{\sqrt{\nabla S \cdot D \nabla S}} \right) \right)$.

23. Verify (6.103).

24. Verify that in two spatial dimensions, $\nabla \cdot \left(\frac{\nabla S}{|\nabla S|} \right)$ is the curvature of the level surface of the function S.

25. The following are the rules for a simple finite automaton on a rectangular grid of points:

   (a) The state space consists of three states, 0, 1, and 2, 0 meaning at rest, 1 meaning excited, and 2 meaning refractory.

   (b) A point in state 1 goes to state 2 on the next time step. A point in state 2 goes to 0 on the next step.

(c) A point in state 0 remains in state 0 unless at least one of its nearest neighbors is in state 1, in which case it goes to state 1 on the next step.

Write a computer program that implements these rules. What initial data must be supplied to initiate a spiral? Can you initiate a double spiral by supplying two stimuli at different times and different points?

26. (a) Numerically simulate spiral waves for the Pushchino model of Chapter 5, Exercise 13.

(b) Numerically simulate spiral waves for the Pushchino model with

$$
f(V) = \begin{cases} C_1 V & \text{when } V < V_1, \\ -C_2 V + a & \text{when } V_1 < V < V_2, \\ C_3(V-1) & \text{when } V > V_2, \end{cases} \tag{6.140}
$$

and

$$
\tau(V, w) = \begin{cases} \tau_1 & \text{when} \quad V_1 < V < V_2 \\ \tau_1 & \text{when} \quad V < V_1, w > w_1, \\ \tau_2 & \text{when} \quad V > V_2, \\ \tau_3 & \text{when} \quad V < V_1, w < w_1. \end{cases}
$$

Use the parameters $V_1 = 0.0026$, $V_2 = 0.837$, $w_1 = 1.8$, $C_1 = 20$, $C_2 = 3$, $C_3 = 15$, $a = 0.06$, $\tau_1 = 75$, $\tau_2 = 1.0$, $\tau_3 = 2.75$, and $k = 3$. What is the difference between these spirals and those for the previous model?

Answer: There are no stable spirals for this model, but spirals continually form and break apart, giving a "chaotic" appearance.

Chapter 7

Calcium Dynamics

Calcium is critically important for a vast array of cellular functions, as can be seen by a quick look through any physiology book. For example, in this book we discuss the role that Ca^{2+} plays in muscle mechanics, cardiac electrophysiology, bursting oscillations and secretion, hair cells, and adaptation in photoreceptors, among other things. Clearly, the mechanisms by which a cell controls its Ca^{2+} concentration are of central interest in cell physiology.

There are a number of Ca^{2+} control mechanisms operating on different levels, all designed to ensure that Ca^{2+} is present in sufficient quantity to perform its necessary functions, but not in too great a quantity in the wrong places. Prolonged high concentrations of Ca^{2+} are toxic. For example, cellular Ca^{2+} overload can trigger apoptotic cell death, a process in which the cell kills itself. In muscle cells, high intracellular calcium is responsible for prolonged muscle tension and rigor mortis.

There are many reviews of Ca^{2+} physiology in the literature: in 2003 an entire issue of Nature Reviews was devoted to the subject and contains reviews of Ca^{2+} homeostasis (Berridge et al., 2003), extracellular Ca^{2+} sensing (Hofer and Brown, 2003), Ca^{2+} signaling during embryogenesis (Webb and Miller, 2003), the Ca^{2+}-apoptosis link (Orrenius et al., 2003), and the regulation of cardiac contractility by Ca^{2+} (MacLennan and Kranias, 2003). Other useful reviews are Berridge (1997) and Carafoli (2002).

In vertebrates, the majority of body Ca^{2+} is stored in the bones, from where it can be released by hormonal stimulation to maintain an extracellular Ca^{2+} concentration of around 1 mM, while intracellular $\left[Ca^{2+}\right]$ is kept at around 0.1 μM. Since the internal concentration is low, there is a steep concentration gradient from the outside of a cell to the inside. This disparity has the advantage that cells are able to raise their Ca^{2+} concentration quickly, by opening Ca^{2+} channels and relying on passive flow down a steep concentration gradient, but it has the disadvantage that energy must be expended to keep the cytosolic Ca^{2+} concentration low. Thus, cells have finely tuned mechanisms to control the influx and removal of cytosolic Ca^{2+}.

Calcium is removed from the cytoplasm in two principal ways: it is pumped out of a cell, and it is sequestered into internal membrane-bound compartments such as the mitochondria, the endoplasmic reticulum (ER) or sarcoplasmic reticulum

(SR), and secretory granules. Since the Ca^{2+} concentration in the cytoplasm is much lower than either the extracellular concentration or the concentration inside the internal compartments, both methods of Ca^{2+} removal require expenditure of energy. Some of this is by a Ca^{2+}-ATPase, similar to the Na,K-ATPase discussed in Chapter 2, that uses energy stored in ATP to pump Ca^{2+} out of the cell or into an internal compartment. There is also a Na^+–Ca^{2+} exchanger (NCX) in the cell membrane that uses the energy of the Na^+ electrochemical gradient to remove Ca^{2+} from the cell at the expense of Na^+ entry (also discussed in Chapters 2 and 3).

Calcium influx also occurs via two principal pathways: inflow from the extracellular medium through Ca^{2+} channels in the surface membrane and release from internal stores. The surface membrane Ca^{2+} channels are of several different types. For example, voltage-controlled channels open in response to depolarization of the cell membrane, receptor-operated channels open in response to the binding of an external ligand, second-messenger-operated channels open in response to the binding of a cellular second messenger, and mechanically operated channels open in response to mechanical stimulation. Voltage-controlled Ca^{2+} channels are of great importance in other chapters of this book (in particular, for bursting oscillations in Chapter ?? or cardiac cells in Chapter ??), but are not discussed here. We also omit consideration of the other surface membrane channels, concentrating instead on the properties of Ca^{2+} release from internal stores.

Calcium release from internal stores such as the ER is the second major Ca^{2+} influx pathway, and this is mediated principally by two types of Ca^{2+} channels that are also receptors: the ryanodine receptor and the inositol (1,4,5)-trisphosphate (IP_3) receptor. The ryanodine receptor, so-called because of its sensitivity to the plant alkaloid ryanodine, plays an integral role in excitation–contraction coupling in skeletal and cardiac muscle cells, and is believed to underlie Ca^{2+}-induced Ca^{2+} release, whereby a small amount of Ca^{2+} entering the cardiac or skeletal muscle cell through voltage-gated Ca^{2+} channels initiates an explosive release of Ca^{2+} from the sarcoplasmic reticulum. Excitation-contraction coupling is discussed in detail in Chapter 15. Ryanodine receptors are also found in a variety of nonmuscle cells such as neurons, pituitary cells, and sea urchin eggs. The IP_3 receptor, although similar in structure to the ryanodine receptor, is found predominantly in nonmuscle cells, and is sensitive to the second messenger IP_3. The binding of an extracellular agonist such as a hormone or a neurotransmitter to a receptor in the surface membrane can cause, via a G-protein link to phospholipase C (PLC), the cleavage of phosphotidylinositol (4,5)-bisphosphate (PIP_2) into diacylglycerol (DAG) and IP_3 (Fig. 7.1). The water-soluble IP_3 is free to diffuse through the cell cytoplasm and bind to IP_3 receptors situated on the ER membrane, leading to the opening of these receptors and subsequent release of Ca^{2+} from the ER. Similar to ryanodine receptors, IP_3 receptors are modulated by the cytosolic Ca^{2+} concentration, with Ca^{2+} both activating and inactivating Ca^{2+} release, but at different rates. Thus, Ca^{2+}-induced Ca^{2+} release occurs through IP_3 receptors also.

As an additional control for the cytosolic Ca^{2+} concentration, Ca^{2+} is heavily buffered (i.e., bound) by large proteins, with estimates that at least 99% of the total cytoplasmic Ca^{2+} is bound to buffers. The Ca^{2+} in the ER and mitochondria is also heavily buffered.
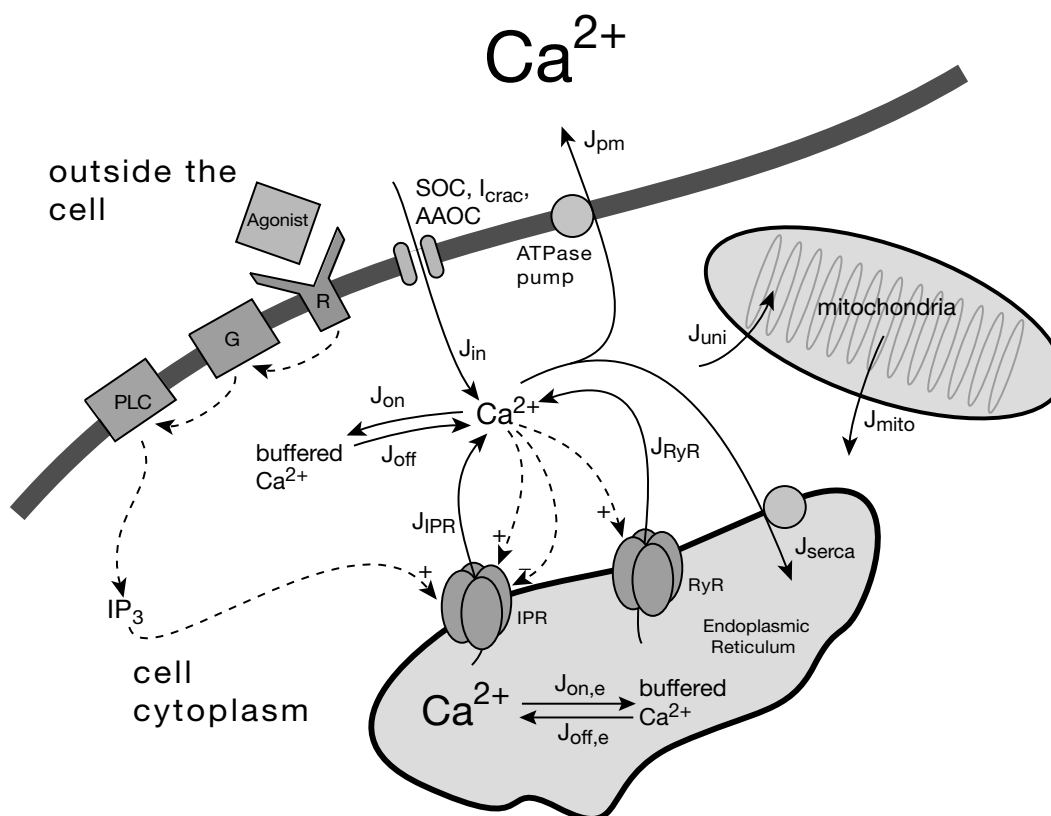
Figure 7.1: Diagram of the major fluxes involved in the control of cytoplasmic Ca^{2+} concentration. Binding of agonist to a cell membrane receptor (R) leads to the activation of a G-protein (G), and subsequent activation of phospholipase C (PLC). This cleaves phosphotidylinositol bisphosphate (PIP_2) into diacylglycerol and inositol trisphosphate (IP_3), which is free to diffuse through the cell cytoplasm. When IP_3 binds to an IP_3 receptor (IPR) on the endoplasmic reticulum (ER) membrane it causes the release of Ca^{2+} from the ER, and this Ca^{2+} in turn modulates the open probability of the IPR and ryanodine receptors (RyR). Calcium fluxes are denoted by solid arrows. Calcium can be released from the ER through IPR (J_{IPR}) or RyR (J_{RyR}), can be pumped from the cytoplasm into the ER (J_{serca}) or to the outside (J_{pm}), can be taken up into (J_{uni}), or released from (J_{mito}), the mitochondria, and can be bound to (J_{on}), or released from (J_{off}), Ca^{2+} buffers. Entry from the outside (J_{in}) is controlled by a variety of possible channels, including store-operated channels (SOC), calcium release activated channels (I_{crac}) and arachidonic acid operated channels (AAOC).

7.1   Calcium Oscillations and Waves

One of the principal reasons that modelers have become interested in calcium dynamics is that the concentration of Ca^{2+} shows highly complex spatio-temporal behavior (Fig. 7.2). Many cell types respond to agonist stimulation with oscillations in the concentration of Ca^{2+}. These oscillations can be grouped into two major types: those that are dependent on periodic fluctuations of the cell membrane potential and the associated periodic entry of Ca^{2+} through voltage-gated Ca^{2+} channels (for example in cardiac cells), and those that occur in the presence of a voltage clamp. The focus in this Chapter is on the latter type, within which group further distinctions can be made by whether the oscillatory calcium flux is through ryanodine or IP_3 receptors. We consider models of both types here, beginning with models of IP_3-dependent Ca^{2+} oscillations.

Calcium oscillations have been implicated in a vast array of cellular control processes. The review by Berridge *et al.* (2003) mentions, among other things, oocyte activation at fertilization, axonal growth, cell migration, gene expression, formation of nodules in plant root hairs, development of muscle, and release of cytokines from epithelial cells. In many cases, the oscillations are a frequency-encoded signal that allows a cell to use Ca^{2+} as a second messenger while avoiding the toxic effects of prolonged high $\left[Ca^{2+}\right]$. For example, exocytosis in gonadotropes is known to be dependent on the frequency of Ca^{2+} oscillations (Tse *et al.*, 1993), and gene expression can also be modulated by Ca^{2+} spike frequency (Dolmetsch *et al.*, 1998; Li *et al.*, 1998). However, there are still many examples where the signal carried by a Ca^{2+} oscillation has not been unambiguously decoded.

The period of IP_3-dependent oscillations ranges from a few seconds to a few minutes. In some cell types these oscillations appear to occur at a constant concentration of IP_3, while in other cell types they appear to be driven by oscillations in $[IP_3]$. Modulation of the IP_3 receptor by other factors such as phosphatases and kinases also plays an important role in setting the oscillation period, while Ca^{2+} influx from outside the cell is another important regulatory mechanism. Thus, there is a tremendous variety of mechanisms that control Ca^{2+} oscillations, and it is not realistic to expect that a single model can capture the important behaviors in all cell types. Nevertheless, most of the models have much in common, and a great deal can be learned about the overall approach by the study of a small number of models. The concept of a cellular calcium-signaling "toolkit" has been introduced by Berridge *et al.* (2003). There are a large number of components in the toolkit (receptors, G proteins, channels, buffers, pumps, exchangers and so on); by expressing those components which are needed, each cell can fine-tune the spatio-temporal properties of its intracellular Ca^{2+}. Models of Ca^{2+} dynamics follow a similar modular approach. Each member of the cellular toolkit has a corresponding module in the modeling toolkit (or if one doesn't exist it can be constructed). To construct whole-cell models one then combines appropriate components from the modeling toolkit.

Often Ca^{2+} oscillations do not occur uniformly throughout the cell, but are organized into repetitive intracellular waves (Rooney and Thomas, 1993; Thomas *et al.*, 1996; Røttingen and Iversen, 2000; Falcke, 2004). One of the most visually impres-
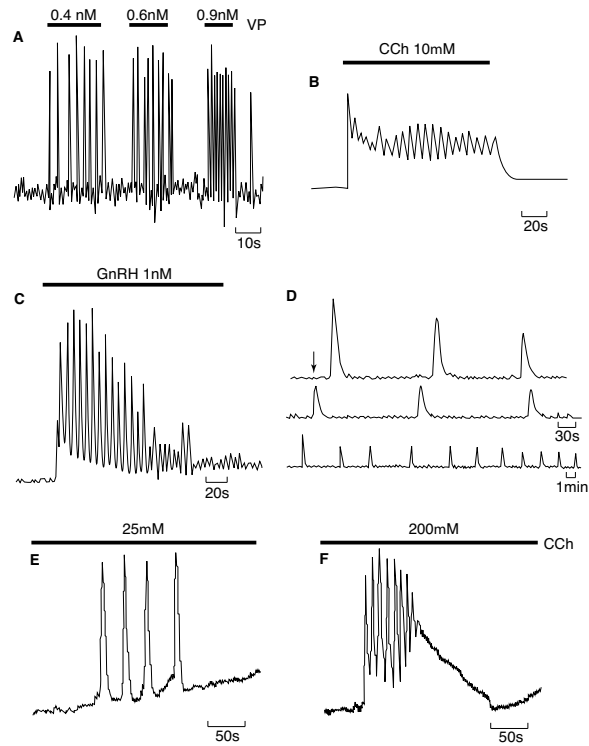
Figure 7.2: Typical calcium oscillations from a variety of cell types. A: Hepatoctyes stimulated with vasopressin (VP). B: Rat parotid gland stimulated with carbachol (CCh). C: Gonadotropes stimulated with gonadotropin-releasing hormone (GnRH). D: Hamster eggs after fertilization. The time of fertilization is denoted by the arrow. E and F: Insulinoma cells stimulated with two different concentrations of carbachol. (Berridge and Galione, 1988, Fig. 2.)
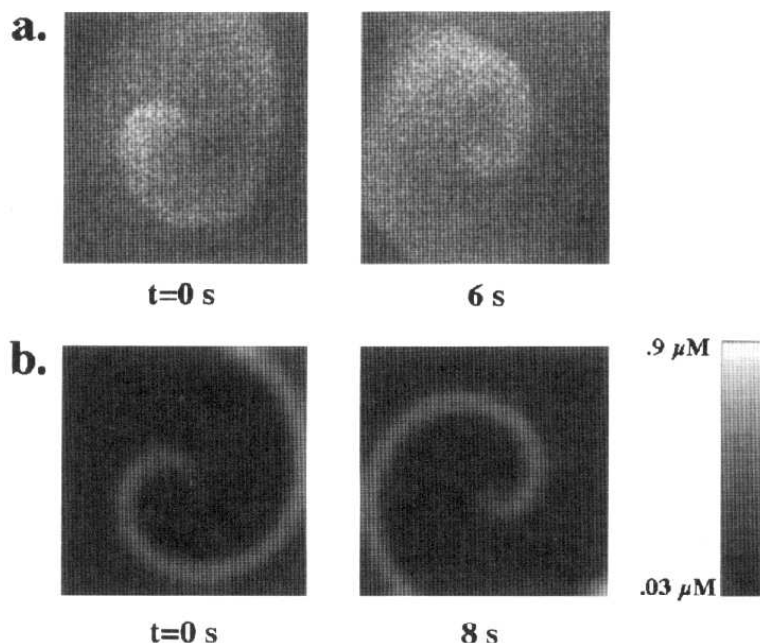
Figure 7.3: A: Spiral Ca^{2+} wave in the *Xenopus* oocyte. The image size is 420×420 μm. The spiral has a wavelength of about 150 μm and a period of about 8 seconds. B: A model spiral wave simulated on a domain of size 250×250 μm, with $[IP_3] = 95$ nM. See Section 7.3.1. (Atri *et al.*, 1993, Fig. 11.)

sive examples of this occurs in *Xenopus* oocytes. In 1991 Lechleiter and Clapham and their coworkers discovered that intracellular Ca^{2+} waves in immature *Xenopus* oocytes showed remarkable spatiotemporal organization. By loading the oocytes with a Ca^{2+}-sensitive dye, releasing IP_3, and observing Ca^{2+} release patterns with a confocal microscope, Lechleiter and Clapham (1992; Lechleiter *et al.*, 1991b) observed that the intracellular waves develop a high degree of spatial organization, forming concentric circles, plane waves, and multiple spirals. Typical experimental results are shown in Fig. 7.3A. The feature of *Xenopus* oocytes that makes these observations possible is their large size. *Xenopus* oocytes can have a diameter larger than 600 μm, an order of magnitude greater than most other cells. In a small cell, a typical Ca^{2+} wave (often with a width of close to 100 μm) cannot be observed in its entirety, and there is not enough room for a spiral to form. However, in a large cell it may be possible to observe both the wave front and the wave back, as well as spiral waves, and this has made the *Xenopus* oocyte an important system for the study of Ca^{2+} waves. Of course, what is true for *Xenopus* oocytes is not necessarily true for other cells, and so one must be cautious about extrapolating to other cell types. The physiological significance of these spatio-temporal patterns is also not apparent.

Another well-known example of an intracellular Ca^{2+} wave occurs across the

cortex of an egg directly after fertilization (Ridgeway *et al.*, 1977; Nuccitelli *et al.*, 1993). In fact, this wave motivated the first models of Ca^{2+} wave propagation, appearing as early as 1978 (Gilkey *et al.*, 1978; Cheer *et al.*, 1987; Lane *et al.*, 1987). Because they do not account for the underlying physiology, these early models have since been superseded (Wagner *et al.*, 1998; Bugrim *et al.*, 2003).

In addition to traveling across single cells, Ca^{2+} waves can be transmitted between cells, forming intercellular waves that can travel over distances of many cell lengths. Such intercellular waves have been observed in intact livers, slices of hippocampal brain tissue, epithelial and glial cell cultures (see Fig. 7.4), and many other preparations (Sanderson *et al.*, 1990, 1994; Charles *et al.*, 1991, 1992; Robb-Gaspers and Thomas, 1995). Not all intercellular coordination is of such long range; synchronized oscillations are often observed in small groups of cells such as pancreatic or parotid acinar cells (Yule *et al.,* 1996) or multiplets of hepatocytes (Tordjmann *et al.*, 1997, 1998).

Although there is controversy about the exact mechanisms by which Ca^{2+} waves propagate (and it is true that the mechanisms differ from cell type to cell type), it is widely believed that in many cell types, intracellular Ca^{2+} waves are driven by the diffusion of Ca^{2+} between Ca^{2+} release sites. According to this hypothesis, the Ca^{2+} released from one group of release sites (usually either IPR or RyR) diffuses to neighboring release sites and initiates further Ca^{2+} release from them. Repetition of this process can generate an advancing wave front of high Ca^{2+} concentration, i.e., a Ca^{2+} wave. Since they rely on the active release of Ca^{2+} via a positive feedback mechanism, such waves are actively propagated. The theory of such waves was presented in Chapter 6. However, when the underlying Ca^{2+} kinetics are oscillatory (i.e., there is a stable limit cycle), waves can propagate by a kinematic, or phase wave, mechanism, in which the wave results from the spatially ordered firing of local oscillators. These waves do not depend on Ca^{2+} diffusion for their existence, but merely on the fact that one end of the cell is oscillating with a different phase than the other end. In this case, Ca^{2+} diffusion serves to synchronize the local oscillators, but the phase wave persists in the absence of Ca^{2+} diffusive coupling.

The most common approach to the study of Ca^{2+} oscillations and waves is to assume that the underlying mechanisms are deterministic. However, even the most cursory examination of experimental data shows that Ca^{2+} dynamics is inherently stochastic in nature. The most prominent of the stochastic events underlying Ca^{2+} oscillations and waves are small localized release events called *puffs*, or *sparks*, and these elementary events, caused by the opening of single, or a small number of, Ca^{2+} release channels, are the building blocks from which global events are built. Calcium puffs, caused by localized release through IPR, have been extensively studied in *Xenopus* oocytes and HeLa cells (Marchant *et al.*, 1999; Sun *et al.*, 1998; Callamaras *et al.*, 1998; Marchant and Parker, 2001; Thomas *et al.*, 2000; Bootman *et al.*, 1997a,b), while calcium sparks, caused by localized release through RyR and occuring principally in muscle cells, were discovered by Cheng *et al.* (1993) and studied by a multitude of authors since (Smith *et al.*, 1998; Izu *et al.*, 2001; Sobie *et al.*, 2002; Soeller and Cannell, 1997, 2002). To study the stochastic properties of puffs and sparks, stochastic models are necessary. In general such models are based on stochastic simulations of Markov state models for the IPR and RyR. We discuss
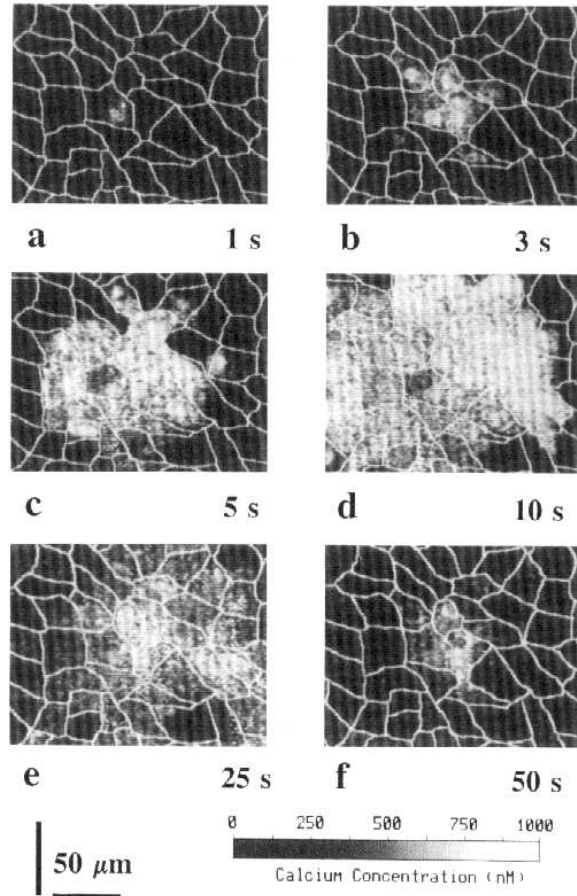
Figure 7.4: Mechanically stimulated intercellular wave in airway epithelial cells. The solid white lines denote the cell borders, and the white dot in the approximate center of frame **a** denotes the place of mechanical stimulation. After mechanical stimulation a wave of increased $[Ca^{2+}]$ can be seen spreading from the stimulated celll through other cells in the culture. The time after mechanical stimulation is given in seconds in the lower right corner of each panel. (Sneyd *et al.*, 1995b, Fig. 4A.). A model for this wave is discussed in Section 7.7.

such models briefly in Section 7.6.

A wide variety of different models have been constructed to study Ca^{2+} oscillations and waves in many different cell types. There is not space enough here to discuss all the models in the literature. Thus, after discussing particular models for each of the most important Ca^{2+} fluxes, we discuss in detail a few models for oscillations and waves. The most comprehensive review of the field is Falcke (2004); this review is almost 200 pages long and is the best yet written of models of Ca^{2+} dynamics.

7.2 Well-Mixed Cell Models: Calcium Oscillations

If we assume the cell is well-mixed, then the concentration of each species is homogeneous throughout. We write c for the concentration of free Ca^{2+} ions in the cytoplasm and note that $c = c(t)$, i.e., c has no spatial dependence. Similarly, we let c_e denote the homogeneous concentration of Ca^{2+} in the ER.

The differential equations for c and c_e follow from conservation of calcium. In words,

Rate of change of total calcium $=$ net flux of calcium into the compartment

or in mathematical notation,

$$\frac{d(vc)}{dt} = \tilde{J}_{\text{net}}, \tag{7.1}$$

where v is the volume of the compartment, and $\tilde{J}_{\text{net}}$ is the net Ca^{2+} flux into the compartment, in units of number of molecules per second. Usually it is assumed that the volumes of the cell and its internal compartments are constant, in which case the conservation equation is written as

$$\frac{dc}{dt} = J_{\text{net}} = \tilde{J}_{\text{net}}/v. \tag{7.2}$$

Here, J_{net} is the net flux into the cytoplasm per cytoplasmic volume, and has units of concentration per second.

In applications where the volume is changing (as, for example, in models of cell volume control, or models of the control of fluid secretion by Ca^{2+} oscillations), it is necessary to use $\tilde{J}_{\text{net}}$ instead of J_{net}.

More specifically, in view of the fluxes shown in Fig. 7.1, we have

$$\frac{dc}{dt} = J_{\text{IPR}} + J_{\text{RyR}} + J_{\text{in}} - J_{\text{pm}} - J_{\text{serca}} - J_{\text{on}} + J_{\text{off}} + J_{\text{uni}} - J_{\text{mito}}, \tag{7.3}$$

For the equation for ER Ca^{2+}, the fact that the cytoplasmic volume is different than the ER volume must be taken into account. Again, in view of the fluxes shown in Fig. 7.1, we have

$$\frac{dc_e}{dt} = \gamma(J_{\text{serca}} - J_{\text{IPR}} - J_{\text{RyR}}) + J_{\text{off,e}} - J_{\text{on,e}}, \tag{7.4}$$

where $\gamma = \frac{v_{cyt}}{v_{ER}}$ is the ratio of the cytoplasmic volume to the ER volume.

Each of the fluxes in these equations corresponds to a component of the Ca^{2+}-signaling toolkit of which there are many possibilities; here, we discuss only those that appear most often in models. In general, these equations are coupled to additional differential equations that describe the gating of the IPR or RyR, or the dynamics of the pumps and exchangers. An example of such a model is discussed in Section 7.2.6. However, before we see what happens when it is all put together, we first discuss how each toolkit component is modelled.

7.2.1 Influx

In general, the influx of Ca^{2+} into a cell from outside is voltage-dependent. However, when Ca^{2+} oscillations occur at a constant voltage (as is typical in non-excitable cells) the voltage dependence is unimportant. This influx is certainly dependent on a host of other factors, including Ca^{2+}, IP_3, arachidonic acid and the Ca^{2+} concentration in the ER. For example, there is evidence that, in some cell types, depletion of the ER causes an increase in Ca^{2+} influx through store-operated channels, or SOCs (Clapham, 1995). There is also evidence that SOCs play a role only at high agonist concentration (when the ER is highly depleted) but that at lower agonist concentrations Ca^{2+} influx is controlled by arachidonic acid (Shuttleworth, 1999). However, the exact mechanism by which this occurs is unknown. What is known is that J_{in} increases as agonist concentration increases; if this were not so, the steady-state level of Ca^{2+} would be independent of IP_3 (see Exercise 1) which it is not. One common model makes the simple assumption that J_{leak} is a linear increasing function of p, the IP_3 concentration, with

$$J_{in} = \alpha_1 + \alpha_2 p, \tag{7.5}$$

for some constants α_1 and α_2.

7.2.2 Mitochondria

Mitochondrial Ca^{2+} handling is a highly complex process, and a number of detailed models have been constructed. For the sake of brevity we do not discuss these models at all; the interested reader is referred to Colegrove *et al.* (2000), Friel (2000), Falcke *et al.* (2000), Grubelnik *et al.* (2001), Marhl *et al.* (2000), Schuster *et al.* (2002) and Selivanov *et al.* (1998). It seems that one function of the mitochondria is to take up and release large amounts of Ca^{2+}, but relatively slowly. Thus, the mitochondria tend to modulate the trailing edges of the waves, reduce wave amplitude, and change the long-term oscillatory behavior. However, this is certainly an over-simplification.

7.2.3 Calcium Buffers

At least 99% of Ca^{2+} in the cytoplasm is bound to large proteins, called Ca^{2+} buffers. Typical buffers are calsequestrin, calbindin, flourescent dyes, and the plasma membrane itself. A detailed discussion of Ca^{2+} buffering, and its effect on oscillations and waves, is given in Section 7.4.
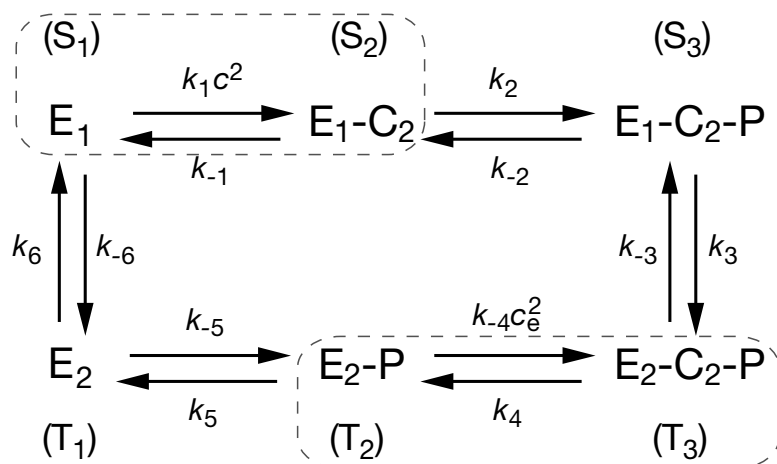
Figure 7.5: Schematic diagram of the SERCA model of MacLennan *et al.* (1997). E_1 is the conformation in which the Ca^{2+} binding sites are exposed to the cytoplasm, and E_2 is the conformation in which they are exposed to the lumen and have a much lower affinity for Ca^{2+}. The P denotes that the pump has been phosphorylated; for simplicity ATP and ADP have been omitted from the diagram. The co-transport of H^+ has also been omitted. By assuming fast equilibrium between the pairs of states in the dashed boxes, a simplified model, shown in Fig. 7.6, can be derived.

7.2.4 Calcium Pumps and Exchangers

Calcium-ATPases

Early models of the Ca^{2+}-ATPase pump were of the Hill equation type (Chapter 1, Section 1.4.4). For example, data from Lytton *et al.* (1992) showed that the flux through the ATPase was approximately a sigmodial function of c, with Hill coefficient of about 2. Thus, a common model is

$$J_{\text{serca}} = \frac{V_p c^2}{K_p^2 + c^2}. \tag{7.6}$$

Such simple models are known to have a number of serious flaws. For example, this flux has no dependence on ER calcium concentration and is always of one sign. However, it is known that with high enough ER Ca^{2+} concentration, it is possible for the pump to reverse, generating ATP in the process.

MacLennan *et al.* (1997) constructed a more detailed model, shown schematically in Fig. 7.5. The pump can be in one of two basic conformations: E_1 and E_2. In the E_1 conformation the pump binds two Ca^{2+} ions from the cytoplasm, whereupon it exposes a phosphorylation site. Once phosphorylated, the pump switches to the E_2 conformation in which the Ca^{2+} binding sites are exposed to the ER lumen and have a much lower affinity for calcium. Thus, Ca^{2+} is released into the ER, the pump is dephosphorylated, and completes the cycle by switching back to

the E_1 conformation. For each Ca^{2+} ion transported from the cytoplasm to the ER, one proton is co-transported from the ER to the cytoplasm. This makes the similarity with the Na,K-ATPase more apparent. (In the models that we discuss here we ignore the effects of H^+ concentration on the pump rate because we are not concerned here with the effects of cellular pH.) The rate limiting step of the transport cycle is the transition from E_1-P-C_2 to E_2-P-C_2.

To calculate the flux in this model is relatively straightforward, and is similar to those that were amply discussed in Chapter 1, so we leave this calculation as an exercise for the interested reader. Solution of these equations gives

$$J = \frac{c^2 - K_1 K_2 K_3 K_4 K_5 K_6 c_e^2}{\alpha_1 c^2 + \alpha_2 c_e^2 + \alpha_3 c^2 c_e^2 + \alpha_4}, \tag{7.7}$$

where the α's are functions of the rate constants, too long and of too little interest to include in full detail. As always, $K_i = k_{-i}/k_i$. If the affinity of the Ca^{2+} binding sites is high when the pump is in conformation E_1, and low when the pump is in conformation E_2, $\frac{k_{-4}}{k_4} \ll \frac{k_1}{k_{-1}}$, so that $K_1 K_4$ is much less than one. However, it is also reasonable to assume that $\frac{k_6}{k_{-6}} = \frac{k_{-3}}{k_3}$ and that $\frac{k_2}{k_{-2}} = \frac{k_5}{k_{-5}}$, in which case $K_2 K_3 K_5 K_6 = 1$. It follows that $K_1 K_2 K_3 K_4 K_5 K_6 \ll 1$ so that the pump can support a positive flux even when c_e is much greater than c.

Notice that if this were a model of a closed system, the law of detailed balance would require that $K_1 K_2 K_3 K_4 K_5 K_6 = 1$. This is not the case here since the cycle is driven by phosphorylation of the pump, so the reaction rates depend upon the concentrations of ATP, ADP and P, and energy is continually consumed (if $J > 0$) or generated (if $J < 0$).

In the original description of the model, MacLennan *et al.* assumed that the binding and release of Ca^{2+} occurs quickly. With this assumption we get a similar expression for the steady-state flux. The process of reducing a model in this way using a fast equilibrium assumption is important and useful, and is explored in the Exercises (see Exercise 7).

In Fig. 7.5 states S_1 and S_2 have been grouped together by a box with a dotted outline, as have states T_2 and T_3. Using the assumption that these pairs of states are in instantaneous equilibrium, we find a simplified schematic diagram of the ATPase, as shown in Fig. 7.6. As c increases, the equilibrium between S_1 and S_2 is shifted further towards S_2. This increases the rate at which S_3 is formed, but decreases the rate at which S_1 is converted to T_1. Thus, the transition from $\bar{S}_1$ to S_3 is an increasing function of c, while the transition from $\bar{S}_1$ to T_1 is a decreasing function of c.

From this diagram, the steady-state flux can be calculated in the same way as before. Not surprisingly, the final result looks much the same, giving

$$J = \frac{c^2 - K_1 K_2 K_3 K_4 K_5 K_6 c_e^2}{\beta_1 c^2 + \beta_2 c_e^2 + \beta_3 c^2 c_e^2 + \beta_4}, \tag{7.8}$$

for constants β_i which are limiting values of the constants α_i that appeared in (7.7).

The Ca^{2+}-ATPases on the plasma membrane are similar to the SERCA ATPases, and are modeled in a similar way.
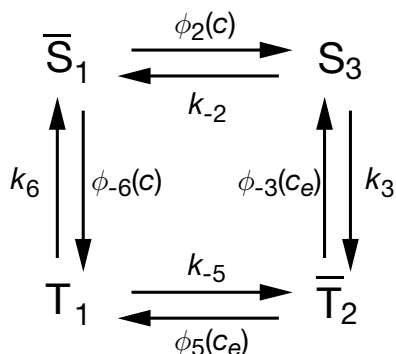
Figure 7.6: Schematic diagram of the simplified version of the SERCA model of MacLennan *et al.* (1997). By assuming fast equilibrium between the pairs of states shown grouped in Fig. 7.5 by the dashed boxes, this diagram in which there are fewer states, but with calcium-dependent transitions, can be derived. The functions in the transition rates are $\phi_2 = c^2 k_2/(c^2 + K_1)$, $\phi_{-3} = k_{-3} K_4 c_e^2/(1 + K_4 c_e^2)$, $\phi_5 = k_5/(1 + K_4 c_e^2)$ and $\phi_{-6} = K_1 k_{-6}/(K_1 + c^2)$.

Calcium exchangers

Another important way in which Ca^{2+} is removed from the cytoplasm is via the action of Na^+-Ca^{2+} exchangers, which remove one Ca^{2+} ion from the cytoplasm at the expense of the entry of three Na^+ ions. They are particularly important for the control of Ca^{2+} in cardiac cells and are discussed further in Chapter 15 in the context of models of excitation-contraction coupling.

7.2.5 IP$_3$ Receptors

A basic property of IP$_3$ receptors is that they respond in a time-dependent manner to step changes of Ca^{2+} or IP$_3$. Thus, in response to a step increase of IP$_3$ or Ca^{2+} the receptor open probability first opens to a peak and then declines to a lower plateau (see Fig. 7.7). This decline is called *adaptation* of the receptor, as it adapts to a maintained Ca^{2+} or IP$_3$ concentration. If a further step is applied on top of the first, the receptor responds with another peak, followed by a decline to a plateau. In this way the IPR responds to *changes* in $[Ca^{2+}]$ or [IP$_3$], rather than to absolute concentrations. Adaptation is a well-known feature of many physiological systems (see, for example, Chapters 16 and 19), and is often characterized by a fast activation followed by a slower inactivation, as seen in the sodium channel in the Hodgkin-Huxley model (Chapter 5).

Adaptation of the IPR is now believed to result, at least in part, from the fact that Ca^{2+} not only stimulates its own release, but also inhibits it on a slower time scale. It is hypothesized that this sequential activation and inactivation of the IP$_3$ receptor by Ca^{2+} is one mechanism underlying IP$_3$-dependent Ca^{2+} oscillations and waves, and a number of models incorporating this hypothesis have appeared
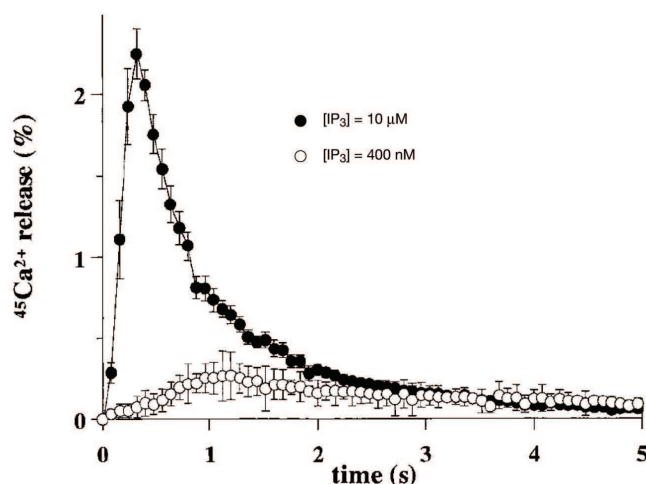
Figure 7.7: Experimental data from Marchant and Taylor (1998). In response to a maintained elevation of IP$_3$, the flux through a hepatocyte IPR (measured here as release of radioactive ^{45}Ca^{2+}), first increases to a peak and then declines to a lower level. **Springer: permission will be needed for this figure, which will also need to be massaged.**

(reviewed by Sneyd *et al.*, 1995b; Tang *et al.*, 1996; Schuster *et al.*, 2002; Falcke, 2004). However, as is described below, there are almost certainly other important mechanisms in operation; some of the most recent models have suggested that the IPR kinetics are of less importance than previously thought, while depletion of the ER might also play in important role.

An eight-state IP$_3$ receptor model

One of the earliest models of the IPR to incorporate sequential activation and inactivation by Ca^{2+} was that of De Young and Keizer (1992).

For this model, it is assumed that the IP$_3$ receptor consists of three equivalent and independent subunits, all of which must be in a conducting state for there to be Ca^{2+} flux. Each subunit has an IP$_3$ binding site, an activating Ca^{2+} binding site, and an inactivating Ca^{2+} binding site, each of which can be either occupied or unoccupied, and thus each subunit can be in one of eight states. Each state of the subunit is labeled S$_{ijk}$, where i, j, and k are equal to 0 or 1, with 0 indicating that the binding site is unoccupied and 1 indicating that it is occupied. The first index refers to the IP$_3$ binding site, the second to the Ca^{2+} activation site, and the third to the Ca^{2+} inactivation site. This is illustrated in Fig. 7.8. While the model has 24 rate constants, because of the requirement for detailed balance, these are not all independent. In addition, two simplifying assumptions are made to reduce the number of independent constants. First, the rate constants are assumed to be

group I
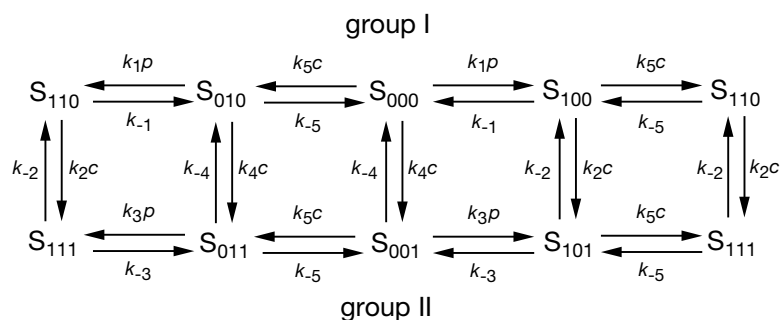
Figure 7.8: The binding diagram for the IP$_3$ receptor model. Here, c denotes $\left[\mathrm{Ca}^{2+}\right]$, and p denotes [IP$_3$].

independent of whether activating Ca^{2+} is bound or not. Second, the kinetics of Ca^{2+} activation are assumed to be independent of IP$_3$ binding and Ca^{2+} inactivation. This leaves only 10 rate constants, $k_1, \ldots, k_5$ and $k_{-1}, \ldots, k_{-5}$. Notice that with these simplifying assumptions, detailed balance is satisfied.

The fraction of subunits in the state S$_{ijk}$ is denoted by x_{ijk}. The differential equations for these are based on mass-action kinetics, and thus, for example,

$$\frac{dx_{000}}{dt} = -(V_1 + V_2 + V_3), \tag{7.9}$$

where

$$V_1 = k_1 p x_{000} - k_{-1} x_{100}, \tag{7.10}$$
$$V_2 = k_4 c x_{000} - k_{-4} x_{001}, \tag{7.11}$$
$$V_3 = k_5 c x_{000} - k_{-5} x_{010}, \tag{7.12}$$

where p denotes [IP$_3$] and c denotes $\left[\mathrm{Ca}^{2+}\right]$. V_1 describes the rate at which IP$_3$ binds to and leaves the IP$_3$ binding site, V_2 describes the rate at which Ca^{2+} binds to and leaves the inactivating site, and similarly for V_3. Since experimental data indicate that the receptor subunits act in a cooperative fashion, the model assumes that the IP$_3$ receptor passes Ca^{2+} current only when three subunits are in the state S_{110} (i.e., with one IP$_3$ and one activating Ca^{2+} bound), and thus the open probability of the receptor is x_{110}^3.

In Fig. 7.9 we show the open probability of the IP$_3$ receptor as a function of $\left[\mathrm{Ca}^{2+}\right]$, which is some of the experimental data upon which the model is based. Bezprozvanny et al. (1991) showed that this open probability is a bell-shaped function of $\left[\mathrm{Ca}^{2+}\right]$. Thus, at low $\left[\mathrm{Ca}^{2+}\right]$, an increase in $\left[\mathrm{Ca}^{2+}\right]$ increases the open probability of the receptor, while at high $\left[\mathrm{Ca}^{2+}\right]$ an increase in $\left[\mathrm{Ca}^{2+}\right]$ decreases the open probability. Parameters in the model were chosen to obtain agreement with this steady-state data. The kinetic properties of the IP$_3$ receptor are equally important: the receptor is activated quickly by Ca^{2+}, but inactivated by Ca^{2+} on a slower time scale. In the model, this is incorporated in the magnitude of the rate constants ($k_5 > k_2$ and $k_5 > k_4$).

k_1	$=$	$400~\mu\mathrm{M}^{-1}\mathrm{s}^{-1}$	k_{-1}	$=$	$52~\mathrm{s}^{-1}$
k_2	$=$	$0.2~\mu\mathrm{M}^{-1}\mathrm{s}^{-1}$	k_{-2}	$=$	$0.21~\mathrm{s}^{-1}$
k_3	$=$	$400~\mu\mathrm{M}^{-1}\mathrm{s}^{-1}$	k_{-3}	$=$	$377.2~\mathrm{s}^{-1}$
k_4	$=$	$0.2~\mu\mathrm{M}^{-1}\mathrm{s}^{-1}$	k_{-4}	$=$	$0.029~\mathrm{s}^{-1}$
k_5	$=$	$20~\mu\mathrm{M}^{-1}\mathrm{s}^{-1}$	k_{-5}	$=$	$1.64~\mathrm{s}^{-1}$

Table 7.1: Parameters of the eight-state IPR model (De Young and Keizer, 1992).
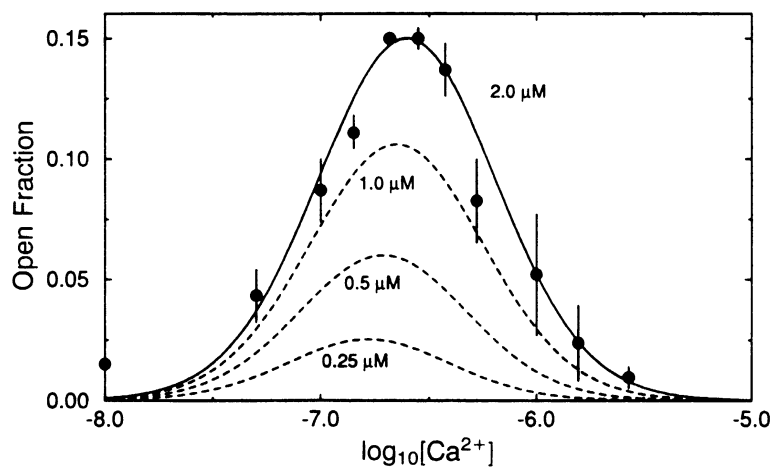
Figure 7.9: The steady-state open probability of the IP$_3$ receptor, as a function of $\left[\mathrm{Ca}^{2+}\right]$. The symbols are the experimental data of Bezprozvanny *et al.* (1991), and the smooth curves are from the receptor model (calculated at four different IP$_3$ concentrations). (De Young and Keizer, 1992, Fig. 2A.)

Reduction of the eight-state IP$_3$ receptor model

The complexity of the eight-state receptor model (seven differential equations and numerous parameters) provides ample motivation to seek a simpler model that retains its essential properties. Since IP$_3$ binds quickly to its binding site and Ca^{2+} binds quickly to the activating site, we can dispense with the transient details of these binding processes and assume instead that the receptor is in quasi-steady state with respect to IP$_3$ binding and Ca^{2+} activation (De Young and Keizer, 1992; Keizer and De Young, 1994; Li and Rinzel, 1994; Tang *et al.*, 1996). Notice that this is implied by the parameter values for the detailed receptor model shown in Table 7.1, where k_1, k_3, and k_5 are substantially larger than k_2 and k_4, and k_{-1}, k_{-3}, and k_{-5} are also larger than k_{-2} and k_{-4}. The process by which fast binding can be used to simplify a complicated model is identical to the reductions for enzyme kinetics used in Chapter 1, and so the details are left as an exercise (Exercise 4).

As shown in Fig. 7.8, the receptor states are arranged into two groups: those without Ca^{2+} bound to the inactivating site (S$_{000}$, S$_{010}$, S$_{100}$, and S$_{110}$, shown in the upper line of Fig. 7.8; called group I states), and those with Ca^{2+} bound to the inactivating site (S$_{001}$, S$_{011}$, S$_{101}$, and S$_{111}$, shown in the lower line of Fig. 7.8; called group II states). Because the binding of IP$_3$ and the binding of Ca^{2+} to the activating site are assumed to be fast processes, within each group the binding states are assumed to be at quasi-steady state. However, the transitions between group I and group II (between top and bottom in Fig. 7.8), due to binding or unbinding of the inactivating site, are slow, and so the group I states are not in equilibrium with the group II states.

Following what by now is a standard procedure, we set

$$y = x_{001} + x_{011} + x_{101} + x_{111}. \tag{7.13}$$

and find that

$$\frac{dy}{dt} = \left[\frac{(k_{-4}K_1K_2 + k_{-2}pK_4)c}{K_4K_2(p + K_1)}\right](1 - y) - \left(\frac{k_{-2}p + k_{-4}K_3}{p + K_3}\right)y. \tag{7.14}$$

This can be written in the form

$$\tau_y(c, p)\frac{dy}{dt} = y_\infty(c, p) - y, \tag{7.15}$$

which is useful for comparison with other models. The open probability is obtained from the equation

$$x_{110} = \frac{pc(1 - y)}{(p + K_1)(c + K_5)}. \tag{7.16}$$

Note that $1 - y$, which is the proportion of receptors that are not inactivated by Ca^{2+}, plays the role of an inactivation variable, similar in spirit to the variable h in the Hodgkin–Huxley equations (Chapter 5). To emphasize this similarity, the reduced model can be written in the form

$$x_{110} = \frac{pc}{(p + K_1)(c + K_5)}h, \tag{7.17}$$

$$\tau_h(c, p)\frac{dh}{dt} = h_\infty(c, p) - h, \tag{7.18}$$
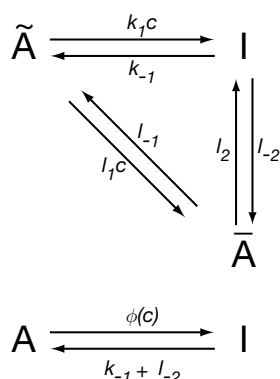
Figure 7.10: Reaction diagram of a Ca^{2+}-dependent transition from state A to state I (c is Ca^{2+} concentration). If $\tilde{A}$ and $\bar{A}$ are in equilibrium, and if $A = \bar{A} + \tilde{A}$, then the upper reaction scheme is equivalent to the lower.

where $h = 1 - y$, and τ_h and h_∞ are readily calculated from the corresponding differential equation for y.

A model with saturating binding rates

Recently it has become clear that the eight-state model has some serious flaws. Most importantly, it has been shown experimentally that the rate of Ca^{2+} binding to the IPR varies only over a single order of magnitude while the concentration of Ca^{2+} varies over four orders of magnitude. It follows that the binding of Ca^{2+} to the IPR cannot follow simple mass action kinetics, but must follow some kinetic scheme that allows for saturation of the binding rate.

Note the similarity of this to models of enzyme kinetics. There, because of the saturation of the reaction rate, simple mass action kinetics are not appropriate to model enzyme reactions, leading to the development of the Michaelis-Menten-type models. We follow a similar approach here to incorporate saturation of the binding rates.

To illustrate the idea, consider the binding reaction scheme shown in Fig. 7.10. If the transitions between $\tilde{A}$ and $\bar{A}$ are faster than other reactions so that these are in instantaneous equilibrium, then

$$c\tilde{A} = L_1\bar{A}, \tag{7.19}$$

where $L_1 = l_{-1}/l_1$. Following what by now should be the routine method to find slow dynamics, we find that

$$\frac{dA}{dt} = (k_{-1} + l_{-2})I - \phi(c)A, \tag{7.20}$$

where $A = \bar{A} + \tilde{A}$

$$\phi(c) = \frac{c(k_1 L_1 + l_2)}{c + L_1}, \tag{7.21}$$

a rate that is saturating in c. Thus, in this simple way, saturating binding kinetics can be incorporated into a model.

Using saturating binding schemes of this type, Sneyd and Dufour (2002) constructed a model of the IPR that was based on the qualitative models of Taylor and his colleagues, and is consistent with the scheme of Hajnóczky and Thomas (1997). In addition to the saturating binding rates, the main features of the model are

1. The IPR can be opened by IP_3 in the absence of Ca^{2+}, but with a lower conductance.

2. The IPR can be inactivated by Ca^{2+} in the absence of IP_3.

3. Once IP_3 is bound, the IPR can spontaneously inactivate, independently of Ca^{2+}.

4. Once IP_3 is bound, the IPR can also bind Ca^{2+} to activate the receptor. Thus, there is an intrinsic competition between Ca^{2+}-mediated receptor activation and spontaneous inactivation.

5. Once the IPR is activated by Ca^{2+} binding, it can be inactivated by binding of additional Ca^{2+}. (This feature of the model is the principal point of disagreement with the qualitative models of Taylor, 1998).

6. Binding of IP_3 and Ca^{2+} is sequential.

Following these assumptions, the model takes the form shown in Fig. 7.11, with corresponding equations

$$\frac{dR}{dt} = \phi_{-2}O - \phi_2 pR + (k_{-1} + l_{-2})I_1 - \phi_1 R, \tag{7.22}$$

$$\frac{dO}{dt} = \phi_2 pR - (\phi_{-2} + \phi_4 + \phi_3)O + \phi_{-4}A + k_{-3}S, \tag{7.23}$$

$$\frac{dA}{dt} = \phi_4 O - \phi_{-4}A - \phi_5 A + (k_{-1} + l_{-2})I_2, \tag{7.24}$$

$$\frac{dI_1}{dt} = \phi_1 R - (k_{-1} + l_{-2})I_1, \tag{7.25}$$

$$\frac{dI_2}{dt} = \phi_5 A - (k_{-1} + l_{-2})I_2, \tag{7.26}$$

where $R + O + A + S + I_1 + I_2 = 1$, and where

$$\phi_1(c) = \frac{(k_1 L_1 + l_2)c}{L_1 + c(1 + L_1/L_3)}, \quad \phi_3(c) = \frac{k_3 L_5}{L_5 + c}, \qquad \phi_5(c) = \frac{(k_1 L_1 + l_2)c}{L_1 + c},$$
$$\phi_2(c) = \frac{k_2 L_3 + l_4 c}{L_3 + c(1 + L_3/L_1)}, \quad \phi_{-2}(c) = \frac{k_{-2} + l_{-4}c}{1 + c/L_5},$$
$$\phi_4(c) = \frac{(k_4 L_5 + l_6)c}{L_5 + c}, \qquad \phi_{-4}(c) = \frac{L_1(k_{-4} + l_{-6})}{L_1 + c}.$$

The parameters were determined by fitting to experimental data and are shown in Table 7.2. We assume that the IPR consists of four identical and independent
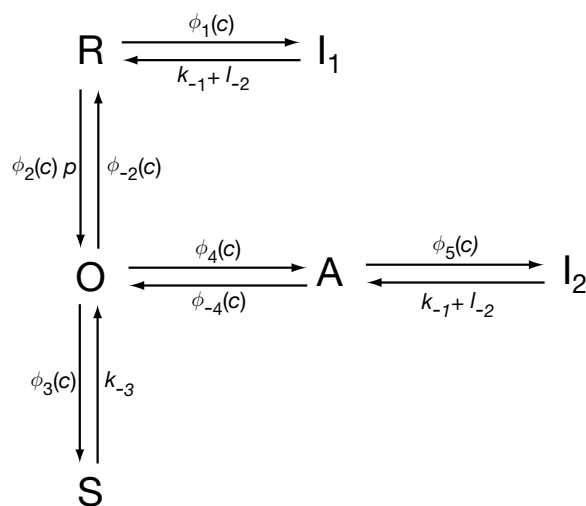
Figure 7.11: Sequential model of the IP$_3$ receptor with saturating binding rates.

subunits, and that it allows Ca^{2+} current when all four subunits are in either the O or the A state. We also assume that the more subunits in the A state, the greater the conductance. One simple way to express this is to write the open probability, P_o, as

$$P_o = (a_1 O + a_2 A)^4, \tag{7.27}$$

for some constants a_1 and a_2. In the original model $a_1 = 0.1$ and $a_2 = 0.9$, but these values can be changed without appreciably changing the fit or the model's behavior.

As a side issue, but an important one, note that the simple phrase "the parameters were determined by fitting to experimental data" covers a multitude of thorny problems. First, it is usually the case that not all the parameters in a model can be unambiguously determined from the available experimental data. This is certainly the case in the IPR model described above, for which, in fact, only a few of the parameters can be pinned down with any confidence. There is no way of getting around this unpleasant fact except either to simplify the model or to collect more experimental data of the appropriate type. Of course, determining which additional experimental data are needed is also not a trivial problem.

Second, the process of determining the parameters from the data is itself complicated. Simple methods such as least-squares fits suffer from serious disadvantages, while more sophisticated methods such as Bayesian inference and Markov Chain Monte Carlo can be more difficult to implement and less robust. A discussion of these issues is far beyond the scope of this text, and the interested reader is referred to (**ref??**).

k_1	$=$	$0.64\ \mu\mathrm{M}^{-1}\mathrm{s}^{-1}$	k_{-1}	$=$	$0.04\ \mathrm{s}^{-1}$
k_2	$=$	$37.4\ \mu\mathrm{M}^{-1}\mathrm{s}^{-1}$	k_{-2}	$=$	$1.4\ \mathrm{s}^{-1}$
k_3	$=$	$0.11\ \mu\mathrm{M}^{-1}\mathrm{s}^{-1}$	k_{-3}	$=$	$29.8\ \mathrm{s}^{-1}$
k_4	$=$	$4\ \mu\mathrm{M}^{-1}\mathrm{s}^{-1}$	k_{-4}	$=$	$0.54\ \mathrm{s}^{-1}$
L_1	$=$	$0.12\ \mu\mathrm{M}$	L_3	$=$	$0.025\ \mu\mathrm{M}$
L_5	$=$	$54.7\ \mu\mathrm{M}$	l_2	$=$	$1.7\ \mathrm{s}^{-1}$
l_4	$=$	$1.7\ \mu\mathrm{M}^{-1}\mathrm{s}^{-1}$	l_6	$=$	$4707\ \mathrm{s}^{-1}$
l_{-2}	$=$	$0.8\ \mathrm{s}^{-1}$	l_{-4}	$=$	$2.5\ \mu\mathrm{M}^{-1}\mathrm{s}^{-1}$
l_{-6}	$=$	$11.4\ \mathrm{s}^{-1}$			

Table 7.2: Parameters of the IPR model with saturating binding rates (Sneyd and Dufour, 2002).

7.2.6 Putting the Pieces Together: Simple Models of Calcium Dynamics

We now have constructed models for most of the fluxes that are important for the control of Ca^{2+}. To put them together into a model of Ca^{2+} dynamics is straightforward; simply choose your favorite model of the IPR (or RyR if appropriate), your favorite models of the ATPases and the influx, and put them all into (7.3) and (7.4).

To illustrate with a simple model, suppose there are only two fluxes, the IPR and SERCA fluxes, so that

$$\frac{dc}{dt} = (k_f P_O + J_{\mathrm{er}})(c_e - c) - J_{\mathrm{serca}}. \tag{7.28}$$

Since the only fluxes are between the ER and the cytoplasm,

$$\frac{dc_e}{dt} = -\gamma \frac{dc}{dt}, \tag{7.29}$$

so that $c + \frac{c_e}{\gamma} = c_t$ is unchanging. Such a model is called a *closed-cell* model (Section 7.2.7). Next, we use a Hill function (Chapter 1) to model the SERCA pump, giving

$$J_{\mathrm{serca}} = \frac{V_p c^2}{K_p^2 + c^2}, \tag{7.30}$$

and, to model the IPR, we use the simplified version of the DeYoung-Keizer model (7.16),

$$P_O = \left(\frac{pc(1-y)}{(p + K_1)(c + K_5)} \right)^3, \tag{7.31}$$

where y satisfies (7.14).

V_p	=	$0.9~\mu\mathrm{Ms}^{-1}$	K_p	=	0.1 s
k_f	=	1.11 s^{-1}	γ	=	5.5
J_{er}	=	0.02 s^{-1}	c_t	=	$2~\mu\mathrm{M}$

Table 7.3: Parameter values of the simple model of calcium dynamics (7.28) and (7.14). The parameter values for the IPR model are given in Table 7.1. The value for γ is based on experimental estimations of the relative volumes of the cytoplasm and the ER, while k_f is a scaling factor that controls the total amount of Ca^{2+} efflux through the IPR; k_f can be loosely interpreted as the product of the IPR density and the single channel current. Although J_{er} is based on estimations of the rate of Ca^{2+} leak from the ER at steady state, there are no reliable data for this parameter.
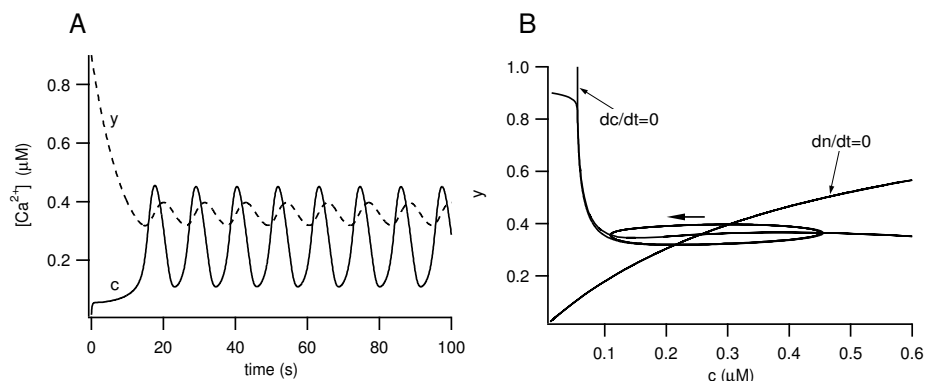
Figure 7.12: Calcium oscillations in a simple model. A: a typical oscillation (for $p = 0.5$). B: the phase portrait.

Note that the flux through the IPR is assumed to be proportional to the concentration difference between the ER and the cytoplasm. This is appropriate only if there is no potential difference across the ER membrane. Even though calcium carries a charge, the flow of calcium does not induce a potential difference because there are counterions that flow freely so that the electrical balance is not upset.

The parameter values are given in Tables 7.3 and 7.1.

Because c_t is fixed, this simple model can be reduced to a two-variable model for which a phase portrait can be constructed. The numerical solution of this model with $p = 0.5$ is shown in Fig. 7.12. The phase portrait is identical in structure to those of several two variable excitable media models, such as the FitzHugh-Nagumo model or the reduced Hodgkin-Huxley model (Chapter 5). The nullcline for the inactivation variable y is a monotone increasing function of c, and the nullcline for c is an "N-shaped" function of c (although on this scale, the N appears to be

shallow). There is a single intersection of the two nullclines. The stability of this fixed point is determined (roughly, but not precisely) by the branch of the c-nullcline on which it lies. On the left-most branch, the fixed point is stable; on the middle branch it is unstable. If the fixed point is unstable, there is a stable periodic limit cycle, corresponding to spontaneous calcium oscillations.

A more complex example

A slightly more realistic model is as follows: If we

1. ignore RyR and mitochondrial fluxes,

2. use the saturating binding model for the IPR,

3. use a four-state Markov model for the SERCA pump, with the transport of a single Ca^{2+} ion for each pump cycle,

4. use a simple Hill function for the plasma membrane pump, and

5. ignore calcium buffering (see Section 7.4)

then we get

$$\frac{dc}{dt} = (k_f P_O + J_{er})(c_e - c) - J_{serca} + J_{in} - J_{pm}, \tag{7.32}$$

$$\frac{dc_e}{dt} = \gamma[J_{serca} - (k_f P_O + J_{er})(c_e - c)], \tag{7.33}$$

where

$$J_{serca} = \frac{c - \alpha_1 c_e}{\alpha_2 + \alpha_3 c + \alpha_4 c_e + \alpha_5 c c_e}, \tag{7.34}$$

$$P_O = (0.1O + 0.9A)^4, \tag{7.35}$$

$$J_{pm} = \frac{V_p c^2}{K_p^2 + c^2}, \tag{7.36}$$

$$J_{er} = \text{constant}, \tag{7.37}$$

$$J_{in} = a_1 + a_2 p. \tag{7.38}$$

The constant J_{er} represents a constant leak from the ER that is necessary to balance the ATPase flux at steady state. Equations (7.32) and (7.33) are coupled to the equations (7.22)-(7.26) describing the IPR. We have used two different pump models here to emphasize the fact that it is possible to mix and match the individual models for the various fluxes. Since there are five parameters describing the SERCA ATPase, and only two parameters describing the plasma membrane ATPase, it is likely that the SERCA pump is overparameterized. If we were fitting the pump models to data this would be a concern since the data may not contain sufficient information to determine all the parameters unambiguously. Here, however, we are content to use some function that can be justified by a mechanistic model and for which the parameters can be adjusted to give reasonable agreement with experimental data. The parameter values are given in Table 7.4.

α_1	$=$	10^{-4}	α_2	$=$	0.007 s
α_3	$=$	$0.06\ \mu M^{-1}s$	α_4	$=$	$0.0014\ \mu M^{-1}s$
α_5	$=$	$0.007\ \mu M^{-2}s$	J_{er}	$=$	0.002 s^{-1}
V_p	$=$	$2.8\ \mu Ms^{-1}$	K_p	$=$	$0.425\ \mu M$
a_1	$=$	$0.003\ \mu Ms^{-1}$	a_2	$=$	0.02 s^{-1}
k_f	$=$	0.96 s^{-1}	γ	$=$	5.4

Table 7.4: Parameter values of the model of Ca^{2+} dynamics (7.32)-(7.38).

Since p corresponds to the concentration of IP$_3$, and thus, indirectly, the agonist concentration, we describe the behavior of this model as p varies. The bifurcation diagram for this model is shown in Fig. 7.13A. As p increases the steady state calcium concentration increases also (because J_{in} increases with p), and oscillations occur for a range of intermediate values of p. Typical oscillations for two different values of p are shown in Fig. 7.13B and C. As p increases the oscillation frequency increases.

Given the variety of models of the IPR, the RyR, the ATPases, and the other fluxes involved in Ca^{2+} dynamics, it is important to think about what a model of Ca^{2+} dynamics can tell us. For example, with nearly any combination of IPR and ATPase models, a whole-cell calcium model that exhibits Ca^{2+} oscillations of approximately the correct form can be constructed. The oscillations in Fig. 7.13 give a reasonably accurate description of Ca^{2+} oscillations in pancreatic acinar cells (the cell type for which this model was originally designed); however, the parameters could be adjusted, practically indefinitely, to obtain oscillations of a wide variety of shapes and properties to describe the behavior in other cell types. The fact that the model exhibits Ca^{2+} oscillations with reasonable properties tells us little about the underlying mechanisms. A great deal more work is needed before we can conclude anything about specific mechanisms in actual cells. This extra work is beyond the scope of this book; the interested reader is referred to the extensive literature on modeling Ca^{2+} dynamics, which can most easily be accessed through Falcke's 2004 review.

7.2.7   Open and Closed Cell Models

The period of a Ca^{2+} oscillation is determined by a number of factors, including the dynamics of the IPR and RyR, the rate of formation and degradation of IP$_3$ (see Section 7.2.8), the rate at which the ER refills after a Ca^{2+} spike, and the rate of Ca^{2+} transport across the cell membrane. One good way to study these latter two effects is to rewrite the model in a slightly different form, one in which membrane Ca^{2+} fluxes can readily be separated from ER fluxes. To do this, we introduce a new variable

$$c_t = c + \frac{c_e}{\gamma}. \tag{7.39}$$
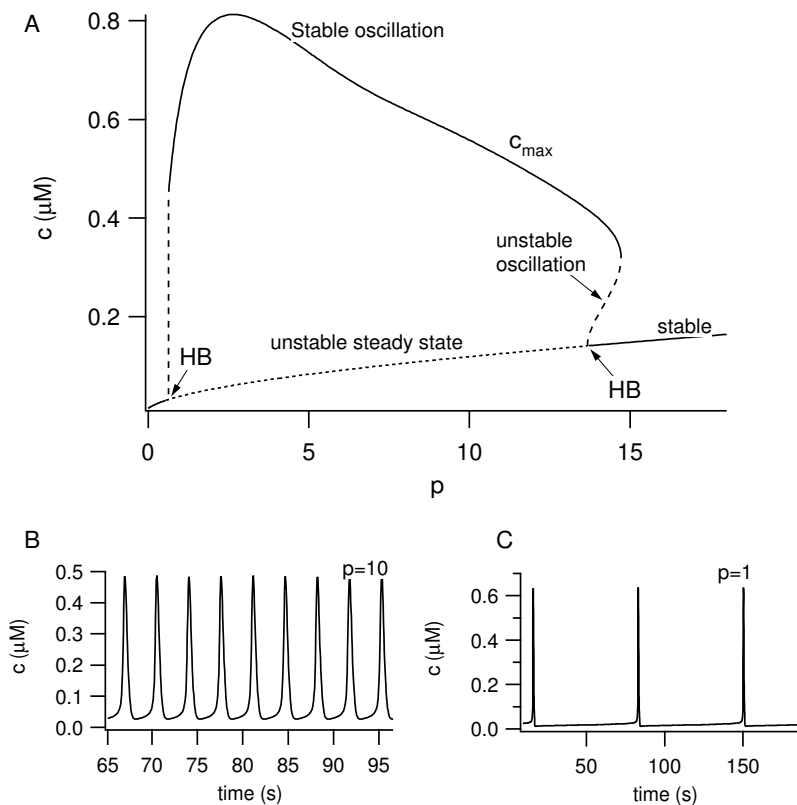
Figure 7.13: A: Simplified bifurcation diagram of the model of calcium dynamics (7.32)-(7.38). Here are plotted the steady state and the maximum of the oscillation, with a solid line denoting stability and a dashed line instability. HB denotes a Hopf bifurcation. Although the branch of oscillations shown here appears to begin at the lower Hopf bifurcation point, such is not the case. The bifurcation diagram is much more complicated in that region and is not shown in full detail here. B and C: typical oscillations in the model for two different values of p.

This new variable c_t is the total amount of Ca^{2+} in the cell (including both the cytoplasm and the ER) divided by the cytoplasmic volume, and is thus a measure of the total Ca^{2+} content of the cell. Rewriting (7.32) and (7.33) in terms of c_t gives

$$\frac{dc_t}{dt} = \delta(J_{in} - J_{pm}), \tag{7.40}$$

$$\frac{dc_e}{dt} = \gamma[J_{serca} - (k_f P_O + J_{er})(c_e - (c_t - \gamma c_e))], \tag{7.41}$$

where, for convenience, we have introduced the scale factor δ into the c_t equation. This scale factor makes it easier to modify the ratio of membrane transport to ER transport without affecting anything else in the model. We could, of course, equally well have written the model in terms of c_t and c, rather than c_t and c_e.

If membrane fluxes are much smaller than ER fluxes, δ is small. This is the case for a number of cell types. When $\delta = 0$, Ca^{2+} neither enters nor leaves the cell, and c_t remains constant. Such a model is called a *closed-cell* model. When $\delta \neq 0$ we have an *open-cell* model, in which the total amount of Ca^{2+} in the cell can change over time.

In some cell types, c_t varies slowly enough that we can gain a reasonable understanding of the calcium dynamics by first understanding the behavior of the closed-cell model. If δ is small enough, the behavior of the open-cell model is similar to that of the closed-cell model (as c_t remains almost constant over short time scales) but is slowly modulated as c_t slowly drifts towards its steady-state. Such an analysis relies on the existence of two time scales; fast changes in c and c_e which are modulated by slow changes in c_t. This approach was first introduced by Rinzel (1985) to study a model of bursting oscillations in pancreatic β-cells, and is discussed in more detail in Chapter **??**.

A particularly interesting use of this formulation arises from the ability to control both δ and c_t experimentally (Sneyd *et al.*, 2004). Application of high concentrations of La^{3+} to the outside of a cell blocks both Ca^{2+} influx and the plasma membrane ATPase, thus reducing δ effectively to zero. Furthermore, pre-loading of cells with photoreleasable Ca^{2+} allows the manipulation of c_t by flashing light. Thus, once La^{3+} has been applied, c_t can be viewed as a control parameter and increased at will (although, unfortunately, not so easily decreased) and the resultant cellular behavior observed. This allows for the detailed testing of model predictions.

7.2.8   IP$_3$ Dynamics

In the above models Ca^{2+} oscillations occur at a constant concentration of IP$_3$. Thus, the role of IP$_3$ is to activate the IPR; once the receptor is activated, Ca^{2+} feedback takes over and the period of oscillations is controlled by the kinetics of Ca^{2+} feedback on the IPR as well as the interaction of the membrane and ER fluxes.

This is certainly an over-simplification. It is known that the rate of production of IP$_3$ is dependent on Ca^{2+}, and it is known that, in some cell types, oscillations in $\left[Ca^{2+}\right]$ are accompanied by oscillations in [IP$_3$] (Hirose *et al.*, 1999; Nash *et al.*, 2001; Young *et al.*, 2003). It is not yet clear if oscillations in [IP$_3$] are *necessary*
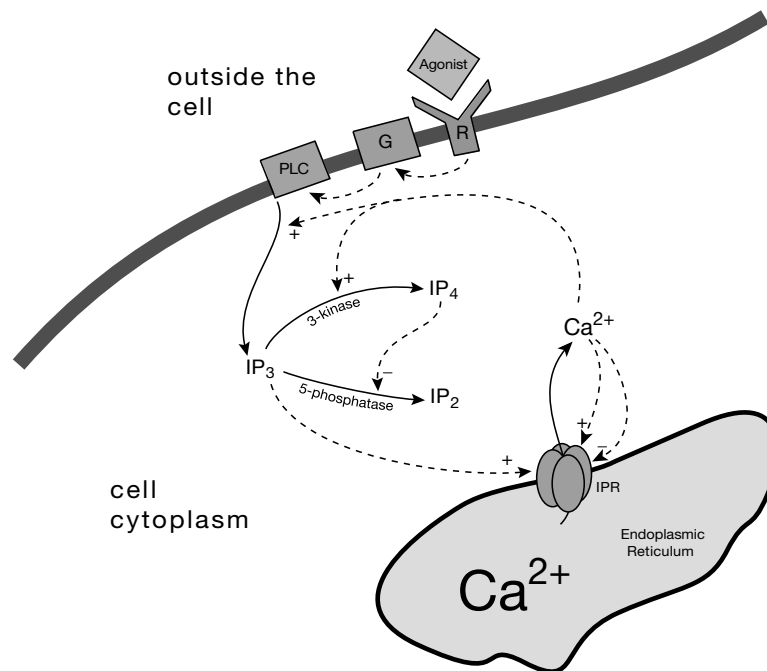
Figure 7.14: Schematic diagram of some of the interactions between Ca^{2+} and IP_3 dynamics. Calcium can activate PLC, leading to an increase in the rate of production of IP_3, and it can also increase the rate at which IP_3 is phosphorylated by the 3-kinase. The end product of phosphorylation by the 3-kinase, IP_4, acts as a competitive inhibitor of dephosphorylation of IP_3 by the 5-phosphatase. Not all of these feedbacks are significant in every cell type.

for Ca^{2+} oscillations, as the former could merely be a passive follower of the latter. Experimental evidence is neither consistent nor conclusive.

There are a number of models of Ca^{2+} dynamics that incorporate the Ca^{2+} dependence of IP_3 production and degradation. Early models were those of Meyer and Stryer (1988, 1991), Swillens and Mercan (1990), De Young and Keizer (1992) and Cuthbertson and Chay (1991); more recent models have been constructed by Shen and Larter (1995), Borghans *et al.* (1997), Dupont and Erneux (1997), Houart *et al.* (1999) and Politi et al. (2006).

There are two principal ways in which Ca^{2+} can influence the concentration of IP_3 and these are sketched in Fig. 7.14. First, activation of PLC by Ca^{2+} is known to occur in many cell types; this forms the basis of the models of Meyer and Stryer (1988) and De Young and Keizer (1992). Second, IP_3 is degraded in two principal ways, each of which is subject to feedback regulation; it is dephosphorylated by IP_3 5-phosphatase to inositol 1,4-bisphosphate (IP_2), or phosphorylated by IP_3 3-kinase to inositol 1,3,4,5-tetrakisphosphate (IP_4). However, since IP_4 is also a substrate for the 5-phosphatase, IP_4 acts as a competitive inhibitor of IP_3 dephosphorylation. In

addition, Ca^{2+} (in the form of a Ca^{2+}-calmodulin complex) can enhance the activity of the 3-kinase.

Intuitively it seems clear that an intricate array of feedbacks such as this could easily give rise to interdependent oscillations in $[IP_3]$ and Ca^{2+}, and the models mentioned above have confirmed that this intuitive expectation is correct. However, few of those models have been used to make predictions which were tested experimentally. Two notable exceptions are the models of Dupont *et al.* (2003) and of Politi et al. (2006).

In hepatocytes, oscillations of Ca^{2+} and IP_3 occur together. Each Ca^{2+} spike causes an increase in the rate of phosphorylation of IP_3, and thus a decline in $[IP_3]$, with a consequent decline in $\left[Ca^{2+}\right]$. However, although both species oscillate, it is not clear that oscillations in $[IP_3]$ are *necessary*. Dupont *et al.* first used a model (Dupont and Erneux, 1997) in which Ca^{2+} influences the rate of the 3-kinase. This model predicted that, if the rate of the 5-phosphatase is increased by a factor of 25, and the rate of IP_3 production also increased, oscillations with the same qualitative properties persist, with only a slight decrease in frequency. Under these conditions, little IP_3 is degraded by the 3-kinase, and thus Ca^{2+} feedback on the 3-kinase cannot play a major role. In other words, these oscillations arise because of the feedback of Ca^{2+} on the IPR.

Dupont *et al.* then devised an experimental test of this model prediction. They increased both the rate of the 5-phosphatase (by direct microinjection of the 5-phosphatase), as well as the rate of production of IP_3 (by increasing the concentration of agonist), and observed that the oscillations remained essentially unchanged, with the predicted decrease in frequency. Thus, under conditions where the degradation of IP_3 is principally through the 5-phosphatase pathway (in which case it is not directly affected by $\left[Ca^{2+}\right]$) there is little change in the properties of the oscillations. The conclusion is that, in hepatocytes, the oscillations are not a result of the interplay between $\left[Ca^{2+}\right]$ and the IP_3 dynamics, but rather a result of Ca^{2+} feedback on the IPR. This work illustrates an excellent interplay between modeling and experimentation.

Similar combined theoretical and experimental studies have been also been performed in CHO cells (Chinese Hamster Ovary cells, which are a cell line). Politi et al. constructed a model incorporating both positive and negative feedback of Ca^{2+} on IP_3, and then tested the consequences of the addition of exogeneous IP_3 buffer. Their analysis is involved and subtle, too much so to be discussed here in detail. However, their conclusion was that Ca^{2+} oscillations in CHO cells are a result of positive feedback of Ca^{2+} on IP_3 production.

It is possible that the response to an exogenous pulse of IP_3 can be used to determine whether or not IP_3 oscillations are a necessary accompaniment to Ca^{2+} oscillations in any given cell type (Sneyd *et al.*, 2006). If both IP_3 and Ca^{2+} are dynamic variables, necessarily oscillating together, then a pulse in IP_3 should perturb the solution off the stable limit cycle, leading to a delay before the oscillations resume. In other words, the phase response curve should exhibit a phase lag. (A phase advance, although theoretically possible, is rarely observed.) If the Ca^{2+} oscillations occur at a constant $[IP_3]$ then the pulse of IP_3 temporarily increases the frequency of the oscillations. These predictions have been tested in two cells types;

in pancreatic acinar cells the IP_3 pulse causes a delay before the next oscillation peak, while in airway smooth muscle cells, the IP_3 pulse causes a temporary increase in oscillation frequency. The model thus predicts that in pancreatic acinar cells the Ca^{2+} oscillations are necessarily accompanied by IP_3 oscillations, while in airway smooth muscle cells they occur for constant $[IP_3]$. However, since this approach yields inconclusive results in hepatocytes (**ref**)), and has not been applied widely to other cell types, it is not yet clear how useful it will prove to be.

7.2.9 Ryanodine Receptors

The second principal way in which Ca^{2+} can be released from intracellular stores is through ryanodine receptors, which are found in a variety of cells, including cardiac cells, smooth muscle, skeletal muscle, chromaffin cells, pituitary cells, neurons, and sea urchin eggs. Ryanodine receptors share many structural and functional similarities with IP_3 receptors, particularly in their sensitivity to Ca^{2+}. Just as Ca^{2+} can activate IP_3 receptors and increase the Ca^{2+} flux, so too Ca^{2+} can trigger Ca^{2+}-induced Ca^{2+} release (CICR) from the sarcoplasmic or endoplasmic reticulum through ryanodine receptors (Endo *et al.*, 1970; Fabiato, 1983). Calcium can also inactivate ryanodine receptors *in vitro*, although it is unknown whether such inactivation plays any important physiological role, or even occurs to any significant extent *in vivo*. Ryanodine receptors are so named because of their sensitivity to ryanodine, which decreases the open probability of the channel. On the other hand, caffeine increases the open probability of ryanodine receptors.

There are many models of the ryanodine receptor but since they are mostly adapted for use in models of excitation-contraction coupling, we discuss them in Chapter 12, Section 12.2.4. Here we discuss one of the few models that has been developed for use in other cell types.

Calcium oscillations in bullfrog sympathetic neurons

Sympathetic neurons respond to caffeine, or mild depolarization, with robust and reproducible Ca^{2+} oscillations. Although these oscillations are dependent on external Ca^{2+}, they occur at a fixed membrane potential and involve the release of Ca^{2+} from the ER via ryanodine receptors, as is indicated by the fact that they are abolished by ryanodine. Typical oscillations are shown in Fig. 7.15.

A simple model of CICR (Friel, 1995) provides an excellent quantitative description of the behavior of these oscillations in the bullfrog sympathetic neuron. Despite the model's simplicity (or perhaps because of it), it is a superb example of how theory can supplement experiment, providing an interpretation of experimental results as well as quantitative predictions that can subsequently be tested.

A schematic diagram of the model is given in Fig. 7.16A. A single intracellular Ca^{2+} store exchanges Ca^{2+} with the cytoplasm (with fluxes J_{L2} and J_{P2}), which in turn exchanges Ca^{2+} with the external medium (J_{L1} and J_{P1}). Thus,

$$\frac{dc}{dt} = J_{L1} - J_{P1} + J_{L2} - J_{P2}, \tag{7.42}$$

$$\frac{dc_e}{dt} = \gamma(-J_{L2} + J_{P2}), \tag{7.43}$$

k_1	$=$	2×10^{-5} s^{-1}	κ_2	$=$	0.58 s^{-1}
k_2	$=$	0.12 s^{-1}	K_d	$=$	0.5 μM
k_4	$=$	0.25 s^{-1}	n	$=$	3
κ_1	$=$	0.013 s^{-1}	γ	$=$	0.24

Table 7.5: Typical parameters of the model of Ca^{2+} oscillations in sympathetic neurons.

where c denotes $\left[\text{Ca}^{2+}\right]$ in the cytoplasm and c_e denotes $\left[\text{Ca}^{2+}\right]$ in the intracellular store as before. The fluxes are chosen in a simple way, as linear functions of the concentrations:

$$\begin{aligned}
J_{L1} &= k_1(c_o - c), & \text{Ca}^{2+}\text{entry}, & \quad (7.44) \\
J_{P1} &= k_2 c, & \text{Ca}^{2+}\text{extrusion}, & \quad (7.45) \\
J_{L2} &= k_3(c_e - c), & \text{Ca}^{2+}\text{release}, & \quad (7.46) \\
J_{P2} &= k_4 c, & \text{Ca}^{2+}\text{uptake}, & \quad (7.47)
\end{aligned}$$

where c_o denotes the external $\left[\text{Ca}^{2+}\right]$, which is assumed to be fixed. (In the experiment shown in Fig. 7.15 c_o was fixed at 1, 0.5 and 0.7 mM). Depolarization induced by the application of high external K$^+$ is modeled as an increase in k_1, the rate of Ca^{2+} entry from the outside, while the application of caffeine (which increases the rate of Ca^{2+} release from the internal store) is modeled by an increase in k_3.

We model CICR in a simple way by making k_3 an increasing sigmoidal function of c, i.e.,

$$k_3 = \kappa_1 + \frac{\kappa_2 c^n}{K_d^n + c^n}, \qquad (7.48)$$

and then determine the parameters of the nonlinear model by fitting to the time course of an oscillation (Table 7.5). A typical result is shown in Fig. 7.16.

Not only does this model provide an excellent quantitative description of the Ca^{2+} oscillation (with a different parameter set than shown in Table 7.5), it also predicts the fluxes that should be observed over the oscillatory cycle. Subsequent measurement of these fluxes confirmed the model predictions. It therefore appears that CICR (at least in bullfrog sympathetic neurons) can be well described by a relatively simple model. It is necessary only for the ryanodine receptors to be activated by Ca^{2+} to generate physiological oscillations — inactivation by Ca^{2+} is not necessary.

7.3 Calcium Waves

In some cell types, Ca^{2+} oscillations occur practically uniformly across the cell. In such a situation, measurement of the Ca^{2+} concentration at any point of the cell gives the same time course, and a well-mixed model is apparently appropriate. More often, however, each oscillation takes the form of a wave moving across the cell;
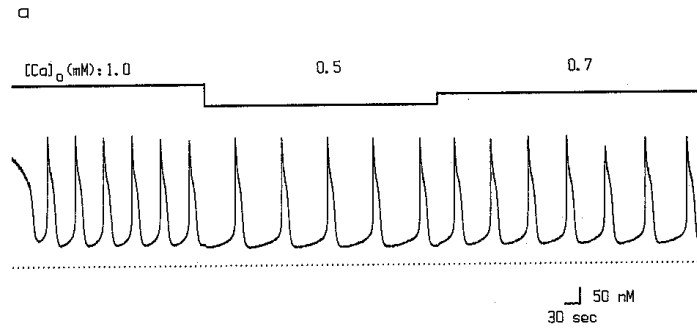
Figure 7.15: Caffeine-induced Ca^{2+} oscillations in sympathetic neurons, and their dependence on the extracellular Ca^{2+} concentration. $[Ca]_0$ stands for c_o. (Friel, 1995, Fig. 5a.)
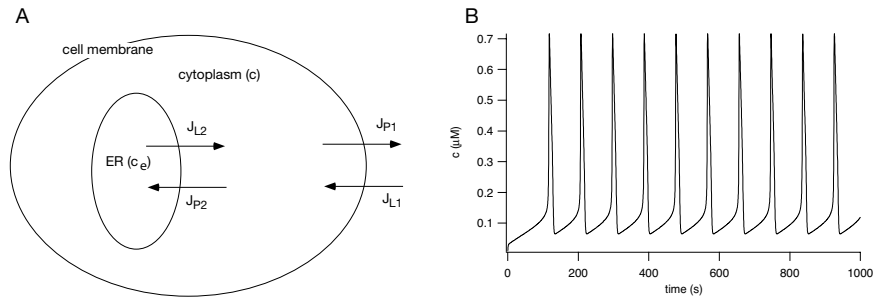
Figure 7.16: A: Schematic diagram of the CICR model of Ca^{2+} oscillations in bullfrog sympathetic neurons. B: Typical oscillation in the model, for $c_o = 1000 \ \mu M$ (i.e. 1 mM), and calculated using the parameters in Table 7.5 **James, please check parameter values again. I changed k_2 to 0.12 because I couldn't get it to oscillate with $k_2 = 0.13$.**.

these intracellular "oscillations" are actually periodic intracellular waves. To model and understand such spatially distributed behavior, inclusion of Ca^{2+} diffusion is necessary. Furthermore, to study objects such as spiral waves of Ca^{2+} (Fig. 7.3) partial differential equation models are again necessary.

When attempting to model spatially distributed calcium dynamics it is tempting to generalize the whole cell model by simply adding a diffusion term to the equation (7.3). However, with a little reflection, one realizes that this cannot be correct for several reasons. First, all of the flux terms represent movement of calcium across a boundary, whether the plasma membrane, the ER or mitochondria. Second, since the cytoplasmic space is highly inhomogeneous, it is not clear that movement of calcium in this space is governed by a standard diffusive process.

A more proper formulation of the model would be to assume that the cell is a three dimensional structure comprised of two interconnected domains, the cytoplasm Ω_c and the ER Ω_e, but ignore all other subdomains, such as mitochondria, Gogli apparati, etc. In the cytoplasm and the ER, calcium is assumed to move by normal diffusion and to react with buffers. Thus,

$$\frac{\partial c}{\partial t} = \nabla \cdot (D_c \nabla c) - J_{on} + J_{off}, \qquad (7.49)$$

in the cytoplasmic domain Ω_c, and

$$\frac{\partial c_e}{\partial t} = \nabla \cdot (D_e \nabla c) - J_{on,e} + J_{off,e}, \qquad (7.50)$$

in the ER Ω_e. Fluxes across the plasma membrane into the cytoplasm lead to the boundary condition

$$D_c \nabla c \cdot n = J_{\text{in}} - J_{\text{pm}}, \text{on } \partial\Omega_{c,m}, \qquad (7.51)$$

while fluxes across the ER into the cytoplasm yield

$$D_c \nabla c \cdot n = -D_e \nabla c_e \cdot n = J_{\text{IPR}} + J_{\text{RyR}} - J_{\text{serca}}, \qquad (7.52)$$

where $\partial\Omega_{c,m}$ is the cell membrane, and $\partial\Omega_e$ is the boundary of the ER, and **n** is the unit outward normal vector to the domain in question. Notice that here we have assumed that there is no direct communication between the ER and extracellular space (although this assumption, as with almost everything in biology, is not without controversy).

It is immediately obvious that these models are far too complicated to make any progress at all, so some simplifying assumptions are needed. This is where homogenization comes to the rescue. The fundamental idea is that since diffusion is rapid over short distances, local variations are smoothed out quickly and it is only necessary to know the average, or mean field, behavior. Thus, one derives mean field equations which describe the behavior over larger space scales. In these descriptions, concentrations c and c_e are assumed to coexist at every point in space, and one finds (see the Appendix to this Chapter)

$$\frac{\partial c}{\partial t} = \nabla \cdot (D_c^{\text{eff}} \nabla c) + \chi_c(J_{\text{IPR}} + J_{\text{RyR}} - J_{\text{serca}}) - J_{\text{on}} + J_{\text{off}}. \qquad (7.53)$$

and

$$\frac{\partial c_e}{\partial t} = \nabla \cdot (D_e^{\text{eff}} \nabla c_e) - \chi_e (J_{\text{IPR}} + J_{\text{RyR}} - J_{\text{serca}}) - J_{\text{on,e}} + J_{\text{off,e}}, \qquad (7.54)$$

where D_c^{eff} and D_e^{eff} are effective diffusion coefficients for the cytoplasmic space and the ER, respectively, and χ_c and χ_e are the surface to volume ratios of these two comingled spaces. It is usually assumed that D_c^{eff} is the same as the calcium diffusion coefficient, and that the cellular cytoplasm is isotropic and homogeneous. Exceptions to the assumption of homogeneity are not uncommon, but exceptions to the isotropic assumption are rare. It is not known, however, how Ca^{2+} diffuses in the ER, or the extent to which the tortuosity of the ER plays a role in determining the effective diffusion coefficient for ER Ca^{2+}. It is typical to assume either that Ca^{2+} does not diffuse in the ER, or that it does so with a restricted diffusion coefficient, $D_e^{\text{eff}} \ll D_c$. Henceforth we delete the superscript eff.

The surface to volume ratios are necessary to get the units correct. In fact, one should notice that a flux term, for example J_{IPR}, in a whole cell model is not the same as in a spatially distributed model; in a whole cell model the flux must be in units of concentration per unit time, while in a spatially distributed model the flux must be in units of number of molecules per unit time per surface area. Multiplication by a surface to volume ratio changes the units to number of molecules per volume. However, it is typical to scale all fluxes to be in units of molecules per unit time per cytoplasmic volume, in which case (7.53) and (7.53) become (after rescaling)

$$\frac{\partial c}{\partial t} = \nabla \cdot (D_c \nabla c) + J_{\text{IPR}} + J_{\text{RyR}} - J_{\text{serca}} - J_{\text{on}} + J_{\text{off}}. \qquad (7.55)$$

and

$$\frac{\partial c_e}{\partial t} = \nabla \cdot (D_e \nabla c_e) - \gamma (J_{\text{IPR}} + J_{\text{RyR}} - J_{\text{serca}}) - J_{\text{on,e}} + J_{\text{off,e}}. \qquad (7.56)$$

where γ is the ratio of cytoplasmic to ER volumes.

However, if the cell is viewed as a long one dimensional object, with calcium homogeneously distributed in each cross-section, then the fluxes across the (cylindrical) wall must be included as source terms in the governing partial differential equation. For example, for a "one-dimensional" cell of length L with no calcium flux at the ends, the boundary conditions are $\frac{\partial c}{\partial x} = 0$ at $x = L$ and $x = 0$, while at each internal point we have

$$\frac{\partial c}{\partial t} = D_c \frac{\partial^2 c}{\partial x^2} + J_{\text{IPR}} + \frac{\rho}{A}(J_{\text{in}} - J_{\text{pm}}) + J_{\text{RyR}} - J_{\text{serca}} - J_{\text{on}} + J_{\text{off}}, \qquad (7.57)$$

where ρ is the cell circumference and A is the cell cross-sectional area. (The derivation of this equation is given in the Appendix to this Chapter.)

There are a number of ways to study reaction-diffusion models of this type, but the two most common (at least in the study of Ca^{2+} waves) are numerical simulation or bifurcation analysis of the traveling wave equations.

7.3.1   Simulation of Spiral Waves in *Xenopus*

One common experimental procedure for initiating waves in *Xenopus* oocytes is to photorelease a bolus of IP_3 inside the cell and observe the subsequent Ca^{2+} activity (Lechleiter and Clapham, 1992). After sufficient time, Ca^{2+} wave activity disappears as IP_3 is degraded, but in the short term, the observed Ca^{2+} activity is the result of Ca^{2+} diffusion and IP_3 diffusion. Another technique is to release IP_3S_3, a nonhydrolyzable analogue of IP_3, which has a similar effect on IP_3 receptors but is not degraded by the cell. In this case, after sufficient time has passed, the IP_3S_3 is at a constant concentration in all parts of the cell.

When a bolus of IP_3S_3 is released in the middle of the domain, it causes the release of a large amount of Ca^{2+} at the site of the bolus. The IP_3S_3 then diffuses across the cell, releasing Ca^{2+} in the process. Activation of IP_3 receptors by the released Ca^{2+} can lead to periodic Ca^{2+} release from the stores, and the diffusion of Ca^{2+} between IP_3 receptors serves to stabilize the waves, giving regular periodic traveling waves. These periodic waves are the spatial analogues of the oscillations seen in the temporal model, and arise from the underlying oscillatory kinetics. If the steady $[IP_3S_3]$ is in the appropriate range (see, for example, Fig. 7.13, which shows that limit cycles exist for $[IP_3]$ in some intermediate range) over the entire cell, every part of the cell cytoplasm is in an oscillatory state. It follows from the standard theory of reaction–diffusion systems with oscillatory kinetics (see, for example, Kopell and Howard, 1973; Duffy *et al.*, 1980; Neu, 1979; Murray, 1989) that periodic and spiral waves can exist for these values of $[IP_3S_3]$. When IP_3, rather than IP_3S_3, is released, the wave activity lasts for only a short time, which is consistent with the theoretical results. When the wave front is broken, a spiral wave of Ca^{2+} often forms (Fig. 7.3A). These results have all been reproduced by numerical simulation; although Atri *et al.* (1993) were the first to do so, most models of Ca^{2+} waves behave in the same qualitative fashion. Depending on the initial conditions, these spiral waves can be stable or unstable. In the unstable case, the branches of the spiral can intersect themselves and cause breakup of the spiral, in which case a region of complex patterning emerges in which there is no clear spatial structure (McKenzie and Sneyd, 1998).

A more detailed understanding of the stability of spiral calcium waves has been developed by Falcke *et al.* (1999, 2000), who showed that an increased rate of Ca^{2+} release from the mitochondria can dramatically change the kinds of waves observed, and that, in extreme cases, the cytoplasm can be made bistable, with an additional steady state with a high resting $\left[Ca^{2+}\right]$. When this happens the spiral waves become unstable, resulting in the emergence of more complex spatio-temporal patterns.

7.3.2   Traveling wave equations and bifurcation analysis

The second principal way in which Ca^{2+} waves are studied is via the traveling wave equations. This is most useful for the study of waves in one spatial dimension. If we introduce the traveling wave variable $\xi = x + st$, where s is the wave speed (see Chapter 6, Section 6.2), we can write (7.57) as the pair of equations

$$c' \;=\; d, \tag{7.58}$$

$$D_c d' \quad = \quad sd - \sum J, \tag{7.59}$$

where $\sum J$ denotes all the fluxes on the right hand side of (7.57), and where a prime denotes differentiation with respect to ξ. Thus, a single reaction-diffusion equation is converted to two ordinary differential equation. In general, these two equations are coupled to the other equations for c_e, p, and the states of the various receptors.

Traveling pulses, traveling fronts, and periodic waves correspond to, respectively, homoclinic orbits, heteroclinic orbits and limit cycles of the traveling wave equations. Thus, by studying the bifurcations of the traveling wave equations we can gain considerable insight into what kinds of waves exist in the model, and for which parameter values. However, such an approach does not give information about the *stability* of the wave solutions of the original reaction-diffusion equations. Stability is much more difficult to determine. Numerical simulation of the reaction-diffusion equations can begin to address the question of stability.

Here we briefly illustrate the method using the model of Section 7.2.6. Adding diffusion of c (but not of c_e) to that model gives

$$\frac{\partial c}{\partial t} \quad = \quad D_c \frac{\partial^2 c}{\partial x^2} + (k_f P_O + J_{er})\,(c_e - c) - J_{serca} + J_{in} - J_{pm}, \tag{7.60}$$

$$\frac{\partial c_e}{\partial t} \quad = \quad \gamma[J_{serca} - (k_f P_O + J_{er})\,(c_e - c)], \tag{7.61}$$

and these two equations are coupled, as before, to the five equations of the 6-state IPR model (Section 7.2.5). (Here, J_{in} and J_{pm} are scaled to be in units of flux per unit cellular length). Rewriting these equations in the traveling wave variable gives

$$c' \quad = \quad d, \tag{7.62}$$

$$D_c d' \quad = \quad sd - (k_f P_O + J_{er})\,(c_e - c) + J_{serca} - J_{in} + J_{pm}, \tag{7.63}$$

$$sc'_e \quad = \quad \gamma[J_{serca} - (k_f P_O + J_{er})\,(c_e - c)], \tag{7.64}$$

coupled to the five receptor equations. Note that, given the units of the parameters in Table 7.4, the natural units for the speed s are $\mu\mathrm{m\,s}^{-1}$.

The results of a two-parameter numerical bifurcation analysis (using AUTO) of these equations, with s and p as the bifurcation parameters, is shown in Fig. 7.17. The behavior as $s \to \infty$ is that of the model in the absence of diffusion, as expected from the general theory (Maginu, 1985). Thus, for large values of s there are two Hopf bifurcations, with a branch of periodic solutions for intermediate values of p. If we track these Hopf bifurcations in the s, p plane they form a U-shaped curve (Fig. 7.17A). To find homoclinic bifurcations corresponding to traveling waves, we take a cross-section of this diagram for a constant value of $s = 10\mu\mathrm{ms}^{-1}$, i.e., for that value of s we plot the bifurcation diagram of c against p (as in Fig. 7.13). The result is shown in Fig. 7.17B. The two Hopf bifurcation points correspond to where the U-shaped curve in panel A intersects the dotted line at $s = 10\mu\mathrm{ms}^{-1}$. Tracking the branch of periodic orbits that emerges from the upper Hopf bifurcation gives a branch that ends in a homoclinic orbit. Tracking this homoclinic orbit in the s, p plane gives the C-shaped curve of homoclinics shown in the inset to panel A. More precisely, only branches of large-period (10,000 s in this case) can be tracked, so the
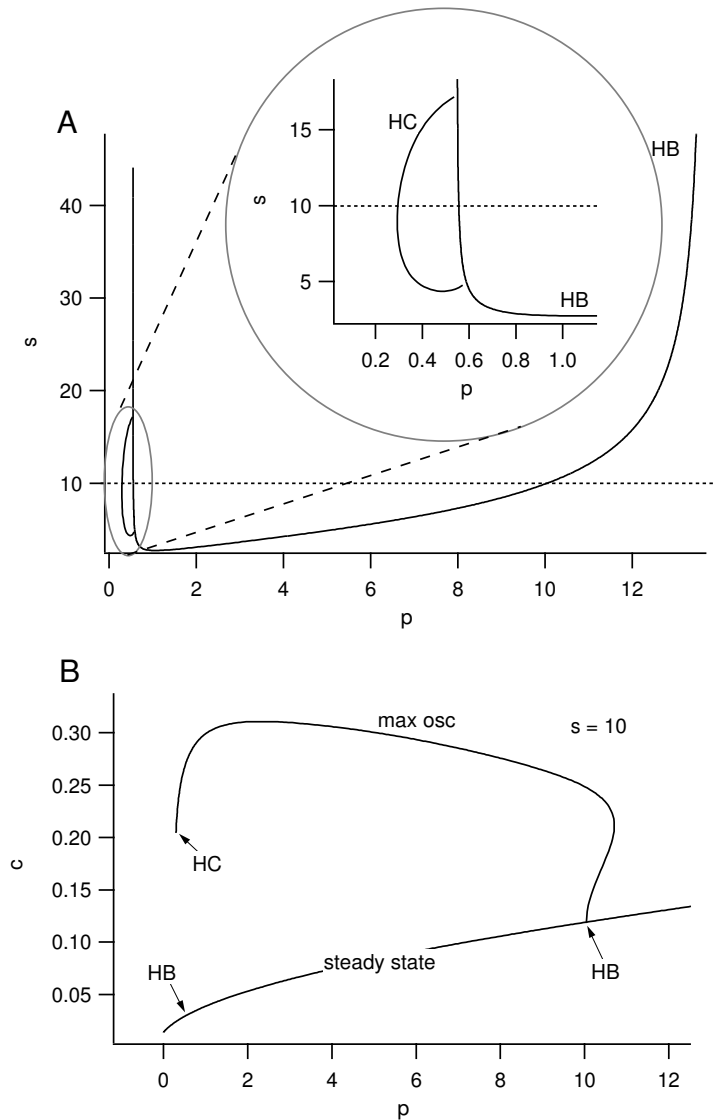
Figure 7.17: A: Two-parameter bifurcation diagram of the traveling wave equations of the model of Ca^{2+} wave propagation. HC — homoclinic bifurcation; HB — Hopf bifurcation. The inset shows a blowup of the branch of homoclinic bifurcations. B: bifurcation diagram obtained by taking a cross-section at $s = 10\mu ms^{-1}$, as shown by the dotted line in panel A. Both panels were computed using the parameter values in Table 7.4, and using $D_c = 25 \ \mu m^2 s^{-1}$. **James, I think s=10 should be deleted from the figure, and units should be added to the axes.**

curve labeled HC in panel A is actually a branch of large-period orbits. However, tracking the branch of orbits of period 1,000 s, or of period 30,000 s gives a nearly identical numerical result so we can be relatively confident that we are tracking a homoclinic orbit.

This branch of homoclinic orbits is the one that gives stable traveling wave solutions of the original reaction-diffusion equation (i.e., of the partial differential equation). This is easily checked numerically by direct simulation; with $p = 0.5$ fixed, and following a large Ca^{2+} stimulus at one end of the (one-dimensional) domain, the wave that results travels at approximately speed 15 $\mu m\, s^{-1}$ (consistent with Fig. 7.17A), and has the same shape as the homoclinic orbit on that C-shaped branch.

The branch of homoclinic orbits predicts traveling waves with speeds of around 10-17 $\mu m\, s^{-1}$, within the physiological range. Furthermore, as p increases, so does the wave speed, consistent with what has been observed experimentally. The ends of the C-shaped homoclinic branch are physiologically important as the upper branch corresponds to the waves that would be observed as p is slowly increased. At some point there is a transition from single traveling pulses to periodic waves, but exactly how that transition occurs is not completely understood (Champneys et al., 2007).

The basic structure of the bifurcation diagram shown in Fig. 7.17, with a C-shaped branch of homoclinic orbits and a U-shaped branch of Hopf bifurcations, seems to be generic to models of excitable systems. The FitzHugh-Nagumo model has the same basic structure, as does the Hodgkin-Huxley model. All models of Ca^{2+} wave propagation (at least all the ones for which this question has been studied) also have the same basic C-U structure in the s, p plane.

7.4 Calcium Buffering

Calcium is heavily buffered in all cells, with at least 99% (and often more) of the available Ca^{2+} bound to large Ca^{2+}-binding proteins of which there are about 200 encoded by the human genome (Carafoli *et al.*, 2001). For example, calsequestrin and calreticulin are major calcium buffers in the endoplasmic and sarcoplasmic reticulum, while in the cytoplasm Ca^{2+} is bound to calbindin, calretinin and parvalbumin, among many others. Calcium pumps and exchangers and the plasma membrane itself are also major Ca^{2+} buffers. In essence, a free Ca^{2+} ion in solution in the cytoplasm cannot do much, or go far, before it is bound to something.

The basic chemical reaction for calcium buffering can be represented by the reaction

$$P + Ca^{2+} \underset{k_-}{\overset{k_+}{\rightleftharpoons}} B, \tag{7.65}$$

where P is the buffering protein and B is buffered calcium. Letting b denote the concentration of buffer with Ca^{2+} bound, and c the concentration of free Ca^{2+}, a simple model of calcium buffering is

$$\frac{\partial c}{\partial t} = D_c \nabla^2 c + f(c) + k_- b - k_+ c(b_t - b), \tag{7.66}$$

$$\frac{\partial b}{\partial t} = D_b \nabla^2 b - k_- b + k_+ c(b_t - b), \tag{7.67}$$

where k_- is the rate of Ca^{2+} release from the buffer, k_+ is the rate of Ca^{2+} uptake by the buffer, b_t is the total buffer concentration, and $f(c)$ denotes all the other reactions involving free Ca^{2+} (for example, release from the IP$_3$ receptors, reuptake by pumps, etc.).

7.4.1 Fast Buffers or Excess Buffers

If the buffer has fast kinetics, its effect on the intracellular Ca^{2+} dynamics can be analyzed simply. If k_- and k_+ are large compared to the time constant of calcium reaction, we take b to be in the quasi-steady state

$$k_- b - k_+ c(b_t - b) = 0, \tag{7.68}$$

and so

$$b = \frac{b_t c}{K + c}, \tag{7.69}$$

where $K = k_-/k_+$. Adding equations (7.66) and (7.67) we find the "slow" equation

$$\frac{\partial}{\partial t}(c + b) = D_c \nabla^2 c + D_b \nabla^2 b + f(c), \tag{7.70}$$

which, after using (7.69) to eliminate b becomes

$$\frac{\partial c}{\partial t} = \frac{1}{1 + \theta(c)}\left(\nabla^2\left(D_c c + D_b b_t \frac{c}{K + c}\right) + f(c)\right) \tag{7.71}$$

$$= \frac{D_c + D_b \theta(c)}{1 + \theta(c)}\nabla^2 c - \frac{2 D_b \theta(c)}{(K + c)(1 + \theta(c))}|\nabla c|^2 + \frac{f(c)}{1 + \theta(c)}. \tag{7.72}$$

where

$$\theta(c) = \frac{b_t K}{(K + c)^2}. \tag{7.73}$$

Note that we assume that b_t is a constant, and does not vary in either space or time.

Nonlinear buffering changes the model significantly. In particular, Ca^{2+} obeys a nonlinear diffusion–advection equation, where the advection is the result of Ca^{2+} transport by a mobile buffer (Wagner and Keizer, 1994). The effective diffusion coefficient

$$D_{\text{eff}} = \frac{D_c + D_b \theta(c)}{1 + \theta(c)} \tag{7.74}$$

is a convex linear combination of the two diffusion coefficients D_c and D_b, so lies somewhere between the two. Since buffers are large molecules, $D_{\text{eff}} < D_c$. If the buffer is not mobile, i.e., $D_b = 0$, then (7.72) reverts to a reaction–diffusion equation. Also, when Ca^{2+} gradients are small, the nonlinear advective term can be ignored (Irving *et al.*, 1990). Finally, the buffering also affects the qualitative nature of the nonlinear reaction term, $f(c)$, which is divided by $1 + \theta(c)$. This may change many properties of the model, including oscillatory behavior and the nature of wave propagation.

If the buffer is not only fast, but also of low affinity, so that $K \gg c$, it follows that

$$b = \frac{b_t c}{K}, \tag{7.75}$$

in which case

$$\theta = \frac{b_t}{K}, \tag{7.76}$$

a constant. Thus, D_{eff} is constant also.

Commonly, it is assumed that the buffer has fast kinetics, is immobile, and has a low affinity. With these assumptions we get the simplest possible model of Ca^{2+} buffers (short of not including them at all) in which

$$\frac{\partial c}{\partial t} = \frac{K}{K + b_t}(D_c \nabla^2 c + f(c)), \tag{7.77}$$

wherein both the diffusion coefficient and the fluxes are scaled by the constant factor $K/(K + b_t)$; each flux in the model can then be interpreted as an *effective* flux, i.e., that fraction of the flux that contributes towards a change in free Ca^{2+} concentration.

In 1986 Neher observed that if the buffer is present in large excess then $b_t - b \approx b_t$, in which case the buffering reaction becomes linear, the so-called excess buffering approximation:

$$\frac{\partial c}{\partial t} = D_c \nabla^2 c + f(c) + k_- b - k_+ c b_t, \tag{7.78}$$

$$\frac{\partial b}{\partial t} = D_b \nabla^2 b - k_- b + k_+ c b_t. \tag{7.79}$$

If we now assume the buffers are fast we recover (7.75) and thus (7.77). In other words, the simple approach to buffering given in (7.77) can be obtained in two ways; either by assuming a low affinity buffer or by assuming that the buffer is present in excess. It is intuitively clear why these two approximations lead to the same result — in either case the binding of Ca^{2+} does little to change the fraction of unbound buffer.

Typical parameter values for three different buffers are given in Table 7.6. BAPTA is a fast, high-affinity buffer, and EGTA is a slow high-affinity buffer, both of which are used as exogeneous Ca^{2+} buffers in experimental work. Parameters for a typical endogenous buffer are also included.

Many studies of Ca^{2+} buffering have addressed the problem of the steady-state Ca^{2+} distribution that arises from the flux of Ca^{2+} through a single open channel (Naraghi and Neher, 1997; Stern, 1992; Smith, 1996; Smith *et al.*, 1996, 2001; Falcke, 2003). Such studies are motivated by the fact that, when a channel opens, the steady-state Ca^{2+} distribution close to the opening of the channel is reached within microseconds. In that context, Smith *et al.* (2001) derived both the rapid buffering approximation and the excess buffering approximation as asymptotic solutions of the original equations.

Despite the complexity of (7.72) it retains the advantage of being a single equation. However, if the buffer kinetics are not fast relative to the Ca^{2+} kinetics, the

Buffer	D_b	k_+	k_-	K
	$\mu\mathrm{m}^2\,\mathrm{s}^{-1}$	$\mu\mathrm{M}^{-1}\mathrm{s}^{-1}$	s^{-1}	μM
BAPTA	95	600	100	0.17
EGTA	113	1.5	0.3	0.2
Endog	15	50	500	10

Table 7.6: Typical parameter values for three different buffers, taken from Smith *et al.*, (2001). BAPTA and EGTA are commonly used as exogenous buffers in experimental work, while Endog refers to a typical endogenous buffer. Typically $b_t = 100\ \mu$M for an endogenous buffer.

only way to proceed is with numerical simulations of the complete system, a procedure followed by a number of groups (Backx *et al.*, 1989; Sala and Hernández-Cruz, 1990; Nowycky and Pinter, 1993; Falcke, 2003).

Of particular current interest are recent observations that buffers with different kinetics have remarkably different effects on the observed Ca^{2+} responses. For example, Dargan and Parker (2003) have shown that in oocytes, the addition of EGTA, a slow buffer with high affinity, "balkanises" the Ca^{2+} response so that local regions tend to respond independently of their neighbors. However, the addition of BAPTA, a fast buffer, has quite different effects, giving slower Ca^{2+} responses that occur globally rather than locally. These results are likely the result of the different effects that these two buffers have on the diffusion of Ca^{2+} between individual release sites (see Section 7.6). Similar studies in pancreatic acinar cells (Kidd *et al.*, 1999) have shown that the addition of EGTA increases the frequency, but decreases the amplitude, of Ca^{2+} spikes, while addition of BAPTA has the opposite effect, decreasing the frequency but maintaining a larger spike amplitude. Furthermore, EGTA broke the response into a number of independent spatially separate release events, as in oocytes. Kidd *et al.* concluded that EGTA disrupts long-range Ca^{2+} diffusion between release sites, thus decreasing the global coordination of Ca^{2+} release, while BAPTA is fast enough to disrupt Ca^{2+} inactivation of the IPR, thus leading to large Ca^{2+} spikes with a lower frequency.

7.4.2   The Existence of Buffered Waves

Since the presence of fast Ca^{2+} buffers changes the nature of the Ca^{2+} transport equation, it is of considerable interest to determine how Ca^{2+} buffering affects the properties of waves. For example, can the addition of a buffer eliminate wave activity? How much do buffers affect the speed of traveling waves? Does the addition of exogeneous buffer, such as a fluorescent Ca^{2+} dye, affect the existence or the speed of the Ca^{2+} waves? First, we address the question of whether buffers can eliminate wave activity.

The form of (7.71) suggests the change of variables

$$w = D_c c + D_b b_t \frac{c}{K+c}, \tag{7.80}$$

so that w is a monotone increasing function of c, since

$$\frac{dw}{dc} = D_c + D_b\theta(c) \tag{7.81}$$

is positive. The unique inverse of this function is denoted by

$$c = \phi(w). \tag{7.82}$$

In terms of w, (7.71) becomes

$$\frac{\partial w}{\partial t} = \frac{D_c + D_b\Theta}{1 + \Theta} \left(\nabla^2 w + f(\phi(w))\right), \tag{7.83}$$

where $\Theta = \frac{b_t K}{(K+\phi(w))^2}$.

Now, we assume that $f(c)$ is of bistable form, with three zeros, $C_1 < C_2 < C_3$, of which C_1 and C_3 are stable. It immediately follows that $f(\phi(w))$ has three zeros $W_1 < W_2 < W_3$, with W_1 and W_3 stable. The proof of existence of a one-dimensional traveling wave solution for (7.83) uses exactly the same arguments as that for the bistable equation presented in Chapter 6 (Sneyd *et al.*, 1998). It follows that a traveling wave-front solution that provides a transition from W_1 to W_3 exists if and only if

$$\int_{W_1}^{W_3} f(\phi(w))dw > 0. \tag{7.84}$$

(If this inequality is reversed, a traveling wave solution still exists, but it moves "backwards", providing a transition from W_3 to W_1.) Using (7.81), we write this condition in terms of c as

$$\int_{C_1}^{C_3} f(c)(D_c + D_b\theta(c))dc > 0. \tag{7.85}$$

In general, this integral cannot be evaluated explicitly. However, for the simple case of cubic bistable kinetics $f(c) = c(1-c)(c-a)$, $0 < a < 1/2$, explicit evaluation of the integral (7.85) shows that traveling waves exist if and only if

$$a < a_c = \frac{1}{2} \frac{D_c - 12D_b b_t K[(3K^2 + 2K)\ln(\frac{K+1}{K}) - (3K + \frac{1}{2})]}{D_c + 12D_b b_t K[(K + \frac{1}{2})\ln(\frac{K+1}{K}) - 1]}. \tag{7.86}$$

One conclusion that can be drawn immediately from (7.85) is that a stationary buffer (i.e., one with $D_b = 0$) has no effect on the existence of traveling waves in the bistable equation. For when $D_b = 0$, the condition (7.85) for the existence of the traveling wave reduces to

$$\int_0^1 f(c)\,dc > 0, \tag{7.87}$$

which is exactly the condition for the existence of a wave in the absence of a buffer.

Note that a_c is a monotonically decreasing function of $D_b b_t/D_c$, and

$$a_c \to a_{c,\min}(K) = -\frac{1}{2} \frac{[(3K^2 + 2K)\ln(\frac{K+1}{K}) - (3K + \frac{1}{2})]}{[(K + \frac{1}{2})\ln(\frac{K+1}{K}) - 1]} \qquad \text{as } D_b \to \infty. \tag{7.88}$$
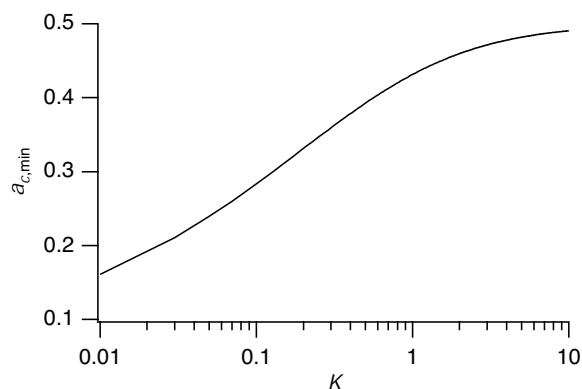
Figure 7.18: Plot of $a_{c,\min}$ against K.

In Fig. 7.18 we give a plot of $a_{c,\min}(K)$ against K. When K is large, the minimum value of a_c is close to 0.5, and thus wave existence is insensitive to D_b. However, when K is small, a_c also becomes small as D_b increases, and so in this case, a mobile buffer can easily stop a wave.

7.5   Discrete Calcium Sources

In all of the models presented so far, calcium release from the ER was assumed to be homogeneous in space. In fact, this is not the case. In *Xenopus* oocytes, for example, IPR are arranged in clusters with a density of about 1 per 30 μm^2, with each cluster containing about 25 IPR. Furthermore, the propagation of Ca^{2+} waves is saltatory, with release "jumping" from one cluster of release sites to another.

To explore the properties of such saltatory waves, and to see the effect of this discrete structure, we assume that calcium is released from discrete release sites but is removed continuously. We consider the equation for calcium concentration

$$\frac{\partial c}{\partial t} = D_c \frac{\partial^2 c}{\partial x^2} - k_s c + L \sum_n \delta(x - nL) f(c). \tag{7.89}$$

The function f is your favorite description of calcium release, and L is the spatial separation between release sites.

Two examples of the release function $f(c)$ that are useful are

$$f(c) = Ac^2(c_e - c), \tag{7.90}$$

and

$$f(c) = AH(c - c^*)(c_e - c), \tag{7.91}$$

where H is the usual Heaviside function. Both of these release functions have calcium dependent release, representing CICR.

The corresponding continuous space model can be found by homogenization (See Exercise 16). It is not difficult to show (and it makes intuitive sense) that in the limit that $\frac{L^2 k}{D_c} \ll 1$, the spatially inhomogeneous problem

$$\frac{\partial c}{\partial t} = D_c \frac{\partial^2 c}{\partial x^2} - k_s c + g(x) f(c), \tag{7.92}$$

where $g(x)$ is periodic with period L, can be replaced by its average

$$\frac{\partial c}{\partial t} = D_c \frac{\partial^2 c}{\partial x^2} - k_s c + G f(c), \tag{7.93}$$

where $G = \frac{1}{L} \int_0^L g(x) dx$.

Since the effective release function $F(c) = G f(c) - k_s c$ is of bistable type, with three zeros $0 < c_1 < c_2$, one would expect there to be traveling waves of calcium release, provided the medium is sufficiently excitable, i.e., provided

$$\int_0^{c_2} F(c) dc > 0. \tag{7.94}$$

However, this condition fails to be correct if $\frac{L^2 k_s}{D_c} \neq 0$.

Waves fail to propagate if there is a standing wave solution. Standing waves are stationary solutions of (7.89), i.e., solutions of

$$0 = D_c \frac{\partial^2 c}{\partial x^2} - k_s c + L \sum_n \delta(x - nL) f(c). \tag{7.95}$$

On the intervals $nL < x < (n+1)L$, this becomes

$$0 = D_c \frac{\partial^2 c}{\partial x^2} - k_s c. \tag{7.96}$$

We find jump conditions at $x = nL$ by (formally) integrating from nL^- to nL^+ to obtain

$$D_c c_x |_{nL^-}^{nL^+} + L f(c_n) = 0, \tag{7.97}$$

where $c_n = c(nL)$.

Now we solve (7.96) to obtain

$$c(x) = (c_{n+1} - c_n \cosh \beta) \frac{\sinh\left(\frac{\beta}{L}(x - nL)\right)}{\sinh \beta} + c_n \cosh\left(\frac{\beta}{L}(x - nL)\right), \tag{7.98}$$

for $nL < x < (n+1)L$, where $c_n = c(nL)$, $\beta^2 = \frac{k_s L^2}{D_c}$, so that

$$c_x(nL^+) = (c_{n+1} - c_n \cosh \beta) \frac{\beta}{L \sinh \beta}. \tag{7.99}$$

Similarly,

$$c_x(nL^-) = -(c_{n-1} - c_n \cosh \beta) \frac{\beta}{L \sinh \beta}. \tag{7.100}$$

It follows that (7.97) is the difference equation

$$\frac{k}{\beta \sinh \beta}(c_{n+1} - 2c_n \cosh\beta + c_{n-1}) + f(c_n) = 0, \qquad (7.101)$$

which is a difference equation for c_n.

Finding solutions of nonlinear difference equations is non-trivial, in general. However, if $f(c)$ is piecewise linear, as it is with release function (7.91), analytical solutions can be found. We seek solutions of (7.101) of the form

$$c_n = \begin{cases} a\mu_0^{-n} & n \leq 0 \\ C - b\mu_f^n & n > 0 \end{cases}, \qquad (7.102)$$

where the steady solution C satisfies

$$\frac{k}{\beta \sinh \beta}(C - 2C\cosh\beta + C) + A(c_e - C) = 0, \qquad (7.103)$$

so that

$$C = c_e \frac{A_f}{2\cosh\beta - 2 + A_f}, \qquad A_f = A\frac{\beta \sinh \beta}{k_s}. \qquad (7.104)$$

The numbers μ_0 and μ_f are both less than one and satisfy the quadratic equations

$$\mu_j - 2\lambda_j + \frac{1}{\mu_j} = 0, \qquad j = 0, f \qquad (7.105)$$

where

$$\lambda_0 = \cosh \beta, \qquad \lambda_f = \cosh \beta + \frac{A_f}{2}, \qquad (7.106)$$

so that

$$\mu_j = \lambda_j - \sqrt{\lambda_j^2 - 1}. \qquad (7.107)$$

It is easy to determine that $\mu_0 = \exp(-\beta)$; the expression for μ_f is more complicated.

We determine the scalars a and b by examining the difference equation for $n = 0$

$$\frac{k}{\beta \sinh \beta}(c_1 - 2c_0 \cosh \beta + c_{-1}) + f(c_0) = 0, \qquad (7.108)$$

and for $n = 1$

$$\frac{k_s}{\beta \sinh \beta}(c_2 - 2c_1 \cosh \beta + c_0) + f(c_1) = 0. \qquad (7.109)$$

Since $c_0 < c^*$ and $c_1 > c^*$ by assumption, $f(c_0) = 0$ and $f(c_1) = A(c_e - C + b\mu_f)$. After some algebraic manipulation we find that

$$a = C\left(\frac{\mu_f - 1}{\mu_f - \frac{1}{\mu_0}}\right), \qquad b = C\left(\frac{1 - \frac{1}{\mu_0}}{\mu_f - \frac{1}{\mu_0}}\right). \qquad (7.110)$$

Now, the condition for the existence of these standing waves is that

$$a \leq c^*, \qquad C - b\mu_f \geq c^*, \qquad (7.111)$$
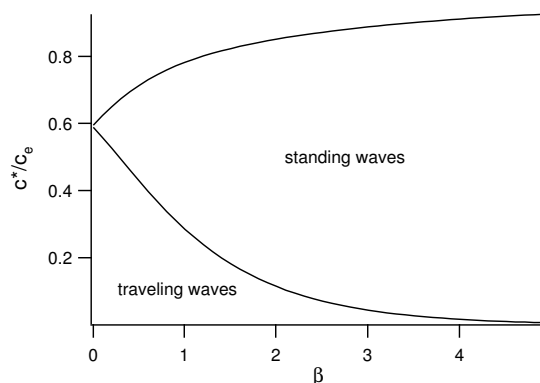
Figure 7.19: Plot of $\frac{a}{c_e}$ (lower curve) and $\frac{C}{c_e} - \frac{b}{c_e}\mu_f$ (upper curve) plotted as functions of $\beta = \sqrt{\frac{kL^2}{D}}$ for $\frac{A}{k} = 5$.

so a plot of a and $C - b\mu_f$ is revealing. In Fig. 7.19 are the two curves $\frac{a}{c_e}$ (lower curve) and $\frac{C}{c_e} - \frac{b}{c_e}\mu_f$ (upper curve) plotted as functions of $\beta = \sqrt{\frac{k_s L^2}{D_c}}$ for $\frac{A}{k} = 5$. The interpretation of this plot is that for a fixed value of β, if $\frac{c^*}{c_e}$ lies in the region below the curve $\frac{a}{c_e}$, then there is a traveling wave, whereas, if $\frac{c^*}{c_e}$ and β lies between the two curves, there is a standing wave, which precludes the possibility of propagation. Thus, in general, the larger β the more excitable the release sites must be ($\frac{c^*}{c_e}$ must be smaller), for propagation to occur. Said another way, discrete release from clumped receptors makes propagation less likely than if the same amount of calcium were released in a spatially continuous and homogeneous fashion. Notice also that for fixed $\frac{c^*}{c_e}$, increasing β sufficiently always leads to propagation failure. Increasing β corresponds to increasing the distance between release sites L or the rate of uptake k_s, or decreasing the calcium diffusion coefficient D_c.

A similar approach to this problem was explored by Sneyd and Sherratt (1997).

7.5.1 The Fire-Diffuse-Fire Model

It is difficult to determine when propagation failure occurs and it is even more difficult to find the speed of propagation in a discrete release model. One approach, which uses techniques that are beyond the scope of this text, was used in Keener (2000b). Another approach is to use a different model. One model that has attracted a lot of attention is the fire-diffuse-fire model (Pearson and Ponce-Dawson, 1998, Keizer *et al.* (1998), Dawson *et al.*, 1999; Coombes, 2001; Coombes and Bressloff, 2003; Coombes *et al.*, 2004).

In this model, once $\left[Ca^{2+}\right]$ reaches a threshold value, c^*, at a release site, that site fires, instantaneously releasing a fixed amount, σ, of Ca^{2+}. Thus, a Ca^{2+} wave is propagated by the sequential firing of release sites, each responding to the Ca^{2+} diffusing from neighboring release sites. Hence the name *fire-diffuse-fire*.

We assume that Ca^{2+} obeys the reaction diffusion equation

$$\frac{\partial c}{\partial t} = D_c \frac{\partial^2 c}{\partial x^2} + \sigma \sum_n \delta(x - nL)\delta(t - t_n), \tag{7.112}$$

where, as before, L is the spacing between release sites. Although this equation looks linear, appearances are deceptive. Here, t_n is the time at which c first reaches the threshold value c^* at the nth release site. When this happens, the nth release site releases the amount σ. Thus, t_n depends in a complicated way on c.

The Ca^{2+} profile resulting from the firing of a single site, site i say, is

$$c_i(x,t) = \sigma \frac{H(t - t_i)}{\sqrt{4\pi D_c(t - t_i)}} \exp\left(-\frac{(x - iL)^2}{4D_c(t - t_i)}\right), \tag{7.113}$$

where H is the Heaviside function. This is the fundamental solution of the diffusion equation with a delta function input at $x = i$, $t = t_i$, and can be found in any standard book on analytical solutions to partial differential equations (see, for example, Keener, 1998, or Kevorkian, 2000). If we superimpose the solutions from each site, we get

$$c(x,t) = \sum_i c_i(x,t) = \sigma \sum_i \frac{H(t - t_i)}{\sqrt{4\pi D_c(t - t_i)}} \exp\left(-\frac{(x - iL)^2}{4D_c(t - t_i)}\right). \tag{7.114}$$

Notice that because of the instantaneous release, $c(x,t)$ is not a continuous function of time at any release site.

Now, suppose that sites $i = N, N-1, \cdots$ have fired at known times $t_N > t_{N-1} > \cdots$. The next firing time t_{N+1} is determined by when c at x_{N+1} first reaches the threshold, c^*, that is,

$$c((N+1)L, t_{N+1}^-) = c^*, \qquad \frac{\partial}{\partial t}c((N+1)L, t_{N+1}^-) > 0. \tag{7.115}$$

Thus, t_{N+1} must satisfy

$$c^* = \sigma \sum_{i \leq N} \frac{1}{\sqrt{4\pi D_c(t_{N+1} - t_i)}} \exp\left(-\frac{L^2(N+1-i)^2}{4D_c(t_{N+1} - t_i)}\right). \tag{7.116}$$

A steadily propagating wave corresponds to having $t_i - t_{i-1} = \text{constant} = \tau$ for all i, i.e., each site fires a fixed time after its leftward neighbor fired. Note that the resulting wave does not propagate with a constant profile, but has a well-defined wave speed L/τ. If such a τ exists, then $t_{N+1} - t_i = \tau(N+1-i)$ and τ is a solution of the equation

$$\frac{c^* L}{\sigma} = \sum_{n=1}^{\infty} \frac{1}{\sqrt{4\pi n\eta}} \exp\left(-\frac{n}{4\eta}\right) \equiv g(\eta), \tag{7.117}$$

where $\eta = \frac{D_c \tau}{L^2}$ is the dimensionless delay.

To find η we need to invert this equation. A plot of $g(\eta)$ is shown in Fig. 7.20. It can be shown that $0 \leq g(\eta) \leq 1$ and that g is monotonic with $g \to 0$ as $\eta \to 0$
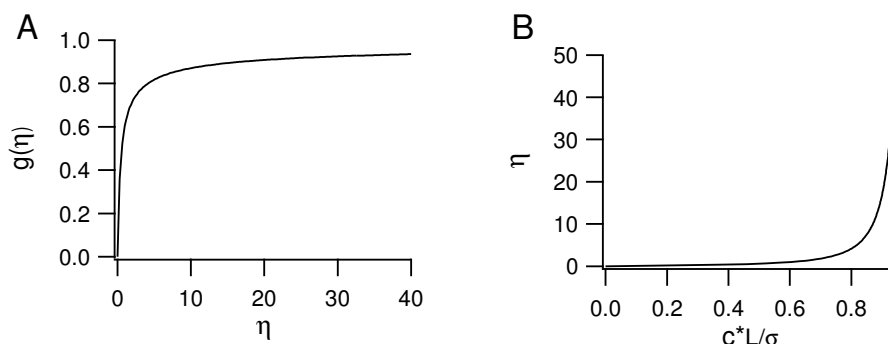
Figure 7.20: A: Plot of $g(\eta)$, where $g(\eta)$ is defined by (7.117). B: Plot of the delay η using (7.117).

and $g \to 1$ as $\eta \to \infty$. It follows that a solution to (7.117) exists only if $\frac{c^*L}{\sigma} < 1$. Thus, when the intercluster distance or the threshold is too large, or the amount of release is too small, there is no propagation. However, when $\frac{c^*L}{\sigma} < 1$ a unique solution of (7.117) is guaranteed, and thus there is a propagating wave.

It is an easy matter to plot the delay as a function of $\frac{c^*L}{\sigma}$ by appropriately reversing the axes of Fig. 7.20A. Thus, in Fig. 7.20B is plotted the dimensionless delay η as a function of $\frac{c^*L}{\sigma}$. It is equally easy to plot the dimensionless velocity $\frac{1}{\eta}$ as a function of $\frac{c^*L}{\sigma}$ (not shown). The result is that the velocity is infinitely large as $\frac{c^*L}{\sigma} \to 0$ and is zero for $\frac{c^*L}{\sigma} \geq 1$.

If a solution of (7.117) exists, then the speed of the wave is proportional to D_c. This is because the velocity is $\frac{L}{\tau} = \frac{D}{\eta L}$. This result is disconcerting for two reasons. First, the speed of propagation of waves in spatially homogeneous reaction diffusion systems usually scales with the square root of D. It follows from simple scaling arguments that since the units of the diffusion coefficient, D_c, are (length)^2 per time, the distance variable can be scaled by $\sqrt{D_c k}$, where k is a typical time constant, to remove all distance units, so that the wave speed scales with $\sqrt{D_c k}$. Second, this disagrees with the result of the previous section showing that if D_c is sufficiently small, there is propagation failure. For the fire-diffuse-fire model, propagation success or failure is independent of D_c.

This mismatch is explained by the fact that the fire-diffuse-fire model has no typical time constants, and is not translationally invariant. Furthermore, since the fire-diffuse-fire model allows only for release of calcium, but no uptake, the calcium transient is unrealistically monotone increasing.

This deficiency of the fire-diffuse-fire model is easily remedied by adding a linear uptake term that is homogeneous in space (Coombes, 2001), so that the model becomes

$$\frac{\partial c}{\partial t} = D_c \frac{\partial^2 c}{\partial x^2} - k_s c + \sigma \sum_n \delta(x - nL)\delta(t - t_n), \qquad (7.118)$$

The analysis of this modified model is almost identical to the case with $k_s = 0$. The fundamental solution is modified slightly by k_s, with the Ca^{2+} profile resulting
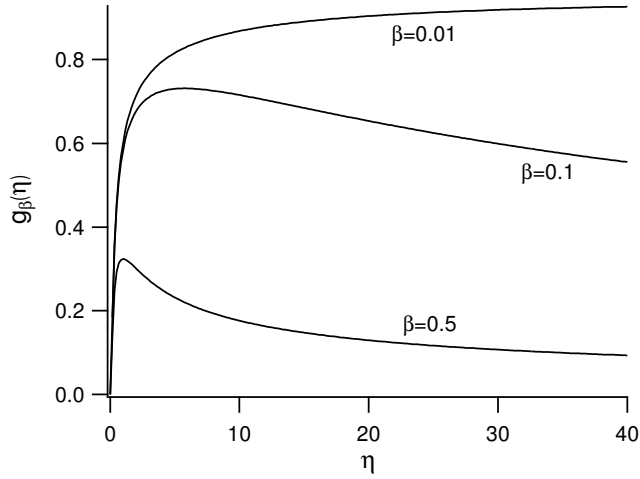
Figure 7.21: Plots of $g_\beta(\eta)$ for three different values of β. Note that g_β is a decreasing function of β for all positive values of η.

from the firing at site i given by

$$c_i(x, t) = \sigma \frac{H(t - t_i)}{\sqrt{4\pi D_c(t - t_i)}} \exp\left(-\frac{(x - iL)^2}{4D_c(t - t_i)} - k_s(t - t_i)\right). \qquad (7.119)$$

Following the previous arguments, we learn that a propagating solution exists if there is a solution of the equation

$$\frac{c^* L}{\sigma} = \sum_{n=1}^{\infty} \frac{1}{\sqrt{4\pi n \eta}} \exp\left(-\frac{n}{4\eta} - \beta^2 n\right) \equiv g_\beta(\eta), \qquad (7.120)$$

where $\eta = \frac{D_c \tau}{L^2}$ is the dimensionless delay, and $\beta^2 = \frac{k_s L^2}{D_c}$ as in the previous section.
    Estimates of the size of β^2 can vary substantially. For example, using $k_s = 143/s$ ($= 1/\alpha_2$ from Table 7.4), $L^2 = 30\mu m^2$ and $D_c = 20\mu m^2/s$, we find $\beta^2 = 172$, whereas with $k_s = 3.78/s$ ($= k_4$ from the Friel model Table 7.5), $L^2 = 4\mu m^2$ (appropriate for calcium release in cardiac cells) and $D_c = 25\mu m^2/s$, we find $\beta^2 = 0.6$. Regardless, the effect of β is significant. Plots of $g_\beta(\eta)$ are shown for several values of β in Fig. 7.21. In particular, if $\beta \neq 0$, the function $g_\beta(\eta)$ is not monotone increasing, but has a maximal value, say $g_{max}(\beta)$, which is a decreasing function of β. Furthermore, $g_\beta(\eta) \to 0$ as $\eta \to 0$ and as $\eta \to \infty$. If $\frac{c^* L}{\sigma} > g_{max}(\beta)$, then no solution of (7.120) exists; there is propagation failure. On the other hand, if $\frac{c^* L}{\sigma} < g_{max}(\beta)$, then there are two solutions of (7.120), although, the physically meaningful solution is the smallest of the two, corresponding to the first time that $c(x, t)$ reaches c^*.
    Denote the maximal value of $g_\beta(\eta)$ by $g_{max}(\beta)$. For larger values of β, the curve $g_{max}(\beta)$ agrees very well with the exponential function $\exp(-\beta)$. This provides us with an approximate criterion for propagation failure, namely, if $\frac{c^* L}{\sigma} > \exp(-\beta)$,

propagation fails. Recall that $\beta = \sqrt{\frac{k_s L^2}{D_c}}$ to see the $\sqrt{D_c}$ dependence in this criterion.

By reversing the axes on Fig. 7.21, one obtains a plot of the dimensionless delay as a function of $\frac{c^* L}{\sigma}$. Notice the significant qualitative difference when $\beta \neq 0$ compared to $\beta = 0$. With $\beta \neq 0$, propagation ceases at a finite, not infinite delay. This implies that propagation fails at a positive, not zero, velocity.

7.6 Calcium Puffs and Stochastic Modeling

In all the models discussed above the release of Ca^{2+} was modeled as deterministic. However, it is now well known that this is not always appropriate. In fact, each Ca^{2+} oscillation or wave is built up from a number of stochastic elementary release events, called *puffs*, each of which corresponds to Ca^{2+} release from a single, or a small group of, IPR. At low concentrations of IP_3, punctate release from single clusters occurs while at high $[IP_3]$ these local release events are coordinated into global intracellular waves (Yao *et al.*, 1995; Parker *et al.*, 1996a, Parker and Yao, 1996). Detailed studies of puffs have been done principally in *Xenopus* oocytes (Marchant *et al.*, 1999; Sun *et al.*, 1998; Callamaras *et al.*, 1998; Marchant and Parker, 2001) and HeLa cells (Thomas *et al.*, 2000; Bootman *et al.*, 1997a,b). Some typical experimental results are shown in Fig. 7.22.

These experimental results raise several important modeling questions. First, when is it appropriate to use deterministic models and when must stochastic behavior be incorporated. Second, how should one best model stochastic Ca^{2+} release through a small number of IPR, and, finally, how can one model the coordination of such local release into global events such as intracellular waves? Although such questions are most obvious from the experimental work in oocytes and HeLa cells, they are also important for the study of Ca^{2+} oscillations in other cell types. As Falcke (2004) has pointed out, stochastic effects appear to be so fundamental and widespread that they raise questions about the applicability of deterministic approaches in general.

7.6.1 Stochastic IPR Models

The basic assumption behind the modeling of Ca^{2+} puffs is that each IPR release event can be modeled as a stochastic Markov process while the diffusion of Ca^{2+}, and the action of the other pumps and Ca^{2+} fluxes can be modeled deterministically. Given a Markov state model of the IPR (for example, as shown in Fig. 7.8 or Fig. 7.11), we can simulate the model by choosing a random number at each time step and using that random number to determine the change of state for that time step. This is done most efficiently using the Gillespie method, as described in Chapter 3, Section 2.9.3.

In general, each transition rate is a function of c and p and thus the transition probabilities are continually changing as the concentrations change. It follows that c and p must be updated at each time step. Such updates are done deterministically, by solving the reaction-diffusion equations for c and p. When the simulated IPR model is in the open state, the reaction-diffusion equation for Ca^{2+} has an additional
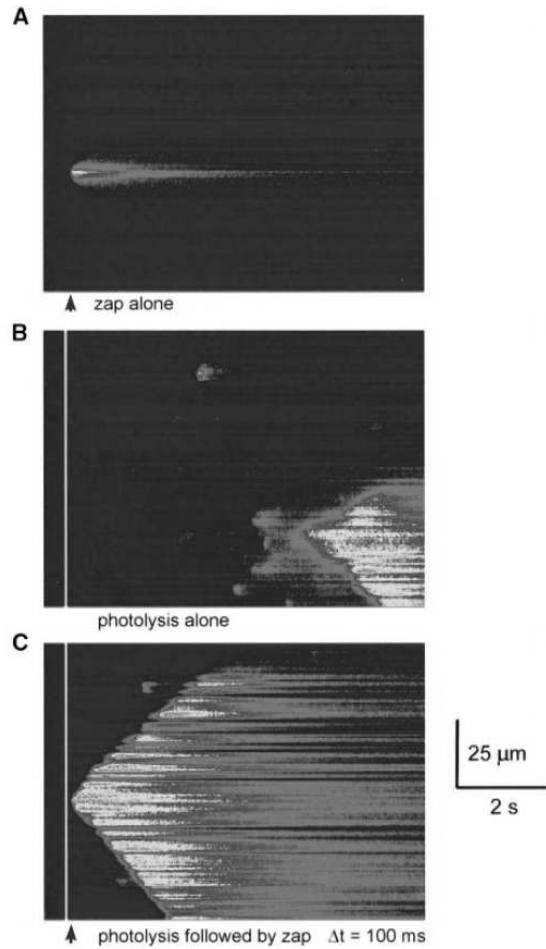
Figure 7.22: Calcium waves and puffs caused by release of Ca^{2+} and IP_3. Lighter colors correspond to higher Ca^{2+} concentrations. A: release of Ca^{2+} by a UV laser zap results in a single localised Ca^{2+} response. B: photolysis of IP_3 across the entire region causes several Ca^{2+} puffs (see, for example, the puff at top center), followed by an abortive wave about 5 seconds after the release of IP_3. C: photolysis of IP_3 followed by release of Ca^{2+} by a UV laser zap. A global wave is initiated immediately by the additional Ca^{2+} release. (Reproduced from Marchant *et al.*, 1999, Fig. 3.) **Springer; we will need permission for this figure, which will also need massaging into grayscale, removal of color bar, etc.**

flux through the IPR. When the simulated IPR model is in some other state, this flux is absent. Thus, we obtain a reaction-diffusion equation for c that is driven by a stochastically varying input.

The first stochastic model of an IPR was due to Swillens *et al.* (1998). Their model is an 18-state model in which the IPR can have 0 or 1 IP_3 bound, 0, 1 or 2 activating Ca^{2+} bound, and 0, 1 or 2 inactivating Ca^{2+} bound. The receptor is open only when it has one IP_3 bound, two Ca^{2+} bound to activating sites, and no Ca^{2+} bound to inactivating sites. The steady-state open probability of the model is constrained to fit the experimental data of Bezprozvanny *et al.* (1991), and it is assumed that Ca^{2+} diffuses radially away from the mouth of the channel. Calcium can build up to high concentrations at the mouth of the channel, and these local concentrations are used in the stochastic simulation of the IPR model.

Simulations of this model show two things in particular. First, channel openings occur in bursts, as Ca^{2+} diffuses away from the mouth of the channel slowly enough to allow rebinding to an activating site. Second, by comparing to experimentally observed distributions of puff amplitudes, Swillens *et al.* (1999) showed that a typical cluster contains approximately 25 receptors, and that within the cluster the IPR are probably separated by no more than 12 nm.

Because of the intensive computations involved in direct stochastic simulation of gating schemes for the IPR, Shuai and Jung approximated a stochastic version of the eight-state model (Section 7.2.5) by a Langevin equation (Shuai and Jung, 2002a,b, 2003. This approach had already been used to study the Hodgkin-Huxley equations by Fox and Lu, 1994). Although 25 receptors in each cluster makes a Langevin equation approach less accurate than direct stochastic simulation, the qualitative behavior agrees well with direct simulation.

Local concentrations

In any stochastic model of the IPR it is impossible to ignore the local high concentrations that occur at the mouth of the channel. Neglect of this factor results either in an IPR model that bears no relation to reality, or a model that does not exhibit realistic Ca^{2+} oscillations. Thus, for a stochastic model of the IPR to be incorporated into a whole-cell model of Ca^{2+} oscillations, it is necessary to somehow relate the Ca^{2+} concentration in the microdomain at the channel mouth to the bulk Ca^{2+} concentration in the cytoplasm of the cell.

This is not easily done, and it is not yet clear exactly how best to incorporate stochastic IPR models into simple whole-cell models of Ca^{2+} oscillations. At the very least, models of Ca^{2+} dynamics that use only the bulk Ca^{2+} concentration cannot be realistic at the level of the IPR. This problem is similar to the problem of how best to model Ca^{2+} release in cardiac cells (Chapter 12, Section 12.2.4). There, the ryanodine receptors release calcium into a very restricted domain, the diadic cleft, and experience Ca^{2+} concentrations much higher than those in the remainder of the cytoplasm. Thus, many recent models of Ca^{2+} dynamics in cardiac cells do not use a single cytoplasmic Ca^{2+} domain, but incorporate various Ca^{2+} microdomains, with greater or lesser complexity.

7.6.2   Stochastic Models of Calcium Waves

Of all the results from stochastic modeling, the most intriguing are those of Falcke (2003a,b) who studied the transition from puffs to waves in *Xenopus* oocytes as [IP$_3$] is increased. At low [IP$_3$] only puffs are observed; there is not enough Ca^{2+} released from each cluster to stimulate Ca^{2+} release from neighboring clusters, and thus the responses are purely local. However, as [IP$_3$] increases, both the sensitivity of, and the amount of Ca^{2+} released from each IPR increases. This allows for the development of global waves that emerge from a *nucleation* site. However, until [IP$_3$] gets considerably larger these global events are rare, and in many cases form only abortive waves that progress a short distance before dying out. Both the interwave time interval, T$_{av}$, and its standard deviation ΔT$_{av}$, decrease as [IP$_3$] increases. Finally, at high [IP$_3$] global waves occur regularly with a well-defined period.

Falcke (2003a,b) showed that all these behaviors can be reproduced by a stochastic version of the eight-state model of Section 7.2.5. The long time interval between successive waves when [IP$_3$] is low is a result almost entirely of the stochastic dynamics. In each time interval there is a chance that one IPR fires, stimulating the firing of the entire cluster, and thus initiating a global wave, but because of the intercluster separation and the low sensitivity of each IPR such events are rare. Hence in this regime both T$_{av}$ and ΔT$_{av}$ are large. Conversely, when [IP$_3$] is large, each IPR is much more sensitive to Ca^{2+}, and the flux through each receptor is larger. Thus, firing of a single IPR is nearly always sufficient to stimulate a global wave. In this case, the interwave period is set, not by stochastic effects, but by the intrinsic dynamics of the IPR, i.e., the time required for the receptor to reactivate and be ready to propagate another wave. These results are most easily seen in Fig. 7.23 which shows experimental data from Marchant and Parker (2001) and the corresponding simulations of Falcke (2003a). The ratio of ΔT$_{av}$/T$_{av}$ remains approximately constant over a wide range of T$_{av}$.

What is particularly interesting about these results is that in the simulations the periodic global waves occur for concentrations of IP$_3$ for which the deterministic version of the model is non-oscillatory. In other words, oscillatory waves are not necessarily the result of oscillatory kinetics. They can result from a stochastic process which, every so often, causes a cluster to fire sufficiently strongly that it initiates a global wave. If the standard deviation of the average time between firings is sufficiently small the resulting almost-periodic responses can appear to be the result of an underlying limit cycle, even when no such limit cycle exists. Such results call into serious question the relevance of deterministic approaches to Ca^{2+} waves and oscillations that are caused by small numbers of stochastic IPR. However, the implications have yet to be fully digested (Keener, 2006).

7.7   Intercellular Calcium Waves

Not only do Ca^{2+} waves travel across individual cells, they also travel from cell to cell to form intercellular waves that can travel across many cells. One of the earliest examples of such an intercellular wave was discovered by Sanderson *et al.* (1990, 1994) who discovered that, in epithelial cell cultures, a mechanical stimu-
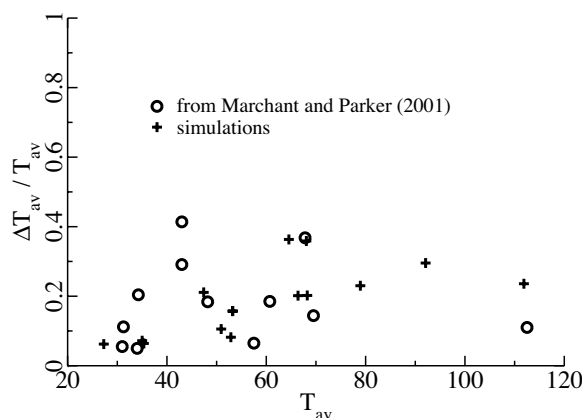
Figure 7.23: Plot of the relative standard deviation $\Delta T_{av}/T_{av}$. The experimental data (open circles) are from Marchant and Parker (2001), while the simulations are from Falcke (2003a).

lus (for example, poking a single cell with a micropipette) can initiate a wave of increased intracellular Ca^{2+} that spreads from cell to cell to form an intercellular wave. Typical experimental results from airway epithelial cells are shown in Fig. 7.4. The epithelial cell culture forms a thin layer of cells, connected by gap junctions. When a cell in the middle of the culture is mechanically stimulated, the Ca^{2+} in the stimulated cell increases quickly. After a time delay of a second or so, the neighbors of the stimulated cell also show an increase in Ca^{2+}, and this increase spreads sequentially through the culture. An intracellular wave moves across each cell, is delayed at the cell boundary, and then initiates an intracellular wave in the neighboring cell. The intercellular wave moves via the sequential propagation of intracellular waves. Of particular interest here is the fact that in the absence of extracellular Ca^{2+}, the stimulated cell shows no response, but an intercellular wave still spreads to other cells in the culture. It thus appears that a rise in Ca^{2+} in the stimulated cell is not necessary for wave propagation. Neither is a rise in Ca^{2+} sufficient to initiate an intercellular wave. For example, epithelial cells in culture sometimes exhibit spontaneous intracellular Ca^{2+} oscillations, and these oscillations do not spread from cell to cell. Nevertheless, a mechanically stimulated intercellular wave does spread through cells that are spontaneously oscillating.

Intercellular Ca^{2+} waves in glial cultures were also studied by Charles *et al.* (1991) as well as by Cornell-Bell *et al.* (1990). Over the past few years there is an increasing body of evidence to show that such intercellular communication between glia, or between glia and neurons, plays an important role in information processing in the brain (Nedergaard, 1994; Charles, 1998; Vesce *et al.*, 1999; Fields and Steven-Graham, 2002; Charles and Giaume, 2002; Lin and Bergles, 2004).

Just as there is wide variety of intercellular Ca^{2+} waves in different cell types, so there is a corresponding variety in their mechanism of propagation. Nevertheless, two basic mechanisms are predominant; propagation by the diffusion of an

extracellular messenger, or propagation by the diffusion of an intracellular messenger through gap junctions. Sometimes both mechanims operate in combination to drive an intercellular wave (see, for example, Young and Hession, 1997). Most commonly the intracellular messenger is IP_3 or Ca^{2+} (or both), but a much larger array of extracellular messengers, including ATP, ADP and nitric oxide, has been implicated.

There have been few models of intercellular Ca^{2+} waves. The earliest were due to Sneyd *et al.* (1994, 1995, 1998) who studied the mechanisms underlying mechanically-induced waves. More recent versions of this basic model have been used to study intercellular coupling in hepatocytes (Höfer, 1999; Höfer *et al.*, 2002; Dupont *et al.*, 2000) and pancreatic acinar cells (Tsaneva-Atanasova *et al.*, 2005), while a different approach was taken by Jung *et al.* (1998). However, detailed studies of the interactions between intracellular and extracellular messengers remain to be done.

7.7.1   A model of mechanically-stimulated intercellular Ca^{2+} waves

Sanderson and his colleagues (Boitano *et al.*, 1992; Sanderson *et al.*, 1994; Sneyd *et al.*, 1994, 1995a,b) proposed a model of mechanically-stimulated intercellular Ca^{2+} waves in epithelial cells (Fig. 7.24). They proposed that mechanical stimulation causes the production of large amounts of IP_3 in the stimulated cell, and this IP_3 moves through the culture by passive diffusion, moving from cell to cell through gap junctions. Since IP_3 releases Ca^{2+} from the ER, the diffusion of IP_3 from cell to cell results in a corresponding intercellular Ca^{2+} wave. Experimental results indicate that the movement of Ca^{2+} between cells does not play a major role in wave propagation, and thus the model assumes that intercellular movement of Ca^{2+} is negligible. Relaxation of this assumption makes little difference to the model behavior, as it is the movement of IP_3 through gap junctions that determines the intercellular wave properties.

In the model, the epithelial cell culture is modeled as a grid of square cells. It is assumed that IP_3 moves by passive diffusion and is degraded with saturable kinetics. Thus, if p denotes $[IP_3]$, then

$$\frac{\partial p}{\partial t} = D_p \nabla^2 p - \frac{V_p p k_p}{k_p + p}. \tag{7.121}$$

When $p \ll k_p$, p decays with time constant $1/V_p$. Ca^{2+} is also assumed to move by passive diffusion, but it is released from the ER by IP_3 and pumped back into the ER by Ca^{2+}-ATPases. The equations are

$$\frac{\partial c}{\partial t} = D_c \nabla^2 c + J_{\text{IPR}} - J_{\text{serca}} + J_{\text{in}}, \tag{7.122}$$

$$\tau_h \frac{dh}{dt} = \frac{k_2^2}{k_2^2 + c^2} - h, \tag{7.123}$$

$$J_{\text{IPR}} = k_f \mu(p) h \left[b + \frac{(1-b)c}{k_1 + c} \right], \tag{7.124}$$
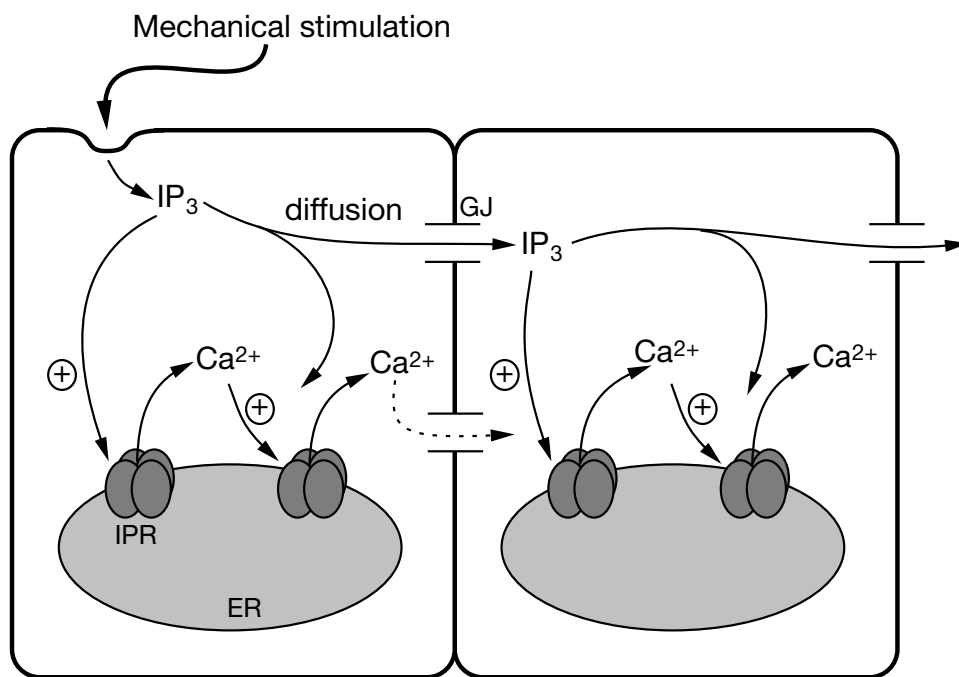
Figure 7.24: Schematic diagram of the model of intercellular Ca^{2+} waves. GJ: gap junction; ER: endoplasmic reticulum; IPR: IP_3 receptor.

$$J_{\text{serca}} = \frac{\gamma c^2}{k_\gamma^2 + c^2}, \tag{7.125}$$

$$J_{\text{in}} = \beta, \tag{7.126}$$

$$\mu(p) = \frac{p^3}{k_\mu^3 + p^3}. \tag{7.127}$$

This was an early model of Ca^{2+} dynamics which is reflected in its relative simplicity. The model for the IPR was based on the model of Atri *et al.* (1993); J_{IPR} is a function of p, c, and a slow variable h, which denotes the proportion of IP_3 receptors that have not been inactivated by Ca^{2+}. Opening by IP_3 is assumed to be instantaneous, as is activation by Ca^{2+}; hence the term $\mu(p)\left[b + \frac{(1-b)c}{k_1+c}\right]$ which is an increasing function of both p and c. The inactivation variable, h, has a steady state which is a decreasing function of Ca^{2+}, and it reaches this steady state with time constant τ_h. Thus, the property of fast activation by Ca^{2+} followed by slower inactivation is built into the model equations.

As usual J_{serca} denotes the removal of Ca^{2+} from the cytoplasm by Ca^{2+}-ATPases in the ER membrane, and is modelled as a simple Hill equation with coefficient 2 (based on the data of Lytton *et al.*, 1992). J_{in} is an unspecified leak of Ca^{2+} into the cytoplasm, either from outside the cell or from the ER. Values of the model parameters are given in Table 12.2.

There is one important difference between this model and others discussed earlier in this chapter; here there is no variable describing the Ca^{2+} concentration in the ER, i.e., no c_e variable. This is equivalent to assuming that depletion of the ER is negligible, so that c_e is constant.

Finally, the internal boundary conditions are given in terms of the flux of IP_3 from cell to cell. If cell n has $[IP_3] = p_n$, it is assumed that the flux of IP_3 from cell n to cell $n+1$ is given by $F(p_n - p_{n+1})$ for some constant F, called the permeability.

Initially, a single cell was injected with IP_3, which was then allowed to diffuse from cell to cell, thereby generating an intercellular Ca^{2+} wave. Figure 7.25 shows a density plot of a numerical solution of the model equations in two dimensions. An intercellular wave can be seen expanding across the grid of cells and then retreating as the IP_3 degrades. As expected for a process based on passive diffusion, the intracellular wave speed (i.e., the speed at which the intercellular wave moves across an individual cell) decreases with distance from the stimulated cell, and the arrival time and the intercellular delay increase exponentially with distance from the stimulated cell. For the values chosen for F, ranging from 1 to 8 $\mu\text{m}\,\text{s}^{-1}$, the model agrees well with experimental data from epithelial, endothelial and glial cells (Demer *et al.*, 1993; Charles *et al.*, 1992). However, the most important model prediction is the value of F needed to obtain such agreement. If F is lower than about 1 $\mu\text{m}\,\text{s}^{-1}$, the intercellular wave moves too slowly to agree with experimental data. Since the value of F is unknown, this prediction provides a way to test the underlying hypothesis of passive diffusion of IP_3.

k_f	$=$	$3\ \mu\mathrm{Ms}^{-1}$	b	$=$	0.11
k_1	$=$	$0.7\ \mu\mathrm{M}$	k_2	$=$	$0.7\ \mu\mathrm{M}$
τ_h	$=$	$0.2\ \mathrm{s}$	k_γ	$=$	$0.27\ \mu\mathrm{M}$
γ	$=$	$1\ \mu\mathrm{Ms}^{-1}$	β	$=$	$0.15\ \mu\mathrm{Ms}^{-1}$
k_μ	$=$	$0.01\ \mu\mathrm{M}$	V_p	$=$	$0.08\ \mathrm{s}^{-1}$
k_p	$=$	$1\ \mu\mathrm{M}$	F	$=$	$2\ \mu\mathrm{m\,s}^{-1}$
D_c	$=$	$20\ \mu\mathrm{m}^2\mathrm{s}^{-1}$	D_p	$=$	$300\ \mu\mathrm{m}^2\mathrm{s}^{-1}$

Table 7.7: Parameters of the model of intercellular Ca^{2+} waves. One important point to note is the difference between D_p and D_c. The value of D_c used here is the effective diffusion coefficient of Ca^{2+}. Although IP$_3$ is a much larger molecule than Ca^{2+}, it diffuses faster through the cell because it is not buffered (Allbritton *et al.*, 1992).
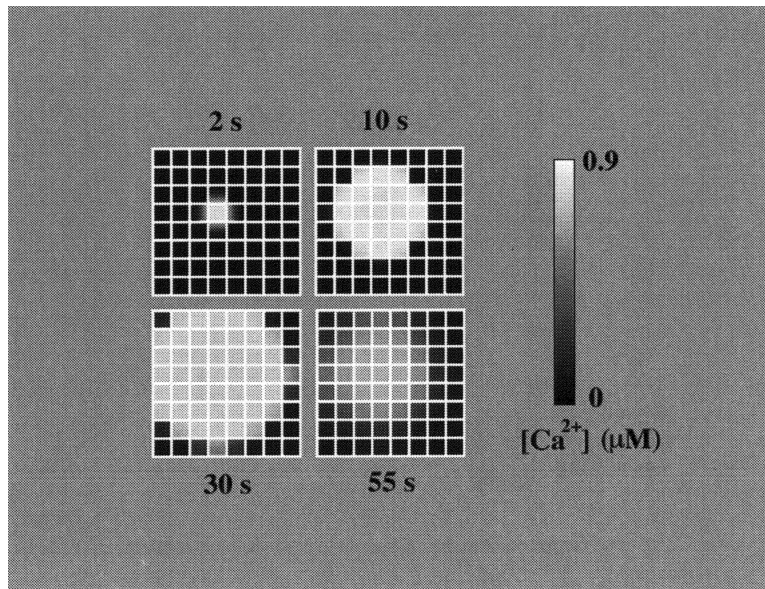
Figure 7.25: Density plot of a two-dimensional intercellular Ca^{2+} wave, computed numerically from the intercellular Ca^{2+} wave model. (Sneyd *et al.*, 1995a, Fig. 4.)
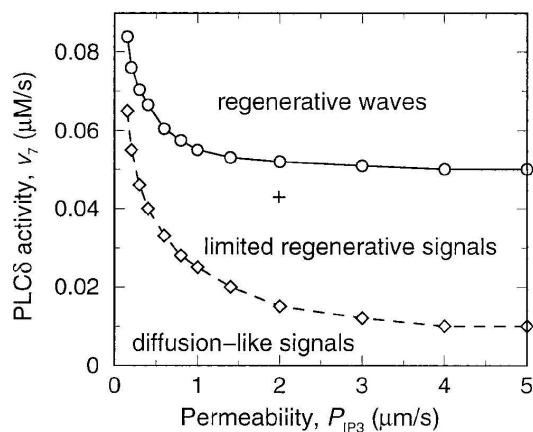
Figure 7.26: Types of intercellular waves in the partially regenerative model as a function of the gap junction permeability of IP$_3$ and the maximal activity of PLCδ (Höfer *et al.*, 2002, Fig. 4.). The intercellular permeability to IP$_3$, here called P_{IP_3} was called F in Table 7.7.1.

7.7.2   Partial regeneration

One of the major questions raised about the previous model was whether an IP$_3$ molecule is able to diffuse through multiple cells without being degraded. It is unlikely that an IP$_3$ molecule could survive long enough to cause intercellular waves propagating distances of up to several hundred micrometers, However, if the production of IP$_3$ is regenerative, for example, by the activation of PLC by increased $\left[\mathrm{Ca}^{2+}\right]$, then the waves could potentially propagate indefinitely, as do action potentials in the axon (Chapter 6). Since, in most cell types the waves eventually stop, this would seem, at first sight, to preclude a regenerative mechanism for IP$_3$ production.

This question was resolved by Höfer *et al.* (2002) who showed that a partially regenerative mechanism could propagate intercellular Ca^{2+} waves much further than would be possible by simple diffusion, but not indefinitely; the waves still eventually terminate. Their model was used to study long-range intercellular Ca^{2+} waves in astrocytes cultured from rat striatum, a preparation in which it is known that the intercellular waves propagate principally through gap junctional diffusion of an intracellular messenger.

The model equations are similar to those in the previous section, with two major exceptions. First, they include the dynamics of c_e, and second, they assume that the rate of production of IP$_3$ by one of the isoforms of PLC, PLCδ, is an increasing function of $\left[\mathrm{Ca}^{2+}\right]$. Thus,

$$\frac{\partial p}{\partial t} = D_p \nabla^2 p + \frac{\nu_7 c^2}{K_{\mathrm{Ca}}^2 + c^2} - k_9 p, \qquad (7.128)$$

where $K_{Ca} = 0.3$ μM, $k_9 = 0.08$ s^{-1}, and ν_7 varies between 0 and 0.08.

Results are shown in Fig. 7.26. When the positive feedback from Ca^{2+} to IP$_3$ production is small (i.e., when the maximal rate of PLCδ activity, ν_7, is small), the intercellular Ca^{2+} wave behaves as if it results from passive diffusion of IP$_3$ from the stimulated cell, as in the model for mechanically-stimulated intercellular Ca^{2+} waves. Conversely, when ν_7 is large the waves become fully regenerative, propagating indefinitely. However, numerical computations show an intermediate range of ν_7 values that give limited regenerative waves; waves that propagate further than they would have had they been governed solely by passive diffusion of IP$_3$, but that eventually terminate and thus are not fully regenerative.

7.7.3 Coordinated oscillations in hepatocytes

Periodic intercellular Ca^{2+} waves propagate across entire lobules of the liver (Nathanson *et al.*, 1995; Robb-Gaspers and Thomas, 1995) and this behavior is mirrored in smaller clusters (doublets and triplets) of coupled hepatocytes. The mechanism for the propagation of these waves appears to be quite different from that proposed for mechanically-stimulated waves. First, the waves in hepatocytes propagate only if each cell is stimulated, i.e., only if each cell has increased IP$_3$. Second, the waves are time periodic. Despite these differences, it is known that the coordination of the waves depends on gap junctional diffusion of an intracellular messenger; in the absence of gap junctional coupling no coordinated wave activity appears, with each cell oscillating independently of its neighbors (Tordjmann *et al.*, 1997). It is also known that there is a increasing gradient of hormone receptor density as one moves from the periportal to the perivenous zone of the liver lobule. This gradient is mirrored in triplets of hepatocytes; when stimulated with noradredaline the cells in the triplet respond in order, with the cell with the highest receptor density responding first. Since each cell in the triplet responds in synchrony to intracellular photorelease of IP$_3$, it follows that the different latencies are the result of different rates of production of IP$_3$.

Based on these observations it has been proposed (Dupont *et al.*, 2000) that the coordinated waves in hepatocyte clusters are phase waves, in which each cell oscillates with a phase slightly different from that of its neighbors. In that model, intercellular synchronization is provided by the diffusion of IP$_3$ through gap junctions. Since each cell produces IP$_3$ at a slightly different rate, the intercellular diffusion of IP$_3$ serves to smooth out the intercellular IP$_3$ gradients, allowing for greater synchronization of the oscillations and the appearance of phase waves. Such synchronization does not persist for a long time, as the cells are essentially uncoupled — in the model there are no oscillations in IP$_3$ driving the Ca^{2+} oscillations, and thus, in the absence of intercellular Ca^{2+} diffusion, the cells act as uncoupled oscillators over a longer time scale. Nevertheless, synchronization persists for long enough to explain experimental observations. A slightly different model, in which the cells are coupled by the intercellular diffusion of Ca^{2+} was proposed by Höfer (1999) and also tested by Dupont *et al.*. According to the latter group, a model based on intercellular diffusion of Ca^{2+} is insufficient to explain all the experimental data.

Similar studies have been done of intercellular waves in pancreatic acinar cells

(Tsaneva-Atanasova *et al.*, 2005) in which it was concluded that the intercellular diffusion of Ca^{2+} alone was able to synchronize intercellular phase waves over a long time period, and that the function of intercellular IP_3 diffusion was to minimize the intercellular IP_3 gradients thus making it easier for Ca^{2+} diffusion to synchronize the oscillators.

However, these results are all still attended by considerable controversy. It is not yet clear how important IP_3 oscillations are for driving Ca^{2+} oscillations in either hepatocytes or pancreatic acinar cells. Much work remains to be done to elucidate the detailed mechanisms underlying these intercellular waves and coupled oscillations.

7.8   Appendix: Mean Field Equations

In Section 7.3, we added diffusion to our model equations in order to study calcium dynamics in a spatially distributed system. However, in doing so, we made use of some very important approximation techniques, which we describe in this Appendix.

7.8.1   Microdomains

Suppose that a substance u is diffusing and reacting in a three dimensional region in which one or two of the dimensions are small compared to the diffusion length scale. (If all dimensions are small compared with a typical diffusion length scale, then it is reasonable to assume that the region is well mixed, and a whole cell model is appropriate.) In this domain,

$$\frac{\partial u}{\partial t} = D\nabla^2 u + f, \tag{7.129}$$

with boundary conditions $\mathbf{n} \cdot D\nabla u = J$ on the boundary of the domain, where $\mathbf{n}$ is the unit outward normal. For this discussion, it is most convenient to assume that (7.129) is in units of dimensionless time, so that D has units of length squared.

Now suppose, for example, that the domain is a long cylindrical tube with crossectional area A that is small compared to D. Because A is small compared to D, we expect that the solution should be nearly uniform in each crossection, varying only slightly from its average value. Thus, we seek an equation describing the evolution of the average value, also called a mean field equation.

To exploit the difference in length scales, we split the Laplacian operator into two, writing

$$\nabla^2 u = u_{xx} + \nabla^2_y u, \tag{7.130}$$

where x is the coordinate along the length of the tube, and y represents the coordinates of the crossection of the tube. The boundary conditions along the sides of the tube are also expressed as $\mathbf{n} \cdot D\nabla_y u = J$, using the coordinate system of the crossection. Here we ignore the boundary conditions at the ends of the tube.

Now the quick and dirty derivation of the mean field equation is to define $\bar{u}$ as the average crossectional value of u,

$$\bar{u} = \frac{1}{A} \int_\Omega u \, dA, \tag{7.131}$$

where Ω is the crossesctional domain, and then to integrate the governing equation (7.129) over Ω, to find

$$\frac{\partial \bar{u}}{\partial t} = D\bar{u}_{xx} + \frac{D}{A} \int_{\Omega} \nabla_y^2 u \, dA + \frac{1}{A} \int_{\Omega} f \, dA. \tag{7.132}$$

Applying the divergence theorem,

$$\int_{\Omega} \nabla_y^2 u \, dA = \int_{\partial\Omega} \mathbf{n} \cdot \nabla_y u \, dS, \tag{7.133}$$

yields

$$\frac{\partial \bar{u}}{\partial t} = D\bar{u}_{xx} + \frac{S}{A}\bar{J} + \bar{f}, \tag{7.134}$$

where

$$\bar{J} = \frac{1}{S} \int_{\partial\Omega} J \, dS, \tag{7.135}$$

with S the circumference of the crossection. Equation (7.134) is the equation governing the behavior of $\bar{u}$.

While this gives the correct answer, some of us (authors and/or readers) may wish for a more systematic derivation. Furthermore, if either J or f depend on u, then it is not clear how to determine $\bar{J}$ or $\bar{f}$.

To this end we introduce a small parameter ϵ where $\epsilon^2 = \frac{A}{D}$, and introduce the scaled coordinate $y = \sqrt{A}\xi$ in terms of which the equation (7.129) becomes

$$\frac{\partial u}{\partial t} = Du_{xx} + \frac{1}{\epsilon^2}\nabla_\xi^2 u + f, \tag{7.136}$$

subject to boundary conditions $\mathbf{n} \cdot \nabla_\xi u = \epsilon \frac{J}{\sqrt{D}}$. Now we seek a solution of (7.136) of the form

$$u = \bar{u} + \epsilon w, \tag{7.137}$$

where w is required to have zero average in each crossection, $\int_{\Omega_\xi} w \, dA_\xi = 0$ and $\bar{u}$ is independent of ξ. It is important to note that $\bar{u}$ and ω are not independent of ϵ, and this is not a power series representation of the solution. Instead, this is a splitting of the solution by a projection operator, say

$$Pu = \int_{\Omega_\xi} u \, dA_\xi, \tag{7.138}$$

and in this notation $\bar{u} = Pu$ and $\epsilon w = u - Pu$.

Now we find equations for $\bar{u}$ and w by substituting (7.137) into (7.136) and then applying the projection operators P and $I - P$. First, applying P (i.e., integrating over Ω_ξ), we find

$$\frac{\partial \bar{u}}{\partial t} = D\bar{u}_{xx} + \frac{1}{\epsilon}\frac{S_\xi}{\sqrt{D}}\bar{J} + \bar{f}, \tag{7.139}$$

where $\bar{J} = \frac{1}{S_\xi} \int_{\partial\Omega_\xi} J \, dS_\xi$, and S_ξ is the circumference of the tube measured in units of ξ. Next, applying the operator $I - P$ we find

$$\frac{1}{\epsilon}\nabla_\xi^2 w = \frac{1}{\epsilon}\frac{S_\xi}{\sqrt{D}}\bar{J} + \bar{f} - f + \epsilon\frac{\partial w}{\partial t} - \epsilon Dw_{xx}. \tag{7.140}$$

The function w must also satisfy the boundary condition $\mathbf{n} \cdot \nabla_\xi w = \frac{J}{\sqrt{D}}$ along the sides of the tube.

Now, if both J and f are known functions, with no dependence on u, then we are done, because (7.139) is the exact mean field equation. No further approximation is needed.

However, if either J or f depend on u, as is typical, then it is necessary to know more about w. In particular, if w is bounded and of order one, then

$$
\begin{aligned}
\bar{J} &= \frac{1}{S_\xi} \int_{\partial\Omega_\xi} J(u) dS_\xi, \\
&= \frac{1}{S_\xi} \int_{\partial\Omega_\xi} J(\bar{u} + \epsilon w) dS_\xi, \\
&= \frac{1}{S_\xi} \int_{\partial\Omega_\xi} \left(J(\bar{u}) + \epsilon J_u(\bar{u})w + O(\epsilon^2) \right) dS_\xi, \\
&= J(\bar{u}) + O(\epsilon^2), \tag{7.141}
\end{aligned}
$$

and similarly, $\bar{f} = f(\bar{u}) + O(\epsilon^2)$. Thus, the mean field equation is

$$
\frac{\partial \bar{u}}{\partial t} = D\bar{u}_{xx} + \frac{1}{\epsilon} \frac{S_\xi}{\sqrt{D}} J(\bar{u}) + f(\bar{u}) + O(\epsilon), \tag{7.142}
$$

or, in terms of the original parameters,

$$
\frac{\partial \bar{u}}{\partial t} = D\bar{u}_{xx} + \frac{S}{A} J(\bar{u}) + f(\bar{u}) + O(\sqrt{\frac{A}{D}}). \tag{7.143}
$$

It remains to establish that w is bounded and of order one. To this end, we seek a solution w of (7.140) as a power series in ϵ, with $\bar{u}$ fixed (that is, ignoring the implicit ϵ dependence of $\bar{u}$),

$$
w = w_1 + \epsilon w_2 + O(\epsilon^2). \tag{7.144}
$$

It is immediate that w_1 must satisfy

$$
\nabla_\xi^2 w_1 = \frac{S_\xi}{\sqrt{D}} \bar{J}, \tag{7.145}
$$

subject to the boundary condition $n \cdot \nabla_\xi w_1 = \frac{J(\bar{u})}{\sqrt{D}}$. Now we let $W(\xi)$ be the fundamental solution of the boundary value problem

$$
\nabla_\xi^2 W = S_\xi \qquad \text{on } \Omega, \tag{7.146}
$$

subject to the boundary condition $n \cdot \nabla_\xi W = 1$ on $\partial\Omega$, and the condition $\int_\Omega W(\xi) dA_\xi = 0$ (which, from the standard theory of Poisson's equation is known to exist). It follows that

$$
w_1 = \frac{J(\bar{u})}{\sqrt{D}} W(\xi). \tag{7.147}
$$

This establishes, at least to our satisfaction, that w is a well-behaved, bounded, function of ϵ, and we are done.

Suppose that instead of a long thin cylinder, the region of interest lies between two flat two dimensional membranes separated by the distance L where $L^2 \ll D$. Suppose also that $Du_z = -J_0$ and $Du_z = J_1$ on the lower and upper membranes, respectively, where z represents the vertical spatial coordinate. In this case, one can show using the same methodology (Exercise 19) that the mean field equation is

$$\frac{\partial \bar{u}}{\partial t} = D\nabla^2 \bar{u} + \frac{1}{L}(J_1(\bar{u}) + J_0(\bar{u})) + f(\bar{u}) + O(\frac{L}{\sqrt{D}}), \qquad (7.148)$$

where $\bar{u} = \frac{1}{L} \int_0^L u \, dz$, and ∇^2 represents the two-dimensional Laplacian operator.

7.8.2 Homogenization; Effective Diffusion Coefficients

As noted in Section 7.3, to take the details of the microstructure of the cytoplasmic and ER boundaries into account is both impractical and of little use. Instead, there is a need to find a mean field description of the calcium concentrations that uses an effective diffusion coefficient.

This need to avoid the details of the microstructure is evident in many other contexts. For example, as is described in Chapter 12, there is a need for equations of action potential propagation in cardiac tissue that do not rely on the details of cellular structure and its interconnectedness.

Homogenization is the very powerful technique by which this is accomplished. In this section we show how homogenization is used to find averaged, or mean field, equations with an effective diffusion coefficient. This same technique is invoked in Chapter 12 to find effective conductances for cardiac tissue. Finally, this technique allows for the derivation of the bidomain equations for calcium, and the bidomain equations for the cardiac action potential.

As a warmup problem, suppose a substance is reacting and diffusing along a one-dimensional region, and that the diffusion coefficient is rapidly varying in space. To be specific, suppose u is governed by the reaction-diffusion equation

$$\frac{\partial u}{\partial t} = \frac{\partial}{\partial x}(D(\frac{x}{\epsilon})\frac{\partial u}{\partial x}) + f(u), \qquad (7.149)$$

Here x is dimensionless, $D(x)$ is a periodic function of period one and of order one, and ϵ is small. We expect that u should have some average or mean field behavior with a characteristic length scale of order one, with small variations from this mean field that are of order ϵ.

To explore this possibility, we introduce two variables,

$$z = x, \qquad \xi = \frac{x}{\epsilon}, \qquad (7.150)$$

which we treat as independent variables. From the chain rule,

$$\frac{\partial}{\partial x} = \frac{\partial}{\partial z} + \frac{1}{\epsilon}\frac{\partial}{\partial \xi}, \qquad (7.151)$$

and the original partial differential equation (7.149) becomes

$$\frac{\partial u}{\partial t} = \frac{\partial}{\partial z}(D(\xi)(\frac{\partial u}{\partial z} + \frac{1}{\epsilon}\frac{\partial u}{\partial \xi})) + \frac{1}{\epsilon}\frac{\partial}{\partial \xi}(D(\xi)(\frac{\partial u}{\partial z} + \frac{\partial u}{\partial \xi})) + f(u). \qquad (7.152)$$

While this equation is clearly more intricate than (7.130), its structure is essentially the same. Thus the calculation that follows is the same as that of the previous section. That is, we seek a solution of (7.152) of the form

$$u = \bar{u} + \epsilon w, \tag{7.153}$$

where $\bar{u}$ is independent of ξ, and w is a periodic function of ξ with zero mean value, $\int_0^1 w \, d\xi = 0$. However, rather than applying the projection operators and then finding power series solutions of these, it is slightly more convenient (and in this case equivalent) to seek power series solutions of (7.152) directly. That is, we set $\bar{u} = u_0 + \epsilon u_1 + O(\epsilon^2)$, and $w = w_1 + \epsilon w_2 + O(\epsilon^2)$, substitute these into (7.152), collect terms of like powers of ϵ, resulting in a hierarchy of equations to be solved,

$$\frac{\partial}{\partial \xi}\left(D(\xi)\left(\frac{\partial w_1}{\partial \xi} + \frac{\partial u_0}{\partial z}\right)\right) = 0, \tag{7.154}$$

and

$$
\begin{aligned}
\frac{\partial}{\partial \xi}\left(D(\xi)\frac{\partial w_2}{\partial \xi}\right) &= \frac{\partial u_0}{\partial t} - \frac{\partial}{\partial z}\left(D(\xi)\left(\frac{\partial u_0}{\partial z} + \frac{\partial w_1}{\partial \xi}\right)\right) \\
&\quad - \frac{\partial}{\partial \xi}\left(D(\xi)\left(\frac{\partial w_1}{\partial z} + \frac{\partial u_1}{\partial z}\right)\right) \\
&\quad - f(u_0).
\end{aligned}
\tag{7.155}
$$

The first of these is readily solved by direct integration. We define $W(\xi)$ to be the periodic function with zero mean that satisfies the differential equation

$$\frac{dW}{d\xi} = \frac{R}{\bar{R}} - 1. \tag{7.156}$$

where $R = \frac{1}{D}$, and $\bar{R} = \int_0^1 R \, d\xi$. Then

$$w_1 = -W(\xi)\frac{\partial u_0}{\partial z}. \tag{7.157}$$

The function $W(\xi)$ determines the small-scale structure of the solution.

Next, we examine the equation (7.155) and observe that w_2 can be periodic only if the right hand side of this equation has zero average with respect to ξ. Thus, it must be that

$$
\begin{aligned}
\frac{\partial u_0}{\partial t} &= \int_0^1 \frac{\partial}{\partial z}\left(D(\xi)\left(\frac{\partial u_0}{\partial z} + \frac{\partial w_1}{\partial \xi}\right)\right) d\xi \\
&\quad + f(u_0), \\
&= D_{\text{eff}}\frac{\partial^2 u_0}{\partial z^2} + f(u_0),
\end{aligned}
\tag{7.158}
$$

where

$$D_{\text{eff}} = \frac{1}{\bar{R}}. \tag{7.159}$$
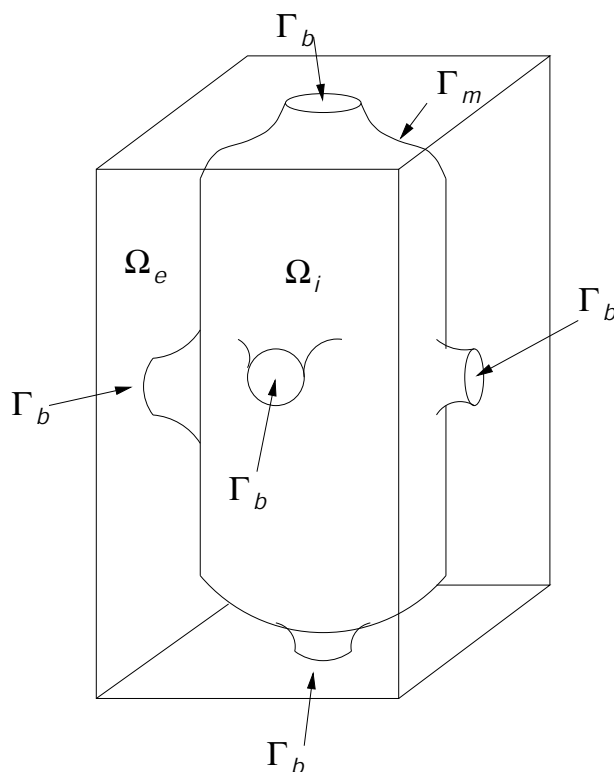
Figure 7.27: Sketch of an idealized single cell.

Equation (7.158) is the mean field equation we seek, and D_{eff} is the effective diffusion coefficient.

Homogenization for the full three dimensional problem follows the same menu. We suppose that a substance is reacting and diffusing in a subregion of three dimensional space, that is subdivided into small periodic subunits Ω, called the microstructure, which are each contained in a small rectangular box. Examples of these are depicted in Figures 7.27 and 7.29. Figure 7.27 depicts a single cell which is connected to its neighbors through small pores, called gap junctions (described in more detail in Chapter 8) which are simply parts of the box wall that connect intracellular space. Thus, the boundary of the cellular subunit, Γ, is composed of two components, cell membrane Γ_m and sides of the box Γ_b.

Similarly, a model of the ER is that it is comprised of a periodic substructure such as those depicted in 7.29. In this figure, Ω_c and Ω_e represent the cytoplasmic and ER domains, Γ_m is the membrane boundary between these and Γ_b is the intersection of the ER with the walls of the box.

We assume that the rectangular box is of length l (although the box need not be a cube), where l is much less than the natural length scale of the problem, in
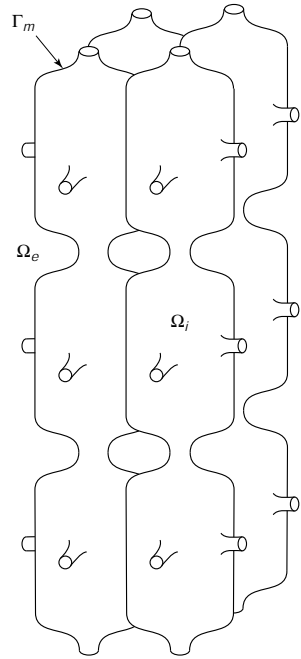
Figure 7.28: Periodic cell structure.
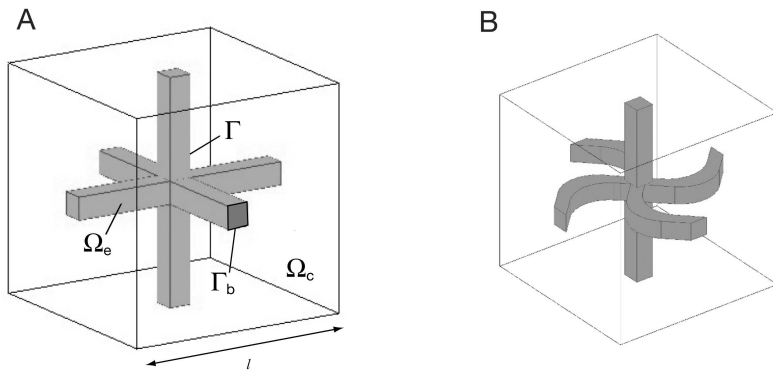
Figure 7.29: Two possible ER microscale structures. The more complicated structure in B results in a non-isotropic effective diffusion tensor. **James, Can you label the membrane boundary Γ_m? Thanks.**

this case $\Lambda = \sqrt{D}$, the diffusion length. Thus, there are two natural length scales, l and Λ, and so $\epsilon = l/\Lambda \ll 1$ is a natural small parameter. Since l is small compared to the diffusion length scale, it is reasonable to assume that the solution is nearly homogeneous in each microstructural unit, and that the microstructure causes only small perturbations to the "background" solution.

Now we suppose that the substance u is diffusing and reacting according to (7.129) in the interior of the three-dimensional subdomain, and that there are fluxes across the membrane given by $\mathbf{n} \cdot D\nabla u = J$. Again, it is convenient to assume that these equations are in units of dimensionless time, so that D has units of length^2. We further assume that J is proportional to l. Notice that the total flux across the boundary of Ω is proportional to the surface area, so that the total flux per unit volume is proportional to $\frac{J}{l}$. In order that this remains bounded in the limit that $\epsilon \to 0$, we assume that $J = lj$.

The standard procedure is to introduce two variables

$$z = \frac{x}{\Lambda}, \qquad \xi = \frac{z}{\epsilon}, \tag{7.160}$$

so that ξ denotes the space variable on the microscale, and z denotes the space variable on the original, or long, scale. Treating z and ξ as independent variables, we write

$$\nabla_x = \frac{1}{\Lambda}\left(\frac{1}{\epsilon}\nabla_\xi + \nabla_z\right), \tag{7.161}$$

where the subscript denotes the space variable with which the gradient derivatives are taken. In these variables, the partial differential equation (7.129) becomes

$$\frac{\partial u}{\partial t} = \nabla_z^2 u + \frac{2}{\epsilon}\nabla_\xi\nabla_z u + \frac{1}{\epsilon^2}\nabla_\xi^2 u + f, \tag{7.162}$$

subject to the boundary condition

$$\mathbf{n} \cdot \left(\nabla_z u + \frac{1}{\epsilon}\nabla_\xi u\right) = \epsilon j \qquad \text{on } \Gamma_m. \tag{7.163}$$

Notice that $\mathbf{n}$ is a dimensionless quantity, containing only directional information about the normal to the boundary and so does not change with changes in space scale.

Once again we have a partial differential equation with the same structure as (7.130). Thus, as before we look for a solution of (7.162) in the form

$$u = \bar{u}(z, t, \epsilon) + \epsilon w(\xi, z, t, \epsilon), \tag{7.164}$$

where $\bar{u}$ is the "background" or mean field solution, varying only on the large space scale and independent of ξ, while ϵw is a correction term periodic in ξ and having zero average value in the variable ξ. Next, we seek power series representations for $\bar{u}$ and w of the form

$$\bar{u} = u_0 + \epsilon u_1 + O(\epsilon^2), \qquad w = w_1 + \epsilon w_2 + O(\epsilon^2). \tag{7.165}$$

Substituting these into (7.162), and (7.163), and equating coefficients of powers of ϵ, gives a hierarchy of equations to be solved sequentially. The leading order equation is

$$\nabla_\xi^2 w_1 = 0 \qquad \text{in } \Omega, \tag{7.166}$$

subject to boundary conditions

$$\mathbf{n} \cdot (\nabla_z u_0 + \nabla_\xi w_1) = 0 \qquad \text{on } \Gamma_m, \tag{7.167}$$

and the next equation in the hierarchy is

$$\frac{\partial u_0}{\partial t} = \nabla_z^2 u_0 + 2\nabla_\xi \nabla_z w_1 + \nabla_\xi^2 w_2 + f, \qquad \text{in } \Omega, \tag{7.168}$$

with boundary conditions

$$\mathbf{n} \cdot (\nabla_z w_1 + \nabla_\xi w_2) = j \qquad \text{on } \Gamma_m. \tag{7.169}$$

The first of these equations can be solved in the way derived by Bensoussan, Lions and Papanicolaou (1978) (this method is discussed in more detail by Auriault and Lewandowska, 1993) by letting

$$w_1 = W(\xi) \cdot \nabla_z u_0, \tag{7.170}$$

where $W(\xi)$ is a fundamental solution satisfying the vector differential equation

$$\nabla_\xi^2 W \;=\; 0 \qquad \text{in } \Omega, \tag{7.171}$$
$$\mathbf{n} \cdot (\nabla_\xi W + I) \;=\; 0 \qquad \text{on } \Gamma_m, \tag{7.172}$$

In addition, to specify $W(\xi)$ uniquely, we require that

$$\int_\Omega W(\xi) dV_\xi = 0. \tag{7.173}$$

We do not actually need to solve (7.168), but simply observe that w_2 can be periodic only if a solvability or consistency condition holds (this is an application of the Fredholm Alternative). The consistency condition is found by integrating the equation (7.168) over the domain Ω, with the result

$$
\begin{aligned}
V_\Omega \frac{\partial u_0}{\partial t} \;&=\; \int_\Omega \nabla_z \cdot (\nabla_z u_0 + \nabla_\xi w_1) dV_\xi + \int_\Omega \nabla_\xi \cdot (\nabla_z w_1 + \nabla_\xi w_2) dV_\xi + \int_\Omega f dV_\xi, \\
&=\; \int_\Omega \nabla_z \cdot (\nabla_z u_0 + \nabla_\xi W \nabla_z u_0) dV_\xi + \int_{\partial\Omega} \mathbf{n} \cdot (\nabla_\xi w_2 + \nabla_z w_1) dS_\xi + \int_\Omega f dV_\xi, \\
&=\; \nabla_z \cdot \left[\int_\Omega (I + \nabla_\xi W) \right] \nabla_z u_0 dV_\xi + \int_{\Gamma_m} j(u_0) dS_\xi + V_\Omega f(u_0), \tag{7.174}
\end{aligned}
$$

and thus

$$\frac{\partial u_0}{\partial t} = \nabla_z \cdot D_{\text{eff}} \nabla_z u_0 + \frac{S_\Omega}{V_\Omega} j(u_0) + f(u_0), \tag{7.175}$$

where V_Ω and S_Ω denote the (dimensionless) volume and surface area of Ω, respectively, and D_{eff}, the (dimensionless) effective diffusion tensor, is given by

$$D_{\text{eff}} = \frac{1}{V_\Omega} \int_\Omega (I + \nabla_\xi W) dV_\xi. \tag{7.176}$$

Expressing this equation in dimensional units, we have

$$\frac{\partial u_0}{\partial t} = D \nabla_x \cdot D_{\text{eff}} \nabla_x u_0 + \chi J(u_0) + f(u_0), \tag{7.177}$$

where χ is the surface area to volume ratio of the microstructure.

Hence, for any given periodic geometry, the effective diffusion tensor (7.176) can be calculated by solving the partial differential equations (7.171) and (7.172). Goel et al. (2006) calculated effective diffusion coefficients for a variety of possible ER microstructures. For the regular structure of Fig. 7.29A the effective diffusion coefficient of Ca^{2+} in the cytoplasm decreases from 250 $\mu m^2 s^{-1}$ to about 100 $\mu m^2 s^{-1}$ as the volume fraction of the ER increases from 0 to 0.9. The more complicated structure of Fig. 7.29B gives non-isotropic diffusion, with the diffusion coefficient in the vertical direction about 50% larger than the diffusion coefficient in the other two directions. **James, there is a notational challenge here, since homogenization produces a dimensionless effective diffusion coefficient, and you report your numerical results in dimensional units. Would it not be better to report the percentage decrease? JK**

7.8.3 Bidomain Equations

The homogenization technique described here can be applied to any spatial domain with a periodic microstructure. Thus, for example, it can be applied to intertwined intracellular and extracellular spaces, or to intertwined cytoplasmic and ER spaces. In each case, one finds descriptions of the mean fields which are defined everywhere in space, so that the two spaces are effectively comingled, hence viewed as a bidomain. The only (slight) complication is that fluxes across common boundaries must be equal in amplitude and opposite in direction. Thus, a flux into intracellular space is a flux out of extracellular space, or a flux into the cytoplasm is also a flux out of the ER. Furthermore, even though the domains share a common interface, their volumes are complementary so that the surface to volume ratios for the two spaces differ.

Exercises

1. Show that in a general model of intracellular Ca^{2+} dynamics in a well-mixed cell, the resting cytosolic Ca^{2+} concentration is independent of Ca^{2+} exchange rates with the internal pools.

2. Murray (1989) discusses a simple model of CICR that has been used by a number of modelers (Cheer *et al.*, 1987; Lane *et al.*, 1987). In the model,

Ca^{2+} release from the ER is an increasing sigmoidal function of Ca^{2+}, and Ca^{2+} is removed from the cytoplasm with linear kinetics. Thus,

$$\frac{dc}{dt} = L + \frac{k_1 c^2}{K + c^2} - k_2 c,$$

where L is a constant leak of Ca^{2+} from the ER into the cytoplasm.

(a) Nondimensionalize this equation. How many nondimensional parameters are there?

(b) Show that when $L = 0$ and $k_1 > 2k_2$, there are two positive steady states and determine their stability. For the remainder of this problem assume that $k_1 > 2k_2$.

(c) How does the nullcline $dc/dt = 0$ vary as the leak from the internal store increases? Show that there is a critical value of L, say L_c, such that when $L > L_c$, only one positive solution exists.

(d) Fix $L < L_c$ and suppose the solution is initially at the lowest steady state. How does c behave when small perturbations are applied to c? How does c behave when large perturbations are applied? How does c behave when L is raised above L_c and then decreased back to zero? Plot the bifurcation diagram in the L, c phase-plane, indicating the stability or instability of the branches. Is there hysteresis in this model?

3. One of the earliest models of Ca^{2+} oscillations was the two-pool model of Goldbeter, Dupont and Berridge (1990). They assumed that IP_3 causes an influx, r, of Ca^{2+} into the cell and that this influx causes additional release of Ca^{2+} from the ER via an IP_3-independent mechanism. Thus,

$$\frac{dc}{dt} = r - kc - f(c, c_e), \tag{7.178}$$

$$\frac{dc_e}{dt} = f(c, c_e), \tag{7.179}$$

$$f(c, c_e) = J_{\text{uptake}} - J_{\text{release}} - k_f c_e, \tag{7.180}$$

where

$$J_{\text{uptake}} = \frac{V_1 c^n}{K_1^n + c^n}, \tag{7.181}$$

$$J_{\text{release}} = \left(\frac{V_2 c_e^m}{K_2^m + c_e^m} \right) \left(\frac{c^p}{K_3^p + c^p} \right). \tag{7.182}$$

Here, $k_f c_e$ is a leak from the ER into the cytoplasm. Typical parameter values are given in Table 20.3. (All the concentrations in this model are with respect to the total cell volume, and thus there is no need for the correction factor γ (cf. 7.4) to take into account the difference in the ER and cytoplasmic volumes.)

(a) Nondimensionalize these equations. How many non-dimensional parameters are there?

k	$=$	10 s^{-1}	K_1	$=$	$1 \ \mu M$
K_2	$=$	$2 \ \mu M$	K_3	$=$	$0.9 \ \mu M$
V_1	$=$	$65 \ \mu Ms^{-1}$	V_2	$=$	$500 \ \mu Ms^{-1}$
k_f	$=$	1 s^{-1}	m	$=$	2
n	$=$	2	p	$=$	4

Table 7.8: Typical parameter values for the two-pool model of Ca^{2+} oscillations (Goldbeter *et al.*, 1990).

(b) Show that in a closed cell (i.e., one without any interaction with the extracellular environment) the two-pool model cannot exhibit oscillations.

(c) How does the steady state solution depend on influx?

(d) Use a bifurcation tracking program such as AUTO to plot the bifurcation diagram of this model, using r as the bifurcation parameter. Find the Hopf bifurcation points and locate the branch of stable limit cycle solutions. Plot some typical limit cycle solutions for different values of r.

4. Complete the details of the reduction of the IP_3 receptor model (Section 7.2.5).

5. Write down the equations for the reduced IP_3 receptor model (Section 7.2.5) when $k_4 = k_2$ and $k_{-4} = k_{-2}$. Let $h = 1 - y$. What is the differential equation for h? Write it in the form

$$\tau_h \frac{dh}{dt} = h_\infty - h. \tag{7.183}$$

Derive this simplified model directly from the state diagram in Fig. 7.8.

6. Write down a reaction scheme like that of Fig. 7.8, but assuming that $2 \ Ca^{2+}$ ions inactivate the receptor in a cooperative fashion. Assume a simple model of cooperativity,

$$S_{ij0} \underset{k_{-2}}{\overset{k_2 c^2}{\rightleftarrows}} S_{ij1}, \tag{7.184}$$

for $i, j = 0$ or 1, and assume that the group I and group II states are each in quasi-steady state. Derive the model equations.

7. Starting with a basic scheme like that of Fig. 7.5 one can construct a large number of variants, each of which has a similar steady-state flux. The purpose of this Exercise is to investigate two simple variants of the basic model, and show that the flux is similar for each. To distinguish between these models on the basis of experimental data is, in general, quite difficult.

(a) First, calculate the expressions for α_1 to α_4 in (7.7) and for β_1 to β_4 in (7.7). (Use of a symbolic manipulation program such as Maple is, as usual, recommended.)

(b) Extend the ATPase model of Section 7.2.4 by assuming that the two Ca^{2+} ions bind sequentially, not simultaneously, and calculate the flux.

(c) Modify the model still further by assuming that the binding of the second Ca^{2+} ion is much faster than binding of the first, and calculate the flux.

(d) Compare these three different expressions for the steady-state flux. Are experimental data of the steady state flux sufficient to distinguish between these models?

8. Does the binding diagram in Fig. 7.8 satisfy the principle of detailed balance (Chapter 1, Section 1.3)?

9. In 2006 Domijan *et al.* constructed a model of Ca^{2+} oscillations that uses a simple model of the IPR (based on an earlier model of Atri et al., 1993):

$$\frac{dc}{dt} = J_{\text{release}} - J_{\text{serca}} + \delta(J_{\text{in}} - J_{\text{pm}}), \qquad (7.185)$$

$$\frac{dc_e}{dt} = \gamma(J_{\text{serca}} - J_{\text{release}}) \qquad (7.186)$$

$$\tau_n \frac{dn}{dt} = \frac{k_2^2}{k_2^2 + c^2} - n, \qquad (7.187)$$

$$\frac{dp}{dt} = \nu\left(\frac{c + (1-\alpha)k_4}{c + k_4}\right) - \beta p, \qquad (7.188)$$

where

$$J_{\text{release}} = \left[k_{\text{flux}}\left(\mu_0 + \frac{\mu_1 p}{k_\mu + p}\right) n \left(b + \frac{V_1 c}{k_1 + c}\right)\right](c_e - c), \quad (7.189)$$

$$J_{\text{serca}} = \frac{V_e c}{k_e + c}, \qquad (7.190)$$

$$J_{\text{pm}} = \frac{V_p c^2}{k_p^2 + c^2}, \qquad (7.191)$$

$$J_{\text{in}} = \alpha_1 + \alpha_2 \frac{\nu}{\beta}. \qquad (7.192)$$

Typical parameter values are given in Table 7.9.

(a) Explain the physiological basis of each term in the model.

(b) What does the parameter ν represent?

(c) The model takes quite different forms when $\alpha = 0$ or $\alpha = 1$. What are the physiological assumptions behind each of these forms?

(d) Using AUTO, plot the bifurcation diagram of the model using ν as the bifurcation parameter. How are the bifurcation diagrams different for $\alpha = 0$ and $\alpha = 1$? (Do not plot every detail of the bifurcation diagrams, but try to find the main branches.)

(e) How would you model a pulse of IP_3 applied by the experimentalist?

δ	$=$	0.01	k_1	$=$	$1.1\ \mu$M
γ	$=$	5.405	k_2	$=$	$0.7\ \mu$Ms^{-1}
k_{flux}	$=$	$6.0\ \mu$Ms^{-1}	k_μ	$=$	$4\ \mu$M
V_p	$=$	$24\ \mu$Ms^{-1}	μ_0	$=$	0.567
k_p	$=$	$0.4\ \mu$M	μ_1	$=$	0.433
V_e	$=$	$20\ \mu$Ms^{-1}	b	$=$	0.111
k_e	$=$	$0.06\ \mu$Ms^{-1}	V_1	$=$	0.889
α_1	$=$	$1\ \mu$Ms^{-1}	α_2	$=$	0.2 s^{-1}
β	$=$	0.08 s^{-1}	k_4	$=$	$1.1\ \mu$M

Table 7.9: Parameters of the model of Ca^{2+} waves in Exercise 9.
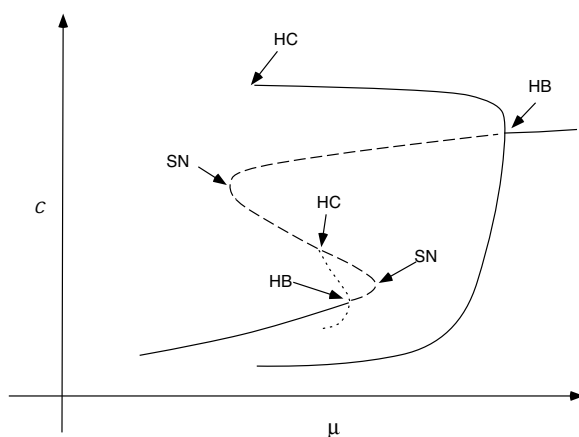
Figure 7.30: Typical bifurcation diagram of the model of Ca^{2+} oscillations in Exercise 10 (not drawn to scale). HB denotes a Hopf bifurcation, SN denotes a saddle-node bifurcation, HC denotes a homoclinic bifurcation.

(f) How does the model respond to an external pulse of IP$_3$? What is the difference between the responses when $\alpha = 0$ and $\alpha = 1$?

10. Suppose that a model of Ca^{2+} oscillations has two variables, c and n. Suppose further that the bifurcation diagram of this model has the structure shown in Fig. 7.30, as a function of some parameter, μ. (This basic structure is common to many models of Ca^{2+} dynamics.) Sketch the phase planes for μ below, at, and above each bifurcation point.

11. (a) Plot the nullclines of the model of CICR in bullfrog sympathetic neurons (Section 7.2.9) and show that they are both N-shaped curves.

(b) Rewrite the model in terms of c and $c_t = c + \frac{c_e}{\gamma}$ and draw the phase portrait and nullclines of the model in these new variables.

(c) Plot the bifurcation diagram of the model of CICR in bullfrog sympathetic neurons (Section 7.2.9) using the external Ca^{2+} concentration c_o

as the bifurcation parameter. Verify the behavior shown in Fig. 7.15, that the period but not the amplitude of the oscillations is sensitive to c_o.

12. Generalize (7.72) to the case of multiple buffers, both mobile and immobile.

13. Prove that (7.83) has a traveling wave solution that is a transition between W_1 and W_3 if and only if

$$\int_{W_1}^{W_3} f(\phi(w))dw > 0. \tag{7.193}$$

14. By looking for solutions to (7.66) and (7.67) of the form $c = A \exp(\xi/\lambda)$, $b = B \exp(\xi/\lambda)$, where λ is the space constant of the wave front and $\xi = x + st$, show that the speed of the wave s is related to the space constant of the wave front by

$$s = \frac{D_c}{\lambda} + \lambda \left[f'(0) - \frac{k_+ b_t (\lambda s - D_b)}{\lambda^2 k_- + \lambda s - D_b} \right]. \tag{7.194}$$

What is the equation in the limit $k_+, k_- \to \infty$, with $k_-/k_+ = K$? Hence show that for the generalized bistable equation,

$$\lambda s < D_{\text{eff}}. \tag{7.195}$$

15. Repeat the analysis of Section 7.4.1, without assuming that b_t is constant. Under what conditions may we assume that b_t is constant?

16. Develop a formal asymptotic expansion (following the method used in the Appendix) to homogenize the equation

$$\frac{\partial c}{\partial t} = D_c \frac{\partial^2 c}{\partial x^2} - kc + g\left(\frac{x}{L}\right) f(c), \tag{7.196}$$

where $g(y)$ is periodic with period 1, in the limit that $\frac{L^2 k}{D_c} \ll 1$. Show that the averaged equation is

$$\frac{\partial c}{\partial t} = D_c \frac{\partial^2 c}{\partial x^2} - kc + Gf(c), \tag{7.197}$$

where $G = \frac{1}{L} \int_0^L g(x)dx$.

17. (a) Find conditions on A guaranteeing that there are traveling waves of calcium release in the spatially homogenized equation (7.93) with the cubic release function (7.90).

    (b) Find conditions on A guaranteeing that there are traveling waves of calcium release in the spatially homogenized equation (7.93) with the piecewise linear release function (7.91).

18. Find the solution of the boundary value problem

$$\nabla^2 W = 2, \tag{7.198}$$

on a circle of radius 1, subject to the boundary condition $n \cdot \nabla W = 1$, and requiring W to have zero average value. (Why is 2 the correct right hand side for this partial differential equation?)

19. Suppose that a substance u reacts and diffuses in a region between two flat two dimensional membranes separated by the distance L where $L^2 \ll D$ (where D is in units of length^2). Suppose also that $Du_z = -J_0$ and $Du_z = J_1$ on the lower and upper membranes, respectively, where z represents the vertical spatial coordinate. Derive the mean field equation for the evolution of u (7.148), and find the leading order correction to the mean field.

Chapter 8

Intercellular Communication

For multicellular organisms to form and operate, cellular behavior must be vastly more complex than what is seen at the single-cell level. Cells must not only regulate their own growth and behavior, they must also communicate and interact with their neighbors to ensure the correct behavior of the entire organism. Intercellular communication occurs in a variety of ways, ranging from hormonal communication on the level of the entire body to localized interactions between individual cells. The discussion in this chapter is limited to cellular communication processes that occur between cells or over a region of a small number of cells. Other forms of communication and control, such as hormone feedback systems, are described in other chapters.

There are two primary ways that cells communicate with neighbors. Many cells (muscle and cardiac cells for example) are connected to their immediate neighbors by gap junctions in the cell membrane that form a relatively nonselective, low-resistance pore through which electrical current or chemical species can flow. Hence, a gap junction is also called an *electrical synapse*. The second means of communication is through a *chemical synapse*, in which the message is mediated by the release of a chemical from one cell and detected by receptors on its neighbor. Electrically active cells such as neurons typically communicate via chemical synapses, which are thus a crucial feature of the nervous system. Chemical synapses are considerably more complex than electrical synapses, and as a result, most of this chapter is devoted to them.

8.1 Chemical Synapses

At a chemical synapse (Fig. 8.1) the nerve axon and the postsynaptic cell are in close apposition, being separated by the *synaptic cleft*, which is about 500 angstroms wide. When an action potential reaches the nerve terminal, it opens voltage-gated Ca^{2+} channels, leading to an influx of Ca^{2+} into the nerve terminal. Increased $\left[Ca^{2+}\right]$ causes the release of a neurotransmitter, which diffuses across the synaptic cleft, binds to receptors on the postsynaptic cell, and initiates changes in its membrane potential. The neurotransmitter is then removed from the synaptic cleft by
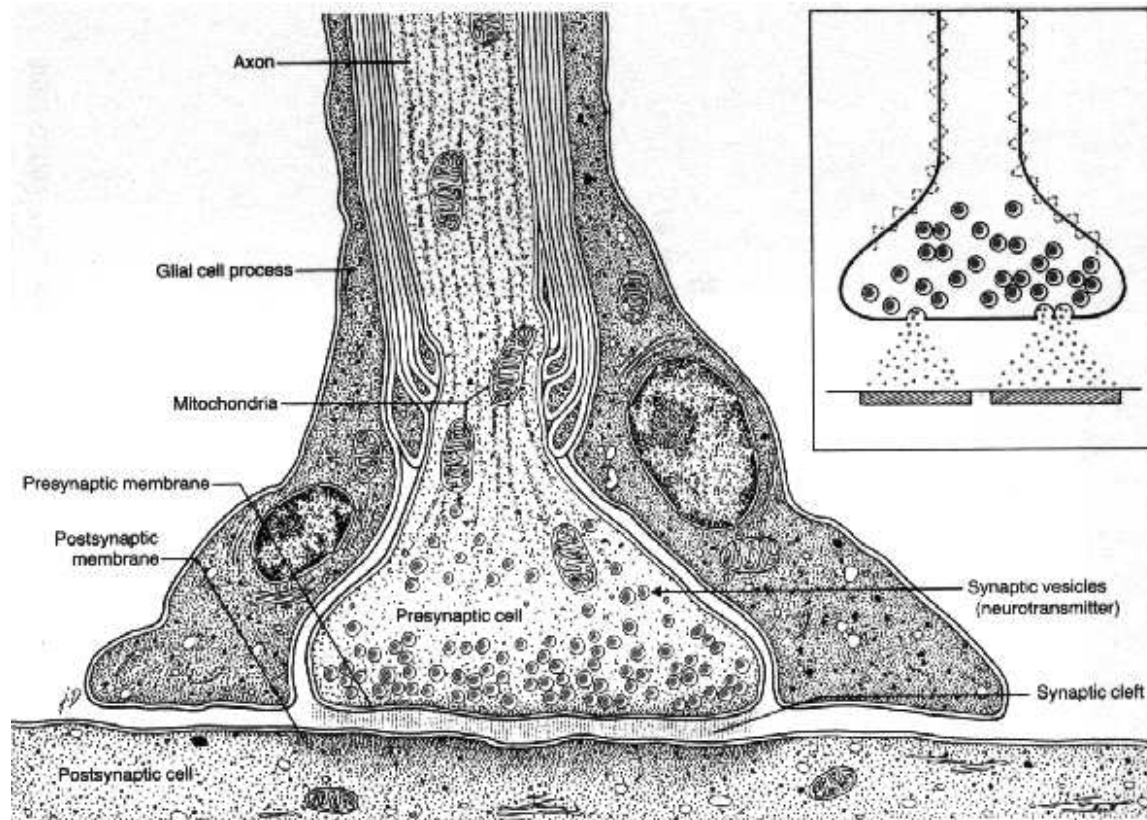
Figure 8.1: Schematic diagram of a chemical synapse. The inset shows vesicles of neurotransmitter being released into the synaptic cleft. (Davis et al., 1985, Fig. 8-11, p. 135.)

diffusion and hydrolysis.

There are over 40 different types of synaptic transmitters, with differing effects on the postsynaptic membrane. For example, acetylcholine (ACh) binds to ACh receptors, which in skeletal muscle act as cation channels. Thus, when they open, the flow of the cation causes a change in the membrane potential, either depolarizing or hyperpolarizing the membrane. If the channel is a sodium channel, then the flow is inward and depolarizing, whereas if the channel is a potassium channel, then the flow is outward and hyperpolarizing. Other receptors, such as those for gamma-aminobutyric acid (GABA), open anion channels (mainly chloride), thus hyperpolarizing the postsynaptic membrane, rendering it less excitable. Synapses are classified as excitatory or inhibitory according to whether they depolarize or hyperpolarize the postsynaptic membrane. Other important neurotransmitters include epinephrine (adrenaline), norepinephrine, dopamine, glycine, glutamate, and serotonin. Of these, dopamine, glycine, and GABA are usually inhibitory, while glutamate and ACh are usually, but not always, excitatory.

Many of these neurotransmitters work by gating an ion channel directly, as described for ACh above. Such channels are called *agonist-controlled* or *ligand-gated* ion channels, and a simple model of an agonist-controlled channel is described in Chapter 3, Section 3.5.4. However, not all neurotransmitters work only in this way. For example, receptors for glutamate, the principal excitatory neurotransmitter in the brain, come in two types — ionotropic receptors, which are agonist-controlled, and metabotropic receptors, which are linked to G-proteins, and act via the production of the second-messenger IP_3 and the subsequent release of Ca^{2+} from the endoplasmic reticulum (as described in Chapter 7).

The loss of specific neurotransmitter function corresponds to certain diseases. For example, *Huntington's disease*, a hereditary disease characterized by flicking movements at individual joints progressing to severe distortional movements of the entire body, is associated with the loss of certain GABA-secreting neurons in the brain. The resulting loss of inhibition is believed to allow spontaneous outbursts of neural activity leading to distorted movements.

Similarly, Parkinson's disease results from widespread destruction of dopamine-secreting neurons in the basal ganglia. The disease is associated with rigidity of much of the musculature of the body, involuntary tremor of involved areas, and a serious difficulty in initiating movement. Although the causes of these abnormal motor effects are uncertain, the loss of dopamine inhibition could lead to overexcitation of many muscles, hence rigidity, or to lack of inhibitory control of feedback circuits with high feedback gain, leading to oscillations, i.e., muscular tremor.

8.1.1 Quantal Nature of Synaptic Transmission

Chemical synapses are typically small and inaccessible, crowded together in very large numbers in the brain. However, neurons also make synapses with skeletal muscle cells, and these are usually much easier to isolate and study. For this reason, a great deal of the early experimental and theoretical work on synaptic transmission was performed on the neuromuscular junction, where the axon of a motorneuron forms a chemical synapse with a skeletal muscle fiber. The response of the muscle cell to a neuronal stimulus is called an *end-plate potential*, or epp.
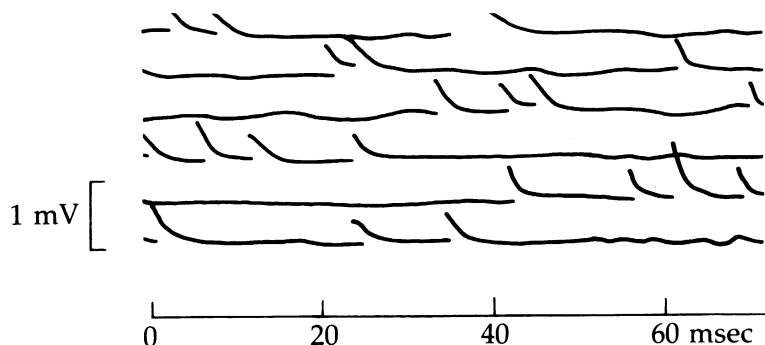
Figure 8.2: Miniature end-plate potentials (epp's) in the frog neuromuscular junction. Each epp has an amplitude of around 1 mV and results from the independent release of a single quantum of ACh. (Kuffler et al., 1984, p. 251, reproducing a figure of Fatt and Katz, 1952.)

In 1952 Fatt and Katz discovered that when the concentration of Ca^{2+} in the synaptic cleft was very low, an action potential stimulated only a small end-plate potential (Fig. 8.2). Further, these miniature end-plate potentials appeared to consist of multiples of an underlying "minimum" epp of the same amplitude as an epp arising spontaneously, i.e., due to random activity other than an action potential. Their findings suggested that an epp is made up of a large number of identical building blocks each of which is of small amplitude.

It is now known that quantal synaptic transmission results from the packaging of ACh into discrete vesicles. Each nerve terminal contains a large number of synaptic vesicles that contain ACh. Upon stimulation, these vesicles fuse with the cell membrane, releasing their contents into the synaptic cleft. Even in the absence of stimulation, background random activity can cause vesicles to fuse with the cell membrane and release their contents. The epp seen in spontaneous activity results from the release of the contents of a single vesicle, while the miniature epp's result from the fusion of a small integer number of vesicles, and thus appear in multiples of the spontaneous epp.

Based on their observations in frog muscle, del Castillo and Katz (1954) proposed a probabilistic model of ACh release. Their model was later applied to mammalian neuromuscular junctions by Boyd and Martin (1956). The model is based on the assumption that the synaptic terminal of the neuron consists of a large number, say n, of releasing units, each of which releases a fixed amount of ACh with probability p. If each releasing site operates independently, then the number of quanta of ACh that is released by an action potential is binomially distributed. The probability that k releasing sites "fire" (i.e., release a quantum of ACh) is the probability that k sites fire and the remaining sites do not, and so is given by $p^k(1-p)^{n-k}$. Since k sites can be chosen from n total sites in $n!/[(k!(n-k)!)]$ ways, it follows that

$$\text{Probability } k \text{ sites fire} = P(k) = \frac{n!}{k!(n-k)!}p^k(1-p)^{n-k}. \qquad (8.1)$$

Under normal conditions, p is large (and furthermore, the assumption of independent release sites is probably inaccurate). However, under conditions of low external Ca^{2+} and high Mg^{2+}, p is small. This is because Ca^{2+} entry into the synapse is required for the release of a quantum of ACh. If only a small amount of Ca^{2+} is able to enter (because the external Ca^{2+} concentration is low), the probability of transmitter release is small. If n is correspondingly large, while $np = m$ remains fixed, the binomial distribution can be approximated by a Poisson distribution. That is,

$$
\begin{aligned}
\lim_{n \to \infty} P(k) &= \lim_{n \to \infty} \left[\frac{n!}{k!(n-k)!} \left(\frac{m}{n} \right)^k \left(1 - \frac{m}{n} \right)^{n-k} \right] \\
&= \frac{m^k}{k!} \lim_{n \to \infty} \left[\frac{n!}{n^k (n-k)!} \left(1 - \frac{m}{n} \right)^{n-k} \right] \\
&= \frac{m^k}{k!} \lim_{n \to \infty} \left(1 - \frac{m}{n} \right)^n \\
&= \frac{e^{-m} m^k}{k!}, \tag{8.2}
\end{aligned}
$$

which is the Poisson distribution with mean, or expected value, m.

There are two ways to estimate m. First, notice that $P(0) = e^{-m}$, so that

$$
e^{-m} = \frac{\text{number of action potentials with no epp's}}{\text{total number of action potentials}}. \tag{8.3}
$$

Second, according to the assumptions of the model, a spontaneous epp results from the release of a single quantum of ACh, and a miniature epp is a linear sum of spontaneous epp's. Thus, m can be calculated by dividing the mean amplitude of a miniature epp response by the mean amplitude of a spontaneous epp, giving the mean number of quanta in a miniature epp, which should be m. As del Castillo and Katz showed, these two estimates of m agree well, which confirms the model hypotheses.

The spontaneous epp's are not of constant amplitude, because the amounts of ACh released from each vesicle are not identical. In the inset to Fig. 8.4 is shown the amplitude distribution of spontaneous epp's. To a good approximation, the amplitudes of single-unit release, denoted by $A_1(x)$, are normally distributed (i.e., a Gaussian distribution), with mean μ and variance σ^2. From this it is possible to calculate the amplitude distribution of the miniature epp's, as follows. If k vesicles are released, the amplitude distribution, denoted by $A_k(x)$, will be normally distributed with mean $k\mu$ and variance $k\sigma^2$, being the sum of k independent, normal distributions each of mean μ and variance σ^2 (Fig. 8.3). Summing the distributions for $k = 1, 2, 3, \ldots$, and noting that the probability of $A_k(x)$ is $P(k)$, gives the amplitude distribution

$$
\begin{aligned}
A(x) &= \sum_{k=1}^{\infty} P(k) A_k(x) \tag{8.4} \\
&= \frac{1}{\sqrt{2\pi\sigma^2}} \sum_{k=1}^{\infty} \frac{e^{-m} m^k}{k! \sqrt{k}} \exp \left[\frac{-(x - k\mu)^2}{2k\sigma^2} \right], \tag{8.5}
\end{aligned}
$$
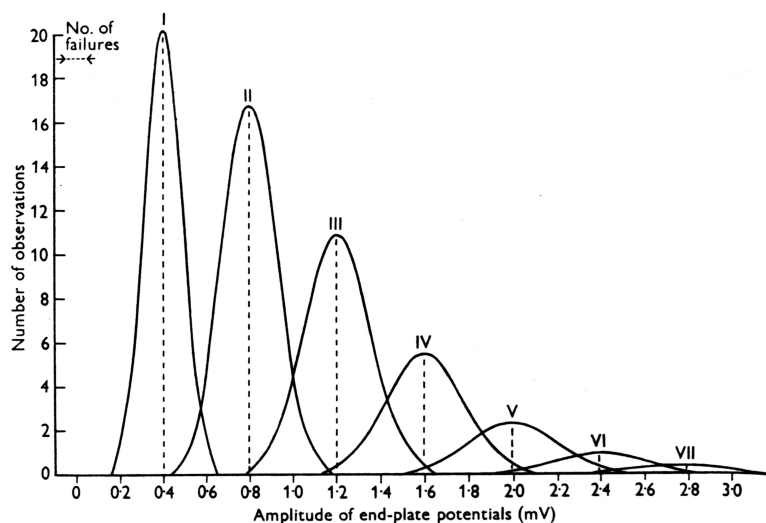
Figure 8.3: Theoretical distributions for epp's consisting of integer multiples of the spontaneous epp, which is the basic building block, or quantum, of the epp. Summation of these curves for all integral numbers of quanta gives the theoretical prediction for the overall amplitude distribution, (8.5), which is plotted in the next figure. (Boyd and Martin, 1956, Fig. 9.)

which is graphed in Fig. 8.4. There are clear peaks corresponding to 1, 2, or 3 released quanta, but these peaks are smeared out and flattened by the normal distribution of amplitudes. There is excellent agreement between the theoretical prediction and the experimental observations, lending further support to the quantal model of synaptic transmission (del Castillo and Katz, 1954; Boyd and Martin, 1956).

8.1.2   Presynaptic Voltage-Gated Calcium Channels

Chemical synaptic transmission begins when an action potential reaches the nerve terminal and opens voltage-gated Ca^{2+} channels, leading to an influx of Ca^{2+} and consequent neurotransmitter release. Based on voltage-clamp data from the squid giant synapse, Llinás et al. (1976) constructed a model of the Ca^{2+} current and its relation to synaptic transmission.

When the presynaptic voltage is stepped up and clamped at a constant level, the presynaptic Ca^{2+} current I_{Ca} increases in a sigmoidal fashion. To model this data, we assume that the voltage-gated Ca^{2+} channel consists of n identical, independent subunits, each of which can be in one of two states, S and O. Only when all subunits are in the state O does the channel admit Ca^{2+} current. Hence

$$S \underset{k_2}{\overset{k_1}{\rightleftharpoons}} O, \qquad (8.6)$$
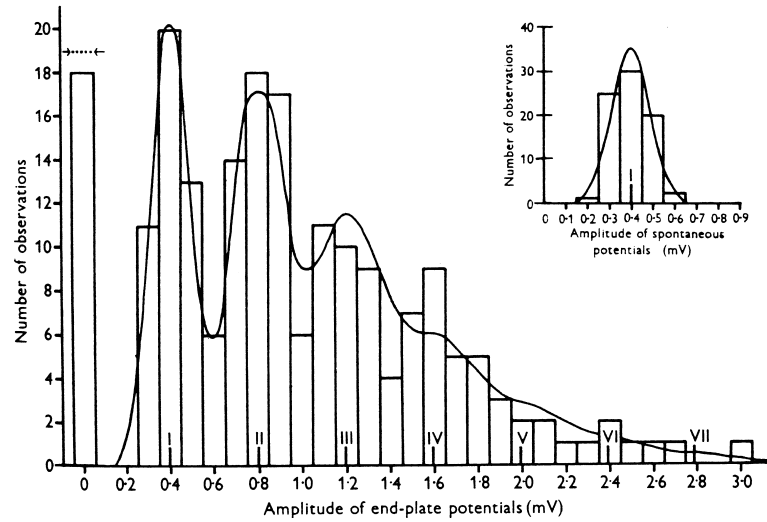
Figure 8.4: Amplitude distribution of miniature epp's. The histogram gives the frequency of the miniature epp as a function of its amplitude, as measured experimentally. The smooth curve is a fit of the theoretical prediction (8.5). The inset shows the amplitude distribution of spontaneous epp's: the smooth curve is a fit of the normal distribution to the data. (Boyd and Martin, 1956, Fig. 8.)
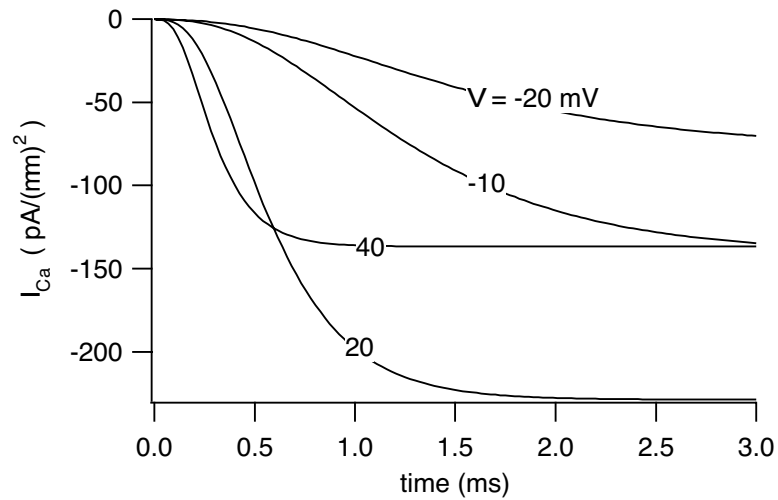
Figure 8.5: Presynaptic Ca^{2+} currents in response to presynaptic voltage steps in a model of squid stellate ganglion.

and the probability that a channel is open is proportional to o^n where o is the probability that a subunit is in the open state. To incorporate the voltage dependence of the channel, the opening and closing rate constants k_1 and k_2 are assumed to be functions of voltage of the form

$$k_1 = k_1^0 \exp\left(\frac{qz_1V}{kT}\right), \qquad k_2 = k_2^0 \exp\left(\frac{qz_2V}{kT}\right), \tag{8.7}$$

where k is Boltzmann's constant, T is the absolute temperature, V is the membrane potential, q is the positive elementary electric charge, z_1 and z_2 are the number of charges that move across the width of the membrane as S $\rightarrow$ O and O $\rightarrow$ S respectively, and k_1^0 and k_2^0 are constants. This is the same type of expression as that for the rate constant seen in Chapter 3 (for example, (3.43) and (3.44)). In Chapter 3, z referred to the number of charges on each ion crossing the membrane by passing through a channel. In this model, z_1 and z_2 denote charges that cross the membrane as a result of a change in the conformation of the channel as it opens or closes. In either case, the result of z charges crossing the membrane is the same, and we have a simple and plausible way to incorporate voltage dependence into the rate constants.

From (8.6) it follows that

$$\frac{do}{dt} = k_1(V)(1 - o) - k_2(V)o. \tag{8.8}$$

We denote the steady state of o by $\hat{o}$,

$$\hat{o}(V) = \frac{k_1(V)}{k_1(V) + k_2(V)}, \tag{8.9}$$

and assume that the membrane potential jumps instantaneously from V_0 to V_1 at time $t = 0$. We also set $o(t = 0) = \hat{o}(V_0)$. Then the solution of the differential equation (8.8) is

$$o(t) = \frac{k_1}{k_1 + k_2}(1 - \exp[-(k_1 + k_2)t]) + \hat{o}(V_1)\exp[-(k_1 + k_2)t], \tag{8.10}$$

where k_1 and k_2 are evaluated at V_0. Now we assume that the single-channel current for an open Ca^{2+} channel, i, is given by the Goldman–Hodgkin–Katz current equation (2.122). Then

$$i = P_{\text{Ca}} \cdot \frac{4F^2}{RT} \cdot V \cdot \frac{c_i - c_e \exp(\frac{-2FV}{RT})}{1 - \exp(\frac{-2FV}{RT})}, \tag{8.11}$$

where c_i and c_e are the internal and external Ca^{2+} concentrations respectively, and P_{Ca} is the permeability of the Ca^{2+} channel. Note that an inward flux of Ca^{2+} gives a negative current. Finally, I_{Ca} is the product of the number of open channels with the single-channel current, and so

$$I_{\text{Ca}} = s_0 i o^n, \tag{8.12}$$

where s_0 is the total number of channels.

By fitting such curves to experimental data, Llinás et al. determined that the best-fit values for the unknowns are $n = 5$, $k_1^0 = 2$ ms^{-1}, $k_2^0 = 1$ ms^{-1}, $z_1 = 1$, and $z_2 = 0$. Hence, the best-fit parameters imply that the Ca^{2+} channel consists of 5 independent subunits, that the conversion of O to S is independent of voltage ($z_2 = 0$), but that the conversion of S to O involves the movement of a single charge across the membrane ($z_1 = 1$) and is thus dependent on the membrane potential.

Typical responses are shown in Fig. 8.5. To plot the curves shown here we used the fixed parameters $c_i = 0.1$ μM, $c_e = 40$ mM, $s_0 = 20$, $P_{Ca} = 10$ μm s^{-1}, $V_0 = -70$ mV. (The internal Ca^{2+} concentration is much smaller than the external concentration, so that the exact number used makes no essential difference to the result. See Exercise 1.) Note that the responses speed up as the voltage step increases, but the plateau level reaches a maximum (in absolute value) and then declines as the size of the voltage step is increased further. This is because of two competing effects that are discussed below.

Because the conversion of a closed subunit to an open subunit involves the movement of a charge across the cell membrane, there must be a current associated with channel opening, i.e., a gating current. This is generally the case when the rate constants for conformational changes of a channel protein are voltage dependent, and these gating currents have been measured experimentally. We do not discuss gating currents any further; the interested reader is referred to Hille (1992) and Armstrong and Bezanilla (1973, 1974, 1977).

Synaptic suppression

At steady state, the percentage of open channels is

$$(o(t = \infty))^5 = \left(\frac{k_1}{k_1 + k_2} \right)^5, \tag{8.13}$$

which is an increasing function of V. However, the single-channel current (8.11) is a decreasing function of V. Thus, the steady state I_{Ca}, being a product of these two functions, is a bell-shaped function of V, as illustrated in Fig. 8.6. There are two time scales in the model; the single channel current depends instantaneously on the voltage, while the number of open channels is controlled by the voltage on a slower time scale. When the voltage is stepped up, the single-channel current decreases instantaneously. However, since there are so few channels open, the instantaneous decrease in the single-channel current has little effect on the total current. On a longer time scale, the channels gradually open in response to the increase in voltage, and this results in the slow monotonic responses to a positive step seen in Fig. 8.5. Of course, if the single-channel current is reduced to zero, no increase in the current is seen as the channels begin to open.

In response to a step *decrease* in voltage, the single-channel Ca^{2+} current increases instantaneously, but in contrast to the previous case where there were few channels open before the stimulus, there are now many open channels. Hence, the instantaneous increase in the single-channel current results in a large and fast increase in the total current. Over a longer time scale, the decrease in the voltage
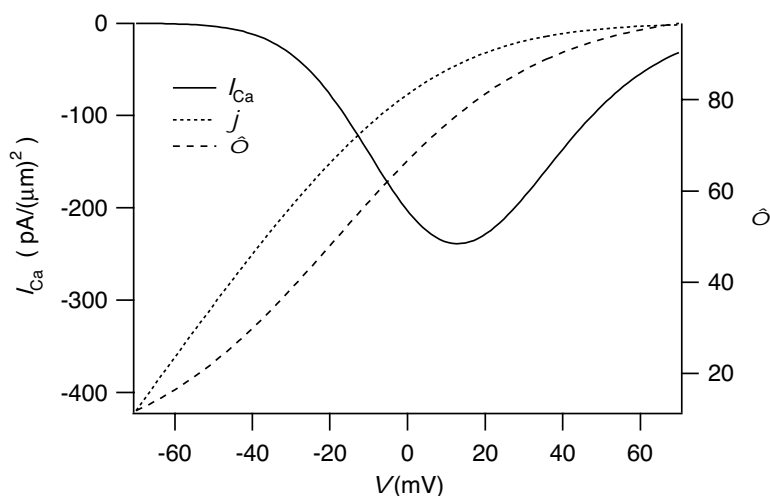
Figure 8.6: Steady-state I_{Ca}, i and $\hat{o}$ as functions of V. Note that the scale for I_{Ca}, and i are shown on the left while the scale for $\hat{o}$ is shown on the right. $\hat{o}$ increases with V while the magnitude of i decreases, their product (the steady state Ca^{2+} current) is a bell-shaped curve. **James, I changed notation so that o and $\hat{o}$ are open probabilities, which I like much better, and it is consistent with what we've done in other chapters (e.g., potassium channels). The axes need to be changed to reflect this (i.e. $0 < \hat{o} < 1$). Also, the label for current in the figure shows j, not i.**

leads to a slow decrease in the number of open channels, and thus a slow decrease in the total current.

These responses are illustrated in Fig. 8.7. When a small positive step is turned on and then off, the Ca^{2+} current I_{Ca} responds with a monotonic increase followed by a monotonic decrease (curve a). When the step is increased to 70 mV, the increase is still monotonic, but the decrease is preceded by a small "bump" as the current initially increases slightly (curve b). For a large step of 150 mV, the initial response is suppressed completely as the single-channel current is essentially zero, but when this suppression is released, a large voltage response is seen, which finally decreases to the resting state (curve c). This phenomenon is called *synaptic suppression*, and the theoretical results agree well with experimental observations.

Response to an action potential

So far we have analytically calculated the response of the model to a voltage step. This was possible because under voltage clamp conditions, the voltage is piecewise constant. However, a more realistic stimulus would be a time-varying voltage corresponding to an action potential at the nerve terminal. It is easiest to find the solution of (8.8) numerically, and this is shown in Fig. 8.8. Given an input $V(t)$ that looks like an action potential, the number of open channels (curve a) and the presy-
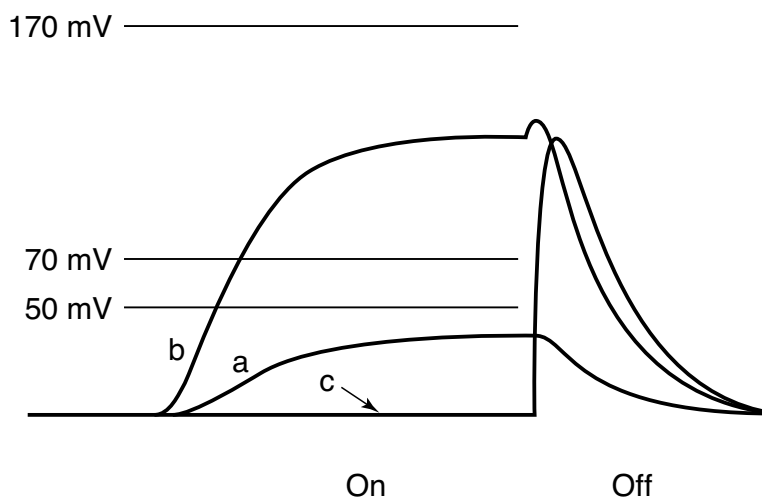
Figure 8.7: Numerical solutions of the Llinás model, demonstrating synaptic suppression of the Ca^{2+} current. These curves are not calculated from the model in the text but are reproduced from Llinás et al., 1976, Fig. 2D, who analyzed the model in a slightly different way. Note that here the Ca^{2+} current is plotted as positive, rather than negative as in Fig. 8.5. See Exercise 2.

naptic Ca^{2+} current (curve b) can be calculated. Figure 8.8 also includes theoretical predictions of the postsynaptic current (curve c) and the postsynaptic membrane potential (curve d). The postsynaptic current is obtained by assuming that it has the same form as the presynaptic current, delayed by 200 ms and amplified appropriately, assumptions that are justified by experimental evidence not discussed here. The postsynaptic membrane potential is obtained by using the postsynaptic current as an input into a model electrical circuit that is described later.

Although the Llinás model provides a detailed description of the initial stages of synaptic transmission and the voltage-gated Ca^{2+} channels, its picture of the postsynaptic response is oversimplified. There are a number of steps between the presynaptic Ca^{2+} current and the postsynaptic current that in this model are assumed to be linearly related. Thus, a decrease in the postsynaptic current is the direct result of a decrease in the presynaptic Ca^{2+} current, leading to a decrease in the concentration of neurotransmitter in the synaptic cleft. However, more detailed models of neurotransmitter kinetics show that at least at the neuromuscular junction, this is not an accurate description.

8.1.3 Presynaptic Calcium Dynamics and Facilitation

One of the fundamental assumptions of the above model (and of the others in this chapter) is that neurotransmitter release is caused by the entry of Ca^{2+} through voltage-sensitive channels into the presynaptic neuron. However, although there is
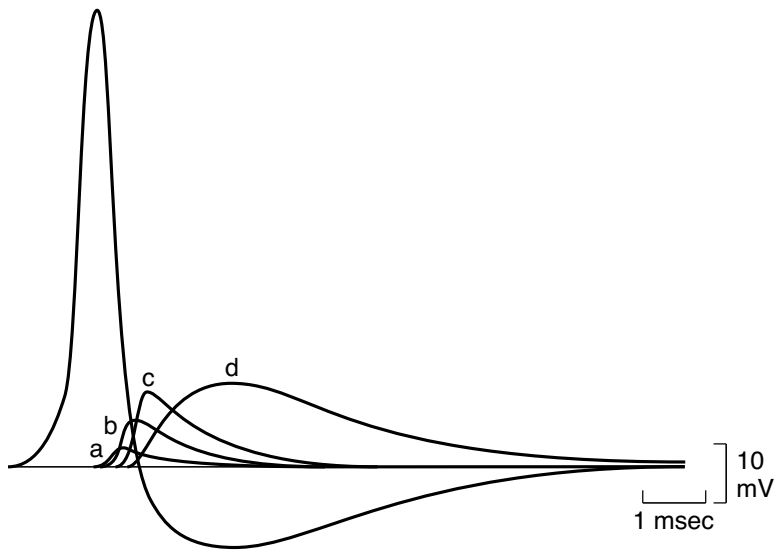
Figure 8.8: Theoretical responses to an action potential. Using the experimentally measured action potential (the leftmost curve in the figure) as input, the model can be used to predict the time courses of (a) the proportion of open channels, (b) the Ca^{2+} current, (c) the postsynaptic current, and (d) the postsynaptic potential. Details of how curve d is calculated are given in the text. Curve c is obtained by assuming that it has the same form as curve b, delayed by 200 ms and amplified. (Llinás et al., 1976, Fig. 2C.)

much evidence in favor of this hypothesis, there is also evidence that cannot be easily reconciled with this model. This has led to considerable controversy; some favor the *calcium hypothesis*, in which transmitter release is the direct result of the influx of Ca^{2+} and the only role of voltage is to cause Ca^{2+} influx (Fogelson and Zucker, 1985; Zucker and Fogelson, 1986; Zucker and Landò, 1986; Yamada and Zucker, 1992). Others favor the *calcium–voltage hypothesis*, in which transmitter release can be triggered directly by the presynaptic membrane potential, with Ca^{2+} playing a regulatory role (Parnas and Segel, 1980; Parnas et al., 1989; Aharon et al., 1994).

The calcium/voltage controversy is particularly interesting because of the role mathematical models have played. In 1985, Fogelson and Zucker proposed a model in which the diffusion of Ca^{2+} from an array of single channels was used to explain the duration of transmitter release and the decay of facilitation. This model was later used as the basis for a large number of other modeling studies, some showing that Ca^{2+} diffusion could not by itself explain all the experimental data, others showing how various refinements of the basic model could result in better agreement with experiment. Experimental and theoretical groups alike used the model as a basis for discussion, and thus, irrespective of the final verdict concerning its accuracy, the Fogelson–Zucker model is an excellent example of the value and use of modeling.

The controversy has shown no signs of abating (Parnas et al., 2002; Felmy et al., 2003), and mathematical models are playing an increasingly important role in the study of the presynaptic terminal. Two Nobel Laureates, Erwin Neher and Bert Sakmann, have both been actively involved in the construction and study of mathematical models of Ca^{2+} entry, binding and diffusion in the presynaptic cell (see, for example, Meinrenken et al., 2003, and Neher, 1998), and current models are now both highly detailed and closely based on experimental data.

Facilitation

One of the major challenges presented by presynaptic Ca^{2+} dynamics is the phenomenon of *facilitation*, which occurs when the amount of neurotransmitter release caused by an action potential is increased by an earlier action potential, provided that the time interval between the action potentials is not too great. There is a lot of evidence that facilitation is primarily a presynaptic mechanism, and thus quantitative explanations have focused on the presynaptic terminal.

One of the earliest hypotheses (Katz and Miledi, 1968) was that facilitation is caused by the buildup of Ca^{2+} in the presynaptic terminal, as the Ca^{2+} introduced by one action potential is not completely removed before the next one comes along, and this hypothesis, in its general form, is still widely accepted.

However, although there is general agreement that buildup of Ca^{2+} is, one way or another, responsible for facilitation, the devil is in the details; there is still no agreement as to where, or in what form, the Ca^{2+} is building up. The *residual free calcium* hypothesis claims that it is an increase in free presynaptic Ca^{2+} that underlies facilitation, and there is considerable evidence in support of this claim (Zucker and Regehr, 2002). For example, Kamiya and Zucker (1994) tested how facilitation responds to a rapid increase of the concentration of Ca^{2+} buffer in the

cytoplasm. This rapid increase was accomplished by the photorelease of a Ca^{2+} buffer, diazo-2. They found that the fast release of diazo-2 into the presynaptic terminal causes a decrease of the synaptic response within milliseconds. Since, on this time scale, the main effect of the added buffers should be to decrease the free Ca^{2+} concentration, it implies that it is the resting free Ca^{2+} concentration that is responsible for facilitation.

Mathematical models of the residual free Ca^{2+} hypothesis (Tang et al., 2000; Matveev et al., 2002; Bennett et al., 2004) have shown that this hypothesis is capable of explaining many experimental results. These models require that the Ca^{2+} facilitation binding site (to the vesicle release machinery) be situated at least 150 nm away from the release binding site, for if this were not so, then every action potential would saturate the facilitation binding site, leading to no increase in neurotransmitter release for subsequent action potentials. In addition, these models require low diffusion coefficients of Ca^{2+} close to the Ca^{2+} channel, and low diffusion coefficients of the exogeneous buffer.

A similar hypothesis is that facilitation is caused by the local saturation of Ca^{2+} buffers close to the mouth of the Ca^{2+} channel, leading to the accumulation of cytoplasmic Ca^{2+} during a train of action potentials, and thus facilitation (Klinghauf and Neher, 1997). Although a mathematical model of this *buffer saturation* hypothesis (Matveev et al., 2004) can explain many experimental results (at least from the crayfish neuromuscular junction) some questions remain. Thus, although there is strong evidence that buffer saturation plays a major role in some experimental preparations (Blatow et al., 2003), in other situations the evidence is inconclusive.

The third hypothesis discussed here was, historically, the first to be proposed. In 1968, Katz and Miledi proposed that facilitation was the result of residual Ca^{2+} bound to the vesicle release site; i.e., if the action potentials followed upon one another too closely there would be not enough time for Ca^{2+} to unbind, making it easier for the subsequent action potential to release neurotransmitter. Although this *residual bound calcium* hypothesis has fallen somewhat out of favor in recent years, due principally to the experiments described briefly above, in which the application of an exogenous buffer was shown to decrease the synaptic response quickly, more recent detailed models have shown that it is, after all, consistent with this experiment (Matveev et al., 2006). Indeed, the residual bound Ca^{2+} hypothesis is superior in some ways, as it does not suffer from the necessity of somewhat artificial requirements, such as the 150 nm separation between the release and the facilitation binding sites, or the small diffusion coefficients around the mouth of the Ca^{2+} channel.

Nevertheless, the question of what causes facilitation is still far from completely resolved. As is often the case, the most likely explanation is a combination of all the above three hypotheses, each acting with different strengths depending on the exact situation.

A model of the residual bound calcium hypothesis

A simple model of the residual bound Ca^{2+} hypothesis does not include any spatial information, but is based entirely on the kinetics of Ca^{2+} binding to the vesicle binding sites. (Bertram et al., 1996). This simplification is justified by experimental

k_1	$=$	3.75×10^{-3} ms$^{-1}\mu$M^{-1}	k_{-1}	$=$	4×10^{-4} ms^{-1}
k_2	$=$	2.5×10^{-3} ms$^{-1}\mu$M^{-1}	k_{-2}	$=$	1×10^{-3} ms^{-1}
k_3	$=$	5×10^{-4} ms$^{-1}\mu$M^{-1}	k_{-3}	$=$	0.1 ms^{-1}
k_4	$=$	7.5×10^{-3} ms$^{-1}\mu$M^{-1}	k_{-4}	$=$	10 ms^{-1}

Table 8.1: Parameter values for the binding model of synaptic facilitation (Bertram et al., 1996).

results showing that the minimum latency between Ca^{2+} influx and the onset of transmitter release can be as short as 200 μs. Since the Ca^{2+} binding site must thus be close to the Ca^{2+} channel, in a simple model we can neglect Ca^{2+} diffusion and assume that Ca^{2+} entering through the channel is immediately available for binding to the vesicle binding site.

It is also assumed that transmitter release is the result of Ca^{2+} entering through a single channel, the so-called Ca^{2+}-domain hypothesis. If the Ca^{2+} channels are far enough apart, or if only few open during each action potential, the Ca^{2+} domains of individual channels are independent.

Our principal goal here is to provide a plausible explanation for the intriguing experimental observation that facilitation increases in a step-like fashion as a function of the frequency of the conditioning action potential train.

We assume that Ca^{2+} entering through the Ca^{2+} channel is immediately available to bind to the transmitter release site, which itself consists of four independent, but not identical, gates, denoted by S$_1$ through S$_4$. Gate S$_j$ can be either closed (with probability C_j) or open (with probability O_j), and thus

$$\text{Ca}^{2+} + \text{C}_j \underset{k_{-j}}{\overset{k_j}{\rightleftharpoons}} \text{O}_j. \tag{8.14}$$

Hence,

$$\frac{dO_j}{dt} = k_j c - \frac{O_j}{\tau_j(c)}, \tag{8.15}$$

where $\tau_j(c) = 1/(k_j c + k_{-j})$, and c is the Ca^{2+} concentration. Finally, the probability R that the release site is activated is

$$R = O_1 O_2 O_3 O_4. \tag{8.16}$$

The rate constants were chosen to give good agreement with experimental data and are shown in Table 8.1. Note that the rates of closure of S$_3$ and S$_4$ are much greater than for S$_1$ and S$_2$, and thus Ca^{2+} remains bound to S$_1$ and S$_2$ for a relatively long time, providing the possibility of facilitation.

To demonstrate how facilitation works in this model, we suppose that a train of square pulses of Ca^{2+} (each of width t_p and amplitude c_p) arrives at the synapse. We want to calculate the level of activation at the end of each pulse and show that this is an increasing function of time. The reason for this increase is clear

from the governing differential equation, (8.15). If a population of gates is initially closed, then a Ca^{2+} pulse begins to open them, but when Ca^{2+} is absent, the gates close. If the interval between pulses is sufficiently short and the decay time constant sufficiently large, then when the next pulse arrives, some gates are already open, so the new pulse activates a larger fraction of transmitter release sites than the first, and so on.

To quantify this observation we define t_n to be the time at the end of the nth pulse,

$$t_n = t_p + (n-1)T, \tag{8.17}$$

where $T = t_p + t_I$ is the period and t_I is the interpulse interval. For any gate (temporarily omitting the subscript j) with $O(0) = 0$, the open probability at the end of the first pulse is

$$O(t_1) = O_\infty(1 - e^{-t_p/\tau_p}), \tag{8.18}$$

where $O_\infty = kc_p\tau_p$ is the steady-state probability corresponding to a steady concentration of Ca^{2+}, c_p, and $\tau_p = \tau(c_p) = 1/(kc_p + k_-)$.

Suppose that $O(t_{n-1})$ is the open probability at the end of the $(n-1)^{st}$ Ca^{2+} pulse. During the interpulse period, O decays with rate constant $\tau(0)$. Thus, at the start of the nth pulse,

$$O(t_{n-1} + t_I) = O(t_{n-1})e^{-t_I/\tau(0)}, \tag{8.19}$$

and so at the end of the nth pulse,

$$\begin{aligned} O(t_n) &= O(t_{n-1})e^{-t_I/\tau(0)}e^{-t_p/\tau_p} + O_\infty(1 - e^{-t_p/\tau_p}) \\ &= \alpha O(t_{n-1}) + O(t_1), \end{aligned} \tag{8.20}$$

where $\alpha = \exp(-(t_I/\tau(0) + t_p/\tau_p)) = \exp(-k_-(T + t_p\frac{c_p}{K}))$ and $K = k_-/k_+$. This is a simple difference equation for $O(t_n)$, which can be solved setting $O(t_n) = A\alpha^n + B$ and substituting into (8.20), from which we find that

$$\frac{O(t_n)}{O(t_1)} = \frac{1 - \alpha^n}{1 - \alpha}. \tag{8.21}$$

Notice that as the interpulse interval gets large ($t_I \to \infty$), $\alpha \to 0$, so that $O(t_n)$ is independent of n. On the other hand, α increases if the Ca^{2+} pulses are shortened (t_p is decreased).

Now we define facilitation as the ratio

$$F_n = \frac{R(t_n)}{R(t_1)}, \tag{8.22}$$

and find that

$$F_n = \left(\frac{1 - \alpha_1^n}{1 - \alpha_1}\right)\left(\frac{1 - \alpha_2^n}{1 - \alpha_2}\right)\left(\frac{1 - \alpha_3^n}{1 - \alpha_3}\right)\left(\frac{1 - \alpha_4^n}{1 - \alpha_4}\right), \tag{8.23}$$

where α_j is the α corresponding to gate j. For the numbers shown in Table 8.1, α_4 is nearly zero in the physiologically relevant range of frequencies, so it can be safely
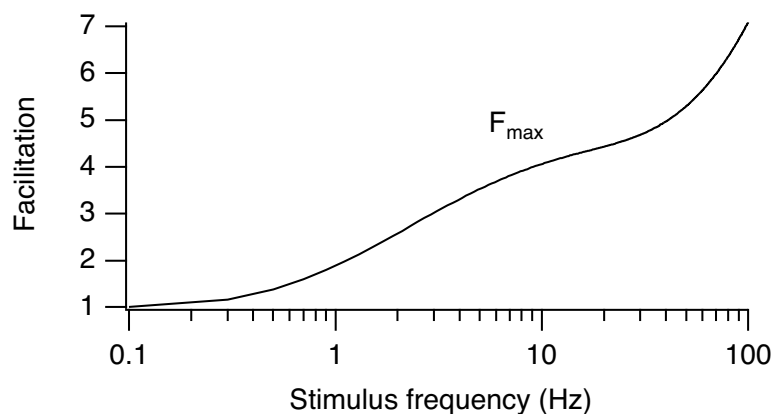
Figure 8.9: Facilitation as a function of stimulus frequency in the binding model for synaptic facilitation, calculated using $t_p c_p = 200\ \mu\text{M ms}$. Here $F_{\max} = \lim_{n \to \infty} F_n$ is the maximal facilitation produced by a pulse train.

ignored. A plot of F_n against the pulse train frequency shows a step-like function, as is observed experimentally. In Fig. 8.9 is shown the maximal facilitation,

$$F_{\max} \;=\; \lim_{n \to \infty} F_n \tag{8.24}$$

$$\;=\; \left(\frac{1}{1 - \alpha_1}\right)\left(\frac{1}{1 - \alpha_2}\right)\left(\frac{1}{1 - \alpha_3}\right), \tag{8.25}$$

which also has a step-like appearance.

A more complex version

A more complex model of the residual bound Ca^{2+} hypothesis takes into account diffusion of Ca^{2+} from the channel to the binding site and the presence of Ca^{2+} buffers (Matveev et al., 2006).

We assume that each of n Ca^{2+} channels are located at discrete positions r_j, $j = 1, \dots, n$, and that there are two Ca^{2+} buffers, one with slower kinetics. Thus, following the discussion of buffers and discrete Ca^{2+} release in Chapter 7, we get

$$\frac{\partial c}{\partial t} \;=\; D_c \nabla^2 c + \sum_{i=1}^{2} k_{-,i} b_i - k_{+,i} c(b_{t,i} - b_i) + \frac{1}{2F} I_{\text{Ca}} \sum_{j=1}^{n} \delta(r - r_j), \tag{8.26}$$

$$\frac{\partial b_i}{\partial t} \;=\; D_b \nabla^2 b_i + \sum_{i=1}^{2} k_{-,i} b_i - k_{+,i} c(b_{t,i} - b_i). \tag{8.27}$$

These equations are solved numerically on the domain illustrated in Fig. 8.10. Calcium channels are clustered into active zones, with 16 channels per zone, and the symmetry of the domain around each active zone is used to reduce the problem
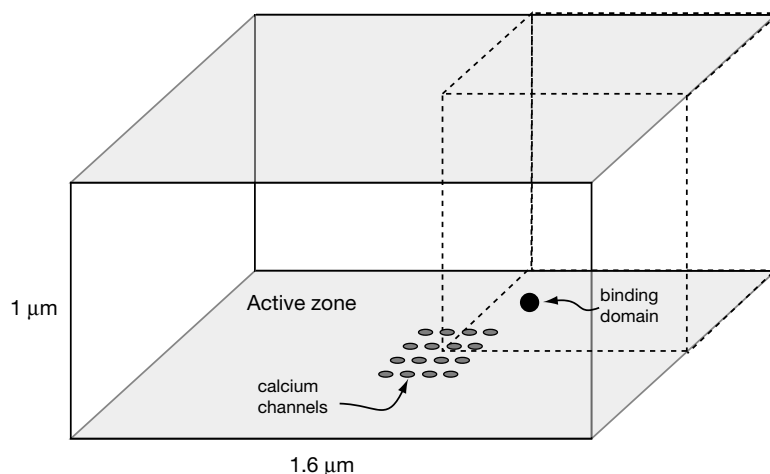
Figure 8.10: Schematic diagram of a presynaptic active zone, the Ca^{2+} channels, and the Ca^{2+} binding site (adapted from Matveev et al., 2006, Fig. 1). The binding domain is situated 130 nm away from the center of the active zone, and about 55 nm from the nearest Ca^{2+} channel.

to one on the quarter box bordered by the dashed lines. In each quarter box there is a single Ca^{2+} binding domain, denoted by the filled circle, which contains multiple Ca^{2+} binding sites, all co-localized. Calcium is pumped out only on the top and bottom surfaces (shaded), while the other surfaces have no-flux boundary conditions, which assumes a regular array of active sites. Calcium pumping is assumed to be by a simple saturating mechanism, with Hill coefficient 1, and is balanced by a constant leak into the cell. Thus, on the shaded boundaries,

$$\frac{\partial c}{\partial n} = J_{\text{leak}} - \frac{V_p c}{K_p + c}, \tag{8.28}$$

where n denotes the normal to the boundary.

The binding domain is assumed to contain two different types of binding sites, one faster (type X), one slower (type Y). The X binding site can bind two Ca^{2+} ions, and thus

$$X \underset{k_{-x}}{\overset{2ck_x}{\rightleftarrows}} CaX \underset{2k_{-x}}{\overset{ck_x}{\rightleftarrows}} Ca_2X, \tag{8.29}$$

while binding sites Y_1 and Y_2 can bind one Ca^{2+} ion each, and thus

$$Y_1 \quad \underset{k_{-1}}{\overset{ck_1}{\rightleftarrows}} \quad CaY_1, \tag{8.30}$$

$$Y_2 \quad \underset{k_{-2}}{\overset{ck_2}{\rightleftarrows}} \quad CaY_2. \tag{8.31}$$
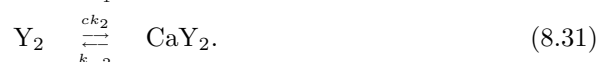
If R denotes the rate of release neurotransmitter, then the rate of increase of R is
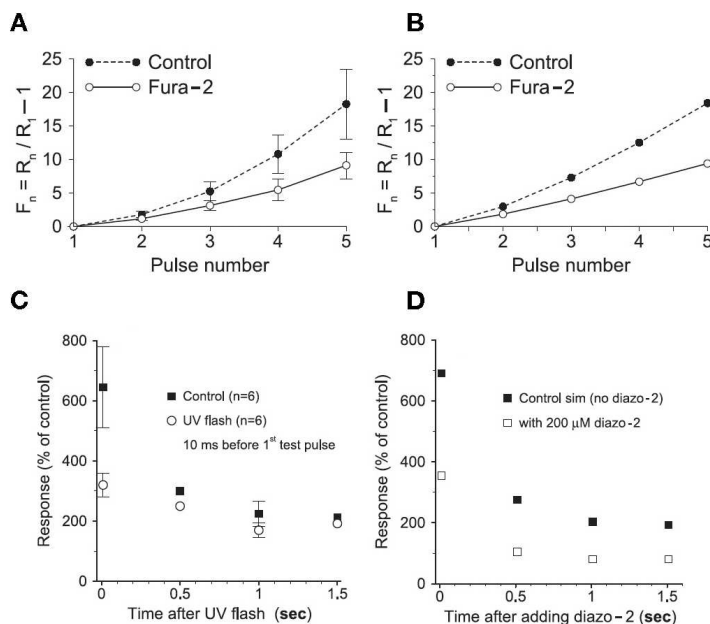
Figure 8.11: Comparison of the residual bound Ca^{2+} model to experimental data. A and B: Facilitation as a function of pulse number, in the presence and absence of exogeneous buffer. Panel A shows the experimental results of Tang et al. (2000), while panel B shows model simulations. In both the experimental data and the model, facilitation increases with pulse number, and has an increasing slope. Addition of exogeneous buffer decreases facilitation. C and D; time dependence of facilitation after the fast release of exogeneous buffer by a UV flash. Panel C is the experimental data of Kamiya and Zucker (1994), while panel D are model simulations. Adapted from Matveev et al., (2006), Figs. 3 and 4. **Springer, we will need permission for this figure.**

assumed to be proportional to $[Ca_2X][CaY_1][CaY_2]$:

$$\frac{dR}{dt} = k_R[Ca_2X][CaY_1][CaY_2] - k_I R. \tag{8.32}$$

Typical model simulations are shown in Fig. 8.11. Significantly, these results show that, in the model, the release of an exogeneous buffer by a UV flash does indeed decrease the synaptic response within milliseconds (Fig. 8.11, panels C and D). Thus, the experimental results of Kamiya and Zucker (1994), which have often been taken as evidence that the residual bound Ca^{2+} hypothesis is incorrect, show no such thing. Although we cannot conclude that the residual bound Ca^{2+} hypothesis is correct, it also cannot be rejected on the basis of such experiments.

8.1.4 Neurotransmitter Kinetics

When the end-plate voltage is clamped and the nerve stimulated (so that the end-plate receives a stimulus of ACh, of undetermined form), the end-plate current first rises to a peak and then decays exponentially, with a decay time constant that is an exponential function of the voltage. Magleby and Stevens (1972) constructed a detailed model of end-plate currents in the frog neuromuscular junction that gives a mechanistic explanation of this observation and shows how a simple model of the receptor kinetics can quantitatively reproduce the observed end-plate currents.

First, Magleby and Stevens showed that the instantaneous end-plate current–voltage relationship is linear, and thus, for a fixed voltage, the end-plate current is proportional to the end-plate conductance. Because of this, it is sufficient to study the end-plate conductance rather than the end-plate current. Since the end-plate conductance is a function of the concentration of ACh, we restrict our attention to the kinetics of ACh in the synaptic cleft.

We assume that ACh reacts with its receptor, R, in enzymatic fashion,

$$\text{ACh} + \text{R} \underset{k_2}{\overset{k_1}{\rightleftharpoons}} \text{ACh} \cdot \text{R} \underset{\alpha}{\overset{\beta}{\rightleftharpoons}} \text{ACh} \cdot \text{R}^*, \tag{8.33}$$
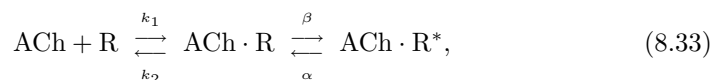
and that the ACh-receptor complex passes current only when it is in the open state $\text{ACh} \cdot \text{R}^*$. We let $c = [\text{ACh}]$, $y = [\text{ACh} \cdot \text{R}]$, and $x = [\text{ACh} \cdot \text{R}^*]$, and then it follows from the law of mass action that

$$\frac{dx}{dt} = -\alpha x + \beta y, \tag{8.34}$$

$$\frac{dy}{dt} = \alpha x + k_1 c (N - x - y) - (\beta + k_2) y, \tag{8.35}$$

$$\frac{dc}{dt} = f(t) - k_e c - k_1 c (N - x - y) + k_2 y, \tag{8.36}$$

where N is the total concentration of ACh receptor, which is assumed to be conserved, and ACh decays by a simple first-order process at rate k_e. The postsynaptic conductance is assumed to be proportional to x, and the rate of formation of ACh is some given function $f(t)$. One option for $f(t)$ is to use the output of the single-domain/bound-calcium model described in the previous section (Exercise 8).

The model equations, as given, are too complicated to solve analytically, and so we proceed by making some simplifying assumptions. First, we assume that the kinetics of ACh binding to its receptor are much faster than the other reactions in the scheme, so that y is in instantaneous equilibrium with c. To formalize this assumption, we introduce dimensionless variables $X = x/N, Y = y/N, C = k_1 c/k_2$, and $\tau = \alpha t$, in terms of which (8.35) becomes

$$\epsilon \frac{dY}{d\tau} = \epsilon X + C(1 - X - Y) - \left(\epsilon \frac{\beta}{\alpha} + 1\right) Y, \tag{8.37}$$

where $\epsilon = \alpha/k_2 \ll 1$. Upon setting ϵ to zero, we find the quasi-steady approximation

$$Y = \frac{C(1 - X)}{1 + C}, \tag{8.38}$$

or in dimensioned variables,

$$y = \frac{c(N - x)}{K + c},$$
(8.39)

where $K = k_2/k_1$. Now we can eliminate y from (8.34) to obtain

$$\frac{dx}{dt} = -\alpha x + \beta \frac{c(N - x)}{K + c}.$$
(8.40)

Next we observe that

$$\frac{dx}{dt} + \frac{dy}{dt} + \frac{dc}{dt} = f(t) - k_e c.$$
(8.41)

In dimensionless variables this becomes

$$\frac{N}{K}\left(\frac{dX}{d\tau} + \frac{dY}{d\tau}\right) + \frac{dC}{d\tau} = F(\tau) - K_e C,$$
(8.42)

where $F(\tau) = \frac{f(t)}{\alpha K}$ and $K_e = k_e/\alpha$ are assumed to be of order one. If we suppose that $N \ll K$, then setting N/K to zero in (8.42), we find (in dimensioned variables)

$$\frac{dc}{dt} = f(t) - k_e c.$$
(8.43)

One further simplification is possible if we assume that $\beta \ll \alpha$. Notice from (8.40) that

$$\frac{dx}{dt} < -\alpha x + \beta(N - x),$$
(8.44)

so that

$$x(t) \le x(0)e^{-(\alpha+\beta)t} + \frac{\beta N}{\alpha + \beta}(1 - e^{-(\alpha+\beta)t}).$$
(8.45)

Once this process has been running for some time, so that effects of initial data can be ignored, x is of order $\frac{\beta N}{\alpha+\beta}$. If $\beta \ll \alpha$, then $x \ll N$, and (8.40) simplifies to

$$\frac{dx}{dt} = -\alpha x + \beta \frac{cN}{K + c}.$$
(8.46)

For any given input $f(t)$, (8.43) can be solved for $c(t)$, and then (8.46) can be solved to give $x(t)$, the postsynaptic conductance.

As mentioned above, the decay of the postsynaptic current has a time constant that depends on the voltage. This could happen in two principal ways. First, if the conformational changes of the receptor were much faster than the decay of ACh in the synaptic cleft, x would be in quasi-equilibrium, and we would have

$$x = \frac{\beta c(t)N}{\alpha[K + c(t)]}.$$
(8.47)

Thus, if c is small, x would be approximately proportional to c. In this case an exponential decrease of c caused by the decay term $-k_e c$ would cause an exponential decrease in the postsynaptic conductance. An alternative possibility is that ACh

degrades quickly in the synaptic cleft, so that c quickly approaches zero, but that the decay of the end-plate current is due to conformational changes of the ACh receptor. According to this hypothesis, the release of ACh into the cleft would cause an increase in x, which then would decay according to

$$\frac{dx}{dt} = -\alpha x \tag{8.48}$$

(since c is nearly zero). In this case, the exponential decrease of end-plate current would be governed by the term $-\alpha x$.

Magleby and Stevens argued that the latter hypothesis is preferable. Assuming therefore that the rate-limiting step in the decay of the end-plate current is the decay of x, α can be estimated directly from experimental measurements of end-plate current decay to be

$$\alpha(V) = Be^{AV}, \tag{8.49}$$

where $A = 0.008$ mV^{-1} and $B = 1.43$ ms^{-1}.

To calculate the complete time course of the end-plate current from (8.46), it remains to determine $c(t)$. In general this is not known, as it is not possible to measure synaptic cleft concentrations of ACh accurately.

A method to determine $c(t)$ from the experimental data was proposed by Magleby and Stevens. First, suppose that β is also a function of V, as is expected, since α is a function of V. Then (8.46) can be written as

$$\frac{dx}{dt} = -\alpha(V)x + \beta(V)W(t), \tag{8.50}$$

where $W(t) = Nc(t)/[K+c(t)]$. Since for any fixed voltage the time course of x can be measured experimentally (recall that the experiments were done under voltage clamp conditions), it follows that $\beta(V)W(t)$ can be determined from

$$\beta(V)W(t) = \frac{dx}{dt} + \alpha(V)x. \tag{8.51}$$

Although this requires numerical differentiation (which is notoriously unstable), the experimental records are smooth enough to permit a reasonable determination of W from the time course of x. Since W is assumed to be independent of V, it can be determined (up to an arbitrary scale factor) from a time course of x obtained for any fixed voltage. Further, if the model is valid, then we expect the same result no matter what voltage is used to obtain W. A typical result for W, shown in Fig. 8.12, rises and falls in a way reminiscent of the responses calculated from the Llinás model described above (Fig. 8.8).

The final unknown is $\beta(V)$, the scale factor in the determination of W. Relative values of β can be obtained by comparing time courses taken at different voltages. If $\beta(V_1)W(t)$ and $\beta(V_2)W(t)$ are time courses obtained from (8.51) at two different voltages, the ratio $\beta(V_1)/\beta(V_2)$ is obtained from the ratio of the time courses. However, because of experimental variability or invalid model assumptions, this ratio may not be constant as a function of time, in which case the ratio cannot be determined unambiguously. Magleby and Stevens used the ratio of the maximum
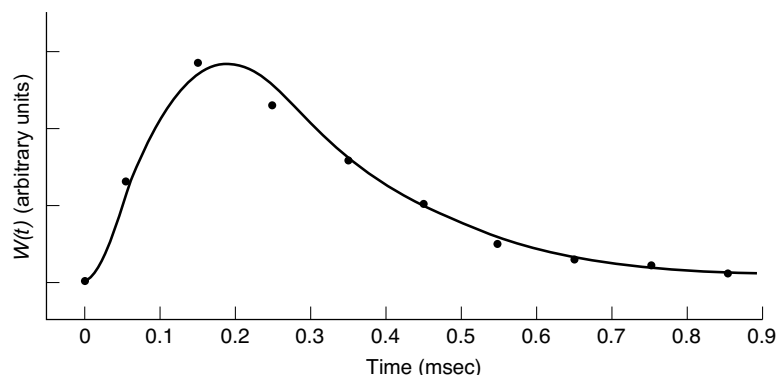
Figure 8.12: $W(t)$ calculated from the time course of x using (8.51). (Magleby and Stevens, 1972, Fig. 4.)

amplitudes of the time courses, in which case $\beta(V_1)/\beta(V_2)$ can be obtained uniquely. They determined that β, like α, is an exponential function of V,

$$\beta(V) = be^{aV}, \tag{8.52}$$

where $a = 0.00315 \text{ mV}^{-1}$ and b is an arbitrary scaling factor.

Equation (8.50) can now be solved numerically to determine the time course of the end-plate current for various voltages. Typical results are shown in Fig. 8.13. Although the model construction guarantees the correct peak response (because that is how β was determined) and also guarantees the correct time course at one particular voltage (because that is how W was determined), the model responses agree well with the experimental records over all times and voltages. This confirms the underlying assumption that W is independent of voltage.

Although the approach of Magleby and Stevens of determining $W(t)$ directly from the data leads to excellent agreement with the experimental data, it suffers from the disadvantage that no mechanistic rationale is given for the function W. It would be preferable to have a derivation of the behavior of W from fundamental assumptions about the kinetics of ACh release and degradation in the synaptic cleft, but such is not presently available.

Neurotransmitter Diffusion

A different style of model is that of Smart and McCammon (1998) or Tai et al. (2003). These groups constructed highly detailed finite element models of the neuromuscular junction, with the model of Tai et al. based directly on anatomical structural information (Stiles and Bartol, 2000). In this region they solved a simple diffusion equation for ACh, with degradation of ACh on selected parts of the boundary. These detailed structural models are still somewhat preliminary, as most of the efforts to date have been in the development of the necessary computational techniques; the models have provided, as yet, little additional physiological insight.
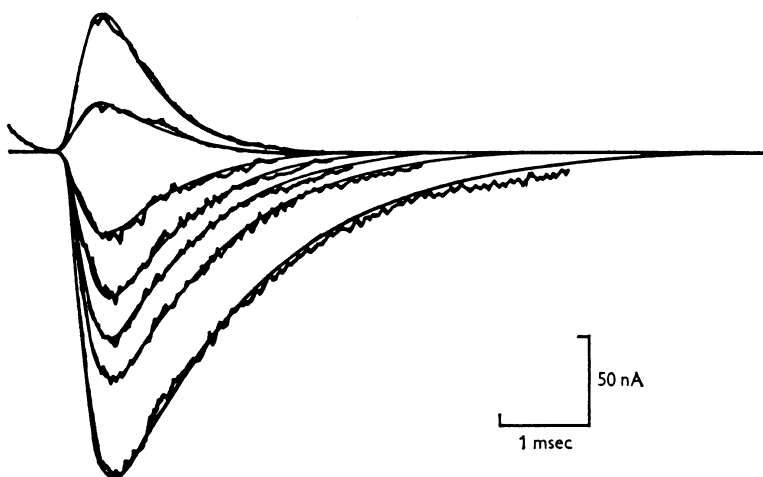
Figure 8.13: End-plate currents from the Magleby–Stevens model. Equation (8.50) was solved numerically, using as input the function plotted in Fig. 8.12. The functions $\alpha(V)$ and $\beta(V)$ are given in the text. The corresponding values for V are, from top to bottom, 32, 20, -30, -56, -82, -106 and -161 mV. The wavy lines are the experimental data; the smooth curves are the model fit. (Magleby and Stevens, 1972, Fig. 6.)

However, they are ideally placed to provide insight into the comparative behavior of different neuromuscular junctions, and are likely to be a highly important style of model in the future.

8.1.5   The Postsynaptic Membrane Potential

Acetylcholine acts by opening ionic channels in the postsynaptic membrane that are permeable to Na^+ and K^+ ions. A schematic diagram of the electrical circuit model of the postsynaptic membrane is given in Fig. 8.14. This model is based on the usual assumptions (see, for example, Chapter 2) that the membrane channels can be modeled as ohmic resistors and that the membrane acts like a capacitor, with capacitance C_m.

The ACh-sensitive channels have a reversal potential V_s of about -15 mV and a conductance that depends on the concentration of ACh. The effects of all the other ionic channels in the membrane are summarized by a resting conductance, g_r and a resting potential V_r of about -70 mV. In the usual way, the equation for the membrane potential V is

$$C_m \frac{dV}{dt} + g_r(V - V_r) + g_s(V - V_s) = 0. \tag{8.53}$$

In general, g_s is a function of the number of ACh receptors with ACh bound, i.e., in the notation of the previous section, $g_s = g_s(x)$. Since x is a function of
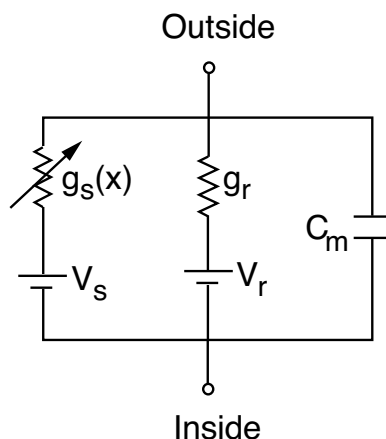
Figure 8.14: Electrical circuit model of the postsynaptic membrane.

time, g_s is also a function of time. Hence,

$$C_m \frac{dV}{dt} + [g_r + g_s(t)]V = g_r V_r + g_s(t)V_s. \tag{8.54}$$

This equation can be reduced to quadratures by using the integrating factor $I = \exp(\frac{1}{C_m} \int (g_r + g_s)dt)$, so in principle, the response of the postsynaptic membrane can be calculated from knowledge of the time course of x. However, since $g_s(t)$ is time dependent, the quadratures can essentially never be evaluated explicitly, so exact formulas are effectively useless.

Suppose, however, that $g_s(t)$ is small compared to g_r. We set $V_1 = V - V_r$ so that

$$\frac{C_m}{g_r}\frac{dV_1}{dt} + V_1 = -\frac{g_s}{g_r}(V_1 + V_r - V_s). \tag{8.55}$$

Now we expect V_1 to be on the order of $\frac{g_s}{g_r}$, so that the term $\frac{g_s}{g_r}V_1$ can be ignored, and we are left with the equation

$$\frac{C_m}{g_r}\frac{dV_1}{dt} + V_1 = -\frac{g_s}{g_r}(V_r - V_s), \tag{8.56}$$

which can be solved exactly.

For example, a simple solution is obtained when g_s is taken to be proportional to x and the input $f(t)$ to the Magleby and Stevens model is assumed to be $\gamma\delta(t)$ for $\frac{\gamma}{K}$ small. In this case,

$$g_s(t) = x(t) = \frac{\gamma\beta N}{K(\alpha - k_e)}\left(e^{-k_e t} - e^{-\alpha t}\right), \tag{8.57}$$

as derived in Exercise 5. The solution of (8.56) is now readily found using standard solution techniques (Exercise 7).
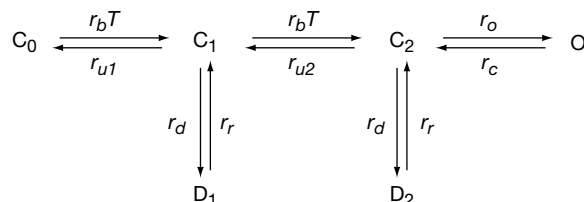
Figure 8.15: Markov model of the AMPA receptor (Patneau and Mayer, 1991). T is the concentration of transmitter.

8.1.6 Agonist-controlled ion channels

The acetylcholine receptor/channel is an example of an agonist-controlled channel, a simple model for which was discussed in Chapter 3, Section 3.5.4. In Section 8.1.5 above, we described an even simpler model of the ACh receptor/channel. There are many other more complex models of the postsynaptic agonist-controlled ion channels. A useful review is that of Destexhe et al. (1998) which briefly discusses a number of the major models of AMPA, NMDA, and GABA receptors.

A typical example is the Markov model of the AMPA receptor (Patneau and Mayer, 1991) shown in Fig. 8.15. This model has three closed states, two desensitized states, and one open state. The receptor can open only from the closed state with two transmitter molecules bound, C_2. The response of this model to a delta function input (i.e., if $T(t) = \delta(t)$) is shown in Fig. 8.16.

This multi-state Markov model of the AMPA receptor can be simplified to a two-state model, without changing the qualitative properties of the impulse response. The two-state model

$$C + T \underset{\beta}{\overset{\alpha}{\rightleftharpoons}} O \tag{8.58}$$
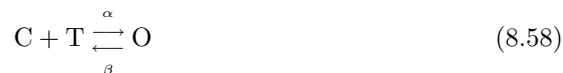
responds to an impulse in much the same as the full model, as can be seen from the dotted line in Fig. 8.16.

8.1.7 Drugs and Toxins

The foregoing models are sufficient to piece together a crude model of synaptic transmission. However, many features were ignored, and there are many situations that can change the behavior of this system. Primary among these are drugs and toxins that affect specific events in the neurotransmission process. For example, the influx of Ca^{2+} is reduced by divalent metal ions, such as Pb^{2+}, Cd^{2+}, Hg^{2+}, and Co^{2+}. By reducing the influx of Ca^{2+}, these cations depress or abolish the action-potential-evoked transmitter release. Certain toxins, including tetanus and clostridial botulinus, are potent inhibitors of transmitter exocytosis, an action that is essentially irreversible. Botulinus neurotoxin is selective for cholinergic synapses and is one of the most potent neuroparalytic agents known. Tetanus toxin is taken up by spinal motor nerve terminals and transported retrogradely to the spinal cord, where it blocks release of glycine at inhibitory synapses. Spread of the toxin throughout the
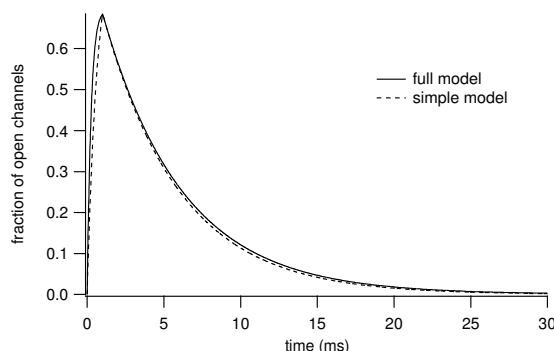
Figure 8.16: Response of the AMPA receptor model to a delta function input. The solid line is from the model shown in Fig. 8.15, with parameter values $r_b = 13 \times 10^6$ M^{-1}s^{-1}, $r_{u1} = 5.9$ s^{-1}, $r_{u2} = 8.6 \times 10^4$ s^{-1}, $r_d = 900$ s^{-1}, $r_r = 64$ s^{-1}, $r_o = 2.7 \times 10^3$ s^{-1}, $r_c = 200$ s^{-1}. The dotted line is from the simplified version of the model, (8.58), with parameters $\alpha = 1.35$ M^{-1}s^{-1}, $\beta = 200$ s^{-1}.

brain and spinal cord can lead to severe convulsions and death. The venom from black widow spider contains a toxin (α-latrotoxin) that causes massive transmitter exocytosis and depletion of synaptic vesicles from presynaptic nerve terminals.

Agents that compete with the transmitter for receptor binding sites, thereby preventing receptor activation, are called receptor antagonists. An example of an antagonist of the ACh receptors of the skeletal neuromuscular junction is curare. By inhibiting ACh binding at receptor sites, curare causes progressive decrease in amplitude and shortening of epp's. In severe curare poisoning, transmission is blocked. Selective antagonists exist for most transmitter receptors. For example, bicuculline is an antagonist of GABA receptors, and is a well-known convulsant.

Agents that mimic the action of natural transmitters are known as receptor agonists. A well-known agonist of ACh receptors in neuromuscular junction is nicotine. Nicotine binds to the ACh receptor and activates it in the same manner as ACh. However, nicotine causes persistent receptor activation because it is not degraded, as is ACh, by ACh-esterase. On the other hand, diisopropylphosphofluoridate (commonly known as nerve gas) is an example of an anticholinesterase, because it inhibits the activity of ACh-esterase, so that ACh persists in the synaptic cleft. Similarly, one effect of cocaine is to prolong the activity of dopamine, by blocking the uptake of dopamine from the synaptic cleft.

Other agents interfere with receptor-gated permeabilities by interfering with the channel itself. Thus, picrotoxin, which blocks GABA-activated Cl$^-$ channels, and strychnine, which blocks glycine-activated Cl$^-$ channels, are potent blockers of inhibitory synapses and known convulsants.
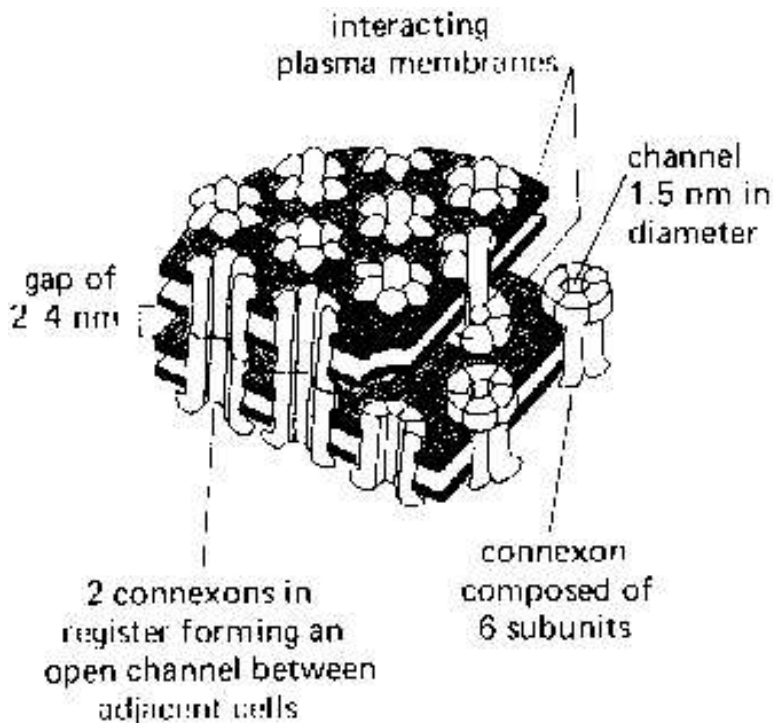
Figure 8.17: Diagram of a region of membrane containing gap junctions, based on electron microscope images and X-ray diffraction data. Each connexon is composed of six gap-junction proteins, called connexins, arranged hexagonally. Connexons in apposed membranes meet in the intercellular space to form the gap junction. (Alberts et al., 1994, Fig. 19-15.)

8.2   Gap Junctions

Gap junctions are small nonselective channels (with diameters of about 1.2 nm) that form direct intercellular connections through which ions or other small molecules can flow. They are formed by the joining of two *connexons*, hexagonal arrays of *connexin* protein molecules (Fig. 8.17). Despite being called electrical synapses, in this chapter we concentrate on models in which membrane potential plays no role, focusing instead on the interaction between intracellular diffusion and intercellular permeability. Electrical aspects of gap junctions are important for the function of cardiac cells and are discussed in that context in Chapter 12. An example of how gap junctions are used for intercellular signaling via second messengers is described in Chapter 7, where we discuss a model of intercellular Ca^{2+} wave propagation.

8.2.1 Effective Diffusion Coefficients

We first consider a one-dimensional situation where a species u diffuses along a line of cells which are connected by gap junctions. Because of their relatively high resistance to flow (compared to cytoplasm), the gap junctions decrease the rate at which u diffuses along the line. Since this is a one-dimensional problem, we assume that each intercellular membrane acts like a single resistive pore with a given permeability F. The effect of gap-junction distribution within the intercellular membrane is discussed later in this chapter.

We assume that Fick's law holds and thus the flux, J, of u is proportional to the gradient of u; i.e.,

$$J = -D\frac{\partial u}{\partial x},\tag{8.59}$$

where D is the diffusion coefficient for the intracellular space. From the conservation of u it follows that in the interior of each cell,

$$\frac{\partial u}{\partial t} = D\frac{\partial^2 u}{\partial x^2}.\tag{8.60}$$

However, u need not be continuous across the intercellular boundary. In fact, if there is a cell boundary at $x = x_b$, the flux through the boundary is assumed to be proportional to the concentration difference across the boundary. Then, conservation of u across the boundary implies that

$$-D\frac{\partial u(x_b^-, t)}{\partial x} = -D\frac{\partial u(x_b^+, t)}{\partial x} = F[u(x_b^-, t) - u(x_b^+, t)],\tag{8.61}$$

for some constant F, called the *permeability coefficient*, with units of distance/time. The $+$ and $-$ superscripts indicate that the function values are calculated as limits from the right and left, respectively.

When the cells through which u diffuses are short compared to the total distance that u moves, the movement of u can be described by an effective diffusion coefficient. The effective diffusion coefficient is defined and is measurable experimentally by assuming that the analogue of Ohm's law holds. Thus, in a preparation of N cells, each of length L, with $u = U_0$ at $x = 0$ and $u = U_1$ at $x = NL$, the effective diffusion coefficient D_e is defined by

$$J = \frac{D_e}{NL}(U_0 - U_1),\tag{8.62}$$

where J is the steady-state flux of u.

To calculate D_e, we look for a function $u(x)$ that satisfies $u_{xx} = 0$ when $x \neq (j + \frac{1}{2})L$ and satisfies (8.61) at $x = (j + \frac{1}{2})L, j = 0, \ldots, N - 1$. Further, we require that $u(0) = U_0$, and $u(NL) = U_1$. Note that we are assuming that the cell boundaries occur at $L/2, 3L/2, \ldots$, and thus the boundary conditions at $x = 0$ and $x = NL$ occur halfway through a cell.

A typical solution u that satisfies these conditions must be linear within each cell, and piecewise continuous with jumps at the cell boundaries. Suppose that the slope of u within each cell is $-\lambda$, and that the jump in u between cells is

$u(x_b^+) - u(x_b^-) = -\Delta$. Then, since there are $N - 1$ whole cells, two half cells (at the boundaries), and N interior cell boundaries, we have

$$(N - 1)\lambda L + 2\lambda \left(\frac{L}{2}\right) + N\Delta = U_0 - U_1. \tag{8.63}$$

Furthermore, it follows from (8.61) that

$$D\lambda = F\Delta. \tag{8.64}$$

We find from (8.62) and (8.63) that

$$
\begin{aligned}
D\lambda &= -D\frac{\partial u}{\partial x} = J = \frac{D_e}{NL}(U_0 - U_1) & (8.65)\\
&= \frac{D_e}{L}(L\lambda + \Delta) & (8.66)\\
&= \lambda D_e \left(1 + \frac{D}{FL}\right), & (8.67)
\end{aligned}
$$

from which it follows that

$$\frac{1}{D_e} = \frac{1}{D} + \frac{1}{LF}. \tag{8.68}$$

8.2.2 Homogenization

The above calculation of the effective diffusion coefficient can be formalized by the process of *homogenization*. Homogenization is an important technique that was described in the Appendix to Chapter 7 and which is seen again in Chapter 12. Homogenization is useful when there are two spatial scales, a microscopic and a macroscopic scale in determining the behavior of the solution on the macroscopic scale while accounting for influences from the microscopic scale, without calculating the full details of the solution on the microscopic scale.

The basic assumption here is that Fick's law holds, but that the diffusion coefficient D is a periodic, rapidly varying function, so that the flux is

$$J = -D(\frac{x}{\epsilon})\frac{\partial u}{\partial x}. \tag{8.69}$$

The dimensionless parameter ϵ is small, indicating that the variations of D are rapid compared to other spatial scales of the problem, in particular, the diffusion length. Thus, cells are assumed to be short compared to the diffusion length scale.

In Section 7.8.2 we calculated that the effective diffusion coefficient is the inverse of the average resistance

$$D_e = \frac{1}{\bar{R}}. \tag{8.70}$$

where

$$\bar{R} = \int_0^1 R(s)\, ds = \int_0^1 \frac{1}{D(s)}\, ds \tag{8.71}$$

is the average resistance.

To apply this result to the specific problem of gap junctions, we take $R(x) = r_c + r_g \sum_k \delta(x - kL)$ to reflect the periodic occurrence of gap junctions with resistance r_g evenly spaced at the ends of cells of length L. Notice that $D = 1/r_c$ is the diffusion coefficient for the intracellular space, while $F = 1/r_g$ is the intercellular permeability. It follows easily that

$$\bar{R} = r_c + \frac{r_g}{L}, \qquad (8.72)$$

which is the same as (8.68).

8.2.3 Measurement of Permeabilities

Although an effective diffusion coefficient is useful when the species of interest diffuses through a large number of cells, in some experimental situations one is interested in how a dye molecule (or a second messenger such as IP_3) diffuses through a relatively small number of cells. In this case the effective diffusion coefficient approximation cannot always be used, and it is necessary to solve the equations with internal boundary conditions (Brink and Ramanan, 1985; Ramanan and Brink, 1990). By calculating exact solutions to the linear diffusion equation with internal boundary conditions (using transform methods, for example) and fitting them to experimental measurements on the movement of fluorescent probes, it is possible to obtain estimates of the intracellular diffusion coefficient as well as the permeability of the intercellular membrane.

The analytic solutions of Brink and Ramanan are useful only when the underlying equations are linear. In many cases, however, the species of interest are also reacting in a nonlinear way. This results in a system of nonlinear diffusion equations coupled by jump conditions at the gap junctions, a system that can only be solved numerically. Two groups have used numerical methods to study problems of this kind. Christ et al. (1994) studied the problem of diffusion through gap junctions, assuming that the diffusing species u decreases the permeability of the gap junction in a nonlinear fashion. A similar model was used by Sneyd et al. (1995a) to study the spread of a Ca^{2+} wave through a layer of cells coupled by gap junctions, and this model is described in Chapter 7.

8.2.4 The Role of Gap-Junction Distribution

It is not always appreciated that the intercellular permeability is strongly influenced by the distribution of gap junctions in the intercellular membrane, although it is a common observation in introductory biology texts that there is a similar relationship between the distribution of stomata on leaves and the rate of evaporation of water through the leaf surface. Individual gap junctions are usually found in aggregates forming larger junctional plaques, as individual gap-junction particles are not easily distinguished from other nonjunctional particles. However, numerical simulations show that the permeability of the intercellular membrane decreases as the gap junction particles aggregate in larger groupings. This raises the intriguing possibility that intercellular permeability may be lowest when the gap-junctional plaques are easiest to see. This in turn provides a possible explanation for the fact that it
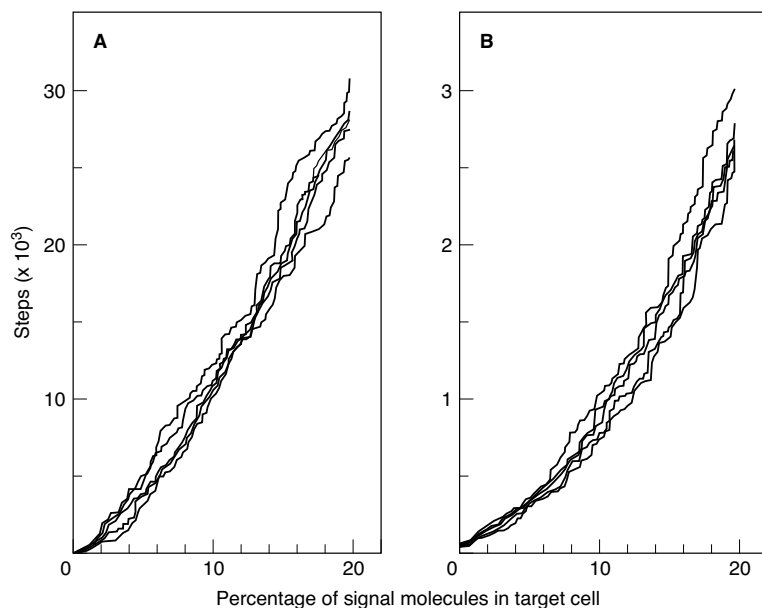
Figure 8.18: Simulation results of the cubic-lattice gap-junction model on a 50 × 50 × 50 lattice with 1000 signal molecules in the source cell at time 0. In A, 100 gap-junction particles are arranged in a compact junctional plaque, while in B they are scattered randomly on the intercellular interface. The random scattering of gap-junction particles results in a greatly increased intercellular transfer rate (note the different scales for the two panels). (Chen and Meng, 1995, Fig. 1.)

has been difficult to establish a direct link between the number of recognizable gap junctions and the intercellular permeability.

Chen and Meng (1995) constructed a cubic lattice model of a two-cell system with a common border. A number of gap-junction particles, with varying degrees of aggregation, were placed on the border lattice points. Marker particles were placed in one of the cubes and followed a random walk over the lattice points of the cube. When they encountered a gap-junction lattice point on the boundary, there was an assigned probability that the marker particle would move across to the other cell. By measuring the time required for a certain percentage of marker particles to cross from one cell to the other, Chen and Meng obtained a quantitative estimate of the efficiency of intercellular transport as a function of gap-junction aggregation. Their results are summarized in Fig. 8.18. When the gap junctions are clumped together into a single junctional plaque, 10,000 time steps were required for the transfer of about 10% of the marker particles. However, when the gap-junction particles were randomly scattered, only 1,000 time steps were required for the same transfer. The magnitude of this discrepancy emphasizes the fact that gap junction distribution can have a huge effect on the rate of intercellular transport.

This result makes intuitive sense. The transfer rate is related to the time it takes
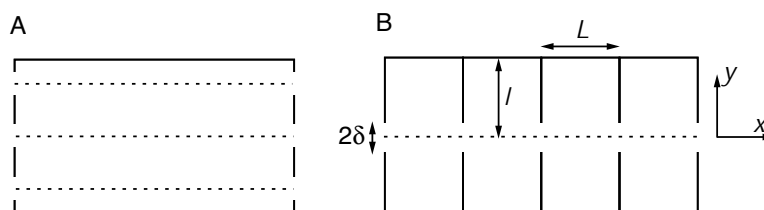
Figure 8.19: A: Sketch of a single rectangular cell with gap-junctional openings in the end faces. B: Sketch of cell array, reduced by symmetry to a single "half-channel."

for a molecule undergoing a random walk to find an exit. It stands to reason that it is easier to find an exit if there are many of them scattered around as opposed to having all of them clumped together in one place.

To get a more analytical understanding of how the distribution of gap junctions affects the diffusion coefficient, we solve a model problem, similar to the one-dimensional problem solved in Section 8.2.1. We consider cells to be two-dimensional rectangles, with a portion of their ends open for diffusive transport (the gap junctions) and the remainder closed (Fig. 8.19A). The dashed lines in this figure are lines of symmetry across which there is no flux in a steady-state problem, so we can reduce the cell configuration to that shown in Fig. 8.19B.

To study diffusion in the x-coordinate direction, we assume that the vertical walls are separated by length L and have regularly spaced openings of width 2δ with centers separated by length $2l$. The fraction of the vertical separator that is open between cells is $\Delta = \delta/l$. To study how the distribution of gap junctions affects the diffusion coefficient, we hold Δ fixed while varying l. When l is small, the gap junctions are small and uniformly distributed, while when l is large, the gap junctions are clumped together into larger aggregates; in either case the same fraction (Δ) of the intercellular membrane is occupied by gap junctions.

Suppose that there are a large number of cells (say N) each of length L connected end to end. We impose a fixed concentration gradient across the array and use the definition (8.62) to define the effective diffusion coefficient for this array.

To find the flux, we solve Laplace's equation subject to no-flux boundary conditions on the horizontal lines $y = 0$ and $y = l$ and on the vertical lines $\delta < y < l, x = pL, p = 0, \ldots, N$. We further divide this region into two subregions, one for $y \geq \delta$ and one for $y \leq \delta$.

Consider first the solution on the upper region. The solution for a single cell $0 \leq x \leq L$ can be found by separation of variables to be

$$u(x, y) = \sum_{n=0}^{\infty} a_n \cos\left(\frac{n\pi x}{L}\right) \cosh\left(\frac{n\pi(y - l)}{L}\right). \tag{8.73}$$

This solution satisfies no-flux boundary conditions at $y = l$ and at $x = 0, L$. Notice also that this solution is periodic, so it is a contender for the solution for any cell.

Now recall that in the one-dimensional case, the solution is piecewise linear, with jumps at the cell boundaries, and that the slope of the solution within each cell is

the same (Section 8.2.1). This suggests that the derivative of the solution in the two-dimensional case should be the same in each cell, or equivalently, the solution in each cell should be the same up to an additive constant. Thus,

$$u(x,y) = \sum_{n=1}^{\infty} A_n \frac{\cosh(n\pi(y-l)/L)}{\cosh(n\pi(\delta-l)/L)} \cos\left(\frac{n\pi}{L}(x-pL)\right) + \alpha_p, \qquad (8.74)$$

for $pL < x < (p+1)L$, $\delta < y < l$, and $p = 0, \ldots, N-1$. We have scaled the unknown constants, A_n, by $\cosh(n\pi(\delta-l)/L)$ for convenience.

On the lower region, a similar argument gives

$$u(x,t) = (U_1 - U_0)\frac{x}{NL} + U_0 + \sum_{n=1}^{\infty} \frac{\cosh(2n\pi y/L)}{\cosh(2n\pi\delta/L)}\left(C_n \sin\frac{2n\pi x}{L}\right), \qquad (8.75)$$

for $0 < x < NL, 0 < y < \delta$. Notice that this solution satisfies a no-flux boundary condition at $y = 0$ and has the correct overall concentration gradient.

Now, to make these into a smooth solution of Laplace's equation we require that $u(x,y)$ and $u_y(x,y)$ be continuous at $y = \delta$. This gives two conditions,

$$\sum_{n=1}^{\infty} A_n \cos\left(\frac{n\pi}{L}(x-pL)\right) = \sum_{n=1}^{\infty}\left(C_n \sin\frac{2n\pi x}{L}\right) + (U_1 - U_0)\frac{x}{nL} + U_0 - \alpha_p, \quad (8.76)$$

and

$$\sum_{n=1}^{\infty} nA_n \tanh\left(\frac{n\pi}{L}(\delta-l)\right)\cos\left(\frac{n\pi}{L}(x-pL)\right) = \sum_{n=1}^{\infty} 2n\tanh\frac{2n\pi\delta}{L}C_n \sin\frac{2n\pi x}{L},$$
$$(8.77)$$

on the interval $pL < x < (p+1)L$.

We determine α_p by averaging (8.76) over cell p. Integrating (8.76) from $x = (p-1)L$ to $x = pL$ gives

$$\alpha_p = \frac{1}{L}\int_{(p-1)L}^{pL}(U_1 - U_0)\frac{x}{NL}\,dx + U_0, \qquad (8.78)$$

since all the trigonometric terms integrate to zero. Hence,

$$\alpha_p = U_0 - (U_0 - U_1)\frac{p-1/2}{N}. \qquad (8.79)$$

Finally, for convenience, we choose $U_0 = N/2$ and $U_1 = -N/2$, which gives $\alpha_p = p + (1+N)/2$. Since this is a linear problem, the values chosen for U_0 and U_1 have no effect on the effective diffusion coefficient.

To obtain equations for the coefficients, we project each of these onto $\cos\frac{k\pi x}{L}$ by multiplying by $\cos\frac{k\pi x}{L}$ and integrating from 0 to L. We find that

$$A_k\frac{L}{2} = F_k + \sum_{n=1}^{\infty} C_n I_{2n,k}, \qquad (8.80)$$

and

$$kA_k \tanh\left(\frac{k\pi}{L}(\delta - l)\right)\frac{L}{2} = \sum_{n=1}^{\infty} 2n \tanh\frac{2n\pi\delta}{L}\left(C_n I_{2n,k}\right), \qquad (8.81)$$

where

$$F_k = \int_0^L \left(\frac{x}{L} - \frac{1}{2}\right)\cos\frac{k\pi x}{L}dx = \frac{L}{n^2\pi^2}((-1)^k - 1), \qquad (8.82)$$

$$I_{n,k} = \int_0^L \sin\frac{n\pi x}{L}\cos\frac{k\pi x}{L}dx = \frac{Ln}{\pi}\left(\frac{1 - (-1)^{n+k}}{n^2 - k^2}\right). \qquad (8.83)$$

There is an immediate simplification possible. Notice that $I_{2n,k} = 0$ and $F_k = 0$ when k is even. Thus, $A_k = 0$ for all even k. Now we eliminate the coefficients A_k from (8.80) and (8.81) to obtain

$$\sum_{n=1}^{\infty} C_n \left(\frac{2n}{k}\frac{\tanh\frac{2n\pi l}{L}\Delta}{\tanh\frac{k\pi l}{L}(1 - \Delta)} + 1\right)\frac{n}{4n^2 - k^2} = \frac{1}{2\pi k^2}, \qquad (8.84)$$

for all odd k, with $\Delta = \delta/l$. Since k can take on any odd positive integer value, (8.84) is an infinite set of equations for the coefficients C_n. Since the solution of the differential equation converges, we can truncate this system of equations and solve the resulting finite linear system numerically.

In terms of this solution, the average flux is

$$J = \frac{D}{l}\int_0^\delta \left.\frac{\partial u}{\partial x}\right|_{x=0} dy = D\left(\frac{\Delta}{L} + \frac{1}{l}\sum_{n=1}^{\infty} C_n \tanh\frac{2n\pi l\Delta}{L}\right), \qquad (8.85)$$

and the effective diffusion coefficient is

$$D_e = D\left(\frac{L}{l}\sum_{n=1}^{\infty} C_n \tanh\frac{2n\pi l\Delta}{L} + \Delta\right). \qquad (8.86)$$

Typical results are shown in Fig. 8.20A, where the ratio D_e/D is shown plotted as a function of l/L for different values of fixed $\Delta = \delta/l$, and in Fig. 8.20B, where D_e/D is shown plotted as a function of Δ for fixed l/L.

There are a number of important observations that can be made. First, notice that in the limit $\Delta \to 1$, or $l/L \to \infty$, $\frac{L}{l}C_n \tanh\frac{2n\pi l\Delta}{L} \to 0$. Thus,

$$\lim_{\Delta \to 1} D_e = D, \qquad (8.87)$$

and

$$\lim_{\frac{l}{L} \to \infty} D_e = D\Delta. \qquad (8.88)$$

Finally, from the numerical solution, it can be seen that D_e is a decreasing function of l/L. Thus, clumping of gap junctions lowers the effective diffusion coefficient compared with spreading them out uniformly, in agreement with numerical experiments described above.
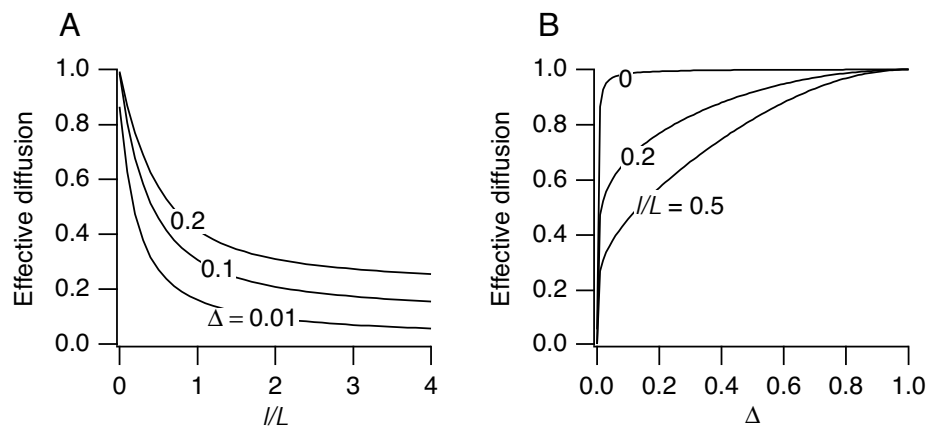
Figure 8.20: A: Effective diffusion ratio D_e/D as a function of the distribution ratio l/L for fixed gap-junction fraction Δ. B: Effective diffusion ratio D_e/D as a function of the gap-junction fraction Δ for fixed distribution ratio l/L.

From Fig. 8.20B we see that when gap junctions are small but uniformly spread, there is little decrease in the effective diffusion coefficient, unless Δ is quite small. Thus, for example, with $\Delta = 0.01$ (so that gap junctions comprise 1% of the membrane surface area) and $l = 0$, the effective diffusion coefficient is about 86% of the cytoplasmic diffusion. On the other hand, with only one large gap junction with $\Delta = 0.01$ in the end membrane of a square cell ($l = 0.5$), the effective diffusion coefficient is reduced to about 27% of the original.

It is interesting to relate these results to the one-dimensional solution (8.68). This two-dimensional problem becomes effectively one-dimensional in the limit $\frac{l}{L} \to 0$, with a piecewise linear profile in the interior of the cells and small boundary or corner layers at the end faces. In this limit, the effective diffusion coefficient satisfies

$$\frac{D}{D_e} = 1 + \mu\frac{1-\Delta}{\Delta},$$
(8.89)

with $\mu = 0.0016$. This formula was found by plotting the curve $\Delta(\frac{D}{D_e} - 1)$ against Δ, which, remarkably, is numerically indistinguishable from the straight line $\mu(1 - \Delta)$. Comparing this with the one-dimensional result, we find that the end-face permeability, F, can be related to the fraction of gap junctions Δ through

$$F = \frac{D}{L}\frac{\Delta}{\mu(1 - \Delta)}.$$
(8.90)

Exercises

1. Use that c_i is small compared to c_e to simplify the Llinás model of presynaptic Ca^{2+} channels (Peskin, 1991). Show that this simplification gives little difference to the behavior of the full model shown in Figs. 8.5 and 8.6.

2. (a) The model of the presynaptic Ca^{2+} current discussed in the text cannot give the curves shown in Fig. 8.7 in response to a voltage jump. Why not?

   (b) Calculate and plot the solution to (8.8) if $V = V_0 + (V_1 - V_0)(H(t) - H(t-4))$, where H is the Heaviside function.

3. Calculate the analytic solution to (8.8) when V is a given function of t.

4. (a) In Fig. 8.13, why are some of the curves positive and some negative?

   (b) Construct a simple function $F(t)$ with the same qualitative shape as the function $W(t)$ used in the Magleby and Stevens model of end-plate currents (Fig. 8.12).

   (c) Calculate the analytic solution to (8.50) for this function F. Compare to the curves shown in Fig. 8.13.

5. In the Magleby and Stevens model of end-plate currents, a simple choice for the release function $f(t)$ results in end-plate conductances with considerable qualitative similarity with those in Fig. 8.13. Suppose there is an instantaneous release of ACh into the synaptic cleft at time $t = 0$. Take $f(t) = \gamma \delta(t)$, where δ is the Dirac delta function and find the conductance x which is the solution of (8.46), to leading order in $\frac{\gamma}{K}$ in the limit that $\frac{\gamma}{K}$ is small. Show that $x(t)$ is always positive. Plot $x(t)$.

6. Peskin (1991) presented a more complex version of the Magleby and Stevens model. His model is based on the reaction scheme

$$\longrightarrow \quad \text{ACh}, \qquad \text{rate } r_T \text{ per unit volume}, \qquad (8.91)$$

$$\text{ACh} + \text{R} \quad \underset{k_2}{\overset{k_1}{\rightleftarrows}} \quad \text{ACh} \cdot \text{R} \quad \underset{\alpha}{\overset{\beta}{\rightleftarrows}} \quad \text{ACh} \cdot \text{R}^*, \qquad (8.92)$$

$$\text{ACh} + \text{E} \quad \underset{k_4}{\overset{k_3}{\rightleftarrows}} \quad \text{ACh} \cdot \text{E} \quad \overset{\gamma}{\longrightarrow} \quad \text{E}, \qquad (8.93)$$

where E is some enzyme that degrades ACh in the synaptic cleft. (The Peskin model differs from the Magleby and Stevens model in two ways, with the assumption of enzymatic degradation of ACh and the assumption that the amount of ACh bound to its receptor is not negligible.)

   (a) Write down the equations for the 6 dependent variables. Use conservation laws to eliminate two of the equations.

   (b) Assume that the reactions involving ACh with R, and ACh with E (with reaction rates $k_i, i = 1, 4$), are fast to obtain expressions for [R] and [E]

in terms of the other variables. Substitute these expressions into the
differential equations for $[\text{ACh} \cdot \text{R}^*]$ and $[\text{ACh}] - [\text{R}] - [\text{E}]$ to find two
differential equations for $[\text{ACh} \cdot \text{R}^*]$ and $[\text{ACh}]$.

(c) Solve these equations when the stimulus is a small sudden release of ACh
(i.e., assume that $r_T = \epsilon \delta(t)$ where ϵ is small - small compared to what?).
Compare this solution with that of Exercise 5.

Remark: After appropriate rescaling and approximation, the equations
are of the form

$$\frac{dx}{dt} = a_1 y - \alpha x \qquad (8.94)$$

$$\frac{dx}{dt} + a_2 \frac{dy}{dt} = \delta(t) - a_3 y, \qquad (8.95)$$

for some constants a_1, a_2 and a_3.

7. Solve (8.56) with $g_s(t) = x(t)$ as found in Exercise 5 and plot the solution.
Compare to $x(t)$ found in Exercise 5 (i.e., (8.57)).

8. The purpose of this exercise is to link together the models of this chapter to
construct a unified model for the synaptic cleft that connects the presynaptic
action potential to the postsynaptic voltage via the concentration of ACh in
the synaptic cleft.

(a) First, use the FitzHugh-Nagumo model (Section 5.2) to construct an
action potential that serves as the input to the overall model. Remark:
the equations

$$\frac{dV_1}{dt} = 100(0.0001(V_1 - V_r)(70 - (V_1 - V_r))((V_1 - V_r) - 7) - w) \quad (8.96)$$

$$\frac{dw}{dt} = 0.25(V_1 - V_r - 5w), \qquad (8.97)$$

do a reasonable job. What is V_r? What value should be chosen for V_r?
Solve these equations and plot the presynaptic action potential, V_1.

(b) Link this presynaptic voltage to the presynaptic Ca^{2+} concentration by
constructing a differential equation for the Ca^{2+} concentration. (Hint:
Take the inward Ca^{2+} current given by the Llinás model of Section 8.1.2
$P_{\text{Ca}} = 0.03 \ \mu\text{ms}^{-1}$ and a linear Ca^{2+} removal with time constant 1
ms works well. Be careful with the units.) Plot the Ca^{2+} transient that
results from the presynaptic action potential calculated in part (a) above.

(c) Link to the model of Ca^{2+}-mediated release of neurotransmitter (Section
8.1.3). Plot, as a function of time, the probability that the release site is
activated.

(d) Next, link to the model of neurotransmitter kinetics in the synaptic cleft
(Section 8.1.4). (Hint: the rate of release of neurotransmitter into the
cleft should be proportional to the number of activated release sites.
Choose this constant of proportionality to be 3×10^6.) Then link this

to the model of the postsynaptic membrane potential, V_2, by letting $g_s(t) = x(t)$. Plot the concentration of ACh and the concentration of open ACh-sensitive channels as functions of time.

(e) Finally, plot V_1 and V_2 on the same graph to compare the input and output voltages of the model.

9. Incorporate the effects of nicotine into a model of ACh activation of receptors.

Chapter 9

Neuroendocrine Cells

There are many hormones that circulate through the body, controlling a diverse array of functions, from appetite to body temperature to blood pH. These hormones are secreted from specialized cells in various glands, such as the hypothalamus and pituitary, the pancreas, or the thyroid. Models of hormone physiology at the level of the entire body are discussed in Chapter 16. Here, we consider models of the cells that secrete the hormones, the *neuroendocrine* cells. They are called neuroendocrine (or sometimes neurosecretory) as they have many of the hallmarks of neurons, such as membrane excitability, but are specialized, not to secrete neurotransmitter into a synaptic cleft, but instead to secrete hormones into the blood. Not only is there a fine line between hormones and neurotransmitters, there is also little qualitative difference between secretion into a synaptic cleft, and secretion into the bloodstream. Thus it does not pay to draw too rigid a distinction between neurons and neuroendocrine cells.

Although, unsurprisingly, there is a great variety of neuroendocrine cells, they have certain characteristics that serve to unify their study. First, they are excitable and therefore have action potentials. Second, the electrical activity usually is not a simple action potential, or periodic train of action potentials (Chapter 5). Instead, the action potentials are characterized by bursts of rapid oscillatory activity interspersed with quiescent periods during which the membrane potential changes only slowly. This behavior is called *bursting*. Third, bursting activity is often closely regulated by the intracellular Ca^{2+} concentration (Chapter 7). Thus, models of neurosecretory cells typically include models of membrane electrical excitability and Ca^{2+} excitability, leading to a fascinating array of dynamic behaviors.

Other factors can also influence bursting; for example, as is described later in this chapter, recent models of bursting in the pancreatic β cell include models of the glycolytic pathway, thus leading to models that incorporate, in a single cell, many of the complexities described in Chapters 1, 5 and 7. Neuroendocrine cells are thus wonderful examples of how multiple complex oscillatory mechanisms can interact, and provide an enormous scope of interesting behaviors to explore.
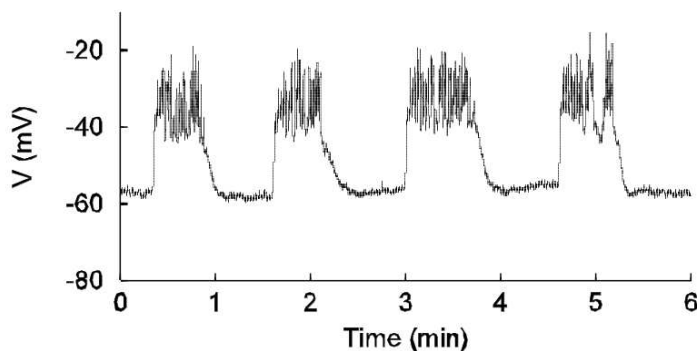
Figure 9.1: Bursting oscillations in the pancreatic β cell. Provided by Richard Bertram. **Needs permission and higher resolution.**

9.1   Pancreatic Beta Cells

In response to glucose, β cells of the pancreatic islet secrete insulin, which causes the increased use or uptake of glucose in target tissues such as muscle, liver, and adipose tissue. When blood levels of glucose decline, insulin secretion stops, and the tissues begin to use their energy stores instead. Interruption of this control system results in diabetes, a disease that if left uncontrolled can result in kidney failure, heart disease, and death. It is believed that electrical bursting, a typical example of which is shown in Fig. 9.1, plays an important (but not exclusive) role in the release of insulin from β cells.

9.1.1   Bursting in the pancreatic beta cell

Bursting in the pancreatic β cell occurs with a wide variety of periods, ranging from a few seconds to a few minutes. Typically, these are divided into three groups; fast bursting, with periods of around 2 to 5 s; medium bursting, with periods of around 10 to 60 s; and slow bursting, with periods of around 2 to 4 minutes.

Although bursting has been studied extensively for many years, most mathematical studies are based on the pioneering work of Rinzel (1985, 1987), which was in turn based on one of the first biophysical models of a pancreatic β cell (Chay and Keizer, 1983). Rinzel's interpretation of bursting in terms of nonlinear dynamics is one of the recent success stories of mathematical physiology and provides an excellent example of how mathematics can be used to understand complex biological dynamical systems.

Models for electrical bursting in pancreatic β cells can be divided into two major groups (well summarized by De Vries, 1995). Earlier models were generally based on the assumption that bursting was caused by an underlying slow oscillation in the intracellular Ca^{2+} concentration (Chay, 1986, 1987; Chay and Cook, 1988; Chay and Kang, 1987; Himmel and Chay, 1987; Keizer and Magnus, 1989). In light

of more recent experimental evidence showing that Ca^{2+} is not the slow variable underlying bursting, more recent models have modified this assumption, relying on alternative mechanisms to produce the underlying slow oscillation (Keizer and Smolen, 1991; Smolen and Keizer, 1992; Bertram and Sherman, 2004; Nunemaker et al., 2006).

One of the first models for bursting was proposed by Atwater et al. (1980). It was based on extensive experimental data, incorporating the important cellular mechanisms that were thought to underlie bursting, and was later developed into a mathematical model by Chay and Keizer (1983). Although the mathematical model includes only those processes believed to be essential to the bursting process and thus omits many features of the cell, it is able to reproduce many of the basic properties of bursting. The ionic currents in the model are:

1. A Ca^{2+}-activated K^+ channel with conductance an increasing function of $c = \left[Ca^{2+}\right]$ of the form

$$g_{K,Ca} = \bar{g}_{K,Ca} \frac{c}{K_d + c},\tag{9.1}$$

for some constant $\bar{g}_{K,Ca}$.

2. A voltage-gated K^+ channel modeled in the same way as in the Hodgkin–Huxley model, with

$$g_K = \bar{g}_K n^4,\tag{9.2}$$

where n obeys the same differential equation as in the Hodgkin–Huxley model (Chapter 5), except that the voltage is shifted by V^*, so that V in (5.28) and (5.29) is replaced by $V + V^*$. For example, $\beta_n(V) = 0.125 \exp[(-V - V^*)/80]$.

3. A voltage-gated Ca^{2+} channel, with conductance

$$g_{Ca} = \bar{g}_{Ca} m^3 h,\tag{9.3}$$

where m and h satisfy Hodgkin–Huxley differential equations for Na^+ gating, shifted along the voltage axis by V'. That is, the inward Ca^{2+} current is modeled by the Na^+ current of the Hodgkin–Huxley model.

Combining these ionic currents and adding a leak current gives

$$C_m \frac{dV}{dt} = -(g_{K,Ca} + g_K)(V - V_K) - 2g_{Ca}(V - V_{Ca}) - g_L(V - V_L),\tag{9.4}$$

where C_m is the membrane capacitance.

To complete the model, there is an equation for the regulation of intracellular Ca^{2+},

$$\frac{dc}{dt} = f(-k_1 I_{Ca} - k_c c),\tag{9.5}$$

where the Ca^{2+} current is $I_{Ca} = \bar{g}_{Ca} m^3 h(V - V_{Ca})$ and where k_1 and k_c are constants. The constant f is a scale factor relating total changes in $\left[Ca^{2+}\right]$ to the changes in free $\left[Ca^{2+}\right]$ (as discussed in the section on Ca^{2+} buffering in Chapter 7) and is usually a small number.
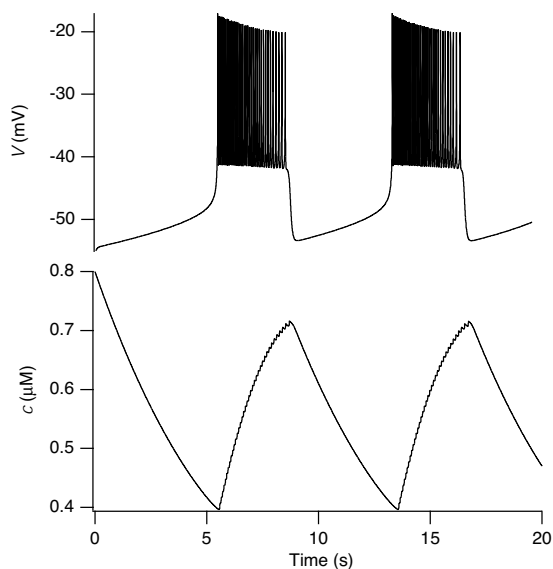
Figure 9.2: Bursting oscillations in the β cell model, calculated using the parameter values in Table 9.1.

For this model it is assumed that glucose regulates the rate of removal of Ca^{2+} from the cytoplasm. Thus, k_c is assumed to be an (unspecified) increasing function of glucose concentration. However, the concentration of glucose is not a dynamic variable of the model, so that k_c can be regarded as fixed, and the behavior of the model can be studied for a range of values of k_c.

A numerically computed solution of this model, shown in Fig. 9.2, exhibits bursts that bear a qualitative resemblance to those seen experimentally. It is also readily seen that there is a slow oscillation in c underlying the bursts, with bursting occurring during the peak of the Ca^{2+} oscillation. The fact that Ca^{2+} oscillations occur on a slower time scale is built into the Ca^{2+} equation (9.5) explicitly by means of the parameter f. As f becomes smaller, the Ca^{2+} equation evolves more slowly, and thus the relative speeds of the voltage and Ca^{2+} equations are directly controlled. It therefore appears that there are two oscillatory processes interacting to give bursting, with a fast oscillation in V superimposed on a slower oscillation in c. This is the basis of the phase-plane analysis that we describe next.

Phase-plane analysis

The β cell model can be simplified by ignoring the dynamics of m and h, thus removing the time dependence (but not the voltage dependence) of the Ca^{2+} current (Rinzel and Lee, 1986). The simplified model equations are

$$C_m \frac{dV}{dt} = -I_{Ca}(V) - \left(\bar{g}_K n^4 + \frac{\bar{g}_{K,Ca} c}{K_d + c} \right) (V - V_K) - \bar{g}_L (V - V_L), \quad (9.6)$$

C_m	=	$1 \ \mu\text{F}/\text{cm}^2$	$\bar{g}_{\text{K,Ca}}$	=	$0.02 \ \text{mS}/\text{cm}^2$
$\bar{g}_{\text{K}}$	=	$3 \ \text{mS}/\text{cm}^2$	$\bar{g}_{\text{Ca}}$	=	$3.2 \ \text{mS}/\text{cm}^2$
$\bar{g}_{\text{L}}$	=	$0.012 \ \text{mS}/\text{cm}^2$	V_{K}	=	$-75 \ \text{mV}$
V_{Ca}	=	$100 \ \text{mV}$	V_{L}	=	$-40 \ \text{mV}$
V^*	=	$30 \ \text{mV}$	V'	=	$50 \ \text{mV}$
K_d	=	$1 \ \mu\text{M}$	f	=	0.007
k_1	=	$0.0275 \ \mu\text{M cm}^2/\text{nC}$	k_c	=	$0.02 \ \text{ms}^{-1}$

Table 9.1: Parameters of the model for electrical bursting in pancreatic β cells.

$$\tau_n(V)\frac{dn}{dt} = n_\infty(V) - n, \tag{9.7}$$

$$\frac{dc}{dt} = f(-k_1 I_{\text{Ca}}(V) - k_c c), \tag{9.8}$$

where $I_{\text{Ca}} = \bar{g}_{\text{Ca}} m_\infty^3(V) h_\infty(V)(V - V_{\text{Ca}})$.

Since f is small, this β cell model separates into a fast subsystem (the V and n equations) and a slow equation for c. The fast subsystem can be studied using phase-plane methods, and then the behavior of the full system can be understood as slow variations of the fast phase plane system.

We first consider the structure of the fast subsystem as a function of c, treating c as a fixed parameter.

When c is low, the Ca^{2+}-activated K$^+$ channel is not activated, and the fast subsystem has a unique fixed point with V high. Conversely, when c is high, the Ca^{2+}-activated K$^+$ channel is fully activated, and the fast subsystem has a unique fixed point with V low, as the high conductance of the Ca^{2+}-activated K$^+$ channels pulls the membrane potential closer to the K$^+$ Nernst potential, about -75 mV. However, for intermediate values of c there are three fixed points, and the phase-plane is much more intricate. Phase-planes of the V, n subsystem for two different intermediate values of c are shown in Fig. 9.3.

In both cases, the lower fixed point is stable, the middle fixed point is a saddle point, and the upper fixed point is unstable. For some values of c the upper fixed point is surrounded by a stable limit cycle, which in turn is surrounded by the stable manifold of the saddle point (Fig 9.3A). However, as c increases (still in the intermediate range), the limit cycle "hits" the saddle point and forms a homoclinic connection (a homoclinic bifurcation). Increasing c further breaks the homoclinic connection, and the stable manifold of the saddle point forms a heteroclinic connection with the upper, unstable, critical point (Fig. 9.3B). There is now no limit cycle.

This sequence of bifurcations can be summarized in a bifurcation diagram, with V plotted against the control parameter c (Fig. 9.4A). The Z-shaped curve is the curve of fixed points, and as usual, the stable oscillation around the upper steady
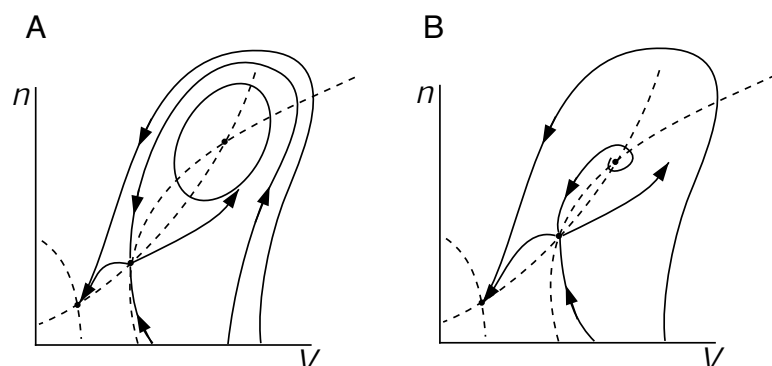
Figure 9.3: Phase-planes of the fast subsystem of the β cell model, for two different values of c, both in the intermediate range. The phase-planes are sketched, not drawn to scale. Nullclines are denoted by dashed lines, and the intersections of the nullclines show the positions of the fixed points. For both values of c there are three fixed points, of which the middle one is a saddle point. However, in A (with $c_{hb} < c < c_{hc}$; see Fig. 9.4) the unstable node is surrounded by a stable limit cycle, while in B (corresponding to $c > c_{hc}$) the limit cycle has disappeared via a homoclinic bifurcation.

state is depicted by the maximum and minimum of V through one cycle. As c increases, oscillations appear via a Hopf bifurcation (c_{hb}) and disappear again via a homoclinic bifurcation (c_{hc}). For a range of values of c the fast subsystem is bistable, with a lower stable fixed point and an upper stable periodic orbit. This bistability is crucial to the appearance of bursting.

We now couple the dynamics of the fast subsystem to the slower dynamics of c. Included in Fig. 9.4A is the curve defined by $dc/dt = 0$, i.e., the c nullcline. When V is above the c nullcline, $dc/dt > 0$, and so c increases, but when V is below the c nullcline, c decreases. Now suppose V starts on the lower fixed point for a value of c that is greater than c_{hc}. Since V is below the c nullcline, c starts to decrease, and V follows the lower branch of fixed points. However, when c becomes too small, this lower branch of fixed points disappears in a saddle-node bifurcation (SN), and so V must switch to the upper branch of the Z-shaped curve. Since this upper branch is unstable and surrounded by a stable limit cycle, V begins to oscillate. However, since V now lies entirely above the c nullcline, c begins to increase. Eventually, c increases enough to cross the homoclinic bifurcation at c_{hc}, the stable limit cycles disappear, and V switches back to the lower branch, completing the cycle. Repetition of this process causes bursting. The quiescent phase of the bursting cycle is when V is on the lower branch of the Z-shaped curve, and during this phase V increases slowly. A burst of oscillations occurs when V switches to the upper branch, and disappears again after passage through the homoclinic bifurcation. Clearly, in this scenario, bursting relies on the coexistence of both a stable fixed point and a stable limit cycle, and the bursting cycle is a hysteresis loop that switches between branches of the Z-shaped curve. Bursting
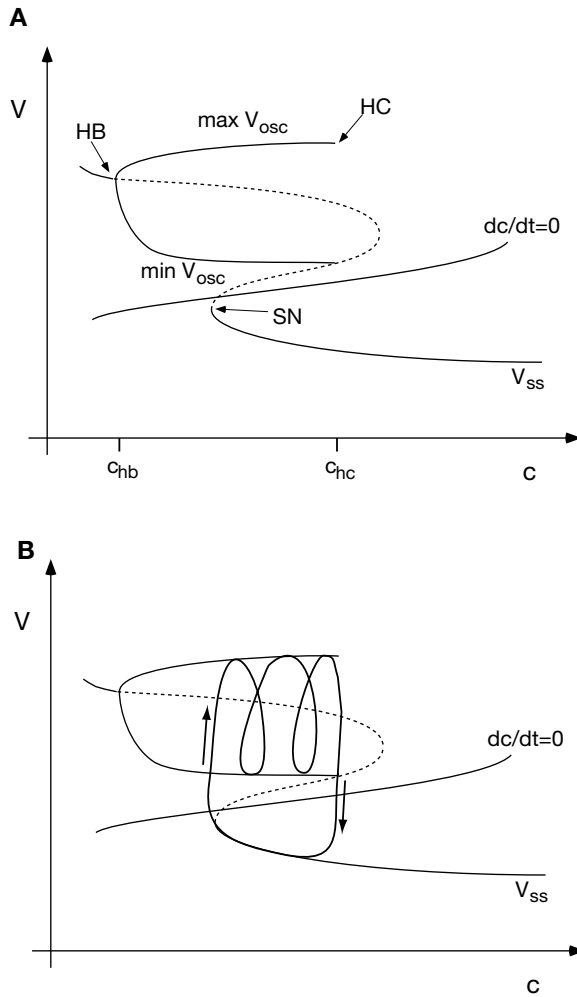
Figure 9.4: A: Sketch of the bifurcation diagram of the simplified β cell model, with c as the bifurcation parameter. V_{ss} denotes the curve of steady states of V as a function of c. A solid line indicates a stable steady state; a dashed line indicates an unstable steady state. The two branches of V_{osc} denote the maximum and minimum of V over one oscillatory cycle. HB denotes a Hopf bifurcation, HC denotes a homoclinic bifurcation, and SN denotes a saddle-node bifurcation. B: A burst cycle projected onto the (V, c) plane. (Adapted from Rinzel and Lee, 1986, Fig. 3.)

also relies on the c nullcline intersecting the Z-shaped curve in the right location. For example, if the c nullcline intersects the Z-shaped curve on its lower branch, there is a unique stable fixed point for the whole system, and bursting does not occur. A projection of the bursting cycle on the (V, c) phase-plane is shown in Fig. 9.4B. The periods of the oscillations in the burst increase through the burst, as the limit cycles get closer to the homoclinic trajectory, which has infinite period.

The relationship between bursting patterns and glucose concentration can also be deduced from Fig. 9.4. Notice that the $\frac{dc}{dt} = 0$ nullcline, given by $c = -\frac{k_1}{k_c} I_{Ca}(V)$, is inversely proportional to k_c. Increasing k_c moves the $\frac{dc}{dt} = 0$ nullcline to the left while decreasing k_c moves it to the right. Thus, when k_c is sufficiently small, the nullcline intersects the lower branch of the V nullcline. On the other hand, if k_c is extremely large, the c nullcline intersects the upper branch of the V nullcline, possibly to the left of c_{hb}. At intermediate values of c, the c nullclines intersects the middle branch of the V nullcline.

Under the assumption that k_c is monotonically related to the glucose concentration, when the glucose concentration is low, the system is at a stable rest point on the lower V nullcline; there is no bursting. If glucose is increased so that the c nullcline intersects the middle V nullcline with $c < c_{hc}$, there is bursting. However, the length of the bursting phase increases and the length of the resting phase decreases with increasing glucose, because Ca^{2+} increases at a slower rate and decreases at a faster rate when k_c is increased. For large enough k_c the bursting is sustained with no rest phase, as c becomes stalled below c_{hc}. Finally, at extremely high k_c values, bursting is replaced by a permanent high membrane potential, with $c < c_{hb}$. This dependence of the bursting phase on glucose is confirmed by experiments.

9.1.2 ER Calcium as a Slow Controlling Variable

There are two major problems with the above model. First, it does not reproduce the wide variety of periods and bursting patterns actually seen in bursting pancreatic β cells, being limited to a narrow range of fast bursting frequencies.

Second, more recent experimental evidence has shown that Ca^{2+} oscillates much too fast to be viewed as a slow control variable. This is illustrated in Fig. 9.5, which shows simultaneous Ca^{2+} and voltage measurements. The bursting oscillations in the voltage are mirrored by bursting oscillations in the cytosolic Ca^{2+} concentration, and the rise in Ca^{2+} concentration is almost as fast as the rise in voltage.

So the question of what controls the length of bursting arises.

One possibility is that ER Ca^{2+} concentration varies much more slowly than cytosolic Ca^{2+} and could provide the necessary control mechanism. This would be the case if most of the Ca^{2+} during active bursting were coming from the extracellular space through transmembrane ion channels, and only a small amount of Ca^{2+} flowed between the cytosol and the ER. If this were the case, ER Ca^{2+} would act like a low pass filter for cytosolic Ca^{2+}, and therefore could be used to detect and regulate the length of bursting activity. The possible usefulness of a low-pass filter is seen in the Ca^{2+} traces shown in Fig. 9.5, where, during a burst, Ca^{2+} concentration oscillates rapidly around a raised baseline. A low-pass filter would measure the length of time that the Ca^{2+} baseline is elevated, but filter out the
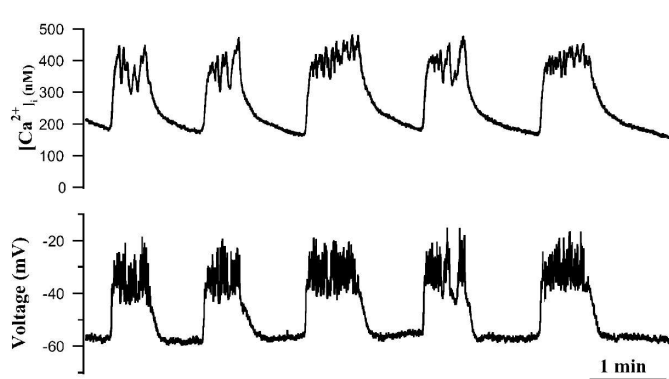
Figure 9.5: Simultaneous Ca^{2+} and voltage measurements from a bursting pancreatic β cell. (Adapted from Zhang et al., 2003, Fig. 4.) **Needs permission and higher resolution.**

rapid oscillations.

Thus, it was proposed by Chay (1996, 1997) that slow variations in ER Ca^{2+} could be an important control mechanism, and could, in addition, generate a wider range of bursting periods. This proposal was analyzed in detail by Bertram and Sherman (2004) who showed that the interaction of a (not very slow) cytosolic Ca^{2+} variable, with a (much slower) ER Ca^{2+} variable, could lead to bursting with a wide range of periods. They named this a *phantom bursting* model, as it can lead to bursting with a period intermediate between that of the slow variables.

The membrane voltage submodel

The electrical part of the phantom bursting model is similar to the Chay-Keizer model, but with slight differences, so we present it in full here. As before, the current is the sum of a Ca^{2+} current, a K^+ current, a Ca^{2+}-sensitive K^+ current, with an additional ATP-sensitive K^+ current, which is important below. The only current not assumed to be at pseudo-steady state is the K^+ current. Thus,

$$C_m\frac{dV}{dt} = -I_{Ca} - I_K - I_{K,Ca} - I_{K,ATP}, \tag{9.9}$$

$$\tau_n\frac{dn}{dt} = n_\infty(V) - n, \tag{9.10}$$

$$I_{Ca} = g_{Ca}m_\infty(V)(V - V_{Ca}), \tag{9.11}$$

$$I_K = g_K n(V - V_K), \tag{9.12}$$

$$I_{K,Ca} = g_{K,Ca}\omega(c)(V - V_K), \tag{9.13}$$

$$I_{K,ATP} = g_{K,ATP}(V - V_K), \tag{9.14}$$

where c denotes the free cytoplasmic Ca^{2+} concentration. The functions m_∞ and n_∞ are given by

$$m_\infty(V) = \frac{1}{1 + e^{(v_m - V)/s_m}}, \tag{9.15}$$

$$n_\infty(V) \quad = \quad \frac{1}{1 + e^{(v_n - V)/s_n}}. \tag{9.16}$$

The variable ω is the fraction of Ca^{2+}-sensitive K^+ channels that are opened by Ca^{2+}, and is close to a step function,

$$\omega(c) = \frac{c^5}{c^5 + k_D^5}. \tag{9.17}$$

The calcium submodel

These equations for the electrical properties of the membrane must be coupled to equations that model the cytoplasmic and ER Ca^{2+} concentrations. The Ca^{2+} model is chosen to be relatively simple; more complex models of Ca^{2+} dynamics are discussed in Chapter 7.

As usual, let c and c_e denote the free concentrations of Ca^{2+} in the cytoplasm and ER respectively. The equations for c and c_e are simple balance of fluxes.

1. I_{Ca}, the transmembrane Ca^{2+} current as discussed above.

2. Pumping of Ca^{2+} across the plasma and ER membranes, denoted by J_{pm} and J_{serca} respectively. Both of these fluxes are assumed to be linear functions of Ca^{2+}. Thus

$$J_{serca} \quad = \quad k_{serca}c, \tag{9.18}$$
$$J_{pm} \quad = \quad k_{pm}c. \tag{9.19}$$

3. J_{leak}, a leak from the ER. This is assumed to be proportional to the difference between the ER and cytosolic concentrations, and thus

$$J_{leak} = k_{leak}(c_e - c). \tag{9.20}$$

Because of Ca^{2+} buffering, only a small fraction of each flux contributes to a change in the free Ca^{2+} concentration. If we assume that buffering is fast and unsaturated, then we need only multiply each flux by a scaling factor to get the change in free Ca^{2+} concentration. This is discussed in detail in Chapter 7, Section 7.4.

We put all these fluxes together to get

$$\frac{dc}{dt} \quad = \quad f_{cyt}(-\alpha I_{Ca} - J_{pm} + J_{leak} - J_{serca}), \tag{9.21}$$
$$\frac{dc_e}{dt} \quad = \quad -\gamma f_{er}(J_{leak} - J_{serca}). \tag{9.22}$$

Here, γ is the ratio of the cytosolic volume to the ER volume, while f_{cyt} and f_{er} are the buffering scaling factors for the cytoplasm and the ER.

The parameter values for this model are given in Table 9.2.

g_{Ca}	$=$	1200 pS	g_{K}	$=$	3000 pS
V_{Ca}	$=$	25 mV	V_{K}	$=$	-75 mV
C_m	$=$	5300 fF	α	$=$	$4.5 \times 10^{-6} \mu$M fA^{-1} ms^{-1}
τ_n	$=$	16 ms	f_{cyt}	$=$	0.01
k_{pm}	$=$	0.2 ms^{-1}	k_D	$=$	0.3 μM
v_n	$=$	-16 mV	s_n	$=$	5 mV
v_m	$=$	-20 mV	s_m	$=$	12 mV
k_{serca}	$=$	0.4 ms^{-1}	f_{er}	$=$	0.01
γ	$=$	5	p_{leak}	$=$	0.0005 ms^{-1}

Table 9.2: Parameters of the model for phantom bursting. The values of $g_{\text{K,Ca}}$ and $g_{\text{K,ATP}}$ used for each simulation are given in the figure captions.

Fast bursting

When the Ca^{2+}-sensitive K$^+$ conductance is high (900 pS), the model exhibits fast bursting, as shown in Fig. 9.6. The ER Ca^{2+} concentration varies little over the course of a burst, and indeed, if c_e is set to be a constant, the solution is nearly identical. As can be seen from the middle panel of Fig. 9.6, although c is slightly slower than V, it changes a lot faster than c_e, and is not obviously a slow variable.

A full analysis of this model requires examining a three dimensional phase space, a difficult exercise. However, even though it is only an approximate analysis, it is useful to analyze this model in the same way as Rinzel's analysis of the Chay-Keizer model, as discussed previously. To do so, we pretend that c is a bifurcation parameter, and draw the bifurcation diagram of V against c (Fig. 9.7). This gives a diagram qualitatively similar to that shown in Fig. 9.4. A Z-shaped curve of steady state solutions becomes unstable at a Hopf bifurcation, and the branch of stable limit cycles intersects the Z-shaped curve of steady states in a homoclinic bifurcation. This gives rise to bistability, where a stable steady state and a stable limit cycle exist simultaneously.

Bursting occurs in the same manner as the Chay-Keizer model. Above the $dc/dt = 0$ nullcline the solution trajectory moves to the right, and lives (approximately) on the branch of stable limit cycles, giving the active phase of the burst. When it moves far enough to the right, it falls off the branch of limit cycles and heads to the lower branch of stable steady states. Since this branch is below the c nullcline, the solution then moves to the left, eventually falling off the saddle-node to repeat the cycle. This way of interpreting the solution is only an approximate one, as it can be seen from Fig. 9.7 that the actual solution follows accurately neither the branch of periodic orbits nor the lower branch of steady states. The upper turning point of the burst is close to osc$_{\text{max}}$, but the lower turning point is not close at all to osc$_{\text{min}}$. Similarly, when the solution falls off the branch of periodic orbits, it does
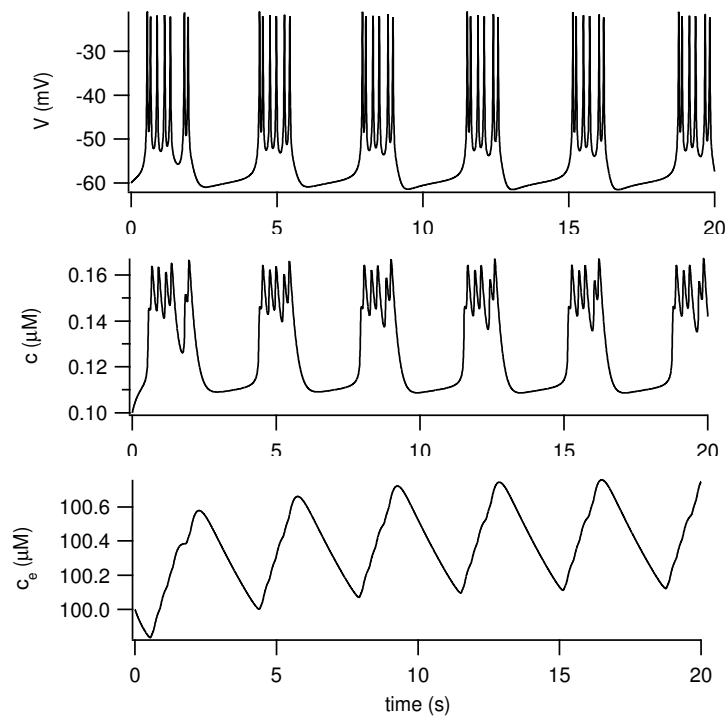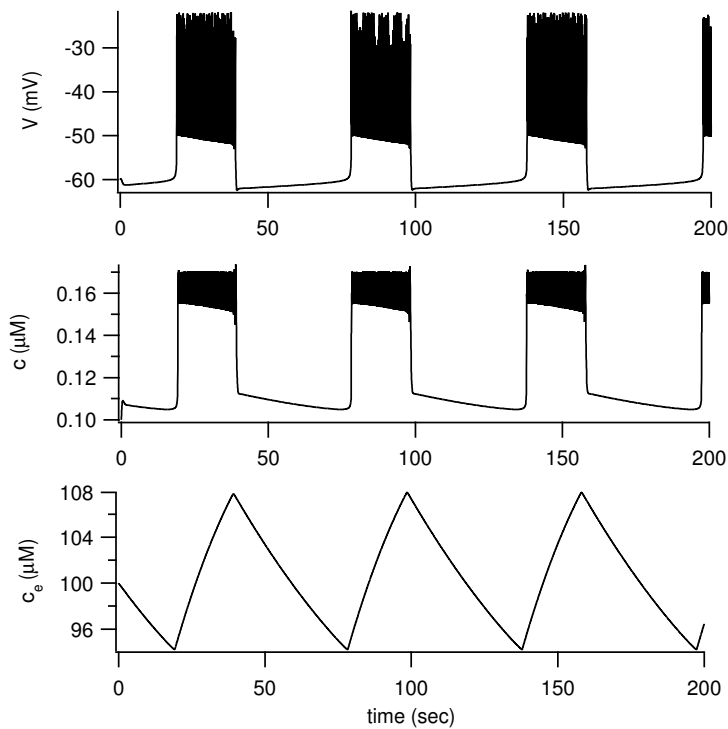
Figure 9.6: Fast bursting oscillations in the phantom bursting model. These solutions were computed with $g_{K,Ca} = 900$ pS and $g_{K,ATP} = 227.5$ pS. Note that the ER Ca^{2+} varies only slightly.
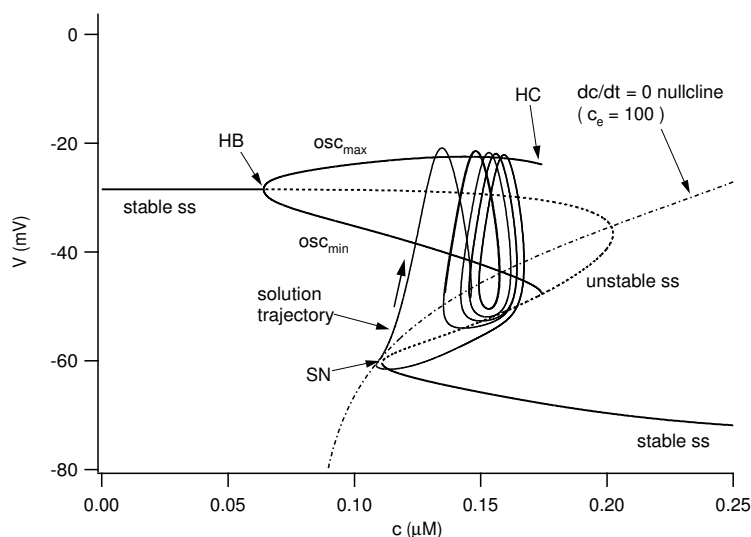
Figure 9.7: Fast bursting in the phantom bursting model (computed with $g_{K,Ca} = 900$ pS and $g_{K,ATP} = 227.5$ pS) superimposed on the bifurcation diagram of the fast subsystem, treating c as the bifurcation parameter. HB — Hopf bifurcation; HC — homoclinic bifurcation; SN — saddle-node bifurcation.

so well before the homoclinic bifurcation, and then does not follow the lower branch of steady states closely. This happens because c is not really a slow parameter after all. In the limit as c becomes infinitely slow, the solution would track much more closely the bifurcation diagram of the fast subsystem. Despite these quantitative disagreements, the phase plane of the fast subsystem is nonetheless a useful way to interpret and understand the solutions of the full system.

However, there is one important difference between this model and the Chay-Keizer model. In this model there is a second slow variable, c_e, and thus the $dc/dt = 0$ nullcline moves as c_e varies (the Z-shaped curve, however, is independent of c_e). From (9.21) we see that the $dc/dt = 0$ nullcline is given by

$$c = \frac{p_{leak}c_e - \alpha I_{Ca}}{k_{pm} + p_{leak} + k_{serca}}, \tag{9.23}$$

and thus, as c_e increases, the nullcline moves to the right. For the fast bursting shown in Fig. 9.6 the changes in c_e are so small that this movement of the null-cline has no effect on the bursting. However, for different parameter values, more interesting behaviors emerge.

Medium bursting

One way to get a longer burst period would be to stretch the Z-shaped curve horizontally, so that the homoclinic bifurcation and the saddle-node are further apart. This can be accomplished by decreasing $g_{K,Ca}$. However, if the c nullcline remains
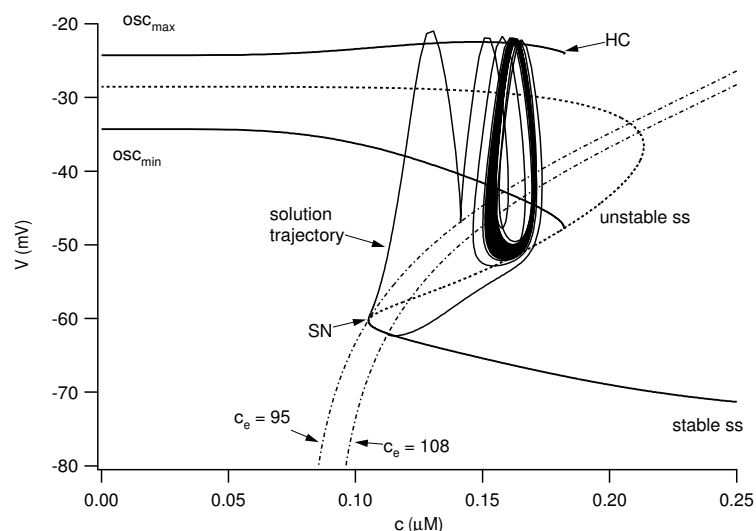
Figure 9.8: Medium bursting in the phantom bursting model (computed with $g_{K,Ca} = 700$ pS and $g_{K,ATP} = 300$ pS) superimposed on the bifurcation diagram of the fast subsystem, treating c as the bifurcation parameter. HC — homoclinic bifurcation; SN — saddle-node bifurcation. The Hopf bifurcation occurs at a negative value of c and so does not appear here. Two $dc/dt = 0$ nullclines are shown, for the maximum and minimum values of c_e over a burst.

unchanged, for small enough $g_{K,Ca}$ it intersects the Z-shaped curve on its upper branch, inside the branch of stable limit cycles. In this case, the limit cycle is a stable solution of the full system, and the solution remains stuck in the active phase.

Now the slow dynamics of c_e come into play. During the active phase c_e increases (see Exercise 4), gradually moving the c nullcline to the right; the oscillations chase the c nullcline to the right, as shown in Fig. 9.8. When the c nullcline iss moved far enough to the right, the solution falls off the limit cycles (i.e., leaves the active phase), moves toward the lower branch of steady state solutions (thus starting the silent phase), and moves to the left towards the saddle-node. However, movement along this lower branch is very slow, as the c nullcline intersects the Z-shaped curve on its lower branch, giving a stable quasi-steady state. The solution is thus forced to move at the same speed as the slow variable c_e, tracking the quasi-steady state as it moves to the left. Eventually, the c nullcline moves sufficiently far to the left that the quasi-steady state disappears, the solution leaves the lower branch of the Z-shaped curve, and the burst cycle repeats.

Thus, in medium bursting the burst cycle relies on the slow movement of the c nullcline, which is caused by the slow increase of c_e during the active phase of the burst, and the slow decrease of c_e during the silent phase. Because the c nullcline moves slowly, this results in medium bursting with a longer period. Both the active and silent phases are longer than for fast bursting, giving a much longer burst period, and the ER Ca^{2+} varies much more over a cycle. Typical solutions are

Figure 9.9: Medium bursting oscillations in the phantom bursting model. These solutions were computed with $g_{K,Ca} = 700$ pS and $g_{K,ATP} = 300$ pS. The active phase is not completely regular due to inadequate numerical resolution of the timestep.

shown in Fig. 9.9.

The effect of agonists

Pancreatic β cells are also regulated by the nervous system. Secretion of acetylcholine from parasympathetic nerves increases the rate of insulin secretion, an effect due partly to changes in the electrical activity and Ca^{2+} dynamics of individual β cells. Since the action of acetylcholine is via the production of IP_3, and consequent release of Ca^{2+} from the ER, it can be modeled by including an additional term for a Ca^{2+} flux through IP_3 receptors (Exercise 3). When IP_3 is raised from 0 to 0.3 μM the burst pattern changes from medium to fast, a change which is observed experimentally.

9.1.3 Slow Bursting and Glycolysis

Bursting in pancreatic β cells is highly sensitive to the level of glucose; as the concentration of glucose increases, so does the active fraction of the burst cycle.

During the active fraction of the burst cycle the Ca^{2+} concentration is raised, and this in turn causes the secretion of insulin. Thus, the rate of insulin secretion is an increasing function of glucose concentration.

This effect of glucose is believed to be mediated by the ATP-sensitive K^+ channel, which is activated by ADP and inhibited by ATP. At low glucose concentrations the ATP/ADP ratio is low, the K^+ channel is open, hyperpolarizing the cell and thus preventing bursting. As glucose increases, so does the ATP/ADP ratio; this decreases the conductance of the ATP-sensitive K^+ channels, thus depolarizing the cell and allowing bursting to occur.

There are two important features of bursting and insulin secretion that we have not, as yet, addressed. First, bursting often occurs with a much longer period than that so far reproduced by the models above, and second, such slow bursting can take a more complex form than that shown in Figs. 9.6 and 9.9. In particular, slow bursting can occur as "compound" bursting, or bursts of bursts, in which each active phase itself consists of alternating active and silent subphases.

One hypothesis is that compound bursting and a long burst period arise from a slow oscillation in the glycolytic pathway (Chapter 1), which causes slow oscillations in the ATP/ADP ratio. One of the earliest quantitative models of this hypothesis was that of Wierschem and Bertram (2004), who showed that, by linking the Goldbeter-Lefevre model of glycolytic oscillations (Chapter 1) to a simple bursting model, the burst pattern could be modulated on a long time scale, to obtain both compound and slow bursting. This initial model, more of a proof of principle than a quantitative model, was quickly followed by much more detailed realizations, first using the Smolen model of glycolytic oscillations (Smolen, 1995; Bertram et al., 2004; Nunemaker et al., 2006), and then linking the Smolen model to the Magnus-Keizer model of mitochondrial metabolism (Magnus and Keizer, 1997, 1998a, 1998b; Bertram et al., 2006).

The later models being too complex to present in full here, we instead examine briefly the original model of Wierschem and Bertram (2004), as it contains most of the essentials of the more complex models.

The glycolysis, electrical and calcium submodels

To model glycolytic oscillations in a simple way we use the reduced Goldbeter-Lefevre model discussed in Chapter 1, Section 1.6. Thus,

$$\tau_c \frac{d[\text{ATP}]}{dt} = v_1 - F([\text{ATP}], [\text{ADP}]), \tag{9.24}$$

$$\tau_c \frac{d[\text{ADP}]}{dt} = F([\text{ATP}], [\text{ADP}]) - v_2[\text{ADP}], \tag{9.25}$$

where (as in (1.125))

$$F([\text{ATP}], [\text{ADP}]) = [\text{ATP}](1 + k_{\text{ADP}}[\text{ADP}])^2. \tag{9.26}$$

The only change introduced to this version of the glycolytic model is the time constant, τ_c, which is convenient for changing the period of the glycolytic oscillations.

g_{Ca}	$=$	1200 pS	g_K	$=$	3000 pS
$g_{K,Ca}$	$=$	300 pS	$g_{K,ATP}$	$=$	350 pS
V_{Ca}	$=$	25 mV	V_K	$=$	-75 mV
C_m	$=$	5300 fF	α	$=$	$2.25 \times 10^{-6} \mu\text{M fA}^{-1} \text{ ms}^{-1}$
τ_n	$=$	16 ms	f	$=$	0.001
k_c	$=$	0.1 ms^{-1}	k_D	$=$	0.3 μM
v_n	$=$	-16 mV	s_n	$=$	5.6 mV
v_m	$=$	-20 mV	s_m	$=$	12 mV
τ_c	$=$	1.2×10^{-6} ms	v_1	$=$	10 mM
v_2	$=$	185	k_{ADP}	$=$	20 mM^{-1}

Table 9.3: Parameters of the model for compound bursting.

The electrical submodel is almost the same as the models discussed previously in this chapter. The currents are described by (9.9)–(9.14) and (9.15), the only difference being that, instead of (9.17), we take

$$\omega(c) = \frac{c}{c + k_D}. \tag{9.27}$$

Finally, the Ca^{2+} submodel is the same as that of the Chay-Keizer model. We thus ignore ER Ca^{2+} to get a single equation for c (as in (9.5)),

$$\frac{dc}{dt} = -f(\alpha I_{Ca} + k_c c). \tag{9.28}$$

All the parameters of the compound bursting model are given in Table 9.3.

Compound bursting

A typical example of compound bursting in this model is shown in Fig. 9.10. The bursting occurs in clusters, with the duration of the active phase increasing and then decreasing through each cluster. As can be seen from the dotted curve, [ATP] is oscillating also; here these oscillations are independent of c and V, although this is not necessarily so in more complex models.

The reason for the compound bursting can be seen if we consider the fast-slow bifurcation structure of the electrical submodel, for various fixed values of [ATP]. As usual, we treat c as a slow variable and construct the bifurcation diagrams using c as a bifurcation parameter.

At all values of [ATP], the curve of steady states (labeled ss in Fig. 9.10) is Z-shaped. The unstable branches of this Z-shaped curve are shown as a dashed line. For low values of c the steady state becomes unstable in a Hopf bifurcation, from
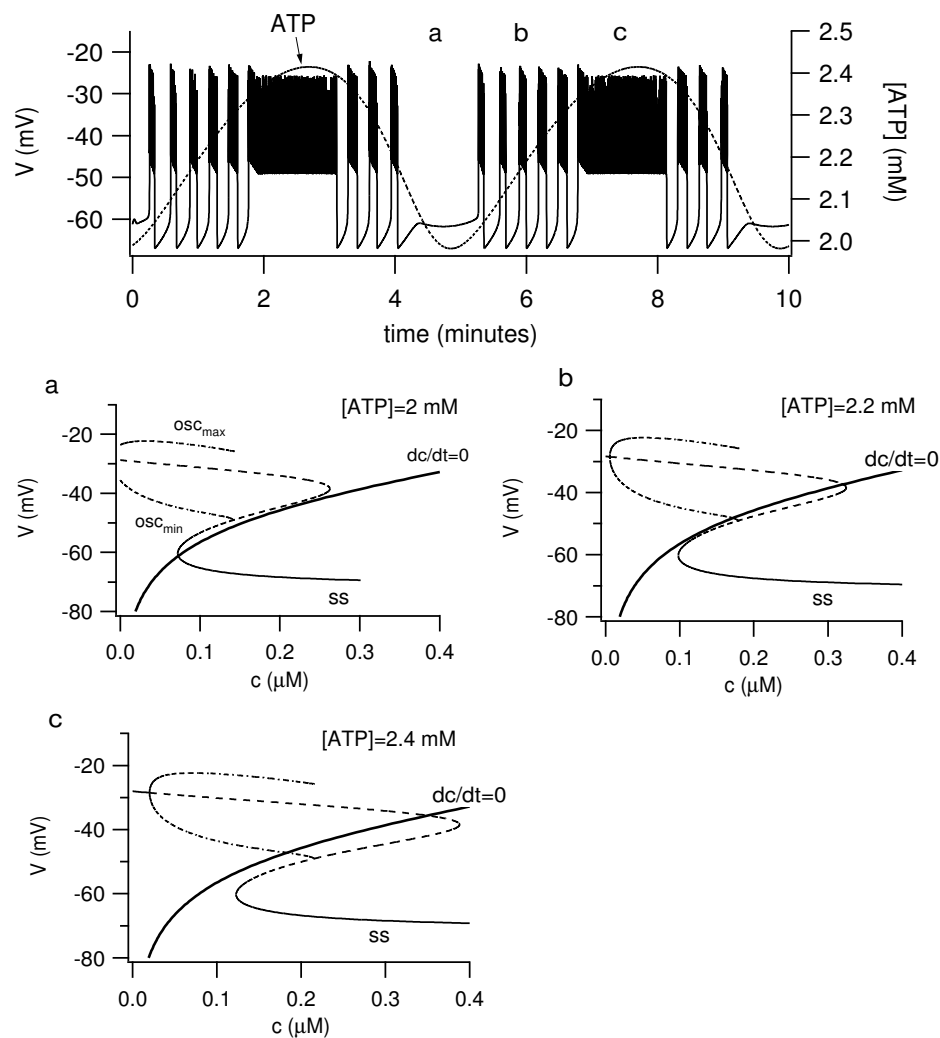
Figure 9.10: Compound bursting in the model with glycolytic oscillations. The upper panel shows a compound bursting pattern, in which the bursts are grouped in clusters that occur in a periodic manner. In panels **a**, **b**, and **c** are shown the bifurcation diagrams corresponding approximately to the regions labeled **a**, **b** and **c** in the top panel. The dashed lines are unstable branches of steady states, and the dot-dash lines are the maximum and minimum of stable periodic solutions.

which emerges a branch of stable periodic solutions (the dot-dash curve, labeled osc_{max} and osc_{min} in Fig. 9.10, panel **a**).

As [ATP] increases, the Z-shaped curve moves to the right, but the $dc/dt = 0$ nullcline remains unchanged. Thus, when [ATP] is low, the $dc/dt = 0$ nullcline intersects the Z-shaped curve on the lower, stable, branch, a situation that gives no bursting at all (panel **a**). Conversely, when [ATP] is high, the $dc/dt = 0$ nullcline intersects the branch of periodic orbits, which leads to a continuous active phase (panel **c**). When [ATP] takes intermediate values, the length of the active phase is either longer or shorter, depending on where the $dc/dt = 0$ nullcline intersects the Z-shaped curve (panel **b**).

Hence, as [ATP] varies over the course of an oscillation, so does the length of the active phase, thus giving compound bursting.

9.1.4 Bursting in Clusters

In the discussion so far, we have ignored the inconvenient fact that isolated pancreatic β cells usually do not burst in a regular fashion. It is not until several thousand cells are grouped into an islet and electrically coupled by gap junctions that regular spiking is seen in any cell. An isolated β cell behaves in a much more irregular fashion, with no discernible pattern of bursting. Indeed, blockage of gap junctions in an islet greatly reduces insulin secretion, and thus intercellular mechanisms that control bursting are of great physiological importance. Figure 9.11 shows how the behavior of an individual cell changes as a function of the number of other cells to which it is coupled.

Channel-Sharing

In 1983, Atwater et al. proposed a qualitative mechanism to account for the difference between the single-cell behavior and the behavior of the cell in a cluster. They proposed that an individual cell contains a small number of Ca^{2+}-sensitive K^+ (K–Ca) channels each of which has a high conductance. At resting V and $\left[Ca^{2+}\right]$, a K–Ca channel is open only infrequently, but the opening of a single channel passes enough current to cause a significant perturbation of the cell membrane potential. Thus, stochastic channel opening and closing causes the observed random fluctuations in V. However, when the cells are electrically coupled in a cluster, each K–Ca channel has a much smaller effect on the potential of each individual cell, as the channel current is spread over the network of cells. Each cell integrates the effects of a large number of K–Ca channels, each of which has only a small influence. The tighter the electrical coupling between cells, the better each cell is able to integrate the effects of all the K–Ca channels in the cluster, and the more regular and deterministic is the overall behavior.

We can use this qualitative explanation as the basis for a quantitative model (Sherman et al., 1988; Chay and Kang, 1988). Initially, we assume infinitely tight coupling of the cells in the cluster, calling the cluster a "supercell," and show how the bursting becomes more regular as the size of the cluster increases.

The equations of the supercell model are similar to those of the β cell model. Recall that in the β cell model the conductance of the K–Ca channel, $g_{K,Ca}$, is given
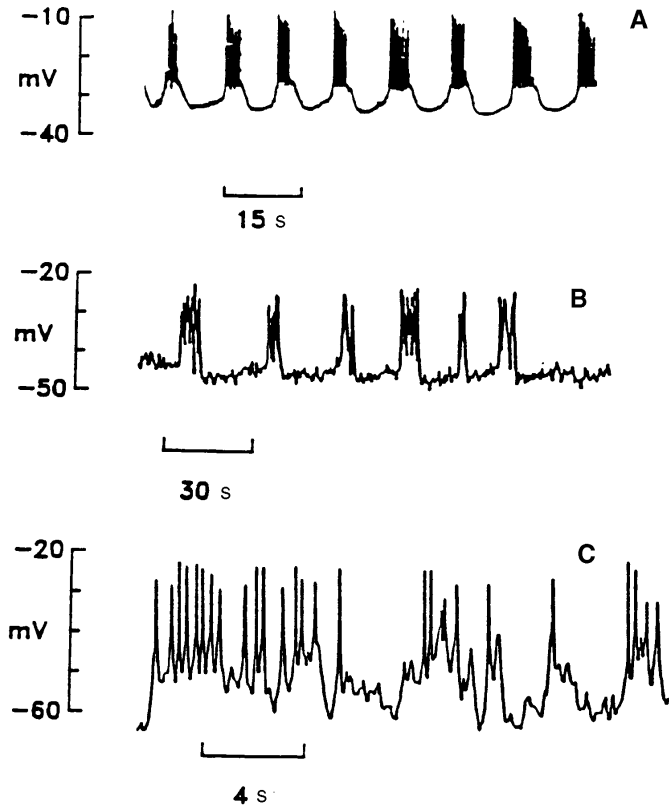
Figure 9.11: Bursting in clusters of β cells, compared to the electrical activity of an isolated β cell (Sherman et al., 1988, Fig. 1). A: Recording from a β cell in an intact cluster (Atwater and Rinzel, 1986), B: Recording from a cluster of β cells, with a radius of 70 μm (Rorsman and Trube, 1986, Fig. 1a). C: Recording from an isolated β cell (Rorsman and Trube, 1986, Fig. 2c).

by

$$g_{K,Ca} = \bar{g}_{K,Ca} \frac{c}{K_d + c}, \tag{9.29}$$

where c, as usual, denotes $\left[Ca^{2+}\right]$. This can be derived from a simple channel model in which the channel has one closed state and one open state, switching from closed to open upon the binding of a single Ca^{2+} ion. Thus

$$C + Ca^{2+} \underset{k_-}{\overset{k_+}{\rightleftharpoons}} O, \tag{9.30}$$

where C is a closed channel and O is an open one. If the rate constants k_+ and k_- are both large compared to the other kinetic parameters of the model, then

$$[O] = \frac{k_+ \left[Ca^{2+}\right]}{k_-}[C] \tag{9.31}$$

$$= \frac{\left[Ca^{2+}\right]}{K_d}(1 - [O]), \tag{9.32}$$

where $K_d = k_-/k_+$. Hence $[O] = \left[Ca^{2+}\right]/(K_d + \left[Ca^{2+}\right])$, from which (9.29) follows.

In the supercell model, (9.30) is interpreted as a Markov rather than a deterministic process, with k_+ denoting the probability per unit time that the closed channel switches to the open state, and similarly for k_-. Thus, the mean open and closed times are, respectively, $1/k_-$ and $1/k_+$. If we let $\langle N_o \rangle$ and $\langle N_c \rangle$ denote the mean number of open channels or closed channels respectively, then at equilibrium we have

$$\frac{\langle N_o \rangle}{\langle N_c \rangle} = \frac{k_+}{k_-}. \tag{9.33}$$

To incorporate the Ca^{2+} dependence of the channel we make

$$\frac{k_+}{k_-} = \frac{\left[Ca^{2+}\right]}{K_d}, \tag{9.34}$$

which gives the steady-state mean proportion of open channels as

$$\langle p \rangle = \frac{\langle N_o \rangle}{\langle N_o \rangle + \langle N_c \rangle} = \frac{\left[Ca^{2+}\right]}{K_d + \left[Ca^{2+}\right]} = \frac{c}{K_d + c}. \tag{9.35}$$

The associated stochastic model is similar to (9.6)–(9.8), with the major difference being that the Ca^{2+}-sensitive K^+ current is governed by the above stochastic process. In other words, p is a random variable denoting the proportion of open channels in a single cell, and is calculated (as a function of time) by numerical simulation of the Markov process described by (9.30). Thus,

$$C_m \frac{dV}{dt} = -I_{Ca} - I_K - \bar{g}_{K,Ca} p (V - V_K), \tag{9.36}$$

$$\tau_n(V) \frac{dn}{dt} = \lambda(n_\infty(V) - n), \tag{9.37}$$

$$\frac{dc}{dt} = f(-\alpha I_{Ca} - k_c c), \tag{9.38}$$

C_m	=	5.3 pF	$\bar{g}_{\mathrm{K,Ca}}$	=	30 nS
$\bar{g}_{\mathrm{K}}$	=	2.5 nS	$\bar{g}_{\mathrm{Ca}}$	=	1.4 nS
V_{Ca}	=	110 mV	V_{K}	=	-75 mV
k_c	=	0.03 ms^{-1}	f	=	0.001
α	=	4.5 μM/C	K_d	=	100 μM
$\bar{\tau}_n$	=	60 ms			

Table 9.4: Parameters of the supercell model for electrical bursting in clusters of pancreatic β cells.

where $I_{\mathrm{Ca}} = \bar{g}_{Ca} m_\infty(V) h(V)(V - V_{\mathrm{Ca}})$ and $I_{\mathrm{K}} = \bar{g}_{\mathrm{K}} n(V - V_{\mathrm{K}})$. The functions appearing in the supercell model are

$$m_\infty(V) = \frac{1}{1 + \exp\left[\frac{4-V}{14}\right]}, \tag{9.39}$$

$$n_\infty(V) = \frac{1}{1 + \exp\left[\frac{-15-V}{5.6}\right]}, \tag{9.40}$$

$$\tau_n(V) = \frac{\bar{\tau}_n}{\exp\left[\frac{V+75}{65}\right] + \exp\left[\frac{-V-75}{20}\right]}, \tag{9.41}$$

$$h(V) = \frac{1}{1 + \exp\left[\frac{V+10}{10}\right]}. \tag{9.42}$$

The other parameters of the model are summarized in Table 9.4. Note that although the form of the model is similar to that of the β cell model, the details have been changed to agree with more recent experimental data. In particular, m_∞ appears only to the first power instead of the third, while n also appears to the first power. Further, the I–V curve of the open Ca^{2+} channel is assumed to be of the form $h(V)(V - V_{\mathrm{Ca}})$, and $h(V)$ is chosen to fit the experimentally observed I–V curve. This has an effect similar to that of the function $h_\infty(V)$ that was used in the β cell model.

One of the most important features of the stochastic model is that the conductance of a single K–Ca channel is an order of magnitude greater than the conductances of the other two channels (Table 9.4). However, each cell contains only a small number of K–Ca channels. Thus, the opening of a single K–Ca channel in an isolated cell has a disproportionately large effect on the membrane potential of the cell; the stochastic nature of each K–Ca channel then causes seemingly random fluctuations in membrane potential (Fig. 9.12).

However, when identical cells are coupled by gap junctions with zero resistance, different behavior emerges. First, since the gap junctions are assumed to have zero resistance, and thus the entire group of cells has the same membrane potential, it is not necessary to treat each cell explicitly. Second, the membrane capacitance and the ionic currents depend on the surface area of the cluster and are therefore
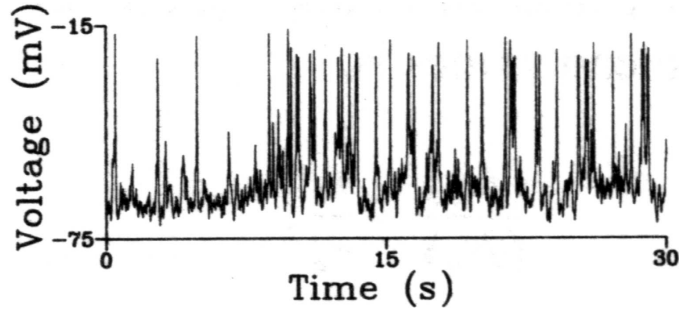
Figure 9.12: Behavior of an isolated cell in the supercell stochastic model. Because of the stochastic nature of each high-conductance K–Ca channel, and because there are few channels in a single cell, no organized bursting appears. (Sherman et al., 1988, Fig. 6).

proportional to the number of cells in the cluster, N_{cell}. Finally, the total number of K–Ca channels is proportional to the total number of cells in the cluster, but the effect of each individual channel on the membrane potential of the cluster is proportional to $1/N_{\text{cell}}$. It follows that the cluster of cells behaves in the same way as a very large single cell with many K–Ca channels, each with a smaller conductance. We expect the cluster of cells to behave in the same manner as a deterministic single-cell model in the limit as $N_{\text{cell}} \longrightarrow \infty$.

To see that this is what happens, we let $\hat{g}$ denote the conductance of a single K–Ca channel and let N_o^i denote the number of open K–Ca channels in the ith cell. Then

$$N_{\text{cell}}C_m\frac{dV}{dt} = -N_{\text{cell}}(I_{\text{Ca}} + I_{\text{K}}) - \hat{g}\sum_{i=1}^{N_{\text{cell}}} N_o^i(V - V_{\text{K}}), \qquad (9.43)$$

and so

$$C_m\frac{dV}{dt} = -(I_{\text{Ca}} + I_{\text{K}}) - \hat{g}\bar{N}\frac{1}{N_{\text{cell}}\bar{N}}\sum_{i=1}^{N_{\text{cell}}} N_o^i(V - V_{\text{K}}) \qquad (9.44)$$

$$= -(I_{\text{Ca}} + I_{\text{K}}) - \bar{g}_{\text{K,Ca}}p(V - V_{\text{K}}), \qquad (9.45)$$

where $\bar{N}$ is the number of K–Ca channels per cell, or the channel density, and where, as before, $\bar{g}_{\text{K,Ca}} = \hat{g}\bar{N}$ is the total K–Ca conductance per cell. Note that in the supercell model $p = \frac{1}{N_{\text{cell}}\bar{N}}\sum_{i=1}^{N_{\text{cell}}} N_o^i$ must be interpreted as the fraction of open channels in the cluster, rather than the fraction of open channels in a single cell. The mean of p is the same in both these cases, but as N_{cell} increases, the standard deviation of p decreases, leading to increasingly regular behavior. As before, p must be obtained by direct simulation of the Markov process. Simulations for different numbers of cells are shown in Fig. 9.13. Clearly, as the size of the cluster increases, bursting becomes more regular.

One obvious simplification in the supercell model is the assumption that the gap junctions have zero resistance and thus that every cell in the cluster has the
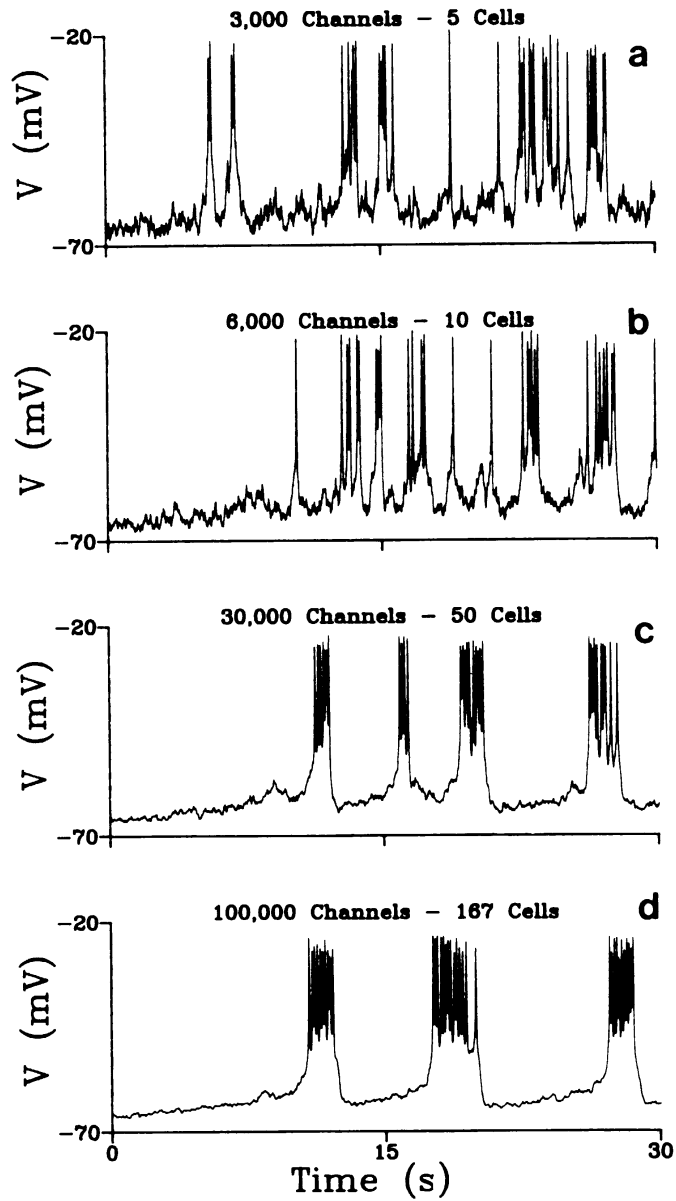
Figure 9.13: Numerical simulations of the supercell model for a cluster of cells ranging in size from 5 to 167 cells. As the size of the cluster increases, more organized bursting appears. (Sherman et al., 1988, Fig. 8.)
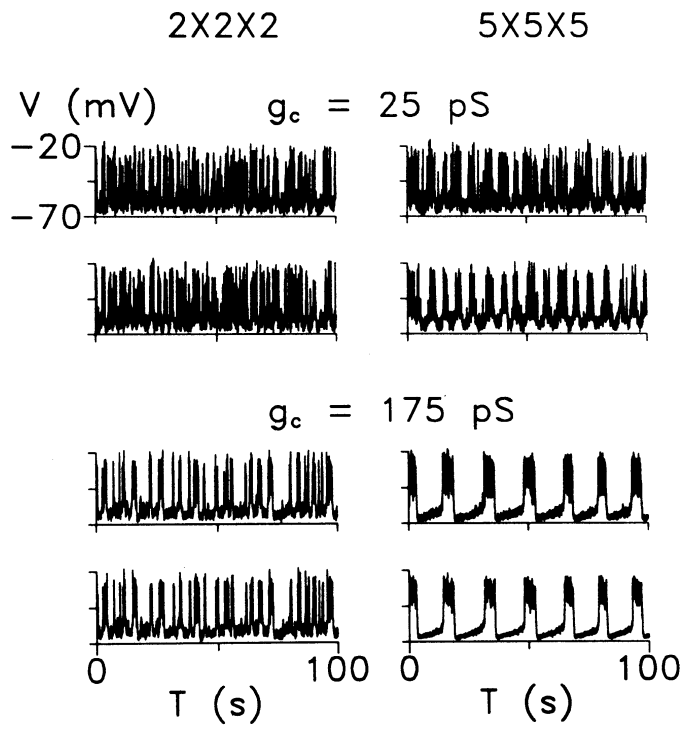
Figure 9.14: Numerical simulations of the multicell model, in which the cells in the cluster are coupled by gap junctions with finite conductance. Results are shown for two cells (upper and lower traces in each pair) from two different cluster sizes ($2 \times 2 \times 2$ cells and $5 \times 5 \times 5$ cells) and two different junctional conductances. (Sherman and Rinzel, 1991, Fig. 3.)

same membrane potential. We can relax this assumption by modeling the cluster
as individual cells coupled by gap junctions with finite conductance (Sherman and
Rinzel, 1991). An individual cell, cell i say, satisfies a voltage equation of the form

$$C_m \frac{dV_i}{dt} = -I_{\text{Ca}}(V_i) - I_{\text{K}}(V_i, n_i) - \bar{g}_{\text{K,Ca}} p_i (V_i - V_{\text{K}}) - g_c \sum_j d_{ij}(V_i - V_j), \quad (9.46)$$

where g_c is the gap junction conductance and where d_{ij} are coupling coefficients,
with value one if cells i and j are coupled, and zero otherwise. As $g_c \to \infty$, the
sum $\sum_j d_{ij}(V_i - V_j)$ must approach zero for every cell in the cluster. If all the
cells are connected by some connecting path (so that there are no isolated cells or
subclusters), then every cell must have the same voltage (see Exercise 9). Thus, in
the limit of infinite conductance,

$$V_i \longrightarrow \bar{V} = \frac{1}{N_{\text{cell}}} \sum_{j=1}^{N_{\text{cell}}} V_j. \qquad (9.47)$$

For large but finite coupling, $V_i = \bar{V} + O(\frac{1}{g_c})$. If we sum (9.46) over all the cells in
the cluster and divide by N_{cell}, we find

$$
\begin{aligned}
C_m \frac{d\bar{V}}{dt} &= -I_{\text{Ca}}(\bar{V}) - I_{\text{K}}(\bar{V}, n) - \bar{g}_{\text{K,Ca}} \frac{1}{N_{\text{cell}}} \sum_{j=1}^{N_{\text{cell}}} p_j (\bar{V} - V_{\text{K}}) + O\left(\frac{1}{N_{\text{cell}}}\right) \quad (9.48) \\
&= -I_{\text{Ca}}(\bar{V}) - I_{\text{K}}(\bar{V}, n) - \bar{g}_{\text{K,Ca}} \bar{p}(\bar{V} - V_{\text{K}}) + O\left(\frac{1}{N_{\text{cell}}}\right), \qquad (9.49)
\end{aligned}
$$

where $\bar{p} = \frac{\sum_i p_i}{N_{\text{cell}}} = \frac{\sum_i p_i \bar{N}}{N_{\text{cell}} N}$ is the proportion of open K–Ca channels in the cluster.
Hence, the model with finite gap-junctional conductance (the *multicell* model) turns
into the supercell model as the gap-junctional conductance and the number of cells
in the cluster approaches infinity.

As expected, synchronized bursting appears as the number of cells in the cluster
increases and the coupling strength increases. Both strong enough coupling and a
large enough cluster size are required to achieve regular bursting. This is illustrated
in Fig. 9.14, where we show numerical simulations for two different cluster sizes and
two different coupling strengths. However, what is not expected (and is therefore
particularly interesting) is that there is a coupling strength at which the length of
the burst period is maximized. The reasons for this have been analyzed in depth in
a simpler system consisting of two coupled cells (Sherman, 1994).

9.1.5   A Qualitative Bursting Model

Just as the essential behaviors of the Hodgkin-Huxley model can be distilled into
the simpler FitzHugh-Nagumo model, giving a great deal of insight into the mech-
anisms underlying excitability, so too can this model for bursting be simplified to
a polynomial model, without losing the essential properties (Hindmarsh and Rose,
1982, 1984; Pernarowski, 1994).
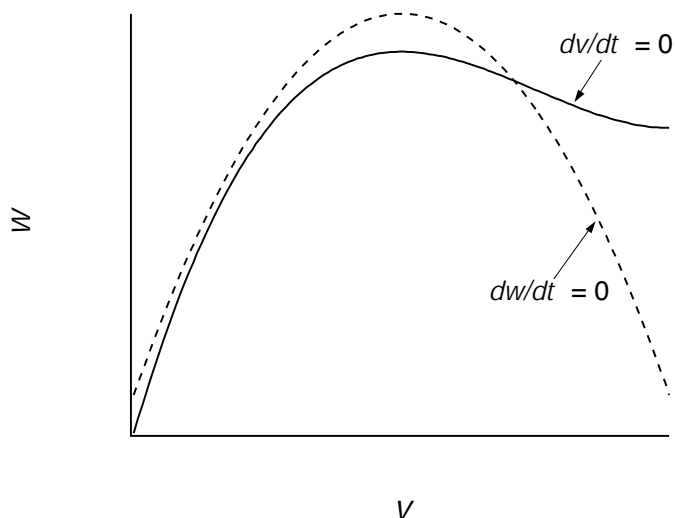
Figure 9.15: Sketch of typical nullclines in the modified FitzHugh–Nagumo model.

Suppose we let v denote the excitatory variable and w the recovery variable (as in Chapter 5). Then, the model equations are

$$\frac{dv}{dt} = \alpha(\beta w - f(v) + I), \tag{9.50}$$

$$\frac{dw}{dt} = \gamma(g(v) - \delta w), \tag{9.51}$$

where I is the applied current and α, β, γ, and δ are constants. As in the FitzHugh–Nagumo model $f(v)$ is cubic, but unlike the FitzHugh–Nagumo model $g(v)$ is not a linear function. In fact, as can be seen from Fig. 9.15, the w nullcline curves around to lie close to the v nullcline to the left of the oscillatory critical point. (Of course, this occurs only for a range of values of the applied current I for which oscillations occur.) As a result, between the peaks of the oscillation, the limit cycle trajectory lies close to both nullclines, and thus both $\dot{v}$ and $\dot{w}$ are small over that portion of the cycle. It follows that the intervals between the spikes are large.

With only a slight change, this modified FitzHugh–Nagumo model can be used as a model for bursting. Following the discussions in this chapter, it should come as no surprise that bursting can arise in this model when bistability is introduced. This can be done by deforming the $\dot{w} = 0$ nullcline so that it intersects the $\dot{v} = 0$ nullcline in three places rather than only one. Since the nullclines lie close to one another in the original model, only a slight deformation is required to create two new critical points. With this change, the new model equations are

$$\frac{dv}{dt} = \alpha(\beta w - f(v) + I), \tag{9.52}$$

$$\frac{dw}{dt} = \gamma(g(v) + h(v) - \delta w), \tag{9.53}$$
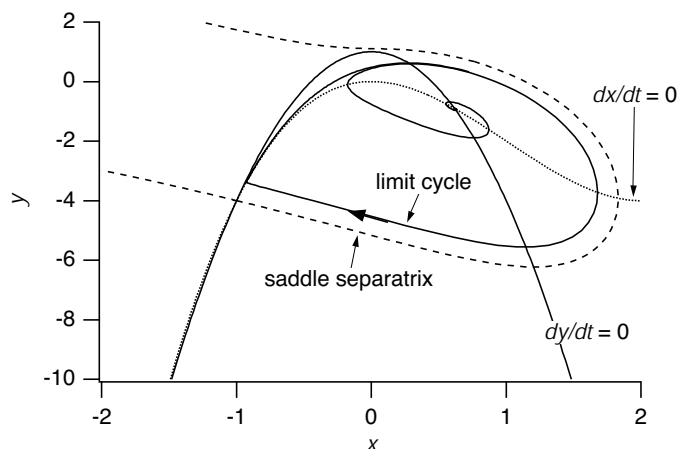
Figure 9.16: Phase-plane of the polynomial bursting model.

where $h(v)$ is chosen such that the nullclines intersect in three places. For convenience, we scale and nondimensionalize the model by introducing the variables $T = \gamma\delta t$, $x = v$, and $y = \alpha\beta w/(\gamma\delta)$, in terms of which variables the model becomes

$$\frac{dx}{dT} = y - \tilde{f}(x), \tag{9.54}$$

$$\frac{dy}{dT} = \tilde{g}(x) - y, \tag{9.55}$$

where $\tilde{f}(x) = \alpha f(x)/(\gamma\delta)$ and $\tilde{g}(x) = \alpha\beta[g(x) + h(x)]/(\gamma\delta^2)$. Note that the form of the model is the same as that of the FitzHugh–Nagumo model, although the functions appearing in the model are different. With appropriate choices for $\tilde{f}$ and $\tilde{g}$ the model exhibits bistability; we use the specific functions

$$\frac{dx}{dT} = y - x^3 + 3x^2 + I, \tag{9.56}$$

$$\frac{dy}{dT} = 1 - 5x^2 - y, \tag{9.57}$$

the phase-plane of which is shown in Fig. 9.16 for $I = 0$.

There are three critical points: a stable node to the left at $x = -\frac{1}{2}(1 + \sqrt{5})$, (the resting state), a saddle point in the middle at $x = -1$, and an unstable node to the right at $x = \frac{1}{2}(-1 + \sqrt{5})$, which is surrounded by a stable limit cycle. As in the models of bursting discussed above, the stable manifold of the saddle point acts as a threshold; if the perturbation from the resting state is large enough that the stable manifold is crossed, the trajectory approaches the stable limit cycle. Smaller perturbations die away to the resting state. This is called *triggered firing*. This bistable phase-plane is essentially the same as the phase-plane shown in Fig. 9.3A, and (9.56)–(9.57) are a simple realization of the qualitative theory developed by Rinzel and others.
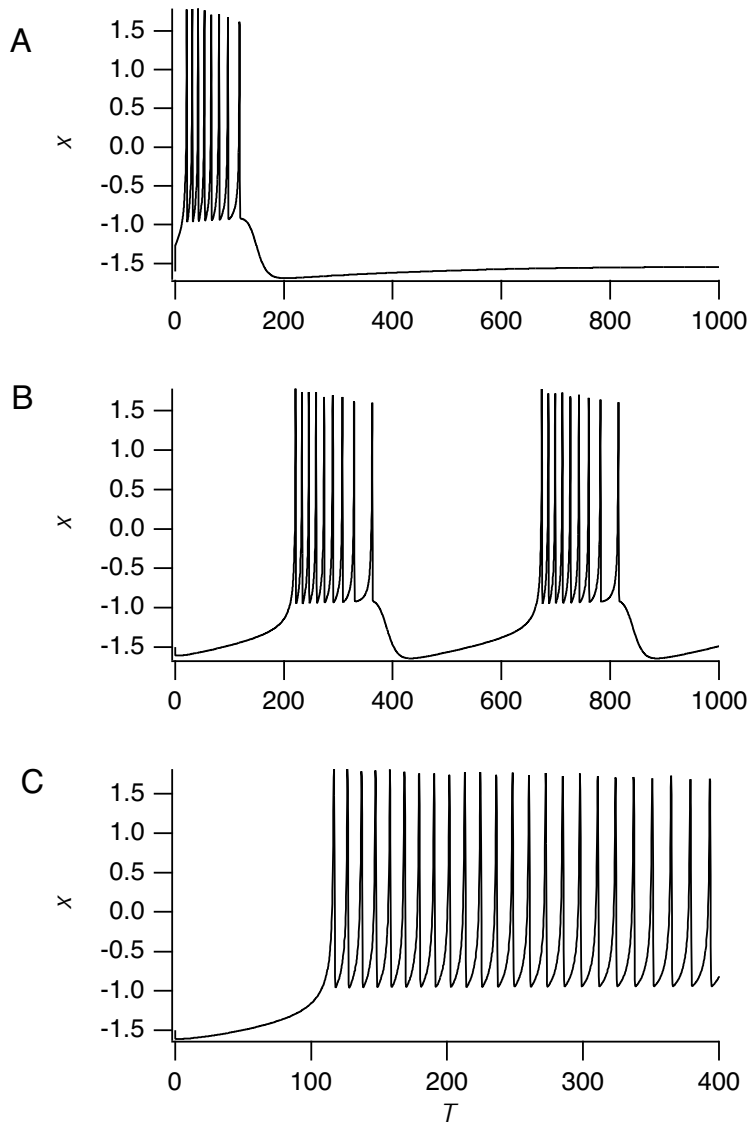
Figure 9.17: Bursting in the polynomial model, calculated numerically from (9.58)–(9.60) for three values of the applied current. A: $I = 0.4$; B: $I = 2$; C: $I = 4$.

To generate bursting in addition to bistability, it is also necessary to have a slow variable so that the voltage can be moved in and out of the bistable regime. This is accomplished in this model by introducing a third variable that modulates the applied current I on a slower time scale. Thus,

$$\frac{dx}{dT} = y - x^3 + 3x^2 + I - z, \tag{9.58}$$

$$\frac{dy}{dT} = 1 - 5x^2 - y, \tag{9.59}$$

$$\frac{dz}{dT} = r[s(x - x_1) - z], \tag{9.60}$$

where $x_1 = -\frac{1}{2}(1 + \sqrt{5})$ is the x-coordinate of the resting state in the two-variable model (9.56)–(9.57), and where I, as before, is the applied current. When $r = 0.001$ and $s = 4$, (9.58)–(9.60) exhibit type I bursting (Fig. 9.17), arising via the same mechanism as in the Rinzel–Lee simplification of the Chay–Keizer model.

9.1.6   Bursting Oscillations in Other Cell Types

As can be seen in Fig. 9.18, bursting oscillations occur not only in pancreatic β cells, but also in a wide range of other types of neurons and neuroendocrine cells. The type of bursting that occurs is also widely variable. Because of the enormously complex dynamical behavior exhibited in these bursting patterns, they have been a popular topic of study among mathematicians, and the theoretical study of bursting oscillations has, by now, far outstripped our corresponding physiological knowledge.

Bursting in the Aplysia neuron

Another well-studied example of bursting is found in the Aplysia R-15 neuron. Analysis of a detailed model by Plant (1981) shows that the mathematical structure of this bursting oscillator is different from that in the β cell model (Rinzel and Lee, 1987). The β cell model has two fast variables, one slow variable, bistability, and a hysteresis loop. At the end of a burst, a homoclinic bifurcation is crossed, leading to an increasing period through the burst. Plant's model, on the other hand, has no bistability, with bursting arising from the presence of two slow variables with their own oscillation. A homoclinic bifurcation is crossed at the beginning and the end of the burst, and so the instantaneous period of the burst oscillations starts high, decreases, and then increases again. The fact that the period is roughly a parabolic function of time has led to the name *parabolic* bursting.

Plant's parabolic bursting model is similar in some respects to the β cell model, incorporating Ca^{2+}-activated K^+ channels and voltage-dependent K^+ channels. However, it also includes a voltage-dependent Na^+ channel that activates and inactivates in typical Hodgkin–Huxley fashion and a slowly activating Ca^{2+} current. The Na^+, K^+, and leak currents form the fast subsystem

$$
\begin{aligned}
C_m \frac{dV}{dt} = \ & -\bar{g}_{Na} m_\infty^3(V) h(V - V_{Na}) - \bar{g}_{Ca} x (V - V_{Ca}) \\
& -\left(\bar{g}_K n^4 + \frac{\bar{g}_{K,Ca} c}{0.5 + c} \right) (V - V_K) - \bar{g}_L (V - V_L),
\end{aligned} \tag{9.61}
$$
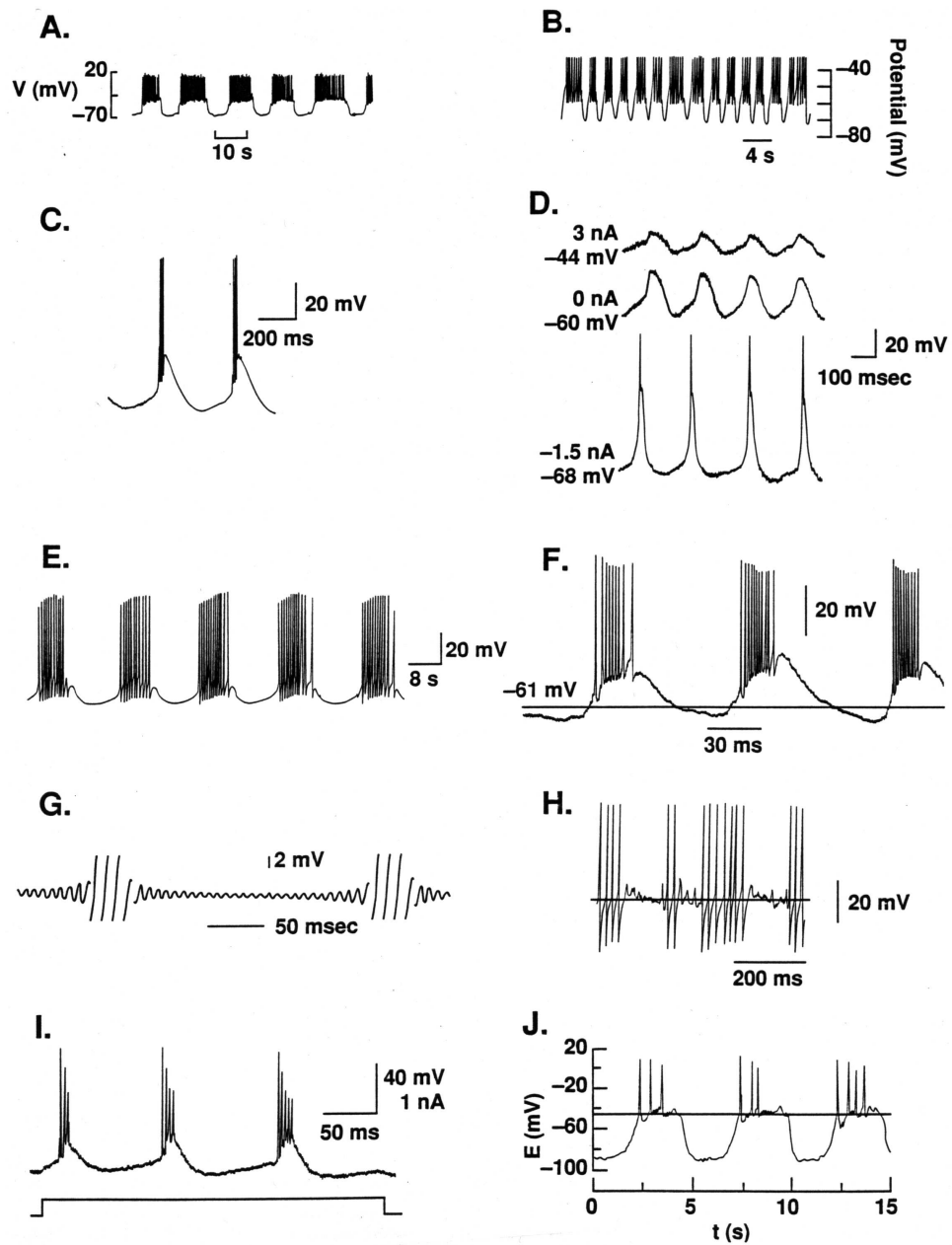
Figure 9.18: Electrical bursting in a range of different cell types. A: Pancreatic β cell. B: Dopamine-containing neurons in the rat midbrain. C: Cat thalamocortical relay neuron. D: Guinea pig inferior olivary neuron. E: *Aplysia* R15 neuron. F: Cat thalamic reticular neuron. G: *Sepia* giant axon. H: Rat thalamic reticular neuron. I: Mouse neocortical pyramidal neuron. J: Rat pituitary gonadotropin-releasing cell. (Wang and Rinzel, 1995, Fig. 2.)

$$\tau_h(V)\frac{dh}{dt} = h_\infty(V) - h, \tag{9.62}$$

$$\tau_n(V)\frac{dn}{dt} = n_\infty(V) - n, \tag{9.63}$$

while the Ca^{2+} current and its activation x form the slow subsystem

$$\tau_x\frac{dx}{dt} = x_\infty(V) - x, \tag{9.64}$$

$$\frac{dc}{dt} = f(k_1 x(V_{Ca} - V) - c). \tag{9.65}$$

The voltage dependence of the variables α_w and β_w with $w = m, n$, or h is of the form

$$\frac{C_1\exp(\frac{V - V_0}{C_2}) + C_3(V - V_0)}{1 + C_4\exp(\frac{V - V_0}{C_5})}, \tag{9.66}$$

in units of ms^{-1}, and the asymptotic values $w_\infty(V)$ and time constants $\tau_w(V)$ are of the form

$$w_\infty(V) = \frac{\alpha_w(\tilde{V})}{\alpha_w(\tilde{V}) + \beta_w(\tilde{V})} \tag{9.67}$$

$$\tau_w(V) = \frac{1}{\lambda\left(\alpha_w(\tilde{V}) + \beta_w(\tilde{V})\right)} \tag{9.68}$$

for $w = m$, n, or h (although $\tau_m(V)$ is not used), with $\tilde{V} = c_1 V + c_2$, $c_1 = 127/105$, $c_2 = 8265/105$. The constants $C_1, \ldots, C_5$ and V_0 are displayed in Table 9.6. Finally,

$$x_\infty(V) = \frac{1}{\exp\{-0.15(V + 50)\} + 1}, \tag{9.69}$$

and $\tau_x = 235$ ms.

The parameter values of the Plant model for parabolic bursting are given in Tables 9.5 and 9.6.

For a fixed x, the bifurcation diagram of the fast subsystem as c varies is shown in Fig. 9.19. Note that in general, V_{ss} is a function of both c and x, and therefore the fast subsystem is properly described by a bifurcation surface. However, since surfaces are more difficult to draw and understand, we first examine a cross-section of the bifurcation surface for fixed x and then discuss how the important points behave as x varies. As before, c_{hb} denotes the value of c at which a Hopf bifurcation to periodic orbits occurs, and c_{hc} denotes the value of c where the periodic solutions disappear in a homoclinic bifurcation. The bifurcation diagram is similar to that of the fast subsystem of the β-cell model (Fig. 9.4), except that the branch of periodic solutions around the upper branch of the Z-shaped curve does not extend past the lower "knee" of the Z-shaped curve. In fact, c_{hc} appears to coincide with the saddle-node bifurcation at the knee of the Z-shaped curve. Hence, there is no bistability in the model, and a simple one-variable slow subsystem is insufficient to give bursting, because it is unable to move the fast subsystem in and out of the region where the

C_m	=	1 μF/cm^2	$\bar{g}_{\text{K,Ca}}$ = 0.03 mS/cm^2
$\bar{g}_{\text{Ca}}$	=	0.004 mS/cm^2	V_{Ca} = 140 mV
$\bar{g}_{\text{Na}}$	=	4.0 mS/cm^2	V_{Na} = 30 mV
$\bar{g}_{\text{K}}$	=	0.3 mS/cm^2	V_{K} = -75 mV
$\bar{g}_{\text{L}}$	=	0.003 mS/cm^2	V_{L} = -40 mV
f	=	0.0003 ms^{-1}	k_1 = 0.0085 mV^{-1}
λ	=	1/12.5	

Table 9.5: Parameters of the Plant model for parabolic bursting.

	C_1	C_2	C_3	C_4	C_5	V_0
α_m	0	—	0.1	-1	-10	50
β_m	4	-18	0	0	—	25
α_h	0.07	-20	0	0	—	25
β_h	1	10	0	1	10	55
α_n	0	—	0.01	-1	-10	55
β_n	0.125	-80	0	0	—	45

Table 9.6: Defining values for the rate constants α and β in the Plant parabolic bursting model.
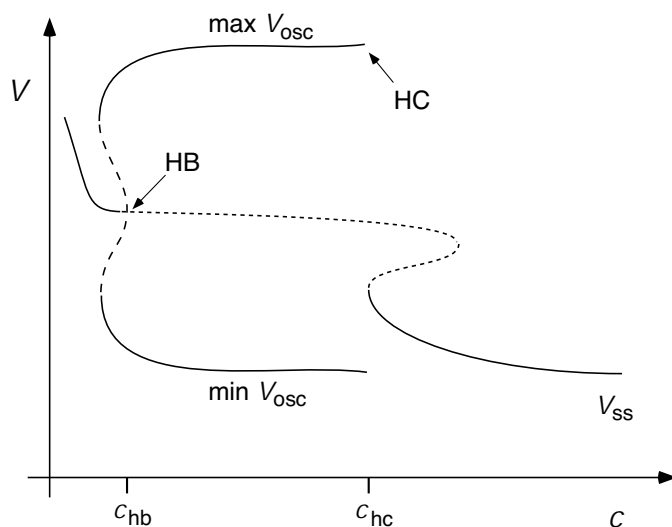
Figure 9.19: Sketch (not to scale) of the bifurcation diagram of the fast subsystem of the parabolic bursting model, with $x = 0.7$. The notation is similar to that used in Fig. 9.4. Note that the homoclinic bifurcation coincides with the lower knee of the Z-shaped curve of steady states and that the oscillations arise via a subcritical Hopf bifurcation instead of a supercritical one as in the β-cell model.

oscillations occur, as in the β-cell model. However, because the parabolic bursting model has two slow variables, x and c, a slow oscillation in these variables moves c backward and forward across the homoclinic bifurcation, leading to bursts of fast oscillations during one portion of the slow oscillations.

In Fig. 9.20A we plot c_{hc} and c_{hb} as x varies. Note that the curves in Fig. 9.19 correspond to taking a cross-section of Fig. 9.20 for a fixed value of x (the dashed line). In region J_{ss} there is a single stable fixed point of the fast subsystem, while in region J_{osc} the fast subsystem has stable oscillations. Now suppose that the slow subsystem has a periodic solution. In the parabolic bursting model, slow oscillations do not occur independently of the fast subsystem but rely on the interaction between the fast and slow variables, the details of which do not concern us here. Similar results are obtained when the slow variables oscillate independently of the fast variables, acting as a periodic driver of the fast subsystem (Kopell and Ermentrout, 1986). In any case, these oscillations correspond to closed curves in the (x, c) phase-plane, three possible examples of which are shown in Fig. 9.20B. In case **a**, the dynamics of x and c are such that the slow periodic solution lies entirely within the region J_{ss}; i.e., the fast subsystem "lives" entirely on the lower branch of the Z-shaped curve and does not oscillate. In case **b**, the slow oscillation crosses the line of homoclinic bifurcations into the region J_{osc}, in which region the fast subsystem oscillates rapidly. In case **c**, the slow oscillations are so arranged that the system spends only a small amount of time in region J_{osc}, but not long enough to generate a burst of oscillations. Thus, by tuning the parameters of the underlying slow
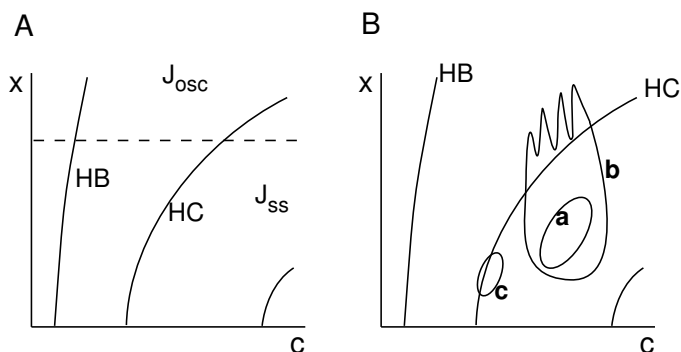
Figure 9.20: A: The Hopf and homoclinic bifurcations in the (x, c) plane, i.e., a projection of the bifurcation surface onto the (x, c) plane. The bifurcation diagram in the previous figure corresponds to a cross-section of this figure for a fixed value of x, as denoted by the dashed line. In the region (labeled J_{osc}) between the two bifurcations, a stable limit cycle exists, while to the right of the homoclinic bifurcation (J_{ss}) there is a unique stable steady state. The rightmost (unlabeled) curve corresponds to where the middle branch of the Z-shaped curve meets the upper branch. B: Three typical slow oscillations in x and c.

oscillation, different patterns of bursts can be obtained from one model. We have already mentioned the parabolic nature of the period of the fast oscillations. This is easily understood in terms of the foregoing analysis. For a burst to occur, the slow oscillation must cross the line of homoclinic bifurcations both at the beginning and at the end of the burst. Since the period of the limit cycle tends to infinity at the homoclinic bifurcation, the interspike interval is large at both the beginning and end of the burst. However, as the slow periodic orbit penetrates further into region J_{osc}, away from the homoclinic bifurcation, the interspike interval decreases.

Classification of bursting oscillations

The earliest classification scheme for the different bursting mechanisms was proposed by Rinzel (1987) and later extended by Bertram et al. (1995). Originally, bursting oscillations were grouped into three classes: type I, with bursts arising from hysteresis and bistability as in the β cell model; type II, with bursts arising from an underlying slow oscillation, as in the Aplysia R-15 neuron; and type III, with bursts arising from a subcritical Hopf bifurcation. However, more recent studies (Izhikevich, 2000) have presented a huge array of different possible bursting behaviors, depending on the underlying bifurcations in the steady state and periodic branches. Many of these possible bursters have no known biophysical implementation.

9.2   Hypothalamic and Pituitary Cells

In pancreatic β cells, the interaction of membrane-based electrical excitability with ER-based Ca^{2+} dynamics is crucial for the generation of fast bursting oscillations. Similar interactions are also known to be important in many cell types, including many types of hypothalamic neurons and pituitary cells. The close relationship between the hypothalamus and pituitary is discussed in Chapter 16. Briefly, hypothalamic neurons secrete hormones which typically travel a short distance along the inferior hypophyseal artery and the portal vein to the pituitary to act there on specific target cells. For example, gonadotropin-releasing hormone (GnRH) is secreted from GnRH cells in the hypothalamus; after traveling to the pituitary it stimulates the release of gonadotropin from pituitary gonadotrophs.

There are already a number of detailed models of electrical and Ca^{2+} excitability in hypothalamic or pituitary cells, and there are sure to be many more as our experimental understanding advances. For example, the release of corticotropin from pituitary corticotrophs in response to corticotropin-releasing hormone (CRH) has been studied in detail by LeBeau et al. (1997, 1998), Shorten et al. (2000) and Shorten and Wall (2000), while the interaction of Ca^{2+} and membrane potential in vasopressin hypothalamic neurons has been studied by Roper et al. (2003, 2004).

9.2.1   The Gonadotroph

One of the best models of this type is an earlier model of the gonadotroph (Li et al., 1994, 1995, 1997) and it is this one that we describe in more detail here. In gonadotrophs, Ca^{2+} spiking occurs in two different ways. First, spontaneous action potentials lead to the influx of Ca^{2+} through voltage-gated channels, and thus Ca^{2+} spikes. Second, in response to the agonist GnRH, gonadotrophs produce inositol trisphosphate (Chapter 7) which releases Ca^{2+} from the endoplasmic reticulum (ER) and leads to oscillations in the cytosolic Ca^{2+} concentration. Both the electrophysiological and agonist-induced Ca^{2+} signaling pathways are well-characterized experimentally (Stojilković and Catt, 1994).

Similarly to the model of the pancreatic β cell, the gonadotroph model consists of two pieces; a model of Hodgkin-Huxley type of the membrane electrical potential, and a model of the intracellular Ca^{2+} dynamics, including IP_3-induced Ca^{2+} release from the ER. Thus, the gonadotroph model is essentially a combination of the models of Chapters 5 and 7 (see Exercise 3). It is, however, more complicated in application, as Li et al. modeled the cell as a spherically symmetric region, with a gradient of Ca^{2+} from the plasma membrane to the interior of the cell. Because the components of the model are no different from what has come before, and because a detailed reproduction of the results is complicated by the inclusion of Ca^{2+} diffusion, we do not present the model in complete detail here, but give instead only an overview of its construction and behavior.

The membrane model

The membrane potential is modeled in the usual way:

$$C\frac{dV}{dt} = -I_{\text{Ca,T}} - I_{\text{Ca,L}} - I_{\text{K}} - I_{\text{K,Ca}} - I_{\text{L}}, \tag{9.70}$$

where the Ca^{2+} current has been divided into T-type and L-type current, I_{K} is the current through K^+ channels, $I_{\text{K,Ca}}$ is the current through Ca^{2+}-sensitive K^+ channels, and I_{L} is a leak current.

Each of these currents is modeled in Hodgkin-Huxley fashion, in much the same way as was discussed above, in the model of the pancreatic β cell. Most importantly, the conductance of the Ca^{2+}-sensitive K^+ channel is assumed to be an increasing function of c_R, the concentration of Ca^{2+} at the plasma membrane. Thus,

$$I_{\text{K,Ca}} = g_{\text{K,Ca}}\frac{c_R^4}{c_R^4 + K_c^4}\phi_K(V), \tag{9.71}$$

where $\phi_K(V)$ denotes the Goldman-Hodgkin-Katz current-voltage relationship (Chapter 3) used here instead of the linear one used in the pancreatic β cell model.

The calcium model

Let c denote the intracellular free concentration of Ca^{2+}, and let c_e denote the free concentration of Ca^{2+} in the ER. Note that both c and c_e are functions of r, the radial distance from the center of the spherically symmetric cell. In the body of the cell, Ca^{2+} can enter the cytoplasm only from the ER, through IP_3 receptors, and can leave the cytoplasm only via the action of SERCA ATPase pumps in the ER membrane. However, on the boundary of the cell, Ca^{2+} can enter or leave via Ca^{2+} currents or plasma membrane Ca^{2+} ATPase pumps.

The equations for c and c_e are thus (Chapter 7, Section 7.3)

$$\frac{\partial c}{\partial t} = D\nabla^2 c + J_{\text{IPR}} - J_{\text{serca}}, \tag{9.72}$$

$$\frac{\partial c_e}{\partial t} = D_e\nabla^2 c_e - \gamma(J_{\text{IPR}} - J_{\text{serca}}), \tag{9.73}$$

where, as usual, D and D_e are the diffusion coefficients of c and c_e respectively, and γ is the scale factor relating ER volume to cytoplasmic volume. On the boundary of the cell, i.e., at $r = R$, we have

$$D\frac{\partial c}{\partial r}\bigg|_{r=R} = -\alpha(I_{\text{Ca,T}} + I_{\text{Ca,L}}) - J_{\text{pm}}, \tag{9.74}$$

$$\frac{\partial c_e}{\partial r}\bigg|_{r=R} = 0, \tag{9.75}$$

where J_{pm} denotes the flux out of the cell due to the action of plasma membrane Ca^{2+} ATPase pumps. The scale factor $\alpha = 1/(2FA_{\text{cell}})$, where A_{cell} is the surface area of the cell, converts the current (in coulombs per second) to a mole flux density (moles per area per second).

The flux through the IP$_3$ receptor, J_{IPR}, is modeled by the Li-Rinzel simplification of the De Young-Keizer model (see Chapter 7 and Exercise 3), while the ATPase pump fluxes, J_{serca} and J_{pm}, are modeled by Hill functions. The exact form of the model equations and the parameter values can be found in the appendix of Li et al. (1997).

Results

When this model is solved for a variety of agonist concentrations (i.e., a variety of IP$_3$ concentrations), the agreement with experimental data is impressive (Fig. 9.21). Before the addition of agonist the cells exhibit continuous spiking; once agonist is applied the frequency of spiking drops dramatically, changing to a more complex burst pattern. At the highest agonist concentrations, bursting is initially suppressed by the agonist, although spiking eventually reappears.

In all cases, the spiking frequency is initially greatly decreased by the agonist, but recovers gradually. This recovery of the spike frequency is an interesting demonstration of the importance of the amount of Ca^{2+} in the ER.

In Fig. 9.22 we show V, c and c_e during the response to agonist stimulation (where c and c_e are averaged over the entire cell). During phase SS-1, before the addition of agonist, the cell exhibits tonic spiking. Upon addition of 0.42 μM IP$_3$, c starts to oscillate and the voltage spikes more slowly (phase T-1). The slowdown of the voltage spiking is caused by the much larger and slower Ca^{2+} spikes, which activate the Ca^{2+}-sensitive K$^+$ current to a much greater extent, thus making it more difficult for a voltage spike to occur. However, as time goes on, Ca^{2+} is lost from the cell by the action of the plasma membrane ATPase (recall that, because of the spatially distributed nature of the model, the concentration of Ca^{2+} is higher at the membrane than in the interior of the cell, which increases the rate at which Ca^{2+} is lost to the outside by the operation of the pump. This overall decline in $\left[\mathrm{Ca}^{2+}\right]$ manifests itself in two principal ways; first, the concentration in the ER declines slowly, and secondly, the baseline of the Ca^{2+} spikes gradually decreases. It is this decrease that causes the slow increase in the frequency of the voltage spikes, as $I_{\mathrm{K,Ca}}$ is gradually decreased.

Eventually, c_e decreases to such an extent that the ER can no longer support large Ca^{2+} spikes, and the oscillations in c become smaller and faster (SS-2 phase). This itself allows for a much greater frequency of the voltage spikes, which thus bring in more Ca^{2+} from the outside, allowing for the stabilization of the ER Ca^{2+} concentration. Upon removal of the agonist, c declines transiently, which causes an increase in the frequency of the voltage spikes. Because these voltage spikes bring in more Ca^{2+}, the ER gradually refills, and the system returns to basal levels (phase T-2).

This model demonstrates the complex interactions between ER Ca^{2+}, cytoplasmic Ca^{2+}, and membrane voltage spiking. It is clearly not the entire story, but it provides an excellent explanation for a wide variety of complex responses.
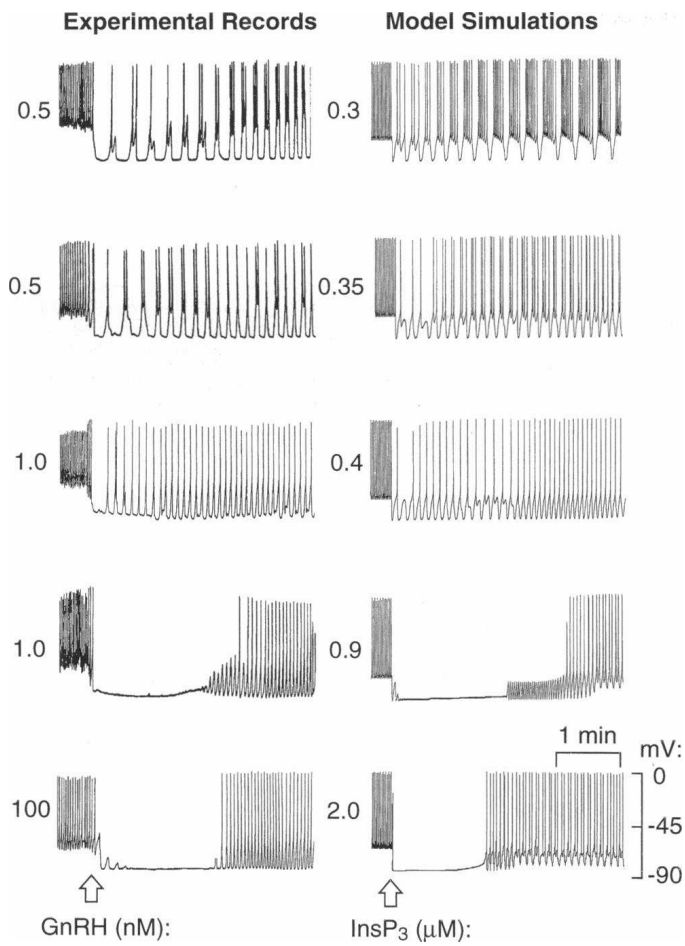
Figure 9.21: The response of gonadotrophs, in experiment and theory, to increasing applications of agonist. In the experiments (left panels), the indicated concentration of GnRH was added at the arrow, while this was simulated in the model (right panels) by addition of the indicated concentrations of IP_3. Li et al. (1997), Fig. 2. **Springer: we will need permission for this figure**.
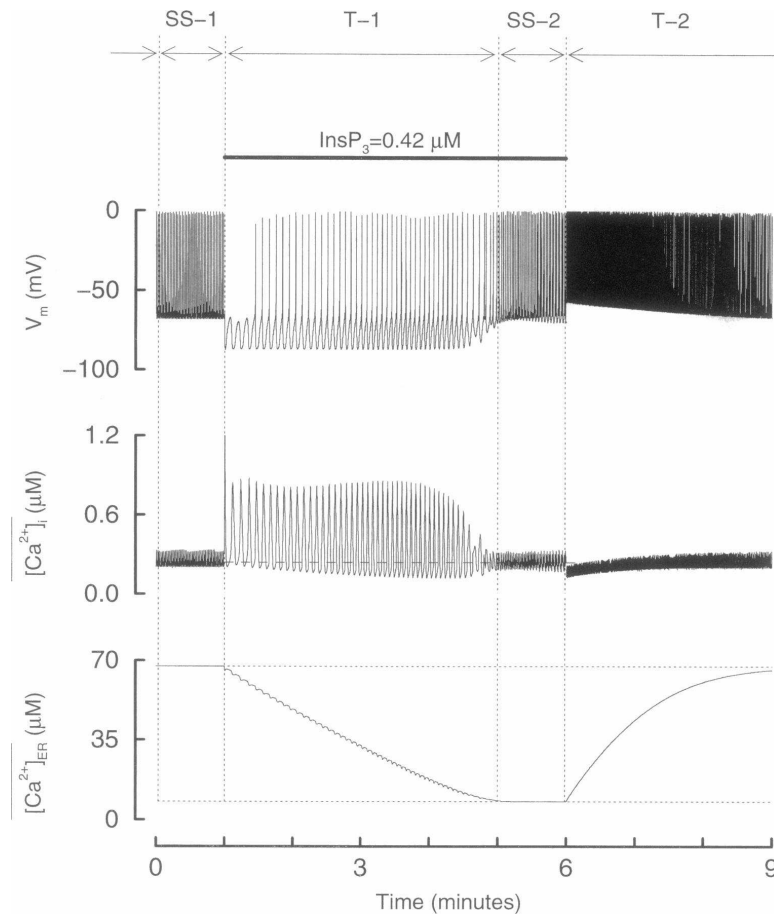
Figure 9.22: Response of a gonadotroph to agonist stimulation, with the different phases labeled. $\overline{[Ca^{2+}]}_i$ and $\overline{[Ca^{2+}]}_{ER}$ are, respectively, the average cytoplasmic and ER Ca^{2+} concentrations over the entire cell. Li et al. (1997), Fig. 3. **Springer: we will need permission for this figure**.

9.3   Exercises

1. (a) Numerically simulate the system of differential equations

$$\frac{dv}{dt} = f(v) - w - gs(v - v_\theta), \tag{9.76}$$

$$5\frac{dw}{dt} = w_\infty(v) - w, \tag{9.77}$$

$$\frac{ds}{dt} = f_s(s) + \alpha_s(x - 0.3), \tag{9.78}$$

$$\frac{dx}{dt} = \beta_x\left((1 - x)H(v) - x\right), \tag{9.79}$$

where $f(v) = 1.35v(1 - \frac{1}{3}v^2)$, $f_s(s) = -0.2(s - 0.05)(s - 0.135)(s - 0.21)$, $w_\infty(v) = \tanh(5v)$, and $H(v) = \frac{3}{2}(1 + \tanh(5x - 2.5))$, and $v_\theta = -2, \alpha_s = 0.002, \beta_x = 0.00025, g = 0.73$.

   (b) Give a fast–slow analysis of this burster. Hint: The equations for v, w comprise the fast subsystem, while those for s, x comprise the slow subsystem.

   (c) Describe the bursting mechanism in this model. For what kind of burster might this be a reasonable model?

2. Compute some numerical solutions of the Rinzel–Lee simplification of the Chay–Keizer β cell model. How does the value of k_c affect the burst length?

3. To the Ca^{2+} submodel of phantom bursting in Section 9.1.2, add a Ca^{2+} flux, J_{IPR}, through IP_3 receptors (see Chapter 7). Assume that the IPR is at steady state, with an open probability given by the Li-Rinzel simplification (Section 7.2.5) of the De Young-Keizer model (Section 7.2.5). Thus

$$J_{IPR} = P_o(c_e - c), \tag{9.80}$$

where

$$P_o = \left(\frac{c}{d_{act} + c}\right)^3 \left(\frac{p}{d_{IP_3} + p}\right)^3 \left(\frac{d_{inact}}{d_{inact} + c}\right)^3, \tag{9.81}$$

where $d_{act} = 0.35$ μM, $d_{inact} = 0.4$ μM, and $d_{IP_3} = 0.5$ μM. Let $g_{K,Ca} = 700$ and $g_{K,ATP} = 230$, so that the model exhibits medium bursting. Show that when p is increased from 0 to 0.3 μM the bursting changes from medium to fast. Explain this in terms of changes to the $dc/dt = 0$ nullcline.

4. In the phantom bursting model of Section 9.1.2, c_e increases during the active phase and declines during the silent phase. Why? Explain this without using any mathematical equations. Then give a mathematical explanation.

5. Investigate the behavior of the model of compound bursting (Section 9.1.3) for the three fixed values of [ATP] shown in Fig. 9.10.

   (a) For each value of [ATP] solve the model equations numerically, and plot them in the V, c phase plane, as well as against time.

(b) Compute the bifurcation diagrams (as shown in Fig. 9.10), and super-impose the model solutions (with varying c) on the bifurcation diagrams (treating c as a bifurcation parameter).

(c) Show that, when [ATP] is small there is no bursting, while when [ATP] is large the active phase is continuous.

(d) Show that, for intermediate values of [ATP], the duration of the active phase depends on [ATP].

(e) Explain why these results should be so, using the bifurcation diagrams to illustrate your answers.

6. If the parameters of the model of compound bursting (Section 9.1.3) are changed slightly to $f = 0.0013$, $v_2 = 188$, $g_{K,ATP} = 357$, what kind of bursting occurs? (This kind of bursting has been called "accordion" bursting.) Explain this behavior by using a fast-slow analysis of the model, and plotting the bifurcation diagrams. Hint: what values are taken by [ATP] over the course of an oscillation, and how do these differ from the values taken in the top panel of Fig. 9.10?

7. Determine the value of I in the Hindmarsh–Rose fast subsystem (9.56), (9.57) for which the trajectory from the unstable node is also the saddle point separatrix.

8. (a) An equation of the form $\frac{d^2x}{dT^2} + F(x)\frac{dx}{dT} + x = 0$ is called an equation in the Liénard form (Minorsky, 1962; Stoker, 1955) and was important in the classical development of the theory of nonlinear oscillators. Show that the polynomial bursting model (9.58)–(9.60) can be written in the *generalized* Liénard form

$$\frac{d^2x}{dT^2} + F(x)\frac{dx}{dT} + G(x,z) = -\epsilon H(x,z), \qquad (9.82)$$

$$\frac{dz}{dT} = \epsilon H(x,z), \qquad (9.83)$$

where ϵ is a small parameter, and where F, G, and H are the polynomial functions

$$F(u) = a[(u - \hat{u})^2 - \eta^2], \qquad (9.84)$$

$$G(u,z) = z + u^3 - \frac{3}{4}u - \frac{11}{27}, \qquad (9.85)$$

$$H(u,z) = \beta(u - \bar{u}) - z. \qquad (9.86)$$

(b) Construct the fast subsystem bifurcation diagram for this polynomial model for the following three different cases with $a = 0.25$, $\beta = 4$, $\hat{u} = -0.954$, and $\epsilon = 0.0025$.

i. $\eta = 0.7$, $\hat{u} = 1.6$. Show that in this case the model exhibits square-wave bursting.

ii. $\eta = 0.7$, $\hat{u} = 2.1$. Show that the model exhibits tapered bursting, resulting from passage through a supercritical Hopf bifurcation.

iii. $\eta = 1.2$, $\hat{u} = 1.0$. Describe the bursting pattern here.

Solve the model equations numerically to confirm the predictions from the bifurcation diagrams. A detailed analysis of this model has been performed by Pernarowski (1994) and de Vries (1995), with a perturbation analysis given by (Pernarowski et al., 1991, 1992).

9. Prove that if D is an irreducible matrix with nonnegative entries d_{ij}, then the only nontrivial solution of the system of equations $\sum_{j=1}^{n} d_{ij}(V_i - V_j) = 0, i = 1, \ldots, N$, is the constant vector.

Remark: An irreducible nonnegative matrix is one for which some power of the matrix has no zero elements. To understand irreducibility, think of the elements of the matrix D as providing connections between nodes of a graph, and d_{ij} is positive if there is a path from node i to node j, but zero if not. Such a matrix is irreducible if between any two points there is a connecting path, with possibly multiple intermediate points. The smallest power of the matrix that is strictly positive is the smallest number of connections that is certain to connect any node with any other node.

Hint: Represent the system of equations as $Av = 0$ and show that some shift $A + \lambda I$ of the matrix A is irreducible and has only nonnegative entries. Invoke the Perron–Frobenius theorem (a nonnegative irreducible matrix has a unique, positive, simple eigenvector with eigenvalue larger in magnitude than all other eigenvalues) to show that the null space of A is one-dimensional, spanned by the constant vector.

Chapter 10

Regulation of Cell Function

In all cells, the information necessary for the regulation of cell function is contained in strands of deoxyribose nucleic acid, or DNA. The nucleic acids are large polymers of smaller molecular subunits called *nucleotides*, which themselves are composed of three basic molecular groups,

- a *nitrogenous base*, which is an organic ring containing nitrogen,

- a 5-carbon (pentose) sugar, either *ribose* or *deoxyribose*,

- an inorganic phosphate group.

Nucleotides may differ in the first two of these components, and consequently there are two specific types of nucleic acids, *deoxyribonucleic acid* (DNA) and *ribonucleic acid* (RNA).

There may be any one of five different nitrogenous bases present in the nucleotides: *adenine* (A), *cytosine* (C), *guanine* (G), *thymine* (T), and *uracil* (U). These are most often denoted by the letters A, C, G, T, and U, rather than by their full names.

The DNA molecule is a long double strand of nucleotide bases, which can be thought of as a twisted, or helical, ladder. The backbone (or sides of the ladder) is composed of alternating sugar and phosphate molecules, the sugar, deoxyribose, having one fewer oxygen atom than ribose. The "rungs" of the ladder are complementary pairs of nitrogenous bases, with G always paired with C, and A always paired with T. The bond between pairs is a weak hydrogen bond that is easily broken and restored during the replication process. In eukaryotic cells (cells that have a nucleus), the DNA is contained within the nucleus of the cell.

The ordering of the base pairs along the DNA molecule is called the genetic code, because it is this ordering of symbols from the four-letter alphabet of A, C, G, and T that controls all cellular biochemical functions. The nucleotide sequence is organized into code triplets, called *codons*, which code for amino acids as well as other signals, such as "start manufacture of a protein molecule" and "stop manufacture of a protein molecule." Segments of DNA that code for a particular product are called *genes*, of which there are about 30,000 in human DNA. Typically, a gene contains

start and stop codons as well as the code for the gene product, and can include large segments of DNA whose function is unclear. One of the simplest known living organisms, *Mycoplasma genitalian*, has 470 genes and about 500,000 base pairs.

DNA itself, although not its structure, was first discovered in the late nineteenth century, and by 1943 it had been shown (although not widely accepted) that it is also the carrier of genetic information. How exactly it accomplishes this, and the structure of the molecule, was not established until the work of Maurice Wilkins and Rosamund Franklin at King's College in London, and James Watson and Francis Crick in Cambridge. Watson, Crick and Wilkins received the 1962 Nobel Prize in Physiology or Medicine, Franklin having died tragically young some years previously in 1958.

In recent years the study of DNA and the genetic code has grown in a way that few would have predicted even 20 years ago. Nowadays, genetics and molecular biology have penetrated deeply into practically all aspects of life, from research and education to business and forensics. Mathematicians and statisticians have not been slow to join these advances. Departments and Institutes of Bioinformatics are springing up in all sorts of places, and there are few mathematics or statistics departments that do not have connections (some more extensive than others, of course) with molecular biologists. It is well beyond the scope of this book to provide even a cursory overview of this vast field. An excellent introduction to molecular biology is the book by Alberts et al. (2002); any reader who is seriously interested in learning about molecular biology will find this book indispensable. Waterman (1995), Mount (2001) and Krane and Raymer (2003) are good introductory bioinformatics texts, while for those who are more mathematically or statistically oriented there are Deonier et al. (2004), Ewens and Grant (2005) and Durrett (2002).

10.1   Regulation of gene expression

An RNA molecule is a single strand of nucleotides. It is different from DNA in that the sugar in the backbone is ribose, and the base U is substituted for T. Cells generally contain two to eight times as much RNA as DNA. There are three types of RNA, each of which plays a major role in cell physiology. For our purposes here, *messenger RNA* (mRNA) is the most important, as it carries the code for the manufacture of specific proteins. *Transfer RNA* (tRNA) acts as a carrier of one of the twenty amino acids that are to be incorporated into a protein molecule that is being produced. Finally, *ribosomal RNA* constitutes about 60% of the *ribosome*, a structure in the cellular cytoplasm on which proteins are manufactured.

The two primary functions that take place in the nucleus are the reproduction of DNA and the production of RNA. RNA is formed by a process called *transcription*, as follows. An enzyme called *RNA polymerase* (or, more precisely, a polymerase complex, as many other proteins are also needed) attaches to some starting site on the DNA, breaks the bonds between base pairs in that local region, and then makes a complementary copy of the nucleotide sequence for one of the DNA strands. As the RNA polymerase moves along the DNA strand, the RNA molecule is formed, and the DNA crossbridges reform. The process stops when the RNA polymerase reaches a transcriptional termination site and disengages from the DNA.

Proteins are manufactured employing all three RNA types. After a strand of mRNA that codes for some protein is formed in the nucleus, it is released to the cytoplasm. There it encounters ribosomes that "read" the mRNA much like a tape recording. As a particular codon is reached, it temporarily binds with the specific tRNA with the complementary codon carrying the corresponding amino acid. The amino acid is released from the tRNA and binds to the forming chain, leading to a protein with the sequence of amino acids coded for by the DNA.

Synthesis of a cellular biochemical product usually requires a series of reactions, each of which is catalyzed by a special enzyme. In prokaryotes, formation of the necessary enzymes is often controlled by a sequence of genes located in series on the DNA strand. This area of the DNA strand is called an *operon*, and the individual genes within the operon are called *structural genes*. At the beginning of the operon is a segment called a *promoter*, which is a series of nucleotides that has a specific affinity for RNA polymerase. The polymerase must bind with this promoter before it can begin to travel along the DNA strand to synthesize RNA. In addition, in the promoter region, there is an area called a *repressor operator*, where a regulatory repressor protein can bind, preventing the attachment of RNA polymerase, thereby blocking the transcription of the genes of the operon. Repressor protein generally exists in two allosteric forms, one that can bind with the repressor operator and thereby repress transcription, and one that does not bind. A substance that changes the repressor so that it breaks its bond with the operator is called an *activator*, or *inducer*.

The original concept of the operon was due to Jacob et al. (1960), closely followed by mathematical studies (Goodwin, 1965; Griffith, 1968a,b; Tyson and Othmer, 1978). The interesting challenge is to understand how the complex networks that regulate genes work, and when, or how gene expression can respond to the need of the organism or changes in the environment.

10.1.1 The *trp* repressor

Tryptophan (*trp*) is an essential amino acid that cannot be synthesized by humans and therefore must be part of our diet. Tryptophan is a precursor for serotonin (a neurotransmitter), melatonin (a neurohormone), and niacin. Improper metabolism of tryptophan has been implicated as a possible cause of schizophrenia, since improper metabolism creates a waste product in the brain that is toxic, causing hallucinations and delusions. Tryptophan can, however, be synthesized by bacteria such as E. coli, and the regulation of tryptophan production serves as our first example of transcriptional regulation.

A number of models of the *trp* repressor have been constructed, of greater or lesser complexity (Bliss et al., 1982; Sinha, 1988; Santillán and Mackey, 2001; Mackey et al., 2004). Here, we present only a highly simplified version of these models, designed to illustrate some of the basic principles.

The *trp* operon is comprised of a regulatory region and a coding region consisting of 5 structural genes that code for three enzymes required to convert chorismic acid into tryptophan. Expression of the *trp* operon is regulated by the Trp repressor protein which is encoded by the trpR gene. In contrast to the *lac* operon, which is described in the next section, the trpR operon is independent of the *trp* operon,

being located some distance on the DNA from the *trp* operon. TrpR protein is able to bind to the operator only when it is activated by the binding of two tryptophan molecules. Thus, we have a negative feedback loop; while tryptophan levels in the cell are low, production of tryptophan remains high. However, once the level of tryptophan builds up, then the Trp repressor blocks further transcription of the operon and, as a result, the synthesis of the three enzymes and consequently of tryptophan itself declines.

The ability to regulate production of a substance in response to its need is characteristic of negative feedback systems. Here, the negative feedback occurs because the product of gene activation represses the activity of the gene. Thus, the tryptophan operon is called a *repressor*.

A simple model of this network is sketched in Fig. 10.1. We suppose that the operon has three states, either free O_f, bound by repressor O_R, or bound by polymerase O_P, and let o_j, $j = f, R, P$ be the probability that the operon is in state j. mRNA (M) is produced only when polymerase is bound, so that

$$\frac{dM}{dt} = k_m o_P - k_{-m} M. \tag{10.1}$$

Note that the dashed lines in Fig. 10.1 correspond to reactions in which the reactants are not consumed. Thus, for example, the production of enzyme does not consume mRNA so that there is no consumption term in (10.1). The probabilities of being in an operon state are governed by the differential equations

$$\frac{do_P}{dt} = k_{\text{on}} o_f - k_{\text{off}} o_P, \qquad \frac{do_R}{dt} = k_r R^* o_f - k_{-r} o_R, \tag{10.2}$$

where $o_P + o_f + o_R = 1$, and R^* denotes activated repressor. Activation of repressor requires binding with two molecules of tryptophan (T) and so we take

$$\frac{dR^*}{dt} = k_t T^2 (1 - R^*) - k_{-t} R^*, \tag{10.3}$$

(scaled so that $R + R^* = 1$.)

According to Bliss et al. (1982), the most important of the enzymes is anthranilate synthase (denoted by E), which is the only enzyme concentration we track here. Enzyme (E) is produced from mRNA, and degraded,

$$\frac{dE}{dt} = k_e M - k_{-e} E, \tag{10.4}$$

and tryptophan production is proportional to the amount of enzyme, so that

$$\frac{dT}{dt} = KE - \mu T - 2\frac{dR^*}{dt}. \tag{10.5}$$

Here μ is the rate of tryptophan utilization and degradation.

For our purposes here, it is sufficient to examine the steady-state solutions of this system, which must satisfy the algebraic equation

$$F(T) \equiv \frac{k_e}{k_{-e}} \frac{k_m}{k_{-m}} \frac{k_{\text{on}}}{k_{\text{off}}} \frac{1}{1 + \frac{k_{\text{on}}}{k_{\text{off}}} + \frac{k_r R^*(T)}{k_{-r}}} = \frac{\mu}{K} T, \tag{10.6}$$
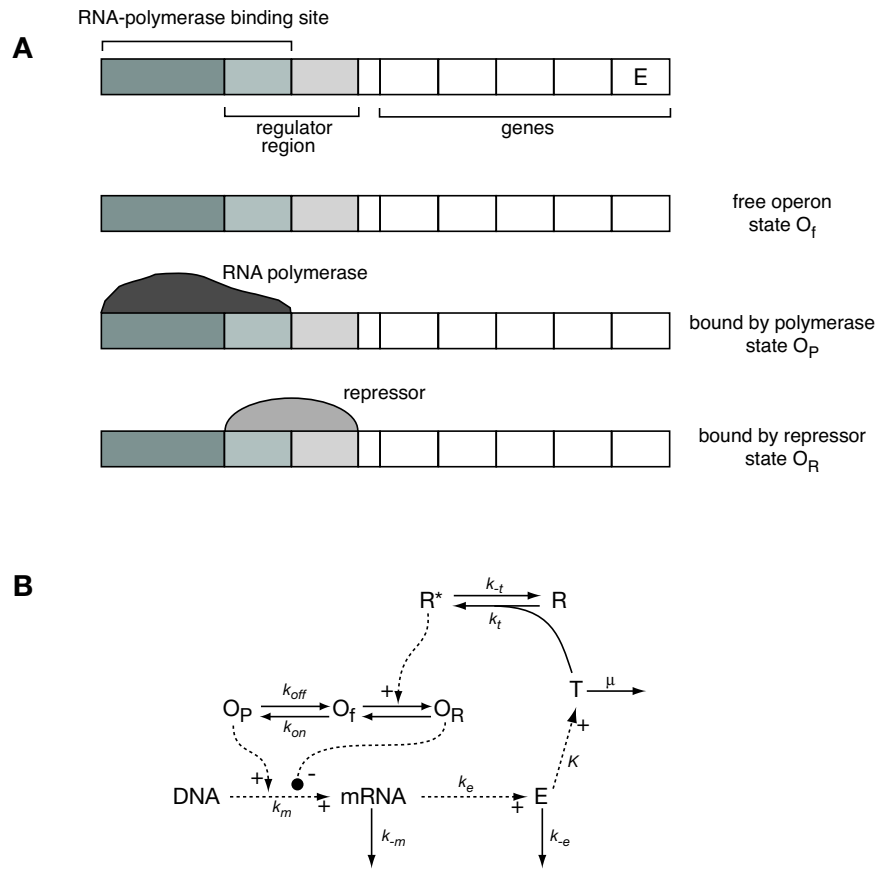
Figure 10.1: A: Control sites and control states of the *trp* operon. B: Feedback control of the *trp* operon. Dashed lines indicate reactions in which the reactants are not consumed.

where

$$R^*(T) = \frac{T^2}{\frac{k_{-t}}{k_t} + T^2}. \tag{10.7}$$

The function $F(T)$ is a positive monotone decreasing function of T, and represents the steady state tryptophan production rate. The right hand side of this equation is a straight line with slope $\frac{\mu}{K}$. Thus, there is a unique positive intersection. Furthermore, as the utilization of tryptophan, quantified by $\frac{\mu}{K}$, increases, the steady state level of T decreases and the production rate $F(T)$ necessary to balance utilization increases, characteristic of negative feedback control.

James, It seems to me that we need a simple sketch of these two functions, $F(T)$ and $\frac{\mu}{K}T$ to illustrate graphically how this negative feedback network works by balancing production with utilization. JK

10.1.2   The *lac* Operon

When glucose is abundant, *E. coli* uses it exclusively as its food source, even when other sugars are present. However, when glucose is not available *E. coli* is able to use other sugars such as lactose, a change that requires the expression of different genes by the bacterium. Jacob, Monod and their colleagues (Jacob et al., 1960; Jacob and Monod, 1961) were the first to propose a mechanism by which this could happen, a mechanism that is now called a *genetic switch*. Forty years ago the idea of a genetic switch was revolutionary, but the original description of this mechanism has withstood the test of time and is used, practically unchanged, in modern textbooks. Mathematicians were quick to see the dynamic possibilities of genetic switches, with the first model, by Goodwin, appearing in 1965, followed by that of Griffith (1968a,b). More recently detailed models have been constructed by Wong et al. (1997), Yildirem and Mackey (2003), Yildirim et al. (2004) and Santillán and Mackey (2004). The structure and function of the *lac* repressor is reviewed by Lewis (2005), while an elegant blend of theoretical and experimental work was presented by Ozbudak et al. (2004). Mackey et al. (2004) review modeling work on both the *lac* operon and the tryptophan operon.

The *lac* operon consists of three structural genes, and two principal control sites. The three genes are *lacZ*, *lacY* and *lacA*, and they code for three proteins involved in lactose metabolism, *β-galactosidase*, *lac* permease, and *β-thiogalactoside acetyl transferase*, respectively. The permease allows entry of lactose into the bacterium. The *β*-galactosidase isomerizes lactose into *allolactose* (an allosteric isomer of lactose) and also breaks lactose down into the simple hexose sugars, glucose and galactose that can be metabolized for energy. The function of the transferase is not known.

Whether or not the operon is on depends on the two control sites. One of these control sites is a repressor, the other is an activator. If a repressor is bound to the repressor binding site, then RNA polymerase cannot bind to the operon to initiate transcription, and the three proteins cannot be produced. Preceding the promoter region of the *lac* operon where the RNA polymerase must bind to begin transcription, there is another region, called a CAP site, which can be bound by a dimeric molecule CAP (*catabolic activator protein*). CAP by itself has no influence

on transcription unless it is bound to cyclic AMP (cAMP), but when CAP is bound to cAMP the complex can bind to the CAP site, thereby promoting the binding of RNA polymerase to the promoter region, allowing transcription.

So, in summary, the three proteins necessary for lactose metabolism are produced only when CAP is bound and the repressor is not bound. This is illustrated in Fig. 10.2.

A bacterium is thus able to switch the *lac* operon on and off by regulating the concentrations of the repressor and of CAP, and this is how the requisite positive and negative feedbacks occur. Allolactose plays a central role here. In the absence of allolactose, the repressor is bound to the operon. However, allolactose can bind to the repressor protein, and prevent it binding to the repressor site. This, in turn, allows activation of the operon, the further production of allolactose (via the action of β-galactosidase), and increased entry of lactose (via the *lac* permease). Hence we have a positive feedback loop.

The second feedback loop operates through cAMP. The CAP protein is formed by a combination of cAMP with a cAMP receptor protein. When there is a large amount of cAMP in the cell, the concentration of CAP is high, CAP binds to the CAP binding site of the operon, thus allowing transcription. When cAMP concentration is low in the bacterium, the reverse happens, turning the operon off. A decrease in extracellular glucose leads to an increase in intracellular cAMP concentration (by an unknown mechanism) thus leading to activation of CAP and subsequent activation of the operon. Conversely, an increase in extracellular glucose switches the operon off.

To summarize, the operon is switched on only when lactose is present inside the cell, and glucose is not available outside (Fig. 10.2). Positive feedback is accomplished by allolactose preventing binding of the repressor. Negative feedback is accomplished by the control of CAP levels by extracellular glucose (Fig. 10.3).

Here we present a mathematical model for this process that is similar to the models of Griffith (1971) (see Exercise 1) and Yildirim and Mackey (2003). For this simple model we ignore the effects of CAP. Our goal is to show how, when there is no lactose available, the operon is switched off, but that as the external lactose concentration increases the operon is switched on (i.e., a genetic switch). Because of our limited goal we do not include the dynamics of CAP in our model.

Let A denote allolactose, with concentration A, and similarly for lactose (L), the permease (P), β-galactosidase (B), mRNA (M), and the repressor (R). We assume that the repressor, normally in its activated state R*, reacts with 2 molecules of allolactose to become inactivated (R), according to

$$\mathrm{R}^* + 2\mathrm{A} \underset{k_{-a}}{\overset{k_a}{\rightleftharpoons}} \mathrm{R}. \tag{10.8}$$

For simplicity, we assume that the operon can be in one of only two states, bound to (activated) repressor and therefore inactive (O_R), or bound by polymerase and therefore producing mRNA (O_P). Thus, the operon reacts with the repressor according to

$$\mathrm{O}_P + \mathrm{R}^* \underset{k_{-r}}{\overset{k_r}{\rightleftharpoons}} \mathrm{O}_R. \tag{10.9}$$
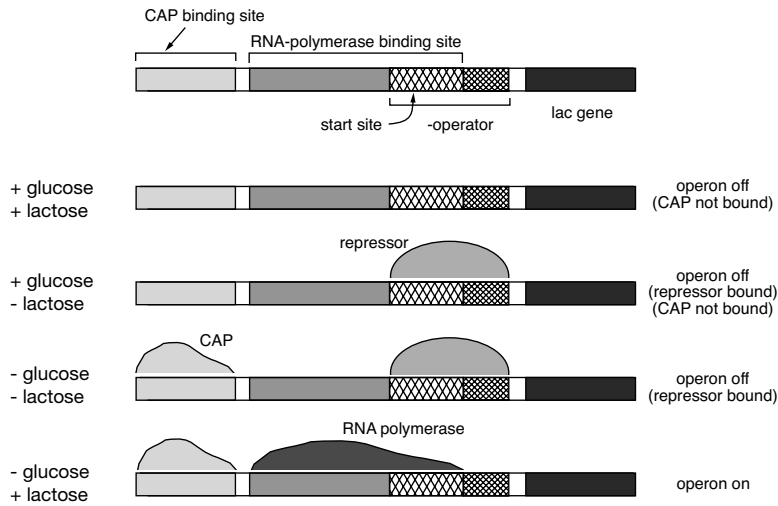
Figure 10.2: Control sites and control states for the *lac* operon.
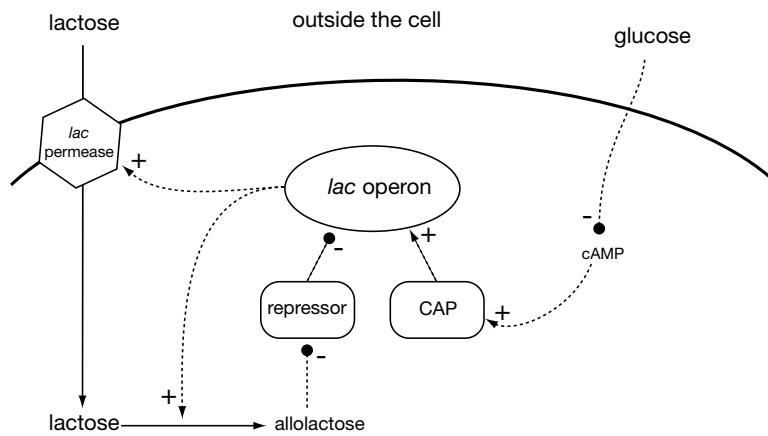
Figure 10.3: Feedback control of the *lac* operon. Indirect effects are denoted by dashed lines, with positive and negative effects denoted by different arrow heads and associated + or - signs.

The probabilities for the operon to be in these states is governed by the equation

$$\frac{do_p}{dt} = k_{-r}(1 - o_p) - k_r R^* o_p, \tag{10.10}$$

since $o_P + o_R = 1$. Since, effectively no repressor is consumed by binding with the operon, the repressor concentration is governed by the differential equation

$$\frac{dR^*}{dt} = k_{-a}R - k_a A^2 R^*, \tag{10.11}$$

where $R + R^* = R_t$.

Assuming each of these reactions is in steady state, we find that

$$R = K_a R^* A^2, \tag{10.12}$$
$$o_R = K_r R^* o_P, \tag{10.13}$$

where $K_i = k_i/k_{-i}$ for $i = a, r$. Thus,

$$R_t = R + R^* = R(1 + K_1 A^2), \tag{10.14}$$

and

$$o_P = \frac{1}{1 + K_r R^*} = \frac{1 + K_a A^2}{1 + K_r R_t + K_a A^2} = \frac{1 + K_a A^2}{K + K_a A^2}, \tag{10.15}$$

where $K = 1 + K_r R_t > 1$. Thus, the *average* production of mRNA is described by the differential equation

$$\frac{dM}{dt} = \alpha_M o_P - \gamma_M M = \alpha_M \frac{1 + K_a A^2}{K + K_a A^2} - \gamma_M M, \tag{10.16}$$

where M is the concentration of mRNA that codes for the enzymes. The constant α_M is a proportionality constant that relates the probability of activated operon to the rate of mRNA production, while γ_M describes the degradation of mRNA. Note that, in the absence of allolactose, there is a residual production of mRNA. This is because the reaction in (10.9) has an equilibrium where O_P is non-zero, even at maximal concentrations of R.

We next assume that the enzymes are produced at a rate linearly proportional to available mRNA and are degraded, so that the concentrations of permease (denoted P) and β-galactosidase (denoted B) are determined by

$$\frac{dP}{dt} = \alpha_P M - \gamma_P P, \tag{10.17}$$
$$\frac{dB}{dt} = \alpha_B M - \gamma_B B. \tag{10.18}$$

Although it might appear that, since their codes are part of the same mRNA, the production rates of P and B are the same, this is not the case. First, mRNA reads the different genes within the operon (*lacZ* and *lacY*) in sequence, making β-galactosidase first and the permease second. Second, the permease must migrate to the cell membrane to be incorporated there. The different times of production,

and the different time delays before these two enzymes can become effective, imply that they have different effective rates of production (see Table **??**).

Lactose that is exterior to the cell, with concentration L_e, is brought into the cell to become the lactose substrate, with concentration L, at a Michaelis–Menten rate proportional to the permease P. Once inside the cell, lactose substrate is converted to allolactose, and then allolactose is converted to glucose and galactose via enzymatic reaction with β-galactosidase, so that

$$\frac{dL}{dt} = \alpha_L P \frac{L_e}{K_{Le} + L_e} - \alpha_A B \frac{L}{K_L + L} - \gamma_L L, \tag{10.19}$$

and

$$\frac{dA}{dt} = \alpha_A B \frac{L}{K_L + L} - \beta_A B \frac{A}{K_A + A} - \gamma_A A. \tag{10.20}$$

To summarize, the model is given by the five equations (10.16)—(10.20). A more complicated mechanism is studied by Wong et al. (1997), while Yildirim and Mackey (2003) include a number of time delays rendering the model a system of delay-differential equations. However, this representation of the reaction mechanism is adequate for our purpose here, to show how a genetic switch can arise in a simple way.

Yildirim and Mackey (2003) devoted a great deal of effort to determine accurate values for the parameters, and slightly modified versions of these are given in Table 10.1, the modifications being necessary because our model is not exactly the same as theirs. The steady state solution is shown in Fig. 10.4, plotted as a function of L_e, the external lactose concentration.

A brief word about how to produce the steady state solution diagram shown in Fig. 10.4. Of course, one could use AUTO (which is how this plot was made). However, if one does not have access to or familiarity with these kinds of sophisticated software packages, then the following do-it-yourself approach is recommended. The easiest method is to plot L_e as a function of A. That is, first use (10.16) to find M as a function of A and then use (10.17) and (10.18) to find P and B as functions of A. Then use (10.20) to find L as a function of A, and finally use (10.19) to find L_e as a function of A.

When L_e is low there is only a single steady state, with a low concentration of allolactose, A; for an intermediate range of values of L_e there are two stable steady states, one (high A) corresponding to lactose usage, the other (low A) corresponding to negligible lactose usage; and for large values of L_e there is again only one stable steady state solution, corresponding to lactose usage. Thus, if L_e increases past a critical value, here around 0.03 mM, the steady state switches from a low usage state to the high usage state as β-galactosidase is switched on. This discontinuous response to a gradually increasing L_e is characteristic of a genetic switch, and results from bistability in the model . This switching on of lactose usage is called *induction*, and this kind of operon is called an *inducer*.

The useage of lactose is switched off at a lower value of L_e than the value at which it is switched on. This feature of hysteretic switches is important because it prevents rapid cycling. That is, when allolactose useage is high, external lactose is consumed and therefore decreases. If the on-switch and off-switch were at the

Table 10.1: Parameters of the *lac* operon model

α_A	=	1.76×10^4 min^{-1}	γ_A	=	0.52 min^{-1}
α_B	=	1.66×10^{-2} min^{-1}	γ_B	=	2.26×10^{-2} min^{-1}
α_P	=	10 min^{-1}	γ_P	=	0.65 min^{-1}
α_M	=	9.97×10^{-4} mM/min	γ_M	=	0.41 min^{-1}
α_L	=	2880 min^{-1}	γ_L	=	2.26×10^{-2} min^{-1}
β_A	=	2.15×10^4 min^{-1}	β_L	=	2.65×10^3 min^{-1}
K	=	6000	K_a	=	2.52×10^4 (mM)$^{-2}$
K_A	=	1.95 mM	K_L	=	9.7×10^{-7} mM
K_{L1}	=	1.81 mM	K_{Le}	=	0.26 mM
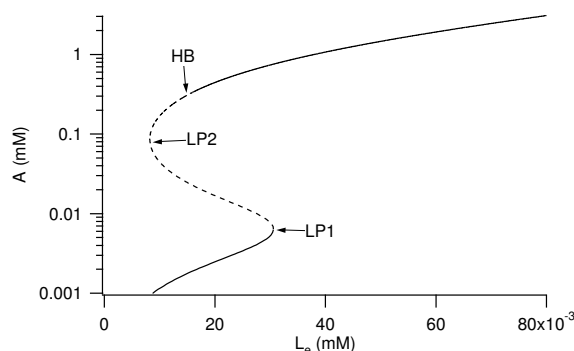
Figure 10.4: Steady states of the *lac* operon model as a function of the external lactose concentration, L_e. Unstable steady states are denoted by a dashed line; LP denotes a limit point and HB denotes a Hopf bifurcation point.

same value, then the lac operon would presumably be switched on and off rapidly, a strategy for resource allocation that seems unfavorable.

The Hopf bifurcation shown in Fig. 10.4 does not appear in more complicated models. It is thus of dubious relevance and we do not pursue it further.

10.2 Circadian Clocks

It has been known for a long time that many organisms have oscillators with a period of about 24 hours, hence circadian from the Latin *circa* = about and *dies* = a day. That humans have such a clock is apparent twice a year when the switch to or from daylight saving time occurs, or whenever one travels by air to a different time zone, and we experience "jet lag". Before the molecular basis of circadian clocks was known, the study of these rhythms focused on properties of generic autonomous oscillators, most typically the van der Pol oscillator, and its response to external stimuli either to entrain the oscillator or to reset the oscillator. There is a vast literature describing this endeavor which we do not even attempt to summarize.

All of this changed in the 1980s when the first genes influencing the 24 hour cycle were discovered. These genes were the *per* (for *period*) gene in *Drosophila* and the *frq* (for *frequency*) gene in the fungus *Neurospora*.

It is now known that circadian clocks are found in many organisms, including cyanobacteria, fungi, plants, invertebrate and vertebrate animals, but as yet, not in the Archaebacteria. Wherever they are found, they employ biochemical loops that are self contained within a single cell (requiring no cell-to-cell interaction). Further, the mechanism for their oscillation is always the same: there are positive elements that activate clock genes that yield clock proteins which act in some way to block the activity of the positive elements. Thus, the circadian clocks are all comprised of a negative feedback loop (the gene product inactivates its own production) with a delay. An excellent review of circadian clocks is found in Dunlap (1999) (see also Dunlap, 1998).

Even before the details of the clocks were known, it was recognized that negative feedback loops with sufficient delay in the feedback could produce oscillatory behavior. The first model of this type (Goodwin, 1965) was intended to model periodic enzyme synthesis in bacteria, and assumed that there were enzymes X_1, X_2, $\cdots X_n$ such that

$$X_1 \to X_2 \to \cdots \to X_n, \tag{10.21}$$

where X_n has an inhibitory effect on the production of X_1. The model equations for the Goodwin oscillator are

$$\frac{dX_1}{dt} \;=\; \frac{\nu_0}{1 + (\frac{X_n}{K_m})^p} - k_1 X_1, \tag{10.22}$$

$$\frac{dX_i}{dt} \;=\; \nu_{i-1} X_{i-1} - k_i X_i, \; i = 2, \ldots, n. \tag{10.23}$$

Oscillations occur in this network only if $n \geq 3$, and if $p > 8$ when $n = 3$ (see Exercise 3).

So the question is not whether negative feedback loops with some source of time delay can produce oscillations. We know they can. Rather, the question is whether enough is known about the details of the biochemistry of circadian clocks to produce reasonably realistic models of their dynamics. There are several intriguing questions. What sets the intrinsic period of the oscillator; that is, what are the mechanisms that give a nearly 24 hour intrinsic cycle? How does phase resetting work?

Drosophila has a molecular circadian system whose investigation has been central to our understanding of how clocks work at the molecular level. Beginning in the morning, *per* and *tim* (for timeless) mRNA levels begin to rise, the result of activation of the clock gene promoters by a heterodimer of CLK (for CLOCK) and CYC (for CYCLE). The protein PER is unstable in the absence of TIM, but is stabilized by dimerization with TIM. Furthermore, the PER/TIM dimer is a target for nuclear translocation, and once it enters the nucleus (within 3 hours of dusk), it interacts with the CLK/CYC heterodimer to inhibit the activity of CLK/CYC, hence shutting down the production of *per* and *tim*. In the night, PER and TIM are increasingly phosphorylated, leading to their degradation. Once they are depleted, the CLK/CYC heterodimer is again activated and the cycle begins again.

Table 10.2: Circadian Clock Genes

System	activator	inhibitor
Synechoccus	*kaiA* (cycle in Japanese)	*kaiC*
Neurospora	*wc-1/wc-2* (WhiteCollar)	*frq* (Frequency)
Drosophila	*Clk/cyc* (Clock/Cycle)	*per tim* (Period/Timeless)
Mouse	*Clock/bmal1*	*per1,2,3* and *cry1,2* (Cryptochrome)

Synchronization with the day/night light cycle and phase resetting occurs because the degradation of TIM is enhanced by light. Thus, exposure to light in the late day when TIM levels are rising delays the clock, while exposure to light in late night and early morning when TIM levels are falling advances the clock.

While the details are different in different organisms, this scenario is typical. However, as is also typical in biochemistry, the names of the main players are different in different organisms, even though their primary function is similar. In Table 10.2 we give a list of the main players in different organisms.

There are several mathematical models of circadian rhythms that are described here. The first (Goldbeter, 1995) is similar in structure to the enzyme oscillator of Goodwin. That is, the PER protein P_0 is (reversibly) phosphorylated into P_1 and then P_2

$$P_0 \rightleftarrows P_1 \rightleftarrows P_2. \tag{10.24}$$

The phosphorylated protein P_2 is then transported into the nucleus where it (P_N) inhibits the production of *per* mRNA (M), closing the negative feedback loop, with a delay because of the phosphorylation steps and nuclear transport.

The equations for the Goldbeter model are as follows:

$$\frac{dM}{dt} = \frac{\nu_s}{1 + (\frac{P_n}{K_I})^4} - \frac{\nu_m M}{K_{m1} + M}, \tag{10.25}$$

$$\frac{dP_0}{dt} = k_s M - \frac{V_1 P_0}{K_1 + P_0} + \frac{V_2 P_1}{K_2 + P_1}, \tag{10.26}$$

$$\frac{dP_1}{dt} = \frac{V_1 P_0}{K_1 + P_0} - \frac{V_2 P_1}{K_2 + P_1} - \frac{V_3 P_1}{K_3 + P_1} + \frac{V_4 P_2}{K_4 + P_2}, \tag{10.27}$$

$$\frac{dP_2}{dt} = \frac{V_3 P_1}{K_3 + P_1} - \frac{V_4 P_2}{K_4 + P_2} - k_1 P_2 + k_2 P_N - \frac{\nu_d P_2}{K_d + P_2}, \tag{10.28}$$

$$\frac{dP_N}{dt} = k_1 P_2 - k_2 P_N. \tag{10.29}$$

Notice that the phosphorylation and dephosphorylation steps in this model are all at Michaelis-Menten rates, appropriate for enzymatic reactions, rather than linear, as in the original model of Goodwin. It is a straightforward matter to simulate these equations and verify that the solutions are periodic with a period of about 24 hours; we leave this verification to the interested reader.

More recently, Leloup and Goldbeter (1998, 2003, 2004) published a model that includes the two proteins PER and TIM, both of which undergo two phosphorylation steps before they form a dimer and then are transported into the nucleus where they

Table 10.3: Parameter values for the 5 variable Goldbeter (1995) circadian clock model.

ν_s	$=$	$0.76~\mu\text{M h}^{-1}$	k_s	$=$	$0.38~\text{h}^{-1}$
ν_m	$=$	$0.65~\mu\text{M h}^{-1}$	k_1	$=$	$1.9~\text{h}^{-1}$
ν_d	$=$	$0.95~\mu\text{M h}^{-1}$	k_2	$=$	$1.3~\text{h}^{-1}$
V_1	$=$	$3.2~\mu\text{M h}^{-1}$	$K_{1,2,3,4}$	$=$	$2~\mu\text{M}$
V_2	$=$	$1.58~\mu\text{M h}^{-1}$	K_I	$=$	$1~\mu\text{M}$
V_3	$=$	$5~\mu\text{M h}^{-1}$	K_{M1}	$=$	$0.5~\mu\text{M}$
V_4	$=$	$2.5~\mu\text{M h}^{-1}$	K_d	$=$	$0.2~\mu\text{M}$

inhibit their own production. The model retains the basic structure of the Goodwin model, but it has the advantage that the effects of changes in the degradation rates of TIM can be studied as a model of how light interacts with the clock.

Another model of the circadian clock (Tyson et al., 1999) takes a different view of the post-translational regulation of PER and TIM, and is motivated by the more recent finding that another clock element *dbt* (doubletime) is important to the phosphorylation of PER. In this model, phosphorylation tags the protein for degradation, rather than activating it for nuclear translocation as in the Goldbeter model. In the Tyson et al. model, DBT protein phosphorylates monomers of PER at a faster rate than it does dimers, which means that PER monomers are much more likely to be degraded than its dimers.

As with the Goldbeter model, the Tyson et al. model does not include TIM, but assumes that dimers of PER inhibit the clock gene. The model equations are

$$\frac{dM}{dt} = \frac{\nu_m}{1 + (\frac{P_2}{P_{\text{crit}}})^2} - k_m M, \tag{10.30}$$

$$\frac{dP_1}{dt} = \nu_p M - \frac{k'_{p1} P_1}{J_p + P_1 + r P_2} - k_{p3} P_1 - 2k_a P_1^2 + 2k_d P_2, \tag{10.31}$$

$$\frac{dP_2}{dt} = k_a P_1^2 - k_d P_2 - \frac{k_{p2} P_2}{J_p + P_1 + r P_2} - k_{p3} P_2. \tag{10.32}$$

The most important assumptions entailed in these equations are, firstl, that both monomer (P_1) and dimers (P_2) bind to DBT, but P_1 is phosphorylated more rapidly (i.e. $k'_{p1} \gg k_{p2}$) and, second, that the DBT-catalyzed reaction is a saturating reaction and that the dimer is a competitive inhibitor of monomer phosphorylation. The extent of competitive inhibition is determined by r, the ratio of enzyme-substrate dissociation constants for the monomer and dimer (see Chapter 1). Here, the parameter r is chosen to be 2.

Next, we suppose that the dimerization reactions are fast (both k_a and k_d are large compared to other rate constants), so that P_1 and P_2 are in quasi-equilibrium. We let $P = P_1 + 2P_2$ be the total amount of PER protein, and observe that since $k_a^2 P_1^2 - k_d P_2 = 0$ (approximately),

$$P_1 = qP, \qquad P_2 = \frac{1}{2}(1-q)P, \qquad q = \frac{2}{1 + \sqrt{1 + 8K_{\text{eq}}P}}. \tag{10.33}$$

Table 10.4: Parameter values for the 2 variable Tyson et al. (Tyson et al., 1999) circadian clock model. Here C_p and C_m are typical concentration for protein and mRNA, respectively.

ν_m	$=$	1 C_m h^{-1}	k_m	$=$	0.1 h^{-1}
ν_p	$=$	0.5 $C_p C_m^{-1}$ h^{-1}	k_{p1}	$=$	10 C_ph^{-1}
k_{p2}	$=$	0.03 C_ph^{-1}	k_{p3}	$=$	0.1 h^{-1}
K_{eq}	$=$	200 C_p^{-1}	P_{crit}	$=$	0.1 C_p
J_p	$=$	0.5 C_p	r	$=$	2
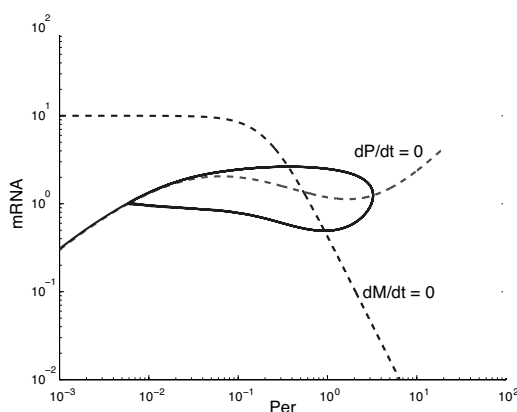
Figure 10.5: Phase portrait for the Tyson et al. circadian clock model.

Now we add (10.31) and (10.32) to find a single equation for P,

$$\frac{dP}{dt} = \nu_p M - \frac{k_{p1}Pq + k_{p2}P}{J_p + P} - k_{p3}P. \tag{10.34}$$

This equation, coupled with (10.30) and the algebraic relationships (10.33) gives a two variable model for the circadian clock.

A nice feature of two variable systems is that they can be studied in the phase plane. The phase portrait for this system is shown in Fig. 10.5, where it can be seen that this system is a canonical excitable system. That is, the $\frac{dM}{dt} = 0$ nullcline is a monotone decreasing curve having a single intersection with the N-shaped $\frac{dP}{dt} = 0$ nullcline. There is a close similarity between this phase portrait and the phase portrait for Ca^{2+} oscillations shown in Fig. 7.12, with M playing a role similar to h and P playing a role similar to c.

The two models of the circadian rhythms presented here give rise to some interesting questions about the mechanisms of these oscillations. No one doubts that there is negative feedback or that negative feedback with delay can produce oscillations. But similarly, no one doubts that oscillations can arise in networks with positive and negative feedback. Thus, both of these models are plausible, but, as yet, is not a definitive answer for which of the two is better.
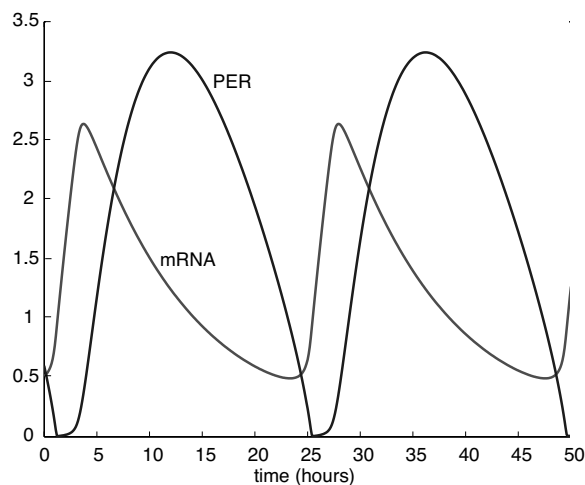
Figure 10.6: Solutions of the Tyson et al. circadian clock model.

Research in circadian rhythms is quite active. Some recent work that relates to the topics of this text include work on the mammalian circadian clock (Leloup and Goldbeter, 2003; Forger and Peskin, 2003, 2004, 2005), and work describing the role of Ca^{2+} in plant circadian clocks (Dodd et al., 2005).

10.3   The Cell Cycle

The *cell-division cycle* is the process by which a cell duplicates its contents and then divides in two. The adult human must manufacture many millions of new cells each second simply to maintain the status quo, and if all cell division is halted, the individual will die within a few days. On the other hand, abnormally rapid cell proliferation, i.e., *cancer*, can also be fatal, as rapidly proliferating cells interfere with the function of "normal" cells and organs. Control of the cell cycle involves, at a minimum, control of cell growth and replication of nuclear DNA in such a way that the size of the individual cells remains, on average, constant.

The cell cycle is traditionally divided into four distinct phases (shown schematically in Fig. 10.7), the most dramatic of which is mitosis or *M phase*. Mitosis is characterized by separation of previously duplicated nuclear material, nuclear division, and finally the actual cell division, called *cytokinesis*. In most cells the whole of M phase takes only about an hour, a small fraction of the total cycle time. The much longer period of time between one M phase and the next is called *interphase*. In some cells, such as mammalian liver cells, the entire cell cycle can take longer than a year. The portion of interphase following cytokinesis is called G_1 *phase* (G for gap), during which cell growth occurs. When the cell is sufficiently large, DNA replication in the nucleus is initiated and continues during *S phase* (S for synthesis). Following S phase is G_2 *phase*, providing a safety gap during which the cell
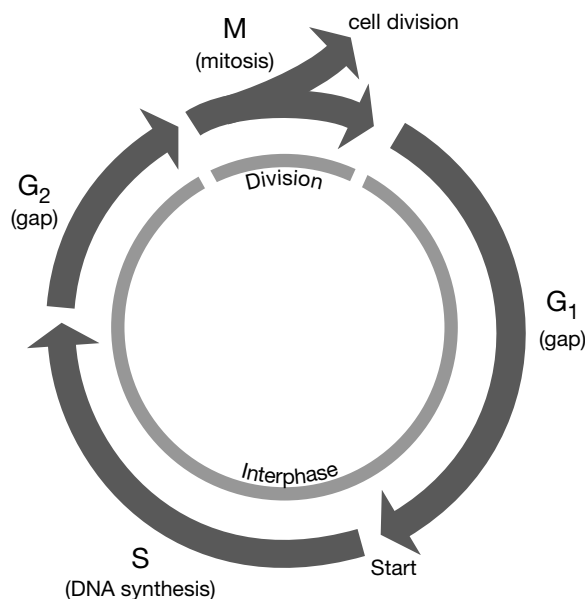
Figure 10.7: Schematic diagram of the cell cycle.

is presumably preparing for M phase, to ensure that DNA replication is complete before the cell plunges into mitosis.

There are actually two controlled growth processes. There is the chromosonal cycle, in which the genetic material is exactly duplicated and two nuclei are formed from one for every "turn" of the cycle. Accuracy is essential to this process, since each daughter nucleus must receive an exact replica of each chromosome. A less tightly controlled process, the cytoplasmic cycle, duplicates the cytoplasmic material, including all of the structures (mitochondria, organelles, endoplasmic reticulum, etc.). This growth is continuous during the G_1, S, and G_2 phases, pausing briefly only during mitosis.

In mature organisms these two processes operate in coordinated fashion, so that the ratio of cell mass to nuclear mass remains essentially constant. However, it is possible for these two to be uncoupled. For example, during *oogenesis*, a single cell (an *ovum*) grows in size without division. After fertilization, during *embryogenesis*, the egg undergoes twelve rapid synchronous mitotic divisions to form a ball consisting of 4096 cells, called the *blastula*.

The autonomous cell cycle oscillations seen in early embryos are unusual. Most cells proceed through the division cycle in fits and starts, pausing at "checkpoints" to ensure that all is ready for the next phase of the cycle. There are checkpoints at the end of the G_1, G_2, and M phases of the cell cycle, although not all cells use all of these checkpoints. During early embryogenesis, however, the checkpoints are inoperable, and cells divide as rapidly as possible, driven by the underlying limit cycle oscillation. The G_1 checkpoint is often called *Start*, because here the cell determines whether all systems are ready for S phase and the duplication of DNA.

Before Start, newly born cells are able to leave the mitotic cycle and differentiate (into nondividing cells with specialized function). However, after Start, they have passed the point of no return and are committed to another round of DNA synthesis and division.

The cell cycle has been studied most extensively for frogs and yeast. Frog eggs are useful because they are large and easily manipulated. Yeast cells are too small for these kinds of studies, but are suitable for cloning and identification of the involved genes and gene products. Since both organisms use fundamentally similar mechanisms to regulate the cell cycle, insights gained from either may usefully be used to build up an overall picture of cell cycle control. The budding yeast *Saccharomyces cerevisiae*, used by brewers and bakers, divides by first forming a bud that is initiated and grows steadily during S and G_2 phases, and finally separates from its mother after mitosis. A similar organism, fission yeast *Schizosaccharomyces pombe*, is also used extensively in cell cycle studies. The cell cycle in mammalian cells is considerably more complex than in either frogs or yeast and we do not consider it in any detail here.

Although there is a great deal of experimental work done on the cell cycle, there is only one major modeling group that specializes in the construction and analysis of cell cycle models (although others such as Albert Goldbeter have published important models). This is the group led by Bela Novak and John Tyson, who, over the last 15 years, have published a series of classic papers, beginning with relatively simple models of the cell cycle and progressing to their most recent, highly complex models. Despite the elegance of this work, there are substantial difficulties facing the novice to this field. Not the least of these difficulties is the proliferation of names. Despite the similarities in basic mechanism, the genes (and proteins) that carry out analogous functions in frog, budding yeast and fission yeast all have different names; when a simple model already contains seven or eight crucial proteins, and each of these proteins has a different name in different organisms, the potential for confusion is clear.

We begin by presenting a generic model for the eukaryotic cell cycle, and discuss the fundamental mechanism that is preserved in mammalian cells. We then specialize this generic model to the specific case of fission yeast. This requires a multitude of names; to keep track of them the reader is urged to make frequent use of Table 10.6 where the analogous names for the generic model and for fission yeast are listed. We end with a brief discussion of cell division in frog eggs after fertilization.

10.3.1   A Simple Generic Model

The fundamental bistability

As with all cellular processes, the cell cycle is regulated by genes and the proteins that they encode. There are two classes of proteins that form the center of the cell cycle control system. The first is the family of *cyclin-dependent kinases* (Cdk), which induce a variety of downstream events by phosphorylating selected proteins. The second family are the *cyclins*, so named because the first members to be identified are cyclically synthesized and degraded in each division cycle of the cell. Cyclin
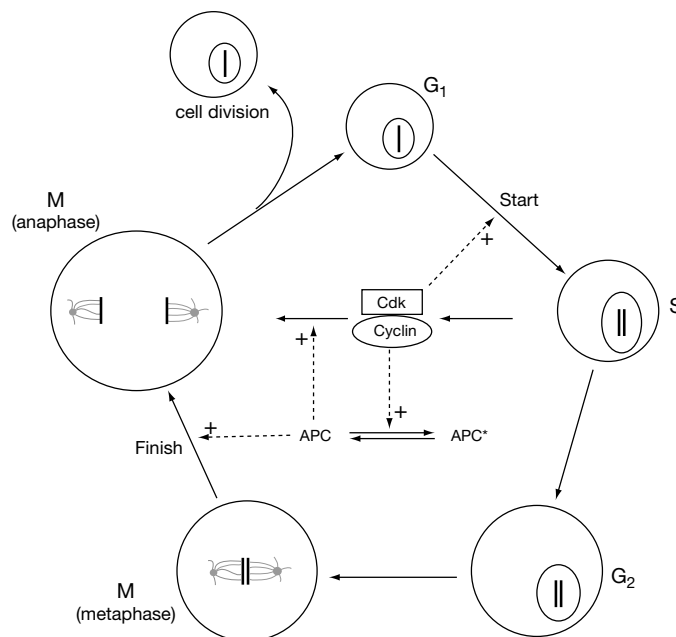
Figure 10.8: Schematic diagram of the primary chemical reactions of the cell cycle. APC* denotes the inactive form of APC. Adapted from Tyson and Novak (2001), Fig. 1.

binds to Cdk molecules and controls their ability to phosphorylate target proteins; without cyclin, Cdk is inactive. In budding yeast cells there is only one major Cdk and nine cyclins, leading to a possibility of nine active cyclin–Cdk complexes. In mammals, the story is substantially more complicated, as there are (at last count) six Cdks and more than a dozen cyclins.

Leland Hartwell and Paul Nurse received the 2001 Nobel Prize in Physiology or Medicine for their work in the 1970s that showed how the cyclin-dependent kinases Cdc2 (in fission yeat), Cdc28 (in budding yeast) and Cdk1 (in mammalian cells) control the cell cycle. Cyclins were discovered in 1982 by Tim Hunt who shared the Nobel Prize with Hartwell and Nurse.

Although the temptation for a modeler is to view the cycle in Fig. 10.7 as a limit cycle oscillator, it is more appropriate to view it as an alternation between two states, G_1 and S-G_2-M. This point of view was first proposed by Nasmyth (1995, 1996) and now forms the basis of practically all quantitative models. Transition between these two states is controlled by the concentration of the Cdk-cyclin complex. In the G_1 state, the concentration of Cdk-cyclin is low, due to the low concentration of cyclin. At Start (see Fig. 10.8) cyclin production is increased and cyclin degradation is inhibited. The concentration of Cdk-cyclin therefore rises (because there is always plenty of Cdk around), and the cell enters S state, beginning synthesis of DNA. At the end of S phase each chromosome consists of a pair of

chromatids. At the end of G_2 the nuclear envelope is broken down and the chromatid pairs are aligned along the metaphase spindle, shown as the lighter grey lines in Fig. 10.8. When alignment is complete (metaphase), a group of proteins that make up the anaphase-promoting complex (APC) is activated. The APC functions in combination with an auxiliary component (either Cdc20 or Cdh1) to label cyclin molecules for destruction, thereby decreasing the concentration of the Cdk-cyclin complex. This initiates a second irreversible transition, Finish, and the chromatids are pulled to opposite poles of the spindle (anaphase). Thus, Start is caused by an explosive increase in the concentration of the Cdk-cyclin complex, while Finish is caused by the degradation of cyclin by APC and the resultant fall in Cdk-cyclin levels.

How do these reactions result in switch-like behavior between G_1 and S-G_2-M, and alternating high and low cyclin concentrations? The switch arises because of the mutually antagonistic interactions between Cdk-cyclin and APC-Cdh1. Not only does APC-Cdh1 inhibit Cdk activity by degrading cyclin, Cdk-cyclin in its turn inhibits APC-Cdh1 activity by phosphorylating Cdh1. Because of this mutual antagonism, the cell can have either low Cdk-cyclin activity and high APC-Cdh1 activity (i.e., G_1), or high Cdk-cyclin activity and low APC-Cdh1 activity (S-G_2-M).

To construct a simple model for this reaction scheme we write down differential equations for the concentrations of cyclin (in this case, Cyclin B, called CycB) and unphosphorylated Cdh1, expressed in arbitrary units. The concentration of Cdk does not appear directly in the model because it is assumed to be present in excess. Because CycB binds tightly to Cdk, the concentration of the Cdk-CycB complex is determined solely by the concentration of CycB. Similarly, the activity of the APC-Cdh1 complex is determined by the concentration of Cdh1.

For each of these reactions we use relatively simple kinetics, either obeying mass action, or following a Michaelis-Menten saturating rate function (Chapter 1). Thus,

$$\frac{d[\text{CycB}]}{dt} = k_1 m - (k_2' + k_2''[\text{Cdh1}])[\text{CycB}], \tag{10.35}$$

$$\frac{d[\text{Cdh1}]}{dt} = \frac{(k_3' + k_3'' A)(1 - [\text{Cdh1}])}{J_3 + 1 - [\text{Cdh1}]} - \frac{k_4[\text{CycB}][\text{Cdh1}]}{J_4 + [\text{Cdh1}]}. \tag{10.36}$$

All the various k's and J's are positive constants, as are A and m. There are a number of important things to note about these equations:

1. CycB is degraded at the intrinsic rate k_2', but is also degraded by APC-Cdh1, with rate constant k_2''. Conversely, Cdh1 is phosphorylated by Cdk-CycB following a Michaelis-Menten saturating rate function. Thus there is mutual inhibition between CycB and Cdh1.

2. The rate of production of Cdh1 is dependent on the concentration of the phosphorylated form, which is $[\text{Cdh1}]_{\text{total}}$ - $[\text{Cdh1}]$. Since units are arbitrary we set $[\text{Cdh1}]_{\text{total}} = 1$.

3. The rate of production of CycB is dependent on the parameter m, which represents the cell mass. This is a crucial assumption. How can a rate constant be dependent on the mass of a cell? Although there must be some way in
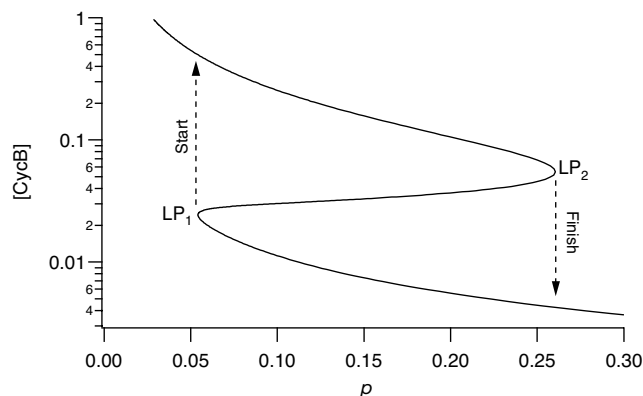
Figure 10.9: Steady states of the two-variable generic model (10.35)–(10.36) plotted against the parameter p. Note the log scale on the vertical axis.

which cell mass controls the kinetics of the cell cycle (because the cell cycle and cell growth are closely coupled, as discussed above) the exact mechanisms by which this occurs are unknown. Of course, it is possible to imagine how it might occur; as the cell mass increases, the ratio of cytoplasmic mass to nuclear mass increases. If a protein is made in the cytoplasm but then moves to the nucleus, the greater the cytoplasmic/nuclear volume ratio, the faster the buildup of this protein in the nucleus. However, such explanations remain speculative. In this simple model we assume that CycB builds up in the nucleus, and thus its rate of production is an increasing function of cell mass, as in (10.36).

4. The constant A is related to the activity of Cdc20. Recall that Cdc20, like Cdh1, can pair up with APC. One job of the APC-Cdc20 complex is to indirectly activate a phosphatase that activates Cdh1.

Letting x_1 denote [CycB] and x_2 denote [Cdh1], the steady states of (10.35)–(10.36) are related by

$$x_1 = \frac{k_1 m}{k_2' + k_2'' x_2}, \tag{10.37}$$

and

$$p = \left(\frac{J_3 + 1 - x_2}{1 - x_2} \right) \left(\frac{x_2}{J_4 + x_2} \right) \left(\frac{k_1}{k_2' + k_2'' x_2} \right), \tag{10.38}$$

where

$$p = \frac{k_3' + k_3'' A}{k_4 m}. \tag{10.39}$$

These solutions are shown in Fig. 10.9 with x_1 plotted as a function of p, using parameter values taken from Table 10.5. However, since A is not specified, the scale on this plot is arbitrary. The easiest way to plot this curve is to view (10.37) and (10.38) as a parametric curve with underlying parameter x_2. For some values of p

there are three steady states, for others only one. The two places where the steady states coalesce are limit points labeled LP_1 and LP_2. (Since this is a two variable system, it is also quite easy to do a phase plane analysis and to verify that the intermediate steady state solution is a saddle point, hence unstable. See Exercise 5.)

We can now trace out an approximate cell cycle loop in Fig. 10.9. Suppose we start at the lower steady state (i.e., the one corresponding to low [CycB]), to the right of LP_1. As m increases (as the cell grows), p decreases and the cell follows the lower steady state. Eventually p decreases so much that LP_1 is reached, the solution falls off the lower steady state and approaches the high steady state. This corresponds to Start (see Fig. 10.8), at which time the concentration of cyclin B increases explosively. At metaphase the concentration of Cdc20 starts to rise, which corresponds to an increase in the parameter A, which increases p. When p increases too far the solution can no longer stay on the upper steady state, and falls back down to the lower steady state (Finish). [CycB] thus falls, A decreases again, the cell divides ($m \to m/2$), and the cell begins the cycle over again.

From this point of view, the cell cycle is a hysteresis loop alternating between two branches of steady states.

Activation of APC

In the previous model, A was a parameter that was increased and decreased at will to mimic the activity of APC-Cdc20. Of course, the story is not this simple as there are a number of reactions that regulate APC activation. In budding yeast Cdh1 is activated by a phosphatase, which is activated by Cdc20. Furthermore, Cdc20 production is increased by cyclin B. Hence, the explosive increase in [CycB] that occurs at Start leads to an increase in Cdc20, and a subsequent increase in Cdh1. However, when Cdc20 is first made it is not active; it is activated by cyclin B only after a time delay, which is the result of a number of intermediate reaction steps between cyclin B and Cdc20 activation. The exact reactions that cause this delay have not yet been identified, so it is modeled by introducing a fictitious enzyme, IE (Intermediate Enzyme), with activated form IEP (the P standing for phosphorylation). Thus, in summary, CycB activates IEP which activates Cdc20 which activates Cdh1 which degrades CycB. This reaction scheme is sketched in Fig. 10.10.

To write the corresponding differential equations we introduce two new variables; activated IE (IEP) and Cdc20. We also let $[\text{Cdc20}]_T$ denote the total concentration of Cdc20, i.e., both the activated and inactivated forms. The rate of production of total Cdc20 is increased by CycB, and thus

$$\frac{d[\text{Cdc20}_T]}{dt} = k_5' + k_5'' \frac{[\text{CycB}]^n}{J_5^n + [\text{CycB}]^n} - k_6[\text{Cdc20}_T]. \qquad (10.40)$$

Note that the activation is assumed to follow a simple model of cooperative kinetics, with Hill coefficient n (Chapter 1).

Similarly, Cdc20 is formed from non-activated Cdc20 (which has concentration $[\text{Cdc20}_T]$ - [Cdc20]) at a rate that is dependent on [IEP], and is removed in two ways; the same intrinsic degradation rate as Cdc20_T, and an additional removal
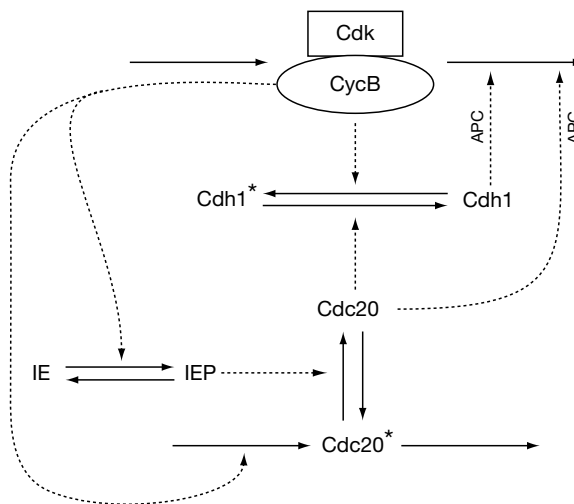
Figure 10.10: Sketch of the reactions involved in the activation of APC. The superscript * indicates an inactive form. IEP denotes the phosphorylated (and active) form of IE. Adapted from Tyson and Novak (2001) Fig. 6.

term corresponding to enzymatic conversion of the active form back to the inactive form. Thus,

$$\frac{d[\text{Cdc20}]}{dt} = \frac{k_7[\text{IEP}]([\text{Cdc20}_T] - [\text{Cdc20}])}{J_7 + ([\text{Cdc20}_T] - [\text{Cdc20}])} - \frac{k_8[\text{Cdc20}]}{J_8 + [\text{Cdc20}]} - k_6[\text{Cdc20}]. \quad (10.41)$$

Finally we include an equation for [IEP];

$$\frac{d[\text{IEP}]}{dt} = k_9 m[\text{CycB}](1 - [\text{IEP}]) - k_{10}[\text{IEP}]. \quad (10.42)$$

Note that IEP is activated at a rate that is proportional to [CycB].

It remains to specify how to model the growth of the cell. For simplicity, we assume that m grows exponentially, and thus

$$\frac{dm}{dt} = \mu m. \quad (10.43)$$

However, this growth law must be modified to take cell division into account. At Start [CycB] grows explosively, but its subsequent fall is the signal that Finish has occurred and the cell should divide. Thus, we assume that the cell divides in half (i.e., $m \rightarrow m/2$) whenever [CycB] falls to some specified low level (in this case 0.05) after Start.

The model now consists of the six differential equations (10.35), (10.36), (10.40), (10.41), (10.42) and (10.43), with $A = [\text{Cdc20}]$ in (10.36). In writing these equations we have made a large number of assumptions. Perhaps the most striking of these is that sometimes the kinetics are assumed to be first order law of mass action
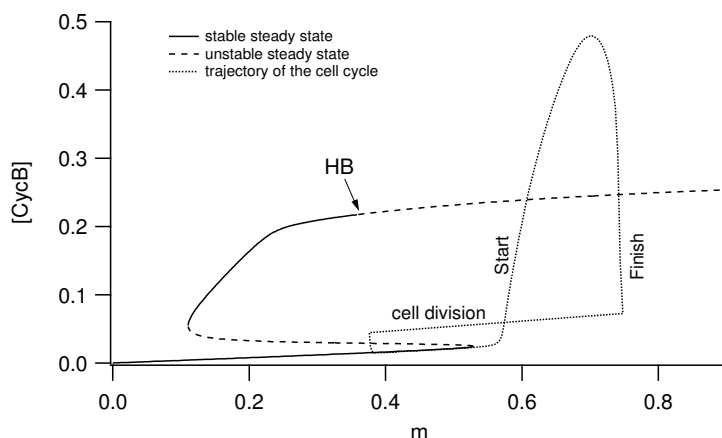
Figure 10.11: Steady states (holding m fixed) of the 6-variable generic model and a superimposed cell cycle trajectory allowing cell growth and division. The parameter values of the model are given in Table 10.5.

Table 10.5: Parameters for the 6-variable generic cell cycle model (10.35), (10.36), (10.40), (10.41), (10.42) and (10.43). Adapted from Tyson and Novak (2001), Table 1.

Component	Rate constants (min^{-1})	Dimensionless constants
CycB	$k_1 = 0.04$, $k_2' = 0.04$, $k_2'' = 1$, $k_2''' = 1$	$[\mathrm{CycB}]_{\mathrm{threshold}} = 0.05$
Cdh1	$k_3' = 1$, $k_3'' = 10$, $k_4' = 2$, $k_4 = 35$	$J_3 = 0.04$, $J_4 = 0.04$
$\mathrm{Cdc20}_T$	$k_5' = 0.005$, $k_5'' = 0.2$, $k_6 = 0.1$	$J_5 = 0.3$, $n = 4$
Cdc20	$k_7 = 1$, $k_8 = 0.5$	$J_7 = 10^{-3}$, $J_8 = 10^{-3}$
IEP	$k_9 = 0.1$, $k_{10} = 0.02$	
m	$\mu = 0.005$	

kinetics, other times they are assumed to be of Michaelis-Menten form, while at other times they are assumed to be cooperative kinetics. Such choices are in large part a judgement call on the part of the original modelers, and depend on the available experimental evidence.

The steady states of this model (i.e., steady states holding m fixed) are shown in Fig. 10.11. As in the simpler 2-variable model (Fig. 10.9) the curve of steady states has two limit points. However, in this more complicated model the upper steady state becomes unstable via a Hopf bifurcation (which we do not investigate any further, the resultant limit cycles being of no interest at this stage). Thus, when the cell cycle trajectory (shown as the dotted line) falls off the lower branch of steady states (at Start) it cannot end up at the upper steady state, as the upper steady state is unstable. Instead, it loops around the upper steady state and [CycB] then falls to a low level (Finish) at which time the mass is divided by 2 (cell division), the solution heads back to the lower steady state branch, and the cycle repeats.

Table 10.6: Cell cycle regulatory proteins

Generic model	Fission yeast
Cdk	Cdc2
CycB	Cdc13
Cdh1	Ste9
Cdc20	Slp1
IE	IE

In this model as it stands, Finish automatically occurs a certain time after Start. Once the trajectory falls off the lower steady-state branch, there is nothing to stop it looping around and initiating Finish when [CycB] falls. In reality there are controls to prevent this from happening if the chromosomes are not aligned properly. However, we omit these controls from this simple model.

A note about units

All the concentrations in this model (and the one that follows) are treated as dimensionless. This explains why, in Table 10.5, all the constants k have units of 1/time, and why the J's are dimensionless. Experimentally, it is possible to measure relative concentrations, but it is not possible to measure absolute concentrations. Thus, we assume that there is some scale factor that could be used to scale all the concentrations rendering them dimensionless, although we not know what the scale factor is. The qualitative behavior of the model remains unchanged by this assumption.

10.3.2 Fission yeast

Having seen how the cell cycle works in a generic model, we now turn to a more complicated model for the cell cycle of fission yeast (Novak et al., 2001; Tyson et al., 2002). This is a particularly interesting model as the cell cycles of various mutants can be elegantly explained by consideration of the corresponding bifurcation diagrams. However, we now need to introduce new names for the major players in the cell cycle. Since the introduction of a list of new names for familiar players has the potential to cause drastic confusion, we urge the reader to pay careful and repeated attention to Table 10.6 where the different names for analogous species are given.

Mitosis-Promoting Factor: MPF

In the generic model, the central player in the cell cycle was the Cdk:cyclin B complex. In fission yeast the cyclin-dependent kinase is called Cdc2 and the B-type cyclin is called Cdc13 (see Table 10.6. Cdc stands for cell division cycle.). The Cdc2:Cdc13 complex that lies at the heart of the cycle is called *Mitosis-Promoting Factor*, or MPF. As before, Cdc2 is active only when it is bound to the cyclin, Cdc13, and thus MPF is the active species that drives the cell cycle.

To understand the regulation of MPF we need to understand how it is formed, degraded and inactivated (Fig. 10.12).
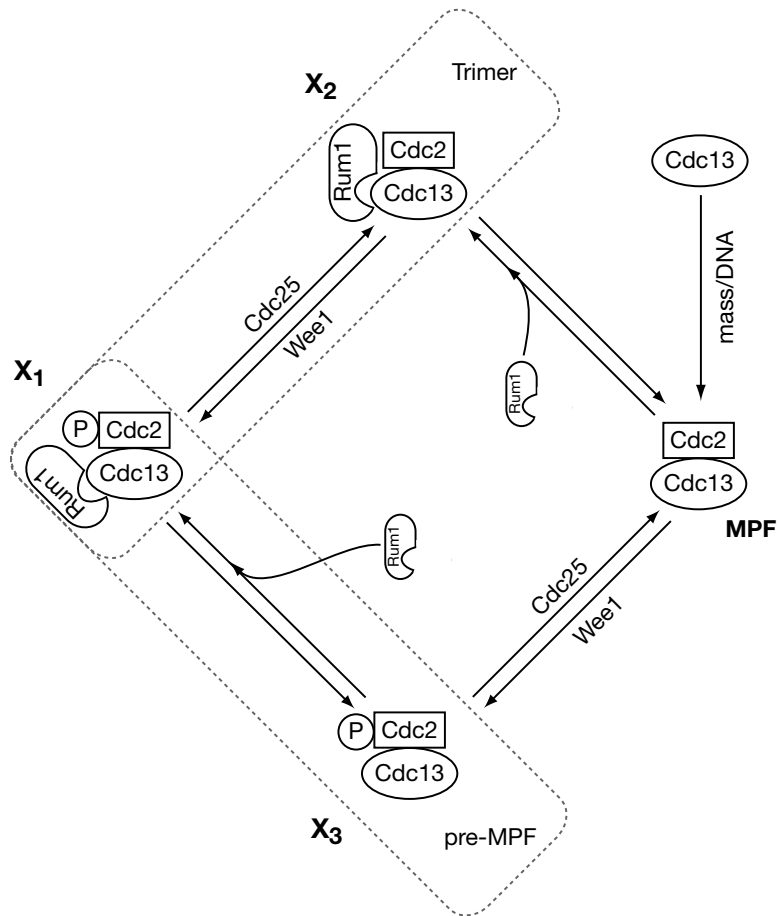
Figure 10.12: Diagram of the states of MPF. In the model of the cell cycle in fission yeast these states are assumed to be at equilibrium. Each of the states is degraded by a pathway that depends on Slp1 and Ste9, but these are omitted from the diagram for clarity. The circled-P denotes a phosphate group.

- MPF is formed when Cdc13 combines with Cdc2; because Cdc2 is present in excess, the rate of this formation is dependent only on how much Cdc13 is present. This rate is assumed to be dependent on the mass of the cell, as Cdc13 can build up inside the nucleus, as discussed previously for CycB.

- The principal degradation pathway is activated by APC, whose auxiliary components, in fission yeast, are called Ste9 and Slp1.

- MPF can be inactivated in two major ways:

    - It can be phosphorylated by the Wee1 kinase to a protein called preMPF. PreMPF in its turn can be dephosphorylated back to MPF by the phosphorylated form of Cdc25.
    - It can be inhibited by the binding of Rum1, to form an inactive trimer.

These reactions are summarized in Fig. 10.12. Since the activities of Rum1, Cdc25 and Slp1 are all controlled by MPF, this gives a highly complex series of feedback interactions. We revisit these below. For now, we focus only on the equations modeling the MPF trimer, Cdc13 and Rum1. We follow the presentation of Novak et al. (2001), who constructed the model using the total amount of Cdc13, the total amount of Rum1, and preMPF, as three of the dependent variables. A different choice of dependent variables gives a different version of the same model.

First, we define the total amount of Cdc13, $[\text{Cdc13}_T]$, as

$$[\text{Cdc13}_T] = X_1 + X_2 + X_3 + [\text{MPF}], \tag{10.44}$$

where X_1, X_2 and X_3 refer to the labeled complexes in Fig. 10.12. As usual, X_1 denotes the concentration of X_1. Similarly, we let

$$[\text{preMPF}] = X_1 + X_3 \qquad \text{and} \qquad [\text{Trimer}] = X_1 + X_2, \tag{10.45}$$

as indicated by the dashed boxes in Fig. 10.12. We also have a conservation equation for Rum1. If we let $[\text{Rum1}_T]$ denote the total amount of Rum1, then

$$[\text{Rum1}_T] = [\text{Rum1}] + [\text{Trimer}] = [\text{Rum1}] + X_1 + X_2. \tag{10.46}$$

We assume that Cdc13, no matter in which state, is degraded at a rate that depends on Slp1 and Ste9, the two components of APC in fission yeast. Thus,

$$\frac{d[\text{Cdc13}_T]}{dt} = k_1 m - (k_2' + k_2''[\text{Ste9}] + k_2'''[\text{Slp1}])[\text{Cdc13}]. \tag{10.47}$$

The equation for preMPF is similar:

$$\begin{aligned} \frac{d[\text{preMPF}]}{dt} &= k_{\text{wee}}([\text{Cdc13}_T] - [\text{preMPF}]) - k_{25}[\text{preMPF}] \\ &\quad -(k_2' + k_2''[\text{Ste9}] + k_2'''[\text{Slp1}])[\text{preMPF}]. \end{aligned} \tag{10.48}$$

Here, k_{wee} and k_{25} are, respectively, the rate constants associated with Wee1 and Cdc25. As described below, they depend on [MPF].

Since k_{wee} and k_{25} depend on [MPF], we need to derive an expression for [MPF] in terms of our chosen dependent variables, $[\text{Cdc13}_T]$, [preMPF] and $[\text{Rum1}_T]$. We begin by deriving an expression for [Trimer]. This we do by assuming that X_1 and X_3 are always in equilibrium, as are X_2 and MPF. Thus

$$[\text{Rum1}][\text{MPF}] \;=\; K_d X_2, \tag{10.49}$$

$$[\text{Rum1}]X_3 \;=\; K_d X_1, \tag{10.50}$$

where K_d is the equilibrium constant for Rum1 binding. From this, and (10.45), it follows that

$$
\begin{aligned}
[\text{Trimer}] &= X_1 + X_2 \\
&= \frac{[\text{Rum1}]}{K_d}(X_3 + [\text{MPF}]) \\
&= \frac{1}{K_d}([\text{Rum1}_T] - [\text{Trimer}])([\text{Cdc13}_T] - [\text{Trimer}]).
\end{aligned}
\tag{10.51}
$$

This quadratic equation for [Trimer] can be easily solved to give

$$[\text{Trimer}] \;=\; \frac{1}{2}\left(\Sigma - \sqrt{\Sigma^2 - 4[\text{Rum1}_T][\text{Cdc13}_T]}\right) \tag{10.52}$$

$$\phantom{[\text{Trimer}]} \;=\; \frac{2[\text{Rum1}_T][\text{Cdc13}_T]}{\Sigma + \sqrt{\Sigma^2 - 4[\text{Rum1}_T][\text{Cdc13}_T]}}, \tag{10.53}$$

where

$$\Sigma = [\text{Cdc13}_T] + [\text{Rum1}_T] + K_d. \tag{10.54}$$

Note that here we have taken the smaller of the two roots, to insure that $[\text{Trimer}] \to 0$ as $[\text{Cdc13}_T] \to 0$.

With this expression for [Trimer] we can find an equation for [MPF] in terms of the other variables. First, since X_1 and X_3 are assumed to be in equilibrium, we have

$$[\text{preMPF}] = X_1 + X_3 = X_3\left(1 + \frac{[\text{Rum1}]}{K_d}\right). \tag{10.55}$$

Also, from conservation of Cdc13 (i.e., from (10.44)) we have

$$[\text{Trimer}] + X_3 + [\text{MPF}] = [\text{Cdc13}_T], \tag{10.56}$$

from which, using (10.55), it follows that

$$[\text{MPF}] = [\text{Cdc13}_T] - [\text{Trimer}] - \frac{[\text{preMPF}]K_d}{K_d + [\text{Rum1}_T] - [\text{Trimer}]}. \tag{10.57}$$

The three major sets of feedbacks

At this point we have differential equations for $[\text{Cdc13}_T]$ and [preMPF], with associated algebraic equations for [Trimer] and MPF. This completes the most complicated part of the model construction. The remainder of the model equations follow
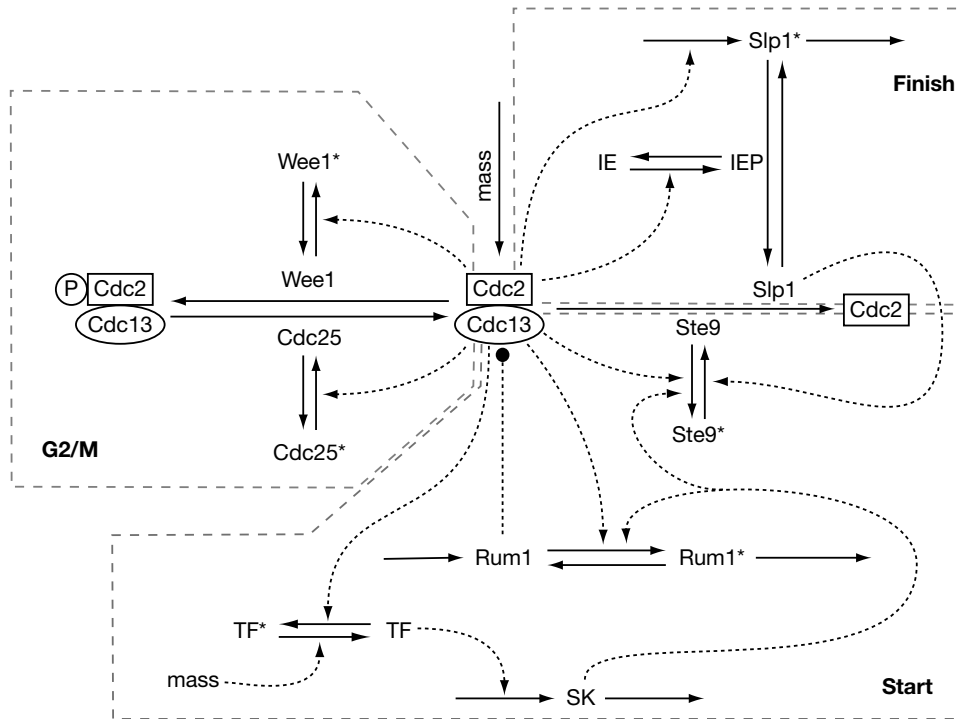
Figure 10.13: Schematic diagram of the feedbacks that control the cell cycle in fission yeast. All the dotted arrows denote activation, with the exception of the arrow with a solid circle on the end, which denotes inhibition. Adapted from Novak et al., (2001), Fig. 2.

in a straightforward manner from the reaction diagram, which is shown in full detail in Fig. 10.13.

This is a complicated reaction diagram; to make sense of it we divide the reactions into three main groups, corresponding to control of Start, Finish, and the G_2/M transition, as indicated by the dashed grey boxes in Fig. 10.13. Each is discussed in turn.

Start This set of feedbacks causes the increase of MPF (i.e., of Cdc2:Cdc13) at Start. There are two mutual inhibition loops. First, MPF inactivates Ste9, thus decreasing the rate of breakdown of MPF. Second, MPF increases the rate of inactivation of Rum1. Since Rum1 inactivates MPF (see Fig. 10.12) this is the second mutual inhibition loop.

Because of these mutual inhibitions, the cell can either have a high concentration of MPF, or a high concentration of Ste9 and Rum1. It cannot have both.

SK denotes a Starter Kinase that helps begin Start by phosphorylating Rum1 to its inactive state, thus relieving the inhibition on MPF. However, once Start begins, SK must be removed to allow MPF to decrease at Finish. Thus, MPF phosphorylates SK's Transcription Factor (TF) to its inactive state. Thus, this negative feedback loop works against the two mutual inhibition loops in Start.

Although this scheme appears to be exactly that of the simple generic model, there are some important differences. One important way in which fission yeast differs from the generic model is that, at Start, the increase of MPF is not explosive. Instead, Start is characterized by a precipitatous drop in [Ste9], which then allows [MPF] to start increasing. In fission yeast, MPF is held very low during G_1, as shown in Fig. 10.14. At Start, Cdc13 begins to accumulate, but MPF activity remains low because Cdc2 is phosphorylated by Wee1.

S/G_2/M The important reactions are sketched in Fig. 10.13, in a more simplified form than in Fig. 10.12, but including the action of MPF on Wee1 and Cdc25. MPF accumulates in the less active, Cdc2-phosphorylated, form, which is sufficient to drive DNA synthesis, but insufficient for mitosis. MPF decreases Wee1 activity by phosphorylating it (Wee1* is the phosphorylated, inactive, form of Wee1). MPF also increases the activity of Cdc25 by phosphorylating it (Cdc25 is the phosphorylated, active, form of Cdc25*). Note that sometimes the phosphorylated state is the inactive state, other times it is the active state. Both of these feedbacks are positive.

The cell spends a long time in G2 phase until it grows large enough for the positive feedback loops on Wee1 and Cdc25 to engage and remove the inhibitory phosphate group from Cdc2. The resulting explosive increase in MPF kicks the cell into mitosis. Hence, fission yeast characteristically has a short G_1 phase and a long S/G_2 phase.

The duration of G_2 is determined by the dynamics of MPF, and its activation and inactivation by Wee1 and Cdc25. In fission yeast, once the cell mass has

increased sufficiently, there is an explosive increase in [MPF] which pushes the cell into mitosis.

Finish This set of feedbacks causes the fast decrease in MPF at Finish (see Fig. 10.11). MPF increases the rate of production of inactive Slp1, which is then activated via the action of IEP, the phosphorylated Intermediate Enzyme. As in the generic model, the identity of IE is unknown. However, its existence is inferred from the significant delays that occur between an increase in MPF levels and an increase in Slp1. Slp1 increases the rate of MPF breakdown in two different ways; first, by promoting its degradation directly, and second, by activating Ste9, which also inactivates MPF.

It is interesting to note that the Start and Finish feedbacks are, essentially, a fast positive feedback (Start) followed by a slower negative feedback (Finish). This arrangement is seen in many physiological systems, including the Hodgkin-Huxley model of the action potential (Chapter 5) and models of the inositol trisphosphate receptor (Chapter 7).

Cell size affects the model in two different ways. First, we assume that the rate of production of MPF is a function of cell size, as discussed previously. Second, the rate of activation of the transcription factor, TF, is also assumed to be dependent on the cell size (see (10.71)). Thus, as the cell grows, the activity of MPF is increased in two different size-dependent ways. TF affects MPF activity via the production of a "starter kinase" (SK). SK initiates Start by downregulating Rum1 and Ste9, which allows $[\text{Cdc13}]_T$ to increase and eventually trigger the G2-M transition.

The model equations

Our job is now to translate the schematic diagrams in Figs. 10.12 and 10.13 into a set of ordinary differential equations. This has been done already for Cdc13_T and preMPF; it is now necessary to repeat this process for the remaining variables in the model. However, since the equations for the remaining variables are much simpler and easier to derive than those for Cdc13_T and preMPF they are presented here without detailed explanations. Also, so that all the equations are together in a single place, the equations for Cdc13_T and preMPF included here as well.

The model equations are

$$\frac{d[\text{Cdc13}_T]}{dt} = k_1 m - (k_2' + k_2''[\text{Ste9}] + k_2'''[\text{Slp1}])[\text{Cdc13}], \qquad (10.58)$$

$$\frac{d[\text{preMPF}]}{dt} = k_{\text{wee}}([\text{Cdc13}_T] - [\text{preMPF}]) - k_{25}[\text{preMPF}]$$
$$- (k_2' + k_2''[\text{Ste9}] + k_2'''[\text{Slp1}])[\text{preMPF}], \qquad (10.59)$$

$$\frac{d[\text{Ste9}]}{dt} = (k_3' + k_3''[\text{Slp1}])\frac{1 - [\text{Ste9}]}{J_3 + 1 - [\text{Ste9}]}$$
$$- (k_4'[\text{SK}] + k_4[\text{MPF}])\frac{[\text{Ste9}]}{J_4 + [\text{Ste9}]}, \qquad (10.60)$$

$$\frac{d[\text{Slp1}_T]}{dt} = k_5' + k_5''\frac{[\text{MPF}]^4}{J_5^4 + [\text{MPF}]^4} - k_6[\text{Slp1}_T], \qquad (10.61)$$

$$\frac{d[\text{Slp1}]}{dt} = k_7[\text{IEP}]\frac{[\text{Slp1}_T] - [\text{Slp1}]}{J_7 + [\text{Slp1}_T] - [\text{Slp1}]}$$

$$-k_8\frac{[\text{Slp1}]}{J_8 + [\text{Slp1}]} - k_6[\text{Slp1}], \tag{10.62}$$

$$\frac{d[\text{IEP}]}{dt} = k_9[\text{MPF}]\frac{1 - [\text{IEP}]}{J_9 + 1 - [\text{IEP}]} - k_{10}\frac{[\text{IEP}]}{J_{10} + [\text{IEP}]}, \tag{10.63}$$

$$\frac{d[\text{Rum1}_T]}{dt} = k_{11} - (k_{12} + k'_{12}[\text{SK}] + k''_{12}[\text{MPF}])[\text{Rum1}_T], \tag{10.64}$$

$$\frac{d[\text{SK}]}{dt} = k_{13}[\text{TF}] - k_{14}[\text{SK}], \tag{10.65}$$

where, as before,

$$[\text{Trimer}] = \frac{2[\text{Rum1}_T][\text{Cdc13}_T]}{\Sigma + \sqrt{\Sigma^2 - 4[\text{Rum1}_T][\text{Cdc13}_T]}}, \tag{10.66}$$

$$\Sigma = [\text{Cdc13}_T] + [\text{Rum1}_T] + K_d, \tag{10.67}$$

$$[\text{MPF}] = [\text{Cdc13}_T] - [\text{Trimer}] - \frac{[\text{preMPF}]K_d}{K_d + [\text{Rum1}_T] - [\text{Trimer}]}. \tag{10.68}$$

We also assume that k_{wee} and k_{25} are, respectively, decreasing and increasing Goldbeter-Koshland functions of [MPF] (recall (1.92), and thus

$$k_{\text{wee}} = k'_{\text{wee}} + (k''_{\text{wee}} - k'_{\text{wee}})G(V_{aw}, V_{iw}[\text{MPF}], J_{aw}, J_{iw}), \tag{10.69}$$

$$k_{25} = k'_{25} + (k''_{25} - k'_{25})G(V_{a25}[\text{MPF}], V_{i25}, J_{a25}, J_{i25}). \tag{10.70}$$

Finally, the concentration of transcription factor, [TF], is assumed to be an increasing Goldbeter-Koshland function of the cell mass, m, but a decreasing function of [MPF], and thus

$$[\text{TF}] = G(k_{15}m, k'_{16} + k''_{16}[\text{MPF}], J_{15}, J_{16}), \tag{10.71}$$

while the mass grows exponentially,

$$\frac{dm}{dt} = \mu m. \tag{10.72}$$

This completes the mathematical description of the reaction diagram in Fig. 10.13. All the parameter values are given in Table 10.7.

The wild type

The cell cycle in this more complex model has a structure similar to that of the 6-variable generic model of Section 10.3.1, and a typical solution is shown in Fig. 10.14. As in the simpler model, the curve of steady states (with m held fixed) is S-shaped. As the cell mass, m, increases, the concentration of MPF also increases until the lower bend of the S is reached, at which point the solution "falls off" the curve of steady states and head towards the stable oscillation (denoted by the dot-dash line in Fig. 10.14A). The resultant sudden increase in [MPF] pushes the cell into M phase.

Table 10.7: Parameters for the model of the cell cycle in fission yeast (10.35)–(10.43). Adapted from Novak et al. (2001), Table II. After Start occurs, the cell mass is divided by two to mimic cell division when $[\text{CycB}] = [\text{CycB}]_{\text{threshold}}$. All the parameters have units 1/min, except for the J's and K_d, which are dimensionless.

Cdc13	
$k_1 = 0.04$, $k_2' = 0.04$, $k_2'' = 1$, $k_2''' = 1$	$[\text{CycB}]_{\text{threshold}} = 0.05$
Ste9	
$k_3' = 1$, $k_3'' = 10$, $k_4' = 2$, $k_4 = 35$	$J_3 = 0.04$, $J_4 = 0.04$
Slp1	
$k_5' = 0.005$, $k_5'' = 0.2$, $k_6 = 0.1$, $k_7 = 1$, $k_8 = 0.25$	$J_5 = 0.3$, $J_7 = J_8 = 10^{-3}$
Rum1	
$k_{11} = 0.1$, $k_{12} = 0.01$, $k_{12}' = 1$, $k_{12}'' = 3$	$K_d = 0.001$
IEP	
$k_9 = 0.1$, $k_{10} = 0.02$	
SK	
$k_{13} = 0.1$, $k_{14} = 0.1$	
TF	
$k_{15} = 1.5$, $k_{16}' = 1$, $k_{16}'' = 2$	$J_{15} = 0.01$, $J_{16} = 0.01$
Wee1	
$k_{\text{wee}}' = 0.15$, $k_{\text{wee}}'' = 1.3$, $V_{aw} = 0.25$, $V_{iw} = 1$	$J_{aw} = 0.01$, $J_{iw} = 0.01$
Cdc25	
$k_{25}' = 0.05$, $k_{25}'' = 5$, $V_{a25} = 1$, $V_{i25} = 0.25$	$J_{a25} = 0.01$, $J_{i25} = 0.01$
m	
$\mu = 0.005$	
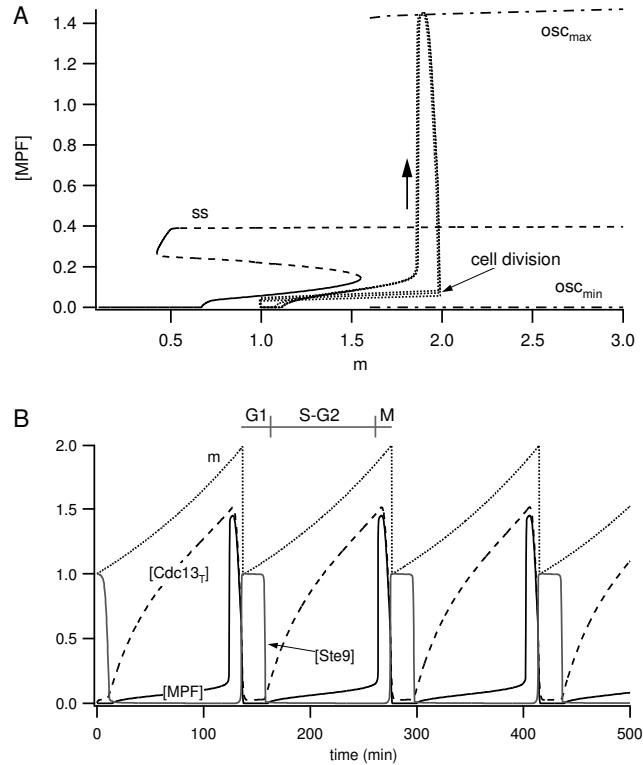
Figure 10.14: A: bifurcation diagram of the cell cycle model of fission yeast, using the wild type parameters in Table 10.7, as a function of m, the cell size. The curve of steady states is labeled ss, with stable branches denoted by solid curves, and unstable branches by dashed curves. A branch of oscillatory solutions exists for larger m. The maximum and minimum of the oscillations are plotted as functions of m, and are labeled osc_{max} and osc_{min} respectively. A solution of the model for several cell cycles is superimposed (dotted line). B: the solution plotted against time for the same cycles shown in A.

Because the stable solution is oscillatory, [MPF] naturally increases and then decreases (Finish), at which point the cell divides, the cell mass is divided by two, and the cycle repeats. A succession of cycles is shown in Fig. 10.14B.

Note that the cell cycle trajectory does not lie exactly on the S-shaped curve of steady states. This is because the cell size is continually changing, never allowing enough time for the solution to reach the steady-state that corresponds to a fixed value of m.

The different phases of the cell cycle are shown on the bar in Fig. 10.14B. During G_1 [MPF] is held very low by Ste9. At the Start transition [Ste9] falls almost to zero, thus allowing [MPF] to increase. This occurs relatively early during the cell cycle, when the cell mass is small. During S/G_2 phase the cell replicates DNA and slowly increases in size until critical mass is reached, whereupon MPF] increases explosively and the cell is pushed into M phase. Thus, the Start transition here does not correspond to an explosive increase of MPF, a major point of difference from the simple generic model described earlier. This serves to emphasize the fact that different cell types have different ways of controlling the cell cycle, and, although there are many similarities between cell types, no single mechanism serves as a universal explanation.

wee1$^-$ cells

One particularly interesting feature of this model is that it can be used to explain the behavior of a number of fission yeast mutants. Here, we discuss only one of these mutants, the wee1$^-$ mutant. Others are discussed in detail in Tyson et al. (2002) and Novak et al. (2001).

The normal fission yeast cell cycle has a short G_1 phase followed by a much longer S/G_2 phase during which most of the cell growth occurs. In the wild type cell, the long S/G_2 phase is caused by the balance between MPF, Wee1 and Cdc25. Because Wee1 inactivates MPF, it is not until [MPF] has increased past a critical threshold that it can inactivate Wee1 and thus allow the explosive growth of MPF at the beginning of M phase.

If Wee1 is knocked out (i.e., as in a wee1$^-$mutant) the inactivation of MPF by Wee1 is prevented, or at least greatly decreased. This allows the explosive increase in [MPF] to happen at a lower value of m, and thus the cell enters mitosis when it is much smaller than in the wild type. However, because the cell cycle occurs for smaller cell sizes, and thus lower overall values of [MPF], the G_1 phase is extended, as it takes longer for Ste9 to be overpowered by MPF (which must happen at the end of G_1, see Fig. 10.14B). Hence, wee1$^-$ cells have an extended G_1 phase, a shortened S/G_2 phase, and at division are approximately half the size of wild type cells. (The word *wee* is Scottish for small. Paul Nurse originally discovered Wee1 in the early 1970s and coined its name after observing that the absence of the gene made cells divide when they were unusually small.)

The phase plane and a cell cycle of the wee1$^-$ mutant is shown in Fig. 10.15. To model the absence of Wee1, the parameter k''_{wee} is decreased to 0.3, thus decreasing the value of k_{wee}, as shown by (10.69). With this change, the S-shaped curve of steady states is shifted to lower values of m, and the solution "falls off" the lower limit point at lower values of m. Thus, mitosis is initiated at lower cell size than
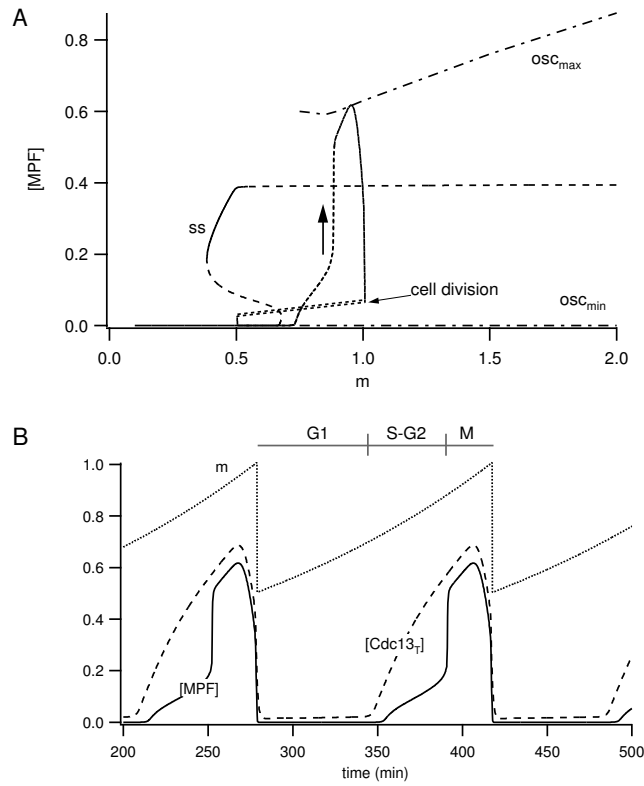
Figure 10.15: A: bifurcation diagram of the wee1$^-$ cell cycle model of fission yeast, using the same parameters in Table 10.7, with $k''_{\text{wee}} = 0.3$. The notation is the same as Fig. 10.14. B: the solution plotted against time for the same cycles shown in A.

in wild type cells. Fig. 10.15B shows that G_1 phase is extended, and that the cell cycle occurs for smaller values of [MPF] than in the wild type.

10.3.3 A Limit Cycle Oscillator in the *Xenopus* Oocyte

There is strong evidence that early embryonic divisions are controlled by a cytoplasmic biochemical limit cycle oscillator. For example, if fertilized (*Xenopus*) frog eggs are enucleated, they continue to exhibit periodic "twitches" or contractions, as if the cytoplasm continued to generate a signal in the absence of a nucleus. Enucleated sea urchin eggs go a step further by actually dividing a number of times before they notice that they contain no genetic material and consequently die. In *Xenopus* the first post-fertilization cell cycle takes approximately one hour, followed by 11 faster cycles (approximately 30 minutes each) during which the cell mass decreases.

These divisions result from a cell cycle oscillator from which some of the checkpoints and controls have been removed. The most detailed model of this oscillator is that of Novak and Tyson (1993a,b; Borisuk and Tyson, 1998), and this is the model we describe here. A simpler model due to Goldbeter is discussed in Exercise 7, and a simplified version of the Novak-Tyson model is discussed in Chapter 10 of Fall et al. (2002).

Because frogs are not yeast, the details of the cell cycle in *Xenopus* oocytes are not exactly the same as those of the cell cycle in fission yeast, although there are major similarities.

In fertilized *Xenopus* oocytes, cell division takes place without any cell growth, so the G_1 checkpoint is removed (or inoperable). The MPF that is critical for getting through the G_2 checkpoint is a dimer of Cdc2 and a mitotic cyclin.

The *cdc*2 gene encodes a cyclin-dependent protein kinase, Cdc2, which, in combination with B-type cyclins, forms MPF, which induces entry into M phase. The activity of the Cdc2-cyclin B dimer (MPF) is also controlled by phosphorylation at two sites, tyrosine-15 and threonine-167. (Tyrosine and threonine are two of the twenty amino acids that are strung together to form a protein molecule. The number 15 or 167 denotes the location on the protein sequence of Cdc2.) These two sites define four different phosphorylation states. MPF is active when it is phosphorylated at threonine-167 only. The other three phosphorylation states are inactive. Active MPF initiates a chain of reactions that controls mitotic events.

Just as in fission yeast, movement between different phosphorylation states is mediated by Wee1 and Cdc25. Wee1 inactivates MPF by adding a phosphate to the tyrosine-15 site. Cdc25 reverses this by dephosphorylating the tyrosine-15 site. A schematic diagram of this regulation is shown in Fig. 10.16. Cyclin B is synthesized from amino acids and binds with free Cdc2 to form an inactive MPF dimer. The dimer is quickly phosphorylated on threonine-167 (by a protein kinase called CAK) and dephosphorylated at the same site by an unknown enzyme. Simultaneously, Wee1 can phosphorylate the dimer at the tyrosine-15 site, rendering it inactive, and Cdc25 can dephosphorylate the same site. Mitosis is initiated when a sufficient quantity of MPF is active.

This regulation of MPF is one point of divergence with the previous model for fission yeast. The other feedbacks are similar to those we have seen before. First, the active form of MPF regulates the activities of Wee1 and Cdc25 (as in the
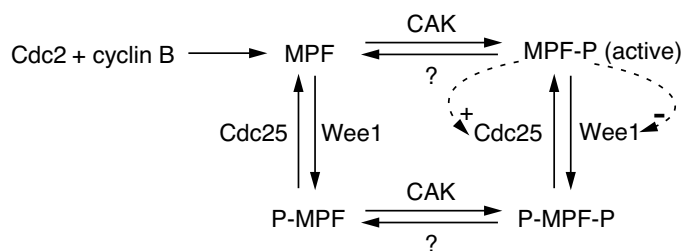
Figure 10.16: Schematic diagram of the regulatory pathway of MPF in *Xenopus* oocytes.

box labeled G2/M in Fig. 10.13), while the degradation of MPF is controlled by a delayed negative feedback loop through an intermediate enzyme (as in the box labeled Finish in Fig. 10.13). In *Xenopus*, the degradation of MPF is controlled by a ubiquitin-conjugating enzyme (UbE) (which is an outdated name for our friend, APC-Cdc20).

We now have a complete verbal description of a model for the initiation of mitosis. In summary, as cyclin is produced, it combines with Cdc2 to form MPF. MPF is quickly phosphorylated to its active form. Active MPF turns on its own autocatalytic production by activating Cdc25 and inactivating Wee1. By activating UbE, which activates the destruction of cyclin, active MPF also turns on its own destruction, but with a delay, thus completing the cycle.

Of course, this verbal description is incomplete, because there are many other features of M phase control that have not been included. It also does not follow from verbal arguments alone that this model actually controls mitosis in a manner consistent with experimental observations. To check that this model is indeed sufficient to explain some features of the cell cycle, it is necessary to present it in quantitative form (Novak and Tyson, 1993).

The chemical species that must be tracked include the Cdc2 and cyclin monomers, the dimer MPF in its active and inactive states, as well as the four regulatory enzymes Wee1, Cdc25, IE, and UbE in their phosphorylated and unphosphorylated states.

First, cyclin (with concentration y) is produced at a steady rate and is degraded or combines with Cdc2 (with concentration c) to form the MPF dimer (r):

$$\frac{dy}{dt} = k_1[A] - k_2 y - k_3 Y c. \tag{10.73}$$

The MPF dimer can be in one of four phosphorylation states, with phosphate at tyrosine-15 (s), at threonine-167 (concentration m), at both sites (concentration n), or at none (concentration r). The movement among these states is regulated by the enzymes Wee1, Cdc25, CAK, and one unknown enzyme ("?"). Thus,

$$\frac{dr}{dt} = -(k_2 + k_{\text{CAK}} + k_{\text{wee}})r + k_3 y c + k_? n + k_{25} s, \tag{10.74}$$

$$\frac{ds}{dt} = -(k_2 + k_{\text{CAK}} + k_{25})s + k_? n + k_{\text{wee}} r, \tag{10.75}$$
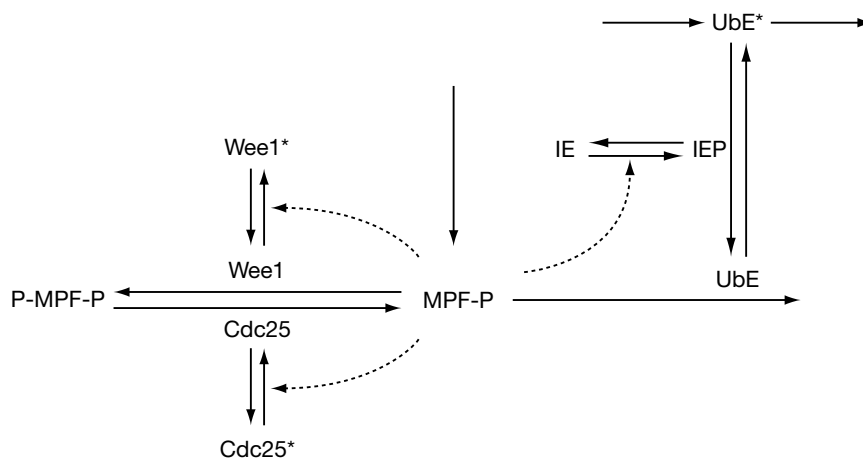
Figure 10.17: Schematic diagram of the regulation of MPF formation and degradation in *Xenopus* oocytes. Note the similarities with Fig. 10.13, the major difference being that the reactions involving the Start transition have been removed. In addition, the rate of production of MPF does not depend on the cell mass, which now does not appear in the model at all.

$$\frac{dm}{dt} = -(k_2 + k_? + k_{\text{wee}})m + k_{\text{CAK}}r + k_{25}n, \tag{10.76}$$

$$\frac{dn}{dt} = -(k_2 + k_? + k_{25})n + k_{\text{wee}}m + k_{\text{CAK}}s. \tag{10.77}$$

Notice that in the above equations, cyclin degradation at rate k_2 is permitted for free cyclin as well as for cyclin that is dimerized with Cdc2. We assume that, if cyclin degrades directly from a phosphorylated dimer, then the phosphate is also immediately removed thus producing free Cdc2. Thus,

$$\frac{dc}{dt} = k_2(r + s + n + m) - k_3 cy. \tag{10.78}$$

These six equations would form a closed system were it not for feedback. Notice that the last equation (10.78) is redundant, since $m + r + s + n + c = \text{constant}$. The feedback shows up in the nonlinear dependence of rate constants on the enzymes Cdc25, Wee1, IE, and UbE. This is expressed as

$$k_{25} = V_{25}'[\text{Cdc25}] + V_{25}''[\text{Cdc25\_P}], \tag{10.79}$$

$$k_{\text{wee}} = V_{\text{wee}}'[\text{Wee1\_P}] + V_{\text{wee}}''[\text{Wee1}], \tag{10.80}$$

$$k_2 = V_2'[\text{UbE}] + V_2''[\text{UbE}^*]. \tag{10.81}$$

In addition, the active states of Cdc25, Wee1, IE, and UbE are governed by Michaelis–Menten rate laws of the form

$$\frac{d[\text{Cdc25\_P}]}{dt} = \frac{k_a m[\text{Cdc25}]}{K_a + [\text{Cdc25}]} - \frac{k_b[\text{PPase}][\text{Cdc25\_P}]}{K_b + [\text{Cdc25\_P}]}, \tag{10.82}$$

Table 10.8: Michaelis–Menten constants for the cell-cycle model of Novak and Tyson (1993).

$K_a/[\text{Cdc25}_{\text{total}}]$	$=$	0.1	$K_b/[\text{Cdc25}_{\text{total}}]$	$=$	0.1
$K_c/[\text{UbE}_{\text{total}}]$	$=$	0.01	$K_d/[\text{UbE}_{\text{total}}]$	$=$	0.01
$K_e/[\text{Wee1}_{\text{total}}]$	$=$	0.3	$K_f/[\text{Wee1}_{\text{total}}]$	$=$	0.3
$K_g/[\text{IE}_{\text{total}}]$	$=$	0.01	$K_h/[\text{IE}_{\text{total}}]$	$=$	0.01

Table 10.9: Rate constants for the cell-cycle model of Novak and Tyson (1993).

$k_1[\text{A}]/[\text{Cdc2}_{\text{total}}]$	$=$	0.01	$k_3[\text{Cdc2}_{\text{total}}]$	$=$	1.0
$V_2'[\text{UbE}_{\text{total}}]$	$=$	$0.015\ (0.03)$	$V_2''[\text{UbE}_{\text{total}}]$	$=$	1.0
$V_{25}'[\text{Cdc25}_{\text{total}}]$	$=$	0.1	$V_{25}''[\text{Cdc25}_{\text{total}}]$	$=$	2.0
$V_{\text{wee}}'[\text{Wee1}_{\text{total}}]$	$=$	0.1	$V_{\text{wee}}''[\text{Wee1}_{\text{total}}]$	$=$	1.0
k_{CAK}	$=$	0.25	$k_?$	$=$	0.25
$k_a[\text{Cdc2}_{\text{total}}]/[\text{Cdc25}_{\text{total}}]$	$=$	1.0	$k_b[\text{PPase}]/[\text{Cdc25}_{\text{total}}]$	$=$	0.125
$k_c[\text{IE}_{\text{total}}]/[\text{UbE}_{\text{total}}]$	$=$	0.1	$k_d[\text{IE}_{\text{anti}}]/[\text{UbE}_{\text{total}}]$	$=$	0.095
$k_e[\text{Cdc2}_{\text{total}}]/[\text{Wee1}_{\text{total}}]$	$=$	1.33	$k_f[\text{PPase}]/[\text{Wee1}_{\text{total}}]$	$=$	0.1
$k_g[\text{Cdc2}_{\text{total}}]/[\text{IE}_{\text{total}}]$	$=$	0.65	$k_h[\text{PPase}]/[\text{IE}_{\text{total}}]$	$=$	0.087

$$\frac{d[\text{Wee1\_P}]}{dt} = \frac{k_e m[\text{Wee1}]}{K_e + [\text{Wee1}]} - \frac{k_f[\text{PPase}][\text{Wee1\_P}]}{K_f + [\text{Wee1\_P}]}, \tag{10.83}$$

$$\frac{d[\text{IE\_P}]}{dt} = \frac{k_g m[\text{IE}]}{K_g + [\text{IE}]} - \frac{k_h[\text{PPase}][\text{IE\_P}]}{K_h + [\text{IE\_P}]}, \tag{10.84}$$

$$\frac{d[\text{UbE}^*]}{dt} = \frac{k_c[\text{IE\_P}][\text{UbE}]}{K_c + [\text{UbE}]} - \frac{k_d[\text{IE}_{\text{anti}}][\text{UbE}^*]}{K_d + [\text{UbE}^*]}. \tag{10.85}$$

The quantities with _P attached correspond to phosphorylated forms of the enzyme quantity. The total amounts of each of these enzymes are assumed to be constant, so equations for the inactive forms are not necessary. PPase denotes a phosphatase that dephosphorylates Cdc25_P.

This forms a complete model with nine differential equations having 8 Michaelis–Menten parameters and 18 rate constants. There are two ways to gain an understanding of the behavior of this system of differential equations: by numerical simulation of the full system of equations using reasonable parameter values, or by approximating the system to a smaller system of equations and studying the simpler system by analytical means.

The parameter values used by Novak and Tyson to simulate *Xenopus* oocyte extracts are shown in Tables 10.8 and 10.9.

While numerical simulation of these nine differential equations is not difficult, to gain an understanding of the basic behavior of the model it is convenient to make some simplifying assumptions. Suppose k_{CAK} is large and $k_?$ is small, as experiments suggest. Then the phosphorylation of Cdc2 on threonine-167 occurs immediately after formation of the MPF dimer. This allows us to ignore the quantities r and s. Next we assume that the activities of the regulatory enzymes, (10.79)–(10.81), can

be approximated by

$$k_{\text{wee}} = \text{constant}, \tag{10.86}$$

$$k_2 = k_2' + k_2''m^2, \tag{10.87}$$

$$k_{25} = k_{25}' + k_{25}''m^2. \tag{10.88}$$

This leaves only three equations for the three unknowns y (free cyclin), m (active MPF), and Cdc2 monomer (q) as follows

$$\frac{dy}{dt} = k_1 - k_2 y - k_3 yq, \tag{10.89}$$

$$\frac{dm}{dt} = k_3 yq - k_2 m + k_{25}n - k_{\text{wee}}m, \tag{10.90}$$

$$\frac{dq}{dt} = -k_3 yq + k_2(m + n), \tag{10.91}$$

where $m + n + q = c$ is the total Cdc2. It follows that the total cyclin $l = y + m + n$ satisfies the differential equation

$$\frac{dl}{dt} = k_1 - k_2 l. \tag{10.92}$$

Any three of these four equations describes the behavior of the system. However, in the limit that k_3 is large compared to other rate constants, the system can be further reduced to a two-variable system for which phase-plane analysis is applicable. With $v = k_3 y$,

$$\frac{dv}{dt} + k_2 v = k_3(k_1 - qv), \tag{10.93}$$

so that $qv = k_1$ to leading order. If k_1 is small, then y is small as well, so that (10.90) becomes

$$\frac{dm}{dt} = k_1 - k_2 m + k_{25}(l - m) - k_{\text{wee}}m. \tag{10.94}$$

The two equations (10.92) and (10.94) form a closed system that can be studied using the phase portrait in the (l, m) plane. In this approximation, $q = c - l$. The nullclines are described by the equations

$$\frac{dl}{dt} = 0 : l = \frac{k_1}{k_2(m)} \tag{10.95}$$

and

$$\frac{dm}{dt} = 0 : l = \frac{k_{\text{wee}}m + k_2(m)m - k_1}{k_{25}(m)} + m, \tag{10.96}$$

which are shown plotted in Fig. 10.18.

For these parameter values, there is a unique unstable steady-state solution surrounded by a limit cycle oscillation. By adjusting parameters, one can have a stable fixed point on the leftmost branch of the "N"-shaped curve corresponding to the G_2 checkpoint, or one can have a stable fixed point on the rightmost branch, yielding an M phase checkpoint. Here a possible control parameter is k_{wee}, since increasing k_{wee} causes the m nullcline to increase. Thus, increasing k_{wee} creates a G_2 checkpoint on the leftmost branch of the "N"-shaped curve.
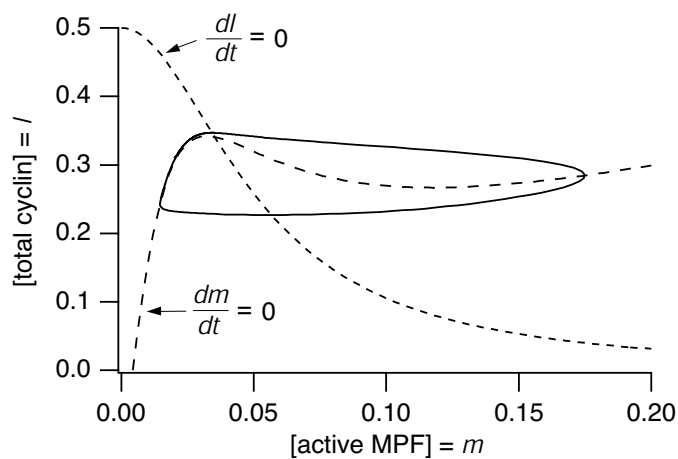
Figure 10.18: Solution trajectory and nullclines for the system of equations (10.92), (10.94). Parameter values are $k_1 = 0.004$, $k_{\text{wee}} = 0.9$, $k_2 = 0.008$, $k_2' = 3.0$, $k_{25} = 0.03$, $k_{25}' = 50.0$.
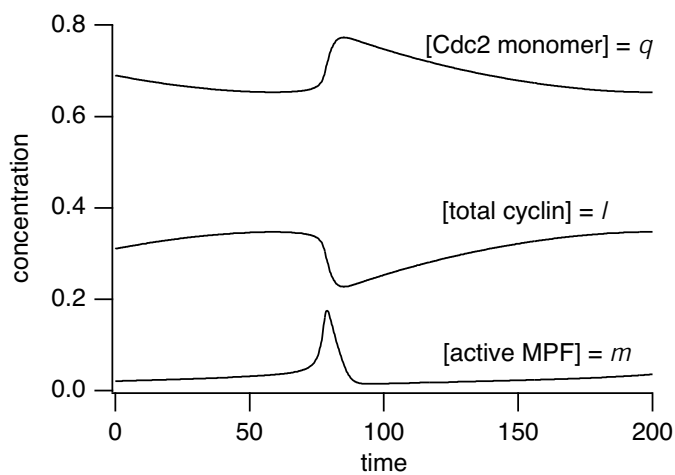
Figure 10.19: Solution for the system of equations (10.90), (10.91), (10.92), plotted as a function of time. Parameter values are the same as in Fig. 10.18.

10.3.4 Conclusion

We are a long way from a complete understanding of the biochemistry of the cell cycle. Here we have seen a few of the main players, although there are major portions of the cell cycle that are still a mystery. With the modern development of biochemistry, many similar stories relating to regulation of cell function are being unfolded. It is likely that in the coming years many of the details of this story will change and many new details will be added. However, the basic modeling process of turning a verbal description into a mathematical model and the consequent analysis of the model will certainly remain an important tool to aid our understanding of these complicated and extremely important processes. Furthermore, as the details of the stories become more complicated (as they are certain to do), mathematical analysis will become even more important in helping us understand how these processes work.

Exercises

1. Suppose that the production of an enzyme is turned on by m molecules of the enzyme according to

$$\text{G} + m\text{P} \underset{k_-}{\overset{k_+}{\rightleftharpoons}} \text{X},$$
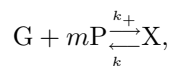
where G is the inactive state of the gene and X is the active state of the gene. Suppose that mRNA is produced when the gene is in the active state and the enzyme is produced by mRNA and is degraded at some linear rate. Find a system of differential equations governing the behavior of mRNA and enzyme. Give a phase portrait analysis of this system and show that it has a "switch-like" behavior.

2. For a simplified lac operon model, assume that external lactose is converted directly into allolactose, and take

$$\frac{dA}{dt} = \alpha_L P \frac{L_e}{K_{Le} + L_e} - \beta_A B \frac{A}{K_A + A} - \gamma_A A. \tag{10.97}$$

eliminating (10.20) from the model.

Give a graphical steady state analysis of the system of equations by plotting the nullclines $\frac{dM}{dt} = 0$ and $\frac{dA}{dt} = 0$ in the $M - A$ phase plane (this is not a true phase plane since it is a four variable system.)

3. Find the steady state solutions of the Goodwin model (10.22)—(10.23) with $n = 3$, and with $k_1 = k_2 = k_3$. Under what conditions is the steady state solution unstable, and under what conditions is the instability an oscillatory instability? Find conditions on the parameters for a Hopf bifurcation.

4. A modification of the Goodwin model that does not require such a high level of cooperativity was formulated by Bliss et al. (1982) and is given by

$$\frac{dx_1}{dt} = \frac{a}{1 + x_3} - b_1 x_1, \tag{10.98}$$
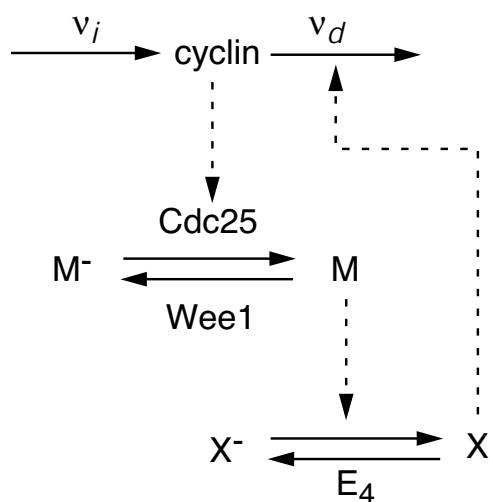
Figure 10.20: Diagram for the minimal cascade mitosis model of Goldbeter (1996).

$$\frac{dx_2}{dt} = b_1 x_1 - b_2 x_2, \tag{10.99}$$

$$\frac{dx_3}{dt} = b_2 x_2 - \frac{c x_3}{K + x_3}. \tag{10.100}$$

Determine the stability of the steady state solution and find any Hopf bifurcation points in the special case that $K = 1$, $b_1 = b_2 < c$, and $a = c\left(\sqrt{\frac{c}{b_1}} - 1\right)$.

5. Sketch the phase portrait for the two variable generic cell cycle model given by (10.35) and (10.36).

6. Instead of using (10.55), the original presentation of the model of Novak et al. (2001) used the expression

$$[\text{MPF}] = \frac{([\text{Cdc13}_T] - [\text{preMPF}])([\text{Cdc13}_T] - [\text{Trimer}])}{[\text{Cdc13}_T]}. \tag{10.101}$$

Show that these two expressions for [MPF] are the same. Hint: make it easier by defining $c_T = [\text{Cdc13}_T]$, $T = [\text{Trimer}]$, $r = [\text{Rum1}]$, $M = [\text{MPF}]$ and $p = [\text{preMPF}]$. There are a number of ways to show this. One way is to start by

$$c_T = c_T + p - p = (c_T - p) + (X_1 + X_3). \tag{10.102}$$

Then show that $X_1 + X_3 = (c_T - p)X_3/M$, and factor out $c_T - p$ to get the result.

7. Goldbeter (1996) developed and studied a "minimal" cascade model for the mitotic oscillator. The model assumes that cyclin B (C) is synthesized at a constant rate and activates Cdc25 kinase. The activated Cdc25 kinase in

Table 10.10: Parameter values for the Goldbeter minimal mitotic cycle model.

K_1	=	0.1	V_{M1}	=	0.5 min^{-1}
K_2	=	0.1	V_2	=	0.167 min^{-1}
K_3	=	0.1	V_{M3}	=	0.2 min^{-1}
K_4	=	0.1	V_4	=	0.1 min^{-1}
ν_i	=	0.023 μM/min	ν_d	=	0.1 μM/min
K_c	=	0.3 μM	K_d	=	0.02 μM
k_d	=	3.33$\times10^{-3}$ min^{-1}			

turn activates Cdc2 kinase (M), and the activated Cdc2 kinase is inactivated by the kinase Wee1. There is also a cyclin protease X that is activated by Cdc2 kinase and inactivated by an additional phosphatase. The differential equations for this reaction scheme (shown in Fig. 10.20) are

$$\frac{dc}{dt} = \nu_i - \nu_d x \frac{c}{K_d + c} - k_d c, \tag{10.103}$$

$$\frac{dm}{dt} = V_1 \frac{1 - m}{K_1 + 1 - m} - V_2 \frac{m}{K_2 + m}, \tag{10.104}$$

$$\frac{dx}{dt} = V_3 \frac{1 - x}{K_3 + 1 - X} - V_4 \frac{x}{K_4 + X}, \tag{10.105}$$

and

$$V_1 = V_{M1} \frac{c}{K_c + c}, \qquad V_3 = V_{M3} m, \tag{10.106}$$

where c denotes cyclin concentration, and m and x denote the fraction of active Cdc2 kinase and the fraction of active cyclin protease, respectively. The parameters ν_i and ν_d are the constant rate of cyclin synthesis and maximum rate of cyclin degradation by protease X, achieved at $x = 1$. K_d and K_c denote Michaelis-Menten constants for cyclin degradation and cyclin activation, while k_d is the rate of nonspecific degradation of cyclin. The remaining parameters V_i and K_i, $i = 1, \ldots, 4$, are the effective maximum rate and Michaelis-Menten constants for each of the four enzymes Cdc25, Wee1, Cdc2, and the protease phosphatase (E_4), respectively. Typical parameter values are shown in Table 10.10.

Simulate this system of equations to show that there is a stable limit cycle oscillation for this model. What is the period of oscillation?

Part II

Chapter 11

The Circulatory System

The circulatory system forms a closed loop for the flow of blood that carries oxygen from the lungs to the tissues of the body and carries carbon dioxide from the tissues back to the lungs (Figs. 11.1 and 11.2). Because it is a closed loop system, there are two pumps to overcome the resistance and maintain a constant flow. The left heart receives oxygen-rich blood from the lungs and pumps this blood into the *systemic arteries*. The systemic arteries form a tree of progressively smaller vessels, beginning with the aorta, branching to the small arteries, then to the arterioles, and finally to the capillaries. The exchange of gases takes place in the capillaries. Leaving the systemic capillaries, the blood enters the *systemic veins*, through which it flows in vessels of progressively increasing size toward the right heart. The systemic veins consist of venules, small veins, and the venae cavae. The right heart pumps blood into the *pulmonary arteries*, which form a tree that distributes the blood to the lungs. The smallest branches of this tree are the pulmonary capillaries, where carbon dioxide leaves and oxygen enters the blood. Leaving the pulmonary capillaries, the oxygenated blood is collected by the pulmonary veins, through which it flows back to the left heart. It takes about a minute for a red blood cell to complete this circuit.

While there is an apparent structural symmetry between the pulmonary and systemic circulations, there are significant quantitative differences in pressure and blood volume. Nevertheless, the output of the right and left sides of the heart must always balance, even though the cardiac output, or total amount of blood pumped by the heart, varies widely in response to the metabolic needs of the body. One of the goals of this chapter is to understand how the cardiac output is determined and regulated in response to the metabolic needs of the body. Questions of this nature have been studied for many years, and many books have been written on the subject (see, for example, Guyton, 1963, or Reeve and Guyton, 1967. A more recent book that discusses several mathematical models of the blood and circulatory system is Ottesen et al., 2004). Here, we consider only the simplest models for the control of cardiac output.

Each beat of the heart sends a pulse of blood through the arteries, and the form of this arterial pulse changes as it moves away from the heart. An interesting problem is to understand these changes and their clinical significance in terms of
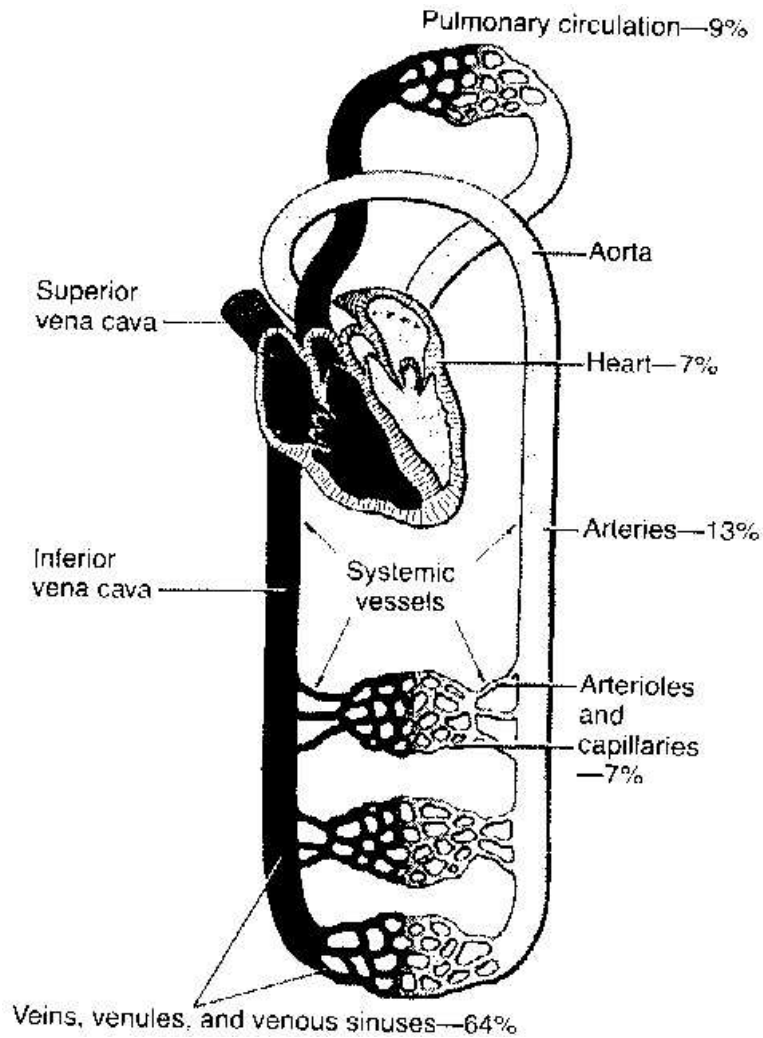
Figure 11.1: Schematic diagram of the circulatory system, showing the systemic and pulmonary circulations, the chambers of the heart, and the distribution of blood volume throughout the system. (Guyton and Hall, 1996, Fig. 14-1, p. 162.)
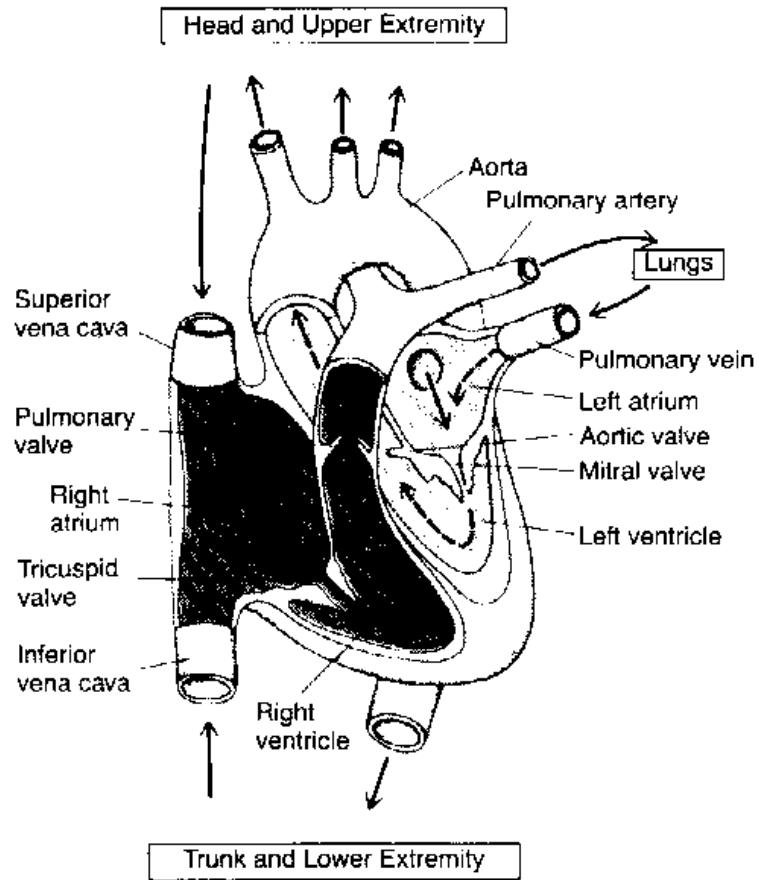
Figure 11.2: Schematic diagram of the heart as a pump. (Guyton and Hall, 1996, Fig. 9-1, p. 108.)

the properties of the blood and the arterial walls. Again, this problem has been studied in great detail, and we present here only a brief look at the earliest and simplest models of the arterial pulse.

11.1 Blood Flow

The term *blood pressure* refers to the force per unit area that the blood exerts on the walls of blood vessels. Blood pressure varies both in time and distance along the circulatory system. *Systolic pressure* is the highest surge of pressure in an artery, and results from the ejection of blood by the ventricles during ventricular contraction, or *systole*. *Diastolic pressure* is the lowest pressure reached during ventricular relaxation and filling, called *diastole*. In the aorta of a normal human, systolic pressure is about 120 mm Hg and diastolic pressure is about 80 mm Hg.

If the effects of gravity are ignored (which they are throughout this book), then one may asume that blood flows solely in response to pressure gradients. The simplest way to characterize a blood vessel is as a *resistance vessel* in which the radius is constant and the flow is linearly proportional to the pressure drop. In a linear resistance vessel, the flow, Q, is related to pressure by the ohmic relationship

$$Q = \frac{\Delta P}{R},\tag{11.1}$$

where ΔP is the pressure drop and R is the resistance. The relationship between resistance and radius of the vessel is dramatic. To understand this dependence suppose that a viscous fluid moves slowly and steadily through a cylindrical vessel of fixed radius. The velocity of the fluid is described by a vector $\mathbf{u}$ that has axial, radial, and angular components. Because the fluid is incompressible and fluid is conserved, it must be that

$$\nabla \cdot \mathbf{u} = 0.\tag{11.2}$$

Furthermore, because momentum is conserved, the Navier–Stokes equations (Segel, 1977) hold:

$$\rho(\mathbf{u}_t + \mathbf{u} \cdot \nabla \mathbf{u}) = -\nabla P + \mu \nabla^2 \mathbf{u},\tag{11.3}$$

where ρ is the constant fluid density, P is the fluid pressure, and μ is the fluid viscosity. (A brief derivation of the conservation and momentum equations in the case of zero viscosity is given in Chapter 20, Section 20.2.1.) If the flow is steady and the nonlinear terms are small compared to viscosity (in an appropriate nondimensional scaling), then

$$\mu \nabla^2 \mathbf{u} = \nabla P.\tag{11.4}$$

This simplification of the Navier–Stokes equation is called the Stokes equation.

The applicability of the Stokes equation to blood flow is suspect for several reasons. The viscosity contribution (the Laplacian) in the Stokes equation is derived from an assumed constitutive law relating stresses and strains in the fluid (Segel, 1977) that is known not to hold in fluids containing long polymers or other complicated chemical structures, including red blood cells. Furthermore, in the capillaries, the large size of the red blood cells compared to the typical diameter of a capillary

suggests that a continuum description is not appropriate. However, we do not concern ourselves with these issues here and accept the Stokes equation description as adequate.

We look for a solution of the Stokes equation whose only nonzero component is the axial component. We define coordinates on the cylinder in the usual fashion, letting x denote distance along the cylinder in the axial direction and letting r denote the radial direction. The angular direction, with coordinate θ, does not enter into this analysis.

First observe that with only axial flow, the incompressibility condition (11.2) implies that $\frac{\partial u}{\partial x} = 0$, where u is the axial component of the velocity vector. Thus, u is independent of x. Then, with a steady flow, (11.4) reduces to the ordinary differential equation

$$\mu \frac{1}{r} \frac{d}{dr} \left(r \frac{d}{dr} u \right) = \frac{dP}{dx} = P_x, \tag{11.5}$$

where P_x is the axial pressure gradient along the vessel. Note also that P_x must be constant, independent of r and x. Because of viscosity, the velocity must be zero at the wall of the cylindrical vessel, $r = r_0$.

Integration of (11.5) from r to r_0 gives

$$u(r) = -\frac{P_x}{4\mu}(r_0^2 - r^2), \tag{11.6}$$

from which it follows that the total flux through the vessel is (*Poiseuille's law*)

$$Q = 2\pi \int_0^{r_0} u(r) r \, dr = -\frac{\pi P_x}{8\mu} r_0^4. \tag{11.7}$$

This illustrates that the total flow of blood through a vessel is directly proportional to the fourth power of its radius, so that the radius of the vessel is by far the most important factor in determining the rate of flow through a vessel. In terms of the cross-sectional area A_0 of the vessel, the flux through the cylinder is

$$Q = -\frac{P_x}{8\pi\mu} A_0^2, \tag{11.8}$$

while the average fluid velocity over a cross-section of the cylinder is given by

$$v = \frac{Q}{A_0} = -\frac{P_x}{8\pi\mu} A_0. \tag{11.9}$$

Note that a positive flow is defined to be in the increasing x direction, and thus a negative pressure gradient P_x drives a positive flow Q. Important controls of the circulatory system are vasodilators and vasoconstrictors, which, as their names suggest, dilate or constrict vessels and thereby adjust the vessel resistance by adjusting the radius.

If there are many parallel vessels of the same radius, then the total flux is the sum of the fluxes through the individual vessels. If there are N vessels, each of

Vessel	D (cm)	A (cm^2)	P(mm Hg)	v (cm/s)
Aorta	2.5	2.5	100	33
Small arteries	0.5	20	100	30
Arterioles	3×10^{-3}	40	85	15
Capillaries	6×10^{-4}	2500	30	0.03
Venules	2×10^{-3}	250	10	0.5
Small veins	0.5	80		2
Venae cavae	3.0	8	2	20

Table 11.1: Diameter, total cross-sectional area, mean blood pressure at entrance, and mean fluid velocity of blood vessels.

cross-sectional area A_0 and with total cross-sectional area $A = NA_0$, the total flux through the system is

$$Q = -\frac{P_x}{8\pi\mu}A_0(NA_0) = -\frac{P_x}{8\pi\mu}A_0 A, \qquad (11.10)$$

and the corresponding average velocity is

$$v = \frac{Q}{A}. \qquad (11.11)$$

Now, for there to be no stagnation in any portion of the systemic or pulmonary vessels, the total flux Q must be the same constant everywhere, implying that $P_x A_0 A$ must be constant. Thus, for a vessel with constant cross-sectional area, the pressure drop must be linear in distance. Furthermore, the pressure drop per unit length must be greatest in that part of the circulatory system for which $A_0 A$ is smallest.

In Table 11.1 are shown the total cross-sectional areas and pressures at entry to different components of the vascular system. The largest pressure drop occurs in the arterioles, and the pressure in the small veins and venae cavae is so low that these are often collapsed. The pressure at the capillaries must be low to keep them from bursting, since they have very thin walls. The numbers in Table 11.1 suggest that the pressure drop per unit length is greatest in the arterioles, about a factor of three times greater than in the capillaries, even though the capillaries are substantially smaller than the arterioles.

When the diameter of a vessel decreases, the velocity must increase if the flux is to remain the same. In the circulatory system, however, a decrease in vessel diameter is accompanied by an increase in total cross-sectional area (i.e., an increase in the total number of vessels), so that the velocity at the capillaries is small, even though the capillaries have very small radius. In fact, according to (11.11), the velocity in a vessel is independent of the radius of the individual vessel but depends solely on the total cross-sectional area of the collection of similar vessels. Once again, from Table 11.1 we see that the velocity drops continuously from aorta to arteries to arterioles to capillaries and then rises from capillaries to venules to veins to venae cavae. The velocity at the vena cava is about half that at the aorta.

11.2 Compliance

Because blood vessels are elastic, there is a relationship between pressure and volume. The blood vessel wall is stretched as a result of the pressure difference between the interior and exterior of the vessel. Obviously, the higher the pressure difference, the more tension in the wall. Also, the larger the radius of the vessel, the larger the tension. However, the thicker the wall the less tension there is. These three observations can be quantified via the relationship, known as Laplace's law,

$$T = \frac{Pr}{M} \tag{11.12}$$

where T is the tension in the wall, P is the transmural pressure, r is the vessel radius and M is the wall thickness.

An application of Laplace's law arises in *dilated cardiomyopathy* in which the heart becomes greatly distended and the radius of the ventricle increases. Much larger wall tension is needed to create the same pressure during ejection of the blood, and so the dilated heart requires more energy to pump the same amount of blood compared to a heart of normal size. A new surgical procedure based on Laplace's law, called ventricular remodeling, removes portions of the ventricular wall in order to improve the function of dilated, failing hearts.

Laplace's law is the motivation for an understanding of compliance. Suppose we have an elastic vessel of volume V, with a uniform internal pressure P. The simplest assumption one can make is that V is linearly related to P, and thus

$$V = V_0 + CP, \tag{11.13}$$

for some constant C, called the *compliance* of the vessel, where V_0 is the volume of the vessel at zero pressure. Although this linear relationship is not always accurate, it is good enough for the simple models that are used here.

The compliance of the venous compartment is about 24 times as great as the compliance of the arterial system, because the veins are both larger and weaker than the arteries. It follows that large amounts of blood can be stored in the veins with only slight changes in venous pressure, so that the veins are often called storage areas. The blood vessels in the lungs are also much more compliant than the systemic arteries.

It is possible for veins and arteries to collapse and for blood flow through the vessel to cease; i.e., the radius becomes zero if the pressure is sufficiently negative. Negative pressures are possible if one takes into account that there is a fluid pressure in the body exterior to the vessels, and P actually refers to the drop in pressure across the vessel wall. The flow of whole blood is stopped at a nonzero radius, primarily because of the nonzero diameter of red blood cells. Thus, when the arterial pressure falls below about 20 mm Hg, the flow of whole blood is blocked, whereas blockage of plasma in arterioles occurs between 5 and 10 mm Hg.

Equation (11.13) is applicable when the vessel has the same internal pressure throughout. When P is not uniform, the compliance of the vessel is modeled by relating the cross-sectional area to the pressure. Again, the simplest assumption to make is that the relationship is linear (see exercise 2), and thus

$$A = A_0 + cP, \tag{11.14}$$

for some constant c. Note that c is the compliance per unit length, since in a cylindrical vessel of length L and uniform internal pressure, $V = AL$, so that $C = cL$. However, here we refer to both C and c as compliance.

For a given flow, the pressure drop in a compliance vessel is different from the pressure drop in a resistance vessel. Further, in a compliance vessel, the flow is not a linear function of the pressure drop. From (11.8) the flux through a vessel is proportional to the product of the pressure gradient and the square of the area. Thus, for a compliance vessel,

$$8\pi\mu Q = -P_x A^2(P), \tag{11.15}$$

where $A(P)$ is the relationship between cross-sectional area and pressure for the chosen vessel. In steady state, the flux must be the same everywhere, so that

$$x = -\frac{1}{8\pi\mu Q} \int_{P_0}^{P(x)} A^2(P)\,dP \tag{11.16}$$

determines the pressure as a function of distance x. If the cross-sectional area of the vessel is given by (11.14), then the flux through a vessel of length L is related to the input pressure P_0 and output pressure P_1 by

$$
\begin{aligned}
RQ &= \frac{1}{3\gamma}(1+\gamma P)^3\big|_{P_1}^{P_0} \tag{11.17}\\[2mm]
&= (P_0 - P_1)\left(1 + \gamma(P_0 + P_1) + \frac{\gamma^2}{3}(P_0^2 + P_0 P_1 + P_1^2)\right), \tag{11.18}
\end{aligned}
$$

where $R = 8\pi\mu L/A_0^2$ and $\gamma = c/A_0$. In the limit of zero compliance, this reduces to the linear ohmic law (11.1). Note that $1/\gamma$ has units of pressure, while R has units of pressure/flow. Thus, R can be interpreted as the flow resistance, as in (11.1).

Since Q is an increasing function of γ, it follows that a given flow can be driven by a smaller pressure drop in a compliance vessel than in a noncompliance vessel. This relationship is viewed graphically in Fig. 11.3, where we plot the scaled flux RQ as a function of pressure drop $\Delta P = P_0 - P_1$ for fixed γ and P_0. Clearly, the higher the compliance, the smaller the pressure drop required to drive a given fluid flux. This explains, for example, why the pressure drop in the veins can be much less than in the arteries, since the compliance of th eveins is much greater than the compliance of the arteries.

We also calculate the volume of blood contained in a vessel with input pressure P_0 and output pressure P_1 to be

$$V = \int_0^L A(x)\,dx = \int_{P_0}^{P_1} A(P)x'(P)\,dP = -\frac{1}{8\pi\mu Q}\int_{P_0}^{P_1} A^3(P)\,dP. \tag{11.19}$$

For a linear compliance vessel (11.14) this is

$$
\begin{aligned}
\frac{V}{V_0} &= \frac{3}{4}\left(\frac{(1+\gamma P)^4\big|_{P_1}^{P_0}}{(1+\gamma P)^3\big|_{P_1}^{P_0}}\right) \tag{11.20}\\[2mm]
&= 1 + \frac{\gamma}{2}(P_0 + P_1) + \frac{\gamma^2}{6}(P_0 - P_1)^2 + O(\gamma^3), \tag{11.21}
\end{aligned}
$$
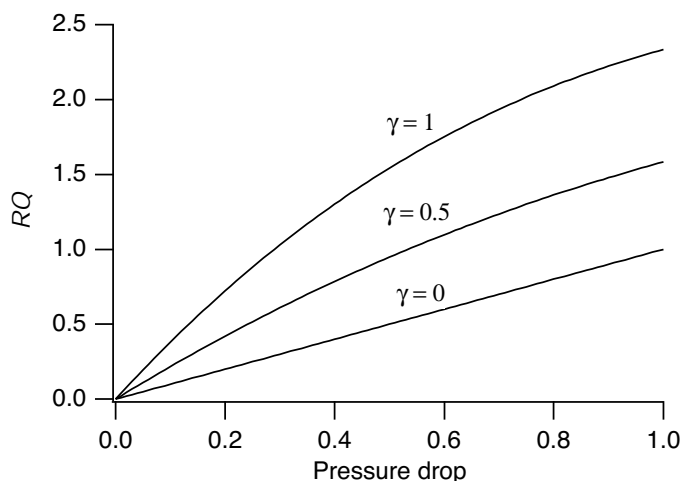
Figure 11.3: Scaled flow RQ (with units of pressure) as a function of pressure drop $\Delta P = P_0 - P_1$ for different values of compliance γ. For all curves $P_0 = 1.0$.

where V_0 is the volume of the vessel at zero pressure. It is left as an exercise (Exercise **??**) to show that when there is no pressure drop across the vessel, so that $P_0 = P_1$,

$$V = V_0 + V_0 \gamma P_0 = V_0 + \frac{V_0}{A_0} cP, \qquad (11.22)$$

which is the same as (11.13).

11.3 The Microcirculation and Filtration

The purpose of the circulatory system is to provide nutrients to and remove waste products from the cellular interstitium. To do so requires continuous filtration of the interstitium. This filtration is accomplished primarily at the level of capillaries, as fluid moves out of the capillaries at the arteriole end and back into the capillaries at the venous end.

The efflux or influx of fluid from or into the capillaries is determined by the local pressure differences across the capillary wall. In normal situations, the pressure drop through the capillaries is substantial, about 25 mm Hg.

A schematic diagram of the capillary network is shown in Fig. 11.4. To get some understanding of how filtration works and why a capillary pressure drop is necessary, we use a simple one-dimensional model of a capillary. We suppose that there is an influx Q_i at $x = 0$ that must be the same as the efflux at $x = L$, where L is the length of the capillary. At each point x along the capillary, there is blood flow q. The (hydrostatic) pressure P_c at each point along the capillary is determined by

$$\frac{dP_c}{dx} = -\rho q, \qquad (11.23)$$
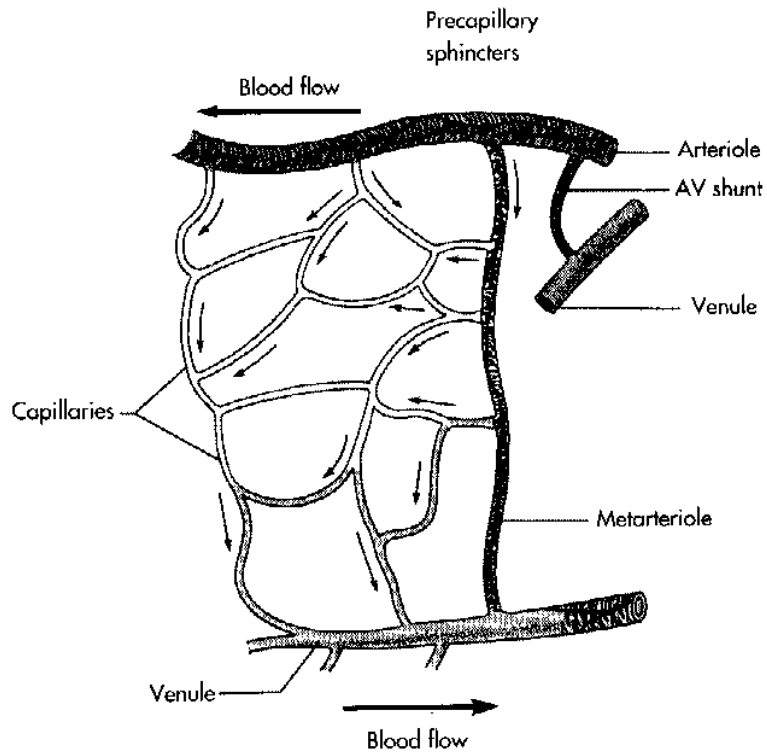
Figure 11.4: Diagram of the capillary microcirculation. (Berne and Levy, 1993, Fig. 28-1, p. 466.)

where ρ is the coefficient of capillary resistance. Flow into or out of the capillary (through the porous capillary wall) is determined by the difference between total internal pressure and total external (interstitial) pressure. The interstitial hydrostatic pressure P_i is typically about -3 mm Hg, and the interstitial fluid colloidal osmotic pressure π_i is about 8 mm Hg, while the plasma colloidal osmotic pressure π_c averages about 28 mm Hg (although it necessarily varies along the length of the capillary; see Exercise 3). Thus, the flow into the capillary is determined by

$$\frac{dq}{dx} = K_f(-P_c + P_i + \pi_c - \pi_i), \tag{11.24}$$

where K_f is the capillary filtration rate.

We assume that only P_c varies along the length of the capillary. Clearly, when P_c is high, fluid is forced out of the capillary, and when P_c drops sufficiently low, fluid is reabsorbed into the capillary.

Equations (11.23) and (11.24) form a linear system of equations, which is readily solved. We use the boundary conditions

$$q(0) = q(L) = Q_i, \tag{11.25}$$

thus giving two boundary conditions for the two linear equations. It is easiest to solve first for q. From (11.24) we see that

$$\frac{d^2q}{dx^2} = -K_f\frac{dP_c}{dx} = K_f\rho q. \tag{11.26}$$

Noting that q is the same at $x = 0$ and $x = L$, it must be symmetric about $x = \frac{L}{2}$, so that

$$q = B\cosh(\beta(x - \frac{L}{2})). \tag{11.27}$$

where $\beta^2 = K_f\rho$. It follows easily from the boundary conditions that $B = \frac{Q_i}{\cosh(\frac{\beta L}{2})}$ and from (11.24) that

$$P_c = P_i + \pi_c - \pi_i - \frac{1}{K_f}\frac{dq}{dx} = P_i + \pi_c - \pi_i - \frac{Q_i\beta}{K_f}\frac{\sinh\beta(x - L/2)}{\cosh\frac{\beta L}{2}}. \tag{11.28}$$

In Exercise 3, this problem is studied in the phase plane, and generalized slightly to include variable osmolarity.

We can also calculate the relationship between the flux and total pressure drop along the length of the capillary. From the solution for P_c it follows that

$$\Delta P_c = P_c(0) - P_c(L) = \frac{2Q_i\beta}{K_f}\tanh\frac{\beta L}{2}, \tag{11.29}$$

and thus

$$Q_i = \frac{\Delta P_c}{R}\frac{\beta L/2}{\tanh\frac{\beta L}{2}}, \tag{11.30}$$

where $R = \rho L$ is the total resistance of the capillary. Notice the similarity of this formula with (11.1), describing the relationship between flow and pressure drop in

a nonleaky vessel. Apparently, leakiness in the vessel ($\beta \neq 0$) has the effect of decreasing the overall resistance of the capillary flow.

Notice that $q(x)$ is minimal, and therefore the interstitial flow is maximal, at $x = L/2$. We define the filtration rate Q_f to be the maximal flux through the interstitium, in this case,

$$Q_f = Q_i - q(L/2). \tag{11.31}$$

It follows that

$$\frac{Q_f}{Q_i} = 1 - \text{sech}\frac{\beta L}{2}. \tag{11.32}$$

The filtration rate depends on the single dimensionless parameter $\beta L = \sqrt{\rho K_f} L$. Thus filtration is enhanced in vessels that are "leaky" (large K_f) and of small radius, since vessel resistance ρ is inversely proportional to r^4.

11.4   Cardiac Output

During a heartbeat cycle, the pressure and volume of the heart change in a highly specific way, most easily seen as a trajectory plotted in the pressure–volume phase plane, shown in Fig. 11.5. Notice that the pressure–volume trajectories, or "loops" are of rectangular shape, and thus the pressure and volume change at different places in the cycle. For example, on the right ascending side of the loop, the pressure increases while volume is constant, which corresponds to the ventricle contracting while the outflow valve is closed. At the top right-hand corner the outflow valve opens, and the volume decreases as the blood is pumped out at a constant pressure. The constant pressure at the top of the loop corresponds to the arterial pressure, while the constant pressure along the bottom of the loop corresponds to the venous pressure. Notice also that the top left corners of the loops lie on the same straight line. Thus, the ventricular volume at the end of a contraction (the end-systolic volume V_{ES}) is a linear function of the arterial blood pressure. Further, in panel B of the same figure, the top left corner of the loop (the end-systolic pressure and volume) is constant, independent of the total volume of blood pumped by the ventricle, suggesting that it depends solely on the arterial pressure.

This suggests that

$$V_{\text{ES}} = V_{\text{min}} + C_s P_a, \tag{11.33}$$

where V_{min} is the intercept on the V axis, and C_s is the slope of the line connecting the three labeled points in Fig. 11.5A. The key observation is that C_s and V_{min} are independent of the arterial pressure and the end-diastolic volume, and are thus intrinsic properties of the ventricle. C_s is, in fact, the compliance of the ventricle at the end of systole. By connecting the lower right corners of the pressure–volume loops, as shown in Fig. 11.5C, we reach a similar conclusion for the end-diastolic volume.

These observations can be summarized in a simple model, in which we determine the total amount of blood pumped by the ventricle, i.e., the *cardiac output*, but ignore the time-dependent changes in volume and pressure over the beat cycle. We view the heart as a compliance vessel whose basal volume and compliance change
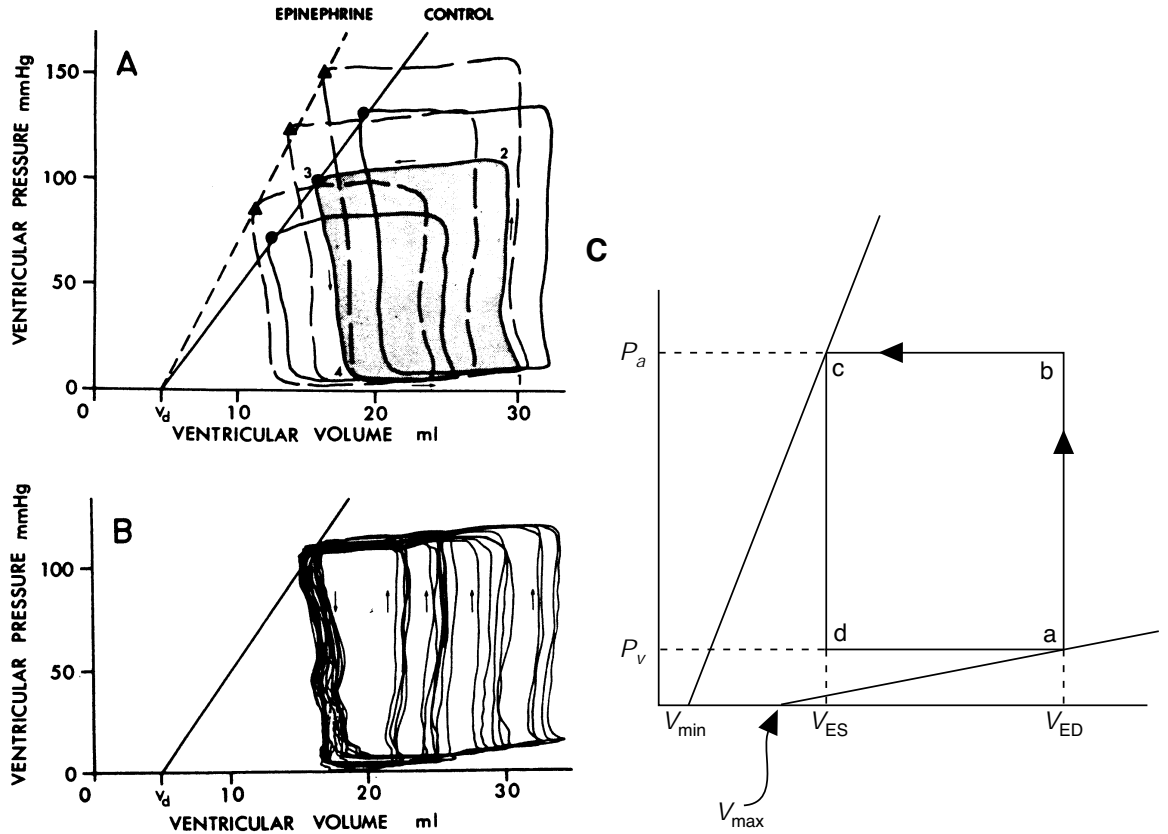
Figure 11.5: Experimental data of the pressure–volume relationship during the heartbeat cycle in the denervated left ventricle of the dog. (Sagawa et al., 1978, Fig. 11.4.) A: Three beats from different end-diastolic volumes and against different arterial pressures are shown in solid lines, with the broken lines representing the same beat cycles in the presence of epinephrine, which enhances the contraction. B: Pressure–volume loops of the same ventricle for four different end-diastolic volumes, but against the same arterial pressure. C: Schematic diagram of the pressure–volume loop (adapted from Hoppensteadt and Peskin, 1992, Fig. 5.5). a: inflow valve closes, b: outflow valve opens, c: outflow valve closes, d: inflow valve opens.

with time. Thus,

$$V = V_0(t) + C(t)P. \tag{11.34}$$

During diastole, when the heart is filling, the heart is relaxed and compliant, so that V_0 and C are large. During this time, the aortic valve is closed, preventing backflow, so that the pressure is essentially the same as the venous pressure. During systole, the heart is contracting and much less compliant, so that C and V_0 are decreased compared to diastolic values. At this time, the mitral valve is closed, preventing backflow into the veins, so that the pressure in the heart is the same as the arterial pressure. Accordingly, the minimal volume (end systolic) is given by (11.33), and the maximal volume V_{ED} (end diastolic) is

$$V_{\mathrm{ED}} = V_{\max} + C_d P_v, \tag{11.35}$$

where P_a and P_v are the arterial and venous pressures, respectively, and C_s and C_d are the compliances of the heart during systole and diastole, respectively. This implies that the *stroke volume* is

$$V_{\mathrm{stroke}} = V_{\max} - V_{\min} + C_d P_v - C_s P_a, \tag{11.36}$$

and the total cardiac output is

$$Q = F V_{\mathrm{stroke}}, \tag{11.37}$$

where F is the heart rate in beats per unit time.

   This expression of cardiac output has some features that agree with reality. For example, if C_s is small compared to C_d, then the cardiac output depends primarily on the venous pressure, or on the rate of venous return. This phenomenon, that cardiac output increases with increasing filling, is commonly referred to as *Starling's law*. While there is some decrease in output due to arterial loading, this effect is not nearly as significant as the increase in output resulting from an increase in venous pressure.

   According to this formula, cardiac output is a linear function of venous pressure. This is not a terrible approximation in normal physiological ranges, although a more accurate formula would show saturation as a function of venous pressure. That is, cardiac output approaches a constant as a function of venous pressure for venous pressure above 10 mm Hg. Cardiac output also saturates at high frequencies because of inadequate fluid filling.

11.5   Circulation

11.5.1   A Simple Circulatory System

To illustrate how all the above pieces fit together to give a model of the circulatory system, consider a simple circulatory system with a single-chambered heart and a resistive closed loop (Fig. 11.6). For the resistive closed loop, we suppose that the total flux is related to the pressure drop through

$$Q = (P_a - P_v)/R, \tag{11.38}$$
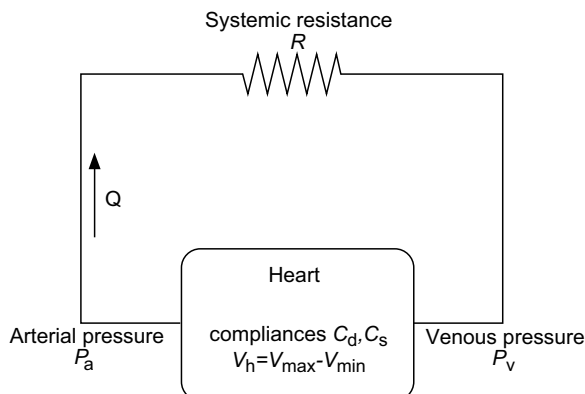
Figure 11.6: Schematic diagram of the simplest circulation model, with a single-chambered heart and a single loop.

so that in steady state the flux through the loop must match the cardiac output, yielding

$$Q = F(V_h + C_d P_v - C_s P_a) = (P_a - P_v)/R, \qquad (11.39)$$

where $V_h = V_{\max} - V_{\min}$. Equation (11.39) gives a relationship between arterial and venous pressure that must be maintained in a steady-state condition. Unfortunately, these are not uniquely determined by this equation, so that this model does not have a unique solution. However, if we model the loop as a compliance vessel, then there is an additional relationship between pressure and total volume that must be satisfied which uniquely specifies the system.

For this simple system, we suppose that the closed circulatory loop consists of a compliance vessel with cross-sectional area given by (11.14). It follows from (11.17) that

$$Q = \frac{1}{3R\gamma} \left((1 + \gamma P_a)^3 - (1 + \gamma P_v)^3 \right), \qquad (11.40)$$

and the total volume of the vessel is given by

$$\frac{V}{V_0} = \frac{3}{4} \left(\frac{(1 + \gamma P_a)^4 - (1 + \gamma P_v)^4}{(1 + \gamma P_a)^3 - (1 + \gamma P_v)^3} \right). \qquad (11.41)$$

These two equations, together with

$$Q = F(V_h + C_d P_v - C_s P_a), \qquad (11.42)$$

give a system of three equations in terms of the four unknowns Q, P_a, P_v, and V. The final equation comes from conservation of blood. Because blood is assumed to be incompressible, and because the heart chambers are assumed to have a fixed volume (as cardiac output is expressed in terms of the average output), it follows that V must be constant. The system is then completely determined. However, because it is nonlinear, a closed-form solution is not apparent, and the easiest way to obtain a solution is to solve the equations numerically.
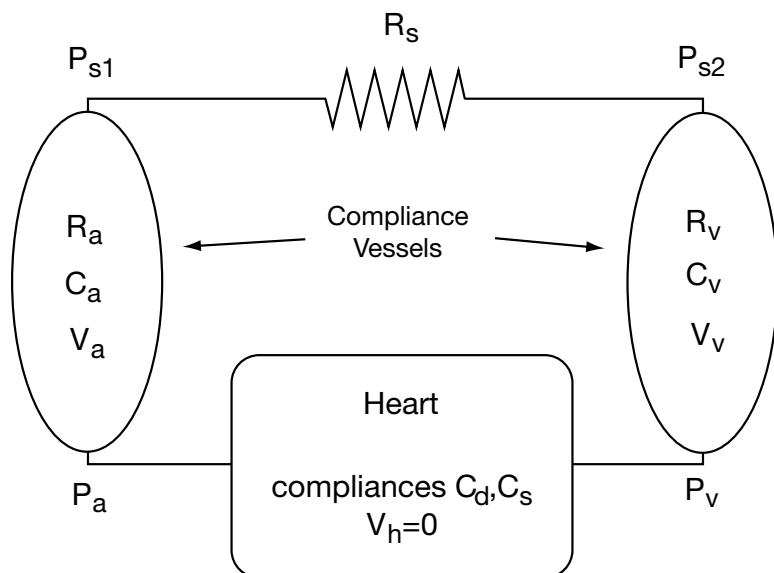
Figure 11.7: Schematic diagram of the two-compartment model of the circulation. The heart and pulmonary system are combined into a single vessel, and the systemic capillaries are modeled as a resistance vessel. The larger arteries and veins are modeled as compliance vessels.

Notice that it is also possible to use these equations to solve an inverse problem. That is, if V, Q, P_v, and P_a are known from measurements, then one could solve for the resistance R and compliances γ, C_d, and C_s.

11.5.2   A Simple Linear Circulatory System

It is difficult to extend the analysis of the previous section to more realistic models because of the complexity of the resulting nonlinear equations. However, much can be learned using linear approximations to the governing equations. The simplest linear model is due to Guyton (1963), in which the circulatory system is represented as a closed loop with two compliance vessels and one pure resistance vessel (Fig. 11.7). The large arteries and veins are each treated as compliance vessels with linearized flow equations, and the systemic capillaries are treated as a resistance vessel with no compliance.

The equations describing this model can be conveniently divided into two groups: those describing the arterial system and those describing the venous system.

Arterial system: Cardiac output is described in terms of the compliance of the ventricle, and so

$$Q = F(C_d P_v - C_s P_a), \tag{11.43}$$

where, for simplicity, we have assumed that $V_h = 0$, i.e., that $V_{\max} = V_{\min}$.

The larger arteries are modeled as a compliance vessel, and thus, from (11.18),

$$Q = \frac{P_a - P_{s1}}{R_a},\tag{11.44}$$

where the nonlinear terms are ignored. This approximation is reasonable if the compliance is small. The parameters are defined in Fig. 11.7. For example, P_a is the arterial pressure, while P_{s1} is the blood pressure at the (somewhat arbitrary) border between the larger arteries and the arterial capillaries, and R_a is the resistance of the larger arteries. Note that although this expression for the flux looks as though the arteries are treated as resistance vessels, this is only because the nonlinear terms are omitted. The compliance of the arteries appears in the relationship between the pressure and the volume of the arteries,

$$V_a = \frac{\gamma V_0}{2}(P_a + P_{s1}) = \frac{C_a}{2}(P_a + P_{s1}),\tag{11.45}$$

where $C_a = c_a V_0/A_0$ is the compliance of the systemic arteries. Note that the volume of the systemic arteries is taken to be zero at zero pressure.

Venous system: We have three similar equations for the venous system, except that the equation for the cardiac output (11.43) is replaced by an equation describing the flow through the capillaries,

$$Q = \frac{P_{s1} - P_{s2}}{R_s}.\tag{11.46}$$

The remaining two equations describe the flow through the veins,

$$Q = \frac{P_{s2} - P_v}{R_v},\tag{11.47}$$

and the volume of blood in the veins,

$$V_v = \frac{C_v}{2}(P_v + P_{s2}).\tag{11.48}$$

At this point, we have a system of six equations in seven unknowns (four pressures, two volumes, and Q). The final equation comes from conservation of volume, according to which

$$V_a + V_v = V_t,\tag{11.49}$$

where V_t is a given constant.

These seven equations, being linear, can be solved for the unknowns. However, before doing so, we make two further simplifications. First, we assume that the systolic compliance, C_s, is nearly zero, and second, that the pressure drops across the larger vessels are small, so that R_a and R_v are quite small, with the result that $P_a = P_{s1}$ and $P_v = P_{s2}$, to a good approximation. This removes two of the variables, leaving the system of five equations:

$$Q \;\;=\;\; FC_dP_v,\tag{11.50}$$

$$Q = \frac{P_a - P_v}{R_s}, \tag{11.51}$$

$$V_a = C_a P_a, \tag{11.52}$$

$$V_v = C_v P_v, \tag{11.53}$$

$$V_a + V_v = V_t. \tag{11.54}$$

The solution of this system is readily found (provided one uses symbolic manipulation software) to be

$$P_a = \frac{(1 + FC_d R_s)V_t}{C_v + (1 + FC_d R_s)C_a}, \tag{11.55}$$

$$P_v = \frac{V_t}{C_v + (1 + FC_d R_s)C_a}, \tag{11.56}$$

$$Q = \frac{FC_d V_t}{C_v + (1 + FC_d R_s)C_a}. \tag{11.57}$$

A number of qualitative features of the circulation can be seen from this solution.

1. As the heart rate increases, the arterial pressure P_a increases to a maximum of V_t/C_a, but as the heart rate falls, the arterial pressure decreases to a minimum of $V_t/(C_v + C_a)$.

2. Conversely, as the heart rate falls, the venous pressure P_v increases to a maximum of $V_t/(C_v + C_a)$. Hence, in heart failure, the arterial pressure falls and the venous pressure rises, until they are equal. With no pressure drop, there is no flow.

3. An increase in the systemic resistance, R_s, leads to a decrease in the cardiac output, an increase in the arterial pressure, and a decrease in the venous pressure.

4. Since $V_a = C_a P_a$ and $V_v = C_v P_v$, an increase in systemic resistance is accompanied by a shift in the blood volume from the venous system to the arterial system, i.e., V_v decreases, and V_a increases.

In reality, systemic resistance varies widely (decreasing, for example, during exercise), but the cardiac output compensates for this variation, keeping the arterial pressure relatively constant. Thus, the above model, which includes no control of cardiac output, needs to be modified to agree with experimental data. Later in this chapter we describe some simple models for regulation of the circulation. Before doing so, however, we consider a more complex model of the circulation, incorporating more compartments.

11.5.3   A Multicompartment Circulatory System

To construct a more detailed linear model of the circulatory system, we assume that the systemic and pulmonary loops each consist of two compliance vessels, the arterial and venous systems, connected by the capillaries, a pure resistance. Further,

we assume that the heart has two chambers, the left and right hearts. A schematic diagram of the model is given in Fig. 11.8. We must write equations for the flow through each of these compartments and keep track of the total volume of blood contained in the system. Unfortunately, the notation can be difficult to follow. We let subscripts a, v, s, and p denote, respectively, arterial, venous, systemic, and pulmonary. So, for example, P_{sa} is the pressure at the entrance to the systemic arteries, and C_{sa} is the compliance of the systemic arteries. Also, subscripts r, l, d, and σ denote, respectively, right, left, diastolic and systolic. Thus, C_{ld} denotes the diastolic compliance of the left heart. Finally, P_{s1} denotes the pressure at the ill-defined border between the systemic arteries and the systemic capillaries, with similar definitions for P_{s2}, P_{p1}, and P_{p2} as indicated in Fig. 11.8.

As before, we write the governing equations in groups.

Systemic arteries:

$$Q = \frac{P_{sa} - P_{s1}}{R_{sa}}, \tag{11.58}$$

$$Q = F(C_{ld}P_{pv} - C_{l\sigma}P_{sa}), \tag{11.59}$$

$$V_{sa} = V_0^s + \frac{C_{sa}}{2}(P_{sa} + P_{s1}). \tag{11.60}$$

Note that here it is assumed that the volume of the systemic arteries at zero pressure is V_0^s, not zero, as was assumed in the previous model.

Systemic veins:

$$Q = \frac{P_{s2} - P_{sv}}{R_{sv}}, \tag{11.61}$$

$$Q = \frac{P_{s1} - P_{s2}}{R_s}, \tag{11.62}$$

$$V_{sv} = \frac{C_{sv}}{2}(P_{sv} + P_{s2}). \tag{11.63}$$

For the venous system, it is reasonable to take the basal volume as zero, because if the blood pressure falls to zero, these vessels collapse. In the arterial system, however, such an approximation is not realistic.

Pulmonary arteries:

$$Q = \frac{P_{pa} - P_{p1}}{R_{pa}}, \tag{11.64}$$

$$Q = F(C_{rd}P_{sv} - C_{r\sigma}P_{pa}), \tag{11.65}$$

$$V_{pa} = V_0^p + \frac{C_{pa}}{2}(P_{pa} + P_{p1}). \tag{11.66}$$

Pulmonary veins:

$$Q = \frac{P_{p2} - P_{pv}}{R_{pv}}, \tag{11.67}$$

Pulmonary system

Systemic system
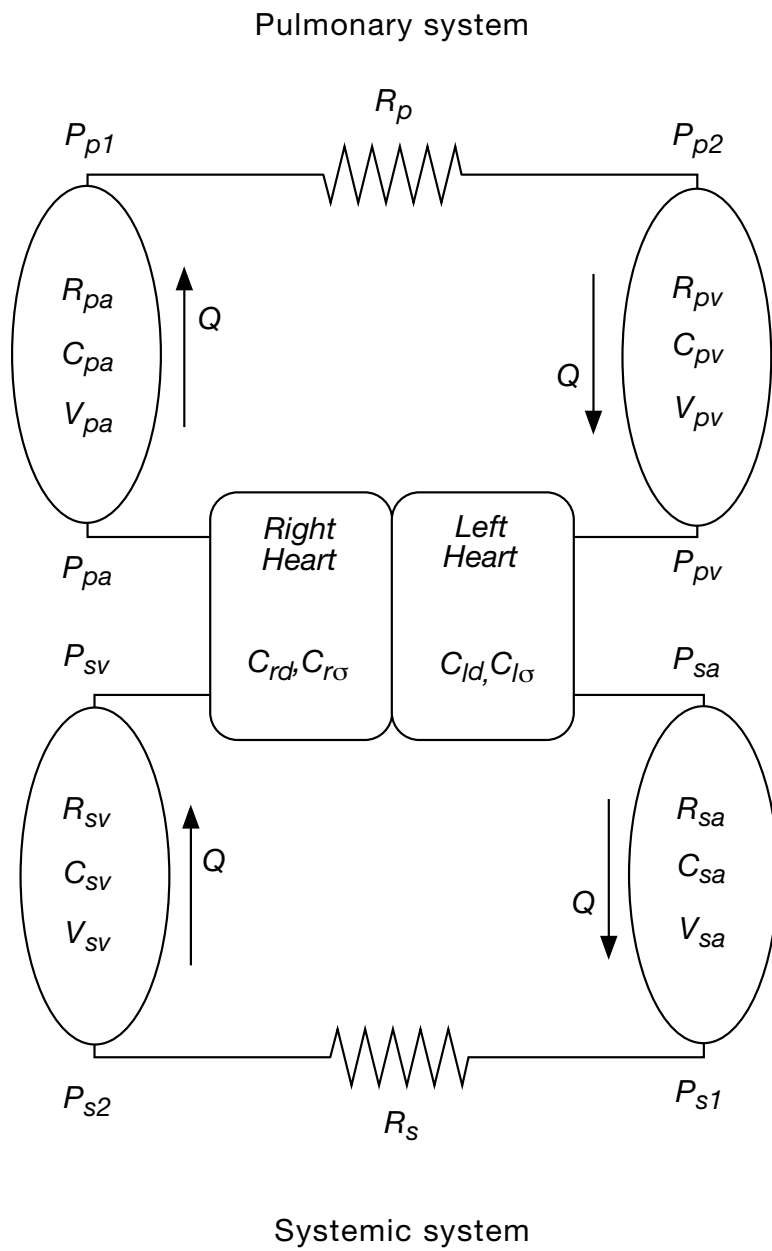
Figure 11.8: Schematic diagram of the multicompartment model of the circulation.

$$Q = \frac{P_{p1} - P_{p2}}{R_p}, \tag{11.68}$$

$$V_{pv} = \frac{C_{pv}}{2}(P_{pv} + P_{p2}). \tag{11.69}$$

At this stage there are 12 equations for 13 unknowns (8 pressures, 4 volumes, and Q). The final equation, as before, comes from the conservation of blood volume, whereby

$$V_{sa} + V_{sv} + V_{pa} + V_{pv} = V_t. \tag{11.70}$$

The capillary and heart volumes need not be included in this equation because they are assumed to be fixed.

This system of equations can be treated in a number of ways. First (using symbolic manipulation software), it is not difficult to find the solution directly. A second approach is to make a number of simplifying assumptions, as was done in the simpler model discussed above. For example, if it is assumed that there is no pressure drop over the arteries or veins (both pulmonary and systemic), then $P_{sa} = P_{s1}$, $P_{sv} = P_{s2}$, and similarly for the pulmonary equations. This removes four variables and four equations, giving a system of nine equations for the remaining nine unknowns. This variation of the model has been discussed by Hoppensteadt and Peskin (1992), and its further study is left as an exercise (Exercise 4).

A second approximation of the full system is to omit the systemic resistance and combine all the pulmonary vessels into a single compliance vessel. This results in a model consisting of only three compliance vessels (Fig. 11.9). It is left as an exercise (Exercise 5) to show that this approximation results from setting R_s and R_p approach zero and by setting $C_{pa} = C_{pv}$ and $R_{pa} = R_{pv}$. For convenience, we write $C_p = 2C_{pa}$, and $R_p = 2R_{pa}$. We also assume that the systolic compliances are negligible.

The equations governing this simplified three compartment model are as follows.

Systemic arteries:

$$Q = \frac{P_{sa} - P_s}{R_{sa}}, \tag{11.71}$$

$$Q = FC_{ld}P_{pv}, \tag{11.72}$$

$$V_{sa} = V_0^s + \frac{C_{sa}}{2}(P_{sa} + P_s). \tag{11.73}$$

Systemic veins:

$$Q = \frac{P_s - P_{sv}}{R_{sv}}, \tag{11.74}$$

$$V_{sv} = \frac{C_{sv}}{2}(P_{sv} + P_s). \tag{11.75}$$

Pulmonary system:

$$Q = \frac{P_{pa} - P_{pv}}{R_p}, \tag{11.76}$$

Pulmonary system
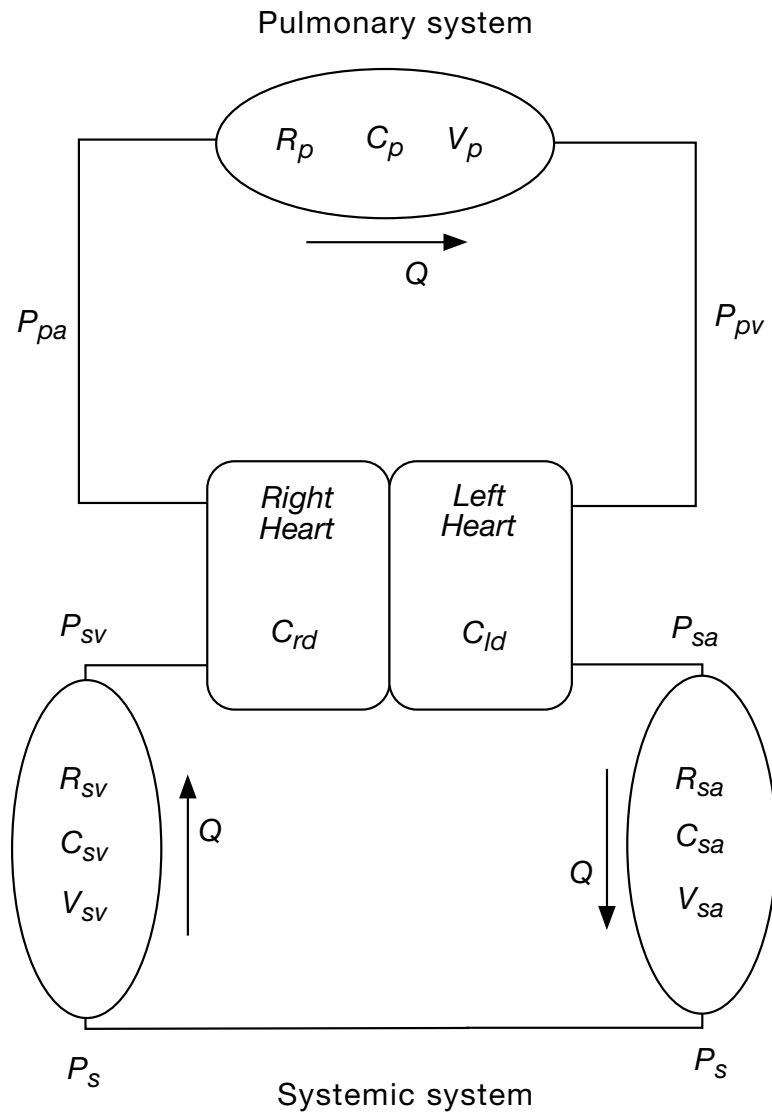
Figure 11.9: Schematic diagram of the simplified three-compartment model, obtained from the one in Fig. 11.8 by letting R_s and R_p go to zero and combining all the pulmonary vessels into one.

$$Q \;\; = \;\; FC_{rd}P_{sv}, \tag{11.77}$$

$$V_p \;\; = \;\; V_0^p + \frac{C_p}{2}(P_{pa} + P_{pv}). \tag{11.78}$$

Conservation of volume:

$$V_{sa} + V_{sv} + V_p = V_t. \tag{11.79}$$

Because this is a linear system, one can solve (preferably using symbolic manipulation software) to obtain

$$P_{sa} \;\; = \;\; Q\left(\frac{1}{FC_{rd}} + R_{sa} + R_{sv}\right), \tag{11.80}$$

$$P_s \;\; = \;\; Q\left(\frac{1}{FC_{rd}} + R_{sv}\right), \tag{11.81}$$

$$P_{sv} \;\; = \;\; \frac{Q}{FC_{rd}}, \tag{11.82}$$

$$P_{pa} \;\; = \;\; Q\left(\frac{1}{FC_{ld}} + R_p\right), \tag{11.83}$$

$$P_{pv} \;\; = \;\; \frac{Q}{FC_{ld}}, \tag{11.84}$$

$$Q \;\; = \;\; \frac{V_e}{\alpha + \frac{C_p}{FC_{ld}} + \frac{C_{sv}+C_{sa}}{FC_{rd}}}, \tag{11.85}$$

where $\alpha = R_{sv}(C_{sa} + C_{sv}/2) + R_{sa}C_{sa}/2 + C_p R_p/2$, and $V_e = V_t - V_0^s - V_0^p$ is the excess volume beyond that which is necessary to fill the system at zero pressure. Clearly, the cardiac output saturates for large F, and

$$\lim_{F\to\infty} Q = Q_\infty = \frac{V_e}{\alpha} = \frac{2V_e}{R_{sv}(2C_{sa} + C_{sv}) + R_{sa}C_{sa} + C_p R_p}. \tag{11.86}$$

We can also see that, as in the simpler model, systemic arterial pressure P_{sa} is an increasing function of heart rate, and systemic venous pressure P_{sv} is a decreasing function of heart rate.

Cardiac output depends linearly on excess blood volume $V_t - V_0^s - V_0^p$. In trauma, if there is substantial blood loss, the cardiac output drops rapidly. If there is no compensatory control (increased heart rate or change of resistance and compliance), loss of 15–20% of blood volume over a period of half an hour is fatal. If reflexes are intact, loss of 30–40% in half an hour is fatal. Notice that in this model (taking $V_t = 5$ liters, $V_0^p + V_0^s = 1.2$ liters) a 20% loss of blood with no compensatory control leads to a 26% loss of cardiac output.

There are ten physical parameters in this system of nine equations, giving nine relationships between parameters if the solution is known from data. We take as typical volumes $V_{sa} = 1$, $V_{sv} = 3.5$, $V_p = 0.5$ (liters), and typical pressures $P_{sa} = 100$, $P_s = 30$, $P_{sv} = 2$, $P_{pa} = 15$, $P_{pv} = 5$ (mm Hg). Total cardiac output is about 5.6 liters/min, with a heart rate of 80 beats per minute and a stroke volume of 0.07 liter. Using these, we find estimates for parameters of $C_{sv} = 0.22$, $R_{sa} = 12.5$,

$R_{sv} = 5.0$, $R_p = 1.78$ mm Hg/(liters/min), and $C_{ld} = 0.014$, $C_{rd} = 0.035$ (liters/mm Hg)/stroke.

As yet, C_{sa} or C_p cannot be determined because V_0^s and V_0^p are unknown. However, these quantities can be estimated using some additional information. To estimate V_0^s and C_{sa}, note that at the heart the arterial pressure varies on a beat-to-beat basis, as does the volume of blood in the arteries. During one beat, the blood ejected from the heart must be accommodated by the compliance of the arteries. Thus,

$$\Delta V = C_{sa}\Delta P, \tag{11.87}$$

where ΔV is the stroke volume, about 0.07 liter, and ΔP is the difference between systolic and diastolic pressure, about 40 mm Hg. Once C_{sa} is known ($C_{sa} = 0.0018$ liter/mm Hg), the resting volume V_0^s can be determined using the given values of volume and pressure in (11.73) as $V_0^s = 0.94$ liters. Assuming that $V_0^s + V_0^p = 1.2$ liters gives $V_0^p = 0.26$ liters. Finally, we substitute this value of V_0^p into (11.78) and solve for C_p to get $C_p = 0.024$ liters/mm Hg.

These numbers correlate with some known features of the adult circulatory system. For example, the venous system is about 24 times more compliant than the arterial system. The ratio found here is $C_{sv}/C_{sa} = 122$, which is too high, but this does not create significant errors in interpretation. Total resistance of the systemic circulation is larger than the pulmonary resistance, and the compliance of the left heart is less than that of the right heart, simply because the left ventricular wall is much thicker than the right.

To gain some understanding of the dependence of the solution on parameters, we calculate the sensitivity σ_{yx}, which is the sensitivity of dependence of the dependent variable y upon changes in the independent variable x. Thus, σ is the proportional change in y for a given proportional change in x, and so

$$\sigma_{yx} = \frac{\Delta y/y}{\Delta x/x} = \frac{x}{y}\frac{\partial y}{\partial x}, \tag{11.88}$$

in the limit as Δx goes to zero. In Table 11.2 are shown the sensitivities, expressed as percentages, for the three-compartment loop using normal parameter values, as shown in the table. For example, the first number in the first column, -5.4, is the sensitivity of the systemic arterial pressure P_{sa} to changes in the systemic arterial compliance C_{sa}.

From this table we infer some interesting features of the human circulatory system. First, the system is relatively insensitive to changes in the arterial compliance C_{sa}. In fact, compliance of the arterial system is insignificant compared to compliance of the other compartments and to a first approximation can be ignored. On the other hand, the system is strongly sensitive to changes in C_{sv}, the venous compliance. Similarly, the solution is relatively insensitive to changes in arterial resistance, R_{sa}, but is relatively sensitive to changes in venous resistance, R_{sv}. Much of the regulation of the cardiac systems occurs through changes in the compliance and resistance of the venous system, and this result demonstrates the efficacy of that choice.

The most common cause of coronary occlusion is *atherosclerosis*, hardening of the arteries. (About half of all deaths in the United States and Europe are the result

	Normal	C_{sa}	C_{sv}	C_p	R_{sa}	R_{sv}	R_p	C_{ld}	C_{rd}	F
		0.0018	0.22	0.024	12.5	5	1.78	0.014	0.035	80
P_{sa}	100	−3	−92	−6	70	−55	−3	2	10	11
P_s	30	−3	−92	−6	−2	12	−3	2	5	7
P_{sv}	2	−3	−92	−6	−2	−84	−3	2	−88	−87
P_{pa}	15	−3	−92	−6	−2	−84	65	−32	12	−20
P_{pv}	5	−3	−92	−6	−2	−84	−3	−98	12	−87
V_{sa}	1	10	−10	−0.7	6	−4	−0.3	0.1	1	1
V_{sv}	3.5	−3	8	−6	−2	4	−3	2	−1	0.7
V_p	0.5	−1	−33	45	−0.6	−18	23	−11	4	−7
Q	5.6	−3	−92	−6	−2	−84	−3	2	12	13

Table 11.2: Sensitivities for the three compartment circulatory system (expressed as percentages).

of atherosclerosis and two thirds of those are the result of a thrombosis (clotting) of one or more coronary arteries.) This occurs when excess cholesterol and fats are deposited in the arteries. These deposits are invaded by fibrous tissue and frequently become calcified, resulting in atherosclerotic plaques and stiffened arterial walls that can be neither constricted nor dilated. While systemic compliance is not extremely important in this model, systemic resistance is significant, and increases in systemic resistance produce increases in arterial pressure.

A person with higher than normal mean arterial pressure is said to have hypertension, or *high blood pressure*. Life expectancy is shortened substantially when mean arterial pressure is 50 percent or more above normal. The lethal effects of hypertension are

1. Increased cardiac workload, leading to congestive heart disease or coronary heart disease, often leading to a fatal heart attack;

2. rupture of a major blood vessel in the brain (a *stroke*), resulting in paralysis, dementia, blindness, or multiple other brain disorders;

3. multiple hemorrhages in the kidneys, leading to renal destruction and eventual kidney failure and death.

One other parameter that has an important effect is the diastolic compliance of the left heart, C_{ld}. As expected, if this compliance decreases, there is a reduction in systemic arterial pressure and a reduction in cardiac output. There is also a noticeable increase in pulmonary blood volume, V_p. Thus, left heart failure, which corresponds to a weakening of the left ventricular muscles and hence decreased cardiac efficiency and decreased compliance, results in excess fluid and fluid congestion in the lungs, known as *pulmonary edema*. Notice that in this model, failure of the left or right heart does not influence the maximal cardiac output Q_∞, although it certainly requires a higher heart rate to effect the same output. Notice, also, that with left or right heart failure, systemic volume changes little, so that one does not expect peripheral edema.

11.6   Cardiovascular Regulation

The circulatory system is equipped with a complex system for the control of arterial pressure and cardiac output. Over the short term (seconds to hours) this control occurs partly at the level of the arterioles and partly at the heart itself. Smooth muscle around the arterioles can constrict or relax, thus changing the resistance, while innervation of the heart can control the cardiac output in response to conditions in the periphery. These short-term mechanisms dampen out the considerable variation that arises in a normal day's activity, from lying down to standing up to running one hundred meters.

There are three major types of peripheral control mechanisms:

1. Local (intrinsic) control of blood flow in the individual tissue, determined mainly by the tissue's need for blood perfusion. Local control is often called *autoregulation.*

2. Neural (extrinsic) control, by which the overall vesicular resistance and cardiac activity are controlled. The baroreceptor reflex is the most widely studied of these extrinsic mechanisms.

3. Humoral control, in which substances dissolved in the blood, such as hormones, ions, or other chemicals, cause changes in flow properties. These feedbacks are mediated by chemoreceptors.

Over the long term (days and months) blood pressure is regulated by renal mechanisms, whereby an increase in arterial pressure causes the kidneys to excrete more fluid, thus decreasing the blood volume and the arterial pressure.

Because of the intricacy of these control mechanisms, it comes as no surprise that feedback instabilities can arise, leading to periodicity in the heart beat rate and the mean arterial pressure. There are a number of different observed oscillations (although the oscillatory behavior is often highly irregular) and none is well understood. The first observations of oscillatory arterial pressure were made by Ludwig in 1847. Some years later, Mayer (1877) discovered arterial pressure oscillations with a frequency of about 0.1 Hz, and these were named *Mayer waves.* Oscillations in arterial pressure with a frequency around that of respiration were discovered by Traube (1865) and Hering (1869) and are called *Traube-Hering waves.* These names are not entirely consistent from author to author; some books such as Guyton and Hall (1996) describe Mayer waves and Traube-Hering waves as the same phenomenon, with the generic name *vasomotor* waves, but other authors such as Cohen and Taylor (2002) or Berne and Levy (1998) make a distinction between the frequencies of Mayer and Traube-Hering waves.

One of the most widely studied oscillations is that of heart rate, which varies periodically with respiration, such oscillations being called *respiratory sinus arrhythmia*, or RSA. The reverse is true also, with the heart rate affecting the rate of breathing. Such *cardiorespiratory coupling*, or *cardioventilatory coupling*, can result in phase locking of heart rate and breathing. Other oscillations in respiration rate, such as *Cheyne-Stokes* breathing, can also occur, and are discussed in Chapter 14.
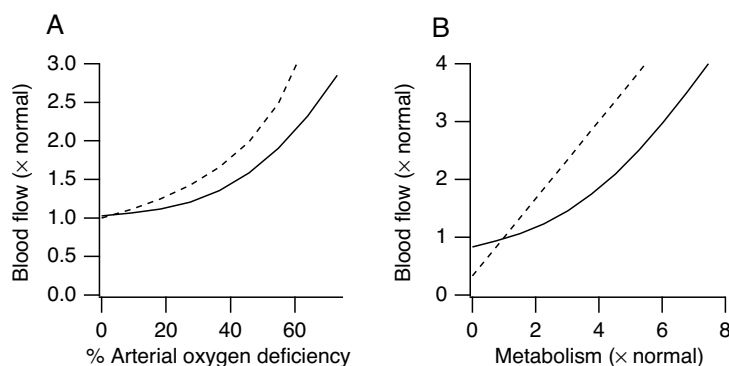
Figure 11.10: Blood flow as a function of arterial pressure if pressure is raised over a period of a few minutes. (Data (solid curve) from Guyton and Hall, 1996, Fig. 17-4, p. 203.) Dashed curve shows the result from the model (11.92).

In summary, there is a confusing plethora of oscillations in heart rate, arterial pressure, and respiration, and these oscillations are almost certainly closely connected in ways we do not yet understand. Although many quantitative models of these oscillations have been constructed (Cohen and Taylor, 2002), there is no unified model that explains all of these behaviors in terms of feedback instabilities of known control mechanisms.

11.6.1 Autoregulation

Autoregulation is a local mechanism that makes flow through a tissue responsive to local oxygen demand but relatively insensitive to arterial pressure. In tissue for which the delivery of oxygen is of central importance (for example, the brain or the heart) the local blood flow is controlled to be slightly higher than required, but no higher.

In dead organs, an increase in arterial pressure produces a linear increase in blood flow, suggestive of a linear-resistance vessel. However, in normally functioning tissue, the arterial pressure can be changed over a large range with little effect on the blood flow (Fig. 15.10). For example, in muscle, with an arterial pressure between 75 mm Hg and 175 mm Hg the blood flow remains within $\pm$10-15% of normal.

The flow through an artery is known to be responsive to the need for oxygen. For example, an eightfold increase in metabolism produces a fourfold increase in blood flow (as shown in Fig. 11.11B). Similarly, if oxygen content falls because of anemia, high altitude, or carbon monoxide poisoning, the blood flow increases to compensate. For example, a reduction to 25% of normal oxygen saturation produces a threefold increase in blood flow, not quite enough to compensate fully for the loss (see Fig. 11.11A).

Although the mechanism for autoregulation is not completely understood, it is most likely that resistance of tissue is responsive to biochemical measures of how hard it is working, such as concentrations of H^+, CO_2, O_2, and lactic acid. The ar-
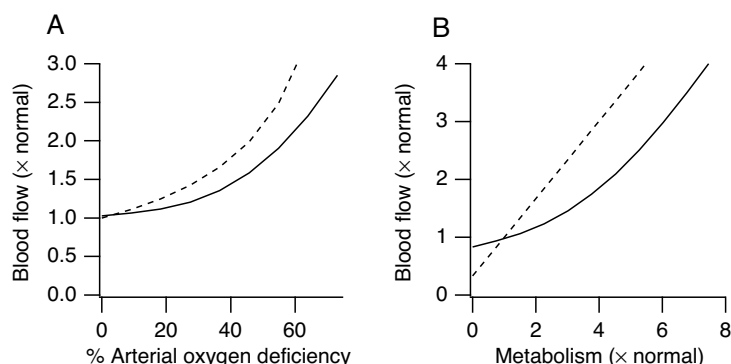
Figure 11.11: A: Blood flow as a function of the percentage of arterial oxygen deficiency, keeping arterial pressure and metabolic rate fixed. (Data (solid curve) from Guyton and Hall (1996), Fig. 17-2, p 200.) Dashed curve shows the result from the model. B: Blood flow as a function of metabolism, keeping arterial pressure and arterial oxygen content fixed at normal levels. (Data (solid curve) from Guyton and Hall, 1996, Fig. 17-1, p. 200.) Dashed curve shows the result from the model.

terioles are highly muscular, and their diameters can change manyfold. The metarterioles (terminal arterioles) are encircled by smooth muscle fibers at intermittent points and are also used to regulate flow.

The arterial blood has the same composition for all tissues of the body so cannot be used as a local control mechanism. This is problematic because it is the arterioles whose resistance is regulated. Here we assume that the resistance of arterioles is a function of the concentration of oxygen in the venous blood. This is possible, since arteries and veins tend to run side by side, and venous concentrations may regulate arterial resistance by release and diffusion of regulatory substances, called *vasodilators*.

An example of how this may work is as follows. If cardiac activity increases and the utilization of oxygen exceeds the supply, ATP is degraded, increasing the concentration of *adenosine*. Adenosine is a vasodilator, which leaks out of the cells into the venous flow to cause local dilation of coronary arteries. Thus, as the oxygen supply decreases, so does the arterial resistance.

A simple model for autoregulation is as follows (Huntsman et al., 1978; Hoppensteadt and Peskin, 1992). We keep track of oxygen consumption and blood flow via

$$([O_2]_a - [O_2]_v)Q \quad = \quad M, \tag{11.89}$$

$$P_a - P_v \quad = \quad RQ, \tag{11.90}$$

where $[O_2]_a$ and $[O_2]_v$ are the arterial and venous oxygen concentrations, respectively, M is the metabolic rate (oxygen consumption per unit time), P_a and P_v are the arterial and venous pressures driving the flow Q through tissue with total resistance R. In this model $[O_2]_a$ is treated as a given constant and $[O_2]_v$ as variable.

Now we assume that there is some linear relationship between arterial resistance and venous oxygen content, say

$$R = R_0 \left(1 + A[O_2]_v\right), \qquad (11.91)$$

where $A > 0$. The assumption of linearity is reasonable in restricted ranges of oxygen content. Here, the parameter A denotes the sensitivity of resistance to oxygen; if $A = 0$ the resistance is unregulated.

These equations can be solved for the flow rate Q to get

$$Q = \frac{1}{1 + A[O_2]_a} \left(MA + \frac{P_a}{R_0}\right), \qquad (11.92)$$

where it is assumed that $P_v = 0$. This is a linear relationship between flow rate and arterial pressure, which, when $A = 0$, reproduces the unregulated situation. However, with $A > 0$, the sensitivity of the flow to changes in arterial pressure varies with arterial oxygen content. Furthermore, this expression shows linear dependence of blood flow on metabolism.

We can estimate the parameters A and R_0 using the data from Fig. 11.10. In the range of pressures between 75 and 175 mm Hg, the curve is well represented by the straight line

$$\frac{Q}{Q^*} = \frac{1}{3} + \frac{2}{3}\frac{P_a}{P^*}, \qquad (11.93)$$

where Q^* and P^* are the normal values of flow and pressure ($Q^* = 5.6$ liters/min., $P^* = 100$ mm Hg). (Remark: Any straight line through P^* and Q^* must be of the form $\frac{Q}{Q^*} = \alpha + (1-\alpha)\frac{P_a}{P^*}$.) Comparing this to the regulated curve (11.92) at normal values,

$$Q = \frac{1}{1 + A[O_2]_a^*} \left(M^*A + \frac{P_a}{R_0}\right), \qquad (11.94)$$

where $[O_2]_a^*$ and M^* are normal values of arterial oxygen and metabolism, respectively ($M^* = Q^*([O_2]_a^* - [O_2]_v^*), [O_2]_a^* = 104$ mm Hg, $[O_2]_v^* = 40$ mm Hg), we find that

$$A = \frac{Q^*}{3M^* - Q^*[O_2]_a^*}, \qquad (11.95)$$

$$R_0 = \frac{P^*(3M^* - Q^*[O_2]_a^*)}{2Q^*M^*}, \qquad (11.96)$$

so that

$$\frac{Q}{Q^*} = \frac{3\frac{M}{M^*}}{\left(1 + 2\frac{P^*}{P_a}\right)\left(3 + \frac{13}{8}\left(\frac{[O_2]_a}{[O_2]_a^*} - 1\right)\right)}, \qquad (11.97)$$

using typical values for $\frac{Q^*[O_2]_a^*}{M^*} = \frac{13}{8}$.

In Fig. 11.10 are shown the data for blood flow as a function of arterial pressure, compared with the model (11.97). The good agreement over the linear range is the result of fitting.

The relationship (11.92) reproduces two other features of autoregulation that are qualitatively correct. It predicts that the flow rate increases as the arterial oxygen

content decreases, and increases linearly with metabolic rate. In Fig. 11.11A is shown the blood flow plotted as a function of arterial oxygen deficiency. Here, the solid curve is taken from data, and the dashed curve is from (11.97). Similarly, in Fig. 11.11B is shown the blood flow plotted as a function of metabolic rate. As before, the solid curve is from data, and the dashed curve is from (11.97). Clearly, the model gives reasonable qualitative agreement for blood flow as a function of arterial oxygen content, and for blood flow as a function of metabolism.

11.6.2   The Baroreceptor Loop

The *baroreceptor loop* is a global feedback control mechanism using the nervous system to adjust the heart rate, the venous resistance, and thereby the venous pressure in order to maintain the arterial pressure at a given level, with the ultimate goal of regulating the cardiac output.

   The need to regulate cardiac output is apparent. During exercise, when the demand for oxygen goes up, cardiac output normally rises at a linear rate, with slope about 5 (since 5 liters of blood are required to supply 1 liter of oxygen). In normal situations, the cardiac output and heart rate are roughly proportional, indicating that the stroke volume remains essentially constant. However, if heart rate is artificially driven up with a pacemaker, with no increase in oxygen consumption, then the cardiac output remains virtually the same, indicating a decrease in stroke volume. Similarly, in exercise with a fixed heart rate (set by a pacemaker), total cardiac output increases to meet the demand.

   The primary nervous mechanism for the control of cardiac output is the *baroreceptor reflex* (Fig. 11.12). This reflex is initiated by stretch receptors, called *baroreceptors* or *pressoreceptors*, located in the walls of the *carotid sinus* and *aortic arch*, large arteries of the systemic circulation. A rise in arterial pressure is detected and causes a signal to be sent to the central nervous system from which feedback signals are sent through the autonomic nervous system to the circulatory system, thereby enabling the regulation of arterial pressure. For example, the baroreceptor reflex occurs when a person stands up after having been lying down. Immediately upon standing, the arterial pressure in the head and upper body falls, with dizziness or loss of consciousness a distinct possibility. The falling pressure at the baroreceptors elicits an immediate reflex, resulting in a strong sympathetic discharge throughout the entire body, thereby minimizing the decrease in blood pressure in the head. This observation suggests that the larger dinosaurs required a well-tuned baroreceptor reflex in order not to faint every time they raised their heads.

   The most important part of the autonomic nervous system for regulation of the circulation is the *sympathetic nervous system*, which innervates almost all the blood vessels, with the exception of the capillaries. The primary effects of sympathetic nervous stimulation are

   1. contraction of small arteries and arterioles (by stimulation of the surrounding smooth muscle) to increase blood flow resistance and thereby decrease blood flow in the tissues;

   2. constriction of the veins, thereby decreasing the amount of blood in the peripheral circulation;
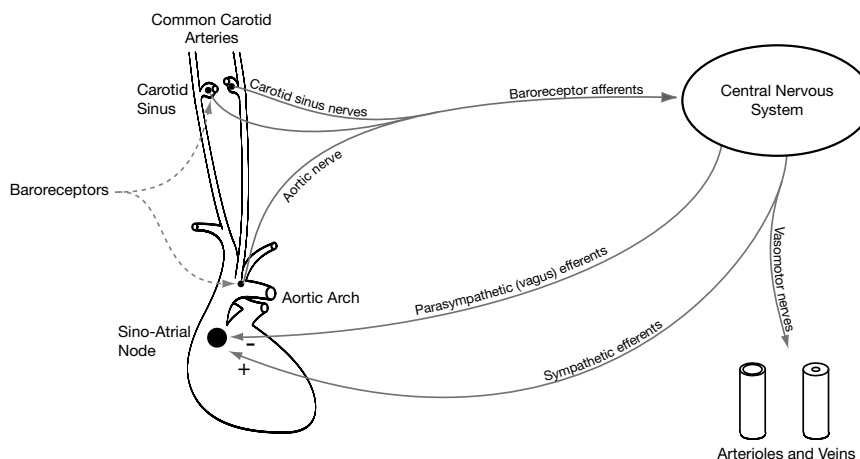
Figure 11.12: Schematic diagram of the baroreceptor reflex pathway. Adapted from Ottesen (1997), Fig. 2.

3. stimulation of the heart muscle, thereby increasing both the heart rate and stroke volume.

The *parasympathetic* or *vagus* nerves have the opposite effect on the heart, namely to decrease the heart rate and decrease the strength of contractility. Strong sympathetic stimulation can increase the heart rate in adult humans to 180–200 beats per minute, and even as high as 220 beats per minute in young adults. Strong parasympathetic stimulation can lower the heart rate to 20–40 beats per minute and can decrease the strength of contraction by 20 to 30 percent.

The effect of the baroreceptors is to increase sympathetic stimulation and decrease parasympathetic stimulation when there is a drop in arterial pressure. This increase in sympathetic activity, in turn, increases the heart rate, the systemic resistance, and the cardiac compliances, and decreases the venous compliance. Notice from Table 11.2 that in the unregulated circulation these changes effect an increase of arterial pressure. Thus, the overall effect of the baroreceptor loop is to maintain the arterial pressure at a desired level.

The sympathetic nervous system is also stimulated by the brain vasomotor center, where an increase in carbon dioxide in the brain acts to cause a widespread vasoconstriction throughout the body. A sympathetic response is also stimulated by fright or anger, and is called the *alarm reaction.*

The sympathetic nervous system acts by three mechanisms. First, it stimulates the contraction of vessels by the release of vasoconstrictors, primarily *norepinephrine.* Simultaneously, the adrenal medullae are stimulated to release epinephrine (adrenaline) and norepinephrine into the circulating blood. These two hormones are carried in the bloodstream to all parts of the body, where they act directly on blood vessels, usually to cause contraction. (Some tissues respond to epinephrine by dilation rather than constriction.) The action of secreted norepinephrine lasts about 30 minutes. Finally, sympathetic nervous activity acts to increase heart rate

and heart contractility.

To include the baroreceptor loop and the sympathetic nervous system in our circulation model, we suppose that the level of sympathetic stimulation is given by S, and that S is related to the deviation of the arterial pressure P_{sa} through a simple linear relationship

$$S = S^* + \beta(P_{sa}^* - P_{sa}), \tag{11.98}$$

so that as arterial pressure decreases, sympathetic stimulation increases. Here, S^* and P_{sa}^* are "normal" values. In animal experiments, blocking all sympathetic activity leads to a drop of arterial pressure from 100 to 50 mm Hg, indicating a continuous basal level of sympathetic firing at normal pressure ($S^* \neq 0$), called *sympathetic tone*, known to be about one impulse per second.

Next, we assume that heart rate F, arterial resistance R_{sa}, and cardiac compliances C_{ld} and C_{rd} are (unspecified) increasing functions of S, while the venous compliance C_{sv} is a decreasing function of S. We account for the metabolic need of the tissue through

$$([O_2]_a - [O_2]_v)Q = M, \tag{11.99}$$

and suppose that the metabolic need is communicated to the tissue through autoregulation via

$$R_{sa} = R(S) + A[O_2]_{sv}. \tag{11.100}$$

This representation is slightly different from that in (11.91), but it has the same interpretation.

Combined with the balance equations (11.71)–(11.79), we have a closed system of equations, which can be solved to find the cardiac output Q as a function of metabolic need M. The solution is complicated, and so we leave the details to the interested reader.

However, it is useful to view the solution of these equations in a slightly different way. We suppose that the effect of baroreceptor feedback is to hold the arterial pressure fixed at some target level and to adjust other parameters such as arterial resistance, venous compliance, and heart rate so that this target pressure is maintained. Then we can view P_{sa} as a parameter of the model and let the heart rate, say, be an unknown. Thus we solve the governing equations, not for the pressures and cardiac output as functions of the heart rate, as with the unregulated flow, but for heart rate and cardiac output as functions of arterial pressure and metabolism. We then obtain

$$F = \frac{\left(\frac{1}{C_{rd}}(2C_{sv} + C_{sa}) + \frac{2}{C_{ld}}C_p\right)(AM + P_{sa}) + \frac{1}{C_{rd}}(P_{sa}C_{sa} - 2V_e)}{(2V_e - P_{sa}C_{sa})(R_{sa} + R_{sv}) - (AM + P_{sa})(C_{sv}R_{sv} + C_pR_p + C_{sa}R_{sv})} \tag{11.101}$$

$$Q = \frac{(C_{ld}(2C_{sv} + C_{sa}) + 2C_{rd}C_p)(AM + P_{sa}) + C_{ld}(P_{sa}C_{sa} - 2V_e)}{C_{ld}(R_{sa}(2C_{sv} + C_{sa}) + R_{sv}C_{sv} - C_pR_p) + 2C_pC_{rd}(R_{sa} + R_{sv})}. \tag{11.102}$$

Although these formulae are somewhat complicated and obscure, here we see a number of features for the controlled circulation that are markedly different from those for the uncontrolled circulation. Most obvious is that heart rate and cardiac
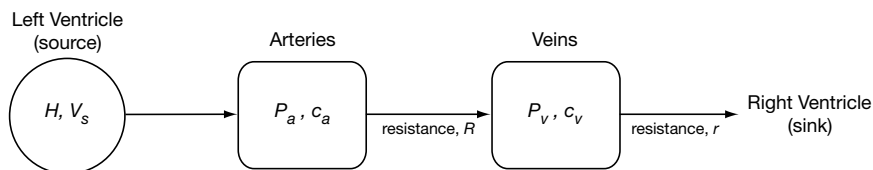
Figure 11.13: The lumped model of the circulatory system used in the model of the baroreceptor loop.

output respond to changes in metabolic need M. In fact, the cardiac output can be increased by increasing the arterial pressure or decreasing the systemic resistances.

These formulae also show some difficulties that the control system faces. Notice that there are parameter ranges for which either the numerator or denominator are negative. These are parameter values for which the solution is not valid, or, said another way, that are outside the range of physical possibility. Thus, for example, certain target pressures P_{sa} cannot be maintained if V_e is either too large or too small. Similarly (and not surprisingly), there are some large values of metabolism and pressure $(AM + P_{sa})$ that are impossible to maintain.

If the heart rate cannot be controlled by the baroreceptor loop, as for example when there is an implanted pacemaker, then F must be viewed as a tuneable parameter of the model rather than an unknown. Instead, some other variables, such as cardiac compliance, are the unknowns. If we suppose that the cardiac compliances are always in the same ratio, then it is easy to see that an increase in heart rate leads to an exactly compensating decrease in compliance and stroke volume, so that the same total output is maintained.

Oscillations in the Baroreceptor Loop

One of the motivations for studying the baroreceptor loop is to try and understand the occurence of oscillations in arterial pressure, such as the Mayer and Traube-Hering waves discussed above. This is not possible with a steady state model like that presented in the previous section. There have been a number of mathematical models of the baroreceptor reflex that concentrate on oscillatory instabilities, the principal ones being that of de Boer et al. (1987), and that of Ottesen (1997) (later studied in a modified form by Fowler and McGuinness, 2005). Here we present a simplifed version of the Ottesen model.

We model the circulatory system as a simple lumped system, in which all the arteries are modeled by a single compliance vessel, as are all the veins, as sketched in Fig. 11.13. This is essentially a *Windkessel* model, a type of model that is discussed in more detail in Section 11.8.2.

The volume of the arterial compartment is $P_a c_a$, and thus

$$\frac{d}{dt}(P_a c_a) = \frac{1}{R}(P_v - P_a) + V_s F, \tag{11.103}$$

where F is the heart rate and V_s is the stroke volume. If we assume that the arterial compliance is constant (i.e., we model only the effects of the baroreceptor loop on

heart rate) then

$$c_a \frac{dP_a}{dt} = \frac{1}{R}(P_v - P_a) + V_s F. \qquad (11.104)$$

Similarly,

$$c_v \frac{dP_v}{dt} = \frac{1}{R}(P_v - P_a) - \frac{1}{r}P_v. \qquad (11.105)$$

We model the changes in heart rate with a sigmoidally increasing function of the arterial pressure (the action of the sympathetic efferents in Fig. 11.12) and a sigmoidally decreasing function of the arterial pressure (the parasympathetic efferents in Fig. 11.12). However, the parasympathetic system is assumed to act with a delay of τ seconds. Thus,

$$\frac{dF}{dt} = \alpha g(P_a(t - \tau)) - \beta(1 - g(P_a)), \qquad (11.106)$$

where g_s is the sigmoidally decreasing function

$$g(P_a) = \frac{\mu^7}{\mu^7 + P_a^7}, \qquad (11.107)$$

for some constant μ. This choice of function for the sympathethic and parasympathetic controls, although highly simplified in this version of the model, is based on experimental data and is discussed in more detail by Danielsen and Ottesen (2004).

Because P_v is so much smaller than P_a it can be neglected in the model, leaving us with the system of delay differential equations

$$c_a \frac{dP_a}{dt} = \frac{-P_a}{R} + V_s F, \qquad (11.108)$$

$$\frac{dF}{dt} = \alpha g(P_a(t - \tau)) - \beta(1 - g(P_a)). \qquad (11.109)$$

The (unique) steady state solution of this system of equations is

$$\bar{P} = \mu \left(\frac{\alpha}{\beta} \right)^{\frac{1}{7}}, \qquad (11.110)$$

$$\bar{F} = \frac{1}{V_s R} \bar{P}. \qquad (11.111)$$

The first step to find oscillatory solutions is to determine where in parameter space this steady state solution becomes unstable. If it becomes unstable via a change of sign of the real part of a complex eigenvalue, then we have a Hopf bifurcation and the existence of a branch of periodic solutions (although, of course, they might not be stable). To investigate stability of the steady solution we follow the usual procedure of linearizing around the steady state solution and calculating the eigenvalues of the resultant linear system. Linearizing (11.110) and (11.111) around the steady state solution gives

$$c_a \frac{dp}{dt} = \frac{-p}{R} + V_s f, \qquad (11.112)$$

$$\frac{df}{dt} = \alpha g'(\bar{P})p(t - \tau) + \beta g'(\bar{P})p, \qquad (11.113)$$

c_a	$=$	1.55 ml/mmHg	R	$=$	1.05 mmHg sec/ml
V_s	$=$	67.9 ml	μ	$=$	93 mmHg
α	$=$	0.84 sec^{-2}	β	$=$	1.17 sec^{-2}

Table 11.3: Parameter values of the model for oscillations in the baroreceptor loop. Taken from Ottesen (1997).

where $P_a = \bar{P} + p$ and $F = \bar{F} + f$, i.e., p and f are the deviations from the steady state.

Now, we look for solutions of the form $p = p_0 e^{\lambda t}$, $f = f_0 e^{\lambda t}$. Substituting into the linearized equations gives

$$\begin{pmatrix} -1/R - c_a\lambda & V_s \\ \alpha g'(\bar{P})e^{-\lambda t} + \beta g'(\bar{P}) & -\lambda \end{pmatrix} \begin{pmatrix} p_0 \\ f_0 \end{pmatrix} = 0. \tag{11.114}$$

This system has a nontrivial solution only if the determinant of the matrix is zero, and thus λ must be a root of the characteristic equation

$$c_a\lambda^2 + \frac{1}{R}\lambda - V_s g'(\bar{P})(\alpha e^{-\lambda t} + \beta) = 0. \tag{11.115}$$

Since $g'(\bar{P}) < 0$, all the real roots of (11.115) have negative real part. Thus, the only way the solution can become unstable is for the real part of a complex root to change sign. Thus, we look for changes of stability by setting $\lambda = iz$ and solving for z. After separating real and imaginary parts, we find

$$c_a z^2 - b^2 = a^2 \cos z\tau, \tag{11.116}$$

$$\frac{z}{R} = a^2 \sin z\tau, \tag{11.117}$$

where $a^2 = -\alpha V_s g'(\bar{P})$ and $b^2 = -\beta V_s g'(\bar{P})$. Squaring both equations and adding gives

$$c_a^2 \xi^2 + \xi \left(\frac{1}{R^2} - 2c_a b^2 \right) + b^4 - a^4, \tag{11.118}$$

where $\xi = z^2$.

As long as care is taken to select the correct root of (11.118), it is a simple matter to solve for ξ, and thus for z and τ. For the parameter values used by Ottesen (shown here in Table 11.3), $z = 1.09$ and $\tau = 1.15$. Thus, the period of the oscillation that occurs when stability is lost is $2\pi/1.09 \approx 5.8$ seconds.

Numerical solution of the differential-delay equations shows that, when $z = 1.09$ and $\tau = 1.15$, the amplitude of the periodic solution is approximately 20 mmHg (Fig. 11.14).

11.7 Fetal Circulation

Because the fetus receives all of its oxygen through the umbilical cord and the placenta, the lungs of the fetus are not used for gas exchange. Instead, the lungs
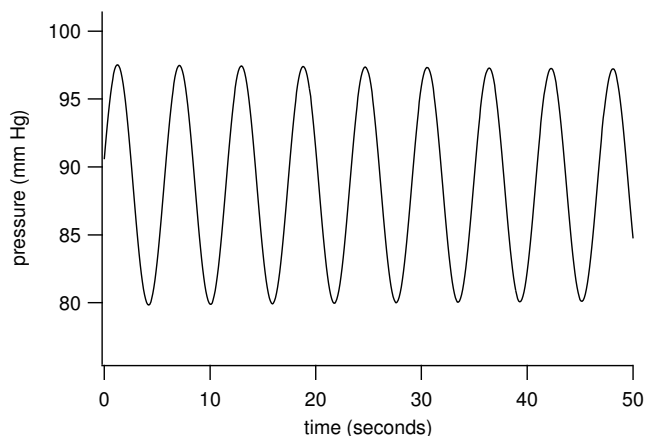
Figure 11.14: Numerical solution of the model of the baroreceptor loop for $\tau = 1.15$. The parameter values are given in Table 11.3.

are collapsed and have high resistance to blood flow: only 12% of the blood flow is through the lungs. This situation is reversed at birth when the newborn takes its first breath, expanding the lungs, and when the umbilical cord constricts.

Necessitated by the high resistance of the pulmonary circulation, the fetal circulatory system has a connection between the pulmonary artery and the aorta, called the *ductus arteriosus*, that shunts blood from the outflow of the right heart directly into the systemic arteries. After birth, the ductus gradually closes.

The ventricular chambers of the developing fetal heart are nearly equal in size. It is only after birth that the load on the left ventricle increases, necessitating additional growth of the left ventricular wall to accommodate an increased demand. To equalize the output of the two hearts, there is a small opening in the interatrial septum, called the *foramen ovale*. On the left side of the septum there is a small flap of tissue that allows flow from the right atrium to the left but prevents the reverse from occurring. In the fetus, this flap is open, but at birth it closes for reasons that become clear below.

To model the fetal circulatory system, we use the same three-compartment model as above with additional connections allowed by the ductus arteriosus and the foramen ovale (Fig. 11.15). Since there is no longer a single loop, we must keep track of the flows in each compartment. These flows are governed by the following equations:

Systemic arteries:

$$Q_s = \frac{P_{sa} - P_s}{R_{sa}}. \tag{11.119}$$

Systemic veins:

$$Q_s = \frac{P_s - P_{sv}}{R_{sv}}. \tag{11.120}$$
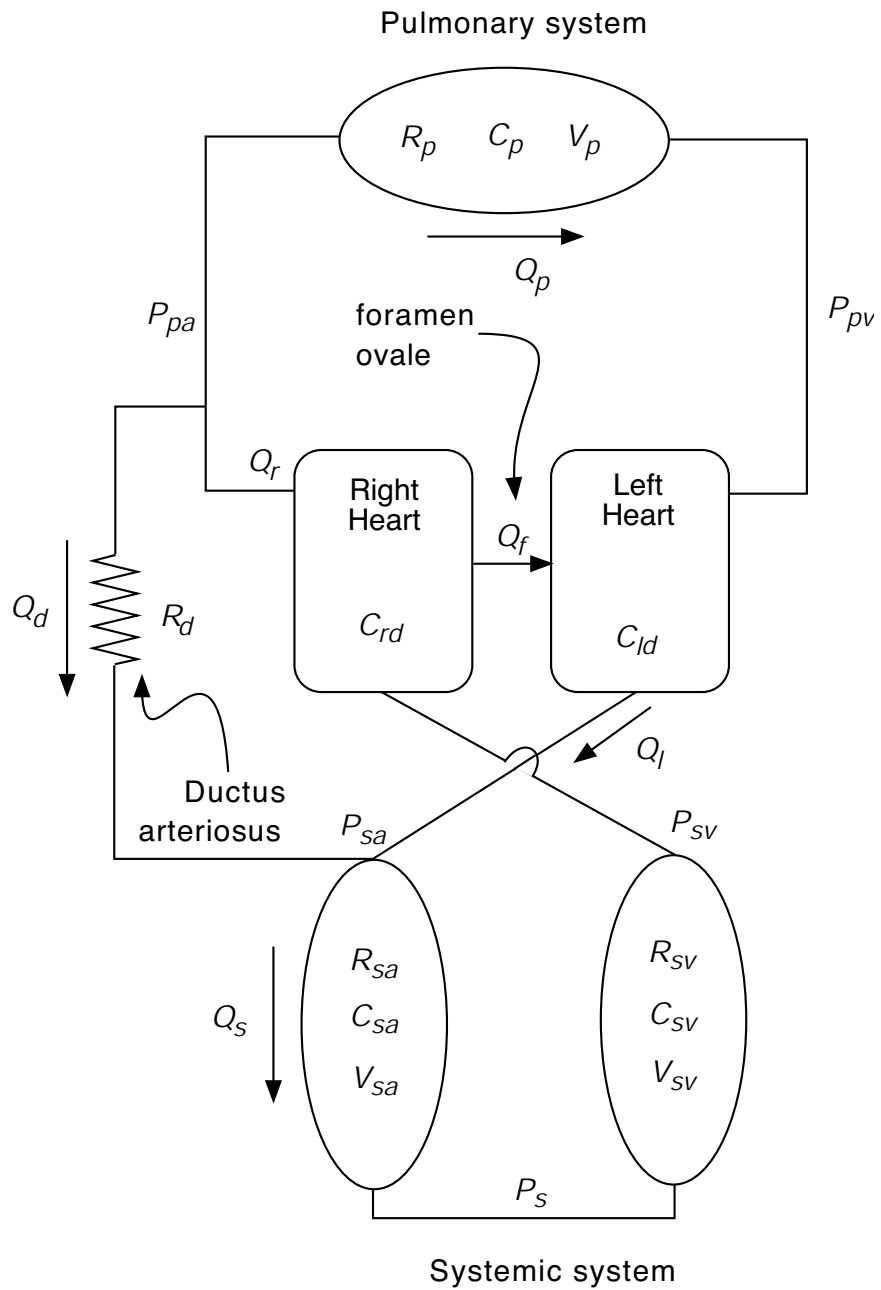
Figure 11.15: Schematic diagram of the fetal circulation. The model is based on the three-compartment model in Fig. 11.9, with additional connections to model the ductus arteriosus and the foramen ovale.

Pulmonary system:

$$Q_p = \frac{P_{pa} - P_{pv}}{R_p}. \tag{11.121}$$

Left heart:

$$Q_l = F(C_{ld}P_{pv} - C_{l\sigma}P_{sa}). \tag{11.122}$$

Right heart:

$$Q_r = F(C_{rd}P_{sv} - C_{r\sigma}P_{pa}). \tag{11.123}$$

The equations for the volumes are unchanged from before.

Since fluid is conserved, flow into any junction must equal the flow out. There are four junctions, and thus there are four conservation laws

$$
\begin{aligned}
Q_l + Q_d &= Q_s, & (11.124) \\
Q_r &= Q_d + Q_p, & (11.125) \\
Q_s &= Q_r + Q_f, & (11.126) \\
Q_p + Q_f &= Q_l, & (11.127)
\end{aligned}
$$

where l = left heart, r = right heart, s = systemic, p = pulmonary, f = foramen ovale, d = ductus arteriosus. Notice that there are only three independent relationships here, as the first three imply the fourth, for the simple reason that total fluid is conserved. As a result, any three flows can be determined as functions of the remaining three.

A quick count shows that there are 14 variables (5 pressures, 3 volumes, and 6 flows), but only 12 equations, including the three equations for the volumes and the equation for the conservation of volume, which are not shown explicitly here. Thus, to characterize the system completely, two additional equations are needed. These are the equation for the ductus,

$$Q_d = \frac{P_{pa} - P_{sa}}{R_d}, \tag{11.128}$$

and the equation for the foramen, modeled as an ideal valve,

$$
\begin{aligned}
P_{sv} &= P_{pv}, & \text{if } Q_f > 0, & (11.129) \\
Q_f &= 0, & \text{if } P_{sv} < P_{pv}. & (11.130)
\end{aligned}
$$

Here, there is no resistance to flow in the forward direction if the valve is open, and if the valve is closed, there is no flow in the backward direction.

There are two possible solutions. First, for the "foramen open" solution, we set $P_{sv} = P_{pv}$ and solve the governing system of equations. This yields a valid solution for all parameter values for which $Q_f > 0$. On the other hand, if we take $Q_f = 0$ (the "foramen closed" solution) and determine all the pressures, we have a valid solution for all parameter values for which $P_{sv} < P_{pv}$. For any set of parameter values there should be one, but only one, solution set.

We begin by looking for the "foramen open" solution. For simplicity, we again suppose that the systolic compliances are negligible, i.e., that $C_{r\sigma} = C_{l\sigma} = 0$. We find

$$Q_f = Q_r \frac{R_d(C_{ld} - C_{rd}) + R_p C_{ld} - C_{rd}(R_{sa} + R_{sv})}{C_{rd}(R_{sa} + R_{sv} + R_p + R_d)}, \tag{11.131}$$

$$Q_d = Q_r \frac{C_{ld}(R_{sv} + R_{sa}) - R_p C_{rd}}{C_{rd}(R_{sv} + R_{sa} + R_d + R_p)}, \tag{11.132}$$

$$Q_s = Q_r \frac{R_p(C_{rd} + C_{ld}) + R_d C_{ld}}{C_{rd}(R_{sa} + R_{sv} + R_p + R_d)}, \tag{11.133}$$

$$Q_p = Q_r \frac{(R_{sa} + R_{sv})(C_{rd} + C_{ld}) + R_d C_{rd}}{C_{rd}(R_{sa} + R_{sv} + R_p + R_d)}, \tag{11.134}$$

$$Q_l = Q_r \frac{C_{ld}}{C_{rd}}. \tag{11.135}$$

In the developing fetus, the left and right hearts are nearly the same. If $C_{rd} = C_{ld} = C_d$, the outputs from the left and right hearts are the same, and $Q_l = Q_r = Q$. With this simplification we find that

$$Q_f = Q_d = Q \frac{R_p - R_{sa} - R_{sv}}{R_{sa} + R_{sv} + R_p + R_d}, \tag{11.136}$$

$$Q_s = Q \frac{2R_p + R_d}{R_{sa} + R_{sv} + R_p + R_d}, \tag{11.137}$$

$$Q_p = Q \frac{2R_{sa} + 2R_{sv} + R_d}{R_{sa} + R_{sv} + R_p + R_d}. \tag{11.138}$$

As long as the pulmonary resistance is larger than the total systemic resistance, the flow Q_f is positive, as required by our initial assumption. Thus, by adjusting the pulmonary resistance R_p, the foramen and the ductus allow blood to be shunted from the lungs to the systemic circulation. Notice that in the extreme case of $R_p = \infty$, we have $Q_f = Q_d = Q, Q_p = 0, Q_s = 2Q$. In other words, if $R_p = \infty$, there is no pulmonary flow, the flow returning from the systemic circulation is equally divided between the left and right hearts for pumping, and the blood pumped by the right heart is shunted from the lungs to the systemic arteries.

At birth, the lungs fill with air and expand, dramatically decreasing the resistance of blood flow in the lungs. Simultaneously, the umbilical cord constricts, dramatically increasing the total systemic resistance $R_{sa} + R_{sv}$. When this happens, the flow through the foramen reverses, and closes the foramen. To find the flow solution in this "foramen closed" situation, we take $Q_f = 0$ and drop the restriction that $P_{sv} = P_{pv}$. It follows immediately from (11.126) and (11.127) that $Q_p = Q_l$, $Q_s = Q_r$, and $Q_d = Q_r - Q_l$. Thus, the flow through the ductus is used to balance the outputs of the left and right sides of the heart.

Furthermore,

$$P_{pv} = \frac{Q_r}{FC_{ld}}, \tag{11.139}$$

$$P_{sv} = \frac{Q_l}{FC_{rd}}, \tag{11.140}$$

$$\frac{P_{sa}}{P_{pa}} = \left(\frac{\frac{1}{FC_{rd}} + R_{sv} + R_{sa}}{\frac{1}{FC_{rd}} + R_{sa} + R_{sv} + R_d}\right)\left(\frac{\frac{1}{FC_{ld}} + R_p + R_d}{\frac{1}{FC_{ld}} + R_p}\right), \quad (11.141)$$

and

$$\frac{P_{pv}}{P_{sv}} = \frac{FC_{rd}(R_{sa} + R_{sv} + R_d) + 1}{FC_{ld}(R_p + R_d) + 1}, \quad (11.142)$$

which is greater than one (as required) as long as $R_p < R_{sa} + R_{sv}$. Thus, remarkably, as soon as the first breath is drawn and the pulmonary resistance drops, the pulmonary venous pressure exceeds the systemic venous pressure, keeping the foramen closed, allowing the skin flap to gradually grow over and seal tightly. In addition,

$$Q_d = Q_r \frac{(\frac{1}{FC_{ld}} + R_p) - (\frac{1}{FC_{ld}} + R_{sa} + R_{sv})}{\frac{1}{FC_{ld}} + R_d + R_p}. \quad (11.143)$$

Thus, immediately after birth, when the left and right heart compliances are the same, the flow through the ductus reverses direction, so that the left heart output exceeds the right heart output, with

$$\frac{Q_l}{Q_r} = \frac{\frac{1}{FC_{rd}} + R_{sa} + R_{sv} + R_d}{\frac{1}{FC_{ld}} + R_p + R_d}. \quad (11.144)$$

For reasons that are not completely understood (probably because of the increased concentration of oxygen in the blood), the ductus gradually closes, so that R_d grows, eventually to ∞. As it does so, the arterial pressure P_{sa} increases, causing the left ventricle to thicken gradually, decreasing its compliance. The end result (taking $R_d \to \infty$) is the solution of the single-loop system found in the previous section, although with parameter values that are not yet the "adult" values.

11.7.1   Pathophysiology of the Circulatory System

Occasionally, the heart or its associated blood vessels are malformed during fetal life, leaving the newborn infant with a defect called a *congenital anomaly*. There are three major types of congenital abnormalities:

1. A blockage, or *stenosis*, of the blood flow at some part of the heart or a major vessel.

2. An abnormality that allows blood to flow directly from the left heart or aorta to the right heart or pulmonary artery, bypassing the systemic circulation.

3. An abnormality that allows blood to flow from the right heart or pulmonary artery to the left heart or aorta, thereby bypassing the lungs.

Patent ductus arteriosus (PDA)

While the ductus arteriosus constricts to a small size shortly after birth, it is several months before flow is completely occluded. In about 1 out of 5500 babies, the ductus never closes, a condition known as *patent ductus arteriosus*. In a child with

a patent ductus, there is a substantial backflow from the left heart into the lungs, so that the blood is well oxygenated, but there is decreased cardiac reserve and respiratory reserve, because insufficient blood is supplied to the systemic arteries. As the child grows and systemic pressure increases, the backflow through the ductus also increases, sometimes causing the diameter of the ductus to increase, thereby worsening the condition. Symptoms of patent ductus include fainting or dizziness during exercise, and there is usually hypertrophy of the left heart.

It can happen that the lungs respond to the excess pulmonary flow by increasing pulmonary resistance, thereby, according to (11.143), reversing the flow in the ductus, shunting blood from the right heart to the aorta, carrying deoxygenated blood directly into the systemic arteries.

Closed foramen ovale in utero

In this situation the circulation is like the circulation after birth, except that the pulmonary resistance exceeds the systemic resistance, $R_p > R_{sa} + R_{sv}$. According to (11.144), the output of the left heart is low compared to the output of the right heart, so that development of the left heart is impaired and the right heart is overdeveloped at birth.

Atrial septal defect (ASD)

If the foramen does not close properly at birth, there remains a hole in the septum between the left and right atria, allowing oxygenated blood to leak from the left heart to the right heart. Assuming that the ductus closes successfully, so that $Q_d = 0$, it follows that

$$Q_p = Q_r = FC_{rd}P_{sv}, \tag{11.145}$$

$$Q_s = Q_l = FC_{ld}P_{pv}, \tag{11.146}$$

$$Q_f = Q_s - Q_r = Q_l - Q_p, \tag{11.147}$$

so that

$$\frac{Q_p}{Q_s} = \frac{Q_r}{Q_l} = \frac{C_{rd}}{C_{ld}}. \tag{11.148}$$

If the left heart has smaller compliance than the right heart, as would be true in an adult, the pulmonary flow exceeds the systemic flow.

ASD and PDA

The configuration here is the same as with the fetal circulation, except that there is no valve to prohibit flow from the left to right atrium. The solution is the "foramen open" solution, for which

$$Q_s - Q_p = Q_f + Q_d = Q_s \left(1 - \frac{R_d C_{rd} + (R_{sa} + R_{sv})(C_{ld} + C_{rd})}{R_d C_{ld} + R_p(C_{ld} + C_{rd})}\right), \tag{11.149}$$

which is negative for typical parameter values. This shows that it is possible to reduce the shunted flow and equalize the pulmonary and systemic flows by *banding*

or surgically constricting the pulmonary artery, thus increasing R_p. The banding procedure works, however, only if $R_d \neq \infty$, that is, only if there is flow through the ductus. Banding has no effect in ASD when the ductus is closed, because in the limit $R_d \to \infty$, the flow through the foramen is

$$Q_f = Q_s \left(1 - \frac{C_{rd}}{C_{ld}} \right), \qquad\qquad (11.150)$$

independent of R_p.

11.8   The Arterial Pulse

The above analysis treats the circulation as if the various pressures in the blood vessels are constant over time. Of course, since the heart pumps blood in a pulsatile manner, this is not the case. Each beat of the heart forms a pressure wave that travels along the arteries, changing shape as it moves away from the heart. Typical experimental data, taken from a dog artery, are shown in Fig. 11.16. It is evident that closer to the heart the pressure pulse is wider and does not have a distinct second wave, and the velocity and pressure waves have different forms. However, as the pulse moves away from the heart, the pressure wave becomes steeper, a second wave develops following the first, and the velocity profile becomes similar to the pressure profile. Since variations in the form of the arterial pulse are often used as clinical indicators (for example, the second wave is usually absent in patients with diabetes or atherosclerosis), it is important to gain an understanding of the physical mechanisms underlying the shape of the pulse in normal physiology. Models to explain the shape of the arterial pulse range from simple linear ones to complex models incorporating the tapering of the arterial walls and its branching structure (Pedley, 1980; Lighthill, 1975; Peskin, 1976), and the modern literature on models of the arterial pulse is vast. Here, we restrict our attention to only the simplest models.

11.8.1   The Conservation Laws

Consider flow in a blood vessel with cross-sectional area $A(x, t)$. For simplicity we assume that the flow is a *plug flow*, with velocity that is a scalar quantity u and is a function of axial distance along the vessel only. Poiseuille flow becomes plug flow in the limit of zero viscosity, and so in the following analysis we omit consideration of viscous forces. The volume of the vessel of length L is $\int_0^L A(x, t) \, dx$, and thus conservation of mass requires that

$$\frac{\partial}{\partial t} \left(\int_0^L A(x, t) \, dx \right) = u(0) A(0, t) - u(L) A(L, t). \qquad (11.151)$$

Taking the partial derivative of (11.151) with respect to L and replacing L by x gives

$$A_t + (Au)_x = 0. \qquad\qquad (11.152)$$
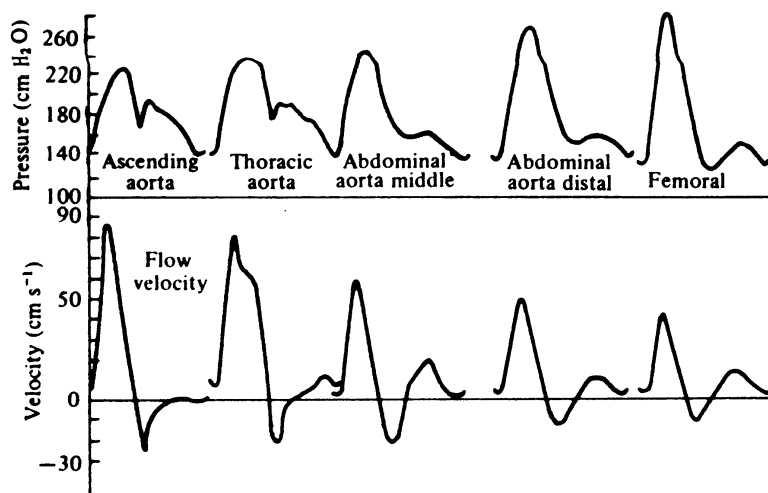
Figure 11.16: The form of the arterial pulse measured in the arteries of a dog. The top panel shows the pressure waveform, and the bottom panel shows the velocity. (Pedley, 1980, Fig. 1.14, taken from McDonald, 1974.)

According to Newton's law, the rate of change of momentum of a fluid in some domain is equal to the net force exerted on the boundary of the domain plus the flux of momentum across the boundary. Thus, conservation of momentum requires that

$$\frac{\partial}{\partial t}\left(\rho \int_0^L A(x,t)u(x,t)\,dx\right) = \rho A(x,t)u^2(x,t)\big|_{x=L}^0 + P(x,t)A(x,t)\big|_{x=L}^0. \quad (11.153)$$

Note that $\rho A(0,t)u(0,t)$ is the rate at which mass enters the vessel across the surface $x = 0$ (i.e., the momentum), so that $\rho A(0,t)u^2(0,t)$ is the rate at which momentum enters the vessel across this surface. Differentiating (11.153) with respect to L and replacing L by x, we find that

$$\rho\left((Au)_t + (Au^2)_x\right) = -(PA)_x. \quad (11.154)$$

This second equation can be simplified by expanding the derivatives and using (11.152) to get

$$\rho\left(u_t + uu_x\right) = -P_x \quad (11.155)$$

as the equation for the conservation of momentum.

For simplicity we assume that the vessel is a linear compliance vessel with

$$A(P) = A_0 + cP. \quad (11.156)$$

One can use a more general relationship between area and pressure, but the basic conclusions of the following analysis remain unchanged. With this expression for the cross-sectional area, the equation for conservation of mass becomes

$$c(P_t + uP_x) + A(P)u_x = 0. \quad (11.157)$$
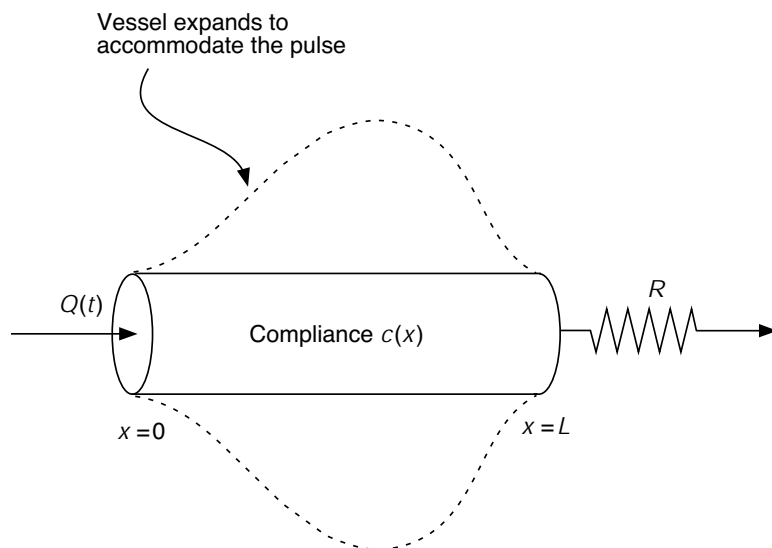
Figure 11.17: Schematic diagram of the *windkessel* model.

11.8.2 The Windkessel Model

One of the earliest models of the heart, dating back to the past century (Frank, 1899; translated by Sagawa et al., 1990), is the *windkessel* model, from the German word meaning an air chamber, or bellows. (The name originally arose because of the similarities between the mechanical conditions in the arterial system and the operation of the *windkessel*, or bellows, of a nineteenth-century fire engine.)

The *windkessel* model is obtained from (11.155) and (11.157) by letting $\rho \to 0$, in which case $P_x = 0$, so that the pressure is a function only of time. Thus, we model the greater arteries as a compliance vessel, extending from $x = 0$ to $x = L$, with time-varying pressure and volume; inflow at $x = 0$ is from the heart, and outflow at $x = L$ is into the peripheral arterial system (Fig. 11.17). However, although the pressure is uniform inside the vessel, the compliance is not, so that the cross-sectional area of the vessel varies with x, the distance along the vessel. In fact, we assume that $c(0) = c(L) = 0$, but that the compliance $c(x)$ is nonzero inside the vessel. Finally, we assume that the outflow from the vessel is into the peripheral system which is modelled as a simple resistance vessel with resistance R.

From (11.157) it follows that

$$u_x(x,t) = \frac{-c(x)P_t}{A_0 + c(x)P}, \tag{11.158}$$

and, integrating from $x = 0$ to $x = L$, we get

$$A_0 u(0,t) = \theta(P)P_t + A_0 u(L,t), \tag{11.159}$$

where

$$\theta(P) = \int_0^L \frac{A_0 c(x)}{A_0 + c(x)P}\, dx. \tag{11.160}$$

We denote $A_0 u(0, t)$ as $Q(t)$, since it is the flow into the vessel from the heart. Further, the outflow from the vessel, $A_0 u(L, t)$, must match the flow through the peripheral system, which we write as P/R (assuming the pressure drop across the peripheral system is also P). Hence, we have the differential equation for P,

$$Q(t) = \theta(P)P_t + \frac{P}{R}. \tag{11.161}$$

From this differential equation we learn that when the heart ejects blood, in which case $Q(t)$ increases quickly, there is a corresponding increase in P (i.e., the vessel fills up and expands). When the flow stops, Q is zero, and the pressure decreases to zero according to $P_t = -P/(\theta(P)R)$. This demonstrates that the major arteries act as a bellows, initially inflating to accommodate the blood from the heart and then contracting to pump the blood through the periphery.

11.8.3 A Small-Amplitude Pressure Wave

If p aan u are small, so that all nonlinear terms in (11.155) and (11.157) can be ignored, we then obtain the linear system

$$\rho u_t + P_x = 0, \tag{11.162}$$

$$cP_t + A_0 u_x = 0. \tag{11.163}$$

By cross-differentiation, we can eliminate u and find a single equation for P, namely

$$P_{tt} = \frac{A_0}{c\rho} P_{xx}, \tag{11.164}$$

which is well known as the *wave equation*.

Solutions of the wave equation include traveling wave solutions, which are functions whose shape is invariant but that move at the velocity $s = \sqrt{\frac{A_0}{c\rho}}$. For arteries, this velocity is on the order of 4 m/s, as can be verified by comparing the arrival times of the pressure pulse at the carotid artery in the neck and at the posterior tibial artery at the ankle.

The general solution of the wave equation (11.164) can be written in the form

$$P(x, t) = f(t - x/s) + g(t + x/s), \tag{11.165}$$

where f and g are arbitrary functions. Note that $f(t - x/s)$ denotes a wave with profile $f(x)$ traveling from left to right, while $g(t + x/s)$ denotes a wave traveling in the opposite direction. It follows that the general solution for u is

$$u = \frac{1}{\rho s}[f(t - x/s) - g(t + x/s)]. \tag{11.166}$$

11.8.4 Shock Waves in the Aorta

Although the linear wave equation can be used to gain an understanding of many features of the arterial pulse, such as reflected waves and waves in an arterial network (Lighthill, 1975), there are experimental indications that nonlinear effects are

also important (Anliker et al., 1971a,b). One particular nonlinear effect that we investigate here is the steepening of the wave front as it moves away from the heart. If the wave front becomes too steep, the top of the front overtakes the bottom, and a shock, or discontinuity, forms, a solution typical of hyperbolic equations. Of course, a true shock is not possible, as blood viscosity and the elastic properties of the arterial wall preclude the formation of a discontinuous solution. Nevertheless, it might be possible to generate very steep pressure gradients within the aorta.

Under normal conditions, no such shocks develop. However, in conditions where the aorta does not function properly, allowing considerable backflow into the heart, the heart compensates by an increase in the ejection volume, thus generating pressure waves that are steeper and stronger than those observed normally. Furthermore, the *pistol-shot* phenomenon, a loud cracking sound heard through a stethoscope placed at the radial or femoral artery, often occurs in patients with aortic insufficiency. It has been postulated that the pistol-shot is the result of the formation of a shock wave within the artery, a shock wave that is possible because of the increased amplitude of the pressure pulse.

To model this phenomenon, recall that the governing equations are

$$c(P_t + uP_x) + A(P)u_x = 0, \tag{11.167}$$
$$\rho(u_t + uu_x) + P_x = 0, \tag{11.168}$$

which can be written in the form

$$w_t + Bw_x = 0, \tag{11.169}$$

where

$$w = \begin{pmatrix} u \\ P \end{pmatrix} \tag{11.170}$$

and

$$B = \begin{pmatrix} u & \frac{1}{\rho} \\ \frac{A(P)}{c} & u \end{pmatrix}. \tag{11.171}$$

Using the method of characteristics (Whitham 1974; Pedley, 1980; Peskin, 1976), we can determine some qualitative features of the solution. Roughly speaking, a characteristic is a curve C in the (x, t) plane along which information about the solution propagates. For example, the equation $u_t + cu_x = 0$ has solutions of the form $u(x, t) = U(x - ct)$, so that information about the solution propagates along curves $x - ct = $ constant in the (x, t) plane. Similarly, characteristics for the wave equation (11.164) are curves of the form $t \pm x/s = $ constant, because it is along these curves that information about the solution travels.

To find characteristic curves, we look for curves in x, t along which the original partial differential equation behaves like an ordinary differential equation. Suppose a characteristic curve C is defined by

$$x = x(\lambda), \quad t = \lambda. \tag{11.172}$$

Derivatives of functions $w(x, t)$ along this curve are given by

$$\frac{dw}{d\lambda} = w_t + w_x \frac{dx}{d\lambda}. \tag{11.173}$$

Notice that with $dx/d\lambda = c$, the partial differential equation $u_t + cu_x = 0$ reduces to the simple ordinary differential equation $u_\lambda = 0$. Thus, curves with $dx/dt = c$ are characteristic curves for this simple equation.

To reduce the system (11.169) to characteristic form, we try to find appropriate linear combinations of the equations that transform the system to an ordinary differential equation. Thus, suppose the matrix B has a left eigenvector ξ^T with corresponding eigenvalue s, so that $\xi^T B = s\xi^T$. We multiply (11.169) by ξ^T, and find that with the identification $dx/d\lambda = s$,

$$0 = \xi^T(w_t + Bw_x) = \xi^T(w_t + sw_x) = \xi^T w_\lambda. \tag{11.174}$$

In other words, along the curve $dx/dt = s$, the original system of equations reduces to the simple ordinary differential equation $\xi^T w_\lambda = 0$.

It is an easy matter to determine that the eigenvalues of B are

$$s = u \pm K(P), \tag{11.175}$$

where

$$K(P) = \sqrt{\frac{A(P)}{\rho c}}, \tag{11.176}$$

with corresponding left eigenvector

$$\xi^T = (\xi_1, \xi_2) = (\rho K(P), \pm 1). \tag{11.177}$$

It follows from $\xi^T w_\lambda = 0$ that

$$u_\lambda \pm \frac{1}{\rho K(P)} P_\lambda = 0 \tag{11.178}$$

along the characteristic curve $dx/d\lambda = u \pm K(P)$, which we denote by $C_\pm$. Now, notice that, since $A(P)$ is linear in P,

$$\frac{1}{\rho K(P)} = 2\frac{d}{dP} K(P), \tag{11.179}$$

so that

$$\frac{d}{d\lambda}(u \pm 2K(P)) = 0. \tag{11.180}$$

In other words, $u + 2K(P)$ is conserved (remains constant) along C_+, the characteristic curve with slope $dx/dt = u + K(P)$, and $u - 2K(P)$ is conserved along C_-, the characteristic curve with slope $dx/dt = u - K(P)$.

Now, to see how this reduction allows us to solve a specific problem, consider the region $x \geq 0$, $t \geq 0$ with $u(0, t) > 0$ specified. For example, $u(0, t)$ could be the velocity pulse generated by a single heartbeat. We suppose that initially, $u(x, 0) = 0, P(x, 0) = P_0$ for all $x \geq 0$, where P_0 is the diastolic pressure.

Pick any point A in the region $x \geq 0$, $t \geq 0$ (Fig. 11.18). There are two characteristics passing through A, one, C_+, with positive slope $u + K(P)$ and one, C_-, with negative slope $u - K(P)$. (Here and in the following we assume that u is
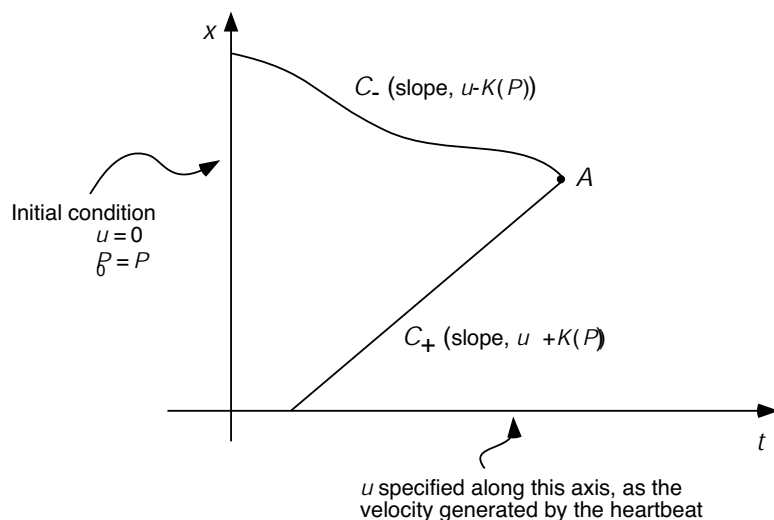
Figure 11.18: Diagram of the characteristics of the arterial pulse equations in the (t, x) plane.

small enough so that C_- always has negative slope.) Following C_- up and to the left, we see that it intersects the vertical axis, where $u = 0$ and $P = P_0$ (because of the specified initial data). Since the quantity $u - 2K(P)$ is conserved on C_-, it must be that $u - 2K(P) = -2K(P_0)$ at the point A. Since A is arbitrary, it follows that $u = 2K(P) - 2K(P_0)$ everywhere in the first quadrant. Thus, $u + 2K(P) = 4K(P) - 2K(P_0)$ is constant along C_+. Hence, $K(P)$ is constant along C_+, as are both P and u, so that C_+ is a straight line. The slope of C_+ is the value of $u + K(P)$ at the intersection of C_+ with the horizontal axis.

To be specific, suppose $u(0, t)$ first increases and then decreases as a function of t, as shown in Fig. 11.19A. (In this figure $u(0, t)$ is shown as piecewise linear, but this is simply for ease of illustration.) To be consistent, since $u = 2K(P) - 2K(P_0)$ everywhere in the first quadrant, $K(P(0, t)) = K(P_0) + \frac{1}{2}u(0, t)$, so that the slope of the C_+ characteristics is $s(t) = \frac{3}{2}u(0, t) + K(P_0)$, which also increases and then decreases as a function of t. With increasing slopes, the characteristics converge, resulting in a steepening of the wave front. If characteristics meet, the solution is not uniquely defined by this method, and shocks develop.

The place a shock first develops can be found by determining the points of intersection of the characteristics. Suppose we have two C_+ characteristics, one emanating from the t-axis at $t = t_1$, described by $x = s(t_1)(t - t_1)$, and the other emanating at $t = t_2$, described by $x = s(t_2)(t - t_2)$. They intersect at any point (t_i, x_i), where

$$t_i = \frac{s(t_2)t_2 - s(t_1)t_1}{s(t_2) - s(t_1)}, \tag{11.181}$$

$$x_i = \frac{s(t_2)s(t_1)(t_2 - t_1)}{s(t_2) - s(t_1)}. \tag{11.182}$$
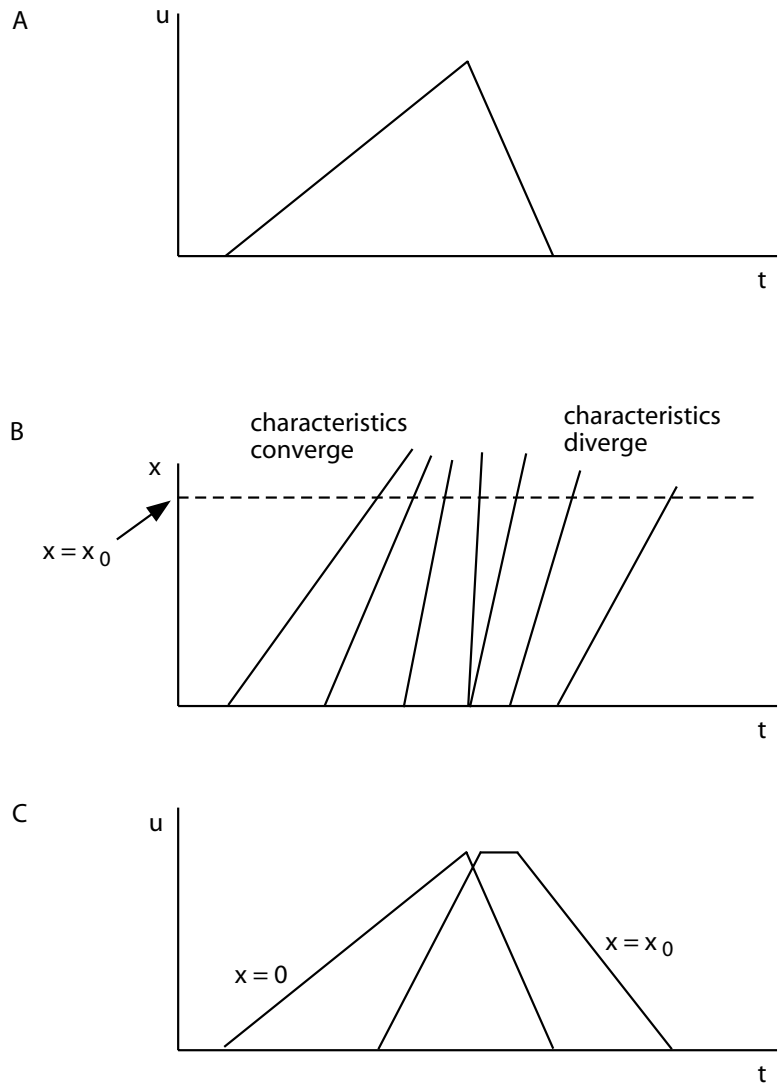
Figure 11.19: A: Sketch of $u(0, t)$. B: Characteristics generated by $u(0, t)$ in the previous figure. C: Plots of $u(x, t)$ for $x = 0$ and $x = x_0$, obtained by taking cross-sections for a fixed x (as indicated by the dotted line in B).

In the limit $t_2 \to t_1$,

$$t_i = \frac{s(t)}{s'(t)} + t, \tag{11.183}$$

$$x_i = \frac{s^2(t)}{s'(t)}, \tag{11.184}$$

which defines parametrically the envelope of intersection points as a function of t, the time of origin of one of the characteristics.

The important point to note is that the first point of shock formation occurs where x_i is smallest. In other words, for data with $s'(t)$ large, the shock develops quickly, and close to $x = 0$. Thus, generally speaking, the steeper the pulse generated by the heart, the sooner and closer a shock forms. This may explain why the pistol-shot occurs in patients with aortic insufficiency but not in other individuals. Using numerical simulations of the model equations, Anliker et al. (1971a,b) have shown that under conditions of aortic insufficiency, a steep pressure gradient can develop within 40 cm of the heart, well within the physiological range.

It is also noteworthy that the slope s depends on diastolic pressure P_0 through $s = \frac{3}{2}u + K(P_0)$. Thus, a decrease in $K(P_0)$, caused either by a decrease of P_0 or a decrease of the function $A(P)$, leads to a decrease of the first location of shock formation x_i.

Notice also that if $s'(t) < 0$, so that $u(0, t)$ is decreasing, no shock can form for positive x. This can also be seen from Fig. 11.19, since, if $u(0, t)$ is a decreasing function of t, the characteristics fan out and do not intersect for positive x.

Exercises

1. Equation (11.7) was derived assuming that the radius of the vessel and pressure drop along the vessel were constant, but then it was used in (11.15) as if the radius was variable. Under what conditions is this a reasonable approximation?

2. Suppose the circumference of a circular vessel at zero pressure is L_0 and is linearly related to the wall tension T via $L = L_0 + \kappa T$. Use Laplace's law to show that the compliance of the vessel is $c = A_0 \frac{\kappa}{\pi M}$ where M is the vessel wall thickness.

3. (a) Choose some parameter values and plot the solution to the filtration equations, (11.27) and (11.28), in the q, P_c phase plane. What is the relationship between the nullcline $q' = 0$ and the solution?

   (b) Modify the model for capillary filtration by allowing the plasma osmotic pressure to vary along the capillary distance. Show that $\pi_c = RT c_c \frac{Q_i}{q}$, where c_c is the concentration of osmolites at $x = 0$, i.e., in the influx.

   (c) For the same parameter values as in the first part of this question, calculate and plot the solution numerically.

   (d) If incoming pressure is unchanged from the first model, what is the effect of osmotic pressure on the filtration rate?

(e) What changes must be made to the incoming pressure and the length of the capillary to maintain the same filtration rate? Hint: Study the phase portrait for this system of equations.

4. Simplify the six-compartment model of the circulation by assuming that there are no pressure drops over the arterial and venous systems (either systemic or pulmonary), and thus, for example, $P_{sa} = P_{s1}$. Assume also that the systolic compliances are negligible (why?). Solve the resultant equations and compare with the behavior of the three-compartment model presented in the text. How do the parameter values change? Are the sensitivities altered? (Calculate the sensitivities using a symbolic manipulation program.)

5. Show that (11.71)–(11.79) can be derived from (11.58)–(11.70) by letting R_s and R_p approach zero and by letting $C_{pa} = C_{pv}$ and $R_{pa} = R_{pv}$.

6. In the three-compartment circulatory model the base volume of the pulmonary circulation V_0^p was calculated using the constraint $V_0^s + V_0^p = 1.2$ liters. Using the fact that the systolic pressure in the pulmonary artery is about 22 mm Hg and the diastolic pressure is about 7 mm Hg, calculate a new value for the volume of the pulmonary circulation. How does this change to the model affect the results?

7. Find the pressures as a function of cardiac output assuming $V_l \neq 0, V_r \neq 0$, where V_l is the basal volume of the left heart, and similarly for V_r (cf. equation (11.39)). Show that

$$Q_\infty = \frac{2C_p V_l/C_{ld} + 2(C_{sv} + C_{sa})V_r/C_{rd} + 2(V_t - V_0^p - V_0^s)}{C_p R_p + C_{sv} R_{sv} + C_{sa}(R_{sa} + 2R_{sv})}. \quad (11.185)$$

8. Explore the behavior of the autoregulation model with $R = R_0 \left(1 + a[O_2]_v\right)/(1 + b[O_2]_v)$.

9. What symptoms in the circulation would you predict from anemia?

   Hint: Anemia refers simply to an insufficient quantity of red blood cells, which results in decreased resistance and oxygen-carrying capacity of the blood.

10. In the fetal circulation, a portion of the systemic flow is diverted to the placenta at the placental arteries for oxygen exchange. Suppose that blood entering the systemic veins from the systemic organs and tissues is completely deoxygenated, as is blood leaving the lungs to enter the left heart. Suppose also that blood leaving the placenta entering the systemic veins is fully oxygenated. What percentage of the total cardiac output should be sent through the placenta in order to maximize the total oxygen exchange?

11. In the model for autoregulation P_a and P_v are given. More realistically, they would be determined, in part at least, by R_s. Construct a more detailed model for autoregulation, including the effects of R_s on the pressures, and show how the arterial and venous pressures, and the cardiac output, depend on M and A.

12. Derive a simplified *windkessel* model by starting with a single vessel with volume $V(t) = V_0 + CP(t)$. Assume that the flow leaves through a resistance R and that there is an inflow (from the heart) of $Q(t)$. Derive the differential equation for P and compare it to (11.161).

13. Frank (1899) described a method whereby the flux of blood out of the heart could be estimated from a knowledge of the pressure pulse, even when the arterial resistance is unknown. Starting with (11.161), assume that during the second part of the arterial pulse, $Q(t) \equiv 0$. Write down equations for the first and second parts of the pulse, eliminate R, and find an expression for Q. Give a graphical interpretation of the expression for Q.

14. In the model for the arterial pulse, set $u(0,t) = at$ for some constant a, and determine the curve in the (t, x) plane along which characteristics form an envelope. Determine the first value of x at which a shock forms.

Chapter 12

The Heart

Of all of the human organs, the heart is in some sense the simplest. All it has to do is pump blood by contracting and expanding about 2.5 billion times during the lifetime of its owner. The heart is also one of the most studied organs of the body, probably because heart failure, either mechanical or electrical, remains the number one cause of death in the Western world.

The heart is a four-chambered pump, consisting of two pumps arranged in series. As is described in Chapter 11, one pump (the right heart) drives blood through the lungs (the pulmonary circulation) and then back to the heart, while the other pump (the left heart) drives the oxygenated blood around the body (the systemic circulation). Coordination of the mechanical activity of the heart is provided by an electrical signal, which is the topic of study in this chapter.

Cardiac tissue is a syncytium of cardiac muscle cells, each of which is contractile in much the same way as is skeletal muscle (Chapter 15), although there are important differences between the two types of striated muscle. Cardiac cells perform two functions in that they are both excitable and contractile. They are excitable, enabling action potentials to propagate, and the action potential causes the cells to contract, thereby enabling the pumping of blood. The electrical activity of the heart is initiated in a collection of cells known as the *sinoatrial node* (SA node) located just below the superior vena cava on the right atrium. The cells in the SA node are autonomous oscillators. The action potential that is generated by the SA node is then propagated through the atria by the atrial cells.

The atria and ventricles are separated by a septum composed of nonexcitable cells, which normally acts as a barrier to conduction of action potentials. There is one pathway for the action potential to continue propagation and that is through another collection of cells, known as the *atrioventricular node* (AV node), located at the base of the atria.

Conduction through the AV node is quite slow, but when the action potential exits the AV node, it propagates through a specialized collection of fibers called the *bundle of HIS*, which is composed of Purkinje fibers. The Purkinje fiber network spreads via tree-like branching into the left and right *bundle branches* throughout the interior of the ventricles, ending on the *endocardial surface* of the ventricles. As action potentials emerge from the Purkinje fiber–muscle junctions, they activate
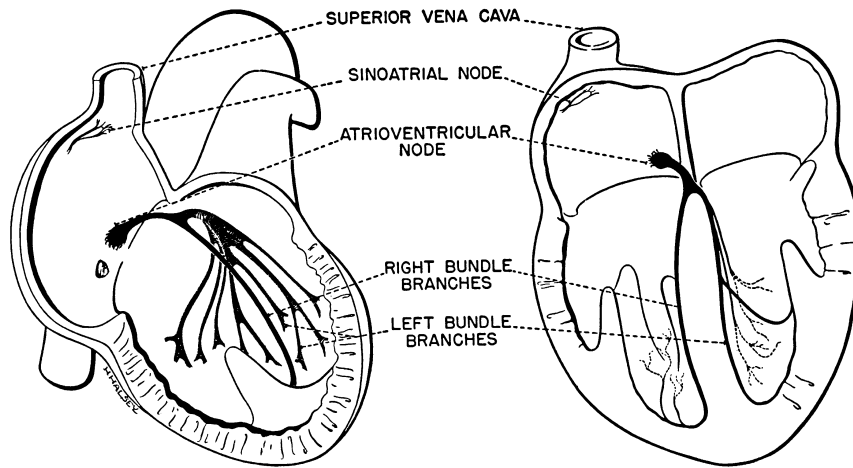
Figure 12.1: Schematic diagram of the cardiac conduction system. (Rushmer, 1976, Fig. 3-9, p. 87).

the ventricular muscle and propagate through the ventricular wall outward to the epicardial surface. A schematic diagram of the cardiac conduction system is shown in Fig. 12.1.

It should be apparent from this introduction that there are a multitude of features of the heart to study. First of all, there is the excitable and contractile function of individual cells, there is the collective oscillatory and pacemaker activity of SA nodal cells, there is one dimensional action potential propagation along Purkinje fibers, there is higher-dimensional propagation in the atrial and ventricular muscle, and, finally, there is the collective behavior of all of these as a unit. In what follows, we describe models of all of these different features of the cardiac system. However, we start with a description of cardiac electrical activity at the organ level that uses the simplest mathematical models and ideas.

12.1   The Electrocardiogram

12.1.1   The Scalar ECG

One of the oldest and most important tools for evaluating the status of the heart and the cardiac conduction system is the *electrocardiogram* (ECG). It has been known since 1877, when the first ECG recording was made, that the action potential of the heart generates an electrical potential field that can be measured on the body surface. When an action potential is spreading through cardiac tissue, there is a wave front surface across which the membrane potential experiences a sharp increase. Along the same wave front, the extracellular potential experiences a sharp decrease. From a distance, this sharp decrease in potential looks like a Heaviside

jump in potential. This rapid change in extracellular potential results from a current source (or sink) because ions are moving into or out of the extracellular space as transmembrane currents.

The body is a *volume conductor*, so when there is a current source somewhere in the body, such as during action potential spread, currents spread throughout the body. Although the corresponding voltage potential is quite weak, no larger than 4 mV, potential differences can be measured between any two points on the body using a sufficiently sensitive voltmeter. Potential differences are observed whenever the current sources are sufficiently strong. There are three such events. When the action potential is spreading across the atria, there is a measurable signal, called the *P wave*. When the action potential is propagating through the wall of the ventricles, there is the largest of all deflections, called the *QRS complex*. Finally, the recovery of ventricular tissue is seen on the ECG as the *T wave*. (The action potential typical of myocardial cells is shown in the upper panel of Fig. 12.2. In these cells the action potential has a rapid upstroke and a relatively rapid recovery separated by a plateau phase of about 300 ms. The physiological basis of the plateau phase, which does not exist in neural cells, is described later in this chapter.) The recovery of the atria is too weak to be detected on the ECG. Similarly, SA nodal firing, AV nodal conduction, and Purkinje network propagation are not detected on the normal body surface ECG because they do not involve sufficient tissue mass or generate enough extracellular current. In Fig. 12.2 is shown a sketch of a typical single electrical ECG event, and a continuous recording is shown in Fig. 12.3a. In hospitals, ECG recordings are made routinely using oscilloscopes, or, if a permanent record is required, on a continuous roll of paper. The paper speed is standardized at 25 mm per second, with a vertical scale of 1 mV per cm, and the paper is marked with a lined grid of 1 mm and darkened lines with 0.5 cm spacing.

The most important use of the single-lead ECG is to detect abnormalities of rhythm. For example, a continuous oscillatory P wave pattern suggests *atrial flutter* (Fig. 12.3b) or *atrial fibrillation* (Fig. 12.3c). A rapid repetition of QRS complexes is *ventricular tachycardia* (Fig. 12.3d), and a highly irregular pattern of ventricular activation is called *ventricular fibrillation* (Fig. 12.3e). The normal appearance of P waves with a few skipped QRS complexes implies a conduction failure in the vicinity of the AV node. Broadening of the QRS complex suggests that propagation is slower than normal, possibly because of conduction failure in the Purkinje network (Fig. 12.4). Spontaneously appearing extra deflections correspond to *extrasystoles*, arising from sources other than the SA or AV nodes.

12.1.2 The Vector ECG

There is much more information contained in the ECG than is available from a single lead. Some of this information can be extracted from the *vector electrocardiogram*. The mathematical basis for the vector ECG comes from an understanding of the nature of a volume conductor. The human body is an inhomogeneous volume conductor, meaning that it is composed of electrically conductive material. If we assume that biological tissue is ohmic, there is a linear relationship between current and potential

$$I = -\sigma \nabla \phi. \tag{12.1}$$
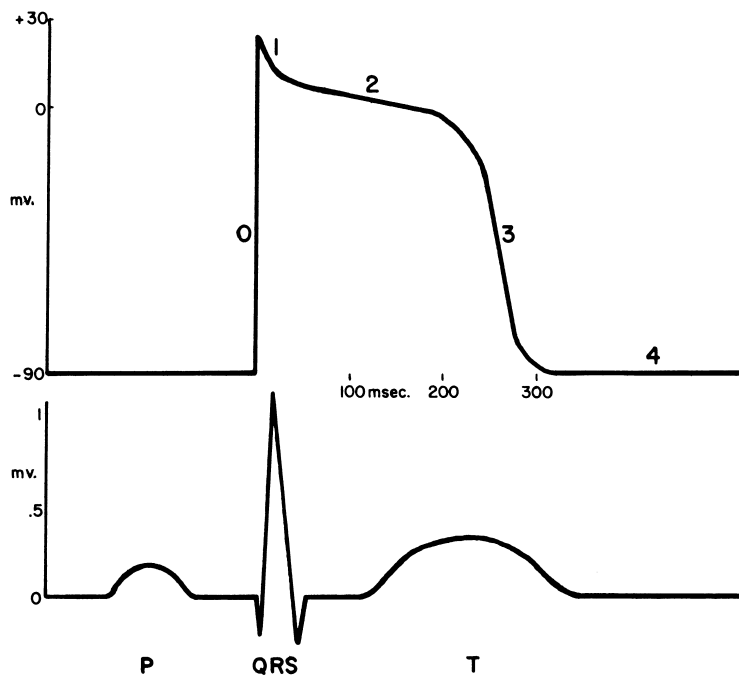
Figure 12.2: Cellular transmembrane potential and electrocardiogram. The upper
tracing represents the transmembrane potential of a single ventricular myocyte and
the lower tracing shows the body surface potential during the same electrical event.
The numbers on the upper tracing designate phases in the action potential cycle:
0: the upstroke, 1: the brief spike, 2: the plateau, 3: the rapid recovery, 4: resting
potential. (Rushmer, 1976, Fig. 8–4, p. 286.)
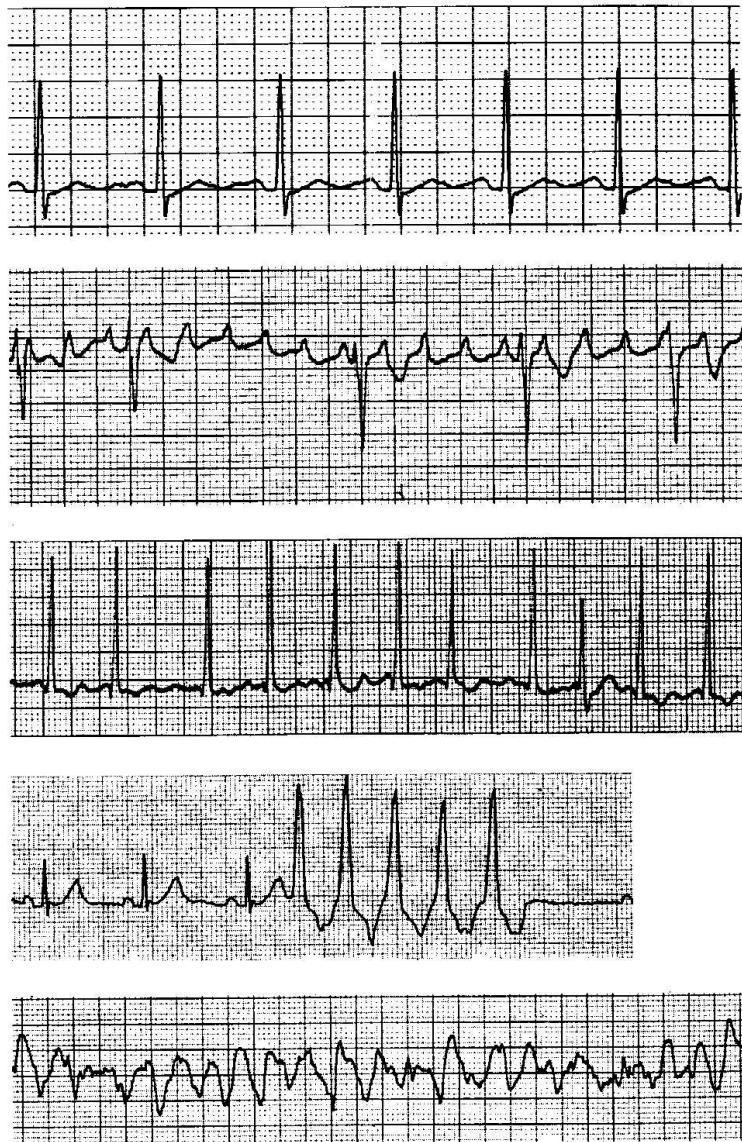
Figure 12.3: A collection of ECG recordings, including (a) Normal ECG recording (lead II) from a sedated 18-year-old male (JPK's son). (b) Atrial flutter showing rapid, periodic P waves, only some of which lead to QRS complexes. (Rushmer, 1976, Fig. 8-29, p. 316.) (c) Atrial fibrillation showing rapid, nonperiodic atrial activity and irregular QRS complexes. (Rushmer, 1976, Fig. 8-28, p. 315.) (d) (Monomorphic) ventricular tachycardia in which ventricular activity is rapid and regular (nearly periodic). (Davis, Holtz, and Davis, 1985, Fig. 17-24, p. 346.) (e) Ventricular fibrillation in which ventricular activity is rapid and irregular. (Rushmer, 1976, Fig. 8-30, p. 317.)
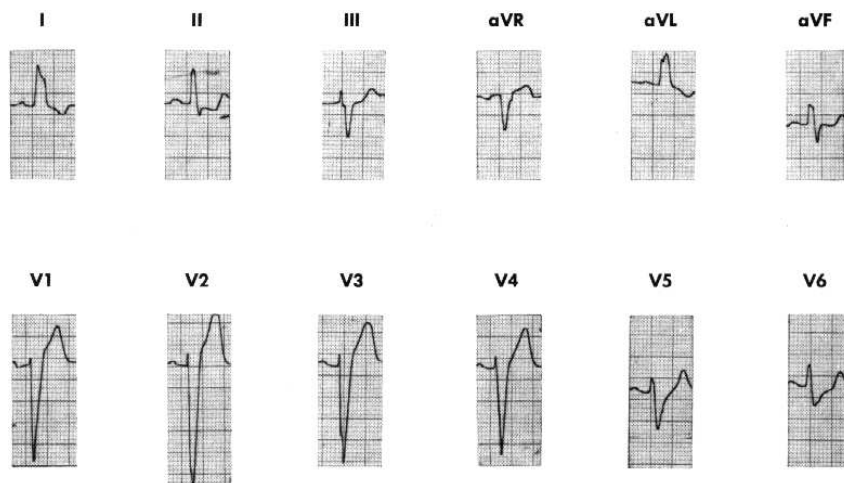
Figure 12.4: ECG from the twelve standard leads, showing left bundle branch block (LBBB), diagnosed as such because of the lengthened QRS complex (0.12 ms), a splitting of the QRS complex in leads V_1 through V_4 into two signals, and a leftward deflection of the heart vector, indicated, for example, by the amplitude shift in lead V_6. (Rushmer, 1976, Fig 8-46, p. 338.)

The conductivity tensor σ is inhomogeneous, because it is different for bone, lung, blood, etc., and it is anisotropic, because of muscle fiber striation, for example. Obviously, current is conserved, so that

$$\nabla \cdot I = -\nabla \cdot (\sigma \nabla \phi) = S, \tag{12.2}$$

where S represents all current sources.

   The most significant current source in the human body is the spreading action potential wave front in the heart. The spreading cardiac action potential is well approximated as a surface of current dipoles. The rapid increase in membrane potential (of about 100 mV) translates into an extracellular decrease of about 40 mV that extends spatially over a distance (the wave front thickness) of about 0.5 mm. If the exact location and strength of this dipole surface and the conductivity tensor for the entire body were known, then we could (in principle) solve the Poisson equation (12.2) to find the body surface potential at all times during the cardiac cycle. This problem is unsolved, and is known as the *forward problem of electrocardiography.*

   What we would really like to know is the operator, say T, called a *transfer function*, that solves (12.2) and yields the *body surface potential* ϕ_B, denoted by

$$\phi_B(t) = T \cdot S(t). \tag{12.3}$$

Even more useful, if the transfer function T were known, one could determine the sources by inverting the forward problem

$$S(t) = T^{-1} \cdot \phi_B(t). \tag{12.4}$$

This problem, known as the *inverse problem of electrocardiography*, is even harder to solve than the forward problem, because it is a numerically unstable mathematical problem.

Since these problems are yet unsolved, we do well to make some simplifications. Our first simplification is to view the action potential upstroke surface as a single current dipole, known as the *heart dipole vector*. We define the heart dipole vector as

$$\mathbf{H}(t) = \int_V \mathbf{J} dV, \tag{12.5}$$

where $\mathbf{J}$ represents the dipole density at each point of the heart, and V is the heart volume. The heart dipole vector is assumed to be located at a fixed point in space, changing only in orientation and strength as a function of time.

Next we assume that the volume conductor is homogeneous and infinite with unit conductance. Then, from standard potential theory (see Exercise 1), at any point x in space,

$$\phi(x,t) = \frac{\mathbf{H}(t) \cdot x}{4\pi|x|^3}, \tag{12.6}$$

where the dipole is assumed to be located at the origin. Thus, at each point on the body surface,

$$\phi_B(x,t) = l_x \cdot \mathbf{H}(t), \tag{12.7}$$

where l_x is a vector, called the *lead vector*, associated with the electrode lead at position x. Of course, for a real person, the lead vector is not exactly $\frac{x}{4\pi|x|^3}$, and some other method must be used to determine l_x. However, (12.7) suggests that we can think of the body surface potential as the dot product of some vector l_x with the heart vector $\mathbf{H}(t)$, and that l_x has more or less the same orientation as a vector from the heart to the point on the body where the recording is made.

Since $\mathbf{H}$ is a three-dimensional vector, if we have three leads with linearly independent lead vectors, then three copies of (12.7) yields a matrix equation that can be inverted to find $\mathbf{H}(t)$ uniquely. In other words, if our goal is to determine $\mathbf{H}(t)$, then knowledge of the full transfer function is not necessary. In fact, additional measurements from other leads should give redundant information.

Of course, the information from additional leads is not redundant, but it is nearly so. Estimates are that a good three-lead system can account for 85% of the information concerning the nature of the dipole sources. Discrepancies occur because the sources are not exactly consolidated into a single dipole, or because the lead vectors are not known with great accuracy, and so on. However, for clinical purposes, the information gleaned from this simple approximation is remarkably useful and accurate.

The next simplification is to standardize the position of the body-surface recordings and to determine the associated lead vectors. Then, with experience, a clinician can recognize features of the heart vector by looking at recordings of the potential at the leads. Or sophisticated (and expensive) equipment can be built that inverts the lead vector matrix and displays the heart vector on a CRT display device.

Cardiologists have settled on 12 standard leads. The first three were established by Einthoven, the "father of electrocardiography" (1860–1927, inventor of the string
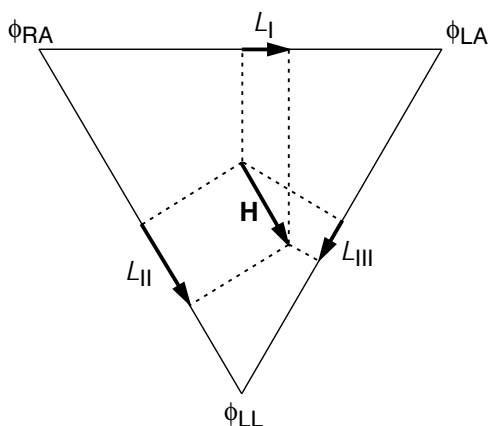
Figure 12.5: The Einthoven triangle showing a typical heart vector $\mathbf{H}$ and associated lead vectors $L_\mathrm{I}, L_\mathrm{II}$ and L_III. Because the body is approximately planar, the lead vectors are assumed to be in the frontal plane.

galvanometer in 1905, 1924 Nobel Prize in physiology) and are still used today. These are the left arm (LA), the right arm (RA), and the left leg (LL). One cannot measure absolute potentials, but only potential differences. There are three ways to measure potential differences with these three leads, namely,

$$V_\mathrm{I} \;=\; \phi_\mathrm{LA} - \phi_\mathrm{RA}, \tag{12.8}$$

$$V_\mathrm{II} \;=\; \phi_\mathrm{LL} - \phi_\mathrm{RA}, \tag{12.9}$$

$$V_\mathrm{III} \;=\; \phi_\mathrm{LL} - \phi_\mathrm{LA}, \tag{12.10}$$

and of course, since the potential drop around any closed loop is zero,

$$V_\mathrm{I} + V_\mathrm{III} = V_\mathrm{II}. \tag{12.11}$$

With these three differences, there are three lead vectors associated with the orientation of the leads, and the potential difference is the amplitude of the projection of the heart vector $\mathbf{H}$ onto the corresponding lead vector. Thus, $L_j = l_j \cdot \mathbf{H}$, and $V_j = |L_j|$ for $j = $ I, II, III.

Einthoven hypothesized that the lead vectors associated with readings $V_\mathrm{I}, V_\mathrm{II}, V_\mathrm{III}$ form an equilateral triangle in the vertical, frontal plane of the body, given by the unit vectors (ignoring an amplitude scale factor) $l_\mathrm{I} = (1,0,0)$, and $l_\mathrm{II} = (\frac{1}{2}, \frac{1}{2}\sqrt{3}, 0)$. The Einthoven triangle is shown in Fig. 12.5. Here the unit coordinate vector (1, 0, 0) is horizontal from right arm to left arm, (0, 1, 0) is vertical pointing downward, and the vector (0, 0, 1) is the third coordinate in a right-handed system, pointing in the posterior direction, from the front to back of the chest. Associated with the frontal plane is a polar coordinate system, centered at the heart, with angle $\theta = 0$ along the x axis, and $\theta = 90°$ vertically downward along the positive y axis.

Of course, the lead vectors of Einthoven are not very accurate. Experiments to measure the lead vectors in a model of the human torso filled with electrolytes produced measured lead vectors $l_{\mathrm{I}} = (0.923, -0.298, 0.241)$, and $l_{\mathrm{II}} = (0.202, 0.972, -0.121)$ (Burger and van Milaan, 1948), which are not in the frontal plane. These lead vectors are known as the *Burger triangle*.

It is fairly easy to glean information about the direction of the heart vector by recognizing the information that is contained in (12.7). The vector ECG is actually a time-varying vector loop (shown in front, top, and side views in Fig. 12.7), and deducing time-dependent information is best done with an oscilloscope. However, one can estimate the mean direction of the vector by estimating the mean amplitude of a wave and then using (12.7) to estimate the mean heart vector. The mean (or time average) of the QRS complex is approximately proportional to the sum of the (positive) maximum and the (negative) minimum.

Since the lead voltage is a dot product of two vectors, a change in mean amplitude of a particular wave suggests either a change in amplitude of the heart vector or a change in direction of the heart vector. For example, the normal QRS and T wave mean dipoles are oriented about $45°$ below horizontal to the left (see Exercise 5). This is close to orthogonal to the lead vector l_{III}, and more or less aligned with lead vector l_{II}. Thus, on a normal ECG, we expect the mean amplitude of a QRS to be small in lead III, large in lead II, and intermediate to these two in lead I. Shifts in these relative amplitudes suggest a shift in the orientation of the heart dipole. For example, an increase in the relative amplitude of the potential difference at lead III and a decrease in amplitude at lead II suggests a shift of the heart vector to the right, away from the left, suggesting a malfunction of the conduction in the left heart.

Although two orthogonal lead vectors suffice to determine the orientation of the heart vector in the vertical plane, for ease of interpretation it is helpful to have more leads. For this reason, there are three additional leads on the frontal plane that are used clinically. To create these leads one connects two of the three Einthoven leads to a central point with 5000 Ω resistors to create a single terminal that is relatively indifferent to changes in potential and then takes the difference between this central potential and the remaining electrode of the Einthoven triangle. These measurements are denoted by aVR, aVL, or aVF, when the third unipolar lead is the right arm, the left arm, or the left foot, respectively. The initial "a" is used to denote an *augmented* unipolar limb lead.

For standard cardiographic interpretation the lead vectors for leads I, aVR$^-$, II, aVF, III, and aVL$^-$ are assumed to divide the frontal plane into equal $30°$ sectors. For example, l_{I} is horizontal, $l_{\mathrm{aVR-}}$ is declined at $30°$, while l_{aVF} is vertical, etc. The superscript for aVR$^-$ denotes the negative direction of the lead vector l_{aVR} (Fig. 12.6).

With these six leads, vector interpretation of the frontal plane orientation of the heart dipole is fast. One looks for the leads with the largest and smallest deflections, and surmises that the lead vector with largest mean amplitude is most parallel to the heart dipole, and the lead vector with the smallest mean deflection is nearly orthogonal to the heart dipole. Thus, in the normal heart situations, readings at leads II and aVR should be the largest in mean amplitude, with positive deflection
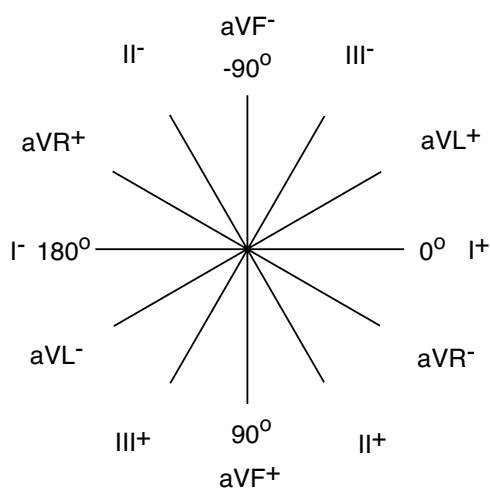
Figure 12.6: The standard six leads for the electrocardiogram (and their negatives).

at lead II, and negative deflection at lead aVR, while the mean deflections from leads III and aVL should be the smallest, being the closest to orthogonal to the normal heart dipole (Fig. 12.7). Deviations from this suggest conduction abnormalities.

Six additional leads have been established to obtain the orientation of the heart dipole vector in a horizontal plane. For these leads, the three leads of Einthoven are connected with three 5000 Ω resistors to form a "zero reference," called the *central terminal of Wilson*. This is compared to a unipolar electrode reading taken from six different locations on the chest. These are denoted by $V_1, V_2, \ldots, V_6$ and are located on the right side of the sternum (V_1), the left side of the sternum (V_2) between the third and fourth ribs, and proceeding around the left chest following just below the fourth rib, ending on the side of the chest directly under the armpit (V_6) (Fig. 12.8).

While a detailed discussion of interpretation of a vector ECG is beyond the scope of this text, there are several features of cardiac conduction that are easy to recognize. Notice from Fig. 12.7 that the normal T wave and the normal QRS complex deflect in the same direction on leads I, II, and aVR (up on I and II, down on aVR). However, the QRS complex corresponds to the upstroke and the T wave to the downstroke of the action potential, so it must be that the activation (upstroke) and recovery (downstroke) wave fronts propagate in opposite directions. Said another way, the most recently activated tissue is the first to recover. The reason for the retrograde propagation of the wave of recovery is not fully understood. Second, an inverted wave (i.e., inverted from what is normal) implies that either the wave is propagating in the retrograde direction, or more typically with novice medical technicians, that the leads have been inadvertently reversed (see Exercise 4).

The amplitude of the QRS complex reflects the amount of muscle mass involved
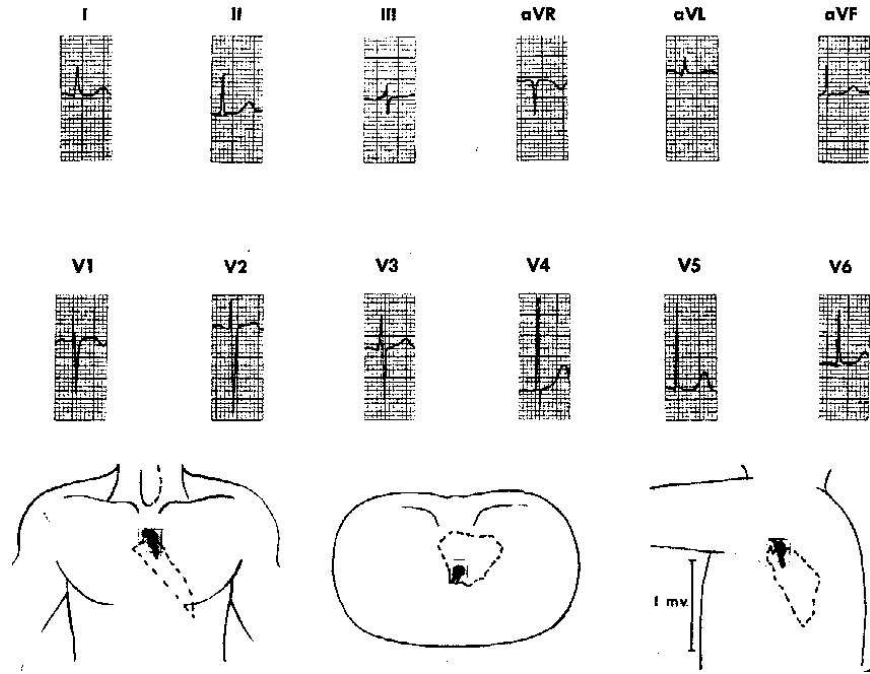
Figure 12.7: Normal ECG and VCG recording from the standard twelve leads in a nine-year old girl. (Rushmer, 1976, Fig. 8-33, p. 320, originally from Guneroth, 1965.)
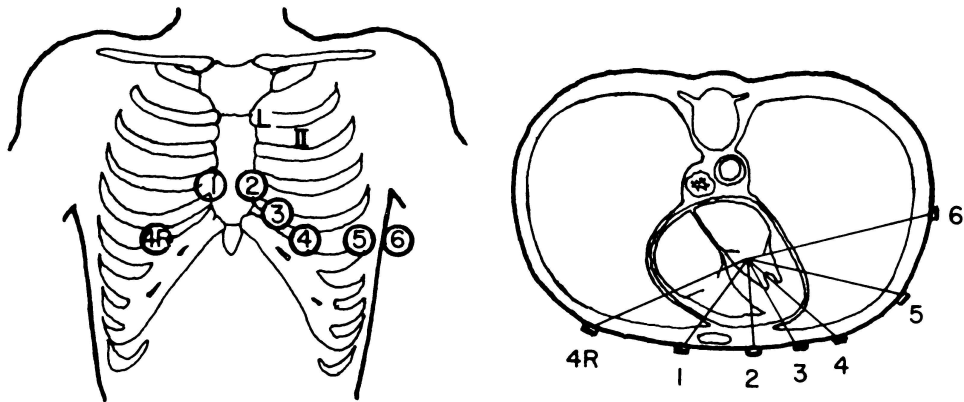
Figure 12.8: Frontal and horizontal cross-sectional views of the thorax in relation to the V-lead positions of Wilson. (Rushmer, 1976, Fig. 8-10, p. 294.)
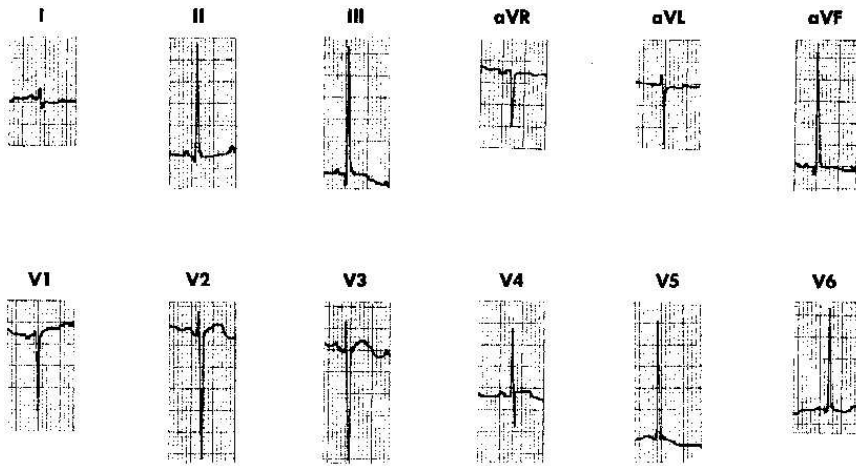
Figure 12.9: Twelve-lead ECG recording for severe left ventricular hypertrophy, particularly noticeable in leads III and aVL. (Rushmer, 1976, Fig. 8-24, p. 331, originally from Guneroth, 1965.)

in propagation. Thus, if the QRS amplitude is extraordinarily large, it suggests *ventricular hypertrophy*. If the ECG vector is leftward from normal, it suggests left ventricular hypertrophy (Fig. 12.9), while a rightward orientation suggests right ventricular hypertropy (Fig. 12.10). On the other hand if an amplitude decrease is accompanied by a rightward change in orientation, a diagnosis of *myocardial infarction* in the left ventricle is suggested, while a leftward orientation with decreased amplitude suggests a myocardial infarction of the right ventricle, as the heart vector is deflected away from the location of the infarction (see Exercises 6 and 7).

12.2   Cardiac Cells

We now turn our attention to developing a more detailed understanding of the physiological basis for the ECG and its abnormalities. We begin with a discussion of individual cardiac cells, and then proceed to describe spatially coupled systems of cells.

The primary cell types of cardiac cells are nodal cells (the sinoatrial (SA) and atrioventricular (AV) nodes), Purkinje fiber cells, and atrial and myocardial cells, each with a slightly different function.

The primary function of SA nodal cells is to provide a pacemaker signal for the rest of the heart. AV nodal cells transmit the electrical signal from atria to ventricles with a delay. Purkinje fiber cells are primarily for fast conduction, to activate the myocardium, and myocardial cells, both atrial and ventricular, are muscle cells and so are contractile as well as excitable.

Because of these different functions, these cell types have different action po-
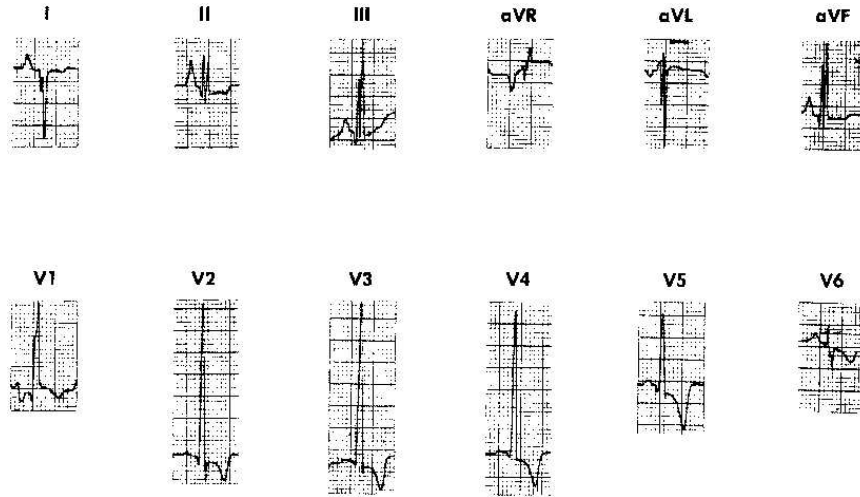
Figure 12.10: Twelve-lead ECG recording for severe right ventricular hypertrophy, particularly noticeable in leads III, V2, and V3. (Rushmer, 1976, Fig. 8-23, p. 330, originally from Guneroth, 1965.)

Ion	Extracellular (mM)	Intracellular (mM)	Nernst Potential (mV)
Na^+	145	15	60
Cl^-	100	5	-80
K^+	4.5	160	-95
Ca^{2+}	1.8	0.0001	130
H^+	0.0001	0.0002	-18

Table 12.1: Ion concentrations in most cardiac cells.

tential shapes, and all are noticeably different than the Hodgkin-Huxley action potential. The action potential for SA nodal cells is the shortest, while both Purkinje fiber cells and myocardial cells have substantially prolonged action potentials (300–400 ms compared to 3 ms for the squid axon), facilitating and controlling muscular contraction. Even within a single cell type, there can be substantial variation. For example, in the ventricles, epicardial, midmyocardial, and endocardial cells have noticeable differences in action potential duration. AV nodal cells vary substantially, to the extent that they are sometimes classified into several different subtypes. Typical action potentials for several cell types are shown in Figs. 12.11, 12.12, and 12.14, and typical ionic concentrations are given in Table 12.1.

12.2.1   Purkinje Fibers

A phenomenological approach

Subsequent to the work of Hodgkin and Huxley, there was substantial work done to apply their modeling approach to many different cell types, including cardiac cells. The first such model describing the action potential of a cardiac cell was proposed by Noble (1962) for Purkinje fiber cells. The primary purpose of the model was to show that the action potential of a Purkinje fiber cell could be captured by a model of Hodgkin–Huxley type. The Noble model is of Hodgkin–Huxley type, expressed in terms of ionic currents and conductances. In this model there are three currents, identified as an inward Na^+ current, an outward K^+ current, and a Cl^- leak current, all of which are assumed to satisfy a linear instantaneous I–V relation,

$$I = g(V - V_{\text{eq}}). \tag{12.12}$$

For the Noble model, all changes in conductances that were measured in Na^+-deficient solutions were assumed to be for currents carried by K^+ ions and are therefore called K^+ currents (thus, the Cl^- current is taken to be zero). While it is now known that not all these currents are carried by K^+ ions, here we follow Noble's original nomenclature.

Following the usual Hodgkin–Huxley formulation, the balance of transmembrane currents is expressed by the conservation law

$$C_m \frac{dV}{dt} + g_{\text{Na}}(V - V_{\text{Na}}) + (g_{\text{K}_1} + g_{\text{K}_2})(V - V_{\text{K}}) + g_{\text{an}}(V - V_{\text{an}}) = I_{\text{app}}, \tag{12.13}$$

where $g_{\text{an}} = 0$ and $V_{\text{an}} = -60$ are the conductance and equilibrium potential, respectively, for the anion Cl^- current (which therefore is not needed). In addition, $V_{\text{Na}} = 40$ and $V_{\text{K}} = -100$.

The Noble model assumes two different types of K^+ channels, an instantaneous, voltage-dependent, channel, and a time-dependent channel. The time-dependent K^+ channel has a similar form to the Hodgkin–Huxley K^+ channel, except that it is about 100 times slower in its response, in order to prolong the action potential plateau. This current is sometimes called the *delayed rectifier current*, because it is delayed and because it is primarily an outward (rectified) current. The conductance for this channel, g_{K_2}, depends on a time-dependent K^+ activation variable n through

$$g_{\text{K}_2} = 1.2n^4. \tag{12.14}$$

The conductance for the instantaneous channel is described empirically by

$$g_{\text{K}_1} = 1.2 \exp\left(-\frac{V + 90}{50}\right) + 0.015 \exp\left(\frac{V + 90}{60}\right). \tag{12.15}$$

The Na^+ conductance for the Noble model is of a form similar to the Hodgkin–Huxley model, being

$$g_{\text{Na}} = 400m^3 h + g_i, \tag{12.16}$$

where $g_i = 0.14$, with the fixed inward bias from g_i enabling a prolonged action potential without necessitating major reworking of the dynamics of h and m.

	C_1	C_2	C_3	C_4	C_5	V_0
α_m	0	—	0.1	-1	-15	-48
β_m	0	—	-0.12	-1	5	-8
α_h	0.17	-20	0	0	—	-90
β_h	1	∞	0	1	-10	-42
α_n	0	—	0.0001	-1	-10	-50
β_n	0.002	-80	0	0	—	-90

Table 12.2: Defining values for rate constants α and β for the Noble model.

The time dependence of the variables m, n, and h is of the form

$$\frac{dw}{dt} = \alpha_w(1 - w) - \beta_w w, \tag{12.17}$$

with $w = m, n$, or h, where α_w and β_w are all of the form

$$\frac{C_1 \exp(\frac{V - V_0}{C_2}) + C_3(V - V_0)}{1 + C_4 \exp(\frac{V - V_0}{C_5})}. \tag{12.18}$$

The constants $C_1, \ldots, C_5$ and V_0 are displayed in Table 12.2.

In the Noble model, $C_m = 12$, which is unrealistically large. This value was used because it gives a correct time scale for the length of the action potential. The choice was justified by arguing that the effective capacitance for a small bundle of cylindrical cells, for which the data were obtained, should be larger than for a single cylindrical cell, the surface area of which is only a small fraction of the total cell membrane area.

Numerical simulations show that the Noble model produces an action potential that has correct features, seen in Fig. 12.11. The sharp upstroke comes from a large, fast, inward Na^+ current, and the plateau is maintained by a continued inward Na^+ current (with conductance g_i), which nearly counterbalances the instantaneous outward K^+ current. Gradually, the slow outward K^+ current is activated, causing repolarization. A small inward Na^+ leak, called the *pacemaker current*, also allows the potential to creep upward, eventually initiating another action potential.

Because of the sharp spike at the beginning of the action potential, it is not possible to reproduce the Purkinje fiber action potential with a two-variable FitzHugh–Nagumo type model. However, by setting $m = m_\infty(V)$, the Noble model can be reduced to a three-variable model that retains the primary qualitative features of the original model.

A physiological approach

While the Noble model succeeds in reproducing the Purkinje fiber action potential with a model of Hodgkin–Huxley type, the underlying physiology is incorrect, primarily because the model was constructed before data on the ionic currents were available. This lack of data was mostly because the voltage-clamp technique was not successfully applied to cardiac membrane until 1964.
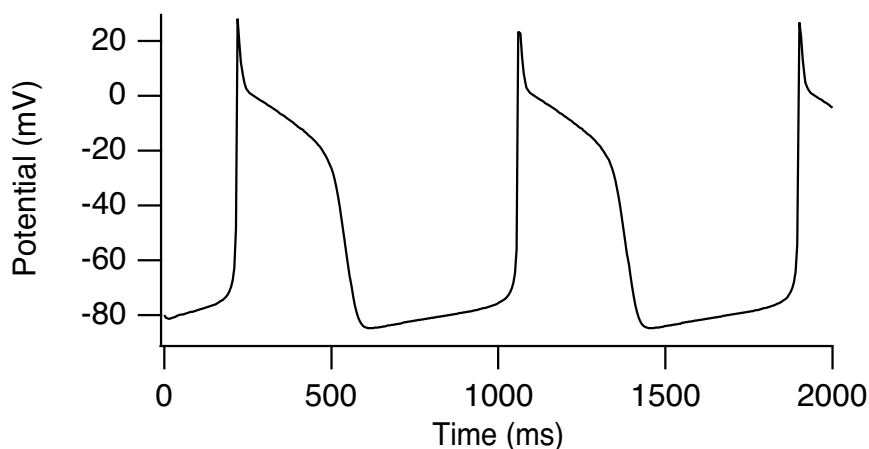
Figure 12.11: Action potential for the Noble model.

The weakness of the physiology in the Noble model is exemplified by the fact that there is no current identified with Ca^{2+} ions, and the inward Na^+ current was given the dual role of generating the upstroke and maintaining the plateau.

In 1975, McAllister, Noble, and Tsien (MNT) presented an improved model for the action potential of Purkinje fibers. This model is based on a "mosaic of experimental results," because unlike the Hodgkin–Huxley model, the required information was not obtained from a single experimental preparation. Furthermore, the model is known to have an inadequate description of the Na^+ current, so that the upstroke velocity is not accurate.

The MNT model is similar to the Noble model in that it is based on a description of transmembrane ionic currents. It is substantially more complicated than most models of its time, having 9 ionic currents and 9 gating variables. There are two inward currents, I_{Na} and I_{si} (called the "slow inward" current). The current I_{Na} resembles the Hodgkin–Huxley Na^+ current and is represented as

$$I_{Na} = \overline{g}_{Na} m^3 h (V - V_{Na}), \tag{12.19}$$

where m and h are activation and inactivation gating variables, respectively, and $V_{Na} = 40$ mV. The inward current I_{si} has slower kinetics than I_{Na} and is carried, at least partly, by Ca^{2+} ions. This current I_{si} has two components and is given by

$$I_{si} = (0.8df + 0.04d')(V - V_{si}), \tag{12.20}$$

where $V_{si} = 70$ mV. The variables d and f are time-dependent activation and inactivation variables, respectively, while d' is only voltage-dependent, being

$$d' = \frac{1}{1 + \exp(-0.15(V + 40))}. \tag{12.21}$$

In the MNT model, there are three time-dependent outward K^+ currents, denoted by I_{K_2}, I_{x_1}, and I_{x_2}. None of these resemble the squid K^+ current from a quantitative point of view, although all are described using an activation variable and no inactivation variable. The current I_{K_2} is called the *pacemaker current* because it is responsible for periodically initiating an action potential, and it is given by

$$I_{K_2} = 2.8\overline{I}_{K_2}s, \tag{12.22}$$

where

$$\overline{I}_{K_2} = \frac{\exp(0.04(V + 110)) - 1}{\exp(0.08(V + 60)) + \exp(0.04(V + 60))}. \tag{12.23}$$

The currents I_{x_1} and I_{x_2} are called *plateau currents* and are governed by

$$I_{x_1} = 1.2x_1\frac{\exp(0.04(V + 95)) - 1}{\exp(0.04(V + 45))}, \tag{12.24}$$

$$I_{x_2} = x_2(25 + 0.385V). \tag{12.25}$$

There is also a time-dependent outward current I_{Cl} carried by Cl^- ions, which is described by

$$I_{Cl} = 2.5qr(V - V_{Cl}), \tag{12.26}$$

where q and r are activation and inactivation variables, and $V_{Cl} = -70$ mV.

Finally, there are several background (leak) currents that are time independent. There is an outward background current of K^+ ions, described by

$$I_{K_1} = \overline{I}_{K_2} + 0.2\frac{V + 30}{1 - \exp(-0.04(V + 30))}, \tag{12.27}$$

where $\overline{I}_{K_2}$ is given by (12.23). There is an inward background Na^+ current described by

$$I_{Na,b} = 0.105(V - 40), \tag{12.28}$$

and, finally, a background Cl^- current, given by

$$I_{Cl,b} = 0.01(V + 70). \tag{12.29}$$

All of the conductances are specified in units of mS/cm^2, and voltage is in mV. The 9 gating variables $m, d, s, x_1, x_2, q, h, f$, and r all satisfy first-order differential equations of the form (12.17), where α_w and β_w are of the form (12.18). The constants $C_1, \ldots, C_5$ and V_0 are listed in Table 12.3.

The action potential for the MNT model is essentially the same as that for the Noble model, so the advantage of the MNT model is that it better isolates and depicts the activity of different channels during an action potential. Of course, because it is more complicated than the Noble model, it is also much harder to understand the model from a qualitative perspective. It therefore illustrates nicely the modeler's dilemma, the constant struggle to balance the demand for quantitative detail and qualitative understanding.

	C_1	C_2	C_3	C_4	C_5	V_0
α_m	0	—	1	-1	-10	-47
β_m	40	-17.86	0	0	—	-72
α_h	0.0085	-5.43	0	0	—	-71
β_h	2.5	∞	0	1	-12.2	-10
α_d	0	—	0.002	-1	-10	-40
β_d	0.02	-11.26	0	0	—	-40
α_f	0.000987	-25	0	0	—	-60
β_f	1	∞	0	1	-11.49	-26
α_q	0	—	0.008	-1	-10	0
β_q	0.08	-11.26	0	0	—	0
α_r	0.00018	-25	0	0	—	-80
β_r	0.02	∞	0	1	-11.49	-26
α_s	0	—	0.001	-1	-5	-52
β_s	5.0×10^{-5}	-14.93	0	0	—	-52
α_{x_1}	0.0005	12.1	0	1	17.5	-50
β_{x_1}	0.0013	-16.67	0	1	-25	-20
α_{x_2}	1.27×10^{-4}	∞	0	1	-5	-19
β_{x_2}	0.0003	-16.67	0	1	-25	-20

Table 12.3: Defining values for α and β for the MNT model.

12.2.2   Sinoatrial Node

Cells within the sinoatrial (SA) node are the primary pacemaker site within the heart. These cells are characterized as having no true resting potential, but instead generate regular, spontaneous action potentials. Unlike most other cells that elicit action potentials (e.g., nerve cells, muscle cells), the depolarizing current is carried primarily by a relatively slow, inward Ca^{2+} current instead of by fast Na^+ currents. There are, in fact, no fast Na^+ currents operating in SA nodal cells. Phase 0 depolarization (recall Fig. 12.2) is primarily due to increased Ca^{2+} conductance. Because the Ca^{2+} channels open more slowly than Na^+ channels (hence, the term "slow inward Ca^{2+} current"), the rate of depolarization (slope of Phase 0) is much slower than found in other cardiac cells (e.g., Purkinje cells, ventricular cells). Repolarization occurs (Phase 3) as K^+ conductance increases and Ca^{2+} conductance decreases. Spontaneous depolarization (Phase 4) is due to a fall in K^+ conductance and to a small increase in Ca^{2+} conductance. A slow inward Na^+ current also contributes to Phase 4, and is thought to be responsible for the pacemaker current. Once this spontaneous depolarization reaches threshold (about -40 mV), a new action potential is triggered.

One of the earliest models of action potential behavior for SA nodal cells is due to Yanagihara et al. (1980). As with all cardiac cell models, the YNI model is of Hodgkin–Huxley type. The YNI model includes four time-dependent currents. These are a fast inward current (incorrectly identified as a Na^+ current) I_{Na}, and the K^+ current I_K, both of which are modeled similar to the Hodgkin–Huxley currents, as well as a slow inward current I_s, and a delayed inward current activated by

	C_1	C_2	C_3	C_4	C_5	V_0
α_m	0	—	1	−1	−10	−37
β_m	40	−17.8	0	0	—	−62
α_h	1.209×10^{-3}	−6.534	0	0	—	−20
β_h	1	∞	0	1	−10	−30
β_p	0	—	-2.25×10^{-4}	−1	13.3	−40
β_d	0	—	-4.21×10^{-3}	−1	2.5	5
α_f	0	—	-3.55×10^{-4}	−1	5.633	−20

Table 12.4: Defining values for α and β for the YNI model.

hyperpolarization I_h. Finally, there is a time-independent leak current I_l.

The conservation of transmembrane current takes the form

$$C_m \frac{dV}{dt} + I_{\text{Na}} + I_{\text{K}} + I_l + I_s + I_h = I_{\text{app}}, \tag{12.30}$$

where

$$I_{\text{Na}} = 0.5m^3 h(V - 30), \tag{12.31}$$

$$I_{\text{K}} = 0.7p \frac{\exp(0.0277(V + 90)) - 1}{\exp(0.0277(V + 40))}, \tag{12.32}$$

$$I_l = 0.8 \left(1 - \exp \left(-\frac{V + 60}{20} \right) \right), \tag{12.33}$$

$$I_s = 12.5(0.95d + 0.05)(0.95f + 0.05) \left(\exp \left(\frac{V - 10}{15} \right) - 1 \right), \tag{12.34}$$

$$I_h = 0.4q(V + 45). \tag{12.35}$$

As usual, the 6 gating variables m, h, p, d, f, and q satisfy first-order differential equations of the form (12.17). Some of the constants α_w and β_w can be written in the form (12.18) with constant values as shown in Table 12.4. Those that do not fit this form are

$$\alpha_p = 9 \times 10^{-3} \frac{1}{1 + \exp(-\frac{V + 3.8}{9.71})} + 6 \times 10^{-4}, \tag{12.36}$$

$$\alpha_q = 3.4 \times 10^{-4} \frac{(V + 100)}{\exp(\frac{V + 100}{4.4}) - 1} + 4.95 \times 10^{-5}, \tag{12.37}$$

$$\beta_q = 5 \times 10^{-4} \frac{(V + 40)}{1 - \exp(-\frac{V + 40}{6})} + 8.45 \times 10^{-5}, \tag{12.38}$$

$$\alpha_d = 1.045 \times 10^{-2} \frac{(V + 35)}{1 - \exp(-\frac{V + 35}{2.5})} + 3.125 \times 10^{-2} \frac{V}{1 - \exp(-\frac{V}{4.8})}, \tag{12.39}$$

$$\beta_f = 9.44 \times 10^{-4} \frac{(V + 60)}{1 + \exp(-\frac{V + 29.5}{4.16})}. \tag{12.40}$$

The behavior of the YNI equations is depicted in Fig. 12.12. The action potential is shaped similarly to the Hodgkin–Huxley action potential but is periodic in time
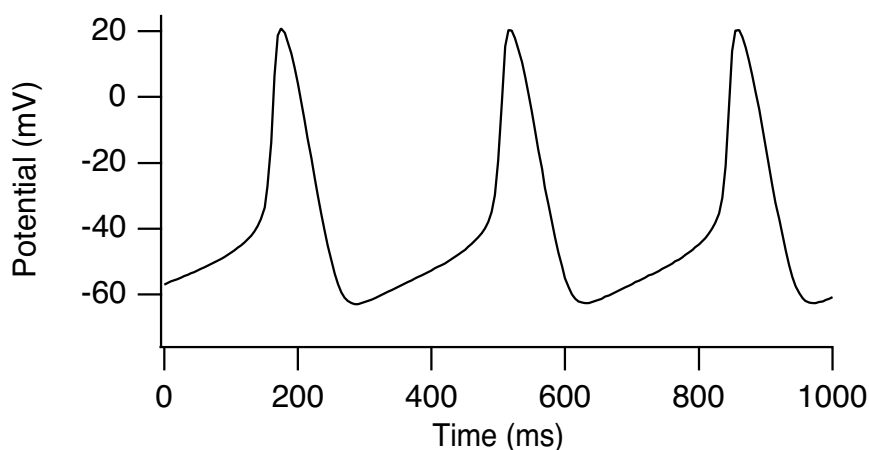
Figure 12.12: Membrane potential for the YNI model of SA nodal behavior.

and slower. The Na$^+$ current is a fast current, and there is little loss in accuracy in replacing $m(t)$ with $m_\infty(V)$. The most significant current in the YNI model is the slow inward current I_s. Not only does this current provide for most of the upstroke, it is also responsible for the oscillation, in that after repolarization by the K$^+$ current, the slow inward current gradually depolarizes the node until threshold is reached and an action potential is initiated.

Because the action potential of the SA node has no initial spike, it is relatively easy to replicate it using a two-variable FitzHugh–Nagumo model. In Fig. 12.13 is shown the periodic activity of a cubic FitzHugh–Nagumo model with action potential spikes similar to those of the YNI model.

12.2.3   Ventricular Cells

The first model for the electrical behavior of ventricular myocardial cells (Beeler and Reuter, 1977) appeared shortly after the MNT equations. Like the models previously described, this model is based on data obtained from voltage-clamp experiments. The Beeler–Reuter equations are less complicated than the MNT equations, as there are only four transmembrane currents that are described, two inward currents, one fast and one slow, and two outward currents, one time independent and one time dependent.

As usual, there is the inward Na$^+$ current

$$I_{\mathrm{Na}} = (4m^3hj + 0.003)(V - 50), \qquad (12.41)$$

which is gated by the variables m, h, and j. Here, Beeler and Reuter found it necessary to include the reactivation variable j, because the reactivation process is much slower than inactivation and cannot be accurately modeled with the single variable h. Thus, the Na$^+$ current is activated by m, inactivated by h, and reactivated by
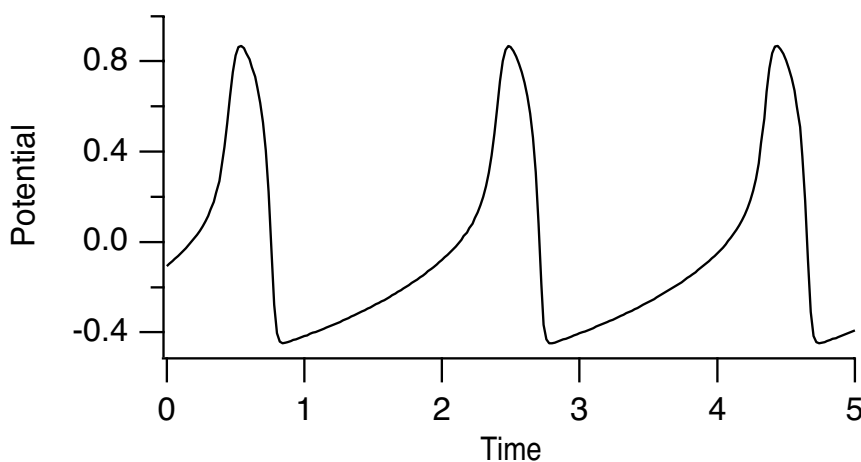
Figure 12.13: The potential $v(t)$ for the FitzHugh–Nagumo model with $f(v,w) = v(1-v)(v-\alpha) - w$, $g(v,w) = w - \gamma v$, with $\epsilon = 0.02$, $\alpha = -0.05$, $\gamma = -0.6$.

j, the slowest of the three variables. The functions h_∞ and j_∞ are identical; it is their time constants that differ. Notice also the inclusion of a Na$^+$ leak current; a similar Na$^+$ leak was included in the Noble and MNT models.

The K$^+$ current has two components, a time-independent current

$$I_K = 1.4 \frac{\exp(0.04(V+85)) - 1}{\exp(0.08(V+53)) + \exp(0.04(V+53))} + 0.07 \frac{v + 23.0}{1.0 - \exp(-0.04(V+23.0))} \tag{12.42}$$

and a time-activated outward current

$$I_x = 0.8x \frac{\exp(0.04(V+77)) - 1}{\exp(0.04(V+35))}. \tag{12.43}$$

The pacemaker K$^+$ current used in the MNT model is not active in myocardial tissue, which is not spontaneously oscillatory.

The primary difference between a ventricular cell and a Purkinje cell is the presence of Ca^{2+}, which is needed to activate the contractile machinery. Later in this chapter, we provide a more modern, detailed account of Ca^{2+} handling in ventricular cells. For the Beeler–Reuter equations, however, the Ca^{2+} influx is modeled by the slow inward current

$$I_s = 0.09fd(V + 82.3 + 13.0287 \ln[\text{Ca}]_i), \tag{12.44}$$

activated by d and inactivated by f. Since the reversal potential for I_s is Ca^{2+} dependent, the internal Ca^{2+} concentration must be tracked, via

$$\frac{dc}{dt} = 0.07(1-c) - I_s, \tag{12.45}$$

	C_1	C_2	C_3	C_4	C_5	V_0
α_m	0	—	1	−1	−10	−47
β_m	40	−17.86	0	0	—	−72
α_h	0.126	−4	0	0	—	−77
β_h	1.7	∞	0	1	−12.2	−22.5
α_j	0.055	−4	0	1	−5	−78
β_j	0.3	∞	0	1	−10	−32
α_d	0.095	−100	0	1	−13.9	5
β_d	0.07	−58.5	0	1	20	−44
α_f	0.012	−125	0	1	6.67	−28
β_f	0.0065	−50	0	1	−5	−30
α_x	0.0005	12	0	1	17.5	−50
β_x	0.0013	−16.67	0	1	−25	−20

Table 12.5: Defining values for α and β for the Beeler–Reuter model.

where $c = 10^7[\text{Ca}]_i$. Since currents are taken as positive outward, the intracellular source of Ca^{2+} is $-I_s$.

The gating variables follow (12.17) where α_w and β_w are of the form (12.18) with constants as displayed in Table 12.5. For these equations, units of V are in mV, conductances are in units of mS/cm^2, and time is measured in milliseconds (ms). A plot of the Beeler–Reuter action potential is shown in Fig. 12.14. The long plateau is maintained by the slow inward (Ca^{2+}) current, and the return to the resting potential is mediated by the slow outward K^+ current I_{x_1}.

It is a fact of modeling that most models have a relatively short lifetime. They are initially proposed because they address a particular problem or feature, but then as weaknesses become apparent, they are supplanted by a new, improved version, whose fate is ultimately similar to the model it replaces. Examples of improved ionic models are those by DiFrancesco and Noble (1985) for Purkinje fiber cells and by Noble and Noble (1984) for the SA node.

Although the Beeler-Reuter model has had a fairly long and robust run of popularity, it too is gradually being replaced by updated models. One of the first modifications to the Beeler–Reuter model was of its Na^+ current. At the time the Beeler–Reuter equations were published, it was not possible to measure accurately the fast Na^+ inward current, because it activates so rapidly. As a result, all the early models (Noble, MNT, BR) used the Hodgkin–Huxley formulation of the Na^+ current. However, it is known that this does not give a sufficiently rapid upstroke for the action potential. This has little effect on the space-clamped action potential, but it has an important effect on the propagation speed for propagated action potentials.

Once appropriate data became available, it was possible to suggest an improved description of the Na^+ current. Thus, a modification of the Na^+ current was proposed by Ebihara and Johnson (1980) (EJ), which has since become the standard for most myocardial simulations.

As of this writing, the most popular detailed model for the electrical activity of ventricular myocytes is the Luo–Rudy (LR-II) model (Luo and Rudy, 1994a,b). An
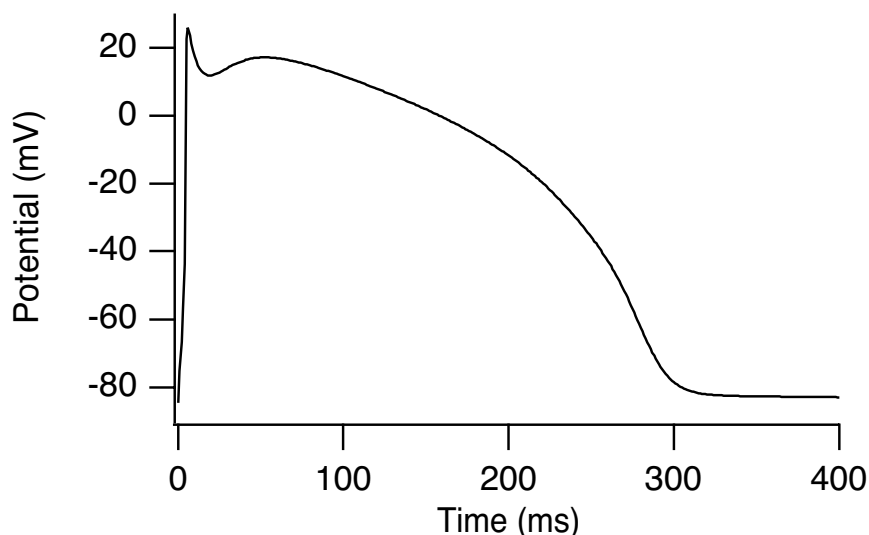
Figure 12.14: Action potential for the Beeler–Reuter equations.

earlier model (LR-I, Luo and Rudy, 1991) was a direct generalization of the Beeler–Reuter model. In Fig. 12.15 is shown a diagram of all the currents included in the LR-II model. Improvements and modifications to the LR-II model are continually being made. For example, many of the currents in the model are being given Markovian formulations, and with these it is feasible to study the effect of mutations to the channel proteins on action potential dynamics (Clancy and Rudy, 1999, 2001).

Other modifications to these models include specialization to human ventricular myocytes, as in ten Tusscher et al. (2004), or to human atrial myocytes as in Courtemanche et al. (1998). The computer codes for many models of cardiac electrical behavior can be found as part of the CellML program, at http://www.cellml.org.

12.2.4 Cardiac Excitation–Contraction Coupling

The final form for a myocardial ionic model has not yet been determined, as there are continual suggestions for improvements and modifications. A major difficulty with the above-mentioned models is with the Ca^{2+} current and the internal Ca^{2+} concentration. In recent years, however, there has been a virtual explosion of information regarding Ca^{2+} handling in cardiac cells, the topic to which we now turn our attention.

Excitation-contraction (EC) coupling is the process whereby an electrical stimulus is converted into muscle contraction. The basic steps of EC coupling in ventricular myocytes are shown in Fig. 12.16. Depolarization of the T-tubule by the action potential causes the opening of L-type Ca^{2+} channels (also called dihydropyridine receptors, or DHPRs) and resultant inward flow of Ca^{2+} current (I_{Ca}). The
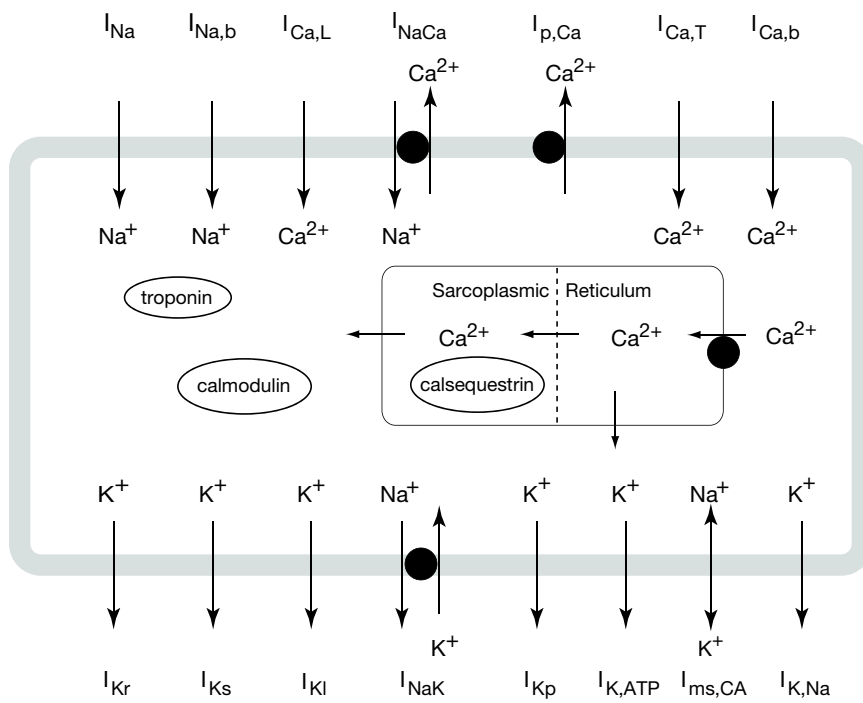
Figure 12.15: Diagram of currents included in the LR-II model.
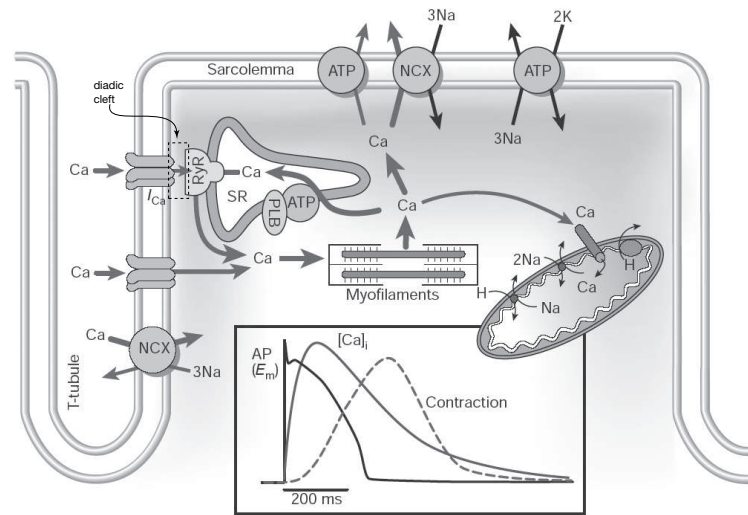
Figure 12.16: The major Ca^{2+} fluxes underlying excitation-contraction coupling in cardiac ventricular myocytes. NCX is the Na^+-Ca^{2+} exchanger; PLB is phospholamban; SR is the sarcoplasmic reticulum. The inset shows the time courses of the action potential (AP), the Ca^{2+} transient and the contraction. Note that the AP happens first, followed by the Ca^{2+} transient and then by contraction. (Bers, 2002, Fig. 1.)**Springer: This figure will need permission.**

Ca^{2+} that enters the cell stimulates the release of additional Ca^{2+} from the SR via ryanodine receptors (RyR) by the process of Ca^{2+}-induced Ca^{2+} release, or CICR (Chapter 7). This Ca^{2+} diffuses through the myoplasm and binds to the myofilaments, causing contraction, before being eventually removed from the myoplasm by ATPases (which pump the Ca^{2+} into the SR or out of the cell) or by the Na^+-Ca^{2+} exchanger (NCX) (which transfers Ca^{2+} to the outside of the cell).

In skeletal muscle the process is slightly different, in that the L-type channels are directly linked to the RyR; a change in conformation of the channel as a result of depolarization causes an immediate change in conformation of the RyR and consequent Ca^{2+} release. Another important difference is that, in skeletal muscle, the T-tubules penetrate into the cell in two places per sarcomere, near the junction of the A and I bands (as shown in Fig. 15.1) while in cardiac cells the T-tubules penetrate only once per sarcomere, at the Z-lines. Here we only discuss EC coupling in cardiac cells.

There is an extensive literature, both experimental and theoretical, on EC coupling. The most comprehensive review of the experimental literature is that of Bers (2001), while the modeling literature is most easily accessed through the reviews of Soeller and Cannell (2004) and Winslow *et al.* (2005). The shorter review by Bers (2002) is a useful introduction to the field.

Although Ca^{2+} fluxes are relatively well understood in many cell types (Chapter 7) the study of Ca^{2+} dynamics in cardiac cells is made much more difficult by the spatial aspects of the problem. Both the L-type Ca^{2+} channels and the RyR release Ca^{2+} into a small volume, the region between the SR and the sarcolemma. This region, called the *diadic cleft*, is only about 15 nm wide with a radius of about 200 nm (although it is not a circular region, it can be reasonably approximated as such), and so has a volume of only about 2×10^{-18} L. Calcium fluxes into such a small volume cause large spatial and temporal gradients that are impossible to measure experimentally and difficult to simulate numerically. Modeling is made even more difficult by the fact that a resting Ca^{2+} concentration of 200 nM (as is typical for the myoplasm of a ventricular myocyte) corresponds to only about 0.2 Ca^{2+} ions in the diadic cleft. In this situation, traditional deterministic and continuous models may not even be applicable. In cardiac cells the diadic clefts are separated longitudinally by approximately 2 μm, the length of a sarcomere.

During a single heart-beat, a total of about 70 μmoles of Ca^{2+} per liter cytosol enters the cell, with about 1% ending up as unbuffered free Ca^{2+} in the myoplasm, giving a myoplasmic concentration of around 600 nM (nmoles per liter cytosol). Since all this influx comes through the diadic cleft there are clearly large and rapid changes in concentration there. Nevertheless, to understand how the Ca^{2+} transient is controlled it is vital to understand what happens inside the diadic cleft, because it is there that Ca^{2+} feeds back on the L-type channels and on the RyR to control the time course of Ca^{2+} influx and release. Thus, we have the situation where a full understanding of the macroscopic properties of the cardiac cell (i.e., the myoplasmic Ca^{2+} concentration and its effect on the sliding filaments), and thus, ultimately, of the whole heart, requires the study of Ca^{2+} dynamics on a much smaller spatial scale. Such problems of how to merge widely differing spatial scales are at the heart of many problems in physiology, particularly those in which one tries to understand the behavior of whole organs by understanding the properties and interactions of single cells.

12.2.5   Common-pool and local-control models

Two of the most important defining characteristics of Ca^{2+} release in cardiac myocytes are high gain and graded release. High gain means that, in response to a small Ca^{2+} influx ($J_{I_{Ca}}$), a much larger amount is released through the RyR (J_{RyR}). In fact, Ca^{2+} influx is about an order of magnitude smaller than Ca^{2+} release from the SR. Graded release means that, if Ca^{2+} influx is smaller, less Ca^{2+} is released from the ER; release is a smooth and continuous function of influx. This is illustrated in Fig. 12.17. Part A of that figure shows the total L-type channel flux and the consequent RyR flux as functions of the membrane potential. The first thing to notice is that $J_{I_{Ca}}$ is a bell-shaped curve of the potential; at low V, the current through each open channel is large, but the probability of opening is small. As V increases, thus increasing the open probability of the channel, the flux increases also. However, as V gets closer to the Ca^{2+} reversal potential of the channel, the current through each open channel begins to fall, leading to a decrease in the total channel flux even though many of the channels are open.

As the L-type channel flux increases smoothly, so does the RyR flux, as can be
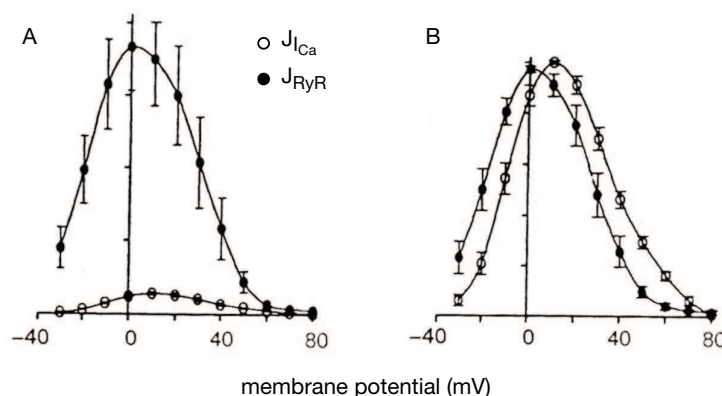
Figure 12.17: Graded release from the rat ventricular myocytes. A: the lower curve is the flux through the L-type channels ($J_{I_{Ca}}$), the upper curve is the consequent flux through the RyR (J_{RyR}). B: the same two curves plotted on a normalized scale. Adapted from Wier *et al.* (1994), Fig. 3. **Springer: This figure will need massaging and permission.**

seen from the upper curve in Fig. 12.17A. Interestingly, comparison of the normalized curves (Fig. 12.17B) shows that the RyR flux decreases at lower voltages than does the L-type channel flux. An explanation for this is that even while the total L-type channel current is an increasing function of voltage, (due to the increased number of open channels), the flux through each individual channel decreases, leading to less effective coupling with the RyR and a resultant decrease in RyR flux.

The two requirements of high gain and graded release appear at first to be contradictory, and so require further explanation. An excitable system (Chapter 5), with a response that is approximately all-or-none, can exhibit high gain without difficulty, but in doing so cannot exhibit a graded release. Conversely, a model that exhibits graded release does not usually exhibit high gain in a stable manner. Many models of Ca^{2+} dynamics in muscle (including those used in Beeler-Reuter and LR-II models) are so-called *common-pool* models, in which it is assumed that Ca^{2+} influx and release both occur into the same well-mixed compartment. This well-mixed compartment could be the myoplasm, as in Fig. 12.18A or a subcompartment such as the diadic cleft, as in Fig. 12.18B. Stern (1992) has shown that such common-pool models, at least in the linear regime, cannot exhibit both high gain and graded release; he introduced, instead, the concept of a *local-control* model, in which the close juxtaposition of the L-type channel and the RyR leads to the formation of a Ca^{2+} synapse in which the opening of an RyR is controlled by the Ca^{2+} coming through a nearby L-type channel. Although each diadic cleft responds in an all-or-none manner (yielding high gain), the stochastic properties of the population of clefts can give a graded response. Since each diadic cleft is separated from its neighbors by approximately 2 μm in a longitudinal direction (the length of the sarcomere) and by about 0.8 μm in a transverse direction (Parker *et al.*, 1996),
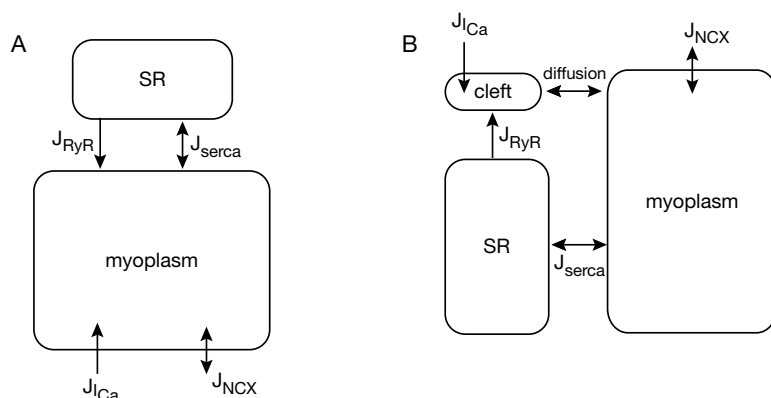
Figure 12.18: Schematic diagrams of two common-pool models. Each model consists of a number of compartments, each of which is assumed to be well-mixed. A: a two-compartment model with only the SR and the myoplasm. The L-type channel current is assumed to flow directly into the myoplasm whence it stimulates the release of further Ca^{2+} release from the SR. B: a three-compartment model in which the diadic cleft (with small volume) is included. J_{NCX} is the Na^+-Ca^{2+} exchange flux. Such common-pool models do not exhibit both a high gain and a graded response.

it can respond in a semi-independent fashion. Statistical recruitment from this large pool of locally-controlled semi-independent release sites can result in graded whole-cell release, even though each individual release site is all-or-none.

Detailed models of local control, incorporating (to greater or lesser extents) the spatial geometry of a single diadic cleft and the stochastic properties of the population of clefts, have been constructed by a number of authors (Stern, 1992; Soeller and Cannell, 1997; Peskoff *et al.*, 1992; Langer and Peskoff, 1996; Stern *et al.*, 1997; Peskoff and Langer, 1998; Smith *et al.*, 1998; Izu *et al.*, 2001; Greenstein and Winslow, 2002; Tameyasu, 2002; Soeller and Cannell, 2003). In general these models are complex and rely on detailed numerical simulations, so we do not discuss them here. We merely comment that there are many unresolved questions in the field, which is an area of intense current research.

As we saw for models of Ca^{2+} dynamics in Chapter 7, models of EC coupling are constructed by combining individual models for each of the various Ca^{2+} fluxes, the most important of which are the L-type Ca^{2+} channel, the RyR, the SERCA pump, and the Na^+-Ca^{2+} exchanger. Here we briefly examine models for each of these fluxes except the SERCA pumps, which are discussed in detail in Chapter 7.

12.2.6   The L-type Ca^{2+} channel

L-type Ca^{2+} channels are activated and inactivated by voltage, and inactivated by high $\left[Ca^{2+}\right]$ (Bers and Perez-Reyes, 1999). During an action potential, voltage-dependent inactivation is much less important than Ca^{2+}-dependent inactivation,
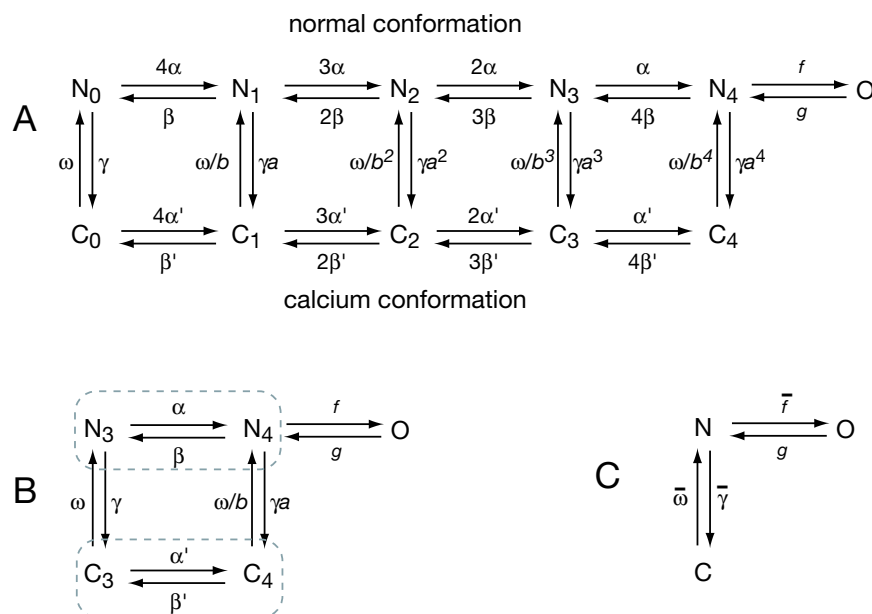
Figure 12.19: A: The full model of the L-type Ca^{2+} channel due to Jafri *et al.* (1998). Activation by voltage occurs because $\alpha = 2e^{0.012(V_m-35)}$ and $\beta = 0.0882e^{-0.05(V_m-35)}$. Inactivation by Ca^{2+} occurs because $\gamma = 0.44 \left[Ca^{2+}\right]_{\text{cleft}}$. To satisfy detailed balance $\alpha' = a\alpha$ and $\beta' = \beta/b$. Other parameter values are $a = 2$, $b = 1.9$, $f = 0.85$ ms^{-1}, $g = 2$ ms^{-1}, and $\omega = 0.02$ ms^{-1}. B: A simplified model obtained by truncating the leftmost three columns. C: The simplest version of the model, obtained by assuming a fast equilibrium between N_3 and N_4, and between C_3 and C_4, as shown by the dashed boxes in part B. It is left as an exercise (Exercise 8) to show that $\bar{\omega} = \omega(\frac{\beta'+\alpha'/b}{\alpha'+\beta'})$, $\bar{\gamma} = \gamma(\frac{\beta+a\alpha}{\alpha+\beta})$ and $\bar{f} = \frac{\alpha f}{\alpha+\beta}$.

and thus we ignore the former.

The most detailed model of the L-type channel is that of Jafri *et al.* (1998), based on an earlier model of Imredy and Yue (1994). It is a model of Monod-Wyman-Changeux type (Chapter 1), a schematic diagram of which is shown in Fig. 12.19. There are two basic conformations of the channel, called, respectively, the normal (top row) and Ca^{2+} (bottom row) conformations. State O is the only open state. Depolarization increases the rate at which the channel moves from left to right along either the normal or Ca^{2+} conformations. However, it is only from the normal conformation that the channel can change to the open state (transition N_4 to O). Binding of Ca^{2+} causes the channel to move from the normal conformation to the Ca^{2+} conformation (i.e., into a conformation from which it cannot access the open state) thus inactivating the receptor.

Good agreement with experimental data can be obtained by simpler versions
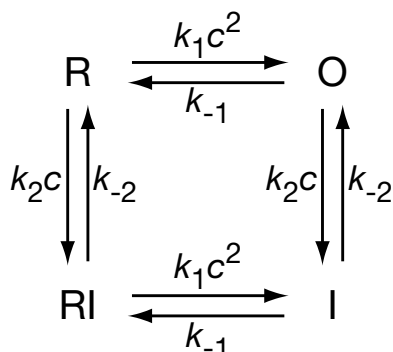
Figure 12.20: Model of the RyR due to Stern *et al.* (1999). R and RI are closed states, O is the open state, and I is the inactivated state. The rate constants depend on c, the $\left[\text{Ca}^{2+}\right]$ in the diadic cleft. Stern *et al.* used the parameters $k_1 = 35\ \mu\text{M}^{-2}\,(\text{ms})^{-1}$, $k_{-1} = 0.06\ (\text{ms})^{-1}$, $k_2 = 0.5\ \mu\text{M}^{-1}\,(\text{ms})^{-1}$, $k_{-2} = 0.005\ (\text{ms})^{-1}$.

of this model (Winslow *et al.*, 2005). First, six channel states are omitted, to get the simpler diagram shown in Fig. 12.19B, and then the two remaining states in the normal conformation are amalgamated by assuming fast equilibrium, as are the remaining two states in the Ca^{2+} conformation (Fig. 12.19C). The details of this model simplification are left as an exercise (Exercise 8).

12.2.7   The ryanodine receptor

One model of the RyR due to Friel has already been described in this book (Chapter 7, Section 7.2.9). For this model it was assumed that activation of the RyR by Ca^{2+} is instantaneous, and that inactivation by Ca^{2+} is unimportant. However, the RyR was assumed to be activated by the cytoplasmic $\left[\text{Ca}^{2+}\right]$ and thus the spatial aspects peculiar to myocytes were not considered. Controversy surrounds the exact properties of RyR in cardiac and skeletal muscle (an excellent review is by Fill and Copello, 2002). There is widespread agreement, first, that (in cardiac myocytes) Ca^{2+} is released through the RyR by a process of Ca^{2+}-induced Ca^{2+} release, giving explosive positive feedback that is crucial for EC coupling, and, second, that the RyR must respond to localized Ca^{2+} concentrations in the diadic cleft and thus have "privileged access" to the Ca^{2+} entering through the L-type channel. However, there must also be some mechanism to terminate flux through the RyR and it is here that agreement ends. A number of mechanisms have been proposed: inactivation by diadic cleft Ca^{2+}, depletion of the SR Ca^{2+}, stochastic fluctuations resulting in RyR closure, and adaptation of the receptor. There is not enough space here to discuss in detail all the hypothetical models and the arguments for and against them. A typical model (Stern *et al.*, 1999) is shown in Fig. 12.20. This model is based on the generic model of an adapting receptor discussed in Chapter 16, Section 16.4. Binding of Ca^{2+} can first open the receptor (state O), but then subsequent, slower, binding of Ca^{2+} can inactivate the receptor (state I).

The application of this class of models to both ryanodine and inositol trisphosphate receptors is discussed by Cheng *et al.* (1995) and Sachs *et al.* (1995).

Shannon *et al.* (2004) modified this basic model by assuming that the SR Ca^{2+} concentration modifies the rate constants, while a number of other groups have developed RyR models of greater or lesser complexity (Scheifer *et al.*, 1995; Keizer and Levine, 1996; Zahradnikova and Zahradnik, 1996; Keizer and Smith, 1998; Fill *et al.*, 2000; Sobie *et al.*, 2002). However, there is still no consensus as to which of this multitude of models best describes RyR behavior *in vivo*.

12.2.8 The Na^+-Ca^{2+} exchanger

All the Ca^{2+} that enters the myocyte through the L-type Ca^{2+} channel must be removed before the next heart beat, otherwise the cell could not attain a steady-state. Most of this removal is effected by the NCX, which, in rabbit, removes more than ten times than does the sarcolemmal Ca^{2+} ATPase. However, it appears that the NCX also allows for Ca^{2+} entry during the beginning of the Ca^{2+} transient. Na^+-Ca^{2+} exchange is reversible, with three Na^+ ions exchanged for one Ca^{2+} ion. Thus, the exchanger is electrogenic; its rate and direction depend on the membrane potential and the intracellular and extracellular Ca^{2+} and Na^+ concentrations. A positive membrane potential increases the exchanger's outward current, thus increasing Ca^{2+} influx, while an increase in intracellular Ca^{2+} leads to Ca^{2+} extrusion, and thus inward exchanger current.

These features can be seen in the model for the exchanger that was discussed in Chapter 2, Section 2.4.3. In that model, the outward Ca^{2+} flux, J, through the exchanger is given by

$$J = \frac{k_1 k_2 k_3 k_4 (c_i n_e^3 - e^{\frac{FV_m}{RT}} c_e n_i^3)}{16 \text{ other terms}}, \tag{12.46}$$

where V_m is the membrane potential, n is Na^+ concentration, c is Ca^{2+} concentration, and subscripts i and e denote, respectively, internal and external concentrations. Notice that the flux of Ca^{2+} is outward whenever

$$\frac{c_i}{c_e} > e^{\frac{FV_m}{RT}} \frac{n_i^3}{n_e^3}. \tag{12.47}$$

Thus, as the membrane depolarizes, the outward flux decreases and reverses for high enough V_m, resulting in Ca^{2+} influx. This is what happens during the beginning of the action potential following depolarization. However, Ca^{2+} influx through the L-type channel and release from the RyR causes a rise in c_i which counterbalances the effects of depolarization, resulting in Ca^{2+} efflux through the exchanger.

12.3 Cellular Coupling

A single cell model, no matter how detailed or precise, can never capture the range of dynamic behaviors of cardiac tissue. This is because many of the behaviors are inherently spatio-temporal, that is, they can occur only in spatially distributed systems of cells, never in single cells.
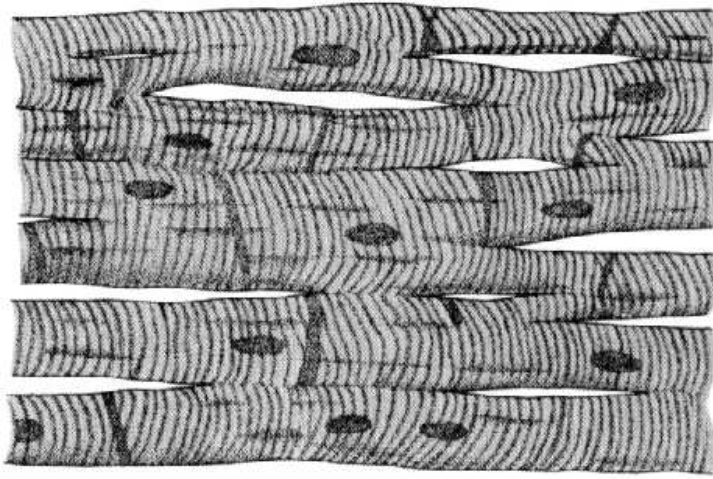
Figure 12.21: Cardiac cell structure. (Guyton and Hall, 1996, Fig. 9-2, p. 108.)

As we will see, spatial coupling of cells has two opposite, but important features. First, coupling between cells tends to synchronize or homogenize their behavior, and second, coupling allows one excited cell to excite its neighbors, so that action potentials can propagate.

Myocardial cells are cable-like, roughly cylindrical, typically 100 μm long and 15 μm in diameter. They are packed together in a three-dimensional irregular brick-like packing, surrounded by extracellular medium (Fig. 12.21). Each cell has specialized contacts with its neighboring cells, mainly in end-to-end fashion, facilitated by a step-like surface that locks into neighboring cells. The opposing cell membranes form the *intercalated disk* structure. While the end-to-end cell membranes are typically separated by about 250 angstroms, there are places, called *junctions*, where the pre- and postjunctional membranes are fused together. The mechanical adhesion of cells is provided by adhering junctions in the intercalated disk, known as *desmosomes* or *tight junctions*. The electrical coupling of cells is provided by gap junctions (Chapter 8).

The intercellular channels provided by the gap junctions are around 20 angstroms in diameter and are characterized as "low-resistance" because the effective resistance is considerably less than what would result from two cell membranes butted together. However, compared to the intracellular cytoplasm, the gap junctions are of high resistance, simply because the cross-sectional area for electrical conduction through gap junctions is greatly reduced (about two percent of the total cross-sectional area).

12.3.1 One Dimensional Fibers

To model a cardiac fiber, we consider a simple one dimensional collection of cylindrical cells (with perimeter p) coupled in end-to-end fashion via gap junctions. From

Chapter 8, we know that in each cell we have the cable equation,

$$p\left(C_m\frac{\partial V}{\partial t} + I_{\text{ion}}\right) = \frac{\partial}{\partial x}\left(\frac{1}{r_c}\frac{\partial V_i}{\partial x}\right) = -\frac{\partial}{\partial x}\left(\frac{1}{r_e}\frac{\partial V_e}{\partial x}\right), \qquad (12.48)$$

with $r_c = \frac{R_c}{A_i}$ and $r_e = \frac{R_e}{A_e}$, where R_c and R_e are the resistivities of intracellular and extracellular space, respectively, A_i and A_e are the average cellular intracellular and extracellular cross-sectional areas, and p is the perimeter of the cell. At the ends of cells (each of length L), there is a jump in intracellular potential, but the intracellular current $-\frac{1}{r_c}\frac{\partial V_i}{\partial x}$ must be continuous. Assuming that gap junctions behave like ohmic resistors, the drop in the potential across the junction is proportional to the current through the junction,

$$\frac{[V_i]}{r_g} = \frac{1}{r_c}\frac{\partial V_i}{\partial x}, \qquad (12.49)$$

where $[V_i]$ is the jump in intracellular potential across the gap junctions and r_g is the effective gap junctional resistance. Here we are also making the assumption that there are no transmembrane currents across the ends of the cell into the small extracellular gap that separates the cells. (Recent evidence suggests that Na^+ channels may have a higher density at the ends of cells than along the cell wall (Kucera et al., 2002) so this assumption may not be valid.) The extracellular potential and current are continuous, unaffected by the gap junctions.

The time constant for this fiber is the same as (4.16). The space constant, however, is affected by the gap-junctional resistance. To find the space constant, we take $I_{\text{ion}} = V/R_m = (V_i - V_e)/R_m$ (linearized around the resting potential) and look for a geometrically decaying solution, with $V_i(x + L) = \mu V_i(x), V_e(x + L) = \mu V_e(x)$ for some constant $\mu < 1$. The constant μ relates to the space constant λ_g through $\mu = e^{-L/\lambda_g}$.

The steady-state solution of this problem can be found analytically. We suppose that for the nth cell, the solution is proportional to

$$\begin{pmatrix} V_i \\ V_e \end{pmatrix}_n = \mu^n \Phi(\mu, x) = \mu^n \begin{pmatrix} \phi_i \\ \phi_e \end{pmatrix}. \qquad (12.50)$$

We also assume that the total current is zero, so that

$$\frac{1}{r_c}\frac{\partial \phi_i}{\partial x} + \frac{1}{r_e}\frac{\partial \phi_e}{\partial x} = 0, \qquad (12.51)$$

and thus

$$\frac{\partial}{\partial x}\left(\frac{1}{r_c + r_e}\frac{\partial \phi}{\partial x}\right) - \frac{p\phi}{R_m} = 0, \qquad \phi = \phi_i - \phi_e. \qquad (12.52)$$

It follows that

$$\phi = \alpha_1 \exp(\lambda x) + \alpha_2 \exp(-\lambda x), \qquad (12.53)$$

where $\lambda^2 = \frac{p}{R_m}(r_c + r_e)$, and

$$\phi_i = \frac{r_c}{r_c + r_e}\phi(x) + \beta, \qquad \phi_e = -\frac{r_e}{r_c + r_e}\phi(x) + \beta. \qquad (12.54)$$

Now there are four boundary conditions that need to be applied to determine the four unknown constants α_1, α_2, β and μ. These boundary conditions are

$$\phi'_e(L) = \mu\phi'_e(0), \qquad \phi'_i(L) = \mu\phi'_i(0), \tag{12.55}$$

requiring the current to be continuous, and

$$\phi_e(L) = \mu\phi_e(0), \qquad \mu\phi_i(0) - \phi_i(L) = \frac{r_g}{r_c}\phi'_i(L), \tag{12.56}$$

requiring continuity of the extracellular potential, and the jump condition (12.49) for the intracellular potential, respectively. It is a somewhat tedious calculation (but Maple makes it easy) to determine that (up to an arbitrary scale factor)

$$\alpha_1 = \mu - \frac{1}{E}, \qquad \alpha_2 = \mu - E, \qquad \beta = 2r_e\frac{(\mu - E)(\mu - \frac{1}{E})}{\mu - 1}, \qquad E = e^{\lambda L}, \tag{12.57}$$

and, most importantly, $\mu < 1$ is a root of the (quadratic) characteristic equation

$$\frac{r_g\lambda}{r_c + r_e} = \frac{R_g}{\lambda L} = 2\frac{(\mu - \frac{1}{E})(\mu - E)}{\mu(E - \frac{1}{E})}, \tag{12.58}$$

where $R_g = \frac{Lpr_g}{R_m}$ is the effective nondimensional gap-junctional resistance.

The behavior of the extracellular, intracellular and transmembrane potentials for this solution is depicted in Fig. 12.22. As can be seen from this plot, the extracellular potential decays smoothly, but the intracellular potential decays with discrete jumps across the gap junctions. Perhaps the most important quantity here is the decay of V intracellularly relative to the decay of V due to gap junctions. If gap junctional resistance is small then the decay of V is essentially exponential throughout the cell, whereas if gap junctional resistance is relatively large, then the cell is nearly isopotential and most of the decay occurs across the gap junctions.

It is not possible to measure the intracellular potential with the detail shown in Fig. 12.22, because cells are usually too small to invade with multiple intracellular electrodes without irreversibly damaging the cell membrane. If the gap-junctional resistance is small compared with the cytoplasmic resistance, then (12.58) has a simplified solution. In particular, if L/λ_g is small (i.e., the length constant is much larger than the length of a single cell), then it must also be that λL is small, so that $E \approx 1 + \lambda L$ and $\mu \approx 1 - \frac{L}{\lambda_g}$. Substituting these into (12.58) gives

$$R_g \approx \left(\left(\frac{L}{\lambda_g}\right)^2 - (\lambda L)^2\right)(1 + O(\lambda L)), \tag{12.59}$$

which implies that

$$\frac{L^2}{\lambda_g^2} \approx R_g + (\lambda L)^2 = R_g + \frac{L^2 p}{R_m}(r_c + r_e). \tag{12.60}$$

The formula (12.60) is used routinely in bioengineering and in linear circuit theory; it implies that resistance along the cable is additive. This is exactly the
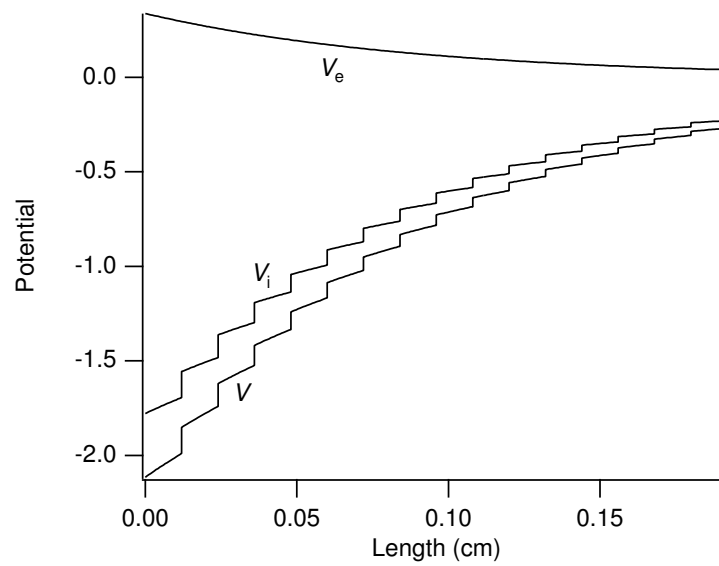
Figure 12.22: Plot of intracellular, extracellular and transmembrane potentials as a function of space, with a constant subthreshold potential maintained at a single point. For this plot cells had $L = 0.012$ cm, $A_i = 4.0 \times 10^{-6}$ cm^2, and a space constant $\lambda_g = 0.09$ cm. $R_m = 7000\,\Omega$cm^2, $R_c = 150\,\Omega$cm, $q_e = 0.5q_i$, $q_i = 5.47 \times 10^{-3}$, where $q_j = \frac{L^2 p}{R_m} r_j$, $j = i, e$. The vertical scale on this plot is arbitrary.

same answer that one finds for the space constant of a uniform continuous cable if the gap-junctional resistance were uniformly distributed throughout the cytoplasm (see below). For most normal cells, the approximation (12.60) is valid. It is only when the gap-junctional resistance is excessively large, such as if there is *ischemia* or if the cells are treated with certain alcohols that block gap junctions, that this formula is substantially wrong.

However, it is also commonly asserted that gap junctions are low resistance and the bulk of the resistance is cytoplasmic in origin. To test this assertion, the effective gap-junctional resistance R_g can be calculated from (12.60). For example, using frog myocardial cells (which are longer than mammalian cells, $L = 131\,\mu$m, radius $= 7.5\,\mu$m), Chapman and Fry (1978) measured a space constant $\lambda_g = 0.328$ cm yielding $(\frac{L}{\lambda_g})^2 = 0.159$. From this they inferred (using $R_m = 1690\,\Omega\text{cm}^2$ and $q_e = 0$) that the effective cytoplasmic resistivity was $R_c = 588\,\Omega\text{cm}$. They were also able to measure the cytoplasmic resistivity directly, and they found $R_c = 282\,\Omega\text{cm}$ so that $q_i = 0.076$. Thus, using (12.60), only 48% of the total resistivity of the cell was attributable to cytoplasmic resistance. The remaining 52% must be from gap-junctional resistance. With these numbers it is difficult to assert that gap junctions are low resistance.

The above space constant calculation represents a situation that is difficult to replicate experimentally. To do so (to enforce the no net current assumption) would require use of a bipolar electrode, with one of the poles placed intracellularly and the other placed extracellularly at a single point along the fiber, thereby holding the transmembrane potential fixed. A more realistic experiment would be to pass a current through the fiber with two extracellular electrodes at different points along the fiber. The associated mathematical problem is to solve the steady version of the cable equation (12.48) with the jump conditions (12.49) subject to the boundary conditions

$$-\frac{1}{r_e}\frac{dV_e}{dx} = I, \qquad \frac{1}{r_c}\frac{dV_i}{dx} = 0, \tag{12.61}$$

at the ends of the fiber at $x = 0, l$. These boundary conditions reflect the fact that current is injected into the extracellular space, but there is no direct current flow into the intracellular space.

The solution of this problem can also be found analytically, although it is more complicated than the previous length constant calculation. Here we state the answer, and relegate the details of the calculation to the Appendix. On the interior of cells the solution is

$$\begin{pmatrix} V_i \\ V_e \end{pmatrix}_j = \frac{1}{r_e + r_c} \begin{pmatrix} r_c \\ -r_e \end{pmatrix} V_j + \begin{pmatrix} 1 \\ 1 \end{pmatrix} (-\beta I x + \gamma_j), \tag{12.62}$$

and $V_j = (A_j + \frac{r_e}{\lambda}I)\sinh \lambda x + B_j \cosh \lambda x$, for $j = 0, 1, \cdots, N-1$, where

$$A_j = \frac{-S}{1-\mu}(\mu c_1 - c_2)f_j, \tag{12.63}$$

$$B_j = \frac{\mu c_1 - c_2}{1-\mu}\left(Cf_j + \frac{1-\mu^N}{1-\mu^{2N}}(\mu^{j+1} + \mu^{N-j-1})\right) - \frac{c_1 - \mu c_2}{1-\mu}, \tag{12.64}$$

$$f_j \;=\; \frac{1 - \mu^{N-j} - \mu^j + \mu^{N+j} + \mu^{2N-j} - \mu^{2N}}{1 - \mu^{2N}}, \qquad (12.65)$$

$$\gamma_{j+1} \;=\; \gamma_n - L\beta I + \frac{\beta}{r_c} K_g\left(\frac{r_e}{\lambda} I(C - 1) + A_j C + B_j S\right), \qquad (12.66)$$

$$C = \cosh \lambda L, \qquad S = \sinh \lambda L, \qquad c_i = \frac{S(1 - \eta_i) + \eta_i K_g(1 - C)}{S(2 + K_g \eta_i + K_g C)}, \qquad (12.67)$$

with $\eta_1 = \frac{1}{\mu}$, $\eta_2 = \mu$, where $\mu < 1$ is the root of the characteristic equation (12.58), and $K_g = \frac{r_g \lambda}{r_c + r_e} = \frac{R_g}{\lambda L}$, $\beta = \frac{r_c r_e}{r_c + r_e}$.

In Fig. 12.23 is shown the transmembrane potential in response to a constant, but small (subthreshold), current stimulus. The current is from right to left, and at the right end the tissue is hyperpolarized, while on the left the tissue is depolarized. If this current stimulus were superthreshold, one would expect an action potential to arise on the left, and (perhaps) propagate to the right.

One can understand this profile as follows. A current that is injected into the extracellular space seeks the path of least resistance. Since there are two possible paths, extracellular space and intracellular space, total current is divided between these two spaces in such a way as to minimize the total resistance. However, to achieve this current-divided profile, current must flow into intracellular space at one end and it must exit the intracellular space at the opposite end, creating the electrode effects of hyperpolarization and depolarization, respectively. In the interior of the fiber, several space constants away from the electrodes, the current in each of the subspaces is essentially constant. However, gap junctional resistance (or any other inhomogeneity of resistance) creates "speed bumps" that the current, while seeking the path of least resistance, circumvents by leaving or entering intracellular space, thereby creating transmembrane currents. At steady state, the membrane potential is depolarized if the transmembrane current is outward and hyperpolarized if it is inward.

The profile of transmembrane current shown in the bottom panel of Fig. 12.23 is called a sawtooth potential (Krassowska et al., 1987) and has been observed in single cells (Knisely et al., 1993) as well as in whole tissue (Zhou et al., 1998), although its physiological significance is debated. In other contexts, regions of localized depolarization and hyperpolarization that are spatially removed from electrodes are referred to as virtual electrodes. These are discussed further in later sections of this chapter. Regardless of the outcome of this debate, it is clear that cardiac tissue is not resistively homogeneous, and the implications of this can be profound.

Because it is impossible to make much headway studying large tissues using a spatially detailed model, some further approximations are helpful. There are two that have proven useful. The first is appropriate when the space constant is large compared to the length of a single cell.

To derive this approximation it is useful to notice that the cable equation with jump condition (12.49) is equivalent to the equation

$$p\left(C_m \frac{\partial V}{\partial t} + I_{\text{ion}}\right) = \frac{\partial}{\partial x}\left(\frac{1}{r_c + \sum \delta(x - nL)r_g} \frac{\partial V_i}{\partial x}\right) = -\frac{\partial}{\partial x}\left(\frac{1}{r_e} \frac{\partial V_e}{\partial x}\right) \quad (12.68)$$
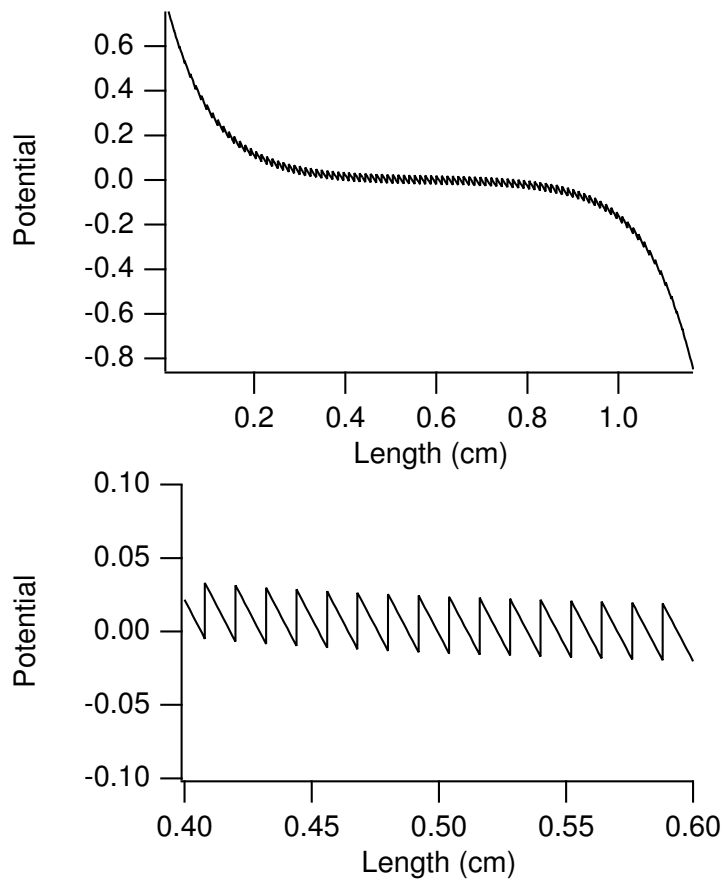
Figure 12.23: Plot of transmembrane potential as a function of space, with a constant applied current. For this plot cells had $L = 0.012$ cm, $A_i = 4.0 \times 10^{-6}$ cm^2, and a space constant $\lambda_g = 0.09$ cm. $R_m = 7000\,\Omega$cm^2, $R_c = 150\,\Omega$cm, $q_e = 0.5q_i$, $q_i = 5.47 \times 10^{-3}$, where $q_j = \frac{L^2 p}{R_m} r_j$, $j = i, e$. The vertical scale on this plot is arbitrary.

with a spatially inhomogeneous resistance. The assumption that the space constant is large compared to the length of a cell implies that the resistance $r_c + \sum \delta(x - nL)r_g$ is a rapidly varying function of space. Thus, one can use homogenization theory (Exercise 19; also see Section 7.8.2, or Keener, 1998) to replace the spatially varying resistance with a spatially averaged, effective resistance. The resulting averaged equation is

$$p\left(C_m \frac{\partial V}{\partial t} + I_{\text{ion}}\right) = \frac{\partial}{\partial x}\left(\frac{1}{r_c + \frac{r_g}{L}} \frac{\partial V_i}{\partial x}\right) = -\frac{\partial}{\partial x}\left(\frac{1}{r_e} \frac{\partial V_e}{\partial x}\right). \tag{12.69}$$

Furthermore, because this is one dimensional in space, we can use that the total current is constant

$$\left(\frac{1}{r_c + \frac{r_g}{L}} \frac{\partial V_i}{\partial x}\right) + \left(\frac{1}{r_e} \frac{\partial V_e}{\partial x}\right) = I_{\text{tot}}, \tag{12.70}$$

to write a single equation involving only the transmembrane potential

$$p\left(C_m \frac{\partial V}{\partial t} + I_{\text{ion}}\right) = \frac{\partial}{\partial x}\left(\frac{1}{r_e + r_c + \frac{r_g}{L}} \frac{\partial V}{\partial x}\right). \tag{12.71}$$

This is the effective cable equation for cardiac fibers.

A different approximation applies when the cytoplasmic resistance r_c and extracellular resistance r_e are small compared to the gap junctional resistance. For simplicity, we set $r_e = 0$, in which case the extracellular potential is constant (so take it to be zero), and $V_i = V$. Set $x = Ly$ and rewrite the cable equation as

$$\frac{\partial^2 V}{\partial y^2} = \epsilon F(V, t), \tag{12.72}$$

subject to the jump conditions

$$\frac{\epsilon}{R_g}[V_i] = \frac{\partial V_i}{\partial y}, \tag{12.73}$$

at the integers $i = n$, where $\epsilon = \frac{p r_c L^2}{R_m}$, $R_g = \frac{r_g p L}{R_m}$ and $F(V, t) = R_m C_m \frac{\partial V}{\partial t} + R_m I_{\text{ion}}$ has units of voltage.

Now we seek a power series solution of (12.72) in ϵ and find that on the interval $n < y < n + 1$,

$$V(y) = V_n + a_n z_n + \frac{1}{2}\epsilon F(V_n) z_n^2, \tag{12.74}$$

where $z_n = y - n$, and V_n and a_n are constants that have yet to be determined. Of course, this implies that

$$\frac{\partial V}{\partial y} = a_n + \epsilon F(V_n) z_n. \tag{12.75}$$

Since $\frac{\partial V}{\partial y}$ must be continuous at $y = n$, it must be that

$$a_{n-1} + \epsilon F(V_{n-1}) = a_n. \tag{12.76}$$

Now substitute this solution into the jump conditions (12.73) to find that

$$\frac{1}{R_g}(V_{n+1} - 2V_n + V_{n-1}) = F(V_n, t) + \frac{\epsilon}{2R_g}(F(V_{n-1}, t) + F(V_n, t)), \qquad (12.77)$$

which, to leading order in ϵ, is the discrete cable equation,

$$\frac{1}{r_g}(V_{n+1} - 2V_n + V_{n-1}) = Lp\left(C_m \frac{\partial V_n}{\partial t} + I_{\text{ion}}(V_n, t)\right), \qquad (12.78)$$

where V_n is the membrane potential of the nth (isopotential) cell.

Which of these approximations is most correct?

Because it is translationally invariant, the effective cable equation implies that propagation, if it occurs, is continuous, and the propagation velocity scales with the inverse square root of the resistance

$$v = \sqrt{\frac{k}{r_c + r_e + \frac{r_g}{L}}}, \qquad (12.79)$$

for some constant k. On the other hand, the discrete cable equation implies that propagation is saltatory, with individual cells becoming excited one at a time, and this excitation jumps from cell to cell in discrete fashion.

Propagation is known to be saltatory (Spach et al., 1981). Data collected on a single strand of rat myocytes (Fast and Kleber, 1993) found that an action potential required about 38 μs to travel 30 μm within a single cell, but it required 118 μs to travel 30 μm if propagation was across the ends of two cells. Hence, propagation through gap junctions led to a delay of about 80 μs. For cells of length 100 μm, this translates into a velocity of 0.8 μm/μs in the cell and 0.48 μm/μs along the fiber. If velocity within cells scales like the inverse square root of resistance, then

$$\left(\frac{0.8}{0.48}\right)^2 = \frac{r_c + r_e + \frac{r_g}{L}}{r_e + r_c}, \qquad (12.80)$$

so that $\frac{r_g}{L} = 1.78(r_e + r_c)$. In other words, according to this estimate, gap junctional resistance represents a substantial portion (here, roughly 65%) of the total resistance.

12.3.2   Propagation Failure

One dimensional propagation in cardiac fibers is expected to occur, since the cable equation is similar to those described in Chapter 6 with excitable dynamics. It is perhaps more interesting and of greater clinical significance to understand the causes of propagation failure. The primary lesson of the discussion that follows is that inhomogeneities of resistance can cause propagation failure.

Branching

On leaving the AV node of the heart, the action potential enters the bundle of HIS. The bundle divides near the upper ventricular septum into right and left branches.

The right bundle continues with little arborization toward the apex of the heart. The left bundle branch divides almost immediately into two major divisions: one anterior and superior, and the second posterior and inferior.

A bundle branch block occurs when the action potential fails to propagate through the entire branch. To understand something about the cause of bundle branch block, we consider a model of propagation in a one dimensional fiber with a junction at which the cable properties suddenly change. Wave fronts are governed by the cable equation

$$C_m R_m \frac{\partial V}{\partial t} = \frac{R_m}{p} \frac{\partial}{\partial x} \left(\frac{A}{R_c} \frac{\partial V}{\partial x} \right) + f(V), \qquad (12.81)$$

where $f(V)$ represents the fast currents, but dynamics due to slower variables are suppressed. We can also modify this equation for propagation in a bundle of fibers by letting p and A be the total membrane perimeter and cross-sectional area, respectively, for the bundle.

Suppose there is a point at which there is a sudden jump in cable properties. This could be due to a sudden change in the size of the cable, or, since this is a one-dimensional model, a splitting of the cable into two for which the total perimeter and cross-sectional area are changed. Thus, on both sides of this discontinuity, the cable equation (12.81) holds, but with different parameters p and A, say p_1, A_1 for $x < 0$, and p_2, A_2 for $x > 0$. At the junction the potential V and the axial current $\frac{A}{R_c} \frac{\partial V}{\partial x}$ must be continuous.

Using upper and lower solution techniques (Fife, 1979), one can demonstrate an important *comparison property* for the cable equation (12.81): If $V_1(x)$ and $V_2(x)$ are two functions that are ordered, with $V_1(x) \leq V_2(x)$, then the solutions of (12.81) with initial data $V_1(x)$ and $V_2(x)$, say $V_1(x,t)$ and $V_2(x,t)$ with $V_1(x,0) = V_1(x)$ and $V_2(x,0) = V_2(x)$, then $V_1(x,t) \leq V_2(x,t)$ for all time $t \geq 0$.

The importance of this theorem is that if we can establish the existence of a standing transitional profile, then traveling profiles of similar type are precluded. The standing wave is an upper bound for solutions and thereby prevents propagation (Pauwelussen, 1981).

Suppose the function $f(V)$ has three zeros, at $V = 0 < \alpha < \beta$. We look for a standing profile that connects $V = 0$ at $x = -\infty$ with $V = \beta$ at $x = \infty$. The standing profile must satisfy the ordinary differential equation

$$\frac{R_m}{p_i} \left(\frac{A_i}{R_c} V_x \right)_x + f(V) = 0, \qquad (12.82)$$

with $i = 1$ for $x < 0$ and with $i = 2$ for $x > 0$. Multiplying these equations by V_x and integrating, we obtain

$$\frac{1}{2} \frac{R_m A_i}{R_c p_i} V_x^2 + F(V) = \begin{cases} 0 & \text{if } i = 1, \\ F(\beta) & \text{if } i = 2, \end{cases} \qquad (12.83)$$

where $F(V) = \int_0^V f(u) du$. Sketches of these two curves are depicted in Fig. 12.24 in the case $F(\beta) > 0$. A connecting trajectory exists if these two curves intersect

at the same level of current. We express the profiles (12.83) in terms of the axial current $I = -\frac{A}{R_c}V_x$ and obtain

$$\frac{1}{2}\frac{R_m R_c}{A_i p_i}I^2 + F(V) = \begin{cases} 0 & \text{if } i = 1, \\ F(\beta) & \text{if } i = 2. \end{cases} \tag{12.84}$$

Intersections of these two curves occur if there is a solution of

$$F(V)\left(\frac{A_1 p_1}{A_2 p_2} - 1\right) = -F(\beta), \tag{12.85}$$

with $F(V) < 0$ in the range $0 < V < \beta$. Since the minimum for $F(V)$ is at $V = \alpha$, there is a solution whenever

$$\frac{A_1 p_1}{A_2 p_2} \geq 1 - \frac{F(\beta)}{F(\alpha)}. \tag{12.86}$$

In the special case that $f(V)$ is the cubic polynomial $f(V) = AV(V - 1)(\alpha - V)$, this condition becomes

$$\frac{A_1 p_1}{A_2 p_2} \geq 1 + \frac{1 - 2\alpha}{\alpha^3(2 - \alpha)}. \tag{12.87}$$

The interpretation is clear. If at a junction along a fiber the product pA increases by a sufficient amount, as specified by (12.86), then propagation through the junction in the direction of increasing pA is not possible. Of course, this criterion for propagation block depends importantly on the excitability of the fiber as expressed through the ratio $\frac{F(\beta)}{F(\alpha)}$, and propagation failure is more likely when the fiber is less excitable. Hence propagation block is time-dependent in that if inadequate recovery time from a previous excitation is allowed, or if recovery is slowed, the likelihood of block at a junction is increased. Further analysis of problems of this type can be found in Lewis and Keener (2000).

Gap-junctional coupling

We expect that gap-junctional resistance can have the similar effect of precluding propagation. To see how gap-junctional resistance affects the success or failure of propagation, we consider the idealized situation of cells of length L coupled at their ends by gap junctions, as described by (12.49) and the cable equation (12.48) with piecewise linear ionic current

$$I_{\text{ion}}(V) = \frac{1}{R_m}\left(H(V - \alpha) - V\right). \tag{12.88}$$

This model recommends itself because it can be solved explicitly, even though it lacks quantitative reliability or a direct physiological interpretation.

As before, we look for a standing solution on the assumption that the existence of a standing solution precludes the possibility of propagation.

The method to solve this standing wave problem is similar to the method used to find the space constant in Section 12.3.1, with two important differences, namely that the solution must be bounded in both directions ($n \to \pm\infty$) rather than only
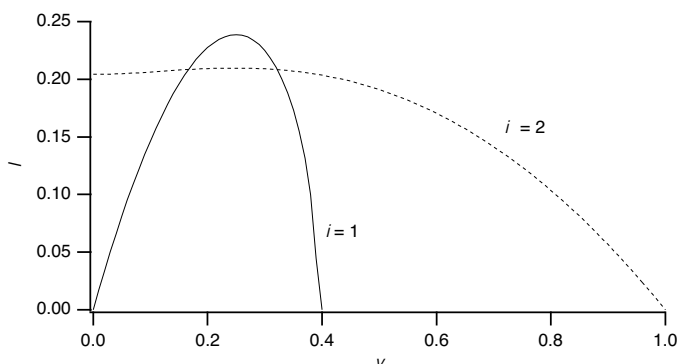
Figure 12.24: The curves (12.84) with $i = 1$ and $\frac{R_m R_c}{2A_i p_i} = 0.04$ and with $i = 2$ and $\frac{R_m R_c}{2A_i p_i} = 1.0$, for $f(v) = v(v-1)(\alpha - v)$, $\alpha = 0.25$. An intersection of the solid curve with the dashed curve guarantees propagation failure.

one, and the transmembrane current is piecewise linear, not linear. We use solutions of the linear problem found before to construct solutions of the nonlinear problem. That is, for $n \geq 0$ we take

$$\left(\begin{array}{c} V_i \\ V_e \end{array} \right)_n = A\mu^n \Phi(\mu, x), \qquad (12.89)$$

and for $n < 0$ we take

$$\left(\begin{array}{c} V_i \\ V_e \end{array} \right)_n = B\mu^{-n} \Phi\left(\frac{1}{\mu}, x \right) + \left(\begin{array}{c} 1+C \\ C \end{array} \right), \qquad (12.90)$$

where $\mu < 1$ is a root of (12.58), and $\Phi(\mu, x)$ is specified by (12.50) and (12.54). Here A, B, and C are as yet undetermined. However, this proposed solution has the feature that $V = V_i - V_e$ approaches 0 as $n \to \infty$, it approaches 1 as $n \to -\infty$, and satisfies all junctional boundary conditions except at the junction between cell $n = -1$ and cell $n = 0$. Futhermore, this proposed solution satisfies the cable equation (12.48) with ionic current $I_{\text{ion}}(V) = -\frac{V}{R_m}$ when $n \geq 0$ and with ionic current $I_{\text{ion}}(V) = \frac{1}{R_m}(1 - V)$ when $n < 0$.

Now, to determine the coefficients A, B, and C, we require that V_e, $\frac{dV_e}{dx}$ and $\frac{dV_i}{dx}$ be continuous at the junction between cell $n = -1$ (at $x = L$) and cell $n = 0$ (at $x = 0$) and that the junctional condition (12.49) be satisfied there as well. A tedious calculation (unless it is done with Maple) yields expressions for $A = B$, and C that are too complicated to be enlightening. However, one also finds that

$$V_0(0) = \frac{1}{2} \frac{E^2 - 2\mu E + 1}{E^2 - 2\mu E + 1 + \frac{1}{2} \frac{r_g \lambda}{r_c + r_e}(E^2 - 1)}, \qquad (12.91)$$

and

$$V_1(L) = 1 - V_0(0). \qquad (12.92)$$
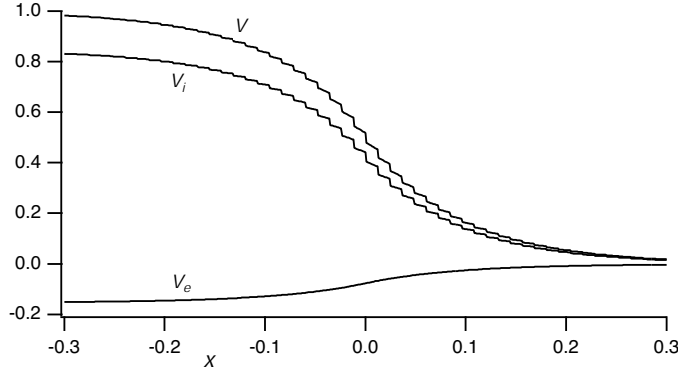
Figure 12.25: Plot of the standing wave solution for cells of length L coupled at their ends by resistive gap junctions. For this plot, cells have $L = 0.012$ cm, $A_i = 4.0 \times 10^{-6}$ cm^2, and a space constant $\lambda_g = 0.09$ cm. $R_m = 7000$ Ωcm^2, $R_i = 150$ Ωcm, $q_e = 0.5 q_i$, where $q_j = \frac{L^2 p}{R_m} r_j$, $j = i, e$.

It follows that $V < \frac{1}{2}$ for cell $n = 0$ at $x = 0$ and $V > \frac{1}{2}$ for cell $n = -1$ at $x = L$ whenever r_g is positive. A plot of this solution is shown in Fig. 12.25.

Finally, to be a valid solution for the piecewise linear ionic current (12.88), it must be that $V_0(0) < \alpha$. This leads to the condition

$$\frac{r_g \lambda}{r_c + r_e} \equiv \frac{R_g}{\lambda L} \geq \frac{1 - 2\alpha}{\alpha} \left(\frac{E - 2\mu + \frac{1}{E}}{E - \frac{1}{E}} \right). \tag{12.93}$$

where $R_g = \frac{L p r_g}{R_m}$.

The interpretation of this formula is complicated by the fact that according to (12.58), μ is a function of R_g. However, the implication of this is that propagation failure occurs if R_g is greater than some critical gap-junctional resistance, say R_g^*, and R_g^* is that value of R_g for which (12.93) is an equality. An equivalent relationship is that

$$\frac{R_g^*}{\lambda L} = 2 \frac{(\mu^* - \frac{1}{E})(\mu^* - E)}{\mu^* (E - \frac{1}{E})}, \tag{12.94}$$

where μ^* is the unique root less than $\frac{1}{E}$ of

$$\frac{1 - 2\alpha}{2\alpha} = \frac{(\mu^* - \frac{1}{E})(\mu^* - E)}{\mu^* (E - 2\mu^* + \frac{1}{E})}. \tag{12.95}$$

One can eliminate μ from these two equations to find the single quadratic equation for R_g^*,

$$\frac{\alpha(1 - \alpha)}{(1 - 2\alpha)^2} \left(\frac{R_g^*}{\lambda L} \right)^2 - \left(\frac{E^2 + 1}{E^2 - 1} \right) \frac{R_g^*}{\lambda L} - 1 = 0. \tag{12.96}$$

This equation has only one positive root.

Now, with a little graphical analysis, one can show that R_g^* is a decreasing function of α for $0 < \alpha < \frac{1}{2}$. This makes good sense, since it implies that propagation is less likely to fail in a more excitable medium (with smaller α) and more likely to fail in a less excitable medium. Further, in the limit of small λL, the positive root of this quadratic equation is

$$R_g^* = \frac{(1 - 2\alpha)^2}{\alpha(1 - \alpha)} + (\lambda L)^2 \left(\frac{1 - 2\alpha + 2\alpha^2}{2\alpha(1 - \alpha)} \right) + O(\lambda L)^3. \qquad (12.97)$$

On the other hand, for large λL, R_g^* is asymptotically linear, with

$$R_g^* = \lambda L \left(\frac{1 - 2\alpha}{1 - \alpha} \right) + O(\lambda L e^{-2\lambda L}). \qquad (12.98)$$

In general, one can show that for $0 < \alpha < \frac{1}{2}$, R_g^* is an increasing function of λL. The interpretation of this is that longer cells are less likely to experience propagation failure than shorter cells with the same excitability.

Additional discussion of this problem can be found in Keener (1991) and Keener (2000).

12.3.3 Myocardial Tissue: The Bidomain Model

Coupling in cardiac tissue is complicated by the fact that the signal is the transmembrane potential, and this necessitates that the intracellular and extracellular spaces be continuously connected and intertwined, so that one can move continuously between any two points within one space without traversing through the opposite space. This is possible only in a three-dimensional domain.

It is impossible to write and solve equations that take into account the fine-structure details of the geometry of these two interleaving spaces. However, the microstructure can be averaged (homogenized) to yield equations that describe the potentials in an averaged, or smoothed, sense, and these are adequate for many situations (although the concerns about inhomogeneities raised by the above discussion still pertain).

In this averaged sense, we view the tissue as a two-phase medium, as if every point in space is composed of a certain fraction of intracellular space and a fraction of extracellular space. Accordingly, at each point in space there are two electrical potentials V_i and V_e, as well as two currents i_i and i_e, with subscripts i and e denoting intracellular and extracellular space, respectively.

The relationship between current and potential is ohmic,

$$i_i = -\sigma_i \nabla V_i, \quad i_e = -\sigma_e \nabla V_e, \qquad (12.99)$$

where σ_i and σ_e are conductivity tensors. The principal axes of the conductivity tensors are the same, owing to the cylindrical nature of the cells, but the conductivities in these directions are possibly different. At any point in space the total current is $i_t = i_i + i_e$, and unless there are extraneous current sources, the total current is conserved, so that $\nabla \cdot i_t = 0$, or

$$\nabla \cdot (\sigma_i \nabla V_i + \sigma_e \nabla V_e) = 0. \qquad (12.100)$$

At every point in space there is a membrane potential

$$V = V_i - V_e. \tag{12.101}$$

The transmembrane current i_T is the current that leaves the intracellular space to enter the extracellular space,

$$i_T = \nabla \cdot (\sigma_i \nabla V_i) = -\nabla \cdot (\sigma_e \nabla V_e). \tag{12.102}$$

For a biological membrane, the total transmembrane current is the sum of ionic and capacitive currents,

$$i_T = \chi \left(C_m \frac{\partial V}{\partial t} + I_{\text{ion}} \right) = \nabla \cdot (\sigma_i \nabla V_i). \tag{12.103}$$

Here χ is the membrane surface-to-volume ratio, needed to convert transmembrane current per unit area into transmembrane current per unit volume. In the typical scaling, $I_{\text{ion}} = -\frac{f(V)}{R_m}$.

Equation (12.103) shows how cardiac tissue is coupled, and it, together with (12.100), is called the *bidomain model*. The bidomain model was first proposed in the late 1970s by Tung and Geselowitz (Tung, 1978) and is now the generally accepted model for electrical behavior of cardiac tissue (Henriquez, 1993). However, it is not actually used that often because it is computationally expensive and there are not many situations where it matters.

Boundary conditions for the bidomain model usually assume that there is no current across the boundary that enters directly into the intracellular space, whereas if there is an injected current, it enters the tissue through the extracellular domain.

Monodomain reduction

Equation (12.103) can be reduced to a monodomain equation for the membrane potential in one special case. Notice that (combining (12.101) and (12.99))

$$\nabla V_i = (\sigma_i + \sigma_e)^{-1} (\sigma_e \nabla V - i_t), \tag{12.104}$$

so that the balance of transmembrane currents becomes

$$\chi \left(C_m \frac{\partial V}{\partial t} + I_{\text{ion}} \right) = \nabla \cdot \left(\sigma_i (\sigma_i + \sigma_e)^{-1} \sigma_e \nabla V \right) - \nabla \cdot \sigma_i (\sigma_i + \sigma_e)^{-1} i_t. \tag{12.105}$$

Here we see that there is possibly a contribution to the transmembrane current from the divergence of the total current. We know that $\nabla \cdot i_t = 0$, so this source term is zero if the matrix $\sigma_i (\sigma_i + \sigma_e)^{-1}$ is proportional to a constant multiple of the identity matrix. In other words, if the two conductivity matrices σ_i and σ_e are proportional, $\sigma_i = \alpha \sigma_e$, with α a constant, then the source term disappears, and the bidomain model reduces to the monodomain model.

$$\chi \left(C_m \frac{\partial V}{\partial t} + I_{\text{ion}} \right) = \nabla \cdot (\sigma \nabla V), \tag{12.106}$$

where $\sigma = \sigma_i (\sigma_i + \sigma_e)^{-1} \sigma_e$. When $\sigma_i = \alpha \sigma_e$, the tissue is said to have equal anisotropy ratios. A one dimensional model with constant conductivities can always be reduced to a monodomain problem.

Plane waves

Cardiac tissue is strongly anisotropic, with wave speeds that differ substantially depending on their direction. For example, in human myocardium, propagation is about 0.5 m/s along fibers and about 0.17 m/s transverse to fibers. To see the relationship between the wave speed and the conductivity tensor we look for plane-wave solutions of the bidomain equations. Plane waves are functions of the single variable $\xi = \mathbf{n} \cdot \mathbf{x} - ct$, where $\mathbf{n}$ is a unit vector pointing in the direction of wave-front propagation. We assume that the ionic current is such that the canonical problem

$$u'' + c_0 u' + f(u) = 0 \qquad (12.107)$$

has a wave-front solution $U(x)$ for some unique value of c_0, the value of which depends on f. The behavior of this solution was discussed in Chapter 6.

In terms of the traveling wave coordinate ξ, the bidomain equations reduce to the two ordinary differential equations

$$\frac{R_m}{\chi} \mathbf{n} \cdot \sigma_i \mathbf{n} V_i'' + c C_m R_m V' + f(V) = 0, \qquad (12.108)$$

$$\mathbf{n} \cdot \sigma_i \mathbf{n} V_i'' + \mathbf{n} \cdot \sigma_e \mathbf{n} V_e'' = 0. \qquad (12.109)$$

Using that $V = V_i - V_e$, we find that

$$V_i' = \frac{\mathbf{n} \cdot \sigma_e \mathbf{n}}{\mathbf{n} \cdot (\sigma_i + \sigma_e)\mathbf{n}} V', \qquad (12.110)$$

$$V_e' = -\frac{\mathbf{n} \cdot \sigma_i \mathbf{n}}{\mathbf{n} \cdot (\sigma_i + \sigma_e)\mathbf{n}} V', \qquad (12.111)$$

and

$$\frac{R_m}{\chi} \frac{(\mathbf{n} \cdot \sigma_i \mathbf{n})(\mathbf{n} \cdot \sigma_e \mathbf{n})}{\mathbf{n} \cdot (\sigma_i + \sigma_e)\mathbf{n}} V_i'' + c C_m R_m V' + f(V) = 0. \qquad (12.112)$$

Now we compare (12.112) with (12.107) and find that the solutions are related through

$$V(\xi) = U\left(\frac{\xi}{\Lambda}\right), \qquad (12.113)$$

where $\Lambda(\mathbf{n})^2 = \frac{R_m}{\chi} \frac{(\mathbf{n} \cdot \sigma_i \mathbf{n})(\mathbf{n} \cdot \sigma_e \mathbf{n})}{\mathbf{n} \cdot (\sigma_i + \sigma_e)\mathbf{n}}$ ($\Lambda(\mathbf{n})$ is the directionally dependent space constant), and the plane-wave velocity is

$$c = \frac{\Lambda(\mathbf{n})}{C_m R_m} c_0. \qquad (12.114)$$

From this we learn that the speed of propagation depends importantly on direction $\mathbf{n}$, but the membrane potential profile is independent of direction except in its spatial scale Λ. This observation allows us to estimate the coefficients of the conductivity tensors σ_i and σ_e. This we do by observing from (12.111) that the total deflection of extracellular potential is dependent on direction. If we denote the total deflection of potentials during the upstroke by ΔV and ΔV_e, then

$$r_d = \frac{\Delta V_{ed}}{\Delta V} = \left(\frac{\sigma_{id}}{\sigma_{id} + \sigma_{ed}}\right), \quad d = L, T \qquad (12.115)$$

where the subscript d denotes the longitudinal (L) or the transverse (T) fiber direction and $\sigma_{id} = \mathbf{n}_d \cdot \sigma_i \mathbf{n}_d$ with $\mathbf{n}_L$ a unit vector along the fiber axis and $\mathbf{n}_T$ a unit vector transverse to the fiber axis, and similarly for σ_{ed}. It follows that

$$\frac{\sigma_{ed}}{\sigma_{id}} = \frac{1 - r_d}{r_d}. \tag{12.116}$$

Measurements on dog myocardium (Roberts and Scher, 1982) find that $\Delta V_{eL} = 74 \pm 7$ mV, $\Delta V_{eT} = 43 \pm 6$ mV. With a typical membrane potential upstroke deflection of $\Delta V = 100$ mV, it follows that

$$\frac{\sigma_{eL}}{\sigma_{iL}} = 0.35, \qquad \frac{\sigma_{eT}}{\sigma_{iT}} = 1.33, \tag{12.117}$$

implying that myocardial tissue has unequal anisotropy ratios. Combining this with the fact that the propagation speed is about three times faster in the longitudinal direction than the transverse direction leads to the conclusion that

$$\frac{\sigma_{iT}}{\sigma_{iL}} = 0.05, \qquad \frac{\sigma_{eT}}{\sigma_{iL}} = 0.07. \tag{12.118}$$

It should be pointed out that one can find a variety of estimates of the anisotropy ratios in the literature.

Virtual Electrodes

It is well accepted that cardiac tissue has unequal anisotropy ratios. Perhaps the most important consequence of unequal anisotropy is seen in the response of the membrane to a current stimulus. Recall from Fig. 12.23 that in a one dimensional cable, the transmembrane response to a current stimulus is local depolarization or hyperpolarization with exponential decay away from the electrode site. In tissue with equal anisotropy ratios, the transmembrane response is roughly the same, except that the isopotential contours are elliptical, with aspect ratio given by the square root of the ratio of the principal eigenvalues of the matrix $\sigma_i(\sigma_i + \sigma_e)^{-1}\sigma_e$.

However, in tissue with unequal anisotropy ratios, the isopotential contours can be much more complicated. An example of these contours is shown in Fig. 12.26. For this plot, the passive bidomain equations (take $I_{\text{ion}} = -V/R_m$) with a constant current point source at the center of the spatial domain were solved using straightforward finite differences. The anisotropy ratios were as in (12.117) and (12.118).

These contours show two striking features. In the central region (shown with a "+"), there is a strong polarizing response, but the isopotential contours are not elliptical, but rather they are "dogbone" shaped, oriented along the axis with largest coupling. For this reason, this is referred to as the dogbone potential. Oriented orthogonal to this dogbone, there are two roughly circular regions of opposite polarity (denoted with a "-"). These are called virtual electrodes, because there is depolarization or hyperpolarization even though there is no actual electrode (Roth, 1992; Wikswo et al., 1995).

Virtual electrodes can result not only from unequal anisotropy ratios but from many other inhomogeneities of resistance, such as fiber curvature, or tissue injury
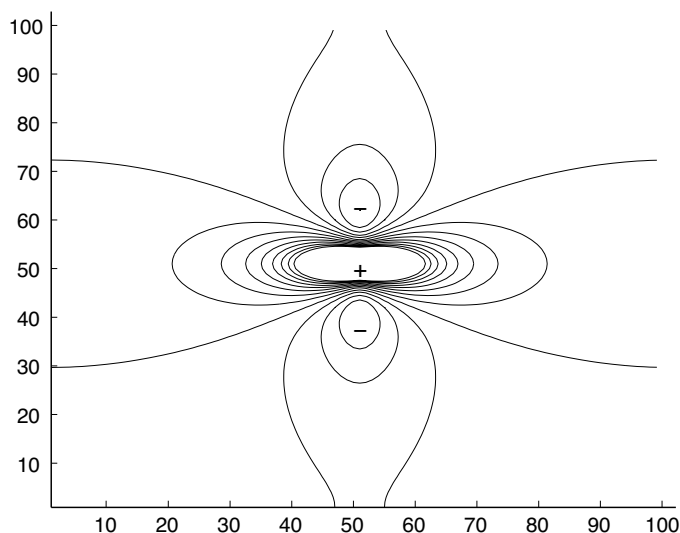
Figure 12.26: Contour plot of dogbone potential and virtual electrodes resulting from current stimulus to an anisotropic bidomain with anisotropy ratios as in (12.117) and (12.118).

(Henriquez et al. 1996, White et al. 1998). Of course, virtual electrodes were also seen above to result from inhomogeneities of resistance along cables. It is believed that virtual electrodes are important determinants of the success or failure of defibrillation, and this interesting topic is discussed below.

The activation sequence

Propagation in myocardial tissue is not planar and neither is it along fibers. In fact, because the initial activation of myocardial tissue occurs at the endocardial surface, myocardial propagation is primarily transverse to fibers. The fiber orientation in myocardial tissue varies through the thickness of the tissue, rotating approximately 120 degrees from epicardium to endocardium (Streeter, 1979). Additionally, the geometry of the ventricles is complicated, and the initiation of action potentials occurs at numerous places on the endocardial surface at the termini of the Purkinje fiber network.

The activation sequence is the spatial and temporal sequence in which the medium is activated by a wave initiated by the SA node. Without belaboring the details, an example of a computed action potential activation sequence for an anisotropic medium is shown in Fig. 12.27. Here is shown a sequence of wave-front surfaces at 20 ms intervals following stimulation on the top surface of a slab of tissue measuring 6 cm × 6 cm × 1 cm. The fiber orientation rotates continuously through 120 deg from top to bottom, and the velocity of propagation along fibers was taken to be three times faster than transverse to fibers. The most noticeable feature of these wave-front surfaces is the distortion from elliptical that occurs because of the
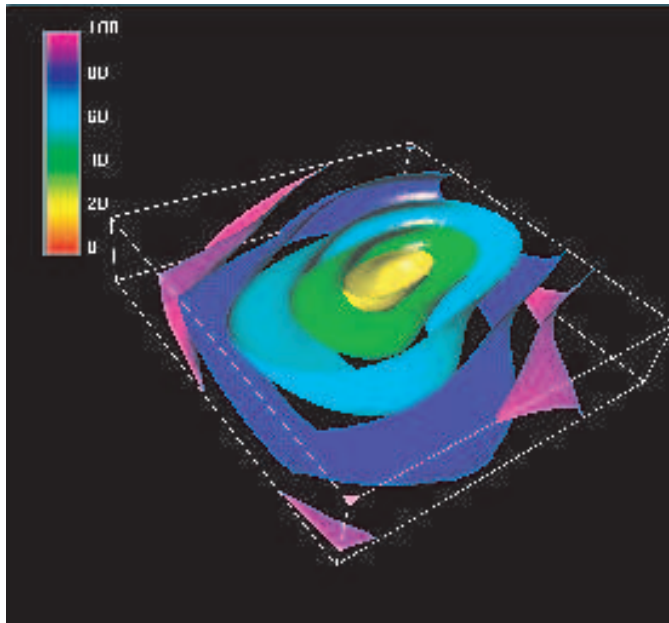
Figure 12.27: Action potential wave fronts at 20 ms intervals in a slab of tissue with rotational anisotropy.

rotational fiber orientation. Furthermore, there is a rotation of the elliptical axes, following the rotation of the fiber axes. However, the fastest propagation is not in the longitudinal fiber direction, as the ellipses rotate by only about 60 degrees. One can also determine (from the simulations) that normal wave-front velocity is always slower than the maximal plane-wave velocity, because of curvature slowing and fiber rotation.

Simulations of this type have also been done for whole heart with realistic geometry and fiber orientation incorporated into the conductivity tensors (see for example, Keener and Panfilov (1996)). Data for the geometry and fiber orientation from Hunter's group (Nielsen et al., 1991) were incorporated into the conductivity tensors. What is noticeable in all of these simulations is that wavefronts are not elliptical, and the direction of fastest propagation is not along fibers, even though the planar velocity is fastest in the direction of fibers. In fact, significant distortions from ellipticity occur because of the variable fiber orientation.

Many of these features of propagation in three-dimensional myocardial tissue have been observed experimentally (see, for example, Taccardi et al., 1992).

12.3.4 Pacemakers

In the previous sections, the emphasis was on how gap junctional coupling enables propagation of action potentials through cardiac tissue. In this section, we describe two other effects of gap junctional coupling, namely synchronization and electrotonic

loading.

Pacemaker Synchrony

The sinoatrial (SA) node is a clump of self-oscillatory cells located on the atrium near the superior vena cava. These cells fire regularly, initiating an action potential that propagates throughout the atrium, eventually terminating at the atrioventricular septum, or conducting into the AV node. SA nodal cells are not identical, but nevertheless fire at the same frequency. They are not synchronous in their firing (i.e., firing all at once), but they are *phase locked*, meaning that during each cycle, each cell fires once and there is a regular pattern to the firing of the cells. The variation of cellular properties in the SA node has two dominant features. There are gradual spatial gradients of the period of the oscillators and random deviations of individual cells from this average gradient.

Three questions concerning the SA pacemaker are of interest. First, since the individual cells all have different natural frequencies, what determines the frequency of the collective SA node? Second, what determines the details of the firing sequence, specifically, the location of the cell that fires earliest in the cycle and the subsequent firing order of the cells in the node? One might anticipate that the leader of the pack is the cell with the highest intrinsic frequency, but as we will see, this is not the case. Third, under what conditions does the SA node lose its ability to initiate the heartbeat (called *sinus node dysfunction*), and is it possible for other regions of (abnormal) oscillatory cells to initiate action potentials? Furthermore, since sinus node dysfunction is a potentially fatal condition, it is of clinical interest to understand how to treat this condition.

To address these questions, we suppose that the SA node is composed of self-oscillatory cells coupled together in a network, and that the action potential of the ith cell can be described by a vector of state variables u_i, which, in the absence of coupling, has dynamics

$$\frac{du_i}{dt} = F(u_i) + \epsilon G_i(u_i). \tag{12.119}$$

Here, the term $F(u)$ represents typical dynamics applicable for every cell, and $\epsilon G_i(u)$ represents the deviation of the dynamics for the ith cell from the average. The parameter ϵ is assumed to be a small positive number, indicating that the variation among cells is small. To specify F, one might use the YNI model or the FitzHugh–Nagumo model (as in Section 12.2), adjusted to allow for autonomous oscillations.

Next we assume that the cells are isopotential and connected discretely through resistive gap-junction coupling and that the extracellular medium is isopotential. Then, when the cells are coupled, we obtain the system of equations

$$\frac{du_i}{dt} = F(u_i) + \epsilon G_i(u_i) + \epsilon D \sum_j d_{ij}(u_j - u_i). \tag{12.120}$$

Here D is a diagonal matrix with entries of zero or one to indicate which of the state variables participate in the coupling. In neuromuscular media, only the intracellular and extracellular potentials participate in the coupling. However, because we have assumed that the extracellular potential is spatially uniform, D has only one nonzero

entry, namely that one corresponding to the intracellular potential. Furthermore, since we have assumed that the extracellular potential is spatially homogeneous, the difference of intracellular potentials between two cells is the same as the difference of their transmembrane potentials .

The coefficients d_{ij} are the coupling coefficients for the network of cells, where d_{ij} is equal to the (positive) coupling strength (inversely proportional to the resistance) between cells i and j. Of course, $d_{ij} = 0$ if cells i and j are not directly coupled, and coupling is symmetric, so that $d_{ij} = d_{ji}$. Without loss of generality, $d_{ii} = 0$.

A simple example for the coupling matrix comes from considering a one dimensional chain of cells coupled by nearest-neighbor coupling, for which $d_{i,i+1} = d_{i,i-1} = d$, the coupling strength between cells, and all other coupling coefficients are zero. The general formulation (12.120) of the problem allows us to consider a wide variety of coupling networks, including anisotropically coupled rectangular grids and hexagonal grids. The parameter ϵ scales the coupling term to indicate that the coupling is weak, so that currents through gap junctions are small compared to transmembrane currents. The evidence for weak coupling is that the wave speed in the SA node is very slow, on the order of 2–5 cm/s, compared with 50 cm/s in myocardial tissue and 100 cm/s in Purkinje fiber. (See Exercise 18 for a possible explanation of why weak coupling might be advantageous.)

Suppose the stable periodic solution of the equation $\frac{du}{dt} = F(u)$ is given by $U(t)$. Then, because ϵ is assumed to be small, one can use multiscale methods (see Section 12.7) to find that $u_i(t) = U(\omega(\epsilon)t + \delta\theta_i(t)) + O(\epsilon)$, where $\omega(\epsilon) = 1 + \epsilon\Omega_1 + O(\epsilon^2)$ and the phase shift $\delta\theta_i$ of each oscillator satisfies the equation

$$\frac{d}{dt}\delta\theta_i = \epsilon\left(\xi_i - \Omega_1 + \sum_{j \neq i} d_{ij}[h(\delta\theta_j - \delta\theta_i) - h(0)]\right). \tag{12.121}$$

The periodic coupling function h and the numbers ξ_i are specified in Section 12.7 and the scalar Ω_1 is as yet undetermined. Notice that each oscillator has frequency $\omega(\epsilon)$ and that the phase is slowly varying by comparison with the underlying oscillation and represents only the variation from the typical oscillation.

While there are many interesting questions that could be addressed at this point, of greatest interest here is to determine the *firing sequence* in a collection of phase-locked oscillators. By firing sequence, we mean the order of firing of the individual cells. If the firing sequence of cells is spatially ordered, then the firing of cells appears as a spreading wave, although it is not a propagated wave, but a *phase wave*. (It is not propagated because it would remain for some time even if coupling were set to zero. The role of coupling is merely to coordinate, not to initiate, the wavelike behavior.)

To determine the approximate firing sequence, we suppose that the cells are phase-locked and that the steady-state phase differences are not too large. This is the case for normal SA nodal cells, since all of the SA nodal cells fire within a few milliseconds of each other during an oscillatory cycle of about one second duration. If the steady-state phase differences are small enough, we can replace $h(\delta\theta_j - \delta\theta_i) - h(0)$ in (12.121) by its local linearization $h'(0)(\delta\theta_j - \delta\theta_i)$. Then the steady states of (12.121) are determined as solutions of the linear system of

equations

$$\sum_j d_{ij} h'(0)(\delta\theta_j - \delta\theta_i) = \Omega_1 - \xi_i. \tag{12.122}$$

We rewrite (12.122) in matrix notation by defining a matrix A with entries $a_{ij} = d_{ij}$ if $i \neq j$ and $a_{ii} = -\sum_{j \neq i} d_{ij}$, and then (12.122) becomes

$$A\Phi = \frac{1}{h'(0)}(\vec{\Omega}_1 - \vec{\xi}), \tag{12.123}$$

where Φ is the vector with entries $\delta\theta_i$, $\vec{\Omega}_1$ is a vector with all entries Ω_1, and the entries of $\vec{\xi}$ are the numbers ξ_i.

A few observations about the matrix A are important. Notice that A is symmetric and has a nontrivial null space, since $\sum_j a_{ij} = 0$. For consistency, we must choose Ω_1 such that the sum of all rows of (12.123) is zero, so that

$$\Omega_1 = \frac{1}{N}\sum_i \xi_i. \tag{12.124}$$

Thus, the bulk frequency of the SA node is determined as the average of the frequencies of the individual oscillators. This is a purely democratic process in which one cell equals one vote, regardless of coupling strength.

Next, since all the nonzero elements of d_{ij} (and hence the off-diagonal elements of A) are positive and A has zero row sums, all the nonzero eigenvalues of A have negative real part. Furthermore, since A is real, symmetric, and nonpositive definite, it has a complete set of N mutually orthogonal, real eigenvectors, say $\{y_k\}$, with corresponding real eigenvalues λ_k. All of the eigenvalues λ_k are negative or zero. If the matrix of coupling coefficients d_{ij} is irreducible, then the constant eigenvector y_1 is the unique null vector of A, and $\lambda_k < 0$ for $k > 1$ (see Chapter 9, Exercise 9). The matrix of coupling coefficients is *irreducible* if all the cells are connected by some electrical path, so that there are no electrically isolated clumps of cells. Suppose also that the eigenvectors are ordered by increasing amplitude of the eigenvalue. The solution of (12.123) is readily expressed in terms of the eigenvectors and eigenvalues of A as

$$\Phi = -\frac{1}{h'(0)}\sum_{k \neq 1}\langle\vec{\xi}, y_k\rangle\frac{y_k}{\lambda_k}. \tag{12.125}$$

The scalar Ω_1 drops out of this expression because the eigenvector y_1 is the constant vector and $\langle y_k, y_1\rangle = 0$ for all $k \neq 1$.

The firing sequence is now determined from Φ. That is, if $\delta\theta_k$ is the largest element of Φ, then the phase of the kth cell is the most advanced and therefore the first to fire, and so on, in decreasing order. It remains to gain some understanding of the relationship between the natural frequencies $\vec{\xi}$ and the firing sequence Φ.

The general principle of how the firing sequence is determined from the natural frequencies $\vec{\xi}$ is apparent from (12.125). The firing sequence is a superposition of the eigenvectors $\{y_k\}$ with amplitudes $\lambda_k^{-1}\langle\vec{\xi}, y_k\rangle$. Thus, eigenvector components of $\vec{\xi}$ that are most influential on the firing sequence are those components for which $\lambda_k^{-1}\langle\vec{\xi}, y_k\rangle$ is largest in amplitude. The expression (12.125) is a filter that suppresses,

A

B
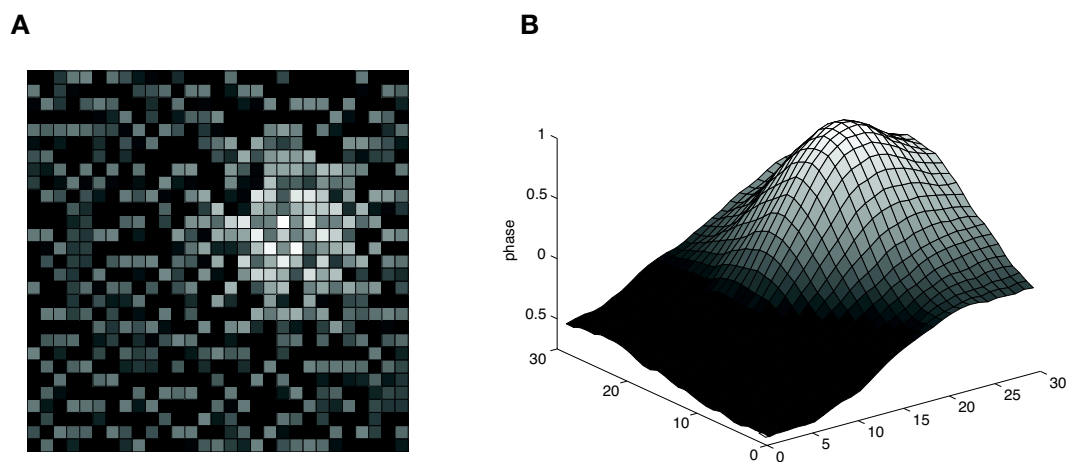
Figure 12.28: A: Natural frequencies ξ_i for a collection of oscillatory cells, lighter being faster, and darker being slower. B: Phase for oscillators in a collection of coupled cells with nearest-neighbor coupling and the natural frequencies depicted in panel A.

or filters out, certain components of $\vec{\xi}$. It follows that a single cell with high natural frequency compared to its coupled neighbors is not necessarily able to lead the firing sequence.

Equation (12.125) for the firing sequence does not give much geometrical insight. Furthermore, it is usually not a good idea to solve matrix problems such as (12.123) using eigenfunction expansions, since direct numerical methods are much faster and easier. To illustrate how (12.125) works, we consider, as an example, a two-dimensional grid of cells coupled by nearest-neighbor coupling. The natural frequencies of the cells are randomly distributed, with the fastest cells concentrated near the center of the grid. The distribution of natural frequencies is depicted in Fig. 12.28A, with darker locations representing the slowest intrinsic frequencies. The firing sequence for this collection of cells is shown in Fig. 12.28B, where cells with advanced (or largest) phase fire earliest in the firing sequence. The initiation of the firing sequence is at the site of a group of fast, but not necessarily the fastest, oscillators. Notice that the phase is smoothed, giving the appearance of wave-like motion moving from the location of largest phase to smallest phase, even though these are phase waves rather than propagated waves. In this figure, the scale of the phase variable is arbitrary.

Critical Size of a Pacemaker

The SA node is a small clump of self-oscillatory cells in a sea of excitable (but nonoscillatory) cells whose function is to initiate the cardiac action potential. SA nodal cells have no contractile function and therefore no contractile machinery.

Thus, when viewed in terms of contractile efficiency, SA nodal cells are a detriment to contraction and a waste of important cardiac wall space. On the other hand, the SA node cannot be too small because presumably it would not be able to generate the current necessary to entrain the rest of the heart successfully. Further it could be that surrounding resting cells drain enough current from the oscillatory cells to quench the pacemaking activity. This drain is called the electrotonic load. Clearly, it is important to have some measure of the critical size of the SA node.

An *ectopic focus* is a collection of cells other than the SA node or AV node that are normally not oscillatory but that for some reason (for example, increased extracellular K^+) become self-oscillatory and manage to entrain the surrounding tissue into a rapid beat. In some situations, particularly in people with scar tissue resulting from a previous heart attack, the appearance of an ectopic focus may be life-threatening.

To understand something about the behavior of a clump of oscillatory cells in an otherwise nonoscillatory medium, we use a simple model with FitzHugh–Nagumo dynamics,

$$\frac{\partial v}{\partial t} = \nabla^2 v + f(v) - w, \tag{12.126}$$

$$\frac{\partial w}{\partial t} = \epsilon(v - \gamma w - \alpha(r/\sigma)), \tag{12.127}$$

where v represents the membrane potential and w the recovery variable for the excitable medium. The function $f(v)$ is of typical "cubic" shape (cf. Chapter 5). The function $\alpha(r)$ is chosen to specify the intrinsic cell behavior as a function of the radial variable r. The number σ is a scale factor that measures the size of the oscillatory region. We take ϵ to be a small positive number and require $\gamma > 0, f'(v)\gamma < 1$ for all v. This requirement on γ guarantees that the steady-state solution of (12.126)–(12.127) is unique. If the domain is bounded, typical boundary conditions are Neumann (no-flux) conditions. Notice that space has been scaled to have unit space constant. We assume radial symmetry for the SA node as well as for the entire spatial domain.

When there is no spatial coupling, there are two possible types of behavior, exemplified by the phase portraits in Figs. 5.15 and 5.16. In these examples, the system has a unique steady-state solution that is globally stable (Fig. 5.15) or has an unstable steady-state solution surrounded by a stable periodic orbit (Fig. 5.16), depending on the location of the intercept of the two nullclines.

The transition from a stable to an unstable steady state is via a subcritical Hopf bifurcation. The Hopf bifurcation is readily found from standard linear analysis. Suppose v^* is the equilibrium value for v (v^* is a function of α). Then the characteristic equation for (12.126)–(12.127) (with no diffusion) is

$$f'(v^*) = \lambda + \frac{\epsilon}{\lambda + \epsilon\gamma}, \tag{12.128}$$

where λ is an eigenvalue of the linearized system. There is a Hopf bifurcation (i.e., λ is purely imaginary) when

$$f'(v^*) = \epsilon\gamma, \tag{12.129}$$

provided that $\epsilon\gamma^2 < 1$. If $f'(v^*) > \epsilon\gamma$, the steady-state solution is an unstable spiral point, whereas if $f'(v^*) < \epsilon\gamma$, the steady-state solution is linearly stable. If ϵ is small, most of the intermediate (increasing) branch of the curve $f(v)$ is unstable, with the Hopf bifurcation occurring close to the minimal and maximal points. Thus, there is a range of values of α, which we denote by $\alpha_* < \alpha < \alpha^*$, for which the steady solution is unstable.

We wish to model the physical situation in which a small collection of cells (like the SA node or an ectopic focus) is intrinsically oscillatory, while all other surrounding cells are excitable, but not oscillatory. To model this, we assume that $\alpha(r)$ is such that the steady solution is unstable for small r, but stable and excitable for large r, so that $\lim_{r\to\infty} \alpha(r) = a < \alpha_*$ and $\lim_{r\to\infty} f'(v^*(r)) < \epsilon\gamma$. As an example, we might have the bell-shaped curve

$$\alpha(r) \;=\; a + (b-a)\exp\left(-\frac{r^2}{R^2}\right), \tag{12.130}$$

$$R^2 \;=\; \log\left(\frac{b-a}{\alpha_* - a}\right), \tag{12.131}$$

with $a < \alpha_* < b < \alpha^*$. The scale factor R was chosen such that $\alpha(1) = \alpha_*$, so that cells with $r < 1$ are self-oscillatory and the cells outside unit radius are nonoscillatory.

Another way to specify $\alpha(r)$ is simply as the piecewise constant function

$$\alpha(r) = \begin{cases} b, & \text{for } 0 < r < 1, \\ a, & \text{for } r > 1, \end{cases} \tag{12.132}$$

with $a < \alpha_* < b < \alpha^*$. The specification (12.132) is particularly useful when used in combination with the piecewise linear function

$$f(v) = \begin{cases} -v, & \text{for } v < \frac{1}{4}, \\ v - \frac{1}{2}, & \text{for } \frac{1}{4} < v < \frac{3}{4}, \\ 1 - v, & \text{for } v > \frac{3}{4}, \end{cases} \tag{12.133}$$

since then all the calculations that follow can be done explicitly (see Exercises 17 and 18).

There are two parameters whose influence we wish to understand and that we expect to be most significant, namely, a, the asymptotic value of $\alpha(r)$ as $r \to \infty$, and σ, which determines the size of the oscillatory region. Note that as a decreases, the cells become less excitable and the wavespeed of fronts decreases. We expect the behavior to be relatively insensitive to variations in b, although this should be verified as well.

With a nonuniform $\alpha(r)$, the uncoupled medium has a region of cells with unstable steady states and a region with stable steady states. With diffusive coupling, the steady state solution is smoothed and satisfies the elliptic equation

$$\nabla^2 v + F(v, r) \;=\; 0, \tag{12.134}$$

$$F(v, r) \;=\; f(v) - w, \tag{12.135}$$

$$w \;=\; \frac{1}{\gamma}\left(v - \alpha\left(\frac{r}{\sigma}\right)\right). \tag{12.136}$$
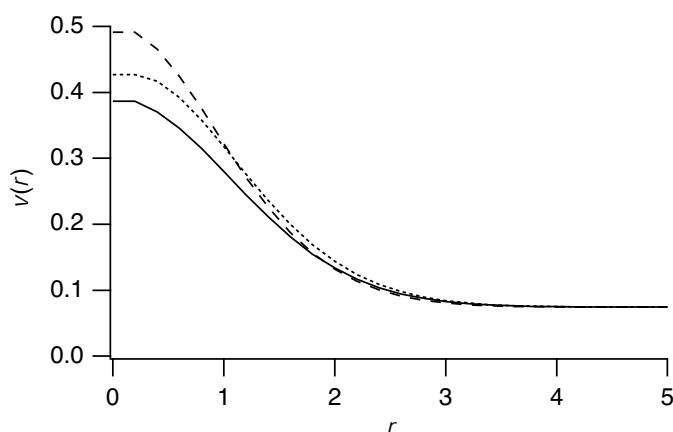
Figure 12.29: Three steady-state solutions with $f(v) = 10.0v(v-1)(0.5-v)$, $\gamma = 0.1$, and $\alpha(r)$ given by (14.23), with $a = 0.104$, $b = 0.5$, $\sigma = 2.25$. The short dashed curve shows the uncoupled solution, the long dashed curve shows the solution for a symmetric one dimensional medium, and the solid curve shows the solution for a spherically symmetric three-dimensional medium.

For each r, since $f'(v)\gamma < 1$, the function $F(v,r)$ is a monotone decreasing function of v having a unique zero, say $v = v^*(r)$, $F(v^*(r),r) = 0$. It follows that there is a unique, stable solution of (12.136), denoted by $v_0(r), w_0(r)$. In fact, this unique solution is readily found numerically as the unique steady solution of the nonlinear parabolic equation

$$\frac{\partial y}{\partial t} = \nabla^2 y + F(y,r). \tag{12.137}$$

This steady-state solution is shown in Fig. 12.29. Here are shown three different steady-state solutions of (12.126)–(12.127); the uncoupled solution (the steady states for the uncoupled medium, i.e., with no diffusive coupling), the solution for a symmetric one dimensional medium, and the solution for a spherically symmetric three-dimensional medium. The three-dimensional solution with spherical symmetry is not much harder to find than the one dimensional solution, because the change of variables $y = Y/r$ transforms (12.137) in three spatial dimensions into the one-dimensional problem

$$\frac{\partial Y}{\partial t} = \frac{\partial^2 Y}{\partial r^2} + rF\left(\frac{Y}{r}, r\right). \tag{12.138}$$

Solutions of this partial differential equation are regular at the origin if we require $Y = 0$ at $r = 0$. Diffusion (i.e., electrotonic coupling) obviously smooths the steady-state solution in the oscillatory region.

The issue of collective oscillation is determined by the stability of the diffusively smoothed steady state as a solution of the partial differential equation system (12.126)–(12.127). To study the stability of the steady state, we look for a solution
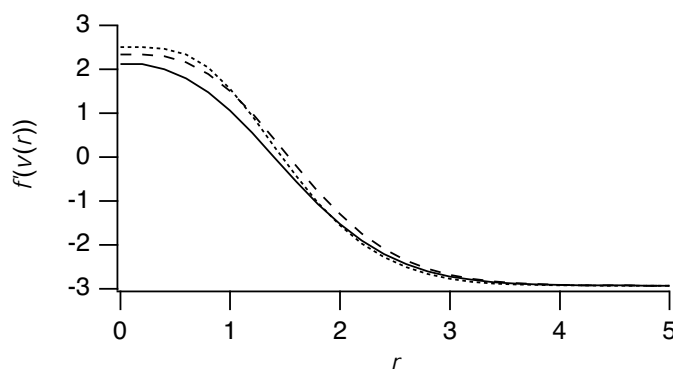
Figure 12.30: The potential function $f'(v(r))$ for three steady profiles $v(r)$. The short dashed curve corresponds to the uncoupled solution, the long dashed curve to the symmetric one dimensional medium, and the solid curve to a spherically symmetric three-dimensional medium.

of (12.126)–(12.127) of the form $v(r) = v_0(r) + V(r)e^{\lambda t}, w = w_0(r) + W(r)e^{\lambda t}$ and linearize. We obtain the linear system

$$\lambda V = \nabla^2 V + f'(v_0(r))V - W, \qquad\qquad (12.139)$$
$$\lambda W = \epsilon(V - \gamma W). \qquad\qquad (12.140)$$

Because of the special form of this linearized system, it can be simplified to a single equation, namely,

$$\nabla^2 V + f'(v_0(r))V = \mu V, \qquad\qquad (12.141)$$

where $\mu = \lambda + \frac{\epsilon}{\lambda + \epsilon\gamma}$. Equation (12.141) has a particularly nice form, being a *Schrödinger equation*. In quantum physics, the function $-f'(v_0(r))$ is the potential energy function, and the eigenvalues μ are the energy levels of bound states. In the present context, we are interested in determining the sign of the real part of λ through $\mu = \lambda + \frac{\epsilon}{\lambda + \epsilon\gamma}$. Notice that the relationship between μ and λ here is of exactly the same form as the characteristic equation for individual cells (12.128). This leads to a nice interpretation for the Schrödinger equation (12.141). Because it is a self-adjoint equation, the eigenvalues μ of (12.141) are real. Therefore, there is a Hopf bifurcation for the medium whenever $\mu = \epsilon\gamma$. The entire collection of coupled cells is stable when the largest eigenvalue satisfies $\mu < \epsilon\gamma$ and unstable if the largest eigenvalue has $\mu > \epsilon\gamma$.

In Fig. 12.30 is shown the potential function $f'(v(r))$ for the three steady profiles of Fig. 12.29. The largest eigenvalue of (12.141) represents an average over space of the influence of $f'(v_0(r))$ on the stability of the steady state. When this value is larger than $\epsilon\gamma$ (the critical slope of $f(v)$ at which Hopf bifurcations of the uncoupled system occur), then the entire medium loses stability to a Hopf bifurcation and gives rise to an oscillatory solution. The condition $\mu > \epsilon\gamma$ is therefore the condition that determines whether a region of oscillatory cells is a source of oscillation. If $\mu < \epsilon\gamma$, the oscillatory cells are held quiescent by the rest of the medium.

Some observations about the size of the eigenvalues μ are immediate. Because $\lim_{r\to\infty} v_0(r) = \lim_{r\to\infty} v^*(r)$, it follows that $f'(v_0(r)) < \epsilon\gamma$ for large r. For there to be a bounded solution of (12.141) that is exponentially decaying at $\pm\infty$, there must be a region of sinusoidal behavior in which $\mu < f'(v_0(r))$. Thus, the largest eigenvalue of (12.141) is guaranteed to be smaller than the maximum of $f'(v_0(r))$. Therefore, if $v_0(r) < \alpha_*$ (so that $f'(v_0(r)) < \epsilon\gamma$ for all r), there are no oscillatory cells, and the steady solution is stable. Furthermore, since the largest eigenvalue is strictly smaller than the maximum of $f'(v_0(r))$ and it varies continuously with changes in $v_0(r)$, there are profiles $\alpha(r)$ having a nontrivial collection of oscillatory cells that is too small to render the medium unstable. That is, there is a critical mass of oscillatory cells necessary to cause the medium to oscillate. Below this critical mass, the steady state is stable, and the oscillation of the oscillatory cells is quenched.

Suppose $f'(v)$ is a monotone increasing function of v in some range $v < v^+$, and suppose that $\alpha(r)$ is restricted so that $v_0(r) < v^+$ for all r. Suppose further that $\alpha(r)$ is a monotone increasing function of its asymptotic value a and a monotone decreasing function of r. Then the steady-state solution $v_0(r)$ is an increasing function (for each point r) of both a and σ. Therefore, the function $f'(v_0(r))$ is an increasing function of a and σ for all values of r, from which it follows—using standard comparison arguments for eigenfunctions (Keener, 1988, or Courant and Hilbert, 1953)—that $\mu(a,\sigma)$, the largest eigenvalue of (12.141), is an increasing function of both a and σ. As a result, if $\alpha(r)$ is restricted so that $v_0(r) < v^+$ for all r, there is a monotone decreasing function of σ, denoted by $\sigma = \Sigma(a)$, along which the largest eigenvalue $\mu(a,\sigma)$ of (12.141) is precisely $\epsilon\gamma$.

This summary statement shows that to build the SA node, one must have a sufficiently large region of oscillatory tissue, and that the critical mass requirement increases if the tissue becomes less excitable or if the coupling becomes stronger. Strong coupling inhibits oscillations, because increasing coupling increases the space constant, and σ was measured in space constant units. Therefore, an increase of the space constant increases the critical size requirement of the oscillatory region. In Fig. 12.31 is shown the critical Hopf curve $\sigma = \Sigma(a)$ for a one dimensional domain and for a three dimensional domain (taking $\epsilon = 0$), both found numerically.

Having established that there is a critical size for a self-oscillatory region above which oscillations occur and below which oscillations are prevented, we would like to examine the behavior of the oscillations. Two types of oscillatory behavior are possible. If the far field $r \to \infty$ is sufficiently excitable, then the oscillations of the oscillatory region excite periodic waves that propagate throughout the medium, as depicted in Fig. 12.32A. On the other hand, it may be that there are oscillations that fail to propagate throughout the entire medium, as depicted in Fig. 12.32B. In Fig. 12.32A, the oscillatory region successfully drives oscillatory waves that propagate throughout the entire medium. Here, $a = 0.2$, $\sigma = 3.0$. In Fig. 12.32B, the oscillatory region is incapable of driving periodic waves into the nonoscillatory region, as the medium at infinity does not support front propagation.

The issue of whether or not the entire medium is entrained to the central oscillator is decided by the relationship between the period of the oscillator and the dispersion curve for the far medium. Roughly speaking, if the period of the cen-
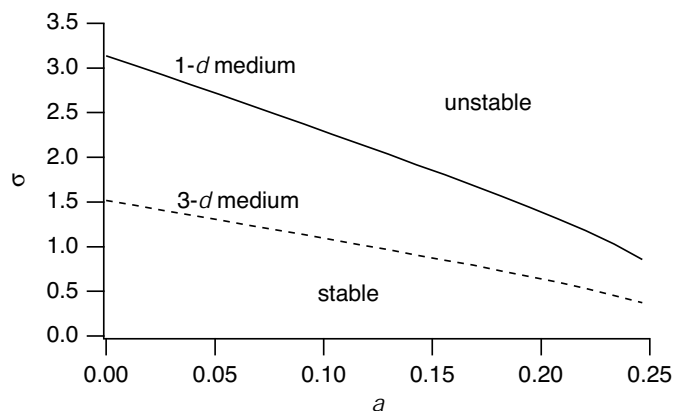
Figure 12.31: The critical curve $\sigma = \Sigma(a)$ along which there is a Hopf bifurcation for the system (12.126)–(12.127), shown solid for a one dimensional and dashed for a three-dimensional medium.
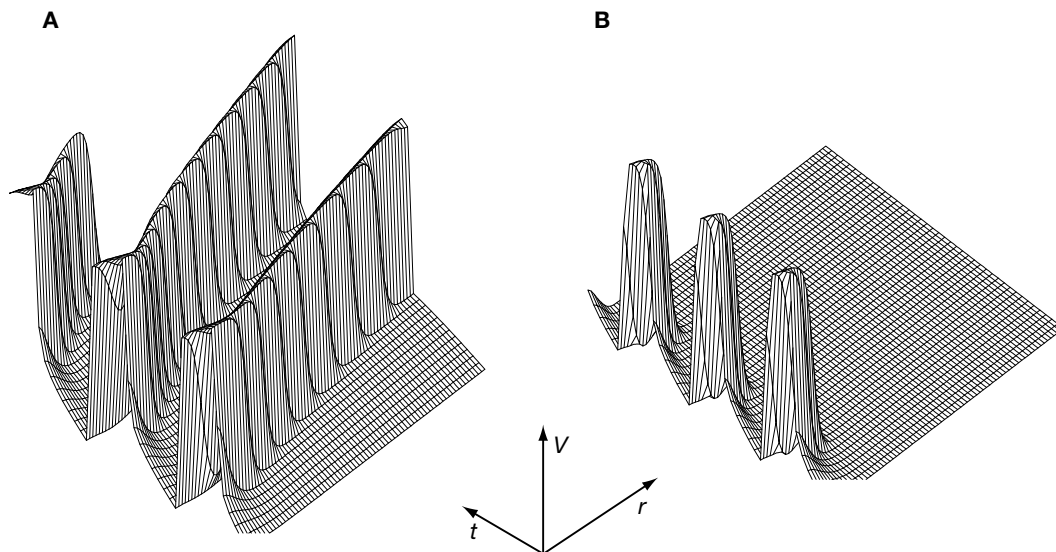
Figure 12.32: A: Waves generated by an oscillatory core that propagate into the nonoscillatory region. The nonlinearity here is the same as in Fig. 12.29 with $\epsilon = 0.1, \gamma = 0.1, a = 0.2, b = 0.5$, and $\sigma = 3.0$. B: Waves generated by an oscillatory core that fail to propagate into the nonoscillatory region. Same parameters as in A, but with $a = 0$.

tral oscillator is large enough compared to the absolute refractory period of the far medium (the knee of the dispersion curve), then waves can be expected to propagate into the far field in one-to-one entrainment. On the other hand, if the frequency of the oscillation is below the knee of the dispersion curve, we expect partial or total block of propagation. Block of propagation occurs as the excitability of the far field, parametrized by a, decreases.

We can summarize how the oscillations of the medium depend on coupling strength. For a medium with fixed asymptotic excitability, if the size of the oscillatory region is large enough, there is oscillatory behavior. However, this critical mass is an increasing function of coupling strength. With sufficiently large coupling, the oscillations of any finite clump of oscillatory cells (in an infinite domain of nonoscillatory cells) are quenched. If coupling is decreased, the critical mass for oscillation decreases. Thus, any clump of oscillatory cells oscillates if coupling is weak enough. However, if coupling is too weak, then effects of discrete coupling may become important, and the oscillatory clump of cells may lose its ability to entrain the entire medium. It follows that if the medium is sufficiently excitable, there is a range of coupling strengths, bounded above and below, in which a mass of oscillatory cells entrains the medium. If the coupling is too large, the oscillations are suppressed, while if the coupling is too weak, the oscillations are localized and cannot drive oscillations in the medium far away from the oscillatory source. On the other hand, if the far region is not sufficiently excitable, then one of these two mechanisms suppresses entrainment for all coupling strengths.

12.4   Cardiac Arrhythmias

Cardiac arrhythmias are disruptions of the normal cardiac electrical cycle. They are generally of two types. There are temporal disruptions, which occur when cells act out of sequence, either by firing autonomously or by refusing to respond to a stimulus from other cells, as in AV nodal block or a bundle branch block. A collection of cells that fires autonomously is called an ectopic focus. Generally speaking, these arrhythmias cause little disruption to the ability of the heart muscle to pump blood, and so if they do not initiate some other kind of arrhythmia, are generally not life-threatening.

The second class of arrhythmias are those that are reentrant in nature and can occur only because of the spatial distribution of cardiac tissue. If they occur in the ventricles, reentrant arrhythmias are of serious concern and life-threatening, as the ability of the heart to pump blood is greatly diminished. Reentrant arrhythmias on the atria are less dangerous, since the pumping activity of the atrial muscle is not necessary to normal function with minimal physical activity, although long-lived atrial reentrant arrhythmias are known to increase the chance of strokes.

12.4.1   Cellular Arrhythmias

By a cellular arryhythmia we mean an action potential response to a stimulus protocol that is not one-to-one. Such arrhythmias are relatively easy to observe in models. Simply apply a periodic stimulus to your favorite model of cellular

activity, vary the period and watch what happens. Of course, it would be nice to obtain some deeper understanding of the cause of these arrhythmias than can be provided by numerical simulation. To that end ideas of dynamical systems theory and discrete maps have been extensively used. Here we present two such examples, APD alternans and Wenckebach patterns in the AV node.

APD Alternans

Yehia et al. (1999) give a comprehensive discussion of the types of rhythms that an isolated cardiac cell can demonstrate under regular pacing. A cell isolated from rabbit ventricular muscle was stimulated periodically and the resulting sequence of action potential durations (APDs) was measured. It was found that for sufficiently large basic cycle length (BCL), after the disappearance of initial transients, each stimulus evoked the same APD. This pattern is referred to as a 1:1 rhythm - one stimulus, one response. For appropriately small BCL, the APD alternated between that of a full action potential and that of a sub-threshold response with APD essentially zero. This pattern is referred to as a 2:1 rhythm since every two stimuli evoked one super-threshold response. This 2:1 rhythm is relatively easy to understand. For large BCL, the cell has sufficient time to recover from the previous action potential before the next stimulus, but for short BCL, there is not sufficient time to recover, and the stimulus delivered during this unrecovered stage elicits a subthreshold response.

More interesting behavior occurs between these two extremes of BCL. For large stimulus amplitude, as BCL is decreased, the 1:1 rhythm is replaced by a rhythm in which there are superthreshold responses with alternating APDs. This 2:2 rhythm is referred to as APD alternans. (2:2 refers to the fact that there are 2 superthreshold responses to 2 stimuli, but the responses are not the same.)

Models of APD alternans trace back to the work of Nolasco and Dahlen (1968). The basic assumption is that APD is a function of the preceding recovery period or diastolic interval (DI). If the cell is assumed to be either excited or recovering, then $BCL = APD + DI$ where

$$\mathrm{APD}_{n+1} = G(\mathrm{DI}) = G(\mathrm{BCL} - \mathrm{APD}_n). \qquad (12.142)$$

In the case of subthreshold responses, where the DI is smaller than some minimum necessary to reestablish excitability, it is assumed that the sub-threshold stimulus has no effect on the cell, but there is an extra BCL during which the cell can recover. Thus, if there are $N - 1$ unsuccessful stimuli, $\mathrm{DI} = N \cdot \mathrm{BCL} - \mathrm{APD}$, so that

$$\mathrm{APD}_{n+1} = G(\mathrm{DI}) = G(N \cdot \mathrm{BCL} - \mathrm{APD}_n). \qquad (12.143)$$

A typical choice for G is an exponential of the form

$$G(\mathrm{DI}) = \mathrm{APD}_{\max} - A \exp\left(-\frac{\mathrm{DI}}{\mu}\right), \qquad \mathrm{DI} > \mathrm{DI}_{\min}, \qquad (12.144)$$

where $\mathrm{APD}_{\max}$, A, μ, and $\mathrm{DI}_{\min}$ are fit to data.

A plot of this map for typical parameter values is shown in Fig. 12.33, where $g_k(\mathrm{APD}) = G(k \cdot \mathrm{BCL} - \mathrm{APD})$. Because this is a one dimensional map, it is
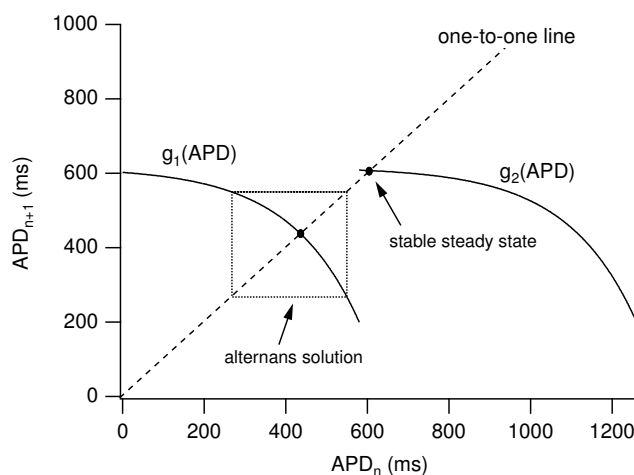
Figure 12.33: A sample APD map exhibiting alternans and bistability. Parameter values are $\text{APD}_{\max} = 616$, $A = 750$, $\mu = 170$, $\text{DI}_{\min} = 100$ and $\text{BCL} = 680$, all with units of ms.

quite easy to study its dynamic behavior. First note that the argument of G must always be greater than $DI_{\min}$. Thus, g_k is defined only if $\text{APD} > k \cdot \text{BCL} - DI_{\min}$. Specifically, the map g_1 is defined only on the interval $(0, \text{BCL} - \text{DI}_{\min})$ which, in Fig. 12.33 is the interval $(0, 580)$. Similarly, the map g_2 is defined only on the interval $(\text{BCL} - \text{DI}_{\min}, 2\text{BCL} - \text{DI}_{\min})$.

Fixed points of these maps are at the intersections of the one-to-one line with the functions $g_k(\text{APD})$. Stability of the fixed points is determined by the slope of $g_k(\text{APD})$ at the fixed point, with stability if $|g_k'(\text{APD}^*)| < 1$, and instability otherwise. Instability of the fixed point gives rise to a period two bifurcation, corresponding to alternans.

Increasing BCL shifts the curves to the right, so apparently for sufficiently large BCL there is a unique fixed point of the g_1 map, which corresponds to a 1:1 rhythm. As BCL is decreased, however, the slope of g_1 at the fixed point becomes more negative, leading, if the slope becomes less than -1, to a period two bifurcation. For the parameter values used in Fig. 12.33, there is also a region of bistability, in which stable alternans coexist with a stable 2:1 rhythm. The stable 2:1 rhythm is the steady state of the g_2 map, i.e., the point where the g_2 graph crosses the one-to-one line. This bistability has been observed experimentally (Hall et al., 1999; Yehia et al., 1999).

The observation that alternans occur in single cells when the slope of the APD curve exceeds one has lead many investigators to speculate that a steep APD restitution curve is responsible for a variety of arrhythmias in cardiac tissue as well, not only single cells. This is now known as the APD restitution hypothesis, and there is an extensive literature describing it, along with the suggestion that flattening the APD restitution curve (with drugs, for example) might prevent certain kinds of

arrhythmias. However, this hypothesis remains highly conjectural. See, for example, Courtemanche et al. (1993), Cytrynbaum and Keener (2002), Qu et al. (2000), Garfinkel et al. (2000), Watanabe et al. (2001).

Discrete maps have been used with great success to study a variety of cellular arrhythmias, see for example Otani and Gilmour (1997), Hall et al. (1999), Glass et al. (1987) and Watanabe et al. (1995).

12.4.2   Atrioventricular Node - Wenckebach Rhythms

In the normal heart, the only pathway for an action potential to travel to the ventricles is through the AV node. As noted above, propagation through the AV node is quite slow compared to propagation in other cardiac cells. This slowed conduction is primarily due to a decreased density of Na^+ channels, which yields a decreased upstroke velocity, as well as a significantly decreased density of gap junctional coupling (Pollack, 1976). With a decrease of Na^+ channel density there is also an increased likelihood of conduction failure.

Propagation failure in the AV node leads to skipped QRS complexes on the ECG, or, more prosaically, skipped heartbeats. A skipped heartbeat once in a while is not particularly dangerous, but it is certainly noticeable. During *diastole* (the period of ventricular relaxation during the heartbeat cycle), the ventricles fill with blood. Following an abnormally long diastolic period, the heart becomes enlarged, and when the next compression (*systole*) occurs, *Starling's law* (i.e., that compression is stronger when the heart is more distended initially, cf. Chapter 11) takes control, and compression is noticeably more vigorous, giving the subject a solid thump in the chest.

AV nodal conduction abnormalities are sorted into three classes. They are all readily visible from ECG recordings by looking at the time interval between the P wave and the QRS complex, i.e., the *P–R interval*. Type I AV nodal block shows itself as an increase in the P–R interval as the SA pacing rate increases. Type III AV nodal block corresponds to no AV nodal conduction whatever and total absence of a QRS complex.

Type II AV nodal block is phenomenologically the most interesting. In the simplest type, there is one QRS complex for every two P waves, a 2:1 pattern. A more complicated pattern is as follows: on the ECG (Fig. 12.34), P waves remain periodic, although the P–R interval is observed to increase gradually until one QRS complex is skipped. Following the skipped beat, the next P–R interval is quite short, but then the P–R lengthening begins again, leading to another skipped beat, and so on. A pattern with n P waves to $n-1$ QRS complexes is called an n-to-$(n-1)$ *Wenckebach pattern*, after the German cardiologist Wenckebach (1904).

A simple mathematical description of AV nodal signal processing can be given as follows: we view the AV node as a collection of cells that fire when they are excited, which happens if their potential reaches a threshold, $\theta(t)$. Immediately after firing, the cells become refractory but then gradually recover. Effectively, at firing, the threshold increases dramatically but then decreases exponentially back to its steady-state value as recovery proceeds. This model ignores the fact that the AV node is self-oscillatory and fires without stimulus with a low frequency of 30–40 per minute. The self-oscillatory nature of the AV node becomes evident only in
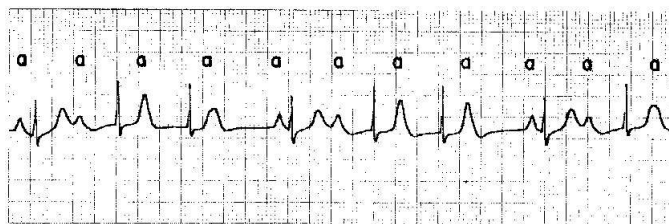
Figure 12.34: ECG recording of a Wenckebach pattern in which every fourth or fifth atrial beat is not conducted. (Rushmer, 1976, Fig. 8-24, p. 313.)

cases of SA nodal failure or at very low SA nodal firing rates. Thus, the model discussed here is valid at high stimulus rates (appropriate for AV nodal block) but not at low stimulus rates.

Input to the AV node comes from the action potential propagating through the atria from the SA node. The AV node experiences a periodic, time-varying potential, say $\phi(t)$. Firing occurs if the input signal reaches the threshold. Therefore, at the nth firing time, denoted by t_n,

$$\phi(t_n) = \theta(t_n). \tag{12.145}$$

Subsequent to firing, the threshold evolves according to

$$\theta(t) = \theta_0 + [\theta(t_n^+) - \theta_0]e^{-\gamma(t-t_n)}, \qquad t > t_n. \tag{12.146}$$

Note that $\theta \to \theta_0$ as $t \to \infty$, and thus θ_0 denotes the base value of the threshold. Further, $\theta = \theta(t_n^+)$ at $t = t_n$, and thus $\theta(t_n^+) - \theta(t_n^-)$ denotes the jump in the threshold caused by the firing of an action potential. To complete the model we must specify $\theta(t_n^+)$. The important feature of $\theta(t_n^+)$ is that it must have some memory, that is, depend in some way on $\theta(t_n^-)$. Therefore, we take

$$\theta(t_n^+) = \theta(t_n^-) + \Delta\theta. \tag{12.147}$$

The simple choice used here is to take $\Delta\theta$ a constant. However, consideration of the threshold in FitzHugh–Nagumo models suggests that (in a more general model) $\Delta\theta$ could also be some decreasing function of $\theta(t_n^-)$, i.e., $\Delta\theta = \Delta\theta(\theta(t_n^-)) = \Delta\theta(\phi(t_n))$, since $\phi(t_n) = \theta(t_n^-)$.

Now we can find the next firing time as the smallest solution of the transcendental equation

$$\phi(t_{n+1}) = \theta_0 + [\theta(t_n^+) - \theta_0] e^{-\gamma(t_{n+1}-t_n)}. \tag{12.148}$$

Equation (12.148) can be rearranged into an equation of the form

$$F(t_{n+1}) = F(t_n) + \Delta\theta e^{\gamma t_n} = G(t_n), \tag{12.149}$$

where

$$F(t) = (\phi(t) - \theta_0)e^{\gamma t}. \tag{12.150}$$

Plots of typical functions $F(t)$ and $G(t)$ are shown in Fig. 12.35. Here we have taken $\phi(t) - \theta_0 = \sin^4(\pi t)$. The dashed lines in this figure follow a few iterates of the map.

The key observation is that the map $t_n \mapsto t_{n+1}$ as defined by (12.149) is the lift of a circle map. Before proceeding with this example, we give a brief introduction to the theory of circle maps.

The first application of circle maps to the behavior of neurons was given by Knight (1972). More detailed discussions of maps and chaos and the like with application to a wide array of biological problems can be found in Glass and Mackey (1988), Glass and Kaplan (1995), and Strogatz (1994).

Circle maps

A circle map is a map of the circle to itself, $f : S^1 \to S^1$, but it is often easier to describe a circle map in terms of its *lift* $F : R \to R$, where F is a monotone increasing function and $F(x + 1) = F(x) + 1$. The two functions f and F are related by

$$f(x) \equiv F(x \bmod 1) \bmod 1. \tag{12.151}$$

(For convenience we normalize the circumference of the circle to be of length 1, rather than 2π.)

The primary challenge from a circle map is to determine when the behavior is periodic and to understand the possible nonperiodic behaviors. The simplest periodic behavior is a period 1 solution, say a point x_0 for which $F(x_0) = x_0 + 1$. This orbit is also said to have *rotation number* one because it rotates around the circle once on each iterate. This is also described as 1:1 phase locking between input and output. A more complicated periodic orbit would be a point x_0 and its iterates x_j with the property that $x_n = x_0 + m$. In other words, the iterates rotate around the circle m times in n iterates. The rotation number is m/n, and there is $m : n$ phase locking, with m output cycles for every n input cycles.

The key fact to understand is that the asymptotic behavior of a circle map is characterized by its *rotation number*, ρ, defined by

$$\rho = \lim_{n \to \infty} \frac{F^n(x)}{n}. \tag{12.152}$$

$F^n(x)$ is the nth iterate of the point x,

$$F^n(x) = F(F^{n-1}(x)), \tag{12.153}$$

where $F^0(x) = x$ and $F^1(x) = F(x)$.

If F is a continuous function, the rotation number has the following properties:

1. ρ exists and is independent of x.

2. ρ is rational if and only if there are periodic points.

3. If ρ is irrational, then the map F is equivalent to a rigid rotation by the amount ρ.

4. If there is a continuous family of maps F_λ, then $\rho(\lambda)$ is a continuous function of λ. Furthermore, if F_λ is a monotone increasing function of λ, then ρ is a nondecreasing function of λ.

5. Generically, if $\rho(\lambda)$ is rational at some value of λ_0, it is constant on an open interval containing λ_0.

Here is what this means in practical terms. Since ρ exists, independent of x, all orbits have the same asymptotic behavior, orbiting the circle at the same rate, independent of initial position. If ρ is rational, the asymptotic behavior is periodic, whereas if ρ is irrational, the motion is equivalent to a rigid rotation. In this case, the behavior is aperiodic, but not complicated, or "chaotic." There are no other types of behavior for a continuous circle map.

The last two features of ρ make the behavior of the orbits so unusual, being a function that is continuous, monotone nondecreasing (if F_λ is an increasing function of λ), yet locally constant at all the rational levels. Such a function is called the *Devil's staircase*. Notice that if ρ is rational on an open interval of parameter space, then phase locking is robust.

The reason for this robustness is that a periodic point with $\rho = p/q$ corresponds to a root of the equation $F^q(x) - x = p$, and roots of equations are generally, but not always, robust, or transversal (i.e., the derivative of $F^q(x) - x$ at a root is nonzero). If a root is transversal, then arbitrarily small perturbations to the equation do not destroy the root, and it persists for a range of parameter values. However, the existence of a periodic point is no guarantee that it is robust. For example, the simple shift $F(x) = x + \lambda$ has periodic points whenever λ is rational, but these periodic points are never isolated or robust.

A detailed exposition on continuous circle maps and proofs of the above statements can be found in Coddington and Levinson (1984, chapter 17).

Now we attempt to apply this theory of circle maps to (12.149). Notice that this is indeed the lift of a circle map, since if t_n and t_{n+1} satisfy (12.149), then so do $t_n + T$ and $t_{n+1} + T$. To find a circle map, we let k_n be the largest integer less than t_n/T and define $\psi_n = (t_n - k_n T)/T$. In these variables the map (12.149) can be written as

$$f(\psi_{n+1}) = (f(\psi_n) + \Delta\theta e^{\gamma T \psi_n})e^{\gamma T \Delta k_n}, \tag{12.154}$$

where

$$f(\psi) = (\Phi(\psi) - \theta_0)e^{\gamma T \psi}, \qquad \Phi(\psi) = \phi(T\psi), \tag{12.155}$$

and $\Delta k_n = k_{n+1} - k_n$.

We can make a few observations about the map $\psi_n \mapsto \psi_{n+1}$. First, and most disconcerting, the map is not continuous. In fact, it is apparent that there are values of t on the unit interval that can never be firing times. For t to be permitted as a firing time it must be the first point at which $F(t)$ reaches the level $G(t_n)$, i.e., the first time that the threshold is reached. At such a point, $F'(t) \geq 0$. Since there are regions for which $F'(t) < 0$, which can therefore never be firing times, this is a map of the unit interval *into*, but not onto, itself. However, the map $t_n \mapsto t_{n+1}$ is order preserving, since $G(t)$ is increasing whenever $F(t)$ is increasing.

Since the entire unit interval is not covered by the map, it is only necessary to examine the map on its range. Examples of the map $\psi_n \mapsto \psi_{n+1}$ are shown in Figs.
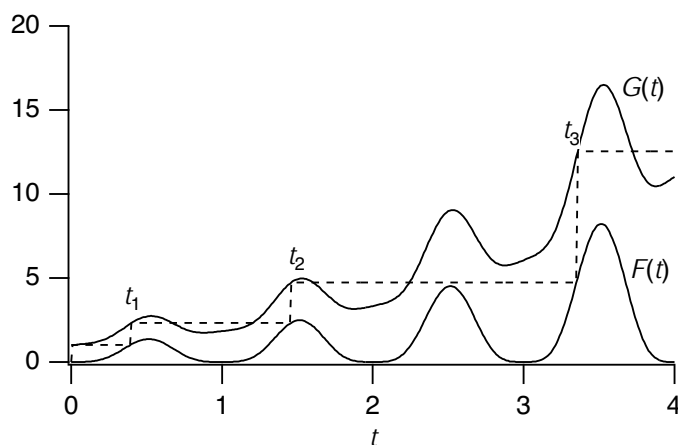
Figure 12.35: Plot of the functions $F(t)$ and $G(t)$ with $\Delta\theta = 1.0$, $\gamma = 0.6$.

12.36–12.39. Here we have plotted the map only on the attracting range of the unit interval. These show important and typical features, namely that the map consists of either one or two continuous, monotone increasing branches. The first branch, with values above the one-to-one curve, corresponds to firing in response to the subsequent input (with $k_{n+1} = k_n + 1$), and the second, with values below the one-to-one curve, corresponds to firing after skipping one beat (with $k_{n+1} = k_n+2$). The skipped beat occurs because when the stimulating pulse arrives, it is subthreshold and so does not evoke a response.

The sequence of figures in Figs. 12.36–12.39 is arranged according to decreasing values of γT. Note that as γ decreases, the rate of recovery from inhibition decreases. For γT sufficiently large, there is a unique fixed point, corresponding to firing in 1:1 response to the input signal. This makes intuitive sense, for when γ is large, the recovery from inhibition is fast, and thus the AV node can be driven at the frequency of the SA node. For large γT the map is relatively insensitive to changes in parameters. As γT decreases, the first branch of the map increases and the value of the fixed point increases, corresponding to a somewhat delayed firing. Furthermore, because the slope of the map in the vicinity of the fixed point is close to 1, the fixed point is sensitive to changes in parameter values (depicted in Fig. 12.37), corresponding to type I AV block.

As the parameter γT is decreased further, the fixed point is lost and a second branch to the map appears (as in Fig. 12.38). Iterations show that subsequent firings become later and later in the input cycle until one beat is skipped, followed by a firing that is relatively early in the input cycle. For this region of parameter space, the map replicates the Wenckebach pattern.

Finally, as γT decreases further, the second branch "slides over" to the left and eventually intersects the one-to-one line, yielding a fixed point. This fixed point corresponds to a periodic pattern of one skipped beat for each successful firing, a two-to-one pattern, and replicates type II AV block.
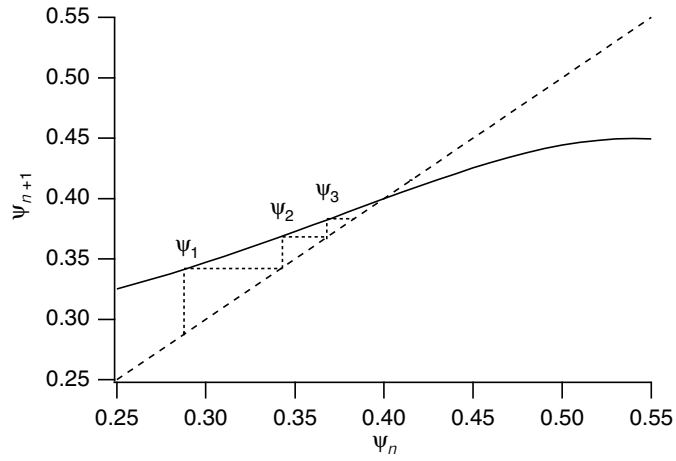
Figure 12.36: Plot of the map $\psi_n \mapsto \psi_{n+1}$ with $\Delta\theta = 1.0$, $\gamma T = 0.8$.
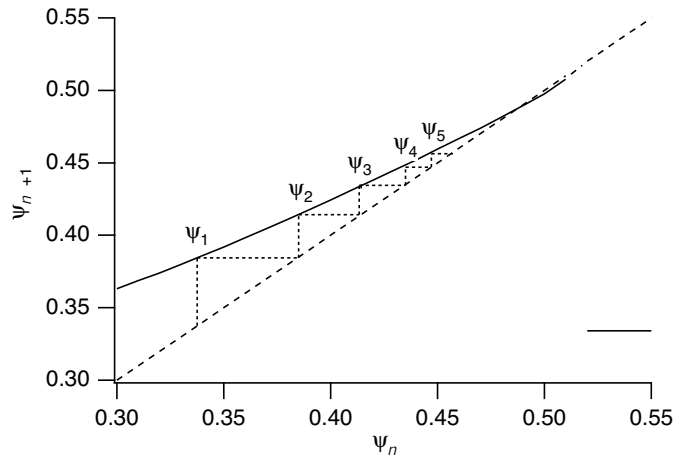
Figure 12.37: Plot of the map $\psi_n \mapsto \psi_{n+1}$ with $\Delta\theta = 1.0$, $\gamma T = 0.695$.
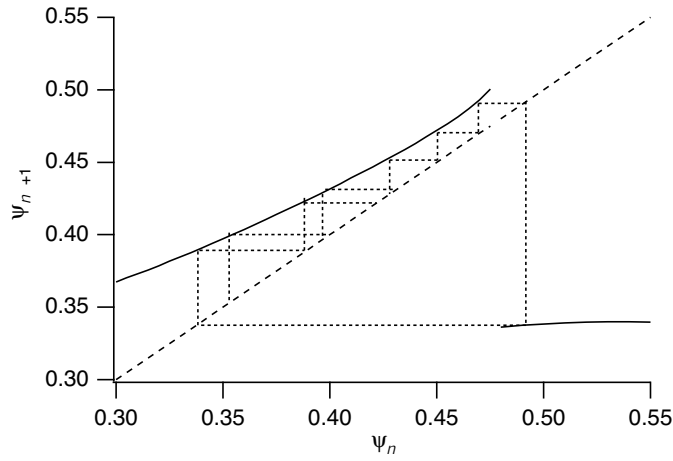
Figure 12.38: Plot of the map $\psi_n \mapsto \psi_{n+1}$ with $\Delta\theta = 1.0$, $\gamma T = 0.67$.
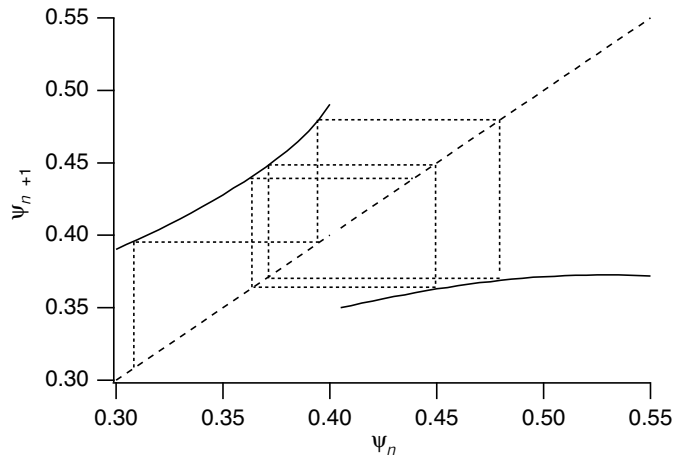
Figure 12.39: Plot of the map $\psi_n \mapsto \psi_{n+1}$ with $\Delta\theta = 1.0$, $\gamma T = 0.55$.

The behavior of the map in the region with no fixed point can be described by the rotation number. For maps of the type (12.149) the rotation number can be defined, analogously to our earlier definition, by

$$\rho = \lim_{n \to \infty} \frac{t_n}{nT}. \tag{12.156}$$

The following features of the rotation number ρ can be verified (Keener, 1980a, 1981):

1. ρ exists and is independent of initial data.

2. ρ is a monotone decreasing function of γT.

3. ρ attains *every* rational level between 0 and 1 on an open interval of parameter space.

For continuous circle maps, it is not certain that every rational level is attained on an open interval of parameter space.

The main consequence of this result is that between 1:1 phase locking and 2:1 AV block, for every rational number there is an open interval of γT on which the rotation with that rational number is attained.

12.4.3   Reentrant Arrhythmias

A reentrant arrhythmia is a self-sustained pattern of action potential propagation that circulates around a closed path, reentering and reexciting tissue as it goes.

The simplest reentrant pattern is one for which the path of travel is one dimensional. These were first studied by Mines (1914) when he intentionally cut a ring of tissue from around the superior vena cava and managed to initiate waves that traveled in only one direction.

A classic example of a one dimensional reentrant rhythm of clinical relevance is one in which an action potential circulates continuously between the atria and the ventricles through a loop, exiting the atria through the AV node and reentering the atria through an *accessory pathway* (or vice versa). Since conduction through the AV node is quite slow compared to other propagation, an accessory pathway that circumvents the AV node usually reveals itself on the ECG by an early, broad deflection of the QRS complex (Fig. 12.40). This deflection is broadened because it depicts propagation through myocardial tissue, which is slow compared to normal propagation through the Purkinje network. This is known clinically as Wolff–Parkinson–White (WPW) syndrome, and is life-threatening if not detected and treated. However, because the associated reentrant rhythm travels essentially along a one dimensional pathway (at least at two points), WPW syndrome is usually curable, as cardiac surgeons can use localized radio frequency waves to burn and permanently obliterate the accessory pathway, restoring a normal single pathway conduction and a normal ECG, and preventing the formation of a closed loop.

Reentrant patterns which are not constrained to a one dimensional pathway are much more problematic. The two primary reentrant arrhythmias of this type are
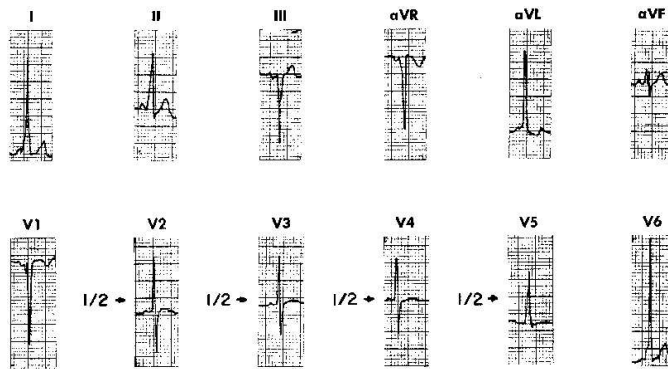
Figure 12.40: Twelve-lead ECG recording of Wolff–Parkinson–White syndrome, identifiable by the shortened P–Q interval (because the AV delay is circumvented) and the slowed QRS upstroke, particularly noticeable in leads II, aVR, and V6. (Rushmer, 1976, Fig. 8-47, p. 339; originally from Guneroth, 1965).

tachycardia and *fibrillation*. Both of these can occur on the atria (*atrial tachycardia* and *atrial fibrillation*) or in the ventricles (*ventricular tachycardia* and *ventricular fibrillation*). When they occur on the atria, they are not immediately life-threatening because the disruption of blood flow is not catastrophic (although over a long term they can cause strokes). However, when they occur on the ventricles, they are life-threatening. Ventricular fibrillation is fatal if it is not terminated quickly. Symptoms of ventricular tachycardia include dizziness or fainting, and sometimes rapid "palpitations."

Tachycardia is often classified as being either *monomorphic* or *polymorphic*, depending on the assumed morphology of the activation pattern. Monomorphic tachycardia is identified as having a simple periodic ECG, while polymorphic tachycardia is usually quasiperiodic, apparently the superposition of more than one periodic oscillation. A typical example of a polymorphic tachycardia is called *torsades de pointes*, and appears on the ECG as a rapid oscillation with slowly varying amplitude (Fig. 12.41). A vectorgram interpretation suggests a periodically rotating mean heart vector.

It is currently believed that the spatio-temporal wave pattern associated with *atrial flutter* is a spiral wave. Because the ventricles are three dimensional, a pattern that appears on the ventricular surface to be spiral-like must, in fact, correspond to a three dimensional reentrant wave, a scroll-wave. A three-dimensional view of a (numerically computed) scroll wave, corresponding to monomorphic V-tach is shown in Fig. 12.42.

Stable monomorphic ventricular tachycardia is rare, as most reentrant tachycardias degenerate into fibrillation. The likely reason for this is that there are a number of potential instabilities, although the mechanism of these instabilities has not been decisively determined. Some possibilities (including the APD alternans instability) are discussed by a number of authors (Courtemanche and Winfree, 1991; Karma, 1993, 1994; Panfilov and Holden, 1990; Panfilov and Hogeweg, 1995; Bar
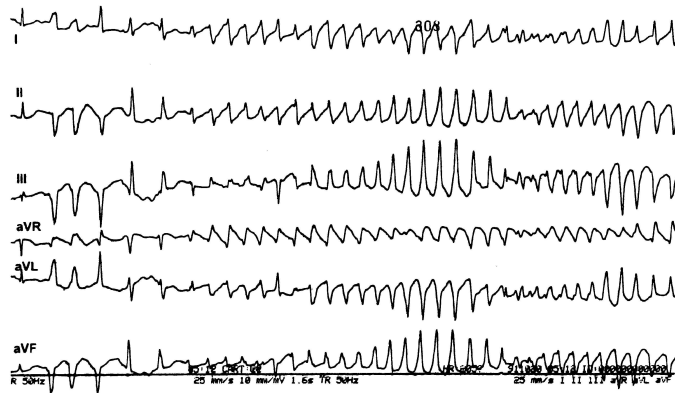
Figure 12.41: A six-lead ECG recording of *torsades de pointes*. (Zipes and Jalife, 1995, Fig. 79-1, p. 886.)
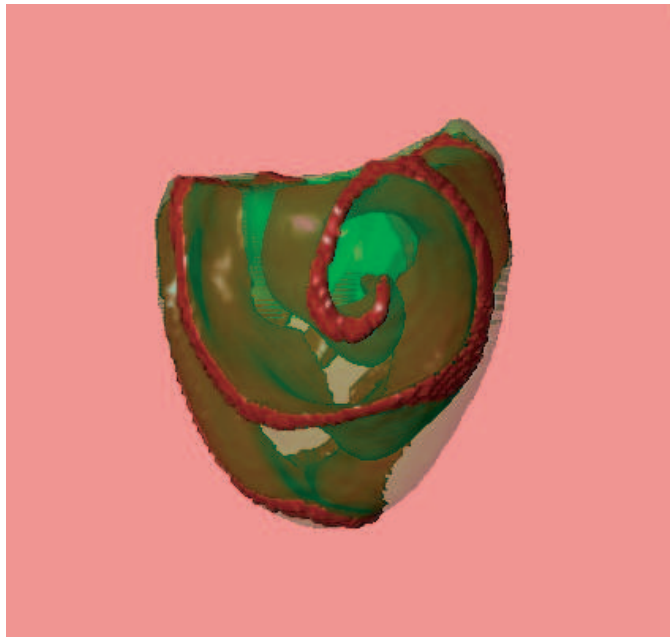
Figure 12.42: Numerically computed scroll wave in ventricular muscle. (Panfilov and Keener, 1995, p. 685, Fig. 3a.)
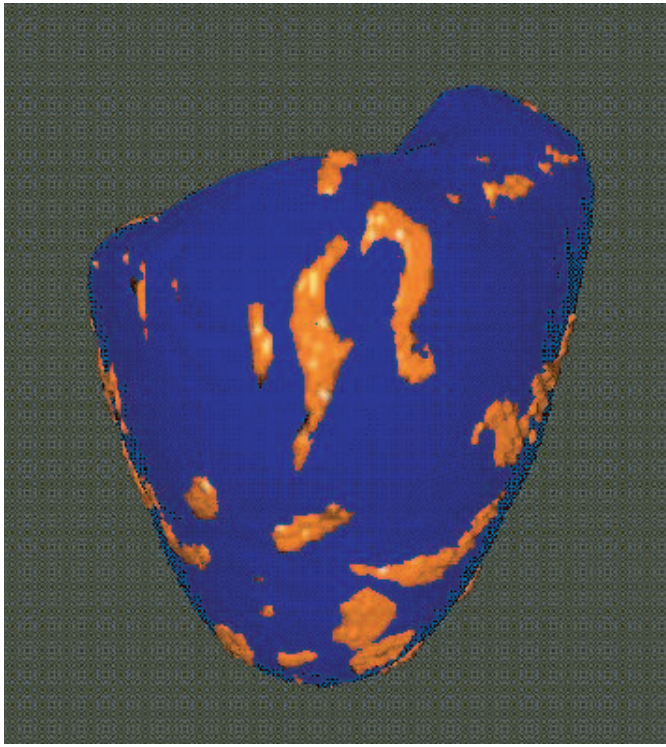
Figure 12.43: Surface view of fibrillatory reentrant activity in the ventricles (computed by A. Panfilov).

and Eiswirth, 1993; Courtemanche et al., 1993). It is currently believed that stable monomorphic V-tach can be maintained only by special physical structures in the cardiac tissue, such as a small conducting pathway through otherwise damaged tissue.

Fibrillation is believed to correspond to the presence of many reentrant patterns moving throughout the ventricles in continuous, perhaps erratic, fashion, leading to an uncoordinated pattern of ventricular contraction and relaxation. A surface view of a (numerically computed) fibrillatory pattern is shown in Fig. 12.43.

There is an extensive literature devoted to the mathematical study of reentrant patterns. The first such theory was due to Wiener and Rosenblueth (1946) who studied a wave circulating around an inexcitable obstacle using a simple automaton model of excitable media. More recent studies have focussed on the behavior of waves in two and three dimensional media using systems of reaction diffusion equations. An interesting consequence of these studies is that it has been shown that a reentrant pattern need not have a physical obstacle around which to circulate, but that there can be a spiral core that is maintained by the dynamics of the surrounding pattern, or with scroll waves, a central filament around which to circulate. This was an important observation because before this, it was generally assumed that

reentrant patterns could only rotate around some physical or anatomical obstacle. Now there is ample experimental confirmation that anatomical obstacles are not necessary to maintain reentrant patterns.

Perhaps the most important mathematical observation about reentrant rhythms was made by Art Winfree (1987) who recognized that reentrant patterns could be characterized by their phase singularities. For any oscillatory dynamical system, one can define a phase as follows. Identify two oscillatory state variables that are not synchronous, i.e., whose extremal values occur at different times, and a phase plot of one against the other will be a closed loop, topologically equivalent to a circle. In fact, one can map the closed loop continuously to a circle, and define the phase of a point on the loop with the angle of the circle to which the point is mapped. Now this map can be continuously extended to the entire plane with the exception of a single point, the phaseless point, or phase singularity. This phaseless point is not unique because it depends on how one chooses the phase map, however, it is certain to exist. One natural way to define the phase ϕ is to take

$$\phi = \arctan\left(\frac{y - y^*}{x - x^*}\right), \tag{12.157}$$

where (x, y) is a point in the phase space, and (x^*, y^*) is a point centrally located within the closed loop.

For a spatially extended system, one can use the phase map to identify a phase for each point in space. However, if the oscillatory pattern is reentrant, that is, if it is maintained by its spatial connectivity, and is not the result of autonomous cellular oscillation, there must be phaseless points. The reason for this is as follows. A feature of an oscillatory pattern is that the variables go through one complete rotation of the phase per oscillation. For a reentrant pattern, all phases are attained somewhere in space at all times, and there is a continuous closed path in space along which the variables cycle through all the phases. However, just as there is a phaseless point at the center of all clocks, so there must be a phaseless point somewhere inside this continuous closed path that cycles through all phases. These phaseless points correspond to the center of spirals in two dimensions and the filaments of scrolls in three dimensions. Of course, there is no requirement that phaseless points be fixed in space and time, but there are precise rules regulating their creation and destruction. Phaseless points in space can be located by noticing that the closed line integral of the gradient of phase is a non-zero integer multiple of 2π if the path P encloses a phase singularity,

$$\oint_P \nabla\phi \cdot d\vec{r} = \begin{cases} 2\pi n, & n = \pm 1, \pm 2, \dots, \text{if } P \text{ encloses a phase singularity}, \\ 0, & \text{otherwise} \end{cases}$$
$$\tag{12.158}$$

Phaseless points are now well-established experimentally. There are currently two ways that experimentalists observe phaseless points in cardiac tissue. The first uses the potential $V(x, t)$ and its delay $V(x, t - \tau)$ for some fixed delay τ (Iyer and Gray, 2001). More recently, with the advent of the ability to simultaneously measure potential and intracellular Ca^{2+} concentration with flourescent dyes, experimentalists are able to use these two variables to create a phase map.

How to Initiate a Reentrant Arrhythmia

While there is a lot of experimental and theoretical work to understand the dynamics of reentrant tachycardias and fibrillation, from a clinical point of view this is somewhat less important. It is of much greater clinical importance to understand how reentrant arrhythmias are formed, how to prevent their formation, or how to terminate them after they have formed.

The problem of how to initiate a reentrant pattern is easily understood by considering two analogies. "The Wave" (often called a "Mexican Wave" due to it first gaining a large international audience at the 1986 World Cup in Mexico City) is a peculiar behavior of football crowds around the world, in which individuals suddenly rise from their seats, wave their arms in the air and then sit down (Farkas et al., 2002). Viewed from an individual perspective there is nothing striking about this behavior (odd, yes, but striking, no). However, the collective behavior is coordinated in such a way that there appears to be a wave propagating around the stadium several times before the participants get weary or the novelty wears off.

If this behavior is viewed as analogous to an excitable system, one sees the resting phase (seated and of sound mind), or excited (standing and waving frantically). If one further assumes that no individual fan goes into the excited phase without stimulus from an excited neighbor, then one has a model of an excitable medium. Of course, in the USA the cheerleaders play the role of an autonomous oscillator that can become excited without provocation (and in some cases, with little cause).

Now, imagine what happens when the cheerleaders wish to initiate a wave. They wave their arms and cheer and in response everyone nearby does the same, initiating a wave that spreads radially outward from its source. But this does not initiate a self-maintained reentrant wave. Some additional ingredient is necessary, namely something to break the symmetry of spread, so that propagation is in one direction but not the other.

To consider a second analogy, suppose there was a large lake surrounded by very fast growing grass, and one wanted to start a grass fire that circulated around the lake continuously. Normally, if one starts a grass fire, the fire will spread, going around the lake in both directions and burning out when the flames meet on the opposite side of the lake. However, to initiate a fire that circulates continuously, two additional conditions must be met. First, there must be a breaking of the symmetry so that the fire initially spreads in only one direction, and second, the lake must be large enough so that by the time the fire has gone around the lake, the grass that was first burned has regrown sufficiently so that it is ready to burn again.

These analogies are actually quite good at describing the problem of initiation of a reentrant pattern in cardiac tissue: there must be some kind of initial stimulus, it must occur at a time and place so that propagation is not symmetric, and there must be some geometrical property that allows the wave to return to reinitiate itself. In a region with no anatomical obstacle around which to circulate, the geometrical problem (actually a topological problem) is how to create a phase singularity.

A simple mathematical model to show how this scenario might work is as follows. Suppose there is a one dimensional closed loop conducting pathway of length L, that is stimulated by an external pacemaker (Fig. 12.44). Suppose also that somewhere in the vicinity of the stimulus site, there is a region of one way block. We know that

such regions can exist, for example, at points of fiber arborization (Section 12.3.2).

Suppose that the external pacemaker fires with period T. We define the instantaneous frequency of stimulus as $\Delta T_{n+1} = t_{n+1} - t_n$, where t_n is the nth firing time of the stimulus site. Now we take a simple kinematic description of propagation along the one-way path and suppose that the speed of propagation on the path is a function of the instantaneous period, $c = c(\Delta T)$. (Typically, c is an increasing function of ΔT, since the longer the recovery time, the faster the speed of propagation.) Then the travel time around the one-way loop is $\frac{L}{c(\Delta T)}$. In cardiac tissue, the speed of an action potential is on the order of 0.5 m/s, so that travel time around the loop (perhaps a few centimeters in length) is much shorter than the period of external stimulus. Thus, the wave going around the loop typically returns to the stimulus site long before the next external stimulus arrives (i.e., we assume that $L/c < T$). If the travel time is smaller than the absolute refractory period T_r of the cells, the stimulus has no effect, and the cells must await the next external stimulus before they fire, so that

$$\Delta T_{n+1} = t_{n+1} - t_n = T \qquad (12.159)$$

if $\frac{L}{c(\Delta T_n)} < T_r$. On the other hand, if the travel time is larger than the T_r but smaller than T, then it stimulates the cells at the stimulus site and initiates another wave around the loop. Thus, the instantaneous period at the stimulus site is

$$\Delta T_{n+1} = t_{n+1} - t_n = \frac{L}{c(\Delta T_n)}, \qquad (12.160)$$

provided that $T > \frac{L}{c(\Delta T_n)} > T_r$.

With this information, we can construct the one dimensional map $\Delta T_n \mapsto \Delta T_{n+1}$ (shown in Fig. 12.45). There are obviously two branches for this map (shown as solid curves). Of interest are the fixed points of this map, corresponding to a periodic pattern of stimulus. The fixed point on the upper branch corresponds to the normal stimulus pattern from the external source, whereas the fixed point on the lower branch corresponds to a high-frequency reentrant pattern. The key feature of this map is that there is hysteresis between the two fixed points. In a "normal" situation (Fig. 12.45A), with L small and T large, the period is fixed at the external stimulus period T. However, as L increases or as T decreases, rendering $L > T_r c(\delta T_n)$, there is a "snap" onto the smaller-period fixed point, corresponding to initiation of a reentrant pattern (Fig. 12.45B). The pernicious nature of the reentrant pattern is demonstrated by the fact that increasing the period of the external stimulus back to previous levels does not restore the low-frequency pattern—the iterates of the map stay fixed at the lower fixed point, even though there are two possible fixed points. This is because the circulating pattern acts as a retrograde source of high-frequency stimulus on the original stimulus site, thereby masking its periodic activity.

Note that there are a number of ways that this reentrant pattern might be initiated. First, there might be a growing diseased or infarcted central region which leads to a gradual increase in L, initiating the reentrant pattern while keeping T fixed. On the other hand, a diseased central region may exist but remain static (L fixed), and the reentrant pattern is initiated following a decrease in T, for example, during strenuous exercise. Thus, a static one-way loop acts like a "period bomb" (rather than a time bomb), ready to go off whenever the period is sufficiently low.
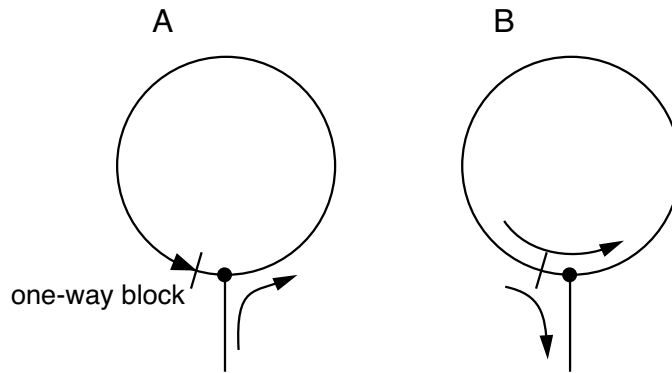
Figure 12.44: Diagram of a conducting path with one-way block, preventing conduction from right to left. A: Conduction of a stimulus around the loop until it encounters refractoriness and fails to propagate further. B: Conduction of a reentrant pattern circulating continuously around the loop and exiting via the entry pathway on every circuit.
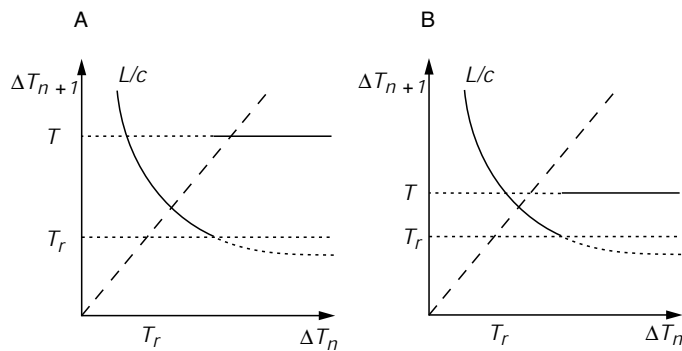
Figure 12.45: Next-interval map for a one-way conducting loop in two cases. A: With T large, so that two stable steady solutions exist. B: With T small, so that the only steady solution corresponds to reentry.

While this simple model of reentry illustrates the basic problem, it probably has little to do with most real reentrant patterns. For example, since reentrant patterns do not require central anatomical obstacles, there must be some way that these patterns can arise in two and three dimensional tissue without a preexisting central anatomical obstacle, or fixed region of one-way conduction block.

One of the earliest mathematical models for initiation of reentrant patterns and fibrillation to address this issue was due to Moe et al. (1964). Theirs was a finite state automaton model in which individual cells had three possible states, resting, excited and refractory, rules for how cells moved through these states in discrete time steps, and rules for how the excited state was propagated from cell to cell. The important feature of their model was that return to rest from the refractory state was spatially and randomly variable. As the spatial variability of the return from refractoriness increased, it was observed that there was an increased propensity for propagated action potentials to break up into multiple reentrant patterns reminiscent of fibrillation.

Finite state automaton models of excitable media have a rich history. They are easy to describe and understand and they are easy to simulate. However, it is important to recognize that these models are analogies to cardiac tissue, and do not have a physiological basis; it is possible (in fact, likely) that some phenomena observed in finite state automata do not occur in realistic ionic based models, and vice versa. In fact, the Moe et al. model is beset with significant difficulties and is probably not an explanation with clinical relevance. One of the difficulties of the model is that it does not employ electrotonic coupling of cells, and it is known that the crucial feature of the model, namely dispersion of refractoriness, is greatly affected by electrotonic coupling. As we saw with SA nodal cells, the effect of electrotonic coupling is to synchronize behavior, and this tends to mask cell-to-cell differences of recovery properties as well.

Nonetheless, the dispersion-of-refractoriness hypothesis, substantially modified, remains one of the best known folklore explanations for fibrillation onset in the cardiology community. Indeed, some form of dispersion of refractoriness, but not necessarily structural, is required for initiation of reentry (Weiss et al., 2006).

One of the challenges in this business is that it is difficult to design experiments in which reentrant arrhythmias are initiated in a way that is clinically relevant. It is known, however, that reentrant arrhythmias can be initiated intentionally by the correct application of point stimuli. This procedure has been described beautifully by Winfree (1987), with many gorgeous color plates, so here we content ourselves with a shorter, less colorful, verbal description of the process.

When a current is injected at some point to resting cardiac tissue, cells in the vicinity of the stimulus are depolarized (recall Fig. 12.23). If the stimulus is of sufficient amplitude and duration, the cells closest to the stimulating electrode may receive a superthreshold stimulus and become excited. Cells further away from the stimulus site receive a subthreshold stimulus, so they return to rest when the stimulus ends. At the border between subthreshold and superthreshold stimulus, a wave front is formed.

Once a transition front is formed, the local conditions of the tissue determine whether the wave moves forward or backward. That is, if the undisturbed medium

is sufficiently excitable, and the initially excited domain is sufficiently large, the wave front moves outward into the unexcited region. If, however, the unaffected medium is not excitable, but partially refractory, or the excited domain is too small, the wave front recedes and collapses.

If the stimulated medium is initially uniform, these two are the only possible responses to a stimulus. However, if the state of the medium in the vicinity of the stimulating electrode is not uniform, then there is a third possible response. Suppose, for example, that there is a gradual gradient of recovery so that a portion of the stimulated region is excitable, capable of supporting wave fronts (with positive wave speed) and the remaining portion of the stimulated region cannot support wave fronts, but only wave backs (i.e., fronts with negative speed). Then, the result of the stimulus is to produce both wave fronts and wave backs.

With a mixture of wave fronts and wave backs, a portion of the wave surface expands, and a portion retracts. Allowed to continue in this way, a circular (two-dimensional) domain evolves into a linked pair of spirals, and a spherical (three-dimensional) domain evolves into a scroll. If the domain is sufficiently large, these become self-sustained reentrant patterns.

In resting tissue with no pacemaker activity, two stimuli are required to initiate a reentrant pattern. The first is required to set up a spatial gradient of recovery (dispersion of refractoriness). Then, if the timing and location of the second is within the appropriate range, a single action potential that propagates in the backward, but not forward, direction can be initiated. This window of time and space is called the *vulnerable window* or *vulnerable period*. If the tissue mass is large enough or if there is a sufficiently long closed one-dimensional path, the retrograde propagation initiates a self-sustained reentrant pattern of activation.

The mechanism of this method of initiation of reentry is well-documented experimentally (Chen et al., 1988; Frazier et al., 1988; Frazier et al., 1989).

While the Winfree scenario reliably initiates reentry, it too lacks clinical relevance because of its reliance on external stimuli. In fact, the cause of the trigger event remains a total enigma. Currently, the most popular hypothesis is that the trigger event is ectopic activity known as Early After Depolarizations (EADs) or Delayed After Depolarizations (DADs). Space does not permit us to give a full description of these events. Suffice it to say that EADs and DADs are thought to be electrical events that are triggered by spontaneous Ca^{2+} release.

While EADs and DADs are universally viewed as proarrhythmic, it has proved difficult to demonstrate a true connection between these events and initiation of reentry. For example, a common level of ventricular ectopy in patients is 2 ectopic beats per minute, or ≈ 1 million ectopic beats per year. Yet sudden cardiac death episodes in these patients occur over months to years, not minutes. In fact, medication to reduce the rate of ectopic activity has actually proven to increase mortality.

In summary, it is known what must happen in order to initiate a reentrant arrhythmia. However, why or how this happens is, for all practical purposes, unknown.

Antiarrhythmic Drugs

We close this section on arrhythmias with a brief description of antiarrhythmic drugs. Antiarrhythmic drugs are agents that have some effect on the cardiac action potential at the cellular level. The most widely used classification scheme for antiarrhythmic drugs, known as the Vaughan Williams scheme, classifies a drug based on the primary cellular mechanism of its antiarrhythmic effect. There are five main classes in the Vaughan Williams classification of antiarrhythmic agents:

The class I antiarrhythmic agents interfere with Na^+ channels. Class I agents are further grouped by the specific effect they have on Na^+ channels, and the effect they have on cardiac action potentials.

Class Ia agents block the fast Na^+ channel. Blocking this channel depresses the phase 0 depolarization (thereby reducing the maximal upstroke velocity, V_{max}), which slows action potential conduction velocity. Agents in this class also cause decreased conductivity and increased refractoriness. Class Ia agents include quinidine, procainamide, and disopyramide.

Class Ib antiarrhythmic agents are Na^+ channel blockers with fast onset and offset kinetics, so that they have little or no effect at slower heart rates, and more effects at faster heart rates. These agents decrease V_{max} in partially depolarized cells with fast response action potentials, decreasing automaticity. They either do not change the action potential duration, or they may decrease the action potential duration. Class Ib agents include lidocaine, mexiletine, tocainide, and phenytoin.

Class Ic antiarrhythmic agents markedly depress the phase 0 depolarization (decreasing V_{max}). They decrease conductivity, but have a minimal effect on the action potential duration. Of the Na^+ channel blocking antiarrhythmic agents (the class I antiarrhythmic agents), the class Ic agents have the most potent Na^+ channel blocking effects. Class Ic agents include encainide, flecainide, moricizine, and propafenone.

Class II agents are beta blockers. They act by selectively blocking the effects of catecholamines at the β_1-adrenergic receptors, thereby decreasing sympathetic activity on the heart. Class II agents include esmolol, propranolol, and metoprolol.

Class III agents predominantly block K^+ channels, thereby prolonging repolarization. Since these agents do not affect the Na^+ channel, conduction velocity is not decreased. The prolongation of the action potential duration and refractory period, combined with the maintenance of normal conduction velocity, is proposed to prevent re-entrant arrhythmias. Class III agents include amiodarone, azimilide, bretylium, clofilium, dofetilide, and sotalol.

Class IV agents are slow Ca^{2+} channel blockers. They decrease conduction through the AV node. Class IV agents include verapamil and diltiazem.

Class V agents are those with other mechanisms, possibly unknown, and include digoxin and adenosine.

The history of antiarrhythmic drugs is interesting and yet tragic. One of the most interesting episodes in this saga was the CAST study (Cardiac Arrhythmia Suppression Test) which was supposed to be an 18 month study of certain type Ic antiarrhythmic drugs. Unfortunately, the test was suspended after only three months when it was realized that the patients receiving the drugs were dying from sudden cardiac death at a rate significantly higher than those receiving placebo.

In other words, the antiarrhythmic drugs were actually pro-arrhythmic. A similar result was found with d-sotolol, a class III antiarrhythmic drug (Waldo et al., 1996). It is now widely recognized that all but class II antiarrhythmic drugs have pro-arrhythmic potential.

This illustrates the important difference between understanding dynamics at the cellular level and understanding the mechanisms for onset and maintenance of spatio-temporal patterns. For example, type I antiarrhythmic drugs all block Na^+ channels thereby slowing depolarization. It might seem that this would make a tachy-arrhythmia less likely because the cells are less excitable. However, it is also the case that Na^+ channel block increases the chances of propagation failure at regions of resistive inhomogeneity, perhaps increasing the possibility of formation of reentrant patterns. Another proposal is that Na^+ channel blockers increase the size of the vulnerable window (Starmer et al., 1991; Starmer et al., 1992).

Similarly, type III antiarrhythmic drugs block K^+ channels, lengthening the action potential. One might think that this would also increase the required size of the tissue necessary to sustain a reentrant pattern. A lengthened action potential is identified clinically as Long QT (LQT) syndrome. Seven different genetic causes of LQT syndrome have been identified, while if it is induced by non-genetic factors, it is called acquired LQT syndrome. People with LQT syndrome, whether genetic or acquired, are now known to be at risk of sudden cardiac death. And while the mechanism by which LQT increases the risk of sudden cardiac death is completely unknown, it is clear that the simple cellular-based reasoning mentioned above has no explanatory power concerning how reentrant arrhythmias are affected by these drugs.

12.5   Defibrillation

Nearly everyone who has ever watched television knows something about defibrillation. They have probably seen medical dramas where the paramedic places paddles on the chest of a man who has unexpectedly collapsed, yells "Clear!" and then a jolt of electricity shakes the body of the victim. Mysteriously, the victim revives. Since they were first made in 1947, defibrillators have saved many lives, and the recent development of implantable defibrillators will no doubt extend the lives of many people who in a previous era would have died from their first heart attack. Implanted defibrillators have become the most often used and most successful treatment for people at high risk of reentrant arrhythmias. However, implantable defibrillators also have significant drawbacks. For example, when they discharge, it is extremely painful, with the consequence that up to 40% of implantees have high levels of anxiety leading to depression.

The goal of a defibrillator is clear. Since during fibrillation different regions of tissue are in different phases of electrical activity, some excited, some refractory, some partially recovered, the purpose of defibrillation is to give an electrical impulse that stimulates the entire heart, so that the electrical activity is once again coordinated and returns to rest as a whole to await the next normal SA nodal stimulus. Said another way, the purpose is to reset the phase of each cardiac cell so that all cells are in phase, and so that there are no remaining phase singularities.
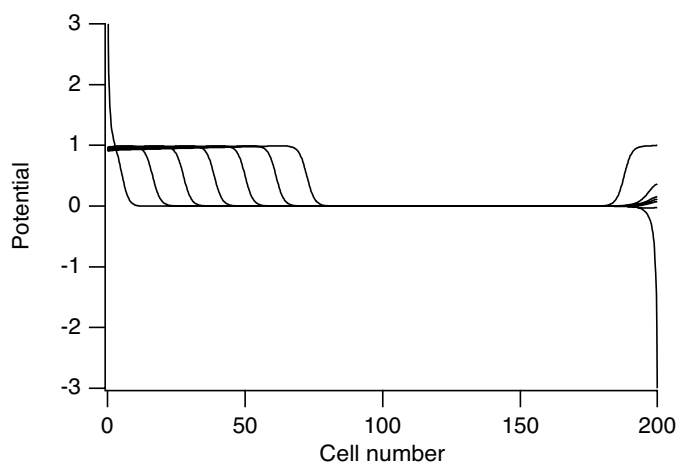
Figure 12.46: Response of a uniform cable to a stimulus of duration $t = 0.2$ applied at the ends of the cable. Traces shown start at time $t = 0.1$ and with equal time steps $\Delta t = 0.2$.

So the questions that need to be addressed are first, how does defibrillation work, and second, are there ways to improve the efficiency of defibrillators?

While it is known that defibrillation works (and is accomplished thousands of times daily around the world), the dilemma is that simple mathematical models fail to explain how this can happen, and indeed, seem to suggest that defibrillation shocks cannot achieve their goal.

To understand the dilemma, consider the numerical calculation shown in Fig. 12.46. Here is shown the result of applying a stimulus to the ends of a bidomain cable. The stimulus on the left is depolarizing and on the right is hyperpolarizing. On the left, a right-moving wave is initiated almost immediately, and on the right a left-moving wave is initiated via anode break excitation (see Chapter 5, Exercise 7). The dilemma is that local stimuli can only have local effects.

A similar conclusion is drawn from Fig. 12.47. Here is shown a periodic traveling wave on a one dimensional bidomain cable, traveling from left to right. (If the left and right ends were connected, this wave would circulate around the ring indefinitely.) What cannot be seen in this figure is that a large stimulus was applied at the ends of the cable between the first and second traces, simulating defibrillation. What can be seen from this figure is that the stimulus has essentially no effect on the traveling wave. This stimulus has no chance of defibrillating the cable, since the effects of the stimulus are localized in space.

The question, then, is how can defibrillation work, if only those regions close to the stimulating source are excited by the stimulus. The likely answer is that the medium into which the stimulus is applied has resistive inhomogeneities that are not accounted for in a uniform cable model.

To see the effect that resistive inhomogeneities might have, consider the effect of a current that is applied to a resistively inhomogeneous one dimensional strand
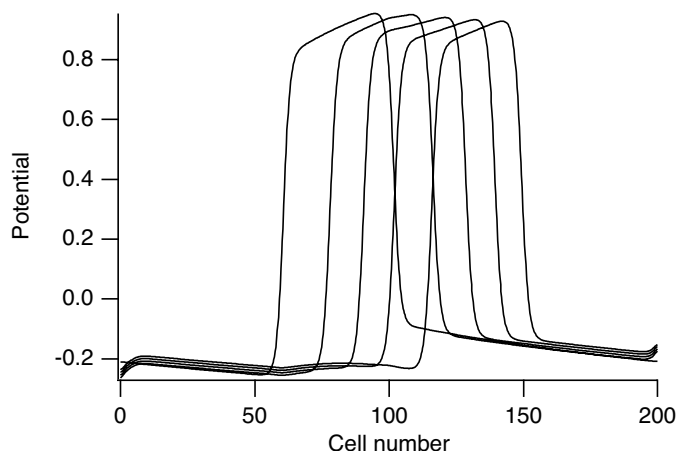
Figure 12.47: A traveling wave in a uniform cable following application of a stimulus at the ends of the cable at a time between the first and second traces.

of cardiac tissue of length L. We take the bidomain model equations (12.48), but now assume that the conductivities $\sigma_i = A_i/R_i$ and $\sigma_e = A_e/R_e$ are continuous but nonconstant to reflect the occurrence of resistive inhomogeneities. Then, the monodomain reduction for a one dimensional cable gives from (12.105)

$$p\left(C_m\frac{\partial V}{\partial t} - \frac{f(V)}{R_m}\right) = \frac{\partial}{\partial x}\left(\frac{\sigma_i\sigma_e}{\sigma_i + \sigma_e}\frac{\partial V}{\partial x}\right) - \frac{\partial}{\partial x}\left(\frac{\sigma_i}{\sigma_i + \sigma_e}\right)I(t), \qquad (12.161)$$

where $I(t)$ is the applied current. The important observation is that if σ_i or σ_e are nonconstant, the new term in (12.161) acts as a source term everywhere throughout the medium, even though the current $I(t)$ is applied locally. The effect of resistive inhomogeneity was already evident in Fig. 12.23. Similarly, in higher dimensions, if $\sigma_i(\sigma_i + \sigma_e)^{-1}$ is inhomogeneous in space, then when the total current i_t is non-zero, there are sources and sinks of transmembrane current in the interior of the domain.

It is useful to introduce dimensionless variables $\tau = t/\tau_m, y = x/\lambda_m$, where $\tau_m = C_m R_m, \lambda_m^2 = \sigma_e D R_m/p$, and we then obtain

$$V_\tau - f(V) = \left(\frac{d}{D}V_y\right)_y - J(\tau)\left(\frac{\Sigma_e d}{\sigma_e D}\right)_y, \qquad (12.162)$$

where $d = \sigma_e\sigma_i/(\sigma_i + \sigma_e)$, D^{-1} is the average value of d^{-1}, Σ_e^{-1} is the average value of σ_e^{-1}, and $J(\tau) = R_m\frac{D}{\Sigma_e}I(\tau)/(p\lambda_m)$. In addition, we have boundary conditions $V_y = -J(\tau)$ at $y = 0$ and at $y = Y = L/\lambda_m$.

There are potentially many different spatial scales for resistive inhomogeneities. At the cellular level, cells are connected by gap junctions and surrounded by extracellular space containing capillaries, collagen fiber, connective tissue, etc. In addition, myocytes are assembled into layers, with extensive interlaminal clefts between these layers (Caulfield and Borg, 1979; Robinson et al., 1983; Hooks et al.,

2002). At larger spatial scales, cells are organized into fibers, there is fiber branching and tapering, and the fiber orientation changes both in the longitudinal and in the transverse directions.

All of these resistive inhomogeneities produce virtual electrodes that affect the outcome of the defibrillation shock. However, here we focus on the effect of resistive inhomogeneities on the spatial scale of individual cells, and so, we suppose that σ_i and σ_e are periodic functions of y, with period $\epsilon = l/\lambda_m$, where l is the cell length. Specifically, we take

$$\sigma_j = \sigma_j\left(\frac{y}{\epsilon}\right), \qquad j = i, e, \tag{12.163}$$

with $\sigma_j(y)$ a function of period 1. Typically, ϵ is a small number, on the order of 0.1.

Now we are able to use homogenization arguments to find the effects of small scale inhomogeneities on the larger scale behavior. The result of a standard multiscale calculation gives (see Exercise 19).

$$V(z, \tau, \eta) = u_0(z, \tau, \epsilon) + \epsilon J(\tau) H(\eta) - \epsilon W(\eta)\frac{\partial u_0(z, \tau)}{\partial z}, \tag{12.164}$$

where $\eta = y/\epsilon$, $W(\eta)$ and $H(\eta)$ are periodic functions with

$$\frac{dW}{d\eta} = 1 - \frac{D}{d}, \qquad \frac{dH}{d\eta} = \frac{\Sigma_e}{\sigma_e} - \frac{D}{d}. \tag{12.165}$$

Furthermore the mean field $u_0(z, t)$ is governed by the equation

$$\frac{\partial u_0}{\partial \tau} - \overline{f\left(V(z, \tau, \eta)\right)} = \frac{\partial^2 u_0}{\partial z^2}, \tag{12.166}$$

where

$$\overline{f\left(V(z, \tau, \eta)\right)} = \int_0^1 f\left(V(z, \tau, \eta)\right) d\eta. \tag{12.167}$$

The interpretation of (12.166) is significant. While a current stimulus is being applied, the response at the cellular level has an effect that is communicated to the tissue on a macroscopic scale through the nonlinearity of the ionic currents. If the current amplitude is sufficiently large (say of order $\frac{1}{\epsilon}$), the effect can be quite significant. (If the ionic current $f(V)$ were linear, the applied stimulus would have no global effect, since then $\overline{f\left(V(z, \tau, \eta)\right)} = f(u_0)$.)

To get some insight into the dynamics while the stimulus is applied, we take the simple model for gap-junctional resistance

$$r_i = r_c + \frac{r_g}{l}\delta(\eta) \tag{12.168}$$

on the interval $0 \leq \eta < 1$, and periodically extended from there. Here, r_c is the intracellular cytoplasmic resistance per unit length, and r_g is the gap-junctional resistance per cell. The function $\delta(\eta)$ is any positive function with small support and area one unit that represents the spatial distribution of the gap-junctional resistance, for example, the Dirac delta function.
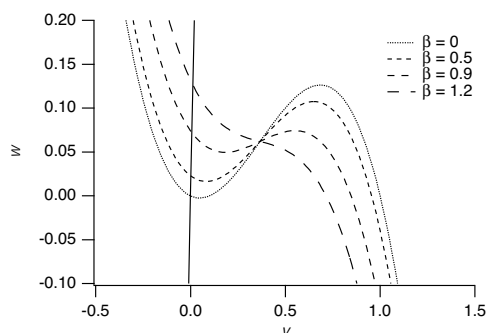
Figure 12.48: Nullclines for FitzHugh–Nagumo dynamics, $w = v(1 - v)(\alpha - v) + \frac{\beta^2}{12}(1 + \alpha - 3v), w = v/\gamma$, modified to include the effects of a current stimulus, for several values of β.

In the specific case that $\delta(\eta)$ is the Dirac delta function, we calculate that

$$W'(\eta) = R_g(1 - \delta(\eta)),\qquad (12.169)$$

where $R_g = \frac{r_g}{r_g + l(r_c + r_e)}$ is the fraction of the total resistance per unit length that is concentrated into the gap junctions. Here we used the fact that $r_i = 1/\sigma_i$. Then, $W(\eta)$ is given by

$$W(\eta) = R_g\left(\eta - \frac{1}{2}\right), 0 \le \eta < 1,\qquad (12.170)$$

$W(\eta + 1) = W(\eta)$, and $H(\eta) = W(\eta)$.

The function $W(\eta)$ is a *sawtooth function*, and according to (12.164), when a stimulus is applied, the membrane potential is the sum of two components, the sawtooth function $W(\eta)$ on the spatial scale of cells and $u(y, \tau)$ on the macroscopic scale of the tissue. The effect of the small-scale oscillatory behavior on the larger scale problem is found by averaging, whereby

$$\overline{F}(u, \beta) = \overline{f\left(V(z, \tau, \eta)\right)} = \int_{-\frac{1}{2}}^{\frac{1}{2}} f(u + \beta\eta)\, d\eta,\qquad (12.171)$$

and $\beta = R_g\epsilon(J(t) - \frac{\partial u}{\partial z})$. In other words, the effect of the current stimulus is to modify the ionic current through local averaging over the cell. The details of the structure of $W(\eta)$ are not important because they are felt only in an average sense. For the cubic model $f(V) = V(V - 1)(\alpha - V)$, $\overline{F}$ can be calculated explicitly to be

$$\overline{F}(V, \beta) = f(V) + \frac{\beta^2}{12}(1 + \alpha - 3V).\qquad (12.172)$$

A plot of this function for different values of β is shown in Fig. 12.48.

Before examining this model for its ability to explain defibrillation, we discuss the simpler problem of direct activation of resting tissue.
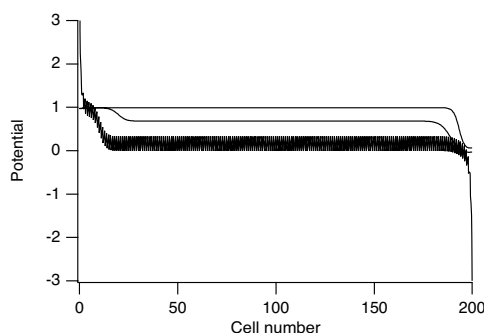
Figure 12.49: Response of a nonuniform cable with regularly spaced high-resistance nodes to a stimulus of duration $t = 0.2$ applied at the ends of the cable. The traces show the response at time $t = 0.15$, during the stimulus, and at times $t = 0.25, 0.35$ after the stimulus has terminated.

12.5.1 The Direct Stimulus Threshold

Direct activation (or field stimulation) occurs if all or essentially all of the tissue is activated simultaneously without the aid of a propagated wave front. According to the model (12.166), it should be possible to stimulate cardiac tissue directly with brief stimuli of sufficiently large amplitude.

A numerical simulation demonstrating how direct stimulation can be accomplished for the bistable equation is shown in Fig. 12.49. In this simulation a one dimensional array of 200 cells was discretized with five grid points per cell, and a brief, large current was injected at the left end and removed at the right end of the cable. In Fig. 12.46 is shown the response to the stimulus when the cable is uniform. Shown here is the membrane potential, beginning at time $t = 0.1$, and at later times with equal time steps $\Delta t = 0.2$. The stimulus duration was $t = 0.2$, so its effects are seen as a depolarization on the left and hyperpolarization on the right in the first trace. As noted above, a wave is initiated from the left from superthreshold depolarization, and a wave from the right is initiated by anode break excitation.

The same stimulus protocol produces a substantially different result if the cable has nonuniform resistance. In Fig. 12.49 is shown the response of the discretized cable with high resistance at every fifth node, at times $t = 0.15, 0.25$, and 0.35, with a stimulus duration of 0.2. The first curve, at time $t = 0.15$, is blurred because the details of the membrane potential cannot be resolved on this scale. However, the overall effect of the rapid spatial oscillation is to stimulate the cable directly, as seen from the subsequent traces.

To analyze this situation, note that since direct activation occurs without the benefit of propagation, it is sufficient to ignore diffusion and the boundary conditions and simply examine the behavior of the averaged ordinary differential equation

$$\frac{dV}{d\tau} = \overline{F}(V, \beta). \tag{12.173}$$

For any resting excitable system, it is reasonable to assume that $f(V) < 0$ for

$0 < V < \theta$, where θ is the threshold that must be exceeded to stimulate an action potential. To directly stimulate a medium that is initially at rest with a constant stimulus, one must apply the stimulus until $V > \theta$. The minimal time to accomplish this is given by the strength–duration relationship,

$$T = \int_0^\theta \frac{dV}{\overline{F}(V, \beta)}. \tag{12.174}$$

Clearly, this expression is meaningful only if β is sufficiently large that $\overline{F}(V, \beta) > 0$ on the interval $0 < V < \theta$. In other words, there is a minimal stimulus level (a threshold) below which the medium cannot be directly stimulated.

12.5.2   The Defibrillation Threshold

While its threshold cannot be calculated in the same way as for direct stimulus, the mechanism of defibrillation can be understood from simple phase-plane arguments. To study defibrillation, we must include the dynamics of recovery in our model equations. Thus, for purposes of illustration, we take FitzHugh–Nagumo dynamics

$$I_{\text{ion}}(v, w) = -f(v) + w, \tag{12.175}$$
$$w_\tau = g(v, w), \tag{12.176}$$

with $f(v) = v(v - 1)(\alpha - v)$, with parameters chosen so that reentrant waves are persistent. This could mean that there is a stable spiral solution, or it could mean that the spiral solution is unstable but some nonperiodic reentrant motion is persistent. Either way, our goal is to demonstrate that there is a threshold for the stimulating current above which reentrant waves are terminated.

The mechanism of defibrillation is easiest to understand for a periodic wave on a one dimensional ring, but the idea is similar for higher-dimensional reentrant patterns. For a one dimensional ring, the phase-portrait projection of a rotating periodic wave is a closed loop. From singular perturbation theory, we know that this loop clings to the leftmost and rightmost branches of the nullcline $w = f(v)$ and has two rapid transitions connecting these branches, and these correspond to wave fronts and wave backs.

According to this model, the effect of a stimulus is to temporarily change the v nullclines and thereby to change the shape of the closed loop. After the stimulus has ended, the distorted closed loop will either go back to a closed loop, or it will collapse to a single point on the phase portrait and return to the rest point. If the latter occurs, the medium has been "defibrillated."

Clearly, if β is small and the periodic oscillation is robust, then the slight perturbation is insufficient to destroy it. On the other hand, if β is large enough, then the change is substantial and collapse may result.

There are two ways that this collapse can occur. First, and easiest to understand, if the nullcline for nonzero β is a monotone curve (as in Fig. 12.48 with $\beta = 1.2$), then the open loop collapses rapidly to a double cover of the single curve $w = \overline{F}(v, \beta)$, from where it further collapses to a single point in phase space. For the specific cubic model, this occurs if $\beta^2 > \frac{4}{3}(1 - \alpha + \alpha^2)$.

The v nullcline need not be monotone to effect a collapse of the periodic loop. In fact, as β increases, the negative-resistance region of the nullcline becomes smaller, and the periodic loop changes shape into a loop with small "thickness" (i.e., with little separation between the front and the back) and with fronts and backs that move with nearly zero speed. Indeed, if the distorted front is at a large enough w "level" (in the sense of singular perturbation theory), it cannot propagate at all and stalls, leading to a collapse of the wave. Another way to explain this is to say that with large enough β, the "excitable gap" between the refractory tail and the excitation front is excited, pushing the wave front forward (in space) as far as possible into the refractory region ahead of it, thereby causing it to stall, and eventually to collapse.

This scenario can be seen in Fig. 12.50, where the results of numerical simulations for a one dimensional nonuniform cable are shown. Earlier, in Fig. 12.47, we showed a wave, propagating to the right, at equal time steps of $\Delta t = 0.55$. To simulate a reentrant arrhythmia, this wave was chosen so that were this cable a closed loop, the wave would circulate around the loop indefinitely without change of shape. It is not apparent from this previous figure that a stimulus of duration $t = 0.3$ was applied at the ends of the cable between the first and second traces, because in a uniform cable a stimulus at the boundary has little effect on the interior of the medium.

In Fig. 12.50 is shown exactly the same sequence of events for a nonuniform cable. This time, however, the applied stimulus (between the first and second traces) induces a rapidly oscillating membrane potential on the spatial scale of cells (not shown), which has the average effect (because of nonlinearity) of "pushing" the action potential forward as far as possible. This new front cannot propagate forward because it has been pushed into its refractory tail and has stalled. In fact, the direction of propagation reverses, and the action potential collapses as the front and back move toward each other.

To illustrate further this mechanism of defibrillation in a two-dimensional domain, numerical simulations were performed using a standard two-variable model of an excitable medium and using the full bidomain model derived in Section 12.8 (Keener and Panfilov, 1996). Parameters for the excitable dynamics were chosen such that spirals are not stable, but exhibit breakup and develop into "chaotic" reentrant patterns (Panfilov and Hogeweg, 1995), thereby giving a reasonable model of cardiac fibrillation (see Chapter 6.5, Exercise 26).

Some time after initiating a reentrant wave pattern, a constant stimulus (of duration about 2.5 times the duration of the action potential upstroke) was applied uniformly to the sides of the rectangular domain. Because the stimulus was applied uniformly along the sides of the domain, the stimulus parameter β was constant throughout the medium.

In Fig. 12.51a is shown an irregular reentrant pattern just before the stimulus is applied. In this picture, the darkest regions are excited tissue, white denotes recovered and excitable tissue, and grey is refractory tissue. Following a stimulus (with $\beta = 0.86$), the excited region expanded to include essentially all of the recovered tissue, as the excitable gap was eliminated by a polarizing stimulus. Shortly thereafter (Fig. 12.51c, $t = 12$) the activation collapsed, leaving behind only recovered
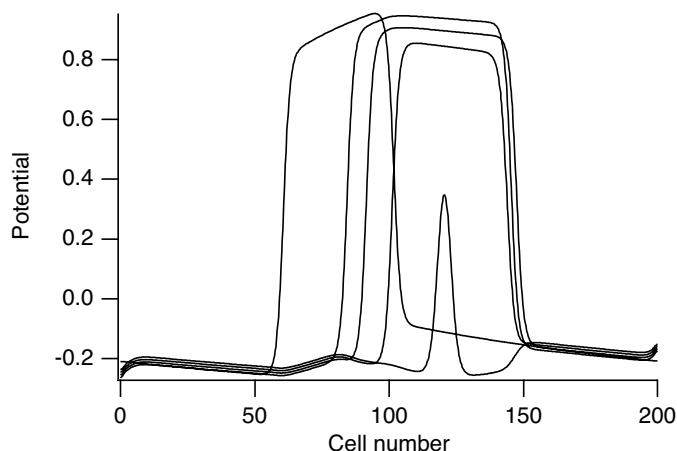
Figure 12.50: A traveling wave in a nonuniform cable following application of a stimulus at the boundary.

or refractory tissue, which shortly thereafter returned to uniform rest. The extensive patterning seen in this last figure shows a mixture of refractory and recovered tissue, but since it contains no excited tissue (except a small patch at the lower left corner that is propagating out of the domain), it cannot become reexcited, but must return to rest. (The similar fates of recovered and refractory regions can be seen in Fig. 12.52b, where the patterning has nearly disappeared.)

Defibrillation is unsuccessful with a smaller stimulus $\beta = 0.84$. The pattern at time $t = 12$ is shown in Fig. 12.52a and is similar to Fig. 12.51c, which was successful. Here, however, after the stimulus and subsequent collapse of much of the excitation, one small excited spot remains at the upper left-hand corner of the medium, which eventually evolves into a double spiral pattern (Fig. 12.52b,c), reestablishing a reentrant arrhythmia.

The primary mechanism of defibrillation still remains uncertain and debated. In this discussion we have focussed on the role of small scale resistive inhomogeneities in defibrillation, and we have ignored the effect of larger scale inhomogeneities. However, there is also a significant body of numerical work exploring the role of large scale virtual electrodes in defibrillation (Efimov et al., 1998; Efimov et al., 2000; Anderson et al., 2000; Eason and Trayanova, 2002). For a theoretical discussion of defibrillation from the viewpoint of phase singularity elimination, see Keener and Cytrynbaum (2003), and Keener (2004).

12.6   Appendix: The Sawtooth Potential

In this appendix, we provide some of the details needed for the calculation of the sawtooth potential solution (12.62)-(12.67). This is a differential-difference boundary value problem that we solve in two steps. First, on the interior of cells the solution must satisfy the cable equation (12.48) with total current $-\frac{1}{r_e}\frac{dV_e}{dx} - \frac{1}{r_c}\frac{dV_i}{dx} = -I$.

(a) (b) (c)
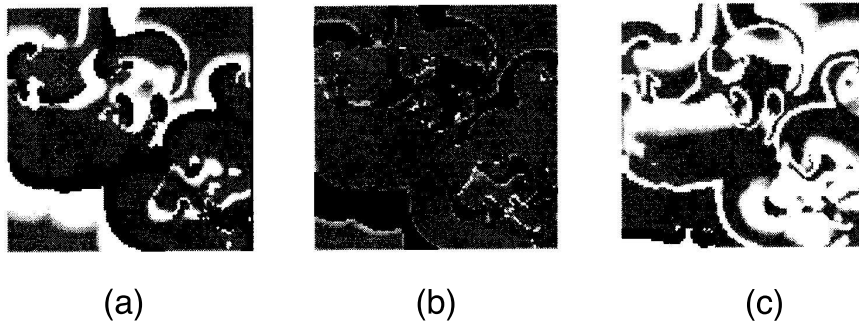
Figure 12.51: Successful defibrillation of a two-dimensional region. **This picture looks quite different from the original one in the book. The gray levels are all wrong. It doesn't make sense as it appears now. JS This is true of several of the figures, not only this one. (for example, Fig. 12.2712.42, etc.) They all need to be fixed. I don't know what we did differently before, but the figure files we are using now (which we got from Springer, maybe?) are not the same as the ones I have for the first edition. JK**
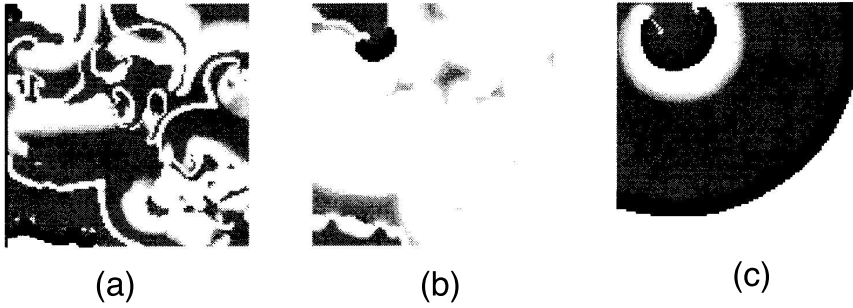
Figure 12.52: Unsuccessful defibrillation of a two-dimensional region.

This solution is

$$\begin{pmatrix} V_i \\ V_e \end{pmatrix} = \frac{1}{r_e + r_c} \begin{pmatrix} r_c \\ -r_e \end{pmatrix} (A \sinh \lambda x + B \cosh \lambda x) + \begin{pmatrix} 1 \\ 1 \end{pmatrix} (-\beta I x + \gamma), \quad (12.177)$$

and $V = A \sinh \lambda x + B \cosh \lambda x$, for $0 < x < L$, with A and B yet to be determined, $\beta = \frac{r_e r_c}{r_e + r_c}$. It is convenient to set $\psi = \frac{1}{r_c} \frac{dV_i(0)}{dx}$ so that $A = a\psi + J$, where $a = \frac{r_e + r_c}{\lambda}$, and $J = \frac{r_e}{\lambda} I$. Now, we suppose that there are a total of N cells, and we denote ψ_j, B_j, and γ_j as the values of ψ, B, and γ for the jth cell, $j = 0, 1, \cdots, N - 1$. The requirement that there be no intracellular current at the ends of the cable is equivalent to the requirement that $\psi_0 = \psi_N = 0$. We impose the conditions that the current and extracellular potentials be continuous and that the jump condition is satisfied at the ends of the cells, and find that

$$\begin{pmatrix} a\psi_{n+1} \\ B_{n+1} \end{pmatrix} = \begin{pmatrix} C & S \\ S + K_g C & C + K_g S \end{pmatrix} \begin{pmatrix} a\psi_n \\ B_n \end{pmatrix} - J \begin{pmatrix} 1 - C \\ K_g(1 - C) - S \end{pmatrix}, \quad (12.178)$$

and

$$\gamma_{n+1} = \gamma_n - \lambda L \frac{\beta}{r_e} J + \frac{\beta}{r_c} K_g (J(C - 1) + a\psi_n C + B_n S), \quad (12.179)$$

where $K_g = \frac{r_g \lambda}{r_e + r_c}$, $C = \cosh \lambda L$, and $S = \sinh \lambda L$.

This is a system of difference equations that we wish to solve subject to the boundary conditions $\psi_0 = \psi_N = 0$. To solve these equations, observe that the matrix has eigenvalues, $\eta_1 = \frac{1}{\mu} > 1$, $\eta_2 = \mu$, where μ is the root of (12.58) with $\mu < 1$. Further, the corresponding right and left eigenvectors are

$$x_i = \begin{pmatrix} S \\ \eta_i - C \end{pmatrix}, \qquad y_i = \begin{pmatrix} S + K_g C \\ \eta_i - C \end{pmatrix}. \quad (12.180)$$

We express the solution of the difference equation (12.178) as a linear combination of the eigenvectors

$$\begin{pmatrix} a\psi_n \\ B_n \end{pmatrix} = \sum_{i=1}^{2} \alpha_{i,n} x_i, \quad (12.181)$$

and write

$$\begin{pmatrix} 1 - C \\ K_g(1 - C) - S \end{pmatrix} = \sum_{i=1}^{2} c_i x_i. \quad (12.182)$$

This decomposes the problem (12.178) into two scalar problems

$$\alpha_{i,n+1} = \eta_i \alpha_{i,n} - J c_i, \qquad i = 1, 2, \quad (12.183)$$

with boundary conditions $\alpha_{1,0} + \alpha_{2,0} = 0$ and $\alpha_{1,N} + \alpha_{2,N} = 0$. The solution of this scalar problem is

$$\alpha_{i,n} = (-1)^i \alpha_0 \eta_i^n - J c_i \frac{\eta_i^n - 1}{\eta_i - 1}, \quad (12.184)$$

which automatically satisfies the boundary condition at $n = 0$. To satisfy the boundary condition at $n = N$, we must have

$$\alpha_0 = -J \frac{\mu}{1 - \mu} \frac{(\mu^N - 1)}{(\mu^{2N} - 1)} \left(c_1 + c_2 \mu^{N-1} \right). \quad (12.185)$$

As a result,

$$a\psi_j = \frac{-S}{1-\mu}(c_1\mu - c_2)f(j),$$

(12.186)

where

$$f(j) = \frac{1 - \mu^{N-j} - \mu^j + \mu^{j+N} + \mu^{2N-j} - \mu^{2N}}{1 - \mu^{2N}}$$

(12.187)

and

$$B_j = \frac{c_1\mu - c_2}{1 - \eta}\left(Cf(j) + \frac{1 - \mu^N}{1 - \mu^{2N}}(\mu^{j+1} + \mu^{N-j-1})\right) - \frac{c_1 - c_2\mu}{1 - \mu}.$$

(12.188)

12.7   Appendix: The Phase Equations

Because coupled oscillators arise so frequently in mathematical biology and physiology, there is an extensive literature devoted to their study. In this book, coupled oscillators play a role in the sinoatrial node and in the digestive system. An important model for the study of coupled oscillators has been the *phase equation*, an equation describing the evolution of the phases of a loosely coupled collection of similar oscillators.

In this appendix we give a derivation of the phase equation. This derivation is similar to that of Neu (1979), using perturbation techniques and a multiscale analysis. A more technical derivation is given by Ermentrout and Kopell (1984). The attempt to describe populations of oscillators in terms of phases was first made by Winfree (1967), and in the context of reaction–diffusion systems, by Ortoleva and Ross (1973, 1974). This was improved by Kuramoto (Kuramoto and Tsuzuki, 1976; Kuramoto and Yamada, 1976). Neu's derivation is also discussed by Murray (1989).

To set the stage, consider the system of equations

$$\frac{dx}{dt} = \Lambda(r)x - \omega(r)y,$$

(12.189)

$$\frac{dy}{dt} = \omega(r)x + \Lambda(r)y,$$

(12.190)

where $r^2 = x^2 + y^2$. Systems of this form are called *lambda–omega* (Λ–ω) systems, and are special because by changing to polar coordinates, $x = r\cos\theta$, $y = r\sin\theta$, (12.189) and (12.190) can be written as

$$\frac{dr}{dt} = r\Lambda(r),$$

(12.191)

$$\frac{d\theta}{dt} = \omega(r).$$

(12.192)

This system has a stable limit cycle at any radius $r > 0$ for which $\Lambda(r) = 0, \Lambda'(r) < 0$. The periodic solution travels around this circle with angular velocity $\omega(r)$. Starting from any given initial conditions, the solution of (12.189) and (12.190) eventually settles onto a regular oscillation with fixed amplitude and period $\frac{\omega(r)}{2\pi}$. Hence, in the

limit as $t \to \infty$, the system is described completely by its angular velocity around a circle.

Now suppose that we have two similar systems, one with a limit cycle of amplitude R_1 and angular velocity ω_1, and the other with a limit cycle of amplitude R_2 and angular velocity ω_2. If there is no coupling between the systems, each oscillates at its own frequency, unaffected by the other, and in the four-dimensional phase space the solutions approaches the torus $r_1 = R_1$, $r_2 = R_2$, moving around the torus with angular velocities $\theta_1' = \omega_1$, $\theta_2' = \omega_2$. Since all solutions eventually end up winding around the torus, and since any solution that starts on the torus cannot leave it, the torus is called an *attracting invariant torus*. The flow on the torus can be described entirely in terms of the rates of change of θ_1 and θ_2. In this case $(\theta_1 - \theta_2)' = \omega_1 - \omega_2$, and so the phase difference increases at a constant rate. Thus, analogously to the one dimensional system discussed above, in the limit as $t \to \infty$, the original system of four-differential equations can be reduced to a two-dimensional system describing the flow on a two-dimensional torus.

If our two similar systems are now loosely coupled, so that each oscillator has only a small effect on the other, it is reasonable to expect (and indeed it can be proved; see Rand and Holmes (1980) for a nice discussion of this, and Hirsch et al. (1977) for a proof) that the invariant torus persists, changing its shape and position by only a small amount. In this case, the longtime solutions for r_1 and r_2 remain essentially unchanged, with $r_1 = R_1 + O(\epsilon)$ and $r_2 = R_2 + O(\epsilon)$, where $\epsilon \ll 1$ is the strength of the coupling. However, the flow *on* the torus could have a drastically different nature, as the phase difference need no longer simply increase at a constant rate. Hence, although the structure of the torus is preserved, the properties of the flow on the torus are not.

In general, the flow on the torus is described by

$$\frac{d\theta_i}{dt} = \omega_i + f_i(r_1, r_2, \theta_1, \theta_2, \epsilon), \qquad i = 1, 2, \tag{12.193}$$

but since $r_1 = R_1 + O(\epsilon)$ and $r_2 = R_2 + O(\epsilon)$, to lowest order in ϵ this simplifies to

$$\frac{d\theta_i}{dt} = \omega_i + h_i(\theta_1, \theta_2, \epsilon), \qquad i = 1, 2. \tag{12.194}$$

In general, R_1 and R_2 appear in (12.194), the so-called *phase equation*, but the independent variables r_1 and r_2 do not. It follows that the full four-dimensional system that describes the two coupled oscillators can be understood in terms of a simpler system describing the flow on a two-dimensional invariant torus.

To derive the equations describing this flow on a torus, we assume that we have a coupled oscillator system that can be written in the form

$$\frac{du_i}{dt} = F(u_i) + \epsilon G_i(u_i) + \epsilon \sum_{j=1}^{N} a_{ij} H(u_j). \tag{12.195}$$

Here, u_i is the vector of state variables for the ith oscillator, the coefficients a_{ij} represent the coupling strength, and the function $H(u)$ determines the effect of coupling. For simplicity, we assume that H is independent of i and j.

To get the special case of SA nodal coupling in (12.120), we take $a_{ij} = d_{ij}$ for $i \neq j$, $a_{ii} = -\sum_{j \neq i} d_{ij}$, and $H(u) = Du$. We take this general form of H to allow for synaptic as well as diffusive coupling.

Next, we assume that when $\epsilon = 0$ we have a periodic solution, i.e., that the equation

$$\frac{du}{dt} = F(u) \tag{12.196}$$

has a stable periodic solution, $U(t)$, scaled to have period one. Note that because of the functions G_i, we are not assuming that each oscillator is identical. Thus, the natural frequency of each oscillator is close to, but not exactly, one.

The model system (12.195) is a classic problem to which the *method of averaging* or the *multiscale method* can be applied. Specifically, since ϵ is small, we expect the behavior of (12.195) to be dominated by the periodic solution $U(t)$ of the unperturbed problem and that deviations from this behavior occur on a much slower time scale. To accommodate two different time scales, we introduce two time-like variables, $\sigma = \omega(\epsilon)t$ and $\tau = \epsilon t$, as fast and slow times, respectively. Here, ω is a function, as yet unknown, of order 1. Treating σ and τ as independent variables, we find from the chain rule that

$$\frac{d}{dt} = \omega(\epsilon)\frac{\partial}{\partial \sigma} + \epsilon \frac{\partial}{\partial \tau}, \tag{12.197}$$

and accordingly, (12.195) becomes

$$\omega(\epsilon)\frac{\partial u_i}{\partial \sigma} + \epsilon \frac{\partial u_i}{\partial \tau} = F(u_i) + \epsilon G_i(u_i) + \epsilon \sum_{j=1}^{N} a_{ij}H(u_j). \tag{12.198}$$

Next we suppose that u_i and $\omega(\epsilon)$ have power series expansions in ϵ, given by

$$u_i = u_i^0 + \epsilon u_i^1 + \cdots, \qquad \omega(\epsilon) = 1 + \epsilon\Omega_1 + \cdots. \tag{12.199}$$

Note that the first term in the expansion for ω is the frequency of the unperturbed solution, U. Expanding (12.198) in powers of ϵ and gathering terms of like order, we find a hierarchy of equations, beginning with

$$\frac{\partial u_i^0}{\partial \sigma} = F(u_i^0), \tag{12.200}$$

$$\frac{\partial u_i^1}{\partial \sigma} - F_u(u_i^0)u_i^1 = G_i(u_i^0) + \sum_{j=1}^{N} a_{ij}H(u_j^0) - \Omega_1\frac{\partial u_i^0}{\partial \sigma} - \frac{\partial u_i^0}{d\tau}. \tag{12.201}$$

Equation (12.200) is easy to solve by taking

$$u_i^0 = U(\sigma + \delta\theta_i(\tau)). \tag{12.202}$$

The phase shift $\delta\theta_i(\tau)$ allows each cell to have different phase shift behavior, and it is yet to be determined.

Next, observe that $\frac{d}{d\sigma}(\frac{dU}{d\sigma} - F(U)) = \frac{\partial U'}{\partial \sigma} - F_u(u_i^0)U' = 0$, so that the operator $LU = \frac{\partial U}{\partial \sigma} - F_u(u_i^0)U$ has a null space spanned by $U'(\sigma + \delta\theta_i(\tau))$. The null space is one

dimensional because the periodic solution is assumed to be stable. It follows that the adjoint operator $L^* y = -\frac{\partial y}{\partial \sigma} - F_u(u_i^0)^T y$ has a one dimensional null space spanned by some periodic function $y = Y(\sigma + \delta\theta_i(\tau))$. (It is a consequence of Floquet theory that the Floquet multipliers of the operator L, say μ_i, and the Floquet multipliers of L^*, say μ_i^*, are multiplicative inverses, $\mu_i \mu_i^* = 1$ for all i. Since a periodic solution has Floquet multiplier 1 and there is only one periodic solution for L, there is also precisely one periodic solution for the adjoint operator L^*. See Exercise 23.) Without loss of generality we scale Y so that $\int_0^1 U'(\sigma) \cdot Y(\sigma)d\sigma = 1$. Therefore, for there to be a periodic solution of (12.201), the right-hand side of (12.201) must be orthogonal to the null space of the adjoint operator L^*. This requirement translates into the system of differential equations for the phase shifts

$$\frac{d}{d\tau}\delta\theta_i = \xi_i - \Omega_1 + \sum_j a_{ij} h(\delta\theta_j - \delta\theta_i), \tag{12.203}$$

where

$$\xi_i = \int_0^1 Y(\sigma) \cdot G_i(U(\sigma))d\sigma, \tag{12.204}$$

$$h(\phi) = \int_0^1 Y(\sigma) \cdot H(U(\sigma + \phi))d\sigma. \tag{12.205}$$

The numbers ξ_i are important because they determine the approximate natural (i.e., uncoupled) frequency of the ith cell. This follows from the fact that when $a_{ij} = 0$, a simple integration gives $\delta\theta_i = \epsilon t(\xi_i - \Omega_1)$, and thus

$$u_i^0 = U(\omega(\epsilon)t + \delta\theta_i) = U((1 + \epsilon\xi_i)t). \tag{12.206}$$

Hence, the uncoupled frequency of the ith cell is $2\pi(1 + \epsilon\xi_i)$. Therefore, ξ_i can (presumably) be measured or estimated without knowing the function $G_i(u)$. The function $h(\phi)$ can be determined analytically for $\Lambda - \omega$ systems (see Exercise 24 or numerically otherwise (see, for example, Exercise 22.)

The function $h(\phi)$ has an important physical interpretation, being a *phase resetting function*. That is, $h(\phi)$ shows the effect of one oscillator on another when the two have phases that differ by ϕ. For example, in the case of two identical oscillators, the two phase shifts are governed by

$$\frac{d}{d\tau}\delta\theta_1 = -\Omega_1 + a_{12}h(\delta\theta_2 - \delta\theta_1) + a_{11}h(0), \tag{12.207}$$

$$\frac{d}{d\tau}\delta\theta_2 = -\Omega_1 + a_{21}h(\delta\theta_1 - \delta\theta_2) + a_{22}h(0). \tag{12.208}$$

Thus, when $a_{12}h(\delta\theta_2 - \delta\theta_1) > 0$, the phase of oscillator 1 is advanced, while if $a_{12}h(\delta\theta_2 - \delta\theta_1) < 0$, the phase of oscillator 1 is retarded. Furthermore, it is not necessarily the case that $h(0) = 0$, so that identical oscillators with identical phases may nonetheless exert a nontrivial influence on each other.

The system of equations (12.203) can be written in terms of phase differences by defining Φ as the vector of consecutive phase differences and defining $\overline{\delta\theta}$ as the

average of the phase shifts, $\overline{\delta\theta} = \frac{1}{N}\sum_{i=1}^{N}\delta\theta_i$. In terms of these variables the system (12.203) can be written in the form

$$\frac{d\Phi}{d\tau} = \Delta + C(\Phi), \tag{12.209}$$

where Δ is the vector of consecutive differences of ξ_i. This is a closed system of $N-1$ equations. *Phase locking* is defined as the situation in which there is a stable steady solution of (12.209), a state in which the phase differences of the oscillators do not change (see Chapter 18).

12.8   Appendix: Homogenization and the Cardiac Bidomain Equations

The homogenization technique that was used in Section 7.8.2 to find effective diffusion coefficients for diffusing and reacting chemical species can also be used to find effective electrical properties of three dimensional cardiac tissue.

We assume that an individual cardiac cell is some small periodic subunit Ω contained in a small rectangular box (Fig. 7.27). The rectangular box is divided into intracellular space Ω_i and extracellular space Ω_e, separated by cell membrane Γ_m. The cells are connected to each other at the sides of the boxes through gap junctions, which are simply parts of the box wall that are contiguous with intracellular space. Thus the boundary of the cellular subunit, $\partial\Gamma$, is composed of two components, cell membrane Γ_m and sides of the box Γ_b.

In either of the intracellular or extracellular spaces, currents are driven by a potential and satisfy Ohm's law $r_c i = -\nabla\phi$, where r_c is the cytoplasmic resistance (a scalar). On the interior of the region, current is conserved, so that

$$\nabla^2\phi = 0. \tag{12.210}$$

Current enters the domain only across boundaries, as a transmembrane current, according to

$$\mathbf{n}\cdot\frac{1}{r_c}\nabla\phi = I_m \tag{12.211}$$

applied in the cell membrane, denoted by Γ_m, and where $\mathbf{n}$ is the outward unit normal to the membrane boundary.

Suppose that x is the original Cartesian coordinate space. To allow for a variable fiber structure we assume that the orientation of the rectangular boxes is slowly varying (so that they are not exactly rectangular, but close enough), and that the axes of the rectangular cellular boxes form a natural "fiber" coordinate system. At each point in space the orientation of the rectangular box is determined by three orthogonal tangent vectors, forming the rows of a matrix $T(x)$. Then the fiber coordinate system is related to the original Cartesian coordinate system through

$$y = Y(x) = \int T(x)dx \tag{12.212}$$

and in the y-coordinate system the Laplacian operator is

$$\nabla^2 \phi = \nabla_y^2 \phi + \kappa \cdot \nabla_y \phi. \tag{12.213}$$

The vector κ is the curvature vector, whose components are the mean curvatures of the coordinate level surfaces. If the components of the matrix T are given by t_{ij}, then the coordinates of κ are $\kappa_j = t_{ik} \frac{\partial t_{ij}}{\partial x_k}$.

To take into account that the boundary of the cells is varying rapidly on the scale of the fiber coordinate system, we introduce the "fast" variable $\xi = \frac{y}{\epsilon}$, where ϵ is the small dimensionless parameter $\epsilon = \frac{l}{\Lambda}$, l is the length of the cell, and Λ is the natural length scale along fibers. We let $z = y$ be the slow variable and assume that κ is a function solely of z, since variations of fiber direction are not noticeable at the cellular level.

Now we apply the homogenization technique described in Chapter 7. For this particular problem, this was first done by Neu and Krassowska (1993; see also Keener and Panfilov, 1997). As the calculation here is nearly identical to that given in Section 7.8.2, we skip directly to the answer. The potential ϕ is given by

$$\phi = \Phi(z) + \epsilon W\left(\frac{z}{\epsilon}\right) \cdot T^{-1} \nabla_z \Phi(z) + O(\epsilon^2 \Phi), \tag{12.214}$$

where the mean field potential Φ satisfies the averaged Poisson equation

$$\nabla \cdot (\sigma_{\text{eff}} \nabla \Phi) = -\chi \frac{1}{S_\xi} \int_{\Gamma_m} I_m(z, \xi) dS_\xi. \tag{12.215}$$

where $\chi = \frac{S_m}{v}$ is the cell surface area per unit volume, a quantity having units of length, and S_ξ is the surface area of Γ_m in units of ξ. $W(\xi)$ is the fundamental solution vector, periodic in ξ with zero surface average value, $\int_{\Gamma_m} W(\xi) d\xi = 0$, and it satisfies the vector partial differential equation

$$\nabla_\xi^2 W(\xi) = 0, \tag{12.216}$$

subject to the boundary condition

$$\mathbf{n} \cdot (\nabla_\xi W(\xi) + I) = 0, \tag{12.217}$$

on Γ_m the membrane wall. Here I is the identity matrix. Finally the effective conductivity tensor is

$$\Sigma = \frac{1}{r_c v} \int_{\Gamma_m} (\nabla_\xi W(\xi) + I) dV_\xi, \tag{12.218}$$

where $\sigma_{eff}(x) = T\Sigma T^{-1}$, and v is the volume of the rectangular box containing the cell.

The derivation of the bidomain model follows quickly from this. We define the potentials in the intracellular and extracellular domains as ϕ_i and ϕ_e, respectively. Then the membrane potential is the difference between the two potentials across the membrane boundary Γ_m between the two domains:

$$\phi = (\phi_i - \phi_e)\left.\right|_{\Gamma_m}. \tag{12.219}$$

At each point of the cell membrane the outward transmembrane current is given by

$$I_m = C_m \frac{d\phi}{dt} + \frac{1}{R_m} f_m(\phi), \tag{12.220}$$

where C_m is the membrane capacitance and f_m/R_m represents the transmembrane ionic current. The parameter R_m is the membrane resistance.

It follows from homogenization (12.214), (12.215) that

$$\phi_i \;\;=\;\; V_i(x) + \epsilon W_i\left(\frac{x}{\epsilon}\right) \cdot T^{-1}\nabla V_i(x) + O(\epsilon^2 V_i), \tag{12.221}$$

$$\phi_e \;\;=\;\; V_e(x) + \epsilon W_e\left(\frac{x}{\epsilon}\right) \cdot T^{-1}\nabla V_e(x) + O(\epsilon^2 V_e), \tag{12.222}$$

and that $V_i(x)$ and $V_e(x)$ satisfy the averaged equations

$$\nabla \cdot (\sigma_i \nabla V_i) = -\nabla \cdot (\sigma_e \nabla V_e) = \chi \frac{1}{S_\xi} \int_{\Gamma_m} I_m(x,\xi) dS_\xi, \tag{12.223}$$

where I_m is the transmembrane current (positive outward). We calculate (using that $\int_{\Gamma_m} W_i dS_\xi = \int_{\Gamma_m} W_e dS_\xi = 0$) that

$$\frac{1}{S_\xi} \int_{\Gamma_m} I_m(x,\xi) dS_\xi = C_m \frac{\partial V}{\partial t} + \frac{1}{S_\xi} \int_{\Gamma_m} \frac{1}{R_m} f_m\left(V + \epsilon H(\xi,x)\right) dS_\xi, \tag{12.224}$$

where

$$H(\xi,x) \;\;=\;\; W_i(\xi) \cdot T^{-1}\nabla V_i(x) - W_e(\xi) \cdot T^{-1}\nabla V_e(x), \tag{12.225}$$

$$V \;\;=\;\; V_i - V_e. \tag{12.226}$$

It follows that

$$\frac{R_m}{\chi}\nabla \cdot (\sigma_i \nabla V_i) = -\frac{R_m}{\chi}\nabla \cdot (\sigma_e \nabla V_e) = C_m R_m \frac{\partial V}{\partial t} + \frac{1}{S_m} \int_{\Gamma_m} f_m\left(V + \epsilon H(\xi,x)\right) dS_\xi. \tag{12.227}$$

In the limit $\epsilon = 0$, the equations (12.227) reduce to the standard bidomain model. With $\epsilon \neq 0$, this model can be used to study the effects of large defibrillating currents.

Exercises

1. (a) The fundamental solution of Poisson's equation in free space with a unit source at the origin ($\nabla^2 \phi = -\delta(x)$) is $\phi(x) = \frac{1}{4\pi|x|}$.

    Find the solution of Poisson's equation with a source at the origin and a sink of equal strength at $x = x_1$, and let $|x_1| \to 0$. What must be assumed about the strength of the source and the sink in order to obtain a nonzero limiting potential?

    (b) Find the solution of Poisson's equation with a dipole source by solving the problem $\nabla^2 \phi = \frac{1}{\epsilon}(\delta(x - \epsilon v) - \delta(x))$ with $|v| = 1$, and then taking the limit $\epsilon \to 0$.

Figure 12.53: ECG recording of a ventricular extrasystole for exercise 3. (Rushmer, 1976, Fig 8-25, p. 314, originally from Guneroth, 1965.)

Figure 12.54: ECG for Exercise 4 (Goldberger and Goldberger, 1994, p. 45).

2. Determine the heart rate for the ECG recording in Fig. 12.3a. The subject was sedated at the time this recording was made. What are the effects of the sedation?

3. Identify the different deflections in the ECG recording shown in Fig. 12.53. What can you surmise about the nature of propagation for the extra QRS complex (called an *extrasystole*). Because of the apparent periodic coupling between the normal QRS and the extrasystole, this rhythm is called a *ventricular bigeminy*.

4. (a) Suggest a diagnosis for the ECG recording in Fig. 12.54.
   Hint: What does the inverted P-wave suggest? What is the heart rate?

   (b) What possible mechanisms can account for the failure of the SA node to generate the heartbeat?

5. Estimate the mean deflection of the QRS complex in each of the six standard leads (I, II, III, aVR, aVL, aVF) in Fig. 12.7 and then estimate the mean heart vector for the normal heartbeat.

6. Improve your skill at reading ECGs by finding the mean heart vector for the QRS complexes in Figs. 12.4, 12.9, and 12.10. Why is hypertrophy the diagnosis for Figs. 12.9 and 12.10? In what direction are the heart vectors deflected in these figures?
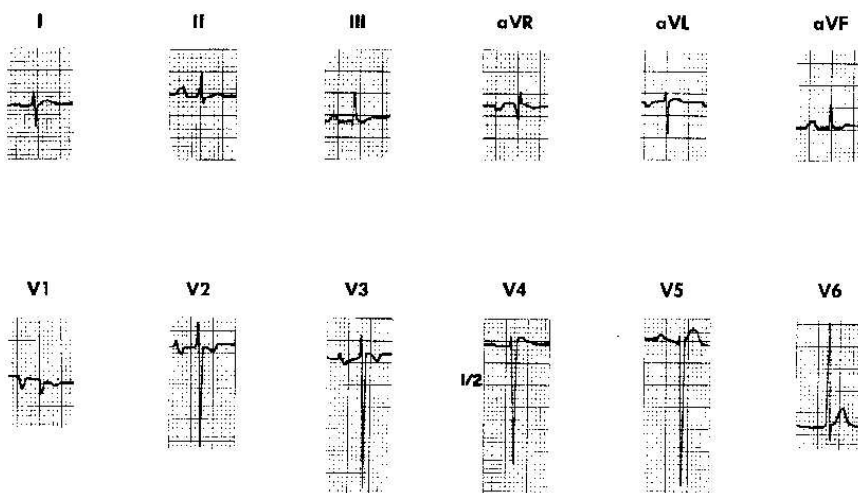
Figure 12.55: ECG for Exercise 7. Can you determine the nature of this abnormality? (Rushmer, 1976, Fig. 8-51, p. 343.)

7. Find the mean heart vector for the ECG recording shown in Fig. 12.55. What mechanism can you suggest that accounts for this vector?

8. By assuming a fast equilibrium between states N_3 and N_4, and between states C_3 and C_4, derive the simplified reaction diagram of Fig. 12.19C for the L-type channel model.

9. Compare the solution of (12.58) with the approximation (12.60). In particular, plot $\frac{\lambda_g^2}{L^2}(Q + r)$ as a function of Q for different values of $\frac{L}{\lambda_g}$.

10. Use cable theory to estimate the effective coupling resistance for cardiac cells in the longitudinal and transverse directions. Assume that cells are 0.01 cm long, 0.00167 cm wide, $\chi = S/v = 2400 \, \text{cm}^{-1}$, $R_m = 7000 \, \Omega\text{-cm}^2$, $R_c = 150 \, \Omega\text{-}$cm, $R_e = 0$, with a longitudinal space constant of 0.09 cm and transverse space constant 0.03 cm (appropriate for canine crista terminalis). What difference do you observe with a transverse space constant of 0.016 cm (appropriate for sheep epicardium)?

11. How should the coupling coefficient r_g be chosen so that the decay rate for the discrete linear model (12.78) with $I_{\text{ion}} = -V/R_m$ matches the space constant of the medium?

12. Using that the longitudinal and transverse cardiac action potential deflections are $\Delta V_{eL} = 74$ mV, $\Delta V_{eT} = 43$ mV, that the membrane potential has $\Delta V = 100$ mV (independent of direction), and that the axial speed of propagation in humans is 0.5 m/s in the longitudinal fiber direction and 0.17 m/s
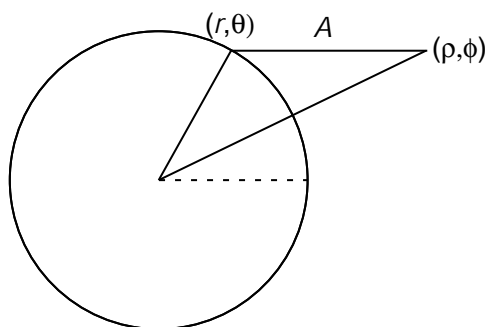
Figure 12.56: Diagram of phase resetting for the Poincaré oscillator (Exercise 14).

in the transverse direction, determine the ratio of coefficients of the conductivity tensors $\frac{\sigma_{eL}}{\sigma_{iL}}$, $\frac{\sigma_{eT}}{\sigma_{iL}}$, and $\frac{\sigma_{iT}}{\sigma_{iL}}$. What are these ratios in dog if the ratio of longitudinal to transverse speeds is 2:1?

13. Determine the conditions under which there is propagation failure at a junction when the ionic current model is

$$I_{\text{ion}} = g_{\text{Na}}hm^2(V)(V_{\text{Na}} - V) + g_{\text{K}}(V_{\text{K}} - V), \qquad (12.228)$$

where

$$m(V) = \begin{cases} 0, & V < V_{\text{K}}, \\ \frac{V - V_{\text{K}}}{V_{\text{Na}} - V_{\text{K}}}, & V_{\text{K}} < V < V_{\text{Na}}, \\ 0, & V > V_{\text{Na}} \end{cases} \qquad (12.229)$$

Reasonable values for the parameters are $V_{\text{K}} = -84$ mV, $V_{\text{Na}} = 66$ mV, $g_{\text{Na}} = 3.33$ mS/cm^2, and $g_{\text{K}} = 0.66$ mS/cm^2, although these numbers are not needed to solve this problem.

14. Consider the following simple model of a forced periodic oscillator, called the *Poincaré oscillator* (also called a *radial isochron clock* or a *snap back oscillator*; Guevara and Glass, 1982; Hoppensteadt and Keener, 1982; Keener and Glass, 1984; Glass and Kaplan, 1995). A point is moving counterclockwise around a circle of radius 1. At some point of its phase, the point is moved horizontally by an amount A and then allowed to instantly "snap back" to radius 1 moving along a radial line toward the origin (see Fig. 12.56).

   (a) Determine the *phase resetting curve* for this process. That is, given the phase θ before resetting, find the phase ϕ after resetting the clock. Plot ϕ as a function of θ for several values of A.

   (b) Show that for $A < 1$ the phase resetting function is a *type 1* map, satisfying $\phi(\theta + 2\pi) = \phi(\theta) + 2\pi$.

   (c) Show that for $A > 1$, the phase resetting function is a *type 0* map, for which $\phi(\theta + 2\pi) = \phi(\theta)$.

(d) Show that there is a *phase singularity*, that is, values of A and θ for which a new phase is not defined (Winfree, 1980).

(e) Construct a map $\theta_n \mapsto \theta_{n+1}$ by resetting the clock every T units of phase, so that

$$\theta_{n+1} = \phi(\theta_n) + T. \qquad (12.230)$$

Show that for $A < 1$, this is a circle map. Determine the values of A and T for which there is one-to-one phase locking.

15. A simple model of the response of an excitable cell to a periodic stimulus is provided by the *integrate-and-fire* model (Knight, 1972; Keener, Hoppensteadt and Rinzel, 1981). In this model the membrane is assumed to be passive unless the threshold is reached, whereupon the membrane "fires" and is immediately reset to zero. The equations describing the evolution of the membrane potential are

$$\frac{dv}{dt} = -\gamma v + S(t), \qquad (12.231)$$

and $v(t^+) = 0$ if $v(t) = v_T$, the threshold. We take the periodic stimulus to be a simple sinusoidal function, $S(t) = S_0 + S_m \sin(\omega t)$.

Let T_n be the time of the nth firing. Formulate the problem of determining T_{n+1} from T_n as a circle map. For what parameter values is this a continuous circle map and for what parameter values is it a discontinuous circle map? (Guevara and Glass, 1982.)

16. Suppose the membrane potential rises at a constant rate λ until it reaches a threshold $\theta(t)$, at which time the potential is reset to zero. Suppose that the threshold is the simple sinusoidal function $\theta(t) = \theta_0 + \theta_m \sin(\omega t)$. Let T_n be the time of the nth firing. Formulate the problem of determining T_{n+1} from T_n as a circle map. For what parameter values is this a continuous circle map and for what parameter values is it a discontinuous circle map? (Glass and Mackey, 1979.)

17. Suppose a constant-current stimulus I is added to a cable with FitzHugh–Nagumo dynamics and piecewise linear function f as in (12.133).

(a) Find the steady-state solution as a function of input current I.

(b) Examine the stability of this steady-state solution. Show that the eigenvalues are eigenvalues of a Schrödinger equation with a square well potential. Find the critical Hopf bifurcation curve. Show that for ϵ sufficiently small, the solution is stable if I is small or large, but there is an intermediate range of I for which the solution is unstable (Rinzel and Keener, 1983).

Hint: Because the function $f(v)$ is piecewise linear, the potential for the Schrödinger equation is a square well potential. Solve the resulting transcendental equations numerically.

18. (a) Carry out the calculations of Section 12.3.4 for a one dimensional piece-wise linear model (12.133) with $\alpha(r)$ specified by (12.132), $b = \frac{1}{2}$. Determine the critical stability curve.

    (b) Generalize this calculation by supposing that the oscillatory cells have coupling coefficient D. What is the effect of the coupling coefficient of the oscillatory cells on the critical stability curve? Show that oscillatory behavior is more likely with weak coupling.

19. (a) Use homogenization theory to show that the averaged approximation of (12.68) is (12.69).

    (b) Use homogenization to separate (12.162) into two equations on different spatial scales. Show that $V \approx u_0(z,\tau) + \epsilon J(\tau)H(\eta) - \epsilon W(\eta)\frac{\partial u_0(z,\tau)}{\partial z}$, where $W'(\eta) = 1 - \frac{D}{d(\eta)}$, $H'(\eta) - \frac{\Sigma_e}{\sigma_e} - \frac{D}{d}$, and u_0 satisfies the averaged equation (12.166). Show that this answer is valid even if $J(\tau) = O(\frac{1}{\epsilon})$. (Hint: Use the projection method rather than a standard power series expansion.)

20. Suppose that the nonlinear function $f(V)$ for an excitable medium is well represented by

$$f(V) = V\left(\frac{V}{\theta} - 1\right), \qquad (12.232)$$

at least in the vicinity of the rest point and the threshold. Find the relationship between minimal time and stimulus strength to directly stimulate the medium.

Hint: Evaluate 12.174.

21. Find the relationship between minimal time and stimulus strength to directly stimulate the medium (as in the previous problem) for the Beeler–Reuter model of myocardial tissue (Section 12.2). To do this, set $m = m_\infty(V)$ and set all other dynamic variables to their steady-state values and then evaluate (12.174).

22. Suppose a collection of FitzHugh–Nagumo oscillators described by

$$\delta\frac{dv}{dt} = f(v) - w, \qquad (12.233)$$

$$\frac{dw}{dt} = v - \alpha, \qquad (12.234)$$

with $f(v) = v(v - 1)(\alpha - v)$ with parameter values $\delta = 0.05$, $\alpha = 0.4$, is coupled through the variable v. Calculate (numerically) the coupling function

$$h(\phi) = \int_0^P y_1(\sigma)v(\sigma + \phi)d\sigma, \qquad (12.235)$$

where y_1 is the first component of the periodic adjoint solution.

23. (a) Consider a linear system of differential equations $\frac{dy}{dt} = A(t)y$ and the corresponding adjoint system $\frac{dv}{dt} = -A^T(t)v$, where $A(t)$ is periodic with period P. Let $Y(t)$ and $V(t)$ be matrix solutions of these equations and suppose that $V^T(0)Y(0) = I$. Show that $V^T(P)Y(P) = I$.

(b) The eigenvalues of the matrix $Y(P)Y^{-1}(0)$ are called the Floquet multipliers for the system $\frac{dy}{dt} = A(t)y$. What does the fact that $V^T(0)Y(0) = V^T(P)Y(P)$ imply about the Floquet multipliers for $\frac{dy}{dt} = A(t)y$ and its adjoint system?

24. Suppose two identical lambda-omega oscillators of the form (12.189-12.189) are coupled through their first variables x, with, in the notation of (12.195),

$$H = \begin{pmatrix} x \\ 0 \end{pmatrix} \tag{12.236}$$

and $a_{12} = a_{21} = \alpha$, and $a_{11} = a_{22} = 0$. Calculate the phase resetting function $h(\phi)$ and determine the stability of in-phase and out-of-phase, phase locked solutions, when $\alpha = \pm 1$.

Chapter 13

Blood

Blood is composed of two major ingredients, the liquid *blood plasma* and several types of cells suspended within the plasma. The cells constitute approximately 40% of the total blood volume and are grouped into three major categories: *erythrocytes* (red blood cells), *leukocytes* (white blood cells), and *thrombocytes* (platelets). The red blood cells remain within the blood vessels, and their function is to transport oxygen and carbon dioxide. The white blood cells fight infection, and thus are able to migrate out of the blood vessels and into the tissues. Platelets are not complete cells, but are small detached fragments of much larger cells called megakaryocytes. Their principal function is to aid with blood clotting.

Leukocytes themselves are subdivided into a number of categories; *granulocytes* (approximately 65%), *lymphocytes* (30%), *monocytes* (5%) and *natural killer* cells. Granulocytes are subdivided into *neutrophils* (95%), *eosinophils* (4%) and *basophils* (1%). Neutrophils phagocytose (i.e., ingest) and destroy small foreign bodies like bacteria, basophils help mediate inflammatory reactions by secreting histamine, while eosinophils help to destroy parasites and modulate allergic responses.

Monocytes mature into macrophages, which help the neutrophils with the phagocytosis of foreign bodies. Macrophages are much larger than neutrophils and can phagocytose larger microorganisms. They are also responsible for removing dead or damaged cells.

Lymphocytes come in two main types, T and B, whose main functions are the production of antibodies and the removal of virus-infected cells.

The types and functions of blood cells are summarized in Table 13.1.

In this chapter we consider only a small number of mathematical questions associated with these cell types. A more general study of lymphocytes and the immune system would require an entire volume all to itself. A good basic introduction to immunology is Janeway et al. (2004), while a more detailed discussion of mathematical models and the immune system is given by Nowak and May (2001) and Perelson (2002).

637

Type of cell	Main functions	cells/liter
Red blood cells (erythrocytes)	transport oxygen and carbon dioxide	5×10^{12}
White blood cells (leukocytes)		
Granulocytes		
Neutrophils	ingest and destroy bacteria	5×10^9
Eosinophils	destroy larger parasites and modulate allergic responses	2×10^8
Basophils	release histamine in certain immune reactions	4×10^7
Monocytes	become macrophages which ingest invading bacteria and foreign bodies, and remove dead or damaged cells	
Lymphocytes		
B Lymphocytes	make antibodies	2×10^9
T Lymphocytes	kill cells infected by virus, and regulate activities of other leukocytes	1×10^9
Natural killer cells (NK)	kill some tumor cells, and cells infected by virus	
Platelets	cell fragments arising from megakaryocytes in bone marrow; initiate blood clotting.	3×10^{11}

Table 13.1: Types and functions of blood cells. The right-hand column shows typical concentrations in human blood. Adapted from Alberts et al. (1994), Table 22-1.

13.1   Blood Plasma

The blood plasma is 89–95% water, with a variety of dissolved substances. The dissolved substances with small molecular weight include bicarbonate, chloride, phosphorus, sodium, calcium, potassium, magnesium, urea, and glucose. There are also large protein molecules including *albumin* and α-, β-, and γ-*globulins*. Of these proteins, albumin has the highest molar concentration in plasma and this makes the greatest contribution to the plasma osmotic pressure.

In addition, gases, such as carbon dioxide and oxygen, are dissolved in the blood plasma. For an ideal gas, the pressure, volume, and temperature are related by the ideal gas law,

$$PV = nkT, \tag{13.1}$$

where P is the pressure, V is the volume, n is the number of gas molecules, k is Boltzmann's constant, and T is temperature in Kelvin. Since concentration is $c = n/V$, for an ideal gas

$$P = ckT. \tag{13.2}$$

This representation of concentration is in units of molecules per volume, and while this seems natural, it is not the usual way that concentrations are represented. To express concentration in terms of moles per unit volume, we multiply and divide (13.2) by Avogadro's number N_A to obtain

$$P = CRT, \tag{13.3}$$

where $C = c/N_A$ and $R = kN_A$ is the universal gas constant.

Air is a mixture of different gases, with 78% nitrogen and 21% oxygen. Each of these gases contributes to the total pressure of the mixture via its *partial pressure*. The partial pressure of gas i, P_i, is defined by

$$P_i = x_i P, \tag{13.4}$$

where x_i is the mole fraction of gas i, and P is the total pressure of the gas mixture. Thus, by definition, the total pressure of a gas mixture is the sum of the partial pressures of each individual gas in the mixture. In an ideal mixture the partial pressure of gas i is equal to the pressure that gas i would exert if it alone were present.

When a gas with partial pressure P_i comes into contact with a liquid, some of the gas dissolves in the liquid. When a steady state is reached, the amount of gas dissolved in the liquid is a function of the partial pressure of the gas above the liquid. If the concentration of the dissolved gas is low enough, thus forming an ideally dilute solution, then P_i is related to the concentration of gas i by

$$c_i = \sigma_i P_i, \tag{13.5}$$

where c_i is the concentration of gas i, and σ_i is called the *solubility*. In general σ_i is a function of the temperature and the total pressure above the liquid. In Table 13.2 are shown the solubilities of important respiratory gases in blood, where it can be seen, for example, that the solubility of carbon dioxide in blood is about 20 times larger than that of oxygen.

Substance	σ
	(Molar/mm Hg)
O_2	1.4×10^{-6}
CO_2	3.3×10^{-5}
CO	1.2×10^{-6}
N_2	7×10^{-7}
He	4.8×10^{-7}

Table 13.2: Solubility of respiratory gases in blood plasma.

13.2   Blood Cell Production and Periodic Hematological Diseases

Blood cells are produced by the bone marrow and must be continually produced over a human's lifetime. For example, one cubic millimeter of blood contains around 5 million erythrocytes. These cells have an average lifetime of 120 days and are estimated to travel through about 700 miles of blood vessels during their life span. Because of aging and rupturing, red blood cells must be constantly replaced. On average, the body must produce 3×10^9 new erythrocytes for each kilogram of body weight every day.

In a child before the age of 5, blood cells are produced in the marrow of essentially all the bones. However, with age, the marrow of the long bones becomes quite fatty and so produces no more blood cells after about age 20. In the adult, most blood cells are produced in the marrow of membranous bones, such as the vertebrae, sternum, ribs, and ilia.

In the bone marrow there are cells, called *pluripotential hemopoietic stem cells*, from which all of the cells in the circulating blood are derived. Remarkably, if endogenous hematopoiesis (blood cell production) is halted in an animal by irradiation, it can be completely restored by the addition of exogeneous stem cells. As stem cells grow and reproduce, a portion of them remains exactly like the original pluripotential cells, maintaining a more or less constant supply of these cells. The larger portion of the reproduced stem cells differentiates to form other cells, called *committed stem cells*, or committed progenitors. The *in vitro* analogue of the committed stem cells are called colony-forming units (CFU). The committed stem cells produce colonies of specific types of blood cells, including erythrocytes, lymphocytes, granulocytes, monocytes, and megakaryocytes.

Although the basic outline of the process is known, the details, both of the mechanisms that control blood cell production, and the exact lineage of each cell type, remain elusive. It seems that hematopoietic stem cells pass through a series of divisions and maturational steps, at each stage of which they progressively lose their potential to change their differentiation pathway (i.e., the choice of what the cell can differentiate to becomes more limited), ending with a fully differentiated cell type such as an erythrocyte. However, it has proven difficult to separate the precursors of one cell type from those of another, leading to considerable uncertainty in the exact cell lineages. A tentative cell lineage diagram is given in Fig. 13.1.
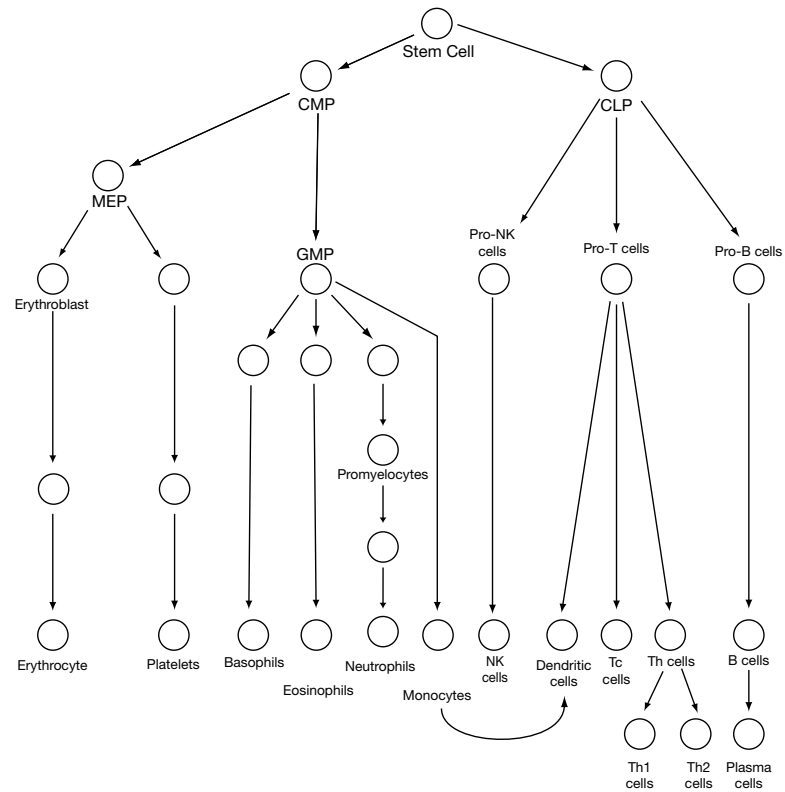
Figure 13.1: Schematic diagram of cell lineage in hematopoiesis. Stem cells differentiate into common myeloid precursors (CMP) and common lymphoid precursors (CLP). CMP then differentiate into megakaryotic/erythroid progenitors (MEP), which differentiate further into erythrocytes and platelets. CMP also give rise to granulocyte-monocyte-megakaryocyte-erythroid common progenitors (GMP), whence come granulocytes and monocytes. CLP differentiate into T lymphocytes, B lymphocytes and natural killer cells. Th cells are helper lymphocytes, while Tc cells are cytotoxic T lymphocytes. Adapted from Kluger et al. (2004), Fig. 1.

Growth and differentiation of blood cells are controlled by an intricate array of soluble factors, or cytokines, that include hematopoietic growth and differentiation factors. However, most cytokines are known to have multiple effects and interactions, and there is no clear distinction between those that control growth and those that control differentiation. Formation of cytokines is itself controlled by factors outside the bone marrow such as, in the case of red blood cells, low oxygen concentration for an extended period of time.

The feedback system that controls erythrocyte production is relatively well understood. The principal factor stimulating red blood cell production is the hormone *erythropoietin*. About 90% of the erythropoietin is secreted by renal tubular epithelial cells when blood is unable to deliver sufficient oxygen. The remainder is produced by other tissues (mostly the liver). When both kidneys are removed or destroyed by renal disease, the person invariably becomes anemic because of insufficient production of erythropoietin.

The role of erythropoietin in bone marrow is twofold. First, it stimulates the production of pre-erythrocytes, called *proerythroblasts*, and it also controls the speed at which the developing cells pass through the different stages. Normal production of red blood cells from stem cells takes 5–7 days, with no appearance of new cells before 5 days, even at high levels of erythropoietin. At high erythropoietin levels the rate of red blood cell production (number per unit time) can be as much as ten times normal, even though the maturation rate of an individual red blood cell varies much less.

Thus, in response to a drop of oxygen pressure in the tissues, an increased production of erythropoietin causes an increase in the rate of production of red blood cells, thus tending to restore oxygen levels. The control mechanisms that operate when the red blood cell count is too high (a condition called polycythemia or erythrocytosis) are less clear. Details of the regulatory system governing red blood cells can be found in Williams (1990), while an excellent review of much of the material discussed in this section can be found in Haurie et al. (1998).

Feedback control of the other types of blood cells is less well understood. Production of granulocytes is controlled by granulocyte colony-stimulating factor (G-CSF), which is produced by a number of tissues, including fibroblasts, and endothelial and epithelial tissue, while megakaryocyte production is controlled, at least in part, by thrombopoietin. These feedback controls are sketched in Fig. 13.2.

13.2.1   Periodic diseases

In most people the production of blood cells is relatively constant. However, there are a number of pathological conditions that exhibit oscillatory behavior. The most widely studied is *cyclical neutropenia*, a condition in which the number of neutrophils periodically drops to a very low level, typically every 19 to 21 days. As it happens, the gray collie suffers from a similar disease, with a period that ranges from 11 to 15 days, and this has greatly helped the study of the disease in humans. In both humans and collies, the periodic variation in neutrophil numbers is accompanied by oscillations in the number of platelets, often the monocytes and eosinophils, and occasionally the lymphocytes. The oscillation period in these other
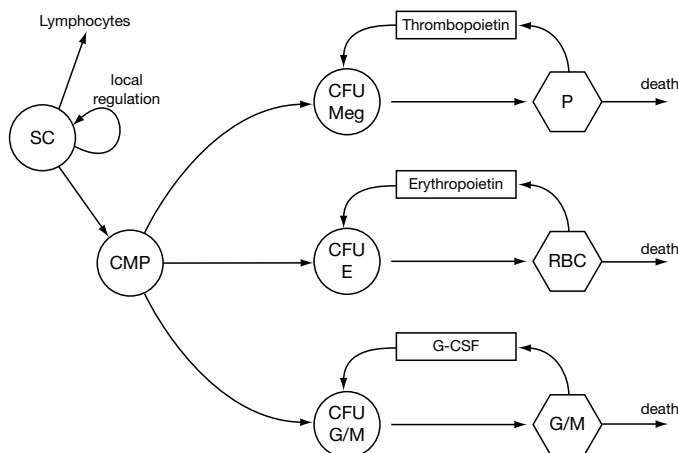
Figure 13.2: Schematic diagram of the control of blood cell production. SC: stem cells. CMP; common myeloid precursors (see Fig. 13.1). CFU: colony-forming units. E: erythrocytes. Meg: megakaryocytes. G/M: granulocytes/monocytes. P: platelets. RBC: red blood cells. The feedback loops in the diagrams are not well understood, but are certainly far more complex than shown here.

cell types is, however, not always the same as that of the neutrophils. Some typical experimental data from 9 different dogs are shown in Fig. 13.3.

Another periodic blood disease is periodic chronic myelogenous leukemia (CML). Being a leukemia, this disease is characterized by the uncontrolled growth of white blood cells. However, this growth can sometimes occur in an oscillatory manner. Data showing oscillations of white blood cell count in a twelve-year-old girl with periodic CML are shown in Fig. 13.4A, and blood cell counts in cyclical neutropenia and CML are compared in Fig. 13.4B. The oscillations in CML occur with a much larger period, and generate much greater numbers of neutrophils, as expected for a leukemia.

Over the last 25 years, there have been a large number of mathematical investigations of these periodic behaviors. Early studies were those of Mackey (1978, 1979a,b), Mackey and Glass (1977), Mackey and Milton (1987), Milton and Mackey (1989), and Bélair et al. (1995), while the recent work of Mackey, Haurie and their colleagues (Haurie et al., 1998; Hearn et al., 1998; Haurie et al., 1999; Haurie et al., 2000; Colijn and Mackey, 2005a,b) have extended the earlier models into much more elaborate versions, with detailed fits to experimental data. Another of the major modeling groups studying periodic hematopoiesis is that of Wichmann, Schmitz and their colleagues (Wichmann et al., 1988; Schmitz et al., 1988, 1990, 1993).

One of the principal goals of the recent modeling work has been to discover the site of action of the feedback that controls blood cell growth and that can lead to oscillatory behavior. Here, we first illustrate the basic modeling concepts by working through a relatively simple delay differential equation model, and then, using a more recent model, study the question of where the feedback occurs.
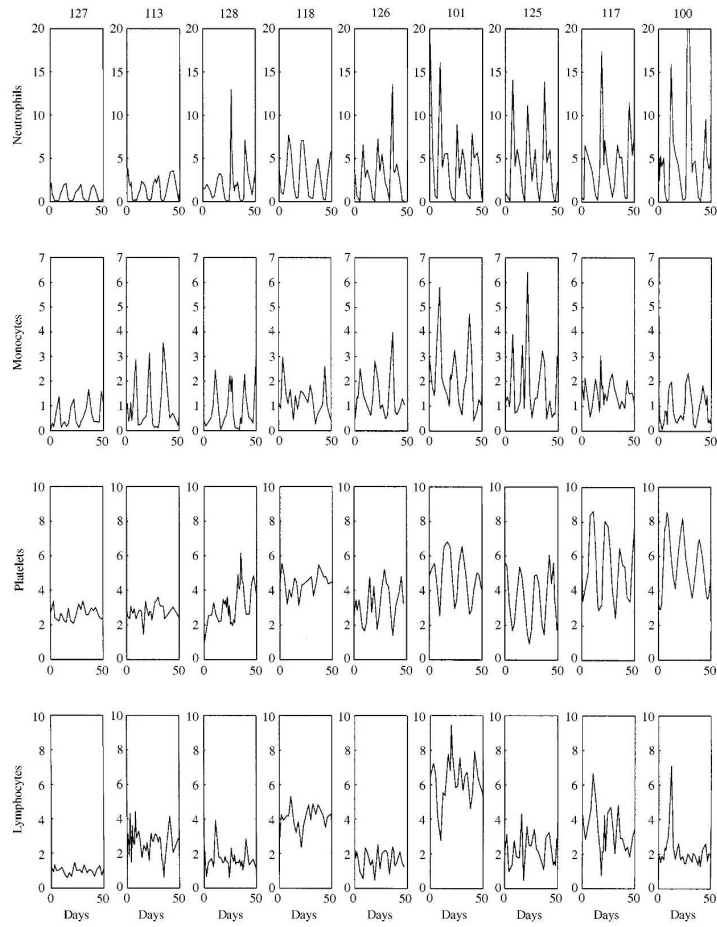
Figure 13.3: Blood counts against time (in days) for nine gray collies with cyclical neutropenia. Units: cells $\times 10^{-5} \mathrm{mm}^{-3}$ for the platelets and cells $\times 10^{-3} \mathrm{mm}^{-3}$ for the other cell types. (Haurie et al. 2000, Fig. 1). **Springer: this figure will need permission**
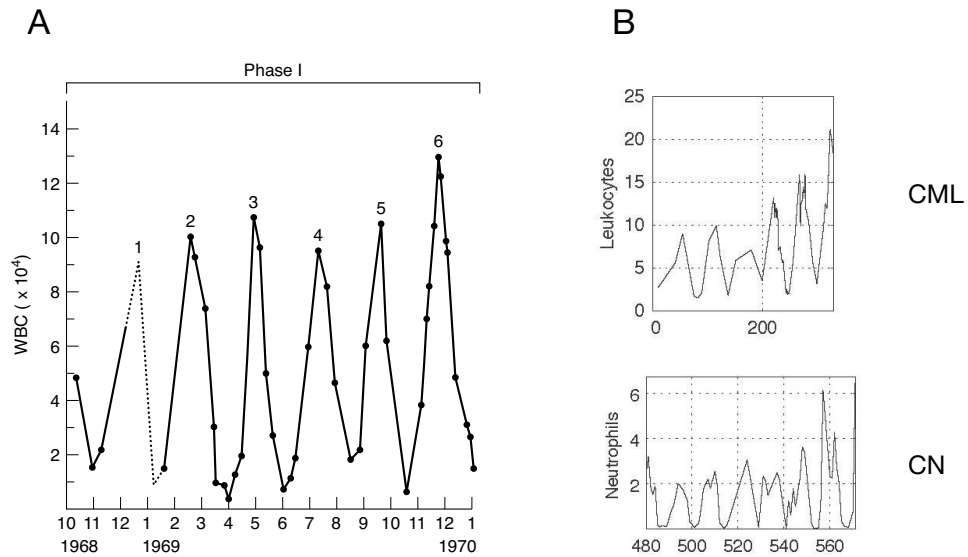
Figure 13.4: A: White blood cell count (per liter) as a function of time for a twelve-year-old girl with periodic CML. (Gatti et al., 1973, Fig. 1.) B: Comparison of blood cell counts in CML and cyclical neutropenia (CN). The CN data is from dog 113 (Fig. 13.3, as reproduced in Colijn and Mackey, 2005b, Fig. 2), while the CML data is from Vodopick et al. (1972), as reproduced in Colijn and Mackey (2005a), Fig. 2. For both sets of data in B the units of cell number are 10^8 per kilogram, and the time scale is days. **Springer: this figure will need massaging and permissions**

13.2.2 A simple model of blood cell growth

We model the blood production cycle as follows (Belair et al., 1995). We let $n(x, t)$ be the density of blood cells at time t that are x units old, i.e., that were released into the bloodstream at time $t - x$. We suppose that as they age, a fixed percentage of them die, but at some age X all cells die. Consider the rate of change of the total number of cells with age in the interval between $x = a$ and $x = b$. Since $n(b, t)$ is the rate at which cells leave the interval $[a, b]$ due to aging, and $n(a, t)$ is the rate at which they enter that interval, the rate of change of total cell number is given by

$$\frac{d}{dt} \int_a^b n(x, t)\, dx = \int_a^b -\beta n(x, t)\, dx - n(b, t) + n(a, t), \qquad (13.6)$$

where β is the death rate of the cells. Differentiating (13.6) with respect to b, and replacing b by x gives the conservation equation,

$$\frac{\partial n}{\partial t} + \frac{\partial n}{\partial x} = -\beta n. \qquad (13.7)$$

In general, the death rate is expected to be a function of age, so that $\beta = \beta(x)$. However, for this model we take the death rate to be independent of age. At any given time the total number of blood cells in circulation is

$$N(t) = \int_0^X n(x, t) dx. \qquad (13.8)$$

Now we suppose that the production of blood cells is controlled by N, and that once a cohort of cells is formed in the bone marrow, it emerges into the bloodstream as mature cells some fixed time d later, about 5 days. Here we ignore the fact that at high levels of feedback (for example, at high levels of erythropoietin, which occurs when oxygen levels are low) cells mature more rapidly. Thus,

$$n(0, t) = F(N(t - d)), \qquad (13.9)$$

where F is some nonlinear production function that is monotone decreasing in its argument. The function F is related to the rate of secretion of growth inducer (erythropoietin, for example) in response to the blood cell population size.

The steady-state solution for this model is easy to determine. We set $\partial n / \partial t = 0$ and find that

$$n(x) = \begin{cases} n(0)e^{-\beta x}, & x < X, \\ 0, & x > X, \end{cases} \qquad (13.10)$$

where $n(0)$ is yet to be determined. If $N_0 = \int_0^X n(x)\, dx$ is the total number of cells in steady state, it follows that

$$N_0 = \int_0^X n(0)e^{-\beta x}\, dx = \frac{n(0)}{\beta}(1 - e^{-\beta X}). \qquad (13.11)$$

At steady state, $F(N_0) = n(0)$, and thus it follows that

$$F(N_0) = \frac{\beta N_0}{1 - e^{-\beta X}}. \qquad (13.12)$$
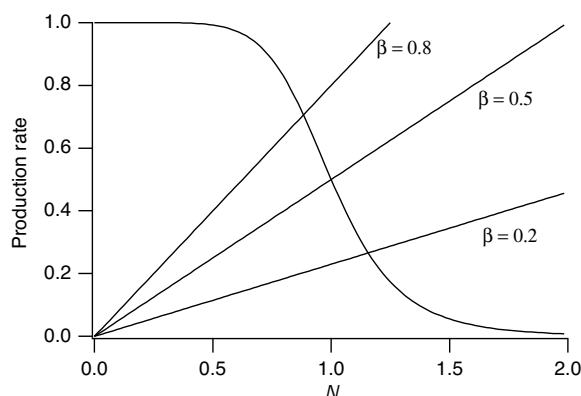
Figure 13.5: Plot of left- and right-hand sides of (13.12) for three different values of β and for $F(N) = \frac{1}{1+N^7}$ and $X = 10$.

Since $F(N_0)$ is a monotone decreasing function of N_0, (13.12) is guaranteed to have a unique solution. In fact, the solution is a monotone decreasing function of the parameter β, indicating that at higher death rates, the cell population drops while the production of cells increases. An illustration of these facts is provided by the graph in Fig. 13.5, where the two curves $F(N)$ and $\frac{\beta N}{1-e^{-\beta X}}$ are plotted as functions of N. Here the function $F(N)$ is taken to be $F(N) = \frac{A}{1+N^7}$, as suggested by data from autoimmune-induced hemolytic anemia in rabbits (Belair et al., 1995).

The next interesting question to ask is whether this steady solution is stable or unstable. It is convenient to integrate the partial differential equation (13.7) to get an ordinary differential equation. Integrating (13.7) from $x = 0$ to $x = X$ gives

$$\frac{dN}{dt} + n(X,t) - n(0,t) = -\beta N. \tag{13.13}$$

Since $n(0,t) = F(N(t-d))$ and $n(X,t) = F(N(t-d-X))e^{-\beta X}$, it follows that $N(t)$ is governed by the delay differential equation

$$\frac{dN}{dt} + F(N(t-d-X))e^{-\beta X} - F(N(t-d)) = -\beta N. \tag{13.14}$$

Note that the steady state of (13.14) is (13.12) as expected.

We now linearize around the steady state, N_0, by looking for solutions of the form $N(t) = N_0(1 + \epsilon e^{\lambda t})$, where $\epsilon \ll 1$. Substituting this form into (13.14), and ignoring all terms of $O(\epsilon^2)$ gives

$$\lambda + F'(N_0)e^{-\lambda(d+X)}e^{-\beta X} - F'(N_0)e^{-\lambda d} = -\beta, \tag{13.15}$$

from which it follows that

$$F'(N_0)e^{-\lambda d}\frac{1 - e^{-(\lambda+\beta)X}}{\lambda + \beta} = 1. \tag{13.16}$$

The roots λ of this equation determine the stability of the linearized solution. If all the roots have negative real part, then the solution is stable, whereas if there are roots with positive real part, the steady solution is unstable. For the remainder of this discussion, we take $\beta = 0$. This implies that all cells die at exactly age X. A different simplification, taking $X \to \infty$, leads to a delay differential equation that is discussed in Chapter 14 (see also Exercise 4).

In the limit $\beta \to 0$, the characteristic equation (13.16) is

$$F'(N_0)(e^{-\lambda d} - e^{-\lambda(d+X)}) = \lambda. \tag{13.17}$$

Since $F'(N_0) < 0$, there are no positive real roots. (The root at $\lambda = 0$ is spurious.)

There is possibly one negative real root; all other roots are complex. It follows that even if the steady solution is stable, the return to steady state is oscillatory rather than monotone. Thus, following rapid disruptions of blood cell population, such as traumatic blood loss or transfusion, or a vacation at a high-altitude ski resort, the blood cell population will oscillate about its steady state.

The only possible way to have a root with positive real part is if it is complex. Furthermore, a transition from stable to unstable can occur only if a complex root changes the sign of its real part, leading to a Hopf bifurcation. If a Hopf bifurcation occurs, it does so with $\lambda = i\omega$. We substitute $\lambda = i\omega$ into (13.17) and separate this into its real and imaginary parts to obtain

$$\begin{aligned} F'(N_0)(\cos{(\omega d)} - \cos(\omega(d + X))) &= 0, \tag{13.18} \\ F'(N_0)(\sin{(\omega d)} - \sin(\omega(d + X))) &= -\omega. \tag{13.19} \end{aligned}$$

There are two ways to solve (13.18). Because cosine is symmetric about any multiple of π, we can take $n\pi - \omega d = n\pi + \omega(d + X)$, or $\omega(2d + X) = 2n\pi$, for any positive integer n. Because cosine is 2π periodic, we could also take $\omega X = 2n\pi$, however, since sine is also 2π periodic, this fails to give a solution of (13.19). With $\omega(2d+X) = 2n\pi$, (13.19) becomes

$$2dF'(N_0)\sin(\omega d) = -\omega d, \tag{13.20}$$

or

$$2dF'(N_0) = -\frac{2n\pi}{2 + \frac{X}{d}}\frac{1}{\sin\left(\frac{2n\pi}{2+\frac{X}{d}}\right)}. \tag{13.21}$$

Finally, we use that $F(N_0) = N_0/X$ to write

$$\frac{N_0 F'(N_0)}{F(N_0)} = -\frac{1}{2}\frac{X}{d}\frac{2n\pi}{2 + \frac{X}{d}}\frac{1}{\sin(\frac{2n\pi}{2+\frac{X}{d}})}. \tag{13.22}$$

For each integer n, this equation defines a relationship between N_0 and X/d at which there is a change of stability and thus, a Hopf bifurcation. If we take F to be of the special form

$$F(x) = \frac{A}{1 + x^p}, \tag{13.23}$$

we can use (13.12) (in the limit $\beta \to 0$) and (13.22) to find an analytic relationship between $dA(= dF(0))$ and X/d at which Hopf bifurcations occur (see Exercise 2).
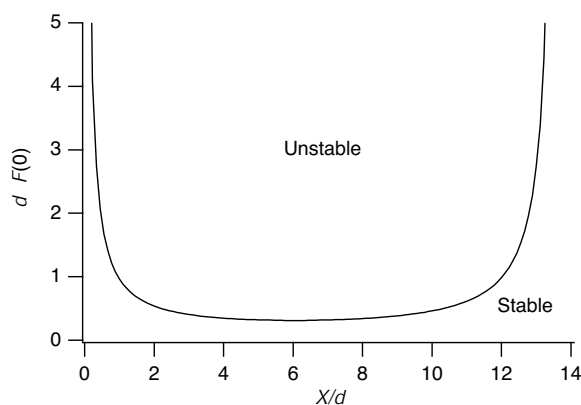
Figure 13.6: Critical stability curve (Hopf bifurcation curve) for cell growth.

Shown in Fig. 13.6 is this curve for $n = 1$ and $p = 7$. The case $n = 1$ is the only curve of interest, since it is the first instability. That is, the steady state solution is unstable for all the critical stability curves with $n > 1$, and so these curves do not lead to physically relevant bifurcations.

The implications of this calculation are interesting. If the nondimensional parameters X/d and $dF(0)$ are such that they lie above the curve in Fig. 13.6, then the steady solution is unstable, and a periodic or oscillatory solution is likely (but since we do not know the direction of bifurcation, this is not guaranteed). On the other hand, if these parameters lie below or to the far right of this curve, the steady solution is stable.

From this we learn that there are three mechanisms by which cell production can be destabilized, and these are by changing the maximal production rate $F(0)$, the expected lifetime X, or the production delay d. If X/d is sufficiently large ($> \approx 14$ for these parameter values), the system cannot be destabilized. However, if X/d is small enough, increasing $F(0)$ is destabilizing. Increasing d is also destabilizing. If $F(0)$ and X are held fixed, then changing d moves $y = dF(0)$ and $x = X/d$ along the hyperbola $yx = $ constant. Thus, decreasing d is stabilizing, as it increases X/d, moving it out of and away from the unstable region.

For normal humans, with $d = 5$ days and $X = 120$ days, there is no instability, since $X/d = 24$. However, any mechanism that substantially shortens X can have a destabilizing effect and can result in oscillatory production of blood cells (Exercise 3). Near the bifurcation, the period of oscillation is $T = \frac{2\pi}{\omega}$, where $\omega(2d + X) = 2\pi$, so that

$$T = 2d + X. \tag{13.24}$$

Thus, for example, a disorder that halves the normal lifetime of blood cells to $X = 60$ days should result in oscillatory blood cell production with a period on the order of 70 days.

13.2.3   Peripheral or local control?

Models of periodic hematopoietic disorders typically fall into one of two classes. The first class of models rely on the observation that in certain disorders, many of the blood cell types show oscillatory behavior, and thus the disease is modeled as generated by local regulation of the stem cell dynamics (Fig. 13.2). In this scenario, the progenitors of each of the cell types have periodic input from the stem cells, and thus the numbers of terminally differentiated cells have the potential to oscillate (although they are not required to). Mackey (1978) and Milton and Mackey (1989) are models of this type.

The other type of model (Morley, 1979; Wichmann et al., 1988; Schmitz et al., 1990) explains the oscillations as the result of instability in the peripheral control feedback (governed by, for example, erythropoietin, or G-CSF, via the cell population, see Fig. 13.2). The model presented in the previous section is of this type.

However, a detailed analysis of peripheral control models suggests that such models, irrespective of the specific mechanisms assumed, are less likely to be an explanation for the observed oscillations (Hearn et al., 1998; Mackey et al., 2003).

To illustrate a peripheral control model, we let x be the density of neutrophils (in number of cells per microliter), let α be their death rate, and let $\mathcal{M}$ denote their rate of production. We do not specify the exact form of $\mathcal{M}$ but use only its qualitative properties. We assume that $\mathcal{M}$ depends on a delayed, weighted average of x. That is, we let $\tilde{x}(t) = \tilde{X}(t - \tau_m)$ where

$$\tilde{X}(t) = \int_{-\infty}^{t} x(s)g(t - s)\,ds \tag{13.25}$$

is the convolution of x with weighting function g, and where τ_m is the minimal maturation delay. A typical choice of g is the gamma distribution,

$$g(\tau) = \begin{cases} 0, & \tau \leq 0, \\ \frac{a^{k+1}}{\Gamma(k+1)}\tau^k e^{-a\tau}, & \tau > 0. \end{cases} \tag{13.26}$$

This gives a good fit to experimental data on the distribution of maturation times, and can be further motivated by the fact that it is the solution of a kth order linear filter (see Exercise 7), if k is an integer. For example, if $k = 0$ then $\tilde{X}$ satisfies the differential equation

$$\frac{d\tilde{X}}{dt} = x - \alpha\tilde{X}, \tag{13.27}$$

so that $\tilde{X}$ can be thought of as a substance that is produced at a rate proportional to x with a natural decay rate α.

The production rate, $\mathcal{M}$, is defined to be some function of $\tilde{x}$, and thus the full model is

$$\frac{dx}{dt} = -\alpha x + \mathcal{M}(\tilde{x}). \tag{13.28}$$

The only additional assumption is that $\mathcal{M}$ is a monotonically non-increasing function of $\tilde{x}$, so that there is negative feedback.

Letting x^* denote the steady state solution, we see that

$$\alpha x^* = \mathcal{M}(x^*), \tag{13.29}$$

which, since $\mathcal{M}$ is monotonically decreasing, has a unique solution. We are interested in the stability of this solution, to determine if it can be unstable, giving rise to oscillatory solutions.

For convenience, let $\mu = \mathcal{M}'(x^*) < 0$ and let $u = x - x^*$. Then, the linearization of (13.28) is

$$\frac{du}{dt} = -\alpha u + \mu \int_{-\infty}^{t-\tau_m} u(s) g(t - s - \tau_m) \, ds. \tag{13.30}$$

Looking for solutions of the form $u = e^{\lambda t}$ gives

$$\lambda + \alpha = \mu \left(\frac{a}{\lambda + a} \right)^{k+1} e^{-\lambda \tau_m}. \tag{13.31}$$

Solutions of this equation with the real part of λ greater than zero correspond to unstable steady states.

It is left to Exercise 9 to show that, if (13.31) has a real solution, it must be negative and lie between $-a$ and $-\alpha$.

Since the only possibility for instability is when λ is complex, we set $\lambda = i\omega$ to find a possible boundary between stability and instability. This gives

$$i\omega + \alpha = \mu \left(\frac{a}{i\omega + a} \right)^{k+1} e^{-i\omega \tau_m}. \tag{13.32}$$

Our goal is to find a curve in the a, μ plane that is a possible stability boundary. We do this by separating (13.32) into real and imaginary parts and finding parametric expressions for $\alpha(\omega)$ and $\mu(\omega)$.

We begin by setting

$$e^{i\theta} = \frac{a + i\omega}{\sqrt{a^2 + \omega^2}}, \tag{13.33}$$

in which case, (13.32) becomes

$$(\alpha + i\omega)(\cos[(k+1)\theta] + i \sin[(k+1)\theta]) = \mu \cos^{k+1} \theta e^{-i\omega \tau_m}. \tag{13.34}$$

Next, equate the real and imaginary parts to get the two equations

$$\alpha - \mu R \cos \omega \tau_m = \omega \tan[(k+1)\theta], \tag{13.35}$$

$$\alpha \tan[(k+1)\theta] = -\mu R \sin \omega \tau_m - \omega, \tag{13.36}$$

where

$$R = \frac{\cos^{k+1} \theta}{\cos[(k+1)\theta]}. \tag{13.37}$$

Finally, solving (13.35) and (13.36) to get α and μ as functions of ω gives

$$\alpha(\omega) = \frac{-\omega}{\tan[\omega \tau_m + (k+1) \tan^{-1}(\omega/a)]}, \tag{13.38}$$

$$\mu(\omega) = \frac{-\omega}{\cos^{k+1}[\tan^{-1}(\omega/a)] \sin[\omega \tau_m + (k+1) \tan^{-1}(\omega/a)]}. \tag{13.39}$$
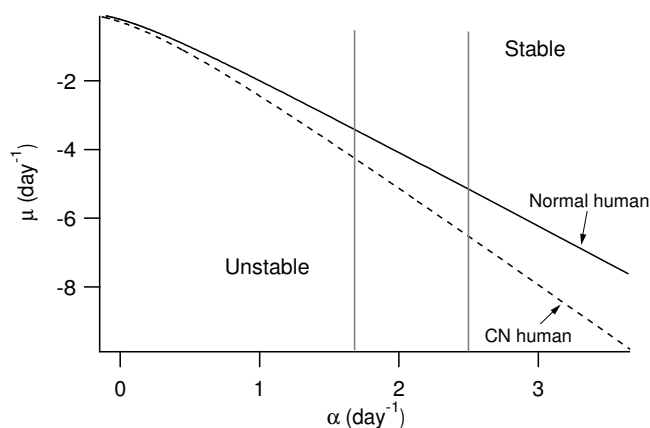
Figure 13.7: Curves that divide the μ-α plane into regions of stability and instability. Parameter values below the curves give an unstable steady state, while parameter values above the curves give a stable steady state. The two vertical lines delineate the region of reasonable values for α. Parameter values are $\tau_m = 3.8$, $a = 0.36$, $k + 1 = 3.15$ (for normal humans) and $\tau_m = 1.2$, $a = 0.53$, $k + 1 = 4.38$ (for CN humans).

Plots of μ against α are shown in Fig. 13.7, the solid curve using the parameters for normal humans, and the dashed curve using the parameters for humans with cyclical neutropenia, i.e., CN humans (Hearn et al., 1998). Typical values for α are between the two vertical lines. **It would be nice to know a little more about CN physiology in order to understand why these parameter values are different. JK**

The stability diagram in Fig. 13.7 has two interesting consequences. First, if the steady state is stable for a normal human, it is also stable for a human with cyclical neutropenia with the same values of μ and α. Thus, changes to the parameters τ, a and m appropriate for cyclical neutropenia are not sufficient to generate instability. Furthermore, it is known experimentally that α is the same in both normal and CN humans. Hence, the only way by which the stable state can become unstable in CN humans is by a decrease in μ, i.e., a decrease in the steady state slope of the production function.

Second, consider the period of the oscillations that arise at the Hopf bifurcations. Recall that, on the curves in Fig. 13.7, the solution has the form $e^{i\omega t}$, and thus has period $2\pi/\omega$. To get reasonable values of α (i.e., between the two vertical lines in Fig. 13.7), ω must be between approximately 0.44 and 0.46. Thus, there is only a narrow window of values for ω that give acceptable behavior, and consequently the period of the resulting oscillations is restricted to be between approximately 14.3 and 13.7 days. Since this range is considerably lower than the period of the observed oscillations, which ranges from 19 to 30 days it suggests that this model does not capture the correct oscillatory mechanism, and thus that CN oscillations

are not caused by instabilities in the peripheral control system.

This conclusion from the linear stability analysis is supported by numerical solution of the model in the nonlinear regime (Hearn et al., 1998), which shows that the period of the oscillation can be made larger only with difficulty, and at the price of having solutions which look quite different from those observed experimentally.

13.3 Erythrocytes

Erythrocytes (red blood cells) are small biconcave discs measuring about 8 μm in diameter. They are flexible, allowing them to change shape and to pass without breaking through blood vessels with diameters as small as 3 μm. Their function is the transport of oxygen from the lungs to the rest of the body, and they accomplish this with the help of a large protein molecule called *hemoglobin*, which binds oxygen in the lungs, later releasing it in tissue. Hemoglobin is the principal protein constituent of mature erythrocytes. A similar protein, *myoglobin*, is used to store and transport oxygen within muscle; mammals that dive deeply, such as whales and seals, have skeletal muscle that is especially rich in myoglobin.

13.3.1 Myoglobin and Hemoglobin

The binding of oxygen with myoglobin and hemoglobin serves as an excellent example of relatively simple chemical reactions that are of fundamental importance in blood physiology. We get some understanding of this process by examining the experimentally determined saturation function for hemoglobin and myoglobin as a function of the partial pressure of oxygen. For myoglobin the saturation curve is much like a standard Michaelis–Menten saturation function, while for hemoglobin it is sigmoidal-shaped (Fig. 13.8). From these curves we see that when the partial pressure of oxygen is at 100 mm Hg (about what it is in the lungs), hemoglobin is 97% saturated. This amount is affected only slightly by small changes in oxygen partial pressure, because at this level the saturation curve is relatively flat. In veins or tissue, however, where the partial pressure of oxygen is about 40 mm Hg, the saturation is about 75%. Furthermore, because this is on a steep portion of the saturation curve, if the metabolic demand for oxygen should decrease the oxygen pressure to, say, 20 mm Hg, then hemoglobin gives up its oxygen readily, reducing its saturation to about 35%. At this value of oxygen partial pressure the saturation of myoglobin is at 90%. Thus, if the tissue is muscle, oxygen is readily transferred from hemoglobin to myoglobin, since the affinity of myoglobin for oxygen is greater than that of hemoglobin.

These saturation curves are of fundamental importance to blood chemistry, so it is of interest to understand why the saturation curves of the two are as they are. We can derive models of these saturation curves from the underlying chemistry (see Section 1.4.4 on cooperativity). Myoglobin consists of a polypeptide chain and a disc-shaped molecular ring called a *heme group*, which is the active center of myoglobin. At the center of the heme group is an iron atom, which can bind with oxygen, forming oxymyoglobin. Hemoglobin consists of four such polypeptide chains (called *globin*) and four heme groups, allowing the binding of four oxygen
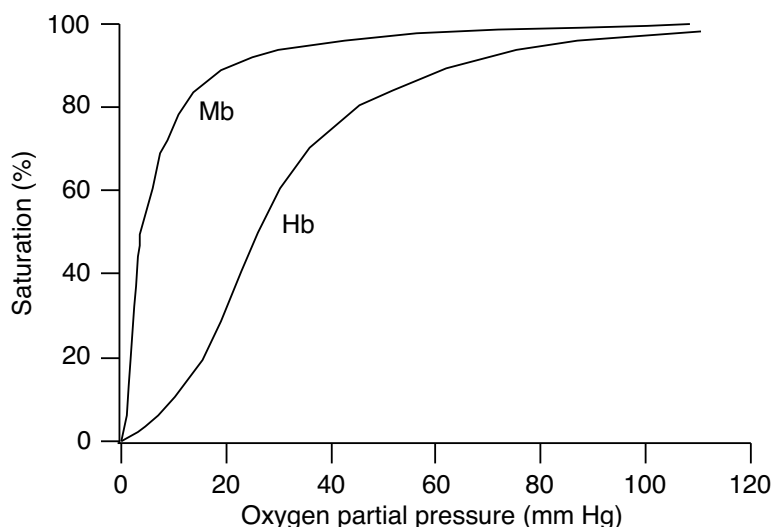
Figure 13.8: Uptake of oxygen by myoglobin and hemoglobin. (Rubinow, 1975, Fig. 2.13, p. 82, taken from Changeux, 1965.)

molecules. When bound with oxygen, the iron atoms in hemoglobin and myoglobin give them their red color. Myoglobin content accounts for the difference in color between red meat such as beef, and white meat such as chicken.

A simple reaction scheme describing the binding of oxygen with myoglobin is

$$O_2 + Mb \underset{k_-}{\overset{k_+}{\rightleftharpoons}} MbO_2.$$
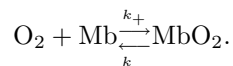
At equilibrium $k_+[Mb][O_2] = k_-[MbO_2]$, so that the percentage of occupied sites is

$$Y = \frac{[MbO_2]}{[Mb] + [MbO_2]} = \frac{[O_2]}{K + [O_2]}, \tag{13.40}$$

where $K = k_-/k_+$.

To compare the function (13.40) with the saturation curve for myoglobin in Fig. 13.8, we must relate the oxygen concentration to the oxygen partial pressure via $[O_2] = \sigma P_{O_2}$. Then, (13.40) becomes

$$Y = \frac{P_{O_2}}{K/\sigma + P_{O_2}} = \frac{P_{O_2}}{K_P + P_{O_2}}, \tag{13.41}$$

and we get a good fit of the myoglobin uptake curve in Fig. 13.8 with $K_P = 2.6$ mm Hg. Notice that the equilibrium constant K_P is in units of pressure rather than concentration, as is more typical. The equilibrium constant K is related to K_P through $K = \sigma K_P$. For the myoglobin saturation curve $K = 3.7\ \mu M$; however, because it is typical to describe concentrations of dissolved gases in units of pressure,
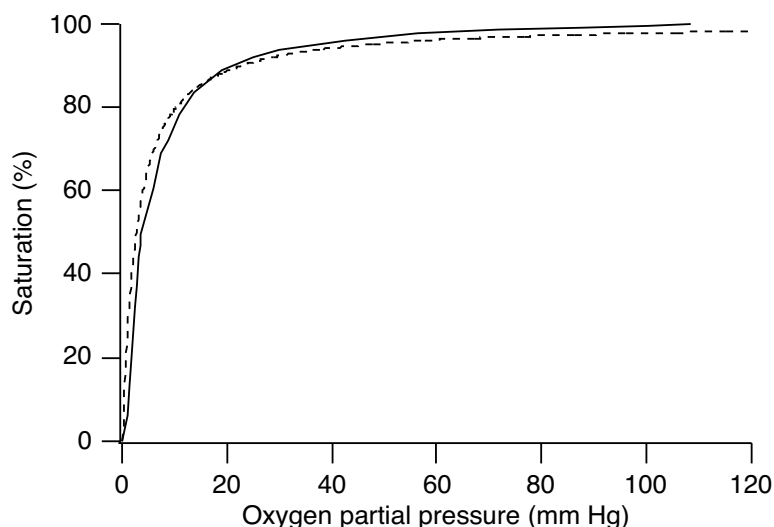
Figure 13.9: Comparison of myoglobin saturation curve (solid) with the curve (13.41) (dashed) with $K_P = 2.6$ mm Hg.

it is also typical to write the equilibrium constant K in these units as $K = 2.6\sigma$ mm Hg. A comparison of the curve (13.41) with the data is shown in Fig. 13.9.

The primary reason that the saturation curve for hemoglobin is significantly different from that for myoglobin is that it has four oxygen binding sites instead of one. A simple kinetic scheme for the formation of oxyhemoglobin is

$$4O_2 + Hb \underset{k_-}{\overset{k_+}{\rightleftarrows}} Hb(O_2)_4,$$
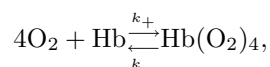
with the corresponding differential equation

$$\frac{d[Hb]}{dt} = k_-[Hb(O_2)_4] - k_+[Hb][O_2]^4. \tag{13.42}$$

At steady state, the percentage of available hemoglobin sites that are bound to oxygen is

$$Y = \frac{[Hb(O_2)_4]}{[Hb(O_2)_4] + [Hb]} = \frac{[O_2]^4}{[O_2]^4 + K^4}, \tag{13.43}$$

where $K^4 = k_-/k_+$. We use the half-saturation level from the hemoglobin uptake curve in Fig. 13.8 to estimate K as $K = 26\sigma$ mm Hg.

While (13.43) (shown as a short dashed curve in Fig. 13.10) reproduces some features of the uptake curve that are qualitatively correct, it is not quantitatively accurate. In fact, one can achieve a much better fit of the data with the Hill equation

$$Y = \frac{[O_2]^n}{[O_2]^n + K^n}, \tag{13.44}$$

with $n = 2.5$ and $K = 26\sigma$ mm Hg. However, there is no adequate theoretical basis for such a model.

A better model keeps track of the elementary reactions involved in the binding process, and is given by

$$O_2 + H_{j-1} \underset{k_{-j}}{\overset{k_j}{\rightleftharpoons}} H_j, \qquad j = 1, 2, 3, 4,$$
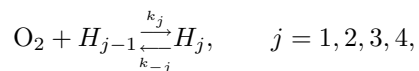
where $H_j = \text{Hb}(O_2)_j$. The steady state for this reaction is attained at

$$[H_j] = \frac{k_{+j}}{k_{-j}} [H_{j-1}][O_2] = \frac{[H_{j-1}][O_2]}{K_j}, \tag{13.45}$$

and the saturation function is

$$Y = \frac{\sum_{j=0}^4 j H_j}{4 \sum_{j=0}^4 H_j}. \tag{13.46}$$

Substituting (13.45) into (13.46) we obtain the saturation function

$$Y = \frac{\sum_{j=0}^4 j \alpha_j [O_2]^j}{4 \sum_{j=0}^4 \alpha_j [O_2]^j}, \tag{13.47}$$

where $\alpha_j = \prod_{i=1}^j K_i^{-1}$, $K_j = k_{-j}/k_{+j}$, $\alpha_0 = 1$.

One can fit the saturation function (13.47) to the hemoglobin uptake curve shown in Fig. 13.8, with the result $K_1 = 45.9, K_2 = 23.9, K_3 = 243.1, K_4 = 1.52\sigma$ mm Hg (Roughton et al., 1972). The striking feature of these numbers is that K_4 is much smaller than K_1, K_2, or K_3, indicating that there is apparently a greatly enhanced affinity of oxygen for hemoglobin if three oxygen molecules are already bound to it. Hemoglobin prefers to be "filled up" with oxygen. The mechanism for this positive cooperativity is not completely understood. (If the binding sites were independent, then K_1 would be the smallest and K_4 would be the largest equilibrium constant; see Exercise 10 and Section 1.4.4.)

Notice that the affinity of oxygen for myoglobin is greater than for any of the binding sites of hemoglobin. In Fig. 13.10 is shown a comparison between the data and the approximate curves (13.43) and (13.47). The Hill equation fit (13.44) is not shown because it is nearly identical to (13.47).

The structure and function of hemoglobin has been intensively studied for over 100 years, and has motivated some of the most important biophysical models of cooperativity (Eaton et al., 1999). Some of the earliest studies were those of Christian Bohr (father of the physicist Niels Bohr) who measured the sigmoidal binding curve of hemoglobin (Bohr et al., 1904), and who also discovered that carbon dioxide lowers the oxygen binding affinity (the Bohr effect). Some years later, the physiologist Adair (Adair, 1925) discovered that hemoglobin contains four binding sites. However, the connection between the sigmoidal binding curve and the number of binding sites was not made explicit until the work of Linus Pauling (1935), who suggested that the binding of oxygen to one binding site, or subunit, could increase the binding affinity to the neighboring subunits, thus leading to a sigmoidal binding curve.
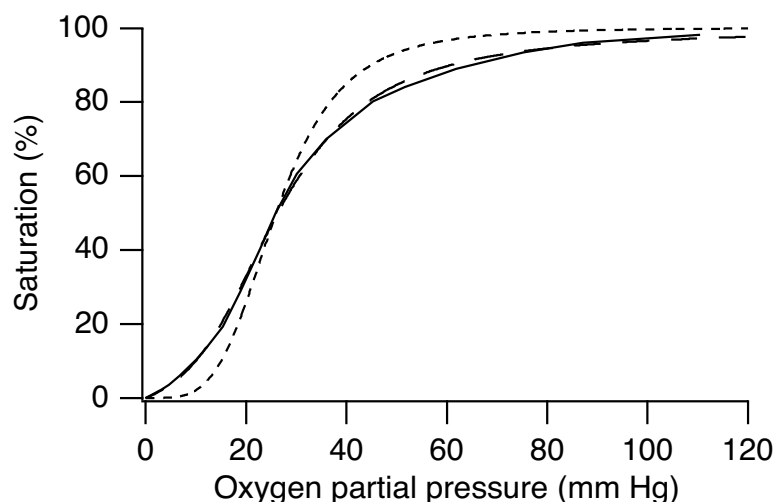
Figure 13.10: Comparison of hemoglobin saturation curve (solid) with the curves (13.43) (short dashed) and (13.47) (long dashed).

The Pauling model was later extended by Koshland, Nemethy and Filmer (1966; Koshland and Hamadani, 2002), giving the so-called KNF, or *sequential*, model.

However, a different model of cooperativity was proposed by Monod, Wyman, and Changeux (1965) The experimental work of Perutz et al. (1964) showed that binding of oxygen resulted in a conformational change in the hemoglobin β subunits, which moved closer together. In the Monod-Wyman-Changeux (MWC) model, hemoglobin is assumed to exist in two structural states, R (relaxed) and T (tense). The R structure has a high affinity for oxygen, while the T structure has a low affinity. As oxygen pressure increases, a greater proportion of hemoglobin exists in the R state, and thus the overall affinity for oxygen increases as oxygen is bound. The major difference from the KNF model is that, in the MWC model, all the subunits switch between the R and T states simultaneously, and are thus always in the same state. However, in the KNF model, the binding of oxygen to one subunit causes a change in the binding affinity of the neighboring subunits, rather than a change in the state of every subunit. The construction of MWC models is discussed in detail in Chapter 1 (also see Exercise 12).

Perutz (1970) proposed a specific physical mechanism that could explain the assumptions used in the MWC model. He proposed that the subunits are connected by salt bridges when hemoglobin is in the T structure. Binding of an oxygen to one subunit could break a salt bridge and destabilize the structure, thus biasing hemoglobin to the R state. The energy required to break the salt bridge upon oxygen binding serves to decrease the affinity of the T structure for oxygen.

Although many refinements of the basic MWC mechanism have been constructed, our understanding of the basic mechanism remains relatively unchanged today. However, there is also experimental evidence for a sequential binding model of

KNF type (Koshland and Hamadani, 2002), and the actual mechanism probably lies somewhere between these two extremes.

13.3.2   Hemoglobin Saturation Shifts

There are a number of factors that affect the binding of oxygen to hemoglobin, the most important of which is the hydrogen ion, which is an allosteric inhibitor of oxygen binding (Chapter 1). As is discussed in Chapter 14, the interactions between oxygen concentration and carbon dioxide concentration (which indirectly changes the hydrogen ion concentration) are important for transport of both oxygen and carbon dioxide.

Carbon monoxide combines with hemoglobin at the same binding site as oxygen (and is a competitive inhibitor), but with an affinity more than 200 times greater. Therefore the carbon monoxide saturation curve is almost identical to the oxygen saturation curve, except that the abscissa is scaled by a factor of about 200. At a carbon monoxide partial pressure of 0.5 mm Hg, and in the absence of oxygen, hemoglobin is 97% saturated with carbon monoxide. If oxygen is present at atmospheric concentrations, then it takes a carbon monoxide partial pressure of only 0.7 mm Hg (about 0.1 percent) to cause oxygen starvation in the tissues (Chapter 17).

Fetal hemoglobin, a different type of hemoglobin found in the fetus, has a considerable leftward shift for its oxygen saturation curve. This allows fetal blood to carry as much as 30% more oxygen at low oxygen partial pressures than can adult hemoglobin. This is important since the oxygen partial pressure in the fetus is always low. The left-shift of the fetal hemoglobin saturation curve is also important for the transfer of oxygen from mother to fetus.

Because it is important in the next section, here we construct a simple model of the allosteric inhibition by hydrogen ions of oxygen binding to hemoglobin. As illustrated in Fig. 13.11, we assume that the hemoglobin molecule can exist in four different states: with H^+ bound (concentration Z), with O_2 bound (concentration Y), with neither bound (concentration X), or with both bound (concentration W). This is, of course, an extreme simplification, as it ignores the cooperative nature of oxygen binding discussed in the previous section and in Chapter 1, but nevertheless the results are qualitatively correct.

Assuming that each reaction is at equilibrium, we find

$$O^4 X \;=\; K_1 Y, \tag{13.48}$$

$$h X \;=\; K_2 Z, \tag{13.49}$$

$$O^4 Z \;=\; \bar{K}_1 W, \tag{13.50}$$

$$X + Y + Z + W \;=\; T_{\text{Hb}}, \tag{13.51}$$

where h denotes $[H^+]$, O denotes $[O_2]$, T_{Hb} denotes the total concentration of hemoglobin, $K_1 = k_{-1}/k_1$ and similarly for K_2, $\bar{K}_1$ and $\bar{K}_2$ (which is needed below). Solving these four equations we find

$$Y + W = \frac{O^4 T_{\text{Hb}}}{\phi(h) + O^4}, \tag{13.52}$$
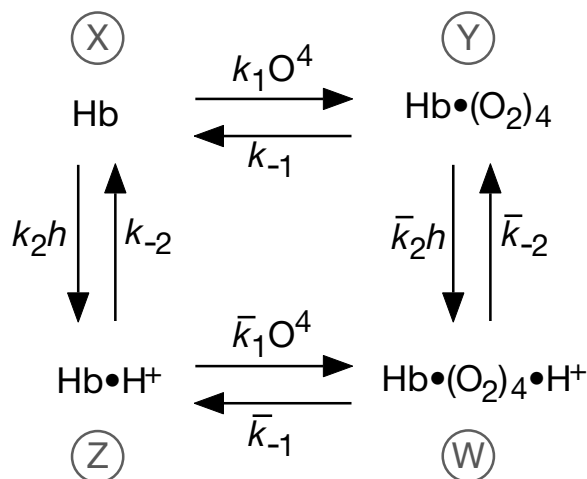
Figure 13.11: Binding diagram for the allosteric binding of hydrogen ions and oxygen to hemoglobin. We assume a single hydrogen ion binding site, and a simplified mechanism for oxygen binding. Hb denotes hemoglobin.

where

$$\phi(h) = \frac{K_1 \bar{K}_1 (K_2 + h)}{K_2 \bar{K}_1 + h K_1}. \tag{13.53}$$

We are interested in determining $Y + W$ as a function of O, since $Y + W$ is the total concentration of hemoglobin with oxygen bound, and thus plotting $Y + W$ as a function of O gives the oxygen saturation curve.

It is easily seen from (13.52) that h does not change the maximal saturation, although it shifts the mid-point of the curve. Since hydrogen ions are an allosteric inhibitor of oxygen binding, we assume that $\bar{K}_1 > K_1$. Note that, in this case, $\phi(h)$ is an increasing function of h, and thus increasing h shifts the saturation curve to the right, as expected.

Before we can discuss the importance of the allosteric effect of hydrogen ions on oxygen binding it is necessary to discuss the mechanism of carbon dioxide transport.

13.3.3 Carbon Dioxide Transport

While oxygen is taken up in the lungs and transported to the tissues, carbon dioxide must be transported in the reverse direction from the tissues to the lungs for removal from the body. In the blood, CO_2 is transported in three main forms. In venous blood a significant amount (about 6%) is present as dissolved CO_2. A slightly greater amount (about 7%) is bound to the globin part of hemoglobin as carbamino compounds, but most CO_2 (87%) is present in the form of bicarbonate ions.

In the tissues CO_2 diffuses down its concentration gradient into the plasma and into the red blood cells. In both plasma and red blood cells it combines with water to form carbonic acid (H_2CO_3), which then dissociates quickly into hydrogen ions

and bicarbonate ions. Thus,

$$\text{CO}_2 + \text{H}_2\text{O} \overset{r_1}{\underset{r_{-1}}{\rightleftarrows}} \text{H}_2\text{CO}_3 \overset{r_2}{\underset{r_{-2}}{\rightleftarrows}} \text{H}^+ + \text{HCO}_3^-. \tag{13.54}$$
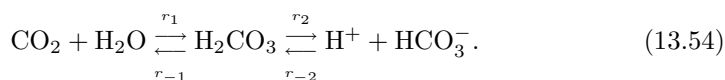
This reaction proceeds slowly in the plasma but much more rapidly in the red blood cells because of the presence there of the enzyme *carbonic anhydrase*, which increases the speed of CO_2 hydration by more than a thousand times. The H^+ formed by the dissociation of carbonic acid binds to the globin part of hemoglobin, and the bicarbonate ion diffuses into the plasma in exchange for Cl^-.

In the lungs the reaction is reversed, as CO_2 diffuses down its concentration gradient to be excreted in the alveolar air and then the expired air. It is important to emphasize that the direction of the carbonic anhydrase reaction (13.54) is determined by the local concentration of CO_2. In the tissues, $[\text{CO}_2]$ is high, which drives reaction (13.54) from left to right, thus storing CO_2 in the blood. In the lungs, $[\text{CO}_2]$ is low, driving the reaction from right to left, thus removing CO_2 from the blood. Of course, carbonic anhydrase speeds up the reaction in both directions; without this increase in speed not enough CO_2 can be stored in the blood to remove it from the body fast enough.

The importance of the allosteric effect of H^+ on oxygen binding to hemoglobin is now apparent. In the tissues, because of the high local CO_2 concentration, the hydration of CO_2 causes an increase in the local concentration of H^+ (i.e., the blood pH falls slightly, from about 7.4 to about 7.35), which in turn results in a decreased affinity of hemoglobin for oxygen, thus increasing oxygen release to the tissues. In the lungs, the reverse occurs; the low local CO_2 concentration causes a decrease in H^+ concentration which results in an increase in hemoglobin oxygen affinity, and thus increased oxygen uptake. This effect of CO_2 concentration on oxygen transport (mediated by the carbonic anhydrase reaction and hydrogen ions), is known as the *Bohr effect*.

It is interesting to note that, from the principle of detailed balance applied to the reaction scheme shown in Fig. 13.11 (i.e., from consistency of the four equilibrium equations) it must be that

$$\frac{K_1}{\bar{K}_1} = \frac{K_2}{\bar{K}_2}. \tag{13.55}$$

It follows that, if $\bar{K}_1 > K_1$ it must also be that $\bar{K}_2 > K_2$. In other words, if H^+ is an allosteric inhibitor of oxygen binding, then oxygen must also be an allosteric inhibitor of H^+ binding. Hence, as CO_2 influences oxygen transport, so too oxygen affects CO_2 transport. In the tissues, where $[\text{O}_2]$ is low, binding of H^+ to hemoglobin is enhanced. This lowers the local H^+ concentration, thus driving the carbonic anhydrase reaction from left to right, and increasing CO_2 storage. The reverse occurs at the lungs. The enhancement of CO_2 transport by low levels of oxygen is called the *Haldane effect*. Note that, according to the principle of detailed balance (at least in this simple model) the Bohr effect implies the Haldane effect, and vice versa.

To construct a mathematical model of CO_2 transport, we assume that the bicarbonate-carbon dioxide reaction is in steady state so that

$$[\text{CO}_2] = R_1 R_2 [\text{H}^+][\text{HCO}_3^-], \tag{13.56}$$

where $R_1 = r_{-1}/r_1$ and $R_2 = r_{-2}/r_2$.

Carbon dioxide enters this system from the tissues and leaves at the lungs. When it does so, bicarbonate is produced or removed. However, since the carbonic anhydrase reaction produces exactly one hydrogen ion for each bicarbonate ion it produces, and since these hydrogen ions must either be free, or bound to hemoglobin, it follows that

$$\Delta[\text{HCO}_3^-] = \Delta h + \Delta Z + \Delta W, \tag{13.57}$$

where Δ denotes the change in concentration. Hence,

$$[\text{HCO}_3^-] = h + Z + W - T_0, \tag{13.58}$$

where $T_0 = h_0 + Z_0 + W_0 - [\text{HCO}_3^-]_0$ is some reference level. In reality each hemoglobin molecule can bind many hydrogen ions, and so the conservation equation should be

$$[\text{HCO}_3^-] = h + n(Z + W) - T_0, \tag{13.59}$$

where n can be as large as 10 or 20, and $T_0 = h_0 + n(Z_0 + W_0) - [\text{HCO}_3^-]_0$. The number n is important, because without it (if $n = 0$), the pH fluctuates widely with changes in bicarbonate (Exercise 13a), whereas in normal blood, practically all the H^+ produced by the carbonic anhydrase reaction is absorbed by hemoglobin. This demonstrates the importance of hemoglobin as a hydrogen ion buffer. Note that, to be consistent, the factor n should also be included in the model for hemoglobin. However, as this would greatly increase the complexity of the binding model without adding anything fundamentally new, we include n in the bicarbonate conservation equation, but not in the binding diagram. A more accurate model gives the same qualitative result.

In addition, the oxygen and carbon dioxide concentrations in arterial and venous blood are unknowns. Their precise values are set by the rate of gas exchange in the lungs and the tissues, the rate of metabolism, and depend to some extent on the properties of the carbonic anhydrase reaction, among other things. Thus, to be strictly correct, we should not treat them as constants, but solve for them as part of a more complicated model. We omit these complications here and treat O and $[\text{CO}_2]$ as known constants, since our primary goal here is to find the other unknowns (X, Y, Z, W and h) as functions of the gas concentrations.

We now have five equations

$$O^4 X = K_1 Y, \tag{13.60}$$
$$hX = K_2 Z, \tag{13.61}$$
$$O^4 Z = \bar{K}_1 W, \tag{13.62}$$
$$X + Y + Z + W = T_{\text{Hb}}, \tag{13.63}$$
$$[\text{CO}_2] = R_1 R_2 h[h + n(Z + W) - T_0], \tag{13.64}$$

to solve for the five unknowns. It is an easy matter to solve (13.60)-(13.63) for X, Y, Z, and W in terms of O^4, h and the other parameters, and substitute these into (13.64). This yields a single equation for $[\text{CO}_2]$ as a function of O^4 and h. This equation can be readily solved numerically for h as a function of $[\text{CO}_2]$ and O^4,

from which one can determine the total amounts of carbon dioxide and oxygen in all their forms. Solution of this equation is left for the exercises (Exercise 13).

The result of this calculation shows that the Bohr effect changes the arterial concentrations of carbon dioxide and oxygen only slightly, but it increases the venous CO_2 and decreases the venous O_2 substantially, giving an increase in the total amount of these that is transported.

As a final note, the most important system for controlling the extracellular acid-base balance is the bicarbonate buffer system. Extracellular fluid contains large amounts of bicarbonate ions, mostly as $Na^+HCO_3^-$. Addition of excess H^+ ions drives the carbonic anhydrase reaction to produce carbon dioxide; the additional CO_2 produced can be removed at the lungs. Conversely, addition of a strong base and the consequent removal of H^+ results in a lowering of $[CO_2]$ and the production of additional H^+. Since the overall levels of bicarbonate and carbon dioxide are controlled by the kidneys and the lungs, respectively, this allows effective and precise control of the pH of extracellular fluid.

13.4   Leukocytes

The *leukocytes* (white blood cells) are the mobile units of the body's immune system. There are six types of white blood cells normally found in the blood. These are the *neutrophils, eosinophils, basophils, monocytes, lymphocytes*, and *natural killer cells* (see Table 13.1 and Fig. 13.1). The neutrophils, eosinophils, and basophils are called *granulocytes*, or in clinical terminology, *polymorphonuclear* (PMN) cells, because they have a granular appearance and have nuclei with a wide variety of shapes (often shaped like a bent sausage). The normal adult human has about 7000 white blood cells per microliter of blood, approximately 62% of which are neutrophils and 30% of which are lymphocytes. The granulocytes and monocytes protect the body against invading organisms mainly by ingesting them, a process called *phagocytosis*.

13.4.1   Leukocyte Chemotaxis

Leukocytes crawl about in tissue by putting out pseudopodal extensions by which they adhere to the fibrous matrix of the tissue. In uniform chemical concentrations of chemical stimulus, their motion is that of a persistent random walk. At random times they undergo random changes in direction. The *persistence time*, the average time between changes of direction, is on the order of a few minutes, and the speed of migration is on the order of 2–20 μm/min.

One important question is how leukocytes are able to find their bacterial targets. The answer is that they move preferentially in the direction of increasing chemoattractant gradients. Exactly how this is accomplished, how this should be modeled, and how well the model represents this behavior is the topic of this section.

Here we derive a simple model for directed motion in a one-dimensional medium (Tranquillo and Lauffenberger, 1987). We assume that the population of cells, c, can be subdivided into two subpopulations, $c = n^+ + n^-$, where superscripts $+$ and $-$ denote right-moving and left-moving cells, respectively. If v^+ is the velocity of

right-moving cells, and v^- is the velocity of left-moving cells, then the flux of cells is given by

$$J_c = v^+ n^+ - v^- n^-. \tag{13.65}$$

We expect that the cell velocity should be a function only of local conditions, so that $v^+ = v^- = v$. In general, v is a function of x and t. Now we write conservation equations for the directional cell species,

$$\frac{\partial n^+}{\partial t} = -\frac{\partial (v n^+)}{\partial x} + p^- n^- - p^+ n^+, \tag{13.66}$$

$$\frac{\partial n^-}{\partial t} = \frac{\partial (v n^-)}{\partial x} + p^+ n^+ - p^- n^-, \tag{13.67}$$

where p^+ is the probability per unit time that a right-moving cell changes direction to become a left-moving cell, and p^- is the probability that a left-moving cell becomes a right-moving cell. These probabilities are also known as *turning rates*.

An equation governing the cell flux J_c is found by differentiating (13.65) and using (13.66) and (13.67), yielding

$$\frac{\partial J_c}{\partial t} - \frac{J_c}{v}\frac{\partial v}{\partial t} = -J_c(p^+ + p^-) - v\frac{\partial (vc)}{\partial x} - vc(p^+ - p^-). \tag{13.68}$$

The steady-state flux is found by setting all time derivatives equal to zero, from which we find that

$$J_c = -v^2 T_p \frac{\partial c}{\partial x} + v(p^- - p^+)T_p c - T_p v\frac{\partial v}{\partial x}c, \tag{13.69}$$

where $T_p^{-1} = p^+ + p^-$.

Now we define phenomenological population migration parameters $\mu = T_p v^2$ as the *random motility coefficient* and $V_c = T_p v(p^- - p^+)$ as the *chemotactic velocity*. Then the equilibrium flux is

$$J_c = -\mu\frac{\partial c}{\partial x} + V_c c - T_p v\frac{\partial v}{\partial x}c. \tag{13.70}$$

Finally, the total cell density is governed by the equation

$$\frac{\partial c}{\partial t} = -\frac{\partial J_c}{\partial x}. \tag{13.71}$$

The movement of cells is governed by three terms in (13.70). The first term, $-\mu\frac{\partial c}{\partial x}$, represents purely random movement of cells, since it gives a diffusive term in (13.71). The second and third terms allow for directed cell movement, since they are proportional to c. The directed motion from the second term is due to a difference in the directional change probabilities, while the directed motion in the third term is due to variation in cell speed with spatial position. The second term is called *chemotaxis*, and the third term is *chemokinesis*.

The next problem is to determine the coefficients of these movement terms and in so doing to understand more about the sensory capabilities of the cells. It is known that cell speed can vary with stimulus concentration, yielding a chemokinetic

effect, and changes in the direction of movements can be biased toward attractant concentration gradients, a chemotactic response. These responses are mediated by cell surface receptors for attractant molecules that can measure the attractant concentration and its spatial gradient.

There is no a priori theory for the dependence of cell speed on attractant concentration, so it must be measured experimentally. For example, with the tripeptide attractant formyl-norleucyl-leucyl-phenylalanine (FNLLP), the data show that leukocyte velocity is a linearly increasing function of the logarithm of concentration over the range of concentrations 10^{-9} M to 10^{-6} M, with velocity about 2–5 μm/min (Zigmond et al., 1981).

Leukocytes determine the presence of an attractant when it binds to receptors on the leukocyte cell surface. When there is a spatial gradient of the attractant, there is also a spatial gradient in the concentration of bound receptors. The side of the cell that experiences a higher concentration of attractant will have a higher concentration of occupied receptors. It has been found experimentally that the fraction of leukocytes that move toward higher attractant concentrations is dependent on this gradient in receptor occupancy. The simplest reasonable expression (Zigmond, 1977) is

$$f = \frac{1}{2}\left(1 + \frac{\chi_0 \frac{\partial N_b}{\partial x}}{1 + \chi_0 \frac{\partial N_b}{\partial x}}\right), \tag{13.72}$$

where f is the fraction of cells moving toward higher concentrations, χ_0 is the chemotactic sensitivity, and N_b is the number of bound cell receptors. Notice that N_b is a function of a, the concentration of chemoattractant, and a is a function of x, so the spatial gradient of N_b is given by $\frac{\partial N_b(a)}{\partial x} = \frac{dN_b}{da}\frac{\partial a}{\partial x}$. For small gradients,

$$f \approx \frac{1}{2}\left(1 + \chi_0 \frac{dN_b}{da}\frac{\partial a}{\partial x}\right), \tag{13.73}$$

while for large gradients, $f \approx 1$. Thus in small gradients, the fraction of cells moving toward higher concentrations is linearly proportional to the gradient, and this fraction approaches 1 as the gradient increases. From data for rabbit leukocytes responding to the peptide attractant formyl-methionyl-methionyl-methionine (FMMM) it is estimated that $\chi_0 = 2 \times 10^{-5}$ cm/receptor.

In a uniform steady state (for which $\frac{\partial n}{\partial x} = 0$), $n^+ p^+ = n^- p^-$, so that

$$f = \frac{n^+}{n^+ + n^-} = \left(1 + \frac{p^+}{p^-}\right)^{-1}. \tag{13.74}$$

Since $T_p = (p^- + p^+)^{-1}$, we find the chemotactic velocity to be

$$V_c = (2f - 1)v = v\frac{\chi_0 \frac{dN_b}{da}\frac{\partial a}{\partial x}}{1 + \chi_0 \frac{dN_b}{da}\frac{\partial a}{\partial x}}. \tag{13.75}$$

For a single homogeneous population of cell receptors, the number of bound receptors is related to the concentration of attractant through a Michaelis–Menten relationship

$$N_b = \frac{N_T a}{K_d + a}, \tag{13.76}$$

where K_d is the receptor dissociation constant and N_T is the total number of cell receptors.

If the function $v = v(a)$ is known, we have a complete model for the flux of cells due to an attractant concentration. In the special case that cell velocity is independent of attractant concentration, and the attractant concentration and gradient are small, this reduces to a well-known model for chemotaxis (Keller and Segel, 1971),

$$J_c = -\mu \frac{\partial c}{\partial x} + \chi c \frac{\partial a}{\partial x}, \tag{13.77}$$

where $\chi = v \chi_0 N_b'(a)$.

13.4.2 The Inflammatory Response

Leukocytes respond to a bacterial invasion by moving up a gradient of some chemical attractant produced by the bacteria and then ingesting the bacterium when it is encountered. Here we present a one-dimensional model (Alt and Lauffenberger, 1987) to determine if and when the leukocytes successfully defend against a bacterial invasion.

There are three concentrations that must be determined. These are the bacterial, attractant, and leukocyte concentrations, denoted by b, a, and c, respectively. The governing equations for these concentrations follow from the following assumptions concerning their behavior:

1. Bacteria diffuse, reproduce, and are destroyed when they come in contact with leukocytes:

$$\frac{\partial b}{\partial t} = \mu_b \frac{\partial^2 b}{\partial y^2} + (k_g - k_d c)b. \tag{13.78}$$

2. The chemoattractant is produced by bacterial metabolism and diffuses:

$$\frac{\partial a}{\partial t} = D \frac{\partial^2 a}{\partial y^2} + k_p b. \tag{13.79}$$

3. The leukocytes are chemotactically attracted to the attractant, and they die as they digest the bacteria, so that

$$\frac{\partial c}{\partial t} = -\frac{\partial J_c}{\partial y} - (g_0 + g_1 b)c. \tag{13.80}$$

For this model we assume that the leukocyte flux is given by (13.77), although more general descriptions are readily incorporated.

To specify boundary conditions we assume that $y = 0$ is the skin surface and that a blood-transporting capillary or venule lies at distance $y = L$ from the skin surface. We assume that the bacteria cannot leave the tissue domain, although the attractant may diffuse into the bloodstream. Leukocytes enter the tissue from the bloodstream at a rate proportional to the circulating leukocyte density c_b. When chemotactic attractant is present, the emigration rate increases, because leukocytes that would

normally flow in the bloodstream tend to adhere to the vessel wall (*margination*) and then migrate into the interstitium. These considerations lead to the boundary conditions

$$\frac{\partial b}{\partial y} = 0 \text{ at } y = 0 \text{ and } y = L, \tag{13.81}$$

$$\frac{\partial a}{\partial y} = \begin{cases} 0 & \text{at } y = 0, \\ -h_a a & \text{at } y = L, \end{cases} \tag{13.82}$$

$$J_c = \begin{cases} 0 & \text{at } y = 0, \\ -(h_0 + h_1 a)(c_b - c) & \text{at } y = L. \end{cases} \tag{13.83}$$

The governing equations are made dimensionless by setting $x = y/L, \tau = k_g t, u = c/c_b, v = b/b_0$, and $w = a/a_0$. We find that

$$\frac{\partial v}{\partial \tau} = \rho_v \frac{\partial^2 v}{\partial x^2} + (1 - \xi u)v, \tag{13.84}$$

$$\frac{\partial w}{\partial \tau} = \rho_w \left(\frac{\partial^2 w}{\partial x^2} + v \right), \tag{13.85}$$

$$\frac{\partial u}{\partial \tau} = \rho_u \left(\frac{\partial^2 u}{\partial x^2} - \alpha \frac{\partial}{\partial x} \left(u \frac{\partial w}{\partial x} \right) \right) - \gamma_0 (1 + v)u, \tag{13.86}$$

where $a_0 = L^2 k_p b_0 / D, b_0 = g_0/g_1, \alpha = \chi a_0/\mu, \rho_v = \frac{\mu_b}{k_g L^2}, \rho_u = \frac{\mu}{k_g L^2}, \rho_w = \frac{D}{k_g L^2}, \xi = k_d c_b/k_g, \gamma_0 = g_0/k_g$.

In nondimensional form the boundary conditions become

$$\frac{\partial v}{\partial x} = 0 \text{ at } x = 0 \text{ and } x = 1, \tag{13.87}$$

$$\frac{\partial w}{\partial x} = \begin{cases} 0 & \text{at } x = 0, \\ -\sigma w & \text{at } x = 1, \end{cases} \tag{13.88}$$

$$\rho_u \left(\frac{\partial u}{\partial x} - \alpha u \frac{\partial w}{\partial x} \right) = \begin{cases} 0 & \text{at } x = 0, \\ \gamma_0 (\beta_0 + \beta_1 w)(1 - u) & \text{at } x = 1, \end{cases} \tag{13.89}$$

where $\sigma = h_a L/D, \beta_0 = \frac{h_0}{g_0 L}, \beta_1 = \frac{h_1 a_0}{g_0 L}$.

There is at least one steady-state solution for this system of equations. It is the *elimination state*, in which $v = w = 0$ and

$$u(x) = \frac{1}{A} \cosh \left(\sqrt{\frac{\gamma_0}{\rho_u}} x \right), \tag{13.90}$$

where $A = \cosh \left(\sqrt{\frac{\gamma_0}{\rho_u}} \right) + \frac{\rho_u}{\gamma_0 \beta_0} \sqrt{\frac{\gamma_0}{\rho_u}} \sinh \left(\sqrt{\frac{\gamma_0}{\rho_u}} \right)$. In this state, all bacteria are eliminated, and the leukocyte density is independent of any bacterial properties. This should represent the normal state for healthy tissue. If γ_0/ρ_u is small, then this steady distribution of leukocytes is nearly constant, at level $(1 + \frac{1}{\beta_0})^{-1}$.

Bacterial diffusion is generally much smaller than the diffusion of leukocytes or of chemoattractant. Typical numbers are $D = 10^{-6}$ cm^2/s, $\mu = 10^{-7}$ cm^2/s, $\mu_b < 10^{-8}$ cm^2/s, $k_g = 0.5$ h^{-1}, and $L = 100$ μm. With these numbers, ρ_u and ρ_w

are relatively large, while ρ_v is small. This leads us to consider an approximation in which bacterial diffusion is ignored, while attractant and leukocyte diffusion are viewed as fast. In this approximation, airborne bacteria can attach to the surface, but they do not move much on the time scale of leukocyte and chemoattractant motion.

Our first approximation is to ignore bacterial diffusion (take $\rho_v = 0$) and then to assume that a bacterial invasion occurs at the skin surface $x = 0$. This is a reasonable assumption for periodontal, peritoneal, and epidermal infections, which are highly localized, slowly moving infections. Then, since we neglect bacterial diffusion, we specify the bacterial distribution by

$$v(x, \tau) = V(\tau)\delta(x), \tag{13.91}$$

where $\delta(x)$ is the Dirac delta function. The governing equation for $V(\tau)$ is

$$\frac{\partial V}{\partial \tau} = (1 - \xi u(0, \tau))V. \tag{13.92}$$

Since $v = 0$ for $x > 0$, the equations for w and u simplify slightly to

$$\frac{\partial w}{\partial \tau} = \rho_w \frac{\partial^2 w}{\partial x^2}, \tag{13.93}$$

$$\frac{\partial u}{\partial \tau} = \rho_u \left(\frac{\partial^2 u}{\partial x^2} - \alpha \frac{\partial}{\partial x} \left(u \frac{\partial w}{\partial x} \right) \right) - \gamma_0 u, \tag{13.94}$$

while the effect of the bacterial concentration at the origin is reflected in the boundary conditions at $x = 0$ (found by integrating (13.85) and (13.86) "across" the origin),

$$\frac{\partial w}{\partial x} = -V, \tag{13.95}$$

$$\rho_u \left(\frac{\partial u}{\partial x} - \alpha u \frac{\partial w}{\partial x} \right) = \gamma_0 V u. \tag{13.96}$$

An identity that is important below is found by integrating (13.94) with respect to x to obtain

$$\gamma_0^{-1} \frac{dU}{dt} = -U - V u(0, \tau) + (\beta_0 + \beta_1 w(1, \tau))(1 - u(1, \tau)), \tag{13.97}$$

where $U(\tau) = \int_0^1 u(x, \tau)dx$ is the total leukocyte population within the tissue.

Our second approximation is to assume that the chemoattractant diffusion is sufficiently large, so that the chemoattractant is in quasi-steady state,

$$\frac{\partial^2 w}{\partial x^2} = 0. \tag{13.98}$$

This implies that $w(x)$ is a linear function of x with gradient

$$\frac{\partial w}{\partial x} = -V. \tag{13.99}$$

Finally, we assume that ρ_u is large (taking $\rho_u \to \infty$), so that the leukocyte density is also in quasi-steady state with $J_c = 0$, that is,

$$\frac{\partial u}{\partial x} + \alpha V u = 0. \tag{13.100}$$

We can solve this equation and find the leukocyte spatial distribution to be

$$u(x, \tau) = U(\tau) F(\alpha V) e^{-\alpha V x}, \tag{13.101}$$

where $F(z) = \frac{z}{1 - e^{-z}}$ is determined by requiring $U(\tau) = \int_0^1 u(x, \tau) dx$.

Now we are able to determine $u(0, \tau), u(1, \tau)$ from (13.101) and $w(1, \tau)$ from (13.88) and (13.99), which we substitute into the equation for total leukocyte mass (13.97) to obtain

$$\gamma_0^{-1} \frac{dU}{d\tau} = (\beta_0 + \beta V) \left(1 - U F(\alpha V) e^{-\alpha V}\right) - (V F(\alpha V) + 1) U, \tag{13.102}$$

where $\beta = \beta_1 / \sigma$. Similarly, from (13.92) and (13.101), we find the equation governing V to be

$$\frac{\partial V}{\partial \tau} = V \left(1 - \xi U F(\alpha V)\right). \tag{13.103}$$

Phase-plane analysis

The system of equations (13.102)–(13.103) is a two-variable system of ordinary differential equations that can be studied using standard phase-plane methods. In this analysis we focus on the influence of two parameters: β, which characterizes the enhanced leukocyte emigration from the bloodstream, and α, which measures the chemotactic response of the leukocytes to the attractant.

One steady-state solution that always exists is $U = (1 + \frac{1}{\beta_0})^{-1}, V = 0$. This represents the elimination state in which there are no bacteria present. Any other steady solutions that exist with $V > 0$ are compromised states in which the bacteria are allowed to persist in the tissue.

We assume that the system is at steady state at time $\tau = 0$ with $U(0) = U_0 = (1 + \frac{1}{\beta_0})^{-1}$ when a bacterial challenge with $V(0) = V_0 > 0$ is presented. We begin the analysis with simple cases for which $\alpha = 0$.

Case I: $\alpha = 0, \beta = 0$.
In this case the system reduces to

$$\gamma_0^{-1} \frac{dU}{d\tau} = \beta_0 - (\beta_0 + 1) U - V U, \tag{13.104}$$

$$\frac{\partial V}{\partial \tau} = V(1 - \xi U). \tag{13.105}$$

There are three nullclines: $\frac{dV}{d\tau} = 0$ on the vertical line $U = \frac{1}{\xi}$ and on the horizontal line $V = 0$, and $\frac{dU}{d\tau} = 0$ on the hyperbola $V = \frac{\beta_0 - (\beta_0 + 1) U}{U}$.

Two types of behavior are possible. If $\xi U_0 < 1$, there are no steady states in the positive first quadrant. The only steady state is at $U = U_0, V = 0$. For
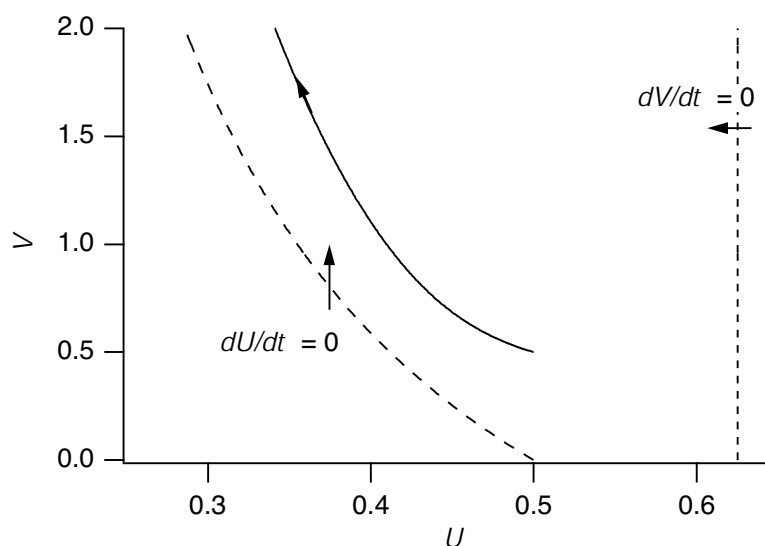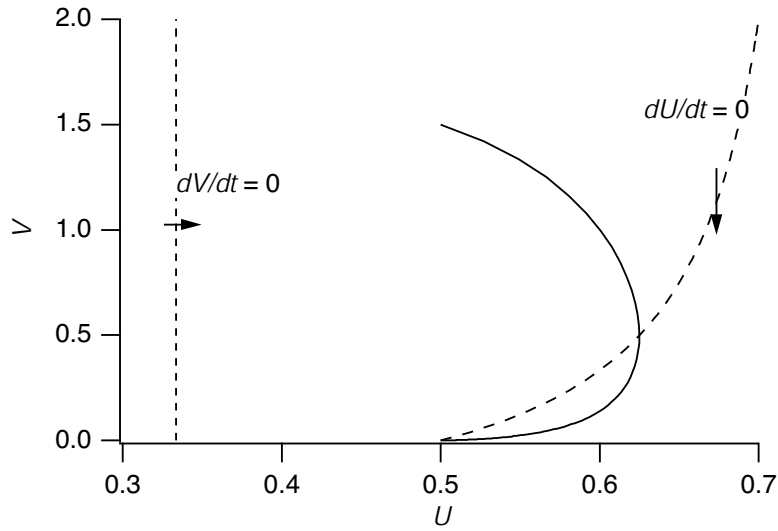
Figure 13.12: Phase portrait for the system (13.102)–(13.103) with "small" $\xi = 1.6$, "small" $\beta = 0.1$, $\alpha = 0$. Other parameters are $\beta_0 = 1.0$, $\gamma_0 = 0.2$, so that $U_0 = 0.5$.

$U \leq U_0$, $\frac{dV}{dt} > 0$, so that U decreases and V increases without bound. The bacterial challenge cannot be met. This situation is depicted in Fig. 13.12. In this and all the following phase portraits, the nullcline for $\frac{dV}{d\tau} = 0$ is shown as a short dashed curve, and the nullcline for $\frac{dU}{d\tau} = 0$ is shown as a long dashed curve. The solid curve shows a typical trajectory starting from initial data $U = U_0$, $V = V_0$.

If $\xi U_0 > 1$, there is a nontrivial steady state in the first quadrant, which is a saddle point. This means that there is a value V^* for which a trajectory starting at $U = U_0$, $V = V^*$ is on the stable manifold of this steady state and divides the line $U = U_0$ into two types of behavior. If $V < V^*$ initially, the trajectory evolves toward the elimination state, while if $V > V^*$ initially, the trajectory is unbounded. Thus, for large enough ξ and small enough initial bacterial population, the challenge can be withstood, but for a larger initial bacterial challenge, the bacterial population wins the competition. The number V^* is a monotone increasing function of ξ, and $\lim_{\xi \to \infty} V^* = \infty$. This follows because to the right of $U = \frac{1}{\xi}$ the stable manifold is an increasing curve as a function of U, so that V^* lies above the the value of V at the saddle point. However, as a function of ξ, the steady-state value of V is monotone increasing as ξ increases, approaching ∞ in the limit $\xi \to \infty$, so $V^* \to \infty$ as well.

The phase portrait for this situation is depicted in Fig. 13.13. In this situation the bacterial challenge is met only if ξ is large enough and V_0 is small enough, so that the leukocytes are effective killers, although with $\alpha = \beta = 0$ they are not good hunters. Note that $\xi = k_d c_b / k_g$, where k_d is the rate at which leukocytes kill bacteria, k_g is the growth rate of the bacteria, and c_b is the leukocyte density in the blood. Hence, large ξ means that leukocytes are effective killers, since they kill
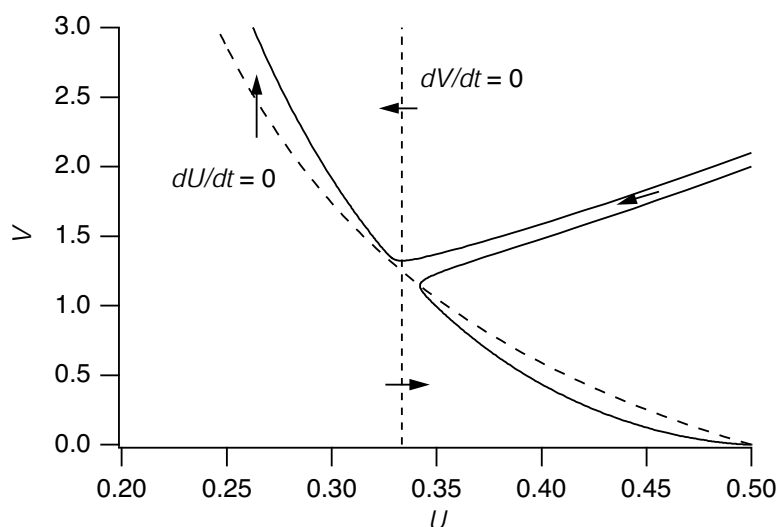
Figure 13.13: Phase portrait for the system (13.102)–(13.103) with "large" $\xi = 3.0$, "small" $\beta = 0.1$, $\alpha = 0$. Other parameters are $\beta_0 = 1.0$, $\gamma_0 = 0.2$, so that $U_0 = 0.5$.

bacteria at a rate exceeding the growth rate of the bacteria.

Case II: $\alpha = 0, \beta > 0$.
Here, the leukocytes can respond to the bacterial challenge by enhanced emigration from the bloodstream, but they cannot localize preferentially within the tissue. The system of equations becomes

$$\gamma_0^{-1}\frac{dU}{d\tau} = (\beta_0 + \beta V)(1 - U) - (V + 1)U, \qquad (13.106)$$

$$\frac{\partial V}{\partial \tau} = V(1 - \xi U). \qquad (13.107)$$

The nullclines for $\frac{dV}{d\tau}$ are unchanged from above. The nullcline $\frac{dU}{d\tau} = 0$ is the hyperbola $V = \frac{\beta_0 - (\beta_0 + 1)U}{(\beta + 1)U - \beta}$. For small β, with $\frac{\beta}{\beta + 1} < U_0$, the behavior of the system changes only slightly from Case I. These phase portraits are as depicted in Figs. 13.12 and 13.13.

If $\xi U_0 < 1$, the bacterial population grows without bound, whereas if $\xi U_0 > 1$, the bacterial population can be eliminated if $V < V^*$ initially. The value V^* is a monotone increasing function of β. Thus, with β small, the leukocytes have an enhanced ability to eliminate a bacterial population. In fact, if $\xi \beta > \beta + 1$ (phase portrait not shown), then $V^* = \infty$, so that a bacterial invasion of any size can be eliminated. Notice that in this case, the bacterial invasion is controlled because the leukocytes are effective killers and they effectively deploy troops to withstand the invasion. There is no mechanism making them more effective hunters.

In all of the above cases, the leukocyte population decreases initially, and if the bacterial population is controllable, the leukocyte population eventually rebounds
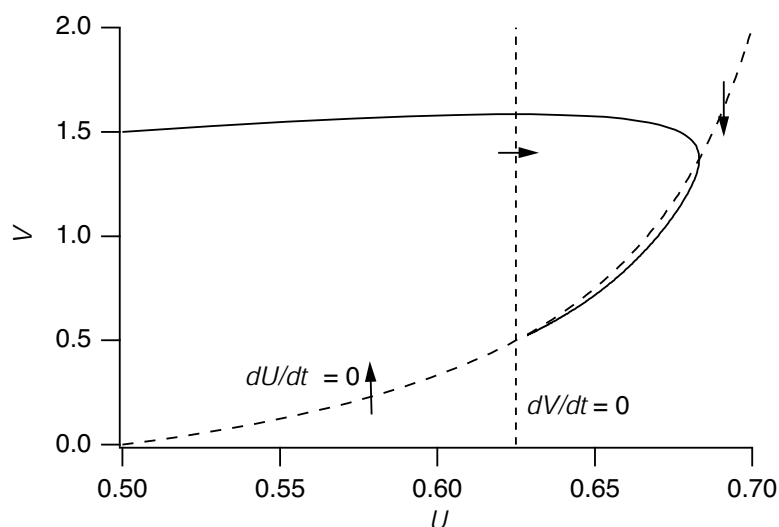
Figure 13.14: Phase portrait for the system (13.102)–(13.103) with "small" $\xi = 1.6$, "large" $\beta = 3.0$, $\alpha = 0$. Other parameters are $\beta_0 = 1.0$, $\gamma_0 = 0.2$, so that $U_0 = 0.5$.

back to normal. If β is large enough, with $\frac{\beta}{\beta+1} > U_0$, then the response to a bacterial invasion is with an initial increase in leukocyte population. If $\xi\beta < \beta + 1$, then the bacterial population is unbounded; the invasion cannot be withstood.

If $\xi\beta > \beta + 1$ and $\xi U_0 < 1$, there is a nontrivial steady state in the positive first quadrant that is a stable attractor. All trajectories starting at $U = U_0$ approach this stable steady-state solution with $U > U_0$. Since $V > 0$ for this steady solution, the bacterial population is controlled but not eliminated. This situation is depicted in Fig. 13.14.

Finally, if $\xi U_0 > 1$, the leukocyte population initially increases and then decreases back to normal as the bacterial population is eliminated. This situation is depicted in Fig. 13.15.

The above information is summarized in Fig. 13.16, where four regions with differing behaviors are shown, plotted in the $(1/\beta, \xi)$ parameter space. The four regions are bounded by the curves $\xi = 1/U_0$ and $\xi = 1 + 1/\beta$ and are identified by the asymptotic state for V, $\lim_{\tau\to\infty} V(\tau)$. For $\xi > 1/U_0$ and $\xi > 1 + 1/\beta$, the bacteria are always eliminated. For $\xi > 1/U_0$ and $\xi < 1 + 1/\beta$, there are two possibilities, either elimination or unbounded bacterial growth, depending on the initial size of the bacterial population. For $\xi < 1/U_0$ and $\xi > 1 + 1/\beta$, the bacteria survive but are controlled at population size V_p, and finally, for $\xi < 1/U_0$ and $\xi < 1 + 1/\beta$, the bacterial population cannot be controlled but becomes infinite.

Case III: $\alpha > 0$, $\beta > 0$.
The primary goal of this model is to determine the effect of the chemotaxis coefficient on the performance of the leukocytes in warding off a bacterial invasion. We have seen so far that with $\alpha = 0$ there are three possible responses to an invasion. The

Figure 13.15: Phase portrait for the system (13.102)–(13.103) with "large" $\xi = 3.0$, "large" $\beta = 3.0$, $\alpha = 0$. Other parameters are $\beta_0 = 1.0$, $\gamma_0 = 0.2$, so that $U_0 = 0.5$.
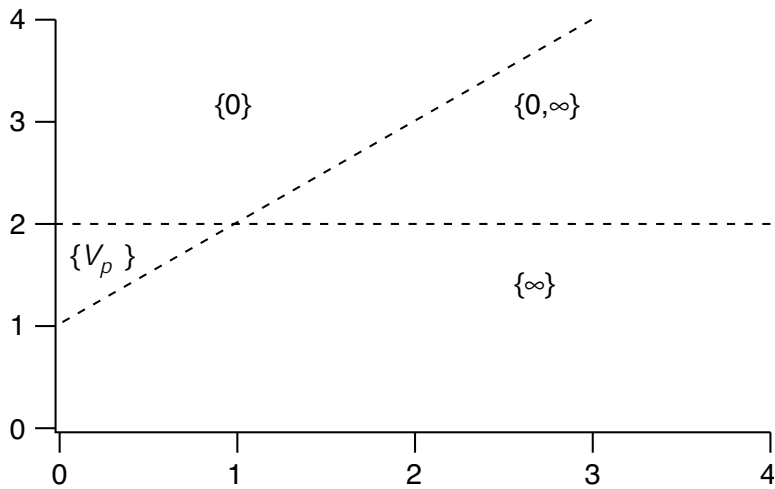
Figure 13.16: Parameter space for the system (13.102)–(13.103) with $\alpha = 0$.

bacteria may become unbounded, they may be controlled at a nonzero steady state, or they may be eliminated, depending on the sizes of the parameters ξ and β. With $\alpha \neq 0$, we expect control and elimination to be enhanced, if only because the bacterial growth rate is a decreasing function of α.

The effect of $\alpha \neq 0$ is seen first of all in the nullclines. The nullclines are the curves

$$\frac{dV}{d\tau} = 0 : U = \frac{1}{\xi F(\alpha V)}, \tag{13.108}$$

and

$$\frac{dU}{d\tau} = 0 : U = \frac{\beta_0 + \beta V}{(\beta_0 + \beta V)F(\alpha V)e^{-\alpha V} + VF(\alpha V) + 1}. \tag{13.109}$$

Both of these are decreasing functions of α, and both asymptote to $U = 0$ as $V \to \infty$. A steady state occurs whenever there is an intersection of these two curves. This condition we write as

$$\frac{1}{\xi} = \frac{\alpha V(\beta_0 + \beta V)}{(1 - e^{-\alpha V}) + \alpha V^2 + \alpha V e^{-\alpha V}(\beta_0 + \beta V)} = G(V). \tag{13.110}$$

One can easily see that $G(0) = U_0$ and that $\lim_{V \to \infty} G(V) = \beta$. This implies that there is an even number of roots if

$$\left(\frac{1}{\xi} - U_0 \right) \left(\frac{1}{\xi} - \beta \right) > 0, \tag{13.111}$$

and an odd number of roots otherwise. An odd number of roots implies that there is at least one steady-state solution in the first quadrant; with an even number there could be no steady states. This leads to four different possible outcomes separated by the curves $\xi = \frac{1}{U_0}$ and $\xi = \frac{1}{\beta}$. These are

1. $\xi < \frac{1}{U_0}, \xi < \frac{1}{\beta}$. There can be zero or two steady states. If there are no steady states, then V becomes infinite. If there are two steady states, one of them is stable and the trajectories for sufficiently small initial bacterial populations approach the stable steady state, where they persist. We can find the boundary between these two cases by looking for a double root of (13.110). We do this by solving (13.110) and the equation $G'(V) = 0$ simultaneously. This gives a curve in the (β, ξ) parameter plane parametrized by V, as follows: For each V, β is a root of the quadratic equation

$$\alpha^2 V^4 \beta^2 \quad - \quad V(-2\alpha^2 V^2 \beta_0 + \alpha V - 2e^{\alpha V} + 2)\beta$$

$$+ \quad \beta_0(\alpha^2 V^2 \beta_0 - \alpha V - 1 + e^{\alpha V}(1 - V^2 \alpha)) = 0, \tag{13.112}$$

and then ξ is given by (13.110) for each V, β. It is an easy matter to determine this curve numerically. The curve is plotted in Fig. 13.17 as a solid curve, shown for the three values of $\alpha = 0.5, 0.75$, and 1.0.

Below this curve in the $(\frac{1}{\beta}, \xi)$ parameter space, there are no steady-state solutions. The phase portrait for this case is similar to that of Fig. 13.12 and is left as an exercise (see Exercise 15). For all trajectories starting at $U = U_0$, $V(\tau) \to \infty$.

Above the "double root" curve there are two steady solutions, one of which is stable. In this situation, some trajectories lead to persistent bacterial populations, while others (with larger initial values) become infinite. This phase portrait has similarities with Fig. 13.13 and is left as an exercise (see Exercise 15).

2. $\xi < \frac{1}{U_0}, \xi > \frac{1}{\beta}$.   Here there is one stable steady state, which is a global attractor. All trajectories approach this steady state, so that the bacterial population is controlled, but it is not eliminated. The phase portrait for this case is quite similar to the previous case, except that there is only one nontrivial steady state, and no saddle point, so there is no separatrix, and all trajectories approach the persistent state.

   It should be noted that with $\xi < \frac{1}{U_0}$, the bacterial population can never be eliminated. However, with $\alpha > 0$, the population is more readily controlled than with $\alpha = 0$.

3. $\xi > \frac{1}{U_0}, \xi < \frac{1}{\beta}$. There is a single steady state in the first quadrant, which is a saddle point and which therefore divides the initial data into two types, those that are eliminated and those that become unbounded. The phase portrait for this case is similar to Fig. 13.13 and is left as an exercise (see Exercise 15).

4. $\xi > \frac{1}{U_0}, \xi > \frac{1}{\beta}$. Here there are no steady-state solutions in the positive quadrant, in which case the bacterial population is always eliminated. Here the effect of chemotaxis can be seen in the transient behavior of the leukocyte population. If the initial bacterial population is small, the leukocyte population initially increases before it decreases back to its equilibrium. If the initial bacterial population is large, then the leukocyte population initially decreases, then increases, and then finally decreases back to steady state, having eliminated the bacterial population. The phase portrait for this case has similarities with Fig. 13.15 and is left as an exercise (see Exercise 15).

In summary, to control a bacterial invasion, the leukocytes must be sufficiently lethal to the bacteria (ξ sufficiently large). They must also be able to recruit new troops, and it is advantageous that they move chemotactically, since they are more effective if $\alpha > 0$. This result is not surprising. However, the significance of this approximate analysis is that the model behaves as we had hoped, suggesting that it is a reasonable model, worthy of more detailed study and development.

13.5   Control of lymphocyte differentiation

The human body can develop considerable specific immunity to various kinds of invading organisms. This so-called *acquired immunity* comes in two different basic versions, both mediated by lymphocytes. First, B lymphocytes make antibodies, soluble proteins that circulate in the blood and help destroy invading organisms (humoral immunity). Second, large numbers of T lymphocytes can be activated to attack and destroy the invaders and cells infected by the invaders (cell-mediated
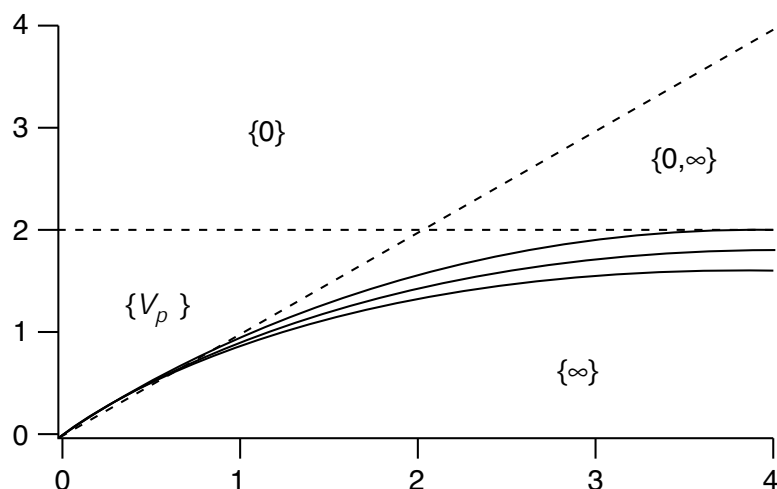
Figure 13.17: Parameter space for the system (13.102)–(13.103) with $\beta_0 = 1.0$, $\alpha > 0$.

immunity). Both types of lymphocytes are derived from common lymphoid precursors (Fig. 13.1); T lymphocytes develop from their precursors in the thymus gland (hence the nomenclature T lymphocyte), while B lymphocytes develop in the bone marrow. B lymphocytes were first discovered in birds, where they develop in an organ spectacularly named the *bursa of Fabricius*, which is not found in mammals.

One remarkable feature of acquired immunity is the combination of extreme specificity with extreme diversity. As T lymphocytes mature in the thymus they develop reactivity for specific antigens; a population of T lymphocytes contains different cells specifically targeted to each of millions of different possible antigens. B lymphocytes exhibit similar diversity and specificity, with many millions of different types of antibodies secreted by B lymphocytes that react to specific antigens. How exactly this occurs is a fascinating physiological and mathematical question, but not one that we consider further here.

T lymphocytes come in different flavors, with the major types being T helper cells, cytotoxic T cells and regulatory T cells. As the name implies, cytotoxic T cells are designed to kill other cells, particularly those infected by invading organisms, while regulatory T cells seem to suppress the actions of both cytotoxic and helper T cells, and play a role in preventing autoimmune disease. The majority of T lymphocytes are T helper cells, which secrete a broad range of soluble mediating factors (*cytokines*) that regulate virtually all aspects of the immune response. Typical cytokines are interleukin-2 (IL2), IL3, IL4 and interferon-γ (IFNγ). Acquired Immune Deficiency Syndrome, or AIDS, attacks the T helper cells in particular, leaving the body highly susceptible to infection.

As can be seen in Fig. 13.1, T helper (Th) cells themselves can differentiate into either Th1 or Th2 subtypes. These two subtypes mediate different responses. Th1 cells secrete IL2 and IFNγ and activate macrophages and cytotoxic T cells
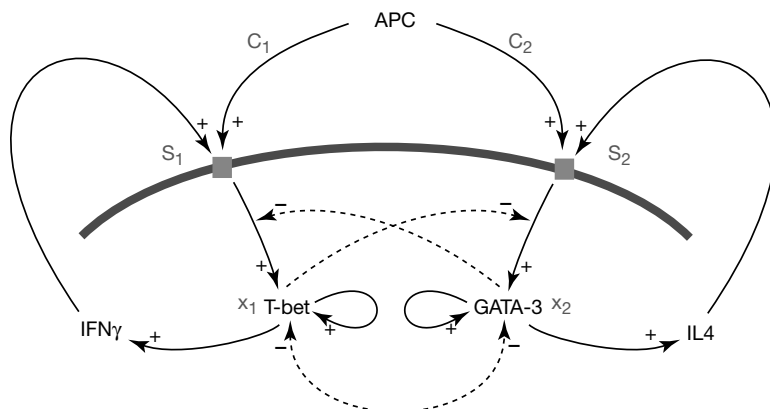
Figure 13.18: Schematic diagram of the pathways involved in the differentiation of Th1 and Th2 cells. Solid lines denote activation, while dashed lines denote inhibition. This diagram only includes a small number of the interactions in the system and is a highly simplified representation.

to destroy invading organisms; Th2 cells make IL4, IL5 and IL13, which activate mast cells, eosinophils, and B lymphocytes, leading to a humoral immune response. Clearly, making the right choice between the Th1 and Th2 pathways can be vital and there is a complex system of controls that ensures that the appropriate response is generated.

Antigen is presented to the Th cells by an antigen presenting cell, or APC. In response to certain types of antigen, APCs secrete IL12, which promotes Th1 differentiation, via the activation of the transcription factor T-bet. T-bet itself also promotes the production of IFNγ which stimulates the APCs to make more IL12, and also stimulates the production of more T-bet. This gives an autocatalytic feedback loop, pushing more cells down the Th1 pathway. IL4, on the other hand, promotes the differentiation of Th2 cells, and, via the activation of the transcription factor GATA-3, leads to the production of further IL4, and an autocatalytic pathway pushing cells down the Th2 pathway. Crosstalk between the two pathways occurs because GATA-3 inhibits the expression of IL12 receptors, while T-bet inhibits GATA-3 activation by IL4. This scheme is sketched in Fig. 13.18. Of course, the actual situation is far more complicated than sketched here. For example, the exact way in which T-bet and GATA-3 stimulate their own production is not clear, and neither is it known exactly how GATA-3 inhibits T-bet. Such interactions are likely to be more indirect than is shown in Fig. 13.18.

A number of groups have constructed models of Th1 and Th2 cell differentiation. One of the earliest was that of Fishman and Perelson (1993, 1994), while more recently Höfer et al. (2004) and Mariani et al. (2004) have constructed detailed models of the gene regulation networks in these cells. Here we follow the model of Yates et al. (2004).

Let x_1 and x_2 denote the concentrations (or expression levels) of T-bet and

σ_1, σ_2	$=$	5 day^{-1}	α_1, α_2	$=$	5 day^{-1}
γ_1	$=$	1	γ_2	$=$	0.5
κ_1, κ_2	$=$	1	μ	$=$	5 day^{-1}
ρ_1, ρ_2	$=$	1	g	$=$	2 day^{-1}
β_1, β_2	$=$	0.05 day^{-1}			

Table 13.3: Parameters of the model of lymphocyte differentiation. These parameters, although reasonable, are not known from experimental data, but are chosen to illustrate the basic behavior of the model.

GATA-3 respectively, and let S_1 and S_2 denote the concentration of cytokines that activate T-bet and GATA-3 respectively. We suppose that the rate of T-bet production is a saturating function of S_1, $\sigma_1 \frac{S_1}{\rho_1 + S_1}$, while the rate at which it catalyzes its own production is $\alpha_1 \frac{x_1^n}{\kappa_1^n + x_1^n}$. The inhibitory effect of GATA-3 on T-bet is included by assuming that both the S_1-dependent and auto-catalytic production of T-bet is inhibited by GATA-3, via the decreasing function $\frac{\gamma_2}{\gamma_2 + x_2}$. Finally, adding a background degradation term $(-\mu x_1)$ and a background production term (β_1) we get

$$\frac{dx_1}{dt} = \beta_1 - \mu x_1 + \left(\frac{\gamma_2}{\gamma_2 + x_2} \right) \left(\alpha_1 \frac{x_1^n}{\kappa_1^n + x_1^n} + \sigma_1 \frac{S_1}{\rho_1 + S_1} \right). \tag{13.113}$$

The equation for x_2 is constructed in the same way, and is essentially a mirror image of the x_1 equation;

$$\frac{dx_2}{dt} = \beta_2 - \mu x_2 + \left(\frac{\gamma_1}{\gamma_1 + x_1} \right) \left(\alpha_2 \frac{x_2^n}{\kappa_2^n + x_2^n} + \sigma_2 \frac{S_2}{\rho_2 + S_2} \right). \tag{13.114}$$

The parameters of the model are given in Table 13.3. Most of the parameters are the same for both T-bet and GATA-3 with the exception of γ_1 and γ_2. Thus, asymmetry appears only in the crosstalk terms, for which the inhibition of T-bet by GATA-3 is more sensitive (i.e., has a lower K_d) than that of GATA-3 by T-bet. **James, Here is a great opportunity to add a simple phase portrait, showing the bistability of this system graphically. In fact, it seems reasonable that this should be a bistable system, but I can't verify that it is or reproduce your figure 13.19. By the way, what is n? It isn't specified in the table. JK**

A plot of the steady-state GATA-3 concentration as a function of S_2 is shown in Fig. 13.19. As the level of stimulation of the GATA-3 pathway increases, the GATA-3 concentration undergoes a sharp increase, while a subsequent decrease in S_2 does not immediately lead to a decrease in GATA-3. This sudden jump corresponds to a change to a Th2 cell from a cell that is neither Th1 nor Th2 (i.e., one with both x_1 and x_2 low). Because of symmetry, a similar curve occurs when the steady-state is plotted against S_1, for fixed $S_2 = 0$. Such switch-like behavior and hysteresis is commonly seen in models of gene transduction pathways (see, for example, Fig. 10.4).
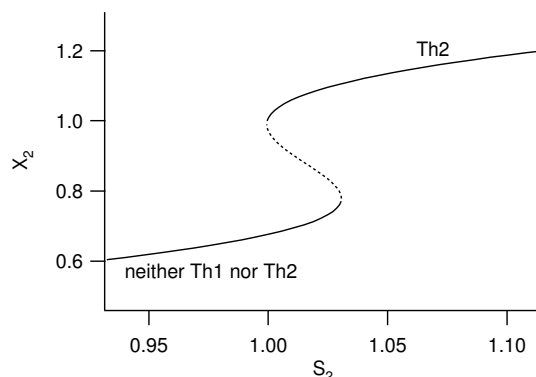
Figure 13.19: Steady-state GATA-3 concentration as a function of S_2, the level of stimulation of the GATA-3 pathway, calculated at $S_1 = 0$. Stable steady-states are denoted by solid lines, unstable by dashed lines.

13.5.1   A population model

The model in the previous section dealt with the dynamics of T-bet and GATA-3 inside a single T cell, showing how the T cell could be pushed down two different pathways, depending on the level of expression of the two transcription factors. However, in a population of cells, the cytokines released from one cell can influence the differentiation pathway of the other cells in the population, leading to a much more complex set of governing equations.

We define $\phi(x_1, x_2, t)$ to be the cell density function, that is, $\phi(x_1, x_2, t)\Delta x_1 \Delta x_2$ is the number of cells expressing T-bet and GATA-3 in the ranges $[x_1, x_1 + \Delta x_1]$ and $[x_2, x_2 + \Delta x_2]$ respectively. Then we let S_1 (the level of T-bet stimulation) be a function of both the intrinsic stimulation by the APC cells (C_1) and the level of T-bet expression in the entire population, $\int x_1 \phi \, dx_1 dx_2$. Thus, (for example)

$$S_1 = \frac{C_1(t) + \int x_1 \phi \, dx_1 dx_2}{\int \phi \, dx_1 dx_2}, \qquad (13.115)$$

with a symmetrical expression for S_2. Crosstalk between the T-bet and GATA-3 pathways is assumed to occur only at the local (cellular) level, but this assumption could be changed in the same way.

The dynamics of ϕ can be determined by a standard conservation argument used many times in this book (see for example, (2.1)), namely

$$\frac{\partial \phi}{\partial t} = f - \nabla \cdot \mathbf{J}, \qquad (13.116)$$

where f is the local rate of production and $\mathbf{J}$ is the flux. The one unusual feature of this conservation law is that the independent variables are the concentrations for T-bet (x_1) and GATA-3 (x_2), so the flux of cells is velocity times density, where by
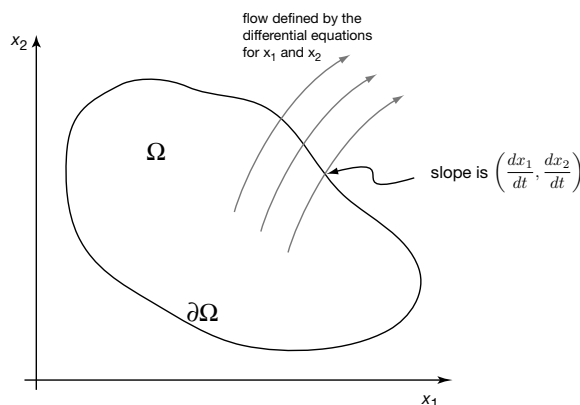
Figure 13.20: Derivation of the population model for lymphocyte differentiation. At each point of the boundary $\partial\Omega$ the flux of ϕ out of the region Ω is in the direction $(\frac{dx_1}{dt}, \frac{dx_2}{dt})$, i.e., the direction of the vector field defined by (13.113) and (13.114).

velocity we mean rate of change of the independent variables. Thus,

$$\mathbf{J} = \left(\begin{array}{c} \frac{dx_1}{dt}\phi \\ \frac{dx_2}{dt}\phi \end{array} \right). \tag{13.117}$$

This is illustrated in Fig. 13.20. Finally, we suppose that cells have a linear growth rate g so that

$$\frac{\partial\phi}{\partial t} = g\phi - \frac{\partial}{\partial x_1}(f_1\phi) - \frac{\partial}{\partial x_2}(f_2\phi), \tag{13.118}$$

where $f_1 = dx_1/dt$ and $f_2 = dx_2/dt$ are defined by (13.113) and (13.114).

Typical numerical solutions of this model are shown in Fig. 13.21. A background concentration of C_1 (3000 units/cell) was applied to a population of cells and on top of this a Th2 stimulus (C_2) was applied. The horizontal axis gives the size of the Th2 stimulus, which was allowed to decay exponentially with a time constant of 24 hours. After 5 days the proportion of Th1 and Th2 cells in the population was measured (plotted on the vertical axis). The initial population had low levels of both T-bet and GATA-3, and were thus neither Th1 nor Th2. We call such undifferentiated cells, Th0 cells.

When the initial C_2 stimulus is low, the background C_1 stimulus causes all the cells to be of Th1 type. However, as the C_2 stimulus increases, the population of cells becomes balanced, differentiating neither to Th1 nor Th2, but remaining as undifferentiated Th0 cells. It is not until the C_2 stimulus becomes sufficiently large that the cells differentiate to Th2. Interestingly, 5 days after the strong Th2 stimulus, the majority of the cells remain as Th2 cells, despite the continued presence of the Th1 stimulus, and the decay of the Th2 stimulus. The cells have been switched to the Th2 pathway by the strong stimulus, and cannot turn back.
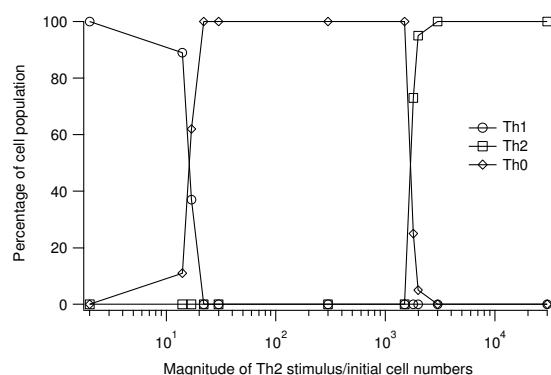
Figure 13.21: Numerical solution of the population model for lymphocyte differentiation. Adapted from Yates et al., Fig. 5B.

13.6 Clotting

13.6.1 The Clotting Cascade

The need for a clotting system is obvious. In any organism with a circulatory system, the loss of the transporters of vital metabolites and waste products has disastrous, perhaps fatal, consequences. However, the occurrence of clots in an otherwise normal circulatory system is also potentially disastrous, as it prevents a flow that is equally important to survival.

The clotting system must be fast reacting, and yet localized. Since all the ingredients for clotting are carried in the blood, there must be some control that prevents propagation. As we know from earlier chapters, a highly excitable system of diffusing species has the possibility, indeed the strong likelihood, of exhibiting traveling waves. For the clotting system, a propagating front would be as disastrous as failure of a clot to form. Thus, the challenge is to understand how a highly excitable system of reacting and diffusing chemicals is built so as not to allow uncontrolled wave propagation.

In fact, there are more than 50 substances in blood and tissue that play a role in the clotting process. Crucial to the process is the enzyme *thrombin*. Thrombin acts enzymatically on *fibrinogen*, converting it to *fibrin*, which then forms the mesh of the clot. However, this is not all, as thrombin is an extremely active enzyme, with many other regulatory roles.

Thrombin is formed when prothrombin, which is carried in the blood, is converted by an enzyme called *prothrombin activator*. Prothrombin activator is formed as the end result of two different enzymatic cascades, which are, however, closely linked. The fastest, called the *extrinsic pathway*, is initiated following tissue trauma. The second pathway, called the *intrinsic pathway*, is initiated following trauma to blood or contact of blood with collagen, or any negatively charged surface, and is not dependent on tissue trauma. However, this second pathway is much slower than the extrinsic pathway. Classic *hemophilia*, a tendency to bleed that occurs in

1 in every 10,000 males in the United States, results from a deficiency of one of the important enzymes in the intrinsic pathway.

A schematic diagram of some of the reactions involved in clotting is shown in Fig. 13.22. Although there is general agreement over the basic pathways, the exact details of the different feedbacks, and their relative importance, remains unknown, and any two papers by different groups are more than likely to contain slightly different clotting schemes. Thus, the details of Fig. 13.22 should not be taken as definitive.

Two important things may be seen immediately from Fig. 13.22. First, the intrinsic and extrinsic pathways are closely linked, and activation of one activates the other. Second, there are multiple positive feedback pathways, leading to an explosive production of fibrin once the system is triggered.

Thirteen of the important factors in the clotting cascade are denoted using Roman numerals as factors I through XIII, although for historical reasons, they also have other names. Here we retain the Roman numeral notation. Of those that have active and inactive states, the active state is denoted by appending the letter "a" to its name. Thus, for example, Xa is the active form of factor X.

The extrinsic pathway is activated when tissue trauma causes the release of a combination of agents called, collectively, *tissue factor* (or tissue thromboplastin). Tissue factor consists primarily of certain phospholipids from the membranes of the damaged tissues, and acts enzymatically to activate factor VII, converting it to factor VIIa. Factor VIIa then acts enzymatically to activate factor X to Xa, which then combines with factor Va on the surface of an activated platelet to form prothrombin activator. As mentioned above, prothrombin activator converts prothrombin to thrombin, from which the clot eventually forms.

The speed of the extrinsic pathway is increased by various positive feedback mechanisms. First, thrombin activates factor V, thus increasing the rate of formation of prothrombin activator. Second, thrombin is one of the substances that activates platelets (described below) to make them sticky and highly reactive (although this particular feedback is not shown in Fig. 13.22). In their reactive form, platelets are a source of the phospholipids with which factor X combines to produce prothrombin activator.

The intrinsic pathway operates in a similar way. Activation of factor XI by collagen leads to the activation of factor IX, which then forms a complex with factor VIIIa on the surface of an activated platelet. This complex can then activate factor X. Again, positive feedback occurs when both Xa and thrombin activate factor VIII.

Thrombin is degraded, so that its activity is not permanent. One of the ways that thrombin is degraded is by binding to the fibrin network, so that thrombin is eventually degraded by the result of its own activity, a negative feedback loop. There are also anticoagulants, such as antithrombin III, that inactivate thrombin. Inhibition of clotting is caused by the activated form of Protein C, PCa, which increases the rate of degradation of both Va and VIIIa, thus decreasing the rate of thrombin production. Since thrombin itself catalyzes the activation of Protein C, inhibition is controlled, at least partially, by a negative feedback loop (Fig. 13.22).

Heparin is another important anticoagulant. Heparin by itself has little or no
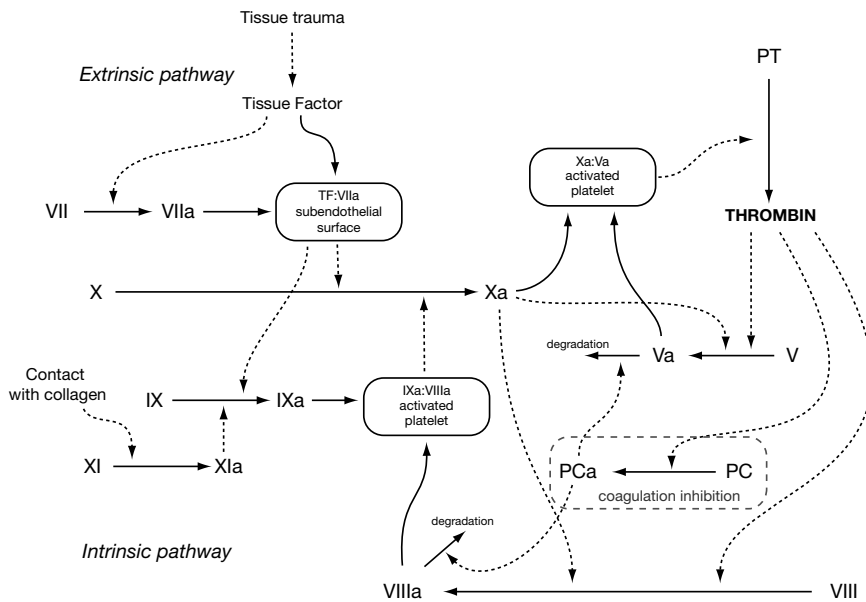
Figure 13.22: Schematic diagram of the extrinsic and intrinsic pathways for blood clotting. PT is prothrombin; PC is protein C; the factors are denoted by Roman numerals (such as VIII, IX or X) with the activated forms denoted by a (for example, VIIIa, IXa or Xa). Solid arrows denote conversion, while dashed arrows indicate catalysis. All the reactions, except those involving PC, activate clotting, and form a system of strong positive feedbacks. Activation of PC is the only reaction that inhibits clotting, and is thus enclosed in a dashed gray box. The boxes with solid lines denote complexes of activated factors that form only on the surface of the exposed subendothelium or of an activated platelet.

anticoagulant effect, but in complex with antithrombin III, the effectiveness of antithrombin III is increased a hundred- to a thousandfold. The concentration of heparin is normally quite slight, although it is produced in large quantities by *mast cells*, located in the connective tissue surrounding capillaries. They are especially abundant in tissue surrounding the capillaries of the lung and of the liver. This is important, because these organs receive many clots that form in the slowly moving venous blood and must be removed. Heparin is widely used in medical practice to prevent intravascular clotting.

13.6.2 Clotting models

Early models of blood clotting focused on the initial enzyme cascades, showing how the sequence of activations could lead to enormous amplification (Hearon, 1948; Levine, 1966). In a similar style, simplified models that attempt to capture the excitability of the system include those of Jesty et al. (1993) and Beltrami and Jesty (1995).

A more complicated approach, involving large systems of differential equations, has been taken by a number of other groups (for example, Nesheim et al., 1984, 1992; Willems et al., 1991; Jones and Mann, 1994; Bungay et al., 2003). Typically, these large models are solved numerically and compared to such experimental data as the rate of rise of thrombin concentration.

Even more complex models, including the effects of blood flow on clot formation, are those of Anand et al. (2003, 2005), or those from Fogelson's group (Fogelson, 1992; Fogelson and Kuharsky, 1998; Fogelson and Tania, 2005; Fogelson and Guy, 2004). Such models are too detailed to present in full here.

13.6.3 In vitro clotting and the spread of inhibition

One particularly interesting model, simple enough to discuss here, is that of Ataullakhanov et al. (2002a,b), based on the earlier model of Zarnitsina et al. (1996a,b). Using either blood, or plasma from which most of the platelets had been removed (platelet-poor plasma, or PPP), they studied the formation of clots in Petri dishes to which small glass beads (or sometimes collagen fibers) had been added to act as clotting foci. One of their more striking observations was that the clot around each bead grows to a certain size and then stops, leaving the clot surrounded by an inhibition zone. The presence of many clotting foci can then result in a checkerboard of clots across the dish, rather than a single merged superclot. In this case, each clot is surrounded by a thin channel of blood in which clotting is inhibited, so that the blood stays liquid for many hours (Fig. 13.23). Blood clots also sometimes form in a banded structure, of similar appearance to a target pattern, but with stationary bands (Fig. 13.24).

To explain these observations, Ataullakhanov et al. proposed a nine-state model of the clotting cascade, where the nine variables are the concentrations of XIa, IXa, Xa, tissue factor, prothrombin, thrombin, VIIIa, Va, and PCa. They then simplified the model by assuming some of the reactions to be in instantaneous equilibrium, in the same manner as has appeared often throughout this book (in Chapters 1 and 2
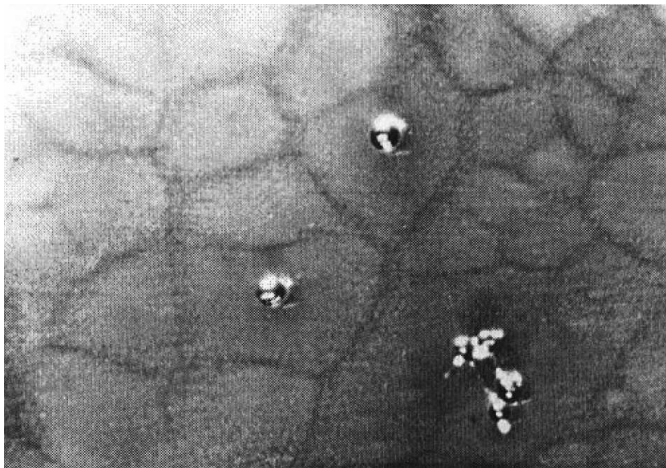
Figure 13.23: Clotting of platelet-poor plasma in a Petri dish, showing the checker-board of clots that has formed 120 minutes after addition of the glass beads. The clots do not merge to form one large superclot, but are separated by darker channels where the plasma remains liquid for many hours. Thus, each clot appears to be surrounded by an inhibition zone. (Ataullakhanov et al., 2002a, Fig. 11b). **Springer; this figure will need permission and massaging. I've taken only the lower panel of the original figure and photoshopped out the letter b that appears in the original.**
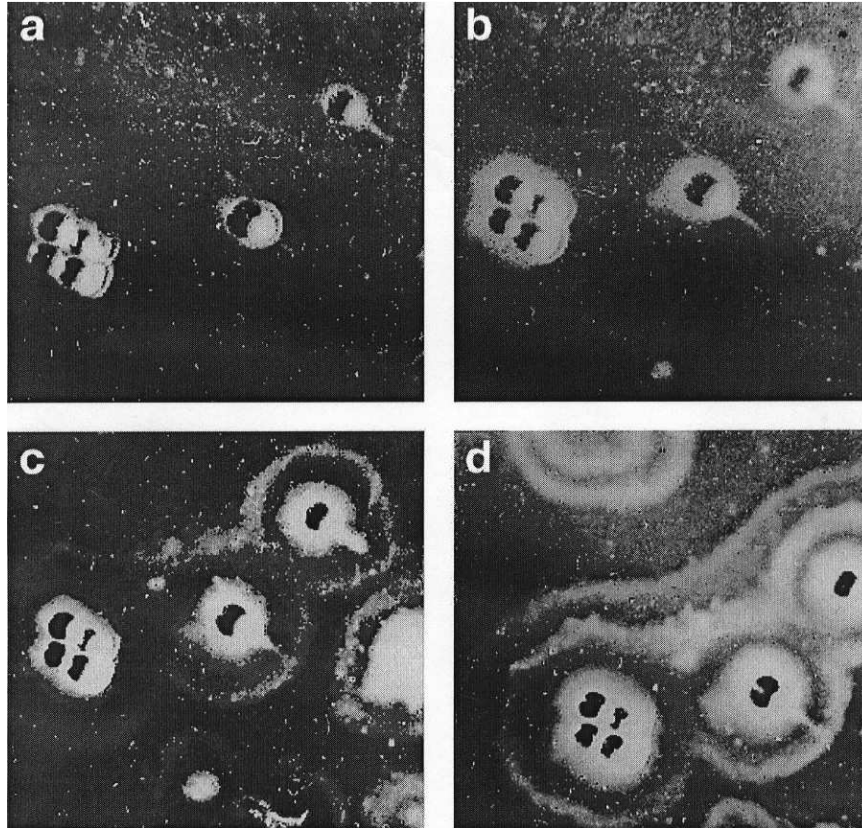
Figure 13.24: Banded clots in platelet-poor plasma in vitro (a) 0 minutes, (b) 12 minutes, (c) 30 minutes, and (d) 60 minutes after addition of the glass beads. (Ataullakhanov et al., 2002a, Fig. 11b). **Springer; this figure will need permission.**
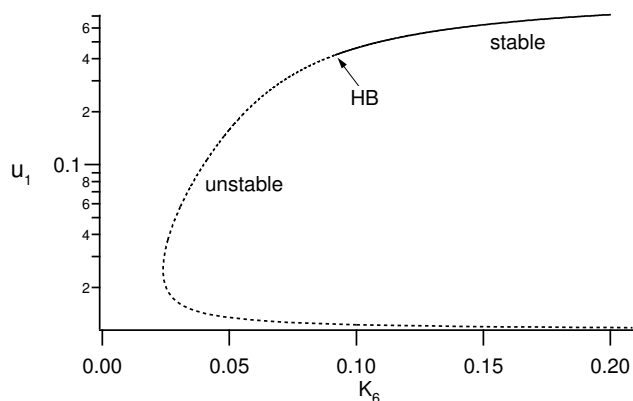
Figure 13.25: Bifurcation diagram of the clotting model (13.119)–(13.121), in the absence of diffusion. The line $u_1 = 0$ is a stable steady state for all values of K_6. Parameter values are $D = 0$, $K_1 = 6.85$, $K_2 = 11$, $K_3 = 2.36$, $K_4 = 0.087$, $K_5 = 17$.

in particular). Nondimensionalization of the equations, and the omission of small terms resulted in the equations

$$\frac{\partial u_1}{\partial t} = D\frac{\partial^2 u_1}{\partial x^2} + K_1 u_1 u_2 (1 - u_1)\frac{(1 + K_2 u_1)}{(1 + K_3 u_3)} - u_1, \qquad (13.119)$$

$$\frac{\partial u_2}{\partial t} = D\frac{\partial^2 u_2}{\partial x^2} + u_1 - K_4 u_2, \qquad (13.120)$$

$$\frac{\partial u_3}{\partial t} = D\frac{\partial^2 u_3}{\partial x^2} + K_5 u_1^2 - K_6 u_3. \qquad (13.121)$$

Here, u_1, u_2 and u_3 are, respectively, the nondimensionalized concentrations of thrombin, factor XIa and PCa. There are a number of things to note about the structure of these equations.

- Production of u_1 is stimulated by u_1 and u_2, but inhibited by u_3.

- Production of u_2 is stimulated by u_1, and thus u_1 and u_2 together form a positive feedback loop.

- Production of u_3 is stimulated by u_1, and thus u_1 and u_3 together form a negative feedback loop.

- The concentration of u_1 is bounded by 1, but the concentrations of u_2 and u_3 are not.

- Each variable is degraded with first order kinetics.

- For simplicity, each variable is assumed to have the same diffusion coefficient.
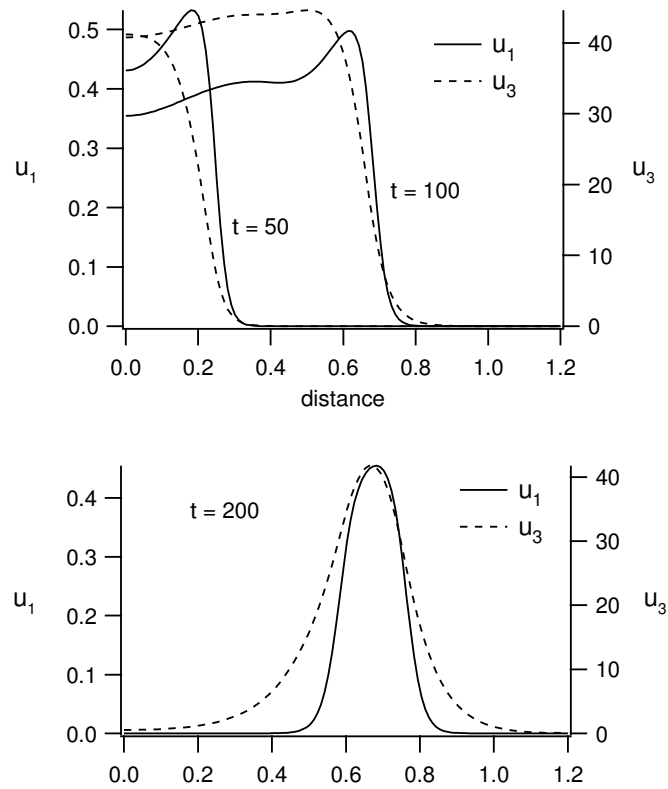
Figure 13.26: A wave of clotting in (13.119)–(13.121) (upper panel), that gradually slows down and turns into a stationary pattern (lower panel). The parameters are $K_6 = 0.066$, $D = 2.6 \times 10^{-4}$, and the times of each plot are given in the figure. The pattern in the lower panel is stable, stationary and persistent.

The steady states of (13.119)–(13.121) are plotted in Fig. 13.25 as functions of K_6. Since the line $u_1 = 0$ is always a stable steady state, the model has two stable steady states when K_6 is large enough. The Hopf bifurcation on the upper branch of steady states leads to a branch of periodic orbits over a narrow range of values of K_6, but since this is of little interest to the present discussion we ignore it from now on.

The model is highly excitable. Small perturbations away from the steady state $u_1 = 0$ decay back to zero, but larger perturbations cause a large and fast increase in the thrombin concentration (Exercise 16). When K_6 is less than the value at the Hopf bifurcation this perturbation eventually dies away to zero, behaving much like an action potential (Chapter **??**). When K_6 is larger than the value at the Hopf bifurcation a super-threshold perturbation causes a transition to the higher steady state.

When diffusion is included, the model can behave much like a typical excitable system, as discussed in Chapter 6. A sufficiently large perturbation away from the steady state $u_1 = 0$ can cause a traveling wave that moves across the domain with a constant speed and shape. Because this is not at all surprising (given the excitable nature of the model) we do not show a picture of this wave.

However, for certain parameter values, something much more interesting happens, as illustrated in Fig. 13.26. Although a traveling wave appears to form in response to the super-threshold perturbation, the wave only travels a short distance before stopping. When the wave stops, it does not die away, but forms a stationary wave that is persistent and stable. This stationary solution corresponds to the experimental observation that the clot spreads only a certain distance before stopping.

Close examination of the solution shows why this happens. Immediately after the perturbation, at $t = 50$, the leading edge of the u_1 wave front (the excitation wave) is in front of the leading edge of the u_3 wave front (i.e., the inhibition wave; Fig. 13.26, upper panel). Thus, the excitation wave is able to propagate into the excitable medium. However, although the inhibition wave starts slower than the excitation wave, it eventually catches up. By $t = 100$, the leading edge of the inhibition wave has overtaken the leading edge of the excitation wave. This slows down the excitation wave, and eventually stops it. By $t = 200$, the inhibition and excitation waves are both stationary, with the inhibition wave forming an inhibition zone around the clot (Fig. 13.26, lower panel).

Thus, this model shows how the interaction of waves of excitation and inhibition can lead to a clot that initially propagates explosively into the blood, but is eventually halted, preventing the uncontrolled spread of clotting.

James, I am not particularly happy with this model but I don't know what to do about it. The standing solution has little to do with real clots and in particular has no features that suggest what it might have to do with stopping the flow of blood. JK

13.6.4   Platelets

The experiments and model discussed in the previous section omit two important features of clotting *in vivo*; the presence of platelets, and the fact that blood is

often flowing past a clot. When these factors are introduced into a clotting model, the question of how clotting is inhibited and controlled becomes considerably more complicated.

As can be seen from Fig. 13.22, activation of the extrinsic pathway depends on the exposure of the subendothelial surface. However, maintenance of the clotting cascade depends on the presence of activated platelets. Thus, a better understanding of clotting *in vivo* depends on more detailed consideration of platelet dynamics, and the effects of fluid flow.

Platelets are minute round or oval discs 2 to 4 micrometers in diameter. They are formed in the bone marrow from *megakaryocytes*, which are large cells in the bone marrow that fragment into platelets. There are normally between 150,000 and 300,000 platelets per microliter of blood, constituting only a small percentage of the volume (≈ 0.3 percent by volume).

A platelet is an active structure with a half-life of 8 to 12 days. Since platelets are cell fragments with no nucleus, they do not reproduce. A platelet normally circulates with the blood in a dormant, or inactivated state, in which it does not adhere to other platelets or to the blood vessel wall. However, when platelets come in contact with a damaged vascular surface or sufficient chemical triggers, they become activated and change their characteristics drastically, as follows:

1. The platelet's surface membrane is altered so that the platelet becomes sticky, capable of adhering to other activated platelets or the subendothelial layer.

2. The platelet secretes chemicals, including large amounts of ADP and thrombaxane A_2, which are capable of activating other platelets.

3. The platelets change from rigid discoidal to highly deformable, extending long, thin appendages called *pseudopodia*.

An important requirement for controlled clotting is that the circulating blood must be able to build a catalytic bed in the vicinity of the injury, even though there is fluid flow. The aggregation of platelets is the means by which a catalytic reactor bed is built, and so is an important part of the process by which the flow of blood from a damaged vessel is halted.

A mathematical model for the aggregation of platelets and the formation of platelet plugs has been formulated and studied by Fogelson (1992) and Fogelson and Guy (2004). The model is a continuum model that assumes that there is a concentration of activated and nonactivated platelets, respectively. Platelets are immersed in blood and are neutrally buoyant, moving with the local fluid velocity. There is some chemical, say ADP, that is released by platelets when they are activated and that has the effect of stimulating nonactivated cells. Activated cells are sticky and form aggregates when they come into contact with each other.

One can readily write conservation equations for the density of inactivated and activated platelets. However, because this is an exercise in fluid and continuum mechanics, which is beyond the scope of this text, we do not reproduce these here. Numerical simulation of these equations then demonstrates how platelet aggregates can form in the vicinity of tissue trauma.
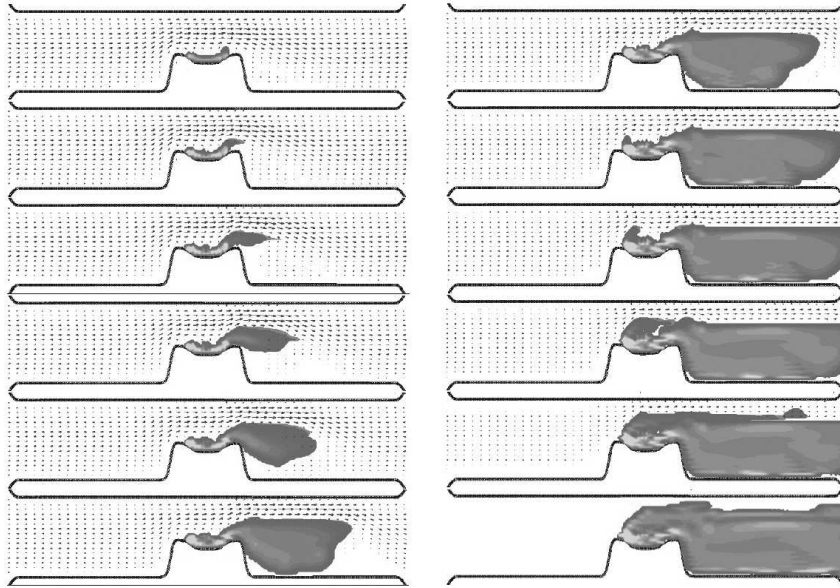
Figure 13.27: Growth of a platelet aggregate in a fluid flow. Fluid is flowing from left to right with velocity vectors shown (the velocity vectors are very small, and difficult to recognize as vectors at this resolution, appearing more like dots). Time is increasing from top left to bottom right, with the panels on the left corresponding to earlier times than the panels on the right. (Fogelson and Guy, Figs. 9 and 10.) **Springer; this figure will need permission and massaging. I've combined two figures from the original publication.**

In Fig. 13.27 are shown a series of snapshots of a (two-dimensional) fluid flow past an obstacle, the top of which is exposed subendothelial layer, and thus capable of activating platelets. The figure shows an aggregate of activated platelets growing from the obstacle, which gradually causes the occlusion of the flow (bottom right panel of Fig. 13.27).

The question remains (and is not addressed by these simulations) of why the platelet system does not exhibit traveling fronts of aggregation. The putative answer is that smooth (undamaged) vascular walls are nonsticky and that they contain inhibitors of ADP, the primary factor in the activation of platelets, and inhibitors of thrombin, and these prevent the uncontrolled spread of activated platelets.

Another interesting study of clotting inhibition is that of Fogelson and Tania (2005), who propose that purely physical mechanisms can play a larger role than previously realized. In their model, there is competition between the tendency of platelets to stick to, and thus cover up, the subendothelial layer (thus inhibiting

formation of the TF:VIIa complex), and the ability of thrombin to activate the platelets. It is essentially a race; if platelets cover the subendothelial layer fast enough, not enough of the IXa:VIIIa or Xa:Va complexes can be formed to maintain the clotting reaction, once the TF:VIIa complex is prevented from forming. A clot is thus prevented from forming, as not enough thrombin can be produced. Formation of the IXa:VIIIa and Xa:Va complexes is also inhibited by the flow, which carries away the reactants by diffusion and convection.

However, if the blood flow is slow enough, or the formation of IXa and VIIIa fast enough, by the time the subendothelial surface is covered up by platelets, enough of the activating complexes have been formed to continue the clotting process.

In this model, purely physical factors such as occlusion of the subendothelial layer, or the transport of reactants by blood flow, are much more significant sources of inhibition than the biochemical mechanisms of inactivation by PCa or antithrombin III.

Exercises

1. What is the volume (per mole) of an ideal gas at room temperature $(27°\,\mathrm{C})$ and 1 atm pressure? What is its volume at body temperature $(98°\,\mathrm{F})$?

2. Find an analytic relationship for the critical stability curve (Section **??**), relating $dF(0)$ to X/d as follows: Use that $F(N) = \frac{F(0)}{1+N^7}$ to solve (13.22) for N_0 as a function of X/d and then determine $dF(0)$ using that $F(N_0) = N_0/X$.

3. A deficiency of vitamin B_{12}, or folic acid, is known to cause the production of immature red blood cells with a shortened lifetime of one-half to one-third of normal. What effect does this deficiency have on the population of red blood cells?

4. Suppose $X \to \infty$ in the red blood cell production model. Show that

$$\frac{dN}{dt} = F(N(t-d)) - \beta N, \qquad (13.122)$$

where $N(t) = \int_0^\infty n(x,t)dx$.

   (a) Find the stability characteristics for the steady-state solution of this equation.

   (b) Show that the period of oscillation $T = 2\pi/\omega$ at a Hopf bifurcation point is bounded between $2d$ and $4d$.

5. Suppose X is finite and $\beta = 0$ in the red blood cell production model. Show that the evolution of N is described by the delay differential equation

$$\frac{dN}{dt} = F(N(t-d)) - F(N(t-d-X)). \qquad (13.123)$$

6. The maturation rate of red blood cells in bone marrow varies as a function of erythropoietin levels. Suppose that x denotes the maturity (rather than chronological age) of a red blood cell. Suppose further that cells are initially formed at maturity $x = -d$, are released into the bloodstream at maturity $x = 0$, age at the normal chronological rate, and die at age $x = X$. Suppose further that the rate of maturation G is a decreasing function of the total circulating red blood cell count N and that the rate of cell production at maturity $x = -d$ is $F(N)$.

(a) Replace the condition (13.9) with an evolution equation of the form (13.7) to account for maturities x in the range $-d < x < 0$. Specify the boundary condition at $x = -d$ and require that the flux be continuous at $x = 0$. Show that the steady state solution is independent of the maturation function $G(N)$.

(b) Provide a linear stability analysis for this modified model. Show that

$$\frac{dn}{dt} = \left(F'(N_0) - \frac{G'(N_0)N_0}{G(N_0)X} \right) \left(n(t - \frac{d}{G(N_0)}) - n(t - \frac{d}{G(N_0)} - X) \right)$$
(13.124)

where $N = N_0(1 + \delta n)$, and $\delta << 1$.

(c) How does the variability of G affect the stability of the steady state solution? Does this variability make the solution more or less likely to become unstable via a Hopf bifurcation?

7. Show that the solution of the kth order linear filter

$$\frac{du_0}{dt} = -\alpha(u_0 - u_1), \tag{13.125}$$

$$\frac{du_1}{dt} = -\alpha(u_1 - u_2), \tag{13.126}$$

$$\ldots$$

$$\frac{du_k}{dt} = -\alpha(u_k - f(t)), \tag{13.127}$$

is given by the convolution

$$u_0(t) = \int_{-\infty}^{t} f(s)g(t - s)ds, \tag{13.128}$$

where $g(t)$ is the gamma distribution of order k,

$$g(t) = \frac{\alpha^{k+1}}{\Gamma(k + 1)} t^k \exp(-\alpha t). \tag{13.129}$$

8. Numerically simulate (13.7) with boundary data (13.9) with parameters chosen from the stable region and from the unstable region.

9. Show that if (13.31) has a real solution, it must be negative and lie between $-a$ and $-\alpha$.

P_{O_2}(mm Hg)	percent saturation
3.08	2.21
4.61	3.59
6.77	6.08
10.15	10.50
12.31	14.09
15.38	19.34
18.77	28.45
22.77	40.33
25.85	50.0
30.15	60.50
36.00	69.89
45.23	80.11
51.69	83.98
61.85	88.95
75.38	93.37
87.08	95.86
110.5	98.07

Table 13.4: Approximate numerical data for the hemoglobin saturation curve.

10. Suppose that a carrier (like hemoglobin) of a molecule (like oxygen) has n independent binding sites, with individual binding and unbinding rates k_+ and k_-. Let c_j denote the concentrations of the state with j molecules bound. Assume concentrations are in steady state.

    (a) Show that $c_j = \binom{n}{j} x^j c_0$, where $\binom{n}{j} = \frac{n!}{j!(n-j)!}$ is the *binomial coefficient* where $x = s_0/K, K = k_-/k_+$, and s_0 is the concentration of the carrier molecule.

    Hint: Keep track of the total number of binding sites.

    (b) Find the saturation function in the case that $n = 4$.

    (c) Show that the four equilibrium constants K_1, K_2, K_3, K_4 defined in (13.45) are given by $(K_1, K_2, K_3, K_4) = K(\frac{1}{4}, \frac{2}{3}, \frac{3}{2}, 4)$.

    (d) Estimate K to give a good fit of this model to the hemoglobin saturation curve. How does this curve compare with the curve (13.47)?

    (e) Determine whether the hemoglobin binding sites are independent. How close are the equilibrium constants here to those found in the text?

11. Approximate numerical data for the hemoglobin saturation curve are found in Table 20.4. Fit these data to a curve of the form (13.47).

    Hint: Suppose we have data points $\{x_i, y_i\}, i = 1, \ldots, n$, that we wish to fit to some function $y = f(x)$, and that the function f depends on parameters $\{\alpha_i\}, i = 1, \ldots, m$. A fit of the data is achieved when the parameters are

picked such that the function

$$F = \sum_{j=1}^{n} (f(x_j) - y_j)^2 \qquad\qquad (13.130)$$

is minimized. To find this fit, start with reasonable estimates for the parameters and then allow them to change dynamically (as a function of a time-like variable t) according to

$$\frac{d\alpha_k}{dt} = -\sum_{j=1}^{n} f(x_j)\frac{\partial f(x_j)}{\partial \alpha_k}. \qquad\qquad (13.131)$$

With this choice,

$$\frac{dF}{dt} = \sum_{k=1}^{m}\sum_{j=1}^{n} f(x_j)\frac{\partial f(x_j)}{\partial \alpha_k}\frac{d\alpha_k}{dt} \le 0, \qquad\qquad (13.132)$$

so that F is a decreasing function of t. A fit is found when numerical integration reaches a steady-state solution of (13.131).

12. Construct a Monod–Wyman–Changeux model (Section 1.4.4) for oxygen binding to hemoglobin and determine the saturation function. Fit to the experimental data given in Table 20.4 and compare to the fit of (13.47).

   In the Monod–Wyman–Changeux model, each binding site is independent. Thus, on the surface it appears that the Monod–Wyman–Changeux model is quite different in principle from the model discussed in the text, in which binding to the fourth binding site is enhanced. However, by considering the solution to Exercise 1.76 of Chapter 1 (and using the parameter values found in the first part of the question), show that this is not really true. In other words, show that the Monod–Wyman–Changeux model indirectly incorporates an enhanced binding to subsequent binding sites, once the initial site is bound.

13. (a) If a 25 mM solution of sodium bicarbonate is equilibrated with carbon dioxide at 40 mm Hg partial pressure, the pH is found to be 7.4. What is the equilibrium constant for the bicarbonate-carbon dioxide reaction?

   (b) If the partial pressure of carbon dioxide is increased until the pH is 6.0, what is the bicarbonate concentration? What is the carbon dioxide partial pressure at this pH? What difference would you expect if this experiment is carried out in whole blood instead of aqueous solution?

   (c) Pick reasonable values for K_1, K_2 and $\bar{K}_1$ and find the oxygen saturation curve as a function of h. (Hint: the parameters must be chosen so that hemoglobin acts as a hydrogen ion buffer at physiological concentrations. So, for example, pick K_1, K_2 and $\bar{K}_1$ so that $(\phi(h))^{1/4} = 26\ \sigma$ mm Hg at pH $= 7.4$. You also have to ensure that $\bar{K}_1 > K_1$ and that K_2 is not too large. Why?)

(d) Use this model to estimate the total amount of CO_2 that is transported from the tissues to the lungs and the total amount of O_2 that iis transported from the lungs to the tissues. (Determine this by solving (13.60) - (13.64) numerically to find h, X, Y, Z and W at a given $[O_2]$ and $[CO_2]$ and finding the difference between arterial and venous quantities.) Remove the Bohr and Haldane effects by setting $K_1 = \bar{K}_1$. How does this change the amount of oxygen and carbon dioxide transported? Typical parameter values are: P_{CO_2} in arterial blood, 39 mm Hg ; P_{CO_2} in venous blood, 46 mm Hg; P_{O_2} in arterial blood, 100 mm Hg; P_{O_2} in venous blood, 40 mm Hg; $R_1 R_2 = 10^{6.1} M^{-1}$; $T_{Hb} = 3$ mM; $n = 10$, $[HCO_3^-] = 25$ mM and pH $= 7.4$ in arterial blood.

14. Develop a detailed model of oxygen and carbon monoxide binding with hemoglobin. How can the fact that CO has 210 times the affinity for binding be used to estimate the equilibrium coefficients?

15. Sketch the phase portraits for the equations (13.102)–(13.103) in Case III $(\alpha > 0, \beta > 0)$ as follows:

(a) $\xi < \frac{1}{U_0}, \xi < \frac{1}{\beta}$. (For example,
   i. $\xi = 1.0$, $\beta = 0.5, \alpha = 0.5, \beta_0 = 1.0, \gamma_0 = 0.2$, and
   ii. $\xi = 1.5$, $\beta = 0.5, \alpha = 1.3, \beta_0 = 1.0, \gamma_0 = 0.2$.)

(b) $\xi < \frac{1}{U_0}, \xi > \frac{1}{\beta}$ (For example, $\xi = 1.8, \beta = 0.6, \alpha = 0.5, \beta_0 = 1.0, \gamma_0 = 0.2$.)

(c) $\xi > \frac{1}{U_0}, \xi < \frac{1}{\beta}$. (For example, $\xi = 2.2, \beta = 0.3, \alpha = 0.5, \beta_0 = 1.0, \gamma_0 = 0.2$.)

(d) $\xi > \frac{1}{U_0}, \xi > \frac{1}{\beta}$. (For example, $\xi = 2.2, \beta = 2.0, \alpha = 0.5, \beta_0 = 1.0, \gamma_0 = 0.2$.)

Locate each of these cases in Fig. 13.17.

16. Show that the clotting model of (13.119)–(13.121) is excitable. Investigate the response to perturbations away from the $u_1 = 0$ steady state. Do this for two different cases: when K_6 is less than the value at the Hopf bifurcation, and when K_6 is larger than the value at the Hopf bifurcation.

Chapter 14

Respiration

The respiratory system is responsible for gas transfer between the tissues and the outside air. Carbon dioxide that is produced by metabolism in the tissues must be moved by the blood to the lungs, where it is lost to the outside air, and oxygen that is supplied to the tissues must be extracted from the outside air by the lungs.

The nose, mouth, pharynx, larynx, trachea, broncheal trees, lung air sacs and respiratory muscles are the structures that make up the respiratory system (Fig. 14.1). The nasal cavities are specialized for warming and moistening inspired air and for filtering the air to remove large particles. The larynx, or "voice box," contains the vocal folds that vibrate as air passes between them to produce sounds. Below the larynx the respiratory system divides into *airways* and *alveoli.* The airways consist of a series of branching tubes that become smaller in diameter and shorter in length as they extend deeper into the lung tissue. They terminate after about 23 levels of branches in blind sacs, the alveoli. The *terminal bronchioles* represent the deepest point of the bronchial tree to which inspired air can penetrate by flowing along a pressure gradient. Beyond the terminal bronchioles, simple diffusion along concentration gradients is primarily responsible for the movement of gases.

Alveoli are thin-walled air sacs that provide the surface across which gases are exchanged (Fig. 14.2). Each lung contains about 300 million alveoli with a combined surface area of about 70–85 square meters. The alveoli are surrounded by respiratory membrane that serve to bring air and blood into close contact with a large surface area. In the lung capillaries, from 70 to 140 ml of blood is spread over the surface area of the lungs.

14.1   Capillary–Alveoli Gas Exchange

14.1.1   Diffusion Across an Interface

Recall from Chapter 13 that the partial pressure of a gas is defined as the mole fraction of the gas multiplied by the total pressure. If a gas with partial pressure P_s is in contact with a liquid, the steady-state concentration U of gas in the liquid
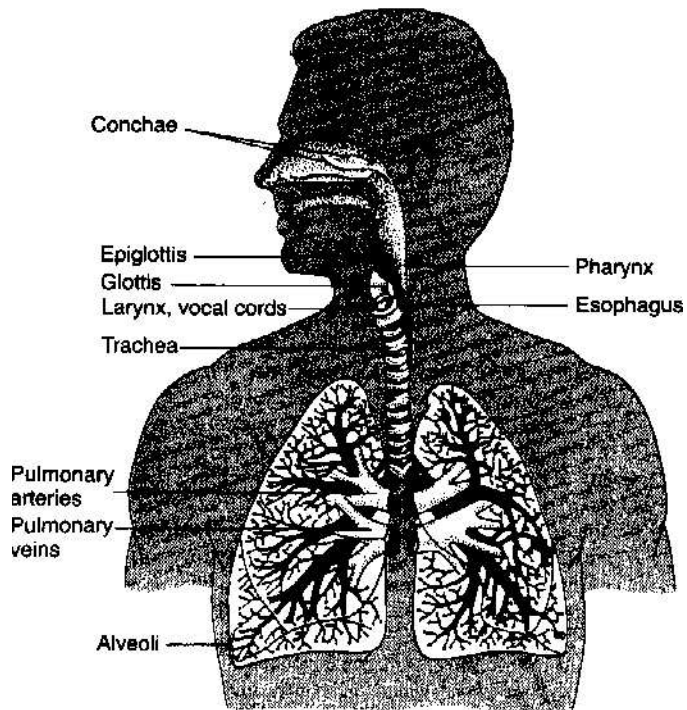
Figure 14.1: Diagram of the respiratory passages. (Guyton and Hall, 1996, Fig. 37-9, p. 486.)
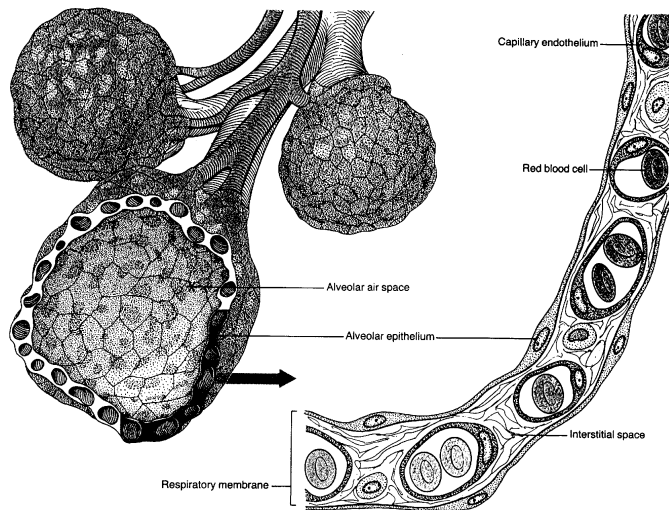
Figure 14.2: The alveoli, or air sacs, of the lung are covered by an extensive network of capillaries that form a thin layer of blood for the exchange of gases. (Davis, Holtz, and Davis, 1985, Fig. 19-4, p. 391.)

is given by

$$U = \sigma P_s, \tag{14.1}$$

where σ is the solubility of the gas in the liquid. Because of this, we define the partial pressure of a dissolved gas with concentration U to be U/σ.

Now suppose that a gas with partial pressure P_g is brought into contact with a liquid within which that same gas is dissolved with concentration U, and thus partial pressure U/σ. If U/σ is not equal to P_g, one expects a net flow of gas across the interface. The simplest model (but not necessarily the most accurate) assumes that the flow is linearly proportional to the difference in partial pressures across the interface, and thus

$$q = D_s \left(P_g - \frac{U}{\sigma} \right), \tag{14.2}$$

where q is the net flux per unit area of the gas (positive when gas is flowing from the gaseous phase to the dissolved phase), and D_s is the *surface diffusion constant.*

14.1.2 Capillary–Alveolar Transport

To understand something about the transport of a gas across the capillary wall into the alveolar space, we begin with the simplest possible model. We suppose that a gas such as oxygen or carbon dioxide is dissolved in blood at some concentration U uniformly across the cross-section of the capillary. The blood flows along a capillary that is bounded by alveolar air space. The partial pressure of the gas in the alveolar space, P_g, is taken to be constant.

Consider a segment of the capillary, of length L, with constant cross-sectional area A and perimeter p. The total amount of the dissolved gas contained in the capillary at any time is $A \int_0^L U(x,t)dx$. Since mass is conserved, we have

$$\frac{d}{dt} \left(A \int_0^L U(x,t)\, dx \right) = v(0)AU(0,t) - v(L)AU(L,t) + p \int_0^L q(x,t)\, dt, \tag{14.3}$$

where $v(x)$ is the velocity of the fluid in the capillary, and q is the flux (positive inward, with units of moles per time per unit area) of gas along the boundary of the capillary. This assumes that diffusion along the length of the capillary is negligible compared to diffusion across the capillary wall. Differentiating (14.3) with respect to L and replacing L by x gives the conservation law

$$U_t + (vU)_x = \frac{pq}{A}. \tag{14.4}$$

Finally, if we assume that the flow velocity v is constant along the capillary, then using (14.2), we obtain

$$U_t + vU_x = \frac{pD_s}{A} \left(P_g - \frac{U}{\sigma} \right) = D_m(\sigma P_g - U), \tag{14.5}$$

where $D_m = \chi D_s/\sigma$, and $\chi = p/A$ is the surface-to-volume ratio. Notice that D_m has units of $(\text{time})^{-1}$, so it is the inverse of a time constant, the *membrane exchange rate.*
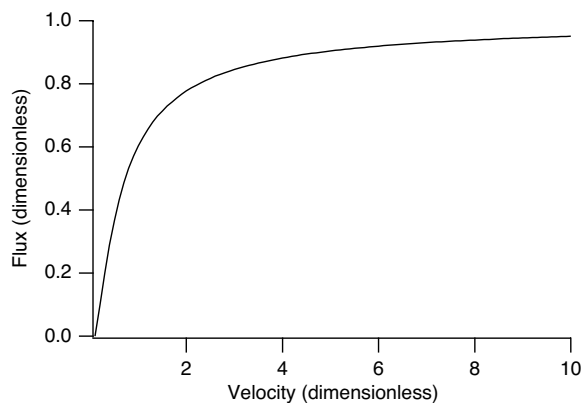
Figure 14.3: Dimensionless transmural flux $\bar{Q}$ as a function of dimensionless flow velocity $\frac{v}{D_m L}$ from (14.9).

At steady state the conservation law (14.5) reduces to the first-order, linear ordinary differential equation

$$v\frac{dU}{dx} = D_m(\sigma P_g - U). \tag{14.6}$$

Note that, as one would expect intuitively, the rate of change of U at the steady state is inversely proportional to the fluid velocity. Now we suppose that the concentration U at the inflow $x = 0$ is fixed at U_0 (at partial pressure $P_0 = U_0/\sigma$). At steady state, the concentration at each position x is given by the exponentially decaying function

$$U(x) = \sigma P_g + (U_0 - \sigma P_g)e^{-D_m x/v}. \tag{14.7}$$

If the exposed section of the capillary has length L, the total flux of gas across the wall is $Q = p \int_0^L q\, dx = vA[U(L) - U_0]$, which is

$$Q = vA\sigma(P_g - P_0)(1 - e^{-D_m L/v}). \tag{14.8}$$

Plotted in Fig. 14.3 is the nondimensional flux

$$\bar{Q} = \frac{Q}{D_m L A\sigma(P_0 - P_g)} = \frac{v}{D_m L}(1 - e^{\frac{-D_m L}{v}}). \tag{14.9}$$

Note that

$$Q \to vA\sigma(P_g - P_0) \tag{14.10}$$

in the limit $D_m L/v \to \infty$. Thus, an infinitely long capillary has only a finite total flux, as the dissolved gas concentration approaches the alveolar concentration along the length of the capillary.

Data on the diffusion of carbon dioxide from the pulmonary blood into the alveolus (Fig. 14.4) suggest that carbon dioxide is lost into the alveolus at an exponential rate, consistent with (14.7). Furthermore, because the solubility of carbon dioxide
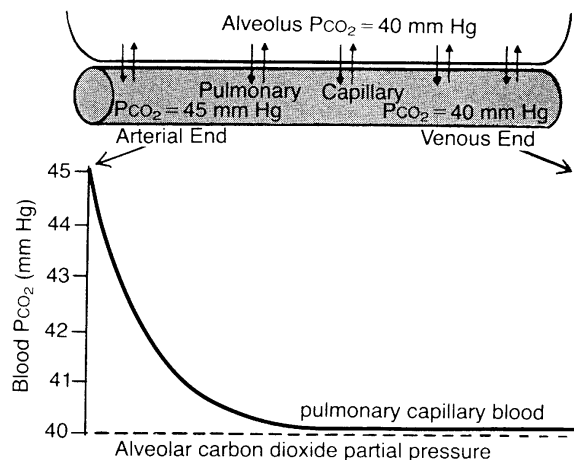
Figure 14.4: Loss of carbon dioxide from the pulmonary capillary blood into the alveolus. (The curve in this figure was constructed from data in Milhorn and Pulley, *Biophys. J.* 8:337, 1968. Figure from Guyton and Hall, 1996, Fig. 40-6, p. 515.)

in water is quite high, the difference between the partial pressure for the entering blood and the alveolar air is small, about 5 mm Hg.

In contrast, the solubility of oxygen in blood is small (about 20 times smaller than carbon dioxide, see Table 13.2), and although the difference in partial pressures is larger, this is not adequate to account for the balance of oxygen inflow and carbon dioxide outflow. That is, if (14.10) is relevant, then, in order to maintain a similar transport, a decrease in σ by a factor of 20 requires a corresponding increase by a factor of 20 for the difference in partial pressures. Thus, if this is the correct mechanism for carbon dioxide and oxygen transport, the difference $P_0 - P_g$ for oxygen should be about twenty times larger than for carbon dioxide. Since $104 - 40 \neq 20(45 - 40)$ (using typical numbers from Figs. 14.4 and 14.5), there is reason to doubt this model.

Secondly, the data in Fig. 14.5 suggest that the uptake of oxygen by the capillary blood is not exponential with distance, but nearly linear for the first third of the distance, where it becomes fully saturated. We consider a model of this below. First, however, we discuss the effects of blood chemistry on gas exchange, which was ignored in the above model.

14.1.3 Carbon Dioxide Removal

Blood chemistry plays a significant role in facilitating the transport of gases between blood and alveoli. To understand something of this facilitation, we first consider a simple model for carbon dioxide transport that takes the carbon dioxide–bicarbonate chemistry into account. We assume that carbon dioxide is converted
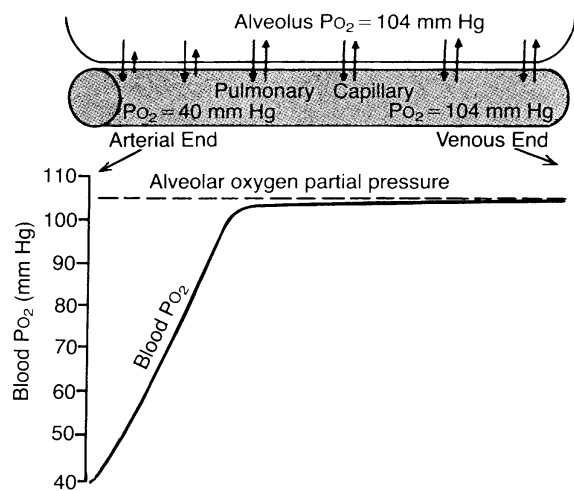
Figure 14.5: Uptake of oxygen by the pulmonary capillary blood. (The curve in this figure was constructed from data in Milhorn and Pulley, *Biophys. J.* 8:337, 1968. Figure from Guyton and Hall, 1996, Fig. 40-1, p. 514.)

to bicarbonate via the reaction

$$CO_2 + H_2O \underset{k_{-1}}{\overset{k_1}{\rightleftharpoons}} HCO_3^- + H^+.$$
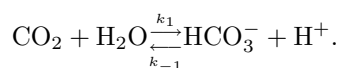
This is the carbonic anhydrase reaction discussed in Section 13.3.3. Because it has little effect, we ignore the intermediary H_2CO_3.

Now we write conservation equations for the two chemical species CO_2 and HCO_3^- (in steady state, and ignoring diffusion within the capillary) as

$$v\frac{dU}{dx} \quad = \quad D_{CO_2}(\sigma_{CO_2}P_{CO_2} - U) + k_{-1}[H^+]V - k_1U, \qquad (14.11)$$

$$v\frac{dV}{dx} \quad = \quad k_1U - k_{-1}[H^+]V, \qquad (14.12)$$

where $U = [CO_2]$, $V = [HCO_3^-]$. Notice that D_{CO_2} is a rate constant, similar to D_m above.

Although this is a linear problem and it can be solved exactly, it is illustrative to use an approximate, singular perturbation technique, as this technique is useful in the next section. First, notice that we can add (14.11) and (14.12) to obtain

$$v\frac{d}{dx}(U + V) = D_{CO_2}(\sigma_{CO_2}P_{CO_2} - U). \qquad (14.13)$$

Now we assume that V equilibrates rapidly, so that it can be taken to be in quasi-steady state. Accordingly, we set $V = K_cU$, where $K_c = \frac{k_1}{k_{-1}[H^+]}$. It follows that, assuming that $[H^+]$ is constant,

$$v(1 + K_c)\frac{dU}{dx} = D_{CO_2}(\sigma_{CO_2}P_{CO_2} - U). \qquad (14.14)$$

This equation is identical in form to (14.6). If we take the inlet conditions to be $U = U_0 = \sigma_{CO_2} P_0$ and $V = V_0 = K_c U_0$, then the total flux Q is

$$Q = vA(1 + K_c)\sigma_{CO_2} (P_0 - P_{CO_2}) \left(1 - e^{-D_{CO_2}L/(v(1+K_c))}\right), \qquad (14.15)$$

and in the limit as $D_{CO_2}L/v \to \infty$,

$$Q \to vA(1 + K_c)\sigma_{CO_2} (P_0 - P_{CO_2}), \qquad (14.16)$$

which is a factor of $1 + K_c$ larger than in (14.10). The only difference between this flux (14.15) and the original (14.8) is that the velocity v has been multiplied by the factor $1 + K_c$. In other words, the conversion of carbon dioxide to bicarbonate via the carbonic anhydrase reaction effectively increases the flow rate by the factor $1 + K_c$.

The equilibrium constant for the bicarbonate–carbon dioxide reaction is known to be $\log_{10}(\frac{k_1}{k_{-1}}) = -6.1$ (see also Exercise 13a). Thus (since $pH = -\log_{10}[H^+]$ with $[H^+]$ in moles per liter), at $pH = 7.4$, we have $K_c = 20$, and the improvement in carbon dioxide transport because of the carbonic anhydrase reaction is substantial.

In words, the improvement in total flux arises because the conversion of bicarbonate to carbon dioxide continually replenishes the carbon dioxide that is lost to the alveolar air. Thus, the carbon dioxide concentration in the capillary does not fall so quickly, leading to an increase in the total flux.

14.1.4 Oxygen Uptake

The chemistry for the absorption of oxygen by hemoglobin has a similar, but non-linear, effect. We take a simple model for the chemistry of hemoglobin (discussed in Section 13.3.1), namely

$$\text{Hb} + 4\text{O}_2 \underset{k_{-2}}{\overset{k_2}{\rightleftharpoons}} \text{Hb}(\text{O}_2)_4.$$
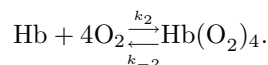
Of course, there are more detailed models of hemoglobin chemistry, but the qualitative behavior is affected little by these details. We write the conservation equations as

$$v\frac{dW}{dx} = D_{O_2}(\sigma_{O_2} P_{O_2} - W) + 4k_{-2}Y - 4k_2 ZW^4, \qquad (14.17)$$

$$v\frac{dY}{dx} = k_2 ZW^4 - k_{-2}Y, \qquad (14.18)$$

$$v\frac{dZ}{dx} = k_{-2}Y - k_2 ZW^4, \qquad (14.19)$$

where $W = [\text{O}_2]$, $Y = [\text{Hb}(\text{O}_2)_4]$, $Z = [\text{Hb}]$, and D_{O_2} is the oxygen exchange rate constant. The last of these equations is superfluous, since total hemoglobin is conserved, and so we take $Z + Y = Z_0$. Notice further that (14.17) and (14.18) can be added to obtain

$$v\frac{d}{dx}(W + 4Y) = D_{O_2}(\sigma_{O_2} P_{O_2} - W). \qquad (14.20)$$

We expect oxygen uptake by hemoglobin to be fast compared to the transmural exchange, so take Y to be in quasi-steady state, setting

$$Y = Z_0 \frac{W^4}{K_{O_2}^4 + W^4}, \tag{14.21}$$

where $K_{O_2}^4 = k_{-2}/k_2$. On substitution into (14.20) we find

$$v \frac{d}{dx}\left(W + 4Z_0 \frac{W^4}{K_{O_2}^4 + W^4}\right) = D_{O_2}(\sigma_{O_2} P_{O_2} - W). \tag{14.22}$$

More generally, if $f(W)$ is the oxygen saturation curve for hemoglobin, then

$$v \frac{d}{dx}(W + 4Z_0 f(W)) = D_{O_2}(\sigma_{O_2} P_{O_2} - W). \tag{14.23}$$

This equation is a nonlinear first-order ordinary differential equation, which, being separable, can be solved exactly. The solution is given implicitly by

$$\int_{W_1}^{W_2} \frac{1 + 4Z_0 f'(W)}{\sigma_{O_2} P_{O_2} - W} dW = \frac{D_{O_2} L}{v}. \tag{14.24}$$

However, this exact solution does not provide much insight. It is more useful to compare (14.23) with (14.14), in which the flux of carbon dioxide was facilitated by the factor K_c. Here, there is facilitation of oxygen flux by the factor $1 + 4Z_0 f'(W)$. Clearly, the two ways to exploit this facilitation are to have a high concentration of hemoglobin and to use a saturation curve with a steep slope in the range of operating values.

The total flux of oxygen is given by

$$\begin{aligned}
Q &= A \int_0^L D_{O_2}(\sigma_{O_2} P_{O_2} - W) dx & (14.25) \\
&= Av \int_0^L \frac{d}{dx}(W + 4Z_0 f(W)) dx & (14.26) \\
&= Av(W + 4Z_0 f(W))|_{W_0}^{W_1}. & (14.27)
\end{aligned}$$

For oxygen, this enhancement is substantial. For normal blood at 100 mm Hg oxygen partial pressure, hemoglobin is 97% saturated, and the hemoglobin of 100 ml of blood carries 19.4 ml of oxygen. By contrast, the same 100 ml of blood contains only 0.3 ml of dissolved (unbound) oxygen. When this hemoglobin is chemically pure, it can combine with a total of 20 ml of oxygen. This implies that (using that 1 mole of a dissolved gas fills 24.6 liters at room temperature) $Z_0 = 2.0$ mM.

Incoming blood has a partial pressure of 40 mm Hg, at which hemoglobin is about 75% saturated and alveolar air is at 104 mm Hg. A reasonable fit of the oxygen saturation curve is given by the function $f(W) = \frac{W^4}{K_{O_2}^4 + W^4}$ with $K_{O_2} = 30\sigma$ mm Hg. A slightly better fit is obtained with the Hill equation $f(W) = \frac{W^n}{K_{O_2}^n + W^n}$, $n = 2.5$, $K_{O_2} = 26\sigma$ mm Hg. Either way, the oxygen flux is increased by hemoglobin by a factor of about 14.
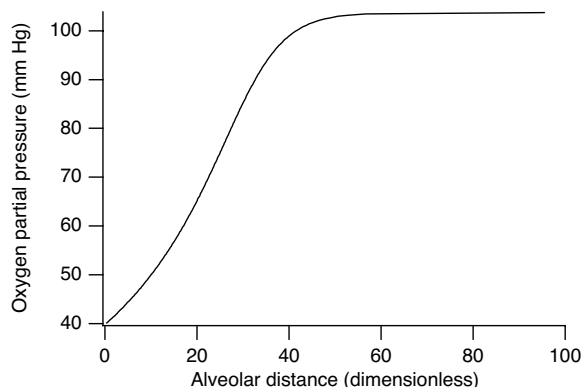
Figure 14.6: Oxygen partial pressure as a function of nondimensional distance $\frac{D_{O_2} x}{v}$.

Finally, using (14.24) we can find the rate of oxygen uptake as a function of length along the capillary. In Fig. 14.6 is shown the partial pressure of oxygen, plotted as a function of the dimensionless distance $D_{O_2} x/v$ along the capillary. The significant observation is that oxygen partial pressure rises steeply and nearly linearly, until it saturates, comparing well with the experimental data shown in Fig. 14.5.

14.1.5 Carbon Monoxide Poisoning

Carbon monoxide poisoning occurs because carbon monoxide competes with oxygen for hemoglobin binding sites. The goal of this section is to see how this competition for hemoglobin affects oxygen exchange and how carbon monoxide can be eliminated from the blood.

To model this problem we assume that the chemistry for carbon monoxide binding with hemoglobin is the same as for oxygen, except that the affinity of carbon monoxide for hemoglobin is much larger (about 200 times) than the affinity of oxygen for hemoglobin. Thus,

$$\text{Hb} + 4\text{CO} \underset{k_{-2}}{\overset{k_2}{\rightleftharpoons}} \text{Hb(CO)}_4.$$
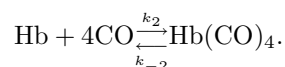
The conservation equations for carbon monoxide gaseous exchange in the alveolus are similar in form to those for oxygen, being (ignoring diffusion of the dissolved gases)

$$v\frac{dU}{dx} = D_{CO}(\sigma_{CO} P_{CO} - U) + 4k_{-3}S - 4k_3 ZU^4, \qquad (14.28)$$

$$v\frac{dS}{dx} = k_3 ZU^4 - k_{-3}S, \qquad (14.29)$$

where $U = [\text{CO}]$, $S = [\text{Hb(CO)}_4]$, $Z = [\text{Hb}]$, and D_{CO} is the carbon monoxide exchange rate constant. The balance of oxygen is governed by (14.17) and (14.18). Conservation of hemoglobin implies that $Z + Y + S = Z_0$.

As before, (14.20) holds, as does

$$v\frac{d}{dx}(U + 4S) = D_{CO}(\sigma_{CO}P_{CO} - U).\tag{14.30}$$

Now we assume that both carbon monoxide and oxygen are in quasi-steady state, so that

$$K_{CO}^4 S = ZU^4, \qquad K_{O_2}^4 Y = ZW^4,\tag{14.31}$$

where $K_{CO}^4 = k_{-3}/k_3, K_{O_2}^4 = k_{-2}/k_2$. It is convenient to introduce scaled variables w and u with $w = K_{O_2}^{-1}W, u = K_{CO}^{-1}U$. It follows from $Z + Y + S = Z_0$ that

$$S = Z_0\frac{u^4}{1 + w^4 + u^4},\tag{14.32}$$

$$Y = Z_0\frac{w^4}{1 + w^4 + u^4},\tag{14.33}$$

so that

$$v\frac{d}{dx}\left(w + 4z_0\frac{w^4}{1 + w^4 + u^4}\right) = D_{O_2}(w^* - w),\tag{14.34}$$

$$v\frac{d}{dx}\left(u + 4\beta z_0\frac{u^4}{1 + w^4 + u^4}\right) = D_{CO}(u^* - u),\tag{14.35}$$

where $z_0 = Z_0/K_{O_2}, \beta = K_{O_2}/K_{CO}, w^* = K_{O_2}^{-1}\sigma_{O_2}P_{O_2}, u^* = K_{CO}^{-1}\sigma_{CO}P_{CO}$.

While we cannot solve this system of differential equations explicitly, the difficulty can be readily seen. Because β is large (on the order of 200), the total carbon monoxide concentration changes as a function of x slowly, much more slowly than does the total oxygen concentration. Thus, w increases quickly to w^*, releasing some carbon monoxide as it does so, while $u + 4\beta z_0\frac{u^4}{1+w^4+u^4}$ remains essentially fixed. As a result, in the length of the alveolus, oxygen is recharged, but very little carbon monoxide is eliminated.

The lethality of carbon monoxide can be seen from a simple steady-state analysis. Suppose that $u = u^*$ is at steady state with the environment, so that no carbon monoxide is gained or lost in the alveoli. The concentration of oxygen in the blood is proportional to $w + 4z_0\frac{w^4}{1+w^4+u^4}$, so that the rate of oxygen transport is proportional to

$$M = w^* + 4z_0\frac{(w^*)^4}{1 + (w^*)^4 + u^4} - w_0 - 4z_0\frac{w_0^4}{1 + w_0^4 + u^4},\tag{14.36}$$

where w_0 is the alveolar input level and w^* is the output level from the alveolus. When there is no carbon monoxide present (i.e., when $u = 0$), the input and output levels are 40 and 104 mm Hg, respectively, so that (with $K_{O_2} = 30\sigma$ mm Hg) $w_0 = 40/30 = 1.333, w^* = 104/30 = 3.47$. Thus, with normal metabolism, the required flow rate has $M = 53$, where we have set $z_0 = 52$. When carbon monoxide is present, this same flow rate must be maintained (as the need of the tissues for oxygen remains unchanged), but now the presence of u in the denominator changes things. Keeping M fixed, we calculate that if u is greater than 4.64, then the incoming blood has $w_0 < 0$, so that the tissue is in oxygen debt. With $\beta = 200$,

$u = 4.64$ is equivalent to a carbon monoxide partial pressure of 0.7 mm Hg, a mere 0.1% by volume. In other words, an ambient concentration of 0.1% carbon monoxide leads to certain death because of oxygen depletion.

Since βz_0 is so large (on the order of 10^4), we can approximate the dynamics of carbon monoxide by

$$4\beta z_0 v \frac{d}{dx}\left(\frac{u^4}{1+(w^*)^4+u^4}\right) = D_{\text{CO}}(u^*-u). \qquad (14.37)$$

If we set

$$F = \frac{u^4}{1+(w^*)^4+u^4}, \qquad (14.38)$$

we find that

$$\frac{dF}{dx} = -\frac{D_{\text{CO}}}{4\beta z_0 v}(1+(w^*)^4)^{1/4}\left(\frac{F}{1-F}\right)^{1/4}, \qquad (14.39)$$

where we have taken $u^* = 0$, assuming that the victim is placed in a carbon-monoxide-free environment. Clearly, the rate of carbon monoxide elimination is proportional to $(1+(w^*)^4)^{1/4}$, which for large w^* is linear in w^*. Thus, (and not surprising) the rate of carbon monoxide elimination can be increased by placing the victim in an environment of high oxygen.

In hospitals it is typical to place a carbon monoxide poisoning victim in an environment of oxygen at 2–2.5 atm. At 2 atmospheres (1 atm = 760 mm Hg), $w^* = (2 \times 760/30) = 50.7$, compared to $w^* = 3.5$ at normal oxygen levels, giving an increase in the rate of carbon monoxide elimination of about 14.

14.2 Ventilation and Perfusion

Gaseous exchange is mediated by the combination of ventilation of the alveoli with inspired air and the perfusion of the capillaries with blood. It is the balance of these two that determines the gas content of the lungs and of the recharged blood.

The most important early studies of ventilation and perfusion were those of Fenn et al. (1946), Rahn (1949), and Riley and Cournand (1949, 1950). A clear non-mathematical discussion is given by West (1985), who also gives a brief summary of the history of such investigations in West (2004).

To see how this balance is maintained, suppose that $\dot{V}$ is the volume flow rate of air that participates in the exchange of the alveolar content. Not all inspired air participates in this exchange, because some inspired air never reaches the terminal bronchioles. The parts of the lung that are ventilated but do not participate in gaseous exchange are called the *anatomical dead space*. In normal breathing, the total amount of inspired air is about 500 ml per breath (men 630 ml; women 390 ml). Of this, 150 ml is anatomical dead space, so only 350 ml participates in alveolar gaseous exchange. With 15 breaths per minute, $\dot{V}$ is about 5250 ml/min.

Now suppose that Q is the volume flow rate of blood into and out of the alveolar capillaries. Cardiac output is about 70 ml per beat, so at 72 beats per minute, Q is about 5000 ml/min. The ratio $\dot{V}/Q$ is called the *ventilation–perfusion ratio*, and it is the most important determinant of lung–blood gas content.

P_{i,O_2}= 150 mm Hg

P_{i,CO_2}= 0 mm Hg

P_{v,O_2}= 40 mm Hg

P_{v,CO_2}= 45 mm Hg
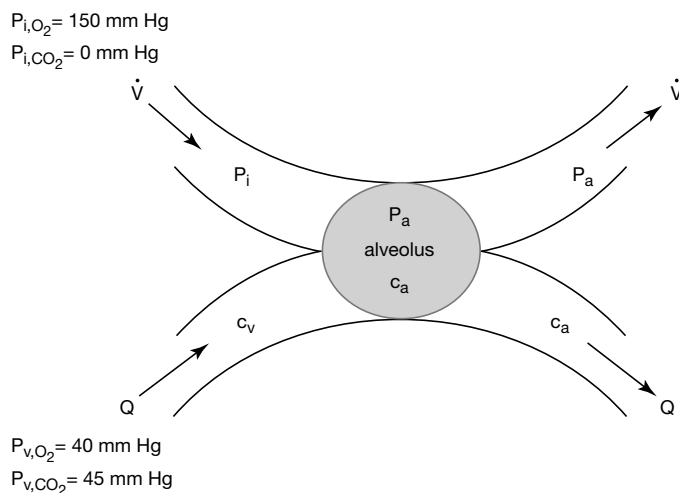
Figure 14.7: Schematic diagram of gas exchange in an alveolus.

If P_i and P_a are the pressures of a gas in the inspired air and in the alveolar air, respectively (see Fig. 14.7), then the rate at which the gas is taken out of the alveolus by ventilation (in moles/sec) is

$$\dot{V}\left(\frac{P_a - P_i}{RT}\right). \tag{14.40}$$

Note that the factor RT is needed to convert pressures to concentrations. Similarly, the rate at which the gas is brought into the alveolus by the blood (again in moles/second) is given by

$$Q(c_v - c_a), \tag{14.41}$$

where c_v and c_a are the venous and alveolar gas concentrations in the blood. Since the rate at which the gas is removed by ventilation must be in balance with the rate at which it is brought in by the blood, it must be that

$$\frac{\dot{V}}{Q} = \frac{(c_v - c_a)RT}{(P_a - P_i)}. \tag{14.42}$$

Textbooks on respiratory physiology typically use different units than those used here, and this can be confusing for those new to the field. Since the gas in the alveolus is always saturated with water vapour and is at body temperature, the partial pressures of alveolar gas are measured at Body Temperature and Pressure, Saturated (BTPS). However, blood gas concentrations are measured in the usual way, at Standard Temperature and Pressure, Dry (STPD). To understand the difference between these units, suppose we have one mole of gas at standard temperature (273 K) and standard pressure (1 atmosphere or 760 mm Hg). Since $PV = nRT$, the STPD volume of the mole of gas, V_{STPD} is

$$V_{\text{STPD}} = \frac{273R}{760}. \tag{14.43}$$

Similarly, for one mole of gas at BTPS, suppose that the total pressure, including the pressue due to water vapour, is P (in mm Hg). At body temperature (310 K), the partial pressure of water vapour is 47 mm Hg, and thus the partial pressure of the mole of gas is $P - 47$ mm Hg. Hence, the BTPS volume of the mole of gas is

$$V_{\text{BTPS}} = \frac{310R}{P - 47}. \tag{14.44}$$

It follows that

$$V_{\text{STPD}} = V_{\text{BTPS}} \frac{273 \times (P - 47)}{310 \times 760} = \frac{P - 47}{863} V_{\text{BTPS}}, \tag{14.45}$$

where the ambient pressure, P, is measured in mm Hg.

To return to gas exchange, if we were considering an inert gas that merely dissolves in blood, (14.42) would be relatively simple. The alveolar concentration c_a would be linearly related to the alveolar pressure P_a by the solubility of the gas. However, in the case of oxygen and carbon dioxide, this relationship is complicated by the blood chemistry.

It is reasonable to assume that the two most important respiratory gases, carbon dioxide and oxygen, are equilibrated when they leave the alveolus in the capillaries. In other words, the partial pressures of carbon dioxide and oxygen in the alveolus and in the blood leaving the pulmonary capillary are the same. Of course, this is not true at high perfusion rates, but it is a satisfactory assumption at normal physiological flow rates.

Because carbon dioxide is quickly converted to bicarbonate, the total blood carbon dioxide (i.e., both free and converted) is given by

$$[CO_2] = \sigma_{CO_2}(1 + K_c)P_{CO_2}. \tag{14.46}$$

In other words, in the notation of Fig. 14.7, $c_a = \sigma_{CO_2}(1 + K_c)P_a$ for carbon dioxide. A similar expression holds for c_v and P_v, where P_v is the pressure of carbon dioxide in the venous blood. In addition, the concentration of carbon dioxide in inspired air is very close to zero ($P_i = 0$). Thus, for carbon dioxide, the ventilation–perfusion ratio must satisfy

$$\frac{\dot{V}}{Q} = \sigma_{CO_2} RT(1 + K_c)\frac{(P_{v,CO_2} - P_{a,CO_2})}{P_{a,CO_2}}, \tag{14.47}$$

where the additional subscript CO_2 is to distinguish these pressures from those of oxygen.

Since $P_{v,CO_2} = 45$ mm Hg we can use (14.47) to plot alveolar CO_2 pressure as a function of the ventilation–perfusion ratio (Fig. 14.8). As $\frac{\dot{V}}{Q}$ increases, the CO_2 partial pressure decreases, as removal of CO_2 from the blood becomes more efficient. When $\frac{\dot{V}}{Q} = 0$, $P_{a,CO_2} = P_{v,CO_2}$ as expected, as no CO_2 is removed from the blood when there is no ventilation.

As described in the previous section, the total amount of oxygen in the blood, $[O_2]_t$, is given by

$$[O_2]_t = W + 4Z_0 f(W), \tag{14.48}$$
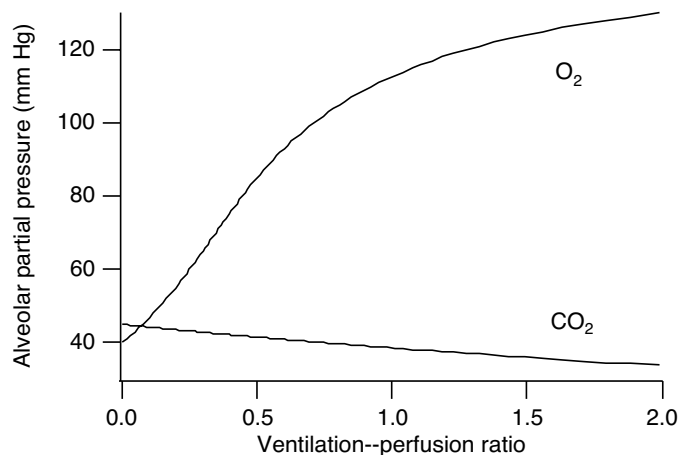
Figure 14.8: Alveolar partial pressure as a function of ventilation–perfusion ratio. Calculated using the parameters $W_v = 40\sigma_{O_2}$ mm Hg (i.e., $P_{v,O_2} = 40$ mm Hg), $K_{O_2} = 30\sigma_{O_2}$ mm Hg, $Z_0 = 2.2$ mM, $RT = 1.7 \times 10^4$ mm Hg/M, $P_{v,CO_2} = 45$ mm Hg, , $K_c = 12$ and $P_{i,O_2} = 150$ mm Hg.

where Z_0 is the total hemoglobin concentration, and W is the concentration of unbound oxygen in the blood. In these terms the ventilation–perfusion ratio must be

$$\frac{\dot{V}}{Q} = \left(\frac{RT}{(P_{i,O_2} - P_{a,O_2})} \right) (W_a - W_v + 4Z_0[f(W_a) - f(W_v)]), \qquad (14.49)$$

where the subscripts a, i, and v have the same interpretations as above. Note that, since we assume that the partial pressure of oxygen in the alveolar air is the same as the partial pressure in the blood leaving the alveolus, we have $W_a = \sigma_{O_2} P_{a,O_2}$. Similarly, $W_v = \sigma_{O_2} P_{v,O_2}$, where $P_{v,O_2} = 40$ mm Hg is a known parameter.

A plot of the alveolar partial pressures of carbon dioxide and oxygen as a function of ventilation–perfusion ratio is shown in Fig. 14.8.

From this figure we see that the alveolar oxygen partial pressure is an increasing function of $\dot{V}/Q$, while the alveolar carbon dioxide partial pressure is a decreasing function thereof. In normal situations, the ventilation–perfusion ratio is about 1. An increase in this ratio is called *hyperventilation*, and a decrease is called *hypoventilation*. During hyperventilation, there is rapid removal of carbon dioxide, and the partial pressure of carbon dioxide in the arterial blood drops below the normal level of 40 mm Hg. This results in less carbon dioxide available for carbonic acid formation, and consequently blood pH rises above the normal level, resulting in *respiratory alkalosis*. In hyperventilation there is no substantial change in oxygen concentration because the hemoglobin is fully saturated.

The opposite situation, in which the ventilation–perfusion ratio drops, increases carbon dioxide content and decreases oxygen content of the arterial blood. The increase of carbon dioxide increases carbonic acid formation and decreases blood pH, a condition referred to as *respiratory acidosis*. To compensate for these changes,
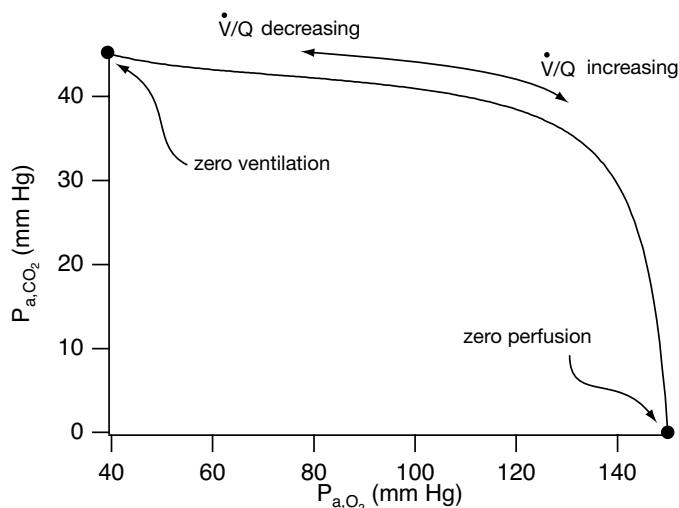
Figure 14.9: Oxygen-carbon dioxide diagram showing how the alveolar partial pressures of oxygen and carbon dioxide are related. Parameter values are the same as used for Fig. 14.8.

the blood gas concentration stimulates the carotid and aortic chemoreceptors to increase the rate of ventilation.

14.2.1   The oxygen-carbon dioxide diagram

Most commonly (partially for historical reasons, as this was the way it was first presented), the ventilation-perfusion ratio is discussed using the *oxygen-carbon dioxide diagram* shown in Fig. 14.9. By combining (14.47) and (14.49) we see that

$$\sigma_{CO_2}(1 + K_c)\frac{(P_{v,CO_2} - P_{a,CO_2})}{P_{a,CO_2}} = \frac{W_a - W_v + 4Z_0[f(W_a) - f(W_v)]}{P_{i,O_2} - P_{a,O_2}}, \quad (14.50)$$

from which one easily determines P_{a,CO_2} as a function of P_{a,O_2}. The resultant curve is plotted in Fig. 14.9. All possible simultaneous alveolar pressures of oxygen and carbon dioxide must lie somewhere on this curve, which is parameterized by $\dot{V}/Q$. As $\dot{V}/Q$ increases we move to the right along the curve, and in the limit as $\dot{V}/Q \to \infty$ we move to the right end-point where $P_{a,O_2} = 150$ mm Hg, the oxygen pressure in inspired air. Similarly, as $\dot{V}/Q$ decreases we move along the curve to the left end-point at which point there is no ventilation and P_{a,O_2} is the venous oxygen pressure, 40 mm Hg.

14.2.2   Respiratory exchange ratio

Different regions of the lung lie on different points of the oxgen-carbon dioxide diagram, the actual point being determined by the local *respiratory exchange ratio*,
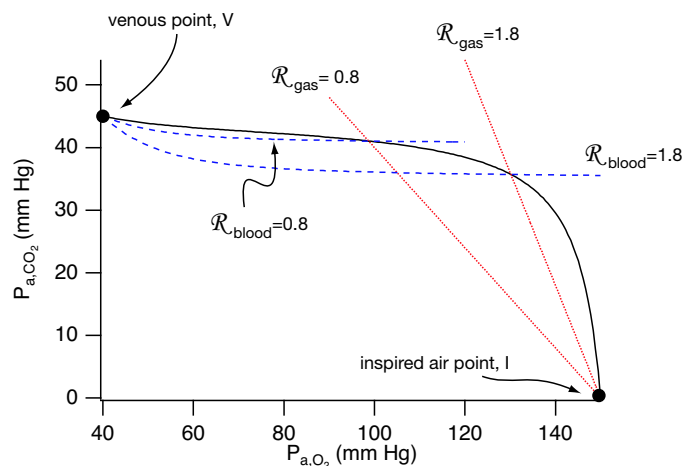
Figure 14.10: Curves of constant respiratory exchange ratio, $\mathcal{R}$, for alveolar gas and blood, superimposed on the oxygen-carbon dioxide diagram.

$\mathcal{R}$, where

$$\mathcal{R} = \frac{\text{volume of carbon dioxide removed}}{\text{volume of oxygen taken up}}. \tag{14.51}$$

This ratio differs throughout the lung.

There is a close relationship between $\mathcal{R}$ and the oxygen-carbon dioxide diagram shown in Fig. 14.9. To see this, we consider curves of constant $\mathcal{R}$ for both the alveolar gas and the alveolar blood. For the alveolar gas,

$$\mathcal{R}_{\text{gas}} = \frac{P_{a,\text{CO}_2} - P_{i,\text{CO}_2}}{P_{i,\text{O}_2} - P_{a,\text{O}_2}} = \frac{P_{a,\text{CO}_2}}{P_{i,\text{O}_2} - P_{a,\text{O}_2}}. \tag{14.52}$$

Thus, in the oxygen-carbon dioxide diagram, curves of constant $\mathcal{R}$ are straight lines that emanate from the inspired air point, I (Fig. 14.10).

The total amount of oxygen taken up by the blood is $W_a + 4Z_0 f(W_a) - [W_v + 4Z_0 f(W_v)]$, while the total amount of carbon dioxide lost is $\sigma_{\text{CO}_2}(1 + K_c)(P_{v,\text{CO}_2} - P_{a,\text{CO}_2})$. Thus

$$\mathcal{R}_{\text{blood}} = \frac{\sigma_{\text{CO}_2}(1 + K_c)(P_{v,\text{CO}_2} - P_{a,\text{CO}_2})}{W_a + 4Z_0 f(W_a) - [W_v + 4Z_0 f(W_v)]}, \tag{14.53}$$

where, as usual, $W_a = \sigma_{\text{O}_2} P_{a,\text{O}_2}$ and $W_v = \sigma_{\text{O}_2} P_{v,\text{O}_2}$. Curves of constant $\mathcal{R}$ are shown in Fig. 14.10. They emanate from the venous point, V, but because of the blood chemistry are non-linear curves, not straight lines.

Since $\mathcal{R}_{\text{gas}}$ must equal $\mathcal{R}_{\text{blood}}$, it follows that the alveolar gas concentrations must lie on the intersection of the two curves $\mathcal{R}_{\text{blood}}$ and $\mathcal{R}_{\text{gas}}$. However, this intersection must lie on the oxygen-carbon dioxide curve shown in Fig. 14.9, since the equation $\mathcal{R}_{\text{gas}} = \mathcal{R}_{\text{blood}}$ is exactly the same as (14.50). Thus, the oxygen-carbon dioxide curve can be thought of as parameterized by either $\dot{V}/Q$ or by $\mathcal{R}$.

One way of showing the relationship between $\dot{V}/Q$ and $\mathcal{R}$ is to combine (14.49) and (14.52) to get

$$\frac{\dot{V}}{Q} = \frac{\mathcal{R}}{P_{a,\mathrm{CO_2}}}RT\Big(W_a - W_v + 4Z_0[f(W_a) - f(W_v)]\Big) \qquad (14.54)$$

$$= \frac{\mathcal{R}}{P_{a,\mathrm{CO_2}}}RT(c_a - c_v), \qquad (14.55)$$

where $c_a = W_a + 4Z_0 f(W_a)$ and $c_v = W_v + 4Z_0 f(W_v)$ are the total concentrations of oxygen in the alveolar blood and venous blood, respectively.

In the upper regions of the lung, $\mathcal{R}$ can be almost as large as 3, while in the lower regions $\mathcal{R}$ can be as low as 0.6. On the level of the entire body, the ratio of total carbon dioxide produced to total oxygen used is called the *respiratory quotient*, or RQ. The oxygen that is taken in by the blood is consumed by metabolic processes to produce carbon dioxide. However, the amount of carbon dioxide produced is generally less than the amount of oxygen consumed, and thus RQ is rarely more than one. When a person uses carbohydrates for body metabolism, RQ is 1.0 because one molecule of carbon dioxide is formed for every molecule of oxygen consumed. On the other hand, when oxygen reacts with fats, a large share of the oxygen combines with hydrogen to form water instead of carbon dioxide. In this mode, RQ falls to as low as 0.7. For a normal person with a normal diet, RQ = 0.825 is considered normal.

14.3 Regulation of Ventilation

While the exchange of gases takes place in the lungs, the control of the rate of ventilation is accomplished in the brain. There, in the respiratory center, is located a chemosensitive area that is sensitive to the concentrations of chemicals in the blood, primarily carbon dioxide. Changes in blood $P_{\mathrm{CO_2}}$ are detected, and this leads to changes in the rate of breathing by activating or inhibiting the inspiratory neurons (described in the next section). In Fig. 14.11 is shown the effect of carbon dioxide on ventilation rate.

To construct a model for this control, we let x denote the partial pressure of carbon dioxide in the blood. Carbon dioxide is produced at rate λ by metabolism and eliminated by ventilation at the lungs. Thus,

$$\frac{dx}{dt} = \lambda - \alpha x \dot{V}, \qquad (14.56)$$

where $\dot{V}$ is the ventilation rate, and we assume that the transport of carbon dioxide through the lungs is linearly proportional to the concentration of carbon dioxide and the ventilation rate.

Now we take the ventilation rate to be the Hill equation

$$\dot{V}(x) = V_m \frac{x^n}{\theta^n + x^n}. \qquad (14.57)$$

in order to replicate the curve shown in Fig. 14.11. Furthermore, there is a substantial delay between ventilation of the blood and the measurement of $P_{\mathrm{CO_2}}$ at the
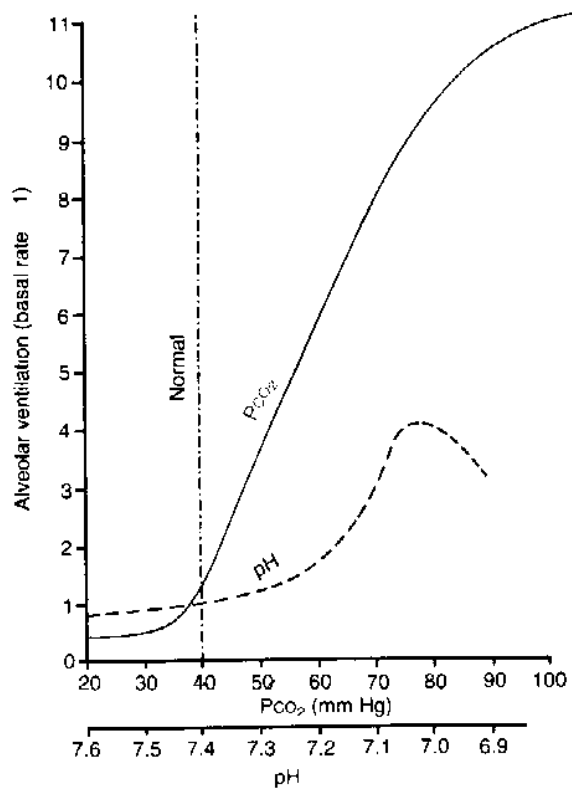
Figure 14.11: Effects of increased arterial P_{CO_2} and decreased arterial pH on the alveolar ventilation rate. (Guyton and Hall, 1996, Fig. 41-3, p. 528.)

λ	=	6 mm Hg/min
V_m	=	80 liter/min
τ	=	0.25 min

Table 14.1: Physical parameters for the Mackey–Glass model of respiratory control.

respiratory center in the brain because the transport of blood from the lungs back to the heart and then to the brain takes time. Thus, the complete model is (Glass and Mackey, 1988)

$$\frac{dx}{dt} = \lambda - \alpha x \dot{V}(x(t-\tau)). \qquad (14.58)$$

Typical parameter values for the model are given in Table 14.1.

Before proceeding further with the analysis of this equation, it is worthwhile to introduce dimensionless variables and parameters. We set $x = \theta y, t = \frac{s}{\alpha V_m}, \tau = \frac{\sigma}{\alpha V_m}$, and $\lambda = \theta \alpha V_m \beta$ and obtain

$$\frac{dy}{ds} = \beta - yF(y(s-\sigma)), \qquad (14.59)$$

where F is a sigmoidal function, monotone increasing with a maximum of 1 as $y \to \infty$.

Because the function $yF(y)$ is monotone increasing in y, there is a unique steady-state solution for (14.59). Furthermore, the steady-state solution is a monotone increasing function of the parameter β, indicating that blood P_{CO_2} and ventilation increase as a function of steady metabolism. However, the dynamic (non-steady-state) situation may be quite different.

To understand more about the dynamic behavior of this equation, we perform a linear stability analysis. We suppose that the steady state is $y = y^*$, and set $y = y^* + Y$, substitute into (14.59), and assume that Y is small enough so that only linear terms of the local Taylor series are necessary. The resulting linearized equation for Y is

$$\frac{dY(s)}{ds} = -F(y^*)Y(s) - y^*F'(y^*)Y(s-\sigma). \qquad (14.60)$$

Solutions of exponential form $Y = Y_0 e^{\mu s}$ exist provided that μ satisfies the characteristic equation

$$\mu + F(y^*) + y^*F'(y^*)e^{-\mu\sigma} = 0. \qquad (14.61)$$

Since there is a monotone relationship between y^* and β, it is convenient to view y^* as an independent parameter.

The function

$$g(y) = F(y) - yF'(y) \qquad (14.62)$$

is important to the analysis that follows and has a nice geometrical interpretation. This function is constructed by drawing a straight line from the point $(y, F(y))$ to $y = 0$ with slope $F'(y)$, as illustrated in Fig. 14.12. The three functions $F(y), F'(y)$, and $g(y)$ are shown in Fig. 14.13, in the case $F(y) = \frac{y^3}{1+y^3}$.
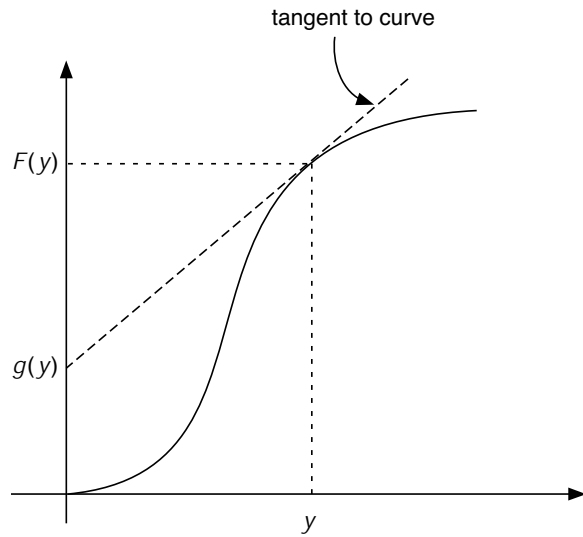
Figure 14.12: Sketch of the construction of the function $g(y) = F(y) - yF'(y)$.
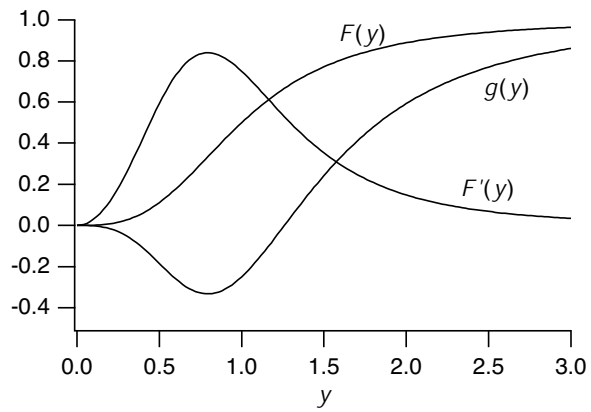
Figure 14.13: Plots of $F(y) = \frac{y^n}{1+y^n}$, $F'(y)$ and $g(y)$, with $n = 3$.
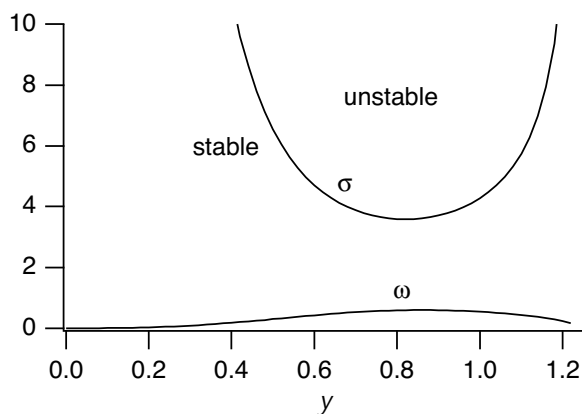
Figure 14.14: Plots of ω and σ at Hopf bifurcation points.

We wish to understand the behavior of the roots of the characteristic equation (14.61). First, observe that if $g(y^*)$ is positive, then all roots of the characteristic equation (14.61) have negative real part, so that the steady solution is stable. This follows, because if the real part of μ is positive, then $|\mu + F(y^*)| > |\mu + y^* F'(y^*)| > |y^* F'(y^*) e^{-\mu\sigma}|$. Note that F, F', and y are all assumed to be positive.

The only real roots of (14.61) are negative. Thus, the only way the real part of a root can change sign is if it is complex, a Hopf bifurcation. To see whether Hopf bifurcations occur, we set $\mu = i\omega$. If this is a root of (14.61), then of necessity, $|i\omega + F(y^*)| = |y^* F'(y^*)|$, and thus $|F(y^*) + i\omega|^2 = [F(y^*)]^2 + \omega^2 = [y^* F'(y^*)]^2$. In this case, it must be that $y^* F'(y^*) > F(y^*)$, which implies that $g(y^*) < 0$. Now, we split (14.61) into real and imaginary parts, obtaining

$$F(y^*) + y^* F'(y^*) \cos \omega\sigma = 0, \qquad (14.63)$$
$$\omega - y^* F'(y^*) \sin \omega\sigma = 0. \qquad (14.64)$$

It follows that $\omega = \sqrt{(y^* F'(y^*))^2 - (F(y^*))^2}$ (provided that $g(y^*) < 0$) and that

$$\tan \omega\sigma = -\frac{\omega}{F(y^*)}. \qquad (14.65)$$

The smallest root of this equation lies in the interval $\frac{\pi}{2} < \omega\sigma < \pi$, and for this root,

$$\sigma = \frac{1}{\omega} \left[\pi + \tan^{-1}\left(-\frac{\omega}{F(y^*)} \right) \right]. \qquad (14.66)$$

We can view this information as follows. For a given y^*, we have the frequency ω and the critical delay σ at which a Hopf bifurcation occurs. If the delay is smaller than this critical delay, then the steady solution is stable, while if the delay is larger, then the steady solution is unstable and an oscillatory solution is likely.

Plots of ω and σ are shown in Fig. 14.14. Steady solutions having σ greater than the critical value of delay (14.66) are unstable. In this case, numerical simulations show that there is a stable periodic solution of the governing equations, shown in
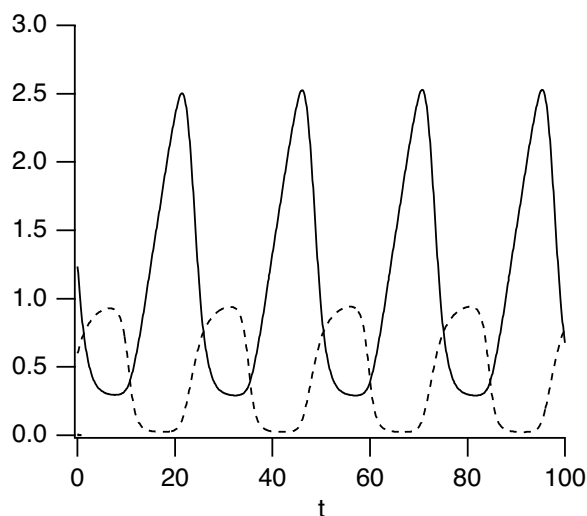
Figure 14.15: Oscillatory solution of the Mackey–Glass equation (14.59) with parameters $y^* = 0.8, \sigma = 10.0$. Solution (carbon dioxide content) is shown as solid curve, ventilation rate is shown as dashed curve.

Fig. 14.15. Here is shown the dimensionless concentration y (shown solid) and the dimensionless ventilation rate $F(y_\sigma)$ (shown dashed) as a function of time, with parameter values $\beta = 0.8, \sigma = 10.0$.

An episode of periodic fluctuation of ventilation, depicted by the periodic solution of Fig. 14.15, is called *Cheyne–Stokes breathing*. It was first described by Cheyne in 1818, but was more widely noticed after being discussed by Stokes (1854). In this condition, the person breathes deeply for a short interval and then breathes slightly or not at all for an additional interval, then repeats the cycle, with a period of 40 to 60 seconds. Notice that Cheyne–Stokes breathing can be caused by an increased delay in the transport of blood to the brain or an increase in the negative feedback gain (the slope of F). The first type (delayed transport) is likely to occur in patients with chronic heart failure, and the second type (increased gain) occurs mainly in patients with brain damage, and is often a signal of impending death.

14.3.1   A more detailed model of respiratory regulation

The model discussed above, due to Mackey and Glass, is one of the simplest models of Cheyne-Stokes breathing. The most widely known model, and possibly the most physiologically realistic, is that of Grodins et al. (1967). The Grodins model describes oxygen, carbon dioxide and nitrogen concentrations in a number of body compartments, including the lungs, the brain and tissues, and has been widely studied (see, for example, Khoo et al., 1982; Fowler et al., 1993; Fowler and Kalamangalam, 2000, 2002; Batzel and Tran, 2000a,b,c; Whiteley et al., 2003; Topor et al., 2004). Here we present a simplified version of the full model; not only does this
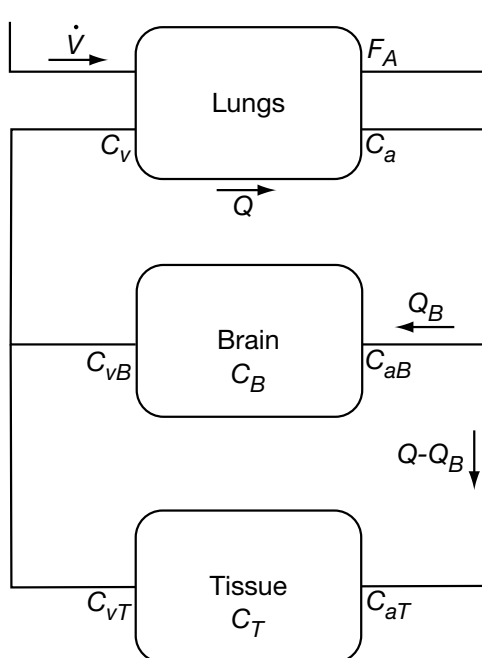
Figure 14.16: Schematic diagram of the Grodins et al. model of ventilation control. The C's denote concentrations at the entry and exit points of the compartments, while F_A is the fraction of carbon dioxide in expired alveolar air.

simplifed model demonstrate reasonable oscillations, it also illustrates the principles behind the construction of the full model.

A schematic diagram of the compartments in the model is given in Fig. 14.16. For simplicity we consider only the carbon dioxide concentrations in each of these compartments. The blood flow through the lungs is Q while the blood flow through the brain compartment is Q_B. The subscripts B and T denote, respectively, quantities in the brain and the tissues. The C's denote concentrations of carbon dioxide at the entry and exit points to the compartments, with a subscript a denoting the arterial side, a subscript v the venous side. Let M_i denote the rate of metabolism in compartment i, and let V_i denote the volume of compartment i. Then, conservation of carbon dioxide gives

$$V_B \frac{dC_B}{dt} = M_B + Q_B(C_{aB} - C_{vB}), \tag{14.67}$$

$$V_T \frac{dC_T}{dt} = M_T + (Q - Q_B)(C_{aT} - C_{vT}). \tag{14.68}$$

Similarly, if we let F denote the volume fraction of carbon dioxide, conservation of carbon dioxide at the lungs gives

$$V_L \frac{dF_A}{dt} = -\dot{V} F_A + \beta Q(C_v - C_a). \tag{14.69}$$

Since V_L and $\dot{V}$ are measured in BTPS while the blood concentrations are measured in STPD (see (14.45)), we include the conversion factor $\beta = 863/(760 - 47)$.

First, we simplify the model by assuming that $C_{vB} = C_B$ and $C_{vT} = C_T$. In other words, the concentration that exits the brain, say, is the same as the concentration in the brain. We also assume that the concentrations C_{aB} and C_{aT} are delayed versions of C_a, and thus

$$C_{aB} = C_a(t - \tau_{aB}), \tag{14.70}$$
$$C_{aT} = C_a(t - \tau_{aT}). \tag{14.71}$$

Similarly, C_v is a delayed version of C_B and C_T, and thus

$$QC_v = Q_B C_B(t - \tau_{vB}) + (Q - Q_B)C_T(t - \tau_{vT}). \tag{14.72}$$

In a more complex version of this model, the time delays depend on the blood flow Q which itself is time-dependent, leading to a far greater complexity. However, for simplicity, we assume both the time delays and the blood flows are constant.

We now convert the variables to partial pressures rather than concentrations. First, each carbon dioxide concentration can be converted to a partial pressure by using (14.46). To simplify the notation we write

$$C_a = K_{CO_2} P_a, \qquad C_v = K_{CO_2} P_v, \qquad \ldots, \tag{14.73}$$

where $K_{CO_2} = \sigma_{CO_2}(1 + K_c)$.

Second, the fractional volume of carbon dioxide in the alveolus, F_A, is related to the alveolar partial pressure of carbon dioxide, P_A, by the relationship

$$F_A = \frac{P_A}{760 - 47}, \tag{14.74}$$

where we assume that the ambient pressure is 760 mm Hg (see (14.45)). This is because the air in the alveolus is saturated with water vapour, which (at body temperature) has a partial pressure of 47 mm Hg, as discussed in Section 14.2. Since it is reasonable to assume that the alveolar air is in equilibrium with the arterial blood we let $P_A = P_a$.

Combining all these assumptions, (14.67)–(14.69) become

$$V_B K_{CO_2} \frac{dP_B}{dt} = M_B + Q_B K_{CO_2}(P_a(t - \tau_{aB}) - P_B), \tag{14.75}$$

$$V_T K_{CO_2} \frac{dP_T}{dt} = M_T + (Q - Q_B)K_{CO_2}(P_a(t - \tau_{aT}) - P_T), \tag{14.76}$$

$$V_L \frac{dP_a}{dt} = -\dot{V}P_a + 863 K_{CO_2} Q(P_v - P_a), \tag{14.77}$$

which we supplement with (14.72), which, in terms of partial pressures, is

$$QP_v = Q_B P_B(t - \tau_{vB}) + (Q - Q_B)P_T(t - \tau_{vT}). \tag{14.78}$$

The model parameters are given in Table 14.2.

Q_B	$=$	0.75 liters/min		Q	$=$	6 liters/min
V_L	$=$	3 liters		V_B	$=$	1 liter
V_T	$=$	39 liters		K_{CO_2}	$=$	0.005/mm Hg
M_B	$=$	0.05 liters/min		M_T	$=$	0.182 liters/min
τ_{aB}	$=$	0.18 min		τ_{aT}	$=$	0.32 min
τ_{vT}	$=$	0.59 min		τ_{vB}	$=$	0.11 min
G_C	$=$	1.8 (9) liters min^{-1} (mm Hg)$^{-1}$		I_C	$=$	49.3 mm Hg
$\dot{V}_{\text{base}}$	$=$	2 liters/min				

Table 14.2: Parameters for the simplified Grodins model of respiratory control. The bracketed value for G_C is the one that was used to generate instability and oscillations (Fig. 14.17).

When $\dot{V}$ is held fixed, the steady state solution of this model is stable and no oscillatory breathing pattern emerges. However, ventilation is dependent on the carbon dioxide concentration in the blood, and thus $\dot{V}$ is dependent on the blood pressures in the model. A number of different authors have chosen different expressions for $\dot{V}$. Here we follow Khoo et al. (1982) and assume that

$$\dot{V} = \dot{V}_{\text{base}} + G_C \max(P_B - I_C, 0), \qquad (14.79)$$

where $\dot{V}_{\text{base}}$ is the base ventilation rate. If the brain carbon dioxide concentration increases above the threshold I_C, the ventilation rate increases (with slope G_C), in order to remove the excess carbon dioxide more effectively.

Typical numerical solutions are shown in Fig. 14.17. When $G_C = 1.8$ the steady state is stable and no oscillations appear. However, when $G_C = 9$ the steady state is unstable and the ventilation rate oscillates with a period close to 60 seconds.

14.4 The Respiratory Center

Breathing is controlled by a neural central pattern generator called the *respiratory center*. The respiratory center is composed of three major groups of neurons located at the base of the brain. The *dorsal respiratory group*, located in the dorsal portion of the medulla, mainly causes inspiration; the *ventral respiratory group* can cause either inspiration or expiration, depending upon which neurons in the group are stimulated; and the *pneumotaxic center*, located above the medulla in the superior portion of the pons, helps control the rate and pattern of breathing.

The basic rhythm of respiration is generated mainly by the dorsal group, by emitting repetitive bursts of inspiratory action potentials. While the basic cause of these bursts is unknown, in primitive animals, neural networks have been found in which one set of neurons stimulates a second set, which in turn inhibits the first set, leading to periodic bursting activity that lasts throughout the lifetime of the animal.

The inspiratory signal is said to be a *ramp signal*, as it begins slowly and increases steadily for about 2 seconds, whereupon it abruptly ceases for the next 3 seconds before a new cycle begins. During normal quiet breathing, the ventral respiratory
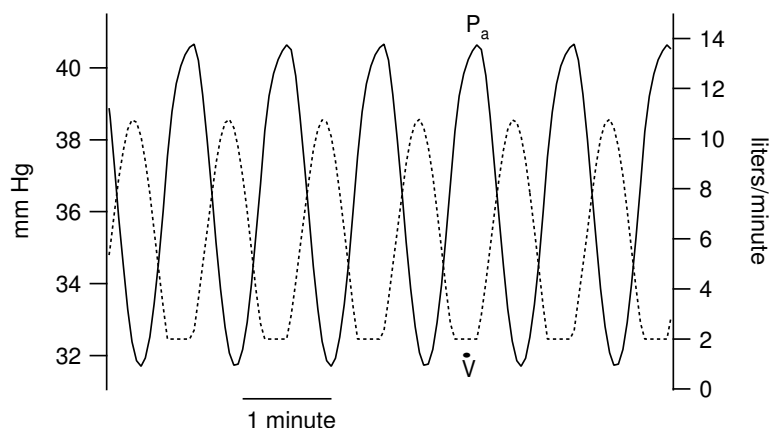
Figure 14.17: Numerical solution of the simplified Grodins model. Arterial carbon dioxide pressure, P_a, is plotted against the left axis, while ventilation ($\dot{V}$) is plotted against the right axis. This solution was calculated with $G_C = 9$. As G_C decreases, the oscillations disappear.

group is almost totally inactive. Expiration results primarily from elastic recoil of the lungs and thoracic cage.

In addition to neural mechanisms operating entirely within the brain, reflex signals from the periphery also help control respiration. Located in the walls of the bronchi and bronchioles throughout the lungs are stretch receptors that transmit signals to the dorsal respiratory group. Thus, when the lungs become overly inflated, the stretch receptors activate a feedback response that switches off the inspiratory ramp and stops further inspiration. This reflex is called the *Hering–Breuer inflation reflex*.

The mechanism for the generation of the respiratory pattern is not known. However, a speculative, qualitative model for a neural network that can control breathing can be built using two neurons, or clumps of neurons, that inhibit each other (von Euler, 1980; Wyman, 1977), as illustrated in Fig. 14.18. (An alternate model is suggested in Exercise 9.) We suppose that there are two neurons with time-dependent outputs (their firing rates) I_1 and I_2 governed by

$$\tau_1 \frac{dI_1}{dt} + I_1 = F_1, \tag{14.80}$$

$$\tau_2 \frac{dI_2}{dt} + I_2 = F_2, \tag{14.81}$$

where F_1 and F_2 are related to the firing rates of inhibitory and excitatory inputs. For simplicity we assume that the arrangement is symmetric, so that the time constants of the neuronal output are the same, $\tau_1 = \tau_2 = \tau$. We further assume that the neurons have steady excitatory inputs, E_1 and E_2, respectively, and that they are cross-inhibited, so that the output from neuron 1 inhibits neuron 2, and
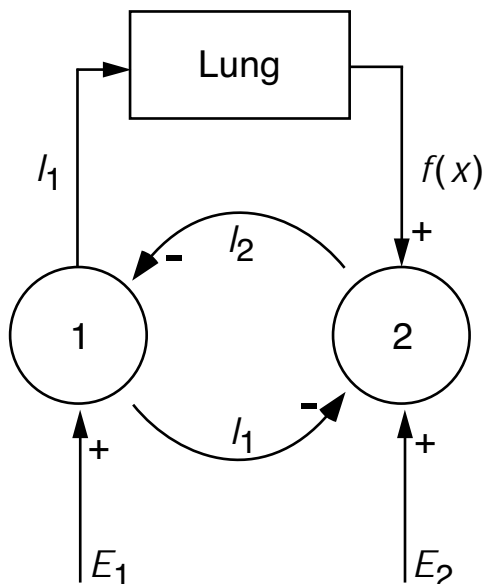
Figure 14.18: A mutual inhibition network for the control of respiration.

vice versa. Thus we take $F_1 = F(E_1 - I_2)$ and $F_2 = F(E_2 - I_1)$. The function $F(x)$ is zero for $x < 0$ (so that the input and output are never negative), and a positive, increasing function of x for $x > 0$. Thus, we have the system of differential equations

$$\tau \frac{dI_1}{dt} + I_1 \;=\; F(E_1 - I_2), \qquad (14.82)$$

$$\tau \frac{dI_2}{dt} + I_2 \;=\; F(E_2 - I_1). \qquad (14.83)$$

At this point there is no feedback from the lungs.

Equations (14.82) and 14.83) are easily studied using phase-plane analysis. There are three different possible phase portraits depending on the relative sizes of E_1 and E_2, two of which are shown in Figs. 14.19. In what follows we assume that $F' > 1$ for all positive arguments, although this restriction can be weakened somewhat. If E_2 is much larger than E_1, so that $E_1 < F(E_2)$ and $E_2 > F(E_1)$, then, as shown in Fig. 14.19A, there is a unique stable fixed point at $I_2 = F(E_1), I_1 = 0$, in which neuron 2 is firing and neuron 1 is quiescent. If E_1 is much larger than E_2, then the reverse is true, namely, there is a unique stable fixed point at $I_1 = F(E_2), I_2 = 0$, with neuron 1 firing and neuron 2 quiescent. There is an intermediate range of parameter values when E_1 and E_2 are similar in size, $E_1 < F(E_2)$ and $E_2 < F(E_1)$, shown in Fig. 14.19B, for which there are three steady states, the two on the axes, and one in the interior of the positive quadrant. The third (interior) steady state is a saddle point, and is therefore unstable.

This neural network exhibits hysteresis. Suppose we slowly modulate the parameter E_1. If it is initially small (compared to E_2, which is fixed at some positive

A

B
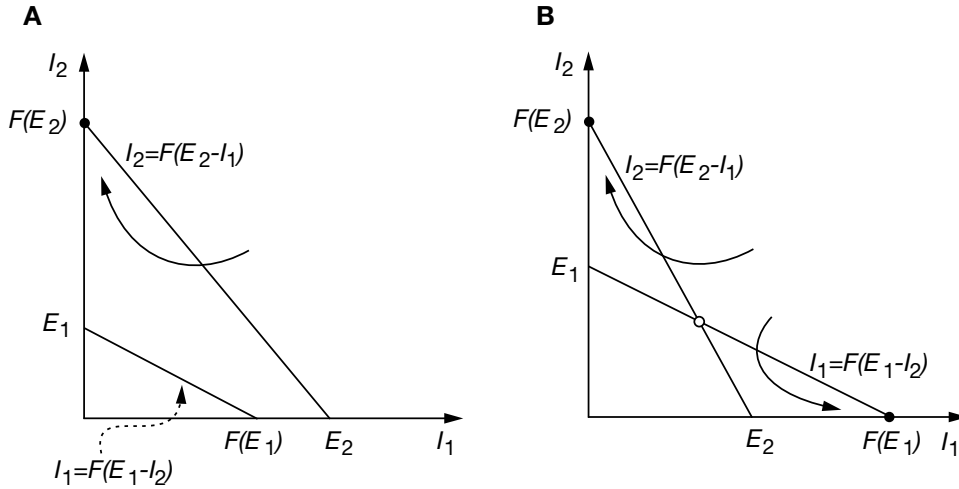
Figure 14.19: A: Phase portrait for mutual inhibition network with $E_1 < F(E_2)$ and $E_2 > F(E_1)$. B: Phase portrait for mutual inhibition network with $E_1 < F(E_2)$ and $E_2 < F(E_1)$.

level), then neuron 2 fires steadily and inhibits neuron 1. As E_1 is increased, this situation remains unchanged, even when E_1 and E_2 are of similar size, when two stable steady solutions exist. However, when E_1 becomes sufficiently large, the steady-state solution at $I_1 = F(E_2), I_2 = 0$ suddenly disappears, and the variables I_1, I_2 move to the opposite steady state at $I_2 = F(E_1), I_1 = 0$. Now if E_1 is decreased, when E_1 is small enough there is a reverse transition back to the steady state at $I_1 = F(E_2), I_2 = 0$, completing the hysteresis loop.

To use this hysteresis to control breathing, we model the diaphragm as a damped mass–spring system driven by I_1, the (firing rate) output from neuron 1, the inspiratory neuron:

$$m\frac{d^2x}{dt^2} + \mu\frac{dx}{dt} + kx = I_1. \tag{14.84}$$

We model the effect of the stretch receptors by a function $f(x)$ that is a monotone increasing function of diaphragm displacement x. The stretch receptors are assumed to excite only neuron 2, so that the output variables are governed by

$$\tau\frac{dI_1}{dt} + I_1 = F(E_1 - I_2), \tag{14.85}$$

$$\tau\frac{dI_2}{dt} + I_2 = F(E_2 - I_1 + f(x)). \tag{14.86}$$

We could allow stretch receptors to inhibit neuron 1 as well.

With this model, oscillation of the diaphragm is assured if the time constant τ is sufficiently small. The stretch receptors act to modulate the excitatory inputs, so that as the lung expands, they excite neuron 2. With $E_2 + f(x)$ sufficiently large, neuron 1, the inspiratory neuron, is switched off. With no inspiratory input, the lung relaxes, returning $f(x)$ toward zero and decreasing the excitation to
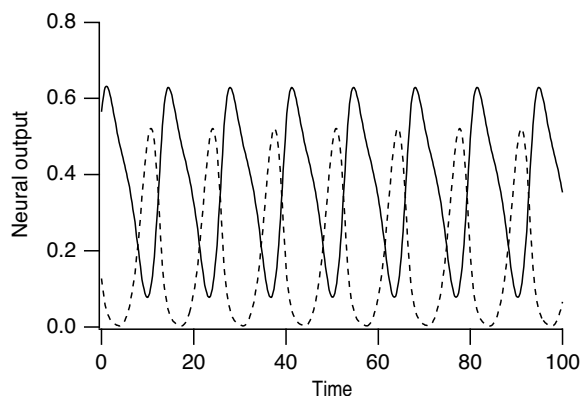
Figure 14.20: Neural output variables I_1 and I_2 (dashed) shown as functions of time.

neuron 2. This removes the inhibition to neuron 1 and allows it to fire once again. Thus, if parameters are adjusted properly, the hysteresis loop is exploited, and the inspiration–expiration cycle is established. The oscillations are robust and easily established.

This oscillation can be externally controlled. For example, by increasing E_2, the cycle can be stopped after expiration, whereas by increasing E_1 the inhibition of the stretch receptors can be overridden and inspiration lengthened (as in, take a deep breath, please). Decreasing E_1 shortens the inspiration time and can stop breathing altogether.

In Fig. 14.20 is shown a plot of the two inhibitory variables I_1 and I_2 (shown dashed) plotted as functions of time. Parameter values for this simulation were $\tau = 1.0, m = 0.5, \mu = 5.0, k = 1.0, E_1 = 0.5, E_2 = 0.3$. The function F was specified as $F(x) = \frac{2x^2}{0.2+x}$ for positive x and zero otherwise, and the stretch response curve was taken to be $f(x) = x^3/(1 + x^3)$.

Exercises

1. Give a "proper" mathematical derivation of (14.14) by introducing appropriate dimensionless parameters. What dimensionless parameter must be small for this approximation to be valid?

   Answer: $\epsilon = \frac{D_{CO_2}}{k_{-1}[H^+]}$.

2. (a) Develop a model of carbon dioxide and oxygen transport that includes the oxyhemoglobin buffering reaction and the effect of free hydrogen ions on the concentration of bicarbonate. Does the inclusion of proton exchange improve or hinder the rate at which oxygen and carbon dioxide are transported into or out of the blood?

O_2 in atm	Half-clearance time (min)
0.21	249
1.0	47
2.5	22

Table 14.3: Experimental half-clearance times for elimination of carbon monoxide from the blood (Pace et al., 1950; also see Exercise 3).

Altitude (ft)	Barometric Pressure (mm Hg)	P_{O_2} in air (mm Hg)	Alveolar P_{O_2} (in air) (mm Hg)	O_2 Saturation (in air) (%)	Alveolar P_{O_2} (in oxygen) (mm Hg)
0	760	159	104	97	673
10,000	523	110	67	90	436
20,000	349	73	40	73	262
30,000	226	47	18	24	139

Table 14.4: Alveolar gas concentration and oxygen saturation at different altitudes. The last column shows the alveolar P_{O_2} when breathing pure oxygen at atmospheric pressure. At this pressure, O_2 saturation is 100%. (Guyton and Hall, 1996, Table 43-1, p. 550.)

   (b) Estimate the overall effect of this exchange by assuming that the pH of pulmonary venous blood is about 0.04 lower than that of arterial blood.

3. Construct a simple model for the total oxygen and total carbon monoxide in the blood. Assume that the circulatory system is a well-mixed container and that oxygen is removed by metabolism, while oxygen is added and carbon monoxide eliminated during transport through the lungs. Use the models of Section 14.1.5 to determine reasonable transfer rate functions. Estimate the parameters of the model and use numerical computations to determine the half-clearance times for elimination of carbon monoxide at different oxygen levels. How well does your model fit the experimental data shown in Table 14.3?

4. Suppose the respiratory exchange rate is fixed. Show that there is a linear relationship between the alveolar carbon dioxide and oxygen partial pressures.

5. (a) Assume that regulatory mechanisms maintain the venous oxygen partial pressure at 40 mm Hg and the ventilation–perfusion ratio at 1. Find the alveolar P_{O_2} and the oxygen saturation leaving the alveolus as a function of atmospheric P_{O_2}.

   (b) Data are shown in Table 14.4 for breathing normal air or breathing pure oxygen. What assumption from part 5a is apparently wrong? From the data, determine the venous oxygen partial pressure.

6. (a) Devise a different model of oxygen concentration in which metabolism

and the ventilation-perfusion ratio are held fixed. How do the alveolar P_{O_2} and O_2 saturation vary as a function of atmospheric pressure?

(b) Using data from Table 14.4, estimate the altitude at which incoming alveolar blood has zero P_{O_2}, at normal metabolism.

(c) Determine the red blood cell count (concentration of hemoglobin) that is necessary to maintain constant venous oxygen partial pressure as a function of altitude at fixed metabolism.

7. Find the rate of carbon monoxide clearance as a function of external P_{O_2}, with fixed metabolism and ventilation.

8. (a) Determine the structure of stable steady solutions of (14.82)–(14.83) in the (E_1, E_2) parameter plane using $F(x) = \frac{2x^2}{0.2+x}$ for positive x and zero otherwise.

   (b) Numerically simulate the system of equations (14.84–14.86) using the parameters in the text. Plot the function $E_2 + f(x)$ as a function of time in the above parameter plane to see how hysteresis is exploited by this system.

9. Consider the following as a possible model for the respiratory center. Two neural FitzHugh–Nagumo oscillators have inhibitory synaptic inputs, so that

$$\frac{dv_i}{dt} = f(v_i, w_i) - s_i g_s(v_i - v_\theta), \qquad (14.87)$$

$$\tau_v \frac{dw_i}{dt} = w_\infty(v) - w_i, \qquad (14.88)$$

for $i = 1, 2$. The synaptic input s_i is some neurotransmitter that is released when the opposite neuron fires:

$$\frac{ds_i}{dt} = \alpha_s(1 - s_i)x_j F(v_j) - \beta_s s_i, \quad j \neq i, \qquad (14.89)$$

and the amplitude of the release x_j decreases gradually when the neuron is firing, via

$$\frac{dx_i}{dt} = \alpha_x(1 - x_i) - \beta_x F(v_i)x_i. \qquad (14.90)$$

(a) Simulate this neural network with $f(v, w) = 1.35v(1 - \frac{1}{3}v^2) - w$, $w_\infty(v) = \tanh(5v)$, $F(v) = \frac{1}{2}(1 + \tanh 10v)$, and with parameters $\tau_v = 5$, $v_\theta = -2$, $\alpha_s = 0.025$, $\beta_s = 0.002$, $\alpha_x = 0.001$, $\beta_x = 0.01$, $g_s = 0.19$.

(b) Give an approximate analysis of the fast and slow phase portraits for these equations to explain how the network works.

(c) How does this bursting oscillator compare with those discussed in Chapter 9?

(d) What features of this model make it a good model for the control of the respiratory system and what features are not so good?

$\bar{g}_{Na}$	=	28nS	E_{Na}	=	50mV
$\bar{g}_K$	=	11.2nS	E_K	=	−85mV
$\bar{g}_{NaP}$ =	=	2.8nS	C_m	=	21pF
$\bar{g}_L$	=	2.8nS	E_L	=	−65mV
θ_m	=	−34mV	σ_m	=	−5mV
θ_n	=	−29mV	σ_n	=	−4mV
θ_h	=	−48mV	σ_h	=	6mV
θ_p	=	−40mV	σ_p	=	−6mV
$\bar{\tau}_h$	=	10,000ms	$\bar{\tau}_n$	=	10ms

Table 14.5: Parameter values for the bursting pacemaker neuron of Exercise 10.

10. A simple physiological model for bursting pacemaker neurons has been pro-
posed by Butera et al. (1999). The model is of standard Hodgkin-Huxley type,
of the form

$$C_m \frac{dV}{dt} = -I_{NaP} - I_{Na} - I_K - I_L, \tag{14.91}$$

with ionic currents

$$
\begin{aligned}
I_{Na} &= \bar{g}_{Na} m_\infty^3(V)(1-n)(V - E_{Na}), & (14.92) \\
I_K &= \bar{g}_K n^4(V - E_K), & (14.93) \\
I_{NaP} &= \bar{g}_{NaP} p_\infty(V) h(V - E_{Na}) & (14.94) \\
I_L &= \bar{g}_L(V - E_L), & (14.95)
\end{aligned}
$$

with gating variables n and h governed by differential equations of the form

$$\tau_x(V)\frac{dx}{dt} = x_\infty(V) - x, \qquad x = n, h, \tag{14.96}$$

where

$$x_\infty(V) = \frac{1}{1 + \exp(\frac{V - \theta_x}{\sigma_x})}, \qquad \tau_x = \frac{\bar{\tau}_x}{\cosh(\frac{V - \theta_x}{2\sigma_x})}. \tag{14.97}$$

(a) Simulate this model using E_L as a control parameter (E_L in the range
-65 to -54 mV). How do the burst patterns vary as a function of E_L?

(b) How does this bursting oscillator compare with those discussed in Chap-
ter 9?

Chapter 15

Muscle

Muscle cells resemble nerve cells in their ability to conduct action potentials along their membrane surfaces. In addition, however, muscle cells have the ability to translate the electrical signal into a mechanical contraction, which enables the muscle cell to perform work. There are three types of muscle cells, namely skeletal muscle, which moves the bones of the skeleton at the joints; cardiac muscle, whose contraction enables the heart to pump blood; and smooth muscle, which is located in the walls of blood vessels and contractile visceral organs. Skeletal and cardiac muscle cells have a banded appearance under a microscope, with alternating light and dark bands, and thus they are called *striated muscle*. They have similar (though not identical) contractile mechanisms. Smooth muscle, on the other hand, is not striated, and its physiology is considerably different from the other two types of muscle.

Single skeletal muscle cells are elongated cylindrical cells with several nuclei. Each cell contains numerous cylindrical structures, called *myofibrils*, surrounded by the membranous channels of the sarcoplasmic reticulum (Fig. 15.1). Myofibrils are the functional units of skeletal muscle, containing protein filaments that make up the contractile unit. Each myofibril is segmented into numerous individual contractile units called *sarcomeres*, each about 2.5 μm long. The sarcomere, illustrated schematically in Fig. 15.2, is made up primarily of two types of parallel filaments, designated as thin and thick filaments. Viewed end on, six thin filaments are positioned around each central thick filament in a hexagonal arrangement. Viewed along its length, there are regions where thin or thick filaments are overlapping or nonoverlapping. At the end of the sarcomere is a region, called the *Z-line*, where the line filaments are anchored. Thin filaments extend from the Z-lines at each end toward the center, where they overlap with thick filaments. The regions where there is no overlap, containing only thin filaments, are called *I-bands*, and the regions containing myosin (thick) filaments (with some overlap with thin filaments) are called *A-bands*. The central region of the sarcomere, containing only thick filaments, is called the *H-zone*. During contraction, both the H-zone and the I-bands shorten as the overlap between thin and thick filaments increases.

In striated muscle, contraction is initiated by an action potential transmitted across a synapse from a neuron. This action potential spreads rapidly across the
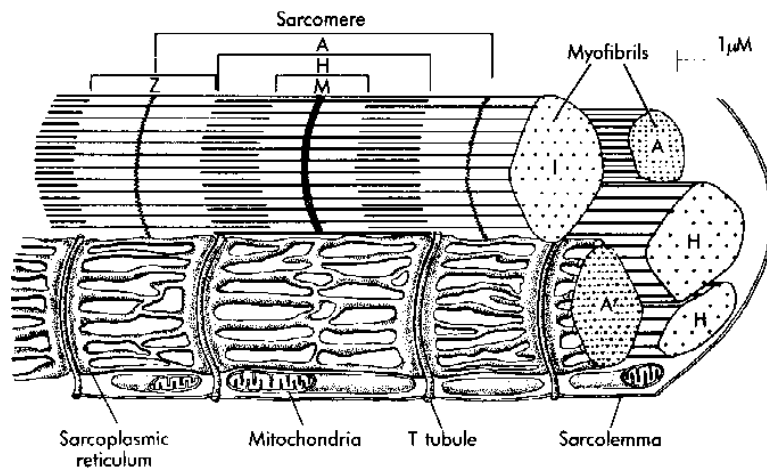
Figure 15.1: Schematic diagram of a skeletal muscle cell. (Berne and Levy, 1993, p. 283, Fig. 17-2.)
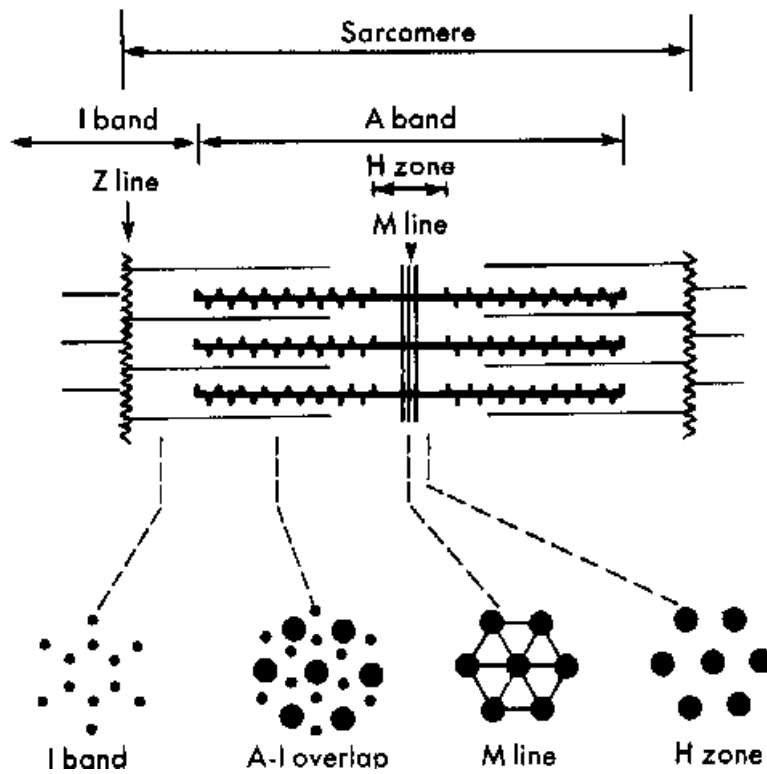
Figure 15.2: Longitudinal section (top panel) and cross-section (lower panels) of a sarcomere showing its organization into bands. (Berne and Levy, 1993, p. 283, Fig. 17-3.)
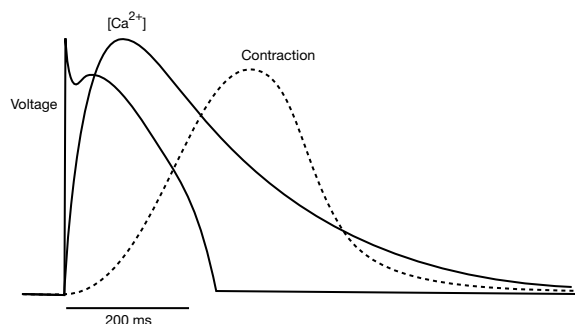
Figure 15.3: The three components of the response of a muscle. The action potential shown here is typical of those seen in cardiac ventricular myocytes (Chapter 12). Adapted from Bers (2002), Fig. 1.

muscle membrane, spreading into the interior of the cell along invaginations of the cell membrane called *T-tubules*. T-tubules form a network in the cell interior, near the junction of the A- and I-bands, and increase the surface area over which the action potential can spread. They enable the action potential to reach quickly into the cell interior. (In cardiac myocytes the T-tubules penetrate into the cell at the level of the Z-lines). In cardiac muscle, voltage-gated Ca^{2+} channels are opened by the action potential, and Ca^{2+} enters the cell, initiating the release of additional Ca^{2+} from the sarcoplasmic reticulum through ryanodine receptors, or RyR (Chapters 7 and 12). In skeletal muscle there is a direct physical connection between the T-tubule and the RyR, and the action potential opens the RyR directly. In either case, the resulting high intracellular Ca^{2+} concentration causes a change in the myofilament structure that allows the thick filaments to bind and pull on the thin filaments, resulting in muscle contraction. There are thus three major components of the response of a muscle, which follow each other in sequence; the action potential, the Ca^{2+} transient, and the contraction. This is shown in Fig. 15.3. The Ca^{2+}-mediated conversion of an electrical stimulus to a mechanical force is called *excitation-contraction coupling*.

15.1 Crossbridge Theory

Thick filaments contain the protein myosin, which is made up of a polypeptide chain with a globular head. These heads constitute the *crossbridges* that interact with the thin filaments to form bonds that act in ratchet-like fashion to pull on the thin filaments. In addition, the myosin heads have the ability to dephosphorylate ATP as an energy source.

Thin filaments contain the three proteins actin, tropomyosin, and troponin. Each actin monomer is approximately spherical, with a radius of about 5.5 nm, and they aggregate into a double-stranded helix, with a complete twist about every 14 monomers. Because the coil is double-stranded, this structure repeats every 7
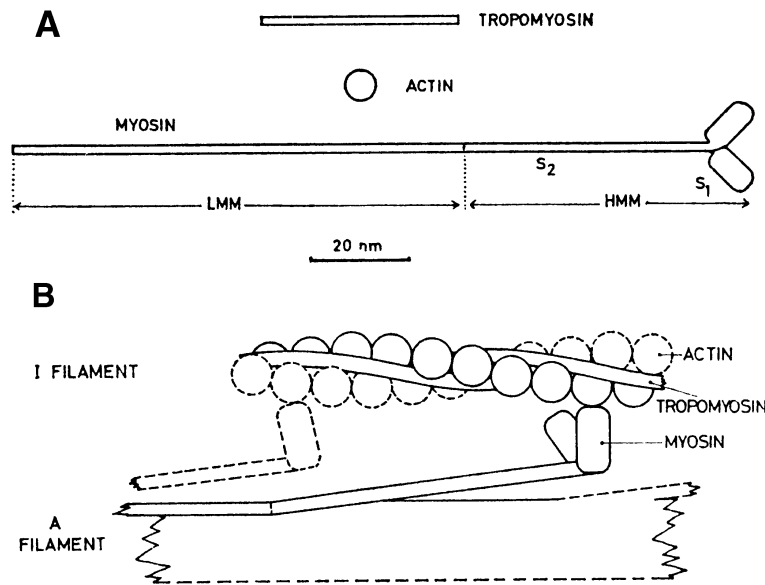
Figure 15.4: A: Scale drawing of actin, myosin, and tropomyosin proteins. B: Scale drawing of the thick and thin filaments (labeled the A and I filaments here), showing the probable way in which the actin, myosin, and tropomyosin proteins fit together. Troponin, which is bound to tropomyosin, is not included in the diagram. (White and Thorson, 1975, Fig. 9, parts A and B (i).)

monomers, or about every 38 nm. Tropomyosin, a rod-shaped protein, forms the backbone of the double-stranded coil. The troponin consists of a number of smaller polypeptides, which include a binding site for calcium as well as a portion that blocks the crossbridge binding sites on the actin helix. When calcium is bound, the confirmation of the troponin–tropomyosin complex is altered just enough to expose the crossbridge binding sites. In Fig. 15.4 we show a scale drawing of the probable way in which the actin, tropomyosin, and myosin proteins fit together.

Contraction takes place when the crossbridges bind and generate a force causing the thin filaments to slide along the thick filaments. A schematic diagram of the crossbridge reaction cycle is given in Fig. 15.5, with the accompanying physical arrangement shown in Fig. 15.6. Before binding and contraction, ATP is bound to the crossbridge heads of the myosin (M), and the concentration of calcium is low. When the calcium concentration increases, calcium ions bind to the troponin–tropomyosin complex, exposing the crossbridge binding sites on the actin filament (A). Where possible, a weak bond between actin and myosin is formed. Release of the phosphate changes the weak bond to a strong bond and changes the preferred configuration of the crossbridge from nearly perpendicular to a bent (foreshortened) position. While the crossbridge is in anything but this energetically preferred, bent state, there is an applied force that acts to pull the thin filament along the thick filament. The movement of the crossbridge to its newly preferred configuration
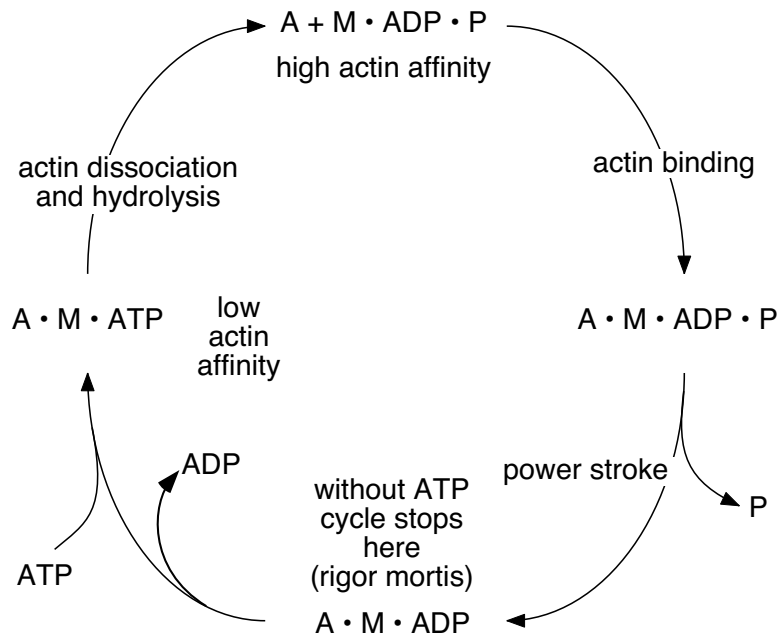
Figure 15.5: Major reaction steps in the crossbridge cycle. M denotes myosin, and A denotes actin.

is called the *power stroke*. Almost immediately upon reaching the preferred bent configuration, the crossbridge releases its ADP and binds another ATP molecule, causing dissociation from the actin binding site and return to its initial perpendicular and unbound position. ATP is then dephosphorylated, yielding ADP, phosphate, and the stored mechanical energy for the next cycle. Thus, during muscle contraction, each crossbridge cycles through sequential binding and unbinding to the actin filament.

To construct quantitative models of crossbridge binding it is necessary to know how many actin binding sites are available to a single crossbridge. One possibility is that the crossbridge must be precisely oriented to the actin binding site, and thus, in each turn of the helix, only one binding site is available to each crossbridge. In other words, from the point of view of the crossbridge, the binding sites have an effective separation of about 38 nm. Because of the physical constraints on each crossbridge, this means that at any time, there is only a single binding site available to each crossbridge. This is the assumption behind the Huxley model, described in detail below.

However, from the distribution of actin binding sites and crossbridges shown in Fig. 15.4, it is plausible that this assumption is not correct. Perhaps, depending on the flexibility of the actin filament, each crossbridge has a number of potential binding sites. In our discussion we concentrate on models for the two extreme cases: first, where each crossbridge has only a single available binding site, and second, where each crossbridge has a continuous array of available binding sites.
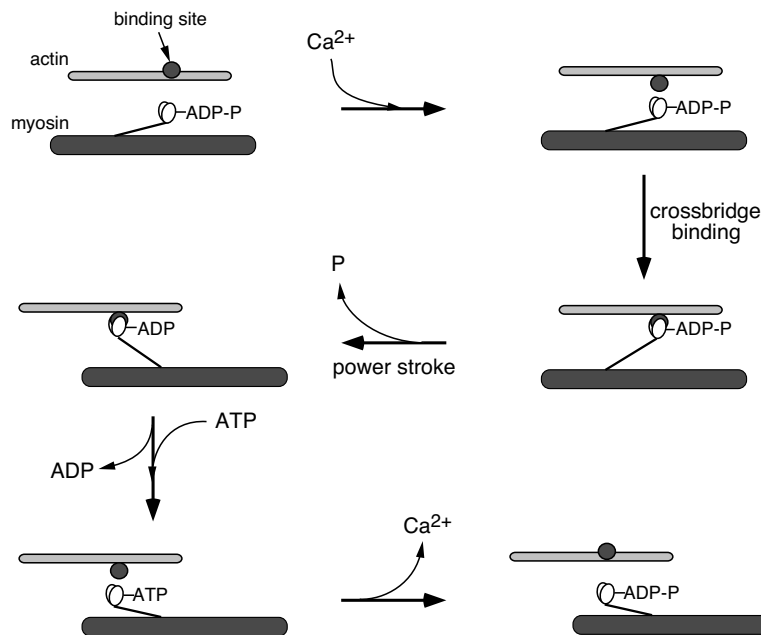
Figure 15.6: Position of crossbridge components during the major steps in the crossbridge cycle.

Intermediate models, in which the crossbridge has a small number of discrete binding sites available, are considerably more complex and are mentioned only briefly.

Because of the sarcomere structure, the tension a muscle develops depends on the muscle length. In Fig. 15.7 we show a curve of isometric tension as a function of sarcomere length. By isometric tension, we mean the tension developed by a muscle when it is held at a fixed length and repeatedly stimulated (i.e., with a high-frequency periodic stimulus). Under these conditions the muscle goes into *tetanus*, a state, caused by saturating concentrations of calcium in the sarcoplasm, in which the muscle is continually attempting to contract. Note that the muscle cannot actually contract, because it is held at constant length, although it must go through the chemistry cycle of the power stroke, since the development of tension requires that energy be consumed.

At short lengths, overlap of the thin filaments causes a drop in tension, but as this overlap decreases (as the length increases) the tension rises. However, when the length is large, there is less overlap between the thick and thin filaments, so fewer crossbridges bind, and less tension develops. When there is no overlap between the thick and thin filaments, the muscle is unable to develop any tension.

Skeletal muscle tends to operate at lengths that correspond to the peak of the isometric length–tension curve, and thus in many experimental setups the tension the muscle develops does not depend significantly on the muscle length. However, the same is not true for cardiac muscle, which considerably complicates theoretical studies of this muscle type. For these reasons we restrict our attention to models
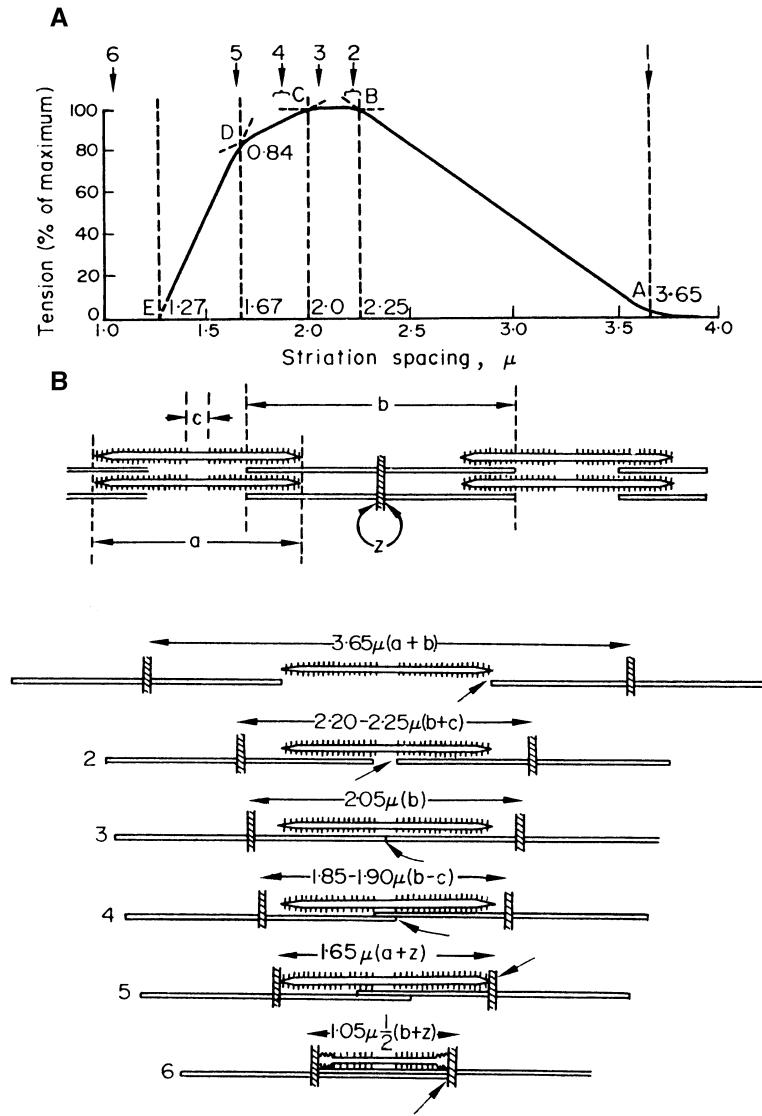
Figure 15.7: A: Isometric tension as a function of the length of the sarcomere. B: schematic diagrams of the arrangement of the thick and thin filaments for the six different places indicated in panel A. (Gordon et al., 1966, reproduced in White and Thorson, 1975, Fig. 14.)

based on data from skeletal muscle. Peskin (1975) presents a detailed description of some theoretical models of cardiac muscle.

15.2   The Force–Velocity Relationship: The Hill Model

One of the earliest models for a muscle is due to A.V. Hill (1938) and was constructed before the details of the sarcomere anatomy were known. Hill observed that when a muscle contracts against a constant load (an *isotonic* contraction), the relationship between the constant rate of shortening v and the load p is well described by the *force–velocity* equation

$$(p + a)v = b(p_0 - p), \tag{15.1}$$

where a and b are constants that are determined by fitting to experimental data in a way that we discuss presently. A typical force–velocity curve is plotted in Fig. 15.8. When $v = 0$, then $p = p_0$, and thus p_0 represents the force generated by the muscle when the length is held fixed; i.e., p_0 is the *isometric* force. As discussed above, the tension generated by a skeletal muscle in isometric tetanus is approximately independent of length, and thus p_0 is also approximately independent of length. When $p = 0$, $v = b p_0 / a$, which is the maximum speed at which a muscle is able to shorten.

In an attempt to explain these observations, we model a muscle fiber as a contractile element with the given force–velocity relationship, in series with an elastic element (Fig. 15.9). In some versions of the model a parallel elastic element is included (see Exercise 1), but as it plays no essential role in the following discussion, it is omitted here. As shown in Fig. 15.9, we let l denote the length of the contractile element, we let x denote the length of the elastic element, so that $L = l + x$ is the total length of the fiber. Then, letting v denote the velocity of contraction of the contractile element, we have

$$v = -\frac{dl}{dt}, \tag{15.2}$$

where, by assumption, v is related to the load on the muscle by the force–velocity equation (15.1). To derive a differential equation for the time dependence of p, we note that because the elastic element is in series with the contractile element, the two experience the same force. We assume that the force generated by the elastic element is a function of its length $p = P(x)$ and then use the chain rule and the force–velocity equation to obtain

$$
\begin{aligned}
\frac{dp}{dt} &= \frac{dP}{dx}\frac{dx}{dt} \\[2mm]
&= \frac{dP}{dx}\left[\frac{dL}{dt} - \frac{dl}{dt}\right] \\[2mm]
&= \frac{dP}{dx}\left[\frac{dL}{dt} + v\right]
\end{aligned}
$$
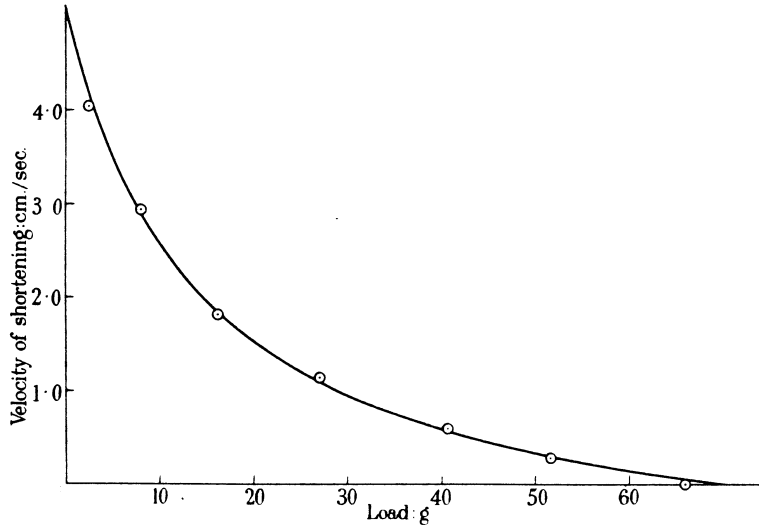
Figure 15.8: The relationship between the load on a muscle and the velocity of contraction (Hill, 1938; Fig. 12). The symbols are the data points, while the smooth curve is calculated from (15.1) using the parameter values $a = 14.35$ grams, $a/p_0 = 0.22$, $b = 1.03$ cm/s. The value of a is equivalent (in Hill's original preparation) to 357 grams (of weight) per square centimeter of muscle fiber (g-wt/cm^2). Note that if p is expressed in grams weight, so also must a be. Since Hill used a muscle of length 38 mm, the value of b is equivalent in Hill's preparation to 0.27 muscle lengths per second, .
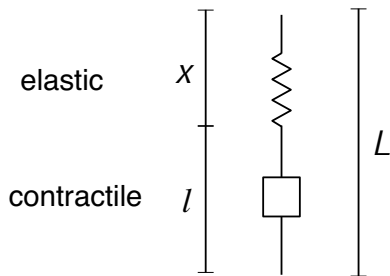
Figure 15.9: Schematic diagram of Hill's two-element model for skeletal muscle. The muscle is assumed to consist of an elastic element in series with a contractile element with a given force–velocity relationship.

$$= \frac{dP}{dx}\left[\frac{dL}{dt} + \frac{b(p_0 - p)}{p + a}\right]. \tag{15.3}$$

It remains to determine dP/dx.

Hill made the simplest possible assumption, that the elastic element is linear, and thus

$$P = \alpha(x - x_0), \tag{15.4}$$

where x_0 is its resting length. Thus, $dP/dx = \alpha$, and the differential equation for p is

$$\frac{dp}{dt} = \alpha\left[\frac{dL}{dt} + \frac{b(p_0 - p)}{p + a}\right]. \tag{15.5}$$

15.2.1   Fitting Data

Suppose a muscle in tetanus is held at a fixed tension until it reaches its isometric length, and then the tension is suddenly decreased and held fixed at a lower value. A typical result is shown in Fig. 15.10A, where the muscle length is plotted against time. As soon as the tension is reduced, the muscle length decreases (plotted in the vertical direction) as the elastic element contracts. After a transition period during which the length exhibits small oscillations (which are not explained by this model), the muscle decreases in length at a constant rate. Plotting the rate of decrease against the constant applied tension gives one point on the force–velocity curve. More specifically, if the tension is stepped from p_0 to p_1, the muscle contracts at the constant rate v, where

$$(p_1 + a)v = b(p_0 - p_1). \tag{15.6}$$

Repeating the experiment for tension steps of different magnitudes (shown in Fig. 15.10B) one finds a series of points on the force–velocity curve, through which one can fit the force–velocity equation to obtain values for a, b, and p_0. Note that this procedure is valid only if p_0 does not change during the course of the experiment. In other words, as the muscle shortens with constant velocity, it must be that p_0 remains unchanged. As discussed above, this is an acceptable assumption for skeletal muscle operating near the peak of the length–tension curve.

Similarly, the characteristics of the elastic element can be determined from the initial step in length. By extrapolating the line of constant speed back to the time of the tension step (the line xyz in Fig. 15.10A), one finds the distance $0z$ which is the change in length of the elastic element. This relies on the assumption that the force–velocity properties of the muscle change instantaneously with the change in tension. Knowing the change in length of the elastic element and the change in tension that produced it allows one to determine α.

15.2.2   Some Solutions of the Hill Model

Isometric tetanus solution

If a muscle at rest is put into tetanus by repeated stimulation, the isometric tension builds up over a period of time. Because the tension is measured isometrically, the
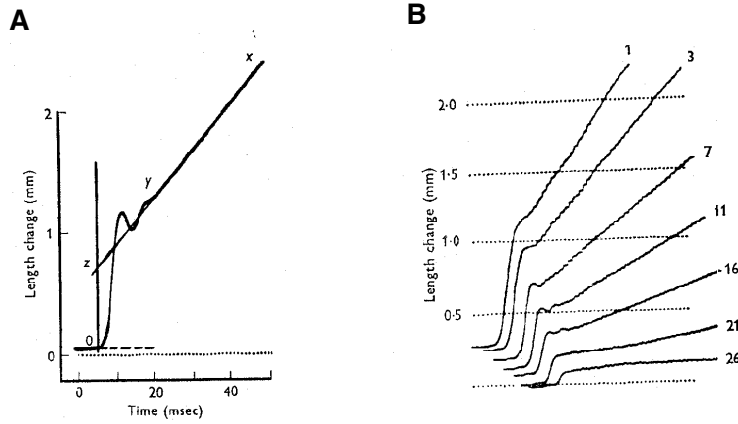
Figure 15.10: A: Plot of length change against time after a step decrease in tension. The length decreases in a sudden jump, and then, after an initial oscillatory phase, decreases at constant velocity. (Jewell and Wilkie, 1958; reproduced in White and Thorson, 1975, Fig. 5.) B: Length change as a function of time from a series of tension step experiments. The baseline of each trace has been shifted for clarity, and each dot on the horizontal axis denotes 1 ms. For each step, the value to the right of the curve denotes the final value of the tension in grams of weight (g-wt). (Jewell and Wilkie, 1958; reproduced in White and Thorson, 1975, Fig. 6.)

length of the muscle does not change, and thus $dL/dt = 0$. Hence, the differential equation for the tension is

$$\frac{dp}{dt} = \alpha \left[\frac{b(p_0 - p)}{p + a} \right].$$ (15.7)

Since this is a first order differential equations, its qualitative behavior is readily understood. The right hand side of the equation has a unique zero at $p = p_0$, and this zero is stable. Thus, all solutions of this equation must approach p_0 as $t \to \infty$.

The solution of this equation can be found explicitly, since this is a separable equation. After separation, we integrate from 0 to t and use the initial condition $p(0) = 0$ to obtain

$$-p - (p_0 + a) \log \left(\frac{p_0 - p}{p_0} \right) = \alpha b t,$$ (15.8)

which describes the time course of the change in tension implicitly. Notice that $p \to p_0$ as $t \to \infty$, as expected.

Release at constant velocity

Suppose a muscle, held originally at its isometric tension p_0, is allowed to contract with constant velocity u. It seems reasonable that the muscle tension should decrease until it reaches the value p_u determined from the force–velocity curve for a
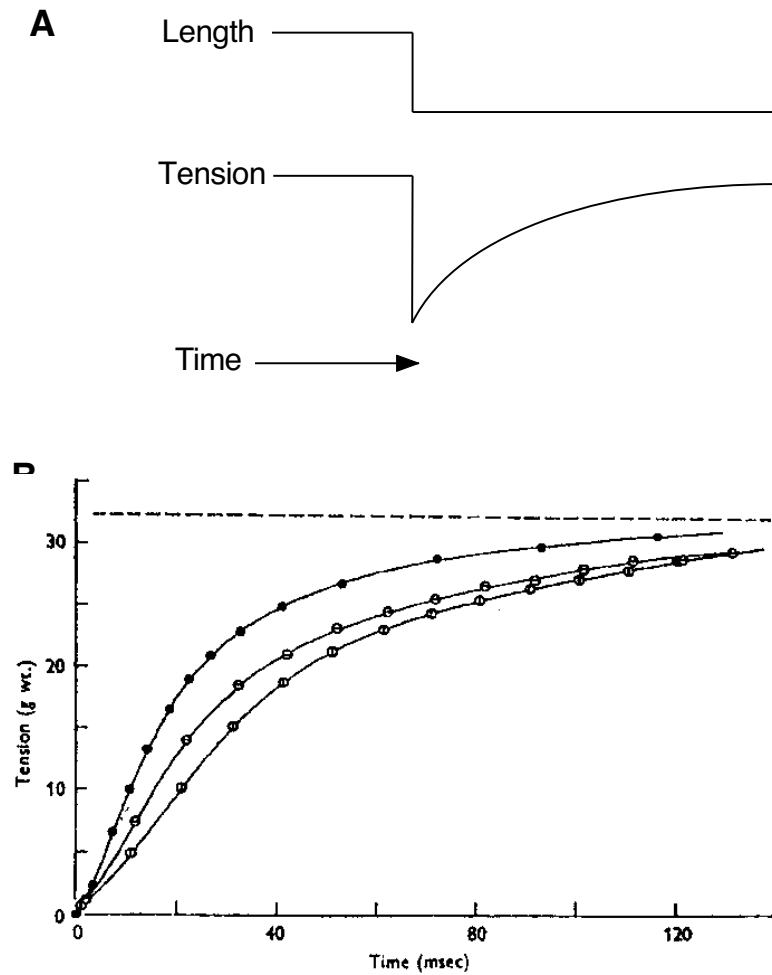
Figure 15.11: A: Schematic diagram of the response to a step decrease in length. B: Comparison of the Hill model to the data of Jewell and Wilkie (1958). The closed circles are computed from the Hill model, while the open circles are data points from two slightly different experimental procedures. (Jewel and Wilkie, 1958; reproduced in White and Thorson, 1975, Fig. 7.)

velocity u. The differential equation for p is

$$\frac{dp}{dt} = \alpha \left[-u + \frac{b(p_0 - p)}{p + a} \right], \tag{15.9}$$

with initial condition $p(0) = p_0$. As before, we assume that p_0 does not change during the course of the contraction.

Again, this is a first order differential equation whose right hand side has a unique, stable, root at $p = p_u$, where p_u is defined by $(p_u + a)u = b(p_0 - p_u)$. The solution is found by separation to be

$$p_0 - p + (p_u + a) \log \left(\frac{p_0 - p_u}{p - p_u} \right) = \alpha t(b + u). \tag{15.10}$$

Notice that $p \to p_u$ as $t \to \infty$, as it must.

Response to a jump in length

Possibly the most interesting solution is the response to a step decrease in length, as this solution has been used to show that the Hill model does not provide an accurate description of all aspects of muscle behavior (Jewell and Wilkie, 1958).

First, Jewell and Wilkie determined the parameters of the Hill model by the series of experiments described above (Fig. 15.10). They then used the Hill model to predict the response of the muscle to a step decrease in muscle length. Suppose that a muscle, originally held at its isometric tension p_0, is suddenly decreased in length. One expects the muscle tension to suddenly decrease, but then slowly increase back to p_0. This is because the isometric tension is independent of length but should take some time to develop at the new length. A typical solution is sketched schematically in Fig. 15.11A.

More precisely, suppose that the length of the muscle as a function of time is given by

$$L(t) = L_1 + L_0 - L_0 H(t), \tag{15.11}$$

where $H(t)$ is the usual Heaviside function, and where L_1 and L_0 are constants, L_0 being the magnitude of the length step. Thus

$$\frac{dL}{dt} = -L_0 \delta(t), \tag{15.12}$$

where $\delta(t)$ denotes the Dirac delta function. Substituting this expression into the differential equation for p gives

$$\frac{dp}{dt} = \alpha \left[-L_0 \delta(t) + \frac{b(p_0 - p)}{p + a} \right], \tag{15.13}$$

$$p(0^-) = p_0. \tag{15.14}$$

Integrating (15.13) (formally) from $t = -\epsilon$ to $t = \epsilon$ and then letting $\epsilon \to 0$, we get

$$p(0^+) - p(0^-) = -\alpha L_0, \tag{15.15}$$

so that the delta function causes a jump of $-\alpha L_0$ in p at the origin. Thus, (15.13) and (15.14) can be rewritten as the initial value problem

$$\frac{dp}{dt} = \alpha \left[\frac{b(p_0 - p)}{p + a} \right], \qquad t > 0, \tag{15.16}$$

$$p(0) = p_0 - \alpha L_0. \tag{15.17}$$

Since we have reduced the problem to the isometric tetanus problem studied earlier (although with a different initial condition), the solution is easily calculated.

The solution calculated from the Hill model in this way does not agree with experimental observations on the tension recovery following a step decrease in length. In fact, the tension recovers less quickly than is predicted by the model, as illustrated in Fig. 15.11B. Here, the model computations (shown as closed circles), consistently lie above the data points (shown as open circles). These observations, made possible by the improvements in experimental technique in the 20 years after Hill's model was first proposed, forced the conclusion that the Hill model has serious defects. In particular, the assumption that the force–velocity relationship (15.1) is satisfied immediately after a change in tension is a probable major source of error. At the same time that Hill's model was shown to have problems, much more was being discovered about the structure of the sarcomere. This motivated the construction of a completely different type of model, based on the kinetics of the crossbridges rather than on heuristic elastic and contractile elements. The first model of this new type was due to Huxley (1957), and is the basis for the majority of subsequent models of muscle behavior.

15.3   A Simple Crossbridge Model: The Huxley Model

To formulate a mathematical model describing crossbridge interactions in a sarcomere, we suppose that a crossbridge can bind to an actin binding site at position x, where x measures the distance along the thin filament to a binding site from the crossbridge, and $x = 0$ corresponds to the position in which the bound crossbridge exerts no force during the power stroke on the thin filament (Fig. 15.12). Crossbridges can be bound to a binding site with $x > 0$, in which case they exert a contractile force, or they can be bound to a site with $x < 0$, in which case they exert a force that opposes contraction. A crossbridge bound to a binding site at x is said to have displacement x. In his original model Huxley assumed that the actin binding sites were sufficiently far apart that each crossbridge could be bound with one and only one binding site. With this assumption, each crossbridge, whether bound or not, can be associated with a unique value of x.

Let ρ denote the number of crossbridges (either bound or unbound) with displacement x. We assume that binding is restricted to occur in some bounded interval, $-x_0 < x < x_0$, and that ρ is a constant independent of x on that interval. In other words, for each displacement x, the number of crossbridges with that displacement is conserved, and we exclude the possibility that all the crossbridges could end up, say, with the same displacement. This assumption was originally designed for
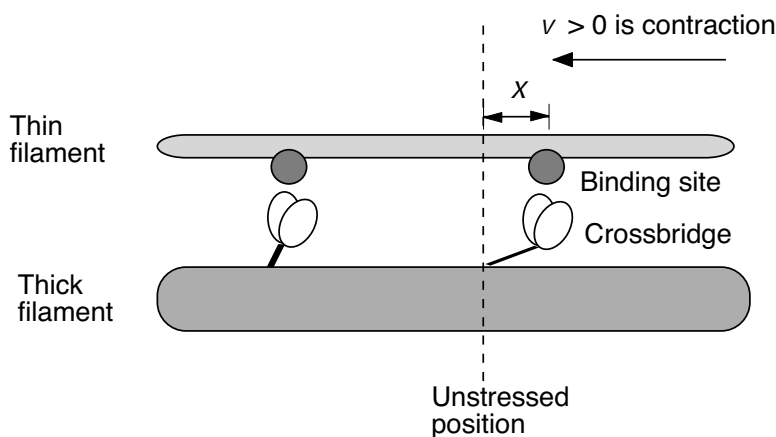
Figure 15.12: Schematic diagram of the Huxley crossbridge model.

the isometric case, in which the muscle has a fixed length, and is not necessarily valid under conditions where the muscle is quickly extended by an external force. For example, in response to a very fast imposed load of sufficient magnitude, each crossbridge could be quickly extended to have a large value of $x > x_0$, thus violating this conservation law, at least in the short time. However, we ignore this complication for now (but see Section 15.8.1).

Finally, we define $n(x, t)$ to be the fraction of crossbridges with displacement x that are bound.

Next, we drastically simplify the reaction mechanism, and assume that a crossbridge can be in one of two states, namely either unbound (U), or strongly bound (B) and thereby generating a force. We suppose further that the binding and unbinding of crossbridges is described by the simple reaction scheme

$$\text{U} \underset{g(x)}{\overset{f(x)}{\rightleftharpoons}} \text{B},$$
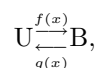
where the rate constants are functions of the displacement x.

The conservation law for the fraction of bound crossbridges can be derived as follows. Consider all the crossbridges that are bound with displacements x between a and b. This total number is given by

$$\rho \int_a^b n(x, t) \, dx. \tag{15.18}$$

The rate of change of this total number is given by the reactions of the crossbridges as well as the fluxes across the boundaries of the interval $[a, b]$. At $x = a$, the flux of crossbridges out of the domain is $\rho v(t) n(a, t)$, while at $x = b$, the flux of crossbridges into the domain is $\rho v(t) n(b, t)$. Here $v(t)$ is the velocity of the actin filament relative to the myosin filament. For notational consistency, we assume that

$v > 0$ denotes muscle contraction. Thus, conservation of crossbridges gives

$$\rho\frac{d}{dt}\int_a^b n(x,t)\,dx = \rho v(t)n(b,t) - \rho v(t)n(a,t) - \rho\int_a^b [f(x)(1-n(x,t)) - g(x)n(x,t)]\,dx, \tag{15.19}$$

and so

$$\int_a^b \frac{\partial}{\partial t}n(x,t)\,dx = v(t)\int_a^b \frac{\partial}{\partial x}n(x,t)dx - \int_a^b [f(x)(1-n(x,t)) - g(x)n(x,t)]\,dx. \tag{15.20}$$

Of course, since a and b are arbitrary, the integral can be dropped, yielding the partial differential equation

$$\frac{\partial n}{\partial t} - v(t)\frac{\partial n}{\partial x} = (1-n)f(x) - ng(x). \tag{15.21}$$

This conservation law and its derivation occur many times in applications, including a number of other places in this book (see for example (2.1), (11.151) (14.3) or (17.31)).

Every time a crossbridge is bound, one ATP molecule is dephosphorylated, so the rate of energy release, ϕ, for this process is given by

$$\phi = \rho\epsilon\int_{-\infty}^{\infty} (1-n(x,t))f(x)dx, \tag{15.22}$$

where ϵ is the chemical energy released by one crossbridge cycle. Since n is, in general, a function of the contraction velocity, so also is ϕ. We also suppose that a bound crossbridge is like a spring, generating a restoring force $r(x)$ related to its displacement. Hence, the total force exerted by the muscle is

$$p = \rho\int_{-\infty}^{\infty} r(x)n(x,t)\,dx. \tag{15.23}$$

To find the force–velocity relationship for muscle, we assume that the fiber moves with constant velocity, and that $n(x,t)$ is equilibrated so that $\partial n/\partial t = 0$. Then, the steady distribution $n(x)$ is the solution of the first-order differential equation

$$-v\frac{dn}{dx} = (1-n)f(x) - ng(x). \tag{15.24}$$

The solution of this differential equation is easily understood. The function $n(x)$ "tracks" the quasi-steady-state solution $\frac{f(x)}{f(x)+g(x)}$ at a rate that is inversely proportional to v. Thus, if v is small, $n(x)$ is well approximated by the quasi-steady-state solution, whereas if v is large, $n(x)$ changes slowly as a function of x. From this we make two observations. First, the force is largest at small velocities. In fact, at zero velocity, the isometric force is

$$p_0 = \rho\int_{-\infty}^{\infty} r(x)\frac{f(x)}{f(x)+g(x)}dx. \tag{15.25}$$
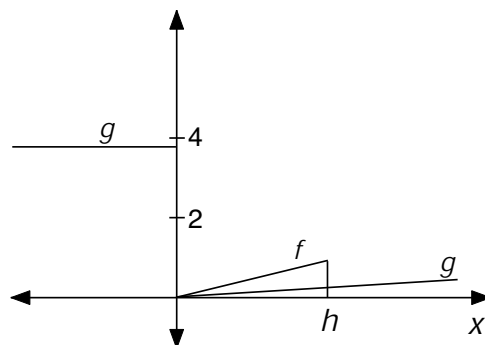
Figure 15.13: The attachment and detachment functions, f and g, in the Huxley model.

Second, at large velocities, the distribution $n(x)$ has small amplitude, and so the force is small. The force decreases because the amount of time during which a crossbridge is close to a binding site is small, and so binding is less likely, with the result that a smaller fraction of crossbridges exerts a contractile force. Another factor is that at higher velocities a greater number of crossbridges are carried into the $x < 0$ region before they can dissociate, hence generating a force opposing contraction. It is intuitively reasonable that at some maximum velocity, the force generated by the crossbridges with $x < 0$ exactly balances the force generated by those with $x > 0$, at which point no tension is generated by the muscle, and the maximum velocity of shortening is attained. We have already seen that this occurs in the Hill force–velocity curve. Crossbridge theory provides an elegant explanation of this phenomenon.

   To obtain quantitative formulas, one must make some reasonable guesses for the functions $f(x)$ and $g(x)$, and then calculate $n(x)$ and p numerically or analytically. Although numerical solutions can always be obtained, there are several choices of $f(x)$ and $g(x)$ for which analytical solutions are possible. The functions that Huxley chose are illustrated in Fig. 15.13 and have the form

$$f(x) \;=\; \begin{cases} 0, & x < 0, \\ f_1 x/h, & 0 \le x \le h, \\ 0, & x > h, \end{cases} \tag{15.26}$$

$$g(x) \;=\; \begin{cases} g_2, & x \le 0, \\ g_1 x/h, & x > 0. \end{cases} \tag{15.27}$$

In this model, the rate of crossbridge dissociation, g, is low when the crossbridge exerts a contractile force, but when x is negative, the crossbridge opposes contraction, and g increases. Similarly, crossbridges do not attach at a negative x ($f = 0$ when $x < 0$), and as x increases, the rate of crossbridge attachment increases as well. This ensures that crossbridge attachment contributes an overall contractile force. At some value h, the rate of crossbridge attachment falls to zero, as it is assumed that crossbridges cannot bind to a binding site that is too far away.
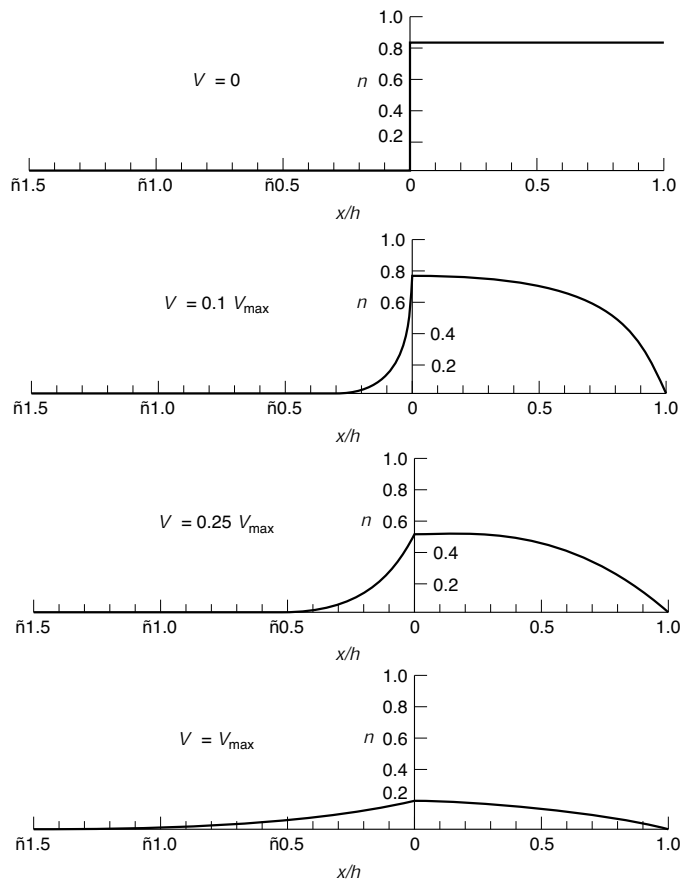
Figure 15.14: Steady-state distributions of n in the Huxley model, for different values of v, plotted as a function of dimensionless space $\frac{x}{h}$. (Huxley, 1957, Fig. 7.) The parameter values for this figure and the next were chosen by Huxley by trial and error to obtain a good fit with experimental data. The values are $F_1 = f_1/(g_1 + f_1) = 13/16$, $G_2 = g_2/(f_1 + g_1) = 3.919$.
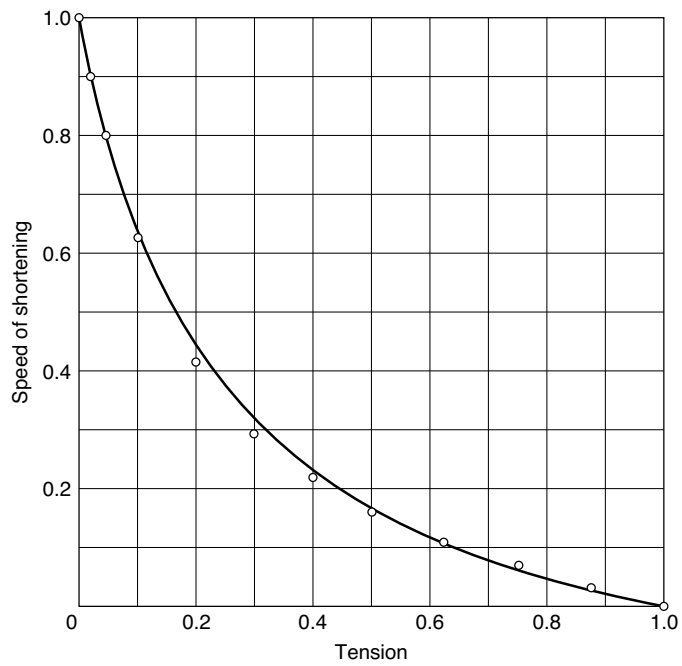
Figure 15.15: The force–velocity curve of the Huxley model (solid curve) compared to Hill's data (open circles). (Huxley, 1957, Fig. 8.) Here, p has been scaled so that $p(0) = 1$. This determines the value used for ρk. Further, the parameters have been scaled so that $v_{\max} = 1$.

The steady-state solution for $n(x)$ is easily obtained by direct piecewise solutions of the differential equation. Let n_I, n_{II} and n_{III} denote, respectively, the steady-state solutions in the regions $x \leq 0$, $0 < x \leq h$ and $h < x$. Then n_I is the solution of the equation

$$-v\frac{dn_I}{dx} = -g_2 n, \tag{15.28}$$

and thus

$$n_I = A e^{g_2 x/v}, \tag{15.29}$$

for some constant A yet to be determined. Note that this solution is bounded as $x \to -\infty$ as it should be.

Next we solve for n_{II}, which satisfies the equation

$$-v\frac{dn_{II}}{dx} + n_{II}\left(\frac{f_1 x}{h} + \frac{g_1 x}{h}\right) = \frac{f_1 x}{h}, \tag{15.30}$$

which has solution

$$n_{II} = \frac{f_1}{f_1 + g_1} + B \exp\left(\frac{x^2(f_1 + g_1)}{2vh}\right), \tag{15.31}$$

for some constant B, also to be determined.

The only bounded solution of the equation for n_{III},

$$-v\frac{dn_{III}}{dt} = g_1 \frac{x}{h} n_{III}, \tag{15.32}$$

is identically zero. This makes physical sense as well, since crossbridges can never be attached for $x > h$, if $v > 0$. Now, to find the unknown constants A and B we require that the solution be continuous at $x = 0$ and $x = h$, and thus

$$n_I(0) = n_{II}(0), \qquad n_{II}(h) = 0. \tag{15.33}$$

It follows easily that

$$B = -\frac{f_1}{f_1 + g_1} e^{-\phi/v}, \tag{15.34}$$

$$A = \frac{f_1}{f_1 + g_1} + B = \frac{f_1}{f_1 + g_1}(1 - e^{-\phi/v}), \tag{15.35}$$

and thus

$$n(x) = \begin{cases} F_1\left[1 - e^{-\phi/v}\right] e^{\frac{x}{2h} G_2 \frac{\phi}{v}}, & x < 0, \\ F_1\left\{1 - \exp\left[\left(\frac{x^2}{h^2} - 1\right)\frac{\phi}{v}\right]\right\}, & 0 < x < h, \\ 0, & x > h, \end{cases} \tag{15.36}$$

where $\phi = (f_1 + g_1)h/2$ has units of velocity, and $F_1 = \frac{f_1}{f_1 + g_1}$, and $G_2 = \frac{g_2}{f_1 + g_1}$ are dimensionless. This steady solution is plotted in Fig. 15.14 for four values of v. Notice the unphysiological implication of this solution, that $n > 0$ for all $x < 0$.

However, only a negligible number of crossbridges are bound at unphysiological displacements, so that these have little effect on the behavior of the model.

Assuming that the crossbridge acts like a linear spring, so that $r(x) = kx$ for some constant k, the force generated by the muscle (defined by (15.23)) can be calculated as a function of the velocity of contraction, and the result compared to the Hill force–velocity equation (15.1). The force–velocity equation calculated from the Huxley model is

$$ p = \frac{\rho k f_1}{f_1 + g_1} \frac{h^2}{2} \left\{ 1 - \frac{v}{\phi}(1 - e^{-\phi/v}) \left(1 + \frac{1}{2G_2^2} \frac{v}{\phi} \right) \right\}, \tag{15.37} $$

which for appropriate choice of parameters gives an excellent fit to the force–velocity curve, as illustrated in Fig. 15.15.

Huxley chose the model parameters by a process of trial and error so that the rate of energy production agreed with experimental data. A good fit is obtained by choosing $F_1 = \frac{f_1}{f_1+g_1} = 13/16$ and $G_2 = \frac{g_2}{f_1+g_1} = 3.919$. One can show that for these parameter values, $4\phi \approx v_{\max}$ (Exercise 5). Since in the Hill model $v_{\max} = bp_0/a$, it follows that $\phi \approx \frac{bp_0}{4a}$. The parameter values that Hill obtained by fitting to data have $p_0/a \approx 4$. Hence, it follows that $\phi \approx b$. This is an elegant way of relating parameter values in the Huxley model to the parameters of the Hill model .

It is useful to see what f_1, g_1 and g_2 are in dimensional units. Brokaw (1976) used $f_1 = 65$ s^{-1}, $g_1 = 15$ s^{-1}, $g_2 = 313.5$ s^{-1} and $h = 10$ nm, to give $f_1 + g_1 = 80$ s^{-1} which gives $\phi = 400$ nm s^{-1} and thus a maximum shortening velocity of 1600 nm s^{-1} per half sarcomere, and a maximum shortening velocity of 3200 nm s^{-1} per sarcomere. Assuming that a sarcomere is 2.5 μm long, each centimeter of muscle contains 4000 sarcomeres. If each sarcomere shortens at 800 nm s^{-1}, a 1 cm length of muscle shortens at 3200×4000 nm/s, which is 1.28 cm/s. From the caption of Fig. 15.8 we see that Hill used a piece of muscle 38 mm long, which corresponds to a maximum shortening velocity of 4.8 cm/s, in good agreement with the measured value shown in Fig. 15.8.

15.3.1   Isotonic Responses

Thus far we have shown how the Huxley model can explain the Hill force–velocity curve using crossbridge dynamics. However, for the model to give an acceptable explanation of muscle dynamics, there is a great deal of additional experimental data with which it should agree. In particular, the model should explain the response of a muscle, first, to a step change in tension (isotonic response) and second, to a step change in length (isometric response). After all, the Hill model was rejected as a satisfactory explanation because of its inability to explain all such data.

It is instructive to consider how one calculates the response of the Huxley model to a step change in tension, as the procedure is not obvious. Suppose a muscle exerts its isometric tension, p_0, at some length L. Then, the steady-state crossbridge distribution is

$$ n_s(x) = \frac{f(x)}{f(x) + g(x)}. \tag{15.38} $$

Now suppose the tension on the muscle is reduced to $p_1 < p_0$ so suddenly that no crossbridges are able to associate or dissociate during the reduction. In a typical

experiment of Civan and Podolsky (1966), a muscle fiber of length 15,000 μm was subjected to a change in tension that changed the fiber length by less than 50 μm, a relative length change of 1/300. Hence, a typical sarcomere of length 2.5 μm changed in length by less than 10 nm, and so the length of each crossbridge was changed by less than 10 nm. A crossbridge is able to absorb such length changes without dissociating from the binding site.

Suppose the extension of each crossbridge decreases by an unknown amount ΔL, and so the crossbridge distribution suddenly changes to $n_s(x + \Delta L)$ and is no longer at steady state. The change in length is found by constraining the new tension to be p_1, and hence ΔL satisfies

$$p_1 = \int_{-\infty}^{\infty} k(x) n_s(x + \Delta L) \, dx. \tag{15.39}$$

Although (15.39) cannot in general be solved analytically, ΔL can be determined numerically, since it is easy to determine p_1 as a function of ΔL.

Following the sudden change in tension, the crossbridge population is not at steady state, so it must change according to the differential equation (15.21) with initial condition $n(x,0) = n_s(x + \Delta L)$ and subject to the constraint that the tension is constant at $p = p_1$. However, during this evolution, v is not constant, as there is some transient behavior before the muscle reaches its steady contraction velocity (cf. Fig. 15.10). However, we can determine an expression for $v(t)$ in terms of $n(x,t)$ that guarantees that the tension remains constant at p_1.

Since p_1 is constant, it must be that $\frac{\partial p_1}{\partial t} = 0$, or

$$0 = \int_{-\infty}^{\infty} k(x) n_t(x,t) dx = \int_{-\infty}^{\infty} k(x) \left(v(t) \frac{\partial n}{\partial x} + (1-n)f(x) - ng(x) \right) dx. \tag{15.40}$$

We solve this for $v(t)$ to get

$$-v(t) = \frac{\int_{-\infty}^{\infty} k(x) \left((1-n)f(x) - ng(x) \right) dx}{\int_{-\infty}^{\infty} k(x) \frac{\partial n}{\partial x} dx}. \tag{15.41}$$

Thus, for the tension to remain constant, the partial differential equation (15.21) must have the contraction velocity specified by (15.41).

Using a slightly different approach, Podolsky et al. (1969; Civan and Podolsky, 1966) showed that the Huxley model does not agree with experimental data in its response to a step change in tension. We saw in Fig. 15.10 that immediately after the tension reduction the muscle length changes also, and after an initial oscillatory period, the muscle contracts with a constant velocity. However, the Huxley model does not show any oscillatory behavior, the approach to constant velocity being monotonic.

Motivated by this discrepancy, Podolsky and Nolan (1972, 1973) and Podolsky et al. (1969) altered the form of the functions f and g to obtain the required oscillatory responses in the Huxley model. Of course, in Huxley's original model no physiological justification was given for the functions f and g, and modification of these functions is therefore an obvious place to start fiddling with the model to

fit the data. Julian (1969) also showed that the Huxley model can be adjusted to give the correct responses to a step change in length. The details of these analyses do not concern us greatly; the main point is that Huxley's crossbridge model has enough flexibility to explain a wide array of experimental data.

15.3.2 Other Choices for Rate Functions

The simple choices for rate functions made by Huxley yield interesting analytical results. However, there are numerous other ways that the rate functions might be chosen. Suppose, for simplicity, that the rate functions $f(x)$ and $g(x)$ have nonoverlapping compact support. Where it is nonzero, we take $f(x)$ to be a constant, $f(x) = \alpha/\epsilon$, on a small interval near the maximum displacement h, say $h - \epsilon \leq x \leq h$, so that actin and myosin bind rapidly in a small interval near h. We expect that α depends on the local calcium concentration. On the support of $f(x)$, $n(x) = 1 - \exp[\alpha(x - h)/(\epsilon v)]$.

The role of $g(x)$ is to break crossbridge bonds. A simple way to accomplish this is to assume that all bonds break at exactly $x = \delta < 0$, in which case

$$n(x) = \begin{cases} 1 - e^{\alpha(x-h)/\epsilon v}, & h - \epsilon \leq x \leq h, \\ (1 - e^{-\alpha/v}), & \delta \leq x \leq h - \epsilon, \\ 0, & \text{elsewhere.} \end{cases} \qquad (15.42)$$

It is left as an exercise (Exercise 6) to show that in the limit as $\epsilon \to 0$ and $\delta \to 0$ the force–velocity curve for this model with a linear restoring force does not produce zero force at some positive velocity, a feature that appears in the Hill force–velocity curve.

A second option is to suppose that bonds break when $x < 0$, and to take $g(x) = \kappa/(\delta - x)$ on $\delta < x < 0$. Note that the rate of bond breakage is infinite at $x = \delta$, and thus all crossbridges are disassociated for $x < \delta$. Then

$$n(x) = \begin{cases} 1 - e^{\alpha(x-h)/\epsilon v}, & h - \epsilon \leq x \leq h, \\ 1 - e^{-\alpha/v}, & 0 \leq x \leq h - \epsilon, \\ (1 - e^{-\alpha/v})\left(1 - \frac{x}{\delta}\right)^{-\kappa/v}, & \delta \leq x < 0, \\ 0, & \text{elsewhere,} \end{cases} \qquad (15.43)$$

in which case $n(x)$ is a continuous function of x with compact support.

Notice that this works only if $v > 0$. The model must be modified if $v < 0$ (See Exercise 9).

Another way to determine the functions f and g is to estimate the energy of the bond as a function of position, and then from Eyring rate theory to determine the rates of reaction of binding and unbinding. This is the approach followed, for example, by Pate (1997). In fact, now that the biochemistry of the crossbridge reactions is known, fairly sophisticated models of this type are possible (Marland, 1998). Other versions of the basic scheme have been constructed by Pate and Cook (1989; 1991), while the models of T.L. Hill and his colleagues (Hill 1974, 1975; Eisenberg and Hill, 1978; Eisenberg and Green, 1980) have combined crossbridge models with detailed studies of the biochemical thermodynamics of the crossbridge cycle.

15.4   Determination of the Rate Functions

So far we have seen that an ad hoc approach to the determination of the functions f, g, and r can generate models that agree in varying degrees with experimental data. Obviously, it is desirable to find some way in which these functions can be determined more systematically, for example, to guarantee the correct form of the force–velocity curve. One way that this can be accomplished is by using a slightly different model for the crossbridge dynamics (Lacker and Peskin, 1986; Peskin, 1975, 1976).

15.4.1   A Continuous Binding Site Model

Recall that the Huxley model was based on the assumption that the actin binding sites are sufficiently separated so that each crossbridge can be associated with a unique binding site. Thus, even when a crossbridge is unbound, the distance of the crossbridge to the nearest binding site is defined. We now make the opposite assumption, that the actin binding sites are continuously distributed, so that myosin can bind anywhere along a thin filament. By analogy, one can think of the thin filament as flypaper, to which the myosin heads stick wherever they touch down. In this case, the variable x denotes the distance between the crossbridge anchor and the binding position, and the crossbridge distribution is described by a function $n(x,t)$ such that $\int_a^b n(x,t)\,dx$ is the fraction of crossbridges (at time t) that are attached with distance to the binding site x in the range $[a,b]$. Note that in this formulation, an unbound crossbridge cannot be associated with a value of x, as x is meaningful only for a bound crossbridge. The total fraction of bound crossbridges is

$$N = \int_{-\infty}^{\infty} n(x,t)\,dx < 1, \tag{15.44}$$

and the total fraction of unbound crossbridges is $1 - N$.

To derive the differential equation for n, we consider the conservation of crossbridges with x in the interval $[a,b]$. Let P denote the pool of crossbridges that are bound with $x \in [a,b]$. If the muscle is contracting at velocity $v > 0$, crossbridges move out of P at the rate $vn(a,t)$ and move into P at the rate $vn(b,t)$. Further, if f is defined such that $\int_a^b f(x)dx$ is the rate at which new crossbridges are formed with $x \in [a,b]$, and if $g(x)$ denotes the rate at which crossbridges with displacement x detach, then the rate of change of crossbridges is

$$\frac{d}{dt}\int_a^b n(s,t)\,ds = v[n(b,t) - n(a,t)] + (1-N)\int_a^b f(s)\,ds - \int_a^b g(s)n(s,t)\,ds. \tag{15.45}$$

Writing $v[n(b,t) - n(a,t)]$ as the integral $v\int_a^b \frac{\partial n}{\partial x}dx$, and noting that since a and b are arbitrary, the integrals can be dropped, we obtain

$$\frac{\partial n}{\partial t} - v(t)\frac{\partial n}{\partial x} = (1-N)f(x) - ng(x). \tag{15.46}$$

Note that in this derivation we assume that the rate of crossbridge attachment is proportional to the fraction of unattached crossbridges, $1 - N$.
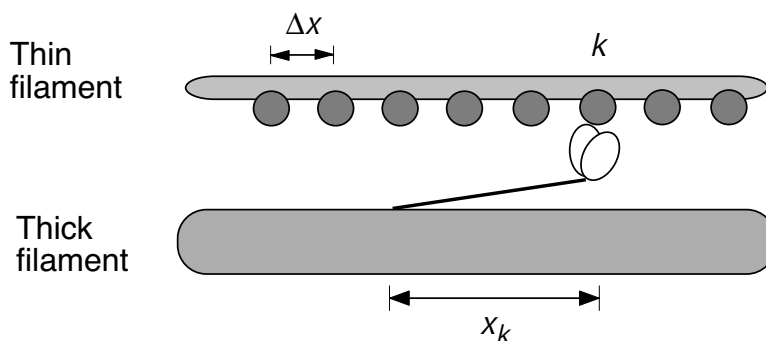
Figure 15.16: Schematic diagram of a crossbridge model with discrete binding sites. The actin binding sites are separated by a distance Δx, and x_k denotes the distance of the kth binding site from the unstressed position of the crossbridge.

The equations for the continuous binding site model are similar to those of the Huxley model, the differences being, first, that the rate of crossbridge attachment is given by $(1 - N)f$ in the continuous binding site model and $(1 - n)f$ in the Huxley model, and, second, that n and f have different units in the two models. In the Huxley model n is dimensionless, while in the continuous binding site model n has dimension of length^{-1}. Similarly, f has dimension of time^{-1} in the Huxley model and dimension of length^{-1} time^{-1} in the continuous binding site model.

In the following discussion we restrict our attention to a simplified version of the continuous binding site model in which all crossbridges attach at some preferred displacement, say, $x = h$. In this case $f(x) = F\delta(x - h)$, where F is the rate of crossbridge attachment. For this choice of f it is most convenient to rewrite the differential equation to incorporate crossbridge attachment as a boundary condition. We do this by integrating (15.46) from $h - \epsilon$ to $h + \epsilon$ and letting $\epsilon \to 0$. The jump in n at $x = h$ is then given by $F(1 - N)/v$, and so (15.46) can be written as

$$\frac{\partial n}{\partial t} - v(t)\frac{\partial n}{\partial x} = -ng(x), \qquad x < h, \tag{15.47}$$

$$n(h, t) = \frac{F(1 - N)}{v}. \tag{15.48}$$

Although in general, N and v are functions of t, we consider only those cases in which they are constant. However, N and n are also functions of v, and we sometimes write $N(v)$ and $n(x, t; v)$ to emphasize this dependence.

15.4.2 A General Binding Site Model

Both the continuous binding site model and the Huxley model can be derived as limiting cases of a more general model (Peskin, 1975). Suppose that on the thin filament there are a discrete number of actin binding sites, with regular spacing Δx (as illustrated in Fig. 15.16). We denote the horizontal distance from the crossbridge (on the thick filament) to the kth binding site by x_k. Finally, let $n_k(t)$ denote the

probability that the crossbridge is attached to site k at time t. Then, if $f(x_k)$ and $g(x_k)$ are the rates at which a crossbridge attaches and detaches respectively from the kth site, we have

$$\frac{dn_k(t)}{dt} = f(x_k)\left[1 - \sum_i n_i(t)\right] - g(x_k)n_k(t). \tag{15.49}$$

Note that the rate of crossbridge attachment is proportional to the probability that the crossbridge is not attached, $1 - \sum_i n_i(t)$.

If we now assume that the $n_k(t)$ are samples of a smooth function, so that

$$n_k(t) = n(x_k(t), t), \tag{15.50}$$

it follows that

$$\frac{dn_k}{dt} = -v\frac{\partial n}{\partial x_k} + \frac{\partial n}{\partial t}, \tag{15.51}$$

where, for consistency with our assumption that v is positive for a contracting muscle, we have defined $v = -dx_k/dt$. Substituting (15.51) into (15.49) gives

$$-v\frac{\partial n}{\partial x_k} + \frac{\partial n}{\partial t} = f(x_k)\left[1 - \sum_{i=-\infty}^{\infty} n(x_k + i\Delta x, t)\right] - g(x_k)n(x_k, t). \tag{15.52}$$

Since this holds for any binding site, the subscript k may be omitted, and thus

$$-v\frac{\partial n}{\partial x} + \frac{\partial n}{\partial t} = f(x)\left[1 - \sum_{i=-\infty}^{\infty} n(x + i\Delta x, t)\right] - g(x)n. \tag{15.53}$$

By taking two different limits of (15.53) we obtain the continuous binding site and Huxley models. Suppose first that the binding sites are so widely spaced that at any given time only one is within reach of any crossbridge. This is modeled by assuming that $n(x, t) = 0$ if $|x| > \Delta x/2$. In this case, the equation (15.53) is applicable only on the interval $|x| \leq \Delta x/2$, and with x in this interval, the only nonzero term in the sum in (15.53) is the term corresponding to $i = 0$. Thus (15.53) becomes

$$-v\frac{\partial n}{\partial x} + \frac{\partial n}{\partial t} = f(x)[1 - n(x, t)] - g(x)n(x, t), \tag{15.54}$$

which is the Huxley model.

If, however, we assume that Δx is small and if we let $n = \hat{n}\Delta x$, $f = \hat{f}\Delta x$, we get

$$-v\frac{\partial \hat{n}}{\partial x} + \frac{\partial \hat{n}}{\partial t} = \hat{f}(x)\left[1 - \sum_{i=-\infty}^{\infty} \hat{n}(x + i\Delta x, t)\Delta x\right] - g(x)\hat{n}. \tag{15.55}$$

In the limit as $\Delta x \to 0$ the sum becomes a Riemann integral, so that

$$-v\frac{\partial \hat{n}}{\partial x} + \frac{\partial \hat{n}}{\partial t} = \hat{f}(x)\left[1 - \int_{-\infty}^{\infty} \hat{n}(s, t)\, ds\right] - g(x)\hat{n}, \tag{15.56}$$

which is the continuous binding site model.

15.4.3 The Inverse Problem

The continuous binding site model (15.47) and (15.48) can be used to determine F, $g(x)$, and $r(x)$ directly from experimental data. (Recall that $r(x)$ is the restoring force generated by a crossbridge with extension x.) The steady-state solution of (15.47) and (15.48) can be written as

$$n(x; v) = \begin{cases} \dfrac{F[1 - N(v)]}{v} \exp\left(\displaystyle\int_x^h \dfrac{-g(s)}{v}\, ds\right), & x < h, \\[2ex] 0, & x > h. \end{cases} \tag{15.57}$$

Integrating (15.57) from $-\infty$ to ∞, we obtain

$$N(v) = \int_{-\infty}^{\infty} n(x; v)\, dx = \frac{F[1 - N(v)]}{v} I(v), \tag{15.58}$$

where

$$I(v) = \int_{-\infty}^{h} \exp\left(\int_x^h \frac{-g(s)}{v}\, ds\right) dx. \tag{15.59}$$

Thus, we can solve for $N(v)$ as

$$N(v) = \frac{FI(v)}{FI(v) + v}. \tag{15.60}$$

Substituting (15.60) into (15.57) we obtain an explicit solution for n,

$$n(x; v) = \frac{F}{FI(v) + v} \exp\left(\int_x^h \frac{-g(s)}{v}\, ds\right). \tag{15.61}$$

Since the average force produced by a crossbridge is

$$p(v) = \int_{-\infty}^{\infty} r(x) n(x; v)\, dx, \tag{15.62}$$

it follows that if F, g, and r are known, then (15.61) can be used to find an explicit expression for the force–velocity curve. This is the direct problem that we considered in the context of the Huxley model. Here we want to solve the inverse problem of determining F, g, and r from knowledge of p. However, additional information is needed to do this.

The energy flux during constant contraction can be measured experimentally; in general it is a function of v. If we assume that the energy flux $\phi(v)$ is proportional to the rate at which crossbridges go through the cycle of binding and unbinding to the actin filament, then ϕ is proportional to the crossbridge turnover rate,

$$\phi(v) = \rho \epsilon F (1 - N(v)), \tag{15.63}$$

where ρ is the total number of crossbridges and ϵ is the energy released during each crossbridge cycle. If the fraction of attached crossbridges during isometric tetanus is known, then F can be calculated from

$$\phi_0 = \rho \epsilon F (1 - N_0), \tag{15.64}$$

where $\phi_0 = \phi(0)$ and $N_0 = N(0)$. Next, $I(v)$ can be calculated from $\phi(v)$ by substituting (15.63) into (15.60), which gives

$$I(v) = v\left(\frac{F\rho\epsilon - \phi(v)}{F\phi(v)}\right) = \frac{\rho\epsilon v[\phi_0 - (1 - N_0)\phi]}{\phi\phi_0}. \tag{15.65}$$

Hence, from experimental knowledge of N_0 and $\phi(v)$ we can calculate explicit expressions for F and $I(v)$.

To find g from $I(v)$, we define the transformation

$$y(x) = \int_x^h g(s)\, ds. \tag{15.66}$$

Since g is positive, y is a monotonic function of x and has an inverse that can be calculated explicitly. Differentiating (15.66) with respect to x, we obtain

$$\frac{dy}{dx} = -g(x), \tag{15.67}$$

from which it follows that

$$x(y) = h - \int_0^y \frac{ds}{\bar{g}(s)}, \tag{15.68}$$

where $\bar{g}$ is defined by $g(x) = g(x(y)) = \bar{g}(y)$, and where we have used the condition $y(h) = 0$, so that $x(0) = h$.

Using these definitions, and also defining $\sigma = 1/v$, we get

$$I(1/\sigma) \;=\; \int_{-\infty}^h e^{-\sigma y}\, dx, \tag{15.69}$$

$$=\; \int_\infty^0 -e^{-\sigma y}\frac{dy}{g(x)}, \tag{15.70}$$

$$=\; \int_0^\infty \frac{1}{\bar{g}(y)} e^{-\sigma y}\, dy. \tag{15.71}$$

The function $I(1/\sigma)$ is the Laplace transform of $1/\bar{g}(y)$, and so $1/\bar{g}(y)$ is obtained as the inverse Laplace transform of $I(1/\sigma)$. Furthermore, g can be obtained as a function of x, since x is defined as a function of y by (15.68). Thus, for given y we can calculate both $\bar{g}(y)$ and $x(y)$. Since $\bar{g}(y) = g(x(y))$, we thus have a parametric representation for $g(x)$.

An explicit formula for $\bar{g}(y)$ can be obtained by using the inversion formula for Laplace transforms. Thus,

$$\frac{1}{\bar{g}(y)} = \frac{1}{2\pi i}\int_{c-i\infty}^{c+i\infty} I(1/\sigma)e^{\sigma y}\, d\sigma, \tag{15.72}$$

where $c > 0$ is arbitrary.

In a similar way, $r(x)$ can be obtained from the force–velocity curve $p(v)$. It is left as an exercise to show that

$$\frac{\epsilon p(1/\sigma)}{\sigma\phi(1/\sigma)} = \int_0^\infty \frac{\bar{r}(y)}{\bar{g}(y)} e^{-\sigma y}\, dy, \tag{15.73}$$

where $\bar{r}(y) = r(x(y))$. Hence

$$\bar{r}(y) = \frac{\epsilon \bar{g}(y)}{2\pi i} \int_{c-i\infty}^{c+i\infty} \frac{p(1/\sigma)}{\sigma \phi(1/\sigma)} e^{\sigma y} \, d\sigma. \qquad (15.74)$$

A specific example

The above analysis can be used to calculate F, g, and r to fit the Hill force–velocity curve and energy flux data (also observed by Hill). First, note that the force–velocity equation (15.1) can be written in the form

$$p(v) = \frac{bp_0 - av}{v + b}. \qquad (15.75)$$

Second, Hill (1938) observed that at constant rate of contraction, the heat flux $\dot{q}$ generated by a contracting muscle is linear, given by

$$\dot{q} = av + \phi_0, \qquad (15.76)$$

where the constant a is the same as in the force–velocity equation, and where ϕ_0 is the energy flux at zero velocity. The energy flux is the sum of two terms: the heat flux and the power used by the muscle. The power of a muscle contracting at speed v is pv (force times velocity), and thus the energy flux, $\phi(v)$, is given by

$$\phi(v) = \dot{q} + pv = \phi_0 + \frac{bv(a + p_0)}{v + b}. \qquad (15.77)$$

Substituting the expression for ϕ into (15.65) and using (15.72), we find that

$$\frac{1}{\bar{g}(y)} = \frac{\rho \epsilon}{\phi_0} \frac{1}{2\pi i} \int_{c-i\infty}^{c+i\infty} \left[\frac{\sigma_+ + N_0(\sigma - \sigma_*)}{\sigma(\sigma - \sigma_*)} \right] e^{\sigma y} \, d\sigma, \qquad (15.78)$$

and

$$\bar{r}(y) = \frac{\epsilon \bar{g}(y)}{2\pi i} \int_{c-i\infty}^{c+i\infty} \left[\frac{p_0 \sigma - a/b}{\sigma(\sigma - \sigma_*)} \right] e^{\sigma y} \, d\sigma, \qquad (15.79)$$

where $\sigma_+ = -(a + p_0)/\phi_0$ and $\sigma_* = -1/b + \sigma_+$. These integrals can be evaluated using the contour Γ shown in Fig. 15.17.

From the residue theorem, we know that the integral around Γ is the sum of the residues inside the contour. Further, it is not difficult to see that the integral over the semicircular part of the contour goes to zero as the radius of the semicircle becomes infinite. Hence

$$2\pi i \sum \text{residues} = \int_\Gamma = \int_{c-i\infty}^{c+i\infty}. \qquad (15.80)$$

Both of the integrals (15.78) and (15.79) have two simple poles inside Γ, one at $\sigma = 0$, the other at $\sigma = \sigma_*$. For the integral (15.78),

the pole at $\sigma = 0$ has residue $N_0 - \sigma_+/\sigma_*$; \qquad (15.81)

the pole at $\sigma = \sigma_*$ has residue $\sigma_+ e^{\sigma_* y}/\sigma_*$; \qquad (15.82)
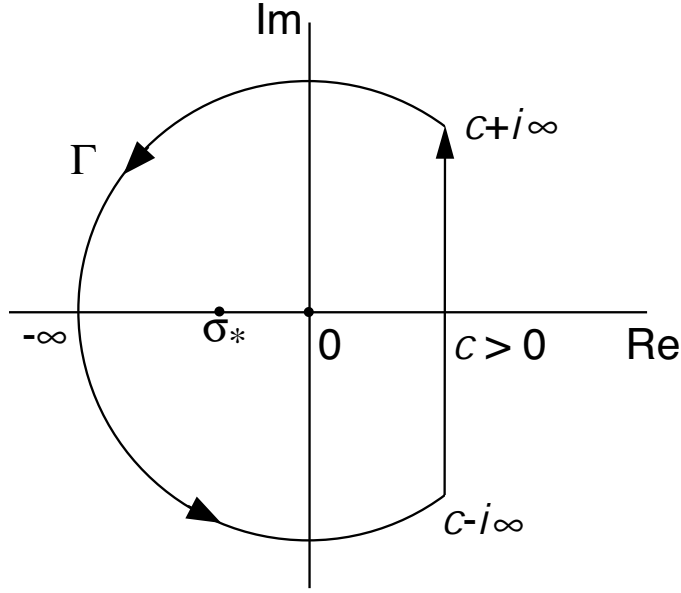
Figure 15.17: Contour for the evaluation of the path integral in the continuous binding site model. (Adapted from Lacker and Peskin, 1986, Fig. 6.)

while for the integral (15.79),

$$\text{the pole at } \sigma = 0 \text{ has residue } \frac{a}{b\sigma_*}; \tag{15.83}$$

$$\text{the pole at } \sigma = \sigma_* \text{ has residue } \left(p_0 - \frac{a}{b\sigma_*}\right) e^{\sigma_* y}. \tag{15.84}$$

Adding these residues for each integral gives, finally,

$$\frac{1}{\bar{g}(y)} = \frac{\rho\epsilon}{\phi_0}\left[N_0 + \frac{\sigma_+}{\sigma_*}(e^{\sigma_* y} - 1)\right], \tag{15.85}$$

$$\bar{r}(y) = \frac{\epsilon\bar{g}(y)}{\phi_0}\left[\frac{a}{b\sigma_*} + \left(p_0 - \frac{a}{b\sigma_*}\right)e^{\sigma_* y}\right]. \tag{15.86}$$

To calculate $x(y)$, use (15.68) from which it follows that

$$x(y) = h - \frac{\rho\epsilon}{\phi_0}\left[\left(N_0 - \frac{\sigma_+}{\sigma_*}\right)y + \frac{\sigma_+}{\sigma_*^2}(e^{\sigma_* y} - 1)\right]. \tag{15.87}$$

This gives a parametric definition of $g(x)$ and $r(x)$.

Finally, we note one important feature of this model. Each crossbridge exerts zero force at some value of $y = y_0$ such that $\bar{r}(y_0) = 0$. Solving for y_0 gives

$$y_0 = \frac{1}{\sigma_*}\ln\left(\frac{a}{a - p_0 b\sigma_*}\right). \tag{15.88}$$
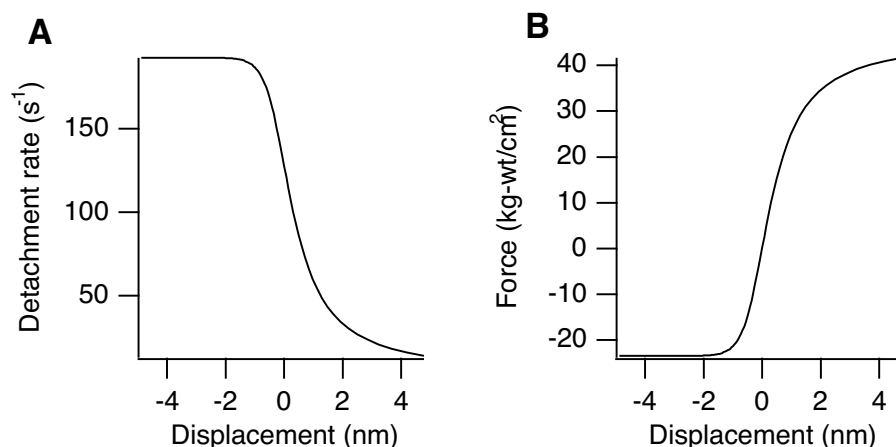
Figure 15.18: Crossbridge detachment rate (A) and force (B) in the continuous binding site model, calculated from (15.85), (15.86), and (15.87), using parameter values $p_0 = 3$ kg-wt/cm^2, $a/p_0 = 0.25$, $b = 0.325$ muscle lengths per second, $\phi_0 = ab$, $F = 125$ s^{-1}, $N_0 = 0.9$, $\phi_0/\rho\epsilon = F(1 - N_0) = 12.5$ s^{-1}. If we require that the crossbridge exerts no force at $x = 0$, then all crossbridges attach at $h = 4.78$ nm, assuming that the length of a half-sarcomere is 1.1 μm.

Hence, if we wish $x = 0$ to correspond to the equilibrium state of the crossbridge (i.e., when it exerts no force) as it was in the Huxley model, h must be chosen so that $x(y_0) = 0$, and thus

$$h = \frac{\rho\epsilon}{\phi_0} \left[\left(N_0 - \frac{\sigma_+}{\sigma_*} \right) y_0 + \frac{\sigma_+}{\sigma_*^2} (e^{\sigma_* y_0} - 1) \right]. \qquad (15.89)$$

Plots of g and r are shown in Fig. 15.18. From these curves we note that as the displacement of the crossbridge becomes more negative, its probability of detachment increases, but the force it exerts decreases. This allows a high isometric force without a corresponding reduction in the maximum contraction velocity; crossbridges initially exert a large force, but tend not to be carried into the region where they oppose contraction.

15.5 The Discrete Distribution of Binding Sites

The Huxley model assumes that at any one time, each crossbridge has only a single actin binding site available for binding, while the continuous binding site model assumes the opposite, that crossbridges can bind anywhere. However, the real situation is probably something in between these two extremes. Depending on the flexibility of the actin filament, it is probable that each crossbridge has a selection of more than one binding site, but it is unlikely that the binding sites are effectively continuous (cf. Fig. 15.4). T.L. Hill (1974, 1975) has constructed a detailed series of models that treat, with varying degrees of accuracy, the intermediate case when

the actin binding sites are distributed discretely but more than one is within reach
of a crossbridge at any time. Detailed consideration of models of this type is left
for the exercises (Exercises 7 and 8).

15.6   High Time-Resolution Data

All the models discussed so far treat crossbridge binding as a relatively simple
phenomenon; either crossbridges are bound or they are not, and there is no con-
sideration of the possibility that each crossbridge might have a number of different
bound states. As we have seen, such assumptions do a good job of explaining muscle
behavior on the time scale of tens of milliseconds. However, as the development of
new experimental techniques allowed the measurement of muscle length and ten-
sion on much shorter time scales, the initial models were improved to take this high
time-resolution data into account. One of the first models to do so was that of
Huxley and Simmons (1971). The Huxley–Simmons model is quite different from
models discussed above, giving a detailed description of how the force exerted by
an *attached* crossbridge can vary with time over a short period, but it does not take
into account the kinetics of crossbridge binding and unbinding to the thin filament.

15.6.1   High Time-Resolution Experiments

As we have already seen (Fig. 15.11B), when muscle length is decreased, the tension
immediately decreases, and then, over a time period of 100 milliseconds or so,
recovers to its original level. When this tension recovery is measured at a higher
time resolution, it becomes apparent that there are two components of the recovery
(Fig. 15.19). The initial drop in tension (which occurs simultaneously with the
change in length) is followed by a rapid, partial recovery, followed in turn by a much
slower complete recovery to the original tension. The slower recovery process is the
one described by the other models discussed in this chapter. Typical experimental
results are shown in Fig. 15.20. In this figure, T_1 denotes the value of the tension
after the initial drop, and T_2 denotes the value of the tension after the initial rapid
recovery. For length increases $(y > 0)$ T_1 is a linear function of the change in
length, while for length decreases $(y < 0)$, the decrease in tension is less than
might be expected from the linear relation. It is likely that because the length
step is not instantaneous but takes about a millisecond to complete, when a larger
length decrease is applied, the rapid recovery process has already begun to take
effect by the time the length decrease has been completed. If this is true (and it
appears plausible from the curves shown in Fig. 15.19), T_1 would be consistently
overestimated for larger, negative, y. From the linearity of the curve for $y > 0$, it
is reasonable to suppose that the relationship between T_1 and y is linear over the
entire range of y, as denoted by the dashed line in the figure.

   In contrast, T_2 is clearly a nonlinear function of y. For small length changes,
the rapid process restores the tension to its original level, but for steps of larger
length, the rapid process results in only partial recovery. The time course of the
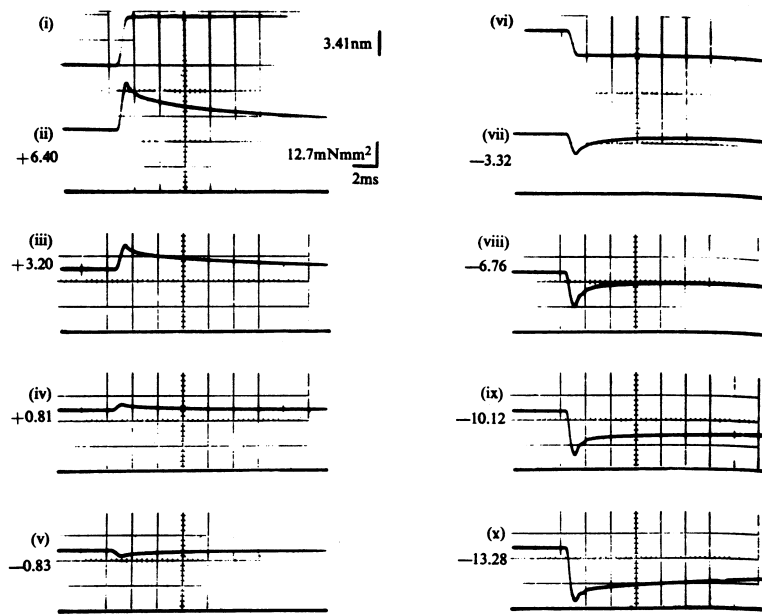
Figure 15.19: Changes in tension after a sudden stretch (ii–iv) or a sudden shortening (v, vii–x). Traces (i) and (vi) show the time course of the length change for traces (ii) and (vii), respectively. The number to the left of each record denotes the amount of the length change (in nm) per half-sarcomere. Note the high time-resolution of the measurements. (Huxley and Simmons, 1971, Fig. 2.)
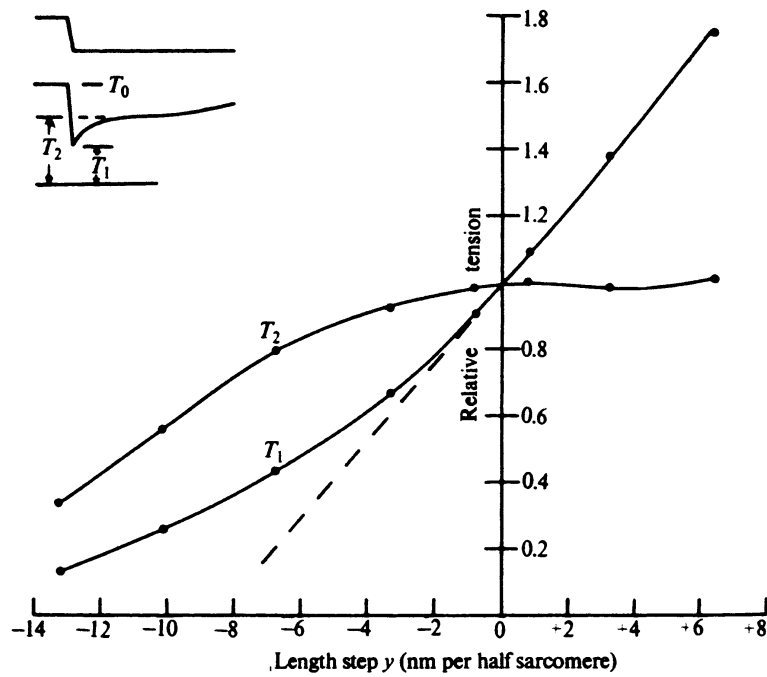
Figure 15.20: Curves of T_1 and T_2 as functions of the length step. As depicted in the inset, T_1 is the minimal tension reached during the step, while T_2 is the value of the tension reached after the quick recovery phase. The upper trace of the inset depicts the time course of the length change. (Huxley and Simmons, 1971, Fig. 3.)

rapid recovery has a dominant rate constant, r, which is well fit by the function

$$r = \frac{r_0}{2} \left(1 + e^{-\alpha y} \right), \tag{15.90}$$

with $r_0 = 0.4$ and $\alpha = 0.5$.

15.6.2 The Model Equations

To model and give a possible explanation of the above results, we assume that a crossbridge consists of two parts: an elastic arm connected to a rotating head that can bind to the actin filament in two different configurations. Recall that in the Huxley model, tension was generated by the crossbridge length, measured as the distance from the base of the crossbridge to the binding site. Here because there are two different possible binding configurations, the tension generated by the crossbridge depends not only on the distance from the base to the binding site, but also on the binding configuration, with different configurations resulting in different total crossbridge lengths. The idea behind this model is that the rapid process to restore tension can be accomplished by a change of the binding configuration, without changing the overall distribution of bound and unbound crossbridges.

As illustrated in Fig. 15.21, the head of the crossbridge is assumed to contain three combining sites, M_1, M_2, M_3, each of which has the ability to bind to a corresponding site, A_1, A_2, A_3, on the actin filament. (To avoid confusion with previous terminology, the M's and A's are called combining sites, rather than binding sites.) The affinity between the combining sites is greatest for $M_3 A_3$, and smallest for $M_1 A_1$. As the head of the crossbridge rotates in the direction of increasing θ, it moves through the sequence of binding configurations, $M_1 A_1$ only, $M_1 A_1$ and $M_2 A_2$, $M_2 A_2$ only, $M_2 A_2$ and $M_3 A_3$, $M_3 A_3$ only. During this progression the crossbridge arm is extended, and thus tension is increased. The two stable configurations of the crossbridge are those in which two consecutive combining sites are attached simultaneously. Because the binding affinity is greater for $M_3 A_3$, the energetically most favorable position for the crossbridge head is for M_2 and M_3 to be bound to A_2 and A_3 simultaneously.

An intuitive explanation of the behavior of this model is as follows. At steady state there is a balance between the tension on the crossbridge arm and the force exerted by the head of the crossbridge. The crossbridge head, in trying to rotate to a position of lower energy, places the elastic crossbridge arm under tension, and so the crossbridge arm, in turn, exerts a contractile force on the muscle. When the muscle is held at a constant length, the sum of all the crossbridge contributions gives the isometric force. If the length of the muscle is suddenly reduced, the tension on the crossbridge arm is suddenly reduced also, and this causes the instantaneous drop in tension seen experimentally. However, over the next few milliseconds, the reduced tension on the arm allows the crossbridge head to rotate to an energetically more favorable position, thus restoring the tension on the arm, and consequently restoring the muscle tension. Hence, the instantaneous drop in tension results from the fact that the elastic crossbridge arm responds instantaneously to a change in length, while the time course of the tension recovery is governed by how fast the crossbridge head rotates, which is, in
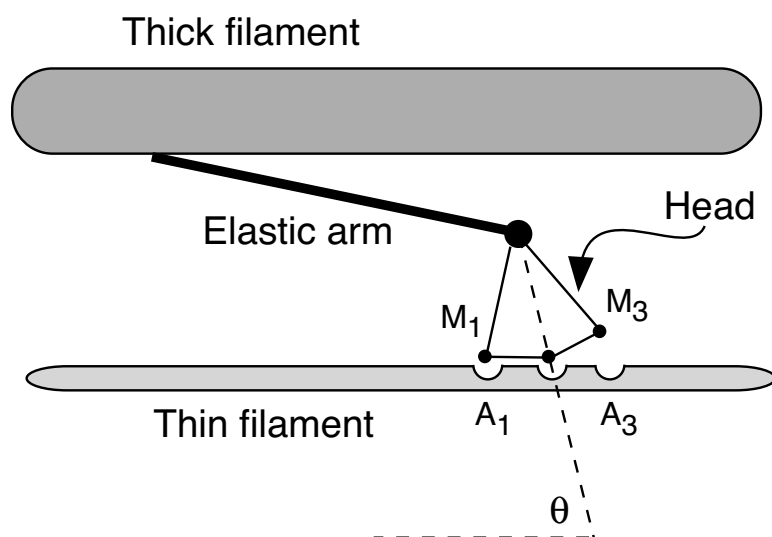
Figure 15.21: Schematic diagram of the Huxley-Simmons crossbridge model. (Adapted from Huxley and Simmons, 1971, Fig. 5).

turn, governed by the kinetics of attachment and detachment of the combining sites.

It is important to note that this description relies on the assumption that during isometric tetanus, all crossbridges have a positive displacement, i.e., $x > 0$. Otherwise, if some crossbridges had $x < 0$, a shortening of the muscle fiber would *increase* the force exerted by these crossbridges, in conflict with the above interpretation. However, in the models discussed so far, this is the case. For example, in the Huxley model the isometric tetanus solution is

$$n(x) = \frac{f(x)}{f(x) + g(x)}, \tag{15.91}$$

which is zero when $f(x) = 0$. Since f is nonzero only when $x > 0$, it follows that all crossbridges have a positive displacement during isometric tetanus. Although this is the case for the Huxley model, this is not necessarily true in experimental situations or in all models.

The model also neglects the effects of those few crossbridges that have such small displacements that a small decrease in length serves to shift them to negative displacements. However, the quantitative effects of this neglect are likely to be small.

To express the model mathematically, we construct a potential-energy diagram for the crossbridge. Recall that the crossbridge head has two stable configurations, one when M_1A_1 and M_2A_2 bonds exist simultaneously, which we denote as position one, and the other when M_2A_2 and M_3A_3 bonds exist simultaneously which we denote as position two. Because these configurations are stable, the potential energy of the crossbridge head reaches a local minimum at positions one and two, and since
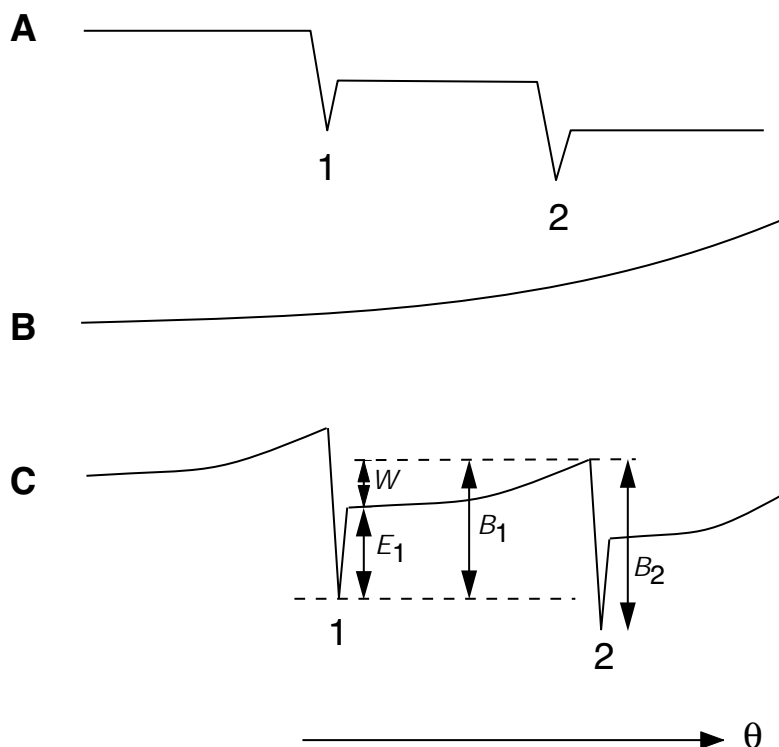
Figure 15.22: A: Potential energy of the crossbridge head. As the head rotates, with increasing θ the combining sites bind consecutively. The potential energy decreases overall from left to right, as it is assumed that M_3 and A_3 have the highest affinity. The two local minima correspond to stable configurations when two consecutive combining sites are bound simultaneously; these are called position one and position two. B: Potential energy due to the elastic energy of the crossbridge arm. C: Total potential energy of the crossbridge, showing the notation used in the model.

position two is energetically favored over position one, it has a lower potential energy (see Fig. 15.22A). However, as the head rotates from position one to position two, the crossbridge arm is extended, which increases the total potential energy of the crossbridge. Thus, adding the potential energy of the crossbridge arm (Fig. 15.22B) to the potential energy of the crossbridge head, we get the total potential energy of the crossbridge (Fig. 15.22C).

Now let n_1 and $n_2 = 1 - n_1$ denote the fraction of crossbridges in positions one and two, respectively, and let y denote the displacement (i.e., length change) of the thick filament relative to the thin filament to be applied. Thus, $y = 0$ corresponds to the steady state before any length change is applied (i.e., the isometric case). Also, let y_1 and y_2 denote the lengths of the crossbridge arm when the head is at positions one and two respectively, before the length change is applied. Let $y_0 = (y_1 + y_2)/2$ (the midway position), and let $h = y_2 - y_1$. Finally, let F_1 and

F_2 denote the tension in the crossbridge arm when the head is in positions one and two, respectively. Then, after the length change is applied,

$$F_1 = K(y+y_1) = K(y+y_0 - h/2), \qquad F_2 = K(y+y_2) = K(y+y_0+h/2), \quad (15.92)$$

where K is the stiffness of the crossbridge arm, assumed to follow Hooke's law. Hence, the average tension, ϕ, on a crossbridge arm is given by

$$\phi = n_1 F_1 + n_2 F_2 = K(y + y_0 - h/2 + hn_2). \qquad (15.93)$$

As the crossbridge head moves from position one to position two, the extending crossbridge arm does work, exerting an average force of approximately $(F_1 + F_2)/2$ over a distance h. Thus the work, W, is given by

$$W = h\frac{F_1 + F_2}{2} = Kh(y + y_0). \qquad (15.94)$$

Now, suppose that a crossbridge moves from position one to position two at kinetic rate k_+ and moves in the opposite direction at kinetic rate k_-. As with barrier models for the ionic current through a membrane channel (Chapter 3), we assume that each of these rates is an exponential function of the height of the potential-energy barrier that the crossbridge must cross in order to jump from one combining configuration to the other. With this assumption, $k_+ = \exp(\frac{-B_1}{kT})$ and $k_- = \exp(\frac{-B_2}{kT})$, where B_1 and B_2 are the barrier heights to move from configuration 1 to 2, and 2 to 1, respectively, T is the absolute temperature and k is Boltzmann's constant. Then,

$$\frac{k_+}{k_-} = \exp\left(\frac{B_2 - B_1}{kT}\right) \qquad (15.95)$$

$$= \exp\left(\frac{B_2 - E_1 - W}{kT}\right) \qquad (15.96)$$

$$= \exp\left(\frac{B_2 - E_1 - Kh(y+y_0)}{kT}\right) \qquad (15.97)$$

$$= A^0 \exp\left(\frac{-Khy}{kT}\right), \qquad (15.98)$$

where $A^0 = \exp\left(\frac{B_2 - E_1 - Khy_0}{kT}\right)$.

When the length of the muscle is changed, the crossbridges redistribute themselves among the two configurations according to the differential equation

$$\frac{dn_2}{dt} = k_+ n_1 - k_- n_2 = k_+ - rn_2, \qquad (15.99)$$

where

$$r = k_+ + k_- = k_-\left[1 + A^0 \exp\left(\frac{-yKh}{kT}\right)\right]. \qquad (15.100)$$

Since r is the time constant for the redistribution of crossbridges, it follows that r is also the time constant for the development of the tension T_2 at the end of the quick
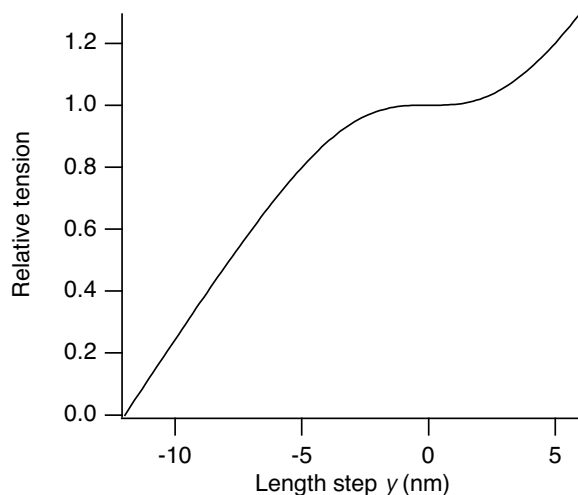
Figure 15.23: Plot of relative steady tension ϕ (15.102) in the Huxley–Simmons model. Parameter values: $\alpha = 0.5\,\text{nm}$, $y_0 = 8\,\text{nm}$, $h = 8\,\text{nm}$. Because we plot relative tension, the numerical value of kT has no effect on the shape of the curve.

recovery. Equation (15.100) is the same as (15.90) if $Kh = \alpha kT$, and $A^0 = 1$, and thus the model shows the correct time course for tension development. At steady state,

$$n_2 = \frac{k_+}{k_+ + k_-} = \frac{1}{2}\left[1 + \tanh\left(\frac{\alpha y}{2}\right)\right], \tag{15.101}$$

where we have used that $k_+/k_- = \exp(-\alpha y)$. Hence, the steady-state tension (which corresponds to T_2) is given by

$$\phi = K(y + y_0 - h/2 + hn_2) = \frac{\alpha kT}{h}\left[y_0 + y - \frac{h}{2}\tanh\left(\frac{\alpha y}{2}\right)\right]. \tag{15.102}$$

A plot of ϕ is given in Fig. 15.23, from which it is seen that the model gives an excellent qualitative description of the experimental data shown in Fig. 15.20.

In summary, although the Huxley–Simmons model does not take later events, such as crossbridge binding and unbinding, into account and is not intended to describe the full tension recovery in the manner of the Huxley model, it nevertheless provides an excellent qualitative description of the initial phase of tension recovery following a step change in length.

15.7 In Vitro Assays

Using reconstituted systems of actin and myosin (so-called *in vitro* assays), it is possible to observe single myosin molecules working their way along an actin strand (Sheetz and Spudich, 1983; Spudich *et al.*, 1985; Uyeda *et al.*, 1990), or single kynesin molecules moving along a microtubule (Howard *et al.*, 1989). If a solution

of myosin fragments, each containing the motor domain, is put on a nitrocellulose-coated glass surface, some of the individual myosin molecules attach to the surface. Upon addition of a solution of ATP and polymerized actin filaments, the individual actin filaments are grabbed by the myosin motor domains which then try to move along the filament. Since the myosins are fixed but the actin filament is not, there is a resulting movement of the actin filament. Individual filaments can then be observed gliding over the field of myosin molecules. By careful regulation of the concentration of the myosin fragments, the average number of myosin molecules moving each actin strand can be controlled. Experimental results show that the speed of gliding increases with the number of myosin molecules that are moving the actin filament, and Pate and Cook (1991) have presented a simple analysis to show why this should be so.

Consider the case when the actin filament is moved by a single myosin molecule. For simplicity, assume that the spacing between actin binding sites is exactly the length of the powerstroke, i.e., 10 nm, and let h denote the length of the powerstroke. The speed of movement is then $h\times$ the mean cycle rate. After the myosin binds and executes a powerstroke it can only rebind to the actin filament at a displacement of $x = h$ nm. Following the notation of the Huxley model (Section 15.3), the rate of rebinding is thus $f(h)$ and the rate of detachment is $g(0)$. Thus the mean time to rebind is $1/f(h)$, the mean time to detach is $1/g(0)$, and the mean cycle time is $1/f(h) + 1/g(0)$. It follows that the speed of the actin filament, v, is given by

$$v = \frac{h}{\frac{1}{f(h)} + \frac{1}{g(0)}}, \tag{15.103}$$

which, using the parameter values of Brokaw (1976), $f(h) = 65 \text{ s}^{-1} \ll g(0) = 313 \text{ s}^{-1}$, is approximated by $v \approx f(h)h$. Thus, the rate-limiting step is the attachment of the myosin to the actin filament.

It is left as an exercise (Exercise 10) to show that, in the limit as the number of bound crossbridges goes to infinity, the gliding rate is given by

$$v \approx \frac{g_2 h}{2}, \tag{15.104}$$

where g_2 is defined by (15.27). Since, for the Huxley parameters, $f(h) < g_2/2$, it follows that the gliding rate increases as the number of bound crossbridges increases, as is observed experimentally.

15.8   Smooth Muscle

Smooth muscle is quite different, both in biochemistry and function, from skeletal or cardiac muscle. Furthermore, there is an enormous diversity of smooth muscle to match its diversity of function. Smooth muscle is found around blood vessels and airways, and is a major component of the hollow internal organs such as the gastrointestinal system (Chapter **??**), the bladder, or the uterus. Unlike skeletal and cardiac muscle, smooth muscle is non-striated as, although it contains both the actin and myosin necessary for contractile function, these proteins are not arranged in regular arrays.

Like striated muscle, smooth muscle is electrically active, with a variety of ion pumps, channels and exchangers in the plasma membrane, that can generate action potentials. Furthermore, contraction requires a rise in the cytoplasmic Ca^{2+} concentration. However, unlike in striated muscle, this rise in Ca^{2+} concentration often occurs via the production of IP_3, and subsequent release of Ca^{2+} from the sarcoplasmic reticulum, as described in Chapter 7.

The most important difference between smooth and striated muscle is the different way in which Ca^{2+} regulates contraction. Recall from earlier in this chapter, in striated muscle the binding of Ca^{2+} to troponin exposes the myosin binding site on the actin filament and allows the crossbridge cycle to generate force. However, smooth muscle contains no troponin. Instead, the crossbridge cycle can occur only when myosin is phosphorylated at a specific site. This phosphorylation is carried out by *myosin light chain kinase* (MLCK), which is activated by Ca^{2+}-calmodulin. Hence, a rise in Ca^{2+} leads to a rise in Ca^{2+}-calmodulin, as Ca^{2+} binds to the calmodulin, leading to increased activation of MLCK, phosphorylation of the myosin, and thus contraction.

Dephosphorylation of the myosin by *myosin light chain phosphatase* (MLCP) prevents the crossbridge cycle occuring. However, this does not necessarily lead to relaxation of the muscle. If dephosphorylation occurs while the myosin is bound to the actin, the crossbridge enters the so-called *latch state*. While in this state the myosin can unbind from the actin only very slowly; thus, no active force can be generated (as the crossbridge cycle cannot occur) but the crossbridge cannot relax, either, as the myosin remains bound. Thus, if all the crossbridges were in the latch state, the muscle would be rigid and unable to relax, but would require little energy to stay in this state. Thus, smooth muscle is able to sustain a load while using little ATP, which allows for the maintenance of organ shape and dimension without undue use of energy. This is illustrated in Fig. 15.24.

15.8.1 The Hai-Murphy model

Most quantitative studies of smooth muscle are based on the work of Hai and Murphy (1989; Murphy, 1994), who assumed that a crossbridge could exist in one of four forms, myosin either unattached or attached, either phosphorylated or not (Fig. 15.25). The rate of crossbridge phosphorylation by MLCK is denoted by k_1, and is a function of the Ca^{2+} concentration, c. The rate of dephosphorylation was assumed by Hai and Murphy to be constant, although it now seems likely that it also depends on Ca^{2+} concentration as well as the level of agonist stimulation. In general, unattached and attached myosin (M and AM respectively) could be phosphorylated at different rates ($k_1(c)$ and $k_5(c)$ respectively) although it is usually assumed that these two rates are the same.

Mihailov et al. (2000) extended the original Hai-Murphy model by including dependence on the crossbridge extension, in the same way as in the Huxley model (Section 15.3). Thus, the rate of attachment and detachment of phosphorylated myosin are $f(x)$ and $g(x)$ respectively, where f and g have the same shape as shown in Fig. 15.13.

However, unphosphorylated myosin cannot attach to actin, and detaches only slowly. Hence, k_7 is smaller than $g(x)$, and there is no reverse reaction.
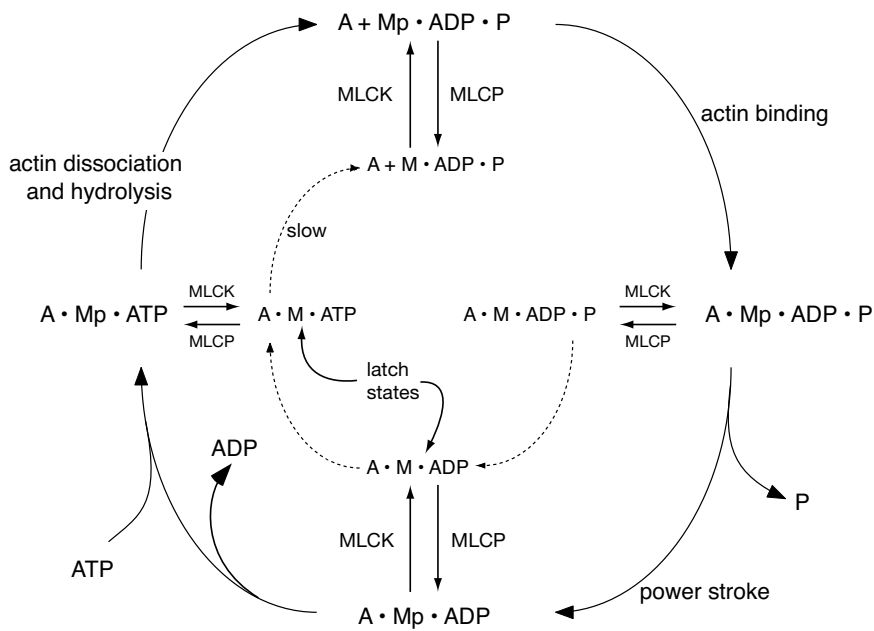
Figure 15.24: Schematic diagram of the eight-state binding model of smooth muscle. The outer ring of solid lines corresponds to the usual crossbridge cycle, but, to enter this cycle, myosin (M) must be in the phosphorylated state (Mp). The inner ring of dotted lines is incomplete, since unphosphorylated myosin cannot bind to actin. MLCK is myosin light chain kinase, MLCP is myosin light chain phosphatase. When the crossbridge is in the latch state it cannot relax quickly, but cannot generate active force either.
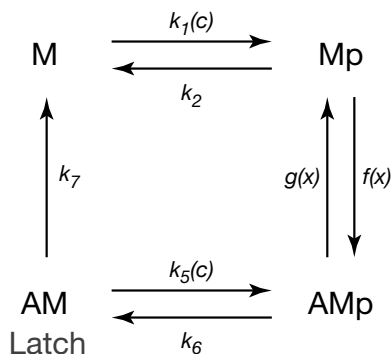
Figure 15.25: Schematic diagram of the Hai-Murphy model of smooth muscle (Hai and Murphy, 1989). M — myosin; Mp — phosphorylated myosin; AMp — attached phosphorylated myosin; AM — attached myosin. MLCK is activated myosin light chain kinase and is a function of the Ca^{2+} concentration (denoted by c), via Ca^{2+}-calmodulin. As in the Huxley model, x is crossbridge displacement.

Because k_7 is small, it is possible that some bound crossbridges experience large negative displacements. This introduces some subtleties into the model equations, which we now describe. Following the Huxley model, we let x be the crossbridge displacement. Then, using standard arguments, the evolution of the density of bound crossbridges is given by

$$\frac{\partial N_{AMp}}{\partial t} - v(t)\frac{\partial N_{AMp}}{\partial x} = k_5(c)N_{AM} + f(x)N_{Mp} - (k_6 + g(x))N_{AMp} \quad (15.105)$$

$$\frac{\partial N_{AM}}{\partial t} - v(t)\frac{\partial N_{AM}}{\partial x} = k_6 N_{AMp} - (k_5(c) + k_7)N_{AM}. \quad (15.106)$$

For an unbound crossbridge, the displacement is the distance to the binding site with which it could bind. Without loss of generality, we assume that $f(x)$ is nonzero only on the interval $0 < x < h$ and that Δx, the distance between binding sites, is greater than h. Thus, N_M and N_{Mp}, the density of crossbridges in states M and Mp, respectively, which are unbound, are only defined for $0 < x < \Delta x$. However, with $v > 0$, it is possible for a bound crossbridge to have displacement anywhere in the interval $-\infty < x < h$. Furthermore, when a bound crossbridge with negative displacement becomes unbound, it becomes an unbound crossbridge with displacement $x + i\Delta x$, where i is the smallest integer for which $x + i\Delta x > 0$. A similar argument holds for $v < 0$ but with positive displacements greater than Δx. Thus, the evolution of N_M is governed by the partial differential equation,

$$\frac{\partial N_M}{\partial t} - v(t)\frac{\partial N_M}{\partial x} = k_2 N_{Mp} - k_1(c)N_M + k_7 \sum_{i=-\infty}^{\infty} N_{AM}(x - i\Delta x, t), \quad (15.107)$$

and similarly for N_M

$$\frac{\partial N_\mathrm{Mp}}{\partial t} - v(t)\frac{\partial N_\mathrm{Mp}}{\partial x} = k_1(c)N_\mathrm{M} - (k_2 + f(x))N_\mathrm{Mp} + \sum_{i=-\infty}^{\infty} g(x - i\Delta x)N_\mathrm{AMp}(x - i\Delta x, t),$$
(15.108)

In addition, the flux of unbound sites with $x = 0$ must match the flux of unbound sites with $x = \Delta x$, so that

$$\frac{\partial N_\mathrm{M}(0, t)}{\partial x} = \frac{\partial N_\mathrm{M}(\Delta x, t)}{\partial x}, \qquad \frac{\partial N_\mathrm{Mp}(0, t)}{\partial x} = \frac{\partial N_\mathrm{Mp}(\Delta x, t)}{\partial x}.$$
(15.109)

One can now show that there is a conserved quantity

$$N_\mathrm{M}(x, t) + N_\mathrm{Mp}(x, t) + \sum_{i=-\infty}^{\infty} \left[N_\mathrm{AMp}(x + i\Delta x, t) + N_\mathrm{AM}(x + i\Delta x, t) \right] = 1. \quad (15.110)$$

for $0 < x < \Delta x$. Under isometric conditions this reduces to $N_\mathrm{M} + N_\mathrm{Mp} + N_\mathrm{AMp} + N_\mathrm{AM} = 1$, since with $v = 0$ it is not possible to have bonds outside the range for which f is nonzero.

The Hai-Murphy cross-bridge model is connected to models of intracellular Ca^{2+} dynamics via $k_1(c)$ and $k_5(c)$ (Koenigsberger et al., 2004, 2005, 2006; Fajmut et al., 2005; Payne and Stephens, 2005; Bursztyn et al., 2007).

15.9   Large-Scale Muscle Models

Ultimately, to model the function and properties of muscle *in situ* it is necessary to consider highly complex models that include the action potential, the calcium transient, crossbridge and thin filament kinetics, the constitutive properties of muscle, and the consequent force and contraction that results from a train of action potentials. Furthermore, these models should use realistic geometries. Although computing facilities are not yet advanced enough to enable simulation of such detailed models in a realistic time frame, much has already been accomplished. Probably the most detailed such investigations (complementing the highly detailed electrical models of Noble's group, summarized in Noble, 2002) are those from the groups of Peter Hunter and Andrew McCulloch (McCulloch, 1995; Hunter *et al.*, 1996a,b; Hunter *et al.*, 1998; McCulloch *et al.*, 1998; Hunter *et al.*, 2003). There is far too little space here to discuss these elaborate models in detail, so the interested reader is referred to the original works.

15.10   Molecular Motors

In all the models described so far, the properties of the muscle result from the collective behavior of a large population of myosin molecules. However, there are many contexts in which movement is achieved by many individual molecules working independently. For example, since cellular components are synthesized at sites (the Golgi apparatus, the endoplasmic reticulum, and the nucleus, for example) that are

far removed from the place where those components are used (the cell membrane, the synapse, etc.) every cell type relies on active transport mechanisms to distribute various cellular components around the cell.

In recent years, a lot of attention has been given to understanding how chemical energy can be transformed into work. Of course, myosin is but one example of a plethora of these molecular machines, or motors. Examples that we have seen already in this text are the ATP-ase ion pumps and exchangers, such as the sodium-potassium ATPase or the SERCA. These motors reside in the cell membrane and use the chemical energy of ATP to pump ions against their gradient, thereby producing work. In the opposite direction, the best-known example is the ATP synthase molecule which manufactures ATP from ADP and phosphate by using the energy in a transmembrane proton gradient (Wang and Oster, 1998; Elston *et al.*, 1998; Mogilner *et al.*, 2002).

A different mechanism (described below) is used to transport large macro-molecules across a membrane, but because ATP is used, this can also be viewed as the action of a molecular motor.

Other motors are used to transport loads over larger space scales. There are three types of molecular transporters (Mallik and Gross, 2004); the myosin, kinesin and dynein motors. Each of them transports its cargo by binding the cargo to its "tail", while simultaneously stepping along a rail system (actin in the case of the myosin motor, microfilaments in the case of kinesin and dynein), in much the same way that a child swings along monkey bars. The kinesin and dynein motor proteins have two heads which cyclically bind and unbind to the rail track, but out of phase, resulting in directed motion along the track. The necessary energy comes from the hydrolysis of ATP. Movement is directed, with most kinesin-family motors transporting their cargo from the nucleus towards the cell periphery, and most dynein-family motors transporting their cargo in the opposite direction along the same microtubule system.

In what follows we give a brief introduction to how pushing and pulling is accomplished by molecular motors. For consistency with the topics in this chapter, it would seem most reasonable to begin with a description of a myosin motor, however, from the perspective of model building and developing the appropriate mathematical framework, we begin with a description of Brownian ratchets. More detailed introductions are given by Mogilner *et al.* (2002) and Riemann (2002), while the mathematical theory is developed in detail by Qian (2000).

15.10.1 Brownian ratchets

Proteins live in a world that is being continually shaken by random movements. If these random motions could be rectified, or biased, then they could be used to perform work. For example, if a particle performs an unbiased random walk on a line then, if there are no outside influences, its mean displacement is zero. However, if every time the particle moves a certain distance in one direction it is prevented by some mechanism from moving back in the opposite direction (i.e., a ratchet), then the original random motion of the particle is "rectified", and the particle experiences a net drift.
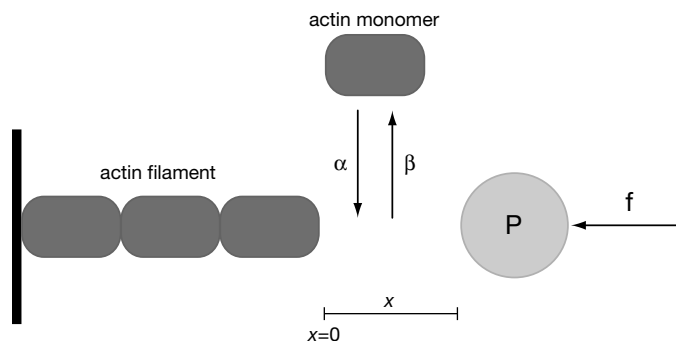
Figure 15.26: Diagram of a polymerization ratchet.

This concept can be understood in a simple way by the way in which a glucose transporter operates (see Chapters **??** and **??**). In the absence of hexokinase, the transporter is merely an exchanger that reaches steady-state when the glucose concentrations are the same on either side of the membrane. However, ATP hydrolysis and phosphorylation of glucose by hexokinase is able rectify the diffusional flux of glucose, eliminating the backflow, thus maintaining a net flux of glucose into the cytoplasm.

Another example is the provided by the translocation of macromolecules through a membrane. For example, the chaperone molecule HSP-70 (heat shock protein, moleular weight 70 kilodaltons) is required for translocation of proteins into the ER and mitochondria. In the absence of HSP-70, macromolecules move through pores in the membrane by simple diffusion, moving forward or backward via a random walk. It is not certain how HSP-70 works, but one proposal (Elston 2000, T. C. Elston, Models of Post-translational Protein Translocation, Biophysical J. 2235-2251, 2000.) is that HSP-70, which is located inside the organelle, binds to the diffusing protein as it enters the organelle, preventing it from sliding back through the pore, thus creating a ratchet.

Another important example of a Brownian ratchet is the polymerization ratchet, a diagram of which is shown in Fig. 15.26. An actin filament that is capable of polymerizing is in contact, from time to time, with a particle, P (which may also have an applied load f). Although P is diffusing it cannot move far to the left as the actin polymer is in the way. However, every so often the Brownian motion of P takes it far enough to the right, providing the opportunity for another actin monomer to polymerize onto the filament, extending the actin filament. The net effect is that the motion of P is biased to the right. Clearly, for this to happen a number of conditions must be satisfied; P must move randomly far enough to the right to make space for an actin monomer to join the filament, and it must stay there long enough to give actin time to bind; also, the polymerizing actin must remain strongly bound to the filament so that the process is not reversed, i.e., so that the collision of P with the actin polymer does not cause the actin at the end to unbind.

We wish to calculate the load-velocity relationship for this system (Peskin *et al.*

(1993). To do so, we let x denote the positive distance between the end of the actin filament and P, and let $p(x,t)$ be the probability density function for the location of the particle P. That is, $\int_a^b p(x,t)\,dx$ is the probability that the particle P lies in the interval $x \in [a,b]$.

There are only two ways that the distance between the end of the polymer and the particle can change; the particle can move to a different position or the length of the actin polymer can change. Correspondingly, $p(x,t)$ can change either because of movement of the particle or because of changes to the length of the polymer. The flux of p due to particle movement is given by

$$J = -D\left(\frac{\partial p}{\partial x} + \frac{f}{kT}p\right), \tag{15.111}$$

where k is Boltzmann's constant, T is absolute temperature, and D is the diffusion coefficient of P. This is the same as the Nernst-Planck relationship for movement of ions in an electric field, where f replaces $qz\frac{\partial\phi}{\partial x}$. Notice that the sign of f is such that it is positive to the left.

Now suppose that monomers bind at rate α and unbind at rate β. Presumably unbinding can occur independent of x, but when it does so, the distance x is suddenly increased by the amount δ. Similarly, if binding occurs, the distance x is suddenly decreased by the amount δ. However, binding can occur only if there is enough room, i.e. only if $x > \delta$.

The rate of change of p depends on these reactions. If $x < \delta$, the rate of change of p is (in words)

$$
\begin{aligned}
\text{rate of change of p} \quad = \quad &\text{transport rate} \\
&+\text{binding rate at position } x + \delta \\
&-\text{unbinding rate at position } x, \tag{15.112}
\end{aligned}
$$

whereas, if $x > \delta$,

$$
\begin{aligned}
\text{rate of change of p} \quad = \quad &\text{transport rate} \\
&+\text{binding rate at position } x + \delta \\
&-\text{unbinding rate at position } x \\
&-\text{binding rate at position } x \\
&+\text{unbinding rate at position } x - \delta. \tag{15.113}
\end{aligned}
$$

In mathematical terms,

$$\frac{\partial p}{\partial t} = D\frac{\partial^2 p}{\partial x^2} + \frac{Df}{kT}\frac{\partial p}{\partial x} + \alpha p(x+\delta,t) - \beta p(x,t), \qquad x < \delta, \tag{15.114}$$

and

$$\frac{\partial p}{\partial t} = D\frac{\partial^2 p}{\partial x^2} + \frac{Df}{kT}\frac{\partial p}{\partial x} + \alpha[p(x+\delta,t) - p(x,t)] + \beta[p(x-\delta,t) - p(x,t)], \qquad x > \delta. \tag{15.115}$$

Since the particle cannot move across the boundary at $x = 0$, we impose the no-flux condition,

$$D\frac{\partial p(0,t)}{\partial x} + \frac{Df}{kT}p(0,t) = 0. \tag{15.116}$$

Finally, we require that p be continuously differentiable at $x = \delta$.

Although this is a fairly simple example of a Brownian ratchet, its full solution is highly non-trivial. This is because the steady state equation is a delay differential equation that must be solved on the infinite half-line, subject to boundary conditions at $x = 0$ and $x = \infty$. However, it is possible to gain an understanding of how this Brownian ratchet works in several limiting cases.

In the limit that α and β are small compared to $\frac{D}{\delta^2}$ (see Exercise 11) we can calculate the steady-state solution for p explicitly. In this case we have

$$\frac{d^2p}{dx^2} + \frac{\omega}{\delta}\frac{dp}{dx} = 0, \qquad x < \delta \text{ and } x > \delta, \tag{15.117}$$

$$\frac{dp(0)}{dx} + \frac{\omega}{\delta}p(0) = 0, \tag{15.118}$$

$$p \text{ continuous at } x = \delta, \tag{15.119}$$

where $\omega = \frac{f\delta}{kT}$. Furthermore, we require that $p \to 0$ as $x \to \infty$. This boundary value problem has solution

$$p = \frac{\omega}{\delta}e^{-\omega x/\delta}, \tag{15.120}$$

so that $\int_0^\infty p(x)dx = 1$.

We now can find the mean ratchet velocity, v. The proportion of positions at which a monomer can bind is $\int_\delta^\infty p(x)\,dx$, and thus the mean rate at which the length of the filament increases due to monomer binding is $\delta\alpha \int_\delta^\infty p(x)\,dx$. Similarly, all filaments can decrease in length due to unbinding of a monomer, and thus the mean rate at which the length of the filament decreases due to monomer unbinding is $\delta\beta$. Taking the difference between these two rates gives the net mean ratchet velocity

$$v = \delta\left(\alpha \int_\delta^\infty p(x)\,dx - \beta\right). \tag{15.121}$$

Substituting for p from (15.120) gives the remarkably simple expression for the force-velocity relation,

$$v = \delta\left[\alpha \exp\left(-\frac{f\delta}{kT}\right) - \beta\right]. \tag{15.122}$$

The stall force, f_0, i.e., the force at which the ratchet velocity is zero, is given by

$$f_0 = -\frac{kT}{\delta}\ln\left(\frac{\beta}{\alpha}\right). \tag{15.123}$$

Note the similarity of this with the Nernst equation (2.103). Notice also that $\frac{\beta}{\alpha}$ is the equilibrium constant for binding of monomer, $\frac{\beta}{\alpha} = \exp(\frac{\Delta G^0}{RT})$, so that

$$f_0 = -\frac{\Delta G^0}{\delta N_A}. \tag{15.124}$$

Thus, the energy used to move the particle against the load is the same as the free energy of binding of the monomer. Clearly, a necessary condition for this polymerization ratchet to push a load is that the binding rate be larger than the unbinding rate.

We can also easily examine this Brownian ratchet in another limit, the fast reaction limit. We suppose that we have an ideal ratchet for which binding of monomer takes place instantly and irreversibly whenever there is sufficient space to bind, i.e., whenever x reaches δ. Thus, the mean velocity of the ratchet is δ divided by the time it takes to diffuse to the right a distance δ starting from position $x = 0$. This time is the mean first exit time $T(0)$, where $T(x)$ satisfies the differential equation

$$D \left(\frac{d^2 T}{dx^2} - \frac{f}{kT} \frac{dT}{dx} \right) = -1, \qquad (15.125)$$

(see Chapter 2, Section 2.9.6) subject to boundary conditions $T'(0) = 0$ (since the boundary at $x = 0$ is a reflecting boundary) and $T(\delta) = 0$. The solution is (see Exercise 30)

$$T(0) = \frac{\delta^2}{D} \left(\frac{kT}{f\delta} \right)^2 \left[\exp\left(\frac{f\delta}{kT} \right) - \frac{f\delta}{kT} - 1 \right], \qquad (15.126)$$

so that

$$v = \frac{D}{\delta} \frac{(\frac{f\delta}{kT})^2}{\exp(\frac{f\delta}{kT}) - 1 - \frac{f\delta}{kT}}. \qquad (15.127)$$

This load-velocity curve is a monotone decreasing function of load f. Notice, however, that for this model there is no stall velocity, because, since the bound monomer is assumed to bind irreversibly, there is the implicit assumption that the binding energy is infinite, which of course, cannot be correct.

Peskin *et al.* (1993) applied this model to the study of filopod protrusion, as well as to propulsion of the bacteria *Listeria monocytogenes*, while a number of elaborations of the basic scheme have been constructed (Mogilner and Oster, 1996, 1999; Simon *et al.*, 1992).

15.10.2 The Tilted Potential

There is another approximate model of the Brownian ratchet that has proven to be quite useful. Rather than thinking of binding and unbinding of a monomer, we suppose that at the fixed positions $x = x_k = k\delta$, the particle P is given a "kick" of energy ΔG, but that it diffuses freely elsewhere, against a load f. Now the probability distribution function $p(x, t)$ for the location of the particle is the solution of the Fokker-Planck equation

$$\frac{\partial p}{\partial t} = \frac{\partial}{\partial x}(V'(x)p) + D\frac{\partial^2 p}{\partial x^2}, \qquad (15.128)$$

where $V(x)$ is the potential energy function with

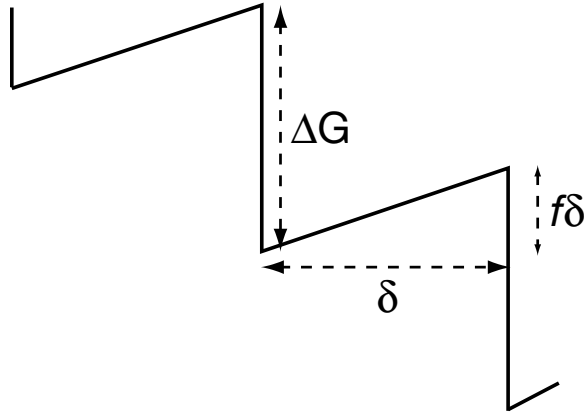$$V'(x) = \frac{Df}{kT} - D\frac{\Delta G}{kT} \sum_n \delta(x - n\delta). \qquad (15.129)$$

Figure 15.27: Diagram of a tilted ratchet potential (15.129)

The potential $V(x)$ shown plotted in Fig. 15.27 is a piecewise linear "staircase", often called a tilted ratchet potential.

One feature of this that is immediately obvious is that the stall load is $f = \Delta G$, because it is the load at which the potential $V(x)$ is periodic. This also makes sense intuitively because at this value the load is exactly balanced by the energy expended.

The second feature of this model is that the load-velocity relationship can be calculated explicitly. To do so we look for a steady periodic solution of the Fokker-Planck equation (15.128). For $x \neq n\delta$, $p(x)$ must satisfy the differential equation

$$\frac{Df}{kT}p + D\frac{dp}{dx} = -J, \tag{15.130}$$

while at the points $x = n\delta$, the solution experiences a jump,

$$\ln p|_{x_n^-}^{x_n^+} = \frac{\Delta G}{kT}, \tag{15.131}$$

so that

$$p(n\delta^+) = p(n\delta^-) \exp\left(\frac{\Delta G}{kT}\right). \tag{15.132}$$

For periodicity, it must be that

$$p(0) = p(\delta) \exp\left(\frac{\Delta G}{kT}\right). \tag{15.133}$$

In addition, we require $\int_0^\delta p(x)dx = 1$. The solution has

$$J = \frac{D}{\delta^2}\omega_l^2 \frac{1 - \exp(\omega_0 - \omega_l)}{(\exp(\omega_0) - 1)(\exp(-\omega_l) - 1) + \omega_l(\exp(\omega_0 - \omega_l) - 1)}, \tag{15.134}$$

where

$$\omega_0 = \frac{\Delta G}{kT}, \qquad \omega_l = \frac{f\delta}{kT}. \tag{15.135}$$

Furthermore,

$$\lim_{f \to 0} J = 2\frac{D}{\delta^2}\frac{\exp(\omega_0) - 1}{\exp(\omega_0) + 1}. \tag{15.136}$$

The mean velocity of the ratchet is given by

$$\left\langle \frac{dx}{dt} \right\rangle = \int_0^\delta J dx = \delta J. \tag{15.137}$$

A motor pulling cargo

The tilted potential Brownian ratchet was motivated as a model for a polymerization ratchet which is pushing a loaded particle. However, another interpretation is that it describes the movement of a molecular motor moving along a track, pulling a load. Elston and Peskiin (2000) extended this idea by assuming that the molecular motor moves in a titled potential, but that the load is attached to the motor by a spring. They then addressed the question of how the velocity of the motor with its load was affected by the flexibility of the spring.

To study this problem, suppose that the molecular motor is a molecule with diffusion coefficient D_1, the cargo molecule has diffusion coefficient D_2, and that the two are connected by a spring with spring constant κ. Thus, the load on the molecular motor is not fixed but is determined by the distance between motor and cargo times the spring constant. One can readily write down the Fokker Planck equation for the location of this motor-cargo complex. Elston and Peskin used asymptotic analysis for large and small κ to determine the velocity of the motor, but their results can also be explained using intuitive physical reasoning.

Suppose the spring is very stiff $\kappa \to \infty$. With no flexibility, the motor-cargo complex is expected to move as a single molecule with an effective diffusion coefficient. Since (recall from Chapter 2) friction is inversely proportional to the diffusion coefficient $f = \frac{kT}{D}$, and we expect friction to be additive, it follows that the diffusion coefficient of the complex should be

$$D_c = \frac{1}{\frac{1}{D_1} + \frac{1}{D_2}} = \frac{D_1 D_2}{D_1 + D_2}. \tag{15.138}$$

The velocity of the complex should be that for a molecule with diffusion coefficient D_c, that is

$$v = 2\frac{D_c}{\delta}\frac{\exp(\omega_0) - 1}{\exp(\omega_0) + 1}. \tag{15.139}$$

In the opposite limit of a soft spring $\kappa \to 0$, one expects the load to be essentially constant. This is because small fluctuations in the separation between cargo and motor change the load very little. Since the load on the cargo must match the velocity times friction coefficient, it must be that

$$F_l = \frac{kT}{D_2}v. \tag{15.140}$$

so that

$$w_l = \frac{\delta}{D_2}v. \tag{15.141}$$

Figure 15.28: Plots of the velocities of the molecular motor-cargo complex in the hard spring limit ($\kappa \to \infty$) and soft spring limit ($\kappa \to 0$), plotted for $\frac{D_2}{D_1} = 0.1$.

This same load is felt by the motor and the motor and cargo must have the same average velocity, so that

$$v = \frac{D_1}{\delta}\omega_l^2 \frac{1 - \exp(\omega_0 - \omega_l)}{(\exp(\omega_0) - 1)(\exp(-\omega_l) - 1) + \omega_l(\exp(\omega_0 - \omega_l) - 1)}, \qquad (15.142)$$

as well. Here we have two relationships between load and velocity that must both be satisifed. Since (15.141) is a monotone increasing relationship between load and velocity and (**??**) is a monotone decreasing relationship between load and velocity, there is a unique intersection of these two curves, hence a unique velocity.

Plots of the velocities in the hard spring limit and in the soft spring limit as a function of the parameter ω_0 are shown in Fig. 15.28. The important observation is that the velocity in the soft spring limit is always larger than in the hard spring limit. Thus, a flexible spring allows a motor to transport its cargo much more efficiently than does a non-flexible spring.

15.10.3   Flashing Ratchets

The brownian ratchet model presented above is a reasonable qualitative model for a molecular motor, however, it does not provide any insight into the actual physical mechanisms by which a molecular motor works.

To build a more mechanistic model of molecular motors, reconsider how an actin-myosin crossbridge works. In the Huxley model, the crossbridge can be in one of two states, bound or unbound. If it is unbound its movement is governed by diffusion and any applied load. If it is bound, then its movement is additionally governed by a force the strength of which is proportional to its deviation from its preferred position.

This is this idea behind a flashing ratchet model. We suppose there are two conformations, bound and unbound, with binding and unbinding rate constants α and β, respectively. In the unbound state the particle (or motor protein) moves by simple diffusion, while in the bound state, it is also driven by the periodic potential $V(x)$. Since $V(x)$ is periodic, there can be no net movement if the protein is always bound. However, if the potential is asymmetric, then net drift is possible, even against a load.

The reason that net movement is possible can be understood as follows. When the particle is bound it is forced to be mostly near the location of the minimum of the potential well; the deeper the potential well, the more narrowly the particle is confined, and the faster it equilibrates. However, when the particle is unbound it is free to move away from the minimum, and the longer it stays unbound, the more uniform the distribution becomes. Now when the particle is bound again, there is some probability that the particle will remain in the same attractive basin and there is some probability that it will be in an adjacent attractive basin. If the potential is asymmetric, then the probability that the particle falls into an adjacent

attractive basin is biased, with one direction preferred over another, decided by the asymmetry of the potential. Thus, if the minimum of the potential well is biased to the left, the particle is more likely to move to the left.

The following is a simple model of an ideal flashing ratchet. We suppose that the periodic potential is deep with each attracting basin between $n\delta$ and $(n+1)\delta$ having its minimum at $x = n\delta + a$, so that binding has the effect of localizing the particle to exactly the minimum at position $x = n\delta + a$. Suppose we start the process with the particle localized at $x = a$. Then, when unbinding occurs, the probability distribution function for the position of the particle is exactly a delta function localized at $x = a$. Now, diffusion renders the distribution a Gaussian with mean $x = a$ and variance $2Dt$. When the next binding occurs, the probability of being in an attractive basin to the right, p_r, is the probability of being to the right of $x = \delta$, while the probability of moving to the left, p_l, is the probability of being to the left of $x = 0$. Thus,

$$p_r(t) = \frac{1}{2}\mathrm{erfc}\left(\frac{\delta - a}{\sqrt{2Dt}}\right), \qquad p_l(t) = \frac{1}{2}\mathrm{erfc}\left(\frac{a}{\sqrt{2Dt}}\right). \tag{15.143}$$

Since the average time spent unbound is $\frac{1}{\alpha}$ and the average time spent bound is $\frac{1}{\beta}$, the average velocity is approximately (making the approximation that the particle moves no more than one position to the left or right),

$$
\begin{aligned}
V &= \delta\frac{\alpha\beta}{\alpha + \beta}\left[p_r\left(\frac{1}{\alpha}\right) - p_l\left(\frac{1}{\alpha}\right)\right] \tag{15.144} \\
&= \frac{\delta\alpha}{2}\frac{\beta}{\alpha + \beta}\left[\mathrm{erfc}\left(\sqrt{\frac{\alpha\delta^2}{2D}}\left(1 - \frac{a}{\delta}\right)\right) - \mathrm{erfc}\left(\sqrt{\frac{\alpha\delta^2}{2D}}\frac{a}{\delta}\right)\right] \tag{15.145} \\
&= \frac{D}{\delta}\frac{\beta}{\alpha + \beta}v\left(\frac{\alpha\delta^2}{2D}\right), \tag{15.146}
\end{aligned}
$$

where

$$v(\eta) = \eta\left[\mathrm{erfc}\left(\sqrt{\eta}\frac{a}{\delta}\right) - \mathrm{erfc}\left(\sqrt{\eta}\left(1 - \frac{a}{\delta}\right)\right)\right]. \tag{15.147}$$

The function $v(\eta)$ is shown in Fig. 15.29 with $\frac{a}{\delta} = \frac{3}{4}$. It is a nonmonotone function of η, with a maximum at about $\eta = 11.5$.

One can easily understand that there should be an optimal rate of switching between the bound and the unbound states. If the switching occurs rapidly (compared to the rate of diffusion), then there is not much time for the distribution to spread out from the localized minimum and hence there is little opportunity to move to an adjacent potential well. On the other hand, if switching is slow, then much of the time spent in the bound state is wasted, since once the asymmetric potential has localized the particle, there is no reason to remain bound.

It is typical in the literature on flashing ratchets that the driving potential is assumed to be asymmetric. If the binding and unbinding rates are independent of position, this is a necessary condition for net directional transport. However, if the binding and unbinding rates are spatially inhomogeneous, then it is not necessary that the potential be asymmetric. The symmetry can be broken by the arrangement
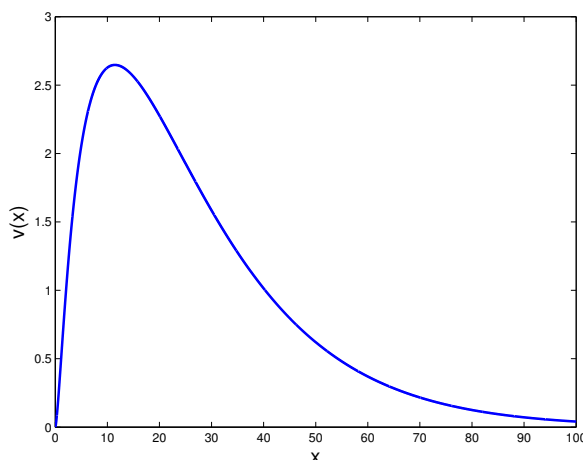
Figure 15.29: Plot of the function $v(x)$ given by (15.147), with $\frac{a}{\delta} = \frac{3}{4}$.

of binding sites relative to the potential well locations. Thus, for example, actin-myosin crossbridge dynamics, wherein the force is assumed to be driven by a simple linear spring, has directed motion because the crossbridge binding site is shifted away from the minimum of the spring potential energy, due to the conformational change that occurs when a weakly bound crossbridge is transformed into a strongly bound crossbridge.

A more detailed analysis of flashing ratchets requires examination of the appropriate Fokker-Planck equations. Suppose that there are a number of chemical states, and that the transition rates between the states are given by $k_{ij}(x)$. Further, assume that in each chemical state the molecule is subject to the potential $\psi_j(x)$. The governing Fokker-Planck equations are then given by

$$\frac{\partial p_j}{\partial t} = \frac{\partial}{\partial x} \left(D\Big((\frac{\psi_j'(x)}{kT} + \frac{f}{kT}) p_j + \frac{\partial p_j}{\partial x} \Big) \right) + \sum_i k_{ij}(x) p_i - \sum_i k_{ji} p_j, \quad (15.148)$$

where $p_j(x, t)$ is the probability distribution for being in state j at position x at time t.

For example, a model of the myosin motor that follows the Huxley crossbridge model would have two states, bound and unbound, with spatially periodic binding and unbinding rates $f(x)$ and $g(x)$, and with a periodic, symmetric potential $\psi(x)$.

This general framework has been used in many studies of real and generic molecular motors. See for example Howard (2001), Reimann (2002), Zwanzig (2001) and references therein.

15.11 Exercises

1. Derive a differential equation for the load in a three-element Hill model with an elastic element in series with a contractile element (as shown in Fig. 15.9) in parallel with an additional elastic element of length L.

2. When a muscle cell dies, its ATP is depleted, with the result that the power stroke stalls and calcium cannot be withdrawn using the Ca^{2+} ATPase. How does this explain rigor mortis?

3. Calculate the response of the Huxley model to a step change in length. In other words, calculate how n changes as a function of t and x, and hence calculate how the tension changes as a function of time following a step change in length.

4. Find the force-velocity relationship for the Huxley model for $v > 0$ with

$$f(x) = \begin{cases} f_{\max}e^{(x-h)/\lambda}, & x < h, \\ 0, & x > h, \end{cases} \tag{15.149}$$

$$g(x) = f_{\max}\left(1 - e^{(x-h)/\lambda}\right), \tag{15.150}$$

$$r(x) = r_{\max}\frac{e^{(x-h)/\lambda} - \alpha}{1 - \alpha}, \tag{15.151}$$

Remark: This model reproduces the Hill force–velocity curve exactly, although it gives poor agreement with the energy flux data.

5. Show that in the Huxley model, $4\phi = v_{\max}$ (at least approximately) if $g_2/(f_1 + g_1) = 3.919$. Hint: to find the maximum velocity set $p = 0$ in (15.37). Then solve numerically for $v_{\max}/\phi$.

6. Assuming that the crossbridges act as linear springs, calculate the force–velocity curve for (15.42) and show that in the limit as $\epsilon \to 0$ and $\delta \to 0$ it does not produce zero force for some positive velocity. Give an intuitive explanation for this.

7. This exercise and the next are based on the discrete binding site models of T.L. Hill (1974,1975). Suppose that each crossbridge is within reach of no more than two binding sites at one time, and that adjacent crossbridges are not within reach of the same two binding sites. Suppose also that adjacent binding sites are separated by a distance Δx, and let x denote the distance of the crossbridge from one of the binding sites, binding site 0, say. Define x such that if the crossbridge is bound to site 0 and has $x = 0$, it exerts no force. Also, let $n_i(x, t), i = 0, -1$, denote the fraction of crossbridges with displacement x that are bound to binding site i.

   (a) Show that the conservation equations are

$$-v\frac{dn_0}{dx} = f(x)[1 - n_0(x) - n_{-1}(x)] - g(x)n_0(x), \tag{15.152}$$

$$-v\frac{dn_{-1}}{dx} = f(x - \Delta x)[1 - n_0(x) - n_{-1}(x)] - g(x - \Delta x)n_{-1}(x). \tag{15.153}$$

where as usual, v denotes the steady contraction velocity.

(b) Derive expressions for the isometric distributions of n_0 and n_{-1}. Compute the isometric force. Show that if the Huxley model is modified to include two binding sites, the isometric force is increased.

(c) Compute the force–velocity curve. Hint: For each v solve the differential equations numerically, using the boundary conditions $n_0(h) = 0$, $n_{-1}(h + \Delta x) = 0$, then substitute the result into the expression for the force and integrate numerically.

(d) Modify the model to include slippage of the crossbridge from one binding site to another. Show that in the limit as slippage becomes very fast, the two differential equations (15.152) and (15.153) reduce to a single equation.

8. Consider the general binding site model (15.53) that incorporates the discrete distribution of binding sites. Why is this equation much harder to integrate than the models we have discussed previously? The isometric solution is considerably easier to calculate than the fully general solution. To do so, let $n_u(x) = 1 - \sum_{-\infty}^{\infty} n(x + i\Delta x)$. Show that

$$1 - n_u(x) = \frac{\sum_{-\infty}^{\infty} \frac{f(x+i\Delta x)}{g(x+i\Delta x)}}{1 + \sum_{-\infty}^{\infty} \frac{f(x+i\Delta x)}{g(x+i\Delta x)}}. \tag{15.154}$$

Use this to calculate the isometric solution $n(x)$.

9. A muscle fiber must be able to produce a force even at negative velocities. For example, if you slowly lower a brick onto a table, your bicep is extending and simultaneously resisting the freefall of the brick. Investigate the behavior of the Huxley model when $v < 0$.

(a) Calculate the force-velocity curve for $v < 0$. Plot the full force-velocity curve using Huxley's parameter values.

(b) Plot $n(x)$ for $v = -0.01$, -0.1 and -1.

(c) Derive an expression for the maximum force as $v \to -\infty$.

10. Show that, in the limit as the number of bound crossbridges goes to infinity, the gliding rate of an actin filament (cf. Section 15.7) is given by

$$v \approx \frac{g_2 h}{2}. \tag{15.155}$$

Hint: When many crossbridges are bound, we recover the Huxley model. Use (15.37) with $p = 0$ to estimate v when $R = \frac{f_1 + g_1}{g_2}$ is small.

11. Use a formal perturbation calculation to find the load-velocity relationship for the polymerization ratchet (15.114) and (15.115) in the limit that α and β are small. That is, introduce a non-dimensional scaling and define an appropriate small parameter ϵ, and then find a power series solution $p = p_0 + \epsilon p_1 + \cdots$ and the corresponding flux $J = J_0 + \epsilon J_1 + \cdots$.

12. Suppose $V(x)$ is the driving potential for a Brownian ratchet, and that $V'(x)$ is periodic with period δ. What is the stall load for the molecular motor driven by the potential $V(x)$?

13. Use a regular perturbation expansion to find the force-velocity curve for the flashing ratchet in the limit that the reaction rates are slow compared to diffusion.

Chapter 16

The Endocrine System

Hormones control a vast array of bodily functions, including sexual reproduction and sexual development, whole-body metabolism, blood glucose levels, plasma calcium concentration, and growth. Hormones are produced in, and released from, diverse places, including the hypothalamus and pituitary, the adrenal gland, the thyroid gland, the testes and ovaries, and the pancreas, and they act on target cells that are often at a considerable physical distance from the site of production. Since they are carried in the bloodstream, hormones are capable of a diffuse whole-body effect, as well as a localized effect, depending on the distance between the production site and the site of action. In many ways the endocrine system is similar to the nervous system, in that it is an intercellular signaling system in which cells communicate via cellular secretions. Hormones are, in a sense, neurotransmitters that are capable of acting on target cells throughout the body, or conversely, neurotransmitters can be thought of as hormones with a localized action.

Despite the analogy with neural transmission, there are significant differences between the endocrine and nervous systems that have important ramifications for mathematical modeling. Not only is the endocrine system extremely complicated, but the data that are presently obtainable are less susceptible to quantitative analysis than, say, voltage measurements in neurons. Further, the distance between the sites of hormone production and action, and the complexities inherent in the mode of transport, make it extraordinarily difficult to construct quantitative models of hormonal control. For these reasons, models in endocrinology are less mechanistic than many of the models presented elsewhere in this book, and thus, in some ways, are less realistic.

There are a number of basic types of hormones. Some, such as epinephrine and norepinephrine, originate from the amino acid tyrosine. Other, water-soluble, hormones are derived from proteins or peptides, while the *steroid* hormones are derived from cholesterol and are thus lipid-soluble. The diversity of the chemical composition of hormones results in a corresponding diversity of mechanisms of hormone action.

Steroid hormones, being lipid-soluble, diffuse across the cell membrane and bind to receptors located in the cell cytoplasm. The resultant conformational change in the receptor leads to activation of specific portions of DNA, thus initiating the

transcription of RNA, eventually (possibly hours or days later) resulting in the production of specific proteins that modify cell behavior. An example of one such hormone is aldosterone, whose effect on epithelial cells is to enhance the production of ion channel proteins, rendering the cell more permeable to sodium.

Other hormones, such as acetylcholine, act by binding to receptors located on the cell-surface membrane and causing a conformational change that results in the opening or closing of ionic channels.

Another important mechanism of hormone action is through second messengers, of which there are several examples in this book. Many hormone receptors are linked to G-proteins; binding of a hormone to the receptor results in the activation of the G-protein, and the triggering of a cascade of enzymatic reactions. For example, in the adenylate cyclase cascade, a wide variety of hormones (including adrenocorticotropin, luteinizing hormone, and vasopressin) cause activation of the G-protein, which in turn activates the membrane-bound enzyme adenylate cyclase. This activation results in an increase in the intracellular concentration of cAMP, and the consequent activation of a number of enzymes, with eventual effects on cell behavior; the specific effects depend on the cell type and the type of hormonal stimulus. In Chapter 7 we described the result of another signaling cascade, the phosphoinositide cascade, in which activation of cell-surface receptors leads to the activation of phospholipase C, the cleavage of phosphotidyl inositol 4,5-bisphosphate, and the resultant production of inositol 1,4,5-trisphosphate (IP_3) and diacylglycerol. As we saw, IP_3 releases Ca^{2+} from internal stores, and this can lead to intracellular Ca^{2+} oscillations and traveling waves.

Hormones can also act by directly converting the receptors into activated enzymes. For example, when insulin binds to a membrane receptor, the portion of the binding protein that protrudes into the cell interior becomes an activated kinase, which then promotes the phosphorylation of several substances inside the cell. The phosphorylation of proteins in the cell leads to a variety of other effects, including the enhanced uptake of glucose.

Much hormonal activity is characterized by oscillatory behavior, with the period of oscillation ranging from milliseconds (β-cell spiking) to minutes (insulin secretion) to hours (β-endorphin). In Table 16.1 are shown examples of pulsatile secretion of various hormones in humans. The pulsatility of normal hormonal activity is not well understood, but has significant implications for the treatment of hormonal abnormalities with drug therapies.

16.1   The Hypothalamus and Pituitary gland

One of the most important components of the endocrine system is the hypothalamus and pituitary gland (Fig. 16.1A). The pituitary gland sits below the hypothalamic region of the brain and is a combination of two different types of cells. The adenohypophysis, or anterior pituitary, is made up of hormone-producing endocrine cells, while the neurohypophysis, or posterior pituitary, consists of secretory neural cells. In fact, the posterior pituitary is a collection of axons of neurons whose cell bodies lie in the hypothalamus. Hormones are synthesized at the cell body and transported to the secretory terminals, where they await release in response to an appropriate

Table 16.1: Examples of pulsatile secretion of hormones in man (Brabant et al., 1992.) Different values correspond to different primary sources.

Hormone	Pulses/Day
Growth hormone	9–16, 29
Prolactin	4–9, 7–22
Thyroid-stimulating hormone	6–12, 13
Adrenocorticotropic hormone	15, 54
Luteinizing hormone	7–15, 90–121
Follicle-stimulating hormone	4–16, 19
β-Endorphin	13
Melatonin	18–24, 12–20
Vasopressin	12–18
Renin	6, 8–12
Parathyroid hormone	24–139, 23
Insulin	108–144, 120
Pancreatic polypeptide	96
Somatostatin	72
Glucagon	103, 144
Estradiol	8–19
Progesterone	6– 6
Testosterone	8–12, 13
Aldosterone	6, 9–12
Cortisol	15, 39

Figure 16.1: A: Schematic diagram of the hypothalamus and pituitary gland. B: Schematic diagram of the pituitary circulation. (Adapted from Berne and Levy, 1998, Figs. 49-1 and 49-2.)
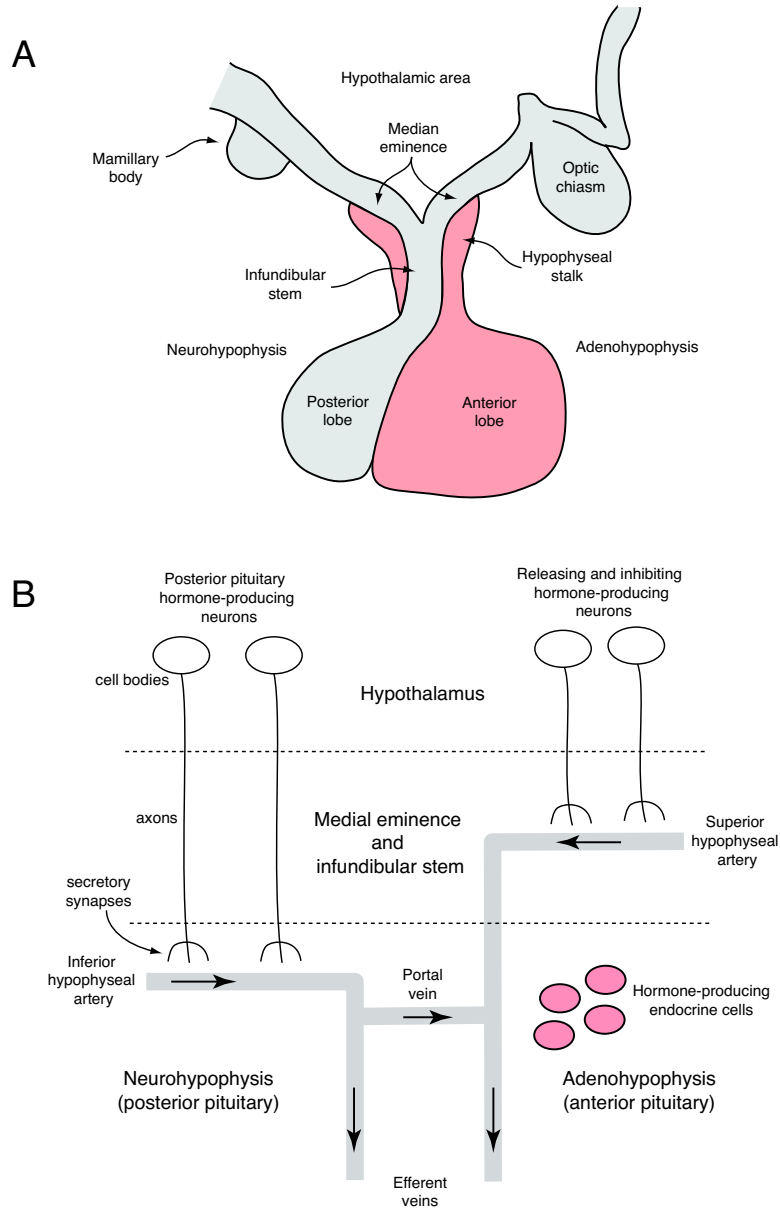
stimulus.

The pattern of blood circulation from the posterior to the anterior pituitary is a crucial part of the function of the gland (Fig. 16.1B). Hormones released from the posterior pituitary enter the inferior hypophyseal artery, whence they can travel through the portal vein to stimulate the endocrine cells of the anterior pituitary. In this way the hypothalamus can exert direct control over the pituitary gland.

Cells in the anterior pituitary can also be stimulated (or inhibited) by hormones released from other hypothalamic neurons that secrete into the superior hypophyseal artery.

Communication between the hypothalamus and pituitary is not all uni-directional. It is possible for hormones secreted from the anterior pituitary to be carried by a reverse blood flow back up to the axons in the median eminence or the cell bodies in the hypothalamus, thus forming a short feedback loop.

Almost all the hormones secreted from the anterior pituitary stimulate the secretion of hormones from target glands in the periphery, such as the thyroid and adrenal glands, or the gonads. This gives a feedforward control system; hormones secreted from the hypothalamic neurons stimulate the secretion of hormones from the anterior pituitary, which in turn stimulate secretion of hormones from target glands in the periphery. For example, secretion of gonadotropin-releasing hormone (GnRH) from the hypothalamus stimulates the secretion of gonadotropins, such as luteinizing hormone (LH) or follicle stimulating hormone (FSH), from the anterior pituitary. These in turn have multiple effects on the gonads, one example of which is stimulating the secretion of estradiol and progesterone from the ovaries.

The enormous complexity of the endocrine system arises partly because the hormones released by the peripheral glands can influence, in their turn, the secretion of the hypothalamus and the anterior pituitary. This allows for a highly complicated system of feedbacks, both positive and negative, most of which involve delays due to the circulation of the blood from one gland to another.

16.1.1 Pulsatile Secretion of Luteinizing Hormone

Luteinizing hormone and follicle-stimulating hormone, known collectively as gonadotropin, have a monthly cycle (in humans) related to ovulation, and also vary periodically on a time scale of hours. Although the precise function of these hourly variations is unclear, they occur in both males and females, and are crucial to development and maturation in both sexes. Gonadotropin is produced by the pituitary gonadotrophs in response to gonadotropin-releasing hormone (GnRH), sometimes called luteinizing-hormone-releasing hormone (LHRH), which is itself produced in the hypothalamus. Periodic variations in gonadotropin secretion are therefore the result of periodic variations in GnRH secretion. In fact, if GnRH secretion is constant rather than pulsatile, the secretion of gonadotropin is greatly reduced, and thus the pulsatility of GnRH secretion has an important regulatory function (Knobil, 1981).

This observation has been used as the basis for clinical treatments of certain reproductive disorders. In women suffering from abnormal GnRH secretion, the pulsatile administration of GnRH can, in some cases, restore normal ovulation and fertility. However, the frequency of the pulse must be controlled carefully. Wildt
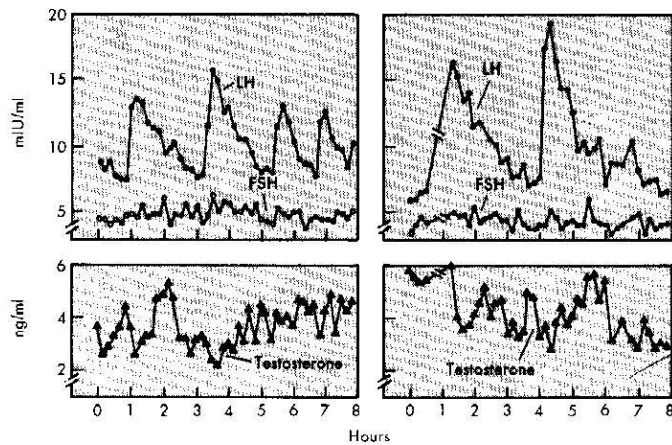
Figure 16.2: Pulsatile secretion of LH, FSH, and testosterone in men. (Berne and Levy, 1993, Fig. 48-15, p. 912.)

et al. (1981) have shown that the secretion of gonadotropin in rhesus monkeys is approximately maximized by the administration of GnRH pulses with a frequency of one per hour. If the frequency of the GnRH pulse is increased to 2 per hour, gonadotropin secretion is inhibited. Conversely, if the frequency is decreased to one pulse every three hours, the rate of secretion of follicle-stimulating hormone (FSH) increases, while the rate of secretion of luteinizing hormone (LH) decreases.

An example of pulsatile secretion of LH and testosterone in males is shown in Fig. 16.2. Although the testosterone secretion is not obviously oscillatory, the fluctuations in LH secretion clearly are.

In males, gonadotropin stimulates the production of testosterone from the testes, while in females it stimulates the production of estradiol from the ovaries. Under some circumstances (see the model for ovulation below) estradiol can stimulate further production of gonadotropin, forming a positive feedback loop. However, estradiol can have both positive and negative feedback effects on the production of gonadotropin. In models of pulsatile testosterone and gonadotropin secretion, negative feedback from estradiol and testosterone to gonadotropin production is the important mechanism.

An early model for LH levels in the rat is that of Shotkin (1974a,b), although this model did not consider oscillatory aspects. One of the earliest models of oscillatory GnRH release is that of Smith (1980, 1983), later extended by Cartwright and Husain (1986) and by Murray (1989). Although these early models are highly simplistic, and phenomenological, they illustrate the basic modeling approach often used to model pulsatile hormone release. A later model of this type is due to Liu and Deng (1991), and was the first to make a serious attempt to determine model parameters by fitting to experimental data, while similar models of the hypothalamus-pituitary-adrenal axis have been constructed by Jelić et al., (2005) and Lenbury and Pornsawad (2005).

A schematic diagram of the Smith model is shown in Fig. 16.3. LHRH, with
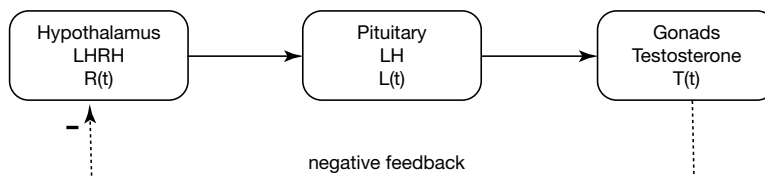
Figure 16.3: Schematic diagram of the Smith model for pulsatile LH release.

concentration R, is produced by the hypothalamus, and stimulates the secretion of LH, with concentration L, from the pituitary. This in turn stimulates the secretion of testosterone, with concentration T, from the testes, which then decreases the rate of LHRH secretion by the hypothalamus. The simplest possible formulation of this model is obtained by assuming that all the reactions, except the feedback of T to R, are linear. In this case

$$\dot{R} = f(T) - b_1 R, \tag{16.1}$$
$$\dot{L} = g_1 R - b_2 L, \tag{16.2}$$
$$\dot{T} = g_2 L - b_3 T, \tag{16.3}$$

where b_i and g_i are positive constants, and $f(T)$ is a decreasing function. This is an example of a feedback repression model, a type of model that was studied in detail in the 1970s by a number of authors (Rapp, 1975,1976; Othmer, 1976; Rapp and Berridge, 1977; Hastings et al., 1977).

Because of the presence of negative feedback, it comes as no surprise that this model can exhibit stable oscillations; the exact conditions under which these occur and are stable are given by Smith (1980).

In a later modification, Murray (1989) introduced a delay into the production of testosterone, replacing the term $g_2 L$ with $g_2 L(t - \tau)$, for some delay τ. They argued that the control of testosterone secretion could occur only after the LH has traveled through the blood to the testes, a process necessarily involving some delay.

Although this gives a minimal increase in model realism, the model remains too simplistic to be a useful model for comparing to data. Nevertheless, it illustrates the basic approach that has been used many times subsequently in the modeling of pulsatile hormone secretion. Typically such models (i) are compartmental, with different compartments for the various hormones and glands, (ii) involve negative or positive feedback, or both, and (iii) use discrete delays, either single or multiple, to model the time taken for the transport of hormones in the blood, and their subsequent action on sites distant from the point of action.

16.1.2   Neural Pulse Generator Models

A completely different approach to modeling pulsatile secretion of LH was taken by Brown et al. (1994), and has since been used in a number of subsequent modeling studies (Brown et al., 2004; MacGregor and Leng, 2005). In this model, pulsatile secretion of LH is assumed to be the result of pulsatile bursts of electrical activity in the hypothalamus, without any need for feedback from the peripheral gland
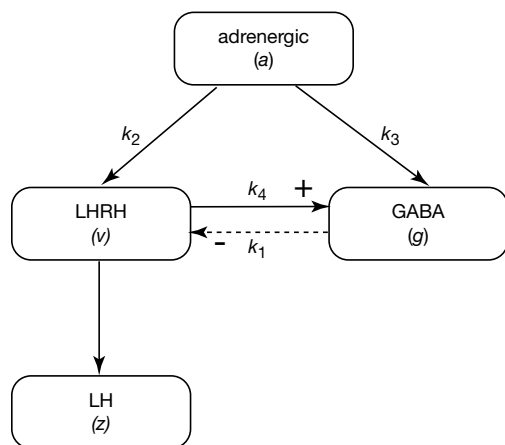
Figure 16.4: Schematic diagram of the neural model for pulsatile LH release.

(although such feedback is not ruled out). Experimental evidence that immortalized LHRH neurons exhibit spontaneous pulsatile electrical activity (Wetsel et al., 1992) lends considerable support to this assumption.

In this model, LHRH neurons stimulate the release of the neurotransmitter GABA from neighboring GABA neurons, which, in turn, decreases the activity of LHRH neurons, thus resulting in a negative feedback loop. Both LHRH and GABA neurons are driven by adrenergic input from the neurotransmitters adrenaline and noradrenaline, which are released from neurons whose cell bodies lie at distant sites in the brainstem. Finally, the activity of LHRH neurons drives the release of LH, with no feedback from LH to LHRH or GABA.

A schematic diagram of this system is given in Fig. 16.4. Each group of neurons is modeled by a single compartment, which assumes complete synchronization within each group. The core of the model is the assumption that the activity of LHRH neurons is intrinsically bistable (see Chapter 5). Thus, if we let v denote the activity of the LHRH neurons, the neurons can be turned off, and not firing (denoted by $v = 0$), or they can be turned on and firing (denoted arbitrarily by $v = 1$). To avoid possible confusion we emphasize that the variable v does not denote the voltage of the synchronized neuron group, merely its activity state. Using the bistable equation to model the activity of the LHRH neurons we get

$$\epsilon \frac{dv}{dt} = v(c - v)(v - 1) - k_1 g + k_2 a(t), \tag{16.4}$$

$$\frac{dg}{dt} = k_3 a(t) + k_4 v - r_g g, \tag{16.5}$$

$$\frac{dz}{dt} = p(v) - r_z z, \tag{16.6}$$

where, as indicated in Fig. 16.4, $a(t)$ denotes a time-dependent adrenergic input, g denotes the activity of GABA neurons, and z denotes the blood concentration of LH. The constants r_g and r_z denote the linear removal rate of g and z respectively. The
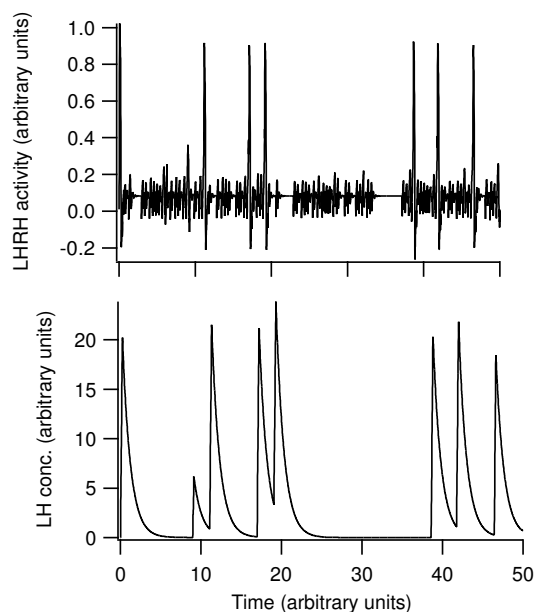
Figure 16.5: Typical results of the neural model for pulsatile LH release. Parameter values are $\epsilon = 1/200$, $c = 0.2$, $k_1 = 1$, $k_2 = 0.02$, $k_3 = 0.02$, $k_4 = 1$, $k_5 = 2.5$, $b_1 = 2$, $b_2 = 0.59$, $b_3 = 10$, $b_4 = 0.1$, $p_1 = 100$, $p_2 = 100$, $p_3 = 0.3$, $d_1 = 1$. All the units are arbitrary.

rate of production of LH is assumed to be some increasing and bounded function of v.

This model has a structure similar to that of the FitzHugh-Nagumo (FHN) model (Chapter 5). Here, however, both the excitatory (v) and inhibitory (g) variables are driven by the same input, and the LH concentration is a filtered version of the LHRH activity. Because of this similarity with the FHN model, we can understand intuitively how this model behaves. If the input a is a low-frequency spike train, each peak of a gives a spike, or a series of spikes in v, as an increase in a is equivalent to an increase in injected current in the FHN model. However, when the frequency of a is high enough, and thus the average level of a is high enough, it is possible that this increases the level of the inhibitory variable, g, to such an extent that further firing of v is prevented. At intermediate frequencies, irregular firing patterns can develop, dependent on the exact balance between excitation and inhibition. Each burst of firing of the LHRH neurons results in a burst of LH release.

A typical solution is shown in Fig. 16.5. The input is given by

$$a(t) = \begin{cases} 3.5, & 0 < t < 0.2, \\ 0, & 0.2 \le t \le 0.21 \end{cases}$$

and then repeated periodically. For this input, LHRH activity is mostly inhibited, but every so often it increases for a short time, resulting in a burst of LH release.

More realistic stochastic inputs were considered by Brown et al. (1994), but these give qualitatively similar results.

Although this model can reproduce patterns of pulsatile LH release that look reasonably realistic, it suffers from the fault of not providing a mechanistic explanation of the pulsatility. Essentially, the pulsatility of hormonal release is assumed to arise from an unexplained pulsatility in a neural network deeper in the brain. Nevertheless, this is as likely an explanation as any other; it is entirely plausible that the origins of pulsatile hormone release lie in neural networks in the brain rather than in an intrinsic oscillatory delayed feedback from the peripheral glands.

Pulsatile release of growth hormone

In humans, and most other mammals, growth hormone (GH) is secreted in a pulsatile manner. In the male rat, which has one of the most defined secretory patterns, pulses occur every three hours, with very little secretion between the pulses. Secretion of GH from the anterior pituitary is stimulated by growth hormone releasing hormone (GHRH) which is secreted from the hypothalamus, and is inhibited by somatostatin, which is also secreted from the hypothalamus. GH, in its turn, activates the production of somatostatin, and inhibits the production of GHRH, both effects occuring with a time delay. In addition, there is evidence that somatostatin can inhibit GHRH neurons directly.

Feedback from the periphery occurs via somatomedins, secreted by the liver and other tissues, which increase the production of both GHRH and somatostatin, and decrease the rate of GH secretion from the pituitary. However, peripheral effects are not included directly in the model discussed below.

A model of this system, similar in style to the model of Section 16.1.2, was constructed and studied by Brown et al. (2004) and by MacGregor and Leng (2005). They showed how, as in the previous model, a train of input pulses to the hypothalamus could be converted into pulsatile release. They also showed how, by mimicking experimental sampling which is done only every 10 minutes or so, the output of the model could be made to look considerably more stochastic, and thus much more realistic.

A schematic diagram of the model structure, and some typical results, are shown in Fig. 16.6.

Pulsatile prolactin secretion

Another model that explains pulsatile hormone secretion by interactions between the hypothalamus and pituitary, without the need for feedback from the periphery is that of Bertram et al. (2006), who modeled the mating-induced prolactin rhythm of female rats. In response to a copulatory stimulus, or an injection of a bolus of oxytocin, the hormone prolactin is secreted by pituitary lactotrophs; in the first 10 days of pregnancy, secretion of prolactin is pulsatile, with regular morning and afternoon surges. Since these rhythms can be observed in ovariectomized rats, it is plausible that the rhythm is generated by interactions between the hypothalamus and the pituitary. Prolactin secretion is regulated principally by the hormone dopamine, which is secreted from the hypothalamus, but, because of the circadian nature of
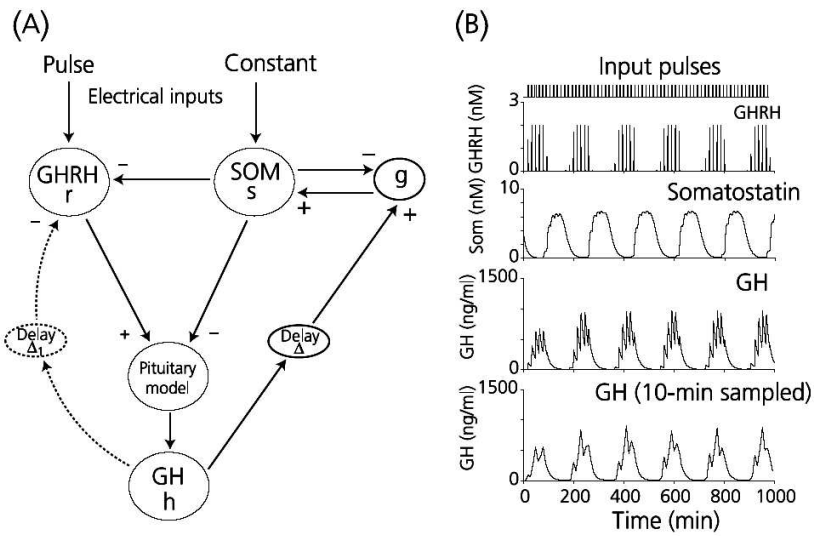
Figure 16.6: Schematic diagram (A) and some typical results (B) of the model for pulsatile GH secretion. The lowest panel of B shows how, by mimicking experimental sampling (which occurs every 10 minutes), the model results can be made to look much more realistic. Reproduced from MacGregor and Leng, 2005, Fig. 6. **Springer: Permission will be needed for this figure. JS.**

the pulsatility, is presumably also influenced by the suprachiasmatic nucleus of the hypothalamus.

The basis for pulsatility in the model is the interaction between dopamine neurons and lactotrophs. Dopamine inhibits the production of prolactin, which in turn activates, with a time delay, the production of dopamine, leading to a classic negative feedback loop, and oscillations. However, Bertram et al. proceed to build a much more complex model on this simple base; the complex model can explain much more of the experimental data, including different surges in morning and afternoon, the persistence of the oscillations after a single brief stimulus, and abrupt termination of the oscillation after 10 days. This work provides a good example of how to build more complex models from simpler ones, ensuring that, at each step, there is a compelling scientific reason for the incorporation of additional complexity.

16.2   Ovulation in Mammals

16.2.1   A Model of the Menstrual Cycle

At birth, the human ovary contains approximately 2 million ovarian *follicles*, which consist of germ cells, or oocytes, surrounded by a cluster of endocrine cells that provide an isolated and protected environment for the oocyte. In the first stage of follicle development, occurring mostly before puberty, and taking anywhere from 13 to 50 years, the cells surrounding the oocyte (the granulosa cells) divide and form several layers around the oocyte, forming the so-called secondary follicle. Subsequent to puberty, these secondary follicles form a reserve pool from which follicles are recruited to begin the second stage of development. In this second stage, follicles increase to a final size of up to 20 mm before they rupture and release the oocyte to be fertilized. The release of the oocyte is called *ovulation*.

A normal menstrual cycle for an adult woman has a period anywhere from 25 to 35 days, and is regulated by the complex interplay of a number of different hormones. In response to the release of LHRH from the hypothalamus, LH and FSH (follicle stimulating hormone) are released from the pituitary. LH and FSH initiate follicle development and control the release of the ovarian hormones, estradiol, inhibin and progesterone. Feedback occurs because the ovarian hormones themselves affect, in multiple ways, the rate of secretion of LH and FSH.

Blood concentrations of all these hormones vary in a systematic manner throughout the menstrual cycle. During the *follicular phase* (which begins after the onset of menstrual bleeding and averages 15 days) LH and FSH levels remain fairly low, while the concentration of estradiol rises. The follicular phase is followed by the *ovulatory phase* (about 1 to 3 days long) during which there is very large increase in LH levels, the so-called LH surge, while the level of estradiol falls rapidly. The final phase, the *luteal phase* (lasting about 13 days), ends with the onset of menstrual bleeding, and is characterized by high levels of progesterone and low levels of LH and FSH.

A model of the menstrual cycle has been constructed by Selgrade, Schlosser and their colleagues (Selgrade and Schlosser, 1999; Schlosser and Selgrade, 2000; Selgrade, 2001; Clark et al., 2002). It consists of two submodels, one for the pituitary
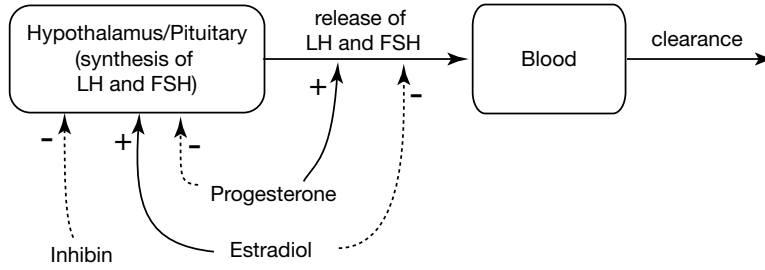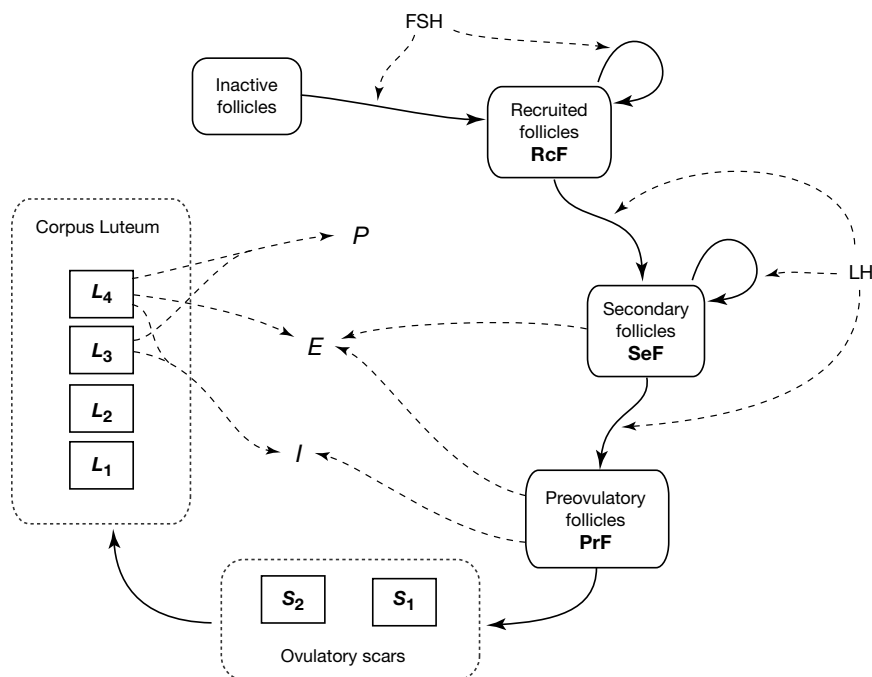
Figure 16.7: Schematic diagram of the pituitary submodel of the model of the menstrual cycle. Adapted from Clark et al., 2002, Fig. 1.

and one for the ovaries. Its most prominent features are, first, the omission of a specific variable for LHRH concentration, and, second, a detailed model of the different stages of the ovary.

The pituitary submodel

A schematic diagram of the pituitary submodel is shown in Fig. 16.7. Both the synthesis and release of LH and FSH are modulated by estradiol and progesterone levels, but in an antagonistic manner. These interactions are not modeled in a mechanistic way, but are described by mathematical functions with the correct qualitative behavior, and thus have a limited biophysical interpretation.

We begin by defining the variables

$$
\begin{aligned}
\mathrm{LH_R} \quad &- \quad \text{amount of LH in the releasable pool,} \\
\mathrm{LH} \quad &- \quad \text{blood concentration of LH,} \\
\mathrm{FSH_R} \quad &- \quad \text{amount of FSH in the releasable pool,} \\
\mathrm{FSH} \quad &- \quad \text{blood concentration of FSH,} \\
E \quad &- \quad \text{blood concentration of estradiol,} \\
P \quad &- \quad \text{blood concentration of progesterone,} \\
I \quad &- \quad \text{blood concentration of inhibin.}
\end{aligned}
$$

Then, based on the feedbacks shown in Fig. 16.7, LH and FSH production and release are modelled by the phenomenological equations

$$\frac{d}{dt}\mathrm{LH_R} = \frac{V_{0L} + \frac{V_{1L}E^8}{K_{mL}^8 + E^8}}{1 + P(t-\tau)/K_{iL}} - \frac{k_L(1 + c_{LP}P)\mathrm{LH_R}}{1 + c_{LE}E}, \tag{16.7}$$

$$\frac{d}{dt}\mathrm{LH} = \frac{1}{v}\frac{k_L(1 + c_{LP}P)\mathrm{LH_R}}{1 + c_{LE}E} - c_L\mathrm{LH}, \tag{16.8}$$

$$\frac{d}{dt}\mathrm{FSH_R} = \frac{V_F}{1 + I(t-\tau)/K_{iF}} - \frac{k_F(1 + c_{FP}P)\mathrm{FSH_R}}{1 + c_{FE}E^2}, \tag{16.9}$$

$$\frac{d}{dt}\mathrm{LH} = \frac{1}{v}\frac{k_F(1 + c_{FP}P)\mathrm{FSH_R}}{1 + c_{FE}E^2} - c_F\mathrm{LH}. \tag{16.10}$$

Figure 16.8: Schematic diagram of the ovary submodel of the model of the menstrual cycle. Adapted from Clark et al., 2002, Fig. 2.

Thus, the rate of production of LH_R is an increasing function of E, but a decreasing function of P, with some time delay, τ. Similarly, the rate of secretion of LH into the blood (i.e., the second term on the right of (16.7) and the first term on the right of (16.8)) is an increasing function of P, but a decreasing function of E. In (16.8) this secretion term is multiplied by the scale factor $1/v$ which takes into account the different volumes of the two compartments. The equations for FSH_R and FSH have the same form, with slightly different functional forms.

The ovary submodel

A schematic diagram of the ovary submodel is shown in Fig. 16.8. Each follicle is assumed to move through 10 different stages, with different rates of hormone production during each stage. This allows for time-dependent rates of hormone release, without the need to build in such time dependence explicitly. The passage of the follicle through the stages is described mostly by linear transitions (making many of the stages act like linear filters, as described briefly in the appendix to Chapter 19, see also Exercises 7 and 7), although some of the transitions are dependent on LH.

Inactive follicles are recruited (i.e., moved into the recruited follicle box, RcF) by FSH (at rate bFSH). Recruited follicles also multiply at a rate proportional to both RcF and FSH. In a similar manner, LH stimulates the movement of follicles

into the secondary phase and then into the preovulatory phase, while simultaneously stimulating an increase in the number of follicles in the secondary phase by a process of positive feedback. Subsequently, the follicle moves through the different phases in a linear fashion. This sequence of steps, as illustrated in Fig. 16.8, is modeled by

$$\frac{d}{dt}\mathrm{RcF} = c\mathrm{FSH} + (c_1\mathrm{FSH} - c_2\mathrm{LH}^\alpha)\mathrm{RcF}, \tag{16.11}$$

$$\frac{d}{dt}\mathrm{SeF} = c_2\mathrm{LH}^\alpha \cdot \mathrm{RcF} + (c_3\mathrm{LH}^\beta - c_4\mathrm{LH})\mathrm{SeF}, \tag{16.12}$$

$$\frac{d}{dt}\mathrm{PrF} = c_4\mathrm{LH} \cdot \mathrm{SeF} - c_5\mathrm{PrF}, \tag{16.13}$$

$$\frac{dS_1}{dt} = c_5\mathrm{PrF} - S_1/k, \tag{16.14}$$

$$k\frac{dS_2}{dt} = S_1 - S_2, \tag{16.15}$$

$$k\frac{dL_1}{dt} = S_2 - L_1, \tag{16.16}$$

$$k\frac{dL_2}{dt} = L_1 - L_2, \tag{16.17}$$

$$k\frac{dL_3}{dt} = L_2 - L_3, \tag{16.18}$$

$$k\frac{dL_4}{dt} = L_3 - L_4. \tag{16.19}$$

To complete the model we need to specify how the levels of estradiol, progesterone and inhibin depend on the various follicle stages. The model assumes that each hormone can be produced only at certain follicle stages, as indicated in Fig. 16.8. Thus we also have the auxiliary equations

$$E = e_0 + e_1\mathrm{SeF} + e_2\mathrm{PrF} + e_3L_4, \tag{16.20}$$

$$P = p(L_3 + L_4), \tag{16.21}$$

$$I = h_0 + h_1\mathrm{PrF} + h_2L_3 + h_3L_4. \tag{16.22}$$

Comparing to data

The model parameters were determined by fitting the model to the data of MacLachlan et al. (1990) who measured blood concentrations of the major hormones over the course of a menstrual cycle. Such a procedure does not determine the parameters to any degree of accuracy, and certainly does not demonstrate that this model is the only possible model that can reproduce the data. Nevertheless, it does show that this model is sufficient to explain many important features of the menstrual cycle.

The parameter values (slightly changed from the original values of Clark et al., 1990) are given in Tables 16.2 and 16.3, and a typical stable oscillatory solution is shown in Fig. 16.9. The LH surge can be clearly seen in the upper panel, while the typical multi-humped solution for the estradiol concentration is shown in the lower panel.

Table 16.2: Parameter values for the pituitary submodel of the model of the menstrual cycle.

LH equations		
k_L	2.5	day^{-1}
c_L	14	day^{-1}
V_{0L}	1263	μg/day
V_{1L}	91000	μg/day
K_{mL}	360	ng/L
K_{iL}	31	nmol/L
c_{LE}	0.005	L/ng
c_{LP}	0.07	L/nmol
τ	2.00	day

FSH equations		
V_F	5700	μg/day
c_F	8.2	day^{-1}
k_F	7.3	day^{-1}
c_{FE}	0.16	(L/ng)^2
K_{iF}	641	U/L
c_{FP}	644	L/nmol
v	2.5	L

Table 16.3: Parameter values for the ovarian submodel and the auxiliary equations of the model of the menstrual cycle.

Ovarian equations		
b	0.004	L/day
c_1	0.006	(L/μg)/day
c_2	0.05	day^{-1}
c_3	0.004	day^{-1}
c_4	0.006	day^{-1}
c_5	1.3	day^{-1}
k	1.43	day
α	0.77	
β	0.16	

Auxiliary equations		
e_0	48	ng/L
e_1	0.1	1/kL
e_2	0.17	1/kL
e_3	0.23	1/kL
p	0.05	(nmol/L)/μg
h_0	274	U/L
h_1	0.5	(U/L)/μg
h_2	0.5	(U/L)/μg
h_3	2	(U/L)/μg
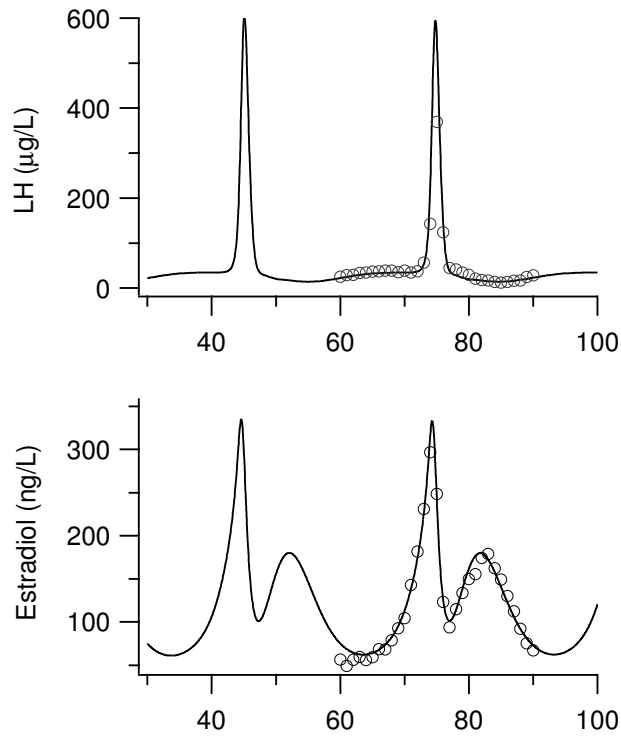
Figure 16.9: An oscillatory solution of the model of the menstrual cycle. The experimental data of MacLachlan et al. (1990) are shown as open circles.

Interestingly, Clark et al. found a second stable limit cycle solution of this same model, a periodic solution that has a slightly smaller period, much less variation in estradiol levels, lower levels of progesterone, and an elevated LH/FSH ratio. Since these features are typical of the disease polycystic ovary syndrome (PCOS), one of the leading causes of female infertility, it is possible that the model might provide a way to investigate proposed treatments. For example, Clark et al. showed that the solution can be switched from the abnormal cycle to the normal cycle by the application of a sufficient amount of exogenous progesterone, but not by the application of too small a dose. Although such conclusions are highly tentative, the possibility of using this model to test proposed treatments is intriguing.

16.2.2   The Control of Ovulation Number

One particularly remarkable feature about ovulation is that, although many follicles begin the second developmental stage, few reach full maturity and ovulate, as the rest atrophy and die. In fact, the number of oocytes reaching full maturity is carefully controlled, so that litter sizes are generally restricted to within a relatively narrow range, and different species have different typical litter sizes. For example, to quote some interesting, if not particularly useful, facts from Asdell (1946), both the dugong and llama have a typical litter size of 1, the crestless Himalayan porcupine typically gives birth to two offspring, while the dingo produces, on average, 3. Different breeds of pigs have litter sizes ranging from 6 to 11.

There must therefore be a complex process that, despite the continuous recruitment of secondary follicles into the second developmental stage, allows precise regulation of the number remaining at ovulation. Further, the temporal periodicity of ovulation is tightly controlled, with ovulation occurring at regularly spaced time intervals.

In addition to questions related to the nature of the control of ovulation, there is the question of efficiency. It appears inefficient to regulate the final number of mature follicles by initiating the growth of many and killing off most of them. One might speculate that it would be more reasonable to initiate growth in only the required number and ensure that they all progress through to ovulation.

Normal ovulation involves growth in both ovaries. However, since removal of one ovary does not change the total number of eggs released during ovulation, the control mechanism is not a local one, but a global one, known to operate through the circulatory system. Maturation of follicles is stimulated by *gonadotropin*, which is released from the pituitary gland. Gonadotropin consists of two different hormones called *follicle-stimulating hormone* (FSH) and *luteinizing hormone* (LH). However, follicles themselves secrete *estradiol*, which stimulates the production of gonadotropin, forming a feedback control loop for the control of follicle maturation (Fig. 16.10).

One of the most elegant models of hormonal control is due to Lacker (1981; Lacker and Peskin, 1981; Akin and Lacker, 1984) and describes a possible mechanism by which mammals control the number of eggs released at ovulation. In the model it is assumed that each follicle interacts with other follicles only through the hormone concentrations in the bloodstream. As follicles mature they become more sensitive to gonadotropin, and their secretion of estradiol increases. The model of
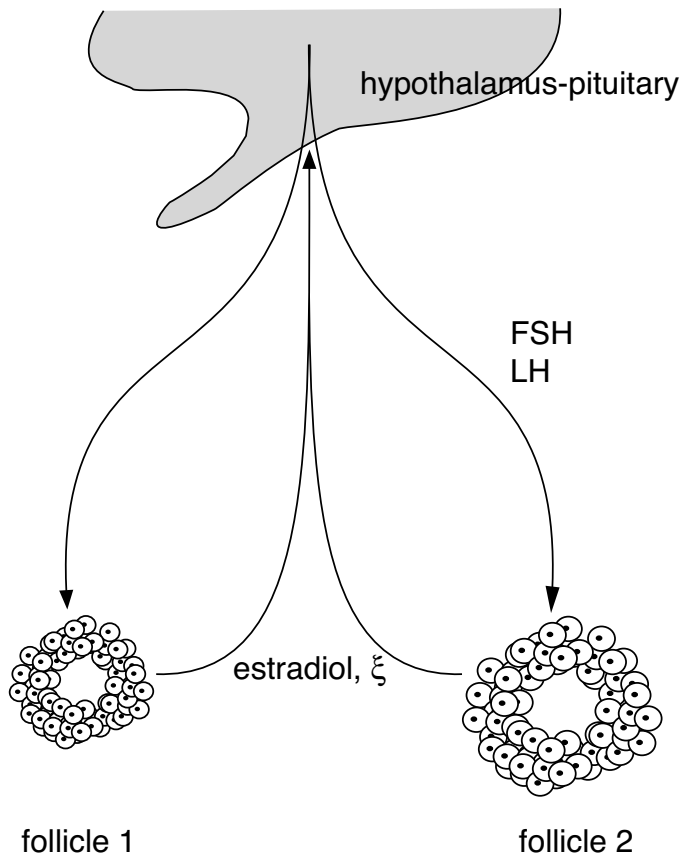
Figure 16.10: Schematic diagram of the Lacker model for ovulation in mammals. (Adapted from Lacker, 1981, Fig. 1.)

this feedback control loop is considerably oversimplified, since it does not incorporate a detailed mechanistic description of how estradiol production depends on gonadotropin or vice versa. However, it provides a phenomenological description of how a global interaction mechanism can be organized to give precise control over the final number of eggs reaching maturity.

The three basic assumptions of the model are that

1. The rate at which follicles secrete estradiol is a marker of follicle maturity.

2. The concentration of estradiol in the blood controls the release of FSH and LH from the pituitary.

3. The concentrations of FSH and LH control the rate of follicle maturation, and at any given instant, the response of each follicle to FSH and LH is a function of the follicle's maturity.

To express these assumptions mathematically, we define the following variables and parameters:

ξ concentration of estradiol,
γ rate of clearance of estradiol from the blood,
V plasma volume,
s_i rate of secretion of estradiol from the ith follicle,
N number of interacting follicles.

Here, all concentrations refer to serum concentrations (i.e., concentrations in the blood). Then, the rate of change of the total estradiol concentration is given by

$$V\frac{d\xi}{dt} = \sum_{i=1}^{N} s_i(t) - \gamma\xi. \tag{16.23}$$

Assuming that the rates of addition and removal of estradiol are much faster than the rate of follicle maturation, we take ξ to be at pseudo-steady state, and thus

$$\xi = \frac{1}{\gamma} \sum_{i=1}^{N} s_i(t) = \sum_{i=1}^{N} \xi_i(t), \tag{16.24}$$

where $\xi_i(t) = s_i(t)/\gamma$ is the contribution that the ith follicle makes to ξ. In general, $d\xi_i/dt$ is a function of both ξ_i and ξ, but does not depend directly on any other $\xi_j, j \neq i$. This is because we assume that local follicle–follicle interactions are not an important feature of the control mechanism, but that follicles interact only via the total estradiol concentration. Hence, the most general form of the model equations is

$$\frac{d\xi_i}{dt} = f(\xi_i, \xi), \qquad i = 1, \ldots, N. \tag{16.25}$$

The function f is called the *maturation function*. Note that the concentrations of FSH and LH do not appear explicitly, as their effect on ξ_i is modelled indirectly by assuming that $\frac{d\xi_i}{dt}$ depends on ξ.

Here we describe one particular form of the maturation function. This form is not based on experimental evidence but is chosen to give the correct behavior. Specifically, we take

$$\frac{d\xi_i}{dt} = f(\xi_i, \xi) = \xi_i\phi(\xi_i, \xi), \qquad i = 1, \ldots, N, \tag{16.26}$$

where

$$\phi(\xi_i, \xi) = 1 - (\xi - M_1\xi_i)(\xi - M_2\xi_i). \tag{16.27}$$

The constants M_1 and M_2 are parameters that are the same for every follicle, so that each follicle obeys the same developmental rules. As a function of ξ_i, for fixed ξ, ϕ is an inverted parabola with a maximum at

$$\xi_{i,\mathrm{max}} = \frac{\xi}{2}\left(\frac{1}{M_1} + \frac{1}{M_2}\right). \tag{16.28}$$

If ξ_i is large or small, the growth of ξ_i is negative, and so this growth rate is fastest for those follicles with maturity within a narrow range, depending on the total estradiol concentration. Thus, with a given initial distribution of follicle maturities, those with ξ_i close to $\xi_{i,\max}$ grow at the expense of the others. Further, since the growth rate f is proportional to ξ_i, the selective growth of the ith follicle leads to an autocatalytic increase in ξ_i.

Numerical solutions

Before we study the behavior of the model analytically, it is helpful to see some typical numerical solutions. The numerical solution of (16.26)–(16.27), with $M_1 = 3.85$, and $M_2 = 15.15$, starting with a group of 10 follicles with initial maturities randomly distributed between 0 and 0.1, shows that the maturity of four or five follicles goes to infinity in finite time, while the other follicles die (Fig. 16.11). Since ovulation is triggered by high, fast-rising estradiol levels, solutions that become infinite in finite time are interpreted as ovulatory solutions. Not only do a similar number of follicles ovulate in each run, they also ovulate at the same time. Hence, ovulatory solutions for ξ_i and ξ_j, say, are ones in which $\xi_i(t)$ and $\xi_j(t) \to \infty$ as $t \to T < \infty$, with $\xi_i/\xi_j \to 1$. These numerical solutions show that the model has the correct qualitative behavior. However, analytic methods give a deeper understanding of how this control is accomplished.

Symmetric solutions

Much of the behavior of the ovulation model can be understood by considering symmetric solutions, in which M of the follicles have the same maturity, while all others have zero maturity. Thus, $\xi_i = \xi/M, i = 1, \ldots, M$, and $\xi_i = 0, i = M + 1, \ldots, N$, in which case the model simplifies to

$$\frac{d\xi}{dt} = \xi + \mu \xi^3, \tag{16.29}$$

where $\mu = -(1 - M_1/M)(1 - M_2/M)$. The solution is given implicitly by

$$\frac{\xi}{\xi_0} \sqrt{\frac{1 + \mu \xi_0^2}{1 + \mu \xi^2}} = e^t, \tag{16.30}$$

where $\xi_0 = \xi(0)$ is the initial value. When $\mu > 0$, $t \to \log\left(\sqrt{(1 + \mu \xi_0^2)/(\mu \xi_0^2)}\right)$ as $\xi \to \infty$, while when $\mu < 0$, t blows up to infinity as $\xi \to \sqrt{-1/\mu}$ (Fig. 16.12). Thus, when $\mu > 0$, ξ becomes infinite in finite time, while when $\mu < 0$, ξ goes to the steady state $\sqrt{-1/\mu}$ as $t \to \infty$. The former solution corresponds to an ovulatory solution, and the time of ovulation, T, is

$$T = \log\left(\sqrt{\frac{1 + \mu \xi_0^2}{\mu \xi_0^2}}\right). \tag{16.31}$$

It follows that if M is between M_1 and M_2, all M follicles progress to ovulation at time T and the other follicles are suppressed, but if M is outside this range, all M
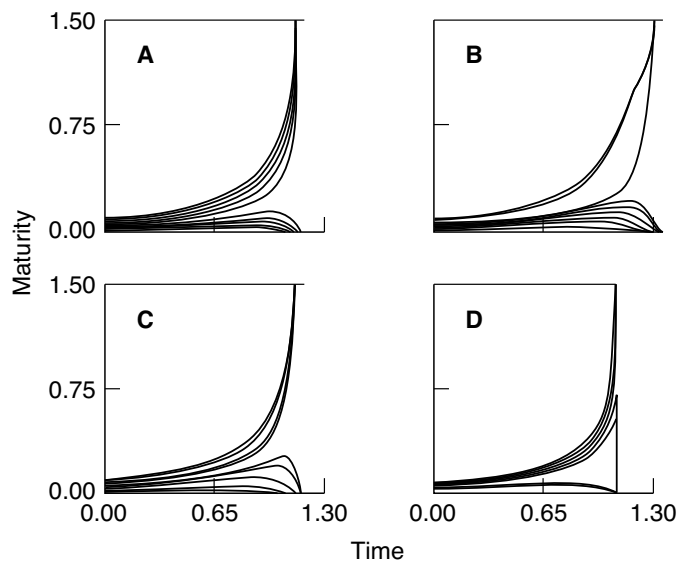
Figure 16.11: Typical numerical solutions of the ovulation model. Each numerical simulation was started with a group of 10 follicles with maturities randomly distributed between 0 and 0.1. Parameter values are $M_1 = 3.85$, $M_2 = 15.15$. In panels A and D five follicles ovulate (their maturity blows up in finite time), while in panels B and C only four ovulate. All other follicles atrophy and die. (Lacker, 1981, Fig. 7.)
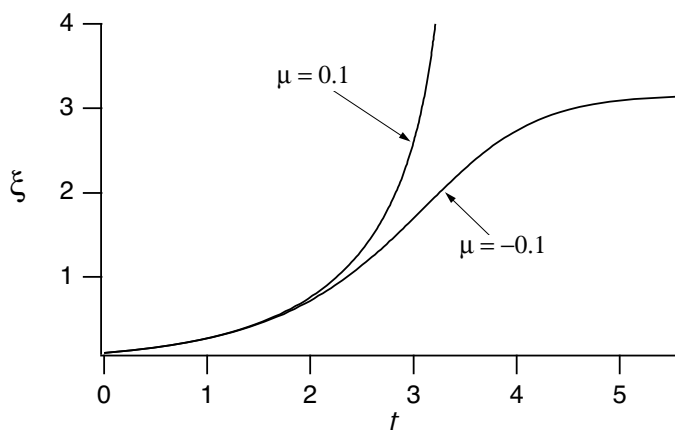
Figure 16.12: Symmetric solutions of the ovulation model for two values of μ. The initial condition was set arbitrarily at $\xi_0 = 0.1$. When $\mu > 0$, the solution blows up in finite time, while when $\mu < 0$, the solution approaches a steady state as $t \to \infty$.

follicles go to the steady (nonovulatory) state

$$\xi_M = \frac{1}{M}\sqrt{\frac{-1}{\mu}} = \frac{1}{\sqrt{(M - M_1)(M - M_2)}}. \tag{16.32}$$

Hence, in the symmetric case, ovulation numbers must be between M_1 and M_2.

Solutions in phase space

To understand these symmetric solutions more fully, and to understand how they relate to the behavior of nonsymmetric solutions, it is helpful to consider the trajectories in the N-dimensional phase space defined by $\xi_i, i = 1, \ldots, N$. Each symmetric solution lies on a line of symmetry l_M of the M-dimensional coordinate hyperplane. This is illustrated in Fig. 16.13 for the case $N = 3$: the l_1 lines are the ξ_1, ξ_2, and ξ_3 axes, the l_2 lines lie in the 2-dimensional coordinate planes, and the l_3 line makes a 45 degree angle with the ξ_1, ξ_2 plane. Note that not all the l_1 and l_2 lines of symmetry are included in the diagram. When M is between M_1 and M_2, l_M contains no critical point, and any trajectory starting on l_M goes to infinity along l_M, reaching infinity in finite time T. However, when M is outside the range of M_1 and M_2, l_M contains a critical point, P_M, and solutions that start on l_M stay on l_M, approaching P_M as $t \to \infty$. In Fig. 16.13, $M_1 = 1.9$ and $M_2 = 2.9$, and so the only possible ovulation number is 2. Thus, each l_1 contains a critical point, P_1, that prevents the ovulation of single follicles, and similarly for l_3. The l_2 lines are the only lines of symmetry not containing a critical point.

The relationship between the symmetric solutions and the general solutions is most easily seen by analyzing the stability of the critical points P_M. Linearizing the model equations (16.25) around P_M gives the linear system (after rearranging
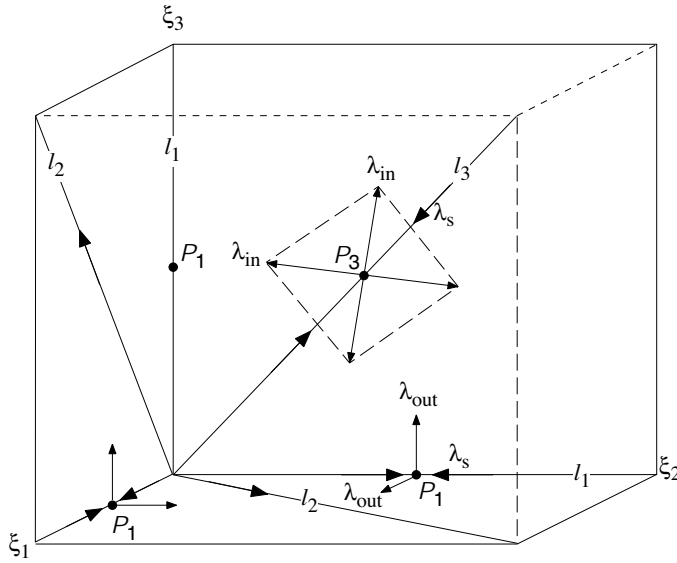
Figure 16.13: Phase space for a system of 3 interacting follicles ($N = 3$) with M_1 and M_2 chosen such that only two follicles ovulate. λ_{out} denotes eigenvalues with eigenvectors that point out of the coordinate hyperplane, while λ_{in} denotes eigenvalues with eigenvectors that are in the coordinate hyperplane. λ_s denotes the eigenvalue with eigenvector in the direction of the line of symmetry.

the variables)

$$\frac{d\tilde{P}}{dt} = A\tilde{P}, \tag{16.33}$$

where $\tilde{P}$ is a small perturbation from P_M and

$$A = \begin{pmatrix} A_1 + B_1 & B_2 \\ 0 & A_2 \end{pmatrix}, \tag{16.34}$$

where A_1 and A_2 are diagonal matrices with diagonal elements a_1 and a_2 respectively, and B_1 and B_2 are matrices with all elements equal to b_1,

$$a_1 = \xi_M \frac{\partial \phi}{\partial \xi_i}\bigg|_{(\xi_M, M\xi_M)}, \qquad a_2 = \phi(0, M\xi_M), \qquad b_1 = \xi_M \frac{\partial \phi}{\partial \xi}\bigg|_{(\xi_M, M\xi_M)}. \tag{16.35}$$

The stability of P_M is determined by the eigenvalues of A, which, because of its block structure, are the eigenvalues of the two diagonal block matrices $A_1 + B_1$ and A_2. Hence, A has an eigenvalue $\lambda_{\text{out}} = a_2$ of multiplicity $N - M$ (from A_2), an eigenvalue $\lambda_s = a_1 + Mb_1 = -2$ of multiplicity 1, and an eigenvalue $\lambda_{\text{in}} = a_1$ of multiplicity $M - 1$, both coming from A_1. To verify the multiplicities of these eigenvalues, note that $A - a_1 I$ is a matrix of rank 1, so has a nullspace of dimension $M - 1$.

In the following discussion we let $Z = (\delta\xi_1, \ldots, \delta\xi_N)$ denote an eigenvector at P_M, and use subscripts to denote the different eigenvectors.

Perturbations along l_M. Corresponding to the simple eigenvalue λ_s is the eigenvector Z_s whose components satisfy $\delta\xi_i = 1, i = 1, \ldots, M$, $\delta\xi_i = 0, i = M + 1, \ldots, N$. Hence, Z_s is in the direction of l_M. Since $\lambda_s < 0$, it follows that l_M is on the stable manifold of P_M. Since symmetry is preserved along l_M, any solution that starts on l_M goes to P_M as $t \to \infty$.

Perturbations orthogonal to l_M in the coordinate hyperplane. Corresponding to the eigenvalue λ_{in} are the eigenvectors $Z_1, \ldots, Z_{M-1}$ whose components are $\sum_{i=1}^{M} \delta\xi_i = 0, \delta\xi_i = 0, i = M + 1, \ldots, N$. Z_1 to Z_{M-1} are independent vectors that lie in the coordinate hyperplane (since all have their last $M - N$ components equal to 0). Since they are also orthogonal to l_M, they span the orthogonal complement of l_M in the coordinate hyperplane.

Perturbations orthogonal to l_M and the coordinate hyperplane. Corresponding to the eigenvalue λ_{out} are the eigenvectors $Z_{M+1}, \ldots, Z_{N-1}$ whose components satisfy $\sum_{i=M+1}^{N} \delta\xi_i = 0, \delta\xi_i = 0, i = 1, \ldots, M$. Finally, there is also the eigenvector Z_N with components $\delta\xi_i = (M - N)b_1, i = 1, \ldots, M$ and $\delta\xi_i = (a_1 - a_2) + Mb_1, i = M + 1, \ldots, N$. All the eigenvectors corresponding to λ_{out} are orthogonal to both l_M and the coordinate hyperplane and span the orthogonal complement of the coordinate hyperplane.

These eigenvectors are illustrated in Fig. 16.13. At the critical point P_1, situated on the ξ_2 axis, there are two independent eigenvectors corresponding to λ_{out}, and these are both orthogonal to l_1, the ξ_2 axis. Note that as the coordinate hyperplane is a line in this case, there are no eigenvectors corresponding to λ_{in}. At P_3 the converse is true. Here there are no eigenvectors corresponding to λ_{out}, as the coordinate hyperplane is the entire space. In three dimensions, the only critical point that could have eigenvectors corresponding to all the eigenvalues $\lambda_s, \lambda_{\text{in}}$, and λ_{out} would be P_2. However, for these parameter values P_2 does not exist as $M_1 < 2 < M_2$.

It remains to determine the stability of each critical point P_M. This is easily done by direct computation of the eigenvalues, which gives

$$\lambda_s = a_1 + Mb_1 = -2, \tag{16.36}$$

$$\lambda_{\text{in}} = a_1 = \frac{(M_1 + M_2)M - 2M_1M_2}{(M - M_1)(M - M_2)}, \tag{16.37}$$

$$\lambda_{\text{out}} = a_2 = -\frac{(M_1 + M_2)M - M_1M_2}{(M - M_1)(M - M_2)}. \tag{16.38}$$

Plots of λ_{in} and λ_{out} as functions of M are shown in Fig. 16.14. For M between M_1 and M_2, P_M does not exist, but for $M > M_2$ and for $M < M^* = M_1M_2/(M_1+M_2)$, λ_{in} and λ_{out} are of opposite signs. For $M^* < M < M_1$, the eigenvalues are both negative. It follows that if there are integers in the interval (M^*, M_1), then there are stable critical points P_M, with $M^* < M < M_1$. All other symmetric critical points are unstable.

Finally, we note (without proof) that there are critical points other than the symmetric ones, but they are all unstable.
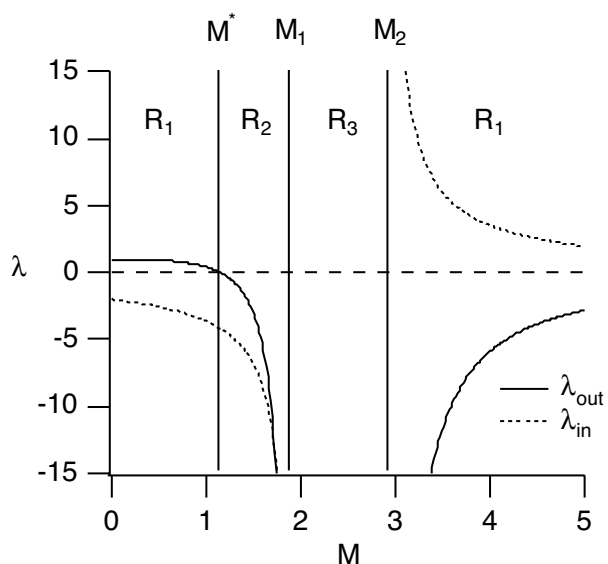
Figure 16.14: The eigenvalues of A as functions of M, calculated with the parameter values $M_1 = 1.9$, $M_2 = 2.9$. In the regions labeled R_1 the steady state P_M is a saddle point; in the region labeled R_2, P_M is stable; and in the region labeled R_3, there are no symmetric critical points, i.e., P_M does not exist for those values of M. Note that only integer values for M have any physical meaning. As described in the text, the eigenvalues λ_{out} and λ_{in} correspond, respectively, to eigenvectors pointing out and in of the symmetric hyperplane.

In summary, when there are no integers in the interval (M^*, M_1) all the critical points are unstable and all the symmetric critical points are saddle points. In fact, from any starting point, all solutions approach infinity along one of the symmetric trajectories, l_M, where $M_1 < M < M_2$. These trajectories become infinite in finite time and are interpreted as ovulatory solutions. However, if there are integers in the interval (M^*, M_1), there are corresponding stable critical points. Any solution that starts in the domain of attraction of one of these stable critical points, P_{M_s} say, approaches P_{M_s} as time increases, and the system becomes "stuck" there. No follicles ovulate, but M_s follicles remain fixed at an intermediate maturity.

Stability of l_M

Although one might expect to observe ovulation numbers anywhere in the range M_1 to M_2, numerical simulations show that only some of these actually occur. This is illustrated in Fig. 16.15, where $M_1 = 3.85$ and $M_2 = 15.15$. In the previous numerical simulations (Fig. 16.11) we started with a fixed number of follicles with random initial maturities normally distributed; in Fig. 16.15, however, follicles mature at random times (generated by a Poisson process), so that the simulation more accurately reflects the physiological situation.

Despite the random entry of follicles into the maturing pool, ovulation occurs at regular intervals, and the ovulation number varies little. Hence, the model generates periodic behavior from stochastic input. Furthermore, although we might expect to see ovulation numbers anywhere in the range 4 to 15, only the ovulation numbers 4 and 5 are observed. An explanation of this observation is found by examining the stability of the symmetric ovulatory solutions. This is done by transforming to a new coordinate system in which the ovulatory solutions, which become infinite in finite time, are transformed into finite critical points. The stability of these finite critical points can then be analyzed using standard linear stability methods.

We begin by noting that the initial ordering of a solution can never change. That is, if ξ_i starts above ξ_j, it remains above ξ_j for all time. This is true because

$$\frac{d}{dt}(\xi_i - \xi_j) = \xi_i \phi(\xi_i, \xi) - \xi_j \phi(\xi_j, \xi) = h(\xi_i, \xi_j, \xi)(\xi_i - \xi_j) \qquad (16.39)$$

for some function h, and as long as ξ_i and ξ_j are bounded, so also is $h(\xi_i, \xi_j, \xi)$. Clearly,

$$\ln(\xi_i(t) - \xi_j(t)) = \ln(\xi_i(0) - \xi_j(0)) + \int_0^t h(\xi_i, \xi_j, \xi) dt. \qquad (16.40)$$

If the right-hand side of this expression is bounded, so also is the left-hand side, so that $\xi_i(t) \neq \xi_j(t)$.

Since the original ordering of the maturities is preserved, we arrange the N follicles in order of maturity, with ξ_1 denoting the follicle with the greatest maturity, and define a new time scale by

$$\tau(t) = \int_0^t \xi_1^2(s) \, ds. \qquad (16.41)$$

As $t \to T$, the finite time of ovulation, $\tau(t) \to \infty$. For as ξ_1 gets large, $d\xi_1/dt \approx \xi_1^3$, and hence ξ_1^2 behaves like $1/(T - t)$ as $t \to T$. Furthermore, ξ_1^2 is positive, and
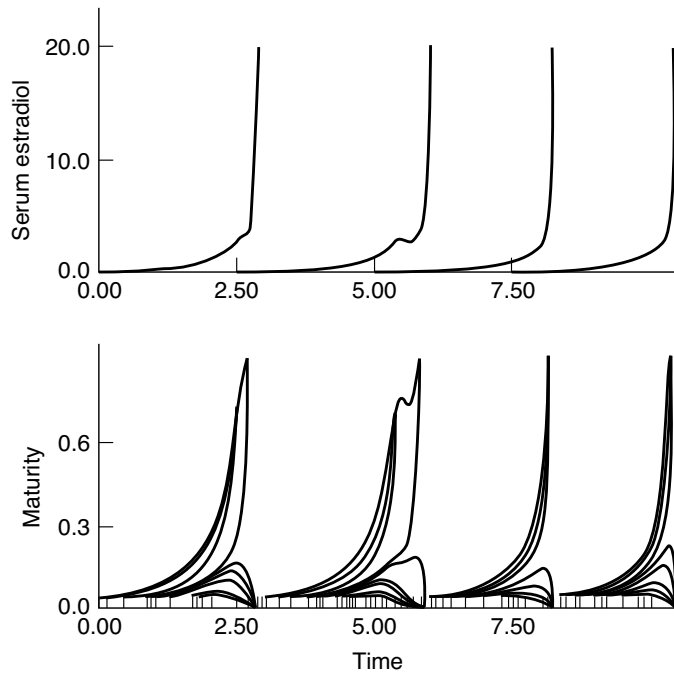
Figure 16.15: Typical solutions when follicles begin to develop at random times, generated by a Poisson process. Each small tick on the horizontal axis marks the initiation of development in a single follicle. Although the parameter values are $M_1 = 3.85$, $M_2 = 15.15$, and thus one might expect to observe ovulation numbers ranging from 4 to 15, only the ovulation numbers 4 and 5 are observed. (Lacker and Peskin, 1981, Fig. 11.)

so τ is an increasing function of t that is therefore invertible. We use the inverse function to define new variables

$$\gamma_i(\tau) = \frac{\xi_i(t(\tau))}{\xi_1(t(\tau))}, \tag{16.42}$$

$$\Gamma(\tau) = \frac{\xi(t(\tau))}{\xi_1(t(\tau))}. \tag{16.43}$$

In terms of these new variables the model equations (16.26)–(16.27) become

$$\frac{d\gamma_i}{d\tau} = \gamma_i \Phi(\gamma_i, \Gamma), \qquad i = 1, \dots, N, \tag{16.44}$$

$$\Gamma = \sum_{j=1}^{N} \gamma_j, \tag{16.45}$$

$$\Phi(\gamma_i, \Gamma) = (1 - \gamma_i)[M_1 M_2 (1 + \gamma_i) - \Gamma(M_1 + M_2)]. \tag{16.46}$$

Note that $\gamma_1(\tau) \equiv 1$, and $0 \le \gamma_i(\tau) \le 1$ for each i.

All ovulatory and anovulatory solutions correspond to critical points of (16.44)–(16.46) of the form

$$\gamma_i = \begin{cases} 1, & i = 1, \dots, M, \\ 0, & i = M + 1, \dots, N. \end{cases} \tag{16.47}$$

Although ovulatory and anovulatory solutions look the same, they can be distinguished by determining whether the original variable ξ is finite. If so, the critical point corresponds to an anovulatory solution.

Equations (16.44)–(16.46) have only two distinct eigenvalues,

$$\lambda_1 = (M_1 + M_2)M - 2M_1 M_2, \tag{16.48}$$
$$\lambda_2 = -(M_1 + M_2)M + M_1 M_2, \tag{16.49}$$

which are plotted in Fig. 16.16. If M lies between M^* and $2M^*$, then both λ_1 and λ_2 are negative, so that the critical point is stable. Otherwise, the critical point is unstable. It follows that only ovulation numbers between M_1 and $2M^*$ are stable, and are therefore observable.

In the numerical simulations shown in Fig. 16.15, $M_1 = 3.85$ and $M_2 = 15.15$, in which case $2M^* = 6.14$. This is consistent with the numerical simulations in which only ovulation numbers 4 and 5 were observed. One possible reason why ovulation number 6 is not observed is that it lies close to the stability boundary. Thus, its domain of attraction is relatively small, and therefore the probability that a random process finds this domain of attraction is also small.

The effect of population size

With this model we can suggest an answer to the question of efficiency, namely, why do so many follicles begin the maturation process, only to atrophy and die? The answer appears to be that the mean time to ovulation is controlled more precisely
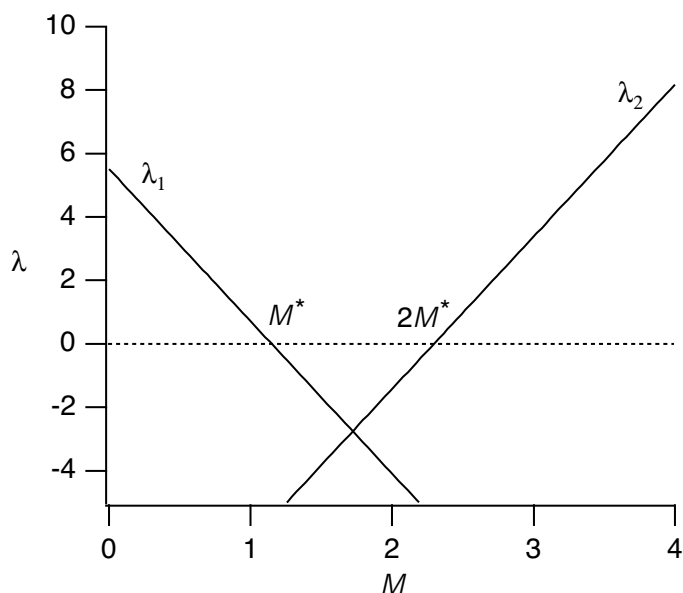
Figure 16.16: The eigenvalues λ_1 and λ_2 of the ovulation model in the transformed variables γ_i and τ.

by a large population than by a small one. This is illustrated in Fig. 16.17. For this figure, the model was simulated for 80 cycles, and the distribution of ovulation numbers and times was plotted for three different population sizes. Each population had the parameter values $M_1 = 6.1, M_2 = 5000$, and thus the expected ovulation numbers lie in the range 7 to 12. As the population size increases, the mean ovulation number decreases, but the shape of the distribution does not change a great deal. However, although the mean ovulation time (shown here centered at 0) does not change as the population size is increased, the distribution sharpens dramatically, and the range of observed ovulation times is dramatically reduced. Thus, while the majority of follicles atrophy and die, they have an important, although not immediately obvious, function: helping to regulate the timing of ovulation. This provides a possible explanation of why women near menopause (i.e., with fewer available oocytes) typically experience menstrual irregularities.

An application of the Lacker model

The Lacker model has been used as a tool to predict the response to ovarian superstimulation (Sarty and Pierson, 2005). A possible treatment for infertility is superstimulation of the ovaries by exogeneous doses of hormones; an equivalent to FSH during the first portion of the ovulation cycle, followed by an equivalent to LH. In one treatment program, the size of the follicles and the level of estradiol were measured over the course of the treatment, with a number of individual follicles followed from day to day. For each follicle followed, this gave a vector $\xi_i(t), \xi(t), \dot{\xi}_i(t),$
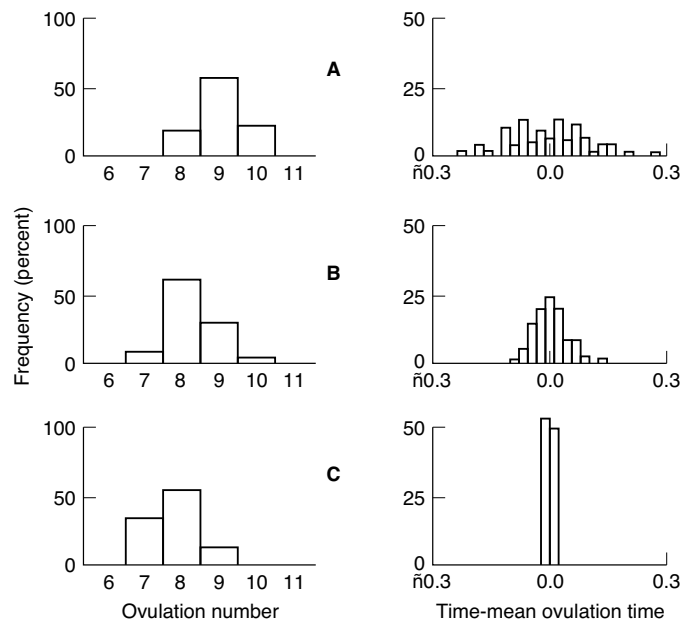
Figure 16.17: The effect of the population size on the distribution of ovulation numbers. In panels A, B, and C, there are, respectively, 10, 100, and 1000 follicles interacting. Parameter values are $M_1 = 6.1$, $M_2 = 5000$. As the follicle population gets larger, the mean ovulation time decreases only slightly, while the standard deviation of the distribution of ovulation times decreases. Thus, larger populations allow more precise control over the ovulation number. (Lacker, 1981, Fig. 13.)

where the derivative is calculated numerically from the data. Model parameters were then chosen so that $\dot{\xi}_i - \xi_i \phi(\xi_i, \xi)$ is as small as possible in the least squares sense.

Because the experimental data were collected during a period of exogenous superstimulation of the ovaries, one should not expect the Lacker model to give a close fit to the data, and indeed it does not. However, the model is a useful predictor of the ratio of ovulating follicles to dominant follicles (defined to be those with a diameter of 19 mm or greater). In particular, the model predicts that faster-growing follicles are less likely to ovulate, i.e., the speed with which the largest follicle reaches the target size of 19 mm is inversely related to probable ovulatory success. This result is similar to others which have shown that follicles from women who did not ovulate show more rapid growth patterns than follicles from women who do. Although the reasons for this are unclear, it gives a clear indication that to increase the number of ovulating follicles, it might be advantageous to slow the rate of follicle growth, possibly by reducing the size of the exogeneous FSH dose.

16.2.3   Other Models of Ovulation

Although this model of ovulation is one of the simplest and most elegant, other, more complex, models have been constructed. For example, Schwarz (1969) and Bogumil et al. (1972) have proposed models that incorporate large numbers of parameters and are based more directly on experimental data.

The Lacker model was extended and generalized by Chávez-Ross et al. (1997) in a study of the possible mechanisms underlying polycystic ovary syndrome, a condition in which many large follicles develop but none becomes predominant, leading to failure of ovulation.

A model of a different type is due to Faddy and Gosden (1995). They constructed a compartmental model of follicle dynamics over the lifetime of an individual female and fit their model to experimental data to obtain follicle growth and death rates as functions of the individual's age. Although this compartmental model does not provide insight into the mechanisms underlying periodic ovulation and a constant ovulation number, it provides an understanding of follicle dynamics over a larger time span.

Most recently, Clément, Monniaux and their colleagues (Clément et al., 1997, 2001, 2002; Clément, 1998; Echenim et al., 2005) have modeled the follicle selection process, in a manner quite different from that of Lacker. In the Clément model, the progress of the granulosa cells through the cell cycle (see Chapter 10) is monitored, with some cells becoming atretic (i.e., dying) and others becoming differentiated. For each follicle, the maturity of the granulosa cells is described by a density function which satisfies a conservation PDE. The rates of entry into apoptosis and differentiation are governed by the blood concentration of FSH, where the rate of FSH production is governed by the total maturity of all the follicles, thus giving feedback between the follicles.

So far (i.e., by 2007), this model has been solved only for a population of five follicles, so it is too early to know whether or not it will prove to be an accurate and useful model of the follicle selection process.

16.3 Insulin and Glucose

Hormones secreted from cells in the pancreas are responsible for the control of glucose, amino acids, and other molecules that are necessary for metabolism. The pancreas contains a large number of secretory cells, grouped into about one million *islets of Langerhans* consisting of approximately 2,500 cells each. There are three principal secretory cell types: the α-cells secrete glucagon, the β-cells secrete insulin (see Chapter 9), and the δ-cells secrete somatostatin. Glucagon and insulin have complementary actions. A high concentration of glucose in the bloodstream (corresponding to an overabundance of nutrients) stimulates the production of insulin, which in turn induces storage of excess nutrient and decreases the rate at which nutrients are mobilized from storage areas such as adipose tissue or the liver. Insulin acts principally on three tissues: striated muscle (including the heart), liver, and adipose tissue. All the actions of insulin apparently stem from its interaction with a specific receptor in the plasma membrane of insulin-sensitive cells. How this interaction leads to the many actions of insulin on the cell is not fully understood. In striated muscle and adipose tissue, one important action of insulin is to stimulate the transport of glucose into the cell by a specific carrier (or carriers) in the plasma membrane. It appears to do this by recruiting glucose carriers to the plasma membrane from intracellular sites where they are inactive. Insulin thus increases the $V_{\max}$ of transport, often as much as 10- to 20-fold. When glucose enters the cell it is rapidly phosphorylated and metabolized.

In the case of the liver, insulin does not increase the rate of transport of glucose into the cell (although it increases the net uptake of glucose). In the liver, insulin acts on a number of intracellular enzymes to increase glucose storage and decrease mobilization of glucose stores. The details of how insulin does this are far from clear.

Glucagon raises the concentration of glucose in the bloodstream. It acts mainly but not entirely on the liver, where it stimulates glycogen breakdown and the formation of glucose from noncarbohydrate precursors such as lactate, glycerol, and amino acids. Glucagon released in the islets stimulates the beta cells in the vicinity to secrete insulin.

Insulin units

Historically, a unit (U) of insulin was defined to be that amount of insulin (in cubic centimeters) that lowers the percentage of blood sugar in a normal rabbit to 0.045 in 2 to 6 hours. The crudity of such a unit was the result of the fact that it was not possible to purify insulin until relatively recently, and thus a bioassay was the only way of determining the amount. An excellent discussion of historical insulin units is given by Lacy (1967).

Later, mouse units became more convenient, and a unit was defined to be the amount of insulin required to produce convulsions in half the mice under standard conditions. A mouse unit is about 1/600 of a rabbit unit. Fortunately, insulin extracted from most animals has equivalent activity in rabbits, mice, and men, although the guinea pig and capybara are exceptions to this rule. Various modifications were made to the conditions of these assays, but with the advent of reasonably

pure preparations of insulin the unit has been redefined as 1/24 milligrams.

16.3.1   Insulin Sensitivity

Insulin resistance (i.e., a lowered ability for insulin to control blood glucose) plays a crucial role in diabetes, and has been implicated in a host of other diseases. Thus there have been a large number of studies of how insulin sensitivity can be measured experimentally (Mari, 2002). In general, these methods involve the addition of exogeneous glucose and/or insulin, and then measurement of the time course of their blood concentrations. One of the most accurate methods is the euglycemic hyperinsulinemic glucose tolerance test (deFronzo et al., 1979). In this test a steady intravenous infusion of insulin is administered, to bring the blood concentration to a steady high level, while simultaneously the blood glucose concentration is clamped by continuous infusion of glucose through a second intravenous infusion. Once a steady state has been reached (which can take over an hour), the amount of glucose needed to maintain the glucose clamp is a measure of insulin sensitivity. At high insulin levels there is little glucose production by the liver, and thus the rate of glucose removal from the blood is due almost entirely to glucose metabolism, including uptake into the periphery. Thus, if insulin sensitivity is higher, it takes more glucose added continuously in the clamp to maintain a steady state; conversely, if insulin sensitivity is low then the high insulin levels will not stimulate much glucose removal, and less added glucose is needed to maintain the steady state. However, since this procedure requires simultaneous IV infusions over a long time, and numerous blood samples, it is difficult to implement.

   Subsequent methods have tried to find ways of determining insulin sensitivity in ways that are easier to apply. Some, such as the intravenous glucose tolerance test (IVGTT; for a mathematical study of this test see Gaetano and Arino, 2000), examine the response to a single intravenous bolus of glucose, while others such as the oral glucose tolerance test (OGTT; Mari et al., 2001) consider the response to a bolus of glucose taken orally. These methods depend crucially on mathematical models of the underlying processes, and most use, in one form or another, the so-called *minimal model* of Bergman et al. (1979).

   The meal tolerance test of Caumo et al. (2000), which is similar to the OGTT, provides a typical example of this kind of approach. In this test, glucose is administered orally and then the blood concentration of both glucose and insulin are measured as functions of time. (As a matter of interest, the meal consisted of 15 g Weetabix, 10 g skimmed milk, 250 ml pineapple juice, 50 g white meat chicken, 60 g wholemeal bread and 10 g polyunsaturated margarine, which seems less than pleasant for the experimental subjects!)

   To build a model of insulin sensitivity, we let $G(t)$, in units of mg/dl, denote the blood concentration of glucose, and let $X(t)$, in units of $\min^{-1}$, denote insulin activity. We assume that G has a base value, G_b, to which it returns in the absence of perturbation, and that G is decreased at a rate proportional to both X and G. Hence,

$$\frac{dG}{dt} = p_1(G_b - G) - XG + \frac{r(t)}{V}, \tag{16.50}$$

where $r(t)$ is the rate at which glucose enters the bloodstream as a result of the

meal, and is not known *a priori.* V is the glucose distribution volume per unit body weight, in units of ml/kg.

Similarly, insulin activity is assumed to increase whenever the concentration of insulin, $I(t)$ (in units of μU/ml), is above its base level, I_b, and is also assumed to decay spontaneously. Thus,

$$\frac{dX}{dt} = p_3(I(t) - I_b) - p_2 X. \tag{16.51}$$

The parameter p_2 has units min^{-1}, while p_3 has units ml $\mu\text{U}^{-1}\text{min}^{-2}$. Notice that at steady state, $X = \frac{p_3}{p_2}(I - I_b)$, so that the ratio $\frac{p_3}{p_2}$ is a measure of insulin sensitivity. That is, the larger $\frac{p_3}{p_2}$, the greater is the insulin activity for a given insulin concentration.

The test for insulin sensitivity is an inverse problem. That is, the glucose and insulin concentrations, $G(t)$ and $I(t)$, are measured quantities, and we wish to determine the ratio $\frac{p_3}{p_2}$.

First, notice that by integrating (16.51) from $t = 0$ to $t = \infty$, we find

$$\frac{p_3}{p_2} = \frac{\int_0^\infty X \, dt}{\int_0^\infty (I(t) - I_b) \, dt}, \tag{16.52}$$

where we have assumed that X is the same at the beginning ($t = 0$) as at the end ($t = \infty$) of the experiment, so that $\int_0^\infty \frac{dX}{dt} \, dt = 0$.

Since $I(t)$ is known, it remains to express $\int_0^\infty X \, dt$ in terms of known quantities. Dividing (16.50) by G and integrating from $t = 0$ to $t = \infty$ we learn that

$$\int_0^\infty \frac{1}{G}\frac{dG}{dt} dt = p_1 \int_0^\infty \frac{G_b - G}{G} dt - \int_0^\infty X \, dt + \frac{1}{V}\int_0^\infty \frac{r(t)}{G} \, dt. \tag{16.53}$$

However, since G is also the same at the beginning and end of the experiment, so that $\int_0^\infty \frac{1}{G}\frac{dG}{dt} dt = 0$, it follows that

$$\int_0^\infty X \, dt = p_1 \int_0^\infty \frac{G_b - G}{G} dt + \frac{1}{V}\int_0^\infty \frac{r(t)}{G} \, dt. \tag{16.54}$$

If we can estimate $r(t)$ the problem is solved. One option is to assume some functional form for $r(t)$, ensuring it peaks at approximately the correct time and has the correct integral (as the total amount of added glucose is known). However, the approach used by Caumo et al. (2000) was to estimate the integral of r/G based on knowledge of G. An alternative model for G is

$$\frac{dG}{dt} = a(G_b - G) + br(t), \tag{16.55}$$

for some unknown constants a and b. The assumption here is that both (16.55) and (16.50) provide reasonable descriptions of the data for $G(t)$, provided a and b are chosen appropriately.

However we can eliminate a and b from the problem as follows. First we integrate (16.55) directly, to get

$$\frac{a}{b} = \frac{\int_0^\infty r(t) \, dt}{\int_0^\infty (G - G_b) \, dt}, \tag{16.56}$$

Next we divide (16.55) by G and integrate, to get

$$\int_0^\infty \frac{r(t)}{G}\,dt = \frac{a}{b} \int_0^\infty \left(\frac{G - G_b}{G}\right)\,dt. \qquad (16.57)$$

Substituting for $\frac{a}{b}$ we find that

$$\int_0^\infty \frac{r(t)}{G}\,dt = \left(\frac{\int_0^\infty r(t)\,dt}{\int_0^\infty (G - G_b)\,dt}\right) \int_0^\infty \left(\frac{G - G_b}{G}\right)\,dt. \qquad (16.58)$$

Since $\int_0^\infty r(t)\,dt$ is the total amount of glucose ingested in the meal, which is known, the combination of (16.52), (16.54) and (16.58) gives an expression for p_3/p_2 entirely in terms of known quantities, as desired.

16.3.2   Pulsatile Insulin Secretion

Insulin secretion oscillates on a number of different time scales, ranging from tens of seconds to more than 100 minutes. The fast oscillations are caused (at least in part) by bursting electrical activity described in Chapter 9. During each burst of action potentials the cytosolic Ca^{2+} concentration rises as Ca^{2+} flows in through voltage-gated Ca^{2+} channels, and this rise in Ca^{2+} stimulates insulin secretion. Oscillations with a much larger period of around 100 minutes are also observed, and are called *ultradian oscillations* (Fig. 16.18). Finally, oscillations with intermediate frequencies of around 10 minutes or so also occur. One of the earliest observations of these oscillations was made in the rhesus monkey by Goodner et al. (1977), and some of their results are reproduced in Fig. 16.19. Glucagon and insulin oscillate out of phase, while insulin and glucose are in phase, with the increase of glucose leading the increase of insulin by an average of about one minute. Oscillations with intermediate frequency are also observed in isolated rat islets (Bergstrom et al., 1989; Berman et al., 1993), although, as can be seen from Fig. 16.20, spectral analysis is usually necessary to determine the principal underlying frequency. Once the underlying trend has been removed, a spectral decomposition of the data shows a frequency peak at about 0.07 min^{-1}, corresponding to a period of 14.5 minutes.

Ultradian insulin oscillations have a number of observable features. First, oscillations occur during constant intravenous glucose infusion and are not dependent on periodic nutrient absorption from the gut. However, damped oscillations occur after a single stimulus such as a meal. Second, glucose and insulin concentrations are highly correlated, with the glucose peak occurring about 10–20 minutes earlier than that of insulin. Third, the amplitude of the oscillations is an increasing function of glucose concentration, while the frequency is not; and fourth, the oscillations do not appear to depend on glucagon.

Although there are many possible mechanisms that are consistent with the above observations, they can all be explained by a relatively simple model (Sturis et al., 1991) in which the oscillations are produced by interactions between glucose and insulin.

A schematic diagram of the model is shown in Fig. 16.21. There are three pools in the model, representing remote insulin storage in the interstitial fluid, insulin in the
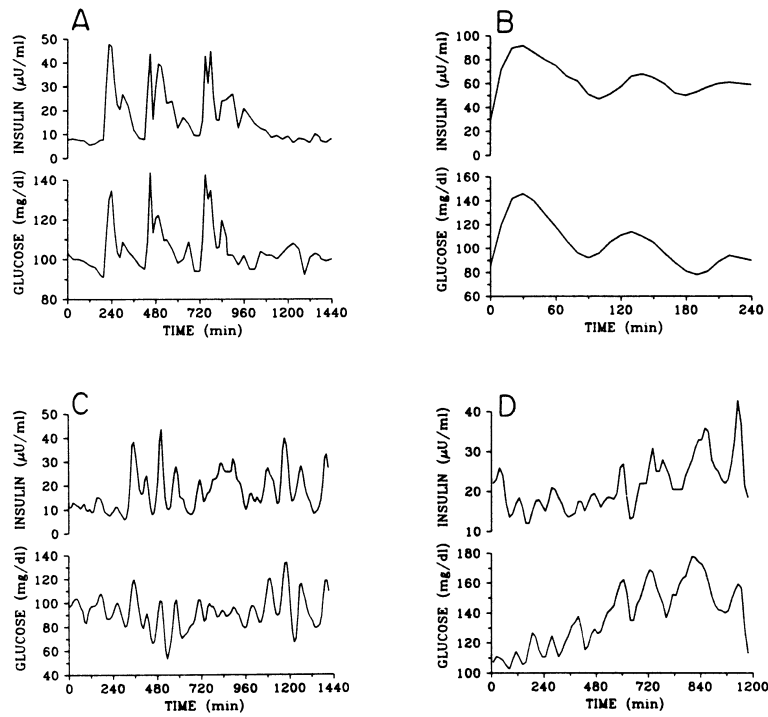
Figure 16.18: Oscillations of insulin and glucose. A: During the ingestion of 3 meals. B: During oral glucose. C: During continuous nutrition. D: During constant glucose infusion. Oscillations with a period of around 120 minutes occur even during constant stimulation (i.e., constant glucose infusion), and occur in a damped manner after a single stimulus such as ingestion of a meal. (Sturis et al., 1991, Fig. 1.)
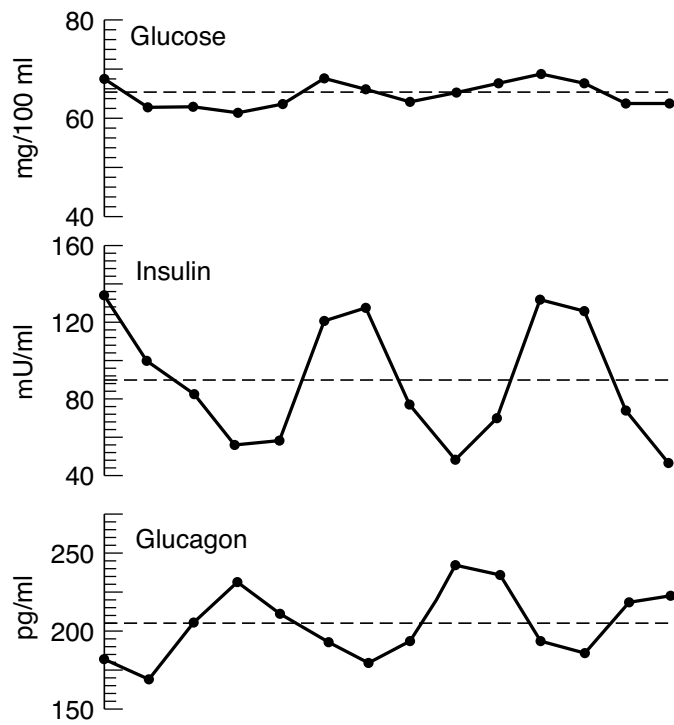
Figure 16.19: Intermediate frequency oscillations of glucose, insulin, and glucagon in monkeys. (Goodner et al., 1977, Fig. 1A.)
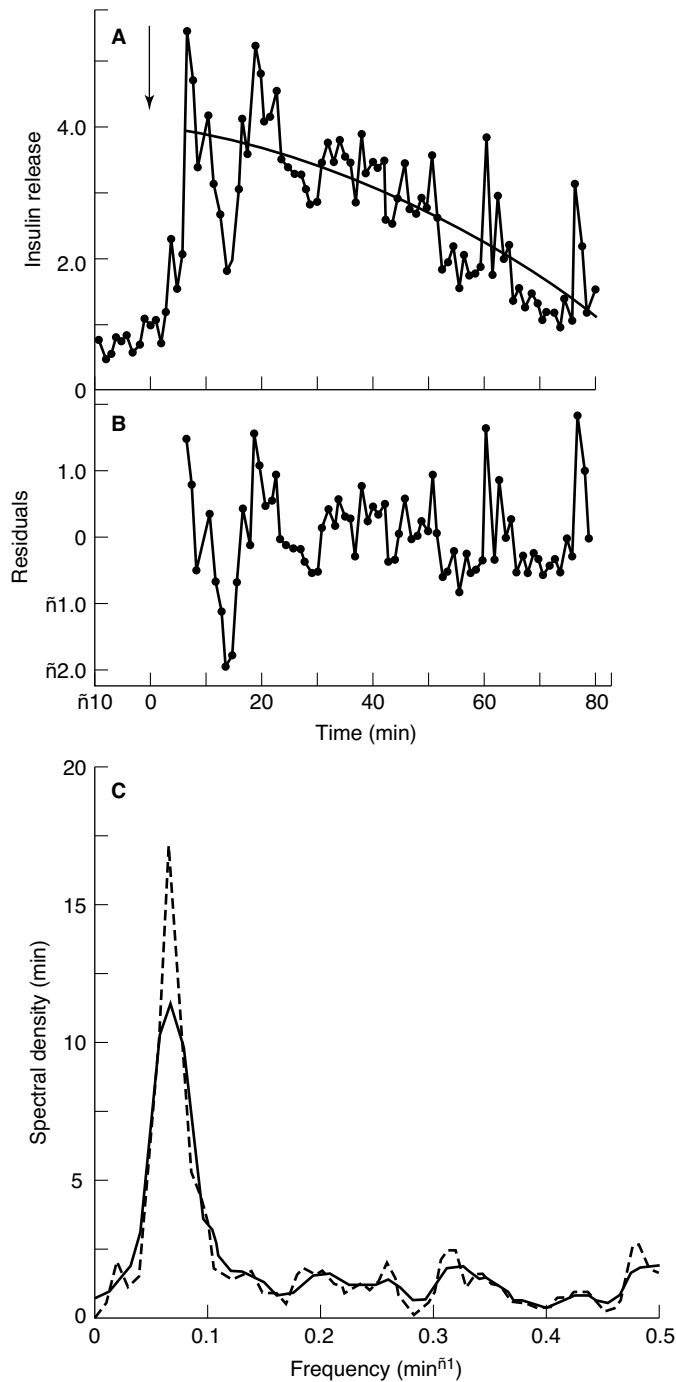
Figure 16.20: A: Oscillations of insulin release in perifused islets. The data indicate a slow time scale decreasing trend (the smooth line) upon which are superimposed faster time scale oscillations. B: When the slow decrease is removed from the data, the residuals exhibit oscillations around 0. C: Spectral analysis of the residuals shows a frequency peak at about 0.07 min^{-1}, corresponding to oscillations with a period of 14.5 minutes. The dashed and continuous lines correspond to two different filters used in the spectral analysis. (Bergstrom et al., 1989. Figs. 1A, C, and 3.)
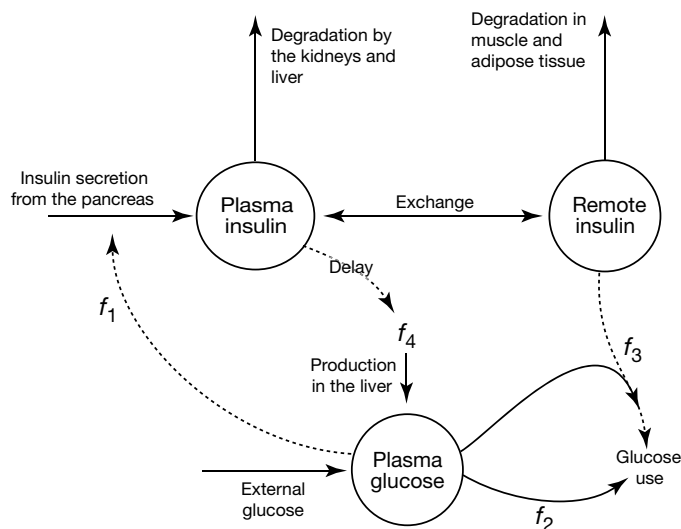
Figure 16.21: Schematic diagram of the model of ultradian insulin oscillations.

blood, and blood glucose. It turns out that two insulin pools are necessary, which is, by itself, an interesting model prediction. There are two delays, one explicit and the other implicit. Although plasma insulin regulates glucose production, it does so only after a delay of about 36 minutes. This delay is incorporated explicitly as a three-stage linear filter. An additional implicit delay arises because glucose utilization is regulated by the remote (interstitial) insulin, and not by the plasma insulin, while glucose has a direct effect (through insulin secretion from the pancreas) on plasma insulin levels.

We let I_p and I_i, in units of mU, denote the amounts of plasma insulin and remote insulin, respectively, and we let G, in units of mg, denote the total amount of glucose. Then the model equations follow from the following assumptions:

1. Plasma insulin is produced at a rate $f_1(G)$ that is dependent on plasma glucose. The insulin exchange with the remote pool is a linear function of the concentration difference between the pools $I_p/V_p - I_i/V_i$ with rate constant E, where V_p is the plasma volume and V_i is the interstitial volume. In addition, there is linear removal of insulin from the plasma by the kidneys and the liver, with rate constant $1/t_p$. Thus,

$$\frac{dI_p}{dt} = f_1(G) - \left(\frac{I_p}{V_p} - \frac{I_i}{V_i} \right) E - \frac{I_p}{t_p}. \qquad (16.59)$$

Note that this equation and the two that follow are written in terms of total amounts of insulin and glucose, rather than concentrations. Formulations using concentrations or total quantities are equivalent, provided that the blood and interstitial volumes remain constant, which we assume.

V_p	3 l	C_2	144 mg l^{-1}
V_i	11 l	C_3	100 mg l^{-1}
V_g	10 l	C_4	80 mU l^{-1}
E	0.2 l min^{-1}	C_5	26 mU l^{-1}
t_p	6 min	U_b	72 mg min^{-1}
t_i	100 min	U_0	4 mg min^{-1}
t_d	12 min	U_m	94 mg min^{-1}
R_m	209 mU min^{-1}	R_g	180 mg min^{-1}
a_1	6.67	α	7.5
C_1	300 mg l^{-1}	β	1.77

Table 16.4: Parameter values for the model of ultradian insulin oscillations.

2. Remote insulin accumulates via exchange with the plasma pool and is degraded in muscle and adipose tissue at rate $1/t_i$:

$$\frac{dI_i}{dt} = \left(\frac{I_p}{V_p} - \frac{I_i}{V_i}\right) E - \frac{I_i}{t_i}. \tag{16.60}$$

3. Plasma glucose is produced at a rate f_4 that is dependent on plasma insulin, but only indirectly, as f_4 is a function of h_3, the output of a three-stage linear filter. The input to the filter is I_p, so glucose production is regulated by plasma insulin but delayed by the filter. There is input $I_G(t)$ from the addition of glucose from outside the system, by eating a meal, say. Finally, glucose is removed from the plasma by two processes. Thus,

$$\frac{dG}{dt} = f_4(h_3) + I_G(t) - f_2(G) - f_3(I_i)G. \tag{16.61}$$

Glucose utilization is described by two terms: $f_2(G)$ describes utilization of glucose that is independent of insulin, as occurs, for example, in the brain, and is an increasing function that saturates quickly. The second removal term, $f_3(I_i)G$, describes insulin-dependent utilization of glucose. f_3 is an increasing, sigmoidal function of I_i.

4. The three-stage linear filter satisfies the system of differential equations

$$t_d\frac{dh_1}{dt} = I_p - h_1, \tag{16.62}$$

$$t_d\frac{dh_2}{dt} = h_1 - h_2, \tag{16.63}$$

$$t_d\frac{dh_3}{dt} = h_2 - h_3. \tag{16.64}$$

The specific functional forms used for $f_1, \ldots, f_4$ are

$$f_1(G) = \frac{R_m}{1 + \exp(\frac{-G}{V_g C_1} + a_1)}, \tag{16.65}$$
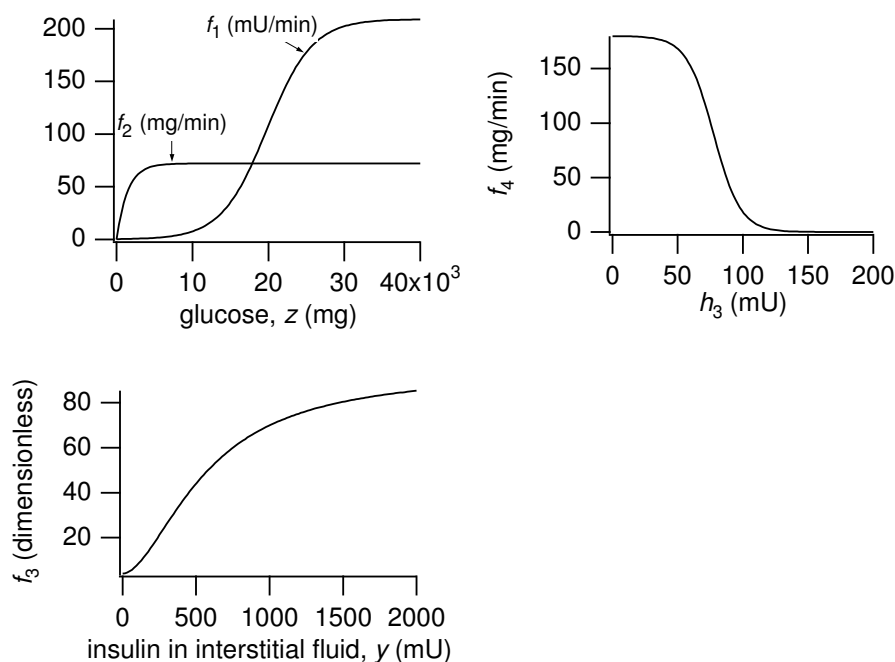
Figure 16.22: Graphs of $f_1, \ldots, f_4$ in the model for ultradian insulin oscillations. The exact forms of these functions are not physiologically significant, but are chosen to give the correct qualitative behavior.

$$f_2(G) \;=\; U_b \left[1 - \exp\left(\frac{-G}{C_2 V_g} \right) \right], \tag{16.66}$$

$$f_3(I_i) \;=\; \frac{1}{C_3 V_g} \left(U_0 + \frac{U_m - U_0}{1 + (\kappa I_i)^{-\beta}} \right), \tag{16.67}$$

$$f_4(h_3) \;=\; \frac{R_g}{1 + \exp[(\alpha(\frac{h_3}{C_5 V_p} - 1)]}, \tag{16.68}$$

where $\kappa = \frac{1}{C_4}\left(\frac{1}{V_i} + \frac{1}{Et_i} \right)$, and these are graphed in Fig. 16.22. The parameter values are given in Table 16.4.

Numerical solution of the model equations shows that a constant infusion of glucose causes oscillations in insulin and glucose. As I increases, the oscillation period remains practically unchanged, but the amplitude increases (Fig. 16.23), in good qualitative agreement with experimental data. However, it is interesting that these oscillations disappear if the compartment of remote insulin is removed from the model. This indicates that the division of insulin into two functionally separate stores could play an important role in the dynamic control of insulin levels. Another prediction of the model is that the oscillations are dependent on the delay in the regulation of glucose production. If the delay caused by the three-stage filter is
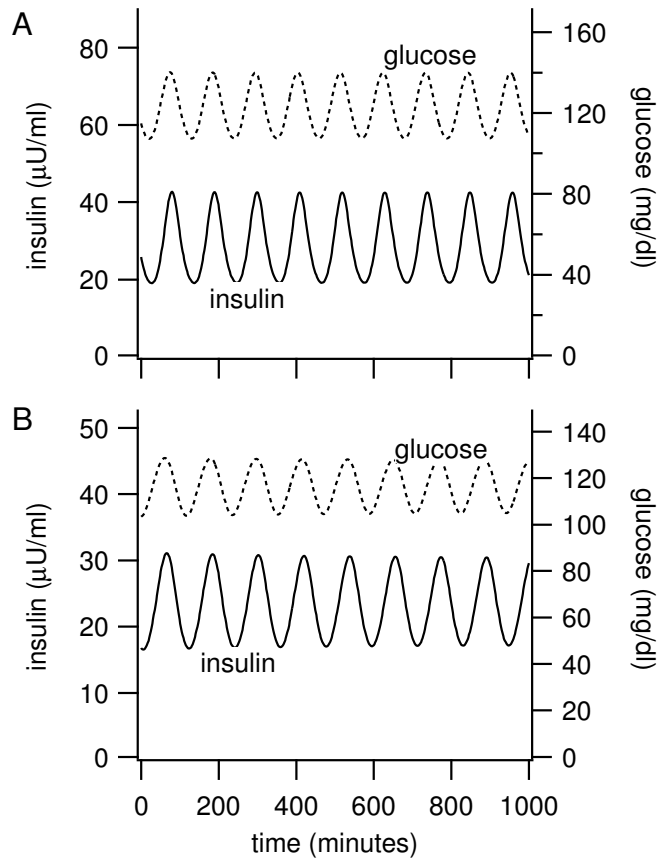
Figure 16.23: Ultradian insulin oscillations in the model. The glucose infusion rates are A: $I = 108$ mg/min, and B: $I = 216$ mg/min. Note that insulin and glucose are expressed in units of concentration. An amount is easily converted to a concentration by dividing by the volume of the appropriate compartment.

either too large or too small, the oscillations disappear (Exercise 8).

The Effect of Oscillatory Insulin Release

Sturis et al. (1995) found experimentally that an oscillatory insulin supply is more efficient at increasing glucose usage than is a constant insulin supply. The experiments were done by the addition of exogeneous insulin, after somatostatin was used to suppress endogeneous insulin production. Tolić et al. (2000) then used a simplified version of the above model for ultradian insulin oscillations to explain how such dependency on insulin oscillations could arise.

16.4 Adaptation of Hormone Receptors

It remains to answer the question of why hormone secretion is pulsatile in the first place. As with many oscillatory physiological systems, there is no completely satisfactory answer to this question. However, one plausible hypothesis has been proposed by Li and Goldbeter (1989). Based on a model of a hormone receptor first constructed by Segel, Goldbeter, and their coworkers (Segel et al., 1986; Knox et al., 1986), Li and Goldbeter constructed a model of a hormone receptor that responds best to stimuli of a certain frequency, thus providing a possible reason for the importance of pulsatility.

Closely linked to this hypothesis is the phenomenon of receptor adaptation. Often, the response to a constant hormone stimulus is much smaller than the response to a time-varying stimulus. In the extreme case, the receptor responds to a time-varying input, but has no response to a steady input, regardless of the input magnitude, a phenomenon called *exact adaptation*. A number of examples of adaptation are described in this book; for example, the models of the IP_3 receptor discussed in Chapter 7 show adaptation in their response to a step-function increase in Ca^{2+} concentration; i.e., their response is an initial peak in the Ca^{2+} release, followed by a decrease to a lower plateau as the receptor is slowly inactivated by Ca^{2+}. Similarly, as described in Chapter 19 biochemical feedback in photoreceptors can result in a system that displays remarkably precise adaptational properties, as embodied in Weber's law. Because of the importance of adaptation in physiological systems, it is interesting to study how adaptation arises in a simple receptor model.

The key assumption is that the hormone receptor can exist in two different conformational states, R and D, and each conformational state can have hormone bound or unbound (Fig. 16.24). For simplicity we assume that the active form of the receptor has hormone bound to the receptor in state R. The addition of hormone to the receptor system causes a change in the proportion of each receptor state, but the total receptor concentration is fixed.

Letting r, x, y, d denote $[R]/R_T, [RH]/R_T, [DH]/R_T$ and $[D]/R_T$ respectively, where R_T is the total receptor concentration, we find the following equations for the receptor system:

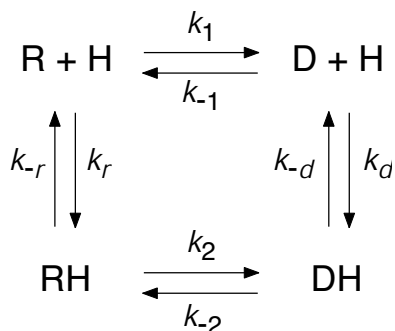$$\frac{dr}{dt} = -[k_1 + k_r H(t)]r + k_{-r}x + k_{-1}d, \qquad (16.69)$$

Figure 16.24: Schematic diagram of a model of a hormone receptor.

$$\frac{dx}{dt} = k_r H(t)r - (k_2 + k_{-r})x + k_{-2}y, \qquad (16.70)$$

$$\frac{dy}{dt} = k_2 x - (k_{-2} + k_{-d})y + k_d H(t)d. \qquad (16.71)$$

Because of the conservation condition $r + x + y + d = 1$ there are only three independent variables, so only three equations are needed. The function $H(t)$ denotes the hormone concentration as a function of time, and is assumed to be known.

Each state of the receptor is assumed to have an intrinsic activity, and the total activity of the receptor is given by the sum over all the receptor states, weighted by the intrinsic activity of the state. Thus, the total activity A of the receptor is

$$A = a_1 r + a_2 x + a_3 y + a_4 d, \qquad (16.72)$$

for some constants $a_1, \ldots, a_4$.

For simplicity, we assume that the binding of the ligand is essentially instantaneous, and thus

$$x = \frac{H(t)r}{K_r}, \qquad (16.73)$$

$$y = \frac{H(t)d}{K_d}, \qquad (16.74)$$

where $K_r = k_{-r}/k_r$ and $K_d = k_{-d}/k_d$. Using a standard quasi-equilibrium reduction, and assuming that $H(t)$ is slowly varying on the time scale of receptor binding, we find the single differential equation for the receptor,**James please check this. I got a different answer than you did and can't find a mistake in this.**

$$\left(1 + \frac{H}{K_r}\right)\frac{dr}{dt} = \frac{k_{-1}K_d + k_{-2}H}{K_d + H}\left(1 - r\left(\frac{K_d + H}{K_d K_1} + \frac{K_r + H}{K_r}\right)\right), \qquad (16.75)$$

where $K_1 = k_{-1}/k_1$, and $k_2 = \frac{k_{-2}K_r}{K_1 K_d}$ in order to satisfy detailed balance. The steady states are given by

$$r_0 = \frac{1}{\frac{K_d + H}{K_1 K_d} + \frac{K_r + H}{K_r}}, \qquad (16.76)$$

$$x_0 \;=\; \frac{Hr_0}{K_r}, \tag{16.77}$$

$$y_0 \;=\; \frac{H\left(1 - \frac{K_r + H}{K_r} r_0\right)}{K_d + H}. \tag{16.78}$$

If $a_4 = 0$, so that the state d is completely inactive, the steady-state activity of the receptor is

$$A \;=\; a_1 r_0 + a_2 x_0 + a_3 y_0 \tag{16.79}$$

$$=\; \frac{a_1 K_1 K_d K_r + H(a_2 K_1 K_d + a_3 K_r)}{K_r K_d (K_1 + 1) + H(K_r + K_1 K_d)}. \tag{16.80}$$

In general, this is a saturating curve as a function of H. However, exact adaptation occurs if A is independent of H, in which case it must be that

$$A = A|_{H=0} = \lim_{H \to \infty} A, \tag{16.81}$$

so that

$$\frac{K_1 a_1}{1 + K_1} = \frac{a_3 K_r + K_1 K_d a_2}{K_r + K_1 K_d}. \tag{16.82}$$

Note that since the right-hand side of (16.82) is the weighted average of a_2 and a_3, exact adaptation is possible only when a_1 is greater than the smaller of a_2 and a_3 (more precisely when $\frac{K_1 a_1}{1 + K_1}$ lies between a_2 and a_3. In general, one expects a_2 to be larger than a_3 (as the RH form of the receptor has a greater intrinsic activity than its inactivated form DH), and thus $a_1 > a_3$ is required for exact adaptation. In other words, the intrinsic activity of the unbound receptor (R form) must be higher than the intrinsic activity of the inactivated receptor, even when the hormone is bound.

In response to a step increase in hormone concentration, the receptor state is first quickly converted to the RH form, which has a high activity, and thus the overall activity initially increases. However, over a longer time period, the RH form gradually converts to the DH form, which has a lower activity than the R (unbound) form. Thus, receptor inactivation decreases the activity back to the basal level. Thus, exact adaptation arises from a process of fast activation and slow inactivation, a mechanism that has appeared in many forms throughout this book.

Exercises

1. By taking partial derivatives of $f(\xi, \xi_i)$ with respect to ξ_i confirm that the model (16.25), when linearized about P_M, takes the form given in (16.33)–(16.35). Calculate the eigenvalues and eigenvectors of the matrix A.

2. This exercise works through the derivation of a Lyapunov function for the Lacker model (Akin and Lacker, 1984). Define $\delta(\xi) = \xi^2$, $\rho(\xi) = \xi^{-2} - 1$, and

$\phi(p_i) = p_i(M_1 + M_2 - M_1 M_2 p_i)$, where $p_i = \xi_i/\xi$. Show that

$$\frac{d\xi_i}{dt} = \delta(\xi)\xi_i[\rho(\xi) + \phi(p_i)], \tag{16.83}$$

$$\frac{d\xi}{dt} = \delta(\xi)\xi[\rho(\xi) + \bar{\phi}], \tag{16.84}$$

$$\frac{dp_i}{dt} = \delta(\xi)p_i[\phi(p_i) - \bar{\phi}], \tag{16.85}$$

where

$$\bar{\phi} = \sum_{i=1}^{n} p_i \phi(p_i). \tag{16.86}$$

Define a new time scale τ by

$$\frac{d\tau}{dt} = \delta(\xi), \tag{16.87}$$

and show that

$$\frac{dp_i}{d\tau} = p_i[\phi(p_i) - \bar{\phi}]. \tag{16.88}$$

Finally, show that

$$V(p_1, \ldots, p_n) = \sum_{i=1}^{n} \int_0^{p_i} \phi(s)\, ds \tag{16.89}$$

is a Lyapunov function for the model by showing that

$$\frac{dV}{d\tau} = \sum_{i=1}^{n} p_i[\xi(p_i) - \bar{\phi}]^2 \geq 0. \tag{16.90}$$

Hint: derive and use the fact that $\sum p_i(\xi(p_i) - \bar{\phi}) = 0$.

3. Since $\gamma_1 \equiv 1$, (16.44)–(16.46) provide no information about ξ_1. Use the original variables to show that $\bar{\xi}_1(\tau) = \xi(t(\tau))$ satisfies the differential equation

$$\frac{1}{2}\frac{d}{d\tau}\bar{\xi}_1^2 = 1 - \bar{\xi}_1^2(\Gamma - M_1)(\Gamma - M_2). \tag{16.91}$$

Find t as a function of τ. Describe how the original variables $\xi_i(t)$ may be obtained once the $\gamma_i(\tau)$ have been obtained by numerical solution of (16.44)–(16.46). Why is it preferable to numerically simulate the model in the transformed variables γ_i rather than the original variables ξ_i?

4. For the model of a hormone receptor assuming fast ligand binding (Section 16.4), calculate the response to a step function, and then to a stimulus of the form $H(t) = 1$ for $0 < t < t_0$, $H(t) = 0$ otherwise (call this stimulus a step pulse). Calculate the response to a series of step pulses, and calculate the width of the pulse and the time between pulses that gives the greatest average activity. Li and Goldbeter (1989) give the details.

5. (From Loeb and Strickland, 1987.) Many cells respond maximally to a hormone concentration that is much too low to saturate the hormone receptors. This can be explained by assuming that the response is dependent on a secondary mediator. Suppose that the hormone, H, combines reversibly with its receptor, R^o, to form the complex HR^o. Suppose that the secondary mediator M is formed at a rate proportional to $[HR^o]$ and is degraded with linear kinetics. Finally, suppose that M combines reversibly with its own receptor, R, to form MR, and that the cellular response is linearly proportional to $[MR]$. What is the fractional receptor occupancy as a function of $[H]$? Show that the fractional response (as a function of $[H]$) has the same shape as the fractional receptor occupancy curve, shifted to the left by a constant factor (when plotted against $\log[H]$). Give a biological interpretation.

6. Consider the model of the activity of the LHRH neurons described by (16.4)–(16.6). Let a be a constant, instead of a function of time.

   (a) How does the steady state depend on a? What are the different possibilities?

   (b) Show that, depending on the values of the other parameters, an increase in a can lead either to an increase or a decrease in excitability.

   (c) Suppose that a is suddenly increased, held constant for a short period of time, and then returned to zero. Plot the solution in the phase plane. What happens as the period of time for which a is raised becomes shorter?

   (d) If $a(t)$ is the delta function, sketch the solution in the phase plane.

7. Find the response of the three-stage linear filter (16.62)-(16.64) to the sinusoidal input $I_p = I_0 + I_1 \sin(\omega t)$.

8. Consider the model of insulin oscillations described in Section 16.3.2.

   (a) Plot the steady states and periodic solutions of the model as, a function of I, and as a function of t_d. Show that, as t_d gets large or small, the oscillations disappear.

   (b) How can the model be modified to omit the remote insulin compartment? How does this change the oscillatory behavior in the model? (Hint: combine both insulin compartments into a single compartment, with all the insulin inputs and outputs going to and from this single compartment, and no exchange term.) How is this approach different from assuming that the exchange between the plasma and remote insulin compartments is fast?

9. In response to a pulse of glucose, the rate of insulin release shows a biphasic response, as shown in Fig. 16.25. First, consider the responses shown in the inset at the top right. These are the responses to two identical glucose steps, each of magnitude 6.9 mmol/l, and each 5 minutes long. Clearly, the response during each glucose step first rises and then decays, while, in addition, the response to the second step is smaller than to the first.
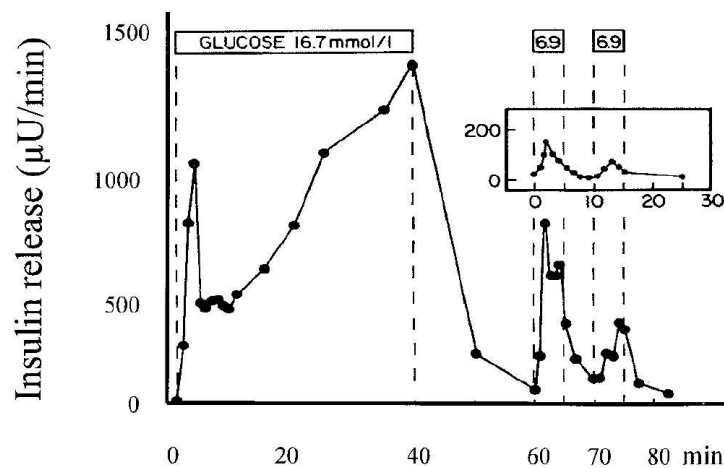
Figure 16.25: The response to glucose of the rate of insulin release in the perfused rat pancreas. The inset at the top right show the response to two glucose steps (each of size 6.9 mmol/l) while directly below the inset is shown the response to two identical glucose steps, but after the pancreas has been primed by the prior addition of 16.7 mmol/l glucose for 40 minutes (Nesher and Cerasi, 2002, Fig. 5). **Springer, this figure will need permission. JS**

Next, consider the curve in the main part of the figure. Initially, a step of 16.7 mmol/l glucose was added for 40 minutes; during this 40 minutes the rate of insulin release shows a clear triphasic behavior, first rising, then falling, then rising again. After this "priming" by glucose, the same two steps as in the inset were applied. Now, the response to these two steps is greatly enhanced, although, as in the inset, the response to the second step is smaller.

Clearly, there are a number of dynamic processes controlling the rate of insulin release, each operating on a different time scale. For instance, addition of glucose clearly first stimulates insulin release, then inhibits then, then stimulates it again. Furthermore, the data in the inset shows that addition of glucose initiates an inhibiting mechanism that is still in operation 5 minutes after cessation of the initial stimulus.

Construct a mathematical model for this behavior. Do not worry about relating your model to specific known physiological mechanisms; construct a system of equations that exhibits approximately the correct behavior. Although there are many possible answers, your model will probably have a number of different variables, one for each of the dynamic processes discussed above and each with a different time constant, with the rate of insulin release modeled as a product of these variables.

Chapter 17

Renal Physiology

The kidneys perform two major functions. First, they excrete most of the end products of bodily metabolism, and second, they control the concentrations of most of the constituents of the body fluids. The main goal of this chapter is to gain some understanding of the processes by which the urine is formed and waste products removed from the bloodstream. The control of the constituents of the body fluids is discussed only secondarily.

The primary operating unit of the kidney is called a *nephron*, of which there are about a million in each kidney (Figs. 17.1 and 17.2). Each nephron is capable of forming urine by itself. The entrance of blood into the nephron is by the *afferent arteriole*, located in the renal cortex, and the tubules of the nephron and the associated peritubular capillaries extend deep into the renal medulla. The principal functional units of the nephron are the *glomerulus*, through which fluid is filtered from the blood; the *juxtaglomerular apparatus*, by which glomerular flow is controlled; and the *long tubule*, in which the filtered fluid is converted into urine.

17.1   The Glomerulus

The first stage of urine formation is the production of a filtrate of the blood plasma. The glomerulus, the primary filter, is a network of up to 50 parallel branching and anastomosing (rejoining) capillaries covered by epithelial cells and encased by *Bowman's capsule*. Blood enters the glomerulus by way of the afferent arteriole and leaves through the *efferent arteriole*. Pressure of the blood in the glomerulus causes the fluid to filter into Bowman's capsule, carrying with the filtrate all the dissolved substances of small molecular weight. The glomerular membrane is almost completely impermeable to all plasma proteins, the smallest of which is albumin (molecular weight 69,000). As a result, the glomerular filtrate is identical to plasma except that it contains no significant amount of protein.

The quantity of filtrate formed each minute is called the *glomerular filtration rate*, and in a normal person averages about 125 ml/min. The filtration fraction is the fraction of renal plasma flow that becomes glomerular filtrate and is typically about 20 percent. Over 99 percent of the filtrate is reabsorbed in the tubules, with
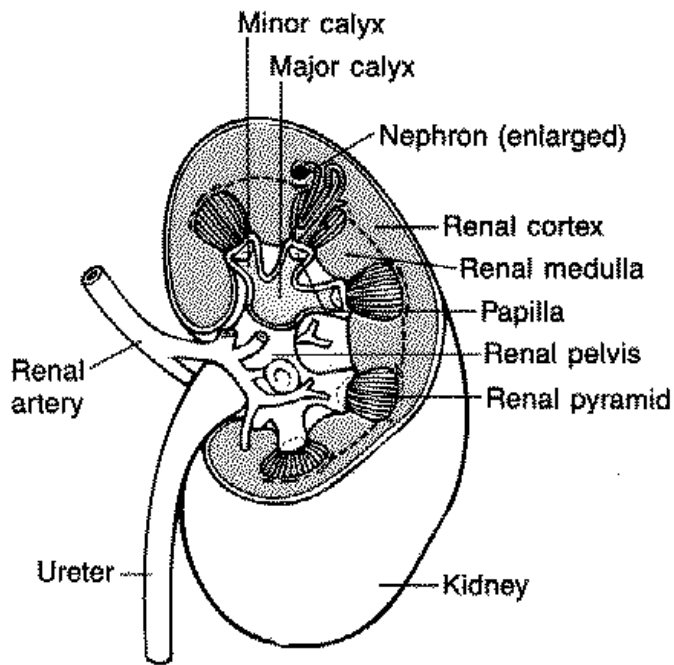
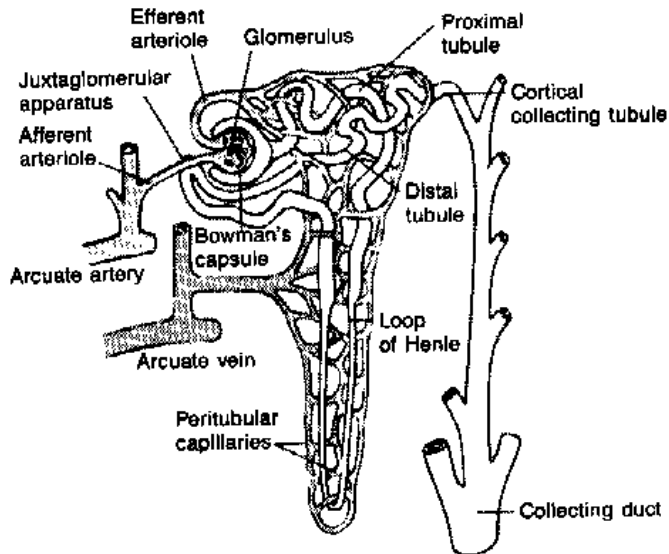Figure 17.1: The kidney. (Guyton and Hall, 1996, Fig. 26-2, p. 317.)

Figure 17.2: The nephron. (Guyton and Hall, 1996, Fig. 26-3, p. 318.)
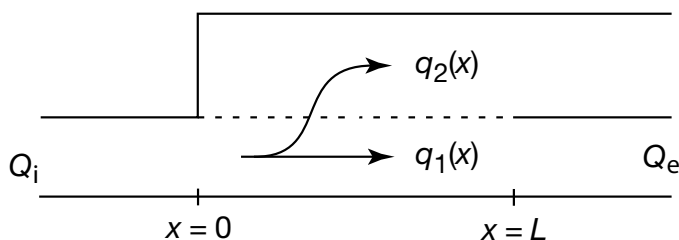
Figure 17.3: Schematic diagram of the glomerular filtration.

the remaining small portion passing into the urine.

There are three pressures that affect the rate of glomerular filtration. These are the pressure inside the glomerular capillaries that promote filtration, the pressure inside Bowman's capsule that opposes filtration, and the colloidal osmotic pressure (cf. Chapter 2, Section 2.7) of the plasma proteins inside the capillaries that opposes filtration.

A mathematical model of the glomerular filter can be described simply as follows. We assume that the glomerular capillaries comprise a one-dimensional tube with flow q_1 and that the surrounding Bowman's capsule is also effectively a one-dimensional tube with flow q_2 (Fig. 17.3). Since the flow across the glomerular capillaries is proportional to the pressure difference across the capillary wall, at steady state the rate of change of the flow in the capillary is

$$\frac{dq_1}{dx} = K_f(P_2 - P_1 + \pi_c), \tag{17.1}$$

where P_1 and P_2 are the hydrostatic fluid pressures in tubes 1 and 2, respectively, π_c is the osmotic pressure of suspended proteins and formed elements of blood, and K_f is the capillary filtration rate. The osmotic pressure of the suspended proteins is given by

$$\pi_c = RTc, \tag{17.2}$$

where c, the concentration expressed in moles per liter, is a function of x, since the suspension becomes more concentrated as it moves through the glomerulus. Since the large proteins bypass the filter, we have the conservation equation

$$c_i Q_i = c q_1, \tag{17.3}$$

where c_i is the input concentration and Q_i is the input flux. It follows that

$$\pi_c = \pi_i \frac{Q_i}{q_1}, \tag{17.4}$$

where $\pi_i = RTc_i$ is the input osmotic pressure. Since the hydrostatic pressure drop in the glomerulus is small compared to the pressure drop in the efferent and afferent arterioles, we take P_1 and P_2 to be constants.

Equation (17.1) along with (17.4) gives a first-order differential equation for q_1, which is easily solved. Setting $q_1(L) = Q_e$ we find that

$$\frac{Q_e}{Q_i} + \alpha \ln\left(\frac{\frac{Q_e}{Q_i} - \alpha}{1 - \alpha}\right) = 1 - K_f L \frac{\pi_i}{\alpha Q_i}, \tag{17.5}$$

where Q_e is the efflux through the efferent arterioles, L is the length of the filter, and $\alpha = \pi_i/(P_1 - P_2)$.

Finally, we assume that the pressures and flow rates are controlled by the input and output arterioles, via

$$P_a - P_1 = R_a Q_i, \tag{17.6}$$
$$P_1 - P_e = R_e Q_e, \tag{17.7}$$

and that the flow out of the glomerulus into the proximal tubule is governed by

$$P_2 - P_d = R_d(Q_i - Q_e), \tag{17.8}$$

where P_a, P_e, and P_d are the afferent arteriole, efferent arteriole, and descending tubule pressures, respectively, and R_a, R_e, and R_d are the resistances of the afferent and efferent arterioles and proximal tubule, respectively. Typical values are $P_1 = 60, P_2 = 18, P_a = 100, P_e = 18, P_d = 14 - 18, \pi_i = 25$ mm Hg, with $Q_i = 650, Q_d = Q_i - Q_e = 125$ ml/min.

The flow rates and pressures vary as functions of the arterial pressure. To understand something of this variation, in Fig. 17.4 is shown the renal blood flow rate Q_i and the glomerular filtration flow rate as functions of the arterial pressure. It is no surprise that both of these are increasing functions of arterial pressure P_a.

The strategy for numerically computing this curve is as follows: with resistances R_a and R_e and pressures P_e, P_d, and π_i specified and fixed at typical levels, we pick a value for glomerular filtrate $Q_d = Q_i - Q_e$. For this value, we solve (17.5) (using a simple bisection algorithm) to find both Q_i and Q_e. From these, the corresponding pressures P_a, P_1, and P_2 are determined from (17.6) and (17.7), and plotted.

For this model, the filtration rate varies substantially as a function of arterial pressure. However, in reality (according to data shown in Fig. 17.5), the glomerular filtration rate remains relatively constant even when the arterial pressure varies between 75 to 160 mm Hg, suggesting that there is some autoregulation of the flow rate.

17.1.1 Autoregulation and Tubuloglomerular Oscillations

The need for autoregulation of the glomerular filtration rate is apparent. If the flow rate of filtrate is too slow, then we expect reabsorption to be too high, and the kidney fails to eliminate necessary waste products. On the other hand, at too high a flow rate, the tubules are unable to reabsorb those substances that need to be preserved and not eliminated, so that valuable substances are lost into the urine.

The glomerulus controls the rate of filtration by detecting the concentration of NaCl at the top of the thick ascending limb, most probably by detecting the chloride
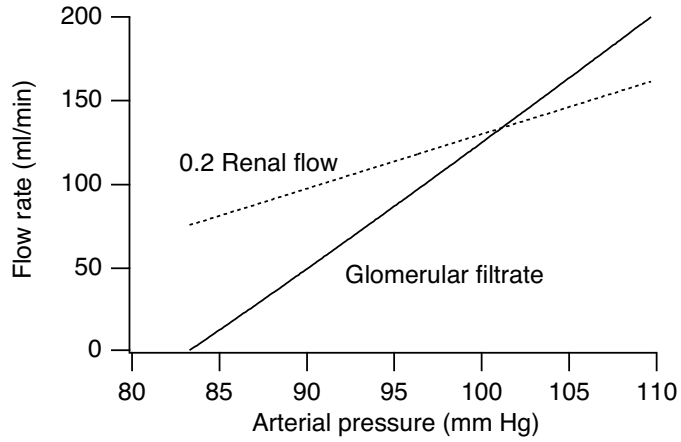
Figure 17.4: Unregulated glomerular filtration and renal blood flow plotted as functions of arterial pressure, with $P_d = 18$, $P_e = 0$ mm Hg.
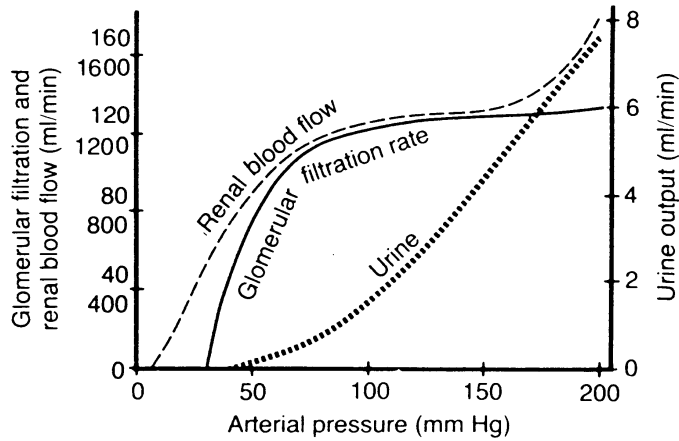

Figure 17.5: Autoregulation of renal blood flow and glomerular filtration rate but lack of autoregulation of urine flow during changes in renal arterial pressure. (Guyton and Hall, 1996, Fig. 26-13, p. 327.)
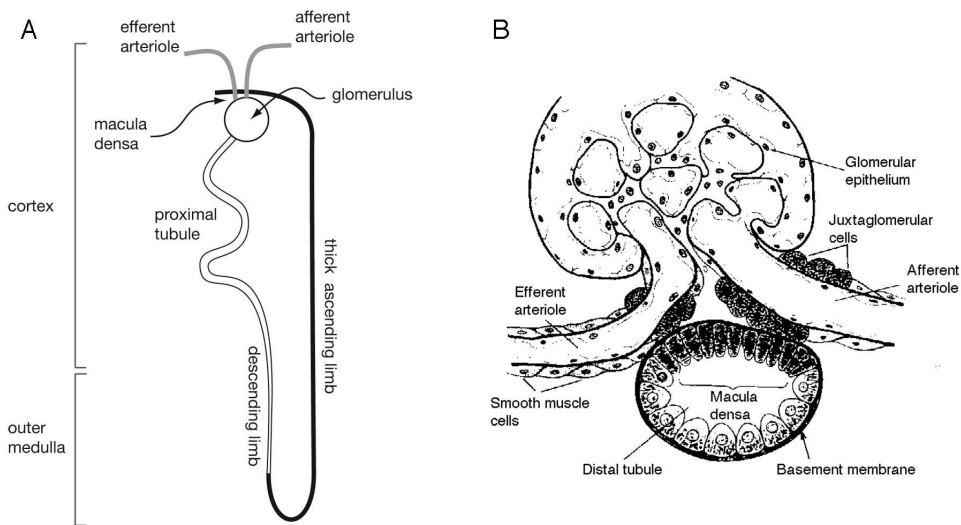
Figure 17.6: A: Schematic diagram of a short nephron, showing how the thick ascending limb ascends to the region of the glomerulus, enabling autoregulation of the glomerular filtration rate. Adapted from Pitman et al. (2004), Fig. 1. B: Structure of the juxtaglomerular apparatus. (Guyton and Hall, 1996, Fig. 26-14, p. 328.)

concentration. After its descent into the renal medulla, the loop of Henle returns to the proximity of the afferent and efferent arterioles at the glomerulus (Fig. 17.6A). The *juxtaglomerular complex* consists of *macula densa* cells in the distal tubule and *juxtaglomerular cells* in the walls of the afferent and efferent arterioles (as depicted in Fig. 17.6B).

As described in Section 17.2, the principal function of the thick ascending limb of the loop of Henle is the pumping of Na^+ out of the tubule into the interstitial space; it is almost entirely impermeable to water. Thus, the slower the rate of flow through the tubule, the greater the amount of Na^+ can be transported out of the thick ascending limb, with Cl^- following passively. A low flow rate causes excessive reabsorption of Na^+ and Cl^- ions, resulting in too large a decrease of these ionic concentrations at the end of the loop. Conversely, a high flow rate results in a higher concentration of Na^+ and Cl^- at the macula densa.

The macula densa cells respond to decreases of NaCl concentration (by a mechanism not completely understood), by releasing a vasodilator that decreases the resistance of the afferent arterioles. Simultaneously, the juxtaglomerular cells release renin, an enzyme that enables the formation of angiotensin II, which constricts the efferent arterioles. The simultaneous effect of these is to increase the flow of filtrate through the glomerulus. Conversely, an increase in the concentration of NaCl at the macula densa has the effect of decreasing the resistance of the afferent arteriole, and increasing the resistance of the efferent arteriole, thus decreasing the rate of filtration and the flow along the tubule.

It comes as no surprise that a control system such as this can result in oscillations in the rate of fluid flow along the loop of Henle (Fig. 17.7). These oscillations were first described in halothane-anesthetized Sprague-Dawley rats by Leyssac and Baumbach (1983), and have since been studied in detail by both modelers and experimentalists (Leyssac and Holstein-Rathlou, 1989; Holstein-Rathlou and Marsh, 1990; Holstein-Rathlou et al., 1990, 1991; Layton et al., 1991, 1995, 1997, 2000; Pitman et al., 1993, 2004). A useful recent review is that of Just (2006).

A simple model of tubuloglomerular oscillations (Layton et al., 1991) focuses on the role of the chloride concentration in the thick ascending limb. We model the thick ascending limb as a one-dimensional tube, through which Cl^- is transported by fluid flow, while being removed actively (of course, it is the Na^+ that is removed actively, but since Cl^- follows passively the effect is the same).

If we let $y = 0$ and $y = L$ denote, respectively, the beginning and end of the thick ascending limb of length L, and let $C(y, \tau)$ denote the Cl^- concentration at y at time τ, then conservation of Cl^- gives

$$\frac{\partial C}{\partial \tau} + \phi \frac{\partial C}{\partial y} = -R(C), \tag{17.9}$$

where $R(C)$ denotes the rate of removal of Cl^- from the tube via the pumping of Na^+, and ϕ denotes the velocity of fluid flow along the tube. For our simple model we assume that Cl^- is removed by a first order process,

$$R(C) = -r_c C. \tag{17.10}$$

When the NaCl concentration at the macula densa is changed, the resistance of the afferent arteriole changes only after a time delay. Thus, ϕ is a function of the
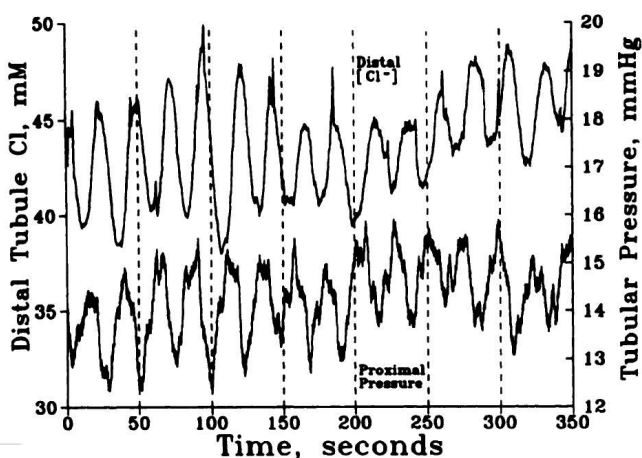
Figure 17.7: Oscillations in distal tubule chloride concentration (top) and proximal tubule pressure (bottom). From Holstein-Rathlou and Leyssac, 1987. **Springer: we'll need permission for this figure**.

Cl^- concentration at the macula densa at some previous time, i.e., a function of $C(L, \tau - \bar{\tau})$. The functional form of ϕ has been established by experimental studies to be of the form

$$\phi(C) = F_{\mathrm{op}} + \Delta F \tanh(\alpha(\bar{C} - C)). \tag{17.11}$$

Notice that ϕ is a decreasing function of C. The constant $\bar{C}$ is the Cl^- concentration for which ϕ has an inflection point.

Finally, we assume that the input Cl^- concentration is known, $C(0, t) = C_0$.

We now rescale y, τ and C, setting $y = Lx$, $\tau = \frac{L}{F_{\mathrm{op}}} t$, $\bar{\tau} = \frac{L}{F_{\mathrm{op}}} \bar{t}$, and $C = C_0 c$, so that the conservation law becomes the delayed partial differential equation

$$\frac{\partial c}{\partial t} + F(c(1, t - \bar{t})) \frac{\partial c}{\partial x} = -\mu c, \tag{17.12}$$

where

$$F(c) = 1 + K_1 \tanh(K_2(\bar{c} - c)), \tag{17.13}$$

and $\mu = r_c \frac{L}{F_{\mathrm{op}}}$, subject to the boundary condition, $c(0, t) = 1$.

The first step in our analysis is to examine the steady state solution. The steady state solution, $s(x)$, is the solution of

$$F(s(1)) \frac{\partial s}{\partial x} = -\mu s, \tag{17.14}$$

so is

$$s(x) = s(0) e^{-kx}, \tag{17.15}$$

where $k = \frac{\mu}{F(s(1))}$. Since $s(0) = 1$, and $s(1) = e^{-k}$, for consistency it must be that

$$kF(e^{-k}) = \mu. \tag{17.16}$$

Since F is a decreasing function of its argument, there is a unique value of k for which (17.16) holds, and hence a unique steady state solution.

Layton et al. made the additional assumption that in normal, steady, operating conditions, $c(1,t) = \bar{c}$ and chose the Cl$^-$ uptake rate to be $\mu = -\ln \bar{c} = k$. In order to allow for abnormal operating conditions, we do not make this additional assumption here.

To understand something about this control mechanism, we calculate the sensitivity of $s(1)$ to changes in $s(0)$. The sensitivity σ is defined as

$$\sigma = \frac{s(0)}{s(1)} \frac{ds(1)}{ds(0)}. \tag{17.17}$$

Since

$$s(1) \exp\left(\frac{\mu}{F(s(1))}\right) = s(0), \tag{17.18}$$

it follows (after implicit differentiation) that

$$\sigma = \frac{1}{1 - \frac{k^2}{\mu} e^{-k} F'(e^{-k})} = \frac{1}{1 + \frac{k}{\mu}\gamma}, \tag{17.19}$$

where $\gamma = -ke^{-k}F'(e^{-k})$. Since, $F'(e^{-k}) < 0$, this implies that $s(1)$ becomes less sensitive to changes in input $s(0)$ as $F'(s(1))$ decreases (i.e., as F becomes steeper). Notice that with no control, $F'(c) = 0$ so that $\sigma = 1$.

The sensitivity is also changed by changes in the Cl$^-$ removal rate. Sensitivity is smallest (and γ is largest) when $\mu = \ln \bar{c}$. (This is an approximate statement because the derivative of γ with respect to μ is nearly, but not exactly, zero at $\mu = \ln \bar{c}$.) However, as μ deviates from this optimal value, the steady solution $s(1)$ deviates from $\bar{c}$, leading to a flatter feedback response. With F' smaller in magnitude, so also is γ.

Oscillations in the macula densa Cl$^-$ concentration, and thus in the other variables such as flow rate and glomerular pressure, can occur if the steady state solution becomes unstable via a Hopf bifurcation. This is not the only possible instability mechanism, but it is a reasonable one to look for. The stability of $s(x)$ can be determined by writing $c(x,t) = s(x) + \epsilon u(x,t)$ and then expanding (17.12) to first order in ϵ. This gives

$$\frac{\partial u}{\partial t} + F(e^{-k})\frac{\partial u}{\partial x} = -\mu u + kF'(e^{-k})e^{-kx}u(1, t - \bar{t}), \tag{17.20}$$

with the boundary condition $u(0,t) = 0$.

We now look for solutions for u of the form $u(x,t) = f(x)e^{\lambda t}$, where $f(0) = 0$. Substituting this into (17.20) gives

$$\frac{\mu}{k}f'(x) = -(\mu + \lambda)f(x) + kF'(e^{-k})e^{-kx}f(1)e^{-\lambda \bar{t}}, \tag{17.21}$$

which can be solved to give

$$f(x) = \frac{1}{\lambda}kF'(e^{-k})f(1)e^{-\lambda \bar{t}}\left[e^{-kx} - e^{-\frac{k}{\mu}(\mu + \lambda)x}\right]. \tag{17.22}$$

For consistency, it must be that

$$f(1) = \frac{1}{\lambda}kF'(e^{-k})f(1)e^{-\lambda\bar{t}}\left[e^{-k} - e^{-\frac{k}{\mu}(\mu+\lambda)}\right], \tag{17.23}$$

from which it follows that λ must be a root of

$$\lambda = \gamma e^{-\lambda\bar{t}}(e^{-\frac{k}{\mu}\lambda} - 1) = -2\gamma e^{-\lambda(\bar{t}+\frac{k}{2\mu})}\sinh\left(\frac{k\lambda}{2\mu}\right), \tag{17.24}$$

where $\gamma = -kF'(e^{-k})e^{-k}$. Note that $\gamma > 0$ is related to the sensitivity of the feedback regulation in (17.19).

The only parameter values for which a Hopf bifurcation can occur are those for which λ has zero real part and nonzero imaginary part. If λ has zero real part we can take $\lambda = i\omega$. Substituting $\lambda = i\omega$ into (17.24) and equating real and imaginary parts gives the two equations

$$0 = 2\gamma\sin\left(\omega\left(\bar{t} + \frac{k}{2\mu}\right)\right)\sin\left(\frac{k\omega}{2\mu}\right), \tag{17.25}$$

$$\omega = -2\gamma\cos\left(\omega\left(\bar{t} + \frac{k}{2\mu}\right)\right)\sin\left(\frac{k\omega}{2\mu}\right). \tag{17.26}$$

The only nontrivial solution of the first of these has

$$\omega = \frac{n\pi}{\bar{t} + \frac{k}{2\mu}}, \quad n = 1, 2, 3, \ldots. \tag{17.27}$$

Thus, the curves in parameter space at which there are Hopf bifurcations are given by

$$\gamma = (-1)^{n+1}\frac{\omega}{2\sin(\frac{k\omega}{2\mu})}, \qquad \omega = \frac{n\pi}{\bar{t} + \frac{k}{2\mu}}, \quad n = 1, 2, 3, \ldots. \tag{17.28}$$

A plot of the curves (17.28) is given in Fig. 17.8 for $n = 1, 2, 3, 4$ with $\frac{k}{\mu} = 1$. The primary instability occurs at the curve corresponding to $n = 1$, while higher frequency instabilities occur at the other curves. Typical corresponding solutions (calculated numerically) are shown in Fig. 17.9.

The main point of this plot is to demonstrate the importance of the two parameters, the time delay, $\bar{t}$, and the sensitivity feedback parameter, γ, on the onset of oscillations. Since the primary critical curve is monotone decreasing, oscillations occur if either of these parameters is sufficiently large (but both must be nonzero). The role of the other parameter of the problem, the rate of Cl^- removal from the thick ascending limb, is more subtle to unravel. As can be seen from (17.28), the primary critical curve is moved around a bit if $\frac{k}{\mu}$ is changed, but the basic shape of the curve is unchanged. What is more significant is that changes in μ lead to changes in the parameter γ. In fact, if μ deviates from its optimal value at $\mu = -\ln\bar{c}$, then γ decreases. Thus, the primary effect of changes of μ from its optimal value is to make oscillations less likely. Another way to express this is that if the delay $\bar{t}$ is sufficiently large, then there are two values of μ that are Hopf Bifurcation points, one below and one above the optimal removal rate at $\mu = -\ln\bar{c}$. A plot of this critical curve is shown in Fig. 17.10.
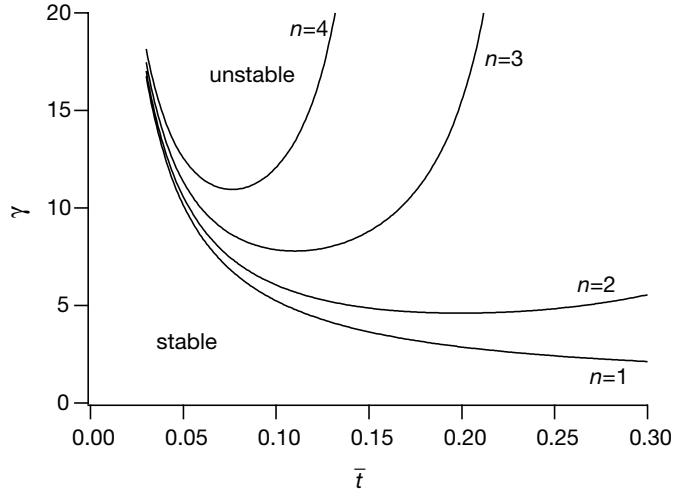
Figure 17.8: Plot of (17.28) for $n = 1, 2, 3, 4$. The steady state solution is stable below the $n = 1$ curve, and unstable above it.
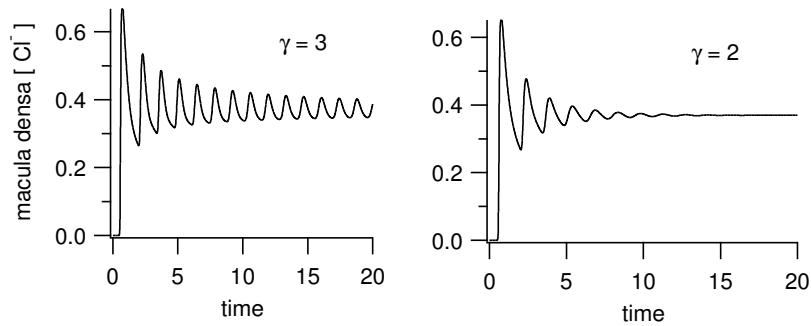
Figure 17.9: Typical oscillatory solutions of the model of tubuloglomerular oscillations, for two different feedback strengths. For both panels, $\bar{t} = 0.2$, $\frac{k}{\mu} = 1$. The Cl^- concentration is plotted in dimensionless units, where the concentration at the start of the thick ascending limb is 1. The time is also dimensionless; to get seconds, multiply by 15.5.
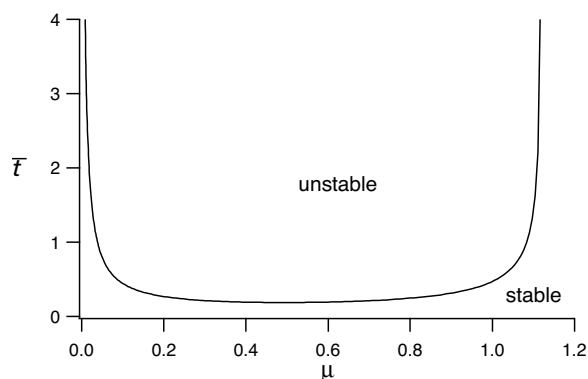
Figure 17.10: Critical curve in the $\mu, \bar{t}$ parameter space along which there are Hopf Bifurcations for the glomerular feedback model. Parameter values are $K_1 = 1$, $K_2 = 10$, $\bar{c} = e^{-0.5}$.

A much more complex model of tubuloglomerular oscillations was constructed by Holstein-Rathlou and Marsh (1990), and the simple model above was compared in detail to this more complex model by Layton et al. (1991).

17.2   Urinary Concentration: The Loop of Henle

The challenge of any model of urine formation is to see how concentrating and diluting mechanisms work together to determine the composition of the urine and to regulate the interstitial contents, and then to account quantitatively for the concentrating ability of particular species. The challenge is substantial. For example, for humans, the maximal urine concentrating ability is 1200 mOsm/liter, while some desert animals, such as the Australian hopping mouse, can concentrate urine to as high as 10,000 mOsm/liter. It is not understood how such high urine concentrations can be obtained. It is also necessary that the kidney be able to produce a dilute urine under conditions of high fluid intake.

A normal 70 kg human must excrete about 600 mOsm of solute (waste products of metabolism and ingested ions) every day. The minimal amount of urine to transport these solutes, called the *obligatory urine volume* is

$$\text{obligatory volume} \quad = \quad \frac{\text{total solute/day}}{\text{maximal urine concentration}} \qquad (17.29)$$

$$= \quad \frac{600 \text{ mOsm/day}}{1200 \text{ mOsm/L}} = 0.5\text{L/day}. \qquad (17.30)$$

This explains why severe dehydration occurs from drinking seawater. The concentration of salt in the oceans averages 3% sodium chloride, with osmolarity between 2000 and 2400 mOsm/liter. Drinking 1 liter of water with a concentration of 2400 mOsm/liter provides 2400 mOsm of solute that must be excreted. If the maximal urine concentration is 1200 mOsm/liter, then 2 liters of urine are required to rid the
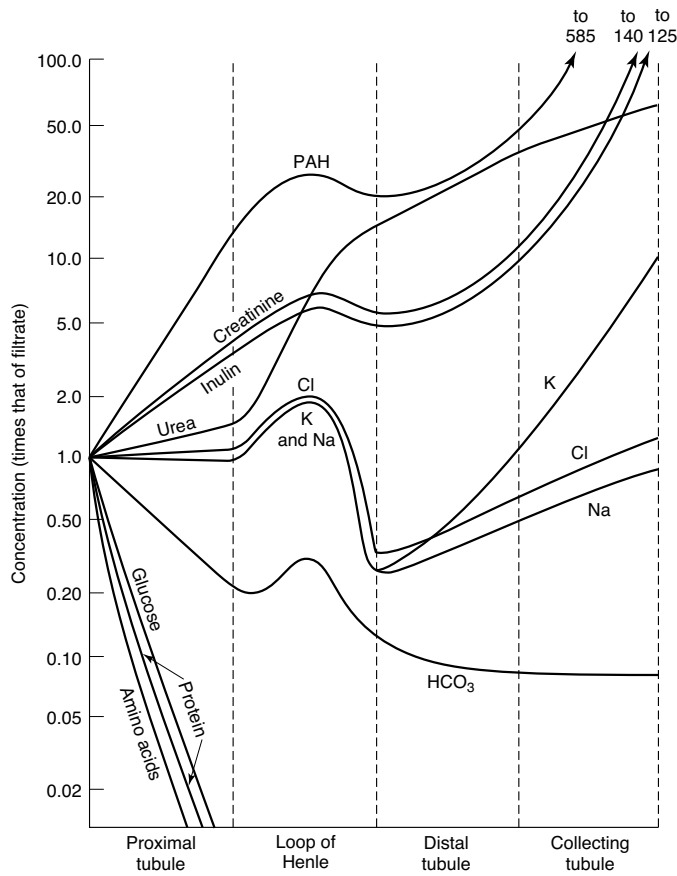
Figure 17.11: Relative concentrations of various substances as functions of distance along the renal tubule system. (Guyton and Hall, 1996, Fig. 27-11, p. 341.)

body of this ingested solute, a deficit of 1 liter, which must be drawn from the interstitial fluid. This explains why shipwreck victims who drink seawater are rapidly dehydrated, while (as Guyton and Hall have kindly pointed out) the victim's pet Australian hopping mouse can drink all the seawater it wants with impunity.

Urinary concentration or dilution is accomplished primarily in the loop of Henle. After leaving Bowman's capsule, the glomerular filtrate flows into a tubule having five sections: the *proximal tubule*, the *descending limb of the loop of Henle*, the *ascending limb of the loop of Henle*, the *distal tubule*, and, finally, the *collecting duct*. These tubules are surrounded by capillaries, called the *peritubular capillaries*, that reabsorb the fluid that has been extracted from the tubules. In Fig. 17.11 are shown the relative concentrations of various substances at different locations along the tubular system.

The purpose of the proximal tubule is to extract much of the water and dissolved chemicals (electrolytes, glucose, various amino acids, etc.) to be reabsorbed into
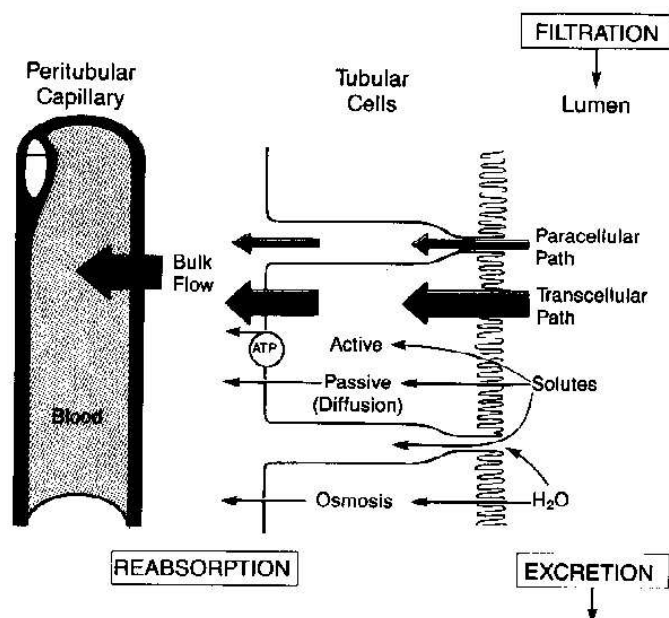
Figure 17.12: Schematic diagram of the reabsorption of water and solutes in the proximal tubule. (Guyton and Hall, 1996, Fig. 27-1, p. 332.)

the bloodstream while concentrating the waste products of metabolism. It is this concentrate that eventually flows as urine into the bladder. The proximal tubular cells have large numbers of mitochondria to support rapid active transport processes. Indeed, about 65 percent of the glomerular filtrate is reabsorbed before reaching the descending limb of the loop of Henle. Furthermore, glucose, proteins, amino acids, acetoacetate ions, and the vitamins are almost completely reabsorbed by active cotransport processes through the epithelial cells that line the proximal tubule.

Any substance that is reabsorbed into the bloodstream must first pass through the tubular membrane into the interstitium and then into peritubular capillaries. There are three primary mechanisms by which this transport takes place, all of which we have seen before (Fig. 17.12). First, there is active transport of Na^+ from the interior of the epithelial cells into the interstitium, mediated by a Na,K-ATPase. Although this pump actively pumps K^+ into the cell from the interstitium, both sides of the tubular epithelial cells are so permeable to K^+ that virtually all of the K^+ leaks back out of the cell almost immediately.

There are secondary transporters that use the gradient of Na^+ ions (established by the ATPase) to transport other substances from the tubular lumen into the interior of the epithelial cell. The most important of these are cotransporters of glucose and amino acid ions, but the epithelial cells of the proximal tubule also contain transporters of phosphate, calcium, and magnesium ions. There is also a transporter that exchanges hydrogen ions for Na^+ ions across the membrane of the epithelial cell membrane into the tubule. The third mechanism of transport is that

of water across cell membranes, mediated by osmotic pressure (see Chapters 2 and 18).

The descending limb of the loop of Henle is lined with thin epithelial cells with few mitochondria, indicating minimal metabolic activity; it is highly permeable to water and moderately permeable to Na^+, urea, and most ions. The ascending limb of the loop of Henle begins with a thin wall but then about halfway up becomes grossly thickened. In contrast to the descending limb, the ascending limb is highly impermeable to water and urea. The cells of the thick ascending limb are similar to those of the proximal tubule, suited for strong active transport of Na^+ and Cl^- ions from the tubular lumen into the interstitial fluid.

The thick segment travels back to the region of the glomerulus, where it passes between the afferent and efferent arterioles, forming the juxtaglomerular apparatus, where much of the feedback control of the flow rate takes places. Passing beyond this point, the tubule becomes the distal tubule, the function of which is similar to that of the ascending limb of the loop of Henle.

Finally, the flow enters the descending collecting duct, which gathers the flow from several nephrons and descends back through the cortex and into the outer and inner zones of the medulla. The flow from the collecting duct then flows out of the kidney through the ureter on the way to the bladder. The cells lining the collecting duct are sensitive to a number of hormones that act to regulate their function as well as the final chemical composition of the urine. Primary among these hormones are *aldosterone* and *antidiuretic hormone* (ADH). Aldosterone determines the rate at which Na^+ ions are transported out of the tubular lumen, and ADH determines the permeability of the collecting duct to water, and thereby determines the final concentration of the urine. When there is no ADH present, the collecting duct is impermeable to water, but with ADH present, the permeability of the collecting duct allows water to be reabsorbed out of the collecting duct, leaving behind a more highly concentrated urine.

Putting this all together, we arrive at a qualitative summary of how a nephron operates. Along the ascending limb of the loop of Henle portion of the tubule, Na^+ is absorbed into the interstitium, either passively (in the thin ascending limb) or actively (in the thick ascending limb). This creates a high Na^+ concentration in the interstitium, which then serves to draw water out of the descending limb and allows Na^+ to reenter the descending limb. Hence, fluid entering the descending limb is progressively concentrated until, at the turning point of the loop, the fluid osmolarity is about 1200 mOsm/liter (compared to the entering fluid, which is about 300 mOsm/liter). Clearly, because the fluid entering the ascending limb is so concentrated, Na^+ extraction from the ascending limb is enhanced, which further enhances water extraction from the descending limb, and so on. This positive feedback process is at the heart of the countercurrent mechanism, to be discussed in more detail below. As the fluid ascends the ascending limb, Na^+ is continually extracted until, at the level of the juxtaglomerular apparatus, the fluid in the tubule is considerably more dilute than the original filtrate. However (and this is the crucial part), the dilution process results in a steep gradient of Na^+ concentration in the interstitium, a gradient that can, when needed, concentrate the urine.

When there is no ADH present, the dilute urine formed by the loop of Henle

proceeds through the collecting duct essentially unchanged, resulting in a large quantity of dilute urine. In the presence of large amounts of ADH, the collecting duct is highly permeable to water, so that by the time the filtrate reaches the level of the turning point of the loop of Henle, it is essentially at the same concentration as the interstitium, about 1200 mOsm/liter, thus giving a small quantity of concentrated urine.

It is important to emphasize that the principal functions of the loop of Henle are, first, the formation of dilute urine, which allows water to be excreted when necessary, and, second, the formation of the interstitial gradient in Na^+ concentration, which allows for the formation of a concentrated urine when necessary. The importance of the loop of Henle in creating the interstitial gradient of Na^+ concentration is underlined by the fact that although all vertebrates can produce dilute urine, only birds and mammals can produce hyperosmotic urine, and it is the kidneys of only these animals that contain loops of Henle.

17.2.1   The Countercurrent Mechanism

Solutes are exchanged between liquids by diffusion across their separating membranes. Since the rate of exchange is affected by the concentration difference across the membrane, the exchange rate is increased if large concentration differences can be maintained. One important way that large concentration differences can be maintained is by the *countercurrent mechanism*. As is described below, the countercurrent mechanism is important to renal function. Other examples of the countercurrent mechanism include the exchange of oxygen from water to blood through fish gills and the exchange of oxygen in the placenta between mother and fetus.

Suppose that two gases or liquids containing a solute flow along parallel tubes of length L, separated by a permeable membrane. We model this in the simplest possible way as a one-dimensional problem, and we assume that solute transport is a linear function of the concentration difference. Then the concentrations in the two one-dimensional tubes are given by

$$\frac{\partial C_1}{\partial t} + q_1 \frac{\partial C_1}{\partial x} = d(C_2 - C_1), \qquad (17.31)$$

$$\frac{\partial C_2}{\partial t} + q_2 \frac{\partial C_2}{\partial x} = d(C_1 - C_2). \qquad (17.32)$$

The mathematical problem is to find the outflow concentrations, given that the inflow concentrations, the length of the exchange chamber, and the flow velocities are known. It is a relatively easy matter to generalize this model to allow for an interstitium (see Exercise 5).

We assume that the flows are in steady state and that the input concentrations are C_1^0 and C_2^0. Then, if we add the two governing equations and integrate, we find that

$$q_1 C_1 + q_2 C_2 = k \text{ (a constant).} \qquad (17.33)$$

Pretending that k is known, we eliminate C_2 from (17.32) and find the differential equation for C_1,

$$\frac{dC_1}{dx} = \frac{d}{q_1 q_2} \left(k - (q_1 + q_2) C_1 \right), \qquad (17.34)$$

from which we learn that

$$C_1(x) = \kappa + (C_1(0) - \kappa)e^{-\lambda x}, \tag{17.35}$$

where $\kappa = \frac{k}{q_1+q_2}$ and $\lambda = d\left(\frac{q_1+q_2}{q_1 q_2}\right)$.

There are two cases to consider, namely when q_1 and q_2 are of the same sign and when they have different signs. If they have the same signs, say positive, then the input is at $x = 0$, and it must be that $C_1(0) = C_1^0, C_2(0) = C_2^0$, from which, using (17.33), it follows that

$$\frac{C_1(L)}{C_1^0} = \frac{1 + \gamma\rho}{1 + \rho} + \rho\frac{1 - \gamma}{1 + \rho}e^{-\lambda L}, \tag{17.36}$$

where $\gamma = C_2^0/C_1^0, \rho = q_2/q_1, \lambda = \frac{d}{q_1}(1 + \frac{1}{\rho})$.

Suppose that the goal is to transfer material from vessel 1 to vessel 2, so that $\gamma < 1$. We learn from (17.36) that the output concentration from vessel 1 is an exponentially decreasing function of the residence length dL/q_1. Furthermore, the best that can be done (i.e., as $dL/q_1 \to \infty$) is $\frac{1+\gamma\rho}{1+\rho}$.

In the case that q_1 and q_2 are of opposite sign, say $q_1 > 0, q_2 < 0$, the inflow for vessel 1 is at $x = 0$, but the inflow for vessel 2 is at $x = L$. In this case we calculate that

$$\frac{C_1(L)}{C_1^0} = \frac{-\gamma\rho + (1 - \rho + \gamma\rho)e^{-\lambda L}}{e^{-\lambda L} - \rho}, \tag{17.37}$$

where $\gamma = C_2(L)/C_1^0 = C_2^0/C_1^0, \rho = -q_2/q_1 > 0, \lambda = \frac{d}{q_1}(1 - \frac{1}{\rho})$, provided that $\rho \neq 1$. In the special case $\rho = 1$, we have

$$\frac{C_1(L)}{C_1^0} = \frac{q_1 + \gamma dL}{q_1 + dL}. \tag{17.38}$$

Now we can see the substantial difference between a cocurrent (q_1 and q_2 of the same sign) and a countercurrent (q_1 and q_2 with the opposite sign). At fixed parameter values, if $\gamma < 1$, the expression for $C_1(L)/C_1^0$ in (17.36) is always larger than that in (17.37), implying that the total transfer of solute is always more efficient with a countercurrent than with a cocurrent.

In Fig. 17.13 is shown a comparison between a countercurrent and a cocurrent. The dashed curves show the transfer fraction $C_1(L)/C_1^0$ for a cocurrent, plotted as a function of the residence length dL/q_1, with input in tube 2, $C_2^0 = C_2(0) = 0$. The solid curves show the same quantity for a countercurrent, with input concentration $C_2^0 = C_2(L) = 0$.

In the limit of a long residence time (large dL/q_1), the transfer fraction becomes $1 - \rho + \gamma\rho$ if $\rho < 1$, and γ if $\rho > 1$. Indeed, this is always smaller than the result for a cocurrent, $\frac{1+\gamma\rho}{1+\rho}$.

17.2.2 The Countercurrent Mechanism in Nephrons

The countercurrent mechanism works slightly differently in nephrons because the two parallel tubes, the descending branch and the ascending branch of the loop
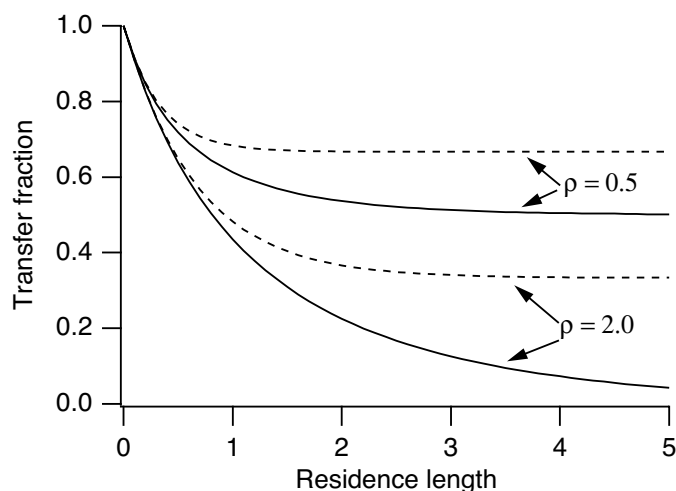
Figure 17.13: Transfer fraction for a cocurrent (dashed) and a countercurrent (solid) when $\gamma = 0$ plotted as a function of residence length.

of Henle, are connected at their bottom end. Thus the flow and concentration of solute out of the descending tube must match the flow and concentration of solute into the ascending tube.

Mathematical models of the urine-concentrating mechanism have been around for some time, but all make use of the same basic physical principles, namely, the establishment of chemical gradients via active transport processes, the movement of ions via diffusion, and the transport of water by osmosis. The unique feature of the nephron is its physical organization, which allows it to eliminate waste products while controlling other quantities. In what follows we present a model similar to that of Stephenson (1972, 1992) of urinary concentration that represents the gross organizational features of the loop of Henle. A number of other models are discussed in a special issue of the *Bulletin of Mathematical Biology* (volume 56, number 3, May 1994), while two useful reviews of mathematical work on the kidney are Knepper and Rector (1991) and Roy et al. (1992).

We view the loop of Henle as consisting of four compartments, including three tubules, the descending limb, the ascending limb, and the collecting duct, and a single compartment for the interstitium and peritubular capillaries (Fig. 17.14). The interstitium/capillary bed is treated as a one-dimensional tubule that accepts fluid from the other three tubules and loses it to the venules. It is an easy generalization to separate the peritubular capillaries and interstitium into separate compartments, but little is gained by doing so. In each of these compartments, one must keep track of the flow of water and the concentration of solutes. For the model presented here, we track only one solute, Na^+, because it is believed that the concentration of Na^+ in the interstitium determines over 90 percent of the osmotic pressure.

We assume that the flow in each of the tubes is a simple plug flow (positive in the positive x direction) with flow rates q_d, q_a, q_c, q_s for descending, ascending,
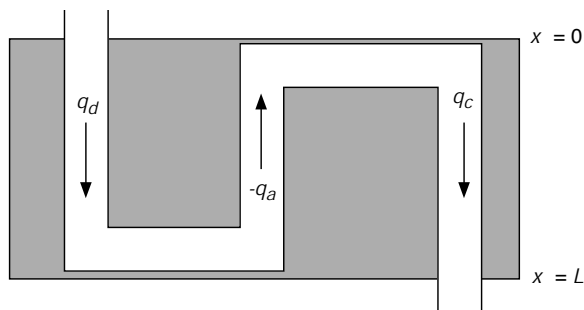
Figure 17.14: Diagram of the simple four-compartment model of the loop of Henle.

collecting, and interstitial tubules, respectively. Similarly, the concentration of solute in each of these is denoted by c_d, c_a, c_c, c_s. The tubules are assumed to be one-dimensional, with glomerular filtrate entering the descending limb at $x = 0$, turning from the descending limb to the ascending limb at $x = L$, turning from the ascending limb to the collecting duct at $x = 0$, and finally exiting the collecting duct at $x = L$. We assume that the interstitium/capillary compartment drains at $x = 0$ with no flow at $x = L$.

Descending limb: The flux of water from the descending limb to the interstitium is controlled by the pressure difference and the osmotic pressure difference; hence

$$\frac{1}{k_d}\frac{dq_d}{dx} = P_s - \pi_s - P_d + 2RT(c_d - c_s), \tag{17.39}$$

where P_d and P_s are the hydrostatic pressures in the descending tubule and interstitium, π_s is the colloidal osmotic pressure of the interstitium, and k_d is the filtration rate for the descending tubule. The factor two multiplying the osmotic pressure due to the solute is to take into account the fact that the fluid is electrically neutral, and the flow of Na$^+$ ions is followed closely by the flow of chloride ions, both of which contribute to the osmotic pressure. The transport of Na$^+$ ions from the descending limb is governed by simple diffusion, so that at steady state we have

$$\frac{d(q_d c_d)}{dx} = h_d(c_s - c_d), \tag{17.40}$$

where h_d is the permeability of the descending limb to Na$^+$ ions.

Ascending limb: The ascending limb is assumed to be impermeable to water, so

that

$$\frac{dq_a}{dx} = 0,\qquad\qquad(17.41)$$

and the flow of Na$^+$ out of the ascending limb is by an active process, so that

$$\frac{d(q_a c_a)}{dx} = -p.\qquad\qquad(17.42)$$

The pump rate p certainly depends in nontrivial ways on the local concentrations of various ions. However, for this model we take p to be a constant. This simplifying assumption causes problems with the behavior of the model at low Na$^+$ concentrations, because there is nothing preventing the Na$^+$ concentration to become negative. Although the Na$^+$-ATPase is actually a Na,K-ATPase, the epithelial cells are highly permeable to K$^+$, and so we assume that K$^+$ can be safely ignored. For simplicity, we also ignore the fact that the Na$^+$ transport properties of the thin ascending limb are different from those of the thick ascending limb, and we assume active removal along the entire ascending limb.

Collecting duct: The flow of water from the collecting duct is also controlled by the hydrostatic and osmotic pressure differences, via

$$\frac{1}{k_c}\frac{dq_c}{dx} = P_s - \pi_s - P_c + 2RT(c_c - c_s),\qquad\qquad(17.43)$$

and the transport of Na$^+$ from the collecting duct is governed by

$$\frac{d(q_c c_c)}{dx} = h_c(c_s - c_c).\qquad\qquad(17.44)$$

Here, k_c and h_c are the permeability of the collecting duct to water and Na$^+$, and are controlled by ADH and aldosterone, respectively.

Conservation equations: Finally, because total fluid is conserved,

$$\frac{dq_s}{dx} = -\frac{d}{dx}(q_d + q_a + q_c),\qquad\qquad(17.45)$$

and because total solute is conserved,

$$\frac{d(q_s c_s)}{dx} = -\frac{d}{dx}(q_d c_d + q_a c_a + q_c c_c).\qquad\qquad(17.46)$$

To complete the description, we have the relationship between pressure and flow in a tube,

$$\frac{dP_j}{dx} = -R_j q_j,\qquad\qquad(17.47)$$

for $j = d, a, c, s$. However, for renal modeling it is typical to take each pressure to be constant. Typical values for the pressures are $P_d = 14\text{–}18$ mm Hg, $P_a = 10\text{–}14$ mm Hg, $P_c = 0\text{–}10$ mm Hg, $P_s = 6$ mm Hg, and $\pi_s = 17$ mm Hg.

This description of the nephron consists of eight first-order differential equations in the eight unknowns q_j and c_j, for $j = d, a, c, s$. To complete the description, we need boundary conditions. We assume that the inputs $q_d(0)$ and $c_d(0)$ are known and given. Then, because the flow from the descending limb enters the ascending limb, $q_d(L) = -q_a(L)$ and $c_d(L) = c_a(L)$. Furthermore, $q_s(L) = 0$. At $x = 0$, flow from the ascending limb enters the collecting duct, so that $q_a(0) = -q_c(0)$ and $c_a(0) = c_c(0)$. Finally, since total fluid must be conserved, what goes in must go out, so that $q_d(0) + q_s(0) = q_c(L)$.

It is useful to nondimensionalize the equations by normalizing the flows and solute concentrations. Thus, we let

$$x = Ly, Q_j = \frac{q_j}{q_d(0)}, C_j = \frac{c_j}{c_d(0)} \text{ for } j = d, a, c, s,$$

and the dimensionless parameters are

$$\rho_j = \frac{q_d(0)}{2LRTc_d(0)k_j}, \Delta P_j = \frac{P_j + \pi_s - P_s}{RT2c_d(0)}, H_j = \frac{Lh_j}{q_d(0)}, \text{ for } j = d, c.$$

In this scaling $Q_d(0) = C_d(0) = 1$.

Three of these equations are trivially solved. In fact, it follows easily from (17.41), (17.45), and (17.46) that

$$Q_a = Q_a(0) = Q_a(L), \tag{17.48}$$

$$Q_d + Q_a + Q_c + Q_s = Q_c(L), \tag{17.49}$$

$$Q_dC_d + Q_aC_a + Q_cC_c + Q_sC_s = Q_c(L)C_c(L). \tag{17.50}$$

Two more identities can be found. If we use (17.40) to eliminate $c_d - c_s$ from (17.39), we obtain

$$\rho_d\frac{dQ_d}{dy} + \Delta P_d = C_d - C_s = -\frac{1}{H_d}\frac{d(Q_dC_d)}{dy}, \tag{17.51}$$

from which it follows that

$$\rho_d(Q_d - 1) + \frac{1}{H_d}(Q_dC_d - 1) = -\Delta P_dy. \tag{17.52}$$

Similarly, we use (17.44) to eliminate $c_c - c_s$ from (17.43) to obtain

$$\rho_c\frac{dQ_c}{dy} + \frac{1}{H_c}\frac{d(Q_cC_c)}{dy} = -\Delta P_c, \tag{17.53}$$

which integrates to

$$\rho_c(Q_c - Q_c(0)) + \frac{1}{H_c}(Q_cC_c - Q_c(0)C_c(0)) = -\Delta P_cy. \tag{17.54}$$

As discussed above, we assume that the Na$^+$ concentration in the ascending limb is always sufficiently high so that the Na$^+$–K$^+$ pump is saturated and the pump rate is independent of concentration, in which case the solution of (17.42) (in nondimensional variables) is

$$Q_aC_a = Q_aC_a(0) - Py, \tag{17.55}$$

where $P = \frac{pL}{c_d(0)q_d(0)}$ is the dimensionless Na$^+$ pump rate.

Having solved six of the original eight differential equations, we are left with a system of two first-order equations in two unknowns. The two equations are

$$\rho_d \frac{dQ_d}{dy} = -\Delta P_d + C_d - C_s, \qquad (17.56)$$

$$\rho_c \frac{dQ_c}{dy} = -\Delta P_c + C_c - C_s, \qquad (17.57)$$

subject to boundary conditions $Q_d = 1, Q_c = -Q_a$ at $y = 0$, and $Q_d = -Q_a$ at $y = 1$, where C_c, C_s, and C_d are functions of Q_d and Q_c. Although there are three boundary conditions for two first-order equations, the number Q_a is also unknown, so that this problem is well posed. Our goal in what follows is to understand the behavior of the solution of this system.

Formation of urine without ADH

The primary control of renal dialysis is accomplished in the collecting duct, where the amount of ADH determines the permeability of the collecting duct to water and the amount of aldosterone determines the permeability of the collecting duct to Na$^+$. Impairment of normal kidney function is often related to ADH. For example, the inability of the pituitary to produce adequate amounts of ADH is called *"central" diabetes insipidus*, and results in the formation of large amounts of dilute urine. On the other hand, with *"nephrogenic" diabetes insipidus*, the abnormality resides in the kidney, either as a failure of the countercurrent mechanism to produce an adequately hyperosmotic interstitium, or as the inability of the collecting ducts to respond to ADH. In either case, large volumes of dilute urine are formed.

Various drugs and hormones can have similar effects. For example, alcohol, clonidine (an antihypertensive drug), and haloperidol (a dopamine blocker) are known to inhibit the release of ADH. Other drugs such as nicotine and morphine stimulate the release of ADH. Drugs such as lithium (used to treat manic-depressives) and the antibiotic tetracyclines impair the ability of the collecting duct to respond to ADH.

The second important controller of urine formation is the hormone aldosterone. Aldosterone, secreted by zona glomerulosa cells in the adrenal cortex, works by diffusing into the epithelial cells, where it interacts with several receptor proteins and diffuses into the cell nucleus. In the cell nucleus it induces the production of the messenger RNA associated with several important proteins that are ingredients of Na$^+$ channels. The net effect is that (after about an hour) the number of Na$^+$ channels in the cell membrane increases, with a consequent increase of Na$^+$ conductance. Aldosterone is also known to increase the Na,K-ATPase activity in the collecting duct, as well as in other places in the nephron (a feature not included in this model), thereby increasing Na$^+$ removal and also K$^+$ excretion into the urine. For persons with *Addison's disease* (severely impaired or total lack of aldosterone), there is tremendous loss of Na$^+$ by the kidneys and accumulation of K$^+$. Conversely, excess aldosterone secretion, as occurs in patients with adrenal tumors (Conn's syndrome), is associated with Na$^+$ retention and K$^+$ depletion.

To see the effect of these controls we examine the behavior of our model in two limiting cases. In the first case, we assume that there is no ADH present, so that $\rho_c = \infty$, and that there is no aldosterone present, so that $H_c = 0$. In this case it follows from (17.53) that $Q_c = Q_c(0) = -Q_a$ and that $C_c = C_c(0) = C_a(0)$. In other words, there is no loss of either water or Na^+ from the collecting duct: the collecting duct has effectively been removed from the model.

It remains to determine what happens in the descending and ascending tubules. The flow is governed by the single differential equation

$$\rho_d \frac{dQ_d}{dy} = C_d - C_s - \Delta P_d = f(Q_d, Q_a, y), \tag{17.58}$$

where, from (17.50), (17.52), and (17.55),

$$C_d = \frac{1}{Q_d}(1 + \rho_d H_d(1 - Q_d) - \Delta P_d H_d y), \tag{17.59}$$

$$C_s = \frac{(P + \Delta P_d H_d)(1 - y)}{Q_d + Q_a} - \rho_d H_d, \tag{17.60}$$

subject to the boundary conditions $Q_d(0) = 1, Q_d(1) = -Q_a$. As before, Q_a is a constant, as the ascending limb is impermeable to water, and C_a is a linearly decreasing function of y.

We view this problem as a nonlinear eigenvalue problem, since it is a single first-order differential equation with two boundary conditions. The unknown parameter Q_a is the parameter that we adjust to make the solution satisfy the two boundary conditions. It is reasonable to take ρ_d to be small, since the descending tubule is quite permeable to water. In this case, however, the differential equation (17.58) is singular, since a small parameter multiplies the derivative. We overcome this difficulty by seeking a solution in the form $y = y(Q_d, \rho_d)$ satisfying the differential equation

$$f(Q_d, Q_a, y) \frac{dy}{dQ_d} = \rho_d \tag{17.61}$$

subject to boundary conditions $y = 0$ at $Q_d = 1$ and $y = 1$ at $Q_d = -Q_a$.

With ρ_d small we have a regular perturbation problem in which we seek y as a function of Q_d as a power series of ρ_d, which is solved as follows. We assume that y has a power series representation of the form

$$y = y_0 + \rho_d y_1 + \rho_d^2 y_2 + O(\rho_d^2), \tag{17.62}$$

substitute into (17.61), expand in powers of ρ_d, collect like powers of ρ_d, and then solve these sequentially. We find that

$$y = 1 - \frac{Q_a + Q_d}{PQ_d - \Delta P_d H_d Q_a}\left[1 - \Delta P_d(Q_d + H_d)\right] + O(\rho_d). \tag{17.63}$$

Notice that $y = 1$ at $Q_d = -Q_a$. Now we determine Q_a by setting $y = 0$, $Q_d = 1$ in (17.63), and solving for Q_a. To leading order in ρ_d we find that

$$-Q_a = 1 - \frac{P + H_d \Delta P_d}{1 - \Delta P_d} + O(\rho_d). \tag{17.64}$$

It is now a straightforward matter to plot y as a function of Q_d, and then rotate the axes so that we see Q_d as a function of y. This is depicted with a dashed curve in Fig. 17.15 (using formulae that include higher-order correction terms for ρ_d). For comparison we also include the curves calculated for the case where ADH is present; the details of that calculation are given below. Note that in either the presence or absence of ADH, Q_a is always independent of y, while in the absence of ADH, Q_c is also independent of y. Once Q_d is determined as a function of y, it is an easy matter to plot the concentrations C_d and C_a as functions of y, as shown in Fig. 17.16.

From these we can draw some conclusions about how the loop of Henle works in this mode. Sodium is extracted from the descending limb by simple diffusion and from the ascending loop by an active process. The Na^+ that is extracted from the ascending loop creates a large osmotic pressure in the interstitial region that serves to enhance the extraction of water from the descending loop. This emphasizes the importance of the countercurrent mechanism in the concentrating process. As the fluid proceeds down the descending loop, its Na^+ concentration is continually increasing, and during its passage along the ascending loop, its Na^+ concentration falls. At the lower end of the loop the relative concentration of the formed urine (i.e., of substances that are impermeable, such as creatinine) is $\frac{1}{Q_d(1)}$. This quantity represents the "concentrating ability" of the nephron in this mode. Since $C_a(0) < C_d(0)$, as can be seen from Fig. 17.16, by the time the fluid reaches the top of the ascending loop, it has been diluted. Furthermore, comparing the value of $Q_d(1)(= Q_c)$ in the absence of ADH (dashed curve in Fig. 17.15) to the value of $Q_c(1)$ in the presence of ADH (solid curve in Fig. 17.15) shows that the flux out of the collecting duct is higher in the absence of ADH. Hence, combining these two observations, we conclude that in the absence of ADH, the nephron produces a large quantity of dilute urine, while in the presence of ADH, it produces a smaller quantity of concentrated urine. This is consistent with the qualitative explanation of nephron function given earlier in the chapter.

In Fig. 17.17 are shown the solute concentration C_a and the flow rate Q at the upper end of the ascending tubule as functions of dimensionless pump rate P. The formed urine is dilute whenever this solute concentration is less than one. The fact that this concentration can become negative at larger pump rates is a failure of the model, since the pump rate in the model is not concentration dependent.

Formation of urine with ADH

In the presence of ADH, the collecting tube is highly permeable to water, so that, since the concentration of Na^+ in the interstitium at the lower end of the tube is high, additional water can be extracted from the collecting duct, thereby concentrating the dilute urine formed by the loop of Henle.

To solve the governing equations in this case is much harder than in the case with no ADH. This is because the equations governing the flux (17.56) and (17.57) are both singular in the limit of zero ρ_d and ρ_c. Furthermore, one can show that the quasi-steady solution (found by setting $\rho_d = \rho_c = 0$ in (17.56) and (17.57)) cannot be made to satisfy the boundary conditions at $y = 1$, suggesting that the solution has a boundary layer. To avoid the difficulties associated with boundary layers, it is
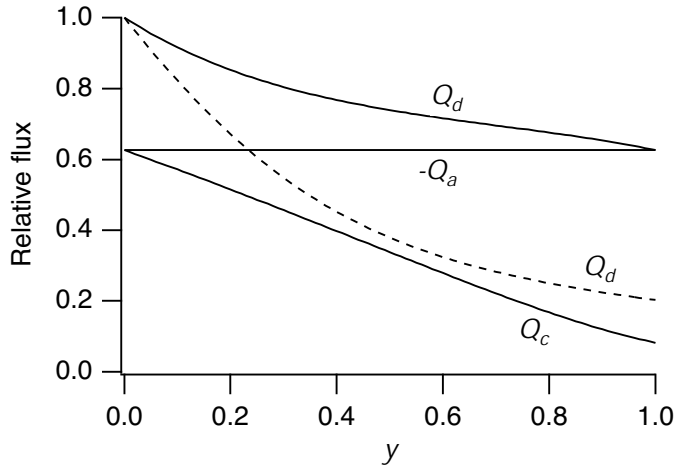
Figure 17.15: The flux of fluid in the loop of Henle, with ADH present (solid curve, $\rho_c = 2.0$) and without ADH present (dashed curve, $\rho_c = \infty$). Parameter values are $P = 0.9$, $\Delta P_d = 0.15$, $H_d = 0.1$, $\rho_d = 0.15$, $H_c = 0$.
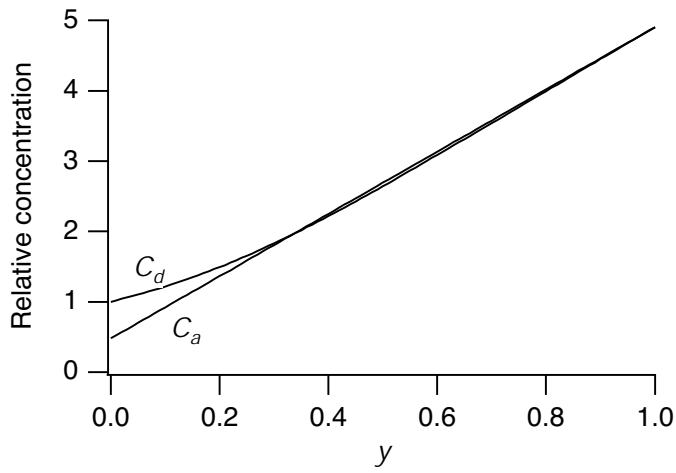

Figure 17.16: The solute concentration in the descending (C_d) and ascending (C_a) tubules with no ADH present ($\rho_c = \infty$), plotted as a function of distance y for the parameter set as in Fig. 17.15.
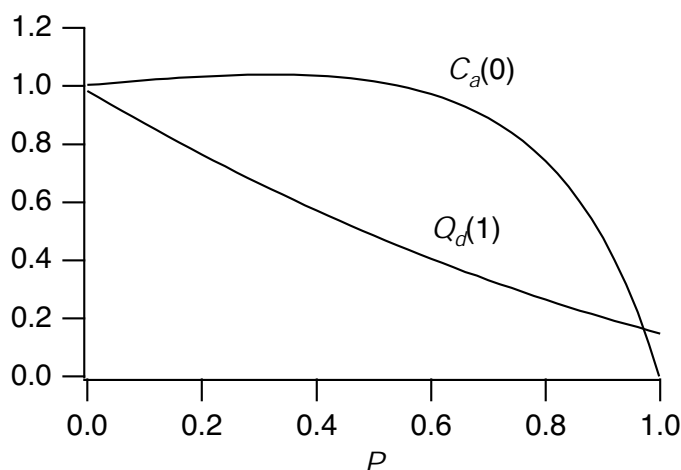
Figure 17.17: The solute concentration and the flow rate at the upper end of the ascending tubule plotted as functions of pump rate P when there is no ADH or aldosterone present ($\rho_c = \infty, H_c = 0$). Dilution occurs if the solute concentration is less than one. Parameter values are $\Delta P_d = 0.15, H_d = 0.1, \rho_d = 0.15$.

preferable to formulate the problem in terms of the solute flux $S_d = Q_d C_d$, because according to (17.51) this function is nearly linear and does not change rapidly when ρ_d is small.

In the case that ADH is present but there is no aldosterone ($H_c = 0$), the governing equations are

$$\frac{dS_d}{dy} = H_d\left(\frac{S_s}{Q_s} - \frac{S_d}{Q_d}\right) = H_d F_d(S_d, Q_c), \tag{17.65}$$

$$\rho_c \frac{dQ_c}{dy} = -\Delta P_c + \frac{S_c(0)}{Q_c} - \frac{S_s}{Q_s} = F_c(S_d, Q_c), \tag{17.66}$$

where

$$S_s = P(y-1) + S_d(1) - S_d, \tag{17.67}$$

$$Q_s = -1 - Q_a - Q_c + Q_c(1) - \frac{1 - S_d - \Delta P_d H_d y}{\rho_d H_d}, \tag{17.68}$$

$$Q_d = 1 + \frac{1 - S_d - \Delta P_d H_d y}{\rho_d H_d}, \tag{17.69}$$

subject to boundary conditions $S_d(0) = 1, Q_c(0) = 1 + \frac{1 - S_d - \Delta P_d H_d}{\rho_d H_d}$, and $Q_d(1) = -Q_a$.

These equations are difficult to solve because there are two unknown functions, S_d and Q_c, and an unknown constant Q_a, subject to three boundary conditions. One way to solve them is to introduce the constants Q_a and $Q_c(1)$ as unknown variables satisfying the obvious differential equations $\frac{dQ_a}{dy} = \frac{dQ_c(1)}{dy} = 0$, and to solve the
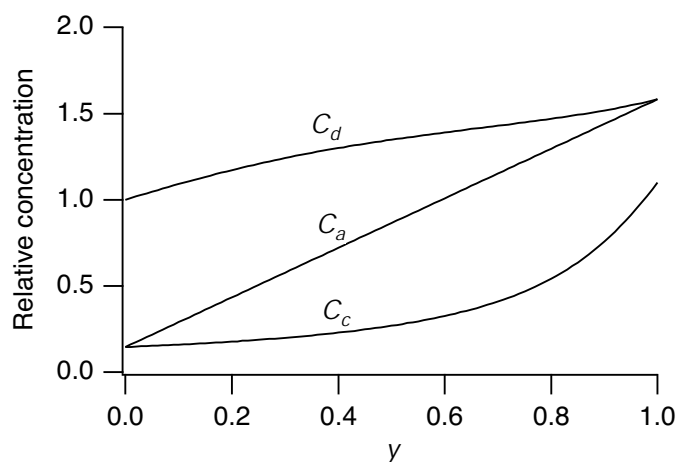
Figure 17.18: Solute concentrations in the loop of Henle and the collecting duct, plotted as functions of y for $P = 0.9, \Delta P_d = 0.15, \Delta P_c = 0.22, H_d = 0.1, \rho_d = 0.15$ and with $\rho_c = 2.0, H_c = 0$.

expanded fourth-order system of equations in the four unknowns $S_d, Q_c, Q_a, Q_c(1)$ with four corresponding boundary conditions (adding the requirement that $Q_c = Q_c(1)$ at $y = 1$).

These equations were solved numerically using a centered difference scheme for the discretization and Newton's method to find a solution of the nonlinear equations (see Exercise 9). Typical results are shown in Fig. 17.18. Here we see what we expected (or hoped), namely that the collecting duct concentrates the dilute urine by extracting water. In fact, we see that the concentration increases on its path through the descending loop, decreases in the ascending loop, and then increases again in the collecting duct. This behavior is similar to the data for Na^+ concentration shown in Fig. 17.11.

The effect of the parameter ρ_c is shown in Figs. 17.19 and 17.20. In these figures are shown the solute concentrations and the flow rates at the bottom and top of the loop of Henle and at the end of the collecting duct. Here we see that the effect of ADH is, as expected, to reconcentrate the solute and to further reduce the loss of water.

The asymptotic value of $C_c(1)$ as $\rho_c \to 0$ is the maximal solute concentration possible and determines, for example, whether or not the individual can safely drink seawater without dehydration. The asymptotic value of $1/Q_c(1)$ represents the highest possible relative concentration of impermeable substances such as creatinine.

Further generalizations

This model shows the basic principles behind nephron function, but the model is qualitative at best, and there are many questions that remain unanswered and many generalizations that might be pursued. For example, the model could be improved by incorporating a better representation of the interstitial/capillary bed flow, taking
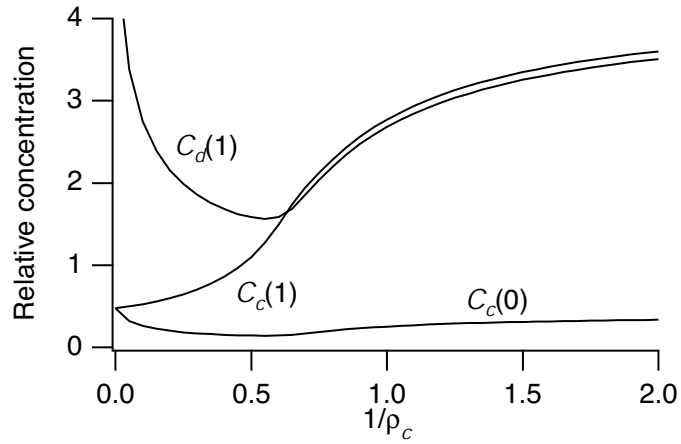
Figure 17.19: Solute concentrations at the bottom and top of the loop of Henle and at the end of the collecting duct plotted as functions of inverse permeability $\frac{1}{\rho_c}$, with $P = 0.9$, $\Delta P_d = 0.15$, $\Delta P_c = 0.22$, $H_d = 0.1$, $\rho_d = 0.15$, and $H_c = 0$.
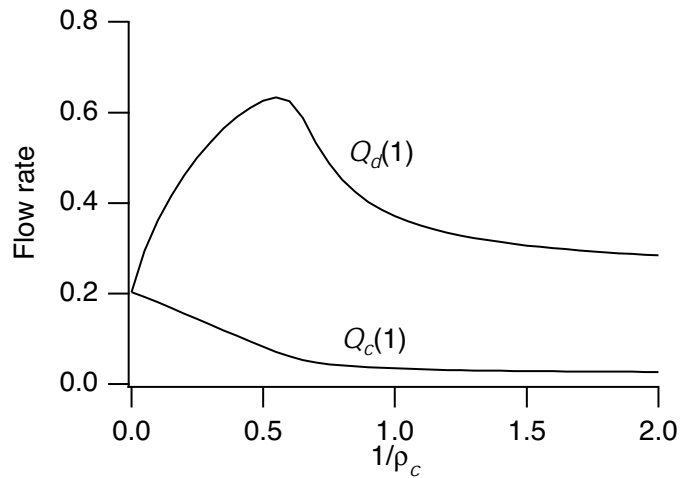

Figure 17.20: Fluid flow rates at the bottom of the loop of Henle and at the end of the collecting duct plotted as functions of inverse permeability $\frac{1}{\rho_c}$, with $P = 0.9$, $\Delta P_d = 0.15$, $\Delta P_c = 0.22$, $H_d = 0.1$, $\rho_d = 0.15$, and $H_c = 0$.

into account that the peritubular capillaries issue directly from the efferent arteriole of the glomerulus, thus determining the hydrostatic and osmotic pressures in the capillary bed. The model is also incorrect in that the active pumping of Na^+ out of the ascending limb is not concentration dependent, and as a result negative concentrations can occur for certain parameter values.

It is a fairly easy matter to add equations governing the flux of solutes other than Na^+, as the principles governing their flux are the same. One can also consider a time-dependent model in which the flow of water is not steady, by allowing the cross-sectional area of the tubules to vary. Nonsteady models are difficult to solve because they are stiff, and there is a substantial literature on the numerical analysis and simulation of time-dependent models (Layton et al., 1991).

Nephrons occur in a variety of lengths, and models describing kidney function have been devised that recognize that nephrons are distributed both in space and in length (Layton et al., 2004; Layton and Layton, 2003, 2005a,b) . These models are partial differential equations, and again, because of inherent stiffness, their simulation requires careful choice of numerical algorithms (Layton et al., 1995; Layton and Layton, 2002, 2003).

17.3   Models of Tubular Transport

So far in this chapter we have discussed glomerular filtration and the formation of urine. The third major group of models in renal physiology are those of the transport of water and solutes by the various epithelial cells that line the tubules. The most important of these models are undoubtedly those of Alan Weinstein; see, for example, Weinstein (1994, 1998, 2000, 2003).

Two of the most significant questions addressed by these models is how the epithelial cell layer can transport water against an osmotic gradient, so-called *uphill* transport, or under conditions of little or no osmotic gradient, so-called *isotonic* transport. These questions were the subject of some of the earliest models (see, for instance, Weinstein and Stephenson, 1981), and remain important today. Discussion of simple models of uphill and isotonic water transport are deferred to Chapter 18, Section 18.1.2, as these questions are also important in the gastrointestinal system.

Models of tubular transport usually also include descriptions of solute transport by both active and passive mechanisms. Typical solutes include Na^+, K^+, HCO_3^-, Cl^-, H, HPO_4, NH_4, glucose and PO_4, giving rise to complex models with a multitude of variables and parameters. Because the epithelial cells in different parts of the nephron have different permeabilities, pumps and exchangers, there are different models for the collecting duct, the ascending and descending limbs, and the proximal tubule. As is described in Chapter 18, the lateral intercellular spaces (the spaces between the epithelial cells) play a crucial role in water and solute transport in models of this type, and are usually included explicitly in the models.
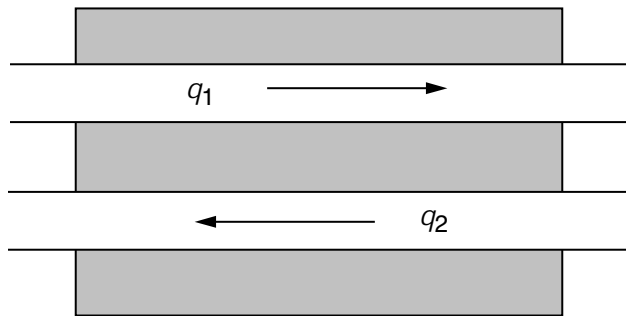
Figure 17.21: Diagram of a countercurrent flow mediated by an interstitium, for Exercise 5.

Exercises

1. The flow of glomerular filtrate and the total renal blood flow increase by 20 to 30 percent within 1 to 2 hours following a high-protein meal. How can this feature be incorporated into a model of renal function and regulation of glomerular function?

   Hint: Amino acids, which are released into the blood after a high protein meal, are cotransported with Na^+ ions from the filtrate in the proximal tubule. Thus, high levels of amino acids leads to high reabsorption of Na^+ in the proximal tubule, and therefore, lower than normal levels of Na^+ at the macula densa.

2. Show that (17.16) has a unique positive root.

3. How much water must one drink to prevent any dehydration after eating a 1.5 oz bag of potato chips? (See Exercise 19 in Chapter 2.) Remark: A mole of NaCl is 58.5 grams and it dissociates in water into 2 osmoles.

4. Why is alcohol a diuretic? What is the combined effect on urine formation of drinking beer (instead of water) while eating potato chips? What is the combined effect on urine formation of drinking beer while smoking cigarettes?

   Hint: Alcohol inhibits the release of ADH, while nicotine stimulates ADH release.

5. Construct a simple model of the countercurrent mechanism that includes an interstitial compartment (Fig. 17.21). Show that inclusion of the interstitium has no effect on the overall rates of transport. Allow the solute to diffuse in the interstitium, but not escape the boundaries.

   Hint: View the interstitium as a tube with zero flow rate.

6. Generalize the four-compartment model for the loop of Henle by separating the interstitium and peritubular capillaries into separate compartments, allowing no flow across $x = 0$ or $x = L$ for the interstitium.

7. What changes in the exchange rates of the four compartment model for the loop of Henle might better represent the geometry of the loop of Henle, as depicted in Fig. 17.2?

   Remark: Some features to consider include the location of the thickening of the ascending and descending limbs and the location of the junction of the peritubular capillaries with the arcuate vein.

8. Formulate a time-dependent four-compartment model of urine concentration that tracks the concentration of both Na^+ ions and urea.

9. Develop a numerical computer program to solve the equations of renal flow in the case that both ADH and aldosterone are present. It is preferable to formulate the problem in terms of the unknowns S_d and S_c and to expand the system of equations to a fourth-order system by allowing $S_d(1)$ and $S_c(1)$ to be unknowns that satisfy the simple differential equations $\frac{dS_d(1)}{dy} = 0$ and $\frac{dS_c(1)}{dy} = 0$. With the 4 unknowns, $S_d(y), S_c(y), S_d(1)$, and $S_c(1)$, the Jacobian matrix is a banded matrix, and numerical algorithms to solve banded problems are faster and more efficient than full matrix solvers.

10. Generalize the renal model to include a concentration-dependent Na^+ pump in the ascending tubule. Does this change in the model guarantee that the flux and concentrations are nowhere negative?

Chapter 18

The Gastrointestinal System

Although the detailed structure of the gastrointestinal tract (GI tract) varies from region to region, there is a common basic structure, outlined in the cross-section shown in Fig. 18.1. It is surrounded by a number of heavily innervated muscle layers, arranged both circularly and longitudinally. Contraction of these muscle layers can mix the contents of the tract and move food in a controlled manner in the appropriate direction. Beneath the muscle layer is the *submucosa*, consisting mostly of connective tissue, and beneath that is a thin layer of smooth muscle called the *muscularis mucosae*. Finally, there is the *lamina propria*, a layer of connective tissue containing capillaries and many kinds of secreting glands, and then a layer of epithelial cells, whose nature varies in different regions of the tract.

In addition to the muscle layers, there are two principal layers of neurons; the myenteric plexus, between the longitudinal and circular muscle layers, and the submucosal plexus, which lies in the submucosa. In general, stimulation of the myenteric plexus increases the rate and intensity of the rhythmic contractions of the gut, and increases the velocity of conduction of waves of excitation along the gut wall. The submucosal plexus is mainly sensory, receiving signals from stretch receptors in the gut wall, and from the gut epithelium. The GI tract is also heavily innervated, which can control the activity of the entire gut, or part of it.

18.1 Fluid Absorption

The primary function of the gastrointestinal tract is to absorb nutrients from the mix of food and liquid that moves through it. To accomplish this, the absorptive surface of the intestines consists of many folds and bends called *valvulae conniventes*, which increase the surface area of the absorptive mucosa about threefold. Located over the entire surface of the mucosa of the small intestine are millions of *villi*, which project about 1 mm from the surface of the mucosa and enhance the absorptive area another tenfold. The absorptive surface of the villi consists of epithelial cells that are characterized by a brush border, consisting of as many as 1000 *microvilli* 1 μm in length and 0.1 μm in diameter. The brush border increases the surface area exposed to the intestinal material by another twentyfold. The combination of all
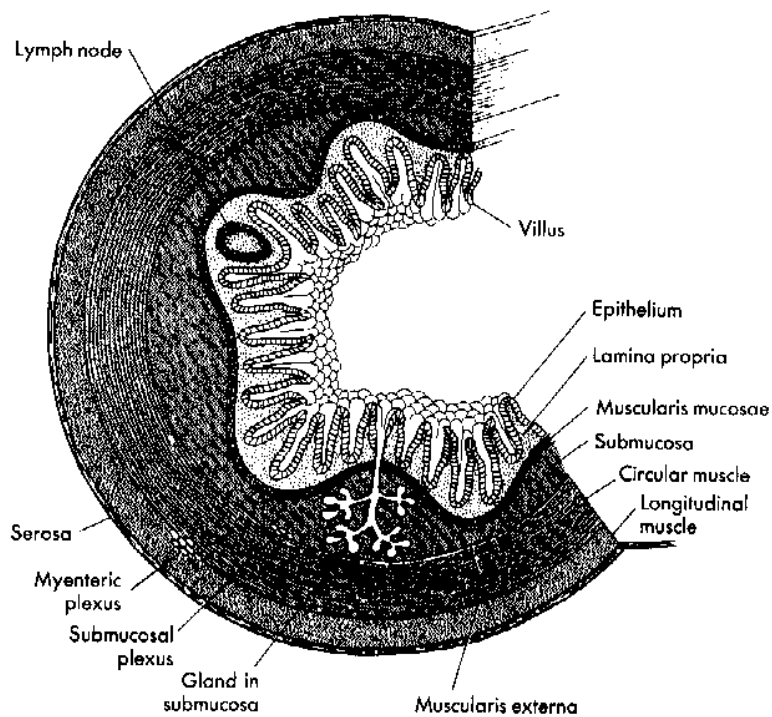
Figure 18.1: Cross-section of the gastrointestinal tract. The outermost layers of the tract consist of smooth muscle, while the innermost layer consists of epithelial cells. The epithelial cell layer contains many gastric pits, glands that secrete hydrochloric acid, and thus the stomach lumen is highly acidic. (Berne and Levy, 1993, Fig. 38-1, p. 616.)

surface protrusions yields an absorptive surface area of about 250 square meters—about the surface area of a tennis court.

Epithelial cells are responsible for the absorption of nutrients and water from the intestine. The absorption of chemical nutrients, for example glucose and amino acids, is by the same process as in the kidney, via cotransporters with sodium.

For many years, it was believed that water is absorbed, or transported through cells, simply because the membrane is porous to water. In this scenario, the movement of ions, either by passive diffusion or by active transport, sets up osmotic gradients which, in turn, drive the flow of water across the membrane. Recall that this is the basic assumption underlying the cell-volume control models described in Chapter 2. However, the discovery in 1992 of transmembrane proteins that allow only (or at least mostly) water to permeate, called *aquaporins*, has changed this view dramatically (Reuss and Hirst, 2002). The first aquaporin to be discovered was AQP1, discovered in 1992 by Agre and his colleagues (Preston et al., 1992). Agre received the 2003 Nobel Prize in Chemistry for this discovery. Aquaporins have since been identified in practically every living organism, and have such high selectivity to water that they repel even H_3O^+ and hydrogen ions. The fact that water flow is through transmembrane protein structures means that, although it is driven by osmotic gradients, it is genetically regulated, and that malfunctioning channels may be associated with many diseases of the kidneys, skeletal muscle and other organs. A review by Agre et al. (2002) discusses a number of areas in which the discovery of aquaporins has had a major impact on our understanding of physiology and pathophysiology.

To complicate matters further, there is evidence that water can be transported actively, by co-transport with a solute (Loo et al., 2002; Zeuthen, 2000). This view has been challenged by other researchers, who claim that the water transport is osmotically driven but that the solute accumulates in spatially restricted areas not amenable to experimental access (Lapointe et al., 2002). However, it remains an intriguing possibility that, if true, would necessitate significant rethinking of models of water transport.

Although the control of absorption and transport of water is perhaps more complicated than first thought, osmosis appears to be the primary driving force. This being the case, one particularly important question arises; how can an epithelial cell layer transport water against its osmotic gradient (*uphill* transport)? Water transport under such conditions is observed in both the gastrointestinal system and the kidney. A related question is the mechanism of *isotonic* transport, in which the transported fluid has the same osmolality of the fluid into which it is transported.

Here we present two models for water transport via osmosis; the first is a simpler model that includes no spatial information, while the second, due to Diamond and Bossert (1967), shows how the maintenance of a standing gradient of solute concentration in a restricted spatial area can lead to isotonic and uphill water transport.

18.1.1   A Simple Model of Fluid Absorption

In general, GI tract epithelial cells are not permeable to water on their lumenal side. However, there are 0.7–1.5 nm pores through the *tight junctions* between
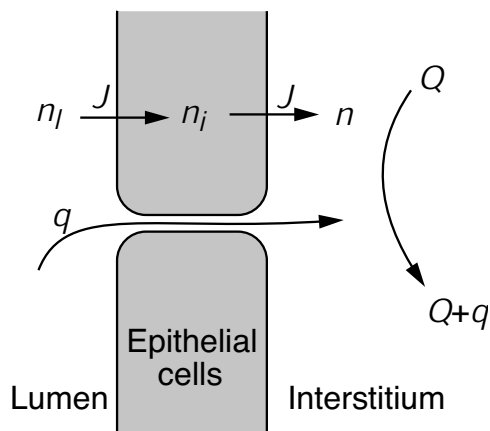
Figure 18.2: Diagram for osmotic transport of water across the epithelial cell wall. J denotes the flow of Na^+, q denotes the flow of water, and Q denotes capillary blood flow.

epithelial cells that permit water to diffuse readily between the lumen and the interstitium. The absorption of water through these pores is driven primarily by the sodium gradient between the lumen and the interstitium. Sodium is transported to the interior of the epithelial cell by passive transport and then is removed from the interior to the interstitium by a sodium–potassium ATPase. The sodium is transported from the interstitium by capillary blood flow.

To model the transport of water by the epithelial cell lining, we consider a small section of the epithelial gastrointestinal tract as two well-mixed compartments, the lumen and the interstitium, separated by a membrane (Fig. 18.2). We suppose that the sodium concentration in the lumen is n_l and in the cell interior is n_i, and that the concentration of all osmolites in the interstitium is n. The flow of sodium J from the lumen to the interior of the cells is assumed to be passive (i.e., we ignore the effects of the membrane potential; see Exercise 1), and so

$$J = g(n_i - n_l), \tag{18.1}$$

for some constant g. Sodium flux from the cell interior to the interstitium is via an active sodium–potassium ATPase,

$$J = f(n_i), \tag{18.2}$$

for some saturating function f. The flow of water q through the tight junctions is driven by the osmotic pressure difference between the lumen and the interstitium, so that

$$Rq = n - n_l, \tag{18.3}$$

where R is the resistance (in appropriate units) of the tight junctions. Finally, we assume that there is a flow into and out of the interstitium provided by capillary flow. The influx of fluid is Q with an incoming concentration of osmolites n_0, while the outflow of osmolites is $Q + q$ at concentration n. At steady state, the conservation of sodium implies that

$$g(n_l - n_i) = f(n_i) \tag{18.4}$$

and

$$(Q + q)n - Qn_0 = f(n_i). \tag{18.5}$$

The behavior of this system of three algebraic equations is relatively easy to sort out. Since f is a positive, monotone increasing function of its argument, there is a one-to-one relationship between n_l and n_i,

$$n_l = n_i + \frac{1}{g}f(n_i). \tag{18.6}$$

We can use (18.3) to eliminate n from (18.5) and obtain

$$Rq^2 + (RQ + n_l)q + Q(n_l - n_0) - f(n_i) = 0. \tag{18.7}$$

Because the rate of sodium removal is dependent on the sodium concentration, we take $f(n) = \frac{Q_f n^3}{N^3 + n^3}$, for some constants Q_f and N.

It is valuable to nondimensionalize this problem by scaling all concentrations by N, setting $u_j = n_j/N$ and $y = q/Q$. Then (18.7) becomes

$$\rho y^2 + (\rho + u_l)y + \kappa = 0, \tag{18.8}$$

where $\kappa = u_i - u_0 + (1 - \gamma)\beta F(u_i) = 0, \rho = RQ/N, \gamma = g/Q$, and $\beta = \frac{Q_f}{gN}$, and (18.6) becomes

$$u_l = u_i + \beta F(u_i), \tag{18.9}$$

where $F(u) = \frac{u^3}{1+u^3}$. There are four nondimensional parameters, namely u_0, the (relative) concentration of incoming interstitial osmolites; ρ, the resistance of the tight junctions to water; γ, the relative permeability of the lumenal cell wall to sodium; and β, the maximal velocity of active sodium transport (which depends primarily on the density of sodium pumps).

The easiest way to solve these equations for y as a function of u_l is to view the solution as the curve $y = y(u_i)$, $u_l = u_l(u_i)$, parametrized by u_i, since for each u_i, u_l is readily determined from (18.9), and then y is determined from (18.8). Observe that (18.8) is a quadratic polynomial in y that has at most one positive root. In fact, the larger root of this polynomial is positive if and only if $\kappa < 0$. Furthermore, the positive root is a monotone decreasing function of κ.

There are several behaviors of the solution depending on the parameter values. However, the behavior that is of most interest here occurs when $\beta(\gamma - 1)$ is a large positive number. In this case, κ is an "N"-shaped function of u_i, negative at $u_i = 0$, increasing for small values of u_i, then decreasing and finally increasing and eventually becoming positive for large u_i.
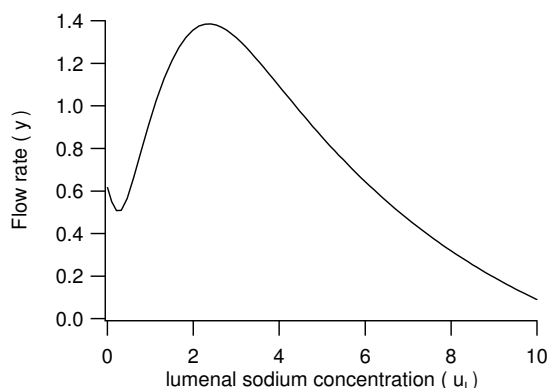
Figure 18.3: Flux of water through the epithelial membrane plotted as a function of lumenal sodium concentration, with parameter values $\rho = u_0 = \beta = 1$, $\gamma = 10$.

For much of parameter space this "N"-shaped behavior for κ translates into "N"-shaped behavior for the positive root of (18.8). That is, with $u_l = 0$, there is a positive root. This root initially decreases to a minimal value and then increases to a maximal value, whereupon it decreases and eventually becomes negative, as a function of u_l. This behavior is depicted in Fig. 18.3, with parameter values $\rho = u_0 = \beta = 1, \gamma = 10$.

The implications of this are interesting. It implies that one can maximize the absorption of water by adjusting the sodium level of the lumenal water. Thus, hydration occurs more quickly with fluids containing electrolytes than with pure water, as many high-performance athletes (such as road cyclists and long-distance runners) already know. However, too much sodium has the opposite effect of dehydrating the interstitium. This is a local effect only, as water is reabsorbed further along the tract.

When a person becomes dehydrated, large amounts of aldosterone are secreted by the adrenal glands. Aldosterone greatly enhances the transport of sodium by epithelial cells by activating the production of channel and pump proteins, which increases the passive and active transport of sodium. Indeed, a person can acclimatize to heavy exercise in hot weather, as over a period of weeks increased aldosterone secretion from the adrenal cortex prevents excessive sodium loss in sweat, thus dispensing with the need for dietary sodium supplements. Loss of potassium can still, however, be a problem.

In this model the presence of aldosterone can be modeled by increasing g, the conductivity of sodium transport from the lumen, and/or by increasing Q_f, the maximal rate of active sodium pumping. It is easy to see that the total flux of sodium $J = f(n_i)$ and the flux of water q both increase if either g or Q_f (or both) are increased. However, this increase is not without bound, since in the limit $g \to \infty$, we have $n_i \to n_l$, so that

$$\lim_{g \to \infty} J = f(n_l), \tag{18.10}$$

and

$$\lim_{g \to \infty} q = Q \left(\frac{n_0}{n_l} - 1 \right) + \frac{f(n_l)}{n_l}, \qquad (18.11)$$

when $R = 0$. Thus, if a person is dehydrated, aldosterone production works to increase sodium absorption and decrease water loss.

Now we can construct a simple model of water content and sodium concentration as a function of distance along the intestinal length. We suppose that the *chyme* (the mixture of food, water, and digestive secretions entering from the stomach) moves as a plug flow with constant velocity. Water is removed from the chyme by osmosis and sodium is removed by the epithelial cells at local rates determined by the local sodium concentration. In steady state,

$$\frac{dQ_w}{dx} = -q(n_l), \qquad (18.12)$$

$$\frac{d(n_l Q_w)}{dx} = -J(n_l), \qquad (18.13)$$

where Q_w is the flow of water in the intestine, x is the distance along the intestine, and $q(n_l)$ and $J(n_l)$ are the removal rates of water and sodium, such as those suggested above. The analysis of this system of equations is straightforward and is left as an exercise (Exercise 2).

There are two common abnormalities that can occur in this process. *Constipation* occurs if the movement of feces through the large intestine is abnormally slow, allowing more time for the removal of water and therefore hardening and drying of the feces. Any pathology of the intestines that obstructs normal movement, including tumors, ulcers, or forced inhibition of normal defecation reflexes, can cause constipation.

The opposite condition, in which there is rapid movement of the feces through the large intestine, is known as *diarrhea*. There are several causes of diarrhea, the most common of which is infectious diarrhea, in which a viral or bacterial infection causes an inflammation of the mucosa. Wherever it is infected, the rate of secretion of the mucosa is greatly increased, with the net effect that large quantities of fluid are made available to aid in the elimination of the infectious agent.

For example, the toxins of cholera and other diarrheal bacteria stimulate immature epithelial cells (which are constantly being produced) to release large amounts of sodium and water, presumably to combat the disease by washing away the bacteria. However, if this excess secretion of sodium and water cannot be overcome by the absorption by mature, healthy cells, the result can be lethal because of serious dehydration. In most instances, the life of a cholera victim can be saved by intravenous administration of large amounts of sodium chloride solution to make up for the loss.

18.1.2 Standing-Gradient Osmotic Flow

In order for water transport to occur by osmosis it appears at first glance that the extracellular fluid must be hypertonic, i.e., have a higher solute concentration than the cell cytoplasm. For, if it were not, how could water be transported osmotically
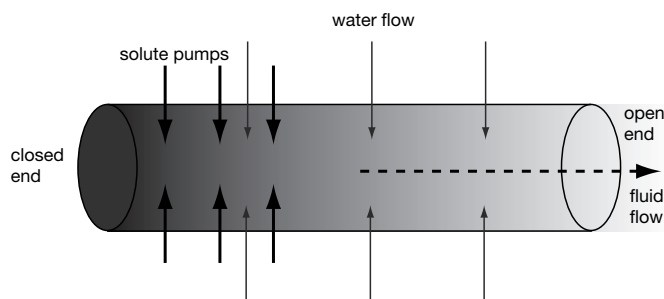
Figure 18.4: Schematic diagram of a long, narrow, tube in which solute-linked water transport occurs. The open end is the side to which fluid is secreted.

out of the cell? However, it has been known for many years that many types of epithelia (such as in the intestine and the kidney) are capable of transporting water in the absence of an osmotic gradient, or even against an osmotic gradient. Furthermore, the transported fluid itself is very close to isotonic. Both of these observations are difficult to reconcile with simple theories of solute-linked transport.

To explain such observations, Diamond and Bossert (1967; their model was an extension of the original idea of Curran and MacIntosh, 1962) proposed the standing-gradient osmotic flow model, a model that was, until recently, the basis for most quantitative explanations of solute-linked water transport. The standing gradient model was analyzed mathematically by Segel (1970; see also Lin and Segel, 1974), and Weinstein and Stephenson (1981) analyze a slight variant of this model.

One important characteristic of solute-linked water transport by epithelia is that, at the ultrastructural level, such epithelia have long, narrow channels, open at the end out of which water is flowing, and closed at the other end. This channel is sometimes the lateral intercellular space (long, narrow channels between neighboring cells), but it can also be infoldings of the basilar membrane. Because this is such a common feature of transporting epithelial cells Diamond and Bossert proposed that it was this anatomical feature that was responsible for the ability of epithelia to secrete (almost) isotonic fluid in an isotonic environment, and they constructed a mathematical model to show how this could be.

Before embarking on the mathematical presentation, it is helpful first to gain an intuitive feel for how such a process works. Suppose we have a long, narrow tube, closed at one end and open at the other, as shown in Fig. 18.4A. When solute is actively pumped into the closed end of the tube, the higher solute concentration in this restricted space is not immediately dissipated by diffusion, and thus a localized concentration gradient is set up across the tube wall, drawing water into the tube from the cytoplasm. However, water transport into the tube sets up a flow of water, which washes the solute out of the tube into the extracellular medium. Thus, a localized high solute concentration can be used to drive water flow even in the absence of concentration gradients on a larger spatial scale.

Suppose that solute-linked water transport occurs in a long, narrow, cylindrical tube of length L and radius r, closed at one end (Fig. 18.4). Solute is actively

transported across the border of the tube, from the cell cytoplasm into the tube, and water follows passively, driven by the osmotic pressure difference.

Let $N(x)$ be the rate of active solute transport, with units of moles per unit area per unit time, across the boundary of the cylindrical tube. Usually, N is non-zero only at that portion of the channel close to the closed end. Also, let $v(x)$ be the velocity of the fluid flow at point x, where a positive velocity denotes flow in the direction of increasing x, and let $c(x, t)$ be the concentration of the solute in the tube at position x.

The differential equations for c and v are derived by standard conservation arguments. For a circular tube of radius r,

$$\pi r^2 \frac{\partial c}{\partial t} = -\pi r^2 \frac{\partial J}{\partial x} + 2\pi r N(x),$$

$$= -\pi r^2 \frac{\partial}{\partial x}\left(vc - D\frac{\partial c}{\partial x}\right) + 2\pi r N(x), \tag{18.14}$$

$$\tag{18.15}$$

since $J = vc - D\frac{\partial c}{\partial x}$ is the flux per unit area of solute in the tube.

In steady state, this gives

$$D\frac{d^2 c}{dx^2} - \frac{d}{dx}(vc) + \frac{2N(x)}{r} = 0. \tag{18.16}$$

Similarly, the velocity of water along the tube is v and the flow per unit area of water entering the tube driven by osmotic pressure is $P(c(x) - c_0)$, where c_0 is the concentration of solute everywhere outside the cylindrical tube. Thus, in steady state, conservation of water implies that

$$\frac{dv}{dx} = \frac{2P}{r}(c(x) - c_0). \tag{18.17}$$

At the closed end there is no flow of water or solute, and thus

$$v(0) = \frac{dc(0)}{dx} = 0. \tag{18.18}$$

However, because this is a third order system, we need a third boundary condition. For this we assume that the open end of the channel opens into a large space for which c is everywhere c_0, so take

$$c(L) = c_0. \tag{18.19}$$

Notice that this boundary condition is an approximation only; a more accurate model would determine the movement of solute and water in the tube as well as in the surrounding space. However, $c = c_0$ is a reasonable approximation if solute is quickly transported away from the end of the tube, and is thus forced to remain at a constant concentration there. This is the same approximation that is made in all introductory textbooks that discuss the heat equation for a one dimensional conducting rod, with ends held at a fixed temperature by a large heat bath. Notice

also that a similar problem occurs at the external sides of the tube walls, since anywhere solute is removed, the concentration cannot be identically c_0 there, even though that is the assumption we make.

Several features of the solution can be deduced without completely solving the equations. First, integrating (18.16) and (18.17) over the length of the tube, and applying the boundary conditions, one finds that

$$v(L)c_0 - D\frac{dc(L)}{dx} = \int_0^L \frac{2N(x)}{r}dx, \qquad (18.20)$$

and

$$v(L) = \frac{2LP}{r}(\bar{c} - c_0), \qquad \bar{c} = \frac{1}{L}\int_0^L cdx. \qquad (18.21)$$

The second of these tells us that the higher the average concentration of solute in the tube, the higher the efflux velocity.

The concentration of solute in the efflux, c_e, is defined to be the rate of total solute pumped into the tube, divided by the total flow out of the tube

$$c_e = \frac{2\pi r \int_0^L N(x)\,dx}{\pi r^2 v(L)} = \frac{2\int_0^L N(x)\,dx}{rv(L)}. \qquad (18.22)$$

Clearly, c_e is not the same as c_0, In fact, from (18.20),

$$c_e = c_0 - \frac{D}{v(L)}\frac{dc(L)}{dx}. \qquad (18.23)$$

Thus, the greater the fluid velocity at the mouth of the channel, the lower the efflux concentration, and the closer the efflux fluid is to isotonic.

Some typical solutions are shown in Fig. 18.5. We take $N(x)$ to be the step function $N(x) = N_0 H(aL - x)$, so that solute is pumped into the tube only in the region $0 < x < aL$, with $a = 0.1$. For $x > aL$, the concentration of solute decreases along the length of the tube and, depending on the parameters, the efflux can be almost isotonic with the background solution. For the parameters given in the caption to Fig. 18.5, the efflux concentration is 0.434 μM when $N_0 = 0.3$, and is 0.344 when $N_0 = 0.1$. As the length of the channel decreases, but with solute actively pumped into only the 10% of the channel closest to the closed end ($a = 0.1$), the efflux concentration increases; for a short channel (with these same parameter values) the efflux concentration can be almost ten times the background concentration. This is because in a short channel the solute diffuses out of the tube relatively rapidly so that the osmotic driving force is decreased, and there is less space over which osmotic balance can be achieved.

The solutions shown in Fig. 18.5 were computed numerically using a shooting method. Since we know $v(0) = 0$ and $\frac{dc(0)}{dx} = 0$, we can guess a value of $c(0)$, and then solve the initial value problem numerically to determine $c(L)$. If $c(L)$ is smaller than c_0, we increase the initial value for c, while if $c(L)$ is too large we reduce the initial value for c. Thus, by trial and error (or more systematically, using bisection), we can determine the value $c(0)$ that gives the correct boundary value at L.
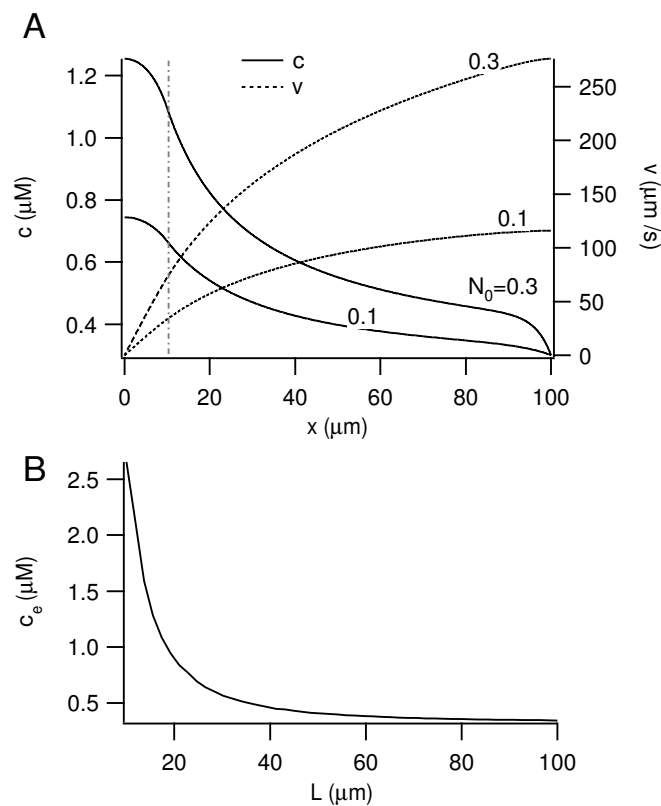
Figure 18.5: A: The standing concentration gradient of solute in the tube and the associated fluid velocity, computed numerically. Parameters are $D = 1000\ \mu\text{m}^2\,\text{s}^{-1}$, $r = 0.05\ \mu\text{m}$, $c_0 = 0.3\ \mu\text{M}$, $P = 0.2\ \mu\text{m}\,\text{s}^{-1}\,\mu\text{M}^{-1}$, and $L = 100\ \mu\text{m}$. $N(x) = N_0$ on the region $0 \leq x \leq aL$, $a = 0.1$ (i.e., to the left of the vertical dashed line) and is zero elsewhere. Two different values were used for N_0 (in units of nanomoles per square meter per second); $N_0 = 0.3$ and $N_0 = 0.1$. B: the efflux solute concentration as a function of L with other parameters the same as in A ($N_0 = 0.1$).

James, because this problem is stiff, I don't believe that forward Euler can be trusted. I've tried several other integration methods in Matlab and none work, at least for D = 1000. The problem is that integration fails before the end is reached. I'm completely stumped. JK

Although this numerical method is direct, there are difficulties because the problem is stiff. Near $x = L$, the solution of the differential equations is close to a saddle point, and shooting into a saddle point is notoriously unstable. Said another way, if D is small (in a way made precise below), then this problem is singular, since a small number multiplies the largest derivative.

Thus, the second way to find solutions of this problem is with perturbation arguments, taking advantage of small parameters. To study the problem in the small diffusion limit (which is the limit in which numerical solutions are most difficult to obtain), we nondimensionalize the problem, setting $y = \frac{x}{L}$, $u = \frac{c}{c_0}$ and $w = \frac{vr}{c_0 PL}$, and substituting into the equations to get

$$\epsilon \frac{d^2 u}{dy^2} - \frac{d}{dy}(wu) \;=\; -2n(y), \tag{18.24}$$

$$\frac{dw}{dy} \;=\; 2(u-1), \tag{18.25}$$

where $\epsilon = \frac{Dr}{L^2 c_0 P}$ and $n(x) = \frac{N(x)}{c_0^2 P}$, with the corresponding boundary conditions

$$w(0) = \frac{du}{dy}(0) \;=\; 0, \tag{18.26}$$

$$u(1) \;=\; 1. \tag{18.27}$$

For the parameter values shown in Fig. 18.5, $\epsilon = 0.08$. Notice that while we call this the small diffusion limit, the diffusion coefficient is not really a parameter that can be freely varied, but is fixed for the particular solute. For the analysis that follows ϵ is required to be small, and this can be accomplished by many combinations of parameters, including cytoplasmic concentration, permeability, tube length or tube radius, which are not *a priori* fixed. Thus, we could equally well identify this as the long tube limit or the high permeability limit.

To find the "outer" solution we set $\epsilon = 0$, which gives the reduced system of equations

$$w_o \frac{du_o}{dy} + 2(u_o - 1) \;=\; 2n(y), \tag{18.28}$$

$$\frac{dw_o}{dy} \;=\; 2(u_o - 1), \tag{18.29}$$

Since this is a second order system, rather than a third order system, we can satisfy only two of the three boundary conditions. Which one of the three to drop is not apparent until one examines the boundary layer equations, as is done next. However, in anticipation of that result, we solve the reduced system subject to the conditions $w_o(0) = \frac{du_o(0)}{dy} = 0$.

Now, since $\frac{du_o(0)}{dy} = 0$, for consistency it must be that

$$u_o(0)(u_o(0) - 1) = n(0). \tag{18.30}$$

The unique positive root of this quadratic equation, say u_d (which is also greater than 1), is the initial value for $u_o(y)$. Now, the solution of the outer problem is

readily determined. If $n(y)$ is a step function, $n(y) = n_0 H(a - y)$, with $0 < a < 1$, then for $0 < y < a$, u_o is constant, and $w_o(y)$ is linear in y,

$$u_o(y) = u_d, \qquad w_o(y) = 2(u_d - 1)y. \tag{18.31}$$

For $a < y < 1$, $w_o(y)u_o(y) = w_a u_d$, where $w_a = w(a) = 2a(u_d - 1)$. Then,

$$\frac{dw_o}{dy} = 2\left(\frac{w_a u_d}{w_o} - 1\right), \tag{18.32}$$

which can be integrated to find

$$-w_o + w_a - w_a u_d \ln\left(\frac{w_o - w_a u_d}{w_a - w_a u_d}\right) = 2(y - a), \tag{18.33}$$

so that $w_o(y)$ and $u_o(y)$ are determined implicitly. A plot of this outer solution is shown in Fig. 18.6.

The outer solution cannot satisfy the boundary condition at $y = 1$. In fact, $u_o(1)$ is certain to be greater than one. To satisfy the condition $u(1) = 1$, we seek a boundary layer correction to the outer solution. We introduce the scaled variable

$$\xi = \frac{y - 1}{\epsilon}, \tag{18.34}$$

and in terms of this variable the original system of equations becomes

$$\frac{d^2 u}{d\xi^2} - \frac{d}{d\xi}(wu) = -2\epsilon n(y), \tag{18.35}$$

$$\frac{dw}{d\xi} = 2\epsilon(u - 1). \tag{18.36}$$

To leading order in ϵ, we have the boundary layer equations

$$\frac{d^2 u_i}{d\xi^2} - \frac{d}{d\xi}(w_i u_i) = 0, \tag{18.37}$$

$$\frac{dw_i}{d\xi} = 0, \tag{18.38}$$

where the subscript i is intended to denote that this as the "inner" solution. This system is also easily solved. w_i is constant and clearly must be equal to $w_o(1)$, so that the boundary layer equation for u_i reduces to

$$\frac{d^2 u_i}{d\xi^2} - w_o(1)\frac{du_i}{d\xi}u_i = 0, \tag{18.39}$$

with general solution

$$u_i(\xi) = A + B\exp(w_o(1)\xi). \tag{18.40}$$

Now we see why this boundary layer is located at $y = 1$. Since the solution $u_i(\xi)$ is bounded in the limit $\xi \to -\infty$, but not in the limit $\xi \to \infty$, it can be a boundary layer solution only on the right, not the left. We pick the constants A and B so
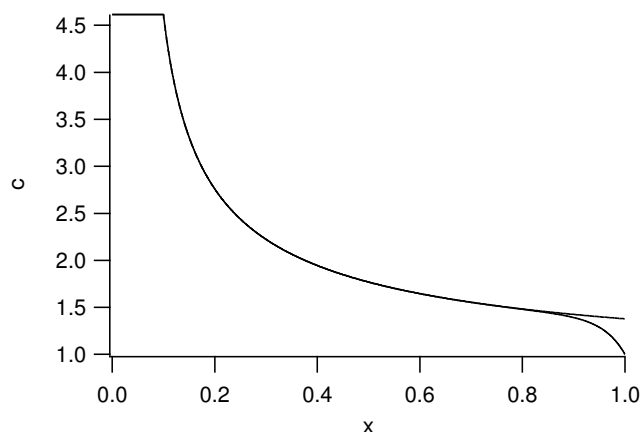
Figure 18.6: The outer solution $u_0(y)$ (shown dashed) and uniformly valid composite solution, computed with the same parameter values as in Fig. 18.5, with $N_0 = 0.3$. Note that the two solutions agree well everywhere except in the boundary layer close to $y = 1$ where the boundary layer correction changes rapidly in order to satisfy the boundary condition at $y = 1$.

that $u_i(0) = 1$ and so that it matches the outer solution, i.e., $\lim_{\xi \to -\infty} = u_o(1)$. Thus,

$$u_i(\xi) = u_o(1) + (1 - u_o(1)) \exp(w_o(1)\xi) + O(\epsilon). \qquad (18.41)$$

Finally, the composite solution, or uniformly valid solution, is given by

$$u(y) = u_o(y) + (1 - u_o(1)) \exp\left(\frac{1}{\epsilon} w_o(1)(y - 1)\right) + O(\epsilon). \qquad (18.42)$$

A plot of this composite solution is also shown in Fig. 18.6.

A different scaling is necessary if the tube is short or permeability is small. As before we let $y = \frac{x}{L}$, and $u = \frac{c}{c_0}$ but take $W = \frac{vL}{D}$, and find

$$\frac{d^2 u}{dy^2} - \frac{d}{dy}(Wu) + 2m(x) = 0, \qquad (18.43)$$

where $m(x) = \frac{L^2 N(x)}{Drc_0}$, and

$$\frac{dW}{dx} = 2\eta(u - 1), \qquad (18.44)$$

where $\eta = \frac{c_0 P L^2}{Dr} = \frac{1}{\epsilon}$. The boundary conditions are unchanged from before.

With $\eta \ll 1$, this is a regular perturbation problem whose solution is readily found as a power series in η. We leave the details of this calculation as an exercise. However, the result is that to leading order in η, but expressed in terms of original dimensional variables,

$$\bar{c} = c_0 + \frac{N_0}{Dr}\left(1 - \frac{1}{3}a^2\right)aL^2. \qquad (18.45)$$
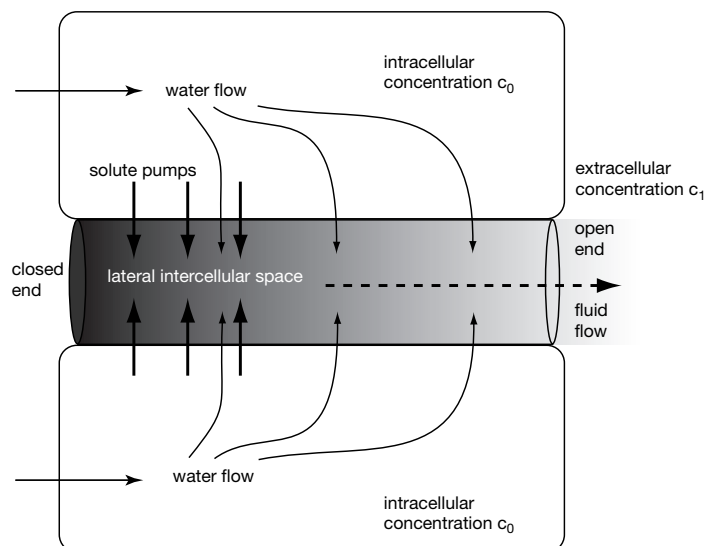
We recover the efflux velocity from (18.21).

Figure 18.7: Schematic diagram of the standing gradient model with separated intracellular and extracellular regions.

18.1.3 Uphill water transport

In the model of the previous section, the background concentration everywhere outside the cylindrical tube was assumed to be the same, c_0. Thus, the model demonstrated that a standing gradient of solute concentration can transport water between regions of identical osmolality, and do so in such a way that the transported fluid is as close to this background osmolality as desired.

However, in many cases an epithelial cell layer can do something even more surprising; it can transport water against an osmotic pressure difference, yet using only osmosis to do so. How this works can be seen by a simple modification of the standing gradient model (Weinstein and Stephenson, 1981).

Instead of assuming that the concentration everywhere outside the cylindrical tube is the same, we divide the external region into intracellular and extracellular regions, with concentrations c_0 and c_1, respectively (Fig. 18.7), with $c_0 > c_1$. The model equations remain the same as previously, with the one exception that the boundary condition for c at $x = l$ is $c(L) = c_1$.

The solution of this system of equations has the same general features as before, namely solute concentration is a decreasing function of x. Anywhere that $c > c_0$, water is drawn from the cell into the tube, while anywhere that $c < c_0$, water is drawn from the tube into the cell. The net flux is determined by (18.21). Accordingly, if the average concentration in the tube is greater than that in the cell, there is a net positive fluid velocity at the open end. Conversely, if the average concentration in the tube is less than that in the cell, there is a net negative fluid velocity at the open end, drawing water into the cell.

So an interesting question is to determine under what conditions there is net

fluid outflow when $c_1 < c_0$.

In the small diffusion (long tube length) limit, the net flow is always positive, regardless of how small c_1 might be. This is because, in the small diffusion limit, the concentration drops below c_0 only in a thin boundary layer, and the net velocity is affected by this only slightly.

In the small tube length (large diffusion, small permeability) limit, the flow can go either way. It is easy to determine that

$$\bar{c} = c_1 + a\frac{N_0}{r}\frac{L^2}{D}\left(1 - \frac{1}{3}a^2\right),\qquad(18.46)$$

from which the direction of net flow is also easily determined.

18.2 Gastric Protection

The inner surface of the gastrointestinal tract is a layer of columnar epithelial cells that actively secrete mucus and a fluid rich in bicarbonate. The mucus is highly viscous and coats the cells with a 0.5–1.0 mm thick layer that is insoluble by other gastric secretions and creates a lubricating boundary for the intestinal wall. In addition, this layer of cells is studded with a large number of gastric pits (Fig. 18.8). Each gastric pit contains *parietal cells* that secrete hydrochloric acid through an active transport process, leading to a pH of about 1 in the stomach lumen. Since the pH of the blood supplying the surface epithelium is about 7.4, there is a large H^+ concentration gradient (approximately a millionfold increase in concentration of hydrogen) across each epithelial cell. Clearly, the epithelial cells must be protected from the high lumenal acidity. It is believed that the secretion of mucus and bicarbonate by epithelial cells plays an important role in gastric protection.

18.2.1 A Steady-State Model

To model gastric protection (following Engel et al., 1984) we assume that the lumenal surface of the gastric mucosa is a plane located at $x = 0$, where x is a coordinate measured perpendicular to the mucosal wall, while the mucus layer is of uniform thickness l. Thus, the mucus–lumen interface lies at $x = l$, as illustrated in Fig. 18.9. Inside the mucus layer H^+ and HCO_3^- react according to

$$H^+ + HCO_3^- \underset{k_-}{\overset{k_+}{\rightleftharpoons}} H_2O + CO_2.\qquad(18.47)$$
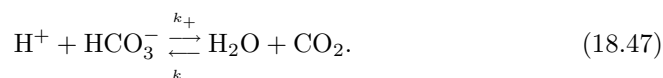
This bicarbonate buffering system is one of the most important buffering systems in the body, and its role in the transport of carbon dioxide is discussed in Chapter 14.

In the time-dependent problem, each species obeys a reaction–diffusion equation, such as

$$\frac{\partial\,[H^+]}{\partial t} = D_{H^+}\frac{\partial^2\,[H^+]}{\partial x^2} - k_+\left[H^+\right]\left[HCO_3^-\right] + k_-\left[CO_2\right],\qquad(18.48)$$
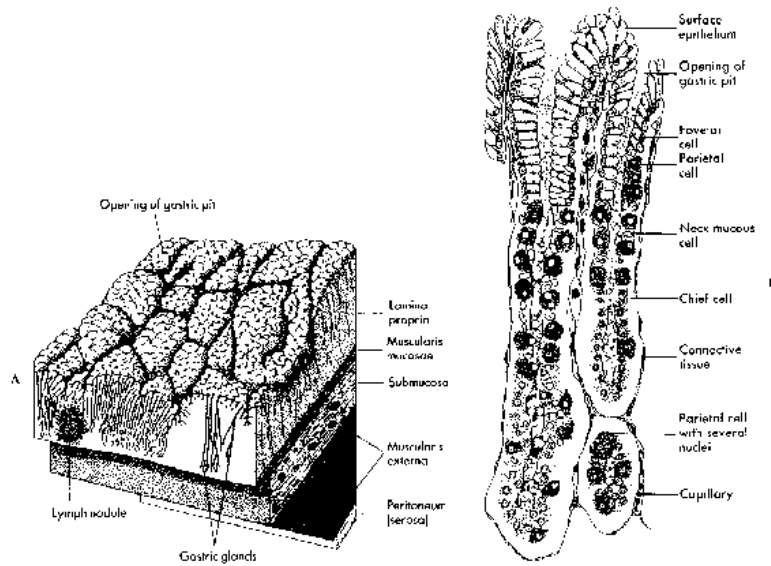
Figure 18.8: Closeup view of the gastric mucosa and two gastric pits. The epithelium of the gastric wall contains large numbers of gastric pits, each of which is lined by parietal cells that secrete HCl. (Berne and Levy, 1993, Fig. 39-9, p. 659.)
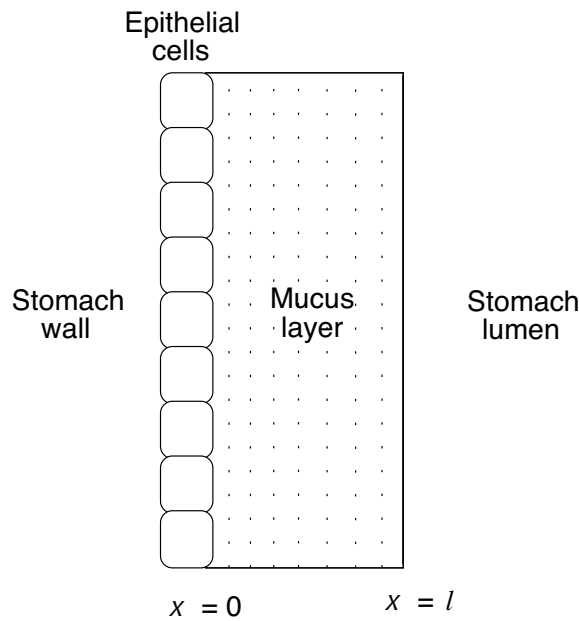

Figure 18.9: Schematic diagram of the mucus layer in the model for gastric protection.

where $D_{\mathrm{H^+}}$ is the diffusion coefficient of $\mathrm{H^+}$ in the mucus layer. However, at steady state the time derivatives are zero, and the partial derivatives with respect to x become ordinary derivatives. Thus, at steady state,

$$D_{\mathrm{H^+}} \frac{d^2\left[\mathrm{H^+}\right]}{dx^2} = D_{\mathrm{HCO_3^-}} \frac{d^2\left[\mathrm{HCO_3^-}\right]}{dx^2} = k_+\left[\mathrm{H^+}\right]\left[\mathrm{HCO_3^-}\right] - k_-\left[\mathrm{CO_2}\right] \quad (18.49)$$

$$D_{\mathrm{CO_2}} \frac{d^2\left[\mathrm{CO_2}\right]}{dx^2} = -k_+\left[\mathrm{H^+}\right]\left[\mathrm{HCO_3^-}\right] + k_-\left[\mathrm{CO_2}\right]. \quad (18.50)$$

To complete the formulation of the problem we add boundary conditions at the epithelial and lumenal boundaries of the mucus layer. On the lumenal side we assume that $[\mathrm{H^+}] = [\mathrm{H^+}]_l$ and $[\mathrm{CO_2}] = [\mathrm{CO_2}]_l$ are constant and known, determined by the concentration of the contents of the gastrointestinal tract, while $\left[\mathrm{HCO_3^-}\right]$ is given by the equilibrium relation

$$\left[\mathrm{HCO_3^-}\right]_l = \frac{k_-}{k_+}\frac{\left[\mathrm{CO_2}\right]_l}{\left[\mathrm{H^+}\right]_l}. \quad (18.51)$$

On the epithelial side we assume that the fluxes of $\mathrm{HCO_3^-}$ and $\mathrm{CO_2}$ are known, as these chemicals are actively secreted by the epithelial cells, and thus, from Fick's law,

$$D_{\mathrm{HCO_3^-}} \frac{d\left[\mathrm{HCO_3^-}\right]}{dx} = -\bar{J}, \quad (18.52)$$

$$D_{\mathrm{CO_2}} \frac{d\left[\mathrm{CO_2}\right]}{dx} = -\bar{I}, \quad (18.53)$$

at $x = 0$, for some known constants $\bar{J}$ and $\bar{I}$. Finally, we assume that the flux of $\mathrm{H^+}$ across the boundary at $x = 0$ is proportional to the concentration difference across the boundary; i.e.,

$$D_{\mathrm{H^+}} \frac{d\left[\mathrm{H^+}\right]}{dx} = P_{\mathrm{H^+}}\left(\left[\mathrm{H^+}\right] - \left[\mathrm{H^+}\right]_{\mathrm{epi}}\right), \quad (18.54)$$

where $P_{\mathrm{H^+}}$ is the permeability and $[\mathrm{H^+}]_{\mathrm{epi}}$ is the concentration of $\mathrm{H^+}$ in the epithelial cells. Since the concentration of $\mathrm{H^+}$ in the epithelial cells is low compared to the concentration external to the cell, we set $[\mathrm{H^+}]_{\mathrm{epi}}$ to zero, and thus require

$$D_{\mathrm{H^+}} \frac{d\left[\mathrm{H^+}\right]}{dx} = P_{\mathrm{H^+}}\left[\mathrm{H^+}\right] \quad (18.55)$$

at $x = 0$.

To study this system of equations, we introduce nondimensional variables $y = x/l$, $u = \left[\mathrm{H^+}\right]/\left[\mathrm{H^+}\right]_l$, $v = \left[\mathrm{HCO_3^-}\right]/\left[\mathrm{H^+}\right]_l$, $w = \left[\mathrm{CO_2}\right]/\left[\mathrm{H^+}\right]_l$, in terms of which the model becomes

$$\epsilon \frac{d^2 u}{dy^2} = uv - \zeta w, \quad (18.56)$$

$$\frac{d^2 u}{dy^2} = \gamma \frac{d^2 v}{dy^2} = -\beta \frac{d^2 w}{dy^2}, \quad (18.57)$$

where $\beta = D_{CO_2}/D_{H^+}, \gamma = D_{HCO_3^-}/D_{H^+}, \epsilon = \frac{D_{H^+}}{k_+ l^2 [H^+]_l}, \zeta = \frac{k_-}{k_+ [H^+]_l}$. The boundary conditions at $y = 1$ $(x = l)$ are

$$u(1) = 1, \qquad v(1) = \zeta\alpha, \qquad w(1) = \alpha, \tag{18.58}$$

and the boundary conditions at $y = 0$ are

$$\frac{du}{dy}(0) = \lambda u(0), \qquad \gamma\frac{dv}{dy}(0) = -J, \qquad \beta\frac{dw}{dy}(0) = -I, \tag{18.59}$$

where $\alpha = \frac{[CO_2]_l}{[H^+]_l}, J = \frac{\bar{J}l}{D_{H^+}[H^+]_l}, I = \frac{\bar{I}l}{D_{H^+}[H^+]_l}, \lambda = \frac{P_{H^+}l}{D_{H^+}}$. Integrating (18.57) from 0 to y and using the boundary conditions (18.59) we obtain

$$\frac{du}{dy} - \lambda u(0) = \gamma\frac{dv}{dy} + J = -\beta\frac{dw}{dy} - I. \tag{18.60}$$

Integrating (18.59) from y to 1 and applying the boundary conditions (18.58) gives

$$u - 1 - \lambda u(0)(y - 1) = \gamma(v - \zeta\alpha) + J(y - 1) = -\beta(w - \alpha) - I(y - 1). \tag{18.61}$$

From this we obtain v and w as functions of u and y:

$$v(y) = \zeta\alpha \ + \frac{1}{\gamma}[u(y) - 1 - (\lambda u(0) + J)(y - 1)], \tag{18.62}$$

and

$$w(y) = \alpha - \frac{1}{\beta}[u(y) - 1 + (I - \lambda u(0))(y - 1)]. \tag{18.63}$$

Thus, we can write the model as

$$\epsilon\frac{d^2 u}{dy^2} = uv - \zeta w = f(u(y), y), \tag{18.64}$$

$$\frac{du}{dy}(0) = \lambda u(0), \qquad u(1) = 1. \tag{18.65}$$

From the molecular weights of the chemicals, we estimate $\beta \approx 0.14$ and $\gamma \approx 0.13$. The forward and reverse rates of the bicarbonate reaction are, respectively, $k_- = 11$ s^{-1} and $k_+ = 2.6 \times 10^{10}$ cm^3·mol^{-1}·s^{-1}. Other experimentally determined quantities include $\bar{J} = 1.4 \times 10^{-10}$ mol·cm^{-2}·s^{-1}, $[H^+]_l = 140$ mM, $l = 0.05$ cm, $D_{H^+} = 1.75 \times 10^{-5}$cm^2·s^{-1}, and $P_{H^+} = 1.3 \times 10^{-5}$cm·s^{-1}. From these parameter values we see that $\epsilon = O(10^{-7})$ and $\zeta = O(10^{-6})$ are small parameters, while $\lambda = 0.037$ and $J = 0.0003$.

We now use singular perturbation theory to solve this two-point boundary value problem. This approach is possible because ϵ, which is the ratio of the rate of diffusion through the mucus to the rate of reaction, is small. Outside of a thin layer the bicarbonate reaction is in a pseudo-steady state at each point in space; in this region, diffusion of hydrogen ions or bicarbonate plays little role. It is only within the thin layer that the bicarbonate concentration is determined by the balance of reaction and diffusion. This allows the representation of the solution in

two different spatial variables, one describing the solution outside this thin layer, and one describing the solution inside it. The solutions are then matched to obtain a uniformly valid solution. As described below, although the bicarbonate reaction is in local chemical equilibrium outside the thin layer, the bulk of the reaction actually occurs within the thin layer. For the parameter values used here, the thin layer occurs at $y = 0$, but this need not necessarily be so. If the acidity of the lumen is low enough, the thin reaction layer occurs within the mucus layer (see Exercise 4).

The outer solution

We look for a solution of the form

$$u = u_0 + \epsilon u_1 + \cdots, \tag{18.66}$$

substitute into the differential equation, and equate coefficients of powers of ϵ. This gives a hierarchy of equations for the outer solution. To lowest order in ϵ we have

$$0 = f(u_0, y), \tag{18.67}$$

$$\frac{du_0}{dy}(0) = \lambda u_0(0), \qquad u_0(1) = 1. \tag{18.68}$$

Obviously, both boundary conditions cannot be satisfied, so we drop the boundary condition at $y = 0$ and keep the boundary condition at $y = 1$. There are good physical reasons for this choice. As discussed above, the balance of reaction and diffusion is important only in a thin layer around $y = 0$. Thus, if we ignore diffusion (by setting $\epsilon = 0$) we do not expect to be able to satisfy the boundary condition at $y = 0$. (This is also the correct mathematical choice, because, as is discussed below, there is a "corner layer" at $y = 0$; the other choice, ignoring the boundary condition at $y = 1$, fails to produce a valid solution.)

The equation $f(u_0, y) = 0$ is the quadratic polynomial in u_0,

$$\beta u_0^2 + [\zeta\gamma(\alpha\beta + 1) - \beta + \beta(J + \lambda u_0(0))(1 - y)]u_0$$
$$+ \zeta\gamma[(\lambda u_0(0) - I)(1 - y) - \alpha\beta - 1] = 0, \tag{18.69}$$

so it can be solved exactly. The easiest way to represent this solution is to find y as a function of u_0, since (18.69) is linear in y. However, because ζ is small, we find that

$$u_0(y) = 1 + (\lambda u_0(0) + J)(y - 1) + O(\zeta), \tag{18.70}$$

and

$$v = O(\zeta). \tag{18.71}$$

Next we set $y = 0$ in (18.69) and solve for $u_0(0)$ to get

$$u_0(0) = \frac{1 - J}{1 + \lambda} + O(\zeta), \tag{18.72}$$

from which it follows that

$$u_0(y) = 1 - \frac{\lambda + J}{\lambda + 1}(1 - y) + O(\zeta), \qquad (18.73)$$

$$w(y) = \alpha + \frac{J + I}{\beta}(1 - y) + O(\zeta). \qquad (18.74)$$

Hence, to leading order, there is no HCO_3^- in the mucus layer, and H^+ and CO_2 vary linearly with distance through the mucus layer.

The inner solution

The outer solution (18.73) does not satisfy the boundary condition at $y = 0$. A uniformly valid solution of this problem must include a "corner layer," that is, a solution with large second derivative, which therefore changes slope, but not value (at least to lowest order), in a small region close to $y = 0$. The corner layer here results from the fact that the boundary condition at $y = 0$ is expressed in terms of the derivative of u at 0. Hence, to satisfy the boundary condition, the derivative of u must change quickly. It is beyond the scope of this book to give a detailed description of the construction of this corner layer (see Engel et al., 1984, or, for a more general description, Keener, 1988, or Holmes, 1995). Suffice it to say that the corner layer is found by introducing a scaled variable $\tilde{y} = y/\sqrt{\epsilon}$ (which eliminates ϵ from the second derivative term in (18.64)) and then seeking a power series solution in powers of $\sqrt{\epsilon}$. The result is a modification of the outer solution by the addition of a term of the form

$$\sqrt{\epsilon}e^{-\mu y/\sqrt{\epsilon}}, \qquad (18.75)$$

which is of small amplitude and satisfies the boundary condition at the origin. As a result, to leading order in ϵ, the outer solution provides a uniformly valid representation of the solution on the entire interval $0 < y < 1$. A sketch of the solution is given in Fig. 18.10.

Physical interpretation of the corner layer

There is an interesting interpretation of the corner layer in terms of the physiology of the problem. Recall that the boundary conditions at $y = 0$ for the original problem are

$$\frac{du}{dy}(0) = \lambda u(0), \qquad \gamma\frac{dv}{dy}(0) = -J, \qquad \beta\frac{dw}{dy}(0) = -I. \qquad (18.76)$$

The outer solution does not satisfy these boundary conditions. Instead, if we evaluate the derivatives of the outer solution to leading order, we find that

$$\frac{du_0}{dy}(0) = \lambda u_0(0) + J, \qquad \frac{dv_0}{dy}(0) = 0, \qquad \beta\frac{dw_0}{dy}(0) = -I + J. \qquad (18.77)$$

In other words, to lowest order, the bicarbonate flux J can be replaced by a flux of hydrogen ions in the opposite direction with the same magnitude, and the CO_2 flux must be altered to compensate. Thus the original problem, which has a bicarbonate
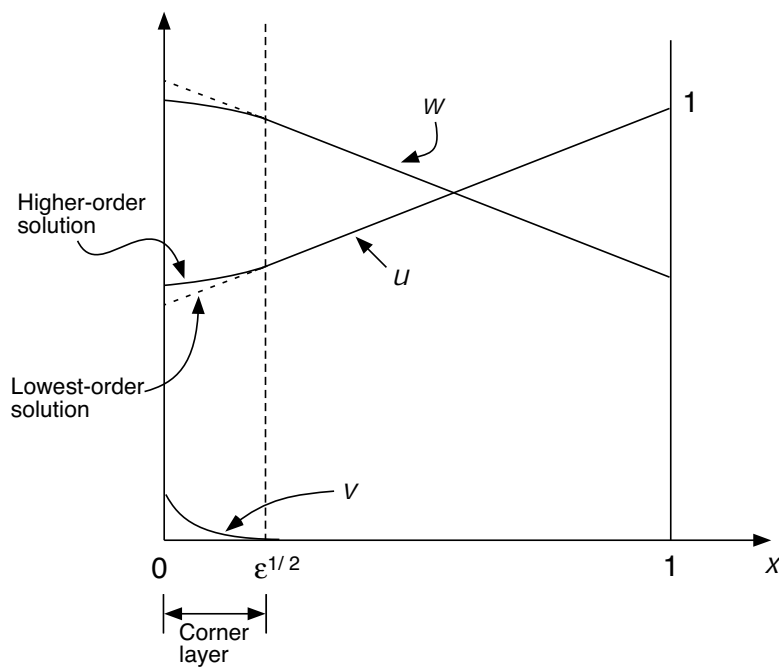
Figure 18.10: Sketch (not to scale) of the solution to the model for gastric protection. (Adapted from Engel et al., 1984, Fig. 10.)

source at $y = 0$, is replaced by a simpler problem that has a H^+ sink and a CO_2 source at $y = 0$ and no H^+–HCO_3^- reaction. This implies that each bicarbonate molecule that exits the epithelium reacts immediately with a hydrogen ion, with the consequent disappearance of the hydrogen ion. Hence, to lowest order, all the chemical reaction occurs within the corner layer.

In dimensional variables, the outer solution is

$$\left[H^+\right] = \left[H^+\right]_l - \frac{\bar{J} + P_{H^+}\left[H^+\right]_l}{D_{H^+} + P_{H^+}l}(l - x), \tag{18.78}$$

$$\left[CO_2\right] = \left[CO_2\right]_l + \frac{\bar{J} + \bar{I}}{D_{CO_2}}(l - x), \tag{18.79}$$

and thus, at the epithelial surface,

$$\left[H^+\right]_0 = \frac{D_{H^+}\left[H^+\right]_l - \bar{J}l}{D_{H^+} + P_{H^+}l}. \tag{18.80}$$

Using experimentally determined values for the parameters, we find that $\left[H^+\right]_0 = 135$ mM, a decrease of only 3.5%, which is too small to protect the epithelial cells from high lumenal acidity. Thus, this simple model of the mucus layer is insufficient to explain how the epithelial layer is protected.

18.2.2 Gastric Acid Secretion and Neutralization

The primary difficulty with the above model for gastric protection is that the flux of bicarbonate, J, is too small to cause a sufficient reduction of hydrogen ions at the surface of the epithelial cells. A model that addresses this shortcoming by examining the relationship between hydrochloric acid secretion and the release of bicarbonate was constructed by Lacker and his coworkers (de Beus et al., 1993).

Hydrochloric acid is secreted from the parietal cells of the oxyntic glands using a number of reactions. First, water in the cells is dissociated into hydrogen and hydroxyl ions in the cell cytoplasm. The hydrogen ions are actively secreted via a hydrogen–potassium ATPase. In addition, chloride ions are actively secreted and sodium ions are actively absorbed, via separate ATPases. The result is a high concentration of hydrochloric acid in the lumen. At the same time, carbon dioxide combines with hydroxyl ions (catalyzed by carbonic anhydrase) to form carbonic acid and thence bicarbonate. This bicarbonate diffuses out of the cell into the extracellular medium and is transported by the capillary blood flow. The direction of capillary blood flow is from the oxyntic cell in the gastric pit to the epithelial lining of the lumen. Since the epithelial cells are downstream of the oxyntic cells, they absorb bicarbonate from the blood and then secrete it into the mucus. Thus, as acid production increases, so does the rate at which bicarbonate is secreted into the lumen by the epithelial cells. According to de Beus et al., the lack of this feature in the Engel model caused an underestimation of the rate of bicarbonate secretion from the epithelial layer.

De Beus et al. estimated the model parameters from the available experimental literature and showed that analytic solutions in certain simplified cases agreed well

with the full solution. Of particular interest is their reproduction of the *alkaline tide*. As the rate of H^+ secretion into the lumen increases, the downstream $[H^+]$ (i.e., the gastric venous $[H^+]$) *decreases*. This reinforces the major idea behind this model, that secretion of HCO_3^- by the epithelial cells is driven by H^+ secretion by the oxyntic cells, so that gastric protection is automatically increased as the lumenal $[H^+]$ increases.

Over longer time scales the secretion of gastric acid is controlled by a complex network of positive and negative feedback processes involving the enteric and central nervous systems and a number of different cell types. For example, food stimulates the production of gastrin by G cells, which in turn stimulates the production of H^+ from parietal cells. However, gastrin also stimulates the production of somatostatin from D cells (in the corpus of the stomach) which inhibits the production of H^+ from the parietal cells. Gastrin also acts on enterochromaffin-like cells (ECL cells) in the corpus to stimulate the secretion of histamine, which enhances acid secretion and potentiates the effect of gastrin on parietal cells. To further complicate matters, D cells in the antrum produce somatostatin in response to high H^+ concentrations to form another negative feedback loop by inhibiting the production of gastrin by the antral G cells.

In addition to these control mechanisms, the numbers of G, ECL,D and parietal cells are controlled by additional feedback mechanisms that operate over a time scale of days to weeks, so that gastric acid secretion can be modulated by long-term changes in food ingestion.

A complicated model of this system has been constructed and analyzed by Joseph et al., (2002). Their principal conclusion was that the action of somatostatin was the most crucial feedback mechanism for maintaining a stable acid balance in the stomach.

18.3   Coupled Oscillators in the Small Intestine

One principal function of the gastrointestinal tract is to mix ingested food and move it through the tract in the appropriate direction. It does this by contraction of the layers of smooth muscle illustrated in Fig. 18.1, contractions that are controlled on a number of different levels. At the lowest level, each smooth muscle cell has intrinsic electrical activity, which can be oscillatory in nature. At higher levels, the properties of the local oscillations are modified by extrinsic and intrinsic neuronal stimulation, or chemical stimuli. Different parts of the tract have different kinds of contractile behavior. Here, we focus on the electrical activity of the smooth muscle of the small intestine. The small intestine is itself divided into three different sections: the first 25 cm or so after the pylorus (the passage from the stomach to the small intestine, controlled by the pyloric sphincter) is called the *duodenum*; the next section, comprising about 40% of the length of the small intestine, is called the *jejunum*; while the remainder is called the *ileum*. However, although this nomenclature is useful for understanding some of the experimental results we present here, we do not distinguish between the electrical activity of different sections of the small intestine.
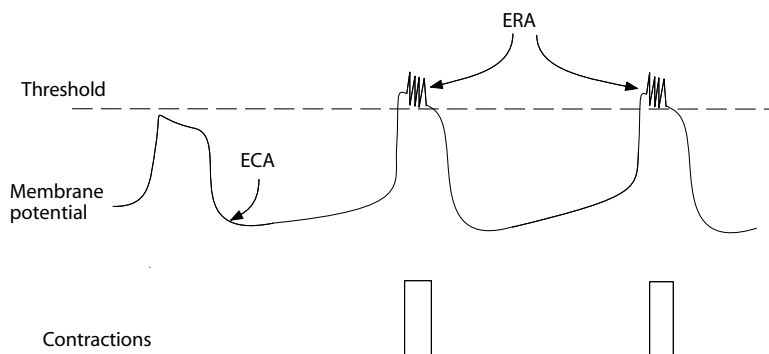
Figure 18.11: Schematic diagram of electrical control activity (ECA), electrical response activity (ERA), and muscular contraction. (Adapted from Sarna, 1989, Fig. 2.)

18.3.1 Temporal Control of Contractions

Smooth muscle cells throughout the gastrointestinal tract exhibit oscillations in their membrane potential, with periods ranging from 2 to 40 cycles/min. A typical example of this *electrical control activity*, or ECA, is shown in Fig. 18.11. Although depolarization of the cell membrane potential can cause muscular contractions, this happens only if the membrane potential is depolarized past a threshold, in which case the potential begins to oscillate, or burst, at a much higher frequency. Whether or not bursting occurs depends on the level of neuronal or chemical stimulation. In this way, contractile activity depends on the local oscillatory properties of the smooth muscle cells, as well as on the higher-level control processes. Electrical bursts are termed *electrical response activity*, or ERA. Muscular contractions cannot occur with a frequency greater than that of the ECA, and thus the properties of the local ECA constrain the possible types of muscular contraction.

Often, when faced with cellular oscillators, modelers seek to understand the cellular mechanisms that cause such behavior; this book contains many examples of this approach. Here, by contrast, we examine what happens when a large number of oscillators are coupled to one another, without concern for the exact mechanisms underlying each oscillation. Although this approach cannot determine a direct relationship between cellular properties and global behavior, it provides greater insight into how coupled oscillators can give rise to organized wave activity of the type that is frequently seen in the stomach and small intestine.

18.3.2 Waves of Electrical Activity

If each local oscillator were uncoupled from its neighbors, we expect there would be no organized waves of contraction moving along the intestine. However, the main point of this section is that weak coupling between the oscillators causes the propagation of waves of ECA and ERA along the intestine.

The importance of coupling between the local oscillators is demonstrated in the

top panel of Fig. 18.12, where is shown the experimentally measured frequency of segments of the small intestine in the intact intestine, and in segments that have been dissociated from one another by circumferential cuts across the intestine. In the intact intestine, the frequency of the ECA is constant over the entire region close to the pylorus, even though the intrinsic frequency is steadily decreasing over this region. At approximately 60 cm from the pylorus the ECA frequency begins to decrease. In the frequency plateau (the region of constant frequency) region, each oscillator is phase-locked to its neighbor, resulting in organized waves that move along the intestine away from the pylorus. This is illustrated in the top panel of Fig. 18.13, where the oscillation peaks in neighboring parts of the intestine are connected by solid lines. The slope of the solid line gives the speed of the wave along the intestine, and the fact that subsequent lines are regularly spaced, parallel and straight, shows that the waves are repetitive and highly organized. Following the frequency plateau is a region where the ECA frequency decreases along the intestine, and the corresponding waves are not phase-locked and therefore much less regular (lower panel of Fig. 18.13).

Note that phase locking (i.e., oscillation with the same frequency) does not necessarily imply that there is wave-like behavior. A *phase wave* occurs when there is a constant advance (or delay) of phase from one point to the next along the length of the intestine.

When the segments are uncoupled, each shows oscillatory ECA, but with an intrinsic frequency that decreases with distance from the pylorus; the frequency plateau disappears in the isolated segments. It appears that in the intact intestine, the highest-frequency segment closest to the pylorus entrains the nearby oscillators, which have similar but lower frequencies. However, when the difference in intrinsic frequency is too large, entrainment is not possible: the frequency plateau breaks down, and the waves lose regularity. This is illustrated further in the lower panel of Fig. 18.12, which shows the effect of a single cut in the intestine part of the way along the frequency plateau. To the left of the cut, the ECA frequency is entrained to the same high frequency as that of the frequency plateau in the intact intestine. To the right of the cut, a new frequency plateau emerges as the highest-frequency oscillator again entrains its neighbors. In this case the frequency of the second plateau is lower than that of the first, as it is entrained to an oscillator with a lower frequency, but it extends further to the right, into the region where the intact intestine has a variable ECA frequency.

There is some evidence to suggest that ECA frequency decreases along the intestine in a stepwise fashion, and this is illustrated in Fig. 18.14. The frequency plateaus are separated by regions where the amplitude of the oscillation is variable. Often, however, the wave activity in subsequent plateaus is less organized than in the first, as the oscillations are not so closely phase-locked.

18.3.3   Models of Coupled Oscillators

The two primary means by which the waves of electrical activity in the intestine have been studied are with numerical simulations of large coupled systems of oscillators and with rigorous mathematical analysis of approximating "phase equations."
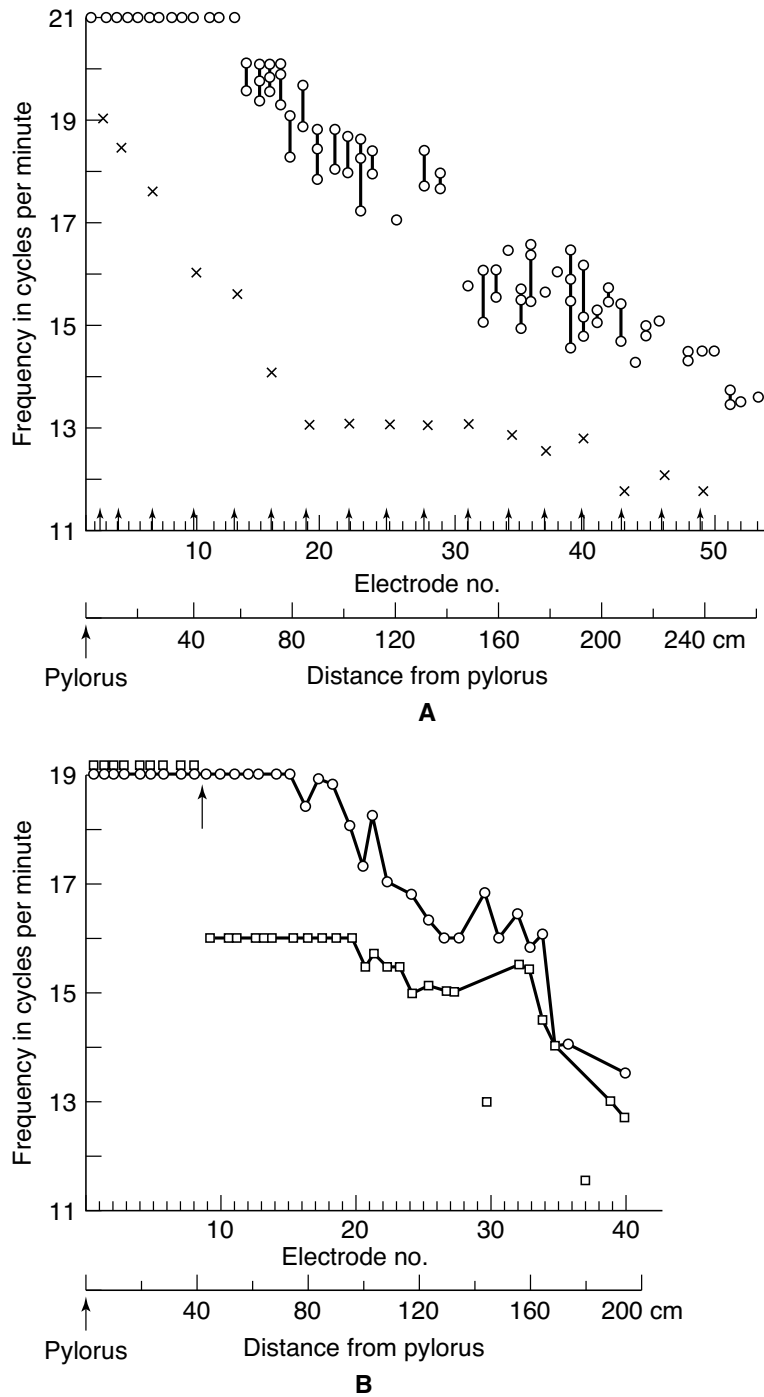
Figure 18.12: A: Intact (circles) and intrinsic frequency (crosses) of ECA in dog small intestine. The intrinsic frequencies were obtained by cutting across the small intestine at the places indicated by the arrows so as to disrupt oscillator coupling. B: The effect of a single cut (at the arrow) across the small intestine. To the right of the cut a frequency plateau still occurs, but now at a lower frequency than in the intact intestine. To the left of the cut the frequencies are unchanged. (Sarna, 1989, Fig. 10.)
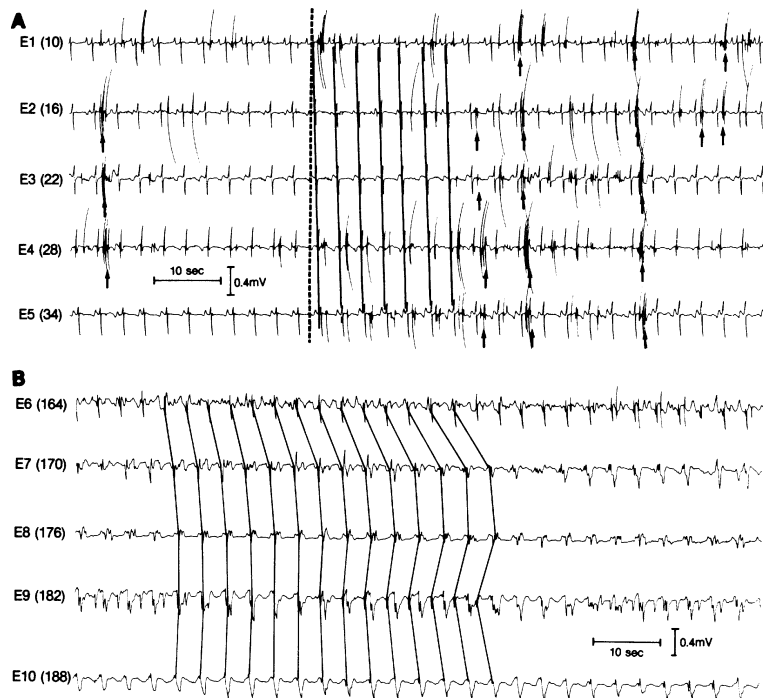
Figure 18.13: Experimental recordings from dog small intestine. A: Recordings taken from the frequency plateau region close to the pylorus. Solid lines connect the peaks of the ERA; these lines are straight and parallel, indicating the propagation of regular wave trains in this region. B: Recordings taken from the variable frequency region. The peaks of the ERA are not well organized, indicating that regular wave propagation has broken down. (Sarna, 1989, Fig. 11 A and B.)
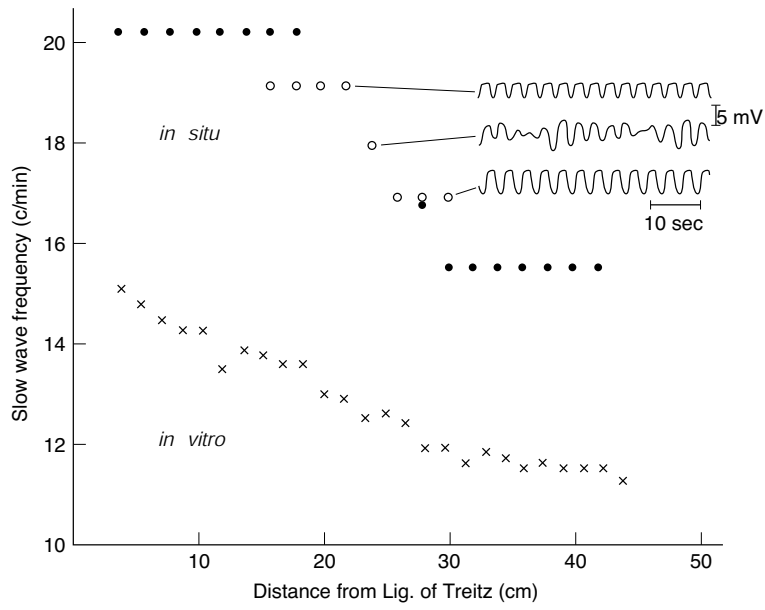
Figure 18.14: Frequency of the ECA in the cat. As the distance from the ligament of Treitz increases, the *in vitro* measurements (crosses) show a steady decline in frequency, while the *in vivo* measurements (open and filled circles) show clear frequency plateaus. (Diamant and Bortoff, 1969, Fig. 2.) (The ligament of Treitz marks the beginning of the jejunum.)

Numerical investigations

A number of investigators have used numerical simulations to study the behavior of chains of coupled oscillators in the small intestine (Nelsen and Becker, 1968; Diamant et al., 1970; Sarna et al., 1971; Robertson-Dunn and Linkens, 1974; Brown et al., 1975; Patton and Linkens, 1978). As a typical example, Diamant et al. (1970) coupled from 5 to 25 van der Pol oscillators with frequencies that decreased along the chain. Each oscillator was coupled to its nearest neighbor with the lower frequency in a procedure called forward coupling, and the coupling was assumed to be resistive. Numerical simulations showed that the oscillators are organized into frequency plateaus, whose lengths increased as the coupling strength increased. Because the coupling was in the forward direction only, the frequency plateaus lay above the intrinsic frequencies of the individual oscillators. The frequency plateaus were separated by regions in which the local frequency waxed and waned.

The phase equations

The mathematical study of waves of electrical activity on the small intestine begins with the assumption that there are $n+1$ coupled oscillators, described by the system of equations

$$\frac{du_i}{dt} = F_i(u_i) + \epsilon \sum_{j=1}^{n+1} a_{ij} H(u_j), \tag{18.81}$$

where u_i is the vector of independent variables describing the ith oscillator, and where a_{ij} are the coupling coefficients. The oscillators are assumed to be nearly identical, so that the behavior of each oscillator is described approximately by some periodic function, denoted by $u_i = U(\omega(\epsilon)t + \delta\theta_i(t))$, where $\delta\theta_i$ is the *phase shift* of the oscillator and is presumed to be slowly varying. Then, the equations (18.81) can be reduced (using multiscale or averaging techniques) to equations describing the phase shifts of the individual oscillators, of the form

$$\frac{d}{d\tau}\delta\theta_i = \xi_i - \Omega_1 + \sum_{j=1}^{n+1} a_{ij} h(\delta\theta_j - \delta\theta_i) + O(\epsilon^2), \qquad i = 1, \ldots, n+1, \tag{18.82}$$

for some periodic function h, where $\tau = \epsilon t$ is a slow time. The phase equations are asymptotically valid in the limit that the coupling is weak and the oscillators are similar. A derivation of the phase equations is given in Section 12.7, where the function h and the constants ξ_i and Ω_1 are determined. As a reminder, recall that $2\pi(1 + \epsilon\xi_i)$ is the natural (uncoupled) frequency of the ith oscillator, and that $\omega(\epsilon) = 1 + \epsilon\Omega_1 + O(\epsilon^2)$.

When each oscillator is coupled only to its nearest neighbors in a linear chain, the equations are

$$\frac{du_i}{dt} = F_i(u_i) + \epsilon(u_{i+1} - u_i) + \epsilon(u_{i-1} - u_i). \tag{18.83}$$

Here, the term $\epsilon(u_{i+1} - u_i)$ is deleted if $i = n + 1$, and the term $\epsilon(u_{i-1} - u_i)$ is deleted if $i = 1$. Then, the phase equations are of the form (18.82), where $a_{ij} = 1$

if $j = i + 1$ or if $j = i - 1$, $a_{ii} = -a_{i,i+1} - a_{i,i-1}$, and all other elements of a_{ij} are zero. We find equations for the consecutive phase differences $\phi_i = \delta\theta_{i+1} - \delta\theta_i$ to be

$$\frac{d\phi_i}{d\tau} = [\Delta_i + h(\phi_{i+1}) + h(-\phi_i) - h(\phi_i) - h(-\phi_{i-1})] + O(\epsilon^2), \tag{18.84}$$

where $\Delta_i = \xi_{i+1} - \xi_i$ is a measure of the amount of detuning of the oscillators, i.e., how much the natural frequencies vary along the chain. The term $h(-\phi_{i-1})$ is omitted if $i = 1$, and the term $h(\phi_{i+1})$ is omitted if $i = n$. Finally, we take h to be odd, in which case the phase difference equation becomes

$$\dot{\phi} = \beta\Delta + K\mathbf{H}(\phi), \tag{18.85}$$

where $\phi = (\phi_1, \ldots, \phi_n)$, $\beta\Delta = (\Delta_1, \ldots, \Delta_n)$, and $\mathbf{H} = (h(\phi_1), \ldots, h(\phi_n))$, and K is a tridiagonal matrix with -2 on the diagonal and 1 above and below the diagonal. Here, the dot denotes differentiation with respect to the slow time $\tau = \epsilon t$. The parameter β has been introduced as a control parameter for the amplitude of the gradient of the uncoupled oscillator frequency (i.e., the strength of the detuning).

Some simple solutions

Before discussing how frequency plateaus arise in the phase equation, it is useful to consider the solution in some simpler cases.

Two coupled oscillators

For two coupled oscillators there is only a single phase equation,

$$\frac{d\phi}{d\tau} = \beta\Delta - 2h(\phi). \tag{18.86}$$

A phase-locked solution is one for which the phase difference between neighboring oscillators does not change, i.e., ϕ is constant. Thus, phase-locked solutions are found by setting $d\phi/d\tau = 0$ and solving for Δ. This gives

$$\beta\Delta = 2h(\phi). \tag{18.87}$$

Since h is 2π-periodic and odd, we can solve (18.87) only if $\beta\Delta$ is not too large, as otherwise it would be greater than the maximum value of $2h$. In a common example, $h(\phi)$ is taken to be $\sin(\phi)$, in which case $|\beta\Delta|$ must be less than two for a phase-locked solution to exist. Since $\beta\Delta$ measures the amount of detuning, a phase-locked solution exists if and only if the two oscillators have natural frequencies that are not too different. If $\beta\Delta$ is small enough, the phase difference established between the oscillators (at least to lowest order in ϵ) is given by the solution of (18.87).

Three coupled oscillators

When three oscillators are coupled, the two phase difference equations are

$$\frac{d\phi_1}{d\tau} = \beta\Delta_1 - 2h(\phi_1) + h(\phi_2), \tag{18.88}$$

$$\frac{d\phi_2}{d\tau} = \beta\Delta_2 - 2h(\phi_2) + h(\phi_1), \tag{18.89}$$

and so a phase-locked solution occurs if

$$\frac{2\beta\Delta_1 + \beta\Delta_2}{3} = h(\phi_1), \tag{18.90}$$

$$\frac{2\beta\Delta_2 + \beta\Delta_1}{3} = h(\phi_2). \tag{18.91}$$

Clearly, this can be solved only if $|\beta(2\Delta_1+\Delta_2)|$ and $|\beta(2\Delta_2+\Delta_1)|$ are small enough.

It is important to note that if solutions for ϕ_1 and ϕ_2 exist, ϕ_1 does not necessarily equal ϕ_2. Thus, although the oscillators are phase-locked, the phase difference between the first and second oscillators is not necessarily the same as the phase difference between the second and third. If the phase differences are unequal, there is not a regular (constant speed) phase wave moving along the chain. Hence, phase locking does not necessarily imply a wavelike behavior.

To have a regular phase wave, the phase differences must be both constant and *equal* along the chain of oscillators. In this case, the peak of the wave moves at a constant speed down the oscillator chain. For the case of three coupled oscillators, phase wave solutions exist if $\Delta_1 = \Delta_2$. In other words, if the frequency difference between the first and second oscillators is the same as the difference between the second and third, and if this difference is not too large, then a phase wave solution exists.

This highlights the fact that in general, we can specify the frequency gradient along the oscillator chain and then solve for the phase differences, or we can specify the phase differences and then solve for the required frequency gradient, but we cannot specify the phase difference and the frequency gradient, expecting a phase wave.

A chain of coupled oscillators

The equations for a phase-locked steady-state solution for a chain of $n + 1$ coupled oscillators are given by

$$\beta\Delta + K\mathbf{H}(\phi) = 0. \tag{18.92}$$

This is a system of n equations in n unknowns. In general, we can view the frequencies as given and the phase differences as unknown, or we can specify the phase differences and view the frequency differences as unknown. For example, if we seek a solution that is both phase-locked and has a phase wave, we need $\phi_1 = \phi_2 = \cdots = \phi_n$. Letting $h(\phi_i) = \eta$, we obtain $\Delta_1 = \Delta_n = \eta/\beta$ and $\Delta_i = 0$ for $i = 2, \ldots, n-1$. Thus, a phase wave solution exists only if all the middle oscillators have the same frequency, ω say, while the first oscillator is tuned to $\omega - \eta/\beta$ and the last oscillator to $\omega + \eta/\beta$. Note that η can be either positive or negative, as different signs correspond to waves moving in opposite directions.

This observation poses a dilemma for the application of the phase equation to the electrical waves in the small intestine. Recall that ECA in the small intestine has a frequency plateau in the region close to the pylorus, and in this plateau, waves appear to be traveling away from the pylorus. These are phase-locked, with constant phase difference along the intestine. However, each segment of the small intestine has a natural oscillation frequency that decreases with distance from the
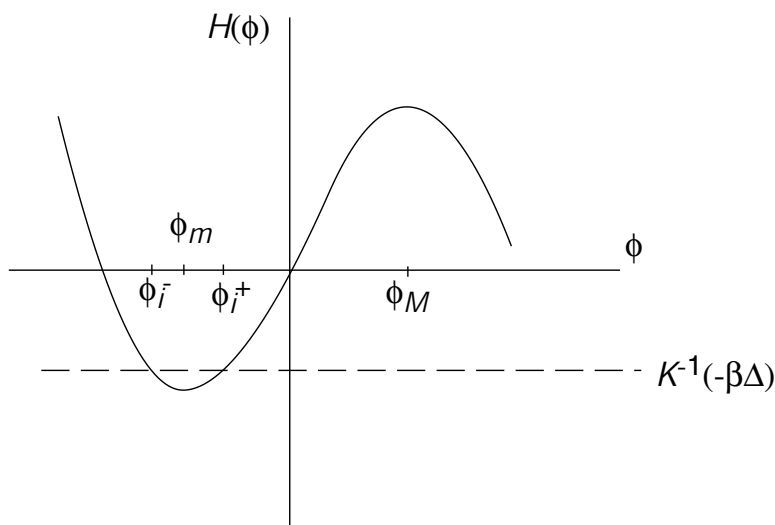
Figure 18.15: The roots of the ith component of the phase difference equation.

pylorus. These two observations are inconsistent with the phase equations, for which a constant phase difference implies a constant natural frequency on the interior of the chain.

Frequency plateaus

One partial solution to this dilemma was given by Ermentrout and Kopell (1984). They showed that on each plateau, the phase differences are not exactly constant, but make small oscillations, being locked only in an average sense, a phenomenon sometimes called *phase trapping*.

For simplicity, we assume that $h(\phi)$ is odd and 2π-periodic, with a maximum M at ϕ_M and a minimum m at ϕ_m, qualitatively like $\sin\phi$ (Fig. 18.15). Critical points of the differential equation (18.85) are solutions of

$$\mathbf{H}(\phi) = K^{-1}(-\beta\Delta), \tag{18.93}$$

which has a solution if and only if every component of $K^{-1}(-\beta\Delta)$ lies between m and M. Let

$$\beta_0 = \max\{\beta : m \leq (K^{-1}(-\beta\Delta))_i \leq M, \text{ for every } i\}. \tag{18.94}$$

When $\beta < \beta_0$, for every i there are two solutions to the scalar equation $h(\phi_i) = (K^{-1}(-\beta\Delta))_i$. These solutions, which we denote by ϕ_i^+ and ϕ_i^-, are shown in Fig. 18.15.

Since each component of ϕ can have one of two values, there are 2^n possible steady states when $\beta < \beta_0$. Because of the definition of β_0, there is some value j such that the roots ϕ_j^+ and ϕ_j^- coalesce and disappear as β crosses β_0. Thus, as β crosses β_0, all the critical points coalesce in pairs and disappear. This follows

because every critical point can be matched with another that agrees with it in every component $i \neq j$, one having jth component ϕ_j^+, the other having jth component ϕ_j^-. When $\beta < \beta_0$ the members of the pair differ only in the jth component; when $\beta = \beta_0$ the members of the pair are identical, and when $\beta > \beta_0$ there is no solution for the jth component, and so both solutions fail to exist.

There is one particular pair of critical points that is of interest for reasons that are explained below. Let $\xi_j(\beta)$ denote the critical point whose kth component is ϕ_k^- for all $k \neq j$, and whose jth component is ϕ_j^+. Also, let $\xi_0(\beta)$ denote the critical point with the kth component equal to ϕ_k^- for all k. Clearly, as $\beta \to \beta_0$, ξ_j coalesces with ξ_0 and the two critical points disappear.

Finally, to complete the preliminaries, we restrict Δ to be of a particular form. Since experimental data suggest that the natural frequencies of the oscillators decrease approximately linearly along the small intestine, it is reasonable to take $\Delta = (-1, \ldots, -1)$, corresponding to a linear decrease in frequency along the oscillator chain. We also assume that there is an even number of oscillators in the chain (an odd number of phase differences), i.e., that n is odd, with $n = 2j - 1$, and thus the central phase difference is at position j. For this choice of Δ and n, the solution of (18.93) fails first at the jth component; that is, if j is the position of the middle phase difference, then $\phi_j^+ \to \phi_j^-$ as $\beta \to \beta_0$. This is easily seen by noting that $K^{-1}(\beta\Delta)$ has kth component $-\beta k(n+1-k)/2 < 0$ (Exercise 5). Hence $\phi_k^\pm(\beta) < 0$ for all k as long as $\beta < \beta_0$. Further, when $n = 2j - 1$, $k(n+1-k) = k(2j-k)$, which is greatest when $k = j$. Since the jth component of the solution to (18.93) is the one with the greatest modulus, it follows that the jth component is the first to "hit" the minimum and disappear.

We now return to the particular pair of steady states, ξ_0 and ξ_j, defined above. Linear stability analysis of the system (18.85) shows that ξ_0 is a stable node, while ξ_j is a saddle point with one positive and $n-1$ negative eigenvalues. Further, both branches of the unstable manifold at ξ_j tend to ξ_0 as $\tau \to \infty$, and thus the closure of the unstable manifold forms a closed loop.

We can get some insight into the meaning of this last statement and why it is true by considering the special case $n = 2$. It is convenient to introduce the change of variables $\psi = K^{-1}\phi$, in which case the system of differential equations (18.85) becomes

$$\dot{\psi} = K^{-1}\beta\Delta + \mathbf{H}(K\psi), \tag{18.95}$$

or, in the specific case that $n = 2$,

$$\dot{\psi}_1 = \beta + h(\psi_2 - 2\psi_1), \tag{18.96}$$
$$\dot{\psi}_2 = \beta + h(\psi_1 - 2\psi_2). \tag{18.97}$$

This is a two-dimensional system whose phase portrait is easily studied. First, note that since (18.85) is a flow on a torus, so also is this system. The torus for (18.85) is the domain $0 \le \phi_i \le 2\pi, i = 1, \ldots, n$, with the boundary at $\phi_i = 0$ "identified" with, or equivalent to, the boundary at $\phi_i = 2\pi$. Here, however, the boundaries of the torus are modified, being the four straight lines

$$\psi_1 - 2\psi_2 = 0, -2\pi, \tag{18.98}$$
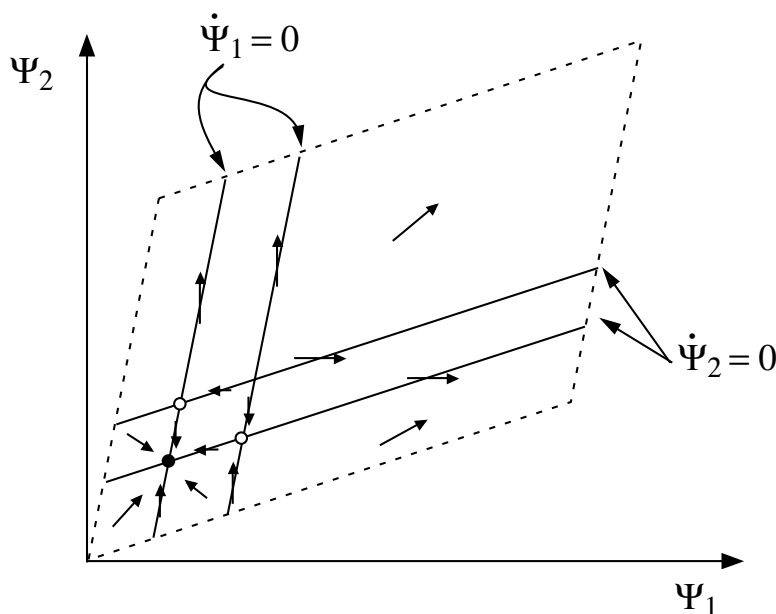$$\psi_2 - 2\psi_1 = 0, -2\pi. \tag{18.99}$$

Figure 18.16: Phase portrait for the two-dimensional system of equations (18.98)–(18.99). The stable critical point is denoted by a filled circle, and the two saddle points by open circles.

These bounding lines are shown dashed in Fig. 18.16. Now, the flow on this torus can be understood by first examining the nullclines $\dot{\psi}_1 = 0$ and $\dot{\psi}_2 = 0$. There are four such curves,

$$\psi_2 - 2\psi_1 = -\phi_\pm, \tag{18.100}$$
$$\psi_1 - 2\psi_2 = -\phi_\pm, \tag{18.101}$$

where the numbers $-\phi_\pm$ satisfy $h(-\phi_\pm) = -\beta$, as depicted in Fig. 18.15. The nullclines are shown in Fig. 18.16 by solid lines.

Clearly, there are four critical points. By sketching in a few elements of the vector field, we can see that the critical point at the leftmost and lowest position is the only stable critical point (denoted by a filled circle), two of the critical points are saddle points (denoted by open circles), and the fourth is an unstable node. We also see that the stable critical point is a global attractor. That is, every trajectory, excluding the other critical points, tends to the unique stable critical point as time goes to infinity. It follows that the unstable manifold of each saddle point forms a closed loop; both closed loops are therefore invariant manifolds.

In general, for arbitrary n, when $\beta < \beta_0$ there is a closed invariant manifold containing the two steady states, ξ_j and ξ_0. Furthermore, this loop is a smooth invariant attracting cycle on which ϕ_j completes a full rotation from 0 to 2π but on which the other ϕ's do not. In other words, as ϕ_j moves through the 2π-cycle,

all the other $\phi_k, k \neq j$, vary without making a full cycle. This is illustrated in Fig. 18.17 by orbit A. Orbit B, however, experiences a full 2π cycle in angle θ_2 for every 2π cycle of θ_1. It follows that the invariant attracting manifold formed by the two branches of the unstable manifold of ξ_j is homotopic to (i.e., is continuously deformable into) the circle $\phi_k = 0, k \neq j, 0 \leq \phi_j \leq 2\pi$.

The crucial result proved by Ermentrout and Kopell is that this invariant attracting manifold exists even when $\beta > \beta_0$. Thus, although steady states of the phase difference equations disappear when $\beta > \beta_0$, a smooth, invariant, attracting manifold that is homotopic to the circle $\phi_k = 0, k \neq j, 0 \leq \phi_j \leq 2\pi$, persists. Since it contains no critical points, this manifold is an attracting limit cycle. This stable limit cycle corresponds to a pair of frequency plateaus in the chain of coupled oscillators. To see this, define the average frequency of the kth oscillator to be

$$\omega(\epsilon) + \lim_{T \to \infty} \frac{1}{T} \int_0^T \delta\theta'_k(t)\, dt, \tag{18.102}$$

provided that the limit exists. Here, a prime denotes differentiation with respect to t. Note that if $\delta\theta'_k$ is constant, the frequency is exactly $\omega(\epsilon) + \delta\theta'_k$, as expected. Subtracting $\delta\theta'_k$ from $\delta\theta'_{k+1}$ gives the average phase difference as

$$\lim_{T \to \infty} \frac{\epsilon}{T} \int_0^T \phi'_k(\tau)\, d\tau. \tag{18.103}$$

Around the attracting limit cycle, this simplifies to

$$\frac{\epsilon}{T_0} \int_0^{T_0} \phi'_k(\tau)\, d\tau, \tag{18.104}$$

where $T_0(\beta)$ is the period of the limit cycle on the torus. However, we readily calculate that

$$\int_0^{T_0} \phi'_k(\tau)\, d\tau = \begin{cases} 0, & k \neq j, \\ 2\pi, & k = j. \end{cases} \tag{18.105}$$

It follows that the first j oscillators all have the same average frequency, as do the oscillators from $j + 1$ to n. Between the jth and the $(j + 1)$st oscillators there is a frequency jump of $2\pi\epsilon/T_0(\beta)$.

It is important to note that the phase differences $\phi_k, k \neq j$, make small oscillations about the constant ϕ_k^-, but are not identically constant. Thus, on each frequency plateau, the phases are not locked, but only "trapped" on average over each cycle. In contrast to some experimental data, one therefore does not expect to see exactly regular propagating waves appearing on each plateau, since such waves require phase locking at each instant and a constant phase difference along the plateau. The precise reasons for this discrepancy are, as yet, unknown.

Numerical solutions

Numerical solutions of the phase equation for two different values of β are shown in Fig. 18.18. Once β is greater than the critical value β_0 a pair of plateaus emerges, and as β is increased further, multiple plateaus appear. Comparison of Fig. 18.12
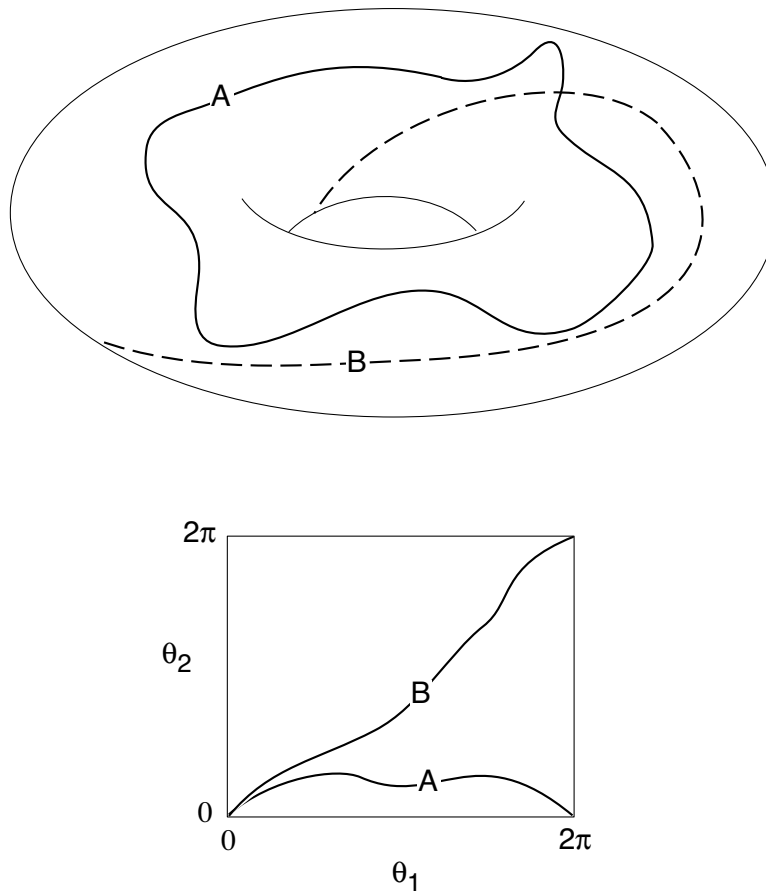
Figure 18.17: Schematic diagram of two orbits on a torus, drawn two different ways. The upper panel shows the orbits on a torus, while the lower panel has unfolded the torus into a square, periodic in both directions. Orbit A is homotopic to the circle $\theta_2 = 0$, while orbit B is not.
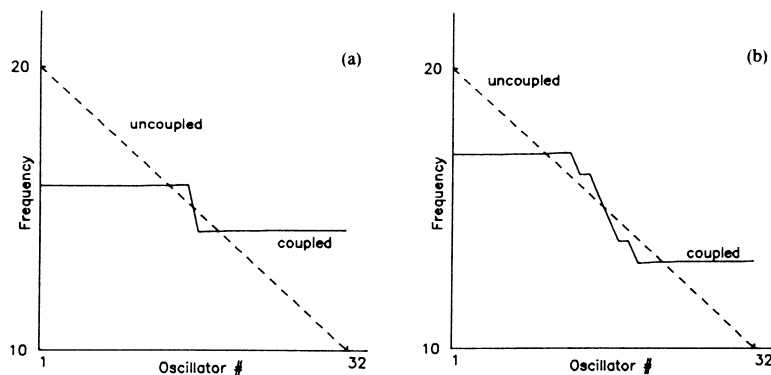
Figure 18.18: Frequency plateaus in a chain of 32 coupled oscillators. For these numerical simulations the phase equation was chosen to be $\dot\phi_k = -10/31 + \delta(\sin\phi_{k+1} - 2\sin\phi_k + \sin\phi_{k-1})$. (a): $\delta = 32$, (b): $\delta = 18$. Note that decreasing δ while leaving the intrinsic oscillator frequencies unchanged is equivalent to increasing β. (Ermentrout and Kopell, 1984, Fig. 4.1.)

with Fig. 18.18 shows that the above model differs from experimental results in an important way. In the model, the frequency of the plateau lies between the maximum and minimum natural frequencies of the oscillators in the plateau; a plateau cannot have a higher frequency than all of its constituent oscillators, as is seen in the experimental data. However, the above simple model can be extended to obtain better qualitative agreement with experiment. For example, the coupling between cells can be made stronger in one direction than the other (nonisotropic coupling) or it can be made nonuniform along the oscillator chain, in which case the phase difference equation can reproduce the asymmetrical behavior exhibited by the experimental system.

   However, despite this qualitative agreement, it must be admitted that the simple model presented here does not give a quantitative explanation of the properties of frequency plateaus in the small intestine. It is an excellent example of how, to obtain an analytical understanding of a particular phenomenon, it is often necessary to study a model that has been reduced to caricature by successive approximations. Although hope of quantitative agreement is thereby lost, such simple models often permit a substantial understanding of the underlying structure.

18.3.4   Interstitial Cells of Cajal

There is, of course, much more than coupled oscillators involved in the control of the gastrointestinal electrical activity. In particular, in recent years it has become clear that the interstitial cells of Cajal (ICC) play an extremely important role in the regulation of ECA, although we still have only a limited understanding of exactly what that role is.

   ICC were first discovered by Santiago Ramon y Cajal in 1911 (Cajal, 1893, 1911) who called them "primitive neurons" and theorized that they were modulators of

smooth muscle contraction, modulated by the nervous system in their turn. ICC can be divided into two groups. In most regions of the gastrointestinal tract, ICC form a thin layer between the longitudinal and circular layers of smooth muscle. These are called *myenteric* ICC. The second group of ICC, the *intramuscular* ICC, are distributed through the smooth muscle cells themselves. We now know that ICC are the pacemaker cells that drive the electrical slow wave in gastrointestinal smooth muscle, and that isolated smooth muscle cells cannot oscillate independently (Sanders, 1996; Čamborová et al., 2003; Takaki, 2003; Hirst and Ward, 2003; Hirst and Edwards, 2004). Although far more is known about the biophysical properties of myenteric ICC than of intramuscular ICC, the mechanisms controlling pacemaker activity are still far from clear. IP_3-dependent release of Ca^{2+} from internal stores such as the endoplasmic reticulum (see Chapter 7) is clearly one important mechanism, and this released Ca^{2+} acts on Ca^{2+}-sensitive ionic channels, particularly a Ca^{2+}-sensitive Cl^- current. It is likely that Ca^{2+} release from the mitochondria also plays an important role. However, no more definite mechanism has yet been proposed and confirmed in detail. ICC are also modulated by the enteric nervous system; it seems that innervation of the GI tract is directed more to the ICC than to the smooth muscle itself (Hirst and Edwards, 2004). The question of how ICC operate, how they are modulated by the nervous system, and how they in turn control smooth muscle contractility, is a fascinating area in which modeling is likely to play an increasingly important role over the next few years.

The importance of ICC for generating pacemaker potentials underlines the important similarities between the GI tract and the heart. In both organs, neurons innervate pacemaker cells, which in turn coordinate their activity in some way to control muscle motility. In the pacemaker cells and the muscle cells of both the GI tract and the heart, the control of internal Ca^{2+}, via IP_3 receptors, ryanodine receptors, and Ca^{2+}-sensitive ion channels, plays a crucial role. These similarities are shown schematically in Fig. 18.19.

18.3.5 Biophysical and Anatomical Models

The most detailed biophysical model of gastrointestinal electrical activity to date is that of Miftakhov et al. (1999), who constructed a model of a "functional unit" of the small intestine. In addition to the smooth muscle cells themselves, this functional unit included a number of different neurons in the enteric nervous system (each with dendritic, somatic and axonal components), as well as the dynamics of neurotransmitters and calcium in the synapses. In this model local distension of the gut wall causes a response in mechanoreceptors (dendritic, somatic and axonal in sequence), stimulation of a response in a secondary neuron, and thence stimulation of the smooth muscle cell by opening of L-type Ca^{2+} channels and a consequent increase of Ca^{2+} concentration inside the smooth muscle cell, causing contraction. The generated force itself feeds back to stimulate the mechanoreceptors again, resulting in multiple contractions in response to the initial isolated stimulus.

The enormous number of parameters and equations required to construct this model, the almost complete lack of experimental data about most of these parameters, and the relative lack of experimental data against which such a model can be tested, raises a number of thorny questions about model identifiability. How much
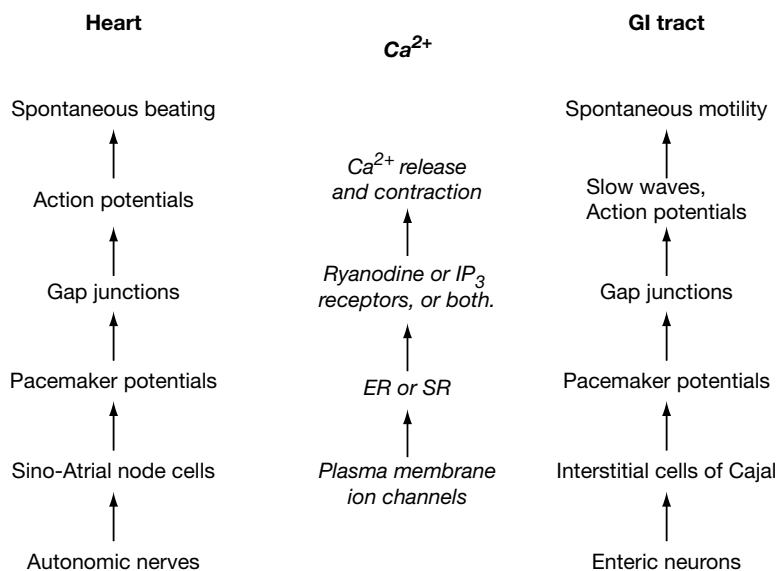
Heart

Ca^{2+}

GI tract

| Spontaneous beating | | Spontaneous motility |

↑

Ca^{2+} release and contraction

Action potentials

Slow waves, Action potentials

↑   ↑   ↑

Ryanodine or IP$_3$ receptors, or both.

Gap junctions

Gap junctions

↑   ↑   ↑

ER or SR

Pacemaker potentials

Pacemaker potentials

↑   ↑   ↑

Sino-Atrial node cells

Plasma membrane ion channels

Interstitial cells of Cajal

↑   ↑

Autonomic nerves

Enteric neurons

Figure 18.19: Schematic diagram showing the similarities between the GI tract and the heart. Adapted from Takaki, 2003, Fig. 15.

model complexity can be justified by experimental data, and how much is absolutely necessary to answer the scientific question under investigation, are difficult questions that have no generic answers; each model must be treated on its own merits. Although there is no doubt that complex biophysical models will be required before we can have a complete understanding of how a syncytium of smooth muscle and its associated innervation works to propel food along the gut, it is perhaps premature to place too much reliance on such complex models at this stage.

A different approach is taken by Pullan et al. (2004) in their detailed anatomical model of the stomach. Instead of studying a highly detailed biophysical model on a simple geometry, they constructed a complex geometry but used only highly simplified biophysical models. Using data from the visible human project (Spitzer et al., 1996) they constructed a geometrically accurate stomach upon which a finite element grid could be superimposed and the model equations solved. However, they model the electrical activity using the FitzHugh-Nagumo equations (Chapter 5). Thus, although the model shows how a wave of electrical excitation can spread around the stomach, as yet it offers little insight into the detailed mechanisms or significance of ECA, or into the behavior of a syncytium of coupled smooth muscle oscillators. However, as more detailed and accurate biophysical models become available they can (relatively) easily be incorporated into the detailed geometrical model.

The electrical activity of the stomach can be measured by an electrogastrogram (EGG) in the same way that the electrical activity of the heart can be measured by an ECG (Chapter 12). The earliest such recordings were those of Alvarez (1922)

and Davis et al. (1957). However, even today EGG recordings, particularly those aimed at measuring electrical activity in the intestines, are difficult to make and to interpret (Bradshaw et al., 1997, 1999; Allescher et al., 1998). The difficulties are clear; each heartbeat is a single event, localized, relatively precise, and repeated many times in succession. Gastrointestinal electrical activity has none of these attributes, being diffuse, changing in nature and frequency along the length of the stomach and intestines, and continuously occurring.

Exercises

1. Modify (18.1) to account for the effects of the membrane potential on sodium flux. How does membrane potential affect the transport of water?

2. Use the model of local sodium removal and osmotic transport of water to analyze the removal of water and sodium along the length of the intestinal tract.

   (a) Give a phase-plane analysis for the system. What is the trajectory of sodium and water if sodium is initially quite high? What is the trajectory of sodium and water if sodium is initially quite low? How does this compare with the trajectory when there is no sodium?

   (b) If the flow of water from the intestine is assumed to depend solely on the sodium concentration, then the flow can become negative, which is clearly unphysiological. How might this assumption be modified and justified on physical grounds?

   Hint: As the chyme dries, one expects the continued extraction of water to become more difficult.

3. For the the model of Section 18.1.2, find the average concentration of solute in a tube for which $\eta = \frac{c_0 P L^2}{Dr}$ is small. Use this to find the efflux velocity and efflux concentration. Under what conditions on parameters can water be pumped into pure water?

4. (a) Find two terms of the power series representation of the solution of (18.69) in powers of ζ. Find $u(0)$ to the same order in ζ.

   (b) It appears from the leading-order solution that $u(0)$ is negative if $J > 1$. Show that this is not correct, but that $u(0) > 0$ for all positive values of J. Show that when $J > 1$, the bulk of the reaction occurs in a thin layer contained within the mucus layer, and that the epithelial surface is completely protected. What is the physical interpretation of the condition $J > 1$?

5. Show that the kth component of $K^{-1}(\beta\Delta)$ in (18.93) is $\alpha_k = -\beta k(n+1-k)/2$.

   Hint: Verify that $(K\alpha)_i = \beta$.

6. What steady phase-locked solutions are possible for two coupled identical oscillators? What stable, steady, phase-locked solutions are possible?

7. Describe the behavior expected from two coupled oscillators when $\beta\Delta = -2-\epsilon$ and $h(\phi) = \sin\phi$ for $\epsilon \ll 1$. Check your prediction numerically. This behavior is called *rhythm splitting*, and is discussed in more detail in Murray (1989).

8. In Exercise 22 of Chapter 12 the coupling function $h(\theta)$ is calculated for a collection of coupled FitzHugh–Nagumo equations. Solve the phase equation with this coupling function numerically with arbitrary initial data to determine $\phi(t)$. How quickly do identical FitzHugh–Nagumo oscillators synchronize?

9. Extend the previous question (and refer to Chapters 7 and 8) to study the synchronization of intracellular calcium oscillations. Suppose two cells, each with a well-mixed interior, are coupled by a membrane through which Ca^{2+} can diffuse through gap junctions. Suppose further that each cell exhibits intracellular calcium oscillations of slightly different periods (i.e., each cell has a slightly different background IP_3 concentration). Using your favorite model for calcium oscillations, determine the coupling function numerically, and thus determine how fast such synchronization occurs, as a function of the intercellular permeability of Ca^{2+}.

Chapter 19

The Retina and Vision

The visual system is arguably the most important system through which our brain gathers information about our surroundings, and forms one of our most complex physiological systems. In vertebrates, light entering the eye through the lens is detected by photosensitive pigment in the photoreceptors, converted to an electrical signal, and passed back through the layers of the retina to the optic nerve, and from there, through the visual nuclei, to the visual cortex of the brain. At each stage, the signal passes through an elaborate system of biochemical and neural feedbacks, the vast majority of which are poorly, if at all, understood.

Although there is great variety in detail between the eyes of different species, a number of important features are qualitatively conserved. Perhaps the most striking of these features is the ability of the visual system to adapt to background light. As the background light level increases, the sensitivity of the visual system is decreased, which allows for operation over a huge range of light levels. From a dim starlit night to a bright sunny day, the background light level varies over 10 orders of magnitude (Hood and Finkelstein, 1986), and yet our eyes continue to operate across all these levels without becoming saturated with light. The visual system accomplishes this by ensuring that its sensitivity varies approximately inversely with the background light, a relationship known as *Weber's Law* (Weber, 1834) and one that we discuss in detail in the next section.

Because of this adaptation, the eye is more sensitive to changes in light level than to a steady input. When a space-independent pulse of light is shone on the entire eye, the retina responds with a large-amplitude signal at the beginning followed by a decrease to a lower plateau. Similarly, at the end of the impulse, a large negative transient is followed by a return to a plateau. Response to transients with adaptation in steady conditions is characteristic of inhibitory feedback, or *self-inhibition*, which occurs at a number of levels in the retina. Furthermore, the retina is sensitive to particular frequencies of flashing light, with the most sensitive frequency being a function of the background light level.

Adaptation is also manifested spatially. When a time-independent strip of light is applied to the retina, the response is greatest at the edges of the pattern. These response variations are known as *Mach bands* and are due to *lateral inhibition*, which plays a similar role in space as self-inhibition plays in time. For example, in the
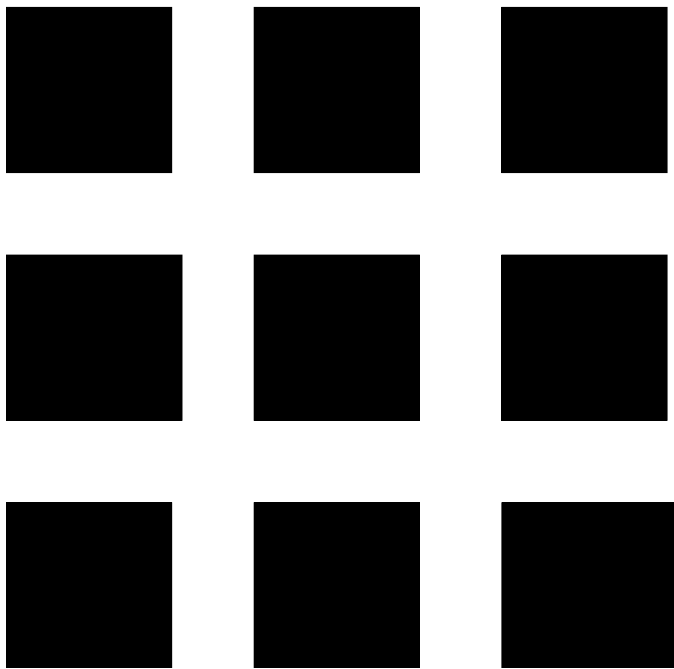
Figure 19.1: Test pattern with which to observe the effects of self-inhibition and lateral inhibition.

interior of a uniformly bright part of the visual field, neurons are inhibited from all sides, while regions near the edge receive little inhibition from their dimly illuminated neighbors and therefore appear brighter. The result is contour enhancement. The effect of lateral inhibition can be seen in the white intersections of Fig. 19.1. In particular, if one looks intently at one of the white intersections, the remaining intersections appear to have a gray or darkened interior, and the center of the white strips appear slightly darkened compared to their edges, because of lateral inhibition.

The visual system operates on many levels, ranging from the biochemistry of the photopigments, to the cellular electrophysiology of the individual retinal cells, to the neural pathways responsible for image processing, to the large-scale structure of the visual cortex. Because of this complexity, there is still much debate over the mechanisms of adaptation, and the place where it occurs. Certainly, adaptation occurs in psychophysical experiments (i.e., with human subjects who report what they detect); one example of this has already been seen in Fig. 19.1. As another example, psychophysical measurement of the threshold-versus-intensity function shows Weber-Law behavior. Plots of the ratio $\delta I/I$, where δI is the brightness of the smallest detectable flash superimposed on the background I, shows that $\delta I/I$ is approximately constant over a range of background light levels. Although relating these psychophysical results to specific mechanisms is not an easy task, it is clear that adaptation occurs at the very lowest level of the visual system, inside the photoreceptors themselves.

Obviously, there is insufficient space here for a detailed study of all these aspects of the visual system. Here we concentrate on retinal mechanisms and omit discussion of mechanisms at the level of the visual cortex. The latter questions are better addressed in specialist books on neuroscience. For a more comprehensive view of the visual system, the reader is referred to the excellent book by Nicholls, Martin, and Wallace (1992); other discussions of visual processing can be found in Graham (1989), Blakemore (1990), Landy and Movshon (1991), and Spilmann and Werner (1990). A review of the connection between psychophysical experiments and the underlying physiology is given by Hood (1998), while an excellent earlier review of psychophysical experiments is Barlow (1972).

19.1   Retinal Light Adaptation

The first stage of visual processing occurs in the retina, a structure consisting of at least five major neuronal cell types (Fig. 19.2). After entering the eye, light passes through all the cell layers of the retina before being absorbed by photosensitive pigments in the photoreceptors in the final layer of cells. (A functional reason for this arrangement is not known.) Photoreceptors come in two varieties: rods, which operate in conditions of low light, and cones, which operate in bright light conditions and detect color. In the dark, photoreceptors have a resting membrane potential of around -40 mV, and they hyperpolarize in response to light. The light response is graded, with larger light stimuli resulting in larger hyperpolarizations. Note that this is different behavior from typical neurons, in which the action potential is a depolarization and is all-or-nothing, as described in Chapter 5. Photoreceptors
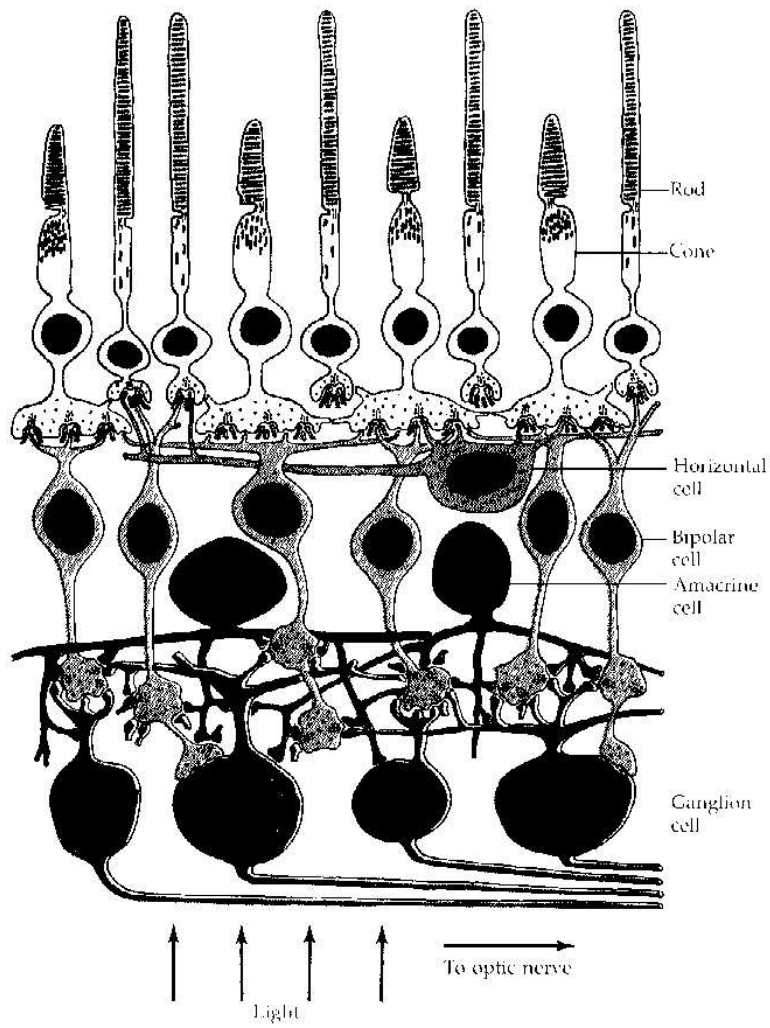
Figure 19.2: Schematic diagram of the layers of the retina. (Nicholls et al., 1992, Chapter 16, Fig. 14, p. 583.)

make connections to both horizontal cells and bipolar cells. Each horizontal cell makes connections to many photoreceptors (and, often, to bipolar cells), and is coupled to other horizontal cells by gap junctions. The bipolar cells form a more direct pathway, coupling photoreceptor responses to ganglion cells, but this is also a simplification. Amacrine cells connect only to bipolar cells and ganglion cells, and their precise function is unknown. Ganglion cells (which fire action potentials, unlike photoreceptors and horizontal cells) are the output stage of the retina and form the optic nerve. The interconnections among the retinal cells are complex and not well understood; there has been a great deal of work done on how the retina detects features such as moving edges and orientation, while ignoring much of the information presented to it. Here, we describe only the simplest models.

19.1.1 Weber's Law and Contrast Detection

One of the basic features of the retina is *light adaptation*, the ability to adapt to varying levels of background light. Over a wide range of light levels, the sensitivity of the retina is observed to be approximately inversely proportional to the background light level. This fact is known as *Weber's law*, or the *Weber–Fechner law*. There are three common definitions of sensitivity. It can mean *psychophysical sensitivity*, defined as 1/threshold, where the threshold is the minimal stimulus necessary to elicit an observable response when superimposed on a given background. Weber's law describes the fact that in psychophysical experiments the threshold increases as the background light level increases.

A second definition of sensitivity is the one used most in this chapter. In response to a small light flash, the membrane potential of a photoreceptor (or horizontal cell) first decreases and then returns to rest (recall that the voltage hyperpolarizes in response to a light flash). If $V(I, I_0)$ is the maximum deviation of the membrane potential in response to a light flash of magnitude I on a background of I_0, then the *peak sensitivity* is

$$S(I_0) = \left. \frac{\partial V}{\partial I} \right|_{I=I_0} . \tag{19.1}$$

In the physiology literature (for example, Fain et al., 2001) the sensitivity is defined as the amplitude of the voltage response to a small flash divided by the intensity of the flash (in units of photons per area). Since $V(I, I_0) \approx \frac{\partial V(I,I_0)}{\partial I}|_{I=I_0} I$, these two definitions are equivalent as long as one uses only small flashes.

The third definition of sensitivity is the *steady-state sensitivity*. If $V_0(I_0)$ is the steady response as a function of the background light level, then the steady-state sensitivity is defined to be dV_0/dI_0.

Light adaptation serves two fundamentally important purposes. First, it helps the retina handle the wide range of light levels in which the eye must operate. The eye functions in a range of light levels that spans about 10 log units, from a starlit night to bright sunlight. (Light intensities are typically plotted on a dimensionless logarithmic scale. For example, if I_0 is a standard unit of light intensity, and the intensity of the light stimulus is I, then $\log(\frac{I}{I_0}) = \log I - \log I_0$, so that on a logarithmic scale, the unit scale I_0 only shifts $\log \frac{I}{I_0}$). Further, the retina is so

sensitive that it can reliably detect as few as 20 photons, and can even, although less reliably, detect single photons.

The two requirements of operation over a wide range of light levels and high sensitivity in the dark are in conflict. Without control mechanisms, a retina that can detect single photons would be saturated, and hence blinded, by bright light. In bright light, there is a *saturation catastrophe*, in which every photoreceptor is saturated, each sending the same signal to the brain, so that no contrast in the scene can be detected. However, for the human retina this saturation catastrophe is about 10 log units above the level of no response. This range of light sensitivity is achieved partly by the use of two different types of photoreceptors, rods and cones, having different sensitivities, rods operating in dim light and cones in bright light. However, by itself, two types of photoreceptors are inadequate to account for the observed range of light sensitivity.

The second effect of light adaptation is to send a signal to the brain that is dependent only on the contrast in the scene, not on the background light level. When a scene is observed with different background light levels, the amount of light reflected from an object in that scene varies considerably. For example, if you read a book inside where the light is relatively dim, it looks the same as if you were to read it outside in bright light. This happens despite the fact that the amount of light reflecting off the black letters outside is considerably more than the amount of light reflecting off the white page inside. Nevertheless, in both situations we see a white page and black text. Clearly, the eye is measuring something other than the total amount of light coming from an object. In fact, the eye measures the contrast in the scene, which, since it is dependent only on the reflectances of the objects, is independent of the background light level. As another striking example of the importance of contrast detection, consider a black and white television screen. When the television is switched off the screen is uniformly gray. When the television is switched on there is no mechanism for making parts of the screen darker. Nevertheless, we still see deep blacks on the screen. Of course, those parts of the screen that look black do so only in contrast to those other parts of the screen which are brighter.

Contrast detection is a consequence of Weber's law, as can be seen from the following argument of Shapley and Enroth-Cugell (1984). Suppose we observe an object superimposed on a background, where the background reflectance is R_b, the object reflectance is R_o, and the background light level is I. As the receptive field of a retinal neuron moves across the boundary of the object, the stimulus it receives changes from IR_b to IR_o, a difference of $IR_o - IR_b$. Since, according to Weber's law, the sensitivity of the cell is inversely proportional to IR_b (the amount of light reaching the cell from the background), the cell's response will be approximately proportional to $(IR_o - IR_b)/(IR_b) = (R_o - R_b)/R_b$, which is dependent only on the contrast in the scene.

19.1.2   Intensity–Response Curves and the Naka–Rushton Equation

Light adaptation in photoreceptors can be clearly seen in the experimental results reproduced in Fig. 19.3 (also discussed in detail by Fain et al., 2001). In that experiment, a salamander rod was presented with a series of light flashes superimposed on backgrounds of different intensities and the resultant photocurrent was measured. (Although we have not yet discussed the photocurrent in receptors, it is reasonable to assume that the voltage shows similar qualitative responses. The photocurrent is discussed in detail in Section 19.2). Three important features can be easily seen. First, as the intensity of the flash increases (for any fixed background) the magnitude of the response increases with the intensity of the flash, but eventually saturates. Second, as the background light level increases, a larger flash is needed to evoke a response of a given size. Thus, the rod is adapting. Third, in response to the step of light at the beginning of the lowest trace (background light level 1.57) the response shows a clear initial peak followed by relaxation to a lower steady level. This relaxation to a lower steady level is a consequence of the adaptation of the receptor.

Around each background light level the peak of the flash response is approximately described by the Naka–Rushton equation (Naka and Rushton, 1966; yet another incarnation of the Michaelis-Menten equation described in detail in Chapter 1)

$$\frac{R_{\mathrm{peak}}}{R_{\mathrm{max}}} = \frac{I}{I + \sigma(I_0)},$$ (19.2)

where R_{peak} is the peak of the response, R_{max} is the maximal response to a saturating flash, I is the intensity of the flash, and I_0 is the background light level. The response is half maximal when $I = \sigma$. It is experimentally observed that as I_0 increases, so does σ. Thus at higher background light levels it takes a larger flash to obtain a half-maximal response, as would be expected from an adapting receptor.

Much of this information can be elegantly summarized by intensity–response curves (Fig. 19.4), a set of curves that repays careful consideration. For a fixed background light level I_0, we consider the response to a family of superimposed light flashes, positive or negative, and plot the peak of the flash response against the intensity of the flash. Note that Fig. 19.4 shows photoreceptor voltage plotted against flash intensity (instead of photocurrent as in Fig. 19.3) and the vertical axis is reversed.

Let $V(I, I_0)$ denote the peak response to a flash of intensity I on a background of I_0. It turns out that the entire set of flash responses can be described by using the Naka–Rushton equation

$$\frac{V(I, I_0)}{V_{\mathrm{max}}} = \frac{I}{I + \sigma(I_0)}$$ (19.3)

as a template and moving it across and down slightly to describe the higher background light levels (see Exercise 1). From Fig. 19.4 it can be seen that σ is an increasing function of I_0. Thus, as the background light level increases, the response curve maintains its shape, but shifts to higher light levels and moves down
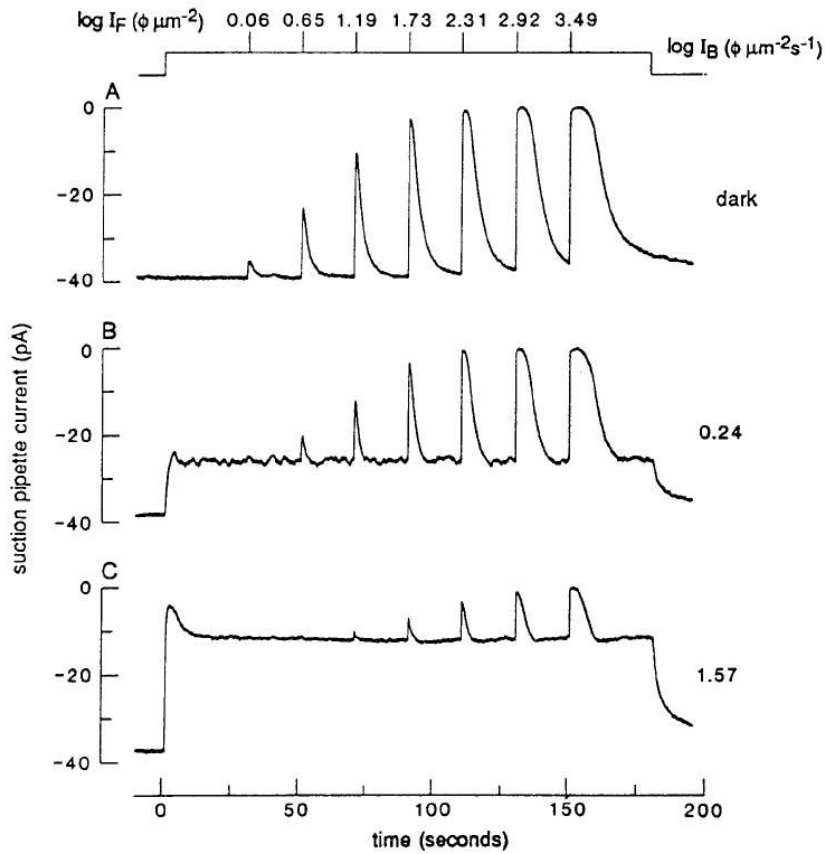
Figure 19.3: Light adaptation in a salamander rod. I_F is the intensity of the light flash and I_B is the intensity of the background, both in units of photons per μm^2. The suction pipette current is the total photocurrent through the rod; models for the photocurrent are discussed in Section 19.2. However, note that a decrease in photocurrent corresponds to a hyperpolarization of the photoreceptor. The timing of the flashes is shown at the top of the figure. Reproduced from Matthews (1990). **Springer; This figure will need permissions. JS**
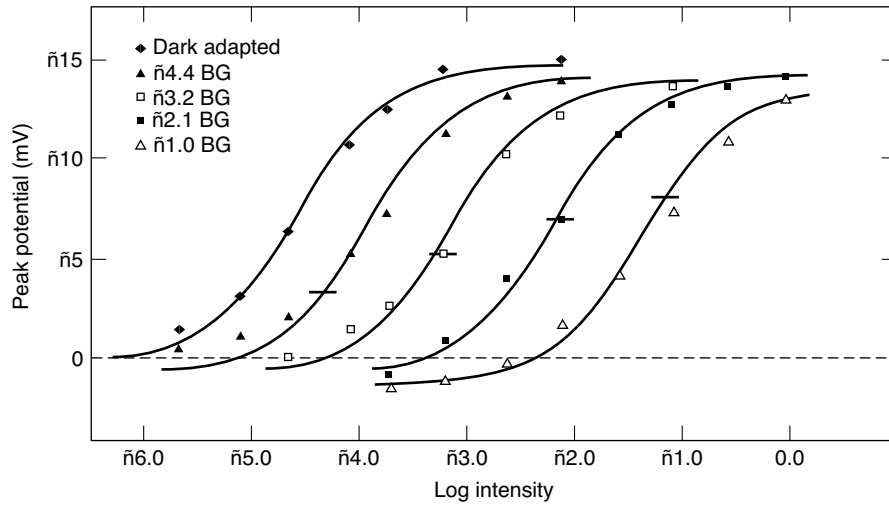
Figure 19.4: Intensity response curves measured in a red-sensitive cone of the turtle. The peak of the response to a light flash (either increasing or decreasing) is plotted against the log of the intensity of flash. Each data set corresponds to a different background light level, and the smooth curves are drawn by using the Naka–Rushton equation, (19.3), as a template, and shifting it across and down for the higher background light levels. The short horizontal lines denote the resting hyperpolarization for each background light level. The membrane potential has been scaled to be zero in the dark (Normann and Perlman, 1979, Fig. 7).

slightly (although this shift is not accounted for in (19.3)). Note that since I and σ are positive, the Naka–Rushton equation is always well defined.

In contrast to the peak response, the steady response, depicted by the small horizontal lines in Fig. 19.4, is a much shallower function of the background light level. In this way retinal neurons can detect contrast over a wide range of light levels without saturating. The steep Naka–Rushton intensity–response curves around each background light level give a high sensitivity to changes superimposed on that background, but the shallower dependence of the steady response on the background light level postpones saturation.

In the experimental literature, adaptation is often discussed in terms of changes in sensitivity so it is useful to present a brief discussion of this approach here also. Sensitivity (at least in the way we use it here) is defined by

$$S(I_0) = \left. \frac{dV(I, I_0)}{dI} \right|_{I=I_0}. \tag{19.4}$$

Note that the sensitivity, S, is a function of the background light level, which is the whole point of adaptation. If V satisfies the Naka-Rushton equation then

$$S = V_{\max} \frac{\sigma(I_0)}{(I_0 + \sigma(I_0))^2}. \tag{19.5}$$

Defining S_D to be the sensitivity in the dark, it follows that $S_D = V_{\max}/\sigma(0)$ and thus

$$\frac{S(I_0)}{S_D} = \frac{\sigma(I_0)\sigma_D}{[I_0 + \sigma(I_0)]^2}. \tag{19.6}$$

We know that σ is an increasing function of I_0, but until now have not specified what the function is. If we specify σ to be a linear increasing function of I_0, i.e.,

$$\sigma = \sigma_D + kI_0, \tag{19.7}$$

for some constant, k, then

$$\frac{S(I_0)}{S_D} = \frac{(\sigma_D + kI_0)\sigma_D}{[I_0(1 + k) + \sigma_D]^2}. \tag{19.8}$$

Notice that as I_0 gets large so that $kI_0 \gg \sigma_D$ then S/S_D is proportional to $1/I_0$, which is Weber's Law. Fortunately, $\sigma(I_0)$ measured experimentally is close to linear for many photoreceptors (Perlman and Normann, 1998).

Many experimental measurements have shown that the relative sensitivity can be well fit by the expression

$$\frac{S}{S_D} = \frac{A}{A + I_0}, \tag{19.9}$$

where A is some constant to be determined by fitting to the data. Because this expression for the sensitivity satisfies all the necessary criteria (it is equal to 1 when $I_0 = 0$, it goes to zero as $I_0 \to \infty$, and it is approximately proportional to $1/I_0$ for a range of I_0) and is very simple, it has been used often in the literature (for example Baylor and Hodgkin, 1974; Baylor et al., 1980; Fain, 1976). Although (19.9) differs from the expression for the sensitivity (19.8) given by the Naka–Rushton equation, it is left as an exercise (Exercise 2) to show that the two expressions for the sensitivity are practically indistinguishable.

19.2   Photoreceptor Physiology

Since we know from the results in Fig. 19.3 that adaptation occurs at the level of the individual photoreceptor, we construct a model of the biochemistry and electrophysiology of a photoreceptor to see how such adaptation can come about. As a preliminary to the construction of such a model, we present a brief discussion of the physiology of the vertebrate photoreceptor. (Because of the significant differences between vertebrate and invertebrate photoreceptors we consider only the former here.) More detailed discussions are given in Fain and Matthews (1990), McNaughton (1990), and Pugh and Lamb (1990). A selection of detailed articles is given in Hargrave et al. (1992) and an excellent review of adaptation in vertebrate photoreceptors is given by Fain et al. (2001).

Vertebrate photoreceptors are composed of two principal segments: an outer segment that contains the photosensitive pigment, and an inner segment that contains the necessary cellular machinery. A connecting process, called an axon, connects the inner segment to a *synaptic pedicle*, which communicates with neurons (such as horizontal and bipolar cells) in the inner layers of the retina. In rods, the photosensitive pigment is located on a stack of membrane-enclosed disks that take up the majority of the space in the outer segment, while in cones, the pigment is located on invaginations of the outer segment membrane. The connecting process does not transmit action potentials, and hence the name "axon" is somewhat misleading. Photoreceptors respond in a graded manner to light, and give an analogue, rather than a digital, output.

In the dark, the resting membrane potential is about -40 mV. Current, carried by Na^+ and Ca^{2+} ions, flows into the cell through light-sensitive channels in the outer segment, and is balanced by current, carried mostly by K^+ ions, flowing out through K^+ channels in the inner segment. Thus, in the dark there is a circulating current of about 35–60 pA. In the dark, the light-sensitive channels are held open by the binding of 3 molecules of cGMP. Ionic balance is maintained by a Na^+–K^+ pump in the inner segment that removes 3 Na^+ ions for the entry of 2 K^+ ions, and a Na^+–Ca^{2+}, K^+ exchanger in the outer segment that removes 1 Ca^{2+} and 1 K^+ for the entry of 4 Na^+ ions. The Na^+–Ca^{2+}, K^+ exchanger is the principal method for Ca^{2+} extrusion from the cytoplasm.

The light response begins when a photon of light strikes the photosensitive pigment, initiating a series of reactions (described in more detail below) that results in the activation of rhodopsin, and its subsequent binding to a G-protein, transducin. The bound transducin exchanges a molecule of GDP for GTP and then binds to cGMP-phosphodiesterase (PDE), thereby activating PDE to PDE*. Since the rate of hydrolysis of cGMP by PDE* is greater than by PDE, this leads to a decline in [cGMP] and subsequent closure of some of the light-sensitive channels. As the light-sensitive conductance decreases, the membrane potential moves closer to the reversal potential of the inner segment K^+ conductance (about -65 mV), hyperpolarizing the membrane.

Light adaptation is mediated by the cytoplasmic free Ca^{2+} concentration. When the light-sensitive channels close, the entry of Ca^{2+} is restricted, as about 10–15% of the light-sensitive current is carried by Ca^{2+}. However, since the Na^+–Ca^{2+}, K^+ exchanger continues to operate, the intracellular $\left[Ca^{2+}\right]$ falls. This decrease in
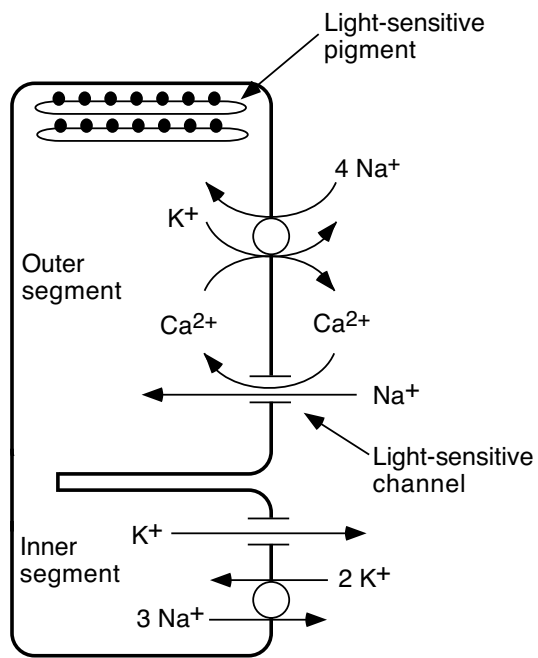
Figure 19.5: Schematic diagram of a photoreceptor, showing the major ionic currents and pumps that regulate phototransduction. (Adapted from McNaughton, 1990.)
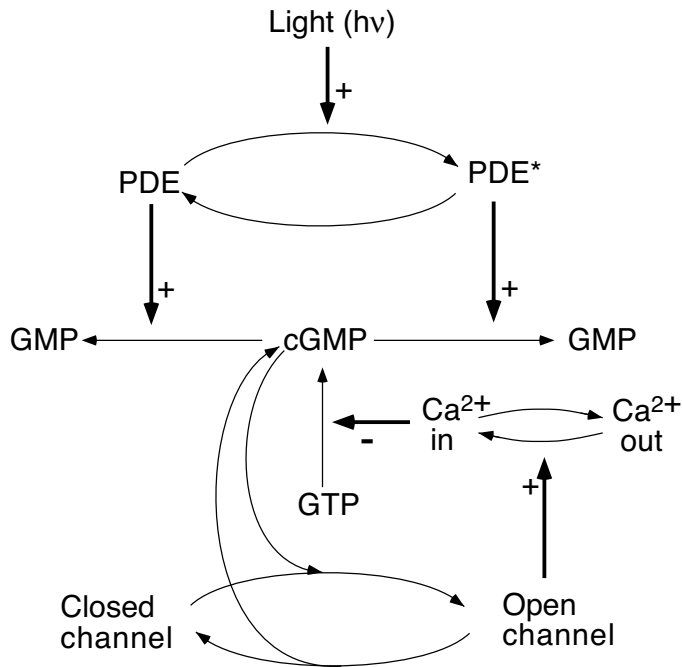
Figure 19.6: Schematic diagram of the major reactions involved in light adaptation. The initial cascade, leading to the activation of PDE, is condensed into a single step here, but is considered in more detail in Fig. 19.7. (Adapted from Sneyd and Tranchina, 1989.)

$[Ca^{2+}]$ increases the activity of an enzyme called guanylate cyclase that makes cGMP from GTP. Thus, a decrease in $[Ca^{2+}]$ results in an increase in the rate of production of cGMP, reopening the light-sensitive channels, completing the feedback loop. A schematic diagram of the reactions involved in adaptation is given in Fig. 19.6. Although it is likely that there are other important reactions involved in phototransduction (for example, Ca^{2+} may affect the activity of PDE), the above scheme incorporates many essential features of the light response.

The mechanisms of phototransduction are similar in rods and cones, with one important difference being the light-sensitive pigment contained in the cell. In rods, rhodopsin consists of retinal and a protein called *scotopsin*, while in cones, the rhodopsin consists of retinal and different proteins, called *photopsins*. The primary effect of this compositional difference is that in rods, rhodopsin absorbs light in a range of wavelengths centered at 505 nm, while the rhodopsin in cones absorbs light in a range of wavelengths centered at 445 (blue cones), 535 (green cones), and 570 (red cones) nm. Night blindness is caused by insensitivity of rods because of inadequate amounts of rhodopsin, often associated with vitamin A deficiency. Colorblindness, on the other hand, occurs when green or red cones are missing or when blue cones are underrepresented. Colorblindness is a genetically inherited disorder. Another important difference between rods and cones is that the light

response of a cone is much faster than that of a rod, due principally to its smaller size.

There are a number of models of phototransduction, some of which (Baylor et al., 1974a,b; Carpenter and Grossberg, 1981) were constructed before the molecular events underlying adaptation were well known. More detailed models include those of Tranchina and his colleagues for turtle cones (Sneyd and Tranchina, 1989; Tranchina et al., 1991), Forti et al. (1989) for newt rods, and Tamura et al. (1991) for primate rods. These models have confirmed that feedback of Ca^{2+} on the activity of guanylate cyclase is indeed sufficient to explain many features of the light response in both rods and cones. Detailed models of the initial cascade and the activation process have been constructed by Cobbs and Pugh (1987) and Lamb and Pugh (1992). The recent models of Hamer (Hamer 2000a,b, 2005), building upon the earlier model of Nikonov et al. (1998), provide by far the most detailed quantitative fit of a model to experimental data, while a detailed stochastic view of the initial reactions in the cascade is given by Hamer et al. (2003).

19.2.1   The Initial Cascade

Although the main consequence of the absorption of light by a photoreceptor is the conversion of PDE to a more active form, and a resultant decline in the concentration of cGMP, there are many biochemical steps between these events (Fig. 19.7). Absorption of a photon causes the isomerization of 11-cis retinal to the all-trans form, and this in turn causes a series of isomerizations of rhodopsin, ending with metarhodopsin II. Metarhodopsin II is converted to metarhodopsin III, which is, in turn, hydrolyzed to opsin and all-trans retinal. The activated form of rhodopsin is metarhodopsin II, called R^* here. In the dark, the G-protein transducin is in its deactivated form, T-GDP. After absorption of a photon, R^* binds to T-GDP and catalyzes the exchange of GDP for GTP. This exchange reduces the affinity of R^* for transducin, and also causes transducin to split into an α subunit, T_α-GTP, and a $\beta\gamma$ subunit, $T_{\beta\gamma}$. It is T_α-GTP that then binds to PDE, forming the complex PDE^*-T_α-GTP, which is the activated form of the PDE. The cycle is completed when the GTP is dephosphorylated to GDP, the PDE leaves the complex, and the T_α subunit recombines with the $T_{\beta\gamma}$ subunit forming the deactivated form of transducin again. All of these reactions occur in the membrane that contains rhodopsin, and are thus influenced by the speed at which the various proteins can diffuse within the membrane, an aspect that we do not consider here (but see Lamb and Pugh, 1992).

Although it is possible to model this sequence of reactions in detail (Exercise 4), we do not do so here, as it appears that nonlinearities in the initial stages of the light response have little effect on adaptation at low light levels. This allows the considerable simplification of modeling the initial stages of the light response as a simple multistage linear system.

We model the initial cascade as a sequence of linear reactions,

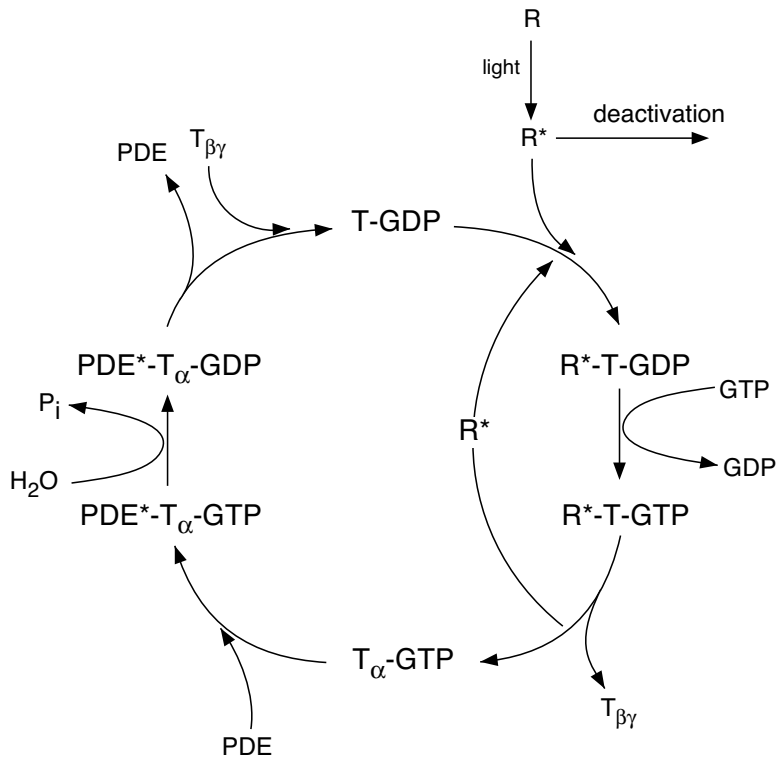$$\frac{dr}{dt} = l_1 I(t) - l_2 r, \tag{19.10}$$

Figure 19.7: Schematic diagram of the biochemical reactions involved in the initial steps of phototransduction. (Adapted from Stryer, 1986, Fig. 6.)

$$\frac{dg_1}{dt} = l_3 r - l_4 g_1, \tag{19.11}$$

$$\frac{dg_2}{dt} = l_5 g_1 - l_6 g_2, \tag{19.12}$$

$$\frac{dg}{dt} = l_7 g_2 - l_8 g, \tag{19.13}$$

where $l_1, \ldots, l_8$ are rate constants, r is the concentration of R*, g is the concentration of transducin, and g_1 and g_2 are hypothetical intermediate states between the formation of activated rhodopsin and the activation of transducin. These intermediate states need not occur in this specific location, but could be included anywhere preceding the activation of PDE. Two intermediate states are used because there is evidence that to get acceptable agreement with data, at least four stages are needed before the activation of PDE (Cobbs and Pugh, 1987). The transfer function (see Appendix 19.8) of this linear system is

$$H(\omega) = \frac{\eta}{(1 + i\omega\tau_1)^4}, \tag{19.14}$$

where $\eta = l_1 l_3 l_5 l_7 \tau_1^4$, and where we have assumed that $l_2 = l_4 = l_6 = l_8 = 1/\tau_1$. The impulse response $K(t)$ of the system is given by

$$K(t) = \frac{\eta}{\tau_1 3!} \left(\frac{t}{\tau_1}\right)^3 e^{-t/\tau_1}. \tag{19.15}$$

Finally, we let p denote the concentration of PDE*, and let P_0 denote the total concentration of PDE, to get

$$\frac{dp}{dt} = s(t)(P_0 - p) - k_1 p, \tag{19.16}$$

where

$$s(t) = \int_{-\infty}^{t} I(\tau) K(t - \tau) \, d\tau. \tag{19.17}$$

If $P_0/p \ll 1$ then $P_0 - p \approx P_0$, in which case the deactivation of PDE* is linear (Hodgkin and Nunn, 1988).

19.2.2 Light Adaptation in Cones

We can now incorporate the model of the initial cascade into a complete model for excitation and adaptation by including equations for the concentrations of cGMP, Ca^{2+}, and Na^+, as well as the membrane potential. First, we scale p by P_0, and then let $x = [cGMP]/[cGMP]_{dark}$, $y = \left[Ca^{2+}\right] / \left[Ca^{2+}\right]_{dark}$, and $z = \left[Na^+\right] / \left[Na^+\right]_{dark}$, so that $x = y = z = 1$ in the dark. We also shift the membrane potential V so that $V = 0$ in the dark.

cGMP is produced at some rate dependent upon Ca^{2+} concentration, given by $g(y)$, an unknown function to be determined. cGMP is hydrolyzed by both the

active (at rate proportional to xp) and the inactive (at rate proportional to $x(1-p)$) forms of PDE, although the rate of hydrolysis by PDE* is faster than by PDE. Thus,

$$\frac{dx}{dt} = g(y) - \gamma xp - \delta x(1-p) = g(y) - (\gamma - \delta)xp - \delta x. \qquad (19.18)$$

Note that the units of $g(y)$, γ, and δ are s^{-1}. (The assumptions behind (19.18) are not as simple as they may seem; see Exercise 5.)

The light-sensitive channel is held open by three cGMP molecules, and, in the physiological regime, has a current–voltage relation proportional to e^{-V/V^*}, for some constant V^*. In general, one expects the number of open light-sensitive channels to be a sigmoidal function of x, as in (1.70), with a Hill coefficient of 3. However, since x is very small in the dark (and becomes even smaller in the presence of light), few light-sensitive channels ever open, and thus the light-sensitive current J_{ls} is well represented by

$$J_{ls} = Jx^3 e^{-V/V^*}, \qquad (19.19)$$

for some constant J, with units of current.

Calcium enters the cell via the light-sensitive current, of which approximately 15% is carried by Ca^{2+}, and is pumped out by the Na^+–Ca^{2+}, K^+ exchanger. Assuming that the Na^+–Ca^{2+}, K^+ exchanger removes Ca^{2+} with first-order kinetics, the balance equation for Ca^{2+} is

$$\beta \frac{dy}{dt} = \frac{\kappa}{2F\nu y_d} Jx^3 e^{-V/V^*} - k_2 y, \qquad (19.20)$$

where ν is the cell volume, κ is the fraction of the light-sensitive current carried by Ca^{2+}, F is Faraday's constant, k_2 is the rate of the exchanger, and y_d denotes $\left[Ca^{2+}\right]_{dark}$. To incorporate Ca^{2+} buffering, we assume that the ratio of bound to free Ca^{2+} is β, and that the buffering is fast and linear. This means that the rate of change of $\left[Ca^{2+}\right]$ must be scaled by β (a detailed discussion of Ca^{2+} buffering is given in Chapter 7, Section 7.4). Typically, β is approximately 99.

Similarly, the balance equation for Na^+ is derived by assuming that the exchanger brings 4 Na^+ ions in for each Ca^{2+} ion it pumps out, and that the rate of the $Na^+ - K^+$ pump is a linear function of Na^+. Further, most of the light-sensitive current not carried by Ca^{2+} is carried by Na^+. Thus,

$$\frac{dz}{dt} = \frac{1-\kappa}{F\nu z_d} Jx^3 e^{-V/V^*} + \frac{4k_2 y_d}{z_d} y - k_3 z, \qquad (19.21)$$

where z_d denotes $\left[Na^+\right]_{dark}$.

Some parameter relationships can be determined and the equations for y and z simplified by using the fact that $x = y = 1$, $V = 0$ must be a steady state. From this it follows that

$$k_2 = \frac{J\kappa}{2F\nu y_d} \qquad (19.22)$$

and

$$k_3 = \frac{(1-\kappa)J}{F\nu z_d} + \frac{4k_2 y_d}{z_d} = \frac{J(1+\kappa)}{F\nu z_d}, \qquad (19.23)$$

so that

$$\tau_y \frac{dy}{dt} = x^3 e^{-V/V^*} - y, \tag{19.24}$$

$$\tau_z \frac{dz}{dt} = \left(\frac{1-\kappa}{1+\kappa}\right) x^3 e^{-V/V^*} + \left(\frac{2\kappa}{1+\kappa}\right) y - z, \tag{19.25}$$

where $\tau_z = \frac{F\nu z_d}{J(1+\kappa)}$ and $1/\tau_y = \beta k_2$.

Finally, we derive an equation for the membrane potential. Since the exchangers and pumps transfer net charge across the cell membrane, there are four sources of transmembrane current: the light-sensitive current, the Na^+–K^+ pump current, the Na^+–Ca^{2+}, K^+ exchange current, and the light-insensitive K^+ current, which is modeled as an ohmic conductance. Also note that for every 1 Ca^{2+} ion pumped out of the cell, one positive charge enters, and for every 3 Na^+ ions pumped out, one positive charge leaves. Thus

$$C_m \frac{dV}{dt} = Jx^3 e^{-V/V^*} - \frac{Fk_3 z_d \nu}{3} z - G(V - E) + (Fk_2 y_d \nu)y, \tag{19.26}$$

where G and E are, respectively the conductance and reversal potential of the light-insensitive K^+ channel, and C_m is the capacitance of the cell membrane. Recall that the potential V is measured relative to the potential in the dark. Using (19.22) and (19.23), the voltage equation becomes

$$C_m \frac{dV}{dt} = Jx^3 e^{-V/V^*} - \frac{J(1+\kappa)}{3} z - G(V - E) + \frac{J\kappa}{2} y, \tag{19.27}$$

and then using that $V = 0$, $y = z = 1$ must be a steady state, we get

$$J = \frac{-6GE}{4+\kappa}. \tag{19.28}$$

Substituting this expression back into the voltage equation gives

$$\tau_m \frac{dV}{dt} = -\left(\frac{6E}{4+\kappa}\right) x^3 e^{-V/V^*} + 2\left(\frac{1+\kappa}{4+\kappa}\right) Ez - (V - E) - \left(\frac{3E\kappa}{4+\kappa}\right) y, \tag{19.29}$$

where $\tau_m = C_m/G$ is the membrane time constant.

In summary, the model equations are

$$\frac{dx}{dt} = g(y) - (\gamma - \delta)xp - \delta x, \tag{19.30}$$

$$\tau_y \frac{dy}{dt} = x^3 e^{-V/V^*} - y, \tag{19.31}$$

$$\tau_z \frac{dz}{dt} = \left(\frac{1-\kappa}{1+\kappa}\right) x^3 e^{-V/V^*} + \left(\frac{2\kappa}{1+\kappa}\right) y - z, \tag{19.32}$$

$$\tau_m \frac{dV}{dt} = -\left(\frac{6E}{4+\kappa}\right) x^3 e^{-V/V^*} + 2\left(\frac{1+\kappa}{4+\kappa}\right) Ez - (V - E) - \left(\frac{3E\kappa}{4+\kappa}\right) y. \tag{19.33}$$

s_1	$=$	1.59 mV	s_2	$=$	1130
E	$=$	-13 mV	V^*	$=$	35.7 mV
τ_y	$=$	0.07 s	k_1	$=$	35.4 s^{-1}
γ	$=$	303 s^{-1}	δ	$=$	5 s^{-1}
κ	$=$	0.1	η	$=$	52.5 s^{-1}
τ_1	$=$	0.012 s	τ_m	$=$	0.016 s
τ_z	$=$	0.04 s			

Table 19.1: Parameter values for the model of light adaptation in turtle cones. (Tranchina et al., 1991.)

Determination of the unknowns

The unknown function $g(y)$ (the Ca^{2+}-dependent rate of cGMP production) is determined by requiring the steady-state membrane potential to be the logarithmic function

$$V_0 = -s_1 \log(1 + s_2 I_0), \qquad (19.34)$$

for some constants s_1, s_2. The form of this steady-state relation gives very good agreement with experimental data from turtle cones (although it does not give exact Weber's law behavior). This results in a long and complicated expression for $g(y)$ that we do not give here, as its analytic form has no physiological significance (see Exercise 3). Its shape, however, is of interest, and that can be determined only after the parameters are determined by fitting to experimental data.

Some of the parameters are known from experiment. For example, κ, the proportion of the light-sensitive current carried by Ca^{2+}, is known to be 0.1–0.15, while τ_z, the time constant for Na^+ extrusion, is known to be around 0.04 s. Similarly, from measurements of the current/voltage relation of the light-sensitive channel, V^* is known to be 35.7 mV. The remaining unknown parameters (s_1, s_2, E, τ_y, k_4, γ, δ, η, τ_1, and τ_m) are determined by fitting the first-order transfer function of the model to experimental data (typical experimental data are shown in Fig. 19.22). The results of this parameter estimation are given in Table 19.4.

Model predictions and behavior

The most interesting prediction of the model is the shape of the feedback function $g(y)$ that mediates light adaptation. A plot of g is given in Fig. 19.8. In the physiological regime, $g(y)$ is well approximated by the function $A(y)$, where

$$A(y) = 4 + \frac{91}{1 + (y/0.34)^4}. \qquad (19.35)$$

In other words, as $\left[Ca^{2+}\right]$ falls, the rate of cGMP production by guanylate cyclase rises along a sigmoidal curve, with a Hill coefficient of 4. This prediction of the model has been confirmed experimentally (Koch and Stryer, 1988), thus lending quantitative support to the hypothesis that the modulation of guanylate cyclase activity by $\left[Ca^{2+}\right]$ is sufficient to account for light adaptation in turtle cones.
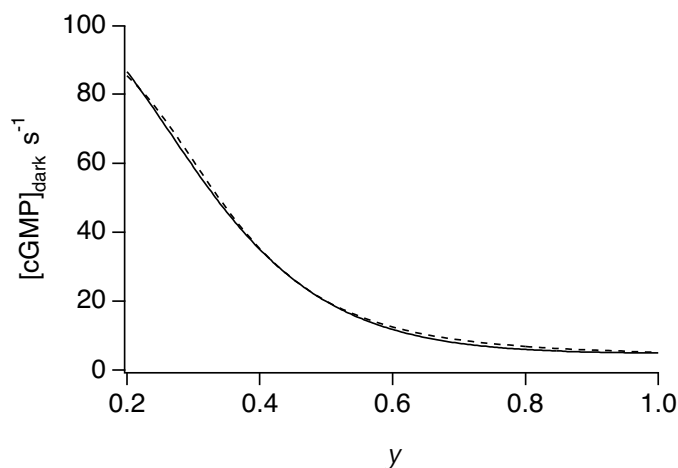
Figure 19.8: Predicted and measured activities of guanylate cyclase as functions of the Ca^{2+} concentration. The solid line denotes $g(y)$ (theoretical prediction), and the dotted line denotes $A(y)$ (experimental measurement). For convenience, the activity of guanylate cyclase is expressed in units of $[cGMP]_{dark}$ per second.

The model exhibits constant contrast sensitivity over a range of lower light levels. As I_0 increases, the contrast sensitivity first increases and then decreases slightly, in agreement with the results of Daly and Normann (1985); the impulse response becomes biphasic; and the time-to-peak decreases as the response speeds up. Further, the intensity–response curves agree well with the Naka–Rushton equation (19.3) and shift to the right and slightly down as I_0 increases (Fig. 19.9), again in good agreement with experimental data. Some of these properties of the model are explored further in Exercise 3.

An unexpected prediction of the model is that [cGMP] does not fall much as the background light level is increased. For example, if the background light level is changed so that the sensitivity decreases by a factor of 1000, [cGMP] decreases by less than a factor of two (see Sneyd and Tranchina, 1989, Fig. 4). This gives a possible explanation for the puzzling observation that even though a decrease in [cGMP] is believed to underlie light adaptation, such decreases are sometimes not experimentally observed (DeVries et al., 1979; Dawis et al., 1988). In other words, the model predicts that even though a decrease in [cGMP] may indeed mediate light adaptation, the actual decrease may be too small to measure reliably.

The model agrees quantitatively with experiment in a number of other ways (discussed in detail by Tranchina et al., 1991), lending further support to the hypothesis that it provides an excellent description of many features of light adaptation. Similar conclusions have been reached by Forti et al. (1989), who modeled phototransduction in newt rods, and Tamura et al. (1991), who modeled adaptation in primate rods. It thus appears that although Ca^{2+} feedback on the activity of guanylate cyclase cannot explain all features of light adaptation in rods and cones (Fain et al., 2001), it is one of the principal mechanisms.
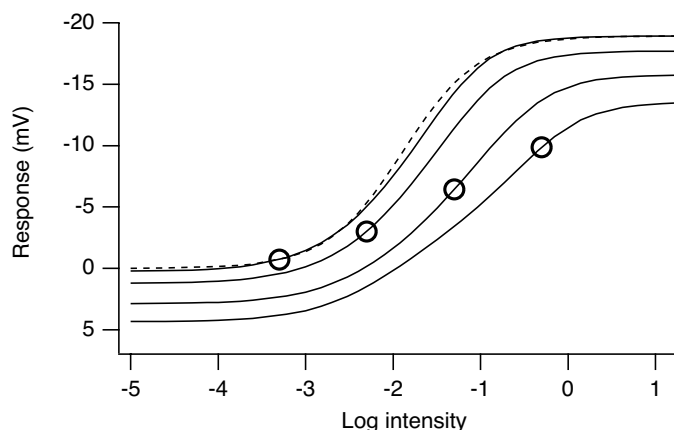
Figure 19.9: Intensity–response curves from the model for adaptation in turtle cones. The dotted line is the Naka–Rushton equation, and the solid lines are the model results. The open symbols denote the steady states for 4 different light levels.

19.3 A Model for Adaptation in Amphibian Rods

The most elegant models of phototransduction in amphibian and vertebrate rods are those of Hamer, Tranchina and their colleagues. Hamer (2000a,b) fitted a modified version of the earlier model of Nikonov et al. (1998) to a set of flash responses from the larval tiger salamander rod. Hamer also attempted to reproduce in a qualitative way a wider array of experimental data, including step responses from newt rods and responses to highly saturating flashes. This model was then extended by Hamer et al. (2003, 2005) to consider the single-photon response.

Hamer's model differs from the above model for adaptation in cones in two principal ways. First, it includes a more detailed description of Ca^{2+} buffering and, second, it models only the photocurrent, not the voltage. This latter feature makes the model simpler in some respects.

The initial cascade is modeled by two reactions only,

$$\frac{dR^*}{dt} = I(t) - \frac{1}{\tau_R}R^*, \tag{19.36}$$

$$\frac{dE^*}{dt} = \nu R^* - \frac{1}{\tau_E}E^*, \tag{19.37}$$

where R^* and E^* denote, respectively, the number of activated rhodopsin and PDE molecules, and as before, $I(t)$ is the light input, and ν, τ_R and τ_E are constants.

Calcium (c) and cGMP (g) concentrations are the only other model variables. The rate of production of cGMP is dependent on c, and is given by an expression similar to (19.35). Also, cGMP is degraded by E^* as well as at some background rate. Thus,

$$\frac{dg}{dt} = \frac{A_{\max}}{1 + (\frac{c}{K_{Ca}})^{n_c}} - (\beta_{dark} + \beta_E E^*)g. \tag{19.38}$$

τ_R	$=$	0.42 s		τ_E	$=$	1.2 s
ν	$=$	$1735\ \mathrm{s}^{-1}$		b_t	$=$	$395\ \mu\mathrm{M}$
γ	$=$	$100\ \mathrm{s}^{-1}$		k_{on}	$=$	$0.17\ \mu\mathrm{M}^{-1}\mathrm{s}^{-1}$
k_{off}	$=$	$2.35\ \mathrm{s}^{-1}$		c_{min}	$=$	$0.005\ \mu\mathrm{M}$
K_c	$=$	$0.219\ \mu\mathrm{M}$		n_c	$=$	2.85
A_{max}	$=$	$4.461\ \mu\mathrm{M\,s}^{-1}$		β_E	$=$	$1.68 \times 10^{-5}\ \mathrm{s}^{-1}$
β_{dark}	$=$	$0.136\ \mathrm{s}^{-1}$		n_g	$=$	2.21
α	$=$	$0.78\ \mu\mathrm{M\,s}^{-1}\,\mathrm{pA}^{-1}$		J_{dark}	$=$	72.3 pA

Table 19.2: Parameters of the model of light adaptation in amphibian rods (Hamer, 2000a).

The Ca^{2+} equations are similar to those discussed in Chapter 7. Calcium enters the cell via a light-sensitive current, is pumped out by membrane ATPases, and is buffered. Thus,

$$\frac{dc}{dt} = \alpha f J_{\mathrm{dark}} - \gamma(c - c_{\mathrm{min}}) - k_{\mathrm{on}}(b_t - b)c + k_{\mathrm{off}}b, \qquad (19.39)$$

$$\frac{db}{dt} = k_{\mathrm{on}}(b_t - b)c - k_{\mathrm{off}}b. \qquad (19.40)$$

Here, J_{dark} is the light-sensitive current in the dark, f is the fraction of open light-sensitive channels, and α is a constant that converts Ca^{2+} current to Ca^{2+} concentration flux. The model of Ca^{2+} pumping is highly simplified, as it is assumed that the pumps remove Ca^{2+} at a linear rate which is zero at c_{min}, while the buffering model is the same as that discussed in Chapter 7, Section 7.4. Hence, b_t is the total concentration of buffer, and b is the concentration of buffer bound to Ca^{2+}.

It remains to specify the form of f, the fraction of open light-sensitive channels. As in the model for adaptation in cones, we assume that f is a power of g, and thus

$$f = \left(\frac{g}{g_{\mathrm{dark}}}\right)^{n_g}, \qquad (19.41)$$

where g_{dark} is the concentration of cGMP in the dark.

The parameter values of the model are given in Table 19.2.

Panels A and D in Fig. 19.10 show the data and the model fit. The model was fit to a set of flash responses from the larval tiger salamander and excellent quantitative agreement was obtained. However, Hamer then proceeded to make a series of more ambitious comparisons wherein the model response was compared to a series of step responses (panels B and E) and a series of highly saturating flash responses (panels C and F). Not all the data are from the same cell type so a direct quantitative fit to all the data is not appropriate, but qualitative comparisons can still be made. Comparison of panels B and E shows that the model, although it captures the initial nose on the step response, fails to capture the details of the declining phase when the step is switched off, with recovery in the model being faster and less oscillatory than the data. Similarly, panels C and F show that the responses to highly saturating flashes are again too fast, although the phenomenon of highly extended responses to bright flashes is clearly apparent.
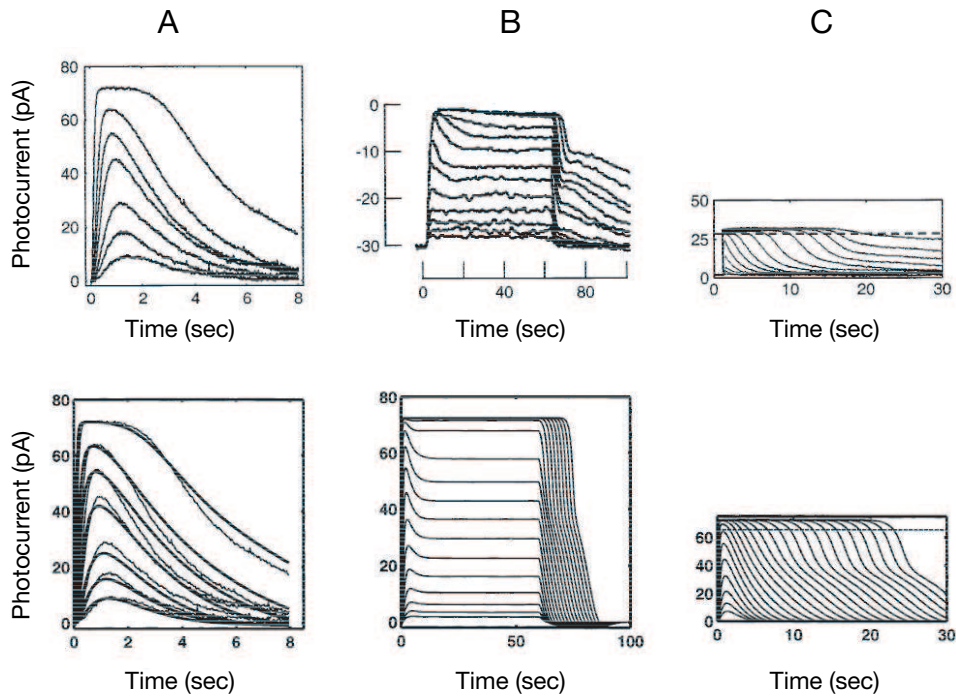
Figure 19.10: Experimental data and model fits from Hamer (2000a). Panels A, B and C show experimental data. A; flash responses from larval tiger salamander rods. B; Step responses from Newt rods (Forti et al., 1989; Torre et al., 1990). C; Highly saturated flash responses from Pepperberg et al. (1992). Panels D, E and F show the corresponding model responses. D; the model parameters were determined by a quantitative fit to the data in panel A. The smooth lines are the model responses, which are superimposed on the experimental data shown in panel A. E and F; the model responses are qualitatively similar to the experimental results, although significant quantitative differences remain. Figure adapted from Figs. 1 and 9 of Hamer (2000a).**Springer: This figure will need permission and massaging. I've taken bits from two different figures. JS**

These disagreements between model and experiment in the bright flash and bright step regime are almost certainly the result of mechanisms that have been omitted from such simple models. For example, nonlinearities in the initial stages of the light response are likely to be important for bright flashes, a feature that is lacking in both models discussed above (but see Exercise 4). In addition, Ca^{2+}-dependent modulation of cGMP production is not the only mechanism for adaptation (Fain et al., 2001). For example, Ca^{2+} is also known to modulate the light-dependent channels directly, with a decrease in $\left[Ca^{2+}\right]$ causing an increase in the affinity of the channels for cGMP. It has also been proposed that Ca^{2+} modulates early steps in the phototransduction cascade, possibly by altering the gain of activation of PDE by rhodopsin in possible combination with modulation of the PDE activity. In a theoretical study, Koutalos et al. (1995) estimated that, in dim lights, about 80% of adaptation in salamander rods is mediated by the action of Ca^{2+} on guanylate cyclase, while at bright lights (6 log units brighter) about 60% is mediated by the action of Ca^{2+} on the activity of PDE. However, whatever the exact details, according to Fain et al. (2001) there is no compelling evidence for adaptation being mediated by any messenger other than Ca^{2+}.

19.3.1   Single-photon responses

One of the most striking features of phototransduction is that not only can a rod respond to a single photon, it does so in a reproducible way that varies little from photon to photon. At first glance this might seem uninteresting, until one realizes that a single photon response is mediated by a single rhodopsin molecule. Since the behavior of a single molecule must, necessarily, be stochastic in nature, how can this produce a reproducible single-photon response? Baylor et al. (1979) were the first to study in detail this question, which has long been considered one of the most puzzling and important problems in photoreceptor physiology.

To consider the problem in slightly more detail, suppose that the decay of an activated rhodopsin molecule is a poisson process, with rate k_0. We are interested in the probability distribution for how long the rhodopsin molecule stays in the activated state, as this determines how many PDE molecules (on average) are activated.

Following the methods described in Chapter 2, Section 2.9.1, we know that if the rhodopsin molecule is activated at time $t = 0$, the probability that it remains activated at time t is given by P_{R^*}, which is the solution of the differential equation

$$\frac{dP_{R^*}}{dt} = -k_0 P_{R^*}. \tag{19.42}$$

where $P_{R^*}(0) = 1$. Thus, $P_{R^*}(t) = e^{-k_0 t}$. It follows that the probability distribution function for the time that the rhodopsin molecule stays activated is $k_0 P_{R^*}(t) = k_0 e^{-k_0 t}$. This *activated time distribution* has mean, μ, and standard deviation, σ, both equal to $1/k_0$ and thus

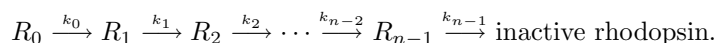$$\frac{\sigma}{\mu} = 1. \tag{19.43}$$

This ratio, called the coefficient of variation, is a non-dimensional measure of the spread of the distribution.

Thus, a single inactivation step results in an activation lifetime that is highly variable, much more variable than is seen in experimental data. However, if rhodopsin is inactivated in a series of phosphorylation steps the variation is significantly decreased (Baylor et al., 1979; Rieke and Baylor, 1998a,b; Whitlock and Lamb, 1999; Field and Rieke, 2002; Hamer et al., 2003).

To see this, suppose that upon light activation, rhodopsin starts in state R_0, where R_i denotes rhodopsin that has been phosphorylated i times. Suppose further that each state R_i activates PDE at the same rate. This second assumption is not necessary, but simplifies the analysis considerably. Finally, assume that there is a maximum of n phosphorylation sites and the rhodopsin is inactivated when all the sites are phosphorylated.

The corresponding Markov model is

$$R_0 \xrightarrow{k_0} R_1 \xrightarrow{k_1} R_2 \xrightarrow{k_2} \cdots \xrightarrow{k_{n-2}} R_{n-1} \xrightarrow{k_{n-1}} \text{inactive rhodopsin.}$$

The total time that rhodopsin is active is the time it takes to get from state R_0 to the inactive state R_n. From Chapter 2, Section 2.9.1 we know that the probability distribution function for the time of inactivation is $\frac{dP_n}{dt} = k_{n-1}P_{n-1}$, where $P_k(t)$ is the probability of being in state k at time t, and is found as the solution of

$$\frac{dP_0}{dt} = -k_0 P_0, \tag{19.44}$$

$$\frac{dP_1}{dt} = k_0 P_0 - k_1 P_1, \tag{19.45}$$

$$\vdots \tag{19.46}$$

$$\frac{dP_{n-1}}{dt} = k_{n-2}P_{n-2} - k_{n-1}P_{n-1}. \tag{19.47}$$

with $P_0(0) = 1$, and $P_k(0) = 0$ for $k > 0$. In other words, P_{n-1} is the impulse response of an $n - 1$-stage linear filter (Appendix 19.8). For any n this system is easily solved using Fourier transforms (or any other method suitable for linear systems), and the mean and standard deviation calculated. For example, when $n = 3$, the distribution of the activated time has coefficient of variation

$$\frac{\sigma}{\mu} = \frac{\sqrt{k_2^2 k_1^2 + k_0^2 k_1^2 + k_0^2 k_2^2}}{k_2 k_1 + k_1 k_0 + k_2 k_0}, \tag{19.48}$$

which is less than one, since all the rate constants are positive. In particular, if the reaction sites are independent so that $k_0 = 3k_2$, $k_1 = 2k_2$, then $\frac{\sigma}{\mu} = \frac{7}{11}$.

In the special case that all the k_i's are equal, inactivation is by an n-step Poisson process, and the coefficient of variation is given by the simple formula

$$\frac{\sigma}{\mu} = \frac{1}{\sqrt{n}}. \tag{19.49}$$

Clearly, as the number of phosphorylation steps increases, the coefficient of variation decreases. Essentially, stochastic variation in any one of the steps is partially canceled out by variation in another of the steps, leading to lower variability over

the entire length of the cascade. **James, I don't agree with this last sentence, or at least I don't understand it. The process is an n step Poisson process. Both the variance and the mean for a Poisson process grow like n, the number of steps. So the variance is growing, not decreasing. I don't know what one means by the variation of one step; how is it defined?. To say that variation in one step is canceled out by variation in another step is ill-defined, or perhaps blatantly false. The easiest fix here is to eliminate the sentence, but if you still want some kind of heuristic explanation, that will require a bit more thought.**

A unified model

Although multiple phosphorylation steps provides a plausible answer to how a single photon can generate a reproducible response, to understand how phototransduction works at all light levels it is necessary to construct a single model that can reproduce not only the single-photon response, but also the responses to flashes and steps of light, both bright and dim. This constitutes a severe set of tests against which to validate any model of phototransduction, and it was not until 2005 that such a model appeared (Hamer et al., 2005).

19.4   Lateral Inhibition

Thus far we have considered only the responses of individual photoreceptors. However, spatial interactions in the retina also play an important role in regulation of the light response. Some of the earliest studies of this were done in the retina of the horseshoe crab *Limulus polyphemus*. As a side issue, it is interesting to note that the photoreceptors of the horseshoe crab (and other invertebrates) operate along quite different lines than those of vertebrates (Dorlöchter and Stieve, 1997). In fact, the mechanisms underlying the photoresponse in invertebrates have a great deal in common with the mechanisms underlying generic Ca^{2+} dynamics in other cell types, as discussed in detail in Chapter 7. However, despite these intriguing similarities we do not discuss invertebrate phototransduction in any further detail.

In 1967 Haldan Hartline won (one third of) the Nobel prize in Physiology and Medicine for his work on the retina of the horseshoe crab. Together with his colleague, Floyd Ratliff, he published in the 1950s a series of papers that showed how lateral inhibition played an important role in the horseshoe crab retina (Hartline et al., 1956; Hartline and Ratliff, 1957, 1958; Ratliff and Hartline, 1959).

The *Limulus* eye is a compound eye containing about 1000 ommatidia. Nerve fibers from each ommatidium come together to form the optic nerve, while lateral interconnections arise from a layer of nerve fibers directly behind the ommatidia. Two classic experiments are shown in Fig. 19.11. In A are shown the results of applying a light step (or ramp in the lower panel) to a single receptor. When lateral inhibition is removed (by the simple expedient of shining light only ever on a single receptor) then the receptor responds in a step-like fashion (open triangles). However, if the light stimulus is applied to the entire eye, thus allowing lateral inhibition, the receptor responds by accentuating the edges of the step or ramp (open
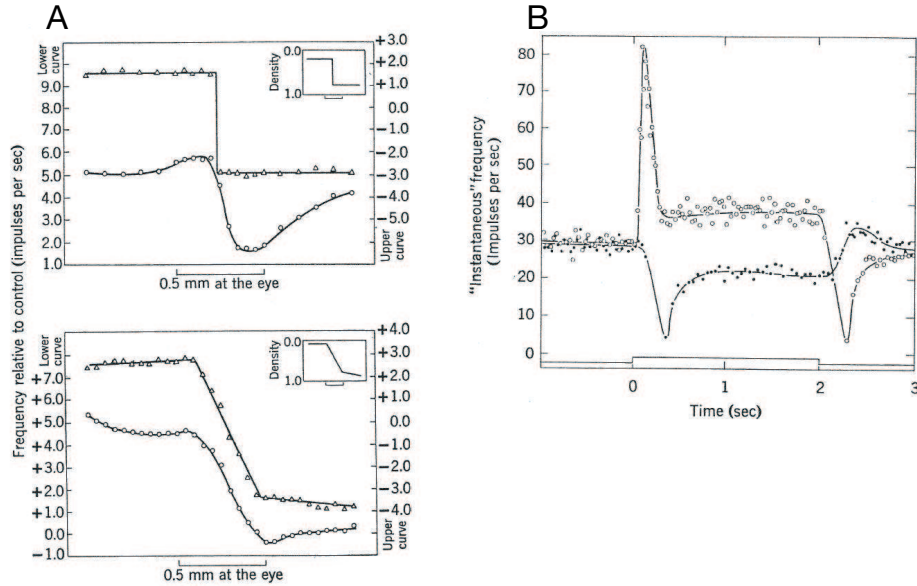
Figure 19.11: Lateral inhibition in the *Limulus* eye. A: the response to a step or a ramp. The open triangles show the response of a single receptor as a light step (or ramp) is moved across it, in conditions that eliminate lateral inhibition (i.e., only a single receptor was illuminated). The open circles correspond to the same experiment with lateral inhibition (i.e., when the step or ramp was applied to the entire eye and moved across the receptor). B: simultaneous excitatory and inhibitory responses in neighboring receptors. One receptor (filled circles) was illuminated uniformly, while the other (open circles) was stimulated with light as indicated in the trace along the bottom of the graph. The stimulated receptor responds with a transient peak followed by adaptation and a return to a lower plateau (as in the vertebrate photoreceptors discussed above). The neighboring receptor, which is not directly stimulated by the light, is inhibited by the response of the first receptor. Reproduced from Ratliff, 1961. **Springer: This figure will need permission**

circles). The temporal development of inhibition is shown in panel B. In a manner reminiscent of the responses of vertebrate photoreceptors (as is discussed above), receptors respond to a light stimulus with a transient peak followed by adaptation to a lower steady level. When the light is removed the behavior is reversed, with a transient dip followed by recovery. A neighboring non-illuminated receptor (filled circles) responds in the opposite way as it is inhibited by the stimulated receptor.

To explain their results, Hartline and Ratliff formulated the Hartline-Ratliff equations which describe the steady response of a receptor subject to lateral inhibition. If r_p is the response of the pth receptor and e_p is the excitation applied to the pth receptor, then

$$r_p = e_p - \sum_{j=1}^{n} K_{p,j}(r_j - r_{p,j}^0), \tag{19.50}$$

where $K_{p,j}$ is the inhibitory coupling coefficient from the jth receptor to the pth receptor, and $r_{p,j}^0$ is the threshold below which the response of receptor j cannot inhibit receptor p. $K_{p,j}$ decreases with distance from cell p, while r^0 increases with distance. Thus the decline of inhibition with distance is built into the model.

Although there have been a number of detailed studies of the Hartline-Ratliff equations and the *Limulus* eye (Knight et al., 1970; Hartline and Knight, 1974; Ratliff et al., 1974; Brodie et al., 1978a,b; Grzywacz et al., 1992), we do not discuss them here. Instead we discuss a simpler version of the model due to Peskin (1976).

19.4.1   A Simple Model of Lateral Inhibition

We suppose that E is the excitation of a receptor by light and that I is the inhibition of the receptor from its neighbors. The photoreceptor response is $R = E - I$. A light stimulus L causes an excitation E in the receptor and E decays with time constant τ. The response of the receptor R provides an input into a layer of inhibitory cells, which are laterally connected, and so the inhibition spreads laterally by diffusion and decays with time constant 1. The model equations are

$$\tau \frac{\partial E}{\partial t} = L - E, \tag{19.51}$$

$$\frac{\partial I}{\partial t} = \nabla^2 I - I + \lambda R, \tag{19.52}$$

$$R = E - I. \tag{19.53}$$

Space-independent behavior

If the light stimulus is spatially uniform, then spatial dependence can be ignored, and the model equations reduce to the ordinary differential equations

$$\tau \frac{dE}{dt} = L - E, \tag{19.54}$$

$$\frac{dI}{dt} + (\lambda + 1)I = \lambda E. \tag{19.55}$$

If L is a unit step applied at time $t = 0$, then the response at subsequent times is

$$R \;\; = \;\; E - I \tag{19.56}$$

$$= \;\; \frac{1}{\lambda + 1} - \frac{k - 1}{k - \lambda - 1} e^{-kt} + \frac{\lambda k}{(k - \lambda - 1)(\lambda + 1)} e^{-(\lambda+1)t}, \tag{19.57}$$

where $k = 1/\tau$. R is graphed in Fig. 19.12A, from where it can be seen that the response is an initial peak followed by a decay to a plateau.

Time-independent behavior

If the input is steady, so that time derivatives vanish, then $E = L$ and

$$\nabla^2 I = (\lambda + 1)I - \lambda L. \tag{19.58}$$

Suppose there is an edge in the pattern of light, represented by

$$L(x, y) = \left\{ \begin{array}{ll} 1, & x > 0, \\ 0, & x < 0. \end{array} \right. \tag{19.59}$$

Then the solution for I is

$$I = \left\{ \begin{array}{ll} \frac{\lambda}{\lambda+1}\left(1 - \frac{1}{2}e^{-x\sqrt{\lambda+1}}\right), & x > 0, \\ \frac{\lambda}{\lambda+1}\frac{1}{2}e^{x\sqrt{\lambda+1}}, & x < 0, \end{array} \right. \tag{19.60}$$

where I and dI/dx are required to be continuous at $x = 0$. However, since $E = L$, $R = E - I$ is discontinuous at $x = 0$. Graphs of E and $R = E - I$ are shown in Fig. 19.12B. R exhibits Mach bands at the edge of the light stimulus.

19.4.2 Photoreceptor and Horizontal Cell Interactions

Lateral inhibition in the vertebrate retina results from different processes than in the invertebrate. In the vertebrate retina photoreceptors and horizontal cells form layers of cells through which their potential can spread laterally. The output from the photoreceptors is directed toward the horizontal cells, but the response of the horizontal cells also influences the photoreceptors, forming a feedback loop with spatial interactions. A detailed model of receptor/horizontal cell interactions was constructed by Krausz and Naka (1980), and the model parameters were determined by fitting to experimental data from the catfish retina. The model is depicted in Fig. 19.13.

In this model, receptor and horizontal cells are assumed to form continuous sheets, within which voltage spreads continuously. The coupling coefficient for voltage spread in the sheet of receptors differs from that in the horizontal cell sheet. The receptors feed forward to the horizontal cells, with transfer function $\hat{A}$, and the horizontal cells feed back to the receptors with transfer function $\hat{k}$. The receptor response is the excitation due to light minus that due to horizontal cell feedback.

We first consider the model where the voltage spreads laterally in the horizontal cell layer, but not in the photoreceptor layer. To specify this model we must first
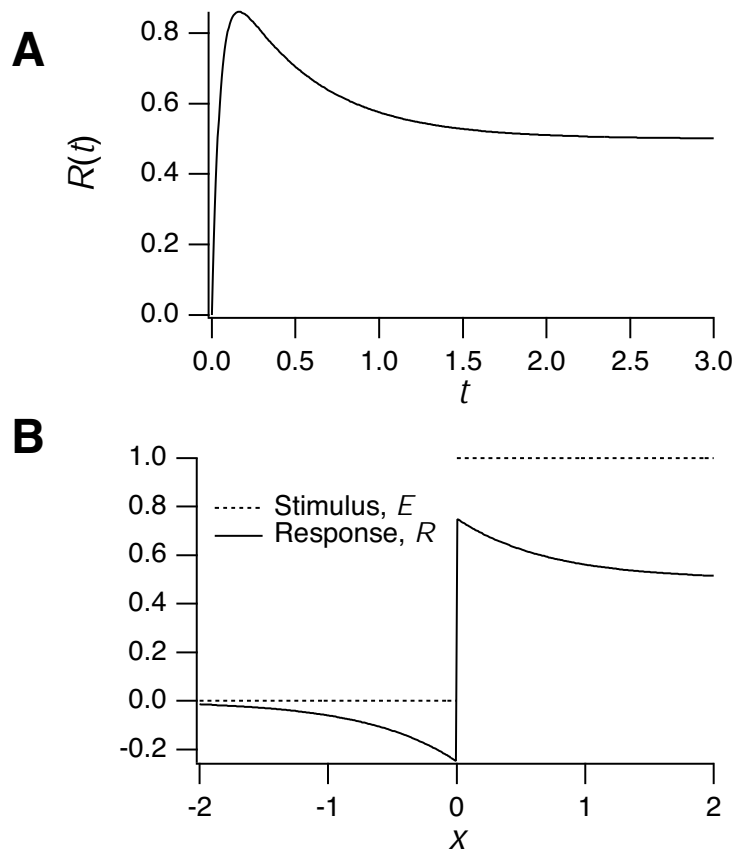
Figure 19.12: Solutions of the qualitative model for lateral inhibition in the retina, calculated with the parameters $\lambda = 1$, $k = 20$. A: The space-independent response. B: The steady response to a band of light extending from $x = 0$ to $x = \infty$.
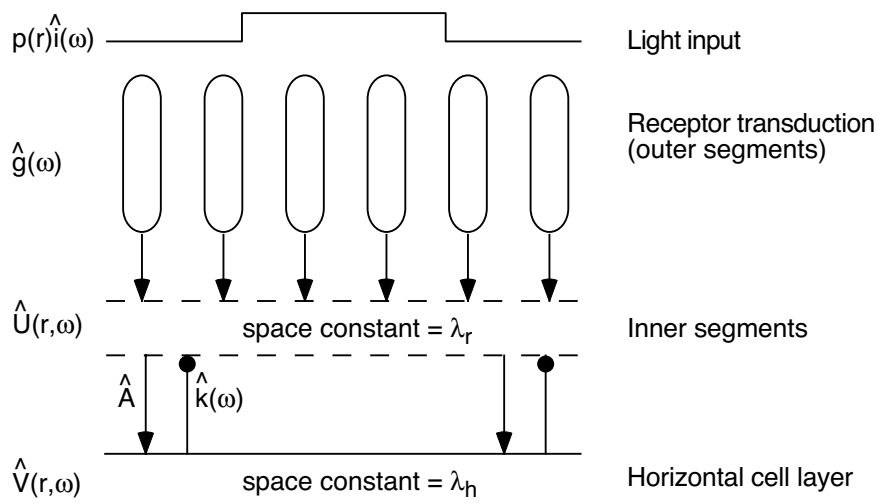
Figure 19.13: Schematic diagram of the lateral inhibition model of Krausz and Naka. (Adapted from Krausz and Naka, 1980.)

determine how voltage spreads within a cell layer. The primary assumption is that the horizontal cell layer is effectively a continuous two-dimensional sheet of cytoplasm, and spread of current within this layer can be modeled by the passive cable equation (Chapter 4), with a source term describing the current input from the photoreceptor layer. If the variations of light around the mean are small it is reasonable to assume that the ionic currents are passive and that the governing equation is linear. Thus, from (8.12) we have

$$\tau_h \frac{\partial V}{\partial t} + V = \lambda_h^2 \nabla^2 V + R_h I_{\text{ph}}, \tag{19.61}$$

where τ_h is the membrane time constant, λ_h is the membrane space constant, R_h is the membrane resistivity, and I_{ph} is the current input from the photoreceptor layer.

To simplify the model, we assume that the light input, and all subsequent responses, are radially symmetric, functions only of the distance from the center of the stimulus. We suppose that the light input is $Ii(t)p(r)$, i.e., modulated temporally by $i(t)$ and spatially by $p(r)$. We let $\hat{U}(r, \omega)$ denote the Fourier transform of receptor potential at position r, and let $\hat{g}(\omega)$ denote the transfer function of the linear stages of receptor phototransduction. Then, in the frequency domain we have

$$\hat{U} = Ip(r)\hat{g}(\omega)\hat{i}(\omega) - \hat{k}(\omega)\hat{V}. \tag{19.62}$$

U is influenced by two terms, the first due to excitation by light, and the second due to inhibitory feedback from horizontal cells, with transfer function $\hat{k}(\omega)$. Finally, taking the feedforward transfer function to be $\hat{A}(\omega)$, and taking $V = \hat{V}e^{i\omega t}$, we obtain

$$\lambda_h^2 \nabla^2 \hat{V} - (1 + i\omega\tau_h)\hat{V} = -\hat{A}(\omega)\hat{U}. \tag{19.63}$$

Although we expect the qualitative behavior of the Krausz–Naka model to be similar to that of Peskin's model, the goal of this model is to obtain quantitative agreement with experiment by fitting it directly to data.

We simplify (19.62) and (19.63) by a change of variables. We set

$$\Phi \;=\; \frac{\hat{U}}{I\hat{g}(\omega)\hat{i}(\omega)}, \tag{19.64}$$

$$\Psi \;=\; \frac{\hat{V}}{I\hat{g}(\omega)\hat{i}(\omega)\hat{A}(\omega)}, \tag{19.65}$$

and from (19.63) find that

$$\nabla^2 \Psi - \frac{1}{\alpha^2(\omega)}\Psi = -\frac{p(r)}{\lambda_h^2}, \tag{19.66}$$

where

$$\alpha^2(\omega) = \frac{\lambda_h^2}{1 + i\omega\tau_h + \hat{A}(\omega)\hat{k}(\omega)}. \tag{19.67}$$

It is left as an exercise (Exercise 10) to show that the solution of (19.66), assuming an infinite domain, is

$$\Psi = \frac{1}{\lambda_h^2}\int_0^\infty p(s)G(r,s)\,s\,ds, \tag{19.68}$$

where G, the fundamental solution, is given by

$$G(r,s) = \left\{ \begin{array}{ll} I_0(r/\alpha)K_0(s/\alpha), & r < s, \\ K_0(r/\alpha)I_0(s/\alpha), & r > s. \end{array} \right. \tag{19.69}$$

Here I_0 and K_0 are modified Bessel functions of the first and second kind of order zero. (Unfortunately, I_0 is standard notation for the modified Bessel function of the first kind, but it should not be confused with the background light level.) Of particular interest is the case of a circular spot of light of radius R,

$$p(s) = \left\{ \begin{array}{ll} 1, & s < R, \\ 0 & s > R. \end{array} \right. \tag{19.70}$$

In this case, we can use the identities $\frac{d}{dz}(zK_1(z)) = zK_0(z)$ and $\frac{d}{dz}(zI_1(z)) = zI_0(z)$ to evaluate the integral (19.68) with the result that

$$\Psi(r,\omega) = \frac{1}{\lambda_h^2}F(r,R,\omega), \tag{19.71}$$

where

$$F(r,R,\omega) = \left\{ \begin{array}{ll} \alpha^2[1 - (R/\alpha)I_0(r/\alpha)K_1(R/\alpha)], & r < R, \\ \alpha R I_1(R/\alpha)K_0(r/\alpha), & r > R. \end{array} \right. \tag{19.72}$$

λ_h	$=$	0.267 mm
τ_h	$=$	0 ms
$\hat{A}$	$=$	3.77
τ	$=$	24.8 ms
t_0	$=$	0.022 ms

Table 19.3: Parameters of the Krausz–Naka model for catfish retinal neurons. These parameters correspond to the model in which there is no coupling between photoreceptors.

Fitting to data

Krausz and Naka determined the model parameters by fitting the ratio of the uniform field response to the spot response to experimental data (Fig. 22.14). The field response (i.e., taking $R \to \infty$) can be calculated from (19.66) by setting $p(r) \equiv 1$, in which case the constant solution for Ψ is easily seen to be $\Psi(r, \omega)_{\text{field}} = \alpha^2/\lambda_h^2$. Thus,

$$\frac{\hat{V}_{\text{spot}}}{\hat{V}_{\text{field}}} = \frac{\Psi(r, \omega)_{\text{spot}}}{\Psi(r, \omega)_{\text{field}}} = \frac{1}{\alpha^2} F(r, R, \omega). \tag{19.73}$$

For fixed values of r and R, $\alpha(\omega)$ can be determined to give good agreement between model and experiment. Note that by taking response ratios, dependence on the feedforward steps within each photoreceptor is eliminated. Thus, attention is focused on the interactions between the horizontal cells and the photoreceptors. However, the model cannot distinguish between $\hat{A}$ and $\hat{k}$, since only the product of these terms appear. So, for simplicity, it is assumed that $\hat{A}$ is a constant gain, with no frequency dependence, and that $\hat{k}$ has unity gain. Values for $\hat{k}(\omega)$ are obtained at each frequency, and then $k(t)$ determined from an inverse Fourier transform. The result is well approximated by

$$k(t) = \frac{3}{\tau} e^{-(t-t_0)/\tau} [1 - e^{-(t-t_0)/\tau}]^2, \tag{19.74}$$

a sigmoindal-shaped rising curve followed by exponential decay. The parameters t_0 and τ are, respectively, the feedback delay and the feedback time constant. The function $k(t)$ has an important physiological interpretation, as it describes the feedback from horizontal cells to photoreceptors; in response to a delta function input from the horizontal cells, the photoreceptor response is given by $-k(t)$. Parameters resulting from the fit are given in Table 19.3. The membrane time constant of the horizontal cells was found to be small in all cases, and so was set to zero. Hence, the potential of the horizontal cell layer responds essentially instantaneously to a stimulus. However, the time constant for the response of the photoreceptor layer to horizontal cell feedback is significant.

Predicting the response to a moving grating

As a test of the model, Krausz and Naka calculated the response to a 1-dimensional moving grating, and compared the result to experimental data. A moving grating
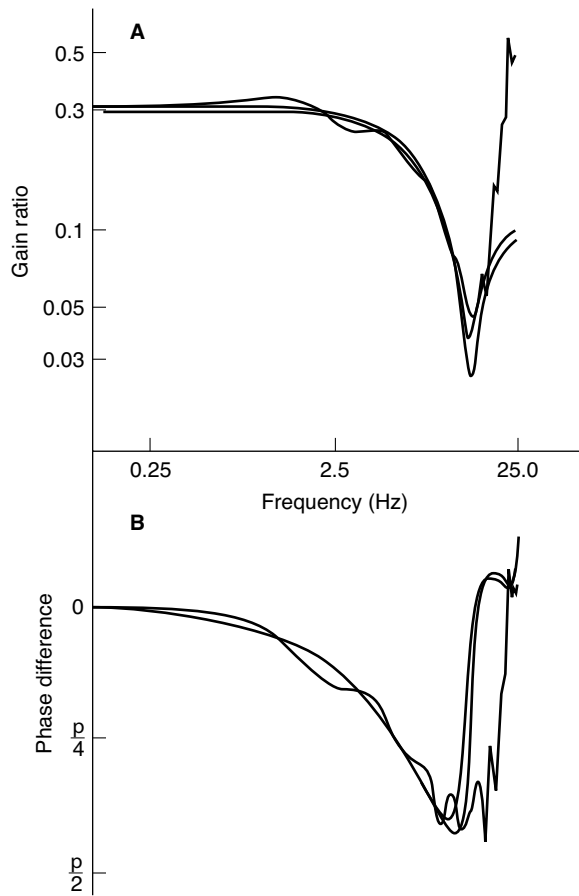
Figure 19.14: Spot-to-field transfer function measured in the catfish retina. The wavy traces are the experimental results, and the two smooth curves are results from the model, using two slightly different parameter sets, one of which is given in Table 19.3. (Krausz and Naka, 1980, Fig. 4.)

provides a light stimulus of the form $l = l(t - x/c)$, where c is the speed of the grating. We look for solutions of the form $V = V(\xi)$, where $\xi = t - x/c$, in which case the differential equation (19.61) becomes

$$\frac{\lambda_h^2}{c^2} V'' - \tau_h V' - V = -R_h I_{\mathrm{ph}}, \tag{19.75}$$

where a prime denotes differentiation with respect to ξ. Taking Fourier transforms with respect to ξ, and recalling that in the frequency domain the input to the horizontal cell layer is given by $\hat{A}\hat{U}$, we find that

$$(1 + i\omega\tau_h)\hat{V} = -\frac{\omega^2 \lambda_h^2}{c^2}\hat{V} + \hat{A}\hat{U}. \tag{19.76}$$

Assuming that the light input is given by $Ie^{i\omega\xi}$, then $\hat{U}$ satisfies

$$\hat{U} = I\hat{g}(\omega) - \hat{k}(\omega)\hat{V}. \tag{19.77}$$

Hence,

$$
\begin{aligned}
\Psi(\omega) &= \frac{\hat{V}}{\bar{I}\hat{g}(\omega)\hat{A}} \\
&= \frac{1}{1 + i\omega\tau_h + \hat{A}\hat{k} + \omega^2\lambda_h^2/c^2} \\
&= \left(\frac{\alpha^2}{\lambda_h^2}\right)\frac{c^2}{c^2 + \omega^2\alpha^2}.
\end{aligned} \tag{19.78}
$$

Krausz and Naka showed that the model predictions for the rectilinear stimulus predict experimental results accurately, confirming that the model provides a general quantitative description of the horizontal cell response that is not limited to the data upon which it was based.

Receptor coupling

Receptors are electrically coupled by gap junctions, and the potential spreads through the receptor layer in a continuous fashion, as it does in the horizontal cell layer, but with a different space constant, λ_r (Lamb and Simon, 1977; Detwiler and Hodgkin, 1979). To incorporate receptor coupling, we need only add spatial coupling for the receptor layer. In the frequency domain, we have

$$
\begin{aligned}
\lambda_r^2 \nabla^2 \Phi - (1 + i\omega\tau_r)\Phi - \hat{k}(\omega)\hat{A}(\omega)\Psi &= -p(r), \tag{19.79} \\
\lambda_h^2 \nabla^2 \Psi - (1 + i\omega\tau_h)\Psi &= -\Phi, \tag{19.80}
\end{aligned}
$$

where τ_r is the membrane time constant for the receptor cell layer. Writing $q_r = (1 + i\omega\tau_r)/\lambda_r^2$ and $q_h = (1 + i\omega\tau_h)/\lambda_h^2$ and substituting (19.80) into (19.79) gives

$$\left(\nabla^2 - \frac{1}{\gamma^2}\right)\left(\nabla^2 - \frac{1}{\delta^2}\right)\Psi = \frac{p(r)}{\lambda_h^2 \lambda_r^2}, \tag{19.81}$$

where $1/\gamma^2$ and $1/\delta^2$ are defined by

$$\frac{1}{\gamma^2} + \frac{1}{\delta^2} = q_r + q_h, \tag{19.82}$$

$$\frac{1}{\gamma^2\delta^2} = q_r q_h + \frac{\hat{A}(\omega)\hat{k}(\omega)}{\lambda_h^2 \lambda_r^2}. \tag{19.83}$$

Note that γ and δ are analogous to α in (19.66).

Now we define $\chi(r, \gamma)$ to satisfy

$$\left(\nabla^2 - \frac{1}{\gamma^2}\right)\chi(r, \gamma) = -p(r). \tag{19.84}$$

Since the operator $\left(\nabla^2 - \frac{1}{\gamma^2}\right)$ has a unique inverse, we use $\chi(r, \gamma)$ to eliminate p in (19.81) and find that

$$\left(\nabla^2 - \frac{1}{\delta^2}\right)\Psi = \frac{-\chi(r, \gamma)}{\lambda_h^2 \lambda_r^2}. \tag{19.85}$$

Similarly, by symmetry

$$\left(\nabla^2 - \frac{1}{\gamma^2}\right)\Psi = \frac{-\chi(r, \delta)}{\lambda_h^2 \lambda_r^2}. \tag{19.86}$$

Subtracting these two equations, we obtain

$$\Psi(r, \omega) = \frac{1}{\lambda_h^2 \lambda_r^2}\left(\frac{\gamma^2\delta^2}{\gamma^2 - \delta^2}\right)[\chi(r, \gamma) - \chi(r, \delta)]. \tag{19.87}$$

Solving (19.85) for $\nabla^2\Psi$, substituting into (19.80), and using the expression for Ψ then gives

$$\Phi(r, \omega) = \frac{1}{\lambda_r^2}\left(\frac{\gamma^2\delta^2}{\gamma^2 - \delta^2}\right)\left[\left(q_h - \frac{1}{\gamma^2}\right)\chi(r, \gamma) - \left(q_h - \frac{1}{\delta^2}\right)\chi(r, \delta)\right]. \tag{19.88}$$

Since (19.84) for χ is of the same form as (19.66) for Ψ, its solution takes the same form. Thus, (19.87) and (19.88) give an explicit solution to the general problem of electrical flow in two coupled cell layers connected by reciprocal pathways.

19.5 Detection of Motion and Directional Selectivity

It seems intuitively obvious that the detection of motion is one of the most important jobs of the visual system of an animal, either prey and predator, and it is believed to be one of the oldest features of the visual system (Nakayama, 1985; a detailed review of motion detection is given by Clifford and Ibbotson, 2003). It is known that, in some vertebrates at least, directional selectivity arises in the retina itself, with directionally sensitive ganglion cells (often called DSGCs) responding preferentially to motion in a certain direction (Barlow and Levick, 1965; Taylor et al., 2000; Vaney
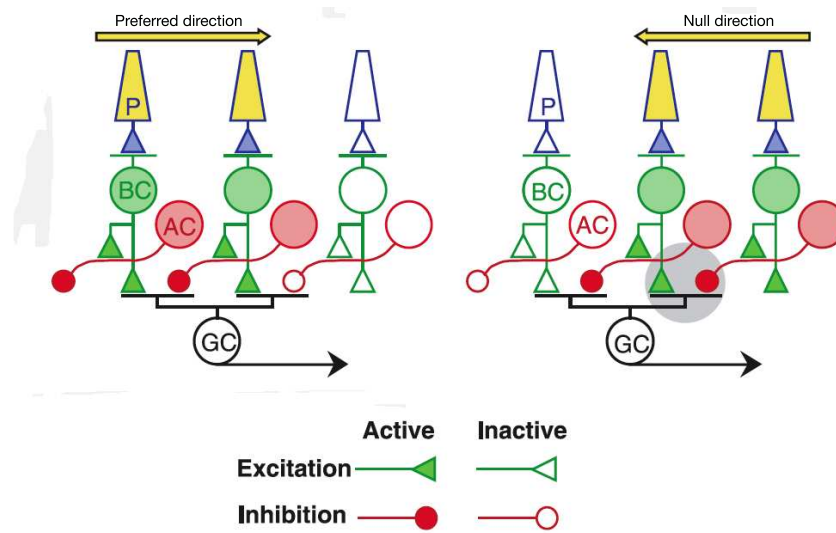
Figure 19.15: Proposed mechanism for directional selective ganglion cells. P — photoreceptor; BC — bipolar cell; AC — amacrine cell. When motion is in the null direction the inhibitory and excitatory inputs at the ganglion cell cancel out (as shown by the dashed box), giving a smaller response. Thus, directional selectivity arises from the asymmetry of the connections from amacrine cells to ganglion cells. Adapted from Taylor et al., 2000, Fig. 1.
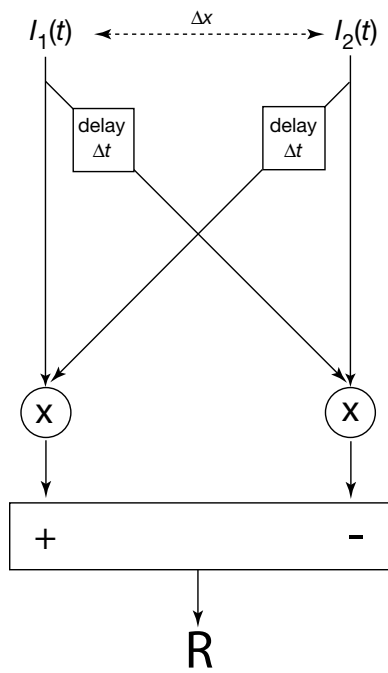
Figure 19.16: Schematic diagram of a simple Reichardt detector. Two spatially separated inputs are delayed, cross-multiplied and subtracted to get a response, R, whose sign depends on the direction of motion.

et al., 2001; Vaney and Taylor, 2002). A qualitative model for how such direction selectivity arises is sketched in Fig. 19.15. According to this scheme, directional selectivity arises because of the asymmetry of the connections between amacrine and ganglion cells. When motion is in the preferred direction the inhibitory effects of the amacrine cell layer are all in the reverse direction, and thus act too late to inhibit the ganglion cell responses. However, when motion is in the null direction the amacrine cells feed forward making the excitation and inhibition happen at the same time at the same place, thus decreasing the ganglion cell response.

The earliest quantitative model of motion detection was that of Hassenstein and Reichardt (1957; Reichardt, 1961; Borst and Egelhaaf, 1989; an introduction for the non-expert is given by Borst 2000), a model that was based on experimental work on the beetle *Chlorophanus* and that has become a classic in the field. A schematic diagram of a simple Reichardt detector is shown in Fig. 19.16. Two photoreceptors (inputs I_1 and I_2), separated by a distance Δx, feed forward to the output stage (a ganglion cell, for example). Input I_1 is delayed by Δt and multiplied by I_2, while the mirror image procedure is applied to I_2. Finally, the results are subtracted to get the response, R.

For ease of notation, let $\Delta x = h$ and $\Delta t = k$. Then, if the light stimulus is $s(x, t)$, it follows that

$$
\begin{aligned}
R(t) &= I_1(t)I_2(t-k) - I_1(t-k)I_2(t) & (19.89)\\
&= s(0,t)s(h,t-k) - s(0,t-k)s(h,t), & (19.90)
\end{aligned}
$$

where for convenience we have assumed that the first photoreceptor, I_1, is at $x = 0$.

This motion detector has two important properties. First, when the response is integrated over a sufficiently long time, the steady components of I_1 and I_2 have no effect; only those portions of the input that correspond to a moving signal are detected. Although this is not true for an arbitrary input, it is true for realistic light stimuli. Second, when the velocity of the stimulus is reversed, the integral of the response changes sign. Thus, the sign of the integral of R determines the direction of motion.

Both these properties can be simply illustrated by using a stimulus of the form $s(x, t) = s_0 + s_1(x - ct)$, where c is the speed at which the stimulus is moved across the two receptors. Two basic forms for s_1 cover almost the entire range of physiological stimuli; periodic, with mean zero, or with compact support (i.e., non-zero only on some finite region). An example of the first case is a flicker stimulus presented to the eye, while an example of the second case is a moving bar. We consider only these two cases. With this expression for s_1 we get

$$
\begin{aligned}
R(t) &= s_0 \left[s_1(h - ct + ck) - s_1(h - ct) + s_1(-ct) - s_1(-ct + ck) \right] \\
&\quad + s_1(-ct)s_1(h - ct + ck) - s_1(-ct + ck)s_1(h - ct). \quad (19.91)
\end{aligned}
$$

When this is integrated from $t = -\infty$ to ∞ all the terms in the square brackets cancel out (as s_1 either has mean zero, or compact support, by assumption). Thus

$$
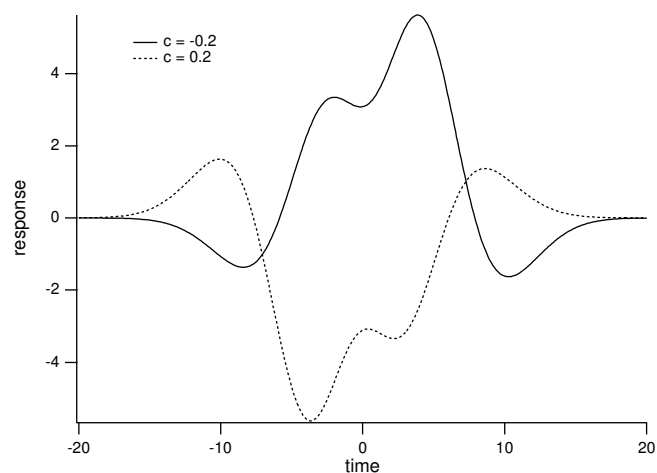\int R(t)\, dt = \int s_1(-ct)s_1(h - ct + ck) - s_1(-ct + ck)s_1(h - ct)\, dt. \quad (19.92)
$$

Figure 19.17: Response of a simple Reichardt detector to the stimulus $s(x,t) = 10[1 + e^{-(x-ct-1)^2} + 0.8e^{-(x-ct+0.2)^2}]$. (Calculated with the values $\Delta x = 0.5$, $\Delta t = 0.2$). When c changes sign, the response is close to a reflection through the origin of the first response. In fact, it is not an exact reflection, but the integrals of the two responses are of the same amplitude with opposite sign.

Now, denote the response for stimulus speed c, as $R_c(t)$. Since

$$\int R_{-c}(-t)\,dt = \int s_1(-ct)s_1(h-ct-ck) - s_1(-ct-ck)s_1(h-ct)\,dt = -\int R_c(t) \tag{19.93}$$

(use the change of variables $\tau = t - k$), it follows that

$$\int R_c(t) + R_{-c}(-t)\,dt = 0. \tag{19.94}$$

Thus, if the velocity of the stimulus is reversed, the response is close to a reflection through the origin of the original response, having exactly the same integral, of opposite sign. We illustrate this in Fig. 19.17.

19.6   Receptive Fields

The output stage of the retina is the layer of ganglion cells, which extend through the optic nerve to the lateral geniculate nucleus, from there transmitting signals to the visual cortex. Each ganglion cell responds by a series of action potentials, with the information encoded in the frequency and duration of the wave train. Thus, ganglion cells transmit a digital signal typical of neurons. The input stage of ganglion cells is highly organized. Each ganglion cell responds only to light in a well-defined part of the retina, called the *receptive field* of the cell, and these receptive fields are organized into two concentric, mutually antagonistic regions,
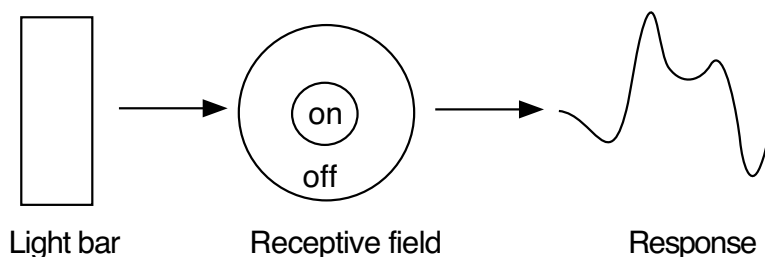
Figure 19.18: Diagram of the center-surround arrangement of the receptive field of an on-center retinal ganglion cell, and its response to a wide bar moving across the receptive field. (Adapted from Rodieck, 1965, Fig. 1.)

the center and the surround (Fig. 19.18). Although in reality the story is not quite so simple (see Troy and Shou, 2002, for an excellent modern review) we discuss only simple receptive fields of this type. This center-surround organization was discovered by Kuffler (1953, 1973) and is considered one of the landmark discoveries in visual science. Interestingly, one of Kuffler's early colleagues was FitzHugh, of later FitzHugh-Nagumo fame (Barlow, FitzHugh and Kuffler, 1957).

The center can be either excitatory (*on-center*) or inhibitory (*off-center*). A white figure moved across the receptive field of an on-center cell gives the same response as a black figure moved across the receptive field of an off-center cell. A typical response curve for a bar moving across the receptive field is shown in Fig. 19.18. Note that the ganglion cell has a large response to the edges of the bar, but responds much less to the maintained stimulus in the middle of the bar. This is reminiscent of the Mach bands seen in the Krausz–Naka model. There are different types of on/off responses for ganglion cells. Some respond to both "on" and "off," while others respond only to one or the other. Some ganglion cells are directionally dependent, responding to a stimulus only if it enters the receptive field from a particular direction. Other ganglion cells are color dependent.

The different responses of the on-center and off-center ganglion cells are the result of their connections to different types of bipolar cells. On-center and off-center ganglion cells synapse to bipolar cells that respond, respectively, to light increments and decrements. These different bipolar cell responses are due, in turn, to their different responses to glutamate released at the synapse with the photoreceptor.

Recall that, in the dark the photoreceptor is depolarized and thus there is a continual release of glutamate at the synapse with the bipolar cell. A light stimulus causes hyperpolarization of the photoreceptor and a consequent decrease in glutamate release. To see what effect this decrease in glutamate has on the bipolar cell, consider first an on-center bipolar cell. These bipolar cells express glutamate receptors (metabotropic glutamate receptors) that, when bound to glutamate, activate intracellular pathways that result in the closure of cAMP-gated Na^+ channels and hyperpolarization of the cell (contrast this with the ACh-sensitive channels discussed in Chapter 8, Section 8.1.5). Thus, in the dark, on-center bipolar cells are hyperpolarized due to the high levels of glutamate released by the photoreceptor. When the photoreceptor is stimulated by light glutamate levels fall, the Na^+ chan-
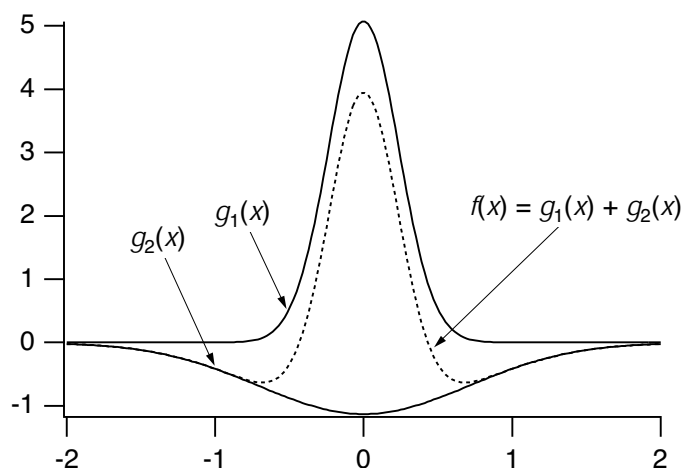
Figure 19.19: The addition of two Gaussian distributions, one with positive sign denoting the excitatory center, and one with negative sign denoting the inhibitory surround, gives the response function $f(x)$, which weights the light stimulus according to its position in space. Computed using $\sigma_1 = 3, \sigma_2 = 1, g_1 = 3, g_2 = 1$.

nels in the bipolar cells open and the bipolar cell depolarizes, sending a positive signal to the ganglion cell.

The off-center bipolar cell expresses a different type of glutamate receptor (an ionotropic, or AMPA, receptor) that responds to glutamate by depolarizing the cell. Thus, in the dark these bipolar cells are depolarized. When stimulated by light the photoreceptors release less glutamate and the off-center bipolar cell hyperpolarizes, thus sending a negative signal to the ganglion cell.

Although it is not yet entirely understood how the center-surround field occurs, it is likely that it is mediated by feedback from horizontal cells to photoreceptors. Horizontal cells synapse with photoreceptors over a considerable area and are connected to one another by gap junctions. It is thus plausible that negative feedback from the surround to the ganglion cell is mediated by feedback from the horizontal cell layer to the photoreceptors in the center, and thus to the bipolar cell and the ganglion cell.

One of the earliest models of ganglion cell behavior was constructed by Rodieck (1965). In this model it is assumed that the response of a ganglion cell is a weighted sum of the responses from each part of the receptive field, with negative weights for the inhibitory part of the field and positive weights for the excitatory part. Here we consider only on-center cells, as the model is the same for off-center cells, with reversed signs. We also consider the model in one spatial dimension only, as the extension to two dimensions introduces greater algebraic complexity, but no new concepts.

Suppose that the steady response to a step change in illumination of a small area dx centered at the point x is given by $f(x)dx$. From consideration of experimental data, Rodieck showed that $f(x)$ can be described as the sum of two Gaussians,
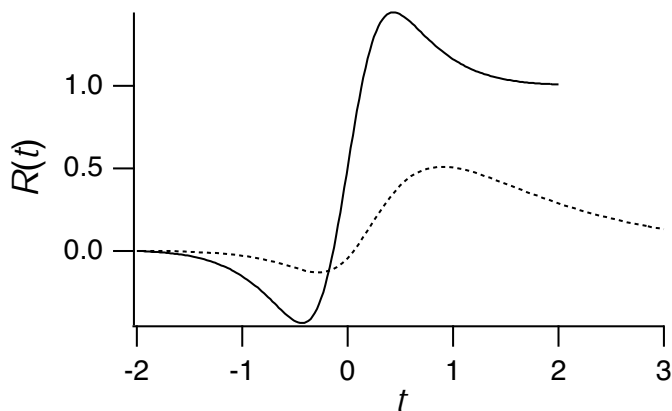
Figure 19.20: Response of a ganglion cell to a moving bar of semi-infinite width. Solid line assuming that the response at each point x is infinitely fast; dotted line assuming that each point x responds to the light stimulus according to (19.99). Both curves were calculated with $\sigma_1 = 3$, $\sigma_2 = 1$, $g_1 = 3$, $g_2 = 1$, $c = 1$.

one contributing a positive component from the center and the other contributing a negative component from the surround. Thus,

$$f(x) = \frac{g_1\sigma_1}{\sqrt{\pi}}e^{-\sigma_1^2 x^2} - \frac{g_2\sigma_2}{\sqrt{\pi}}e^{-\sigma_2^2 x^2}, \tag{19.95}$$

which is plotted in Fig. 19.19. The constants g_1 and g_2 are the gains of the excitatory center and inhibitory surround, respectively, and the parameters σ_1 and σ_2 control their radial size. Now suppose that the response of the ganglion cell is infinitely fast, and that the cell is stimulated with a semi-infinite bar, extending from $x = -\infty$ to $x = ct$, so that the edge of the bar is moving from left to right with speed c. Then, the response of the ganglion cell, $R(t)$, is

$$R(t) \quad = \quad \int_{-\infty}^{ct} f(x)\,dx \tag{19.96}$$

$$= \quad g_1\left[\frac{1}{2} + \frac{1}{\sqrt{\pi}}\mathrm{erf}(ct/\sigma_1)\right] + g_2\left[\frac{1}{2} + \frac{1}{\sqrt{\pi}}\mathrm{erf}(ct/\sigma_2)\right], \tag{19.97}$$

where $\mathrm{erf}(x)$, the error function, is defined by

$$\mathrm{erf}(x) = \frac{2}{\sqrt{\pi}}\int_0^\infty e^{-x^2}\,dx. \tag{19.98}$$

From the plot of R given in Fig. 19.20 (solid line) it can be seen that the ganglion cell responds preferentially to the edge of the bar, as is seen in experimental data.

In reality, the response of the ganglion cell is not infinitely fast, but the response to a step of light has an initial peak followed by a decrease to a lower plateau. Thus, in Rodieck's model, the time-dependent response to a step input is taken to be

$$h(t) = \left[1 + te^{-t}\right]H(t), \tag{19.99}$$

where $H(t)$ is the Heaviside function. This is a simple way to incorporate the dynamic behavior of the earlier retinal stages. More general forms for the response produce little difference in the overall response.

To illustrate the temporal behavior of the overall response, we calculate the response to the moving bar, extending from $x = -\infty$ to $x = ct$. Since the edge of the moving bar reaches an element at position x at time $t = x/c$, the response of an element at position x is $f(x)h(t - x/c)dx$. Integrating over the entire domain gives

$$R(t) \;=\; \int_{-\infty}^{\infty} f(x)h(t - x/c)\, dx, \tag{19.100}$$

$$=\; \underbrace{\int_{-\infty}^{ct} f(x)\, dx}_{\text{steady term}} + \underbrace{\int_{-\infty}^{ct} f(x)(t - x/c)e^{x/c-t}\, dx}_{\text{transient term}}, \tag{19.101}$$

which is graphed in Fig. 19.20 (dotted line). If $f(x)$ decays sufficiently rapidly at $\pm\infty$, the transient term goes to zero as $t \to \infty$, leaving only the steady response. Of course, since retinas are not infinite in extent, f is zero outside a bounded domain, and so such decay is guaranteed. Further, in the limit as $c \to 0$, keeping ct fixed, the transient term again approaches zero. That is, if the bar moves slowly, the effect of $h(t)$ is small, again as expected. On the other hand, as $c \to \infty$, $R(t)$ approaches $h(t) \int_{-\infty}^{\infty} f(x)\, dx$, which is exactly the response to a space-independent flash. Verifications of these statements are left for the exercises (Exercise **??**).

Not only should a model incorporate the temporal dynamics of the receptive field responses, it should also incorporate the fact that the responses of the center and surround have different temporal kinetics. Thus, the most accurate models include an additional temporal filter in the response of the surround, the so-called Gaussian center-surround model (Frishman et al., 1987; Victor, 1987, 1988; Troy and Shou, 2002). However, since these models quickly become quite complicated we do not discuss them in any further detail here.

Cells higher up in the visual pathway, in the lateral geniculate nucleus and the visual cortex, have progressively more complex receptive fields, designed to make particular cells respond maximally to stimuli of particular orientation or direction of movement. The above model serves as a brief introduction to the type of modeling involved in the analysis of receptive fields. A more detailed discussion of receptive fields is given by Kuffler et al. (1984) and Troy and Shou (2002).

19.7   The Pupil Light Reflex

The control of pupil size is yet another way in which the eye can adjust to varying levels of light intensity. While the adjustment of pupil size accounts for much less of visual adaptation than those mechanisms described earlier, it is nonetheless an important control mechanism.

The size of the pupil of the eye is determined by a balance between constricting and dilating mechanisms. Pupil constriction is caused by contraction of the circularly arranged pupillary constrictor muscle, which is innervated by parasympathetic fibers. The motor nucleus for this muscle is the Edinger–Westphal nucleus located

in the oculomotor complex of the midbrain. Dilation is controlled by contraction of the radially arranged pupillary dilator muscle innervated by sympathetic fibers and by inhibition of the Edinger–Westphal nucleus.

The effect of the pupil light reflex is to control the retinal light flux

$$\phi = IA, \tag{19.102}$$

where I is the illuminance (lumen mm^{-1}) and A is the pupil area (mm^2). It performs this function by acting like the aperture of a camera. When light is shined on the retina, the pupil constricts, thereby decreasing ϕ. However, there is a latency of $\approx$ 180–400 ms following a change in light input before changes in pupil size are detected.

This combination of negative feedback with delay may lead to oscillations of pupil size. These oscillations were first observed by a British army officer, Major Stern, who noticed that pupil cycling could be induced by carefully focusing a narrow beam of light at the pupillary margin. Initially, the retina is exposed to light, causing the pupil to constrict, but this causes the iris to block the light from reaching the retina, so that the pupil subsequently dilates, re-exposing the retina to light, and so on indefinitely.

Longtin and Milton (1989) developed a model for the dynamics of pupil contraction and dilation. In their model it is assumed that the light flux ϕ is transformed after a time delay τ_r into neural action potentials that travel along the optic nerve. The frequency of these action potentials is related to ϕ by

$$N(t) = \eta F \left(\ln \left[\frac{\phi(t - \tau_r)}{\bar{\phi}} \right] \right), \tag{19.103}$$

where $F(x) = x$ for $x \geq 0$ and $F(x) = 0$ for $x < 0$, $\bar{\phi}$ is a threshold retinal light level (the light level below which there is no response), and η is a rate constant. The notation $\phi(t - \tau_r)$ is used to indicate dependence on the flux at time τ_r in the past.

This afferent neural action potential rate is used by the midbrain nuclei, after an additional time delay τ_t, to produce an efferent neural signal. This signal exits the midbrain along preganglionic parasympathetic nerve fibers, which terminate in the ciliary ganglion where the pupillary sphincter is innervated. Neural action potentials at the neuromuscular junction result in the release of neurotransmitter (ACh), which diffuses across the synaptic cleft, thus generating muscle action potentials and initiating muscle contraction. These events are assumed to require an additional time τ_m.

The relationship between iris muscle activity x and the rate of arriving action potentials $E(t)$ is not known. We take a simple differential relationship

$$\tau_x \frac{dx}{dt} + x = E(t), \tag{19.104}$$

where

$$E(t) = \gamma F \left(\ln \left[\frac{\phi(t - \tau)}{\bar{\phi}} \right] \right), \tag{19.105}$$

and $\tau = \tau_r + \tau_t + \tau_m$ is the total time delay in the system.

Finally, we close the model by assuming some relationship between iris muscle activity x and pupil area A as $A = f(x)$. For example, one reasonable possibility is the Hill equation

$$A = f(x) = \Lambda_0 + \frac{\Lambda \theta^n}{x^n + \theta^n}, \tag{19.106}$$

for which area is a decreasing function of activity, with maximal area $\Lambda + \Lambda_0$ and minimal area Λ_0. It follows that the differential equation governing iris muscle activity is

$$\tau_x \frac{dx}{dt} + x = \gamma F \left(\ln \left[\frac{I(t-\tau)f(x(t-\tau))}{\bar\phi} \right] \right) \tag{19.107}$$

$$= g(x(t-\tau), I(t-\tau)). \tag{19.108}$$

19.7.1   Linear Stability Analysis

Because $f(x)$ is a decreasing function of x, a steady solution of (19.108) is assured when the input $I(t)$ is constant. We identify this value of x as x^*, satisfying $x^* = g(x^*, I)$. Linearized about x^*, the delay differential equation becomes

$$\tau_x \frac{dX}{dt} + X = -GX(t-\tau), \tag{19.109}$$

where $G = -g_x(x^*, I) = -\gamma \frac{f'(x^*)}{f(x^*)}$ is called the *gain* of this negative feedback system. If we set $X = X_0 e^{\mu t}$, we find the characteristic equation for μ to be

$$\tau_x \mu + 1 = -Ge^{-\mu\tau}. \tag{19.110}$$

If $|G| < 1$, there are no roots of this equation with positive real part; the solution is linearly stable. Since $G > 0$, there are no positive real roots of this characteristic equation. The only possible way for the solution to become unstable is through a Hopf bifurcation, whereby a root of (19.110) with nonzero imaginary part changes the sign of its real part. If we set $\mu = i\omega$, we can separate (19.110) into real and imaginary parts, obtaining

$$G \cos \omega\tau = -1, \tag{19.111}$$
$$G \sin \omega\tau = \tau_x \omega. \tag{19.112}$$

From these two expressions, we readily find a parametric representation of the critical stability curve to be

$$G = \frac{-1}{\cos \eta}, \qquad \frac{\tau}{\tau_x} = \frac{-\eta}{\tan \eta}. \tag{19.113}$$

The first instability curve is plotted in Fig. 19.21, with the gain G plotted as a function of the dimensionless delay τ/τ_x. It is easily seen that on the critical curve G is a decreasing function of τ/τ_x. If the delay is larger than the critical delay, the steady solution is unstable and there is a stable periodic solution of the full differential delay equation (19.108), corresponding to periodic cycling of pupil size with constant light stimulus.
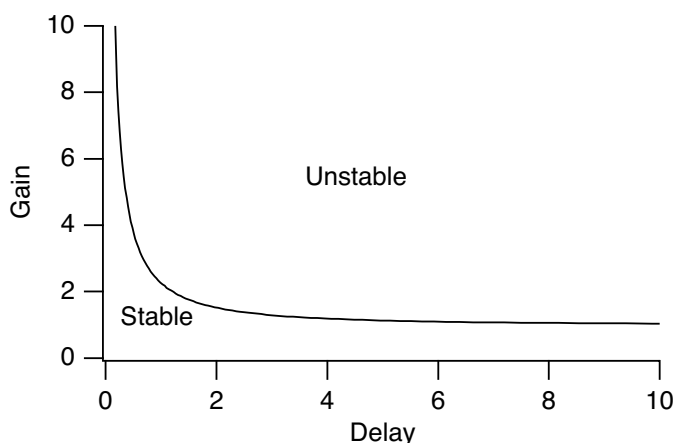
Figure 19.21: Critical stability curve for the pupil light reflex.

19.8 Appendix: Linear Systems Theory

One of the most widely used tools in the study of the visual system is linear systems analysis. Here we have assumed that the basic tools of linear function theory, such as Fourier transforms, delta functions, and the convolution theorem, are familiar to readers. There are numerous books that provide the necessary background, for example, Papoulis (1962), Stakgold (1997) and Haberman (2003).

The essential idea of linear systems theory is that for any linear differential equation $L[u] = f(t)$, where $L[\cdot]$ is a time-autonomous differential operator, the Fourier transform of the solution can be written as

$$\hat{u}(\omega) = T(\omega)\hat{f}(\omega), \tag{19.114}$$

where $\hat{f}(\omega)$ is the Fourier transform of the input function $f(t)$, and $T(\omega)$ is called the *transfer function* for this linear system. Note that if $f(t)$ is the delta function, then $\hat{u} = T(\omega)$, and thus the transfer function is the Fourier transform of the impulse response. The transfer function can also be found by assuming an input of the form $f = e^{i\omega t}$ and looking for an output of the form $u = T(\omega)e^{i\omega t}$. Thus, the amplitude and phase of the sinusoidal input are modulated by the amplitude and phase of the transfer function. Such sinusoidally varying inputs are commonly used in experimental studies of the visual system; by varying the frequency of the stimulus and measuring (at each fixed frequency) the amplitude and phase of the output, the transfer function can be experimentally determined.

Once the transfer function (and thus the impulse response) of a linear system is known, its response to any input can be calculated. Intuitively, any function $f(t)$ can be considered a superposition of impulses, and thus the response to the input $f(t)$ is the sum of the responses to these impulses. Thus, if $K(t)$ is the impulse response of the linear operator L, the solution to $L[u] = f(t)$ is $u(t) = \int_{-\infty}^{t} f(\tau)K(t - \tau)\,d\tau$. Although this exposition is far too brief for a complete presentation of the theory, the main point is that, for a linear system, experimental

measurement of the transfer function suffices for a complete determination of the system. For a detailed discussion of impulse responses, Green's functions, and fundamental solutions of differential equations, the reader is referred to Stakgold (1997), Haberman (2003) or Kevorkian (1990).

One of the simplest mathematical realizations of a linear system is the linear differential equation

$$\frac{dx}{dt} + ax = f(t), \qquad a > 0, \tag{19.115}$$

where $f(t)$ is the input to the system. If we assume that $f(t) = e^{i\omega t}$, and look for solutions of the form $x = A(\omega)e^{i\omega t}$, we get

$$A(\omega) = \frac{1}{a + i\omega}. \tag{19.116}$$

This is the transfer function of (19.115). It can also be calculated by taking the Fourier transform of (19.115). The inverse Fourier transform of the transfer function is $H(t)e^{-at}$, where H is the Heaviside function, which is the impulse response of (19.115) (Exercise 12). If we now solve (19.115) directly by using the integrating factor e^{at} we get

$$\left(x(t)e^{at}\right)' = f(t)e^{at}, \tag{19.117}$$

and thus, integrating from $-\infty$ to t and assuming the solution is bounded at $-\infty$, we get

$$x(t) = \int_{-\infty}^{t} f(\tau)e^{-a(t-\tau)} \, d\tau. \tag{19.118}$$

Thus the response to a general input is the convolution of the input with the impulse response, as claimed above.

This approach is easily extended to multiple linear differential equations, as in (19.10)—(19.13). The transfer function and impulse response of those equations is calculated in exactly the same way; we assume an input of the form $I(t) = e^{i\omega t}$ and look for solutions of the form $g(t) = H(\omega)e^{i\omega t}$.

Typical experimental data are shown in Fig. 19.22. The light input to the system is modulated around a mean level, and the output is the membrane potential of a turtle horizontal cell. Here there are five different background light levels, corresponding to the five curves in the figure. Gain is measured in units of mV photon^{-1} and plotted relative to gain in the dark.

As can be seen from Fig. 19.22, when the background light level increases by one log unit in intensity (indicated by moving from filled squares to open circles, or from open circles to filled triangles, etc.), the relative gain at low frequency decreases by approximately one log unit. Hence, over a range of light levels the low-frequency gain is inversely proportional to I_0, and thus the steady-state sensitivity obeys Weber's law. At high frequencies and low background light levels, Weber's law breaks down, and the gain becomes nearly independent of the background light level. It is important to note that the steady-state sensitivity is not the same as the peak sensitivity. In photoreceptors, however, for reasons that are not clear, both the steady state and peak sensitivity follow Weber's law approximately. From this data it can also be seen that turtle horizontal cells respond best to stimuli of a given
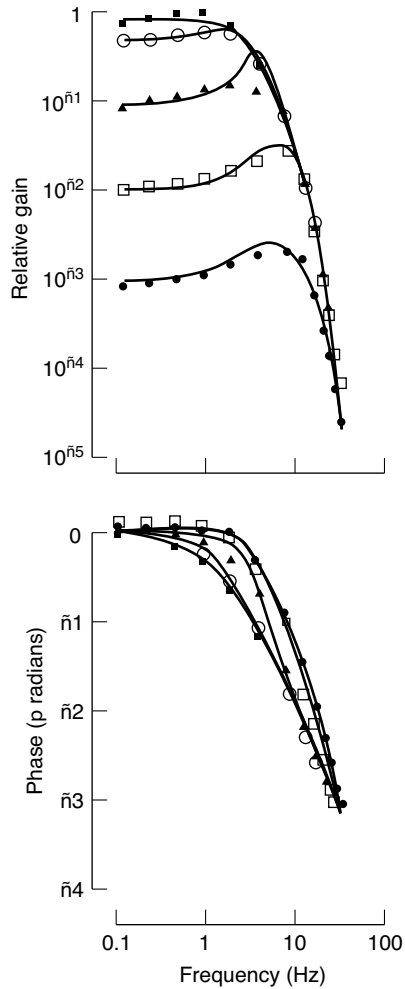
Figure 19.22: A family of temporal frequency responses from turtle horizontal cells, measured at five different mean light levels. (From top to bottom, the filled square, open circle, filled triangle, open square, and filled circle denote background lights of intensity, respectively, -4, -3, -2, -1, and 0 log units.) Symbols are experimental data, and the smooth curves are from the model of Tranchina et al. (1984), which is not described here. The data are presented in a typical Bode plot format, with the amplitude plotted in the upper panel, the phase difference in the lower. (Tranchina et al., 1984, Fig. 1.)

frequency. At the two highest light levels the data is clearly band-pass in nature, with a maximal response at around 10 Hz.

One significant problem is that most realistic systems are nonlinear, so a transfer function cannot be defined (since solutions are not the linear superposition of fundamental solutions). However, if the amplitude of the sinusoidal input is small, so that $I(t) = \epsilon e^{i\omega t}$, then the response should also be small, of the form $\epsilon T(\omega)e^{i\omega t} + O(\epsilon^2)$. If ϵ is small enough, and higher-order terms can be neglected, the response of the system is well described by the *first-order transfer function* $T(\omega)$.

Of course, the response of retinal cells to stimuli is not linear, and therefore one can determine only their first-order frequency response. However, measurement of the amplitudes of higher harmonics ($e^{2i\omega t}, e^{3i\omega t}, e^{4i\omega t}$, etc.) in response to an input of the form $e^{i\omega t}$ indicates that nonlinearities have little effect for the light stimuli used in the experiments. Thus, the behavior of retinal cells can be described well by their first-order frequency responses.

Suppose $V_0(x)$ denotes the response to a steady input x. If the input is of the form $I(t) = I_0 + \epsilon e^{i\omega t}$, then the output is of the form $V(t) = V_0(I_0) + \epsilon V_1(w; I_0)e^{i\omega t} + O(\epsilon^2)$. The function $V_1(w; I_0)$ is the first-order transfer function, or first-order frequency response. When $\omega = 0$, this becomes $V_0(I_0 + \epsilon) = V_0(I_0) + \epsilon V_1(0; I_0) + O(\epsilon^2)$. However, expanding $V_0(I_0 + \epsilon)$ in a Taylor series around I_0 gives $V_0(I_0 + \epsilon) = V_0(I_0) + \epsilon V_0'(I_0) + O(\epsilon^2)$, from which it follows that the steady-state sensitivity is

$$\frac{dV_0}{dI_0} = V_1(0; I_0), \qquad\qquad (19.119)$$

an identity that is of considerable use.

19.9 Exercises

1. Show that changing σ in the Naka-Rushton equation (19.3) translates the curve along the $\log I$ axis.

2. Compare the two expressions (19.8) and (19.9) for the sensitivity. (Hint: choose the arbitrary values $\sigma_D = 0.1$, $k = 1$ and plot (19.8), then adjust the value of A until the curves look the same.)

3. In this exercise, some of the solutions of the model of light adaptation in turtle cones are obtained (Section 19.2.2).

   (a) Before one can calculate solutions of the model, the expression for $g(y)$ must be derived. By requiring the steady state solution of the model to be

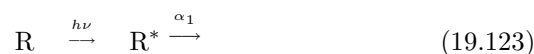$$V_0 = -s_1 \log(1 + s_2 I_0), \qquad\qquad (19.120)$$

   show that

$$g(y) = \left(y e^{E(1-y)/V^*}\right)^{1/3}\left(\delta + \frac{(\gamma - \delta)\eta(e^{-E(1-y)/s_1} - 1)}{s_2 k_1 + \eta(e^{-E(1-y)/s_1} - 1)}\right). \qquad (19.121)$$

Plot $g(y)$ (using the parameters given in Table 19.4) and compare to the functional form found experimentally (19.35), i.e.,

$$A(y) = 4 + \frac{84}{1 + (y/0.34)^4}.$$ (19.122)

(b) Calculate the impulse responses of the model for a range of background light levels. For each background light level I_0, let the magnitude of the impulse be I_0 also. Do this for $I_0 = 0.5, 0.05, 0.005, 0.0005$ and 0.00005. How close to linear are the responses? What can be said about the contrast sensitivity?

(c) Scale each of the impulse responses calculated above so that each has a maximum value of 1, and plot them all on the same graph. How do the impulse responses change as the light level increases?

(d) Replace $g(y)$ by $A(y)$ and recalculate the steady state V_0 and the impulse responses (at the same background light levels as in part (b) above). Are there any significant differences?

4. In 1989, Forti et al. published a model of phototransduction in newt rods. In many respects their model is similar to the model discussed here. However, one major difference is in how they chose to model the initial stages of the light response. Instead of using a linear filter (which is, to be sure, a bit simplistic), Forti et al. assumed that the initial stages of the light response could be modeled by the reactions

$$R \quad \xrightarrow{h\nu} \quad R^* \xrightarrow{\alpha_1} \qquad\qquad\qquad (19.123)$$

$$R^* + T \quad \xrightarrow{\epsilon} \quad R^* + T^* \qquad\qquad\qquad (19.124)$$

$$T^* \quad \xrightarrow{\beta} \qquad\qquad\qquad\qquad\qquad (19.125)$$

$$T^* + P \quad \underset{\tau_2}{\overset{\tau_1}{\rightleftharpoons}} \quad T^* + P^* \qquad\qquad\qquad (19.126)$$
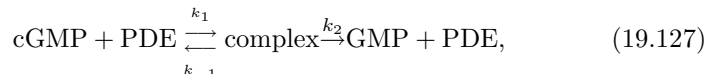
Here, R denotes rhodopsin, T denotes transducin and P denotes PDE. The * superscript denotes the activated form, and $h\nu$ denotes the action of light. The parameter values of the model are given in Table 19.4. (These are not exactly the reactions assumed by Forti et al. as we have omitted the inactivated rhodopsin state. However, this makes almost no difference to the results presented here.)

(a) Write down the differential equations for this system of reactions, assuming the amount of rhodopsin is not limiting, and solve them numerically. Plot $P^*(t)$ for a variety of stimuli, each 10 ms in duration, with magnitudes 0.2, 0.5, 1, 2, 5, 10, 20, 50, 100 and 500. What can you conclude about the linearity of the response when the magnitude of the stimulus is small? What can you conclude about the linearity of the response as the magnitude of the stimulus increases?

T_0	$=$	$1000~\mu\mathrm{M}$	P_0	$=$	$100~\mu\mathrm{M}$
α_1	$=$	$20~\mathrm{s}^{-1}$	ϵ	$=$	$0.5~\mathrm{s}^{-1}\,\mu\mathrm{M}^{-1}$
τ_1	$=$	$0.1~\mathrm{s}^{-1}\,\mu\mathrm{M}^{-1}$	τ_2	$=$	$10~\mathrm{s}^{-1}$
β_1	$=$	$10.6~\mathrm{s}^{-1}$			

Table 19.4: Parameter values for the model of the initial stages of the light response in newt rods (Forti et al., 1989). P_0 is the total amount of PDE, and T_0 is the total amount of transducin.

(b) Compare the model in part (a) with the detailed reaction scheme in Fig. 19.7. Where do they disagree? Modify the model so that it agrees better with the more detailed reaction scheme. (Hint: the conservation equation for transducin must be considered more carefully, as must the differential equation for T*.) Solve the new model numerically for the same stimuli as part (a), and compare with the solutions of the Forti et al. model. Explain the differences.

(c) Compare the model of part (a) to the linear cascade model in the book. Where are they similar? Where are they not similar? Why?

5. cGMP is hydrolyzed to GMP by PDE or PDE* in an enzymatic reaction, and as was described in Chapter 1, such reactions do not necessarily follow the law of mass action. Assuming that cGMP reacts with PDE according to

$$\mathrm{cGMP} + \mathrm{PDE} \underset{k_{-1}}{\overset{k_1}{\rightleftharpoons}} \mathrm{complex} \overset{k_2}{\rightarrow} \mathrm{GMP} + \mathrm{PDE}, \tag{19.127}$$

derive the conditions under which (19.18) may be expected to apply, keeping in mind that [PDE] is much larger than [cGMP], and thus the usual approximation of enzyme kinetics does not apply. (See also Exercise **??** of Chapter 1, and Sneyd and Tranchina, 1989.)

6. Show that the current generated by the electrogenic exchange pumps should not be ignored in the modeling of a photoreceptor. (Hint: By writing down the balance equations for Na^+ and Ca^{2+} show that the outward current generated by the electrogenic Na^+–K^+ exchanger in the inner segment must be approximately a third of the total inward light-sensitive current.) How significant is the current generated by the Na^+–$\mathrm{Ca}^{2+}, \mathrm{K}^+$ exchanger in the outer segment? Should the electrogenic pumps be included in the model if the model is compared to photocurrent measurements and not to voltage measurements?

7. Find the solution of (19.44)-(19.47) in the case that $k_i = k$ for all i. Find the mean and variance for the time of inactivation.

8. Calculate the response of the lateral inhibition model (Section 19.4) when the light stimulus is a strip of width $2a$, modulated sinusoidally with frequency ω. Show that as a increases (i.e., as the stimulus goes from a spot to a uniform field), the gain at $x = 0$ becomes more band-pass in nature.

Hint: Show that the solution for $\hat{I}$ is of the form

$$
\hat{I} = \begin{cases} \frac{\lambda \hat{L}}{(i\omega\tau+1)(1+\lambda+i\omega)}[1 + A\cosh[x\sqrt{1+\lambda+i\omega}], & |x| < a, \\ B\exp(-|x|\sqrt{1+\lambda+i\omega}), & |x| > a, \end{cases} \tag{19.128}
$$

and require that $\hat{I}$ and its derivative be continuous at $|x| = a$. Define the gain as the response divided by the stimulus, and calculate the amplitude of the gain at $x = 0$ as a function of ω and a. (The details are given in Peskin (1976)).

9. Calculate the response of the lateral inhibition model (Section 19.4) to a moving step of light. Show that as the speed tends to zero, the response approaches the response to a steady step, while as the speed goes to infinity, the response behaves like the response to a step of light presented simultaneously to the entire retina. (This question is taken from Peskin (1976)).

Hint: to exhibit the space-like limit write R as a function of $x + ct$, where c is the speed of the moving step. To exhibit the time-like limit, write R as a function of $t + x/c$.

10. Derive (19.69) and verify (19.71). Hints: Show first that everywhere except $r = s$, G satisfies the modified Bessel equation of order zero, $z^2\frac{d^2u}{dz^2} + z\frac{du}{dz} - z^2u = 0$. Two independent solutions of the modified Bessel equation are the modified Bessel functions of the first and second kind. Then show that the jump condition at $r = s$ is

$$
\left.\frac{dG}{dr}\right|_{r=s^+} - \left.\frac{dG}{dr}\right|_{r=s^-} = -\frac{1}{s}, \tag{19.129}
$$

and use the fact that the Wronskian W is

$$
W(K_\nu, I_\nu) = K_\nu(z)\frac{d}{dz}I_\nu(z) - I_\nu(z)\frac{d}{dz}K_\nu(z) = \frac{1}{z}. \tag{19.130}
$$

11. Show that the Krausz–Naka model (Section 19.4.2) is similar to the Peskin model (Section 19.4.1), with a few more details. Thus, investigate the response of the Krausz–Naka model to a space-independent light step and a time-independent bar of light. Demonstrate Mach bands and adaptation, as in the Peskin model.

12. (a) By taking the Fourier transform of (19.115) show that the transfer function is given by (19.116).

   (b) Calculate the impulse response of (19.115) by solving the differential equation directly. (Hint: first integrate from $t = -\epsilon$ to $t = \epsilon$ and let $\epsilon \to 0$ to obtain a jump condition at $t = 0$. Then use that jump condition as an initial condition for the differential equation.)

Chapter 20

The Inner Ear

The mammalian ear has three major components: the outer, middle, and inner ears
(Fig. 20.1A). The outer ear consists of a cartilaginous flange, the *pinna*, incorpo-
rating a resonant cavity that connects to the *ear canal* and finally to the *tympanic
membrane*. It performs an initial filtering of the sound waves, increasing the sound
pressure gain at the tympanic membrane in the 2 to 7 kHz region. It also aids sound
localization. Bats, for example, have highly developed pinnae, with a high degree
of directional selectivity. Although less efficient in humans, the outer ear accounts
for our ability to distinguish whether sounds come from above or below, in front or
behind.

   The function of the middle ear is to transmit the sound vibrations from the
tympanic membrane to the cochlea. Because of the much higher impedance of
the cochlear fluid, the middle ear also functions as an impedance-matching device,
focusing the energy of the tympanic membrane on the oval window of the cochlea.
If not for impedance matching, much of the energy of the sound waves in air would
be reflected by the cochlear fluid. This impedance matching is carried out by
the *ossicles*, three small bones, the *malleus, incus*, and *stapes*, that connect the
tympanic membrane to the oval window. The tympanic membrane has a much
higher surface area than the oval window, and the ossicles act as levers that increase
the force at the expense of velocity, resulting in the required concentration of energy
at the oval window.

   Most of the events central to hearing occur in the inner ear, in particular the
cochlea. The vestibular apparatus (the semicircular canals and the otolith organs)
are also in the inner ear, but their principal function is the detection of movement
and acceleration, not sound. The cochlea is a tube, about 35 mm long, divided longi-
tudinally into three compartments and twisted into a spiral (Fig. 20.1B). The three
compartments are the *scala vestibuli*, the *scala tympani*, and the *scala media*, and
they wind around the spiral together, preserving their spatial orientation. Reiss-
ner's membrane separates the scala vestibuli from the scala media, which in turn
is separated from the scala tympani by the *spiral lamina* and the *basilar membrane*
(Fig. 23.2A). The scala vestibuli and the scala tympani are filled with *perilymph*,
a fluid similar to extracellular fluid, while the scala media is filled with *endolymph*,
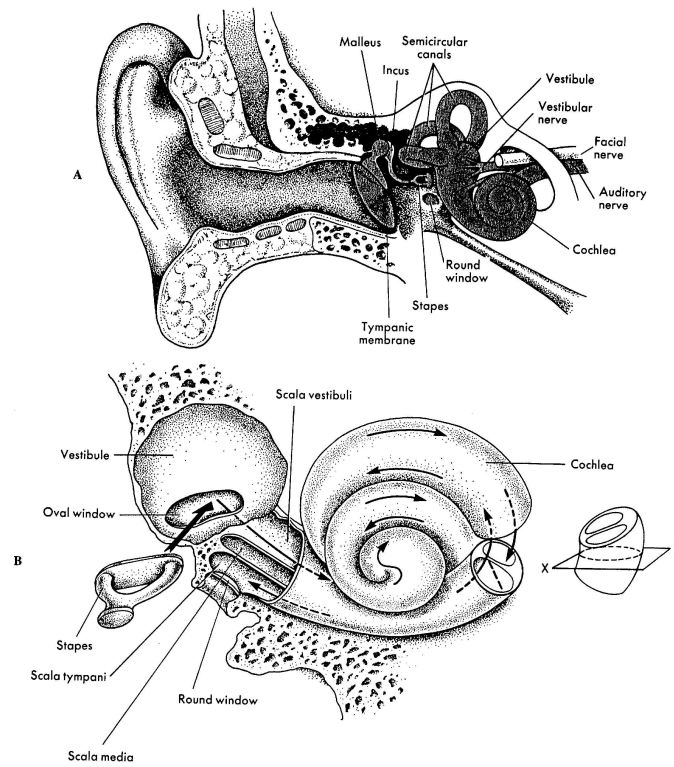a fluid with a high K^+ concentration and a low Na^+ concentration. Sound waves

Figure 20.1: Location and structure of the cochlea. A: Location of the cochlea in relation to the middle ear, the tympanic membrane, and the outer ear. B: Diagram of the cochlea at increased magnification, showing its spiral structure and the relative positions of the two larger internal compartments, the scala vestibuli and the scala tympani. (Berne and Levy, 1993, Fig. 10-6.)
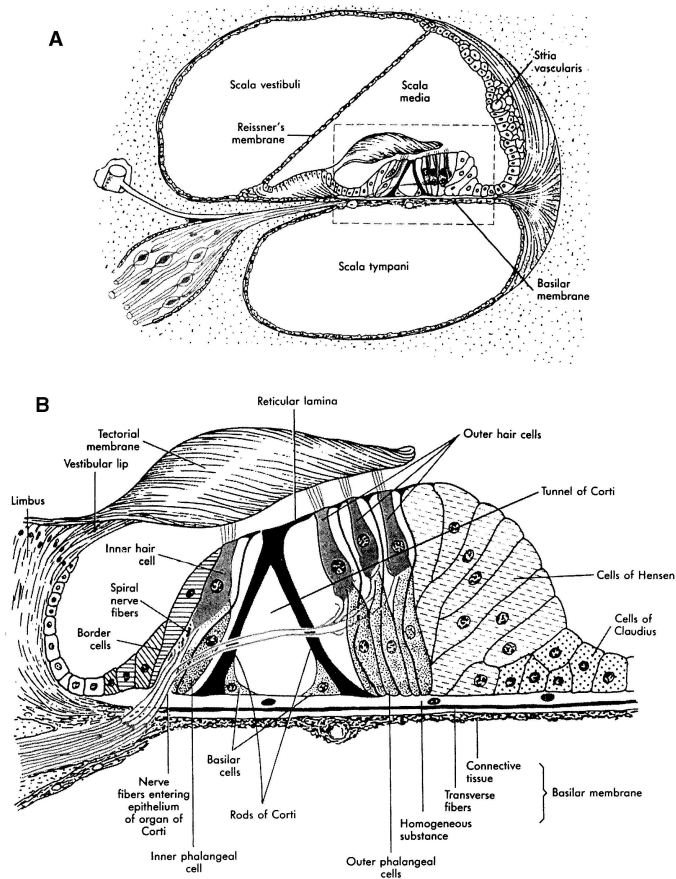
Figure 20.2: Location and structure of the cochlea, continued. A: Cross-section of the cochlea in the plane indicated by the inset in Fig. 23.1B. B: Enlarged view of the organ of Corti, including the basilar membrane, the tectorial membrane, and the hair cells. (Berne and Levy, 1993, Fig. 10-6.)

transmitted through the middle ear are focused by the stapes onto the oval window, an opening into the scala vestibuli. The resultant waves in the perilymph travel along the length of the scala vestibuli, creating complementary waves in the basilar membrane and the scala tympani. At the end of the cochlea, an opening between the scala vestibuli and the scala tympani, the *helicotrema*, equalizes the local pressure in the two compartments. Because the perilymph is essentially incompressible, it is necessary for the scala tympani also to have an opening analogous to the oval window; otherwise, conservation of mass would preclude movement of the stapes. The opening in the scala tympani is called the *round window*. Inward motion of the stapes at the oval window is compensated for by the corresponding outward motion of fluid at the round window.

Transduction of sound into electrical impulses is carried out by the *organ of Corti* (Fig. 23.2B), which sits on top of the basilar membrane. *Hair cells* in the organ of Corti have hairs projecting out the top, and these hairs touch a flap called the *tectorial membrane* that sits over the organ of Corti. Waves in the basilar membrane create a shear force on these hairs, which in turn causes a change in the membrane potential of the hair cell. This is transmitted to nerve cells, and from there to the brain.

20.1   Frequency Tuning

The task of the cochlea is to identify the constituent frequencies of a sound wave, and thus identify the sound. The different ways in which this is accomplished in different animals fall into three principal groupings: mechanical tuning of the hair cells, mechanical tuning of the basilar membrane, and electrical tuning of the hair cells (Hudspeth, 1985; Eatock et al., 2006).

One of the earliest theories of frequency tuning was that of Helmholtz (1875) who proposed that the ear consists of an array of sharply tuned elements, each resonating with a particular frequency. Although this is far from the full story, resonance plays an important role. For example, in many lizards, the length of the hair bundles on the hair cells increases systematically from the base to the apex. In much the same way that a longer string produces notes of lower pitch, the longer hair cell bundles respond preferentially to inputs of lower frequency, while the short bundles are tuned to higher frequencies. Thus, the input frequency can be determined by the position of maximal stimulation. In mammals, the basilar membrane itself acts as a frequency analyzer, and this is discussed in the next section. The third tuning mechanism results from the properties of ionic channels in the hair cell membrane. Each hair cell is an electrical resonator, with a band-pass frequency response. The input frequency that gives the greatest response is a function of the biophysical properties of the hair cell, and the systematic variation of these properties along the length of the cochlea allows the cochlea to distinguish between frequencies based on the position of maximal response.

We do not discuss the first tuning mechanism further, but concentrate on the remaining two. We begin by looking at models of the basilar membrane that demonstrate mechanical tuning, and then discuss models for resonance of the hair cell membrane potential.
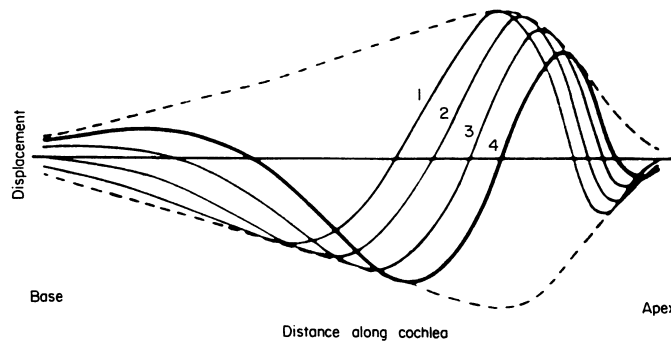
Figure 20.3: Membrane waves and their envelope in the cochlea. The solid lines show the deflection of the basilar membrane at successive times, denoted (in order of increasing time) by 1, 2, 3, 4. The dashed line is the envelope of the membrane wave, and remains constant over time. (von Békésy, 1960, Fig. 12-17.)

20.1.1 Cochlear Macromechanics

In mammals, vibrations of the stapes set up a wave with a particular shape on the basilar membrane. The amplitude envelope of the wave is first increasing, then decreasing, and the position of the peak of the envelope is dependent on the frequency of the stimulus (von Békésy, 1960; fortunately, since original editions of this book are difficult to find, it is now available through the Acoustical Society of America), as illustrated in Fig. 20.3. The wave speed decreases as it moves along the membrane, resulting in a continual decrease in phase, and an apparent increase in frequency. Low-frequency stimuli have a wave envelope that peaks closer to the apex of the cochlea (i.e., near the helicotrema), and as the frequency of the stimulus increases, the envelope peak moves toward the base of the cochlea, as illustrated in Fig. 20.4.

The amplitude of the envelope is a two-dimensional function of distance from the stapes and frequency of stimulation; the curves shown in Fig. 20.4 are cross-sections of the function for fixed frequency. Another way to present the data is to give cross-sections for a fixed distance. This gives the envelope amplitude as a function of frequency, for a fixed distance from the stapes, i.e., the frequency response of the basilar membrane for that fixed distance. Frequency responses measured by von Békésy are shown in Fig. 20.5, from which it can be seen that each part of the basilar membrane responds maximally to a certain frequency, and as the frequency increases, the site of maximum response moves toward the stapes. In this way the cochlea determines the frequency of the incoming signal from the place on the basilar membrane of maximal amplitude, the so-called *place theory* of hearing.

Although questions have been raised concerning the accuracy of von Békésy's results (he performed his experiments, somewhat gruesomely, on cadavers, but it is believed that the properties of the basilar membrane in a living person are different), in all theoretical studies of cochlear mechanics, the experimental results of von Békésy, and the associated place theory, have been the gold standard by which
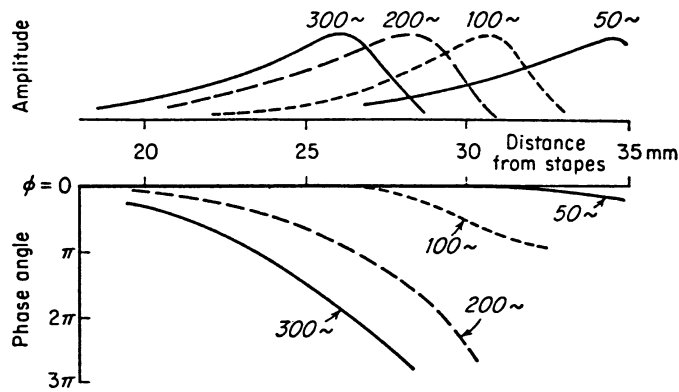
Figure 20.4: Amplitude and phase of the cochlear membrane wave for four different frequencies. As the frequency of the wave increases, the peak of the wave envelope moves toward the base of the cochlea (i.e., toward the oval and round windows). (von Békésy, 1960, Fig. 11-58. p. 462.)
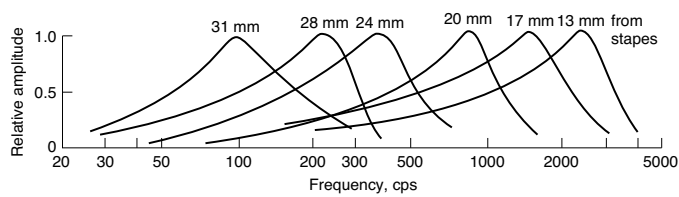

Figure 20.5: Frequency responses of the basilar membrane measured at different distances from the stapes. Only the amplitude is shown. Close to the stapes, the basilar membrane responds preferentially to tones of high frequency, while farther away from the stapes, the membrane responds preferentially to tones of lower frequencies. (von Békésy, 1960, Fig. 11-49.)

model performance has been judged.

The name "basilar membrane" is misleading, as it is not a true membrane. This is shown by the fact that when it is cut, the edges do not retract. Thus it is not under tension; resistance to movement comes from the bending elasticity. The stiffness of the basilar membrane decreases exponentially from the base to the apex, with a length constant of about 7 mm. Although the width of the cochlea decreases from the base to the apex, the width of the basilar membrane increases in this direction.

Models for waves on the basilar membrane can be distinguished by the types of equations used for the membrane and the fluid. Early models by Ranke (1950) and Zwislocki (1965) assumed the perilymph to be incompressible and inviscid, and modeled the basilar membrane as a damped, forced harmonic oscillator, with no elastic coupling along the length of the membrane. Ranke used deep-water wave theory, while Zwislocki used shallow-water wave theory, leading to considerable controversy over which was the best approach. These models were developed by many authors, the best known being due to Peterson and Bogert (1950), Fletcher (1951), Lesser and Berkley (1972), and Siebert (1974). Subsequent models by Steele (1974), Inselberg and Chadwick (1976), Chadwick et al. (1976), Chadwick (1980), and Holmes (1980a,b, 1982) used more sophisticated representations of the basilar membrane as an elastic plate and incorporated fluid viscosity and the geometry of the plate. Surveys of experimental and theoretical results can be found in Dallos et al. (1990, 1996). Here we give an overview of some of the earlier and simpler models, as they provide elegant demonstrations of how the basilar membrane and the perilymph can interact to give the types of waves observed by von Békésy.

20.2 Models of the Cochlea

20.2.1 Equations of Motion for an Incompressible Fluid

The fluid in the cochlea surrounding the basilar membrane is incompressible, and assumed to be inviscid. The equations of motion of this fluid are well known, and are derived in many places (e.g., Batchelor, 1967).

We let $\mathbf{u} = (u_1, u_2, u_3)$ be the fluid velocity, p the pressure, and ρ the density of the fluid. The mass of fluid in a fixed volume V can change only in response to fluid flux across the boundary of the volume. Thus,

$$\frac{d}{dt}\int_V \rho dV = -\int_S \rho(\mathbf{u} \cdot \mathbf{n})\, dS, \tag{20.1}$$

where S is the surface of V, and $\mathbf{n} = (n_1, n_2, n_3)$ is the outward unit normal to V. Similarly, the momentum of the fluid in a fixed domain V can change only in response to applied forces or to the flux of momentum across the boundary of the domain. Thus (for an inviscid fluid) conservation of momentum implies that

$$\frac{d}{dt}\int_V \rho u_i\, dV = -\int_S [(\mathbf{u} \cdot \mathbf{n})\rho u_i + p n_i]\, dS. \tag{20.2}$$

Using the divergence theorem to convert surface integrals to volume integrals, we

obtain

$$\int_V \left(\frac{\partial \rho u_i}{\partial t} + \rho \nabla \cdot (u_i \mathbf{u}) + \frac{\partial p}{\partial x_i} \right) dV \;\;=\;\; 0, \tag{20.3}$$

$$\int_V \frac{\partial \rho}{\partial t} + \nabla \cdot \mathbf{u} \, dV \;\;=\;\; 0. \tag{20.4}$$

Finally, since V is arbitrary, and assuming that the density ρ is constant, it follows that

$$\rho \frac{\partial \mathbf{u}}{\partial t} + \rho (\nabla \cdot \mathbf{u}) \mathbf{u} + \nabla p \;\;=\;\; 0, \tag{20.5}$$

$$\nabla \cdot \mathbf{u} \;\;=\;\; 0. \tag{20.6}$$

When the fluid motions are of small amplitude, as is expected to be true in the cochlea, the nonlinear terms may be ignored, yielding

$$\rho \frac{\partial \mathbf{u}}{\partial t} + \nabla p \;\;=\;\; 0, \tag{20.7}$$

$$\nabla \cdot \mathbf{u} \;\;=\;\; 0. \tag{20.8}$$

An important special case is when $\mathbf{u} = \nabla \phi$ for some potential ϕ (an irrotational flow), in which case (20.7) and (20.8) become

$$\rho \frac{\partial \phi}{\partial t} + p \;\;=\;\; 0, \tag{20.9}$$

$$\nabla^2 \phi \;\;=\;\; 0, \tag{20.10}$$

where p is normalized so that the constant of integration is zero.

20.2.2   The Basilar Membrane as a Harmonic Oscillator

One of the simplest models of the cochlea combines (20.9) and (20.10) with the equation of a damped, forced harmonic oscillator. One of the clearest presentations of this model is due to Lesser and Berkley (1972). In their model, the cochlea is assumed to have a configuration as shown in Fig. 20.6. Thus, letting subscripts 1 and 2 denote quantities in the upper and lower compartments, respectively, we have two copies of (20.9) and (20.10),

$$\rho \frac{\partial \phi_1}{\partial t} + p_1 = \rho \frac{\partial \phi_2}{\partial t} + p_2 \;\;=\;\; 0, \tag{20.11}$$

$$\nabla^2 \phi_1 = \nabla^2 \phi_2 \;\;=\;\; 0, \tag{20.12}$$

where the pressure is determined only up to an arbitrary constant.

Each point of the basilar membrane is modeled as a simple damped harmonic oscillator with mass, damping, and stiffness that vary along the length of the membrane. Thus, the movement of any part of the membrane is assumed to be independent of the movement of neighboring parts of the membrane, as there is no direct lateral coupling. The position of the basilar membrane, $y = \eta(x,t)$, is specified by

$$m(x) \frac{\partial^2 \eta}{\partial t^2} + r(x) \frac{\partial \eta}{\partial t} + k(x)\eta = p_2(x, \eta(x,t), t) - p_1(x, \eta(x,t), t), \tag{20.13}$$
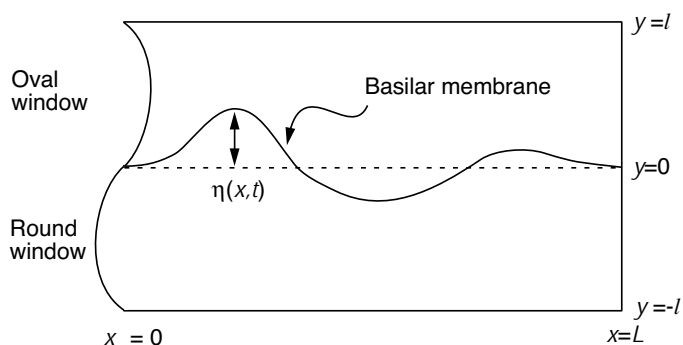
Figure 20.6: Schematic diagram of the cochlea, adapted from the model of Lesser and Berkley (1972). The cochlea is modeled as having two rectangular compartments filled with fluid, separated by the basilar membrane. The upper compartment corresponds to the scala vestibuli, and the lower compartment to the scala tympani. For simplicity, the scala media, shown in Fig. 20.1, is omitted from the model.

where $m(x)$ is the mass per unit area of the basilar membrane, $r(x)$ is its damping coefficient, and $k(x)$ is its stiffness (Hooke's constant) per unit area.

Boundary conditions are determined by requiring that the fluid velocity at the boundary matches the velocity of the boundary. Thus,

$$\frac{\partial \eta}{\partial t} = \frac{\partial \phi_1}{\partial y} = \frac{\partial \phi_2}{\partial y}, \qquad y = \eta(x,t), \ 0 < x < L. \tag{20.14}$$

We further assume that there is no vertical motion at the top, so that

$$\frac{\partial \phi_1}{\partial y} = 0, \qquad y = l, \ 0 < x < L. \tag{20.15}$$

As formulated, this is a very difficult free boundary problem. A significant simplification occurs if we assume that the displacement is small. Then, the leading order linear problem has a driving force which is the pressure difference evaluated at $y = 0$, rather than at $y = \eta$, so that

$$m(x)\frac{\partial^2 \eta}{\partial t^2} + r(x)\frac{\partial \eta}{\partial t} + k(x)\eta = p_2(x,0,t) - p_1(x,0,t). \tag{20.16}$$

The boundary conditions also simplify to

$$\frac{\partial \eta}{\partial t} = \frac{\partial \phi_1}{\partial y} = \frac{\partial \phi_2}{\partial y}, \qquad y = 0, \ 0 < x < L. \tag{20.17}$$

There are a number of ways to specify how the system is externally forced. One way, due to Lesser and Berkley, is to assume that the motion of the stapes in contact with the oval window determines the position of the oval window. Since $\partial \phi/\partial x$ is the x component of the fluid velocity, the boundary condition at $x = 0$ is

$$\frac{\partial \phi_1}{\partial x} = \frac{\partial F(y,t)}{\partial t}, \qquad 0 < y < l, \tag{20.18}$$

where $F(y, t)$ is the specified horizontal displacement of the oval window. Further, we assume that there is no horizontal motion at the far end, so that at $x = L$

$$\frac{\partial \phi_1}{\partial x} = 0, \qquad 0 < y < l. \tag{20.19}$$

20.2.3   An Analytical Solution

Because of the inherent symmetry of the problem, we seek solutions that are odd in y (Exercise 1). Thus, we consider only the problem in the upper region and drop the subscript 1.

When the input has a single frequency, $F(y, t) = \hat{F}(y) e^{i\omega t}$, then $\phi(x, y, t)$ is of the form $\hat{\phi}(x, y; \omega) e^{i\omega t}$ and similarly for the other variables. Looking for solutions of this form for all the variables, we obtain the equations

$$\nabla^2 \hat{\phi} \;=\; 0, \qquad \hat{p} + i\omega\rho\hat{\phi} = 0, \tag{20.20}$$

$$\frac{\partial \hat{\phi}}{\partial y} \;=\; i\omega\hat{\eta}, \qquad i\omega\hat{\eta}Z = -\hat{p} \qquad \text{on } y = 0, \tag{20.21}$$

$$\frac{\partial \hat{\phi}}{\partial x} \;=\; U_0 \qquad\qquad \text{on } x = 0, \tag{20.22}$$

$$\frac{\partial \hat{\phi}}{\partial x} \;=\; 0 \qquad\qquad \text{on } x = L, \tag{20.23}$$

$$\frac{\partial \hat{\phi}}{\partial y} \;=\; 0 \qquad\qquad \text{on } y = l, \tag{20.24}$$

where $Z = i\omega m + r + k/(i\omega)$ and $U_0 = i\omega\hat{F}$. By looking for solutions in the frequency domain, we have transformed the differential equations on the basilar membrane into algebraic equations. The term $i\omega Z$ is the frequency response of the damped harmonic oscillator, and Z, the *impedance*, is a function of x. Also note that in (20.21) the pressure is assumed to be an odd function of y.

Finally, we nondimensionalize the model equations by scaling x and y by L, Z by $i\omega\rho L$, and $\hat{\phi}$ by $U_0 L$; rearranging; and dropping the hats we get **James, I have always found this "then dropping the hats" to be quite distasteful. I have always thought that changes of variables should be explicit, so that readers do not have to reconstruct them. Jim**

$$\nabla^2 \phi \;=\; 0, \tag{20.25}$$

$$\frac{\partial \phi}{\partial y} \;=\; \frac{2\phi}{Z}, \qquad \text{on } y = 0, \tag{20.26}$$

$$\frac{\partial \phi}{\partial x} \;=\; 1 \qquad \text{on } x = 0, \tag{20.27}$$

$$\frac{\partial \phi}{\partial x} \;=\; 0 \qquad \text{on } x = 1, \tag{20.28}$$

$$\frac{\partial \phi}{\partial y} \;=\; 0 \qquad \text{on } y = \sigma, \tag{20.29}$$

where $\sigma = l/L$.

The analytical solution of this problem can be found using standard Fourier series (Lesser and Berkley, 1972). We look for solutions of the form

$$\phi = x\left(1 - \frac{x}{2}\right) - \sigma y\left(1 - \frac{y}{2\sigma}\right) + \sum_{n=0}^{\infty} A_n \cosh[n\pi(\sigma - y)]\cos(n\pi x), \qquad (20.30)$$

for some as yet undetermined constants A_n. Since ϕ satisfies all the boundary conditions except (20.26), we use (20.26) to determine the unknown coefficients A_n. This gives

$$\sigma \quad + \sum_{n=0}^{\infty} n\pi A_n \sinh(n\pi\sigma)\cos(n\pi x)$$

$$-\frac{2}{Z}\left[x(1 - \frac{x}{2}) + \sum_{n=0}^{\infty} A_n \cosh(n\pi\sigma)\cos(n\pi x)\right] = 0. \qquad (20.31)$$

Multiplying by $\cos(m\pi x)$, and integrating from 0 to 1, we find

$$A_m \alpha_m = f_m, \qquad (20.32)$$

where

$$\alpha_m = \frac{1}{Z}\cosh(m\pi\sigma) - \frac{1}{2}n\pi \sinh(m\pi\sigma) \qquad (20.33)$$

and

$$f_m = \sigma\delta_{m0} - \int_0^1 \frac{x(2-x)\cos(m\pi x)}{Z}\,dx = -\frac{2}{m^2\pi^2}. \qquad (20.34)$$

The coefficients A_n can now be evaluated explicitly, and substituted into (20.30). Typical results are shown in Fig. 20.7. The wave envelope has the same qualitative shape as von Békésy's results (Fig. 20.3), and the peak of the wave envelope moves toward the base of the cochlea as the frequency is increased.

20.2.4 Long-Wave and Short-Wave Models

Although the Fourier solution shows that the behavior of the Lesser and Berkley model is qualitatively correct, it would be nice to get a better analytical understanding of the behavior of the basilar membrane. There are two classic approximations of the model equations that allow further analytical investigation. The long-wave approximation, studied by Zwislocki and others, assumes that the wavelength is long compared to the depth of the cochlea, and the short-wave approximation of Ranke assumes the opposite, that the cochlea is effectively infinitely deep. Experiments suggest that the depth of the cochlea has little effect on the cochlear wave, supporting the short-wave theory. Indeed, even if one side of the cochlea is completely removed, there is little effect on the wave. However, neither model gives a complete description of cochlear behavior (Zwislocki, 1953).

Both short-wave and long-wave models can be derived as approximate cases of the model described in Section 20.2.2. To show this, we use a generalized form of the previous model (Siebert, 1974), as illustrated in Fig. 20.8. The only change is
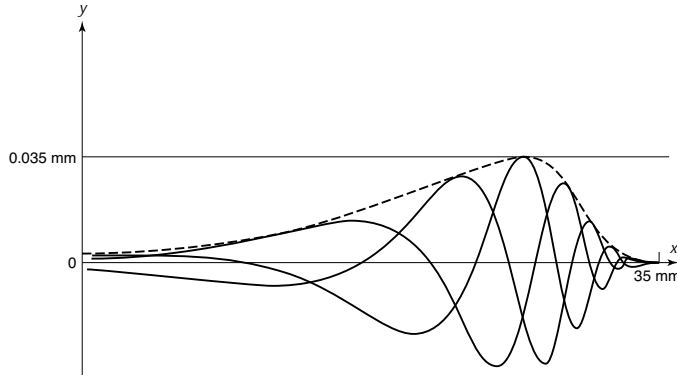
Figure 20.7: Results from the Lesser and Berkley model, showing a typical wave on the basilar membrane and the wave envelope. Parameters are $m = 0.05$ g/cm^2, $k = 10^7 e^{-1.5x}$ dynes/cm^3, $r = 3000 e^{-1.5x}$ dynes sec/cm^3, $\omega = 1000$/sec. The perilymph was assumed to have the same density as water, 1 g/cm^3. (Lesser and Berkley, 1972, Fig. 6.)

to assume that there is a direct mechanical forcing at the two ends of the basilar membrane. Modifying the equation of membrane motion (20.16) to include this direct forcing gives

$$m(x)\frac{\partial^2 \eta}{\partial t^2} + r(x)\frac{\partial \eta}{\partial t} + k(x)\eta = p_2(x,0,t) - p_1(x,0,t) + F_0(t)\delta(x) - F_L(t)\delta(x-L).$$
(20.35)

As before, we assume that the forcing is at a single frequency with $F_0(t) = F_0 e^{i\omega t}$ and $F_L(t) = F_L e^{i\omega t}$. It follows from (20.17), (20.20), and (20.35) that

$$\nabla^2 p(x,y) = 0, \tag{20.36}$$

$$-i\omega\eta = \frac{1}{i\omega\rho}\frac{\partial p(x,0)}{\partial y}, \tag{20.37}$$

$$Y(x)p(x,0) = -i\omega\eta(x) + \eta_0\delta(x) - \eta_L\delta(x-L), \tag{20.38}$$

where $Y = 2/Z, \eta_0 = \frac{F_0}{Z(0)}, \eta_L = \frac{F_L}{Z(L)}$, and where we have dropped the hats associated with the Fourier transform.

Because Laplace's equation is separable on a rectangular domain, we use Fourier series to write the solution of (20.36) as

$$p(x,y) = \sum_{n=-\infty}^{\infty} \alpha_n \frac{\cosh[2\pi n(y-l)/L]}{\cosh(2\pi nl/L)} e^{2\pi inx/L}, \tag{20.39}$$

where we have used the boundary condition $\partial p/\partial y = 0$ on $y = l$. It follows that

$$-i\omega\eta = \frac{1}{i\omega\rho}\frac{\partial p(x,0)}{\partial y} = -\frac{1}{i\omega\rho}\sum_{n=-\infty}^{\infty}\alpha_n \frac{2\pi n}{L}\tanh(2\pi nl/L)e^{2\pi inx/L}. \tag{20.40}$$
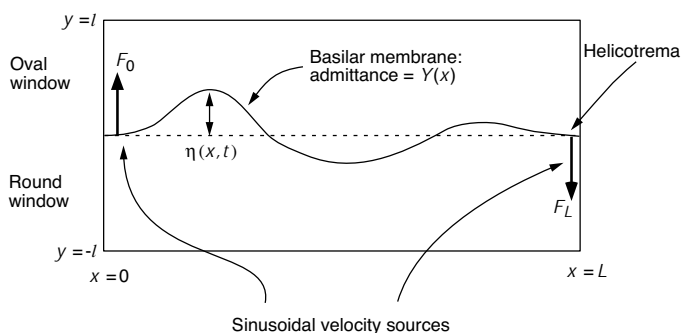
Figure 20.8: Schematic diagram of the cochlea model of Siebert (1974). It differs from the model of Lesser and Berkley in the boundary conditions at $x = 0$ and $x = L$, where it is assumed that there is direct mechanical forcing at both ends of the membrane.

Since our only interest is in the behavior of the basilar membrane, from now on we restrict our attention to $p(x, 0)$, which we denote by $p(x)$.

Equation (20.40) has been approximated in two principal ways. The first assumes that the depth of the cochlea is small compared to the wavelengths of the waves on the basilar membrane, the so-called *long-wave*, or *shallow-water*, approximation. The second approach, the *short-wave*, or *deep-water*, approximation, assumes that the wavelengths of the membrane waves are short compared to the cochlear depth.

The shallow-water approximation

In the shallow-water approximation, the wavelengths of the waves on the basilar membrane are assumed to be greater than the depth of the cochlea. As a consequence, we assume that $\alpha_n = 0$ for all $n > N$, for some integer N such that $Nl/L \ll 1$. Since the sum over n includes only those terms with $nl/L \ll 1$, it follows that for each term in the sum, $\tanh(2\pi nl/L)$ can be approximated by the lowest-order term in its Taylor expansion. Thus, $\tanh(2\pi nl/L) \approx 2\pi nl/L$, and so (20.40) becomes

$$-i\omega\eta \approx -\frac{l}{i\omega\rho} \sum_{n=-\infty}^{\infty} \alpha_n \left(\frac{2\pi n}{L}\right)^2 e^{2\pi i n x/L}. \tag{20.41}$$

However, a similar argument applied to (20.39) implies that

$$p(x) = \sum_{n=-\infty}^{\infty} \alpha_n e^{2\pi i n x/L}, \tag{20.42}$$

and thus, combining this with (20.41), we have

$$-i\omega\eta \approx \frac{l}{i\omega\rho} \frac{d^2 p}{dx^2}. \tag{20.43}$$

Combining this with (20.37) and (20.38), we get a single equation for $p(x)$,

$$Y(x)p(x) = \frac{l}{i\omega\rho}\frac{d^2p(x)}{dx^2} + \eta_0\delta_0(x) - \eta_L\delta_L(x). \qquad (20.44)$$

To convert the delta functions in this equation into boundary conditions, we integrate the differential equation (20.44) from $x = -\epsilon$ to $x = +\epsilon$ and let $\epsilon \to 0$ and find that

$$\frac{dp}{dx} = -i\omega\rho\eta_0 \qquad \text{at } x = 0, \qquad (20.45)$$

where we have assumed that $dp/dx = 0$ at $x = 0^-$, which is outside the boundaries of the cochlea. Similarly, integrating from $x = L - \epsilon$ to $x = L + \epsilon$ and letting $\epsilon \to 0$ gives

$$\frac{dp}{dx} = i\omega\rho\eta_L \qquad \text{at } x = L. \qquad (20.46)$$

Note that when $\eta_0 = 1$ and $\eta_L = 0$ (and since $p + i\omega\rho\phi = 0$), these boundary conditions are the same as (20.27) and (20.28) used in the Lesser–Berkley model.

The analysis of this equation exploits the fact that $Y(x)$ is a slowly varying function. To see what this means mathematically, note that $i\omega\rho Y(x)/l$ has dimensional units of length^{-2}, which determines the length scale (wavelength) of the spatial oscillations of $p(x)$. On the other hand, $Y(x)$ varies exponentially with a length constant of $\lambda^{-1} \approx 0.7$ cm. If the ratio of these two length constants is small, then we assert that $Y(x)$ is a slowly varying function. Furthermore, there is a rescaling of space, $x = z/q$, of (20.44), putting it into the dimensionless form

$$\frac{d^2p}{dz^2} + g^2(\epsilon z)p(z) = 0, \qquad (20.47)$$

where ϵ is a small positive number and $g^2(\epsilon z) = \frac{-i\omega\rho Y(z/q)}{lq^2}$ is of order one in amplitude and slowly varying in z. Note that q is an arbitrary length scale, chosen so that g^2 is of order one in amplitude; by assumption, $\lambda/q \ll 1$.

As a specific example, suppose that $m = 0, k(x) = k_0 e^{-\lambda x}, r(x) = r_0 e^{-\lambda x}$, in which case

$$\frac{i\omega\rho Y(x)}{l} = \frac{-2\omega^2\rho}{lk_0}\frac{e^{\lambda x}}{1 + i\omega r_0/k_0}. \qquad (20.48)$$

We set $q^2 = \frac{2\omega^2\rho}{lk_0}$, and then define ϵ by

$$\epsilon = \frac{\lambda}{2q}. \qquad (20.49)$$

If the parameters are such that $\epsilon \ll 1$, we have a slowly varying oscillation.

Problems of this type are well known in the theory of oscillations and can be solved approximately using multiscale analysis (Kevorkian and Cole, 1996; Keener, 1988). We wish to find approximate solutions of (20.47). If g were a constant ($\epsilon = 0$), the solution of (20.47) would be simply

$$p(z) = Ae^{igz} + Be^{-igz}. \qquad (20.50)$$

However, since g is assumed to be slowly varying, we expect this basic solution to be a reasonable local (but not global) approximation. To find a solution that has a longer range of validity, we introduce two scales, a slow scale variable $\sigma = \epsilon z$ and a fast variable τ for which $\frac{d\tau}{dz} = f(\epsilon z)$, where f is a function to be determined. It follows that the derivative $\frac{d}{dz}$ must be replaced by partial derivatives

$$\frac{d}{dz} = f(\sigma)\frac{\partial}{\partial\tau} + \epsilon\frac{\partial}{\partial\sigma}. \tag{20.51}$$

In terms of these two variables the original ordinary differential equation (20.47) becomes the partial differential equation

$$f^2(\sigma)\frac{\partial^2 p}{\partial\tau^2} + \epsilon f(\sigma)\frac{\partial^2 p}{\partial\sigma\partial\tau} + \epsilon\frac{\partial}{\partial\sigma}\left(f(\sigma)\frac{\partial p}{\partial\tau}\right) + \epsilon^2\frac{\partial}{\partial\sigma}\left(f(\sigma)\frac{\partial p}{\partial\sigma}\right) + g^2(\sigma)p = 0. \tag{20.52}$$

The obvious choice for f is $f = g$, because then the equation to leading order in ϵ is

$$\frac{\partial^2 p}{\partial\tau^2} + p = 0 \tag{20.53}$$

with general solution

$$P_0 = A(\sigma)e^{i\tau} + B(\sigma)e^{-i\tau}. \tag{20.54}$$

Notice that A and B are functions of the slow variable σ, since this is a partial differential equation.

To determine the functions A and B, we set $p = P_0 + \epsilon P_1 + O(\epsilon^2)$, collect like powers of ϵ, and determine that the equation for P_1 is

$$g^2(\sigma)\left(\frac{\partial^2 P_1}{\partial\tau^2} + P_1\right) = -g(\sigma)\frac{\partial^2 P_0}{\partial\sigma\partial\tau} - \frac{\partial}{\partial\sigma}\left(g(\sigma)\frac{\partial P_0}{\partial\tau}\right). \tag{20.55}$$

Since we want P_1 to be a periodic function of τ, we require that P_1 be "nonsecular," that is, that the right-hand side of (20.55) contain no terms proportional to $e^{i\tau}$ or $e^{-i\tau}$. It follows that

$$\frac{\partial}{\partial\sigma}(gA^2) = 0, \qquad \frac{\partial}{\partial\sigma}(gB^2) = 0, \tag{20.56}$$

or that

$$A(\sigma) = \frac{A_0}{\sqrt{g(\sigma)}}, \qquad B(\sigma) = \frac{B_0}{\sqrt{g(\sigma)}}, \tag{20.57}$$

from which we obtain, to lowest order in ϵ,

$$p = \frac{1}{\sqrt{g(\sigma)}}(A_0 e^{iG(z)} + B_0 e^{-iG(z)}), \tag{20.58}$$

where $G(z) = \int_0^z g(\epsilon z)dz$.

In terms of the original dimensioned variables, this is

$$p(x) = \phi^{-1/2}\left(A_1 \exp\left[i\int_0^x \phi(s)\,ds\right] + B_1 \exp\left[-i\int_0^x \phi(s)\,ds\right]\right), \tag{20.59}$$

where

$$\phi(x) = \sqrt{\frac{-i\omega\rho Y(x)}{l}}. \tag{20.60}$$

The constants A_1 and B_1 are determined from boundary conditions (20.45) and (20.46), and then the membrane displacement is found from the identity $i\omega\eta(x) = -Y(x)p(x)$.

The key feature of this solution is that it is oscillatory with an envelope, whose maximal amplitude and position are determined by the frequency ω. We get some idea of this behavior in the special case $m = 0$, $k(x) = k_0 e^{-\lambda x}$, and $r(x) = r_0 e^{-\lambda x}$ in which case $\phi(x) = \alpha e^{\lambda x/2}$, where $\alpha^2 = \frac{2\omega^2 \rho}{l(k_0 + i\omega r_0)}$. If we let $\alpha = \alpha_r + i\alpha_i$ and suppose that $\frac{\alpha_i}{\lambda} \gg 1$ (not valid at low frequencies), then with $\eta_L = 0$, we find that

$$\eta(x) = -\frac{1}{i\omega}Y(x)p(x) \approx \hat{A}\exp\left(\frac{3\lambda x}{4} - \frac{2\alpha_i}{\lambda}e^{\lambda x/2} + \frac{2i\alpha_r}{\lambda}e^{\lambda x/2}\right). \tag{20.61}$$

This represents an oscillation with exponentially increasing phase and amplitude

$$|\eta| \approx |\hat{A}|\exp\left(\frac{3\lambda x}{4} - \frac{2\alpha_i}{\lambda}e^{\lambda x/2}\right). \tag{20.62}$$

The maximal value of this envelope occurs at

$$x_p = -\frac{2}{\lambda}\ln\left(\frac{4\alpha_i}{3\lambda}\right). \tag{20.63}$$

The location of this maximum is dependent on frequency, as

$$\alpha_i \approx \sqrt{\frac{\rho\omega}{lr_0}}, \tag{20.64}$$

provided that ω is sufficiently large. Thus, for large ω we have

$$x_p = -\frac{1}{\lambda}\ln\left(\frac{16\rho\omega}{9l\lambda^2 r_0}\right). \tag{20.65}$$

The deep-water approximation

The second approach, the *short-wave*, or *deep-water*, approximation, assumes that the wavelength of the membrane waves is short compared to the cochlear depth. In this case the Fourier expansion of $p(x)$ includes only high frequencies, and so $\alpha_n = 0$ whenever $|n| < N$ for some large integer N. However, when $|n| > N$ and $l \gg L$, then $\tanh(2\pi nl/L) \approx \text{sign}(n)$. Thus, (20.40) becomes

$$-i\omega\eta \approx -\frac{1}{i\omega\rho}\sum_{n=-\infty}^{\infty}\alpha_n\frac{2\pi}{L}|n|e^{2\pi inx/L}. \tag{20.66}$$

Now we separate the sum into two pieces by defining two functions,

$$p_+(x) = \sum_{n=0}^{\infty}\alpha_n e^{2\pi inx/L} \tag{20.67}$$

and

$$p_-(x) = \sum_{n=-\infty}^{-1} \alpha_n e^{2\pi inx/L}, \tag{20.68}$$

and then observe that (20.38) becomes

$$Yp = Y(p_+ + p_-) \approx \frac{1}{\omega\rho}\left[\frac{dp_+}{dx} - \frac{dp_-}{dx}\right] + \eta_0\delta_0(x) - \eta_L\delta_L(x), \tag{20.69}$$

which we take to be the governing equation for p.

We can remove the delta function influence from this equation by integrating across the boundaries at $x = 0$ and $x = L$, and assuming that outside the cochlea, $p = 0$. This gives

$$\frac{1}{\omega\rho}[p_+(0) - p_-(0)] = \eta_0, \tag{20.70}$$

$$\frac{1}{\omega\rho}[p_+(L) - p_-(L)] = \eta_L. \tag{20.71}$$

Although p_+ is a linear combination of only positive (spatial) frequencies, the same is not true of Yp_+. However, if we assume that Y is a slowly varying function of x, then the Fourier series of Y with Fourier coefficients b_k has $b_k \approx 0$ whenever $|k| > k_0$, for some number k_0 that is small compared to the dominant frequency of p_+. It follows that

$$Yp_+ = \sum_{k=-\infty}^{\infty} c_k e^{2\pi ikx/L}, \tag{20.72}$$

where $c_k = \sum_{j=0}^{\infty} \alpha_j b_{k-j}$. If the dominant frequencies of p_+ and Y are separated, as stated above, then c_k is small for $k \le 0$. Thus we can approximate Yp_+ by its Fourier series with positive frequencies. A similar argument applies for Yp_-. With these approximations, (20.69) separates into a pair of differential equations for the positive and negative frequencies separately,

$$Y(x)p_\pm(x) \approx \frac{\pm 1}{\omega\rho}\frac{dp_\pm}{dx}, \qquad 0 < x < L. \tag{20.73}$$

These first-order linear equations can be integrated directly to get

$$p_\pm(x) = A_\pm \exp\left[\pm\omega\rho\int_0^x Y(\zeta)\,d\zeta\right] \tag{20.74}$$

for some constants $A_\pm$, so that

$$p = A_+ \exp\left[\omega\rho\int_0^x Y(\zeta)\,d\zeta\right] + A_- \exp\left[-\omega\rho\int_0^x Y(\zeta)\,d\zeta\right]. \tag{20.75}$$

We use the boundary conditions at $x = 0$ and $x = L$ to determine the constants $A_\pm$. From (20.70) and (20.71) it follows that these constants must satisfy the equations

$$A_+ - A_- = \omega\rho\eta_0, \qquad \gamma A_+ - \frac{1}{\gamma}A_- = \omega\rho\eta_L, \tag{20.76}$$

where $\gamma = \exp[\omega\rho \int_0^L Y(\zeta)\,d\zeta]$, from which it follows that

$$A_+ = \frac{\omega\rho}{\gamma^2 - 1}[\gamma\eta_L - \eta_0], \tag{20.77}$$

$$A_- = \frac{\omega\rho}{\gamma^2 - 1}[\gamma\eta_L - \gamma^2\eta_0]. \tag{20.78}$$

For physiological values of Y, $|\gamma| \gg 1$ for all except the lowest frequencies; for example, for the parameter values in Fig. 20.7, $|\gamma| = 40$ when $\omega = 800$, and $|\gamma| = 10^9$ when $\omega = 1500$. Since on physical grounds η_0 and η_L are not large, it follows that $|A_-| \approx -\omega\rho\eta_0 \gg |A_+|$. Finally, from (20.38) and (20.75), we find that the membrane displacement is given by

$$\eta = -i\rho\eta_0 Y(x) \exp\left[-\omega\rho \int_0^x Y(\zeta)d\zeta\right]. \tag{20.79}$$

The amplitude of η can be plotted as a function of x to give the envelope of the wave on the basilar membrane. The frequency response is similarly obtained, by fixing x and plotting $|\eta|$ as a function of ω. Typical results are shown in Fig. 20.9. The qualitative agreement with data is good, with the peak of the wave envelope moving toward the stapes as the frequency increases.

In the special case $m = 0, k(x) = k_0 e^{-\lambda x}, r(x) = r_0 e^{-\lambda x}$, we can calculate the waveform (20.79) to be

$$\eta = 2\eta_0\xi \exp[\lambda x + \beta(1 - e^{\lambda x})], \tag{20.80}$$

where

$$\beta = \frac{2\omega^3\rho r_0}{\lambda(k_0^2 + \omega^2 r_0^2)} + i\frac{2\omega^2\rho k_0}{\lambda(k_0^2 + \omega^2 r_0^2)} = \beta_r + i\beta_i \tag{20.81}$$

and

$$\xi = \frac{\omega\rho}{i\omega\rho + k_0}. \tag{20.82}$$

Here we again see an oscillatory waveform with an envelope of amplitude

$$|\eta| = 2\eta_0|\xi| \exp[\lambda x + \beta_r(1 - e^{\lambda x})], \tag{20.83}$$

the maximum of which occurs at

$$x_p = \frac{-1}{\lambda} \ln\left(\frac{2\omega^3\rho r_0}{\lambda(k_0^2 + \omega^2 r_0^2)}\right). \tag{20.84}$$

According to this expression, the peak of the envelope moves to the left (toward the base of the cochlea) as ω increases. The principal fault of the short-wave model is that the phase of the model waves increases much more than is observed experimentally.

A similar solution was found by Peskin (1976, 1981), who calculated an exact solution to a special case of the cochlear model. In his model the cochlear membrane was taken to be infinitely long, with $r(x)$ and $k(x)$ chosen to be decaying exponential functions with decay rate λ and a fluid container of height $\lambda l = \pi/2$. With these assumptions and simplifications, Peskin found the exact solution using conformal mapping and contour integration techniques.
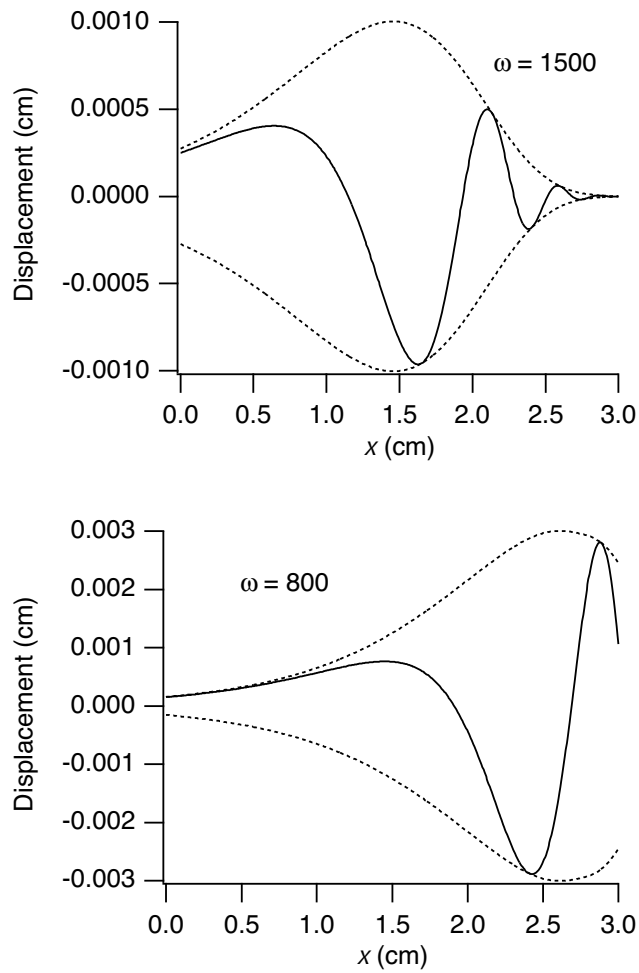
Figure 20.9: Plots of the amplitude of the wave on the basilar membrane for two different frequencies. The envelope of the wave is shown as a dotted line. Calculated from the deep-water approximation (20.75) using the same parameter values as in the Lesser and Berkley model (given in the caption to Fig. 20.7).

20.2.5   More Complex Models

In this chapter we have concentrated on the simpler models of the basilar membrane that assume that the cochlea is two-dimensional and that the basilar membrane can be described by a point impedance function, i.e., that each point of the basilar membrane acts as a damped harmonic oscillator, with no coupling along the length of the membrane except for that imposed indirectly via the fluid motion.

Although the wave motion on the basilar membrane is an important component of the hearing process, many other factors are involved (Pickles, 1982; Rhode, 1984; Hudspeth, 1985). Nonlinearities in the cochlear response and acoustic emissions suggest the presence of active feedback processes that modulate the waveform (Section 20.4). This feedback may occur in the outer hair cells and the organ of Corti. Simple hydrodynamic models do not reproduce the degree of tuning observed in the mammalian cochlea, and the precise tuning mechanism is still controversial. Many other, more complex, models have been constructed (see, for example, Steele, 1974; Steele and Tabor, 1979a,b; Inselberg and Chadwick, 1976; Chadwick et al., 1976; Chadwick, 1980; Holmes, 1980a,b, 1982). In general, these models use similar equations for the fluid flow, but model the basilar membrane in greater detail, including spatial coupling in the membrane. The resultant membrane equations are of fourth order in space, and heavy use is made of asymptotic expansions in the solution of the model equations. A particularly detailed study was performed by Steele (1974), who constructed a series of models ranging from a plate in an infinite body of fluid up to a tapered elastic basilar membrane, a cochlea with rigid walls, and flexible arches of Corti. Recent models are based on finite element descriptions of the basilar membrane, organ of Corti, and the outer hair cells, and incorporate acoustic, electrical and mechanical elements (Ramamoorthy et al., 2007), while the three-dimensional spiral nature of the cochlea has been modeled by Givelberg and Bunn (2001, 2003; Givelberg, 2004).

20.3   Electrical Resonance in Hair Cells

In many lower vertebrates frequency decomposition is performed, not by a wave on the basilar membrane, but by the hair cells themselves. Hair cells in the turtle cochlea and the bullfrog sacculus (to name but two examples) respond preferentially to stimuli of a certain frequency, and this band-pass response is mediated by the ionic channels in the hair cell membrane. At the top of each hair cell is the hair bundle, a group of stereocilia connected to each other at the tips by a thin *fiber*, called a tip link. Each stereocilium is rigid and, in response to a force applied at the tip, pivots around its base rather than bending. It is postulated that the tip links act like elastic springs connected directly to ionic channels such that when the hair bundle is deflected in one direction, the tip links pull channels open, while when the hair bundle is deflected in the opposite direction, the tip links relax and allow channels to close. The mechanically sensitive ion channels are nonselective, and the modulation of current flow through these channels results in hyperpolarization or depolarization of the hair cell membrane. The membrane potential is then modulated by other ionic channels, including K^+ channels, Ca^{2+}-sensitive K^+
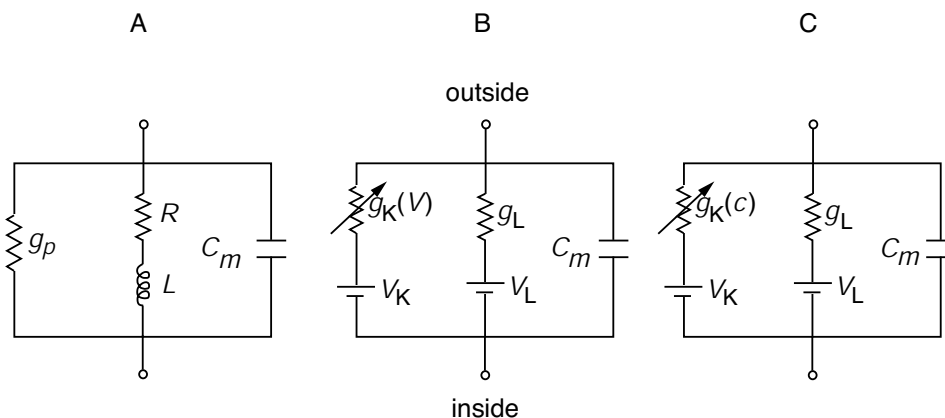
Figure 20.10: Electrical for electrical tuning, adapted from Ashmore and Attwell (1985). A: The basic model, with an inductance in place of ionic currents. B: Voltage-gated K^+ current, with a conductance that is increased by membrane depolarization. C: Ca^{2+}-gated current, with the K^+ conductance controlled by the intracellular concentration of Ca^{2+}, denoted by c.

channels, and voltage-sensitive Ca^{2+} channels. The structure, tuning, sensitivity, and function of hair cells are reviewed by Hudspeth (1985, 1989; Hudspeth and Gillespie, 1994), and these papers give a readable summary of the field.

In response to a step current input, the membrane potential of hair cells exhibits damped oscillations, with a period and amplitude dependent on the size of the step. Thus, each cell has a natural frequency of oscillation and responds best to a stimulus at a similar frequency. Crawford and Fettiplace (1981) and Ashmore and Attwell (1985) have developed simple models for electrical resonance that while not based on the details of known mechanisms, provide a good description of the experimental results. Later work by Lewis and Hudspeth (1988a,b), using a more detailed model, showed that the measured properties of the ionic conductances are sufficient to explain resonance in the hair cells of the bullfrog sacculus.

20.3.1 An Electrical Circuit Analogue

The models of Crawford and Fettiplace (1981) and Ashmore and Attwell (1985) are based on the electrical circuit shown in Fig. 20.10A. In response to a current input I, the voltage V is given by

$$\frac{d^2V}{dt^2} + \gamma\frac{dV}{dt} + \omega_0^2 V = f(t), \tag{20.85}$$

where

$$\gamma = \frac{g_p}{C_m} + \frac{R}{L}, \tag{20.86}$$

$$\omega_0^2 = \frac{g_p R + 1}{L C_m}, \tag{20.87}$$

$$f(t) = \frac{1}{C_m}\frac{dI}{dt} + \frac{IR}{LC_m}. \tag{20.88}$$

It is simplest to demonstrate resonance when $f(t) = e^{i\omega t}$, in which case $V = V_1(\omega)e^{i\omega t}$, where

$$V_1(\omega) = \frac{1}{\omega_0^2 - \omega^2 + i\gamma\omega}. \tag{20.89}$$

Thus, $|V_1|$ has a band-pass frequency response, with a maximum at $\hat{\omega}$, where $\hat{\omega}^2 = \omega_0^2 - \gamma^2/2$. Solutions of (20.85) are of the form $\exp(-\gamma t/2)\exp\left(\pm i\sqrt{\omega_0^2 - \gamma^2/4}\right)$, and thus $\hat{\omega}$ is slightly smaller than the natural frequency of oscillation of the system. However, if damping is small (i.e., if γ is small), the maximum amplitude of the frequency response occurs at approximately the natural frequency of oscillation. The sharpness of the peak of $|V_1|$ is a measure of the degree of tuning of the electrical circuit, with sharper peaks giving greater frequency selectivity. Since

$$\frac{d^2}{d\omega^2}[(\omega_0^2 - \omega^2)^2 + \gamma^2\omega^2]\Big|_{\omega=\hat{\omega}} = 4\gamma^2(2Q^2 - 1), \tag{20.90}$$

where

$$Q = \frac{\omega_0}{\gamma}, \tag{20.91}$$

it follows that Q, often called the *quality factor*, is a useful measure of the degree of tuning. As Q increases, so does the frequency selectivity of the circuit.

We now consider the response of the circuit when the input is a sinusoidally varying current. When $I = e^{i\omega t}$,

$$V_1(\omega) = \frac{\frac{R}{LC_m} + \frac{i\omega}{C_m}}{\omega_0^2 - \omega^2 + i\gamma\omega}, \tag{20.92}$$

which again corresponds to a band-pass filter, with the maximum response occurring at $\hat{\omega}$, where

$$(\hat{\omega}^2)^2 + 2\left(\frac{R}{L}\right)^2\hat{\omega}^2 + \left(\frac{R}{L}\right)^2(\gamma^2 - 2\omega_0^2) = 0. \tag{20.93}$$

Crawford and Fettiplace (1981) used a model of this type (without the leak conductance g_p) to determine the electrical tuning characteristics of hair cells from the turtle cochlea. By comparison of these tuning curves with tuning curves obtained by acoustic stimulation of the hair cells they were able to determine that electrical resonance can account for most of the frequency selectivity of the hair cell.

Although the above circuit exhibits the required resonance, it would be much more satisfactory to explain electrical resonance in terms of components that have a more direct connection to the hair cell. This can be done in at least two ways. In Fig. 20.10B and C two circuits are shown, one involving a voltage-sensitive K^+ conductance, the other a Ca^{2+}-sensitive K^+ conductance, that, formally at least, are equivalent to the circuit in Fig. 20.10A.

Consider first the circuit in Fig. 20.10B. If the leak has a constant conductance, and the K^+ conductance is a function of time and voltage, then

$$I = C_m\frac{dV}{dt} + g_L(V - V_L) + f g_K(V - V_K), \tag{20.94}$$

$$\tau \frac{df}{dt} = f_\infty - f, \tag{20.95}$$

where we take a linear approximation for f_∞,

$$f_\infty = f_r + \mu(V - V_r). \tag{20.96}$$

Here, V_r is assumed to be the resting membrane potential, f_r is the value of f when $V = V_r$, and μ is the slope of the activation curve at the steady state. Note that at steady state,

$$0 = g_L(V_r - V_L) - g_K f_r(V_K - V_r), \tag{20.97}$$

and thus V_L can be eliminated.

It follows that

$$\frac{dI}{dt} + \frac{I}{\tau} = C_m \frac{d^2\tilde{V}}{dt^2} + \left(g_L + g_K f_r + \frac{C_m}{\tau} \right) \frac{d\tilde{V}}{dt} + \left(\frac{g_L + g_K f_r + g_K(V_r - V_K)\mu}{\tau} \right) \tilde{V}, \tag{20.98}$$

where $\tilde{V} = V - V_r$ and where we have linearized the equation around V_r by assuming that $V \approx V_r$. Equation (20.98) is equivalent to (20.85)–(20.88) if

$$L = \frac{\tau}{g_K(V_r - V_K)\mu}, \tag{20.99}$$

$$R = \frac{1}{g_K(V_r - V_K)\mu}, \tag{20.100}$$

$$g_p = g_L + g_K f_r. \tag{20.101}$$

A similar procedure can be followed for the circuit in Fig. 20.10C, in which the K^+ conductance is Ca^{2+}-dependent rather than voltage-dependent, but extra assumptions about the Ca^{2+} kinetics must be made. As a first approximation, it is assumed that Ca^{2+} enters the cell through channels at a rate that is a linear function of voltage, with slope θ, and is removed with first-order kinetics, i.e., at a rate proportional to its concentration. Finally, it is assumed that the proportion of open K^+ channels is linearly related to the Ca^{2+} concentration. Thus,

$$I = C_m \frac{dV}{dt} + g_L(V - V_L) + g_K kc(V - V_K), \tag{20.102}$$

$$W \frac{dc}{dt} = \frac{I_r + \theta(V - V_r)}{F} - pc, \tag{20.103}$$

where c denotes Ca^{2+} concentration, F is Faraday's constant, W is the cell volume, p is the rate of Ca^{2+} pumping, and I_r is the steady Ca^{2+} current when $V = V_r$. The constant k is the rate at which Ca^{2+} activates the K^+ current. Again, linearizing this system about the steady state gives a system that is equivalent to (20.85)–(20.88), provided that

$$L = \frac{WF}{g_K(V_r - V_K)k\theta}, \tag{20.104}$$

$$R = \frac{pF}{g_K(V_r - V_K)k\theta}, \tag{20.105}$$

$$g_p = g_L + g_K kc_r, \tag{20.106}$$

where c_r is the steady Ca^{2+} concentration at the resting potential.

Ashmore and Attwell showed that although the model with the voltage-sensitive K^+ conductance can generate a wide range of optimal frequencies, physiological values for the parameters result in values for the quality factor Q that are an order of magnitude too low. Thus, for reasonable parameters, the model can distinguish between frequencies, but not sharply enough. Experimental values for Q are often 5 or more, while Q values in the model are not above 0.7. This, they argue, is the result of the low value of μ: a physiological value for μ is about 0.33 mV^{-1}, but Q is large enough in the model with μ about 3 mV^{-1}. Thus, it appears that the activation of the K^+ current by voltage is not steep enough to account for the observed resonance in hair cells.

In the third model, however, the activation of the K^+ current by Ca^{2+} can be made much steeper. Here, the effective activation slope of the K^+ channel is $k\theta/(pF)$, which can be made large by decreasing the pump rate p or by increasing the sensitivity of the K^+ channel to Ca^{2+}. Ashmore and Attwell conclude that frequency tuning in hair cells is more likely the result of a Ca^{2+}-sensitive K^+ conductance than of a voltage-sensitive conductance.

20.3.2   A Mechanistic Model of Frequency Tuning

This conclusion has been upheld by the more recent, and more detailed, work of Hudspeth and Lewis (1988a,b). Based on a series of experiments in which they measured the kinetic properties of the ionic conductances in saccular hair cells of the bullfrog, Hudspeth and Lewis constructed a detailed model for electrical resonance in these cells. They concluded that the observed properties of the Ca^{2+}-sensitive K^+ conductance, in concert with a voltage-sensitive Ca^{2+} conductance and a leak, are a sufficient quantitative explanation of frequency tuning in these cells.

A schematic diagram of their model is given in Fig. 20.11. Mechanical deflection of the hair bundle opens transduction channels in the hair bundle allowing the entry of positive ions, mostly K^+. The consequent depolarization of the cell activates voltage-gated Ca^{2+} channels, and the intracellular Ca^{2+} concentration rises. This, in turn, opens Ca^{2+}-sensitive K^+ channels. K^+ ions flow out of the cell, and the cell repolarizes. Ca^{2+} balance is maintained by pumps that remove Ca^{2+} from the hair cell. One crucial, and rather unusual, feature of the model is that K^+ can both enter and leave the cell passively. Since the hair bundle projects into the scala media, the fluid surrounding the hair bundle (the endolymph in the case of hair cells in the cochlea) is of different composition from that surrounding the base of the hair cell, having a high K^+ and a low Na^+ concentration.

We do not present all the many details of the model here. Suffice it to say that it is assumed that there are three significant ionic currents contributing to resonance in the hair cell: a voltage-gated Ca^{2+} current, a Ca^{2+}-activated K^+ current, and a leak current. Thus, for an applied current I,

$$I = C_m \frac{dV}{dt} + I_c + I_{kc} + I_{\text{L}}. \tag{20.107}$$

The voltage-gated Ca^{2+} current I_c and the leak currents are described by similar equations as in the Hodgkin–Huxley model (Chapter 5). The model for the Ca^{2+}-
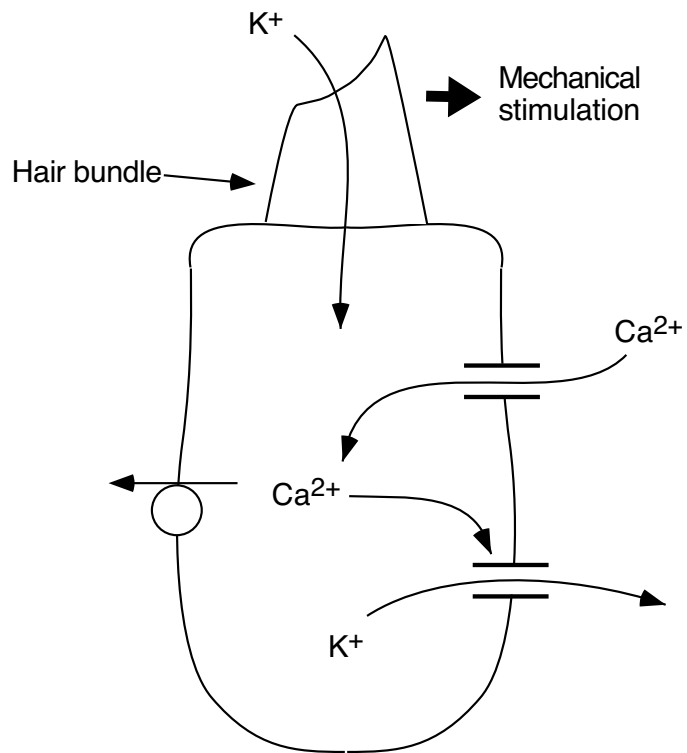
Figure 20.11: Schematic diagram of a model for electrical tuning in hair cells, adapted from Hudspeth (1985).
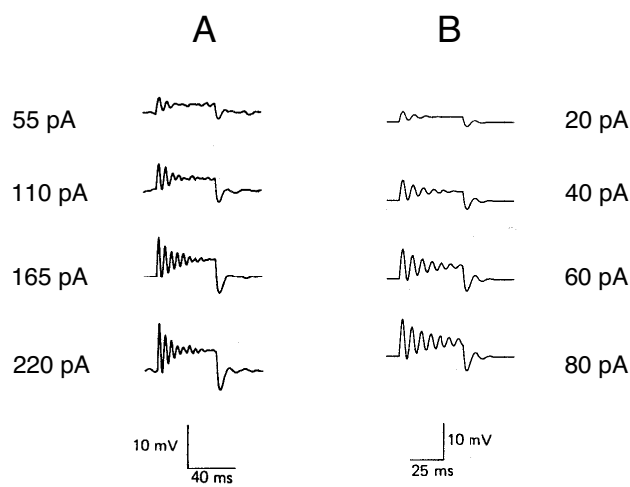
Figure 20.12: A: Responses of bullfrog saccular hair cells to depolarizing current steps. As the current step increases in size, the hair cells show more pronounced oscillatory behavior. (Adapted from Hudspeth and Lewis, 1988b, Fig. 3.) B: Responses of the model to current steps. (Adapted from Hudspeth and Lewis, 1988b, Fig. 6.)

activated K^+ channel, I_{kc}, is considerably more complicated. It is assumed that the channel has three closed states and two open states: binding of two Ca^{2+} ions converts the channel into a state in which it can spontaneously open, while the binding of an additional Ca^{2+} ion can prolong opening. The transition rate constants are dependent on Ca^{2+} and voltage. Finally, Ca^{2+} handling is treated simply by assuming that Ca^{2+} enters through the Ca^{2+} channel and is removed by a first-order process.

The parameters (of which there are about 30) were determined by constraining the model to agree with voltage-clamp data from a single cell, and then the response of the model to current pulses was investigated. It was found that depolarizing current steps induced damped membrane potential oscillations in the model, with a frequency and amplitude dependent on the magnitude of the current step, in close agreement with experimental data (Fig. 20.12).

To simulate a transduction current, a term $I_{\mathrm{T}} = g_{\mathrm{T}}(V - V_{\mathrm{T}})$ is added to the right-hand side of (20.107). The transduction conductance is assumed to be a function of hair cell displacement, which, in turn, is assumed to vary sinusoidally. The resultant model frequency response is band-pass in nature, with the maximal response at frequency 112 Hz and a quality factor of 3. The frequency at which the response is maximal (the resonant frequency) is a function of the model parameters, and realistic changes in the model parameters can account for the range of experimentally observed resonant frequencies in the bullfrog sacculus. In particular, because the resonant frequency is sensitive to g_{kc}, the model predicts that controlling the number of Ca^{2+}-sensitive K^+ channels is one simple way in which cells could tune their frequency response.

20.4 The Nonlinear Cochlear Amplifier

In Chapter 19 we saw that photoreceptors are able to respond in a reliable and reproducible way to single photons; the visual system thus attains the maximum possible sensitivity. Similarly, one of the most extraordinary things about the cochlea is its extreme sensitivity, which appears to be limited only by thermal noise (Manley, 2001).

The ability of the cochlea to detect low amplitude signals is surprising, given that the cochlear fluid would be expected to damp out signals with low power. As Hudspeth (2005) has so graphically expressed it, asking the basilar membrane to vibrate under such conditions is akin to asking a tuning fork to vibrate in honey. As early as 1948, Gold pointed out this difficulty, and proposed the existence of some active mechanism, amplifying the response to small sounds.

Such high sensitivity (as well as sharp frequency tuning) is believed to result from active mechanical amplification by hair cells. The exact molecular basis for such amplification is unclear, and almost certainly differs in different species. In mammals, outer hair cells contract and elongate in response to depolarization and hyperpolarization respectively. Vibrations of the basilar membrane cause lateral movement of the hair bundle on the top of the outer hair cell, which in turn opens and closes ion channels in the stereocilia, leading to changes in membrane potential (Hudspeth, 1997; Nobili et al., 1998; Manley, 2000; Hudspeth et al., 2000). It is fascinating to note that the opening and closing of ion channels in response to movement of the hair bundle is a direct mechanical interaction, and thus extremely fast. Elastic springs (tip links) connect the tip of one stereocilia directly to the ion channel; when the stereocilia moves, the tip link is pulled, thus opening the ion channel. It seems that these changes in the length of the outer hair cell result from the contraction or expansion of billions of proteins within the outer membrane, and that these proteins react to the membrane potential directly, without any need for ATP. However, the exact identity and properties of these proteins remains elusive (Ashmore et al., 2000).

20.4.1 Negative stiffness, adaptation, and oscillations

Non-mammalian vertebrates lack outer hair cells, and it is believed that mechanical amplification is carried out by the hair cells themselves. Hair bundles of the bullfrog sacculus display spontaneous twitches, or oscillations that, when entrained by a stimulus of the resonant frequency, respond with an amplitude about twice that of the initial stimulus.

One possible mechanism for such spontaneous oscillations has been proposed by Martin et al. (2000), and is based on the fact that the hair bundle has a negative stiffness for small displacements. This is an extraordinary result. A typical spring (as taught in first year Math and Physics classes) has a positive stiffness; when perturbed from its rest position, the spring exerts a force that tries to restore the rest position, i.e., a positive displacement gives a positive force, while a negative displacement gives a negative force.

But hair bundles from the bullfrog sacculus have a very much more interesting response (Fig. 20.13A). A small positive displacement results in a negative force,
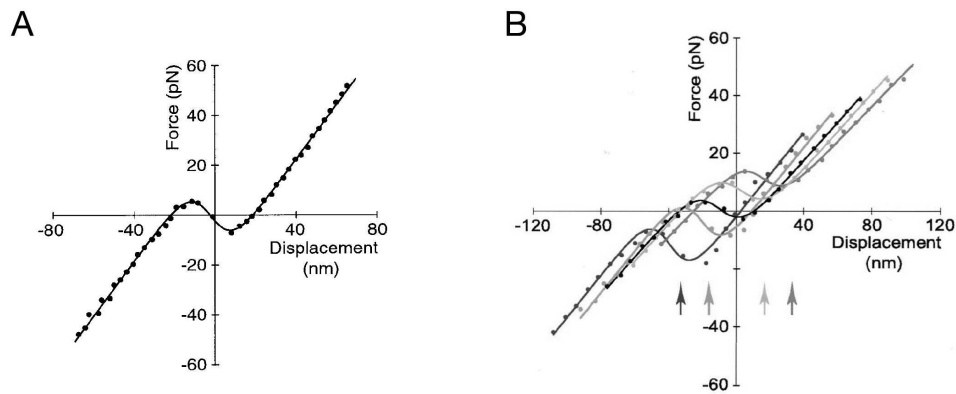
Figure 20.13: A: Negative stiffness in hair bundles from the bullfrog sacculus. Small perturbations from the zero-displacement resting state cause greater displacements, and thus zero displacement is an unstable steady state (Martin et al., 2000, Fig. 1C). B: Adaptation of the force-displacement curve. When a fixed displacement is externally imposed, the force-displacement curve shifts in the direction of the applied displacement, and also moves vertically. The black curve is the force-displacement curve in the absence of any externally imposed displacement, while the other curves, in varying shades of gray, were measured after the imposed displacement had been maintained for 100 ms. The arrows along the bottom show the positions of the externally imposed offset displacements (Martin et al., 2000, Fig. 2). **Springer: this figure will need permissions and massaging. I've amalgamated bits from two different figures. JS**

tending to *increase* the displacement, leading to positive feedback and an unstable rest state. Similarly, a negative displacement causes a positive force. Hence there are two stable rest states; one with a positive displacement, one with a negative displacement.

Furthermore, the hair bundle displays adaptation, in a manner reminiscent of photoreceptor adaptation (Chapter 19). This is illustrated in Fig. 20.13B. If a fixed displacement is externally imposed, the force-displacement curve shifts both horizontally and vertically so as to bring the position of the imposed displacement within the region of negative stiffness. Hence, the response to a step increase in load is an initial large increase in force, followed by a slower relaxation. If the maintained displacement is large enough, this shift of the force-displacement curve results in the disappearance of two steady states in a saddle-node bifurcation.

Thus, spontaneous oscillations can arise. When the hair bundle tries to sit at the stable steady state with positive displacement, the force-displacement curve gradually adapts, shifting up and to the right, until this stable steady state no longer exists. The hair bundle is then forced to flip to the other stable steady state (at a negative displacement), whereupon the process repeats itself in reverse. This results in a spontaneous oscillation where the hair bundle is alternately flipping between the two stable steady states, and the force-displacement curve is continually adapting. It is left as an exercise (Exercise 8) to formulate a mathematical model of this process.

20.4.2 Nonlinear compression and Hopf bifurcations

Another important feature of the cochlea is that low amplitude signals are more sharply tuned than signals of high amplitude, and thus show greater frequency selectivity. Furthermore, there is no audible sound for which the cochlear response is linear; cochlear responses are essentially nonlinear.

Typical experimental data (from a living chinchilla) are shown in Fig. 20.14. At low signal amplitudes the frequency-response curve is sharply peaked, but becomes less so at high amplitudes. Also, at the resonant frequency (shown by the vertical dashed line), the response quickly saturates as the stimulus amplitude increases. This is called *nonlinear response compression*. Stated another way, the velocity of the response to a small-amplitude stimulus is much greater than would be expected were the cochlea to behave in a linear manner.

Eguíluz et al. (2000) have shown that both these properties of the response could result from the proximity of a Hopf bifurcation. Since we have already seen from biophysical models that bullfrog saccular hair cells appear to be dynamically close to a Hopf bifurcation, this provides a plausible and appealing explanation of the responses seen in Fig. 20.13.

In normal form (Wiggins, 2003), the equations for a Hopf bifurcation are

$$\frac{dx}{dt} = \mu x - \omega_0 y - (x^2 + y^2)x, \tag{20.108}$$

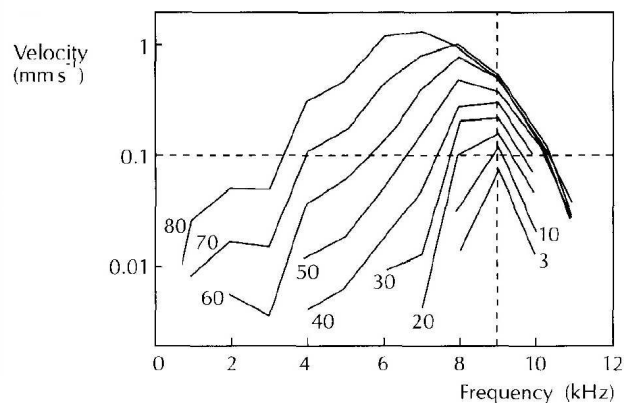$$\frac{dy}{dt} = \omega_0 x + \mu y - (x^2 + y^2)y, \tag{20.109}$$

Figure 20.14: The velocity of one point on the basilar membrane of a live chinchilla, plotted as a function of frequency. Each curve corresponds to a different stimulus amplitude, labeled in decibels. At low stimulus strength the frequency-response curve is sharply peaked, but becomes less so as the stimulus amplitude increases. In addition, the response at the resonant frequency is not a linear function of stimulus amplitude, but saturates (Ruggero, 1992, Fig. 1b). **Springer: this figure will need permission and massaging. JS**

or, in complex form,

$$\frac{dz}{dt} = (\mu + i\omega_0)z - |z|^2 z, \tag{20.110}$$

where $z = x + iy$. This system has a Hopf bifurcation at $\mu = 0$, and the oscillations that appear at the Hopf bifurcation have period $2\pi/\omega_0$, and have the form $z = \sqrt{\mu}e^{i\omega_0 t}$.

If we drive this oscillator with a forcing term $\alpha e^{i\omega t}$, and look for solutions of the form $z = Ae^{i(\omega t + \phi)}$, we get

$$(iA(\omega - \omega_0) - \mu A + A^3)e^{i\phi} = \alpha. \tag{20.111}$$

Since we are interested only in the amplitude, A, of the response, it suffices to take the modulus of both sides of (20.111), from which it follows that

$$\alpha^2 = A^6 - 2\mu A^4 + [\mu^2 + (\omega - \omega_0)^2]A^2. \tag{20.112}$$

For a given stimulus strength (i.e., a given α), we can plot A as a function of stimulus frequency, ω. The results are shown in Fig. 20.15. When α is small, the response has a sharp frequency tuning, and, at the resonant frequency $\omega = \omega_0$, the amplitude shows nonlinear compression. This behavior is qualitatively the same as that seen experimentally (Fig. 20.14). At the resonant frequency, $\omega = \omega_0$, (20.112) becomes

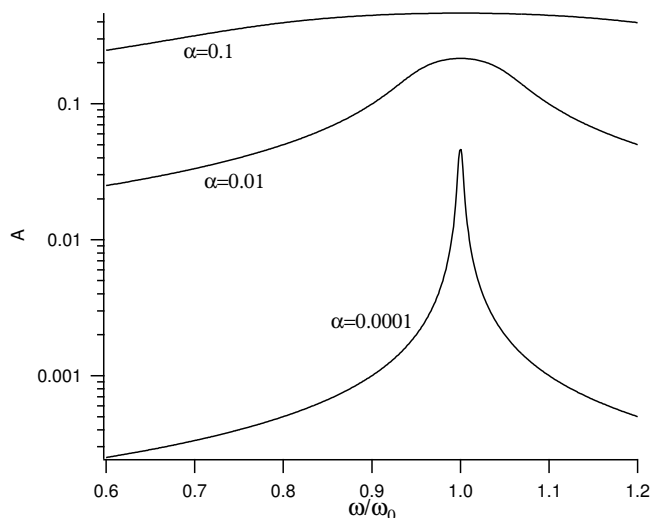$$\alpha = A^3 - \mu A, \tag{20.113}$$

Figure 20.15: The amplitude, A, of the response of (20.108)-(20.109) to an input of the form $\alpha e^{i\omega t}$.

from which we see that, at the Hopf bifurcation point (i.e., when $\mu = 0$) A depends on the 1/3rd power of the input amplitude, and thus the response is nonlinearly compressed, as seen in the experimental data.

It is still unclear whether or not the hair cells of any particular animal actually tune their responses in this way by sitting close to a Hopf bifurcation, and the exact mechanical forces that are responsible for nonlinear compression, sharp tuning, and amplification remain unclear. Nevertheless, this simple theory provides an intriguing explanation of this phenomenon.

Exercises

1. Show that if $F(y, t)$ in the Lesser and Berkley model is an odd function of y, it is sufficient to consider only the solution in the region $0 < y < l$. Hint: show that $\phi_2(y, t) = -\phi_1(-y, t)$ and $p_2(y, t) = -p_1(-y, t)$ satisfy the differential equations for ϕ_2 and p_2. Hence the potential and pressure are odd functions of y.

2. Formulate a model of the cochlea in which the basilar membrane is spatially coupled in the x direction as if it were a damped string. How does the Fourier transform of this problem differ from the Lesser–Berkley model (20.25)–(20.29)?

3. Show that (20.75) describes two waves moving in opposite directions. Hint: Y has an imaginary component, and thus the terms in (20.75) have phases with opposite signs. What are the envelopes of the waves?

4. If the functions $m(x), r(x)$, and $k(x)$ are proportional to the same exponential, then the solution of (20.44) can be found exactly.

   (a) Suppose that $m = m_0 e^{-\lambda x}$, $k(x) = k_0 e^{-\lambda x}$, $r(x) = r_0 e^{-\lambda x}$. Show that (20.44) becomes

$$\frac{d^2 p}{dx^2} + \alpha^2 e^{\lambda x} p = 0, \qquad (20.114)$$

   where $\alpha^2 = \frac{2\omega^2 \rho}{l(i\omega r_0 + k_0 - \omega^2 m_0)}$.

   (b) Show that the transformation $s = \frac{2\alpha}{\lambda} e^{\lambda x/2}$ transforms (20.114) into

$$s\frac{d}{ds}\left(s\frac{dp}{ds}\right) + s^2 p = 0, \qquad (20.115)$$

   which is Bessel's equation of order zero. Thus, the general solution of (20.114) is

$$p(x) = A J_0\left(\frac{2\alpha}{\lambda}e^{\lambda x/2}\right) + B Y_0\left(\frac{2\alpha}{\lambda}e^{\lambda x/2}\right), \qquad (20.116)$$

   where J_0 and Y_0 are the zeroth-order Bessel functions of the first and second kind, or equivalently,

$$p(x) = \tilde{A} H_0^{(1)}(s) + \tilde{B} H_0^{(2)}(s), \qquad (20.117)$$

   where $H_0^{(1)}(s)$ and $H_0^{(2)}(s)$ are the zeroth-order Hankel functions of first and second kind. Use the boundary conditions (20.45) and (20.46) to determine the coefficients $\tilde{A}$ and $\tilde{B}$.

   (c) Use the asymptotic behavior of the Hankel functions (Keener, 1988)

$$H_0^{(1)}(s) \sim \left(\frac{2}{\pi s}\right)^{1/2} e^{i(s-\pi/4)}, \qquad H_0^{(2)}(s) \sim \left(\frac{2}{\pi s}\right)^{1/2} e^{-i(s-\pi/4)}$$

$$(20.118)$$

   to approximate $p(x)$ in the case that $\tilde{B} = 0$. Show that $\eta(x)$ is approximated by (20.61). Under what conditions is this approximation valid?

5. For the long-wave model it was claimed that the phase of η, where η is given by (20.80), does not agree with experimental data. Confirm this by showing that for a fixed ω, the phase increases exponentially with x, and that the phase does not approach zero as ω approaches zero.

6. Compare the location of the envelope maximum x_p for the shallow-water approximation (20.65) in the case $l\lambda = \pi/2$ with that for the deep-water approximation (20.84), for large ω.

7. Let $\eta_0 = 1$, $\eta_L = 0$, and $m = 0.05 e^{-1.5x}$, and let the other parameters be the same as in the Lesser and Berkley model. Use the boundary conditions to solve for A_1 and B_1 in (20.59), and thus calculate the displacement of

the basilar membrane for the shallow-water model. Compare the shallow-water and deep-water models by plotting the displacements for high and low frequencies. How does the behavior of the long-wave model change as l is decreased?

8. Formulate a mathematical model of spontaneous oscillations that incorporates the force-displacement adaptation described in Section 20.4.1, and show that the model can exhibit relaxation oscillations. (Hint: Use a second-order differential equation to model the hair bundle as a damped spring, and at least one additional first-order equation to model adaptation of the spring. The model equations need not be biophysically realistic, but merely a qualitative caricature of the process.)

Part I

Solutions

Selected Solutions to Chapter 1

1. Consider the simple chemical reaction in which two monomers of A combine to form a dimer B, according to

$$A + A \underset{k_-}{\overset{k_+}{\rightleftharpoons}} B. \tag{20.119}$$

(a) Use the law of mass action to find the differential equations governing the rates of production of A and B.

(b) What quantity is conserved? Use this conserved quantity to find an equation governing the rate of production of A that depends only on the concentration of A.

(c) Non-dimensionalize this equation and show that these dynamics depend on only one dimensionless parameter.

Solution

(a) Using the law of mass action, we find the two differential equations

$$\frac{da}{dt} = 2k_- b - 2k_+ a^2, \tag{20.120}$$

$$\frac{db}{dt} = k_+ a^2 - k_- b, \tag{20.121}$$

where $a = [A]$, $b = [B]$ and where the factor 2 in the first equation denotes that 2 molecules of species A are used up or produced by each of the reactions.

(b) Since $\frac{da}{dt} + 2\frac{db}{dt} = 0$, the conserved quantity is $a + 2b = B_0$. Using this conserved quantity, the equation for a becomes
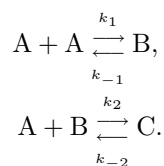
$$\frac{da}{dt} = k_-(B_0 - a) - 2k_+ a^2. \tag{20.122}$$

(c) Introduce dimensionless variables $u = \frac{a}{B_0}$, and $t = \frac{\tau}{k_-}$ and find

$$\frac{du}{d\tau} = 1 - u - \frac{2k_+ B_0}{k_-} u^2. \tag{20.123}$$

The sole dimensionless parameter is $\frac{2k_+ B_0}{k_-}$.

2. In the real world trimolecular reactions are rare, although trimerizations are not. Consider the following trimerization reaction in which three monomers of A combine to form the trimer C,

$$A + A \underset{k_{-1}}{\overset{k_1}{\rightleftharpoons}} B,$$

$$A + B \underset{k_{-2}}{\overset{k_2}{\rightleftharpoons}} C.$$

(a) Use the law of mass action to find the rate of production of the trimer C.

(b) Suppose $k_{-1} \gg k_{-2}, k_2 A$. Use the appropriate quasi-steady state approximation to find the rates of production of A and C, and show that the rate of production of C is proportional to $[A]^3$. Explain in words why this is so.

Solution

(a) Using the law of mass action, we find

$$\frac{da}{dt} = 2k_{-1}b - 2k_1 a^2 + k_{-2}c - k_2 ab, \tag{20.124}$$

$$\frac{db}{dt} = k_1 a^2 - k_{-1}b + k_{-2}c - k_2 ab, \tag{20.125}$$

$$\frac{dc}{dt} = k_2 ab - k_{-2}c, \tag{20.126}$$

where $a = [A]$, $b = [B]$, and $c = [C]$.

(b) If k_{-1} is large compared to other rate constants, then b equilibrates rapidly (as an exponential) to its quasi-steady state,

$$b = \frac{k_1 a^2 + k_{-2}c}{k_{-1} + k_2 a}. \tag{20.127}$$

If we substitute this quasi-steady state approximation into the equations governing c and a, we find

$$\frac{dc}{dt} = \frac{k_2 k_1 a^3 - k_{-2}k_{-1}c}{k_{-1} + k_2 a}, \qquad \frac{da}{dt} = -3\frac{dc}{dt}. \tag{20.128}$$

If $k_{-1} \gg k_2 a$, this further reduces to

$$\frac{dc}{dt} = \frac{k_2 k_1}{k_{-1}} a^3 - k_{-2} c. \tag{20.129}$$

Here, the rate at which the reaction takes place is represented by a cubic term because, since k_{-1} is large, the dimer B comes apart quickly unless it is stabilized by a collision with a third monomer of A.

3. The length of microtubules changes by a process called treadmilling, in which monomer is added to one end of the microtubule and taken off at the other end. To model this process, suppose that monomer A_1 is self-polymerizing in that it can form dimer A_2 via

$$A_1 + A_1 \xrightarrow{k_+} A_2. \tag{20.130}$$

Furthermore, suppose A_1 can polymerize an n-polymer A_n at one end making an $n + 1$-polymer A_{n+1}

$$A_1 + A_n \xrightarrow{k_+} A_{n+1}. \tag{20.131}$$

Finally, degradation can occur one monomer at a time from the opposite end at rate k_-. Find the steady state distribution of polymer lengths after an initial amount of monomer A_0 has fully polymerized.

Solution

The differential equations describing the dynamics are

$$\frac{da_1}{dt} = -2k_+ a_1^2 + 2k_- a_2 + k_- \sum_{j=3}^{\infty} a_j - k_+ a_1 \sum_{j=2}^{\infty} a_j, \tag{20.132}$$

and

$$\frac{da_n}{dt} = k_+ a_{n-1} a_1 - k_+ a_n a_1 - k_- a_n + k_- a_{n+1}, \tag{20.133}$$

for $n \geq 2$. The quantity $A_0 = \sum_{j=1}^{\infty} j a_j$ is conserved by these equations.

In steady state, the system for $n \geq 2$ is a linear system of equations with solution

$$a_n = \alpha \lambda^n, \tag{20.134}$$

with $\lambda = \frac{k_+ a_1}{k_-}$. Of course, it must be that $\lambda < 1$ for this solution to be physically meaningful. To determine α, we substitute this solution into the first equation, and find that $\alpha = \frac{k_-}{k_+}$. It follows that the total amount of monomer is

$$A_0 = \frac{k_-^2 a_1}{(k_+ a_1 - k_-)^2}, \tag{20.135}$$

which in turn implies that

$$a_1 = \frac{1}{2\kappa}(1 + 2\kappa - \sqrt{1 + 4\kappa}), \tag{20.136}$$

where $\kappa = \frac{k_+ A_0}{k_-}$.

??. Suppose that the reaction rates for the three reactant loop of Fig. 1.1 do not satisfy detailed balance. What is the net rate of conversion of A into B when the reaction is at steady state?

Solution

The rate at which A is steadily converted into B is

$$\frac{k_1 k_3 k_2 - k_2 k_1 k_3}{k_1 k_3 + k_1 k_2 + k_3 k_2 + k_3 k_2 + k_3 k_1 + k_2 k_1 + k_2 k_1 + k_3 k_2 + k_3 k_1} \qquad (20.137)$$

Of course, this can only happen if energy is supplied (for example, if one of the reactions depends on the hydrolysis of ATP.)

5. Consider an enzymatic reaction in which an enzyme can be activated or inactivated by the same chemical substance, as follows:

$$\mathrm{E} + \mathrm{X} \underset{k_{-1}}{\overset{k_1}{\rightleftharpoons}} \mathrm{E}_1, \qquad (20.138)$$

$$\mathrm{E}_1 + \mathrm{X} \underset{k_{-2}}{\overset{k_2}{\rightleftharpoons}} \mathrm{E}_2, \qquad (20.139)$$

$$\mathrm{E}_1 + \mathrm{S} \xrightarrow{k_3} \mathrm{P} + \mathrm{Q} + \mathrm{E}. \qquad (20.140)$$

Suppose further that X is supplied at a constant rate and removed at a rate proportional to its concentration. Use quasi-steady-state analysis to find the nondimensional equation describing the degradation of X,

$$\frac{dx}{dt} = \gamma - x - \frac{\beta x y}{1 + x + y + \frac{\alpha}{\delta} x^2}. \qquad (20.141)$$

Identify all the parameters and variables, and the conditions under which the quasi-steady state approximation is valid.

Solution

We begin by defining X to be the concentration of X, e_1 to be the concentration of E_1, and similarly for s, e and e_2. We then use the law of mass action to write the differential equations for the reaction system

$$\frac{dX}{dt} = k_{-1}e_1 + k_{-2}e_2 - k_1 eX - k_2 e_1 X + a - bX, \qquad (20.142)$$

$$\frac{de_1}{dt} = k_{-2}e_2 - k_2 e_1 X - k_3 e_1 s - k_{-1}e_1 + k_1 eX, \qquad (20.143)$$

$$\frac{de_2}{dt} = k_2 e_1 X - k_{-2}e_2. \qquad (20.144)$$

The fact that X is supplied at a constant rate and removed at a rate proportional to its concentration is represented by the terms $a - bX$ in the equation (20.142) for X. We also have the conservation law

$$e + e_1 + e_2 = e_t, \qquad (20.145)$$

where e_t is the (constant) total amount of enzyme. Notice that, because of this conservation law, we do not need an additional equation for the dynamics of e.

Next, we non-dimensionalize the equations. A reasonable scaling for e, e_1, and e_2 is e_t, so we set $e = e_t z$, $e_1 = e_t z_1$, and $e_2 = e_t z_2$. We do not yet know how to scale X, so for the present we leave it unscaled. The removal rate of X provides a typical time constant, so we set $t = b\tau$. With these new variables, the equations become

$$\frac{dX}{d\tau} = \frac{k_{-1}e_t}{b}z_1 + \frac{k_{-2}e_t}{b}z_2 - \frac{k_1 e_t}{b}zX - \frac{k_2 e_t}{b}z_1 X + \frac{a}{b} - X, \quad (20.146)$$

$$\frac{dz_1}{d\tau} = \frac{k_{-2}}{b}z_2 - \frac{k_2}{b}z_1 X - \frac{k_3}{b}z_1 s - \frac{k_{-1}}{b}z_1 + \frac{k_1}{b}(1 - z_1 - z_2)X \quad (20.147)$$

$$\frac{dz_2}{d\tau} = \frac{k_2}{b}z_1 X - \frac{k_{-2}}{b}z_2. \quad (20.148)$$

$$1 = z + z_1 + z_2. \quad (20.149)$$

Notice that the equations for z_1 and z_2 describe exponential processes with exponential rates of decay at least as big as $\frac{k_{-1}}{b}$ and $\frac{k_{-2}}{b}$. Thus, if these two numbers are large compared to one it is legitimate to approximate the solution of these equations by their steady state solutions,

$$0 = \frac{k_{-2}}{b}z_2 - \frac{k_2}{b}z_1 X - \frac{k_3}{b}z_1 s - \frac{k_{-1}}{b}z_1 + \frac{k_1}{b}(1 - z_1 - z_2)X \quad (20.150)$$

$$0 = \frac{k_2}{b}z_1 X - \frac{k_{-2}}{b}z_2, \quad (20.151)$$

from which we find that

$$z_1 = \frac{k_1 k_{-2} X}{k_{-2}k_3 s + k_{-2}k_{-1} + k_{-2}k_1 X + k_1 k_2 X^2}, \quad (20.152)$$

$$z_2 = \frac{k_2}{k_{-2}}z_1 X. \quad (20.153)$$

We substitute these into the equation for X, finding

$$\frac{dX}{d\tau} = \frac{a}{b} - X - \frac{e_t}{b}\frac{k_{-2}k_1 k_3 s X}{k_{-2}k_{-1} + k_{-2}k_3 s + k_{-2}k_1 X + k_2 k_1 X^2}, \quad (20.154)$$

Now, to make the equation look "pretty", we set $s = Sy$, $X = \bar{X}x$, where $S = \frac{k_{-1}}{k_3}$, $\bar{X} = \frac{k_{-1}}{k_1}$ and find

$$\frac{dx}{d\tau} = \frac{a}{\bar{X}b} - x - \frac{e_t k_1}{b}\frac{yx}{1 + y + x + \frac{k_2 k_{-1}}{k_{-2}k_1}x^2}, \quad (20.155)$$

which is

$$\frac{dx}{d\tau} = \gamma - x - \frac{\beta xy}{1 + y + x + \alpha x^2}, \quad (20.156)$$

where $\gamma = \frac{k_1 a}{k_{-1}b}$, $\beta = \frac{k_1 e_t}{b}$, $\alpha = \frac{k_2 k_{-1}}{k_{-2}k_1}$.

6. Using the quasi-steady-state approximation, show that the velocity of the reaction for an enzyme with an allosteric inhibitor (Section 1.4.3) is given by

$$V = \left(\frac{V_{\max}K_3}{i + K_3}\right)\left(\frac{s(k_{-1} + k_3 i + k_1 s + k_{-3})}{k_1(s + K_1)^2 + (s + K_1)(k_3 i + k_{-3} + k_2) + k_2 k_{-3}/k_1}\right),$$
(20.157)

Identify all parameters. Under what conditions on the rate constants is this a valid approximation? Show that this reduces to (1.59) in the case $K_1 = \kappa_1$.

Solution

Applying the law of mass action to the reaction in Fig.1.2, we find that

$$\frac{de}{dt} = (k_{-1} + k_2)x + k_{-3}y - k_1 se - k_3 ie, \qquad (20.158)$$

$$\frac{dy}{dt} = k_{-1}z + k_3 ie - k_1 sy - k_{-3}y, \qquad (20.159)$$

$$\frac{dz}{dt} = k_3 ix + k_1 sy - (k_{-3} + k_{-1})z. \qquad (20.160)$$

$$\frac{ds}{dt} = -k_1(e + y)s + k_{-1}z + k_{-1}x \qquad (20.161)$$

where $e = [\mathrm{E}]$, $y = [\mathrm{EI}]$, and $z = [\mathrm{EIS}]$. We do not need a differential equation for $x = [\mathrm{ES}]$ because of the conservation law

$$e_0 = e + x + y + z. \qquad (20.162)$$

If k_{-3} and either of k_{-1} or k_2 are large compared to $k_1 e_0$, then reactions of e, y, and z are fast compared to s, regardless of the amount of s and i. In this case, the quasi-steady state approximation is valid and we set $\frac{de}{dt} = \frac{dy}{dt} = \frac{dz}{dt} = 0$. This gives the three equations

$$(k_{-1} + k_2)(e_0 - e - y - z) + k_{-3}y - k_1 se - k_3 ie = 0, \quad (20.163)$$

$$k_{-1}z + k_3 ie - k_1 sy - k_{-3}y = 0, \quad (20.164)$$

$$k_3 i(e_0 - e - y - z) + k_1 sy - k_{-3}z - k_{-1}z = 0. \quad (20.165)$$

To find the velocity of the reaction, i.e., the rate at which product is produced, we need to solve (20.163)–(20.165) for x. Since this is a linear system this can be done by hand, although it is tedious. It is much more convenient to use a symbolic manipulation package to find the solution. A simple Maple code (in file allosteric.mp) for solving these equations is

```
readlib(unassign):
unassign('x','y','z'):
fun1 := (k1*s + k3*i)*(e0-x-y-z) - km1*x - km3*y - k2*x:
fun2 := (km3+k1*s)*y - km1*z - k3*i*(e0-x-y-z) :
fun3 := (km3 + km1)*z - k3*i*x - k1*s*y :
sols := solve({fun1=0,fun2=0,fun3=0},{x,y,z}):
assign(sols):
simplify(x);
```

This gives the solution

$$x = \frac{(k_3 i + k_{-3} + k_{-1} + k_1 s)k_1 s e_0 k_{-3}}{(k_{-3} + k_3 i)(k_3 i(k_1 s + k_{-1}) + ((k_2 + k_{-1} + k_1 s)(k_{-1} + k_{-3} + k_1 s)))} \tag{20.166}$$

It remains only to write the velocity V in the form

$$\begin{aligned} V &= \frac{dp}{dt} = k_2 x \\ &= \left(\frac{k_2 e_0 K_3}{K_3 + i}\right) \frac{s(\kappa_3 i + \kappa_2 + s)}{\kappa_3 i(s + K_1) + (s + \kappa_2)(s + \kappa_1)} \end{aligned} \tag{20.167}$$

where $V_{\max} = k_2 e_0 4$, $\kappa_3 = \frac{k_3}{k_1}$, $K_1 = \frac{k_{-1}}{k_1}$, $\kappa_1 = \frac{k_{-1} + k_2}{k_1}$, $\kappa_2 = \frac{k_{-3} + k_{-1}}{k_1}$ which is the required answer. Notice that the maximum velocity occurs when all the enzyme is in the ES form (so there is no) inhibition), and so the maximum velocity is $k_2 e_0$. In the special case that $K_1 = \kappa_1$, V reduces to

$$V = \left(\frac{k_2 e_0 K_3}{K_3 + i}\right) \frac{s}{(s + K_1)} \tag{20.168}$$

which is the same as (1.59).

7. (a) Derive the expression (1.76) for the fraction of occupied sites in a Monod–Wyman–Changeux model with n binding sites.

   (b) Modify the Monod–Wyman–Changeux model shown in Fig.1.4 to include transitions between states R_1 and T_1, and between states R_2 and T_2. Use the principle of detailed balance to derive an expression for the equilibrium constant of each of these transitions. Find the expression for Y, the fraction of occupied sites, and compare it to (1.72).

Solution

   (a) It is often the case that to prove a result for general n, it is instructive to work through the proofs for several special cases. The case of $n = 2$ is done in the text, so here we begin with the case $n = 3$.

   The binding diagram for $n = 3$ is shown in Fig.20.16. Assuming that each reaction is at equilibrium we get

$$\begin{aligned} r_1 &= 3sK_1^{-1}r_0, & (20.169) \\ r_2 &= 3s^2 K_1^{-2}r_0, & (20.170) \\ r_3 &= s^3 K_1^{-3}r_0, & (20.171) \end{aligned}$$

and similarly,

$$\begin{aligned} t_1 &= 3sK_3^{-1}t_0, & (20.172) \\ t_2 &= 3s^2 K_3^{-2}t_0, & (20.173) \\ t_3 &= s^3 K_3^{-3}t_0. & (20.174) \end{aligned}$$
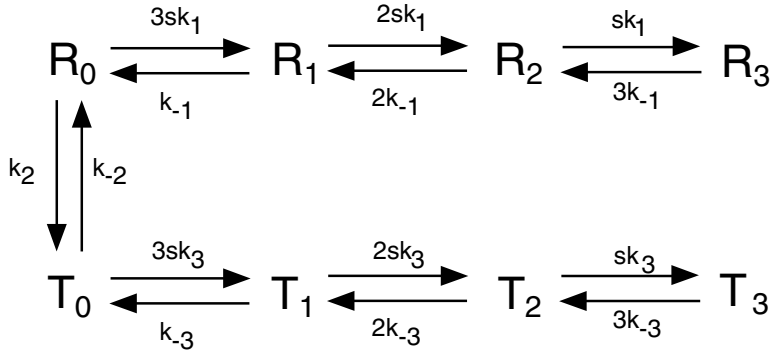
Figure 20.16: Diagram of the states of the protein and the possible transitions in an eight-state Monod-Wyman-Changeux model (i.e., the $n = 3$ case).

By definition, the saturation function is

$$Y = \frac{r_1 + 2r_2 + 3r_3 + t_1 + 2t_2 + 3t_3}{3(r_0 + r_1 + r_2 + r_3 + t_0 + t_1 + t_2 + t_3)}. \qquad (20.175)$$

Using the above relations, we quickly see that

$$
\begin{aligned}
r_1 + 2r_2 + 3r_3 &= 3sK_1^{-1}r_0 + 6(sK_1^{-1})^2 r_0 + 3(sK_1^{-1})^3 r_0 \\
&= 3r_0 sK_1^{-1}(1 + K_1^{-1})^2, \qquad (20.176)
\end{aligned}
$$

and

$$
\begin{aligned}
t_1 + 2t_2 + 3t_3 &= 3sK_3^{-1}t_0 + 6(sK_3^{-1})^2 t_0 + 3(sK_3^{-1})^3 t_0 \\
&= 3t_0 sK_3^{-1}(1 + K_3^{-1})^2. \qquad (20.177)
\end{aligned}
$$

Similarly,

$$
\begin{aligned}
3(r_0 + r_1 + r_2 + r_3) &= 3r_0(1 + 3sK_1^{-1} + 3(sK_1^{-1})^2 + (sK_1^{-1})^3) \\
&= 3r_0(1 + sK_1^{-1})^3. \qquad (20.178)
\end{aligned}
$$

and

$$
\begin{aligned}
3(t_0 + t_1 + t_2 + t_3) &= 3t_0(1 + 3sK_3^{-1} + 3(sK_3^{-1})^2 + (sK_3^{-1})^3) \\
&= 3t_0(1 + sK_3^{-1})^3. \qquad (20.179)
\end{aligned}
$$

Finally, we use that

$$t_0 = K_2^{-1}r_0, \qquad (20.180)$$

so that

$$
\begin{aligned}
Y &= \frac{r_1 + 2r_2 + 3r_3 + t_1 + 2t_2 + 3t_3}{3(r_0 + r_1 + r_2 + r_3 + t_0 + t_1 + t_2 + t_3)} \\
&= \frac{3r_0 sK_1^{-1}(1 + K_1^{-1})^2 + 3t_0 sK_3^{-1}(1 + K_3^{-1})^2}{3r_0(1 + sK_1^{-1})^3 + 3t_0(1 + sK_3^{-1})^3} \\
&= \frac{3sK_1^{-1}(1 + K_1^{-1})^2 + 3K_2^{-1}sK_3^{-1}(1 + K_3^{-1})^2}{3(1 + sK_1^{-1})^3 + 3K_2^{-1}(1 + sK_3^{-1})^3}, \qquad (20.181)
\end{aligned}
$$

as expected.

The calculation for the general case (depicted in Fig. 20.17) should now be clear. We first observe that

$$Y = \frac{\sum_1^n i r_i + \sum_1^n i t_i}{n(\sum_0^n r_i + \sum_0^n t_i)}. \tag{20.182}$$

From the assumption that all reactions are at chemical equilibrium we find

$$r_1 = n s K_1^{-1} r_0, \tag{20.183}$$

$$r_2 = \left(\frac{n-1}{2}\right) s K_1^{-1} r_1 = \left(\frac{n-1}{2}\right) n (s K_1^{-1})^2 r_0, \tag{20.184}$$

$$r_3 = \left(\frac{n-2}{3}\right)\left(\frac{n-1}{2}\right) n (s K_1^{-1})^3 r_0, \tag{20.185}$$

$$\vdots$$

$$r_i = \frac{n!}{(n-i)!i!}(s K_1^{-1})^i r_0. \tag{20.186}$$

Thus,

$$\begin{aligned}
\sum_{i=1}^n i r_i &= r_0 \sum_{i=1}^n i \frac{n!}{(n-i)!i!}(s K_1^{-1})^i \\
&= r_0 n (s K_1^{-1}) \sum_{i=1}^n \frac{(n-1)!}{(n-i)!(i-1)!}(s K_1^{-1})^{i-1} \\
&= r_0 n (s K_1^{-1}) \sum_{i=0}^{n-1} \frac{(n-1)!}{(n-1-i)!i!}(s K_1^{-1})^i \\
&= r_0 n (s K_1^{-1})(1 + s K_1^{-1})^{n-1}. \tag{20.187}
\end{aligned}$$

(because of the binomial expansion formula $(1+x)^k = \sum_{j=0}^k \frac{k!}{(k-j)!j!} x^j$). Similarly,

$$\begin{aligned}
n \sum_{i=0}^n r_n &= n r_0 \sum_0^n \frac{n!}{(n-i)!i!}(s K_1^{-1})^i \\
&= n r_0 (1 + s K_1^{-1})^n. \tag{20.188}
\end{aligned}$$

The same argument works for the T states (using, of course, K_3 instead of K_1). We substitute these expressions into (20.182), and use that $t_0 = K_2^{-1} r_0$ to find

$$Y = \frac{s K_1^{-1}(1 + s K_1^{-1})^{n-1} + K_2^{-1}[s K_3^{-1}(1 + s K_3^{-1})^{n-1}]}{(1 + s K_1^{-1})^n + K_2^{-1}(1 + s K_3^{-1})^n}. \tag{20.189}$$
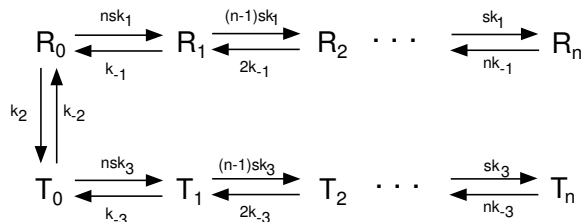
as required.

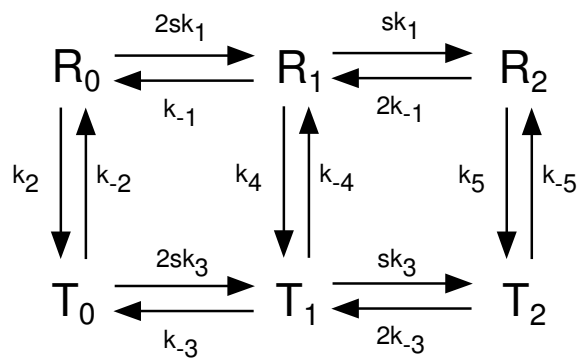Figure 20.17: Diagram of the states of the protein and the possible transitions in the general case.

Figure 20.18: Diagram of the states of the protein and the possible transitions when R_1-T_1 and R_2-T_2 are allowed.

(b) The new binding diagram is shown in Fig.20.18. Applying detailed balance around the reaction loop R_0-T_0-T_1-R_1 gives

$$2sk_2k_3k_{-4}k_{-1} = 2sk_1k_4k_{-3}k_{-2}, \qquad (20.190)$$

so that

$$K_1K_4 = K_2K_3, \qquad (20.191)$$

where, as usual, $K_i = k_{-i}/k_i$. Thus, K_4 is determined by K_1, K_2 and K_3. Similarly, from the R_1-T_1-T_2-R_2 reaction loop

$$K_1K_5 = K_3K_4. \qquad (20.192)$$

Do these transitions make any difference to the calculation of Y? No, they do not, because the additional equilibrium constraints

$$r_1 = K_4t_1, \qquad (20.193)$$
$$r_2 = K_5t_2, \qquad (20.194)$$

are automatically satisfied. To see this, notice that the equilibrium conditions

$$r_1 = 2sK_1^{-1}r_0, \qquad t_1 = 2sK_3^{-1}t_0, \qquad (20.195)$$

used before imply that

$$\begin{aligned} r_1 &= 2sK_1^{-1}r_0 \\ &= 2sK_1^{-1}K_2t_0 \\ &= 2sK_1^{-1}K_2\left(\frac{t_1K_3}{2s}\right) \\ &= K_1^{-1}K_2K_3t_1 \\ &= K_4t_1. \end{aligned} \qquad (20.196)$$

It follows similarly that $r_2 = K_5t_2$ is automatically satisfied. Thus, because of the constraints on the reaction rates, the additional transitions are automatically in equilibrium and so the expression for Y is unchanged.

8. An enzyme-substrate system is believed to proceed at a Michaelis-Menten rate. Data for the (initial) rate of reaction at different concentrations is shown in Table 20.1.

(a) Plot the data V vs. s. Is there evidence that this is a Michaelis-Menten type reaction?

(b) Plot V vs. V/s. Is this data well approximated by a straight line?

(c) Use linear regression and (1.46) to estimate K_m and $V_{\max}$. Compare the data to the Michaelis-Menten rate function using these parameters. Does this provide a reasonable fit to the data?

Table 20.1: Data for Problem 8.

Substrate Concentration (mM)	Reaction Velocity (mM/s)
0.1	0.04
0.2	0.08
0.5	0.17
1.0	0.24
2.0	0.32
3.5	0.39
5.0	0.42

Solution

(c) Rewrite the equation (1.46) as

$$V_{\max} - \frac{V}{s}K_m = V. \qquad (20.197)$$

For each experiment, there is one such equation, so with seven data points we have the linear system of equations

$$A \begin{pmatrix} V_{\max} \\ K_m \end{pmatrix} = \begin{pmatrix} 1.0 & -0.40 \\ 1.0 & -0.40 \\ 1.0 & -0.32 \\ 1.0 & -0.26 \\ 1.0 & -0.16 \\ 1.0 & -0.11 \\ 1.0 & -0.08 \end{pmatrix} \begin{pmatrix} V_{\max} \\ K_m \end{pmatrix} = \begin{pmatrix} 0.04 \\ 0.08 \\ 0.16 \\ 0.26 \\ 0.32 \\ 0.39 \\ 0.42 \end{pmatrix} = b.$$

$$(20.198)$$

To find the linear regression solution (also called the least-squares solution) of this system, solve the normal equations

$$A^T A \begin{pmatrix} V_{\max} \\ K_m \end{pmatrix} = A^T b, \qquad (20.199)$$

which in this case is the 2×2 system

$$\begin{pmatrix} 7.0000 & -1.7354 \\ -1.7354 & 0.5351 \end{pmatrix} \begin{pmatrix} V_{\max} \\ K_m \end{pmatrix} = \begin{pmatrix} 1.6700 \\ -0.2967 \end{pmatrix}, \qquad (20.200)$$

having the solution $V_{\max} = 0.5160$, $K_m = 1.1189$. A plot of the line $y = V_{\max} - K_m x$ is shown with data points in Fig. 20.19, and a plot of the reaction velocity with data points is shown in Fig. 20.20. This solution can be found by running the Matlab code ex_Burk.m.

9. Suppose the maximum velocity of a chemical reaction is known to be 1 mM/s, and the measured velocity V of the reaction at different concentrations s is shown in Table 20.2.
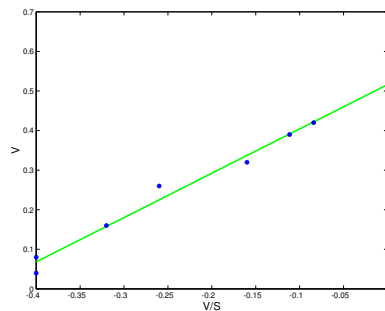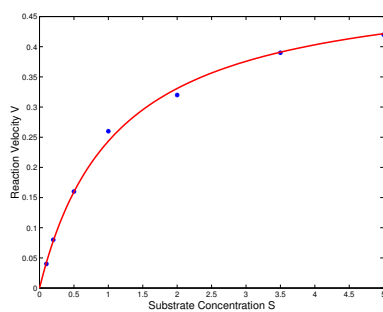
Figure 20.19:

Figure 20.20: Michaelis-Menten growth curve for data of Problem 8.

Table 20.2: Data for Problem 9.

Substrate Concentration (mM)	Reaction Velocity (mM/s)
0.2	0.01
0.5	0.06
1.0	0.27
1.5	0.50
2.0	0.67
2.5	0.78
3.5	0.89
4.0	0.92
4.5	0.94
5.0	0.95

(a) Plot the data V vs. s. Is there evidence that this is a Hill type reaction?

(b) Plot $\ln(\frac{V}{V_{\max}-V})$ vs. $\ln(s)$. Is this approximately a straight line, and if so, what is its slope?

(c) Use linear regression and (1.71) to estimate K_m and the Hill exponent n. Compare the data to the Hill rate function with these parameters. Does this provide a reasonable fit to the data?

Solution

(c) Rewrite the equation (1.71) as

$$-n \ln K_m + n \ln s = \ln\left(\frac{V}{V_{\max} - V}\right), \qquad (20.201)$$

and view n and $-n \ln K_n$ as unknown variables. For each experiment, there is one such equation, so with ten data points we have the linear system of equations

$$A\begin{pmatrix} -n\ln K_m \\ n \end{pmatrix} = \begin{pmatrix} 1.0 & -1.6094 \\ 1.0 & -0.6931 \\ 1.0 & 0 \\ 1.0 & 0.4055 \\ 1.0 & 0.6931 \\ 1.0 & 0.9163 \\ 1.0 & 1.2528 \\ 1.0 & 1.3863 \\ 1.0 & 1.5041 \\ 1.0 & 1.6094 \end{pmatrix} \begin{pmatrix} -n\ln K_m \\ n \end{pmatrix} = \begin{pmatrix} -4.5951 \\ -2.7515 \\ -0.9946 \\ 0 \\ 0.7082 \\ 1.2657 \\ 2.0907 \\ 2.4423 \\ 2.7515 \\ 2.9444 \end{pmatrix} = b.$$

$$(20.202)$$

To find the linear regression solution of this system, solve the normal equations

$$A^T A \begin{pmatrix} -n\ln K_m \\ n \end{pmatrix} = A^T b, \qquad (20.203)$$

which in this case is the 2×2 system

$$\begin{pmatrix} 10.0000 & 5.4649 \\ 5.4649 & 12.8990 \end{pmatrix} \begin{pmatrix} -n\ln K_m \\ n \end{pmatrix} = \begin{pmatrix} 3.8616 \\ 25.8358 \end{pmatrix}, \qquad (20.204)$$

having the solution $n = 2.4$, $K_m = 1.47$. A plot of the line $y = n \ln s - n \ln K_m$ is shown with data points in Fig. 20.21, and a plot of the reaction velocity with data points is shown in Fig. 20.22. This solution can be found by running the Matlab code ex_Hill.m.

11. (a) Find the velocity of reaction for an enzyme with three active sites.

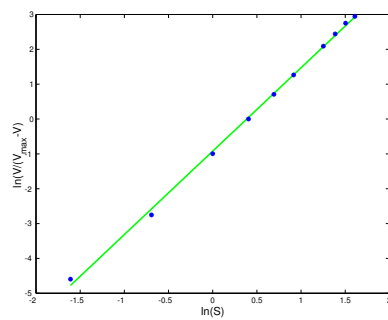(b) Under what conditions does the velocity reduce to a Hill function with exponent three? Identify all parameters.
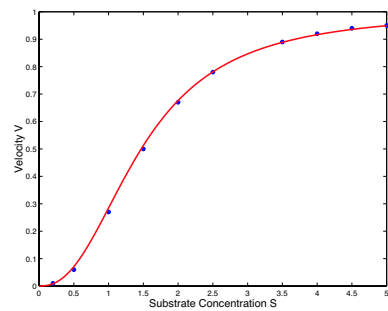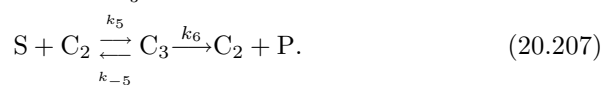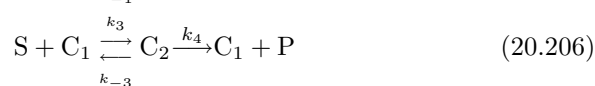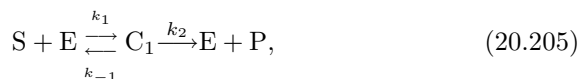
Figure 20.21:

Figure 20.22: Hill curve for data of Problem 9.

(c) What is the relationship between rate constants when the three sites are independent? What is the velocity when the three sites are independent?

Solution

(a) For an enzyme with three active sites, the reaction mechanism is represented by

$$S + E \underset{k_{-1}}{\overset{k_1}{\rightleftharpoons}} C_1 \overset{k_2}{\longrightarrow} E + P, \tag{20.205}$$

$$S + C_1 \underset{k_{-3}}{\overset{k_3}{\rightleftharpoons}} C_2 \overset{k_4}{\longrightarrow} C_1 + P \tag{20.206}$$

$$S + C_2 \underset{k_{-5}}{\overset{k_5}{\rightleftharpoons}} C_3 \overset{k_6}{\longrightarrow} C_2 + P. \tag{20.207}$$

Using the law of mass action, one can write down the rate equations for the 6 concentrations [S], [E], $[C_1]$, $[C_2]$, $[C_3]$, and [P]. However, because the amount of product [P] can be determined by quadrature, and because the total amount of enzyme molecule is conserved, we only need four equations for the four quantities [S], $[C_1]$, $[C_2]$, and $[C_3]$. These are

$$\frac{ds}{dt} = -k_1 se + k_{-1}c_1 - k_3 sc_1 + k_{-3}c_2 - k_5 sc_2 + k_{-5}c_3 \tag{20.208}$$

$$\frac{dc_1}{dt} = k_1 se - (k_{-1} + k_2)c_1 - k_3 sc_1 + (k_4 + k_{-3})c_2, \tag{20.209}$$

$$\frac{dc_2}{dt} = k_3 sc_1 - (k_4 + k_{-3})c_2 - k_5 sc_2 + (k_6 + k_{-5})c_3, \tag{20.210}$$

$$\frac{dc_3}{dt} = k_5 sc_2 - (k_6 + k_{-5})c_3, \tag{20.211}$$

where $s = [S]$, $c_1 = [C_1]$, $c_2 = [C_2]$, $c_3 = [C_3]$, and $e + c_1 + c_2 + c_3 = e_0$. Proceeding as before, we invoke the quasi-steady-state assumption that $\frac{dc_1}{dt} = \frac{dc_2}{dt} = \frac{dc_3}{dt} = 0$ (Under what conditions is this a valid assumption?), and solve for c_1, c_2, and c_3 to get (this is easily done using the maple file three_sites.mp)

$$c_1 = \frac{K_2 K_3 se_0}{s^3 + K_3 s^2 + K_3 K_2 s + K_3 K_2 K_1}, \tag{20.212}$$

$$c_2 = \frac{K_3 s^2 e_0}{s^3 + K_3 s^2 + K_3 K_2 s + K_3 K_2 K_1}, \tag{20.213}$$

$$c_3 = \frac{s^3 e_0}{s^3 + K_3 s^2 + K_3 K_2 s + K_3 K_2 K_1}, \tag{20.214}$$

where

$$K_1 = \frac{k_{-1} + k_2}{k_1}, \qquad K_2 = \frac{k_4 + k_{-3}}{k_3}, \qquad K_3 = \frac{k_6 + k_{-5}}{k_5}. \tag{20.215}$$

It follows that the velocity of the reaction is

$$V = k_2c_1 + k_4c_2 + k_6c_3 \tag{20.216}$$

$$= e_0 \frac{k_2 K_2 K_3 s + k_4 K_3 s^2 + k_6 s^3}{s^3 + K_3 s^2 + K_3 K_2 s + K_3 K_2 K_1}. \tag{20.217}$$

We recover a Hill function with exponent three in the limit that $K_2 \to 0$, $K_3 \to 0$, while $K_1 K_2 K_3$ remains bounded and nonzero.

(b) With three independent binding sites, $k_4 = 2k_2$, $k_6 = 3k_2$, $k_1 = 3k_5$, $k_3 = 2k_5$, $k_{-5} = 3k_{-1}$, $k_{-3} = 2k_{-1}$, so that $K_3 = 2K_2$, and $K_1 = \frac{1}{3}K_2$. It follows that

$$V = 3\frac{k_2 s}{s + K_2}, \tag{20.218}$$

where $K_2 = \frac{k_2 + k_{-1}}{k_5}$.

13. Suppose that a substrate can be broken down by two different enzymes with different kinetics. (This happens, for example, in the case of cAMP or cGMP, which can be hydrolyzed by two different forms of phosphodiesterase—see Chapter 19).

   (a) Write the reaction scheme and differential equations, and nondimensionalize, to get the system of equations

   $$\frac{d\sigma}{dt} = -\sigma + \alpha_1(\mu_1 + \sigma)x + \alpha_2(\mu_2 + \sigma)y, \tag{20.219}$$

   $$\epsilon_1 \frac{dx}{dt} = \frac{1}{\lambda_1}\sigma(1 - x) - x, \tag{20.220}$$
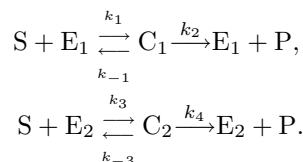
   $$\epsilon_2 \frac{dy}{dt} = \frac{1}{\lambda_2}\sigma(1 - y) - y. \tag{20.221}$$

   where x and y are the nondimensional concentrations of the two complexes. Identify all parameters.

   (b) Apply the quasi-steady-state approximation to find the equation governing the dynamics of substrate σ. Under what conditions is the quasi-steady state approximation valid?

   (c) Solve the differential equation governing σ.

   (d) For this system of equations, show that the solution can never leave the positive octant $\sigma, x, y \geq 0$. By showing that $\sigma + \epsilon_1 x + \epsilon_2 y$ is decreasing everywhere in the positive octant, show that the solution approaches the origin for large time.

Solution

   (a) The chemical equations for the two reactions are

   $$S + E_1 \underset{k_{-1}}{\overset{k_1}{\rightleftarrows}} C_1 \overset{k_2}{\longrightarrow} E_1 + P,$$

   $$S + E_2 \underset{k_{-3}}{\overset{k_3}{\rightleftarrows}} C_2 \overset{k_4}{\longrightarrow} E_2 + P.$$

As usual we let lower letters denote concentrations. Applying the law of mass action gives

$$\frac{ds}{dt} = k_{-1}c_1 + k_{-3}c_2 - k_1se_1 - k_3se_2, \qquad (20.222)$$

$$\frac{dc_1}{dt} = k_1se_1 - (k_{-1} + k_2)c_1, \qquad (20.223)$$

$$\frac{dc_2}{dt} = k_3se_2 - (k_{-3} + k_4)c_2. \qquad (20.224)$$

Since the total amounts of the enzymes are conserved,

$$e_1 + c_1 = e_t, \qquad (20.225)$$

$$e_2 + c_2 = e_T, \qquad (20.226)$$

and we can eliminate e_1 and e_2 to find

$$\frac{ds}{dt} = k_{-1}c_1 + k_{-3}c_2 - k_1s(e_t - c_1) - k_3s(e_T - c_2), \quad (20.227)$$

$$\frac{dc_1}{dt} = k_1s(e_t - c_1) - (k_{-1} + k_2)c_1, \qquad (20.228)$$

$$\frac{dc_2}{dt} = k_3s(e_T - c_2) - (k_{-3} + k_4)c_2. \qquad (20.229)$$

The most natural nondimensionalization of the concentrations is

$$x = \frac{c_1}{e_t}, \qquad (20.230)$$

$$y = \frac{c_2}{e_T}, \qquad (20.231)$$

$$\sigma = \frac{s}{s_0}, \qquad (20.232)$$

where s_0 is the initial amount of substrate. Since it is not immediately obvious how to scale time, we set $t = \mu\tau$, and wait until later to determine μ. This change of variables gives

$$\frac{d\sigma}{dt} = k_{-1}\frac{\mu e_t}{s_0}x + k_{-3}\frac{\mu e_T}{s_0}y - \mu k_1\sigma e_t(1 - x) - \mu k_3\sigma e_T(1 - y), \quad (20.233)$$

$$\frac{1}{\mu}\frac{dx}{dt} = k_1s_0\sigma(1 - x) - (k_{-1} + k_2)x, \qquad (20.234)$$

$$\frac{1}{\mu}\frac{dy}{dt} = k_3s_0\sigma(1 - y) - (k_{-3} + k_4)y. \qquad (20.235)$$

Now we want to exploit the fact that there is far more substrate than either enzyme, and pick μ in a way that emphasizes that under these conditions, x and y are "fast" variables, compared to σ. Notice that all the linear terms proportional to σ on the right hand side of (20.233) are

multiplied by either e_t or e_T, suggesting that this variable is slow. This also suggests that we should pick $\mu = \frac{1}{k_1 e_t + k_3 e_T}$ in which case we find

$$\frac{d\sigma}{dt} = -\sigma + \frac{e_t(k_{-1} + k_1 s_0 \sigma)}{s_0(k_1 e_t + k_3 s_0 e_T)} x + \frac{e_T(k_{-3} + k_3 \sigma)}{s_0(k_1 e_t + k_3 e_T)} y \tag{20.236}$$

$$\frac{k_1 e_t + k_3 e_T}{k_{-1} + k_2} \frac{dx}{dt} = \frac{k_1 s_0}{k_{-1} + k_2} \sigma(1 - x) - x, \tag{20.237}$$

$$\frac{k_1 e_t + k_3 e_T}{k_{-3} + k_4} \frac{dy}{dt} = \frac{k_3 s_0}{k_{-3} + k_4} \sigma(1 - y) - y. \tag{20.238}$$

which is

$$\frac{d\sigma}{dt} = -\sigma + \alpha_1(\mu_1 + \sigma)x + \alpha_2(\mu_2 + \sigma)y, \tag{20.239}$$

$$\epsilon_1 \frac{dx}{dt} = \frac{1}{\lambda_1}\sigma(1 - x) - x, \tag{20.240}$$

$$\epsilon_2 \frac{dy}{dt} = \frac{1}{\lambda_2}\sigma(1 - y) - y. \tag{20.241}$$

where $\epsilon_1 = \frac{k_1 e_t + k_3 e_T}{k_{-1} + k_2}$, $\epsilon_2 = \frac{k_1 e_t + k_3 e_T}{k_{-3} + k_4}$, $\lambda_1 = \frac{k_{-1} + k_2}{k_1 s_0}$, $\lambda_2 = \frac{k_{-3} + k_4}{k_3 s_0}$, $\mu_1 = \frac{k_{-1}}{k_1 s_0}$, $\mu_2 = \frac{k_{-3}}{k_3 s_0}$, $\alpha_1 = \frac{k_1 e_t}{k_1 e_t + k_3 e_T}$, and $\alpha_2 = \frac{k_3 e_T}{k_1 e_t + k_3 e_T}$, with $\alpha_1 + \alpha_2 = 1$.

(b) Under the assumption that both ϵ_1 and ϵ_2 are small, we set $\epsilon_1 = \epsilon_2 = 0$ and find the quasi-steady state solution

$$x = \frac{\sigma}{\lambda_1 + \sigma}, \tag{20.242}$$

$$y = \frac{\sigma}{\lambda_2 + \sigma}. \tag{20.243}$$

We substitute these expressions into the differential equation for σ to get the equation for σ,

$$\frac{d\sigma}{dt} = -\sigma + \alpha_1 \sigma \frac{\mu_1 + \sigma}{\lambda_1 + \sigma} + \alpha_2 \sigma \frac{\mu_2 + \sigma}{\lambda_2 + \sigma}. \tag{20.244}$$

(c) The equation (20.244) can be solved by separating variables. First, we rewrite it as

$$\frac{(\lambda_1 + \sigma)(\lambda_2 + \sigma)}{\sigma(\theta_1 \sigma + \theta_2)} d\sigma = -dt. \tag{20.245}$$

where

$$\theta_1 = \lambda_1 + \lambda_2 - \alpha_1(\mu_1 + \lambda_2) - \alpha_2(\mu_2 + \lambda_1) \tag{20.246}$$

$$\theta_2 = \lambda_1 \lambda_2 - \alpha_1 \mu_1 \lambda_2 \alpha_2 \mu_2 \lambda_1. \tag{20.247}$$

(It is important to notice that $\alpha_1 + \alpha_2 = 1$.) Notice that in original dimensioned parameters these are

$$\theta_1 = k_3 \frac{k_1 e_t k_2 + e_T k_4 k_1}{(k_1 e_t + k_3 e_T)k_1 k_3 s_0} \tag{20.248}$$

$$\theta_2 = \frac{1}{(k_1 e_t + k_3 e_T)k_1 s_0 k_3 s_0} k_1 e_t k_2(k_{-3} + k_4) + k_3 e_T k_4(k_{-1} + k_2) \tag{20.249}$$
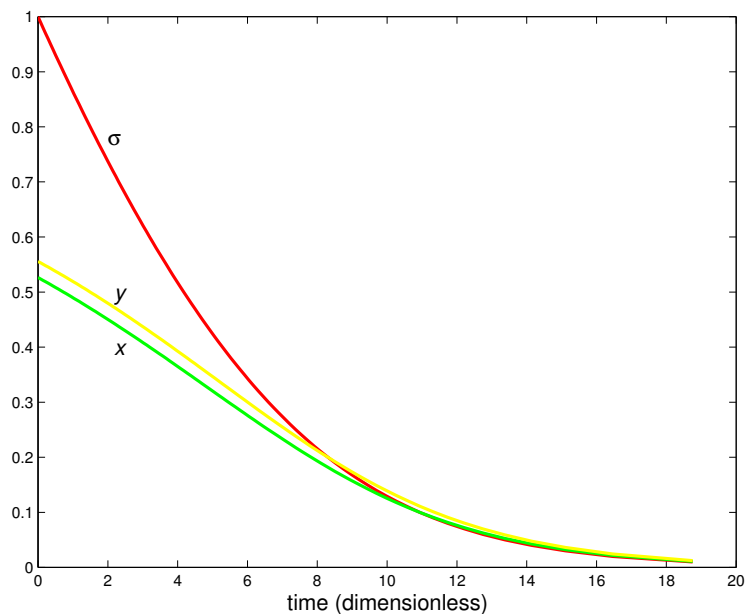
Figure 20.23: Plots of σ, x and y for the parameters $\mu_1 = 0.5$, $\mu_2 = 0.6$, $\lambda_1 = 0.9$, $\lambda_2 = 0.8$, $\beta = 2$ **This figure needs to be redone using newly defined parameters.**

both positive.

We integrate both sides of (20.245) to find

$$-\frac{\sigma}{\theta_1} - \frac{\lambda_1\lambda_2 \ln(\sigma)}{\theta_2} + \left(\frac{\lambda_1\lambda_2}{\theta_2} - \frac{\lambda_1 + \lambda_2}{\theta_1} + \frac{\theta_2}{\theta_1^2}\right)\ln(\theta_1\sigma + \theta_2) = t + K, \quad (20.250)$$

for some constant K. To determine K, we apply the initial condition $\sigma(0) = 1$, from which it follows that

$$K = -\frac{1}{\theta_1} + \left(\frac{\lambda_1\lambda_2}{\theta_2} - \frac{\lambda_1 + \lambda_2}{\theta_1} + \frac{\theta_2}{\theta_1^2}\right)\ln(\theta_1 + \theta_2). \quad (20.251)$$

Thus,

$$\frac{1 - \sigma}{\theta_1} - \frac{\lambda_1\lambda_2 \ln(\sigma)}{\theta_2} + \left(\frac{\lambda_1\lambda_2}{\theta_2} - \frac{\lambda_1 + \lambda_2}{\theta_1} + \frac{\theta_2}{\theta_1^2}\right)\ln\left(\frac{\theta_1\sigma + \theta_2}{\theta_1 + \theta_2}\right) = t. \quad (20.252)$$

We can now plot the solutions. (This is most easily done by considering t to be a function of σ, and then reversing the axes.) The results, for one particular choice of the parameters, are shown in Fig.20.23. This calculation is done in maple using the file two_enzymes.mp.

It is important to realize that the graphs for x and y are incorrect at small times, since at $t = 0$, x and y are nonzero. This is not physically possible, since all the enzymes start in the unbound form. Hence, using the quasi-steady state approximation we have constructed a solution that is incorrect close to $t = 0$. To correct this requires a knowledge of how to construct asymptotic series solutions to equations of this type (i.e., to singular perturbation problems), a subject which is beyond the scope of this text. This is discussed briefly in the Appendix of this Chapter, as well as in Murray (1989) and Lin and Segel (1988).

However, for larger times this solution is reasonably accurate.

(d) To show that solutions of equations (20.219)-(20.221) cannot leave the positive octant, it suffices to show that they cannot cross the boundary. The boundary consists of the three planes, $x = 0$, $y = 0$, and $\sigma = 0$. When $x = 0$, $dx/dt = \frac{\sigma}{\lambda_1}$ which is strictly positive everywhere in the first octant (and hence on the boundary), except at the origin (which is a critical point of the system). Similarly, when $y = 0$, $dy/dt = \frac{\sigma}{\lambda_2} > 0$ except at the origin, and when $\sigma = 0$, $d\sigma/dt = \alpha_1\mu_1 x + \alpha_2\mu_2 y > 0$ except at the origin. It follows that no solution can leave the first octant.

To show that the solution approaches the origin for large time, we add the three equations together, weighted by 1, $\lambda_1\alpha_1$, and $\lambda_2\alpha_2$ respectively to find

$$\frac{d}{dt}(\sigma + \epsilon_1\lambda_1\alpha_1 x + \epsilon_2\lambda_2\alpha_2 y) = \alpha_1(\mu_1 - \lambda_1)x + \alpha_2(\mu_2 - \lambda_2)y \quad (20.253)$$

(since $\alpha_1 + \alpha_2 = 1$).

Now observe that

$$\mu_1 - \lambda_1 = -\frac{k_2}{k_1 s_0} < 0, \qquad \mu_2 - \lambda_2 = -\frac{k_4}{k_3 s_0} < 0, \qquad (20.254)$$

so that $\sigma + \epsilon_1\lambda_1\alpha_1 x + \epsilon_2\lambda_2\alpha_2 y$ decreases whenever x and y are non-negative. However, we already know that x and y cannot be zero unless $\sigma = 0$ as well. Thus $\sigma + \epsilon_1\lambda_1\alpha_1 x + \epsilon_2\lambda_2\alpha_2 y$ is always decreasing, and so approaches zero for large time.

14. For some enzyme reactions (for example, the hydrolysis of cAMP by phosphodiesterase in vertebrate retinal cones) the enzyme is present in large quantities, so that e_0/s_0 is not a small number. Fortunately, there is an alternate derivation of the Michaelis-Menten rate equation that does not require that $\epsilon = \frac{e_0}{s_0}$ be small. Instead, if one or both of k_{-1} and k_2 are much larger than $k_1 e_0$, then the formation of complex c is a rapid exponential process, and can be taken to be in quasi-steady state. Make this argument systematic by introducing appropriate non-dimensional variables and then find the resulting quasi-steady state dynamics. (Segel, 1988; Frenzen and Maini, 1988; Segel and Slemrod, 1989; Sneyd and Tranchina, 1989).

Solution

We introduce dimensionless variables

$$\sigma = \frac{s}{s_0}, \quad x = \frac{c}{e_0}, \quad \tau = k_1 e_0 t, \tag{20.255}$$

in terms of which equations (1.26) and (1.28) become

$$\frac{d\sigma}{dt} = \alpha x - \sigma(1-x), \tag{20.256}$$

$$\frac{dx}{dt} + Kx = \frac{s_0}{e_0}\sigma(1-x), \tag{20.257}$$

where $\alpha = \frac{k_{-1}}{k_1 s_0}$, and $K = \frac{k_2 + k_{-1}}{k_1 e_0} \gg 1$. Because K is large compared to one, the dynamics of x are such that x equilibrates rapidly and exponentially, regardless of the amplitude of $\frac{s_0}{e_0}$. Thus, in quasi-steady state

$$Kx = \frac{s_0}{e_0}\sigma(1-x), \tag{20.258}$$

which in dimensioned variables is exactly (1.44) found before. Thus, this approximation gives the same answer as the quasi-steady state analysis described in the text.
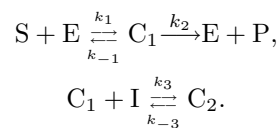
16. In the case of noncompetitive inhibition, the inhibitor combines with the enzyme-substrate complex to give an inactive enzyme-substrate-inhibitor complex which cannot undergo further reaction, but the inhibitor does not combine directly with free enzyme or affect its reaction with substrate. Use the quasi-steady-state approximation to determine that the velocity of this reaction is

$$V = V_{\max}\frac{s}{K_m + s + \frac{i}{K_i}s}. \tag{20.259}$$

Identify all parameters. Compare this velocity with the velocity for other types of inhibition discussed in the text.

Solution

For this case the reaction scheme is

$$S + E \underset{k_{-1}}{\overset{k_1}{\rightleftharpoons}} C_1 \overset{k_2}{\longrightarrow} E + P,$$

$$C_1 + I \underset{k_{-3}}{\overset{k_3}{\rightleftharpoons}} C_2.$$

and from the law of mass action the governing equations are

$$\frac{ds}{dt} = -k_1 se + k_{-1}c_1, \tag{20.260}$$

$$\frac{de}{dt} = -k_1 se + (k_{-1} + k_2 c_1, \tag{20.261}$$

$$\frac{dc_1}{dt} = k_1 se - (k_{-1} + k_2 + k_3 i)c_1 + k_{-3}c_2, \tag{20.262}$$

$$\frac{dc_2}{dt} = k_3 c_1 i - k_{-3}c_2, \tag{20.263}$$

$$\frac{dp}{dt} = k_2 c_1, \tag{20.264}$$

where $s = [S]$, $i = [I]$, $c_1 = [C_1]$, and $c_2 = [C_2]$. We know that $e+c_1+c_2 = e_0$. Observe that if $k_{-1} + k_2 + k_3 i$ and k_{-3} are large compared to $k_1 e_0$, then the reactions of c_1 and c_2 are fast compared to s and the quasi-steady state approximation is valid. We set $\frac{dc_1}{dt} = \frac{dc_2}{dt} = 0$, so that

$$0 = k_1 s(e_0 - c_1 - c_2) - (k_{-1} + k_2 + k_3 i)c_1 + k_{-3}c_2, \qquad (20.265)$$
$$0 = k_3 c_1 i - k_{-3} c_2. \qquad (20.266)$$

We need to know c_1 since this determines the velocity of the reaction. We easily find that

$$k_{-3}c_2 = k_3 c_1 i, \qquad (20.267)$$

so that

$$c_1 = \frac{k_1 s e_0}{k_{-1} + k_2 + k_1 s + \frac{k_3}{k_{-3}} i s}, \qquad (20.268)$$

yielding the velocity of reaction

$$V = K_2 c_1 = V_{\max} \frac{s}{K_m + s + \frac{i}{K_i} s}, \qquad (20.269)$$

where $K_m = \frac{k_{-1}+k_2}{k_1}$, $K_i = \frac{k_{-3}k_1}{k_3}$, and $V_{\max} = k_2 e_0$.

20. (a) Nondimensionalize (1.26) to (1.29) in a way appropriate for the equilibrium approximation (rather than the quasi-steady-state approximation of Section 1.4.2). Hint: Recall that for the equilibrium approximation, the assumption is that $k_1 e_0$ and k_{-1} are large compared to k_2. You should end up with equations that look something like

$$\epsilon \frac{d\sigma}{d\tau} = \alpha x - \beta \alpha \sigma (1 - x), \qquad (20.270)$$

$$\epsilon \frac{dx}{d\tau} = \beta \sigma (1 - x) - x - \epsilon x, \qquad (20.271)$$

where $\epsilon = k_2/k_{-1}$, $\alpha = e_0/s_0$ and $\beta = s_0/K_1$.

(b) Find the behavior, to lowest order in ϵ for this system. (Notice that the slow variable is $\sigma + \alpha x$.)

(c) To lowest order in ϵ, what is the differential equation for σ on this time scale?

(d) Rescale time to find equations valid for small times.

(e) Show that, to lowest order in ϵ, $\sigma + \alpha x = $ constant for small times.

(f) Without calculating the exact solution, sketch the solution in the phase plane, showing the initial fast movement to the slow manifold, and then the movement along the slow manifold.

Solution

1024

(a) Nondimensionalize (1.26) to (1.29) in a way appropriate for the equilibrium approximation (rather than the quasi-steady-state approximation of Section 1.4.2). Hint: Recall that for the equilibrium approximation, the assumption is that $k_1 e_0$ and k_{-1} are large compared to k_2. You should end up with equations that look something like

$$\epsilon \frac{d\sigma}{d\tau} = \alpha x - \beta\alpha\sigma(1-x), \tag{20.272}$$

$$\epsilon \frac{dx}{d\tau} = \beta\sigma(1-x) - x - \epsilon x, \tag{20.273}$$

where $\epsilon = k_2/k_{-1}$, $\alpha = e_0/s_0$ and $\beta = s_0/K_1$.

(b) Find the behavior, to lowest order in ϵ for this system. (Notice that the slow variable is $\sigma + \alpha x$.)

(c) To lowest order in ϵ, what is the differential equation for σ on this time scale?

(d) Rescale time to find equations valid for small times.

(e) Show that, to lowest order in ϵ, $\sigma + \alpha x = $ constant for small times.

(f) Without calculating the exact solution, sketch the solution in the phase plane, showing the initial fast movement to the slow manifold, and then the movement along the slow manifold.

Solution

Since $e + c = e_0$, we let $c = e_0 x$, and scale s by s_0, the initial amount of substrate, $s = s_0\sigma$. There are two reasonable scalings for time. One could take $\tau = k_2 t$, to emphasize behavior on a long time scale, or $\tau = k_{-1}t$ to emphasize behavior on a short time scale. With $\tau = k_2 t$, the equations are

$$\epsilon \frac{d\sigma}{d\tau} = \alpha x - \alpha\beta\sigma(1-x), \tag{20.274}$$

$$\epsilon \frac{dx}{d\tau} = \beta\sigma(1-x) - (1+\epsilon)x, \tag{20.275}$$

where $\alpha = \frac{e_0}{s_0}$, $\beta = \frac{k_1}{k_{-1}}s_0 = \frac{s_0}{K_1}$.

The quasi-steady state approximation for these equations is apparent. We set ϵ to zero to obtain $x - \beta\sigma(1-x) = 0$, or

$$x = \frac{\beta\sigma}{1+\beta\sigma}. \tag{20.276}$$

The slow behavior is found by adding together the two equations to find

$$\frac{d}{dx}(\sigma + \alpha x) = -x. \tag{20.277}$$

Eliminating x, we find

$$\frac{d}{dx}(\sigma + \alpha\frac{\beta\sigma}{1+\beta\sigma}) = -\frac{\beta\sigma}{1+\beta\sigma}. \tag{20.278}$$

The problem with this equation is, of course, that it cannot satisfy the correct initial data. Thus, we need a different scaling of time to study the initial behavior. If, instead, we take $\tau = k_{-1}t$, we find

$$\frac{d\sigma}{d\tau} = \alpha x - \alpha\beta\sigma(1-x), \tag{20.279}$$

$$\frac{dx}{d\tau} = \beta\sigma(1-x) - (1+\epsilon)x, \tag{20.280}$$

Here, setting ϵ to zero, we find that $\sigma + \alpha x = 1$ (using initial data $\sigma(0) = 1$, $x(0) = 0$), and then

$$\frac{d\sigma}{d\tau} = 1 - \sigma - \beta\sigma(\alpha - 1 + \sigma). \tag{20.281}$$

Although the analytical solution to this equation can be found, it is sufficiently informative to observe that the solution moves rapidly along the curve $\sigma + \alpha x = 1$ until it reaches the quasi-equilibrium value at $x = \frac{\beta\sigma}{1+\beta\sigma}$, from where the slow evolution (20.277) takes over.

Selected Solutions to Chapter 2

1. A rule of thumb (derived by Einstein) is that the diffusion coefficient for a globular molecule satisfies $D \sim M^{-1/3}$ where M is the molecular weight. Determine how well this relationship holds for the substances listed in Table 2.2 by plotting D and M on a log-log plot.

   Solution

   A log-log plot of D against M is given in Fig. 20.24, with the best-fit straight line shown as a dashed line. The equation of the best-fit line is $D = -4.2473 - 0.41658M$, which has slope reasonably close to $-1/3$.

2. A fluorescent dye with a diffusion coefficient of $D = 10^{-7}$ cm^2/s and binding equilibrium of $K_{\mathrm{eq}} = 30$ mM is used to track the spread of hydrogen ($D_h = 4.4 \times 10^{-5}$cm^2/s). Under these conditions the measured diffusion coefficient is 8×10^{-6}cm^2/s. How much dye is present? (Assume that the dye is a fast buffer of hydrogen and that the amount of hydrogen is much less that K_{eq}.)

   Solution

   Use that

   $$D_{\mathrm{eff}} = \frac{D_h + D_B \frac{w_0}{K_{eq}}}{1 + \frac{w_0}{K_{eq}}}, \qquad (20.282)$$

   so that

   $$w_0 = K_{eq}\left(\frac{D_h - D_{\mathrm{eff}}}{D_{\mathrm{eff}} - D_B}\right). \qquad (20.283)$$

   With these numbers we find that $w_0 = 0.14$M.

3. Segel, Chet and Henis (1977) used (2.21) to estimate the diffusion coefficient for bacteria. With the external concentration C_0 at 7×10^7ml^{-1}, at times t = 2, 5, 10, 12.5, 15, and 20 minutes, they counted N of 1,800, 3,700, 4,800, 5,500, 6,700, and 8,000 bacteria, respectively, in a capillary of length 32 mm with 1 μl total capacity. In addition, with external concentrations C_0 of 2.5, 4.6, 5.0, and 12.0 $\times 10^7$ bacteria per milliliter, counts of 1,350, 2,300, 3,400, and 6,200 were found at $t = 10$ minutes. Estimate D.
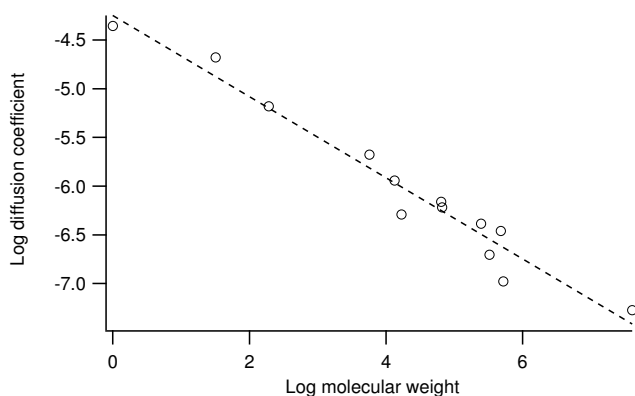
Figure 20.24: Log-log plot of diffusion coefficient D versus molecular weight M for exercise 1. The dashed line is the best-fit straight line, with equation $D = -4.2473 - 0.41658M$.

Solution

According to the formula (20.284)

$$D = \frac{\pi N^2}{4C_0^2 A^2 T}.$$ (20.284)

the ratio $\frac{N^2}{T}$ should be a constant. In fact, this number varies between 1.6×10^6 and 3.2×10^6, giving an estimate of $D = 0.7\text{-}1.5 \times 10^{-6} \text{cm}^2/\text{s}$. For the second data set, with T fixed, the estimate is $D = 0.56\text{-}1 \times 10^{-6} \text{cm}^2/\text{s}$.

4. Calculate the effective diffusion coefficient of oxygen in a solution containing 1.2×10^{-5} M/cm^3 myoglobin. Assume that the rate constants for the uptake of oxygen by myoglobin are $k_+ = 1.4 \times 10^{10}$cm^3 M^{-1}s^{-1}, and $k_- = 11$ s^{-1}.

Solution

Use (2.34)

$$D_{\text{eff}} = \frac{D + D_B \frac{w_0}{K_{eq}}}{1 + \frac{w_0}{K_{eq}}},$$ (20.285)

to calculate that $K_{eq} = 5.11 \times 10^{-5}$cm^{2}s^{-1}, which is essentially indistiguishable from that of myoglobin.

5. Find the maximal enhancement for diffusive transport of carbon dioxide via binding with myoglobin using $D_s = 1.92 \times 10^{-5}$ cm^2/s, $k_+ = 2 \times 10^8$ cm^3/M·s, $k_- = 1.7 \times 10^{-2}$/s. Compare the amount of facilitation of carbon dioxide transport with that of oxygen at similar concentration levels.

Solution

Calculate $\rho = \frac{D_c k_+ e_0}{D_s k_-}$, with $D_c = 5.1 \times 10^{-7} \text{cm}^2/\text{s}$ for myoglobin, $D_s = 1.92 \times 10^{-5}\text{cm}^2/\text{s}$ for carbon dioxide, $k_+ = 2 \times 10^8 \text{cm}^3\text{M}^{-1}\text{s}^{-1}$, and $k_- = 1.7 \times 10^{-2}\text{s}^{-1}$, and find $\rho = 3.1 \times 10^8 e_0 \text{cm}^3\text{M}^{-1}$. Compare this with oxygen using $D_s = 2.1 \times 10^{-5}\text{cm}^2/\text{s}$, $k_+ = 1.4 \times 10^{10}\text{cm}^3\text{M}^{-1}\text{s}^{-1}$, and $k_- = 11\text{s}^{-1}$, and find $\rho = 3.1 \times 10^7 e_0\text{cm}^3\text{M}^{-1}$, which is smaller by a factor of about 10.

6. Devise a model to determine the rate of production of product for a "one-dimensional" enzyme capsule of length L in a bath of substrate at concentration S_0. Assume that the enzyme is confined to the domain $0 \le x \le L$ and there is no flux through the boundary at $x = 0$. Assume that the enzyme cannot diffuse within the capsule but that the substrate and product can freely diffuse into, within, and out of the capsule. Show that the steady state production per unit volume of enzyme is less than the production rate of a reactor of the same size in which substrate is homogeneously mixed (infinite diffusion).

Solution

We assume that the reaction is a standard Michaelis-Menten type reaction, with

$$\text{S} + \text{E} \underset{k_{-1}}{\overset{k_1}{\rightleftharpoons}} \text{C} \overset{k_2}{\longrightarrow} \text{P} + \text{E}.$$
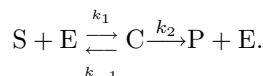
Then the concentrations of substrate, enzyme, and product in the enzymatic region are governed by the system of equations

$$\frac{\partial s}{\partial t} = D_s \frac{\partial^2 s}{\partial x^2} + k_{-1}c - k_1 se, \tag{20.286}$$

$$\frac{\partial c}{\partial t} = k_1 se - k_{-1}c - k_2 c, \tag{20.287}$$

$$\frac{\partial p}{\partial t} = D_p \frac{\partial^2 p}{\partial x^2} + k_2 c, \tag{20.288}$$

where, because enzyme does not diffuse, $c + e = e_0$. Using the quasi-steady state approximation

$$c = \frac{e_0 s}{(s + K_m)}, \tag{20.289}$$

with $K_m = \frac{k_{-1}+k_2}{k_1}$. It follows that at steady state,

$$0 = D_s s_{xx} - k_2 \frac{e_0 s}{(s + K_m)}, \tag{20.290}$$

$$0 = D_p p_{xx} + D_s s_{xx}. \tag{20.291}$$

It follows that the total rate of production is

$$R = -D_p p_x(L) = D_s s_x(L). \tag{20.292}$$

We introduce nondimensional variables $\sigma = \frac{s}{K_m}$, $y = \frac{x}{L}$, and find

$$0 = \sigma_{yy} - \alpha \frac{\sigma}{(\sigma + 1)}, \tag{20.293}$$

where $\alpha = \frac{L^2 k_2}{D_s}\frac{e_0}{K_m}$, with $\sigma'(0) = 0$ and $\sigma(0) = \frac{s_0}{K_m}$ and the rate of production is

$$R = \frac{D_s K_m}{L}\sigma_y(1) = k_2 L e_0 \frac{D_s}{k_2 L^2}\frac{K_m}{e_0}\sigma_y(1) = \frac{k_2 L e_0}{\alpha}\sigma_y(1), \qquad (20.294)$$

so that the effectiveness of the reaction, i.e., the rate of production per total amount of enzyme is

$$E = \frac{k_2}{\alpha}\sigma_y(1). \qquad (20.295)$$

The easiest way to solve this problem numerically is using "shooting", i.e., solve an initial value problem with $\sigma'(0) = 0, \sigma(1) = \sigma_1$ to determine both σ_0 and the rate of production, and then to plot rate of production as a function of σ_0.

Run the following maple code to see this solution.

```
N=100;
dx = 1/N;

%first a typical profile
s(1) = .1;
a=30;
t(1) = 0;

for j=1:N
s(j+1) = s(j)+dx*t(j);
t(j+1) = t(j) + dx*a*s(j)/(1+s(j));
end
x=.01*[0:N];
figure(1);
plot(x,s,'r',x,s./(1+s),'b');
legend('substrate concentration','local reaction rate')
xlabel('x')
ylabel('s');
title('Solution Profile');

%Now look at several values of external concentration:

M=20;
s1=.0001;
s2=.001;
s3=.01;
s4=.1;
S=[s1*[1:M],s1*M+s2*[1:M],(s1+s2)*M+s3*[1:M],(s1+s2+s3)*M+s4*[1:M]];
T=zeros(1,4*M);
for j=1:N
S = S + dx*T;
T = T +dx*a*S./(1+S);
```

```
end
E=T/a;
Se=S./(S+1);


figure(2);
plot(S,E,'r',S,Se,'b','linewidth',2)
legend('Difussion-limited Reactor','Well-stirred Reactor',4);
title('Effective Production Rate');
xlabel('External Substrate Concentration');
```

9. Red blood cells have a passive exchanger that exchanges a single Cl^- ion for a bicarbonate (HCO_3^-) ion. Develop a model for this exchanger and find the flux.

   Solution

   This is exactly the exchanger model (2.61) with $m = n = 1$.

10. Almost immediately upon entering a cell, glucose is phosphorylated in the first reaction step of glycolysis. How does this rapid and nearly unidirectional reaction affect the transmembrane flux of glucose as represented by (2.57)? How is this reaction affected by the concentration of ATP?

    Solution

    To solve this problem one must first modify the differential equation (2.52), replacing $-J$ by the removal term $-k_r s_i$, where k_r is the ATP dependent rate of phosphorylation. Now the system of equations is nonlinear and the formula for J is the same as before (2.57) where s_i is the solution of the quadratic equation

    $$C_2 s_i + C_1 s_i - s_e k k_- k_+ c_0 = 0, \qquad (20.296)$$

    where $C_2 = 2k_p k_r (k + k_- + k_+ s_e)$, and $C_1 = kk_- k_+ c_0 + k_r (2k_+ k s_e + 4kk_- + 2s_e k_+ k_- + 2k_-^2)$.

12. Simplify the model of the Na^+-Ca^{2+} exchanger (Fig. 2.9) by assuming that the binding and unbinding of Na^+ and Ca^{2+} are fast compared to the exchange processes between the inside and the outside of the cell. Write the new model equations and calculate the steady-state flux. Hint: The assumption of fast equilibrium gives

    $$k_1 c_i x_1 = k_{-1} n_i^3 x_2, \qquad (20.297)$$
    $$k_3 n_e^3 y_2 = k_{-3} c_e y_1. \qquad (20.298)$$

    Then introduce the new variables $X = X_1 + X_2$ and $Y = Y_1 + Y_2$ and derive the equations for X and Y.

Solution

Suppose that we know the initial concentrations of Ca^{2+} and Na^+ on both sides of the membrane. Call these $\bar{c}_i$, $\bar{c}_e$, $\bar{n}_i$ and $\bar{n}_e$. Then, in the case that the two volumes are equal, conservation of Ca^{2+} and Na^+ gives

$$c_i + c_e = \bar{c}_i + \bar{c}_e, \tag{20.299}$$

$$n_i + n_e = \bar{n}_i + \bar{n}_e. \tag{20.300}$$

The fact that one $Ca^{2+}$is transferred for 3 Na^+ gives the additional conservation condition

$$3(c_i - \bar{c}_i) + (n_i - \bar{n}_i) = 0. \tag{20.301}$$

Substitute these three equations into $n_e^3 c_i = n_i^3 c_e$ to get

$$\left(\frac{\bar{n}_i + \bar{n}_e - n_i}{n_i} \right)^3 = \frac{3\bar{c}_e - \bar{n}_i + n_i}{3\bar{c}_i - n_i + \bar{n}_i}. \tag{20.302}$$

The left hand side of this equation is a decreasing function of n_i, positive for $0 < n_i < \bar{n}_i + \bar{n}_e$ and unbounded at $n_i = 0$. The right hand side is positive and increasing for $\bar{n}_i - 3\bar{c}_e < n_i < 3\bar{c}_i + \bar{n}_i$ and unbounded at $n_i = 3\bar{c}_i + \bar{n}_i$. Since $\bar{n}_i - 3\bar{c}_e < \bar{n}_i + \bar{n}_e$, there is a unique intersection point of the two curves, and this intersection point lies between 0 and $\bar{n}_i + \bar{n}_e$, as it must.

13. Simplify the model of Fig. 2.11 by assuming fast binding of Na^+ and K^+, and draw the reaction diagram of the simplified model. Calculate the expression for the steady-state flux. Hint: combine the states X_1, X_2 and X_3 into a single state, X, and similarly for Y_1, Y_2 and Y_3. Then use the equilibrium conditions

$$x_1 = K_1 x_2 \kappa_i^2, \tag{20.303}$$

$$n_i^3 x_2 = K_2 x_3, \tag{20.304}$$

$$y_3 = K_5 n_e^3 y_2, \tag{20.305}$$

$$\kappa_e^2 y_2 = K_6 y_1, \tag{20.306}$$

where $K_i = k_{-i}/k_i$, n denotes $[Na^+]$, and κ denotes $[K^+]$, to derive the differential equations for X and Y.

Solution

If we assume that the binding and unbinding of Na^+ and Ca^{2+} are fast reactions compared to the exchange process between the inside and outside of the cell, we can simplify the reaction scheme shown in Fig. 2.9. In Fig. 20.25 we show the same model as in Fig. 2.9 but now states X_1 and X_2 are assumed to be in equilibrium (as shown by the dashed box) and similarly for states Y_1 and Y_2. (For this problem, this is somewhat dangerous, since the binding rates are concentration dependent and so at sufficiently low concentrations the assumption that these rates are faster than the exchange rates is incorrect. Nevertheless, we shall continue.)
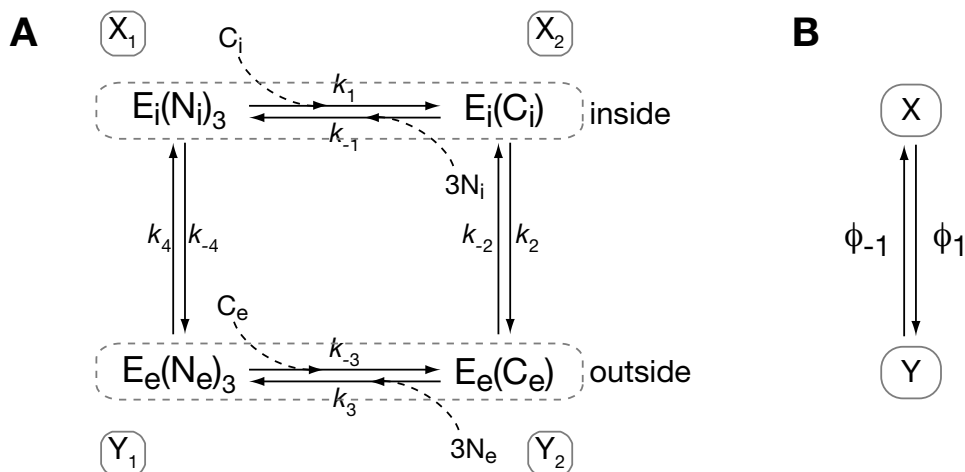
A

B

Figure 20.25: A:Schematic diagram of a simple model of the Na^+-Ca^{2+} exchanger. B: Diagram of the two-state model obtained by assuming fast equilibrium between the states in dashed boxes. The functions ϕ_1 and ϕ_{-1} are defined in (20.317) and (20.318).

The assumption of fast equilibrium gives

$$\begin{aligned}
k_1 c_i x_1 &= k_{-1} n_i^3 x_2, & (20.307) \\
k_3 n_e^3 y_2 &= k_{-3} c_e y_1, & (20.308)
\end{aligned}$$

and thus

$$\begin{aligned}
c_i x_1 &= K_1 n_i^3 x_2, & (20.309) \\
n_e^3 y_2 &= K_3 c_e y_1. & (20.310)
\end{aligned}$$

Now introduce two lumped states; $X = X_1 + X_2$ and $Y = Y_1 + Y_2$, with corresponding fractions $x = x_1 + x_2$ and $y = y_1 + y_2$. From (20.309) and (20.310) it follows that

$$\begin{aligned}
x &= x_1 \left(1 + \frac{c_i}{K_1 n_i^3} \right) & (20.311) \\
&= x_2 \left(1 + \frac{K_1 n_i^3}{c_i} \right), & (20.312) \\
y &= y_1 \left(1 + \frac{K_3 c_e}{n_e^3} \right) & (20.313) \\
&= y_2 \left(1 + \frac{n_e^3}{K_3 c_e} \right). & (20.314) \\
& & (20.315)
\end{aligned}$$

We find the differential equation for x by adding together the differential

1034

equations for x_1 and x_2. Thus,

$$\frac{dx}{dt} = k_4 y_1 - k_{-4} x_1 + k_{-2} y_2 - k_2 x_2. \tag{20.316}$$

Notice that the rates in this equation are all "slow" compared to the assumed fast binding and unbinding rates. Substituting the equilibrium solution and using that $x + y = 1$, we find

$$\begin{aligned}
\frac{dx}{dt} &= \left(\frac{n_e^3 k_4 + k_{-2} K_3 c_e}{n_e^3 + K_3 c_e}\right)(1-x) - \left(\frac{k_{-4} K_1 n_i^3 + k_2 c_i}{K_1 n_i^3 + c_i}\right) x, \tag{20.317} \\
&= \phi_{-1}(1-x) - \phi_1 x. \tag{20.318}
\end{aligned}$$

Thus, the four-state model depicted in Fig. 20.25A has been condensed down to the simpler two-state model

$$X \underset{\phi_{-1}}{\overset{\phi_1}{\rightleftharpoons}} Y, \tag{20.319}$$

shown in Fig. 20.25B. To find the steady-state flux, J, we set $dx/dt = 0$ in (20.317), solve for x, and substitute into

$$J = k_4 y_1 - k_4 x_1, \tag{20.320}$$

finding

$$J = \frac{k_2 k_4 (c_i n_e^3 - e^{\frac{FV}{RT}} c_e n_i^3)}{\eta}, \tag{20.321}$$

where

$$\begin{aligned}
\eta &= n_e^3 k_4 K_1 n_i^3 + n_e^3 k_4 c_i + k_{-2} K_3 c_e K_1 n_i^3 + k_{-2} K_3 c_e c_i + \\
&\quad k_{-4} K_1 n_i^3 n_e^3 + k_{-4} K_1 n_i^3 K_3 c_e + k_2 c_i n_e^3 + k_2 c_i K_3 c_e \tag{20.322}
\end{aligned}$$

14. Simplify the model of Fig. 2.11 by assuming fast binding of Na^+ and K^+, and draw the reaction diagram of the simplified model. Calculate the expression for the steady-state flux. Hint: combine the states X_1, X_2 and X_3 into a single state, X, and similarly for Y_1, Y_2 and Y_3. Then use the equilibrium conditions

$$\begin{aligned}
x_1 &= K_1 x_2 \kappa_i^2, \tag{20.323} \\
n_i^3 x_2 &= K_2 x_3, \tag{20.324} \\
y_3 &= K_5 n_e^3 y_2, \tag{20.325} \\
\kappa_e^2 y_2 &= K_6 y_1, \tag{20.326}
\end{aligned}$$

where $K_i = k_{-i}/k_i$, n denotes $[Na^+]$, and κ denotes $[K^+]$, to derive the differential equations for X and Y.
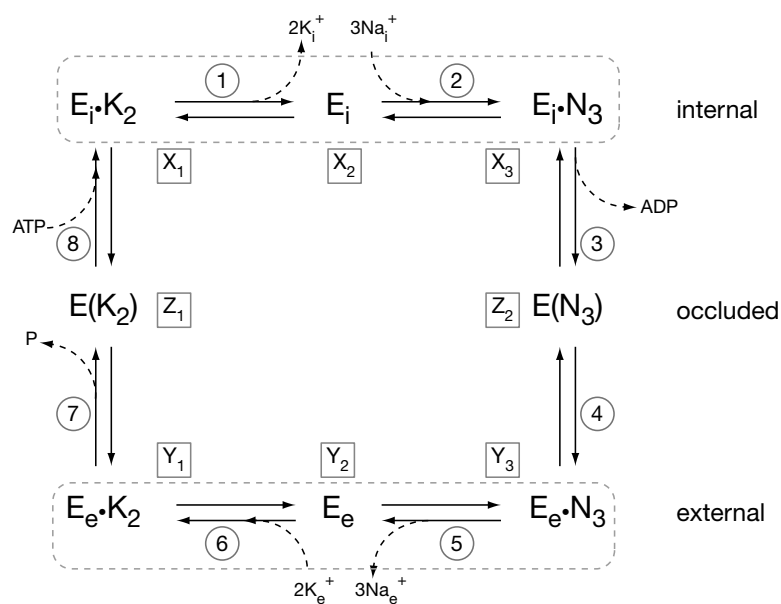
Solution

Figure 20.26: Model of the Na,K-ATPase based on the Post-Albers scheme. The model is simplified by assuming fast equilibrium between the boxed states.

We assume that the binding of Na^+ and K^+, either inside or outside, is so fast compared to the other reactions that it can be assumed to be at equilibrium. This is denoted by the dashed grey boxes in Fig. 20.26. Setting transitions 1, 2, 5 and 6 to be at equilibrium gives

$$x_1 = K_1 x_2 \kappa_i^2, \tag{20.327}$$

$$n_i^3 x_2 = K_2 x_3, \tag{20.328}$$

$$y_3 = K_5 n_e^3 y_2, \tag{20.329}$$

$$\kappa_e^2 y_2 = K_6 y_1, \tag{20.330}$$

where $K_i = k_{-i}/k_i$, n denotes $[Na^+]$, and κ denotes $[K^+]$. We now introduce two new variables by lumping together all the states that are connected by fast equilibria. Thus, let

$$x = x_1 + x_2 + x_3, \tag{20.331}$$

$$y = y_1 + y_2 + y_3. \tag{20.332}$$

Using (20.327) to (20.330) then gives

$$x = x_1 \left(1 + \frac{1}{K_1 \kappa_i^2} + \frac{n_i^3}{K_2 K_1 \kappa_i^2} \right), \tag{20.333}$$

$$= x_2 \left(1 + K_1 \kappa_i^2 + \frac{n_i^3}{K_2} \right), \tag{20.334}$$

$$= x_3 \left(1 + \frac{K_2}{n_i^3} + \frac{K_1 K_2 \kappa_i^3}{n_i^3} \right), \tag{20.335}$$

and

$$y = y_1 \left(1 + \frac{K_6}{\kappa_e^2} + \frac{K_5 K_6 n_e^3}{\kappa_e^2} \right), \tag{20.336}$$

$$= y_2 \left(1 + \frac{\kappa_e^2}{K_6} + K_5 n_e^3 \right), \tag{20.337}$$

$$= y_3 \left(1 + \frac{1}{K_5 n_e^3} + \frac{\kappa_e^2}{K_5 K_6 n_e^3} \right). \tag{20.338}$$

It follows that the differential equations for x and y are

$$\frac{dx}{dt} = k_8[\text{ATP}]z_1 + k_{-3}[\text{ADP}]z_2 - k_{-8}x_1 - k_1\kappa_i^2 x_1, \tag{20.339}$$

$$= k_8[\text{ATP}]z_1 + k_{-3}[\text{ADP}]z_2 - (\phi_{-8} + \phi_3)x, \tag{20.340}$$

$$\frac{dy}{dt} = k_{-7}[\text{P}_i]z_1 + k_4 z_2 - k_7 y_1 - k_{-4} y_3, \tag{20.341}$$

$$= k_{-7}[\text{P}_i]z_1 + k_4 z_2 - (\phi_7 + \phi_{-4})y, \tag{20.342}$$

where

$$\phi_3 = \frac{k_3}{\left(1 + \frac{K_2}{n_i^3} + \frac{K_1 K_2 \kappa_i^2}{n_i^3} \right)}, \tag{20.343}$$

$$\phi_{-4} = \frac{k_{-4}}{\left(1 + \frac{1}{K_5 n_e^3} + \frac{\kappa_e^2}{K_5 K_6 n_e^3} \right)}, \tag{20.344}$$

$$\phi_7 = \frac{k_7}{\left(1 + \frac{K_6}{\kappa_e^2} + \frac{K_5 K_6 n_e^3}{\kappa_e^2} \right)}, \tag{20.345}$$

$$\phi_{-8} = \frac{k_{-8}}{\left(1 + \frac{1}{K_1 \kappa_i^2} + \frac{n_i^3}{K_2 K_1 \kappa_i^2} \right)}. \tag{20.346}$$

Thus, finally, the full model shown in Fig. 2.11 simplifies to the four-state model shown in Fig. 20.27.

The steady-state flux through this model can be calculated by first calculating the steady-state expressions for x, y and z_1 (note that $x + y + z_1 + z_2 = 1$ so that only three of the ATPase states are independent) and then substituting them into the equation for the flux, $J = \phi_3 x - k_{-3}z_2$. Similarly to what we obtained in (2.83) it turns out that

$$J = \frac{\phi_3 k_4 \phi_7 k_8[\text{ATP}] - k_{-3}\phi_{-4}k_{-7}\phi_{-8}[\text{ADP}][\text{P}_i]}{16 \text{ other terms}}, \tag{20.347}$$

$$= \frac{[\text{ATP}]n_i^3 \kappa_e^2 - [\text{ADP}][\text{P}_i]\kappa_i^2 n_e^3 (\prod_{i=1}^{8} K_i)}{135 \text{ other terms}}. \tag{20.348}$$
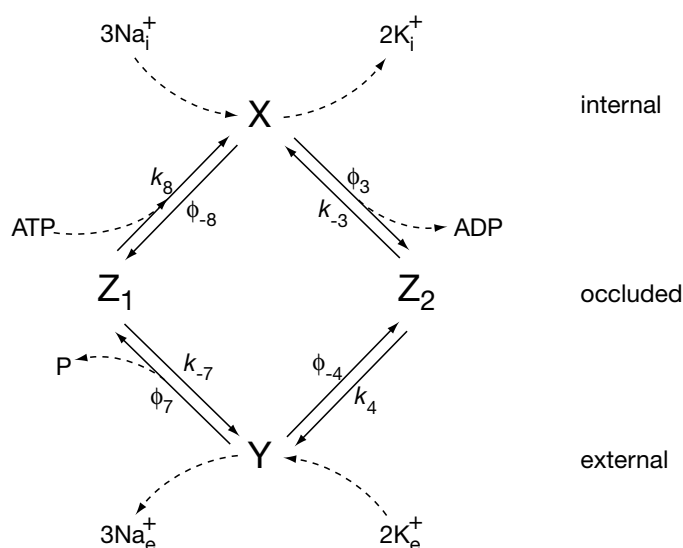
Figure 20.27: Four-state model of the Na,K-ATPase, derived by simplification of the Post-Albers scheme of Fig. 2.11. The expressions for the ϕ's are given in (20.343) to (20.346).

15. The process by which Ca^{2+} is taken up into the sarcoplasmic reticulum (SR) in muscle and cardiac cells is similar to the Na,K-ATPase, but simpler. Two intracellular Ca^{2+} ions bind with a carrier protein with high affinity for Ca^{2+}. ATP is dephosphorylated, with the phosphate bound to the carrier. There is a conformational change of the carrier protein that exposes the Ca^{2+} to the interior of the SR and reduces the affinity of the binding sites, thereby releasing the two ions of Ca^{2+}. The phosphate is released and the conformation changed so that the Ca^{2+} binding sites are once again exposed to the intracellular space.

Formalize this reaction and find the rate of Ca^{2+} uptake by this pump.

Solution

The system of differential equations is (where $sc = u$, and $scp = v$, $c_i p = w$)

$$\frac{ds_e}{dt} = k_{-e}u - k_e s_e c_e + J, \tag{20.349}$$

$$\frac{dc_e}{dt} = k_e s_e c_e - k_{-e}sc + k_{-a}scp - k_a sc, \tag{20.350}$$

$$\frac{dv}{dt} = k_a sc - k_{-a}scp + k_{-i}s_i c_i p - k_i v, \tag{20.351}$$

$$\frac{ds_i}{dt} = k_i v - k_{-i}s_i c_i p - J, \tag{20.352}$$

$$\frac{dw}{dt} = k_i v - k_{-i} s_i w - k_p w + k_{-p} c_e, \tag{20.353}$$

with the conservation law $c_e + w + v + u = c_0$. Solving these in steady state we find that

$$J = c_0 \frac{K_p s_e - K_{-p} s_i}{s_e k_e + K_0 + s_i K_i + s_e * s_i K_{ei}}, \tag{20.354}$$

where $K_p = k_p k_i k_e k_a$, $K_{-p} = k_{-i} k_{-a} k_{-p} k_{-e}$, $K_e = k_e(k_i k_p + k_{-a} k_p + k_i k_a + k_a k_p)$, $K_i = k_{-i}(k_{-e} k_{-a} + k_{-p} k_a + k_{-p} k_{-e} + k_{-p} k_{-a})$, $K_{ei} = k_e k_{-i}(k_{-a} + k_a)$, $K_e = k_{-i}(k_{-a} + k_{-a} k_p + k_e k_a k_{-i})$, $K_0 = k_i k_{-p} k_{-e} + k_i k_{-e} k_p + k i k_{-p} k_a + k_i k_a k_p + k_{-a} k_{-p} k_{-e} + k_{-e} k_{-a} k_p$

16. Calculate the flux of the Ran-GTP nuclear transporter. Use the information given in the text to estimate the concentrating ability of this transporter, assuming there is no difference in potential across the nuclear membrane.

   Solution

   There are seven species to track. These are the carrier protein E_i and E_e, (denoted e_i and e_e), the carrier protein bound to cargo, $C \cdot E_i$ and $C \cdot E_e$ (denoted x_i and x_e), the carrier protein bound to Ran-GTP, y_i and y_e, and carrier protein bound to Ran-GDP, z_e. We ignore Ran-GDP bound to carrier on the interior of the nucleus since RanGAP is in the cytoplasm only. and assume that there is no Ran-GDP in the nucleus. The differential equations are

$$\frac{de_i}{dt} = -k_{c+} e_i c_i + k_{c-} x_i - k_{GTP_i} e_i + k_{GTP-} y_i, \tag{20.355}$$

$$\frac{de_e}{dt} = -k_{c+} e_e c_e + k_{c-} x_e - k_{GTP_e} e_e + k_{GTP-} y_e - k_{GDP_e} e_e + k_G\text{(20.356)}$$

$$\frac{dx_i}{dt} = kx_e - kx_i + k_{c+} e_i c_i - k_{c-} x_i, \tag{20.357}$$

$$\frac{dx_e}{dt} = -kx_e + kx_i + k_{c+} e_e c_e - k_{c-} x_e, \tag{20.358}$$

$$\frac{dy_i}{dt} = ky_e - ky_i + k_{GTP_i} e_i - k_{GTP-} y_i, \tag{20.359}$$

$$\frac{dy_e}{dt} = ky_i - ky_e + k_{GTP+} e_e - k_{GTP-} y_e - k_{hyd+} y_e + k_{hyd-} z, \tag{20.360}$$

$$\frac{dz}{dt} = k_{GDP_e} e_e - k_{GDP-} z + k_{hyd+} y_e - k_{hyd-} z. \tag{20.361}$$

   The flux of protein is given by $J = k_{c+} e_e c_e + k_{c-} x_e$. Now find the steady flux using Maple.

17. Suppose that two compartments, each of one liter in volume, are connected by a membrane that is permeable to both K^+ and Cl^-, but not to water or protein (X). Suppose further that, as illustrated in Fig. 20.28, the extracellular compartment initially contains 300 mM K^+ and 300 mM Cl^-, while the intracellular compartment initially contains 200 mM protein, with valence -2, and 400 mM K^+.

Figure 20.28: The initial configuration for Exercise 17.

(a) Is the starting configuration electrically and osmotically balanced?

(b) Find the concentrations at equilibrium.

(c) Why is $[K^+]_i$ at equilibrium greater than its starting value, even though $[K^+]_i > [K^+]_e$ initially? Why does K^+ not diffuse from right to left to equalize the concentrations?

(d) What is the equilibrium potential difference?

(e) What would happen if the connecting membrane were suddenly made permeable to water? How large is the osmotic pressure developed?

Solution

(a) It is both electrically and osmotically balanced, since there can be no water flow there is no osmotic pressure.

(b) At equilibrium, $[K^+]_i = 490$ mM, $[K^+]_e = 210$ mM, $[Cl^-]_i = 90$ mM and $[Cl^-]_e = 210$ mM.

(d)
$$V = \frac{kT}{q} \ln(\frac{210}{490}) = 25.7 mV \qquad (20.362)$$

at 25°C.

18. Suppose the intracellular macromolecule X can bind b molecules of the ion S via $X + bS \rightleftharpoons XS_b$. What is the effect of this buffering on the Gibbs-Donnan equilibrium potential?

Solution

When the reaction is at equilibrium, $k_+[X][S]_i^b = k_-[XS]$, where $[X] + [XS] = X_0$, and for charge electroneutrality, $z_x[X] + (z_x - b)[XS] + z[S']_i = z[S]_i$,

$z[S']_e = z[S]_e$. Finally, $[S']_e[S]_e = [S']_i[S]_i$ so that the movement of both S and S' is opposed by the same potential difference. This system of equations can be reduced to the single algebraic equation

$$y - \frac{1}{y} = \frac{\beta K}{K + y^b} + x_0, \qquad (20.363)$$

where $y = \frac{[S]_i}{[S]_e}$, $K = \frac{k_-}{k_+[S]_e^b}$, $\beta = \frac{b}{z}$, $x_0 = (\beta - \frac{z_x}{z})\frac{X_0}{[S]_e}$. This system of equations cannot be solved analytically, but it can be solved numerically. In fact, the left side of the equation is a monotone increasing function of y for $y > 0$, while the right side of the equation is a monotone decreasing function of y, so that there is a unique positive solution.

19. A 1.5 oz bag of potato chips (a typical single serving) contains about 200 mg of Na^+. When eaten and absorbed into the body, how many osmoles does this bag of potato chips represent?

Solution

The gram molecular weight of sodium is 23, while the gram molecular weight of chloride is 35.5. Therefore 200 mg of sodium is 8.7×10^{-3} moles of sodium. Since salt has equal amounts of sodium and chloride, 200 grams of sodium gives 0.174 osmoles.

20. (a) Confirm that π_s in (2.137) has units of pressure.

(b) Confirm the statement that a pressure of 25 atm corresponds to a column of water over 250 meters high.

(c) Consider a vertical tube with a cross-sectional area of 1 cm^2. The bottom of the tube is closed with a semi-permeable membrane and 1 gram of sugar is placed in the tube. The membrane-closed end of the tube is then put into an inexhaustible supply of pure water at $T = 300$K. What will be the height of the water in the tube at equilibrium? (The weight of a sugar molecule is 3×10^{-22} gm, and the density of water is 1 gm/cm^3).

(d) Two columns with cross-sectional area 1 cm^2 are initially filled to a height of one meter with water at $T = 300°$ K. Suppose 0.001 gm of sugar is dissolved in one of the two columns. How high will the sugary column be when equilibrium is reached?.

(e) Suppose in the previous question 1 gm of sugar is dissolved in one of the two columns. What is the equilibrium height of the two columns?

Solution

(a) The units of RcT are 10^3Jm$^{-3} = 10^3$Nm$^{-2} = 10^3$Pa.

(b) If $\rho gh = 25$atm $= 2.533 \times 10^6$N m^{-2}, then $h = 256.6$ m.

(c) Since a gram of sugar has $\frac{1}{3} \times 10^{22}$ molecules, $\frac{nkT}{\rho gA} = 14.12$m^2. The column will have height 3.76m.

(d) $h_1 = \frac{h_0}{2} + \frac{1}{2}\sqrt{h_0^2 + \frac{2nkT}{\rho gA}} = 1.007$m.

(e) There is not enough water to balance the osmotic pressure.

23. Suppose 90% of the Na^+ in the bath of a squid axon is replaced by inert choline, preserving electroneutrality. What happens to the equilibrium potentials and membrane potentials?

Solution

Using typical ionic concentrations for squid axon from Table 2.1, the normal sodium Nernst potential is 55.7 mV. With 90% choline in the extracellular space, the sodium Nernst potential drops to -3.5 mV, and the resting potential decreases as well. For example, with Nernst potentials $V_{Na} = 56$ mV, $V_K = $ -77 mV, $V_{Cl} = $ =-68 mV, and with conductances g_{Na}=0.01 mS/cm^2, g_K= 0.367 mS/cm^2, and g_{Cl}=0.1 mS/cm^2, the resting potential is

$$V_r = \frac{g_{Na}V_{Na} + g_K V_K + g_{Cl}V_{Cl}}{g_{Na} + g_K + g_{Cl}} = -72.3\text{mV}, \qquad (20.364)$$

while with 90% choline the resting potential is $V_r = -73.6$ mV.

27. Since the Na,K-ATPase is electrogenic, the pump rate P in the pump-leak model must also include effects from the membrane potential. What effect does membrane potential have on the expression (2.167) and how does this modification affect the solution?

Solution

Since a negative voltage potential opposes the net outward current of the Na,K ATPase, a reasonable model for the flux P is (in non-dimensional units)

$$P = \rho u^3 \exp(v) = \frac{\rho u^3}{y} \qquad (20.365)$$

It is easy to solve the resulting model equations and determine that the solution is qualitatively similar to that shown in Fig 2.17, however, the pump reaction rate ρ must be larger to achieve the same potential as in Fig. 2.17.

28. Use (2.221) to simulate a diffusion process, and verify that the mean and variance of the process are 0 and $2Dt$, respectively, as expected.

Solution

A simple Matlab code to simulate a diffusion process is the following

```
D = 1;
N = 100;
X = zeros(N,1);
U = X;
```

```
dt = .01;
sqdt = sqrt(2*dt*D);
k_end = 100;
for k = 1:k_end
dx = sqdt*randn(N,1);
X = X + dx;
U(:,k) = X;
end
T = [1:k]*dt;

figure(1)
plot(T,U)

figure(2)
plot(T,mean(U),T,var(U))
```

29. Find the steady state probability distribution for the Ornstein-Uhlenbeck process.

   Solution

   The Fokker-Planck equation for the Ornstein-Uhlenbeck process is

   $$\frac{\partial p}{\partial t} = \frac{\partial}{\partial x}(xp) + \frac{\partial^2 p}{\partial x^2}. \tag{20.366}$$

   At steady state $(\frac{\partial p}{\partial t} = 0)$, it must be that

   $$xp + \frac{dp}{dx} = 0, \tag{20.367}$$

   from which it follows that

   $$p(x) = \frac{1}{\sqrt{2\pi}} \exp(-\frac{x^2}{2}), \tag{20.368}$$

   which is normalized so that $\int_{-\infty}^{\infty} p(x)dx = 1$.

30. A small particle (with diffusion constant D and viscosity ν) experiences a constant load F directed to the left but is not permitted to move into the region with $x < 0$. Suppose that the particle is initially at $x = 0$. What is the expected time to first reach location $x = \delta$?

   Solution

   We solve the mean first exit time problem for $T(0)$, where $T(x)$ satisfies the differential equation

   $$D\frac{d^2 T}{dx^2} - \frac{F}{\nu}\frac{dT}{dx} = -1, \tag{20.369}$$

subject to boundary conditions $T'(0) = 0$ and $T(\delta) = 0$. The solution is

$$T(0) = \frac{\nu^2}{F^2}(D \exp(\frac{F\delta}{\nu D}) - \frac{F\delta}{\nu} - D).$$

(20.370)

31. Suppose that a molecule enters a spherical cell of radius 5 μm at its boundary. How long will it take for the molecule to move by diffusion to find a binding target of radius 0.5 nm located at the center of the cell? Use a diffusion coefficient of 10^{-6}cm^2/s. (Hint: In higher dimensions the differential equation for the mean first exit time is $\nabla^2 T = -1$.)

Solution

We solve a mean first exit time problem for a diffusing particle in spherical geometry,

$$D\nabla^2 T = -1$$

(20.371)

subject to boundary conditions $\frac{\partial T}{\partial r}(R) = 0$ and $T(r_0) = 0$, where R is the outer radius of the sphere and r_0 is the radius of the target region. In spherical coordinates, the equation (20.371) is

$$\frac{D}{r^2}\frac{\partial}{\partial r}(r^2\frac{\partial T}{\partial r}) = -1,$$

(20.372)

and the solution is

$$T(r) = \frac{1}{3D}(R^3(\frac{1}{r_0} - \frac{1}{r}) + \frac{1}{2}(r_0^2 - r^2)),$$

(20.373)

so that $T(R) \approx \frac{R^3}{3Dr_0} \approx 833$ s.

Selected Solutions to Chapter 3

1. Show that the GHK equation (3.2) satisfies both the independence principle and the Ussing flux ratio, but that the linear I–V curve (3.1) satisfies neither.

   Solution

   (a) GHK equation

   To see whether the GHK flux equation satisfies the Ussing flux ratio we must first find some expression for the one way fluxes. This is most simply done by setting either the external or the internal concentrations to zero. For example, the outward flux is obtained by setting the external concentration of the ion to zero. Thus, setting $c_e = 0$ in (2.121) we get

   $$|J_{\text{out}}| = P_S \frac{zFV}{RT} \frac{c_i}{1 - \exp\left(\frac{-zVF}{RT}\right)}, \qquad (20.374)$$

   and similarly, setting $c_i = 0$ in (2.121) we get

   $$|J_{\text{in}}| = P_S \frac{zFV}{RT} \frac{c_e \exp\left(\frac{-zVF}{RT}\right)}{1 - \exp\left(\frac{-zVF}{RT}\right)}. \qquad (20.375)$$

   Note that we take the absolute value of the fluxes as the Ussing flux ratio assumes that all fluxes are positive.

   Taking the ratio of these gives

   $$\left|\frac{J_{\text{in}}}{J_{\text{out}}}\right| = \frac{c_e}{c_i} \exp\left(\frac{-zVF}{RT}\right), \qquad (20.376)$$

   which is the Ussing flux ratio.

   The GHK current also satisfies the independence principle. This follows immediately from the fact that J_{in} and J_{out} are linear functions of the concentrations. Thus, a doubling of c_i, say, results in a doubling of J_{out}, which is the independence principle.

   It's important to note that the Ussing flux ratio and independence are *not* equivalent. There are simple models for ionic flow that satisfy the Ussing flux ratio but not independence; some of these are discussed in Keener and Sneyd (1998).

(b) The linear equation

First note that, since the current does not depend linearly on either c_i or c_e, the linear $I - V$ curve cannot satisfy the independence principle.

However, it is not possible to use the above procedure to find the inward and outward fluxes, as the linear $I-V$ curve is not valid in the limit where either the internal or external concentration tends to zero. (As a side note, it is important to note how this makes the GHK formulation more useful for many situations. Although in reality there is never a single ion type present and so this singular limit never causes any problems, it is nice not to have to deal with the associated mathematical difficulties that can arise when the linear $I - V$ curve is used.)

Instead of calculating the inward and outward fluxes separately, we use the formulation of the Ussing flux ratio in (??). In other words, if we assume that $c_i = c_i'$, and thus the outward fluxes are the same, then the Ussing flux ratio can be reformulated as

$$\frac{I'}{I} = \frac{J_{\text{out}}' - J_{\text{in}}'}{J_{\text{out}} - J_{\text{in}}} \tag{20.377}$$

$$= \frac{J_{\text{out}}'\left(1 - \frac{J_{\text{in}}'}{J_{\text{out}}'}\right)}{J_{\text{out}}\left(1 - \frac{J_{\text{in}}}{J_{\text{out}}}\right)} \tag{20.378}$$

$$= \frac{1 - \frac{J_{\text{in}}'}{J_{\text{out}}'}}{1 - \frac{J_{\text{in}}}{J_{\text{out}}}} \tag{20.379}$$

$$= \frac{1 - \frac{c_e'}{c_i'}\exp\left(\frac{-VF}{RT}\right)}{1 - \frac{c_e}{c_i}\exp\left(\frac{-VF}{RT}\right)} \tag{20.380}$$

$$= \frac{c_i - c_e'\exp\left(\frac{-VF}{RT}\right)}{c_i - c_e\exp\left(\frac{-VF}{RT}\right)}. \tag{20.381}$$

Now we need only note that the linear $I - V$ curve does not satisfy this equation, and thus does not satisfy the Ussing flux ratio.

The astute reader may be wondering why we bothered to rederive (20.381) when it is already derived in the book. The answer is that the derivation in the book relies on the use of the independence principle, and thus is no good for our purposes. After all, if the linear $I - V$ curve doesn't satisfy the independence principle, it thus will automatically not satisfy any other equation that depends on the independence principle for its derivation. However, the derivation of the Ussing flux ratio given above does not use the independence principle, which shows that we may indeed use (20.381) to see whether the linear $I - V$ curve obeys the Ussing flux ratio.

3. In Section 3.3.1 the PNP equations were used to derive I–V curves when two ions with opposite valence are allowed to move through a channel. Extend this analysis by assuming that two types of ions with positive valence and one

type of ion with negative valence are allowed to move through the channel. Show that in the high concentration limit, the negative ion obeys a linear I–V curve, but the two positive ions do not. Details can be found in Chen, Barcilon, and Eisenberg (1992), equations (43)–(45).

Solution

First we write down the differential equations and boundary conditions that apply to this three-ion case. Let c_1 and c_2 denote the concentrations of the positive ions S_1 and S_2, and c_3 the concentration of the negative ion S_3. Then we extend (3.23)–(3.25) in the book by adding a second positive ion to get

$$-\bar{J}_1 = \frac{dc_1}{dx} + c_1 \frac{d\phi}{dx}, \tag{20.382}$$

$$-\bar{J}_2 = \frac{dc_2}{dx} + c_2 \frac{d\phi}{dx}, \tag{20.383}$$

$$-\bar{J}_3 = \frac{dc_3}{dx} - c_3 \frac{d\phi}{dx}, \tag{20.384}$$

$$\frac{d^2\phi}{dx^2} = -\lambda^2 (c_1 + c_2 - c_3), \tag{20.385}$$

where the terms are as defined in the book. The first three equations govern the flux of the ions through the channel, while the last equation is Poisson's equation.

When formulating the boundary conditions we must remember to keep the solutions on either side of the membrane electrically neutral. This is most easily done with the introduction of two new parameters, l and r, that govern the relative proportions of c_1 and c_2 on either side of the membrane. Thus,

$$\begin{array}{ll} c_1(0) = lc_i, & c_1(1) = rc_e, \\ c_2(0) = (1-l)c_i, & c_2(1) = (1-r)c_e, \\ c_3(0) = c_i, & c_3(1) = c_e, \\ \phi(0) = v, & \phi(1) = 0. \end{array} \tag{20.386}$$

Now that we have the equations, we want to construct solutions for the long-channel limit $(\lambda \gg 1)$ and the short channel limit $(\lambda \ll 1)$.

(a) The long-channel limit

Just as in the book, letting $\lambda \to \infty$ gives

$$c_1 + c_2 = c_3, \tag{20.387}$$

which happens to satisfy both boundary conditions (and thus we can avoid the difficulties of a full matched asymptotic expansion procedure).

If we now add the three flux differential equations we get

$$\frac{d}{dx}(c_1 + c_2 + c_3) = -\bar{J}, \tag{20.388}$$

where $\bar{J} = \bar{J}_1 + \bar{J}_2 + \bar{J}_3$ is an unknown constant to be determined from the boundary conditions. Thus

$$c_1 + c_2 + c_3 = -\bar{J}x + \bar{K}, \tag{20.389}$$

for some other constant, $\bar{K}$. Applying the boundary conditions now gives $\bar{K} = 2c_i$ and $-\bar{J} = 2c_e + 2c_i$. Thus

$$c_1 + c_2 + c_3 = 2[(c_e - c_i)x + c_i], \tag{20.390}$$

whence it follows (using (20.387)) that

$$c_1 + c_2 = c_3 = (c_e - c_i)x + c_i. \tag{20.391}$$

Hence, the concentration profile of c_3 in the channel is linear, but those of c_1 and c_2 not necessarily so. The profiles of c_1 and c_2 sum to a linear profile, but this does not mean that the individual profiles must be linear also.

We now solve for $\phi(x)$. Forming (20.382) + (20.383) - (20.384) gives

$$(c_1 + c_2 + c_3)\frac{d\phi}{dx} = -\tilde{J}, \tag{20.392}$$

where $\tilde{J} = -\bar{J}_1 - \bar{J}_2 + \bar{J}_3$. Thus

$$[(c_e - c_i)x + c_i]\frac{d\phi}{dx} = -\tilde{J}, \tag{20.393}$$

which can now be solved for ϕ by separation of variables. One integration gives

$$\phi(x) = -\frac{\tilde{J}}{2(c_e - c_i)}\ln[2(c_e - c_i)x + 2c_i] + \tilde{K}, \tag{20.394}$$

for some other constant $\tilde{K}$. We now determine $\tilde{J}$ and $\tilde{K}$ from the boundary conditions $\phi(0) = v$, $\phi(1) = 0$. Plugging in these conditions and solving then gives

$$-\frac{\tilde{J}}{2(c_e - c_i)} = \frac{v}{\ln\left(\frac{c_i}{c_e}\right)}, \tag{20.395}$$

$$\tilde{K} = -\frac{\ln(2c_e)v}{\ln\left(\frac{c_i}{c_e}\right)}. \tag{20.396}$$

Substituting into the expression for ϕ then gives

$$\phi(x) = \frac{v}{\ln\left(\frac{c_i}{c_e}\right)}\ln[2(c_e - c_i)x + 2c_i] - \frac{\ln(2c_e)v}{\ln\left(\frac{c_i}{c_e}\right)} \tag{20.397}$$

$$= \frac{v}{\ln\left(\frac{c_i}{c_e}\right)}\ln\left[\frac{(c_e - c_i)x + c_i}{c_e}\right]. \tag{20.398}$$

Since we are going to be using the ratio c_i/c_e often in the following pages, we define

$$c = c_i/c_e \tag{20.399}$$

to make things look a little simpler.

Finally, we want to find each flux. This is most easily done by solving for c_1, c_2 and c_3. Of course, we already have an expression for $c_3(x)$, namely (20.391 above. Hence, it follows immediately that

$$-\bar{J}_3 = \frac{dc_3}{dx} - c_3\frac{d\phi}{dx} \tag{20.400}$$

$$= \frac{c_e - c_i}{\ln(c)}[\ln(c) - v]. \tag{20.401}$$

Since $\ln(c)$ is the Nernst potential of S$_3$, we see immediately that S$_3$ obeys a linear $I - V$ curve, as claimed.

Calculating the fluxes of c_1 and c_2 takes somewhat longer, but is no more difficult in concept. We shall illustrate the procedure for c_1 only, since the calculations for c_2 are practically identical.

Start with the differential equation for c_1:

$$\frac{dc_1}{dx} + c_1\frac{d\phi}{dx} = -\bar{J}_1. \tag{20.402}$$

Since $\phi(x)$ is known, this differential equation can be solved by using an integrating factor. Multiply through by e^ϕ to get

$$\frac{d}{dx}(c_1 e^\phi) = -\bar{J}_1 e^\phi. \tag{20.403}$$

Now note that

$$e^\phi = [(1 - c)x + c]^{v/\ln(c)}. \tag{20.404}$$

Thus, integrating (20.403), we get

$$c_1 e^\phi = \left(\frac{\ln(c)}{v + \ln(c)}\right)\left(\frac{-\bar{J}_1[(1 - c)x + c]^{\frac{v+\ln(c)}{\ln(c)}}}{1 - c}\right) + K, \tag{20.405}$$

for some constant K.

$\bar{J}_1$ and K can now be determined from the boundary conditions. At $x = 0$ we get

$$lc_i e^v = \left(\frac{\ln(c)}{v + \ln(c)}\right)\left(\frac{-\bar{J}_1 c^{\frac{v+\ln(c)}{\ln(c)}}}{1 - c}\right) + K \tag{20.406}$$

$$= \left(\frac{\ln(c)}{v + \ln(c)}\right)\left(\frac{-\bar{J}_1 c e^v}{1 - c}\right) + K, \tag{20.407}$$

while at $x = 1$

$$rc_e = \left(\frac{\ln(c)}{v + \ln(c)}\right)\left(\frac{-\bar{J}_1}{1 - c}\right) + K. \tag{20.408}$$
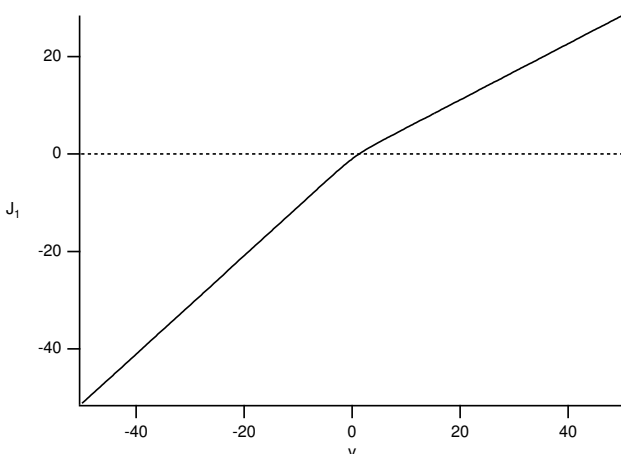
Figure 20.29: Plot of $\bar{J}_1$ against v. The flux is mostly a fairly straight function of v, except around the reversal potential where it looks more like a GHK flux relationship. Parameters were chosen arbitrarily as $c_i = 1$, $c_e = 2$, $r = 0.7$, $l = 0.4$.

Solving these two equations for $-\bar{J}_1$ and K gives

$$-\bar{J}_1 = \left(\frac{v + \ln(c)}{\ln(c)}\right) \frac{(lc_i e^v - rc_e)(1 - c)}{ce^v - 1}, \qquad (20.409)$$

$$K = rc_e - \frac{lc_i e^v - rc_e}{ce^v - 1}, \qquad (20.410)$$

and thus, finally,

$$c_1 = \frac{1}{ce^v - 1}\left\{(lc_i e^v - rc_e)[(1 - c)x + c] + c_i e^v (r - l)[(1 - c)x + c]^{v/\ln(c)}\right\}. \tag{20.411}$$

Note that in passing we have obtained the expression for the flux of S_1, namely (20.409). It's interesting to note a few things about this flux expression. Firstly, it has the correct reversal potential (fortunately); although it looks like it has multiple zeros it actually doesn't, as when $v = -\ln(c)$ the zeros on the top and bottom lines cancel out. Secondly, it looks very like the GHK flux equation, with the exception that is multiplied by the linear v term on the top of the fraction. Thus, in this case the flux of S_1 is a combination of both the GHK and the linear flux expressions.

The calculations for $\bar{J}_2$ and c_2 are essentially identical, so we won't reproduce them here.

(b) Short-channel limit

In the limit of a short channel, or small ionic concentrations on either side of the membrane, the calculations are exactly the same as those in

the book (equations (3.27)–(3.30)). Thus,

$$\frac{d^2\phi}{dx^2} = 0, \tag{20.412}$$

from which it follows that $d\phi/dx = -v$ and that the flux of each ion satisfies the GHK current equation (equation (3.31) of the book).

14. Suppose that a channel consists of k identical, independent subunits, each of which can be open or closed, and that a current can pass through the channel only if all units are open.

  (a) Let S_j denote the state in which j subunits are open. Show that the conversions between states are governed by the reaction scheme

$$S_0 \underset{\beta}{\overset{k\alpha}{\rightleftarrows}} S_1 \ldots S_{k-1} \underset{k\beta}{\overset{\alpha}{\rightleftarrows}} S_k. \tag{20.413}$$

  (b) Derive the differential equation for x_j, the proportion of channels in state j.

  (c) By direct substitution, show that $x_j = \binom{k}{j} n^j (1-n)^{k-j}$, where $\binom{k}{j} = \frac{k!}{j!(k-j)!}$ is the *binomial coefficient*, is an invariant manifold for the system of differential equations, provided that

$$\frac{dn}{dt} = \alpha(1-n) - \beta n. \tag{20.414}$$

Solution

  (a) First, let α be the rate at which a single subunit opens, and let β be the rate at which a single subunit closes. The channel can move from state S_0 to state S_1 by having any one of its subunits open. Since there are k subunits, this can occur in any of k different ways. With the rate of opening of an individual subunit being α, it follows that the rate at which S_0 converts to S_1 is given by $k\alpha$. However, the reverse conversion from S_1 to S_0 can occur only at the base rate β, since there is only a single subunit that can close.

  In general, the transition from state S_j to state S_{j+1} can be written as

$$S_j \underset{(j+1)\beta}{\overset{(k-j)\alpha}{\rightleftarrows}} S_{j+1}. \tag{20.415}$$

  (b) The solution to part (a) above gives immediately the solution to part (b) by applying the law of mass action:

$$\frac{dx_j}{dt} = (k-j+1)\alpha x_{j-1} + (j+1)\beta x_{j+1} - [j\beta + (k-j)\alpha]x_j. \tag{20.416}$$

(c) Strictly speaking, since we are given the answer we need only check that it works. However, before doing that it is useful to gain some insight into where this answer comes from.

Note that, from conservation we must have $x_0 + x_1 + \cdots + x_k = 1$. Thus, we have $k + 1$ bits that change over time but always must add to give 1. The trick is in using the identity

$$1 = [n + (1 - n)]^k, \tag{20.417}$$

and recognizing that the right hand side has the desired number of terms (i.e., $k + 1$ of them). Hence, if we ensure that x_0 corresponds to the first term of $[n + (1 - n)]^k$, x_1 to the second, and so forth, we automatically ensure that the x_js always sum to one. That is where the expression for x_j comes from; it is the $j + 1$st term in the expansion of $[n + (1 - n)]^k$. However, it remains to be seen whether we can find a differential equation for n that is consistent with this. First, take d/dt of the equation $x_j = \binom{j}{k} n^j (1 - n)^{k-j}$ to get

$$\frac{dx_j}{dt} = \frac{dn}{dt} \binom{k}{j} \left[j n^{j-1}(1 - n)^{k-j} - (k - j)n^j(1 - n)^{k-j-1} \right]. \tag{20.418}$$

Second, take the expressions for x_j, x_{j+1} and x_{j-1}, substitute them into the right hand side of (20.416), and equate to (20.418). This gives

$$\frac{dn}{dt} \binom{k}{j} \left[j n^{j-1}(1 - n)^{k-j} \quad - \quad (k - j)n^j(1 - n)^{k-j-1} \right] =$$

$$- \quad [j\beta + (k - j)\alpha] \binom{k}{j} n^j (1 - n)^{k-j}$$

$$+ \quad (k - j + 1)\alpha \binom{k}{j - 1} n^{j-1}(1 - n)^{k-j+1}$$

$$+ \quad (j + 1)\beta \binom{k}{j + 1} n^{i+1}(1 - n)k \tag{20.419}$$

Now divide through by $\binom{k}{j} n^{j-1}(1 - n)^{k-j-1}$ to get

$$(j - kn)\frac{dn}{dt} = j\alpha(1 - n)^2 + (k - j)\beta n^2 - [i\beta + (k - j)\alpha]n(1 - n), \tag{20.420}$$

and thus, factoring out α and β on the right hand side, and cancelling out the common factor, we get

$$\frac{dn}{dt} = \alpha(1 - n) - \beta n, \tag{20.421}$$

as required.

Note that this argument works for all $0 < j < k$. The arguments for $j = 0$ and $j = k$ are similar, but simpler.

15. Consider the model of the Na$^+$ channel shown in Fig. 3.11. Show that if α and β are large compared to γ and δ, then x_{21} is given (approximately) by

$$x_{21} \;=\; \left(\frac{\alpha}{\alpha+\beta}\right)^2 h, \qquad\qquad (20.422)$$

$$\frac{dh}{dt} \;=\; \gamma(1-h) - \delta h, \qquad\qquad (20.423)$$

while conversely, if γ and δ are large compared to α and β, then (approximately)

$$x_{21} \;=\; m^2\left(\frac{\gamma}{\gamma+\delta}\right), \qquad\qquad (20.424)$$

$$\frac{dm}{dt} \;=\; \alpha(1-m) - \beta m. \qquad\qquad (20.425)$$

Solution

(a) Case I: α and β large

In problems of this sort, where there are some fast rates and some slow ones, the general procedure is to divide all the variables into groups such that every variable within a group is at equilibrium with all the other variables in that group. When α and β are large we see that there is an obvious grouping to use, by letting group I consist of S_{00}, S_{10} and S_{20}, while letting group II consist of S_{01}, S_{11} and S_{21}. Note that, since α and β are large all the variables in group I are in equilibrium with each other, but not necessarily with the variables in group II.

Within group I we see that

$$2\alpha x_{00} \;=\; \beta x_{10} \qquad\qquad (20.426)$$

$$\alpha x_{10} \;=\; 2\beta x_{20}. \qquad\qquad (20.427)$$

We also let

$$x = x_{00} + x_{10} + x_{20}. \qquad\qquad (20.428)$$

Similarly, within group II we have

$$2\alpha x_{01} \;=\; \beta x_{11} \qquad\qquad (20.429)$$

$$\alpha x_{11} \;=\; 2\beta x_{21}. \qquad\qquad (20.430)$$

and we also let

$$h = x_{01} + x_{11} + x_{21}. \qquad\qquad (20.431)$$

Note that $h + x = 1$.

Using (20.429) and (20.430) to express x_{01} and x_{11} in terms of x_{21}, and substituting into (20.431) then gives

$$x_{21} = \left(\frac{\alpha}{\alpha+\beta}\right)^2 h. \qquad\qquad (20.432)$$

Finally, the differential equation for h is

$$
\begin{aligned}
\frac{dh}{dt} &= \gamma(x_{00} + x_{10} + x_{20}) - \delta(x_{01} + x_{11} + x_{21}) \\
&= \gamma x - \delta h \\
&= \gamma(1 - h) - \delta h,
\end{aligned}
\tag{20.433}
$$

as required.

(b) Case II: γ and δ large

This is slightly more complicated, due to the presence of three variable groupings rather than two, as in the previous case.

We let group I consist of x_{00} and x_{01}. We have $\gamma x_{00} = \delta x_{01}$, and we let $x = x_{00} + x_{01}$.

Similarly, we let group II consist of x_{10} and x_{11}. We have $\gamma x_{10} = \delta x_{11}$, and we let $y = x_{10} + x_{11}$.

Finally, we let group III consist of x_{20} and x_{21}. We have $\gamma x_{20} = \delta x_{21}$, and we let $h = x_{20} + x_{21}$.

It now follows that $h = \frac{\delta}{\gamma} x_{21} + x_{21}$ and thus

$$
x_{21} = \left(\frac{\gamma}{\gamma + \delta} \right) h.
\tag{20.434}
$$

Next we derive the differential equations for x, y and h. Inspection of the binding diagram quickly gives

$$
\frac{dx}{dt} = \beta y - 2\alpha x,
\tag{20.435}
$$

$$
\frac{dy}{dt} = 2\alpha x + 2\beta h - (\beta + \alpha)y,
\tag{20.436}
$$

$$
\frac{dh}{dt} = \alpha y - 2\beta h.
\tag{20.437}
$$

We now use the same trick that was used in Exercise 14. Since $x + y + h = 1$, we can write $x + y + h = (n + (1 - n))^2$, to get $h = n^2$, $y = 2n(1 - n)$, and $x = (1 - n)^2$. Substituting these expressions into the differential equation for h (or x or y of course) then gives

$$
\frac{dn}{dt} = \alpha(1 - n) - \beta n,
\tag{20.438}
$$

as required.

16. Show that (3.120) has two negative real roots. Show that when $\beta = 0$ and $a \le \frac{-\lambda_1}{\lambda_1 - \lambda_2}$, then (3.121)–(3.123) have two possible solutions, one with $\alpha + \delta = -\lambda_1$, $\gamma = -\lambda_2$, the other with $\alpha + \delta = -\lambda_2$, $\gamma = -\lambda_1$. In the first solution inactivation is faster than activation, while the reverse is true for the second solution.

Solution

First we have to show that the equation

$$f(\lambda) \equiv \lambda^2 + (\alpha + \beta + \gamma + \delta)\lambda + (\alpha + \delta)(\beta + \gamma) - \alpha\beta = 0 \qquad (20.439)$$

has two real roots. This is most easily done by noticing that $f(\lambda)$ is a quadratic in λ, with $f(0) > 0$ and $f'(0) > 0$. Hence, from inspection of the graph of f the roots of f have negative real part. Furthermore,

$$(\alpha+\beta+\gamma+\delta)^2 - 4[(\alpha+\delta)(\beta+\gamma)-\alpha\beta] = [(a+\delta)-(\beta+\gamma)]^2 + 4\alpha\beta > 0, \quad (20.440)$$

from which it follows that the roots must be real and negative.

Now let $\beta = 0$. We then have to solve the equations

$$\alpha + \gamma + \delta = -\lambda_1 - \lambda_2, \qquad (20.441)$$
$$\gamma(\alpha + \delta) = \lambda_1\lambda_2, \qquad (20.442)$$
$$\alpha = a(\lambda_1 - \lambda_2). \qquad (20.443)$$

Letting $z = \alpha + \delta$, we get from the first two equations

$$z^2 + (\lambda_1 + \lambda_2)z + \lambda_1\lambda_2 = 0, \qquad (20.444)$$

and thus

$$2z = -\lambda_1 - \lambda_2 \pm (\lambda_1 - \lambda_2). \qquad (20.445)$$

Hence

$$\alpha + \delta = -\lambda_2, \qquad \text{or } \alpha + \delta = -\lambda_1, \qquad (20.446)$$

which are the two desired solutions.

There is a further constraint on the solutions however. Since all the parameters must be non-negative (from the physiological constraints), these solutions are only acceptable if α and δ are both positive. This can only occur if

$$\alpha < -\lambda_1, \qquad (20.447)$$

that is, if $a \leq \frac{-\lambda_1}{\lambda_1 - \lambda_2}$, as required. Note that λ_1 and λ_2 are both negative, with $\lambda_2 < \lambda_1 < 0$, and thus if $\alpha < -\lambda_1$ we must also have $\alpha < -\lambda_2$.

24. Find the most likely event for the binomial distribution

$$P(h) = \frac{n!}{h!(n-h)!}p^h(1-p)^{(n-h)} \qquad (20.448)$$

when n is large. Show that the probability of this event approaches 1 in the limit $n \to \infty$.

Solution

Using Stirling's formula,

$$
\begin{aligned}
\ln P \quad = \quad & \ln(n!) - \ln(h!) - \ln((n-h)!) + h\ln(p) + (n-h)\ln(1-p) \\
\approx \quad & n\ln(n) - h\ln(h) - (n-h)\ln(n-h) + h\ln(p) + (n-h)\ln(1-p).
\end{aligned}
$$

Differentiate this with respect to h to find

$$
\frac{1}{P}\frac{dP}{dh} = -\ln(h) + \ln(n-h) + \ln(p) - \ln(1-p) \tag{20.449}
$$

which is zero at $h = np$. Now evaluate $\ln P$ at $h = np$ to find

$$
\begin{aligned}
\ln P \quad \approx \quad & n\ln(n) - np\ln(np) - n(1-p)\ln(n-np) + np\ln(p) + n(1-p)\ln(1-p) \\
= \quad & n\ln(n) - np\ln(n) - n(1-p)\ln(n) = 0 \tag{20.450}
\end{aligned}
$$

so that in the limit $n \to \infty$, $P \to 1$.

Selected Solutions to Chapter 4

2. (a) Find the fundamental solution K of the linear cable equation satisfying

$$-\frac{d^2 K}{dX^2} + K = \delta(X - \xi), \quad -\infty < X < \infty, \qquad (20.451)$$

where $\delta(X - \xi)$ denotes an *inward* flow of positive current at the point $X = \xi$.

(b) Use the fundamental solution to construct a solution of the cable equation with inhomogeneous current input

$$-\frac{d^2 V}{dX^2} + V = I(X). \qquad (20.452)$$

Solution

(a)
$$K(X, \xi) = \frac{1}{2} e^{-|X-\xi|}. \qquad (20.453)$$

(b)
$$V(X) = \int_{-\infty}^{\infty} I(\xi) K(X, \xi) \, d\xi = \frac{1}{2} \int_{-\infty}^{\infty} I(\xi) e^{-|X-\xi|} \, d\xi. \qquad (20.454)$$

4. (a) Use Laplace transforms to find the solution of the semi-infinite (time-dependent) cable equation with clamped voltage

$$V(X, 0) = 0 \qquad (20.455)$$

and current input
$$\frac{\partial V(0, T)}{\partial X} = -r_i \lambda_m I_0 H(T), \qquad (20.456)$$

where H is the Heaviside function.

1058

Hint: Use the identity

$$\frac{2}{s\sqrt{s+1}} = \frac{1}{s+1-\sqrt{s+1}} - \frac{1}{s+1+\sqrt{s+1}}, \tag{20.457}$$

and then use

$$\mathcal{L}^{-1}\left\{\frac{e^{-a\sqrt{s}}}{s+b\sqrt{s}}\right\} = e^{b^2T+ab}\operatorname{erfc}\left(\frac{a}{2\sqrt{T}} + b\sqrt{T}\right), \tag{20.458}$$

where $\mathcal{L}^{-1}$ denotes the inverse Laplace transform.

(b) Show that

$$V(X,T) \to r_i\lambda_m I_0 e^{-X} \tag{20.459}$$

as $T \to \infty$.

Solution

(a)

$$V(X,T) = \frac{r_i\lambda_m I_0}{2}\left\{e^{-X}\operatorname{erfc}\left(\frac{X}{2\sqrt{T}} - \sqrt{T}\right) - e^X\operatorname{erfc}\left(\frac{X}{2\sqrt{T}} + \sqrt{T}\right)\right\}, \tag{20.460}$$

where erfc is the complementary error function,

$$\operatorname{erfc}(x) = \frac{2}{\sqrt{\pi}}\int_x^\infty e^{-y^2}\,dy. \tag{20.461}$$

Selected Solutions to Chapter 5

1. Show that, if $k > 1$, then $(1 - e^{-x})^k$ has an inflection point, but $(e^{-x})^k$ does not.

   Solution

   For $f(x) = (1 - e^{-x})^k$, $f''(x) = k(1 - e^{-x})^{k-2}e^{-x}(ke^{-x} - 1))$ which is zero if $x = \ln(k)$. Whereas for $g(x) = e^{-kx}$, $g''(x) = k^2 e^{-kx}$ has no zeros.

2. Explain why replacing the extracellular Na^+ with choline has little effect on the resting potential of an axon. Calculate the new resting potential with 90% of the extracellular Na^+ removed. Why is the same not true if K^+ is replaced? (Assume the conductances are constant.)

   Solution

   Replacing 90% of the extracellular sodium by choline reduces the Nernst potential by $\frac{RT}{F}\ln(10) = 2.63\frac{RT}{F}$. Since the sodium rest conductance is quite small, this changes the rest potential by very little. On the other hand, a similar replacement for extracellular potassium would have a more substantial effect of the rest potential since the potassium conductance is not small at rest.

10. The Hodgkin–Huxley equations are for the squid axon at 6.3°C. Using that the absolute temperature enters the equations through the Nernst equation, determine how changes in temperature affect the behavior of the equations. In particular, simulate the equations at 0°C and 30°C to determine whether the equations become more or less excitable with an increase in temperature.

    Solution

    At 0°C, all Nernst potentials are reduced by a factor of 0.977, whereas at 30°C, all Nernst potentials are increased by a factor of 1.085. At 0°C, the rest potential is -63.4mV making the axon more excitable, while at 30°C the rest potential is -67.3 mV, making the axon less excitable.

11. Show that a Hopf bifurcation occurs in the generalized FitzHugh–Nagumo model when $f_v(v^*, w^*) = -\epsilon g_w(v^*, w^*)$, assuming that

$$f_v(v^*, w^*)g_w(v^*, w^*) - g_v(v^*, w^*)f_w(v^*, w^*) > 0.$$

On which side of the minimum of the v nullcline can this condition be satisfied?

Solution

A Hopf bifurcation occurs when the Jacobian of the linearized system has two eigenvalues that are purely imaginery. For a two-variable system, this occurs when the determinant of the Jacobian is positive and the trace is zero. For the generalized Fitzhugh-Nagumo system, this can occur when the steady state is located on the middle branch of the v nullcline, to the right of the minimum.

Selected Solutions to Chapter 6

1. Show that the (U, W) phase-plane of the bistable equation, (6.6) and (6.7), has three steady states, two of which are saddle points. What is the nature of the third steady state? Show that the slope of the unstable manifold at the origin is given by the positive root of $\lambda^2 - c\lambda + f'(0) = 0$ and is always larger than c. What is the slope of the stable manifold at $(U, W) = (1, 0)$? Show that the slopes of both these manifolds are increasing functions of c.

Solution

The phase plane of the bistable equation is described by the two equations

$$U' = W, \tag{20.462}$$
$$W' = cW - f(U), \tag{20.463}$$

where f has a generic "cubic" shape, with three roots, at $U = 0$, α and 1. Thus, the steady states are obtained by setting the two right hand sides equal to zero, from which we get $W = 0$ and $f(U) = 0$. It follows immediately (from the constraints on $f(U)$) that there are three steady states in the phase plane, $(U, W) = (0, 0)$, $(\alpha, 0)$ and $(1, 0)$.

To determine the linear stability of each steady states we construct the linearized system around that steady state. At the steady state $U = U_0$, the linearized system is governed by the matrix

$$A = \begin{pmatrix} 0 & 1 \\ -f'(U_0) & c \end{pmatrix}. \tag{20.464}$$

As usual, the eigenvalues and eigenvectors of A determine the linear stability of U_0. The eigenvalues of A are the roots of the equation

$$\lambda^2 - c\lambda + f'(U_0) = 0 \tag{20.465}$$

and thus the eigenvalues, $\lambda\pm$, are given by

$$2\lambda_\pm = c \pm \sqrt{c^2 - 4f'(U_0)}. \tag{20.466}$$

1061

Each eigenvalue has an associated eigenvector, $\xi_\pm$, obtained by solving the linear system

$$(A - \lambda_\pm I)\xi_\pm = 0. \tag{20.467}$$

This immediately gives

$$\xi_\pm = \begin{pmatrix} 1 \\ \lambda_\pm \end{pmatrix}. \tag{20.468}$$

We are now in a position to answer all the parts of this Exercise. First note that if $f'(U_0) < 0$ then (20.465) must necessarily have one real positive root, and one real negative root, in which case $(U_0, 0)$ will be a saddle point. Since, $f'(0) < 0$ and $f'(1) < 0$, we conclude that $(0,0)$ and $(1,0)$ are saddle points. Furthermore, since $f'(\alpha) > 0$, it follows that, at the steady state $(\alpha, 0)$, the eigenvalues can be either real or complex, but in either case must have positive real part, since $c > 0$. Thus $(\alpha, 0)$ is linearly unstable.

Next we consider the slope of the unstable manifold at the origin. From (20.468) we see that the unstable manifold at the origin is in the direction of the vector $(1, \lambda_+)$, where

$$2\lambda_+ = c + \sqrt{c^2 - 4f'(0)} > c. \tag{20.469}$$

Since this vector has slope λ_+, it follows that the slope of the unstable manifold at the origin is λ_+. From (20.469) it is clear that λ_+ is an increasing function of c.

Similarly, the stable manifold at $(1,0)$ is in the direction of the eigenvector $(1, \lambda_-)$, where

$$2\lambda_- = c - \sqrt{c^2 - 4f'(1)} < 0. \tag{20.470}$$

It remains only to show that (20.470) defines an increasing function of c. However, this is easily seen by differentiating with respect to c:

$$2\lambda_-'(c) = 1 - \frac{c}{\sqrt{c^2 - 4f'(1)}} > 0 \tag{20.471}$$

where the last inequality results from the fact that $f'(1) < 0$ and thus $\sqrt{c^2 - 4f'(1)} > c$.

2. Use cable theory to find the speed of propagation for each of the axons listed in Table 4.1, assuming that the ionic currents are identical and the speed of propagation for the squid giant axon is 21 mm/ms.

Solution

According to (6.21)

$$s = \frac{c\lambda_m}{\tau_m}, \tag{20.472}$$

where c depends only on the ionic conductances. Here, we are assuming that c is the same for all the cell types in Table 4.1.

For the squid giant axon

$$\frac{c\lambda_m}{\tau_m} = \frac{c \times 6.5 \text{ mm}}{1 \text{ ms}} = 21 \text{ mm/ms}, \qquad (20.473)$$

from which it follows that $c = 21/6.5 = 3.23$. We now just use that value for c to calculate the wave speeds for the other axons.

lobster giant axon $s = 3.23 \times \frac{2.5 \text{ mm}}{2 \text{ ms}} = 4 \text{ mm/ms}$
crab giant axon $s = 3.23 \times \frac{2.4 \text{ mm}}{7 \text{ ms}} = 1.1 \text{ mm/ms}$
earthworm giant axon $s = 3.23 \times \frac{4 \text{ mm}}{3.6 \text{ ms}} = 3.6 \text{ mm/ms}$
marine worm giant axon $s = 3.23 \times \frac{5.4 \text{ mm}}{0.9 \text{ ms}} = 19.4 \text{ mm/ms}$
mammalian cardiac cell $s = 3.23 \times \frac{1.5 \text{ mm}}{8.4 \text{ ms}} = 0.58 \text{ mm/ms}$
barnacle muscle fiber $s = 3.23 \times \frac{2.8 \text{ mm}}{4.6 \text{ ms}} = 2 \text{ mm/ms}$

4. Construct a traveling wave solution to the piecewise linear bistable equation, (6.1) and (6.3). Show that the wave travels with speed $\frac{1-2\alpha}{\sqrt{\alpha-\alpha^2}}$. (Construct the solution by using the techniques presented in Section 6.3.1.)

   Solution

   We want to solve

   $$V_t = V_{xx} + f(V) \qquad (20.474)$$
   $$f(V) = -V + H(V - \alpha). \qquad (20.475)$$

   Change variables to $\xi = x - ct$ to get $V'' + cV' - V + f(V) = 0$. We look for a solution of the form shown in Fig. 20.30. Note that the ξ axis is divided into two regions; region I, $\xi < 0$, where $V > \alpha$, and region II, $\xi > 0$, where $V < \alpha$. We solve the differential equation on each region separately and then stick the pieces together by ensuring the solution has a continuous derivative at $\xi = 0$.

   Region I On region I we have

   $$V_I'' + cV_I' - V_I = -1, \qquad V_I(0) = \alpha, \qquad (20.476)$$

   which has solution
   $$V_I = 1 + (\alpha - 1)e^{\lambda_+ \xi}, \qquad (20.477)$$
   where $2\lambda_+ = -c + \sqrt{c^2 + 4} > 0$. Here, we have used the fact that the solution must be bounded as $\xi \to -\infty$ in order to eliminate one of the possible exponential solutions.

   Region II On region II we have

   $$V_{II}'' + cV_{II}' - V_{II} = 0, \qquad V_{II}(0) = \alpha, \qquad (20.478)$$

   which has solution
   $$V_{II} = \alpha e^{\lambda_- \xi}, \qquad (20.479)$$
   where $2\lambda_- = -c - \sqrt{c^2 + 4} > 0$. Again we have used the fact that V_{II} must be bounded as $\xi \to \infty$.
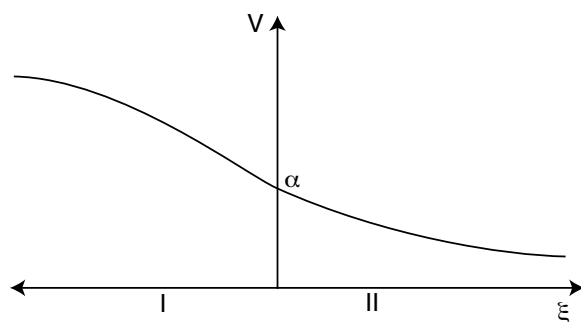
Figure 20.30: Schematic diagram of the traveling wave for Exercise 4.

Now force the derivative to be continuous at $\xi = 0$, i.e., $V_I'(0) = V_{II}'(0)$. This gives

$$\lambda_+(\alpha - 1) = \alpha\lambda_- \qquad (20.480)$$

from which it follows that

$$c^2 = \frac{(1 - 2\alpha)^2}{\alpha - \alpha^2} \qquad (20.481)$$

as required.

6. (a) Solve the bistable equation

$$v_t = v_{xx} + v(0.1 - v)(v - 1) \qquad (20.482)$$

numerically and plot a traveling wave.

(b) Solve the FitzHugh-Nagumo equations

$$
\begin{aligned}
v_t &= v_{xx} + v(0.1 - v)(v - 1) - w & (20.483)\\
w_t &= 0.1(v - w) & (20.484)
\end{aligned}
$$

numerically and plot a traveling wave.

Solution

(a) There are a number of ways of solving this nonlinear diffusion equation in one spatial dimension, and they can be programmed relatively simply in almost any language. However, probably the easiest way to solve PDEs like this is to use the capabilities of XPPAUT. This will not be nearly as fast as a compiled program such as Fortran, but is much easier to program.

If we discretize in space, but not in time, we get a large system of (stiff) ODEs, one for each spatial grid point, which we can then solve with XPPAUT. In fact, XPPAUT is designed to make it easy to solve such systems. Let x_i, $0 \le i \le n$, denote the ith spatial grid point, let v_i denote

the approximate solution at x_i, and use centred differences to discretise v_{xx}. Then

$$\frac{dv_i}{dt} = \frac{v_{i+1} - 2v_i + v_{i-1}}{(\Delta x)^2} + v_i(0.1 - v_i)(v_i - 1) \qquad (20.485)$$

for $1 \leq i < n$. At the boundaries we specify no flux by introducing a phantom grid point x_{-1}, such that $v_{-1} = v_1$, and similarly at the other end. Thus

$$\frac{dv_0}{dt} = \frac{2v_1 - 2v_0}{(\Delta x)^2} + v_0(0.1 - v_0)(v_0 - 1) \qquad (20.486)$$

$$\frac{dv_n}{dt} = \frac{-2v_n + 2v_{n-1}}{(\Delta x)^2} + v_n(0.1 - v_n)(v_n - 1) \qquad (20.487)$$

For initial conditions, we put the solution at the leftmost grid points at 0.9. This initiates a waves which travels from left to right across the domain.

This large system of ODEs can be programmed in XPPAUT as follows:

```
# Declare the variables
# Initial conditions
v[0..5](0)=0.9
# Initialise the rest of the domain
v[6..100](0)=0
#
param delx=1.0  diff=1.0
#
!lam=diff/(delx*delx)
#
# Define right hand sides of the pdes
bistab(v)=v*(1-v)*(v-0.1)
#
v[1..99]'  = lam*(v[j-1]-2.0*v[j]+v[j+1]) + bistab(v[j])
# No-flux boundary conditions
v0'  = lam*(-2.0*v0+2.0*v1)  + bistab(v0)
v100'  = lam*(2.0*v99-2.0*v100)  + bistab(v100)
#
#
@ total=200, dt=0.1, xlo=0, xhi=200, ylo=0, yhi=1,  meth=gear, yp2=v4,yp3=v50,yp4=v80,nplot=4
done
```

All that remains is to save the output into a file, read it into the plotting program of your choice and plot the waves. A typical solution is shown in Fig. 20.31.

(b) The procedure for solving the FitzHugh-Nagumo model is similar. Again, it is easiest to use XPPAUT. The code is

---

```
# Declare the variables
v[0..5](0)=1.0
v[6..100](0)=0
w[0..100](0)=0
```
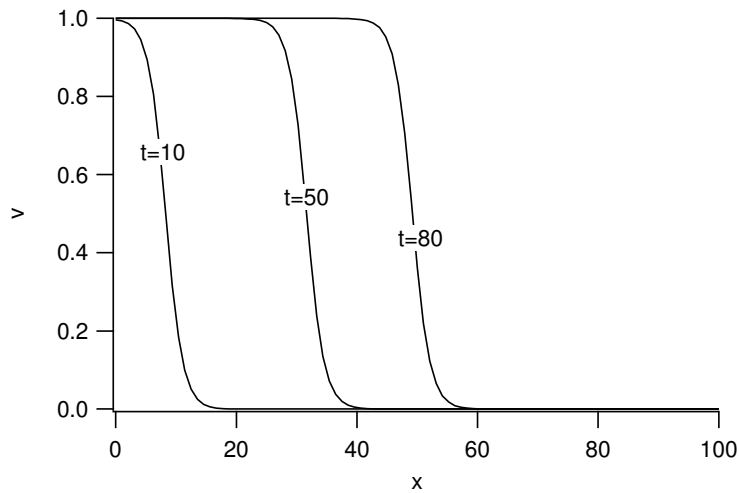
Figure 20.31: Traveling wave in the bistable equation

```
#
param delx=4.0  diff=5.0
#
!lam=diff/(delx*delx)
#
# Define right hand sides of the pdes
bistab(v)=v*(1-v)*(v-0.1)
#
v0'  = lam*(-2.0*v0+2.0*v1)  + bistab(v0) -w0
v[1..99]'  = lam*(v[j-1]-2.0*v[j]+v[j+1]) + bistab(v[j]) - w[j]
v100'  = lam*(2.0*v99-2.0*v100)  + bistab(v100)  -w100
#
# The diff eqn for w
w[0..100]'  = 0.01*(v[j]-w[j])
# No-flux boundary conditions
#
#
@ total=500, dt=0.1, xlo=0, xhi=500, ylo=-0.3, yhi=1,  meth=gear, yp2=v4,yp3=v50,yp4=v80,nplot=4
done
```

A typical solution is shown in Fig. 20.32

7. Find the speed of traveling fronts for barnacle muscle fiber using the Morris–
Lecar model (Chapter 5, (5.72)–(5.73)).

Answer: About 6 cm/s.

Solution

Information must be combined from two other chapters. The details of the
model are in Chapter 5, while the details of the diffusion are in Chapter 4.
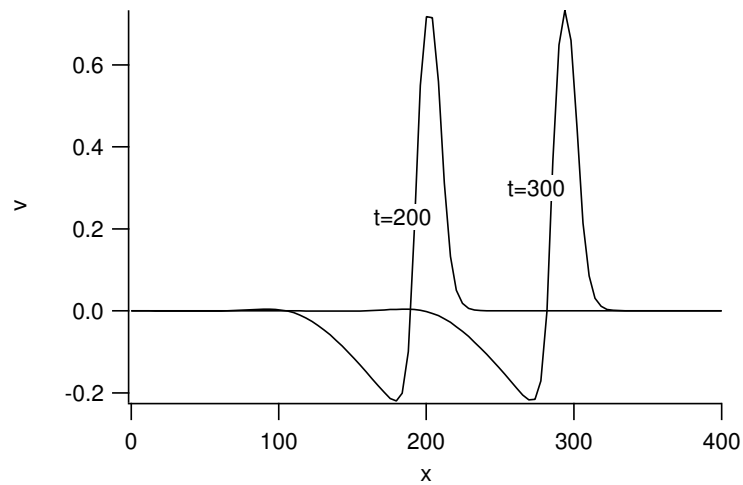
Figure 20.32: Traveling wave in the FitzHugh-Nagumo equations

From (4.14) we have

$$\tau_m \frac{\partial V}{\partial t} + R_m(I_{\text{ion}} - I_{\text{app}}) = \lambda_m^2 \frac{\partial^2 V}{\partial x^2}, \qquad (20.488)$$

and thus

$$C_m \frac{\partial V}{\partial t} + I_{\text{ion}} - I_{\text{app}} = \frac{\lambda_m^2}{R_m} \frac{\partial^2 V}{\partial x^2}. \qquad (20.489)$$

The values of λ_m and R_m are given in Table 4.1. All the other model parameters are given in Table 12. There is only one tricky one, the value for I_{app}, where one must be careful to use the correct units. Since C_m is in units of $\mu\text{F/cm}^2$ and V and T are in units of mV and ms respectively, we see that I_{app} must be given in units of $\mu\text{A/cm}^2$. Hence, $I_{\text{app}} = 60 \ \mu\text{A/cm}^2$.

As in Exercise 6 we use XPPAUT and the method of lines, i.e., we discretize the equations in space and then use XPPAUT to solve the resulting stiff system of ODEs. Then we saved the results to a file and used IGOR to plot the waves and calculate the wave speed. The XPPAUT code is given below. From the two sample waves in Fig. 20.33 we see that the wave travelled 4 cm in about 0.66 seconds, giving a wave speed of close to 6 cm/sec. As can be seen from the code, these waves were calculated with no-flux boundary conditions on a domain of length 10 cm. Initially V was set at 0 at the left-most 6 grid points.

XPPAUT code for Exercise 7.

```
# Declare the variables
V[0..5](0)=0.0
V[6..100](0)=-36.755
```
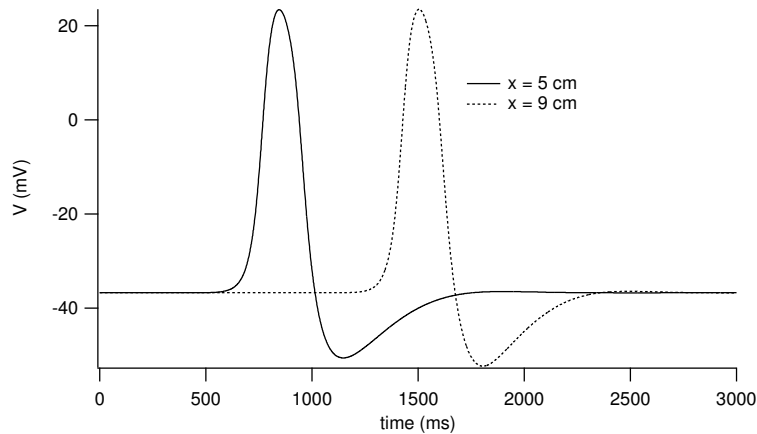
Figure 20.33: Traveling waves in the Morris-Lecar model of Exercise 7, plotted as functions of time at two fixed points in space.

```
w[0..100](0)=0.070198
#
# Declare the parameters
#
param   Iapp=60.0   cm=20.0      gca=4.4   gk=8
param   gl=2         phi=0.04 vee1=-1.2      vee2=18  vee3=2  vee4=30
param   vca=120      vk=-84    vl=-60
param   taum=4.6     Rm=0.23   lamm=0.28
#
param delx=0.1
!diff=lamm*lamm/Rm
#
!lam=diff/(delx*delx)
#
minf(V)=0.5*(1+tanh((V-vee1)/vee2))
winf(V)=0.5*(1+tanh((V-vee3)/vee4))
lambda(V)=cosh((V-vee3)/(2*vee4))
Iion(V,w)=gca*minf(V)*(V-vca)+gk*w*(V-vk)+gl*(V-vl)
#
# Define right hand sides of the pdes
#
V[1..99]'  = (1/cm)*( lam*(V[j-1]-2.0*V[j]+V[j+1]) - Iion(V[j],w[j]) + Iapp )
# No-flux boundary conditions
V0'  = (1/cm)*( lam*(-2.0*V0+2.0*V1)  - Iion(V0,w0) + Iapp )
V100'  = (1/cm)*( lam*(2.0*V99-2.0*V100)   - Iion(V100,w100) + Iapp )
w[0..100]'  = phi*lambda(V[j])*(winf(V[j])-w[j])
#
#
@ total=300, dt=0.1, xlo=0, xhi=300, ylo=-70, yhi=40,  meth=gear, yp2=V4,yp3=V50,yp4=V80,nplot=4
done
```

9. Show that $1/p'(\lambda_1) + 1/p'(\lambda_2) + 1/p'(\lambda_3) = 0$, where p is defined by (6.58).

Hence, show that $h(1) = 0$, where h is defined by (6.64). Show also that $\lambda_1/p'(\lambda_1) + \lambda_2/p'(\lambda_2) + \lambda_3/p'(\lambda_3) = 0$ and thus $h'(1) = 0$. Finally, show that $h''(1) = p'(\lambda_1)/\lambda_1^2 - 2$.

Solution

Use the fact that λ_1, λ_2 and λ_3 are all roots of $p(\lambda)$. Thus, $p(\lambda) = (\lambda - \lambda_1)(\lambda - \lambda_2)(\lambda - \lambda_3)$ and so $p'(\lambda_1) = (\lambda_1 - \lambda_2)(\lambda_1 - \lambda_3)$, $p'(\lambda_2) = (\lambda_2 - \lambda_1)(\lambda_2 - \lambda_3)$ and $p'(\lambda_3) = (\lambda_3 - \lambda_2)(\lambda_3 - \lambda_1)$. From these identities it follows immediately that $1/p'(\lambda_1) + 1/p'(\lambda_2) + 1/p'(\lambda_3) = 0$ and $\lambda_1/p'(\lambda_1) + \lambda_2/p'(\lambda_2) + \lambda_3/p'(\lambda_3) = 0$.

It follows that $h(1) = 1 + \frac{p'(\lambda_1)}{p'(\lambda_2)} + \frac{p'(\lambda_1)}{p'(\lambda_3)} = p'(\lambda_1)\left(\frac{1}{p'(\lambda_1)} + \frac{1}{p'(\lambda_2)} + \frac{1}{p'(\lambda_3)}\right) = 0$ as required. Furthermore,

$$h'(s) = -1 - \frac{\lambda_2}{\lambda_1 s}\frac{p'(\lambda_1)}{p'(\lambda_2)}\exp(-\lambda_2 \ln(s)/\lambda_1) - \frac{\lambda_3}{\lambda_1 s}\frac{p'(\lambda_1)}{p'(\lambda_3)}\exp(-\lambda_3 \ln(s)/\lambda_1),$$

(20.490)

and thus

$$h'(1) = -1 - \frac{\lambda_2}{\lambda_1}\frac{p'(\lambda_1)}{p'(\lambda_2)} - \frac{\lambda_3}{\lambda_1}\frac{p'(\lambda_1)}{p'(\lambda_3)} \tag{20.491}$$

$$= -\frac{p'(\lambda_1)}{\lambda_1}\left(\frac{\lambda_1}{p'(\lambda_1)} + \frac{\lambda_2}{p'(\lambda_2)} + \frac{\lambda_3}{p'(\lambda_3)}\right) \tag{20.492}$$

$$= 0 \tag{20.493}$$

as required.

Finally, a straightforward calculation shows that

$$h''(1) = \frac{p'(\lambda_1)}{\lambda_1}\left(\frac{\lambda_2}{p'(\lambda_2)} + \frac{\lambda_3}{p'(\lambda_3)} + \frac{\lambda_2^2}{\lambda_1 p'(\lambda_2)} + \frac{\lambda_3^2}{\lambda_1 p'(\lambda_3)}\right) \tag{20.494}$$

$$= \frac{p'(\lambda_1)}{\lambda_1}\left(-\frac{\lambda_1}{p'(\lambda_1)} + \frac{\lambda_2^2}{\lambda_1 p'(\lambda_2)} + \frac{\lambda_3^2}{\lambda_1 p'(\lambda_3)}\right) \tag{20.495}$$

$$= -1 + \frac{p'(\lambda_1)}{\lambda_1^2}\left(\frac{\lambda_2^2}{\lambda_1 p'(\lambda_2)} + \frac{\lambda_3^2}{\lambda_1 p'(\lambda_3)}\right) \tag{20.496}$$

$$= -1 + \frac{p'(\lambda_1)}{\lambda_1^2}\left(1 - \frac{\lambda_1^2}{p'(\lambda_1)}\right) \tag{20.497}$$

$$= -2 + \frac{p'(\lambda_1)}{\lambda_1^2} \tag{20.498}$$

as required, where we have used the fact that

$$\frac{\lambda_1^2}{p'(\lambda_1)} + \frac{\lambda_2^2}{p'(\lambda_2)} + \frac{\lambda_3^2}{p'(\lambda_3)} = 1. \tag{20.499}$$

10. The results of Exercise 9 can be generalized. Use contour integration in the complex plane to show that for an nth order polynomial $p(z) = z^n + \cdots$ with

simple roots $z_k, k = 1, \ldots, n$,

$$\sum_{k=1}^{n} \frac{z_k^j}{p'(z_k)} = 0, \qquad (20.500)$$

provided that $n > j + 1$. In addition, show that

$$\sum_{k=1}^{n} \frac{z_k^{n-1}}{p'(z_k)} = 1. \qquad (20.501)$$

Solution

First, note that $1/p(z)$ has simple poles at $z = z_i$. Second,

$$\text{residue at } z_i = \lim_{z \to z_i} \frac{z - z_i}{p(z)} = \frac{1}{p'(z_i)}. \qquad (20.502)$$

Now take as our contour, C, a circle of radius R, centred at the origin. If R is large enough, C contains all the poles of $1/p(z)$ and we know from the residue theorem that the integral of $1/p(z)$ around C is equal to $2\pi i$ times the sum of the residues at the poles, z_i.

However, in the limit as $R \to \infty$, the integral of $1/p(z)$ around C tends to zero. (This is most easily seen by letting $z = Re^{i\theta}$ and converting the integral around C to an integral over θ. Then

$$\int_C \frac{1}{p(z)} \, dz = \int_0^{2\pi} \frac{iRe^{i\theta}}{p(Re^{i\theta})} \, d\theta = \int_0^{2\pi} f(R) \, d\theta \qquad (20.503)$$

for some function $f(R) = O(R^{1-n})$. As $R \to \infty$, $|f| \to 0$ and so the integral vanishes.)

Thus, letting $R \to \infty$, it follows immediately from the residue theorem that

$$0 = \sum_{k=1}^{n} \frac{1}{p'(z_k)}. \qquad (20.504)$$

The same argument can be applied to every function $\frac{z^j}{p(z)}$, for $j < n - 1$, and thus

$$0 = \sum_{k=1}^{n} \frac{z_k^j}{p'(z_k)}, \qquad 0 \le j < n - 1. \qquad (20.505)$$

When $j = n-1$, the integral around C now becomes of order R^n/R^n (because of the additional factor of R introduced by the change of integration variable to $d\theta$). In this case

$$\lim_{R \to \infty} \int_C \frac{z^{n-1}}{p(z)} \, dz \;=\; \lim_{R \to \infty} \int_0^{2\pi} \frac{R^{n-1}e^{i(n-1)\theta} iRe^{i\theta}}{p(Re^{i\theta})} \, d\theta \qquad (20.506)$$

$$=\; \int_0^{2\pi} i d\theta \qquad (20.507)$$

$$=\; 2\pi i. \qquad (20.508)$$

It remains only to apply the residue theorem again. Equating the integral over C to the sum of the residues gives

$$2\pi i = 2\pi i \sum_{k=1}^{n} \frac{z_k^{n-1}}{p'(z_k)}, \qquad (20.509)$$

as required.

11. Show that the duration of the absolute refractory period of the traveling pulse for the generalized FitzHugh–Nagumo model is (approximately)

$$T_{\mathrm{ar}} = \int_{w_-}^{w_0} \frac{dw}{G_-(w)}, \qquad (20.510)$$

where w_0 is that value of w for which $c(w) = 0$.

Solution

From Fig. 6.7, and from the definition of w_+ and w_-, we see that the refractory phase starts at $w = w_-$, as that is where the back of the wave jumps down. For all values of w such that $c(w) < 0$ it is not possible to initiate another wave, as no wave front from $V_-(w)$ to $V_+(w)$ exists (the only possible transitions from $V_-(w)$ to $V_+(w)$ are moving backwards, and thus cannot be wave fronts). This is exactly what is meant by the absolute refractory period; the period when no stimulus, no matter how large, can initiate another wave front. So the absolute refractory period lasts as long as w is between w_- and w_0.

Since $\frac{dw}{dt} = G_-(w)$ during the refractory period it follows that

$$T_{\mathrm{ar}} = \int_{w_-}^{w_0} \frac{dw}{G_-(w)}, \qquad (20.511)$$

as required.

Of course, once $w < w_0$ a stimulus of sufficient strength can initiate another wave, and so the system, although still refractory, is not absolutely refractory.

12. Show that in the limit as the period approaches infinity, (6.85) and (6.86) reduce to the equations for a solitary pulse (6.62) and (6.63).

Solution

Since the period of the wave is ξ_2, letting the period tend to infinity corresponds to taking the limit $P \to \infty$. Note that we don't let $\xi_1 \to \infty$ also, because we want the solitary pulse to have a finite width. Since $\lambda_1 < 0$ and the real parts of λ_2 and λ_3 are positive, it follows that the terms involving $e^{\lambda_1 P}$ will disappear, while the terms involving $e^{\lambda_2 P}$ and $e^{\lambda_3 P}$ will become large.

Taking the limit as $P \to \infty$ of (6.85) thus gives

$$\frac{-1}{-p'(\lambda_1)} + \frac{e^{-\xi_1 \lambda_2}}{p'(\lambda_2)} + \frac{e^{-\xi_1 \lambda_3}}{p'(\lambda_3)} + \epsilon^2 \alpha = 0, \qquad (20.512)$$

which is the same as (6.63).

Similarly, taking the limit as $P \to \infty$ of (6.86) gives

$$\frac{-e^{\xi_1 \lambda_1}}{-p'(\lambda_1)} + \frac{1}{p'(\lambda_2)} + \frac{1}{p'(\lambda_3)} + \epsilon^2 \alpha = 0, \tag{20.513}$$

from which, using the identity $\frac{1}{p'(\lambda_1)} + \frac{1}{p'(\lambda_2)} + \frac{1}{p'(\lambda_3)} = 0$ it follows that

$$\frac{e^{\xi_1 \lambda_1}}{p'(\lambda_1)} - \frac{1}{p'(\lambda_1)} + \epsilon^2 \alpha = 0, \tag{20.514}$$

and hence (6.62).

14. (Fisher's equation.) The goal of this exercise is to find traveling wave solutions of the equation

$$u_t = u_{xx} + f(u), \tag{20.515}$$

where $f(u) = u(1-u)$. This equation, sometimes known as Fisher's equation, is commonly used in mathematical ecology and population biology to model traveling waves. In this context u corresponds to a population density or a gene density.

(a) Convert to the traveling wave coordinate $\xi = x + ct$, where $c \geq 0$ is the wave speed, and show that the PDE converts to the system of ODEs

$$\begin{aligned} u' &= w & (20.516) \\ w' &= cw - u(1-u). & (20.517) \end{aligned}$$

(b) What are the steady states of the ODE system? Determine the stability of the steady states and sketch the phase plane, including the directions of the eigenvectors at the saddle point.

(c) Show that a biologically relevant traveling wave cannot exist when $c < 2$.

(d) Starting at the saddle point $(1,0)$, follow the stable manifold backwards in time. Show that while doing so, this stable manifold cannot leave the first quadrant across the u axis.

(e) Show that if $c \geq 2$ there exists a line, $u = mw$, such that the stable manifold of the saddle point cannot be above this line.

(f) Use this to draw a conclusion about the existence of traveling wave solutions to Fisher's equation.

Solution

(a) In the traveling wave coordinate $\xi = x + ct$ we get

$$cu' = u'' + u(1-u), \tag{20.518}$$

where a prime denotes differentiation with respect to ξ. Introducing the variable $w = u'$ gives the required system.
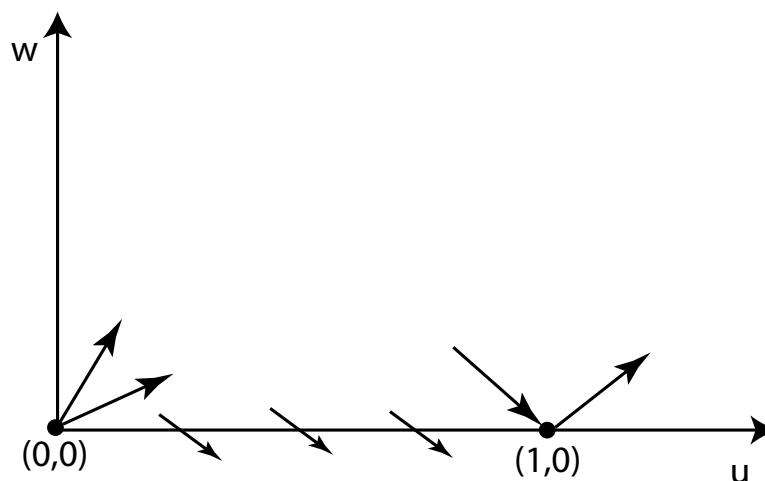
Figure 20.34: Sketch of the phase plane of Fisher's equation (Exercise 14).

(b) The steady states are clearly $(0,0)$ and $(1,0)$. The Jacobian matrix around a steady state (u_0, w_0) is

$$J = \begin{pmatrix} 0 & 1 \\ -f'(u) & c \end{pmatrix}. \tag{20.519}$$

At $(0,0)$ the eigenvalues are

$$2\lambda_\pm = c \pm \sqrt{c^2 - 4}. \tag{20.520}$$

Thus, when $0 < c < 2$ the origin is an unstable spiral. When $c > 2$ the origin is an unstable node.

At $(1,0)$ the eigenvalues are

$$2\lambda_\pm = c \pm \sqrt{c^2 + 4}, \tag{20.521}$$

and thus $(1,0)$ is a saddle point.

The directions of the eigenvectors at the saddle point are determined by solving the system $J\eta = \lambda_\pm\eta$. For example, suppose that the eigenvalue λ_- has corresponding eigenvector $\eta = \begin{pmatrix} \eta_1 \\ \eta_2 \end{pmatrix}$. Then, since $J\eta = \lambda_-\eta$ it follows from the first component of the matrix equation that $\eta_2 = \lambda_-\eta_1$. Since $\lambda_- < 0$ we thus know that η must point into quadrants II and IV. This gives us enough information to sketch the phase plane, as shown in Fig. 20.34.

(c) First note that a traveling wave corresponds to a heteroclinic orbit, starting at $(0,0)$ and ending at $(1,0)$. If the origin is an unstable spiral then

any trajectory leaving the origin will pass through all four quadrants as it spirals out, and thus u becomes negative along the trajectory. Since u corresponds to a population density or a gene density, it cannot be negative. Thus no acceptable traveling wave solution exists when $c < 2$.

(d) From Fig. 20.34 we see that the only possible heteroclinic orbit from $(0,0)$ to $(1,0)$ is the stable manifold of $(1,0)$. If we can trace the stable manifold backwards in time and show that it begins at the origin we will thus have constructed a traveling wave solution.

Now, on the u axis, $w' = -f(u) < 0$ when $0 < u < 1$, and thus for $0 < u < 1$ all the trajectories on the u axis point down (illustrated in Fig. 20.34). It follows immediately that if we trace the stable manifold backwards in time it cannot cross the u axis between $0 < u < 1$.

(e) Consider the line L, given by $w = mu$. If we can show that no trajectories cross L from above to below then we will have the desired result. This holds if $w'/u' \geq m$ which is true only if

$$m^2 - cm + (1 - u) \leq 0. \tag{20.522}$$

Thus, if we can choose an m such that

$$m^2 - cm + 1 \leq 0. \tag{20.523}$$

we will have the desired result.

Consider the quadratic

$$m^2 - cm + 1 = 0. \tag{20.524}$$

This has roots $c/2 \pm \sqrt{c^2 - 4}/4$. If $c \geq 2$ there are two positive roots of (20.524) and thus a range of m for which (20.523) holds. Hence the result. The phase plane and the line L are sketched in Fig. 20.35.

(f) For any $c \geq 2$, follow the stable manifold of $(1,0)$ backwards in time. It cannot leave the first quadrant across the u axis, and neither can it cross the line L. It is thus forced to head to the origin as $\xi \to -\infty$, giving a heteroclinic orbit and thus a traveling wave solution.

It follows that a traveling wave solution exists for all $c \geq 2$.

15. Here we examine Fisher's equation (20.515) again in a more general form. Suppose $f(0) = f(1) = 0$, $f'(0) > 0$, $f'(1) < 0$, and $f(u) > 0$ for $0 < u < 1$.

(a) Show that when $c = 0$ there are no trajectories with $u \geq 0$ connecting the two rest points $u = 0$ and $u = 1$.

(b) Show that if there is a value of c for which there is no heteroclinic connection with $u \geq 0$, then there is no such connecting trajectory for any smaller value of c.

(c) Show that if there is a value of c for which there is a connecting trajectory with $u \geq 0$, then there is a similar connecting trajectory for every larger value of c.
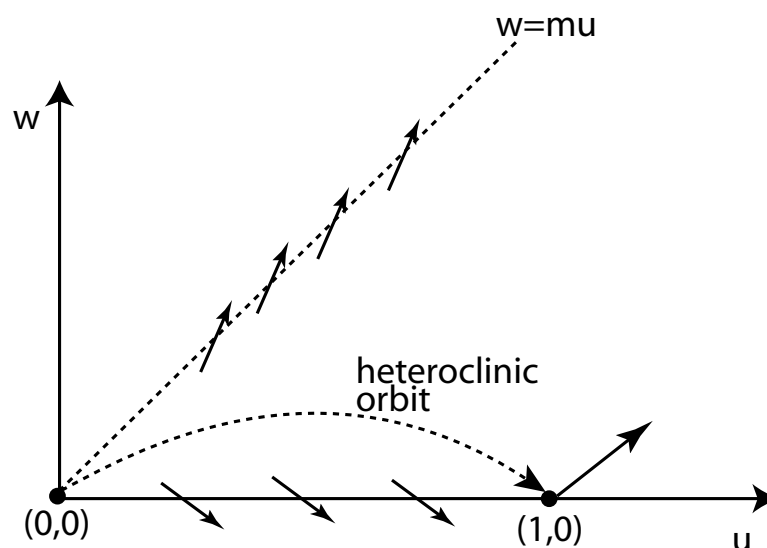
Figure 20.35: Sketch of the phase plane of Fisher's equation (Exercise 14), showing the line L and a sketch of the heteroclinic orbit.

(d) Let μ be the smallest positive number for which $f(u) \le \mu u$ for $0 \le u \le 1$. Show that a heteroclinic connection exists for all $c \ge 2\sqrt{\mu}$.

Solution

Recall from Exercise 14 that we need to consider the ODE system

$$u' = w \tag{20.525}$$
$$w' = cw - f(u). \tag{20.526}$$

As in Exercise 14, the point $(1, 0)$ is a saddle point whose stable manifold has slope $\lambda_- = \frac{1}{2}(c - \sqrt{c^2 + 4f'(0)})$. The origin is an unstable steady state. The phase plane portrait is the same as sketched in Fig. 20.34.

(a) When $c = 0$, $w' = -f(u)$, which is always negative when $0 < u < 1$. Any solution leaving the origin cannot go into the first quadrant as then it would have $u > 0$ and $w' > 0$ which contradicts $w' = -f(u)$. Similarly, it cannot go into the fourth quadrant as then it would have $u' > 0$ with $w < 0$ which contradicts $u' = w$. Hence the result.

(b) Suppose that a heteroclinic connection does not exist for $c = c_0$. We know that, since the stable manifold of $(1, 0)$ cannot enter quadrant I across the u axis, it must enter quadrant I across the w axis (Fig. 20.36). Consider any $c_1 < c_0$. Since λ_- is an increasing function of c, it follows that $l_-(c_1) < l_-(c_0)$, i.e., the stable manifold at $(1, 0)$ has rotated in a clockwise direction (Fig. 20.36).
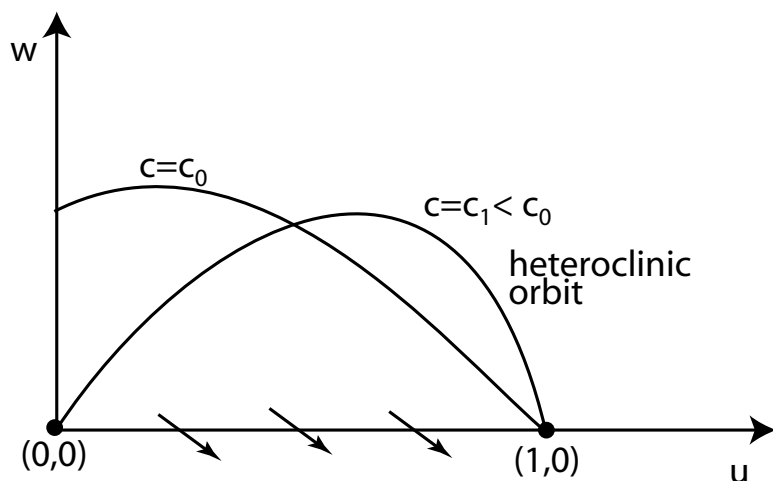
Figure 20.36: Sketch of the situation when a heteroclinic connection exists for $c_1 < c_0$, with no such connection existing for c_0. As discussed in Exercise 15 this leads to a contradiction at the intersection point of the two solutions.

Suppose a heteroclinic connection exists for c_1. Then we would have the situation shown in Fig. 20.36 in which the heteroclinic connection for c_1 intersects the stable manifold for c_0, and has a greater slope at the point of intersection. However, from the differential equations we see that w'/u' is an increasing function of c, i.e., for a fixed u and w, as c decreases, the slope of the trajectory there must also decrease. Hence, the situation illustrated in Fig. 20.36 is not possible, and no such heteroclinic connection can exist for c_1.

(c) Suppose that a heteroclinic connection exists for $c = c_0$ and let $c = c_1 > c_0$. Now we have the situation sketched in Fig. 20.37. The stable manifold for $c = c_1$ initially lies below the stable manifold for $c = c_0$ (since λ_- is an increasing function of c). The two solutions cannot cross (or we would get the same contradiction as we got in the previous part of this question), and the stable manifold cannot enter the first quadrant across the u axis. The only possibility is that it connects to the origin, thus forming a heteroclinic connection, as required.

(d) The argument is the same as in Exercise 14 so we won't show all the details. As before we construct a line $w = mu$ and choose m so that solutions cannot cross this line from above to below. In terms of $f(u)$ the required condition is

$$m^2 - cm + \frac{f(u)}{u} \leq 0, \qquad (20.527)$$

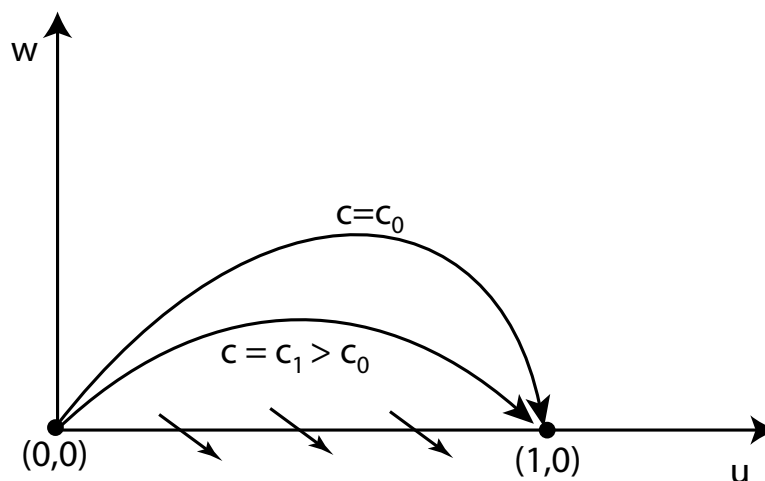for all $0 < u < 1$. By the definition of μ we see that $f(u)/u \leq \mu$ for all

Figure 20.37: Sketch of the situation when a heteroclinic connection exists for c_0.

$0 < u < 1$ and thus it suffices to have

$$m^2 - cm + \mu \le 0. \tag{20.528}$$

This has a range of possible m when $c^2 \ge 4\mu$, i.e., $c \ge 2\sqrt{\mu}$, as required.

17. Construct a traveling wave solution for the equation $v_t = v_{xx} + f(v)$ with $v(-\infty, t) = 0$ and $v(+\infty, t) = 1$ where $f(v) = 0$ for $0 < v < q$, $f(v) = 1 - v$ for $q < v < 1$. What is the speed of propagation? For what values of q does the wave exist? Plot the traveling wave on the same graph as the traveling wave for the piecewise linear bistable equation, making sure that q and α are chosen so that the two waves are traveling with the same speed.

Solution

We use the same techniques as in Exercise 4. In the traveling wave coordinate $\xi = x + ct$ we have $v'' - cv' + f(v) = 0$. As for the piecewise linear bistable equation (Exercise 4) we divide the ξ axis into two regions: Region I ($\xi < 0$) and Region II ($\xi > 0$). We also set $v(0) = q$, which specifies the position of the wave along the ξ axis.

In Region I denote the solution by v_I. We have

$$v_I'' - cv_I' = 0 \tag{20.529}$$

and thus

$$v_I = \frac{A}{c}e^{c\xi}, \tag{20.530}$$

for some constant A. Note that we have eliminated the arbitrary constant by applying the boundary condition at $-\infty$.

In Region II denote the solution by v_{II}. We have

$$v_{II}'' - cv_{II}' - v_{II} = -1, \qquad (20.531)$$

and thus

$$v_{II} = 1 + Be^{\lambda_- \xi}, \qquad (20.532)$$

for some constant B, and where

$$2\lambda_- = c - \sqrt{c^2 + 4}. \qquad (20.533)$$

Note that to satisfy the boundary condition at ∞ we only use the negative root.

Now apply the constraints $v_I(0) = v_{II}(0) = q$ and $v_I'(0) = v_{II}'(0)$, which give $A/c = 1 + B = q$ and $A = \lambda_- B$. Thus, $B = q - 1$, $A = cq$ and

$$c = \frac{\lambda_-(q - 1)}{q}. \qquad (20.534)$$

Solving this last equation for c gives

$$c = \frac{1 - q}{\sqrt{q}}. \qquad (20.535)$$

Clearly, the wave exists for all q such that $0 < q < 1$.

We now need to choose q and a so that

$$\frac{1 - q}{\sqrt{q}} = \frac{1 - 2\alpha}{\sqrt{\alpha - \alpha^2}}. \qquad (20.536)$$

In Fig. 20.38 we plot the wave speed as a function of q and of α for the two different equations. For example, if we choose $\alpha = 0.4$ and $q = 0.7$ the waves travel with similar speeds. Plots of the two waves are given in Fig. 20.39. As one would expect, the traveling wave of the bistable equation rises more slowly, due to the fact that $f(u) < 0$ when u is close to zero, and thus pulls the wave front down.

18. Show that the equation $v_t = v_{xx} + f(v)$, where $f(0) = f(1) = 0$, has a traveling wave solution connecting $v = 0$ to $v = 1$ only if $\int_0^1 f(v)\,dv > 0$. Interpret the results of Exercises 4 and 17 in light of this result.

Solution

Let $\xi = x + ct$. Then the PDE becomes $cv' = v'' + f(v)$. Multiply by v' to get

$$c(v')^2 = v''v' + f(v)v'. \qquad (20.537)$$

Let
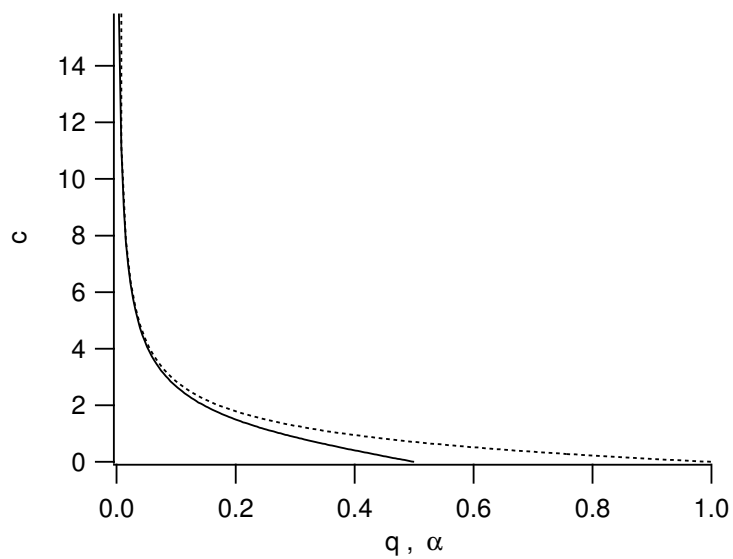
$$F(v) = \int_0^v f(s)ds. \qquad (20.538)$$

Figure 20.38: Wave speed as a function of q (dotted line) and of α (solid line). The dotted line refers to Exercise 17 while the solid line is for the piecewise linear bistable equation (Exercise 4).
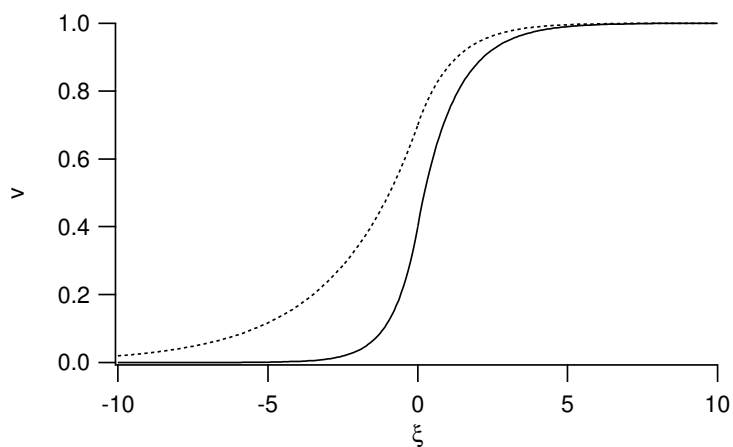

Figure 20.39: The traveling wave of Exercise 17 (dotted line) and of the piecewise linear bistable equation (solid line).

Then $\frac{d}{d\xi}F(v) = f(v)v'$. Hence, from (20.537) we see that

$$c(v')^2 = \frac{1}{2}\frac{d}{d\xi}(v')^2 + \frac{d}{d\xi}F(v). \qquad (20.539)$$

Now integrate from $\xi = -\infty$ (i.e., $v = 0$) to $\xi = \infty$ (i.e., $v = 1$) to get

$$c\int_{-\infty}^{\infty}(v')^2\,d\xi = \left.\frac{(v')^2}{2}\right|_{\xi=-\infty}^{\xi=\infty} + F(v)|_{\xi=-\infty}^{\xi=\infty} = 0 + \int_0^1 f(v)\,dv. \qquad (20.540)$$

Hence

$$c = \frac{\int_0^1 f(v)\,dv}{\int_{-\infty}^{\infty}(v')^2\,d\xi}. \qquad (20.541)$$

It follows that $c > 0$ (and thus a traveling wave solution exists) only when $\int_0^1 f(v)\,dv > 0$, as required.

For the bistable equation, $\int_0^1 f(v)\,dv > 0$ only when $\alpha < 1/2$, while for the choice of f in Exercise 17 the integral is always positive when $0 < q < 1$. This explains why the wave exists for all q, $0 < q < 1$, but only exists for $0 < \alpha < 1/2$.

20. Use perturbation arguments to estimate the error in the calculated speed of propagation when Euler's method (forward differencing in time) with second-order centered differencing in space is used to approximate the solution of the bistable equation.

Solution

Use perturbation arguments to approximate the solution of the numerical problem with a traveling front solution of the bistable equation. (See Section 6.2.3.)

22. What is the eikonal-curvature equation for (6.96) when the medium is anisotropic and D is a symmetric matrix, slowly varying in space?

Solution

Generalize (10.11) by calculating $\nabla\cdot(D\nabla u)$ using components of D as d_{ij}, and use this to generalize (10.12). The result is that $S_t = \sqrt{\nabla S \cdot D\nabla S}\left(c_0\sqrt{k} + \nabla\cdot\left(\frac{D\nabla S}{\sqrt{\nabla S\cdot D\nabla S}}\right)\right)$.

23. Verify (6.103).

Solution

Use Cramer's rule to find the inverse of a matrix with three column vectors, say t_1, t_2, and t_3. Use the fact that the determinant of such a matrix is $t_1\cdot(t_2\times t_3)$. Then apply this to the transpose of the Jacobian matrix $\frac{\partial X_j}{\partial \xi_i}$.

24. Verify that in two spatial dimensions, $\nabla \cdot \left(\frac{\nabla S}{|\nabla S|} \right)$ is the curvature of the level surface of the function S.

Solution

If $x = X(t), y = Y(t)$ is the parametric representation of a smooth level-surface curve, then $S(X(t), Y(t)) = 0$. Use this and derivatives of this expression with respect to t to show that $\nabla \cdot \left(\frac{\nabla S}{|\nabla S|} \right) = \pm \frac{Y_t X_{tt} - Y_{tt} X_t}{(X_t^2 + Y_t^2)^{3/2}}$.

Selected Solutions to Chapter 8

2. Murray (1989) discusses a simple model of CICR that has been used by a number of modelers (Cheer *et al.*, 1987; Lane *et al.*, 1987). In the model, Ca^{2+} release from the ER is an increasing sigmoidal function of Ca^{2+}, and Ca^{2+} is removed from the cytoplasm with linear kinetics. Thus,

$$\frac{dc}{dt} = L + \frac{k_1 c^2}{K + c^2} - k_2 c,$$

where L is a constant leak of Ca^{2+} from the ER into the cytoplasm.

   (a) Nondimensionalize this equation. How many nondimensional parameters are there?

   (b) Show that when $L = 0$ and $k_1 > 2k_2$, there are two positive steady states and determine their stability. For the remainder of this problem assume that $k_1 > 2k_2$.

   (c) How does the nullcline $dc/dt = 0$ vary as the leak from the internal store increases? Show that there is a critical value of L, say L_c, such that when $L > L_c$, only one positive solution exists.

   (d) Fix $L < L_c$ and suppose the solution is initially at the lowest steady state. How does c behave when small perturbations are applied to c? How does c behave when large perturbations are applied? How does c behave when L is raised above L_c and then decreased back to zero? Plot the bifurcation diagram in the L, c phase-plane, indicating the stability or instability of the branches. Is there hysteresis in this model?

Solution

   (a) The nondimensional form of the equation is

$$\frac{dc}{dt} = l + \frac{kc^2}{1 + c^2} - c.$$
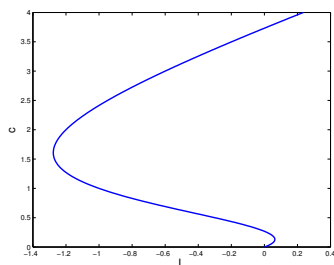
with two free parameters, l and k.

Figure 20.40: Bifurcation diagram for Exercise 2 with $\frac{k_1}{k_2} = 4$.

(b) With $L = 0$, the steady states are determined by the equation

$$\frac{k_1 c^2}{1 + c^2} - k_2 c = 0$$

The roots of this equation are $c = 0$ and

$$c_\pm = \frac{k_1}{2k_2} \pm \frac{1}{2}\sqrt{(\frac{k_1}{k_2})^2 - 4},$$

which are real and positive provided $k_1 > 2k_2$.

The slope of the polynomial $f(c) = \frac{k_1 c^2}{1+c^2} - k_2 c$ is negative at $c = 0$ and at $c = c_+$, and positive at $c = c_-$. Thus, the steady solutions at $c = 0, c_+$ are stable, and unstable at $c = c_-$

(c) The function $f(c)$ has a unique minimum at $c = c^*$, say. If $L < f(c^*)$, then $L + f(c) = 0$ has three roots, whereas, if $L > f(c^*)$, there is only one root.

(d) The easiest way to plot the bifurcation diagram is to make a plot of the curve $L = -f(c)$ and then reverse the axes. An example of such is shown in Fig. 20.40. There is no hysteresis because L is restricted to be positive.

3. One of the earliest models of Ca^{2+} oscillations was the two-pool model of Goldbeter, Dupont and Berridge (1990). They assumed that IP_3 causes an influx, r, of Ca^{2+} into the cell and that this influx causes additional release of Ca^{2+} from the ER via an IP_3-independent mechanism. Thus,

$$\frac{dc}{dt} = r - kc - f(c, c_e), \tag{20.542}$$

$$\frac{dc_e}{dt} = f(c, c_e), \tag{20.543}$$

$$f(c, c_e) = J_{\text{uptake}} - J_{\text{release}} - k_f c_e, \tag{20.544}$$

where

$$J_{\text{uptake}} = \frac{V_1 c^n}{K_1^n + c^n}, \tag{20.545}$$

k	$=$	$10\ \text{s}^{-1}$	K_1	$=$	$1\ \mu\text{M}$
K_2	$=$	$2\ \mu\text{M}$	K_3	$=$	$0.9\ \mu\text{M}$
V_1	$=$	$65\ \mu\text{Ms}^{-1}$	V_2	$=$	$500\ \mu\text{Ms}^{-1}$
k_f	$=$	$1\ \text{s}^{-1}$	m	$=$	2
n	$=$	2	p	$=$	4

Table 20.3: Typical parameter values for the two-pool model of Ca^{2+} oscillations (Goldbeter *et al.*, 1990).

$$J_{\text{release}} \quad = \quad \left(\frac{V_2 c_e^m}{K_2^m + c_e^m}\right)\left(\frac{c^p}{K_3^p + c^p}\right). \tag{20.546}$$

Here, $k_f c_e$ is a leak from the ER into the cytoplasm. Typical parameter values are given in Table 20.3. (All the concentrations in this model are with respect to the total cell volume, and thus there is no need for the correction factor γ (cf. 7.4) to take into account the difference in the ER and cytoplasmic volumes.)

(a) Nondimensionalize these equations. How many non-dimensional parameters are there?

(b) Show that in a closed cell (i.e., one without any interaction with the extracellular environment) the two-pool model cannot exhibit oscillations.

(c) How does the steady state solution depend on influx?

(d) Use a bifurcation tracking program such as AUTO to plot the bifurcation diagram of this model, using r as the bifurcation parameter. Find the Hopf bifurcation points and locate the branch of stable limit cycle solutions. Plot some typical limit cycle solutions for different values of r.

Solution

(a) To nondimensionalize, set $u = c/K_1$, $v = c_e/K_2$ and $t = \tau/k$ to get the system

$$\frac{du}{dt} = \mu - u - \frac{1}{\epsilon}f(u,v), \tag{20.547}$$

$$\frac{dv}{dt} = \frac{\eta}{\epsilon}f(u,v), \tag{20.548}$$

$$f(u,v) = \beta\left(\frac{u^n}{u^n+1}\right) - \left(\frac{v^m}{v^m+1}\right)\left(\frac{u^p}{\alpha^p+u^p}\right) - \delta v, \tag{20.549}$$

where $\alpha = K_3/K_1$, $\beta = V_1/V_2$, $\eta = K_1\gamma/K_2$, $\delta = k_f K_1/V_2$, $\mu = \nu/(kK_1)$ and $\epsilon = kK_1/V_2$.

(b) Notice that $f(u,v)$ is a monotone decreasing function of v and so to find the nullclines it is easiest to solve for v as a function of u.
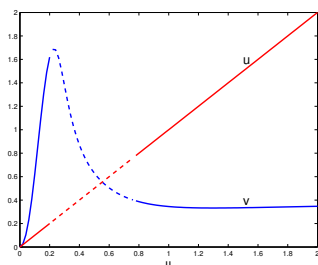
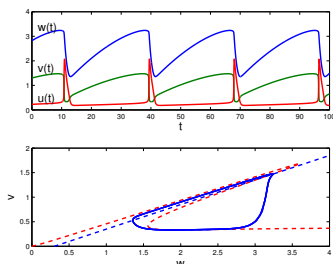Figure 20.41: Steady state solutions as a function of μ for Exercise 3.

Figure 20.42: Solution and phase portrait for Exercise 3 with $\mu = 0.3$.

(c) There is no interaction with the extracellular environment if $\nu = k = 0$. In this case, $\gamma c + \frac{c_e}{\gamma}$ is constant, so the system of two equations can be reduced to a single first order differential equation, whose solutions cannot oscillate.

(d) The easiest way to find the dependence of the steady state solution on μ is to first solve $f(u, v) = 0$ for v as a function of u, and then to plot the curve $\mu = u$ in the $\mu - v$ plane. A plot of the steady state solutions as a function of μ is shown in Fig. 20.41.

(e) Introducing the variable $w = u + v/\eta$ we find

$$\frac{dw}{dt} = \mu - (w - v/\eta), \qquad (20.550)$$

$$\frac{dv}{dt} = \frac{\eta}{\epsilon} F(w, v). \qquad (20.551)$$

Note that w plays the role of c_t as discussed in Section 7.2.7, and is a measure of the total Ca^{2+} load of the cell. When $\epsilon \ll 1$, w changes more slowly than does v, i.e., transport to and from the ER is much faster than transport in and out of the cell. A phase portrait is shown in Fig. 20.42.

(f) One can easily find the two Hopf bifurcation points by calculating where

the trace of the linearization vanishes. The dashed portion of the steady state curves in Fig. 20.41 are where the trace is positive, hence the solutions are unstable.

4. Complete the details of the reduction of the IP_3 receptor model (Section 7.2.5).

Solution

To carry out this calculation, write the differential equations governing the states in group I, say, to get

$$\frac{dx_{000}}{dt} = -x_{000}(k_5c + k_1p + k_4c) + k_{-5}x_{010} + k_{-1}x_{100} + k_{-4}x_{001} \quad (20.552)$$

$$\frac{dx_{100}}{dt} = -x_{100}(k_5c + k_{-1} + k_2c) + k_{-5}x_{110} + k_1px_{000} + k_{-2}x_{101} \quad (20.553)$$

$$\frac{dx_{010}}{dt} = -x_{010}(k_{-5} + k_1p + k_4c) + k_5cx_{000} + k_{-1}x_{110} + k_{-4}x_{011} \quad (20.554)$$

The differential equation for the fourth receptor state, x_{110}, is superfluous because of the definition

$$y = x_{001} + x_{011} + x_{101} + x_{111}, \quad (20.555)$$

and the constraint

$$x_{000} + x_{010} + x_{100} + x_{110} = 1 - y. \quad (20.556)$$

Now, using the assumption that the group I binding sites are in quasi-steady state, the quasi-steady-state equations are obtained by balancing the fast terms on the right-hand sides of (20.552)–(20.554). The underlying assumption here is that if these terms are not balanced, then the dynamics of the group I variables quickly adjust to bring them into balance. Thus,

$$x_{000}(k_5c + k_1p) = k_{-5}x_{010} + k_{-1}x_{100}, \quad (20.557)$$
$$x_{100}(k_5c + k_{-1}) = k_{-5}x_{110} + k_1px_{000}, \quad (20.558)$$
$$x_{010}(k_{-5} + k_1p) = k_5cx_{000} + k_{-1}x_{110}. \quad (20.559)$$

These are solved together with the constraint (20.556) to find the group I state probabilities. An identical procedure applied to the group II receptor states gives the quasi-steady-state relationships for the group II states. The result is

$$\frac{x_{000}}{K_1K_5} = \frac{x_{010}}{K_1c} = \frac{x_{100}}{K_5p} = \frac{x_{110}}{pc} = \frac{(1-y)}{(p+K_1)(c+K_5)}, \quad (20.560)$$

$$\frac{x_{001}}{K_3K_5} = \frac{x_{011}}{K_3c} = \frac{x_{101}}{K_5p} = \frac{x_{111}}{pc} = \frac{y}{(p+K_3)(c+K_5)}, \quad (20.561)$$

where $K_i = k_{-i}/k_i$.

It now remains to derive the differential equation for y. Notice that y changes on a slow time scale, since any changes in y involve Ca^{2+} leaving or binding to the inactivating site, a process that is assumed to be slow. Thus, we write the differential equations for the group II sites by adding together the four equations for its constituents,

$$\frac{dy}{dt} = k_4 c(x_{000} + x_{010}) + k_2 c(x_{100} + x_{110}) - k_{-4}(x_{001} + x_{011}) - k_{-2}(x_{101} + x_{111}). \tag{20.562}$$

The important observation is that with this addition, all the "fast" terms cancel, and we are left only with terms involving small rate constants. This is called the "slow manifold" equation. Substitute all the quasi-steady-state expressions to find (7.14).

7. Starting with a basic scheme like that of Fig. 7.5 one can construct a large number of variants, each of which has a similar steady-state flux. The purpose of this Exercise is to investigate two simple variants of the basic model, and show that the flux is similar for each. To distinguish between these models on the basis of experimental data is, in general, quite difficult.

   (a) First, calculate the expressions for α_1 to α_4 in (7.7) and for β_1 to β_4 in (7.7). (Use of a symbolic manipulation program such as Maple is, as usual, recommended.)

   (b) Extend the ATPase model of Section 7.2.4 by assuming that the two Ca^{2+} ions bind sequentially, not simultaneously, and calculate the flux.

   (c) Modify the model still further by assuming that the binding of the second Ca^{2+} ion is much faster than binding of the first, and calculate the flux.

   (d) Compare these three different expressions for the steady-state flux. Are experimental data of the steady state flux sufficient to distinguish between these models?

Solution

For convenience we label the pump states S_i and T_i, $i = 1, 2, 3$, as shown in Fig. 7.5, and let s_i and t_i denote, respectively, the fraction of pumps in state S_i and T_i. Because of the conservation constraint

$$\sum_{i=1}^{3}(s_i + t_i) = 1 \tag{20.563}$$

only five of these variables are independent.

At steady state, the flux of Ca^{2+} from the cytoplasm to the ER is given by the difference between the forward and reverse rates of any of the reaction steps. (Note that this difference must be same for each reaction step otherwise the model would not be at steady state.) Thus, if we let J denote the Ca^{2+} flux

from the cytoplasm to the ER, we have

$$
\begin{aligned}
J &= k_1 s_1 c^2 - k_{-1} s_2 & (20.564) \\
&= k_2 s_2 - k_{-2} s_3 & (20.565) \\
&= k_3 s_3 - k_{-3} t_3 & (20.566) \\
&= k_4 t_3 - k_{-4} t_2 c_e^2 & (20.567) \\
&= k_5 t_2 - k_{-5} t_1 & (20.568) \\
&= k_6 t_1 - k_{-6} s_1, & (20.569)
\end{aligned}
$$

where c denotes $\left[\mathrm{Ca}^{2+}\right]$ in the cytoplasm and c_e denotes $\left[\mathrm{Ca}^{2+}\right]$ in the ER. We thus have six equations for six unknowns (s_1, s_2, s_3, t_1, t_2 and J), which can be solved to find J as a function of the rate constants.

Solution of these equations gives

$$
J = \frac{c^2 - K_1 K_2 K_3 K_4 K_5 K_6 c_e^2}{\alpha_1 c^2 + \alpha_2 c_e^2 + \alpha_3 c^2 c_e^2 + \alpha_4}, \tag{20.570}
$$

where the αs are functions of the rate constants, too long and of too little interest to include in full detail. As always, $K_i = k_{-i}/k_i$. If the affinity of the Ca^{2+} binding sites is high when the pump is in conformation E_1, it follows that K_2 is small (i.e., $k_{-2} \ll k_2$). Similarly, if the affinity of the binding sites is low when the pump is in conformation E_2, it follows that K_4 is also small. (Note that, given the way we have written the diagram, k_{-4} is the rate at which ER Ca^{2+} binds to the pump in conformation E_2.) Since K_2 and K_4 are thus small, it follows that the pump can support a positive flux even when c_e is much greater than c.

If this were a model of a closed system, the law of detailed balance would require that $K_1 K_2 K_3 K_4 K_5 K_6 = 1$. Fortunately, this is not so here. Because the cycle is driven by phosphorylation of the pump, the reaction rates depend upon the concentrations of ATP, ADP and P, and energy is continually being consumed (if $J > 0$) or generated (if $J < 0$).

In the original description of the model, MacLennan *et al.* assumed that the binding and release of Ca^{2+} occurred quickly. If we make this assumption we get a similar expression for the steady-state flux. However, the process of how one reduces the model in this way is important and useful, and thus worth considering in detail.

In Fig. 7.5 states S_1 and S_2 have been grouped together by a box with a dotted outline, and so have states T_2 and T_3. If we assume that these pairs of states are in instantaneous equilibrium it follows that

$$
\begin{aligned}
c^2 s_1 &= K_1 s_2, & (20.571) \\
t_3 &= K_4 c_e^2 t_2. & (20.572)
\end{aligned}
$$

Now let

$$
\begin{aligned}
\bar{s}_1 &= s_1 + s_2 & (20.573)
\end{aligned}
$$

$$= s_1 \left(1 + \frac{c^2}{K_1} \right) \tag{20.574}$$

$$= s_2 \left(1 + \frac{K_1}{c^2} \right), \tag{20.575}$$

and

$$\bar{t}_2 = t_2 + t_3 \tag{20.576}$$

$$= t_2 (1 + K_4 c_e^2) \tag{20.577}$$

$$= t_3 \left(1 + \frac{1}{K_4 c_e^2} \right). \tag{20.578}$$

Thus

$$\frac{d\bar{s}_1}{dt} = k_{-2} s_3 - k_2 s_2 + k_6 t_1 - k_{-6} s_1 \tag{20.579}$$

$$= k_{-2} s_3 - \left(\frac{c^2 k_2}{c^2 + K_1} \right) \bar{s}_1 + k_6 t_1 - \left(\frac{K_1 k_{-6}}{K_1 + c^2} \right) \bar{s}_1, \tag{20.580}$$

$$\frac{d\bar{t}_2}{dt} = k_3 s_3 - k_{-3} t_3 + k_{-5} t_1 - k_5 t_2 \tag{20.581}$$

$$= k_3 s_3 - \left(\frac{k_{-3} K_4 c_e^2}{1 + K_4 c_e^2} \right) \bar{t}_2 + k_{-5} t_1 - \left(\frac{k_5}{1 + K_4 c_e^2} \right) \bar{t}_2. \tag{20.582}$$

From these equations we can write down a simplified schematic diagram of the ATPase, as shown in Fig. 7.6. As c increases, the equilibrium between S_1 and S_2 will be shifted further towards S_2. This will tend to increase the rate at which S_3 is formed, but decrease the rate at which S_1 is converted to T_1. Thus, the transition from $\bar{S}_1$ to S_3 is an increasing function of c, while the transition from $\bar{S}_1$ to T_1 is a decreasing function of c.

From this diagram we can calculate the steady-state flux in the same way as before. Not surprisingly, the final result looks much the same, giving

$$J = \frac{c^2 - K_1 K_2 K_3 K_4 K_5 K_6 c_e^2}{\beta_1 c^2 + \beta_2 c_e^2 + \beta_3 c^2 c_e^2 + \beta_4}, \tag{20.583}$$

for some constants β that are not the same as the constants α that appeared previously.

The Ca^{2+}-ATPases on the plasma membrane are similar to the SERCA ATPases, and are modeled in the same way.

16. Develop a formal asymptotic expansion (following the method used in the Appendix) to homogenize the equation

$$\frac{\partial c}{\partial t} = D_c \frac{\partial^2 c}{\partial x^2} - kc + g \left(\frac{x}{L} \right) f(c), \tag{20.584}$$

where $g(y)$ is periodic with period 1, in the limit that $\frac{L^2 k}{D_c} \ll 1$. Show that the averaged equation is

$$\frac{\partial c}{\partial t} = D_c \frac{\partial^2 c}{\partial x^2} - kc + Gf(c), \qquad (20.585)$$

where $G = \frac{1}{L} \int_0^L g(x) dx$.

Solution

A formal asymptotic expansion requires a small parameter. Introduce the nondimensional variables $y = \sqrt{\frac{k}{D_c}} x$, and $\tau = kt$, in terms of which the equation becomes

$$\frac{\partial c}{\partial \tau} = \frac{\partial^2 c}{\partial y^2} - c + \frac{1}{k} g(\frac{y}{\epsilon}) f(c), \qquad (20.586)$$

where $\epsilon = \sqrt{\frac{kL^2}{D_c}}$.

Now introduce two (assumed to be) independent spatial variables $\xi = \frac{y}{\epsilon}$ and $z = y$, and use the chain rule to find that

$$\frac{\partial}{\partial y} = \frac{1}{\epsilon} \frac{\partial}{\partial \xi} + \frac{\partial}{\partial z}.$$

In terms of these variables, the equation becomes

$$\frac{1}{\epsilon^2} \frac{\partial^2 c}{\partial \xi^2} + \frac{2}{\epsilon} \frac{\partial^2 c}{\partial \xi \partial z} + \frac{\partial^2 c}{\partial z^2} - c + \frac{1}{k} g(\xi) f(c) - \frac{\partial c}{\partial \tau} = 0.$$

Now seek a power series solution $c = c_0(z, \tau) + \epsilon^2 c_2(\xi, z, \tau) + O(\epsilon^3)$, and require that c_2 be periodic in ξ. It follows that c_2 must satisfy

$$\frac{\partial^2 c_2}{\partial \xi^2} = \frac{\partial c_0}{\partial \tau} - \frac{\partial^2 c_0}{\partial z^2} + c_0 - \frac{1}{k} g(\xi) f(c_0).$$

However, the requirement that c_2 be periodic in ξ implies that the right hand side of this equation have zero integral, i.e,

$$\int_0^1 (\frac{\partial c_0}{\partial \tau} - \frac{\partial^2 c_0}{\partial z^2} + c_0 - \frac{1}{k} g(\xi) f(c_0).) d\xi = 0.$$

Since c_0 is independent of ξ, this requirement reduces to

$$\frac{\partial c_0}{\partial \tau} - \frac{\partial^2 c_0}{\partial z^2} + c_0 - \frac{1}{k} \int_0^1 g(\xi) d\xi f(c_0) = 0.$$

Rewritten in terms of original dimensioned variables this is

$$\frac{\partial c_0}{\partial t} = D_c \frac{\partial^2 c_0}{\partial x^2} - kc_0 + \frac{1}{L} \int_0^L g(\frac{x}{L}) dx f(c_0) = 0,$$

as expected.

More details about homogenization can be found in Keener (1998) or Holmes (199?).

17. (a) Find conditions on A guaranteeing that there are traveling waves of calcium release in the spatially homogenized equation (7.93) with the cubic release function (7.90).

    (b) Find conditions on A guaranteeing that there are traveling waves of calcium release in the spatially homogenized equation (7.93) with the piecewise linear relaese function (7.91). Ans.: $\frac{c^*}{c_e} < 1 - \sqrt{\frac{k}{A+k}}$.

Solution

(a) $A + \sqrt{(A(A-4k)} - 6k > 0$.

(b) $\frac{c^*}{c_e} < 1 - \sqrt{\frac{k}{A+k}}$.

18. Find the solution of the boundary value problem

$$\nabla^2 W = 2\pi, \qquad\qquad (20.587)$$

on a circle of radius 1, subject to the boundary condition $n \cdot \nabla W = 1$, and requiring W to have zero average value.

Solution

$W(r) = \frac{1}{2}(r^2 - \frac{1}{4})$.

Selected Solutions to Chapter 9

1. Use that c_i is small compared to c_e to simplify the Llinás model of presynaptic Ca^{2+} channels (Peskin, 1991). Show that this simplification gives little difference to the behavior of the full model shown in Figs. 8.5 and 8.6.

   Solution

   With $\frac{c_i}{c_e} = \frac{0.1}{40} = 0.0025$ it is clear that the relative error from ignoring c_i is small. This is also easily seen by plotting the two solutions.

2. (a) The model of the presynaptic Ca^{2+} current discussed in the text cannot give the curves shown in Fig. 8.7 in response to a voltage jump. Why not?

   (b) Calculate and plot the solution to (8.8) if $V = V_0 + (V_1 - V_0)(H(t) - H(t-4))$, where H is the Heaviside function.

   Solution

   (a) In the model, an instantaneous jump in voltage gives an instantaneous jump in I_{Ca}, while the curves in Fig. 8.7 show smooth changes in I_{Ca}.

   (b) Suppose that $o(0) = \hat{o}(V_0)$. If V is instantatneously changed to V_1 at $t = 0$, and then back to V_0 at $t = 4$, we get

   $$o(t) = \begin{cases} o_1(t), & 0 < t \leq 4, \\ o_2(t), & 4 < t, \end{cases} \qquad (20.588)$$

   where

   $$o_1(t) = \frac{k_1(V_1)}{k_1(V_1) + k_2}(1 - e^{-(k_1(V_1)+k_2)t})$$
   $$+\hat{o}(V_0)e^{-(k_1(V_1)+k_2)t}], \qquad (20.589)$$
   $$o_2(t) = \frac{k_1(V_0)}{k_1(V_0) + k_2}(1 - e^{-(k_1(V_s)+k_2)(t-4)})$$
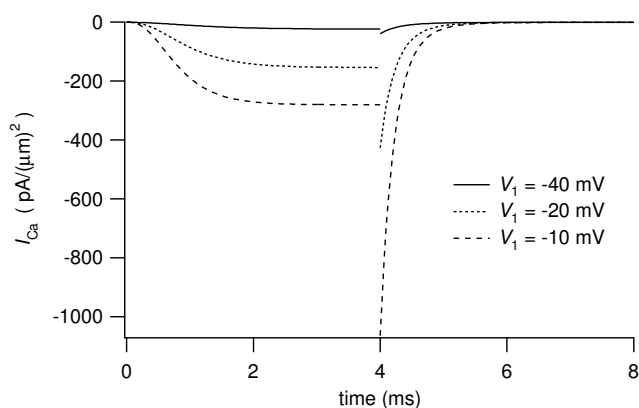 $$+o_1(4)e^{-(k_1(V_s)+k_2)(t-4)}. \qquad (20.590)$$

Figure 20.43: Synaptic suppression in the model of presynaptic Ca^{2+} channels (Exercise 2). Plots of I_{Ca}, calculated from (20.591), for $V_0 = -70$ mV and $V_1 = -40, -20, -10$ mV.

Finally

$$I_{\text{Ca}} = \begin{cases} j(V_1)\,(o_1(t))^n, & 0 < t \le 4, \\ j(V_0)\,(o_2(t))^n, & 4 < t. \end{cases} \tag{20.591}$$

Note that, although $o(t)$ is continuous, I_{Ca} is not. Plots for three values of V_1 are shown in Fig. 20.43.

3. Calculate the analytic solution to (8.8) when V is a given function of t.

Solution

If V is a specified function of t, then k_1 and k_2 are also specified functions of t. Thus, we need to solve

$$\frac{do}{dt} + (k_1(t) + k_2(t))o = k_1(t). \tag{20.592}$$

Multiply this equation by the integrating factor $e^{\int^t (k_1(s)+k_2(s))ds}$ to get

$$\frac{d}{dt}\left(o(t)e^{\int^t (k_1(s)+k_2(s))ds}\right) = s_0 k_1(t)e^{\int^t (k_1(s)+k_2(s))ds}. \tag{20.593}$$

Integrate both sides and solve for $o(t)$ to get

$$o(t) = e^{-\int^t (k_1(s)+k_2(s))ds} \int^t k_1(\tau)e^{\int^\tau (k_1(s)+k_2(s))ds}d\tau + Ce^{-\int^t (k_1(s)+k_2(s))ds}, \tag{20.594}$$

for some constant C. Use the initial condition $o(t = 0) = o_0$ to solve for C, to get

$$o(t) = e^{-\int_0^t (k_1(s)+k_2(s))ds} \int_0^t k_1(\tau) e^{\int^\tau (k_1(s)+k_2(s))ds} d\tau + o_0 e^{-\int_0^t (k_1(s)+k_2(s))ds}.$$
(20.595)

4. (a) In Fig. 8.13, why are some of the curves positive and some negative?

   (b) Construct a simple function $F(t)$ with the same qualitative shape as the function $W(t)$ used in the Magleby and Stevens model (Fig. 8.12).

   (c) Calculate the analytic solution to (8.50) for F. Compare to the curves shown in Fig. 8.13.

   Solution

   (a) Since the *current* is plotted in Fig. 8.13, and not the conductance, the curves change sign when V is on different sides of the Nernst potential of the ACh-sensitive channels (around 15 mV). Thus, when $V < 15$ mV, the current is negative, and when $V > 15$ mV, the current is positive.

   (b) A reasonable approximation of the curve in Fig. 8.12 is given by $W(t) = t^2 e^{-10t}$.

   (c) We need to solve

   $$\frac{dx}{dt} + \alpha x = \beta W(t).$$
   (20.596)

   Multiplying by the integrating factor $e^{\alpha t}$ and integrating gives

   $$x(t) = e^{-\alpha t} \left(x(0) + \beta \int_0^t e^{\alpha \tau} W(\tau) \, d\tau \right).$$
   (20.597)

   Substituting in $W(t) = t^2 e^{-10t}$ and assuming that $x(0) = 0$ then gives

   $$\begin{aligned} x(t) &= \beta e^{-\alpha t} \int_0^t \tau^2 e^{(\alpha - 10)\tau} \, d\tau \\ &= \beta e^{-\alpha t} \left(\frac{[t^2(\alpha - 10)^2 + 2t(10 - \alpha) + 2]e^{(\alpha - 10)t} - 2}{(\alpha - 10)^3} \right) \end{aligned}$$
   (20.598)

   The current, I_{ACh}, is then given by

   $$I_{\text{ACh}} = x(t)(V - V_{\text{ACh}}),$$
   (20.599)

   where $V_{\text{ACh}} = -15$ mV. Plots of I_{ACh} for various values of V are given in Fig. 20.44.

5. In the Magleby and Stevens model of end-plate currents, a simple choice for the release function $f(t)$ results in end-plate conductances with considerable qualitative similarity with those in Fig. 8.13. Suppose there is an instantaneous release of ACh into the synaptic cleft at time $t = 0$. Take $f(t) = \gamma \delta(t)$,
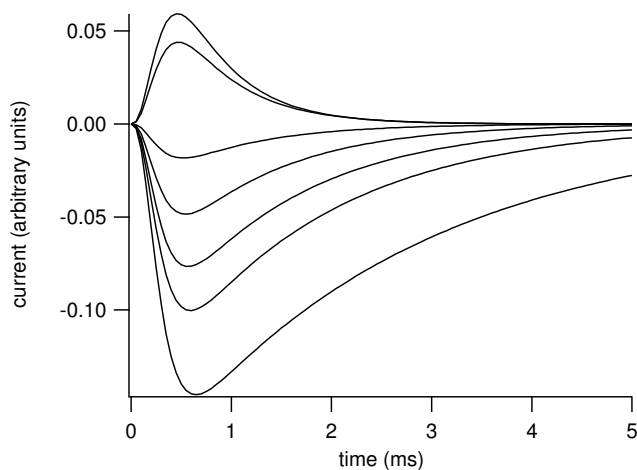
Figure 20.44: Plots of I_{ACh} calculated from (20.599) of Exercise 4. The corresponding values for V are, from top to bottom, 32, 20, -30, -56, -82, -106 and -161 mV, the same values as in Fig. 8.13. The only parameter not specified in the text is b (in $\beta(V)$) which we set arbitrarily at 1.

where δ is the Dirac delta function and find the conductance x which is the solution of (8.46), to leading order in $\frac{\gamma}{K}$ in the limit that $\frac{\gamma}{K}$ is small. Show that $x(t)$ is always positive. Plot $x(t)$.

Solution

With $f(t) = \gamma \delta(t)$, (8.43) becomes

$$\frac{dc}{dt} = \gamma \delta(t) - k_e c, \qquad c(0) = 0. \tag{20.600}$$

As usual, we eliminate the delta function by integrating across the singularity, i.e., by integrating from $-\epsilon$ to ϵ and letting $\epsilon \to 0$. Thus

$$\int_{-\epsilon}^{\epsilon} \frac{dc}{dt}\,dt = \int_{-\epsilon}^{\epsilon} \gamma \delta(t)\,dt - \int_{-\epsilon}^{\epsilon} k_e c\,dt = \gamma - \int_{-\epsilon}^{\epsilon} k_e c\,dt. \tag{20.601}$$

Letting $\epsilon \to 0$, and assuming that c is bounded, gives

$$c(0^+) - c(0^-) = \gamma, \tag{20.602}$$

and thus, since $c(0^-) = 0$ (from the original initial condition) we have

$$\frac{dc}{dt} = -k_e c, \qquad t > 0, \tag{20.603}$$
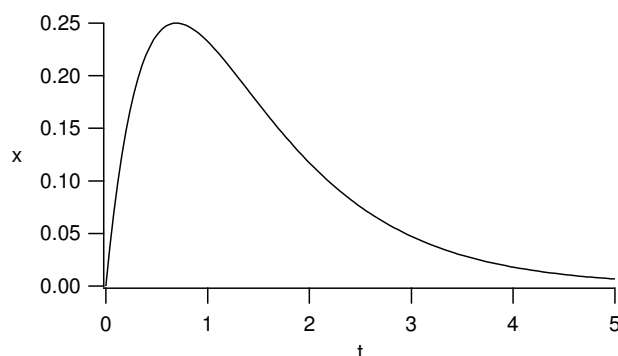
$$c(0) = \gamma. \tag{20.604}$$

Figure 20.45: Plot of $x(t)$ calculated as in Exercise 5, using the parameters $\gamma = 0.1$, $K = 10$, $\alpha = 1$, $\beta = 1$, $N = 100$ and $k_e = 2$.

The equation for x now becomes

$$\frac{dx}{dt} = -\alpha x + \frac{\gamma \beta N e^{-k_e t}}{K + \gamma e^{-k_e t}} \tag{20.605}$$

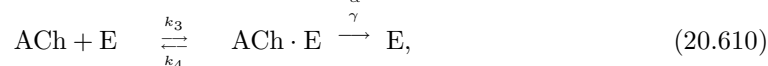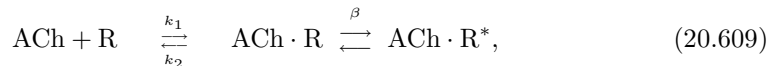which, if $\frac{\gamma}{K}$ is assumed to be small, can be approximated by

$$\frac{dx}{dt} = -\alpha x + \frac{\gamma \beta N}{K} e^{-k_e t}. \tag{20.606}$$

This equation has the solution

$$x_0 = \frac{\gamma \beta N}{K(\alpha - k_e)} (e^{-k_e t} - e^{-\alpha t}), \tag{20.607}$$

satisfying the initial condition $x_0(0) = 0$. A plot of x is given in Fig. 20.45.

6. Peskin (1991) presented a more complex version of the Magleby and Stevens model. His model is based on the reaction scheme

$$\longrightarrow \quad \text{ACh}, \qquad \text{rate } r_T \text{ per unit volume}, \tag{20.608}$$

$$\text{ACh} + \text{R} \quad \underset{k_2}{\overset{k_1}{\rightleftharpoons}} \quad \text{ACh} \cdot \text{R} \quad \overset{\beta}{\underset{\alpha}{\rightleftharpoons}} \quad \text{ACh} \cdot \text{R}^*, \tag{20.609}$$

$$\text{ACh} + \text{E} \quad \underset{k_4}{\overset{k_3}{\rightleftharpoons}} \quad \text{ACh} \cdot \text{E} \quad \overset{\gamma}{\longrightarrow} \quad \text{E}, \tag{20.610}$$

where E is some enzyme that degrades ACh in the synaptic cleft. (The Peskin model differs from the Magleby and Stevens model in two ways, with the assumption of enzymatic degradation of ACh and the assumption that the amount of ACh bound to its receptor is not negligible.)

(a) Write down the equations for the 6 dependent variables. Use conservation laws to eliminate two of the equations.

(b) Assume that the reactions involving ACh with R, and ACh with E (with reaction rates $k_i, i = 1, 4$), are fast to obtain expressions for [R] and [E] in terms of the other variables. Substitute these expressions into the differential equations for [ACh · R*] and [ACh] − [R] − [E] to find two differential equations for [ACh · R*] and [ACh].

(c) Solve these equations when the stimulus is a small sudden release of ACh (i.e., assume that $r_T = \epsilon\delta(t)$ and look for solutions of $O(\epsilon)$). Show that the solution has the same form as (**??**) but that the exponential coefficients are given by the roots of a quadratic polynomial. Choose arbitrary values for the parameters and plot the solution.

Hint: look for solutions of the form $R^* = \epsilon x$, $A = \epsilon y$ and derive the differential equations

$$\frac{dx}{dt} = a_1 y - \alpha x, \tag{20.611}$$

$$\frac{dx}{dt} + a_2 \frac{dy}{dt} = \delta(t) - a_3 y, \tag{20.612}$$

for some constants a_1, a_2 and a_3. Then integrate over the singularity at $t = 0$ to show that $y(0) = 1/a_2$. Solve by finding the eigenvalues and eigenvectors of the resultant homogeneous linear system.

Solution

(a) Let $A = [\text{ACh}]$, $R = [\text{R}]$, $E = [\text{E}]$, $R^* = [\text{ACh} \cdot \text{R}^*]$, $C_1 = [\text{ACh} \cdot \text{R}]$, and $C_2 = [\text{ACh} \cdot \text{E}]$. Then

$$\frac{dA}{dt} = r_T - k_1 AR + k_2 C_1 - k_3 AE + k_4 C_2, \tag{20.613}$$

$$\frac{dR}{dt} = -k_1 AR + k_2 C_1, \tag{20.614}$$

$$\frac{dE}{dt} = -k_3 AE + k_4 C_2 + \gamma C_2, \tag{20.615}$$

$$\frac{dR^*}{dt} = \beta C_1 - \alpha R^*, \tag{20.616}$$

$$\frac{dC_1}{dt} = k_1 AR - k_2 C_1 - \beta C_1 + \alpha R^*, \tag{20.617}$$

$$\frac{dC_2}{dt} = k_3 AE - k_4 C_2 - \gamma C_2. \tag{20.618}$$

From the conservation of E and R we have

$$E + C_2 = \text{constant} = \bar{C}_2, \tag{20.619}$$

$$R + R^* + C_1 = \text{constant} = \bar{C}_1. \tag{20.620}$$

Thus we have the four equations

$$\frac{dA}{dt} = r_T - k_1 AR + k_2(\bar{C}_1 - R - R^*) - k_3 AE + k_4(\bar{C}_2 - E) \tag{20.621}$$

$$\frac{dR}{dt} = -k_1 AR + k_2(\bar{C}_1 - R - R^*), \tag{20.622}$$

$$\frac{dE}{dt} = -k_3 AE + k_4(\bar{C}_2 - E) + \gamma(\bar{C}_2 - E), \tag{20.623}$$

$$\frac{dR^*}{dt} = \beta(\bar{C}_1 - R - R^*) - \alpha R^*. \tag{20.624}$$

(b) Assuming that the two enzymatic reactions are fast we have the pseudo-equilibrium

$$k_1 AR = k_2 C_1, \tag{20.625}$$
$$k_3 AE = k_4 C_2, \tag{20.626}$$

and thus

$$R = \frac{\bar{C}_1 - R^*}{K_R A + 1}, \tag{20.627}$$

$$E = \frac{\bar{C}_2}{K_E A + 1}, \tag{20.628}$$

where $K_R = k_1/k_2$ and $K_E = k_3/k_4$.

Since $\frac{d}{dt}(A - R - E) = r_T - \gamma(\bar{C}_2 - E)$, it follows that

$$\frac{d}{dt}\left(A - \frac{\bar{C}_1 - R^*}{K_R A + 1} - \frac{\bar{C}_2}{K_E A + 1}\right) = r_T - \gamma \bar{C}_2 \frac{K_E A}{K_E A + 1}. \tag{20.629}$$

Furthermore, from (20.624) we have

$$\frac{dR^*}{dt} = \beta(\bar{C}_1 - R - R^*) - \alpha R^*$$

$$= \frac{\beta K_R A}{K_R A + 1}(\bar{C}_1 - R^*) - \alpha R^*. \tag{20.630}$$

(c) Let $A = \epsilon y$, $R^* = \epsilon x$. Then

$$\epsilon \frac{dx}{dt} = \frac{\epsilon \beta K_R y}{\epsilon K_R y + 1}(\bar{C}_1 - \epsilon x) - \epsilon \alpha x, \tag{20.631}$$

and thus, to lowest order in ϵ,

$$\frac{dx}{dt} = \beta K_R \bar{C}_1 y - \alpha x. \tag{20.632}$$

Similarly,

$$\frac{d}{dt}\left(\epsilon y - \frac{\bar{C}_1 - \epsilon x}{\epsilon K_R y + 1} - \frac{\bar{C}_2}{\epsilon K_E y + 1}\right) = \epsilon \delta(t) - \epsilon \gamma \bar{C}_2 \frac{K_E y}{\epsilon K_E y + 1}. \tag{20.633}$$

Since

$$(\bar{C}_1 - \epsilon x)(1 + \epsilon K_R y)^{-1} = \bar{C}_1 - \epsilon(x + \bar{C}_1 K_R y) + O(\epsilon^2), \tag{20.634}$$

it follows that, to lowest order in ϵ,

$$\frac{d}{dt}[y(1 + \bar{C}_1 K_R + \bar{C}_2 K_E) + x] = \delta(t) - \gamma \bar{C}_2 K_E y. \qquad (20.635)$$

Then, let $a_1 = \beta K_R \bar{C}_1$, $a_2 = 1 + \bar{C}_1 K_R + \bar{C}_2 K_E$, and $a_3 = \gamma \bar{C}_2 K_E$ to get

$$\frac{dx}{dt} = a_1 y - \alpha x, \qquad (20.636)$$

$$\frac{dx}{dt} + a_2 \frac{dy}{dt} = \delta(t) - a_3 y. \qquad (20.637)$$

To cope with the delta function we integrate both equations across the singularity, i.e., from $-\epsilon$ to ϵ and then let $\epsilon \to 0$. Assuming bounded solutions, this gives $x(0^+) - x(0^-) = 0$ and $y(0^+) - y(0^-) = 1/a_2$. Thus, (20.636) and (20.637) become

$$\frac{dx}{dt} = a_1 y - \alpha x, \qquad (20.638)$$

$$\frac{dx}{dt} + a_2 \frac{dy}{dt} = -a_3 y \qquad (20.639)$$

on $t > 0$, with the initial conditions $x(0) = 0$, $y(0) = 1/a_2$.
A slight rearrangement now gives

$$\frac{d}{dt}\begin{pmatrix} x \\ y \end{pmatrix} = M \begin{pmatrix} x \\ y \end{pmatrix}. \qquad (20.640)$$

where

$$M = \begin{pmatrix} -\alpha & a_1 \\ \frac{\alpha}{a_2} & \frac{-(a_1 + a_3)}{a_2} \end{pmatrix}. \qquad (20.641)$$

The eigenvalues of M are the roots of

$$\lambda^2 + \lambda\left(\alpha + \frac{a_1 + a_3}{a_2}\right) + \frac{\alpha a_3}{a_2} = 0. \qquad (20.642)$$

Since

$$\left(\alpha + \frac{a_1 + a_3}{a_2}\right)^2 - 4\frac{\alpha a_3}{a_2} = \left(\alpha - \frac{a_3}{a_2}\right)^2 + 2\frac{a_1}{a_2}\left(\alpha + \frac{a_3}{a_2}\right) + \left(\frac{a_1}{a_2}\right)^2 > 0, \qquad (20.643)$$

and since

$$\left(\alpha + \frac{a_1 + a_3}{a_2}\right) > 0 \qquad (20.644)$$

it follows that the roots of (20.642) are both real and negative. Call these roots λ_1 and λ_2, where $\lambda_2 < \lambda_1 < 0$. The eigenvector corresponding to λ_1 is $\begin{pmatrix} a_1 \\ \lambda_1 + \alpha \end{pmatrix}$, and the eigenvector corresponding to λ_2 is $\begin{pmatrix} a_1 \\ \lambda_2 + \alpha \end{pmatrix}$.
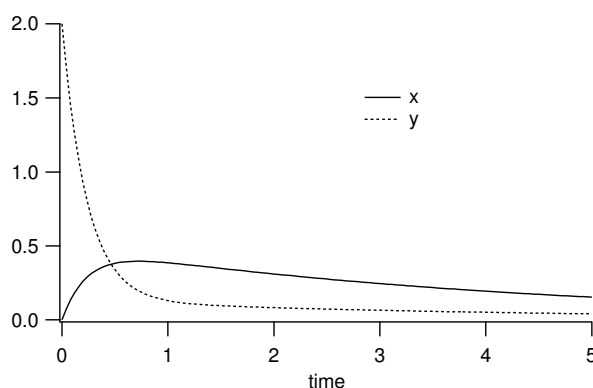
Figure 20.46: Plot of $x(t)$ and $y(t)$ from (20.648) (Exercise 6), using the arbitrarily chosen parameters $a_1 = 0.1$, $a_2 = 0.5$, $a_3 = 1$, $\alpha = 0.5$.

Thus, the general solution is

$$\begin{pmatrix} x \\ y \end{pmatrix} = \kappa_1 \begin{pmatrix} a_1 \\ \lambda_1 + \alpha \end{pmatrix} e^{\lambda_1 t} + \kappa_2 \begin{pmatrix} a_1 \\ \lambda_2 + \alpha \end{pmatrix} e^{\lambda_2 t}, \qquad (20.645)$$

where the constants κ_1 and κ_2 are determined from the initial conditions, $y(0) = 1/a_2$, $x(0) = 0$. Hence

$$\kappa_1 = \frac{1}{a_2(\lambda_1 - \lambda_2)}, \qquad (20.646)$$

$$\kappa_2 = \frac{1}{a_2(\lambda_2 - \lambda_1)}, \qquad (20.647)$$

from which we get, finally,

$$\begin{pmatrix} x \\ y \end{pmatrix} = \frac{1}{a_2(\lambda_1 - \lambda_2)} \begin{pmatrix} a_1 \\ \lambda_1 + \alpha \end{pmatrix} e^{\lambda_1 t} + \frac{1}{a_2(\lambda_2 - \lambda_1)} \begin{pmatrix} a_1 \\ \lambda_2 + \alpha \end{pmatrix} e^{\lambda_2 t}. \tag{20.648}$$

In Fig. 20.46 we plot $x(t)$ and $y(t)$ for arbitrary choices of the parameters.

7. Solve (8.56) with $g_s(t) = x(t)$ as found in Exercise 5 and plot the solution. Compare to $x(t)$ found in Exercise 5 (i.e., (8.57)).

Solution

Let

$$g_s(t) = \frac{\beta N}{K(\alpha - k_e)} \left(e^{-k_e t} - e^{-\alpha t} \right) \qquad (20.649)$$

so that $V_1 = V - V_r$ satisfies the equation

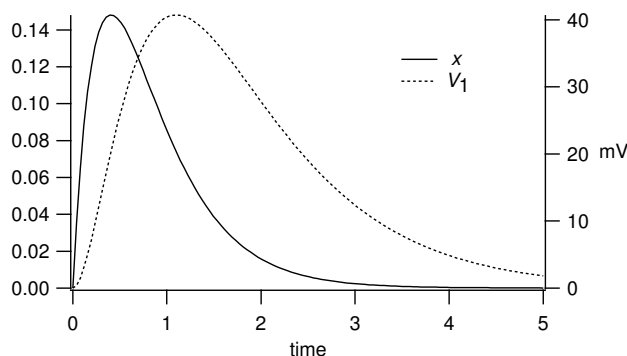$$\frac{dV_1}{dt} + \frac{g_r}{C_m} V_1 = \left(\frac{V_s - V_r}{C_m} \right) g_s(t). \qquad (20.650)$$

Figure 20.47: Comparison of $x(t)$ (Exercise 5) and $V_1(t)$ (Exercise 7), using the same parameters as in Fig. 20.45. Additional parameters are $V_s = -15$, $V_r = -70$, $C_m = 1$, $g_r = 1$. (C_m and g_r are chosen arbitrarily.) V_1 is plotted against the right-hand axis, x against the left.

Multiplying both sides by the integrating factor $e^{g_r t/C_m}$ gives

$$\frac{d}{dt}\left(V_1 e^{g_r t/C_m}\right) = \left(\frac{V_s - V_r}{C_m}\right) g_s(t) e^{g_r t/C_m}, \qquad (20.651)$$

and hence, integrating both sides and dividing by $e^{g_r t/C_m}$, we get

$$V_1 = \frac{(V_s - V_r)\beta N}{K(\alpha - k_e)} \left(\frac{e^{-\alpha t}}{\alpha C_m - g_r} - \frac{e^{-k_e t}}{k_e C_m - g_r}\right) + K e^{-g_r t/C_m}, \qquad (20.652)$$

for some constant K. From the initial condition $V_1(0) = 0$ (which follows since $V(0) = V_r$), it follows that

$$K = \frac{(V_s - V_r)\beta N}{K(\alpha - k_e)} \left(\frac{1}{k_e C_m - g_r} - \frac{1}{\alpha C_m - g_r}\right), \qquad (20.653)$$

and thus

$$V_1 = \frac{(V_s - V_r)\beta N}{K(\alpha - k_e)} \left(\frac{e^{-\alpha t} - e^{-g_r t/C_m}}{\alpha C_m - g_r} - \frac{e^{-k_e t} - e^{-g_r t/C_m}}{k_e C_m - g_r}\right). \qquad (20.654)$$

In Fig. 20.47 we plot $x(t)$ and $V_1(t)$ on the same graph, with V_1 plotted against the right-hand axis in order to facilitate comparison. As can be seen, V_1 responds more slowly than x, due to the time delay inherent in the membrane conductance.

8. The purpose of this exercise is to link together the models of this chapter to construct a unified model for the synaptic cleft that connects the presynaptic action potential to the postsynaptic voltage via the concentration of ACh in the synaptic cleft.

(a) First, use the FitzHugh-Nagumo model (section 5.2) to construct an action potential that serves as the input to the overall model. Remark: the equations

$$\frac{dV_1}{dt} = 100(0.0001(V_1 - V_r)(70 - (V_1 - V_r))((V_1 - V_r) - 7)) \quad (20.655)$$

$$\frac{dw}{dt} = 0.25(V_1 - V_r - 5w), \quad (20.656)$$

do a reasonable job. What is V_r? What value should be chosen for V_r? Solve these equations and plot the presynaptic action potential, V_1.

(b) Link this presynaptic voltage to the presynaptic Ca^{2+} concentration by constructing a differential equation for the Ca^{2+} concentration. (Hint: Take the inward Ca^{2+} current given by the Llinás model of section 8.1.2 $P_{Ca} = 0.03\mu m s^{-1}$ and a linear Ca^{2+} removal with time constant 1 ms works well. Be very careful with the units.) Plot the Ca^{2+} transient that results from the presynaptic action potential calculated in part (i) above.

(c) Link to the model of Ca^{2+}-mediated release of neurotransmitter (section 8.1.3). Plot, as a function of time, the probability that the release site is activated.

(d) Next, link to the model of neurotransmitter kinetics in the synaptic cleft (section 8.1.4). (Hint: the rate of release of neurotransmitter into the cleft should be proportional to the number of activated release sites. Choose this constant of proportionality to be 3×10^6.) Then link this to the model of the postsynaptic membrane potential, V_2, by letting $g_s(t) = x(t)$. Plot the concentration of ACh and the concentration of open ACh-sensitive channels as functions of time.

(e) Finally, plot V_1 and V_2 on the same graph to compare the input and output voltages of the model.

Solution

It is important to use parameters with consistent units. Here we take time in units of ms, voltage in mV and concentration in μM. The XPPAUT code used for this exercise is given in full below.

(a) V_r is the resting potential of the cell, so a reasonable value is $V_r = -70$ mV. The given equations are easily solved (see the equations for v_1 and w in the XPPAUT code below) to get a reasonable presynaptic action potential, as shown in Fig. 20.48A.

(b) $V_1(t)$ can be used it to determine the time course of o in the Llinás model of section 8.1.2, and hence the inward Ca^{2+} current. Thus,

$$\frac{do}{dt} = k_1(V_1(t))(s_0 - o) - k_2(V_1(t))o, \quad (20.657)$$

$$i = P_{Ca} \cdot \frac{4F^2}{RT} \cdot V \cdot \frac{c_i - c_e \exp(\frac{-2FV}{RT})}{1 - \exp(\frac{-2FV}{RT})}, \quad (20.658)$$

$$I_{\text{Ca}} \quad = \quad i\frac{s_0}{n}\left(\frac{o}{s_0}\right)^n. \tag{20.659}$$

Most of the parameters can be taken directly from the text.

It remains to write down a differential equation for c, the presynaptic Ca^{2+} concentration. Great care must be taken with the units. Firstly, since i is a current density, if we write P_{Ca} in units of $\mu m/ms$, we see that the units of I_{Ca} are $(\mu m/ms)(\mu C/liter)$. (Note that this does indeed have units of current density, although written in an unusual way.)

Since c is in units of μM, the differential equation for c is

$$\frac{dc}{dt} = -\left(\frac{A}{2F\nu}\right)I_{\text{Ca}} - k_{\text{out}}c, \tag{20.660}$$

where A and ν are, respectively, the area and volume of the presynaptic region, and k_{out} is some constant rate of Ca^{2+} removal. As suggested, just let $k_{\text{out}} = 1/ms$.

A/ν has units of $1/distance$. If this distance is expressed in units of μm, it follows that $\left(\frac{A}{2F\nu}\right)I_{\text{Ca}}$ has units of $\mu M/ms$, as desired. This combination $\left(\frac{A}{2F\nu}\right)$ is called `factor` in the XPPAUT code for this exercise. Here, we have assumed a spherical presynaptic region, with radius of $20\ \mu m$, which gives $A/\nu = 3/20$.

With these numbers, then, we get the Ca^{2+} transient shown in Fig. 20.48B.

(c) Once we know c as a function of time, $R(t)$ is easily calculated numerically from (8.15) and (??). Note that the parameters in Table 8.1 are all in the correct units and so can be put directly into the model. Note also that there are four differential equations, for O_1 through O_4. The resultant plot of $R(t)$ is given in Fig. 20.48C.

(d) As suggested, let $f(t) = (3 \times 10^6)R(t)$ in (8.36). The equations for x and y depend on V_2, the postsynaptic potential, since α and β both depend on V_2, and likewise the equation for V_2 depends on x, as we take $g_s(t) = x(t)$ as the conductance of the ACh-sensitive postsynaptic channels. As given in the text, the reversal potential of the ACh-sensitive channels, V_s, is assumed to be -15 mV, while the reversal potential of the postsynaptic membrane in the absence of ACh is assumed to be -70 mV, just as for the presynaptic membrane. The other parameters are taken as $C_m = 1$ and $g_r = 1$. Thus, the final model equations are

$$\frac{dx}{dt} \quad = \quad -\alpha(V_2)x + \beta(V_2)y, \tag{20.661}$$

$$\frac{dy}{dt} \quad = \quad \alpha(V_2)x + k_1 a(N - x - y) - (\beta + k_2)y, \tag{20.662}$$

$$\frac{da}{dt} \quad = \quad (3 \times 10^6)R(t) - k_e a - k_1 a(N - x - y) + k_2 y \tag{20.663}$$

$$C_m\frac{dV_2}{dt} \quad = \quad -g_r(V_2 - V_r) - x(t)(V_2 - V_s). \tag{20.664}$$

Note that we have used a, rather than c, to denote [ACh], because c is used here to denote the presynaptic Ca^{2+} concentration.

Plots of x and a are shown in Fig. 20.48D and E.

(e) The plot of V_2 is obtained immediately from the equations above, and a plot of V_1 and V_2 is given in Fig. 20.48F. Note how the membrane potential transient is delayed and spread out by the process of synaptic transmission.
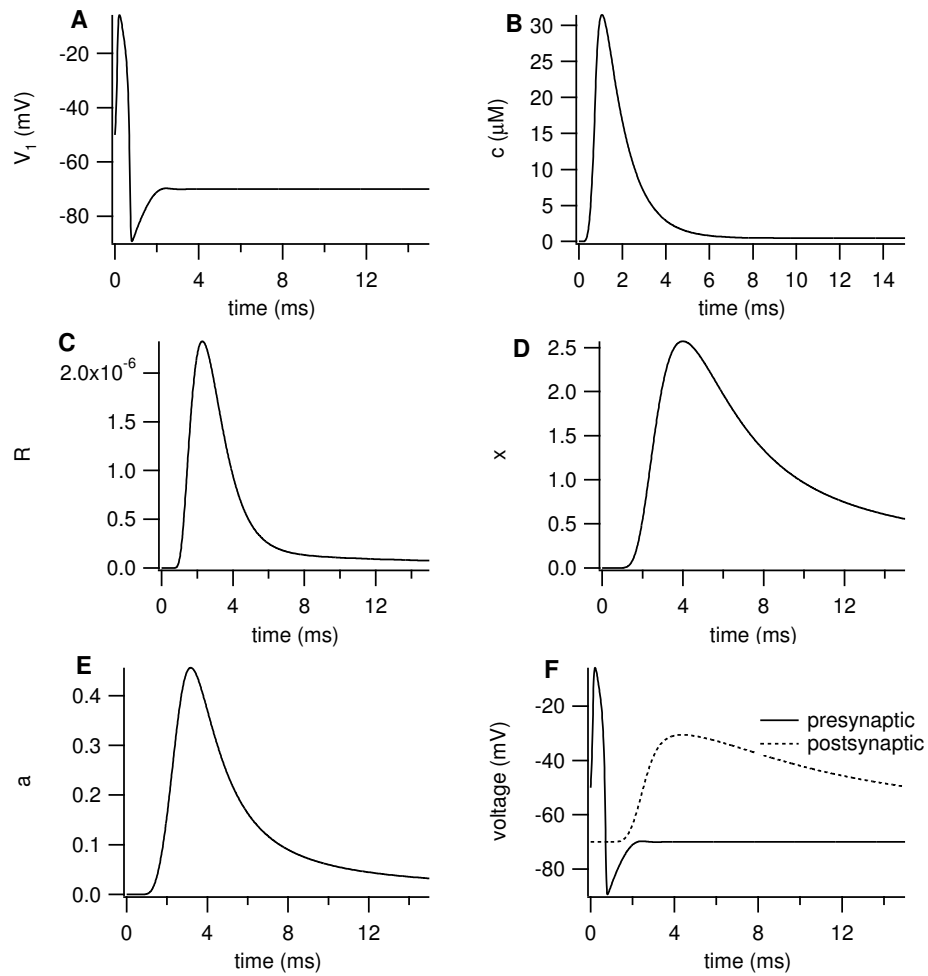
Figure 20.48: Plots from the model of Exercise 8.

XPPAUT code for the full model connecting the presynaptic voltage to the postsynaptic voltage.

```
############################
v1(0)=-50
w(0)=0
o(0)=0
c(0)=0
o1(0)=0
o2(0)=0
o3(0)=0
o4(0)=0
a(0)=0
x(0)=0
y(0)=0
v2(0)=-70
############################
# FHN params
Vr=-70

# Llinas params
param k10=2, k20=1, z1=1, n=5,ci=0.1,ce=4.0e4,PCa=3.0e-2,s0=100

# Voltage-type params
param FRT=.0386   F=96490.0

# Calcium parameters. Radius in microns. Factor converts current to calcium flux.
param kout=1 radius=20
!factor=(3/radius)*(1/(2*F))

# Calcium-stimulated secretion params
param kp1=3.75e-3, km1=4e-4
param kp2=2.5e-3, km2=1e-3
param kp3=5e-4, km3=0.1
param kp4=7.5e-3, km4=10

# Magleby parameters
param bigA=0.008 bigB=1.43   bigN=10
param smalla=0.00315 smallb=1
param k1m=1000, k2m=500, ke=10

# Postsynaptic voltage params
param Vs=-15, gr=1, Cm=1

############################
# Llinas functions
k1(x)=k10*exp(z1*x*FRT)
fac(x)=2*x*FRT
j(x)=PCa*2*F*fac(x)*(ci-ce*exp(-fac(x)))/(1-exp(-fac(x)))
ICa(x,y)=j(x)*(s0/n)*((y/s0)^n)

# calcium-stimulated secretion functions
tau1(x)=1/(kp1*x+km1)
tau2(x)=1/(kp2*x+km2)
tau3(x)=1/(kp3*x+km3)
tau4(x)=1/(kp4*x+km4)
```

```
# Magleby functions
alpha(x)=bigB*exp(bigA*x)
beta(x)=smallb*exp(smalla*x)

#############################
aux R=o1*o2*o3*o4

#############################
# FHN odes for the presynaptic voltage
v1'=100*(0.0001*(v1-Vr)*(70-(v1-Vr))*((v1-Vr)-7)-w)
w'=0.25*(v1-Vr-5*w)

# Llinas odes
o'=k1(v1)*(s0-o) - k20*o

# Calcium odes. Conversion factors are included explicitly, for clarity
c'= -ICa(v1,o)*factor - kout*c

# Calcium-stimulated secretion odes
o1'=kp1*c - o1/tau1(c)
o2'=kp2*c - o2/tau2(c)
o3'=kp3*c - o3/tau3(c)
o4'=kp4*c - o4/tau4(c)

# Magleby odes
x'=-alpha(v2)*x + beta(v2)*y
y'=alpha(v2)*x + k1m*a*(bigN-x-y) - (beta(v2)+k2m)*y
a'=3e6*o1*o2*o3*o4 - ke*a - k1m*a*(bigN-x-y) + k2m*y

# Postsynaptic voltage ode
v2'= (1/Cm)*(-gr*(v2-Vr) - x*(v2-Vs))

#############################
@ total=15, dt=0.01, xlo=0, xhi=15,  ylo=-85, yhi=0, yp1=v1, yp2=v2, bounds=10000, nplot=2
@ meth=gear

done
```

Selected Solutions to Chapter 11

2. For a simplified lac operon model we assume that external lactose is converted directly into allolactose, and take

$$\frac{dA}{dt} = \alpha_L P \frac{L_e}{K_{Le} + L_e} - \beta_A B \frac{A}{K_A + A} - \gamma_A A. \qquad (20.665)$$

eliminating (10.20) from the model.

Give a graphical steady state analysis of the system of equations by plotting the nullclines $\frac{dM}{dt} = 0$ and $\frac{dA}{dt} = 0$ in the $M - A$ phase plane (this is not a true phase plane since it is a four variable system.)

Solution

An example is shown in Fig. 20.49. For this plot, $L_e = 0.15$, and there are three intersections corresponding to three steady state solutions. For smaller values of L_e (say $L_e = 0.05$) there is only one solution with allolactose at a low value, and for larger values of L_e (say $L_e = 0.35$), there is only one solution with allolactose at high values.

3. Find the steady state solutions of the Goodwin model (10.23) with $n = 3$, and with $k_1 = k_2 = k_3 = k$. Under what conditions is the steady state solution unstable, and under what conditions is the instability an oscillatory instability? Find conditions on the parameters of the problem for a Hopf bifurcation.

Solution

It is useful to first non-dimensionalize the problem. We introduce variables $x_1 = \frac{\nu_1 \nu_2}{K_m k_2 k_3} X_1$, $x_2 = \frac{\nu_2}{K_m k_3} X_2$, and $x_3 = \frac{X_3}{K_m}$, $\tau = \alpha t$, where $\alpha = \frac{\nu_0 \nu_1 \nu_2}{K_m k_2 k_3}$, in which case the equations become

$$\frac{dx_1}{d\tau} = \frac{1}{1 + x_3^p} - \mathbf{x}_1, \qquad (20.666)$$

$$\frac{dx_2}{d\tau} = \beta(x_1 - x_2), \qquad (20.667)$$

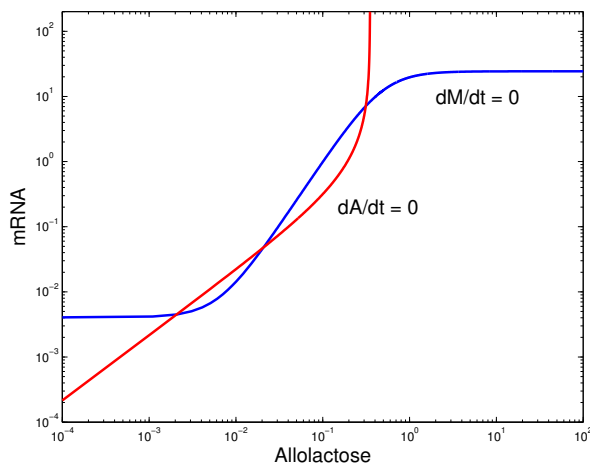$$\frac{dx_3}{d\tau} = \beta(x_2 - x_3), \qquad (20.668)$$

Figure 20.49: Plot of null-clines $\frac{dM}{dt} = 0$ and $\frac{dA}{dt} = 0$ in the $M - A$ phase plane shown for $L_e = 0.15$.

where $\beta = \frac{k}{\alpha}$. In this form it is easy to see that the steady solution is $x_1 = x_2 = x_3 = y$ where y is the (unique - why is it unique?) positive root of $\beta y(1 + y^p) = 1$. Notice that $\beta y < 1$.

The Jacobian matrix at this steady state is

$$J = \begin{pmatrix} -b & 0 & -\phi \\ b & -b & 0 \\ 0 & b & -b \end{pmatrix}, \tag{20.669}$$

where $\phi = \frac{py^p}{y(1+y^p)^2} = p\beta(1 - \beta y) > 0$. The characteristic equation is

$$(\lambda + \beta)^3 + \beta^2 \phi = 0 \tag{20.670}$$

It follows readily that the roots are

$$\lambda_1 = -\beta - b(p(1 - \beta y))^{\frac{1}{3}}, \qquad \lambda_{2,3} = -\beta + b(p(1 - \beta y))^{\frac{1}{3}} \exp(\pm i\frac{\pi}{3}). \tag{20.671}$$

The real part of λ_1 is always negative. The real part of $\lambda_{2,3}$ is

$$R(\lambda_{2,3}) = -\beta + \frac{b}{2}(p(1 - \beta y))^{\frac{1}{3}} \tag{20.672}$$

and the steady solution is unstable if

$$-\beta + \frac{b}{2}(p(1 - \beta y))^{\frac{1}{3}} > 0, \tag{20.673}$$

or equivalently, if

$$p(1 - \beta y) > 8. \tag{20.674}$$

Thus, if $p > 8$, it is possible to find parameter values k so that the steady solution is unstable via a Hopf bifurcation.

4. A modification of the Goodwin model that does not require such a high level of cooperativity was formulated by Bliss, Painter and Marr (Bliss et al. 1982) and is given by

$$\frac{dx_1}{dt} = \frac{a}{1 + x_3} - b_1 x_1, \qquad (20.675)$$

$$\frac{dx_2}{dt} = b_1 x_1 - b_2 x_2, \qquad (20.676)$$

$$\frac{dx_3}{dt} = b_2 x_2 - \frac{c x_3}{K + x_3}. \qquad (20.677)$$

Determine the stability and of the steady state solution and find any Hopf bifurcation points in the special case that $K = 1$, $b_1 = b_2 = b < c$, and $a = c(\sqrt{\frac{c}{b}} - 1)$.

Solution

At steady state, $x_1 = x_2 = \frac{1}{b}\frac{a}{1+x_3}$, where $x_3 = \frac{a}{c}$. The Jacobian matrix is

$$J = \begin{pmatrix} -b & 0 & -a\phi \\ b & -b & 0 \\ 0 & b & -c\phi \end{pmatrix}, \qquad (20.678)$$

where $\phi = \frac{1}{(1+x_3)^2}$, and the characteristic equation is

$$(\lambda + b)^3 + \frac{ab^3}{c} = 0. \qquad (20.679)$$

The roots of the characteristic equation are

$$\lambda_1 = -b - b(\frac{a}{c})^{\frac{1}{3}}, \qquad \lambda_{2,3} = -b + b(\frac{a}{c})^{\frac{1}{3}} \exp(\pm i\frac{\pi}{3}). \qquad (20.680)$$

The real part of $\lambda_{2,3}$ is zero when $a = 8c$, which therefore corresponds to a Hopf bifurcation point.

Selected Solutions to Chapter 12

1. (a) The fundamental solution of Poisson's equation in free space with a unit source at the origin ($\nabla^2 \phi = -\delta(x)$) is $\phi(x) = \frac{1}{4\pi|x|}$.

   Find the solution of Poisson's equation with a source at the origin and a sink of equal strength at $x = x_1$, and let $|x_1| \to 0$. What must be assumed about the strength of the source and the sink in order to obtain a nonzero limiting potential?

   (b) Find the solution of Poisson's equation with a dipole source by solving the problem $\nabla^2 \phi = \frac{1}{\epsilon}(\delta(x - \epsilon v) - \delta(x))$ with $|v| = 1$, and then taking the limit $\epsilon \to 0$.

   Solution

   With a source of strength A at the origin and sink at x_1, the solution of Poisson's equation is

   $$\phi = \frac{A}{4\pi|x|} - \frac{A}{4\pi|x - x_1|} \approx \frac{A}{4\pi}\frac{x \cdot x_1}{|x|^3}, \qquad (20.681)$$

   to leading order in x_1. Thus, (part b), if $x_1 = \epsilon v$, and $A = \frac{1}{\epsilon}$, then

   $$\lim_{\epsilon \to 0} \phi = \frac{1}{4\pi}\frac{x \cdot v}{|x|^3}. \qquad (20.682)$$

2. Determine the heart rate for the ECG recording in Fig. 12.3a. The subject was sedated at the time this recording was made. What are the effects of the sedation?

   Solution

   With 6 beats per 19 subdivisions (of 5 mm each), the overall rate is $\frac{6}{19} \times 300 = 95$ beats per minute. It is likely that this high rate is a consequence of sedation.

3. Identify the different deflections in the ECG recording shown in Fig. 12.53. What can you surmise about the nature of propagation for the extra QRS

complex (called an *extrasystole*). Because of the apparent periodic coupling between the normal QRS and the extrasystole, this rhythm is called a *ventricular bigeminy.*

Solution

The P wave, QRS complex and T wave in this recording appear normal but at a very slow rate (39 per minute). The large broad QRS complex implies slowed conduction (not employing the Purkinje conduction network), hence an origination site somewhere in the ventricular myocardium.

4. (a) Suggest a diagnosis for the ECG recording in Fig. 12.54.
   Hint: What does the inverted P-wave suggest? What is the heart rate?

   (b) What possible mechanisms can account for the failure of the SA node to generate the heartbeat?

Solution

The heart rate is 82 beats per minute (6 beats in 22 5 mm subdivisions $= \frac{6}{22} \times 300$.)

5. Estimate the mean deflection of the QRS complex in each of the six standard leads (I, II, III, aVR, aVL, aVF) in Fig. 12.7 and then estimate the mean heart vector for the normal heartbeat.

Solution

Using that $l_I = (1,0)$, $l_{II} = (\frac{1}{2}, \frac{1}{2}\sqrt{3})$, $l_{III} = (-\frac{1}{2}, \frac{1}{2}\sqrt{3})$, $l_{aVF} = (0,1)$, $l_{aVR} = (-\frac{1}{2}\sqrt{3}, -\frac{1}{2})$, and estimating(from Fig. 12.7) that $L_I = 7$, $L_{II} = 9$, $L_{III} = 0$, $L_{aVR} = -8$, $L_{aVL} = 3$, and $L_{aVF} = 7$, we estimate (using a least squares solution) that the mean heart vector $H = (7.0, 5.8)$.

6. Improve your skill at reading ECGs by finding the mean heart vector for the QRS complexes in Figs. 12.4, 12.9, and 12.10. Why is hypertrophy the diagnosis for Figs. 12.9 and 12.10? In what direction are the heart vectors deflected in these figures?

Solution

From Fig. 12.4 we estimate that $L_I = 9.5$, $L_{II} = 5$, $L_{III} = -4.5$, $L_{aVR} = -8.5$, $L_{aVL} = 7.5$, and $L_{aVF} = 0$, showing a significant deflection in the direction of l_I. The least squares solution is $H = (9.4, 0.3)$.

From Fig.12.9, we estimate that $L_I = 0$, $L_{II} = 28$, $L_{III} = 27$, $L_{aVR} = -13$, $L_{aVL} = -10$, and $L_{aVF} = 0$, showing a significant deflection in the direction of l_{aVF}, and a very large amplitude. The least squares solution is $H = (1.0, 28.0)$.

From Fig. 12.10, we estimate that $L_I = -16$, $L_{II} = 3$, $L_{III} = 15$, $L_{aVR} = 0$, $L_{aVL} = -15$, and $L_{aVF} = 15$, showing a significant deflection in the direction of l_{III}, and a very large amplitude. The least squares solution is $H = (-11.7, 12.7)$.

7. Find the mean heart vector for the ECG recording shown in Fig. 12.55. What mechanism can you suggest that accounts for this vector?

Solution

Notice that the amplitude in all the leads is substantially smaller than normal, suggesting loss of tissue mass (infarction). We can determine the location of this loss by determining the deflection of the heart vector from normal, away from the location of tissue loss. From Fig. 12.55, we estimate that $L_I = -2$, $L_{II} = 4$, $L_{III} = 5$, $L_{aVR} = 0$, $L_{aVL} = -6$, and $L_{aVF} = 6$, yielding $H = (-2.6, 5.6)$, showing a significant deflection in the direction of l_{III}, with a small amplitude. This suggests infarcted (nonconducting) tissue in the left heart.

8. By assuming a fast equilibrium between states N_3 and N_4, and between states C_3 and C_4, derive the simplified reaction diagram of Fig. 12.19C for the L-type channel model.

Solution

We begin by writing the system of differential equations for the full system

$$
\begin{aligned}
\frac{dN_3}{dt} &= \beta N_4 + \omega C_3 - (\alpha + \gamma)N_3, \\
\frac{dN_4}{dt} &= \alpha N_3 + \frac{\omega}{b}C_4 - (\beta + f)N_4 + gO - \gamma a N_4, \\
\frac{dC_3}{dt} &= \gamma N_3 + \beta' C_4 - (\omega + \alpha')C_3, \\
\frac{dC_4}{dt} &= \alpha' C_3 + \gamma a N_4 - (\beta' + \frac{\omega}{b})C_4, \\
\frac{dO}{dt} &= fN_4 - gO.
\end{aligned}
\tag{20.683}
$$

The quasisteady state assumption is that $\beta N_4 = \alpha N_3$ and $\alpha' C_3 = \beta' C_4$. We let $N = N_3 + N_4$ and $C = C_3 + C_4$ so that $N_3 = \frac{\beta}{\alpha+\beta}N$, $N_4 = \frac{\alpha}{\alpha+\beta}N$, $C_3 = \frac{\beta'}{\alpha'+\beta'}C$, $C_4 = \frac{\alpha'}{\alpha'+\beta'}C$. Adding the respective equations, we find

$$
\begin{aligned}
\frac{dN}{dt} &= \omega\frac{\beta' + \alpha'/b}{\alpha' + \beta'}C - \gamma\frac{\beta + a\alpha}{\alpha + \beta}N - f\frac{\alpha}{\alpha + \beta}N + gO, \\
\frac{dC}{dt} &= \gamma\frac{\beta + a\alpha}{\alpha + \beta}N - \omega\frac{\beta' + a'/b}{\alpha' + \beta'}C, \tag{20.684} \\
\frac{dO}{dt} &= f\frac{\alpha}{\alpha + \beta}N - gO. \tag{20.685}
\end{aligned}
$$

From this one can easily read off the transition rates for the diagram of Fig. 12.19C.

10. Use cable theory to estimate the effective coupling resistance for cardiac cells in the longitudinal and transverse directions. Assume that cells are 0.01 cm long, 0.00167 cm wide, $\chi = S/v = 2400\,\text{cm}^{-1}$, $R_m = 7000\,\Omega\text{-cm}^2$, $R_c = 150\,\Omega$-cm, $R_e = 0$, with a longitudinal space constant of 0.09 cm and transverse space constant 0.03 cm (appropriate for canine crista terminalis). What difference do you observe with a transverse space constant of 0.016 cm (appropriate for sheep epicardium)?

Solution

For canine crista terminalis, in the longitudinal direction the gap junctional resistance per cell is $\frac{R_g}{L} = 0.72$, and in the transverse direction it is $\frac{R_g}{L} = 1.77$. For sheep epicardium, $\frac{R_g}{L} = 6.44$. Apparently, sheep epicardium is much less tightly coupled in the transverse direction than canine crista terminalis.

11. How should the coupling coefficient r_g be chosen so that the decay rate for the discrete linear model (12.78) with $I_{\text{ion}} = -V/R_m$ matches the space constant of the medium?

Solution

The decay rate $\mu = \exp\frac{-L}{\lambda_g}$ satisfies $\frac{r_g L p}{R_m} = \mu - 2 + \frac{1}{\mu} = 4\sinh^2(\frac{L}{2\lambda_g})$. Pick r_g accordingly.

12. Using that the longitudinal and transverse cardiac action potential deflections are $\Delta V_{eL} = 74$ mV, $\Delta V_{eT} = 43$ mV, that the membrane potential has $\Delta V = 100$ mV (independent of direction), and that the axial speed of propagation in humans is 0.5 m/s in the longitudinal fiber direction and 0.17 m/s in the transverse direction, determine the ratio of coefficients of the conductivity tensors $\frac{\sigma_{eL}}{\sigma_{iL}}$, $\frac{\sigma_{eT}}{\sigma_{iL}}$, and $\frac{\sigma_{iT}}{\sigma_{iL}}$. What are these ratios in dog if the ratio of longitudinal to transverse speeds is 2:1?

Solution

The ratios $\frac{\sigma_{eL}}{\sigma_{iL}}$ and $\frac{\sigma_{eT}}{\sigma_{iT}}$ follow directly from (12.116). To find the remaining ratios use that

$$\left(\frac{c_L}{c_T}\right)^2 = \frac{\sigma_{iL}\sigma_{eL}}{\sigma_{iL} + \sigma_{eL}}\frac{\sigma_{iT} + \sigma_{eT}}{\sigma_{iT}\sigma_{eT}} \tag{20.686}$$

In the case of human tissue, $\frac{c_L}{c_T} = 3$ so that $\frac{\sigma_{eT}}{\sigma_{iL}} = 0.067$, and $\frac{\sigma_{iT}}{\sigma_{iL}} = 0.05$. For canine tissue for which $\frac{c_L}{c_T} = 2$, $\frac{\sigma_{eT}}{\sigma_{iL}} = 0.15$, and $\frac{\sigma_{iT}}{\sigma_{iL}} = 0.11$.

14. Consider the following simple model of a forced periodic oscillator, called the *Poincaré oscillator* (also called a *radial isochron clock* or a *snap back oscillator*; Guevara and Glass, 1982; Hoppensteadt and Keener, 1982; Keener and Glass, 1984; Glass and Kaplan, 1995). A point is moving counterclockwise around a circle of radius 1. At some point of its phase, the point is moved horizontally by an amount A and then allowed to instantly "snap back" to radius 1 moving along a radial line toward the origin (see Fig. 12.56).
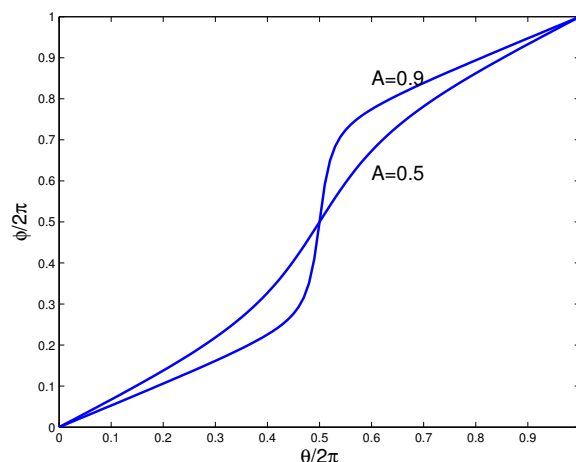
Figure 20.50: Phase resetting curve for the Poincare map with $A = 0.5$ and $A = 0.9$.

(a) Determine the *phase resetting curve* for this process. That is, given the phase θ before resetting, find the phase ϕ after resetting the clock. Plot ϕ as a function of θ for several values of A.

(b) Show that for $A < 1$ the phase resetting function is a *type 1* map, satisfying $\phi(\theta + 2\pi) = \phi(\theta) + 2\pi$.

(c) Show that for $A > 1$, the phase resetting function is a *type 0* map, for which $\phi(\theta + 2\pi) = \phi(\theta)$.

(d) Show that there is a *phase singularity*, that is, values of A and θ for which a new phase is not defined (Winfree, 1980).

(e) Construct a map $\theta_n \mapsto \theta_{n+1}$ by resetting the clock every T units of phase, so that

$$\theta_{n+1} = \phi(\theta_n) + T. \tag{20.687}$$

Show that for $A < 1$, this is a circle map. Determine the values of A and T for which there is one-to-one phase locking.

Solution

(a) The phase resetting curve satisfies the equation

$$\tan \phi = \frac{\sin \theta}{A + \cos\theta}. \tag{20.688}$$

Plots of the phase resetting curve for $A < 1$ (a *type 1*map) are shown in Fig. 20.50, and for $A > 1$ (a *type 0* map) in Fig. 20.51.
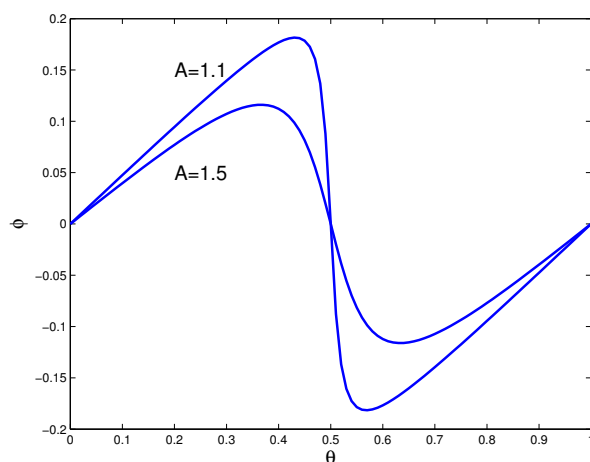
Figure 20.51: Phase resetting curve for the Poincare map with $A = 1.1$ and $A = 1.5$.

(d) There is a phase singularity (or phase indeterminancy) at $\theta = \pi$ when $A = 1$.

(e) The boundary of the one-to-one phase locking region occurs for those values of A and T for which there is a fixed point of the mapping that occurs where the phase resetting curve has slope 1. To have slope 1, it must be that $A + \cos\theta = 0$. This enables us to easily determine the boundary curve for the one-to-one phase locking region, shown plotted in Fig. 20.52.

15. A simple model of the response of an excitable cell to a periodic stimulus is provided by the *integrate-and-fire* model (Knight, 1972; Keener, Hoppensteadt and Rinzel, 1981). In this model the membrane potential $v(t)$ is assumed to be passive unless the threshold is reached, whereupon the membrane "fires" and is immediately reset to zero. The equations describing the evolution of the membrane potential are

$$\frac{dv}{dt} = -\gamma v + S(t), \tag{20.689}$$

and $v(t^+) = 0$ if $v(t) = v_T$, the threshold. We take the periodic stimulus to be a simple sinusoidal function, $S(t) = S_0 + S_m \sin(\omega t)$.

Let T_n be the time of the nth firing. Formulate the problem of determining T_{n+1} from T_n as a circle map. For what parameter values is this a continuous circle map and for what parameter values is it a discontinuous circle map? (Guevara and Glass, 1982.)
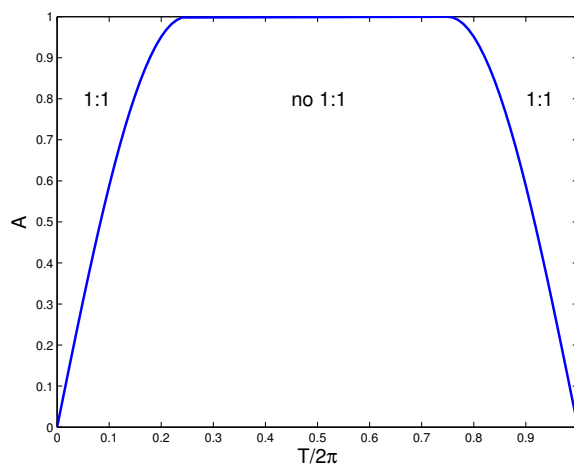
Solution

Figure 20.52: Boundary of the 1:1 phase locking region for the Poincare map in the $T - A$ parameter plane.

Use that the solution of the differential equation is

$$v(t) = C \exp(-\gamma t) + \frac{S_0}{\gamma} + S_m \frac{\gamma \sin(t) - \cos(t)}{\gamma^2 + 1}. \qquad (20.690)$$

If $v(T_n) = V_T$, then the resetting condition implies that

$$C = -\exp(\gamma T_N^+) F(T_N^+), \qquad (20.691)$$

where $F(T) = \frac{S_0}{\gamma} + S_m \frac{\gamma \sin(T) - \cos(T)}{\gamma^2 + 1})$, and the next firing time T_{N+1} must satisfy the implicit equation

$$\exp(\gamma T_{N+1})(F(T_{N+1}) - V_T) = \exp(\gamma T_N) F(T_N). \qquad (20.692)$$

This is a continuous map if $\exp(\gamma T)(F(T) - V_T)$ is a monotone increasing function of its argument, which holds if and only if $S_0 - S_M \geq \gamma V_T$.

16. Suppose the membrane potential rises at a constant rate λ until it reaches a threshold $\theta(t)$, at which time the potential is reset to zero. Suppose that the threshold is the simple sinusoidal function $\theta(t) = \theta_0 + \theta_m \sin(\omega t)$. Let T_n be the time of the nth firing. Formulate the problem of determining T_{n+1} from T_n as a circle map. For what parameter values is this a continuous circle map and for what parameter values is it a discontinuous circle map? (Glass and Mackey, 1979.)

Solution

Since $V(t) = \lambda(t - T_N)$, the next firing time is determined by the requirement

$$\lambda(T_{N-1} - T_N) = \theta_0 + \theta_m \sin(\omega T_{N+1}).\qquad(20.693)$$

This we write as the implicit equation

$$T_{N+1} - \frac{\theta_m}{\lambda}\sin(\omega T_{N+1}) = T_N + \frac{\theta_0}{\lambda}.\qquad(20.694)$$

This is a continuous circle map if and only if $T - \frac{\theta_m}{\lambda}\sin(\omega T)$ is a monotone increasing function, which is the case if and only if $\omega\frac{\theta_m}{\lambda} < 1$.

19. (a) Use homogenization theory to show that the averaged approximation of (12.68) is (12.69).

   (b) Use homogenization to separate (12.162) into two equations on different spatial scales. Show that $V \approx u_0(z, \tau) + \epsilon W(\eta)\left(J(\tau) - \frac{\partial u_0(z,\tau)}{\partial z}\right)$, where $W'(\eta) = 1 - \frac{D}{d(\eta)}$ and u_0 satisfies the averaged equation (12.166). Show that this answer is valid even if $J(\tau) = O(\frac{1}{\epsilon})$.

Solution

Both of these problems can be done at once. For eqn. (12.68), set $d = \frac{1}{r_c + \sum \delta(x - nL)r_g}$, and then $D = \frac{1}{r_c + r_g/L}$. We introduce two length scales $z = y$ and $\eta = \frac{y}{\epsilon}$ and then use the chain rule to replace

$$\frac{\partial}{\partial y} = \frac{1}{\epsilon}\frac{\partial}{\partial \sigma} + \frac{\partial}{\partial z}\qquad(20.695)$$

in terms of which the eqn (12.162) becomes

$$V_\tau - f(V) = \frac{1}{\epsilon^2}\frac{\partial}{\partial \eta}\left(\frac{d}{D}V_\eta\right) + \frac{1}{\epsilon}\frac{\partial}{\partial \eta}\left(\frac{d}{D}V_z\right) + \frac{1}{\epsilon}\frac{\partial}{\partial z}\left(\frac{d}{D}V_\eta\right) + \frac{\partial}{\partial z}\left(\frac{d}{D}V_z\right) - \frac{1}{\epsilon}J(\tau)\left(\frac{\Sigma_e d}{\sigma_e D}\right)_\eta\qquad(20.696)$$

Now we assume that V is of the form

$$V(z, \eta, \tau) = V_0(z, \tau, \epsilon) + \epsilon J(\tau)H(\eta) + \epsilon V_1(z, \eta, \tau) + O(\epsilon^2)\qquad(20.697)$$

and find a hierarchy of equations to be satisfied

$$0 = \frac{\partial}{\partial \eta}\left(\frac{d}{D}\frac{\partial V_1}{\partial \eta}\right) + \frac{\partial}{\partial \eta}\left(\frac{d}{D}\frac{\partial V_0}{\partial z}\right) + \frac{\partial}{\partial \eta}\left(\frac{d}{D}H'(\eta) - \frac{d}{\sigma_e}\right)J(\tau)\qquad(20.698)$$

$$\frac{\partial(V_0 + V_p)}{\partial \tau} - f(V_0 + V_p) = \frac{\partial}{\partial \eta}\left(\frac{d}{D}\frac{\partial V_2}{\partial \eta}\right) + \frac{\partial}{\partial \eta}\left(\frac{d}{D}\frac{\partial V_1}{\partial z}\right) + \frac{\partial}{\partial z}\left(\frac{d}{D}\frac{\partial V_1}{\partial \eta}\right)_z + \left(\frac{d}{D}\frac{\partial V_0}{\partial z}\right)_z\qquad(20.699)$$

The first of these is solved if we take

$$\left(\frac{d}{D}\frac{\partial V_1}{\partial \eta}\right) = K_1 - \left(\frac{d}{D}\frac{\partial V_0}{\partial z}\right),\qquad(20.700)$$

and

$$\left(\frac{d}{D}H'(\eta) - \frac{\Sigma_e d}{\sigma_e D}\right) = K_2. \tag{20.701}$$

The periodic solutions of these are

$$V_1 = W(\eta)\frac{\partial V_0}{\partial z}, \tag{20.702}$$

where

$$W'(\eta) = \frac{D}{d} - 1, \tag{20.703}$$

and

$$H'(\eta) = \frac{\Sigma_e}{\sigma_e} - \frac{D}{d}. \tag{20.704}$$

For the second of these to have a bounded periodic solution, we require that the integral with respect to η vanish, so that

$$\frac{\partial V_0}{\partial \tau} - \int_0^1 f(V_0 + V_p)d\eta = \frac{\partial}{\partial z}\left(\frac{\partial V_0}{\partial z}\right) \tag{20.705}$$

13. Determine the conditions under which there is propagation failure at a junction when the ionic current model is

$$I_{ion} = g_{Na}hm^2(V)(V_{Na} - V) + g_K(V_K - V), \tag{20.706}$$

where

$$m(V) = \begin{cases} 0, & V < V_K \\ \frac{V - V_K}{V_{Na} - V_K}, & V_K < V < V_{Na} \\ 0, & V > V_{Na} \end{cases} \tag{20.707}$$

Reasonable values for the parameters are $V_K = -84$mV, $V_{Na} = 66$mV, $g_{Na} = 3.33$mS/cm^2, and $g_K = 0.66$mS/cm^2, although these numbers are not needed to solve this problem.

Solution

With the change of variables $v = \frac{V - V_K}{V_{Na} - V_K}$, the function I_{ion} can be scaled into the cubic polynomial

$$F(v) = (V_{Na} - V_K)(g_{Na}hm^2(V)(1 - v) - g_K v). \tag{20.708}$$

The condition for failure with this function is

$$\frac{A_1 p_1}{A_2 p_2} \geq 1 - \frac{F(\beta)}{F(\alpha)} = 1 + \frac{(1 + \sqrt{(1 - 4g)})^2(1 - 6g + \sqrt{(1 - 4g)})}{(-1 + \sqrt{(1 - 4*g)})^2/(6g - 1 + \sqrt{(1 - 4g)}}, \tag{20.709}$$

where $g = \frac{g_K}{g_{Na}h}$.

24. Suppose two identical lambda-omega oscillators of the form (12.189-12.189) are coupled through their first variables x, with, in the notation of (12.195),

$$H = \begin{pmatrix} x \\ 0 \end{pmatrix} \tag{20.710}$$

and $a_{12} = a_{21} = \alpha$, and $a_{11} = a_{22} = 0$. Calculate the phase resetting function $h(\phi)$ and determine the stability of in-phase and out-of-phase, phase locked solutions, when $\alpha = \pm 1$.

Solution

This is simply a matter of carrying out the calculation for (12.205). First, rescale time so that $\omega = 2\pi$, so that the period of the uncoupled oscillators is 1. Then the periodic solution for the uncoupled oscillators is

$$U = \begin{pmatrix} x \\ y \end{pmatrix} = \begin{pmatrix} r_0 \cos(2\pi t) \\ r_0 \sin(2\pi t) \end{pmatrix}. \tag{20.711}$$

where r_0 is a root of the equation $\Lambda(r_0) = 0$.

It is a straightforward calculation to verify that the null spaces of the linearized equations and of the adjoint linearized equations are spanned by the function

$$Y = \begin{pmatrix} -\sin(2\pi t) \\ \cos(2\pi t) \end{pmatrix}, \tag{20.712}$$

from which it follows that

$$h(\phi) = \int_0^1 Y(\sigma) H(U(\sigma + \phi)) d\sigma = -\frac{1}{2}\sin(2\pi\phi). \tag{20.713}$$

The equation governing the phase difference $\phi = \delta\theta_1 - \delta\theta_2$ is **Recheck this scaling of ϕ!**

$$\frac{d\phi}{d\tau} = -\frac{1}{2}\alpha \sin(2\pi\phi). \tag{20.714}$$

Thus, if $\alpha = 1$, the in-phase solution $\phi = 0$ is stable and the out-of-phase solution $\phi = \frac{1}{2}$ is unstable, whereas if $\alpha = -1$, the in-phase solution is unstable and the out-of-phase solution is stable.

Selected Solutions to Chapter 13

2. Suppose the circumference of a vessel at zero pressure is L_0 and is linearly related to the wall tension T via $L = L_0 + \kappa T$. Use Laplace's law to show that the compliance of the vessel is $c = A_0 \frac{\kappa}{\pi M}$ where M is the vessel wall thickness.

Solution

Since $L = L_0 + \kappa T$, and $T = \frac{Pr}{M}$, where $L = 2\pi r$, it follows that

$$r = \frac{r_0}{1 - \frac{\kappa P}{2\pi M}}. \tag{20.715}$$

Linearizing this for small P gives

$$r \approx r_0(1 + \frac{\kappa P}{2\pi M}), \tag{20.716}$$

so that the crossectional area A satisfies

$$A \approx A_0(1 + \frac{\kappa P}{\pi M}), \tag{20.717}$$

at least for sufficiently small P. Accordingly, the compliance is $c = A_0 \frac{\kappa}{\pi M}$.

10. In the fetal circulation, a portion of the systemic flow is diverted to the placenta for oxygen exchange. Suppose that blood entering the systemic veins from the systemic organs and tissues is completely deoxygenated, as is blood leaving the lungs to enter the left heart. Suppose also that blood leaving the placenta entering the systemic veins is fully oxygenated. What percentage of the total cardiac output should be sent through the placenta in order to maximize the total oxygen exchange?

Solution

In the model for the fetal circulation, split Q_s into two flows, $Q_s = Q_P + Q_o$, where Q_P is placental flow and Q_o is flow to systemic organs and tissues. The concentration of oxygen entering the right heart is $\frac{Q_P}{Q_P + Q_o} O_{max}$. Thus, the

rate of uptake of oxygen by the lungs is $Q_p \frac{Q_P}{Q_P + Q_o} O_{max}$, whereas, the rate of uptake of oxygen by the systemic organs and tissues is

$$\frac{1}{Q_d + Q_l}(Q_d + Q_l \frac{Q_f}{Q_f + Q_p})\frac{Q_P}{Q_P Q_o}O_{max} \tag{20.718}$$

It follows (after some calculation) that the total oxygen uptake rate is

$$O_{up} = \frac{(q_p^2 - 2q_p + 2q_p q_P - q_P + 1)Q_P}{(q_p - 1)^2}O_{max} \tag{20.719}$$

where $q_p = \frac{Q_p}{Q_T}$ and $q_P = \frac{Q_P}{Q_T}$, with Q_T the total cardiac output. This is maximized when

$$q_P = \frac{1}{2}\frac{(1 - q_p)^2}{1 - 2q_p}, \tag{20.720}$$

which is close to $\frac{1}{2}$ if q_p is not too large. According to Guyton and Hall, actual placental flow percentage is $q_P = 0.55$ and $q_p = 0.12$.

Selected Solutions to Chapter 14

1. What is the volume (per mole) of an ideal gas at room temperature $(27°\,\text{C})$ and 1 atm pressure? What is its volume at body temperature $(98°\,\text{F})$?

   Solution

   From the ideal gas law $PV = nRT$ (where n is the number of moles), the volume, V, of a mole of ideal gas is given by

   $$V = \frac{RT}{P}. \qquad (20.721)$$

   Since $R = 8.315$ J mol^{-1}·K^{-1}, $T = 300.15$ K (corresponding to $27°$ C), and $P = 1$ atm $= 1.01325 \times 10^5$ N · m^{-2}, it follows that

   $$
   \begin{aligned}
   V &= \frac{8.315 \times 300.15}{1.01325 \times 10^5}\text{m}^3 & (20.722) \\
   &= 0.0246 \text{ m}^3 & (20.723) \\
   &= 24.6 \text{ liters.} & (20.724)
   \end{aligned}
   $$

   With $T = 309.82$K (corresponding to $98°$ F, use the conversion $T_F = \frac{9}{5}T_C + 32 = \frac{9}{5}(T_K - 273.15) + 32$),

   $$V = \frac{8.315 \times 309.82}{1.01325 \times 10^5}\text{m}^3 = 25.4 \text{ liters} \qquad (20.725)$$

10. Suppose that a carrier (like hemoglobin) of a molecule (like oxygen) has n independent binding sites, with individual binding and unbinding rates k_+ and k_-. Let c_j denote the concentrations of the state with j molecules bound. Assume concentrations are in steady state.

    (a) Show that $c_j = \binom{n}{j} x^j c_0$, where $\binom{n}{j} = \frac{n!}{j!(n-j)!}$ is the *binomial coefficient* where $x = s_0/K$, $K = k_-/k_+$, and s_0 is the concentration of the carrier molecule.
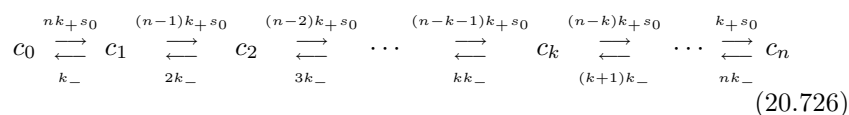
       Hint: Keep track of the total number of binding sites.

(b) Find the saturation function in the case that $n = 4$.

(c) Show that the four equilibrium constants K_1, K_2, K_3, K_4 defined in (13.45) are given by $(K_1, K_2, K_3, K_4) = K(\frac{1}{4}, \frac{2}{3}, \frac{3}{2}, 4)$.

(d) Estimate K to give a good fit of this model to the hemoglobin saturation curve. How does this curve compare with the curve (13.47)?

(e) Determine whether the hemoglobin binding sites are independent. How close are the equilibrium constants here to those found in the text?

Solution

Part (a)

We have the binding scheme

$$c_0 \; \underset{k_-}{\overset{nk_+s_0}{\rightleftarrows}} \; c_1 \; \underset{2k_-}{\overset{(n-1)k_+s_0}{\rightleftarrows}} \; c_2 \; \underset{3k_-}{\overset{(n-2)k_+s_0}{\rightleftarrows}} \; \cdots \; \underset{kk_-}{\overset{(n-k-1)k_+s_0}{\rightleftarrows}} \; c_k \; \underset{(k+1)k_-}{\overset{(n-k)k_+s_0}{\rightleftarrows}} \; \cdots \; \underset{nk_-}{\overset{k_+s_0}{\rightleftarrows}} \; c_n$$

$$(20.726)$$

State c_0 can convert to state c_1 in n different ways (since there are n unoccupied binding sites) and each site reacts at speed k_+s_0. Thus we get

$$nxc_0 = c_1, \qquad (n-1)xc_1 = 2c_2, \qquad (n-2)xc_2 = 3c_3, \qquad \cdots, \qquad (20.727)$$

from which it follows that

$$c_2 \;=\; \frac{n-1}{2}xc_1 = \frac{n(n-1)}{2}x^2c_0, \tag{20.728}$$

$$\vdots \tag{20.729}$$

$$c_i \;=\; \frac{n(n-1)\cdots(n-i-1)}{1\cdot 2\cdot 3\cdots i}x^ic_0, \tag{20.730}$$

which is the desired answer.

Part (b)

The fraction of occupied sites, Y, is given by

$$Y \;=\; \frac{c_1 + 2c_2 + 3c_3 + 4c_4}{4(c_1 + c_2 + c_3 + c_4)} \tag{20.731}$$

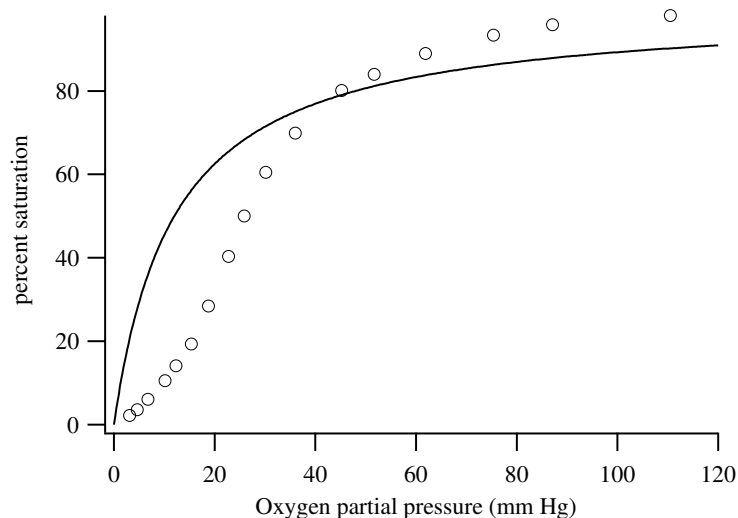$$=\; \frac{x + 3x^2 + 3x^3 + x^4}{1 + 4x + 6x^2 + 4x^3 + x^4}. \tag{20.732}$$

Figure 20.53: Plot of the saturation function when $n = 4$.

Part (c)

From the reaction scheme in (20.726) we see that $k_j = (n - j + 1)k_+$ and $k_{-j} = jk_-$. Hence

$$\frac{k_{-j}}{k_j} = \left(\frac{j}{n - j + 1}\right) K.$$
(20.733)

When $n = 4$ we thus have $K_1 = K/4$, $K_2 = 2K/3$, $K_3 = 3K/2$ and $K_4 = 4K$, as required.

Part (d)

It is not possible to get a good fit to the hemoglobin saturation curve by using independent binding sites, as illustrated in Fig. 20.53. The symbols are the approximate experimental data as given in Table 20.4, and the solid curve is drawn from (20.732) using $K = 12\sigma$ mm Hg. Clearly, with independent and identical binding sites, the saturation function has the incorrect shape and cannot be made to fit the experimentally measured saturation function well.

Part (e)

We conclude from the result of (d) that the binding sites are not independent. The measured values of $K_1, \cdots, K_4$ are quite different from the values obtained if we assume independent binding sites, with $K = 12\sigma$ mm Hg.

P_{O_2}(mm Hg)	percent saturation
3.08	2.21
4.61	3.59
6.77	6.08
10.15	10.50
12.31	14.09
15.38	19.34
18.77	28.45
22.77	40.33
25.85	50.0
30.15	60.50
36.00	69.89
45.23	80.11
51.69	83.98
61.85	88.95
75.38	93.37
87.08	95.86
110.5	98.07

Table 20.4: Approximate numerical data for the hemoglobin saturation curve.

12. Construct a Monod–Wyman–Changeux model (Section 1.4.4) for oxygen binding to hemoglobin and determine the saturation function. Find parameter values so that the saturation curve agrees (at least approximately) with the data in Fig. 20.4. Compare your results to the fit of (13.47).

   In the Monod–Wyman–Changeux model, each binding site is independent. Thus, on the surface it appears that the Monod–Wyman–Changeux model is quite different in principle from the model discussed in the text, in which binding to the fourth binding site is enhanced. However, by considering the solution to Exercise 1.76 of Chapter 1 (and using the parameter values found in the first part of the question), show that this is not really true. In other words, show that the Monod–Wyman–Changeux model indirectly incorporates an enhanced binding to subsequent binding sites, once the initial site is bound.

   Solution

   Most of the work for this question was already done in Chapter 1, where we discussed Monod–Wyman–Changeux models. The MWC model is shown in Fig. 20.54. Equation (1.76) gives the saturation function for an MWC model with n binding sites. In our case $n = 4$, and so we get immediately that

   $$Y = \frac{\frac{s}{K_1}\left(1 + \frac{s}{K_1}\right)^3 + \frac{1}{K_2}\frac{s}{K_3}\left(1 + \frac{s}{K_3}\right)^3}{\left(1 + \frac{s}{K_1}\right)^4 + \frac{1}{K_2}\left(1 + \frac{s}{K_3}\right)^4}. \tag{20.734}$$

   Note also that, as we showed in Exercise **??** of Chapter 1, the incorporation of transitions from R_i to T_i doesn't change the saturation function. By ap-
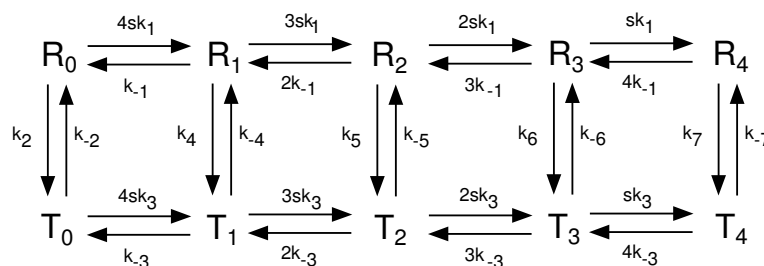
Figure 20.54: Schematic diagram of the Monod–Wyman–Changeux model for oxygen binding to hemoglobin.

propriate choice of the parameters K_1, K_2 and K_3 we can make this MWC saturation function agree closely with the experimental data shown in Table 20.4; typical results are shown in Fig. 20.54.

We did not determine the parameters by a formal fitting procedure to the data, but merely by trial and error. With only three parameters to twiddle this is not a difficult procedure. There are many ways of finding the "best-fit" parameters, in, say, the least-squares sense, but such methods require considerably more programming. Interested readers are referred to ?? for details on such methods.

In a MWC model each binding site is considered to be identical. This appears different from the model discussed in the text, in which the binding of oxygen to the fourth binding site proceeds at quite a different rate. However, this is not really the case. From the principle of detailed balance we know that

$$K_1 K_4 = K_2 K_3, \qquad K_1 K_5 = K_4 K_3, \qquad K_1 K_6 = K_5 K_3, \qquad K_1 K_7 = K_6 K_3. \tag{20.735}$$

From these equations and from the values for K_1, K_2 and K_3 given in the caption to Fig. 20.55 we find that $K_4 = 5.7$, $K_5 = 0.025$, $K_6 = 1.2 \times 10^{-4}$ and $K_7 = 5.3 \times 10^{-7}$.

Since $K_2 \gg 1$ it follows that the state R_0 is greatly preferred over the state T_0. Hence, upon the addition of oxygen, most R_0 gets converted to state R_1. Of course, since K_3/K_1 is so small we know that oxygen will bind much more easily to hemoglobin when it is in the T conformation, but this does not happen for the first binding site as hemoglobin is "locked" into the R conformation. However, $K_7 < K_6 < K_5 < K_4$ and thus, as hemoblobin binds more oxygen the rate at which R is converted to T increases. In other words, the binding of oxygen tends to favour the conversion of the R conformation to the T conformation, and thus facilitates the binding of further oxygen.

13a. Suppose enough sodium bicarbonate is dissolved in water (with neutral pH) to give a 25mM solution, assuming no carbon dioxide is produced. This solution is then equilibrated with carbon dioxide at 40 mm Hg
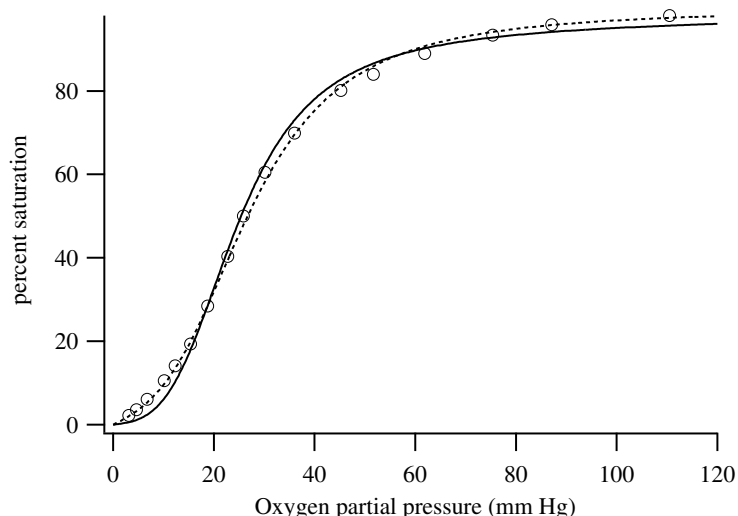
Figure 20.55: Plot of the saturation function of the Monod–Wyman–Changeux model in the previous figure. The solid curve is the MWC model with the parameters $K_1 = 1000\,\sigma$ mm Hg, $K_2 = 1250$, $K_3 = 4.54\,\sigma$ mm Hg. The dashed curve is a plot of (13.47) using the parameter values given in the text.

partial pressure, and the pH is found to be 7.4. What is the equilibrium constant for the bicarbonate-carbon dioxide reaction?

If the partial pressure of carbon dioxide is increased until the pH is 6.0, what is the bicarbonate concentration? What is the carbon dioxide partial pressure at this pH? What difference would you expect if this experiment is carried out in whole blood instead of aqueous solution?

(b) Pick reasonable values for K_1, K_2 and $\bar{K}_1$ and find the oxygen saturation curve as a function of h. (Hint: the parameters must be chosen so that hemoglobin acts as a hydrogen ion buffer at physiological concentrations. So, for instance, pick K_1, K_2 and $\bar{K}_1$ so that $(\phi(h))^{1/4} = 26\ \sigma$ mm Hg at pH $= 7.4$. You also have to ensure that $\bar{K}_1 > K_1$ and that K_2 is not too large. Why?)

(c) Use this model to estimate the total amount of CO_2 that is transported from the tissues to the lungs and the total amount of O_2 that is transported from the lungs to the tissues. (Determine this by solving (13.60) - (13.64) numerically to find h, X, Y, Z and W at a given $[O_2]$ and $[CO_2]$ and finding the difference between arterial and venous quantities.) Remove the Bohr and Haldane effects by setting $K_1 = \bar{K}_1$. How does this change the amount of oxygen and carbon dioxide transported? Typical parameter values are: P_{CO_2} in arterial blood, 39 mm Hg ; P_{CO_2} in venous blood, 46 mm Hg; P_{O_2} in arterial blood, 100 mm Hg; P_{O_2} in venous blood, 40 mm Hg; $R_1 R_2 = 10^{6.1} \mathrm{M}^{-1}$; $T_{Hb} = 3$ mM; $n = 10$,

$[\text{HCO}_3^-] = 25$ mM and pH $= 7.4$ in arterial blood.

Solution

Part (a)

We begin by using the given information to calculate the equilibrium constant of the reaction

$$\text{H}^+ + \text{HCO}_3^- \underset{k_-}{\overset{k_+}{\rightleftharpoons}} \text{CO}_2 + \text{H}_2\text{O}.$$
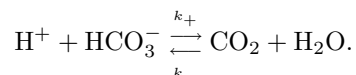
Since the partial pressure of CO_2 is held fixed at 40 mm Hg, and since the solubility of CO_2 is 3.3×10^{-5} M/mm Hg, it follows that $[\text{CO}_2] = 40 \times 3.3 \times 10^{-5}$ M $= 1.32$ mM. Similarly, since the pH is 7.4, $[\text{H}^+] = 10^{-4.4}$ mM $= 4 \times 10^{-5}$ mM.

At equilibrium,

$$K = \frac{k_-}{k_+} = \frac{[\text{H}^+][\text{HCO}_3^-]}{[\text{CO}_2]}. \tag{20.736}$$

To calculate K it remains only to determine $[\text{HCO}_3^-]$. The experiment started with 25 mM of HCO_3^- at pH $= 7$. Since at equilibrium pH $= 7.4$, there are fewer hydrogen ions at equilibrium than at the beginning of the experiment, and for each hydrogen ion that was lost, exactly one bicarbonate ion was lost. Thus,

$$[\text{HCO}_3^-] = 25\text{mM} - \Delta H,$$

However, $\Delta H = 6 \times 10^{-5}$mM is so small that it can be safely ingnored, and we find that

$$K = \frac{(4 \times 10^{-5}) \cdot 25}{1.32} = 7.6 \times 10^{-4} \text{ mM}. \tag{20.737}$$

Part(b)

If the pH is decreased to 6, $[\text{H}^+]$ is increased to 10^{-3} mM. Again, this is so much smaller than 25 mM that there is no appreciable change to the bicarbonate concentration. However, being at equilibrium it must be that

$$[\text{CO}_2] = \frac{[\text{H}^+][\text{HCO}_3^-]}{K} = 33.0 \text{ mM}, \tag{20.738}$$

from which it follows that the partial pressure of CO_2 is

$$P_{\text{CO}_2} = \frac{0.033}{3.3 \times 10^{-5}} = 10^3 \text{ mm Hg}. \tag{20.739}$$

In whole blood hemoglobin acts as a hydrogen ion buffer; as CO_2 reacts with water the H^+ that is produced is taken up by hemoglobin, greatly decreasing changes in blood pH. Hence, to raise the pH of whole blood by a given amount requires a far greater CO_2 partial pressure than is needed for a bicarbonate solution.

Part (c)

We need to choose K_1, $\bar{K}_1$ and K_2 to get reasonable behavior of the O_2 saturation curve. We know (from the experimental data) that, at blood pH (approximately 7.4), the half-maximal saturation occurs at about $[O_2] = 26\sigma$ mm Hg. Thus, we must have $\phi(10^{-7.4}) = (26\sigma)^4$ mm Hg.

We also require that $\bar{K}_1 > K_1$. Thus, we choose $\bar{K}_1 = 10K_1$ (this is not based on experimental data; it is a reasonable choice used to illustrate the behavior of the model). Then,

$$\phi(h) = 10K_1 \frac{K_2 + h}{10K_2 + h}. \tag{20.740}$$

Clearly, if K_2 is much larger than h, changes in h have little effect. So, again arbitrarily, we choose $K_2 = 10^{-7.4}$ M, the same as the normal blood pH.

With these constraints on $\bar{K}_1$ and K_2 we can now choose K_1 to ensure that $\phi(10^{-7.4}) = (26\sigma)^4$ mm Hg. This gives

$$10K_1 \frac{2 \times 10^{-7.4}}{11 \times 10^{-7.4}} = (26\sigma)^4 \text{mm Hg}, \tag{20.741}$$

from which it follows that $K_1 = \frac{20}{11}(26\sigma)^4$ mm Hg.

Plots of the saturation curve with these parameters, and for three different values of the pH, are given in Fig. 20.56. We see that as the pH increases (i.e., as $[H^+]$ decreases), the saturation curves shifts to the left, thus increasing the amount of O_2 bound at a given partial pressure. Conversely, as the pH decreases, the amount of bound O_2 decreases.

Part (d)

There are many ways of solving the equations numerically, but one of the easiest ways is with Maple. The Maple code we used is given below.

The trickiest part of this problem is to make sure the units on the parameters are correct. Since we are working with concentrations of H^+, a good choice is to use Molar units throughout. Thus, we use $K_1 = \frac{20}{11}(26\sigma_{O_2})^4$ M, where $\sigma_{O_2} = 1.4 \times 10^{-6}$ M $(\text{mm Hg})^{-1}$.

The next challenge is to estimate T_0. We choose the arterial blood as the reference state and adjust T_0 until the solution for $[HCO_3^-]$ is close to 25 mM. (Since we are not trying for exact answers, close is good enough). Using the Maple code to try a few values of T_0 we find that $T_0 = -0.022$ M works well. With this value of T_0, $[HCO_3^-] = h + n(Z + W) - T_0 = 25$ mM, while $n(Z + W) = 3$ mM. The value of h in the arterial blood is so small it can be ignored. Without the Bohr effect, $T_0 = -0.0099$ mM works well.

Finally, note that in the calculation of the total oxygen or carbon dioxide content we include the gas in the dissolved state, although the amount of gas in the dissolved state is quite small.
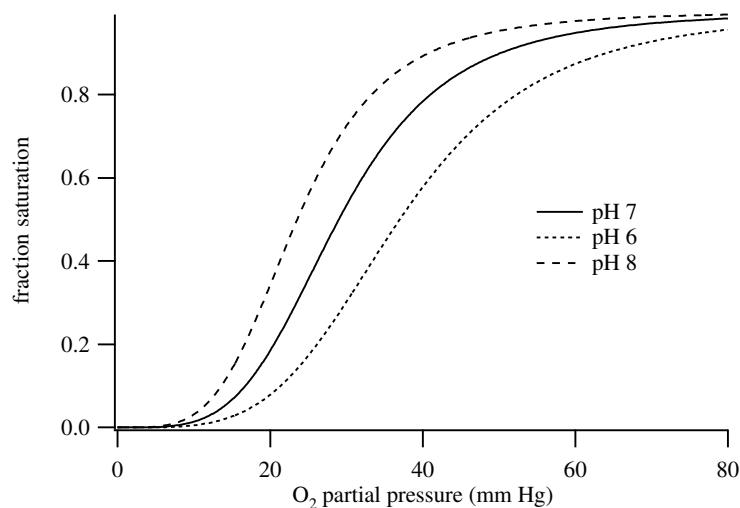
Figure 20.56: Oxygen saturation curves at three different pH values, calculated with the parameter values $K_1 = \frac{20}{11}26^4\sigma^4$ mm Hg^4, $\bar{K}_1 = 10K_1$, $K_2 = 10^{-7.4}$mm Hg.

	With Bohr effect		Without Bohr effect	
	Arterial	Venous	Arterial	Venous
Total CO_2	26.27	30.96	26.36	27.55
Total O_2	3.09	1.93	3.13	2.6

Table 20.5: Summary of results for part (c) of Question 13. All concentrations are in mM.

We are now ready to answer the question; the results are summarized in Table 20.5. We see that, with the Bohr effect, CO_2 is transported at a concentration of $30.96 - 26.27 \approx 4.7$ mM, and O_2 is transported at a concentration of $3.09 - 1.93 \approx 1.2$ mM. However, if the Bohr effect is removed then CO_2 is transported at $27.55 - 26.36 \approx 1.2$ mM, and O_2 is transported at approximately 0.5 mM.

We emphasize that these answers have little quantitative significance, but illustrate the effect only qualitatively. Different choices for K_1, $\bar{K}_1$ and K_2 give different quantitative results.

The Maple code for part (c)

```
readlib('unassign'):
unassign('X','Y','Z','W','sols','h','K1','K2','K1bar',
         'THb','n','T0','R','Ox','C'):

 sigmaO := 1.4*(10^(-6)): sigmaC := 3.3*(10^(-5)):  # Solubilities
 PCarterial:=39:   PCvenous:=46:
 POarterial:=100:  POvenous:=40:
```

```
# Convert the partial pressures to Molar concentrations
# Comment out whichever you don't need
  C:=PCarterial*sigmaC:  Ox:=POarterial*sigmaO:   # Arterial concentrations
  #C:=PCvenous*sigmaC:  Ox:=POvenous*sigmaO:      # Venous concentrations

# Make sure all the concentration units are Molar. That's why
# we have to include the sigmaO in the formula for K1.
# Comment out whichever you don't need
  K1 := (20/11)*(26*sigmaO)^4: K1bar:=10*K1:  T0:=-0.022:  # with Bohr effect
  #K1 := (26*sigmaO)^4:          K1bar:=K1:     T0:=-0.0099:  # without Bohr effect

  K2  := 10^(-7.4):
  THb := 0.003:  n:=10:    R:=10^(6.1):

  fun1 := (Ox^4)*X - K1*Y:
  fun2 := h*X - K2*Z:
  fun3 := (Ox^4)*Z - K1bar*W:
  fun4 := X+Y+Z+W - THb:
  sols := solve({fun1=0,fun2=0,fun3=0,fun4=0}, {X,Y,Z,W}):
  assign(sols):

# Now find h numerically
  hfun := R*h*(h + n*(Z+W) - T0) - C:
  h:=fsolve(hfun=0,h,0..0.00001);

# Now calculate the total bicarbonate and oxygen
  bicarb := h + n*(Z+W) - T0;
  total_co2 := bicarb + C;
  heme_oxygen := Y+W;
  total_oxygen := heme_oxygen + Ox;
```

2. Find an analytic relationship for the critical stability curve (Section **??**), relating $dF(0)$ to X/d as follows: Use that $F(N) = \frac{F(0)}{1+N^?}$ to solve (13.22) for N_0 as a function of X/d and then determine $dF(0)$ using that $F(N_0) = N_0/X$.

Solution

Since

$$F(N_0) = \frac{F(0)}{1 + N_0^p} \tag{20.742}$$

it follows that

$$\frac{F'(N_0)}{F(N_0)} = \frac{-pN_0^{p-1}}{1 + N_0^p}. \tag{20.743}$$

For convenience we introduce the notation

$$\alpha = \frac{2n\pi}{2 + X/d}, \qquad \phi = \frac{1}{2}\frac{\alpha x}{\sin \alpha}. \tag{20.744}$$

Then, from (13.22) and (20.743) it follows that

$$\frac{pN_0^p}{1 + N_0^p} = \phi, \tag{20.745}$$

and hence

$$N_0 = \left(\frac{\phi}{p - \phi} \right)^{\frac{1}{p}}. \tag{20.746}$$

Now use the fact that, at steady state

$$F(N_0) = \frac{N_0}{X}. \tag{20.747}$$

Hence,

$$\frac{F(0)}{1 + N_0^p} = \frac{N_0}{X}, \tag{20.748}$$

and thus

$$dF(0) \quad = \quad d(1 + N_0^p)\frac{N_0}{X} \tag{20.749}$$

$$= \quad \frac{d}{X}\left(\frac{p}{p - \phi} \right)\left(\frac{\phi}{p - \phi} \right)^{\frac{1}{p}}, \tag{20.750}$$

which is the required expression.

3. A deficiency of vitamin B_{12}, or folic acid, is known to cause the production of immature red blood cells with a shortened lifetime of one-half to one-third of normal. What effect does this deficiency have on the population of red blood cells?

Solution

A decreased lifetime corresponds to a decrease in X. The result of a decrease in X depends on the value of $dF(0)$. If $dF(0) > 0.4$ or so, then a decrease in X from the normal value of 120 days may result in the steady state becoming unstable and the appearance of oscillations in the number of red blood cells. If $dF(0)$ is too small, however, the steady state is stable for any value of X.

4. Suppose $X \to \infty$ in the red blood cell production model. Show that

$$\frac{dN}{dt} = F(N(t - d)) - \beta N, \tag{20.751}$$

where $N(t) = \int_0^\infty n(x, t)dx$.

(a) Find the stability characteristics for the steady-state solution of this equation.

(b) Show that the period of oscillation $T = 2\pi/\omega$ at a Hopf bifurcation point is bounded between $2d$ and $4d$.

Solution

With $X \to \infty$, $N(t) = \int_0^\infty n(x,t)\,dx$. Integrate the conservation equation (13.7) from $x = 0$ to $x = \infty$ to find

$$\int_0^\infty \frac{\partial n}{\partial t}\,dx + \int_0^\infty \frac{\partial n}{\partial x}\,dx = -\beta \int_0^\infty n(x,t)\,dx, \qquad (20.752)$$

and thus

$$\frac{\partial}{\partial t}N(t) - n(0,t) = -\beta N(t). \qquad (20.753)$$

The boundary condition (13.9) gives

$$\frac{\partial N(t)}{\partial t} = F(N(t-d)) - \beta N(t), \qquad (20.754)$$

as required.

Part (a)

The steady state solution, N_0, is given by the equation $F(N_0) = \beta N_0$. To determine the stability of this steady state we linearize around N_0. If $N = N_0 + \delta N$, then

$$
\begin{aligned}
\frac{d}{dt}\delta N(t) &= F(N_0 + \delta N(t-d)) - \beta(N_0 + \delta N) & (20.755)\\
&= F(N_0) + F'(N_0)\delta N(t-d) - \beta N_0 - \beta\delta N & (20.756)\\
&= F'(N_0)\delta N(t-d) - \beta\delta N. & (20.757)
\end{aligned}
$$

Looking for solutions of the form $\delta N = e^{\lambda t}$ gives

$$\lambda = F'(N_0)e^{-\lambda d} - \beta. \qquad (20.758)$$

Recall that $F'(N_0) < 0$ and that $\beta > 0$. It thus follows that λ cannot be real and positive. It can be real and negative, in which case the steady state is stable. As in the example discussed in the text, instability can only arise at a Hopf bifurcation, where $\lambda = i\omega$. Substituting this into (20.758) gives

$$
\begin{aligned}
\beta &= F'(N_0)\cos(\omega d) & (20.759)\\
\omega &= -F'(N_0)\sin(\omega d). & (20.760)
\end{aligned}
$$

We can eliminate ω by squaring the equations and adding, to get

$$\omega^2 = (F'(N_0))^2 - \beta^2. \qquad (20.761)$$

Note that we must have $\beta < |F'(N_0)|$. With this expression for ω, (20.759) is a relationship between N_0 and d that must be satisfied for a Hopf bifurcation to exist. Or, since $F(N_0) = \beta N_0$, (20.759) can be interpreted as a relationship between β and d that ensures a Hopf bifurcation.

Part (b)

From (20.759) we see that, for β to be positive we must have $\cos(\omega d) < 0$. Similarly, from (20.760) we must have $\sin(\omega d) > 0$. Combining these two constraints gives

$$\frac{\pi}{2} < \omega d < \pi, \tag{20.762}$$

from which it follows that

$$2d < \frac{2\pi}{\omega} < 4d. \tag{20.763}$$

5. Suppose X is finite and $\beta = 0$ in the red blood cell production model. Show that the evolution of N is described by the delay differential equation

$$\frac{dN}{dt} = F(N(t-d)) - F(N(t-d-X)). \tag{20.764}$$

Solution

Integrate (13.7) from $x = 0$ to $x = X$ to get

$$0 = \int_0^X \frac{\partial n}{\partial t}\, dx + \int_0^X \frac{\partial n}{\partial x}\, dx, \tag{20.765}$$

$$= \frac{\partial}{\partial t} \int_0^X n(x,t)\, dx + n(X,t) - n(0,t), \tag{20.766}$$

$$= \frac{dN}{dt} + n(X,t) - n(0,t), \tag{20.767}$$

$$= \frac{dN}{dt} + n(X,t) - F(N(t-d)). \tag{20.768}$$

Since the death rate of the cells is zero ($\beta = 0$), the solution of the partial differential equation is of the form $n(x,t) = f(x-t)$, so that $n(X,t) = n(0, t-X)$. In other words, the number of cells of age X at time t is equal to the number of cells that entered the bloodstream at time $t - X$. Thus,

$$n(X,t) = F(N(t-d-X)), \tag{20.769}$$

in which case

$$\frac{dN}{dt} = F(N(t-d)) - F(N(t-d-X)), \tag{20.770}$$

as required.

6. The maturation rate of red blood cells in bone marrow varies as a function of erythropoietin levels. Suppose that x denotes the maturity (rather than chronological age) of a red blood cell. Suppose further that cells are initially formed at maturity $x = -d$, are released into the bloodstream at maturity $x = 0$, age at the normal chronological rate, and die at age $x = X$. Suppose further that the rate of maturation G is a decreasing function of the total circulating red blood cell count N and that the rate of cell production at maturity $x = -d$ is $F(N)$.

(a) Replace the condition (13.9) with an evolution equation of the form (13.7) to account for maturities x in the range $-d < x < 0$. Specify the boundary condition at $x = -d$ and require that the flux be continuous at $x = 0$. Show that the steady state solution is independent of the maturation function $G(N)$.

(b) Provide a linear stability analysis for this modified model. Show that

$$\frac{\delta N}{dt} = \left(F'(N_0) - \frac{G'(N_0)N_0}{G(N_0)X} \right) \left(\delta N(t - \frac{d}{G(N_0)}) - \delta N(t - \frac{d}{G(N_0)} - X) \right)$$
(20.771)

where $N = N_0 + \delta N$.

(c) Does the variability of G make the solution more or less likely to become unstable via a Hopf bifurcation?

Solution

(a) For $-d < x < 0$ the governing equation is

$$\frac{\partial n}{\partial t} + \frac{\partial}{\partial x}(G(N)n) = 0,$$
(20.772)

and for $0 < x < X$ the equation is

$$\frac{\partial n}{\partial t} + \frac{\partial n}{\partial x} = 0,$$
(20.773)

with $N = \int_0^X n(x,t)dx$. The boundary condition is that $F(N) = G(N)n(-d,t)$, and the flux at $x = 0$ must be continuous so that $G(N)n(0^-,t) = n(0^+,t)$.

The steady state solution has $n(x) = n_-$ for $x < 0$ and $n(x) = n_0 = \frac{N_0}{X}$ for $x > 0$, where $G(N_0)n_- = n_0$ and $F(N_0) = \frac{N_0}{X}$.

(b) Linearizing the equations about this steady solution, we find

$$\frac{\partial \delta n}{\partial t} + \frac{\partial}{\partial x}(G(N_0)\delta n) = 0,$$
(20.774)

for $-d < x < 0$, and

$$\frac{\partial \delta n}{\partial t} + \frac{\partial \delta n}{\partial x} = 0,$$
(20.775)

for $0 < x < X$, subject to the boundary condition

$$F'(N_0)\delta N = G'(N_0)\delta N n_- + G(N_0)\delta n(-d, t).$$
(20.776)

It follows that $\delta n(0^-, t) = \delta n(-d, t - \frac{d}{G(N_0)})$, and $\delta n(X, t) = \delta n(0^+, t - X)$. Furthermore, as in the previous exercise,

$$\frac{d\delta N}{dt} = n(0^+, t) - n(X, t).$$
(20.777)

Piecing all this together, we find that

$$\frac{\delta N}{dt} = \left(F'(N_0) - \frac{G'(N_0)N_0}{G(N_0)X} \right) \left(\delta N(t - \frac{d}{G(N_0)}) - \delta N(t - \frac{d}{G(N_0)} - X) \right).$$
(20.778)

(c) The stability curves are modifications of (13.22), given by

$$\frac{F'(N_0)N_0}{F(N_0)} - \frac{G'(N_0)N_0}{G(N_0)} = -\frac{G(N_0)X}{d} \frac{n\pi}{2 + \frac{G(N_0)X}{d}} \frac{1}{\sin\left(\frac{2n\pi}{2 + \frac{G(N_0)X}{d}} \right)}.$$
(20.779)

15. Sketch the phase portraits for the equations (13.102)–(13.103) in Case III ($\alpha > 0, \beta > 0$) as follows:

   (a) $\xi < \frac{1}{U_0}, \xi < \frac{1}{\beta}$. (For example,
      i. $\xi = 1.0, \beta = 0.5, \alpha = 0.5, \beta_0 = 1.0, \gamma_0 = 0.2$, and
      ii. $\xi = 1.5, \beta = 0.5, \alpha = 1.3, \beta_0 = 1.0, \gamma_0 = 0.2$.)
   (b) $\xi < \frac{1}{U_0}, \xi > \frac{1}{\beta}$ (For example, $\xi = 1.8, \beta = 0.6, \alpha = 0.5, \beta_0 = 1.0, \gamma_0 = 0.2$.)
   (c) $\xi > \frac{1}{U_0}, \xi < \frac{1}{\beta}$. (For example, $\xi = 2.2, \beta = 0.3, \alpha = 0.5, \beta_0 = 1.0, \gamma_0 = 0.2$.)
   (d) $\xi > \frac{1}{U_0}, \xi > \frac{1}{\beta}$. (For example, $\xi = 2.2, \beta = 2.0, \alpha = 0.5, \beta_0 = 1.0, \gamma_0 = 0.2$.)

Locate each of these cases in Fig. 13.17.

Solution

The easiest way to plot these phase portraits is to use your favourite differential equations package. Here, we used XPPAUT to calculate the nullclines and trajectories, wrote the curves to disk, and then plotted them using a scientific plotting package called Igor Pro (ref). This separation of the calculation stage from the plotting stage lets us use specialist packages for the different jobs, giving a higher quality output.

The XPPAUT code is

```
par xi=2.2 beta=0.3 alpha=0.5 beta0=1.0 gamma0=0.2
u'=gamma0*((beta0+beta*v)*(1-u*fun(alpha*v)*exp(-alpha*v))-(v*fun(v)+1)*u)
v'=v*(1-xi*u*fun(v))
#
fun(v)=alpha*v/(1-exp(-alpha*v))
@yp=v xlo=0 xhi=0.8 yhlo=0 yhi=10
```

The phase planes for (a)i, (a)ii, (b), (c) and (d) are given in Figs. 20.57–20.61 respectively. The location of each of these cases in Fig. 13.17 is shown in Fig. 20.62.
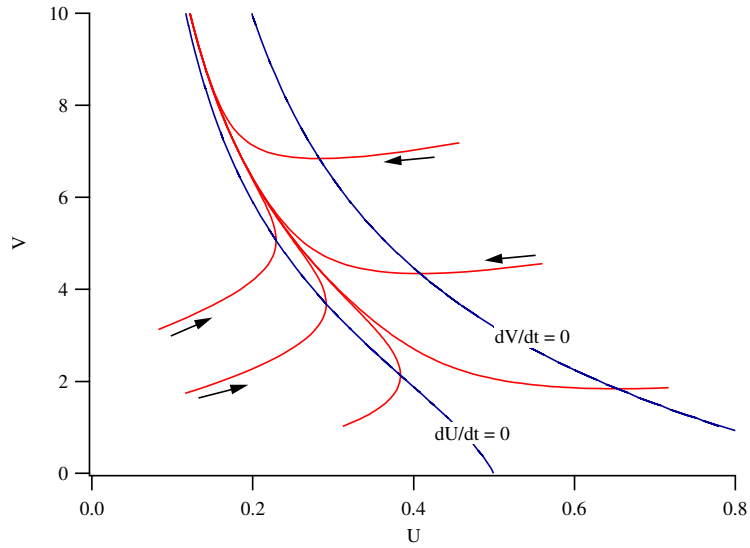
Figure 20.57: Phase plane for Question 15, part (a)i. Parameters are $\xi = 1$, $\beta = 0.5$, $\alpha = 0.5$, $\beta_0 = 1$ and $\gamma_0 = 0.2$
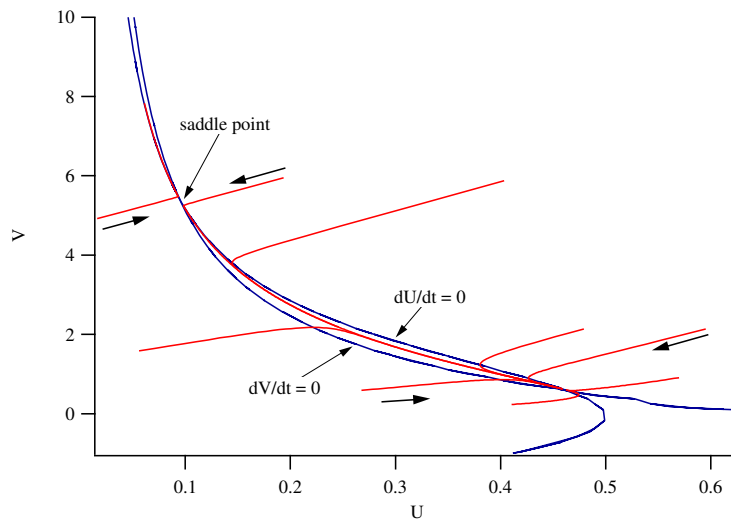

Figure 20.58: Phase plane for Question 15, part (a)ii. Parameters are $\xi = 1.5$, $\beta = 0.5$, $\alpha = 1.3$, $\beta_0 = 1$ and $\gamma_0 = 0.2$
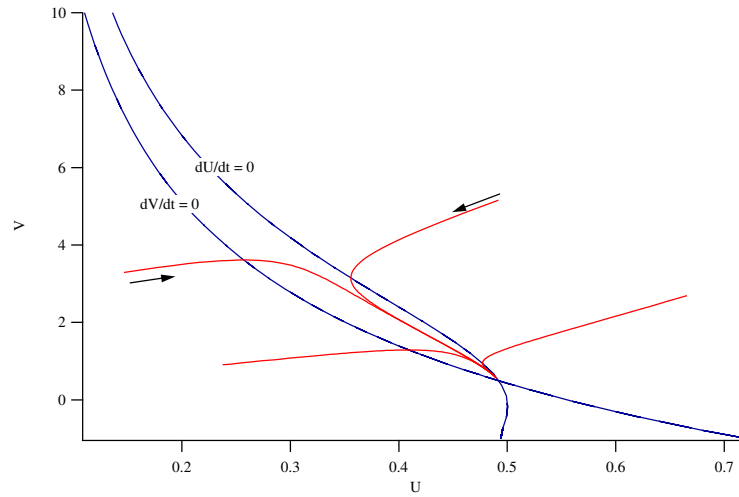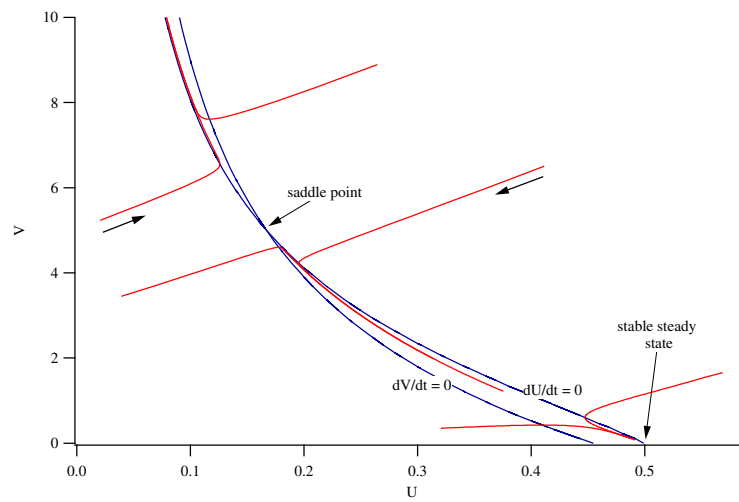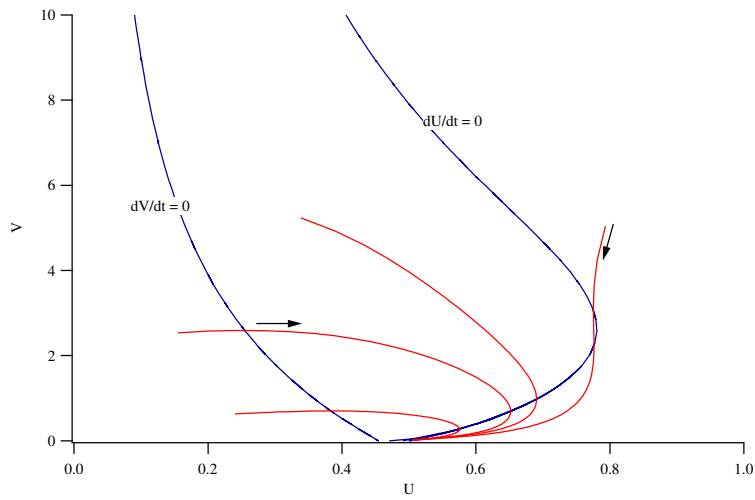
Figure 20.59: Phase plane for Question 15, part (b). Parameters are $\xi = 1.8$, $\beta = 0.6$, $\alpha = 0.5$, $\beta_0 = 1$ and $\gamma_0 = 0.2$

Figure 20.60: Phase plane for Question 15, part (c). Parameters are $\xi = 2.2$, $\beta = 0.3$, $\alpha = 0.5$, $\beta_0 = 1$ and $\gamma_0 = 0.2$

Figure 20.61: Phase plane for Question 15, part (d). Parameters are $\xi = 2.2$, $\beta = 2$, $\alpha = 0.5$, $\beta_0 = 1$ and $\gamma_0 = 0.2$
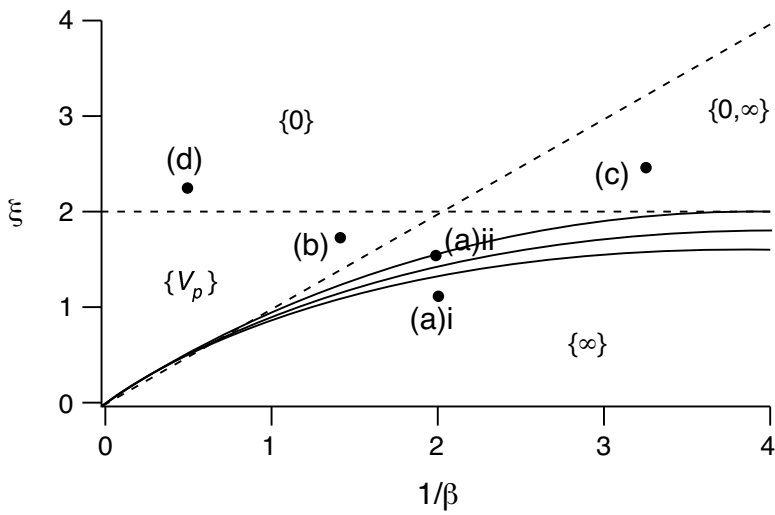

Figure 20.62: The approximate location in Fig. 13.17 of each of the above phase planes.

Selected Solutions to Chapter 16

1. Derive a differential equation for the load in a three-element Hill model with an elastic element in series with a contractile element (as shown in Fig. 15.9) in parallel with an additional elastic element of length L.

   Remark: The total load in the whole unit is divided between the two parallel subunits.

   Solution

   A schematic diagram of a three-element Hill model is shown in Fig. 20.63. From this diagram we see that

   $$F_1 + F_2 = p, \qquad\qquad (20.780)$$

   and thus

   $$\beta(L - L_0) + \alpha(x - x_0) = p, \qquad\qquad (20.781)$$

   from which, since $x + l = L$, it follows that

   $$\beta(x + l - L_0) + \alpha(x - x_0) = p. \qquad\qquad (20.782)$$

   Thus, we have

   $$\frac{dp}{dt} = \frac{dp}{dx}\frac{dx}{dt} = (\beta + \alpha)\left(\frac{dL}{dt} + v\right). \qquad\qquad (20.783)$$

2. When a muscle cell dies, its ATP is depleted, with the result that the power stroke stalls and calcium cannot be withdrawn using the Ca^{2+} ATPase. How does this explain rigor mortis?

   Solution

   At rest, every cell in the body is under a high calcium load, since the calcium concentration outside the cell is much higher than the calcium concentration inside the cell. When the calcium ATPase stops working at death, calcium can no longer be removed from the muscle cell, and the intracellular calcium concentration rises. This prevents the disassociation of the actin and myosin
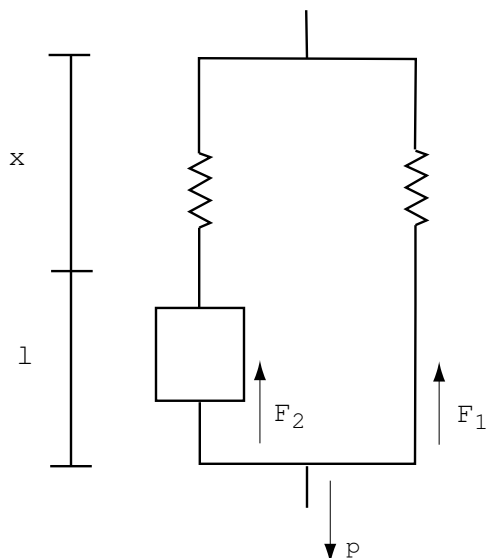
Figure 20.63: A three-element Hill model.

filaments which remain locked together, thus causing rigidity in the muscles. This rigidity lasts until the muscle proteins are broken down, about 15 to 25 hours after death.

3. Calculate the response of the Huxley model to a step change in length. In other words, calculate how n changes as a function of t and x, and hence calculate how the tension changes as a function of time, following a step change in length.

Solution

Before the step change, n is at steady state,

$$n(x) = \frac{f(x)}{f(x) + g(x)}. \tag{20.784}$$

Immediately after a step decrease in length, the x position of each crossbridge is decreased by Δx, but the distribution of bound crossbridges is unchanged. Hence, immediately after the length change

$$n(x, t = 0^+) = \frac{f(x + \Delta x)}{f(x + \Delta x) + g(x + \Delta x)}. \tag{20.785}$$

Thus, to find the evolution of n over space and time, we need to solve the

differential equation

$$\frac{\partial n(x,t)}{\partial t} = (1 - n(x,t))f(x) - ng(x), \tag{20.786}$$

$$n(x,0) = \frac{f(x + \Delta x)}{f(x + \Delta x) + g(x + \Delta x)}. \tag{20.787}$$

Since x acts only as a parameter, this is an ordinary differential equation in t. Note that v does not enter into the equation either, since the length is decreased and then held fixed, i.e., $v = 0$.

Multiplying both sides by the integrating factor $e^{\int (f+g)dt} = e^{-(f(x)+g(x))t}$ gives

$$\frac{\partial}{\partial t}\left(ne^{-(f(x)+g(x))t}\right) = f(x)e^{-(f(x)+g(x))t}, \tag{20.788}$$

and thus

$$n(x,t) = \frac{f(x)}{f(x) + g(x)} + Ke^{-(f(x)+g(x))t}, \tag{20.789}$$

for some constant K. Determining K from the initial condition gives

$$n(x,t) = \frac{f(x)}{f(x) + g(x)} + e^{-(f(x)+g(x))t}\left(\frac{f(x + \Delta x)}{f(x + \Delta x) + g(x + \Delta x)} - \frac{f(x)}{f(x) + g(x)}\right). \tag{20.790}$$

Finally,

$$p(x,t) = \rho k \int_{-\infty}^{\infty} x\, n(x,t)\, dx. \tag{20.791}$$

We now evaluate each of these expressions for the particular choice of f and g used by Huxley, i.e.,

$$f(x) = \begin{cases} 0, & x < 0, \\ f_1 x/h, & 0 < x < h, \\ 0, & x > h, \end{cases} \tag{20.792}$$

$$g(x) = \begin{cases} g_2, & x < 0, \\ g_1 x/h, & x > 0. \end{cases} \tag{20.793}$$

For this choice of f and g we have

$$\frac{f(x)}{f(x) + g(x)} = \alpha(H(0) - H(h)), \tag{20.794}$$

where $\alpha = f_1/(f_1 + g_1)$ and H is the Heaviside function ($H(x) = 0$ when $x < 0$, and $H(x) = 1$ when $x > 1$.) We also have

$$\frac{f(x + \Delta x)}{f(x + \Delta x) + g(x + \Delta x)} - \frac{f(x)}{f(x) + g(x)} = \begin{cases} \alpha, & -\Delta x < x < 0, \\ -\alpha, & h - \Delta x < x < h, \\ 0, & \text{otherwise.} \end{cases} \tag{20.795}$$
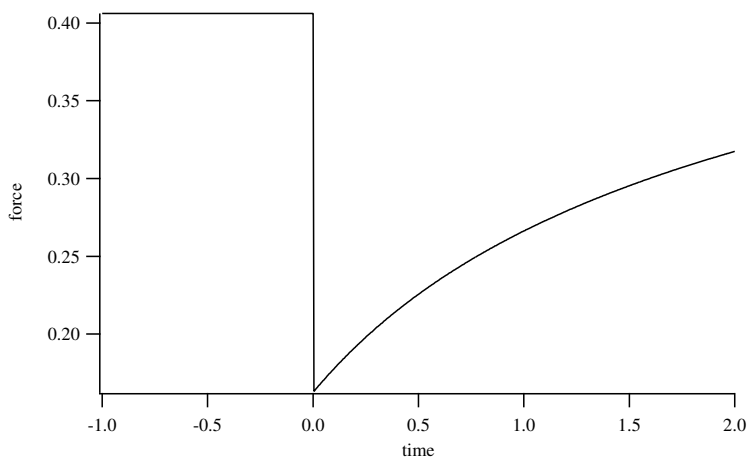
Figure 20.64: The solution for p, calculated from (20.796), using the parameter values $\rho = 1$, $k = 1$, $f_1 + g_1 = 1/2$, $g_1 = 3/32$, $g_2 = 2$, $\Delta x = 0.3$.

Substitute these expressions into (20.790) and (20.791) to get

$$
\begin{aligned}
p(x,t) &= \int_0^h \alpha x \, dx + \alpha \left(\int_{-\Delta x}^0 x\, e^{-g_2 t} \, dx - \int_{h-\Delta x}^h x\, e^{-(f_1+g_1)xt/h} \, dx \right) \\
&= \frac{\rho k \alpha h^2}{2} - \frac{\alpha e^{-g_2 t}(\Delta x)^2}{2} - \alpha \int_{h-\Delta x}^h x\, e^{-(f_1+g_1)xt/h} \, dx. \quad (20.796)
\end{aligned}
$$

At this stage, it's not really very useful to evaluate the final integral analytically. It is, however, useful to note that $p \to \rho k \alpha h^2/2 = p_s$, say, as $t \to \infty$, and that $p < p_s$.

Now, at steady state,

$$
p = \rho k \alpha \int_0^h x \, dx, \qquad (20.797)
$$

and thus it follows that p_s is the steady state force exerted by the muscle. Hence we see from (20.796) that immediately after the length decreases the force decreases also, and then slowly increases back to the resting level. This is all as expected intuitively and agrees qualitatively with the sketch given in Fig. 15.11A of the text.

The solution for p is plotted in Fig. 20.64.

4. Find the force-velocity relationship with

$$
f(x) = \begin{cases} f_{\max} e^{(x-h)/\lambda}, & x < h, \\ 0, & x > h, \end{cases} \qquad (20.798)
$$

$$
g(x) = f_{\max}\left(1 - e^{(x-h)/\lambda}\right), \qquad (20.799)
$$

$$r(x) = r_{\max} \frac{e^{(x-h)/\lambda} - \alpha}{1 - \alpha}, \tag{20.800}$$

1. Remark: This model reproduces the Hill force–velocity curve exactly, although it gives poor agreement with the energy flux data.

Solution

We begin by calculating $n(x)$, the steady-state crossbridge distribution at a constant velocity. For $x > h$, we have the simple differential equation

$$v \frac{dn}{dx} = g(x)n. \tag{20.801}$$

Since $g(x)$ is positive, if $n(x) \neq 0$, it is unbounded as $x \to \infty$. This is clearly inadmissible. Fortunately, $n \equiv 0$ is a solution. Clearly, since $f(x) = 0$ for $x > h$, and thus no crossbridges can ever attach there, the identically zero solution is the one we want. So, $n(x) = 0$ when $x > h$.

Next we solve for the region $x < h$. Since $f(x) + g(x) = f_{\max}$ when $x < h$, it follows that, when $x < h$, $n(x)$ satisfies the differential equation

$$-v \frac{dn}{dx} = f(x) - f_{\max}n. \tag{20.802}$$

To characterize the solution completely we need a boundary condition, and this is supplied by the solution for $x > h$. Because we wish $n(x)$ to be continuous, and because $n(x) = 0$ for $x > h$, it follows that the boundary condition is

$$n(h) = 0. \tag{20.803}$$

This differential equation can be solved using an integrating factor to get

$$n(x) = \frac{f_{\max}\lambda}{f_{\max}\lambda - v} \left(\exp\left(\frac{x-h}{\lambda}\right) - \exp\left(\frac{f_{\max}(x-h)}{v}\right) \right). \tag{20.804}$$

To find $p(v)$, we substitute the expression for $r(x)$ into the formula

$$
\begin{aligned}
p &= \rho \int_{-\infty}^{\infty} r(x)n(x)\,dx \\
&= \rho \int_{-\infty}^{h} r(x)n(x)\,dx \\
&= \frac{\rho r_{\max}\lambda f_{\max}}{(1-\alpha)(f_{\max}\lambda - v)} \int_{-\infty}^{h} \left(e^{(x-h)/\lambda} - \alpha \right) \left(e^{(x-h)/\lambda} - e^{f_{\max}(x-h)/v} \right) \\
&= \frac{1}{2} \frac{\lambda r_{\max}\rho}{\alpha - 1} \left(\frac{2\lambda f_{\max}\alpha - f_{\max}\lambda + 2\alpha v}{f_{\max}\lambda + v} \right). \tag{20.805}
\end{aligned}
$$

(To do this last step we used Maple.)

It helps to write (20.805) in a slightly different form. At $v = 0$ we get

$$p_0 = p(0) = \frac{\lambda r_{\max} \rho}{2} \cdot \frac{2\alpha - 1}{\alpha - 1}. \tag{20.806}$$

and thus, substituting into (20.805) we get

$$p(v) = p_0 \left(\frac{f_{\max} \lambda + (\frac{2\alpha}{2\alpha - 1})v}{f_{\max} \lambda + v} \right). \tag{20.807}$$

It remains only to derive constraints on α so that our solution has the correct form. First, notice that the Hill equation

$$v = \frac{b(p_0 - p)}{p + a} \tag{20.808}$$

implies that

$$p = p_0 \frac{b - (a/p_0)v}{v + b}. \tag{20.809}$$

Thus, for (20.807) to have the same form as (20.809) we need

$$\frac{2\alpha}{2\alpha - 1} < 0. \tag{20.810}$$

Furthermore, in order for p_0 to be greater than zero, we also need

$$\frac{2\alpha - 1}{\alpha - 1} > 0. \tag{20.811}$$

Fortunately, both these constraints can be satisfied by setting $0 < \alpha < 1/2$.

In summary therefore, when $0 < \alpha < 1/2$ and this choice of f and g, with

$$b = f_{\max} \lambda \quad \text{and} \tag{20.812}$$
$$a = \frac{2\alpha}{1 - 2\alpha}, \tag{20.813}$$

Hill's equation is satisfied exactly.

6. Assuming that the crossbridges act as linear springs, calculate the force–velocity curve for (15.42) and show that in the limit as $\epsilon \to 0$ and $\delta \to 0$ it does not produce zero force for some positive velocity. Give an intuitive explanation for this.

Solution

Since the crossbridges act as linear springs, we have

$$r(x) = kx, \tag{20.814}$$

for some constant k. Hence

$$p(v) = k\rho \int_{-\infty}^{\infty} x n(x, v) \, dx \tag{20.815}$$

$$= k\rho \int_{h-\epsilon}^{h} x \left[1 - \exp\left(\frac{\alpha(x - h)}{\epsilon v} \right) \right] dx \tag{20.816}$$

$$+ k\rho \int_{\delta}^{h-\epsilon} x[1 - \exp(-\alpha/v)] \, dx. \tag{20.817}$$

Since we prefer to avoid calculating these integrals (although there are easily done using Maple), we take the desired limits first. In the limit as $\epsilon \to 0$ and $\delta \to 0$ the first integral disappears and we get

$$\lim_{\epsilon \to 0, \delta \to 0} p(v) = \rho k \int_{0}^{h} x(1 - e^{-\alpha/v}) \, dx \tag{20.818}$$

$$= \frac{\rho k h^2}{2} \left(1 - e^{-\alpha/v} \right). \tag{20.819}$$

From this we see that $p(v)$ is nonzero for all $v < \infty$, i.e., no matter how fast the muscle is contracting, it always exerts a force. The explanation for this can be readily seen if we first think about why, in the usual Huxley model, there is some finite velocity at which the muscle generates zero force. This is because, as v increases, more crossbridges are carried into the region $x < 0$ where they exert a negative force. Once v gets high enough, enough crossbridges are carried into the $x < 0$ region that the negative force they exert exactly balances the positive force exerted by all the crossbridges that are bound with $x > 0$.

However, for the choice of f and g used here, in the limit as ϵ and δ tend to zero, the crossbridges detach at $x = 0$ and never exert a negative force. Thus there cannot be a balance between the positive and negative forces, and the force exerted by the muscle cannot be zero for any contraction velocity.

??. This exercise and the next are based on the discrete binding site models of T.L. Hill (1974,1975). Suppose that each crossbridge is within reach of no more than two binding sites at one time, and that adjacent crossbridges do not "see" the same two binding sites. Suppose also that adjacent binding sites are separated by a distance Δ, and let x denote the distance of the crossbridge from one of the binding sites, binding site 0, say. Define x such that if the crossbridge is bound to site 0 and has $x = 0$, it exerts no force. Also, let $n_i(x, t), i = 0, -1$, denote the fraction of crossbridges with displacement x that are bound to binding site i.

(a) Show that the conservation equations are

$$-v \frac{dn_0}{dx} = f(x)[1 - n_0(x) - n_{-1}(x)] - g(x)n_0(x), \tag{20.820}$$

$$-v \frac{dn_{-1}}{dx} = f(x - \Delta)[1 - n_0(x) - n_{-1}(x)] - g(x - \Delta)n_{-1}(x) \tag{20.821}$$

Figure 20.65: Schematic diagram of the crossbridge model with two actin binding sites.

where as usual, v denotes the steady contraction velocity.

(b) Derive expressions for the isometric distributions of n_0 and n_{-1}. Compute the isometric force. Show that if the Huxley model is modified to include two binding sites, the isometric force is increased.

(c) Compute the force–velocity curve. Hint: For each v solve the differential equations numerically, using the boundary conditions $n_0(h) = 0$, $n_{-1}(h + \Delta) = 0$, then substitute the result into the expression for the force and integrate numerically.

(d) Modify the model to include slippage of the crossbridge from one binding site to another. Show that in the limit as slippage becomes very fast, the two differential equations (15.152) and (15.153) reduce to a single equation.

Solution

Part (a)

In Fig. 20.65 we give a schematic diagram of the crossbridge and the two binding sites. From there we see that, if a crossbridge is distance x away from site 0, it must be distance $x - \Delta$ away from site -1. Thus, the rate at which it binds and unbinds to site -1 must be, respectively, $f(x - \Delta)$ and $g(x - \Delta)$. Furthermore, the fraction of crossbridges that are unbound to either site, and thus available for binding, is $1 - n_0 - n_{-1}$. Hence, at steady state (so that $\partial n_0/\partial t = \partial n_{-1}/\partial t = 0$) we have

$$-v\frac{dn_0}{dx} = f(x)[1 - n_0(x) - n_{-1}(x)] - g(x)n_0(x), \qquad (20.822)$$

$$-v\frac{dn_{-1}}{dx} = f(x - \Delta)[1 - n_0(x) - n_{-1}(x)] - g(x - \Delta)n_{-1}(x) \qquad (20.823)$$

as required. We emphasise that $n_{-1}(x)$ is the proportion of crossbridges that are distance x from site 0, but are bound to site -1. These crossbridges are thus extended only a distance $x - \Delta$.

Part (b)

The isometric case is when $v = 0$, in which case we get

$$f(x)[1 - n_0(x) - n_{-1}(x)] = g(x)n_0(x) \qquad (20.824)$$
$$f(x - \Delta)[1 - n_0(x) - n_{-1}(x)] = g(x - \Delta)n_{-1}(x). \qquad (20.825)$$

Solving for n_0 and n_{-1} gives

$$n_0(x) = \frac{f(x)}{\frac{f(x-\Delta)}{g(x-\Delta)}g(x) + f(x) + g(x)}, \tag{20.826}$$

$$n_{-1}(x) = \frac{f(x-\Delta)}{\frac{f(x)}{g(x)}g(x-\Delta) + f(x-\Delta) + g(x-\Delta)} \tag{20.827}$$

To calculate the isometric force we need to calculate the integral

$$p = \rho \int_{-\infty}^{\infty} r(x)n_0(x)\,dx + \rho \int_{-\infty}^{\infty} r(x-\Delta)n_{-1}(x)\,dx. \tag{20.828}$$

Note that the second integral on the right hand side using the argument $x-\Delta$ in the force function. That is because a crossbridge that is distance x away from site 0, but is attached to site -1, is only extended a distance $x-\Delta$.

These isometric distributions and the isometric force can be calculated explicitly for the Huxley model, i.e., using

$$f(x) = \begin{cases} 0, & x < 0, \\ f_1 x/h, & 0 < x < h, \\ 0, & x > h, \end{cases} \tag{20.829}$$

$$g(x) = \begin{cases} g_2, & x < 0, \\ g_1 x/h, & x > 0. \end{cases} \tag{20.830}$$

$$r(x) = kx. \tag{20.831}$$

Plots of $n_0(x)$ and $n_{-1}(x)$ are given in Fig. 20.66. We see that n_0 and n_{-1} are piecewise constant, and that only n_{-1} is nonzero for any $x > h$. A moment's thought explains why this is so. If $x > h$ then the crossbridge cannot bind to site 0 as it is too far away, but it can still bind to site -1 as long as $x < h + \Delta$.

Because the isometric distributions are piecewise constant, to evaluate the force it is easiest to break the integrals up into regions in which n_0 and n_{-1} are piecewise constant. For the first integral we get

$$\int_{-\infty}^{\infty} r(x)n_0(x)\,dx = k\int_0^{\Delta} \frac{xf(x)}{f(x)+g(x)}\,dx + k\int_{\Delta}^{h} \frac{xf(x)}{\frac{f(x-\Delta)}{g(x-\Delta)}g(x)+f(x)+g(x)}\,dx \tag{20.832}$$

while the second gives

$$\int_{-\infty}^{\infty} r(x-\Delta)n_{-1}(x)\,dx = k\int_{\Delta}^{h} \frac{(x-\Delta)f(x-\Delta)}{\frac{f(x)}{g(x)}g(x-\Delta)+f(x-\Delta)+g(x-\Delta)} \tag{20.833}$$

$$+ k\int_{h}^{h+\Delta} \frac{(x-\Delta)f(x-\Delta)}{f(x-\Delta)+g(x-\Delta)}\,dx. \tag{20.834}$$
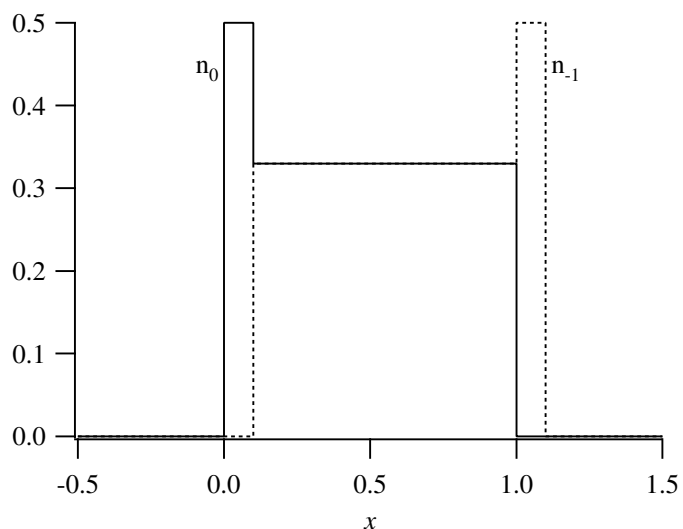
Figure 20.66: Isometric distributions of n_0 and n_{-1}. Parameters are $h = 1$, $\Delta = 0.1$, $f_1 = 0.25$, $g_1 = 0.25$, $g_2 = 2$.

Using Maple to evaluate these integrals and add them (the Maple code is given below) gives

$$p_{\text{two sites}} = \rho k \frac{f_1 h(hg_1 + hf_1 + f_1\Delta)}{(g_1 + f_1)(2f_1 + g_1)}. \tag{20.835}$$

This is the desired expression for the isometric force.

Finally, we compare this expression to the expression calculated for the Huxley model with a single binding site. When there is only a single binding site, we have

$$p_{\text{one site}} = \rho k \int_0^h \frac{f(x)}{f(x) + g(x)} \, dx = \frac{\rho k}{2} \cdot \frac{f_1 h^2}{f_1 + g_1}. \tag{20.836}$$

Subtracting these expressions give

$$p_{\text{two sites}} - p_{\text{one site}} = \frac{\rho k}{2} \cdot \frac{f_1 h(hg_1 + 2f_1\Delta)}{(g_1 + f_1)(2f_1 + g_1)} > 0. \tag{20.837}$$

Hence it follows that the isometric force is greater when there are two binding sites.

Here is the Maple code we used to do these calculations.

```
# fm and gm denote the shifted functions
```

```
# The other notation should be self-explanatory.

        f := f1*x/h: fm := f1*(x-Delta)/h:
        g:=g1*x/h: gm := g1*(x-Delta)/h:
        n0low := f/(g + f):
        n0high := f/( fm*g/gm + f + g):
        nm1low := fm/( f*gm/g + fm+gm):
        nm1high := fm/(fm+gm):

# Calculate the force generated by the $n_0$ crossbridges
        n0int := k*int(x*n0low,x=0..Delta) + k*int(x*n0high,x=Delta..h):
        simplify(n0int);

# Calculate the force generated by the $n_{-1}$ crossbridges
        nm1int := k*int((x-Delta)*nm1low,x=Delta..h) + k*int((x-Delta)*nm1high,x=h..h+Delta):
        simplify(nm1int);

# Now add the two integrals together to get the total force.
        dum1:=simplify(n0int+nm1int);

# Now calculate the isometric force of the Huxley model with a single binding site
        dum2:=k*int(x*n0low,x=0..h);

#Subtract the two forces to see which is greater
        dum1-dum2;
```

Part (c)

This part of the question must be done numerically. For each v we have to solve the differential equations numerically, and then integrate numerically to find the force.

```
% Solve problem 16.11 c in Matlab rather than Fortran

clear
%soecify parameters
global k rho h delta f1 g1 g2 v

Nj = 50;
dv = 1/Nj;
for j = 1:Nj

v = j*dv;

k = 1;
rho = 1;
h = 1;
delta = .1;
f1 = .25;
g1 = .25;
```

```
    g2 = 2;


    %specify the output points
    xspan = [h+delta:-.01:-2];

    %specify initial data

    n0 = [0,0,0,0];

    [T,Y] = ode23('two_sites_deRHS',xspan, n0);
    figure(1)
    %plot(T,Y(:,1),T,Y(:,2),'--','linewidth',2)
    legend('n_0','n_{-1}')

    N = length(T);
    force(j) = -Y(N,3)-Y(N,4);
    V(j) = v;
    end
    figure(2)
    plot(V,force)
    xlabel('v')
    ylabel('p')

    ==================================
    %this is the rhs for the two site muscle model

    function F_prime=deRHS(x,Y)
    global k rho h delta f1 g1 g2 v

    % variables are

    n0 = Y(1);
    nm1 = Y(2);


    xd = x-delta;
    f = (x>=0 & x<=h)*f1*x/h;
    fd = (xd>=0 & xd<=h)*f1*xd/h;

    g = (x<0)*g2 + (x>=0)*g1*x/h;
    gd = (xd<0)*g2 + (xd>=0)*g1*xd/h;

    n0P = -(f*(1-n0-nm1)-g*n0)/v;
    nm1P = -(fd*(1-n0-nm1)-gd*nm1)/v;
    n0IP = x*n0;
```

```
nm1IP = xd*nm1;

F_prime = [n0P;nm1P;n0IP;nm1IP];
```

Hence we have chosen to write a program in Fortran (the full code is given below). For ease of programming, the differential equations are solved using the simple forward Euler method, and stability is ensured by using a small space step. The forward Euler algorithm has many disadvantages, but for a small problem like this it is quick and easy to program, and quite sufficient for the task at hand.

We discretize space in increments of dx. We take our initial condition to $n_0(h + \Delta) = n_{-1}(h + \Delta) = 0$, and then take steps of $-dx$ until we reach $x = -2$, which seems (by trial and error) to be far enough.

At the ith space step (so that $x_i = h + \Delta - idx$), we have

$$n_0(x_{i+1}) = n_0(x_i) + \frac{\Delta x}{v}\Big[f(x_i)(1 - n_0(x_i) - n_{-1}(x_i)) - g(x_i)n_0(x_i)\Big] \quad (20.838)$$

$$n_{-1}(x_{i+1}) = n_{-1}(x_i) + \frac{\Delta x}{v}\Big[f(x_i - \Delta)(1 - n_0(x_i) - n_{-1}(x_i)) \quad (20.839)$$

$$- g(x_i - \Delta)n_{-1}(x_i)\Big]. \quad (20.840)$$

Once n_0 and n_{-1} are obtained the force can be calculated from the equation

$$p(v) = \rho k \int_{-\infty}^{\infty} x n_0(x)\, dx + \rho k \int_{-\infty}^{\infty} (x - \Delta)n_{-1}(x)\, dx. \quad (20.841)$$

To evaluate these integrals numerically we use the trapezoidal rule. If a function $\theta(x)$, say, is known at n equally spaced points x_i, $i = 1, n$, then

$$\int_{x_1}^{x_n} \theta(x)\, dx \approx dx\left(\frac{\theta(x_1)}{2} + \theta(x_2) + \cdots + \theta(x_{n-1}) + \frac{\theta(x_n)}{2}\right), \quad (20.842)$$

where dx is the spacing between the points.

Results are shown in Figs. 20.67 and 20.68. Fig. 20.67 shows the solutions for n_0 and n_{-1}, while Fig. 20.68 shows the computed force-velocity curve.

Here is the complete Fortran code used to obtain these solutions.

```
use globalparams
double precision :: force
integer :: i

k=1.0d0; rho=1.0d0; h=1.0d0; delta=0.1d0; f1=0.25d0; g1=0.25d0; g2=2.0d0

delx = 0.001d0                          ! Choose a nice small number for stability
lower = -2.0d0                          ! The lower bound for the integration.
```
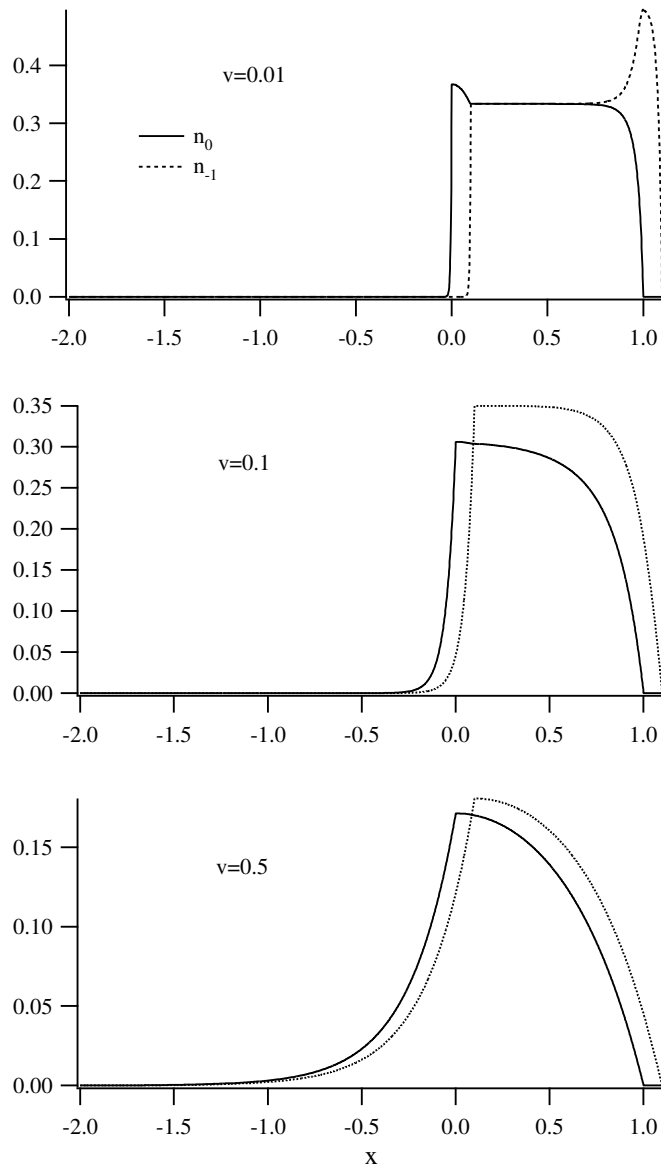
Figure 20.67: Computed solutions of the two binding site model for three different values of v. Note that as v gets smaller the solutions resemble the piecewise constant isometric solutions. Parameters are $h = 1$, $\Delta = 0.1$, $f_1 = 0.25$, $g_1 = 0.25$, $g_2 = 2$.
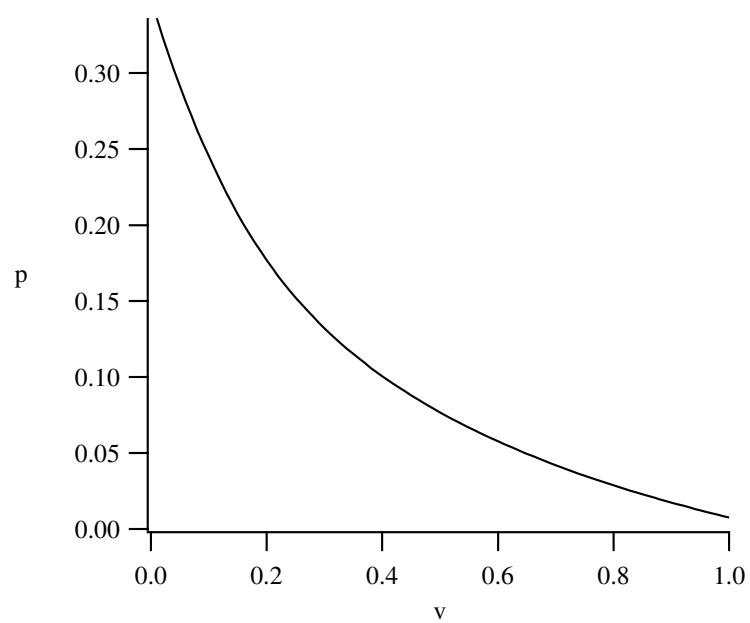
Figure 20.68: The computed force-velocity curve for the two-site model. Parameters are $k = 1$, $\rho = 1$, $h = 1$, $\Delta = 0.1$, $f_1 = 0.25$, $g_1 = 0.25$, $g_2 = 2$.

```fortran
        numsteps=nint((h+delta - lower)/delx)         ! Solve from x=lower to x=h+delta

!  The solution for n$_0$ is stored in the array n0.
!  The solution for n$_{-1}$ is stored in the array nm1.
!  We keep the solutions in arrays (instead of just printing out each value to a file
!  as we compute it) because we need to use n0 and nm1 later in the integration
!  subroutine
        allocate(n0(numsteps))         ! It's most efficient to use allocatable arrays
        allocate(nm1(numsteps))

        open(1,file='c11q7.out')       ! Put the solution into this file
        do i=1,100
            v = i*0.01d0
            call solve_for_n
            call integrate(force)
            print*,v,force
            write(1,*) v,force
        end do
        close(1)


        end
!------------------------
!  We solve the differential equations using the simplest, quickest method, the
!  forward Euler method. It's not a great method, but good enough for rough work
!  like this, and it's easy to program.

        subroutine solve_for_n
        use globalparams
        integer :: i
        double precision :: x

        n0(1)=0.0d0; nm1(1)=0.0d0                 ! Initial conditions
        do i=1,numsteps-1
            x = h+delta - i*delx
            n0(i+1)  = n0(i)  + (delx/v)*( f(x)*(1.0d0-n0(i)-nm1(i)) - g(x)*n0(i) )
            nm1(i+1) = nm1(i) + (delx/v)*( f(x-delta)*(1.0d0-n0(i)-nm1(i)) &
                                 - g(x-delta)*nm1(i)  )
        end do


        end
!------------------------
! Integrate r(x)n0(x) and r(x-Delta)nm1(x) using the trapezoidal rule. Note the
!  shift in the second integral (i.e., in sum2) where we use x2 in place of x1

        subroutine integrate(force)
        use globalparams
        integer :: i
        double precision :: force,x1,x2

        sum1 = (h+delta)*n0(1)/2.0d0
        sum2 = h*nm1(1)/2.0d0
        do i=2,numsteps-1
            x1 = h+delta - float(i)*delx
            x2 = h - i*delx                  ! Shifted by delta: we need r(x-delta)*nm1(x)
            sum1 = sum1 + x1*n0(i)
            sum2 = sum2 + x2*nm1(i)
        end do
        sum1 = delx*k*(sum1 + lower*n0(numsteps)/2.0d0)
```

```
        sum2 = delx*k*(sum2 + (lower-delta)*nm1(numsteps)/2.0d0)
        force = sum1+sum2

        end
!  ------------------------
        function f(x)                    ! Define the function f(x)
        use globalparams
        double precision :: f,x

        if (x<0) f=0
        if (x>h) f=0
        if (x<=h .and. x>=0) f=f1*x/h

        end
!-------------------------
        function g(x)                    ! Define the function g(x)
        use globalparams
        double precision :: g,x

        if (x<0) g=g2
        if (x>=0) g=g1*x/h

        end
!-------------------------
      module globalparams
      implicit none        ! Always a good idea to specify no implicit typing
      double precision :: f1,g1,g2,h,delta,k,rho,v,delx,lower
      double precision,dimension(:),allocatable :: n0,nm1
      integer :: numsteps
      end module globalparams
!------------------------
```

Part (d)

To include a fast slippage of the crossbridge from one binding site to another, we assume that the transitions

$$n_{-1} \underset{k_{-1}}{\overset{k_1}{\rightleftarrows}} n_0 \tag{20.843}$$

occur rapidly. Thus,

$$k_1 n_{-1} = k_{-1} n_0, \tag{20.844}$$

and so

$$n_{-1} = K n_0, \qquad \text{where } K = \frac{k_{-1}}{k_1}. \tag{20.845}$$

Next we add the equations (20.822) and (20.823) to get

$$-v\frac{\partial}{\partial x} n(x) = [f(x) + f(x - \Delta)](1 - n(x)) - [g(x)n_0(x) + g(x - \Delta)n_{-1}(x)], \tag{20.846}$$

where we have defined $n(x) = n_0(x) + n_{-1}(x)$. Noting that $n = (1+K)n_0 = (1+1/K)n_{-1}$ then gives

$$-v\frac{\partial}{\partial x}n(x) = [f(x) + f(x-\Delta)](1 - n(x)) - \left(\frac{g(x) + Kg(x-\Delta)}{1+K}\right)n(x).$$
(20.847)

Thus, the original two equations in n_0 and n_{-1} condense down to a single equation in n.

8. Consider the general binding site model (15.53) that incorporates the discrete distribution of binding sites. (Why is this equation much harder to integrate than the models we have discussed previously? The isometric solution is considerably easier to calculate.) Let $n_u(x) = 1 - \sum_{-\infty}^{\infty} n(x+i\Delta)$. Show that

$$1 - n_u(x) = \frac{\sum_{-\infty}^{\infty} \frac{f(x+i\Delta)}{g(x+i\Delta)}}{1 + \sum_{-\infty}^{\infty} \frac{f(x+i\Delta)}{g(x+i\Delta)}}.$$
(20.848)

Hence calculate the isometric solution $n(x)$.

Solution

The difficulty in integrating the general binding site model arises from how to cope with the boundary conditions. In the previous question we could specify the boundary conditions $n_0(h+\Delta) = n_{-1}(h+\Delta) = 0$, and this was enough to let us compute the solution numerically, i.e., we started at $x = h + \Delta$, secure in the knowledge that we knew the solution there, and then decreased x in jumps of dx, calculating the solution as we go.

But the steady state solution of (15.53) cannot be calculated this way, as dn/dx depends on the solution along the entire range of x values. The only realistic boundary conditions are to assume that $n \to 0$ as $x \to \pm\infty$, and these give no way of "starting" the solution for n. One possible way around this problem is to pick a starting distribution for $n(x)$, and then step the full partial differential equation (15.53) forward in time until a steady state is reached. The techniques for doing this numerically are beyond the scope of this book.

To calculate the isometric solution is easier. First, for simplicity let $n_i = n(x+i\Delta)$, and similarly for f_i and g_i. Then, the isometric steady solution is given by

$$f(x)\left(1 - \sum_{i=-\infty}^{i=\infty} n_i\right) = g(x)n(x).$$
(20.849)

But since

$$\sum_{i=-\infty}^{i=\infty} n(x + i\Delta) = \sum_{i=-\infty}^{i=\infty} n(x + (i+j)\Delta),$$
(20.850)

for any integer j, substituting $x + j\Delta$ for x in (20.849), it follows that

$$f(x + j\Delta)\left(1 - \sum_{i=-\infty}^{i=\infty} n_i\right) = g(x + j\Delta)n(x + j\Delta), \qquad (20.851)$$

for any integer j, and thus

$$n_j = \frac{f_j}{g_j}(1 - \sum_i n_i). \qquad (20.852)$$

Now just sum (20.852) from $j = -\infty$ to $j = \infty$ to get

$$\sum_j n_j = (1 - \sum_i n_i)\sum_j \frac{f_j}{g_j}, \qquad (20.853)$$

and thus (since $\sum_j n_j = \sum_i n_i$)

$$\sum_j n_j = \frac{\sum_j \frac{f_j}{g_j}}{1 + \sum_j \frac{f_j}{g_j}}, \qquad (20.854)$$

as required.

To get the isometric solution we substitute (20.854) into (20.849) to get

$$n(x) = \frac{f(x)}{g(x)} \cdot \frac{1}{1 + \sum_j \frac{f_j}{g_j}}. \qquad (20.855)$$

9. A muscle fiber must be able to produce a force even at negative velocities. For example, if you slowly lower a brick onto a table, your bicep is extending and simultaneously resisting the freefall of the brick. Investigate the behaviour of the Huxley model when $v < 0$.

   (a) Plot $n(x)$ for $v = -0.01$, -0.1 and -1.
   (b) Derive an expression for the maximum force as $v \to -\infty$.

   Solution

   For convenience, we let $v = -u$, where $u > 0$. Then, to find $n(x)$, we need to solve the differential equation

   $$u\frac{dn}{dx} = f(x)(1 - n) - g(x)n, \qquad (20.856)$$

   where f and g are as given for the Huxley model, i.e.,

   $$f(x) = \begin{cases} 0, & x < 0, \\ f_1 x/h, & 0 < x < h, \\ 0, & x > h, \end{cases} \qquad (20.857)$$

   $$g(x) = \begin{cases} g_2, & x < 0, \\ g_1 x/h, & x > 0. \end{cases} \qquad (20.858)$$

   $$r(x) = kx. \qquad (20.859)$$

Part (a)

When the muscle is stretching it must be that that $n(x) = 0$ for all $x < 0$. We thus have to solve for n only on the two regions $0 \leq x \leq h$ and $h \leq x$. Let n_1 denote the solution on $0 \leq x \leq h$, and let n_2 denote the solution on $h \leq x$.

When $0 \leq x \leq h$ we have

$$u\frac{dn_1}{dx} = \frac{f_1 x}{h} - \left(\frac{(f_1 + g_1)x}{h}\right)n_1, \qquad n_1(0) = 0, \tag{20.860}$$

which has solution

$$n_1(x) = \frac{f_1}{f_1 + g_1}\left(1 - e^{\frac{-x^2(f_1+g_1)}{2uh}}\right). \tag{20.861}$$

On the region $h \leq x$ we have

$$u\frac{dn_2}{dx} = -\frac{g_1 x}{h}n_2, \tag{20.862}$$

which has solution

$$n_2(x) = Ce^{\frac{-g_1 x^2}{2hu}}, \tag{20.863}$$

where C is a constant to be determined from the continuity condition

$$n_1(h) = n_2(h). \tag{20.864}$$

Applying this condition gives

$$C = \frac{f_1}{f_1 + g_1}\left(e^{\frac{hg_1}{2u}} - e^{\frac{-hf_1}{2u}}\right), \tag{20.865}$$

and hence

$$n_2(x) = \frac{f_1}{f_1 + g_1}\left(e^{\frac{hg_1}{2u}} - e^{\frac{-hf_1}{2u}}\right)e^{\frac{-g_1 x^2}{2hu}}. \tag{20.866}$$

Plots of $n(x)$, constructed by joining together n_1 and n_2, are given in Fig. 20.69 for three different values of v. Clearly, when v is close to 0 the solution is close to the isometric solution, but as v becomes more negative the crossbridge distribution is skewed to higher x values.

Part (b)

The force is given by

$$p = k\rho \int_0^\infty x n(x)\, dx = k\rho \int_0^h x\, n_1(x)\, dx + k\rho \int_h^\infty x\, n_2(x)\, dx \tag{20.867}$$
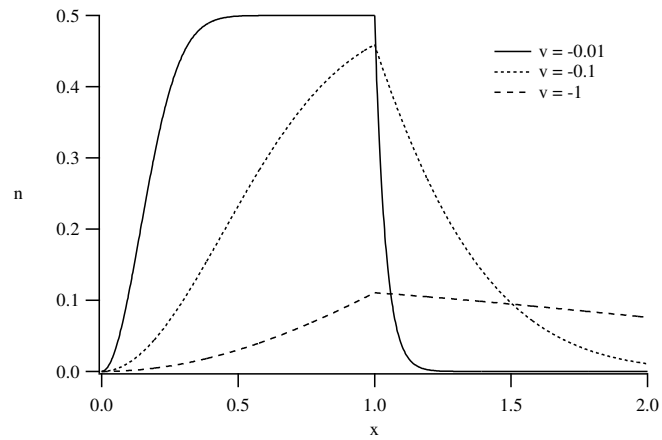
Figure 20.69: Plots of $n(x)$ for three negative values of velocity, i.e., as the muscle lengthens.
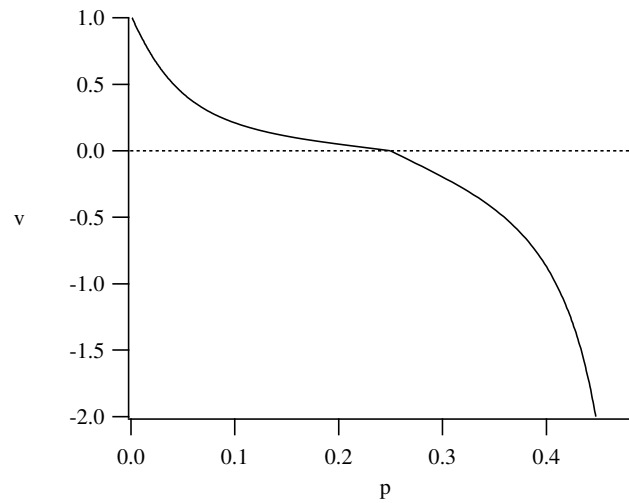

Figure 20.70: The force-velocity curve for positive and negative velocities.

An integral like this is most easily done with a symbolic manipulator such as Maple, which gives the answer

$$p = \frac{hkf_1\rho}{2g_1(f_1+g_1)^2}\left(2g_1 u e^{\frac{-h(f_1+g_1)}{2u}} + g_1 f_1 h + hg_1^2 + 2uf_1\right) \quad (20.868)$$

$$- 2uf_1 e^{\frac{-(f_1+g_1)}{2hu}} - 2ug_1 e^{\frac{-(f_1+g_1)}{2hu}}\Big) \quad (20.869)$$

Since

$$\lim_{u\to\infty} 2g_1 u \left(e^{\frac{-h(f_1+g_1)}{2u}} - e^{\frac{-(f_1+g_1)}{2hu}}\right) = g_1(f_1+g_1)\left(\frac{1}{h}-h\right), \quad (20.870)$$

and

$$\lim_{u\to\infty} 2f_1 u \left(1 - e^{\frac{-(f_1+g_1)}{2hu}}\right) = \frac{f_1(f_1+g_1)}{h}. \quad (20.871)$$

it follows that

$$\lim_{u\to\infty} p = \frac{hkf_1\rho}{2g_1(f_1+g_1)^2}\left[g_1(f_1+g_1)\left(\frac{1}{h}-h\right) + \frac{f_1(f_1+g_1)}{h} + g_1 h f_1(20.872)\right]$$

$$= \frac{1}{2}\frac{kf_1\rho}{g_1}. \quad (20.873)$$

10. Show that, in the limit as the number of bound crossbridges goes to infinity, the gliding rate of an actin filament (cf. Section 15.7) is given by

$$v \approx \frac{g_2 h}{2}. \quad (20.874)$$

Solution When many crossbridges are bound, we recover the original Huxley model. Thus, this problem reduces to calculating an approximate expression for the maximal velocity of the Huxley model, i.e., setting $p = 0$ in (15.37) and solving for v.

(a) Nondimensionalize (15.37) by defining $X = x/h$, $V = \frac{v}{g_2 h}$, and $R = \frac{f_1+g_1}{g_2}$ to get

$$1 - \frac{2V}{R}(1 - e^{-R/(2V)})(1+VR) = 0. \quad (20.875)$$

(b) Since R is small (what is its actual value?), expand V in a power series in R, expand the exponential in a Taylor series, and equate coefficients of powers of R to obtain the answer to lowest order.

11. Use a formal perturbation calculation to find the load-velocity relationship for the polymerization ratchet (15.114) and (15.115) in the limit that α and β are small. That is, introduce a non-dimensional scaling and define an appropriate small parameter ϵ, and then find a power series solution $p = p_0 + \epsilon p_1 + \cdots$ and the corresponding total flux $J = -\int_0^\infty D(\frac{dp}{dx} + \frac{f}{kT}p)dx$.

Solution

Introduce the dimensionless spatial variable $y = \frac{x}{\delta}$ and rewrite the steady versions of (15.114) and (15.115) as

$$0 = \frac{d^2p}{dy^2} + \omega\frac{dp}{dy} + \frac{\delta^2\alpha}{D}p(y+1) - \frac{\delta^2\beta}{D}p(y), \qquad y < 1,$$

$$0 = \frac{d^2p}{dy^2} + \omega\frac{dp}{dy} + \frac{\delta^2\alpha}{D}[p(y+1) - p(x)] + \frac{\delta^2\beta}{D}[p(y-1) - p(x)], \qquad y > 1.$$

where $\omega = \frac{f\delta}{kT}$. We define $\epsilon = \frac{\delta^2\alpha}{D}$ and set $\frac{\delta^2\beta}{D} = \epsilon b$. Then, if $p = p_0 + \epsilon p_1 + \cdots$, the equations for p_0, p_1 etc., are

$$\frac{d^2p_0}{dy^2} + \omega\frac{dp_0}{dy} = 0, \tag{20.876}$$

and

$$\frac{d^2p_1}{dy^2} + \omega\frac{dp_1}{dy} = -p_0(y+1) + bp_0(y), \qquad y < 1,$$

$$\frac{d^2p_1}{dy^2} + \omega\frac{dp_1}{dy} = -[p_0(y+1) - p_0(y)] - b[p_0(y-1) - p_0(y)], \qquad y > 1,$$

subject to the boundary conditions $\frac{dp_j(0)}{dy} + \omega p_j(0) = 0$, and $\lim_{y\to\infty} p(y) = 0$, and the normalization $\int_0^\infty p_j(y)dy = \frac{\delta_{j0}}{\delta}$.

It follows immediately that

$$p_0(y) = \frac{\omega}{\delta}\exp(-\omega y), \tag{20.877}$$

and

$$\frac{dp_1}{dy} + \omega p_1 = \frac{1}{\delta}\left(\exp(-\omega) - \exp(-\omega(y+1)) + b\exp(-\omega y) - b\right), \qquad y < 1,$$

$$\frac{dp_1}{dy} + \omega p_1 = \frac{1}{\delta}\left(-\exp(-\omega(y+1)) + \exp(-\omega y) - b[\exp(-\omega(y-1)) - \exp(-\omega y)]\right), \qquad y > 1,$$

Notice that integration constants were chosen so that $\frac{dp_1}{dy} + \omega p_1$ is 0 at $y = 0$ and is continuous at $y = 1$.

We do not need to solve for $p_1(y)$ to find the total flux. In fact,

$$j_1 = -\int_0^\infty (\frac{dp_1}{dy} + \omega p_1)dy = \frac{1}{\delta}(\exp(-\omega) - b). \tag{20.878}$$

It follows that the total flux (in original variables) is

$$J = \epsilon D j_1 = \delta(\alpha\exp(-\omega) - \beta), \tag{20.879}$$

as determined in the text using heuristic arguments.

12. Suppose $V(x)$ is the driving potential for a brownian ratchet, and that $V'(x)$ is periodic with period δ . What is the stall load for the molecular motor driven by the potential $V(x)$?

SolutionWe seek a periodic solution of the steady Fokker -Planck equation that has zero flux, i.e.,

$$D\frac{dp}{dx} + (V'(x) + \frac{f}{kT})p = 0 \qquad (20.880)$$

This is equivalent to

$$\frac{d}{dx}(\exp(V(x) + \frac{f}{kT}x)p) = 0 \qquad (20.881)$$

and this has a periodic solution if and only if $V(x) + \frac{f}{kT}x$ is a periodic function, that is, if and only if

$$\frac{f\delta}{kT} = V(0) - V(\delta) = \frac{f\delta}{kT} \qquad (20.882)$$

which is therefore the stall load.

13. Use regular perturbation expansion to find the force-velocity curve for the flashing ratchet in the limit that the reaction rates are slow compared to diffusion.

SolutionThe challenge is to calculate the total flux

$$J = -\int_0^\delta \left(\frac{fD}{kT}p_u + D\frac{\partial p_u}{\partial x} + \left(V'(x) + \frac{fD}{kT}\right) p_b + D\frac{\partial p_b}{\partial x} \right) dx \qquad (20.883)$$

First, we introduce the non-dimensional variable, $y = \frac{x}{\delta}$ where δ is the period of the potential $V(x)$. In non-dimensional form the governing equations are

$$0 = \frac{d^2 p_u}{dy^2} + \frac{d}{dy}(\epsilon F p_u) - \epsilon p_u + \epsilon b p_b, \qquad (20.884)$$

$$0 = \frac{d}{dy}((v'(y) + \epsilon F)p_b) + \frac{d^2 p_b}{dy^2} + \epsilon p_u - \epsilon b p_b, \qquad (20.885)$$

where $v'(y) = \frac{\delta^2}{D}V'(\frac{x}{\delta})$, $\epsilon F = \frac{f\delta}{kT}$, $\epsilon = \frac{\delta^2 \alpha}{D}$, $\frac{\delta^2 \beta}{D} = \epsilon b$. Notice that because the transitions are slow, we also expect that the load that can be moved is small and so scale the load by ϵ as well. The flux we wish to calculate is

$$J = -D\int_0^1 \left(\frac{f\delta}{kT}p_u + \frac{\partial p_u}{\partial y} + \left(v'(y) + \frac{f\delta}{kT}\right) p_b + \frac{\partial p_b}{\partial x} \right) dy \qquad (20.886)$$

We introduce a power series representation

$$p_u = p_u^0 + \epsilon p_u^1 + \cdots, \qquad p_b = p_b^0 + \epsilon p_b^1 + \cdots, \qquad (20.887)$$

and find the hierarchy of equations

$$\frac{d^2 p_u^0}{dy^2} = 0, \tag{20.888}$$

$$\frac{d}{dy}\left(v'(y)p_b^0\right) + \frac{d^2 p_b^0}{dy^2} = 0, \tag{20.889}$$

and

$$\frac{d^2 p_u^1}{dy^2} = p_u^0 - b p_b^0 - \frac{d}{dy}(F p_u^0), \tag{20.890}$$

$$\frac{d}{dy}\left(v'(y)p_b^1\right) + \frac{d^2 p_b^1}{dy^2} = -p_u^0 + b p_b^0 - \frac{d}{dy}(F p_b^0). \tag{20.891}$$

Since the solutions must be periodic, it is easy to determine that

$$p_u^0 = K_1, p_b^0 = K_2 \exp(-v(y)), \tag{20.892}$$

with the appropriate normalization

$$\int_0^1 (p_u^0 + p_b^0)dy = \frac{1}{\delta}. \tag{20.893}$$

Next, the periodicity of p_u^1 and p_b^1 require that the right-hand sides of the equations (20.890) and (20.891) have zero integral. (This follows from the Fredholm alternative Theorem and the fact that the null space of the associated adjoint operators have null-spaces spanned by constant functions.) This requirement combined with (20.893) implies that

$$K_1 = \frac{b E_{-v}(1)}{\delta(b+1)E_{-v}(1)}, \qquad K_2 = \frac{1}{\delta(b+1)E_{-v}(1)}, \tag{20.894}$$

where $E_{-v}(y) = \int_0^y \exp(-v(y))dy$.

Now we integrate the equations (20.890) and (20.891) once to find

$$\frac{dp_u^1}{dy} = j_u - F p_u^0 + \int_0^y (p_u^0(\eta) - b p_b^0(\eta))d\eta \equiv J_u, \tag{20.895}$$

$$v'(y)p_b^1 + \frac{dp_b^1}{dy} = j_b - F p_b^0 + \int_0^y (-p_u^0(\eta) + b p_b^0(\eta))d\eta \equiv J_b. \tag{20.896}$$

The constants j_u and j_b are determined by the requirements

$$\int_0^1 \left(j_u - F p_u^0 + \int_0^y (p_u^0(\eta) - b p_b^0(\eta))d\eta\right) dy = 0, \tag{20.897}$$

and

$$\int_0^1 \exp(v(y)) \left(j_b - F p_b^0 + \int_0^y (-p_u^0(\eta) + b p_b^0(\eta))d\eta\right) dy = 0, \tag{20.898}$$

and then the total flux is

$$
\begin{aligned}
J_1 &= \int_0^1 (J_u + J_b + F p_u^0 + F p_b^0) dy \\
&= \int_0^1 \left(j_b - F p_b^0 + \int_0^y (-p_u^0(\eta) + b p_b^0(\eta)) d\eta \right) dy + \frac{F}{\delta}.
\end{aligned}
$$

Working out all the algebra, and expressing the answer in dimensioned units, we find

$$
\begin{aligned}
J &= \frac{D}{\delta} \frac{f\delta}{kT} \frac{1}{\alpha + \beta} \left(\frac{\alpha}{E_v(1) E_{-v}(1)} + \beta \right) \\
&\quad + \frac{\delta \alpha \beta}{\alpha + \beta} \int_0^1 \left(\frac{E_v(y)}{E_v(1)} - y \right) \left(\frac{\exp(-v(y))}{E_{-v}(1)} - 1 \right) dy, \quad (20.899)
\end{aligned}
$$

to leading order in the small parameter $\frac{\delta^2 \alpha}{D}$.

Selected Solutions to Chapter 17

7. Find the response of the three-stage linear filter (16.62)-(16.64) to the sinusoidal input $I_p = I_0 + I_1 \sin(\omega t)$.

Solution

The response to the input $I_p = \exp(I\omega t)$ is

$$h_3 = \frac{1}{(1 + i\omega t_d)^3} \exp(i\omega t) \qquad (20.900)$$

from which it follows, using linearity, that the response of the system to the input $I_p = I_0 + I_1 \sin(\omega t)$ is

$$
\begin{aligned}
h_3 &= I_0 + \frac{1}{2} I_1 \left(\frac{1}{(1 + i\omega t_d)^3} \exp(i\omega t) - \frac{1}{(1 - i\omega t_d)^3} \exp(-i\omega t) \right) \quad (20.901) \\
&= I_0 + \frac{I_1}{(1 + t_d^2 \omega^2)^{3/2}} \sin(\omega t + \phi) \qquad (20.902)
\end{aligned}
$$

where $\sin(\phi) = \frac{3t_d\omega - t_d^3\omega^3}{(1 + t_d^2\omega^2)^{3/2}}$.

Selected Solutions to Chapter 19

3. For the model of Section 18.1.2, find the average concentration of solute in a tube for which $\eta = \frac{c_0 P D}{L r}$ is small. Use this to find the efflux velocity and efflux concentration. Under what conditions on parameters can water be pumped into pure water?

Solution

To leading order in η, the equation governing the solute concentration is (in dimensional units)

$$D\frac{d^2 c}{dx^2} = -\frac{2N(x)}{r}. \tag{20.903}$$

With $N(x) = N_0 H(aL - x)$, we find that

$$c = \begin{cases} c(0) - \frac{N_0}{Dr}x^2, & 0 < x < aL \\ c(L) - 2\frac{N_0}{Dr}aL(x - L) & aL < x < L \end{cases} \tag{20.904}$$

where

$$c(0) = c(L) - \frac{N_0}{Dr}aL^2(a - 2). \tag{20.905}$$

It follows that

$$\bar{c} = c(L) + a\frac{N_0 L^2}{rD}(1 - \frac{1}{3}a^2). \tag{20.906}$$

If the extracellular bath is pure water, then net flow is positive if $a\frac{N_0 L^2}{rD}(1 - \frac{1}{3}a^2) > c_0$.

Selected Solutions to Chapter 20

3. In this question we study some of the solutions of the model of light adaptation in turtle cones (Section 19.2.2).

   (a) Before we can calculate solutions of the model the expression for $g(y)$ must be derived. By forcing the steady state of the model to be

   $$V_0 = -s_1 \log(1 + s_2 I_0), \qquad (20.907)$$

   show that

   $$g(y) = \left(y e^{E(1-y)/V^*} \right)^{1/3} \left(\delta + \frac{(\gamma - \delta)\eta(e^{-E(1-y)/s_1} - 1)}{s_2 k_1 + \eta(e^{-E(1-y)/s_1} - 1)} \right). \qquad (20.908)$$

   Plot $g(y)$ (using the parameters given in Table 20.6) and compare to the functional form found experimentally (19.35), i.e.,

   $$A(y) = 4 + \frac{84}{1 + (y/0.34)^4}. \qquad (20.909)$$

   (b) Calculate the impulse responses of the model for a range of background light levels. For each background light level of I_0, let the magnitude of the impulse be I_0 also. Do this for I_0 = 0.5, 0.05, 0.005, 0.0005 and 0.00005. How linear are the responses? What can be said about the contrast sensitivity?

   (c) Scale each of the impulse responses calculated above so that each has a maximum value of 1, and plot them all on the same graph. How do the impulse responses change as the light level increases?

   (d) Replace $g(y)$ by $A(y)$ and recalculate the steady state V_0 and the impulse responses (at the same background light levels as in part (b) above). Are there any significant differences?

   Solution

Part (a)

Let a subscript 0 denote the steady state of the model. Then, by setting the right hand sides of (**??**)–(**??**) to zero, we get

$$p_0 = \frac{\eta I_0}{k_1 + \eta I_0}, \tag{20.910}$$

$$y_0 = x_0^3 e^{-V_0/V^*}, \tag{20.911}$$

$$g(y_0) = x_0(\delta + (\gamma - \delta)p_0), \tag{20.912}$$

$$z_0 = \left(\frac{1-\kappa}{1+\kappa}\right) x_0^3 e^{-V_0/V^*} + \left(\frac{2\kappa}{1+\kappa}\right) y_0, \tag{20.913}$$

$$V - E = \left(\frac{-6E}{4+\kappa}\right) x_0^3 e^{-V_0/V^*} + 2\left(\frac{1+\kappa}{4+\kappa}\right) E z_0 - \left(\frac{3E\kappa}{4+\kappa}\right) y_0 \tag{20.914}$$

Substituting (20.911) into (20.913) gives

$$z_0 = y_0, \tag{20.915}$$

and thus, from (20.914), that

$$V_0 = E(1 - y_0). \tag{20.916}$$

Furthermore, from (20.911) it follows that

$$\begin{aligned} x_0 &= \left(y_0 e^{V_0/V^*}\right)^{\frac{1}{3}} \\ &= \left(y_0 e^{E(1-y_0)/V^*}\right)^{\frac{1}{3}}. \end{aligned} \tag{20.917}$$

We now have x_0, z_0 and V_0 expressed in terms of y_0. It remains only to express p_0 in terms of y_0 and we are done.

Since $V_0 = -s_1 \log(1 + s_2 I_0)$ it follows that

$$I_0 = \frac{e^{-V_0/s_1} - 1}{s_2}, \tag{20.918}$$

and thus

$$\begin{aligned} p_0 &= \frac{\eta \left(e^{-V_0/s_1} - 1\right)}{k_1 s_2 + \eta \left(e^{-V_0/s_1} - 1\right)}, \\ &= \frac{\eta(e^{-E(1-y_0)/s_1} - 1)}{s_2 k_1 + \eta(e^{-E(1-y_0)/s_1} - 1)}. \end{aligned} \tag{20.919}$$

Substituting (20.917) and (20.919) into (20.912) then gives the required result.

In Fig. 20.71 we show plots of $g(y)$ and $A(y)$. Clearly the two functions agree very well over the plotted range. (For smaller values of y the two functions differ more, but such low values of y are unphysiological and thus we pay them little attention).
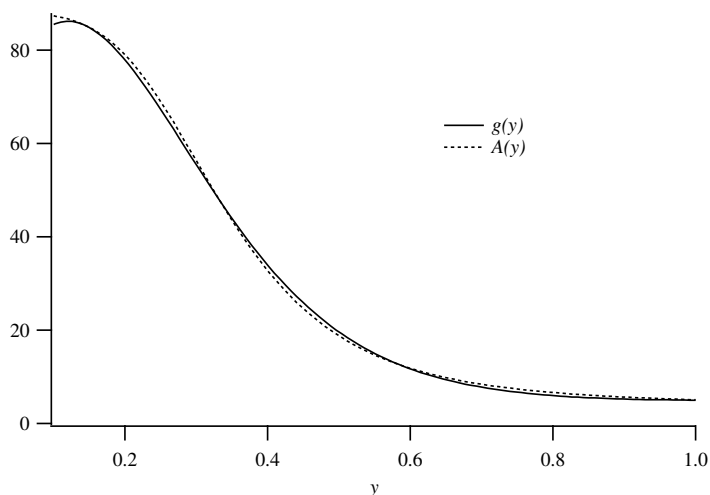
Figure 20.71: Plots of $g(y)$ and $A(y)$, using the parameters given in Table 20.6.

Part (b)

This question involves the numerical solution of the model equations (**??**) – (**??**). One could do this a number of ways; with Maple for instance, or by writing a program in Fortran or C. Here, the differential equations contain no surprises so we choose to use the program *xppaut* (see Appendix **??**) because of its convenience and ease of use.

In Fig. 20.72 we see responses of the model to flashes of fixed contrast superimposed on various background light levels. All the responses were calculated by numerical solution of (**??**)–(**??**), using the .ode file given in full below. To facilitate comparison of the curves, each curve was shifted vertically until its steady state voltage coincided with 0. In other words, these curves are really just plotting deviations from the steady-state voltage. To simulate a 5 ms light flash of strength I_0 superimposed on a background light level of I_0 we let

$$I(t) = I_0 + I_0\delta(t)/200. \qquad (20.920)$$

Note that the factor of 200 is needed because if we approximate an impulse function by using a square pulse of width 0.005 seconds, then that square pulse has to be 200 units high. Thus, dividing by 200 gives us a brief flash of light, of width 5 ms, and of unit height.

Each light flash had the same contrast, and thus if the photoreceptor had constant contrast sensitivity the amplitude of all the responses would be the same. However, we see from the figure that this is not exactly true. Instead, the contrast sensitivity first increases with increasing background light level, and then decreases again. For a background light level between 0.5 and 0.05, the contrast sensitivity is approximately constant.
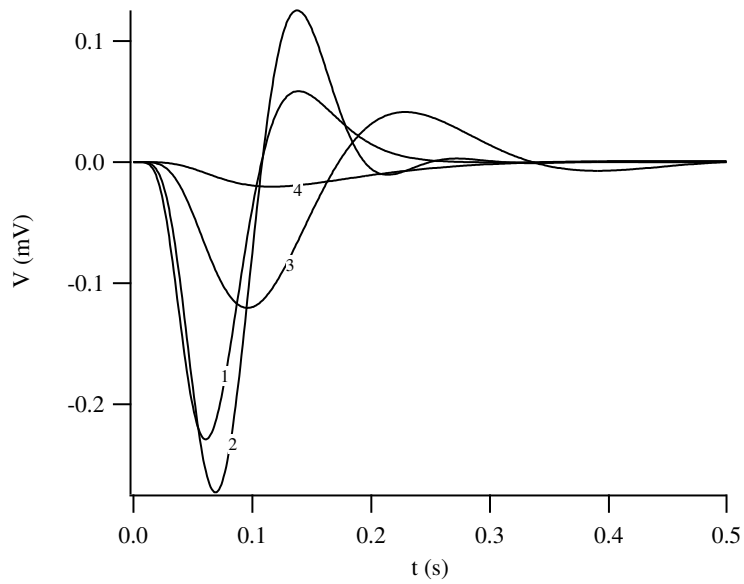
Figure 20.72: Responses of the model of light adaptation in turtle cones, using the parameters given in Table 20.6. For each curve a light flash of length 5 ms and magnitude I_0 was superimposed on a background of I_0 (so that each stimulus had the same contrast). The values for I_0 were (1) 0.5, (2) 0.05, (3) 0.005 and (4) 0.0005. So that we can plot the curves together, each curve is shifted vertically so that the steady state voltage is 0.
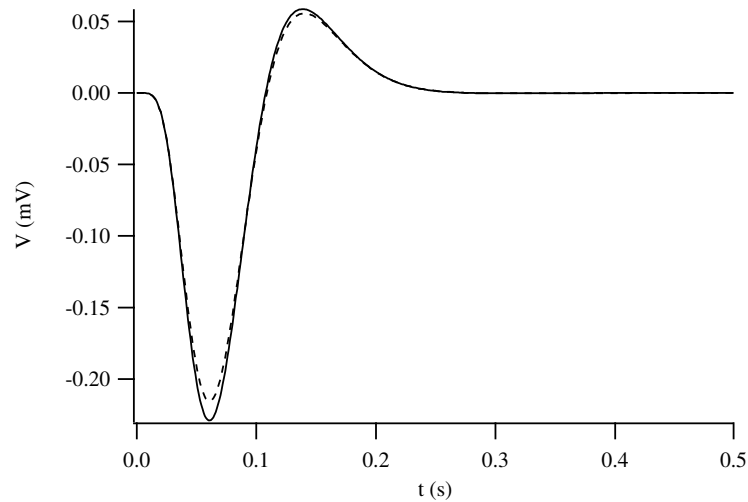
Figure 20.73: Testing the linearity of the flash responses. The solid curve is the same as curve 1 of Fig. 20.72, and is the response to a brief flash of light on top of a background light level of 0.5. The dotted curve is the result of doubling the flash strength and dividing the response by two.

To see if the responses are linear we double the stimulus strength (i.e., just put contrast=2 in the .ode file below) and divide the response by two. If the response is linear the result will exactly match the contrast=1 case. For the lowest three background light levels this is the case, as the curves are essentially identical to the naked eye. Fig. 20.73 shows the solutions for $I_0 = 0.5$; the dotted curve was the one obtained by doubling the stimulus strength and then dividing the response by two. As can be seen from the figure, although the responses are almost exactly linear, there is a slight decrease of the amplitude.

Part (c)

In Fig. 20.74 we show the same flash responses as in Fig. 20.72 normalised to a maximum amplitude of 1. What this figure illustrates is the speed-up of the kinetics of the flash responses. As the background light level increases, the flash responses reach their peak sooner, and develop oscillating tails, i.e., become *biphasic*. This (by the way) is in excellent agreement with experimental data.

Part (d)

When $g(y)$ is replaced by $A(y)$ the flash responses are essentially the same (Fig.20.75). There are, however, minor differences. For instance, we no longer
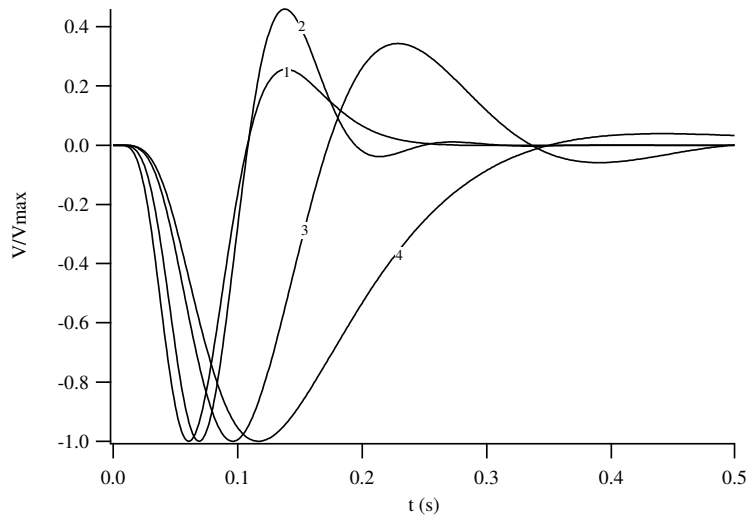
Figure 20.74: The same flash responses as in Fig. 20.72, normalised to a maximum amplitude of 1.

have $V_0 = -s_1 \ln(1 + s_2 I_0)$ and thus the variable Vshift in the .ode file below is no longer of any use. Nevertheless, the steady state is easily calculated and then subtracted from the responses to shift them to the origin. We did this, for example, in the plotting program we used to display the results (Igor Pro; see Appendix ??). It would be a simple matter to automate all this by writing a Fortran program, but the time saved is probably not worth the time invested.

It is a slightly more involved matter to calcuate V_0 as a function of I_0, as no analytical expression is readily obtainable. One option is to write a program that uses a nonlinear solver such as Newton's method to solve for V_0 given I_0. However, *xppaut* has the ability to do this quickly and easily as it provides a friendly interface to AUTO, a program designed to track steady states and bifurcations (see Appendix ??). The .ode file given below shows how to set the options for the AUTO interface, and the options that we used for this question. The result is show in Fig. 20.76. The steady state curves for the two different cases (using $g(y)$ or $A(y)$) cannot be told apart in this graph.

The solutions above were calculated using the following XPPAUT file.

```
#
# contrast=0 gives steady-states.
# contrast=1 gives a stimulus of size I0 on a background of I0.
#
par I0=0.05 contrast=1
par s1=1.59  s2=1130  E=-13  Vstar=35.7
par tauy=0.07 k1=35.4 gam=303 delta=5 kappa=0.1
```
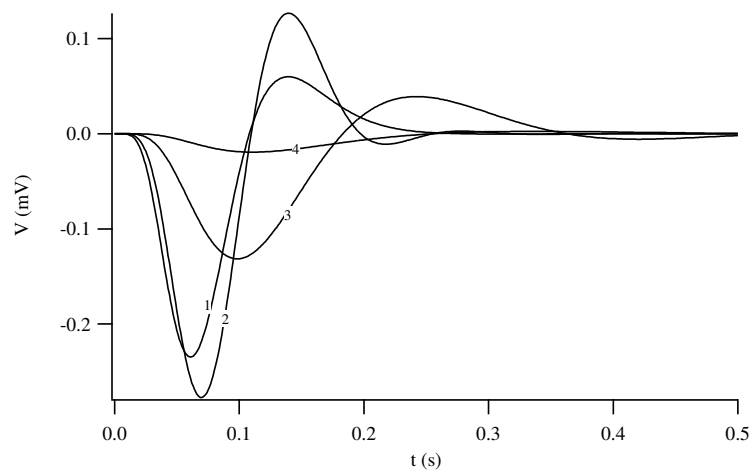
Figure 20.75: Flash responses of the model of light adaptation in turtle cones, using $A(y)$ instead of $g(y)$. Everything else was done exactly the same as in Fig. 20.72.
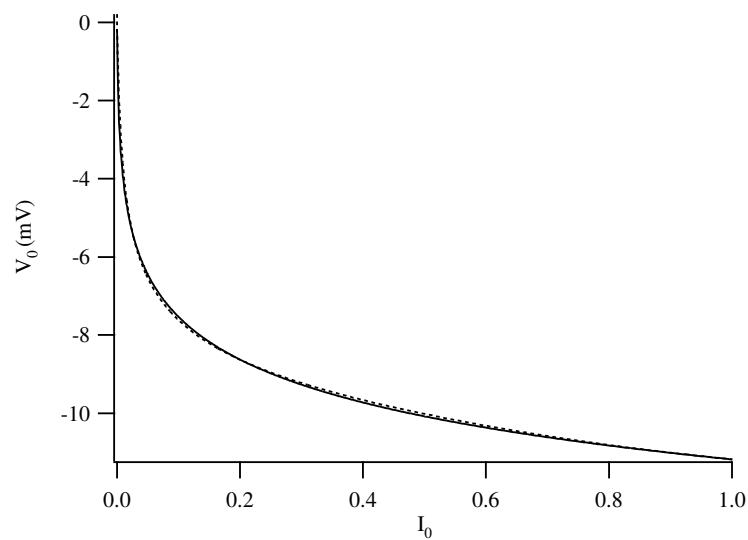

Figure 20.76: Steady state curves $V_0(I_0)$ of the model of light adaptation in turtle cones: solid curve, using $g(y)$; dotted curve, using $A(y)$. The curves are indistinguishable at this resolution.

```
par eta=52.5 tau1=0.012 taum=0.016 tauz=0.04
#
!V0=-s1*ln(1+s2*I0)
#
kernel(t)=(eta/tau1/6)*((t/tau1)^3)*exp(-t/tau1)
s(t)=eta*I0 + contrast*I0*kernel(t)/200
p'=s(t)*(1-p)-k1*p
x'=gfun(y)-(gam-delta)*x*p-delta*x
y'=((x^3)*exp(-V/Vstar)-y)/tauy
z'=(((1-kappa)/(1+kappa))*(x^3)*exp(-V/Vstar)\
    +(2*kappa/(1+kappa))*y-z)/tauz
V'=((-6*E/(4+kappa))*(x^3)*exp(-V/Vstar)+\
    (2*(1+kappa)/(4+kappa))*E*z-(V-E)-\
    (3*E*kappa/(4+kappa))*y)/taum
#
gfun(y)=(y*exp(E*(1-y)/Vstar))^(1/3)*\
        (delta+(gam-delta)*eta*\
        (exp(-E*(1-y)/s1)-1)/s2/\
        (k1+eta*(exp(-E*(1-y)/s1)-1)/s2))
#
# Here's A(y) (still called gfun just to make it easy).
# For part (d) use this gfun instead of the gfun above.
# gfun(y)=4+84/(1+(y/0.34)^4)
#
# Can't put in the actual steady states as functions of I0
# so we just put in the dark steady state.
p(0)=0
x(0)=1
y(0)=1
z(0)=1
V(0)=0
#
# We choose to plot out the shifted voltages
# (which is why we bother to calculate V0 at all)
aux Vshift=V-V0
@ yp=Vshift total=2.5 xlo=0 xhi=0.5 ylo=-0.5 yhi=0.1 dt=0.001
@ ntst=50 nmax=2000 npr=2000 dsmin=0.0001 dsmax=0.01 ds=0.001 parmin=0.00001
@ parmax=1 autoxmin=0.00001 autoxmax=1 autoymin=-12 autoymax=0 autovar=v
done
```

One thing that we should note is that XPPAUT does not handle the initial conditions very elegantly, as they can't be specified as functions of I_0. Thus, every time I_0 is changed during calculation of the curves the steady state must be recomputed (because it is needed to serve as the initial condition). This is most easily done by running up to $t = 5$, say, and then using the last computed point as the initial condition. The AUTO options are set on the last two lines and are used only for the calculation of $V_0(I_0)$ when $A(y)$ is used in place of $g(y)$.

4. In 1989, Forti *et al.* published a model of phototransduction in newt rods. In many respects their model is very similar to the model discussed here. However, one major difference is in how they chose to model the initial stages of the light response. Instead of just using a linear filter (which is, to be sure, a bit of a cheat) they modelled the equations in more detail. Forti *et al.*

T_0	$=$	$1000\ \mu$M	P_0	$=$	$100\ \mu$M
α_1	$=$	20 s^{-1}	ϵ	$=$	0.5 s$^{-1}\,\mu$M^{-1}
τ_1	$=$	0.1 s$^{-1}\,\mu$M^{-1}	τ_2	$=$	10 s^{-1}
β_1	$=$	10.6 s^{-1}			

Table 20.6: Parameter values for the model of the initial stages of the light response in newt rods (Forti et al., 1989). P_0 is the total amount of PDE, and T_0 is the total amount of transducin.

assumed that the initial stages of the light response could be modeled by the reactions

$$R \xrightarrow{h\nu} R^* \xrightarrow{\alpha_1} \tag{20.921}$$

$$R^* + T \xrightarrow{\epsilon} R^* + T^* \tag{20.922}$$

$$T^* \xrightarrow{\beta} \tag{20.923}$$

$$T^* + P \underset{\tau_2}{\overset{\tau_1}{\rightleftarrows}} T^* + P^* \tag{20.924}$$

Here, R denotes rhodopsin, T denotes transducin and P denotes PDE. The * superscript denotes the activated form, and $h\nu$ denotes the action of light. The parameter values of the model are given in Table 20.6. (Actually, these are not the exact same reactions assumed by Forti *et al.* as we have omitted the inactivated rhodopsin state. However, this makes almost no difference to the results presented here.)

(a) Assuming that rhodopsin in present in unlimited quantities, write down the differential equations for this system of reactions, and solve numerically. Plot $P^*(t)$ for a variety of stimuli, each 10 ms in duration, but with magnitudes 0.2, 0.5, 1, 2, 5, 10, 20, 50, 100 and 500. What can you conclude about the linearity of the response when the magnitude of the stimulus is small? What can you conclude about the linearity of the response as the magnitude of the stimulus increases?

(b) Compare the model in part (a) with the detailed reaction scheme in Fig. 19.7. Where do they disagree? Modify the model so that it agrees better with the more detailed reaction scheme. (Hint: the conservation equation for transducin must be considered more carefully, as must the differential equation for T*.) Solve the new model numerically for the same stimuli as part (a), and compare with the solutions of the Forti *et al.* model. Explain the differences.

(c) Compare the model of part (a) to the linear cascade model in the book. Where are they similar? Where are they not similar? Why?

Solution

Part (a)

Denote the light stimulus by $I(t)$, and let R^* denote the concentration of R^* with the same convention for P, P^*, T and T^*. Then we have the conservation laws

$$P + P^* = P_0, \tag{20.925}$$

$$T + T^* = T_0. \tag{20.926}$$

Hence,

$$\frac{dR^*}{dt} = I(t) - \alpha_1 R^*, \tag{20.927}$$

$$\frac{dT^*}{dt} = \epsilon R^*(T_0 - T^*) - \beta_1 T^* + \tau_2 P^*, \tag{20.928}$$

$$\frac{dP^*}{dt} = \tau_1 T^*(P_0 - P^*) - t_2 P^*. \tag{20.929}$$

We solve these equation numerically using *xppaut*. For each curve the light stimulus had a duration of 10 ms, and had the magnitude as described in the caption. Fig. 20.77 shows P^* as a function of t for stimuli of seven different magnitudes. As expected, the responses get larger as the magnitude of the stimulus increases.

It is more enlightening to look at the scaled responses, rather than the actual responses, as this shows us the degree of linearity of the response. Fig. 20.78 shows such scaled responses, each scaled to a stimulus strength of 1. In other words, the solution corresponding to a stimulus strength of 0.2 was scaled by a factor of 5, the solution corresponding to a stimulus strength of 2 was scaled by a factor of $1/2$ and so on. If the responses were exactly linear, the scaled responses would be identical. From Fig. 20.78 we see this is true for the first three (stimulus strengths of 0.2, 1 and 2). However, at the remaining stimulus strengths (10, 20 100 and 500) the magnitude of the response is diminished, and at the highest stimulus strengths the kinetics of the response are considerably faster also. Hence, linearity is lost at these high stimulus strengths.

To solve the equations using XPPAUT we used the Runge-Kutta option with a step size of 0.001.

```
# Declare the variables
r(0)=0
g(0)=0
p(0)=0
# Declare the parameters
par str=0.2 alpha1=20 eps=0.5 T0=1000 P0=100 beta1=10.6
par tau1=0.1 tau2=10
#
# Define right hand sides
r'=str*(heav(t)-heav(t-0.01))-alpha1*r
```
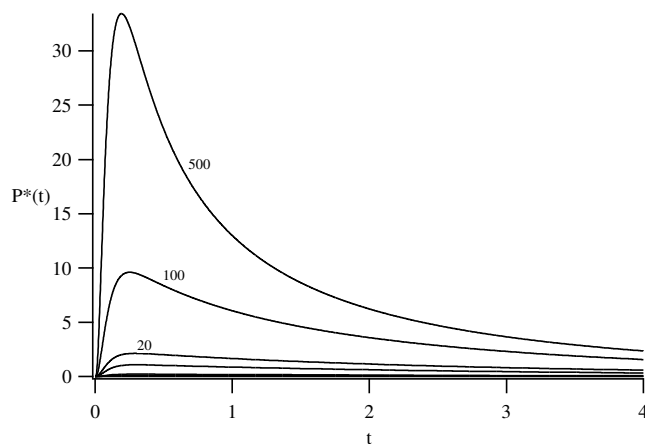
Figure 20.77: Numerical solutions of (20.927)–(20.929). The light stimulus had a duration of 10 ms, and the magnitude was (from the bottom curve to the top curve) 0.2, 1, 2, 10, 20, 100 and 500 (in units of $R^* \, s^{-1}$). So as not to clutter the graph, the stimulus strength is shown on the three uppermost curves but not on the others.
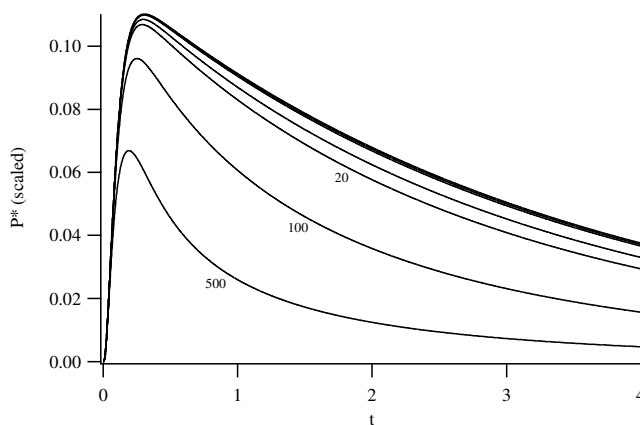

Figure 20.78: Numerical solutions of (20.927)–(20.929), scaled to a stimulus strength of 1. The light stimulus had a duration of 10 ms, and the magnitude was (from the top curve to the bottom curve) 0.2, 1, 2, 10, 20, 100 and 500. So as not to clutter the graph, the stimulus strength is shown on the three lowest curves but not on the others.
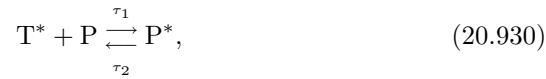
```
g'=eps*r*(T0-g)-beta1*g+tau2*p
p'=tau1*g*(P0-p)-tau2*p
#
@ total=4, dt=0.001
done
```

Part (b)

In the more detailed scheme of Fig. 19.7 we see that the T_α subunit of transducin (i.e., the activated form of transducin) is bound to the activated form of the PDE, and thus (20.929) should really be

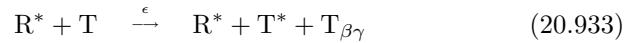$$T^* + P \overset{\tau_1}{\underset{\tau_2}{\rightleftharpoons}} P^*, \tag{20.930}$$

and the conservation law for transducin should therefore be

$$T_0 = T^* + T + P^*. \tag{20.931}$$

Furthermore, the inactivation of T^* requires a $T_{\beta\gamma}$ subunit, and so one should keep track of the $T_{\beta\gamma}$ subunits in order to model the inactivation of transducin.

With these modifications the reaction scheme becomes

$$R \overset{h\nu}{\rightarrow} R^* \overset{\alpha_1}{\rightarrow} \tag{20.932}$$

$$R^* + T \overset{\epsilon}{\rightarrow} R^* + T^* + T_{\beta\gamma} \tag{20.933}$$

$$T^* + T_{\beta\gamma} \overset{\beta}{\rightarrow} T \tag{20.934}$$

$$T^* + P \overset{\tau_1}{\underset{\tau_2}{\rightleftharpoons}} P^*, \tag{20.935}$$

with the corresponding differential equations

$$\frac{dR^*}{dt} = I(t) - \alpha_1 R^*, \tag{20.936}$$

$$\frac{dT^*}{dt} = \epsilon R^* T - \beta_1 T^* T_{\beta\gamma} - \tau_1 T^* P + \tau_2 P^*, \tag{20.937}$$

$$\frac{dP^*}{dt} = \tau_1 T^* P - t_2 P^*. \tag{20.938}$$

The three conservation laws are

$$T_0 = T^* + T + P^*, \tag{20.939}$$
$$T_{\beta\gamma} = T^* + P^*, \tag{20.940}$$
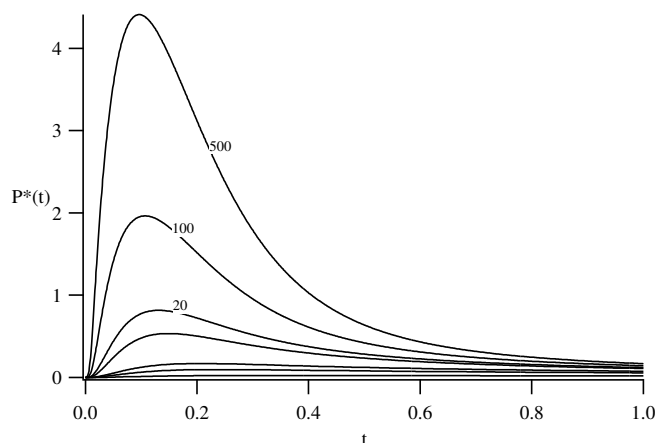$$P_0 = P + P^*. \tag{20.941}$$

Figure 20.79: Numerical solutions of (20.942)–(20.944). The light stimulus had a duration of 10 ms, and the magnitude was (from the bottom curve to the top curve) 0.2, 1, 2, 10, 20, 100 and 500 (in units of $R^* \, \mathrm{s}^{-1}$). So as not to clutter the graph, the stimulus strength is shown on the three uppermost curves but not on the others.

Hence the model is

$$
\frac{dR^*}{dt} \;=\; I(t) - \alpha_1 R^*, \tag{20.942}
$$

$$
\frac{dT^*}{dt} \;=\; \epsilon R^*(T_0 - T^* - P^*) - \beta_1 T^*(T^* + P^*) - \tau_1 T^*(P_0 - P^*) + t_2 P^*, \tag{20.943}
$$

$$
\frac{dP^*}{dt} \;=\; \tau_1 T^*(P_0 - P^*) - t_2 P^*. \tag{20.944}
$$

In Fig. 20.79 we plot numerical solutions of the model equations, calculated for the same stimuli as in Fig. 20.77. The responses of this second model are similar to those of the model of Forti *et al.*, except that they are smaller, and decay more quickly (note the different vertical and horizontal scales).

In Fig. 20.80 we plot the scaled solutions, just as in Fig. 20.78. We see that none of the responses are linear, even at the lowest stimulus strength, and that the responses to the stronger stimuli are greatly attenuated by the nonlinearities in the model.

These results are unsurprising, as the second model contains "stronger" non-linear terms than does the Forti model. In particular, in the Forti model the decay of T* is always linearly proportional to T^*, while in the second model the decay of T* is proportional rather to $(T^*)^2$, as well as to T^*P^*. Thus, when T^* gets large, it decays much faster in the second model than in the Forti model. This causes the smaller responses and the faster decay rates.

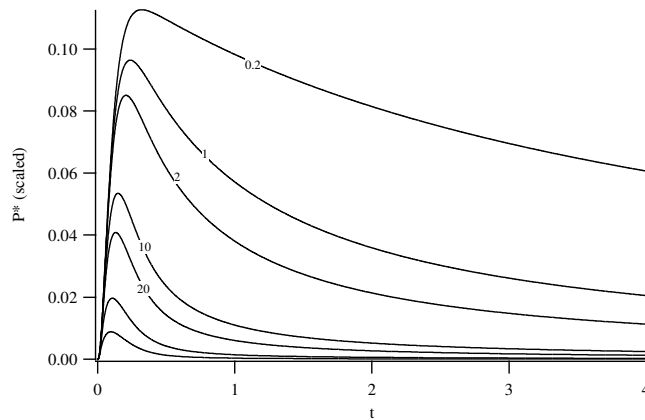To solve the equations using XPPAUT we used the Runge-Kutta option with a step size of 0.001.

Figure 20.80: Numerical solutions of (20.942)–(20.944), scaled to a stimulus strength of 1. The light stimulus had a duration of 10 ms, and the magnitude was (from the top curve to the bottom curve) 0.2, 1, 2, 10, 20, 100 and 500.

```
# Declare the variables
r(0)=0
g(0)=0
p(0)=0
# Declare the parameters
par str=0.2 alpha1=20 eps=0.5 T0=1000 P0=100 beta1=10.6
par tau1=0.1 tau2=10
#
#
# Define right hand sides
r'=str*(heav(t)-heav(t-0.01))-alpha1*r
g'=eps*r*(T0-g-p)-beta1*g*(g+p)+tau2*p-tau1*g*(P0-p)
p'=tau1*g*(P0-p)-tau2*p
#
@ total=4, dt=0.001, xlo=0, xhi=4
done
```

Part (c)

Finally, we compare the models in (a) and (b) to the linear cascade model described in the text, i.e.,

$$\frac{dP^*}{dt} = s(t)(P_0 - P^*) - k_1 P^*, \qquad (20.945)$$

where

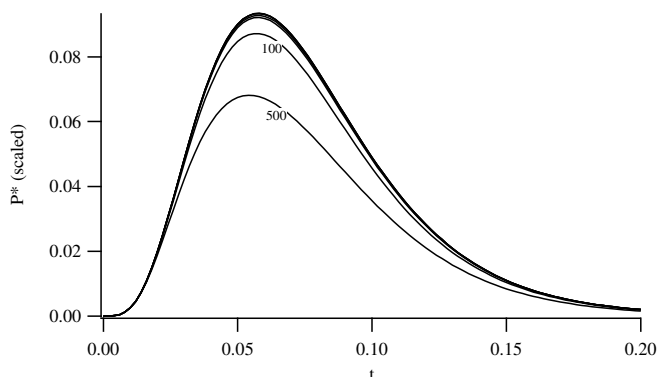$$s(t) = \int_{-\infty}^{t} I(\tau) K(t - \tau) \, d\tau. \qquad (20.946)$$

Figure 20.81: Numerical solutions of (20.945), scaled to a stimulus strength of 1. The light stimulus had a duration of 10 ms, and the magnitude was (from the top curve to the bottom curve) 0.2, 1, 2, 10, 20, 100 and 500.

We solve (20.945) for the same light inputs as in parts (a) and (b). However, care is needed, as the function $I(t)$ in the Forti model (having units of $R^* \, s^{-1}$) does not have exactly the same meaning as $I(t)$ in the linear cascade model (which has units of simply R^*).

In the linear cascade model the actual light input is $l_1 I(t)$, and we do not know the exact value of l_1. However, we shall just choose l_1 so that the response at the smallest light stimulus has the same magnitude as that of the Forti model, and then use that value of l_1 for all the other responses.

For a light stimulus that is 10 ms in duration with a magnitude of 0.2 $R^* \, s^{-1}$, we choose $l_1 = 200 \, s^{-1}$, to get the responses shown in Fig. 20.81. From this graph we see that the responses are linear at all but the highest two stimulus strengths, and of very similar magnitude to the responses of the Forti model. The major difference is in the time scale; the responses of the linear model are approximately 10 times faster than the responses of the Forti model. This is as expected from the physiology; the parameters in the Forti model were chosen to fit data from rods, while the parameters of the linear cascade model were chosen to fit data from cones. Since the light responses of cones are much faster than the responses of rods it stands to reason that this difference will be reflected in the responses of the two models.

In addition to the differences in the speeds, the shapes of the responses differ as well, with the responses of the Forti model weighted more towards the early part of the response. The exact reasons for these detailed differences in shape are not clear, but are obviously a result of the nonlinearities in the initial stages of the Forti model.

6. Show that the current generated by the electrogenic exchange pumps should not be ignored in the modeling. (Hint: By writing down the balance equations

for Na^+ and Ca^{2+} show that the outward current generated by the electrogenic Na^+–K^+ exchanger in the inner segment must be approximately a third of the total inward light-sensitive current.) How significant is the current generated by the Na^+–Ca^{2+},K^+ exchanger in the outer segment? Should the electrogenic pumps be included in the model if the model is compared to photocurrent measurements and not to voltage measurements?

Solution

From Fig. 19.5 we see that there are two pumps that need to be considered in addition to the light-sensitive flux of Na^+ and Ca^{2+}; the Na^+–Ca^{2+},K^+ exchanger in the outer segment and the Na^+–K^+ exchanger in the inner segment. (As it turns out, we need not consider the flux of K^+ in the balance equations as none of the light-sensitive current is carried by K^+.)

We begin by defining some notation. Let

$$
\begin{aligned}
n_1 &= \text{flux of } Na^+ \text{ through the light} - \text{sensitive channel,} \\
n_2 &= \text{flux of } Na^+ \text{ through the } Na^+ : Ca^{2+}, K^+ \text{exchanger,} \\
n_3 &= \text{flux of } Na^+ \text{ through the } Na^+ : K^+ \text{exchanger,} \\
c_1 &= \text{flux of } Ca^{2+} \text{ through the light} - \text{sensitive channel,} \\
c_2 &= \text{flux of } Ca^{2+} \text{ through the } Na^+ : Ca^{2+}, K^+ \text{exchanger.}
\end{aligned}
$$

All these fluxes are counted as positive, and have units of molecules per time.

At steady state we must have no net ionic fluxes and thus

$$
\begin{aligned}
n_1 + n_2 &= n_3, & (20.947) \\
c_1 &= c_2. & (20.948)
\end{aligned}
$$

Furthermore, because the exchangers pump ions in certain ratios we must also have

$$
n_2 = 4c_2. \tag{20.949}
$$

If we now let J_{ls} denote the total light-sensitive current, and assume that Ca^{2+} carries a fraction α of the total light-sensitive current we have

$$
\begin{aligned}
c_1 &= \frac{\alpha J_{ls}}{2q} & (20.950) \\
n_1 &= \frac{J_{ls}(1 - \alpha)}{q}, & (20.951)
\end{aligned}
$$

where q is the unit positive charge.

We can now solve for the current carried by the Na^+–K^+ exchanger in the inner segment, which is given by $qn_3/2$. Since

$$
\begin{aligned}
n_3 &= n_1 + n_2 \\
&= \frac{J_{ls}(1 - \alpha)}{q} + 4y_2
\end{aligned}
$$

$$= \frac{J_{\text{ls}}(1 - \alpha)}{q} + 4y_1$$

$$= \frac{J_{\text{ls}}(1 - \alpha)}{q} + \frac{2\alpha T}{q}$$

$$= \frac{J_{\text{ls}}(1 + \alpha)}{q},$$

it follows that

$$\frac{qn_3}{3} = \left(\frac{1 + \alpha}{3}\right) J_{\text{ls}}. \tag{20.952}$$

Thus, since $\alpha \approx 0.1$ we see that the Na^+–K^+ exchanger in the inner segment generates an outward positive current that is approximately one third as big as the total inward light-sensitive current.

Because $C_m dV/dt = I$, where I includes all the trans-membrane currents, we know that the currents generated by the exchange pumps will affect the voltage responses of the photoreceptor and thus should be included in the model; the omission of these currents is one of the most severe deficiencies of the model for light adaptation presented here.

The current generated by the Na^+–Ca^{2+}, K^+ exchanger in the outer segment is given by $n_2 q/4 = c_2 q = c_1 q = \alpha J_{\text{ls}}/2$. Hence, the Na^+–Ca^{2+}, K^+ exchanger generates a much smaller current than the Na^+–K^+ exchanger and can probably be safely ignored in the modelling.

This problem is only partially avoided by comparing the model to photocurrent measurements, rather than to voltage measurements. The photocurrent is dependent mainly on the number of open channels, which in turn depends on the cGMP concentration. So a good approximation of the photocurrent is obtained by assuming that it is proportional to x^3 (or to $x^3/(K^3 + x^3)$, which is more accurate at higher light levels). With this approximation the membrane voltage of the photoreceptor never appears in the model and thus the exchange pump currents can be ignored. This is the approach taken by Forti *et al.* (1989), for instance.

However, the photocurrent does depend on the membrane potential to a certain extent, as shown in (??), and so a fully accurate model would include the effects of the transmembrane potential on the photocurrent. It's not clear what difference this would make.

8. Calculate the response of the lateral inhibition model (Section 19.4) when the light stimulus is a strip of width $2a$, modulated sinusoidally with frequency ω. Show that as a increases (i.e., as the stimulus goes from a spot to a uniform field), the gain at $x = 0$ becomes more band-pass in nature.

Hint: Show that the solution for $\hat{I}$ is of the form

$$\hat{I} = \begin{cases} \frac{\lambda \hat{L}}{(i\omega\tau + 1)(1 + \lambda + i\omega)}[1 + A\cosh[x\sqrt{1 + \lambda + i\omega}], & |x| < a, \\ B\exp(-|x|\sqrt{1 + \lambda + i\omega}), & |x| > a, \end{cases} \tag{20.953}$$

and then require that $\hat{I}$ and its derivative be continuous at $|x| = a$. Define the gain as the response divided by the stimulus, and calculate the amplitude of the gain at $x = 0$ as a function of ω and a. (The details are given in Peskin (1976)).

Solution

First consider the response of the lateral inhibition model to a stimulus of the form
$$L(x, y, t) = L_1(x)e^{i\omega t}. \tag{20.954}$$

We look for solutions of the form $L = L_1(x)e^{i\omega t}$, $I = I_1(x)e^{i\omega t}$ and $E = E_1(x)e^{i\omega t}$. Substituting these into (19.51)–(**??**) and cancelling out the $e^{i\omega t}$ gives

$$
\begin{align}
E_1 &= \frac{L_1}{1 + i\omega\tau}, \tag{20.955}\\
\nabla^2 I_1 &= \alpha^2 I_1 - \lambda E_1, \tag{20.956}\\
R_1 &= E_1 - I_1, \tag{20.957}
\end{align}
$$

where
$$\alpha^2 = 1 + \lambda + i\omega. \tag{20.958}$$

For a strip of light of width $2a$, modulated sinusoidally, we have

$$
L_1(x) = \begin{cases} \bar{L}, & |x| < a, \\ 0, & \text{otherwise,} \end{cases} \tag{20.959}
$$

where $\bar{L}$ is a constant. Since there is no y dependence $\nabla^2 I_1 = d^2 I_1/dx^2$. Hence we need to solve

$$
\frac{d^2 I_1}{dx^2} = \begin{cases} \alpha^2 I_1 - \frac{\lambda\bar{L}}{1+i\omega\tau}, & |x| < a, \\ \alpha^2 I_1, & \text{otherwise.} \end{cases} \tag{20.960}
$$

We consider the three regions $x < -a$, $|x| < a$ and $x > a$. When $x > a$ we have
$$\frac{d^2 I_1}{dx^2} = \alpha^2 I_1, \tag{20.961}$$

which has solution
$$I_1^{\text{region 1}} = Ae^{-\alpha x}. \tag{20.962}$$

Note that the other exponential solution is discarded because we require the solution to be bounded at infinity.

Similarly, when $|x| < a$ we have

$$\frac{d^2 I_1}{dx^2} = \alpha^2 I_1 - \frac{\lambda\bar{L}}{1 + i\omega\tau}, \tag{20.963}$$

which has solution

$$I_1^{\text{region 2}} = Be^{\alpha x} + Ce^{\alpha x} + \frac{\lambda \bar{L}}{\alpha^2(1 + i\omega\tau)}. \qquad (20.964)$$

Because of the inherent symmetry of the problem we know that the solution must be symmetrical around the origin, and thus $B = C$. Hence

$$I_1^{\text{region 2}} = B(e^{\alpha x} + e^{\alpha x}) + \frac{\lambda \bar{L}}{\alpha^2(1 + i\omega\tau)} \qquad (20.965)$$

$$= D\cosh(\alpha x) + \frac{\lambda \bar{L}}{\alpha^2(1 + i\omega\tau)}, \qquad (20.966)$$

where $D = 2B$.

Finally, on the region $x < -a$ we know from symmetry that

$$I_1^{\text{region 3}} = Ae^{\alpha x}. \qquad (20.967)$$

Thus, in summary,

$$I_1 = \begin{cases} Ae^{-\alpha|x|}, & |x| > a, \\ D\cosh(\alpha x) + \frac{\lambda \bar{L}}{\alpha^2(1+i\omega\tau)}, & |x| < a. \end{cases} \qquad (20.968)$$

We now determine the constants A and D by requiring that

$$I_1^{\text{region 1}}(a) = I_1^{\text{region 2}}(a), \qquad (20.969)$$

$$\frac{dI_1^{\text{region 1}}(a)}{dx} = \frac{dI_1^{\text{region 2}}(a)}{dx}. \qquad (20.970)$$

This gives the two conditions

$$D\cosh(\alpha a) + \frac{\lambda \bar{L}}{\alpha^2(1 + i\omega\tau)} = Ae^{-\alpha a}, \qquad (20.971)$$

$$\alpha D\sinh(\alpha a) = -\alpha Ae^{-\alpha a}, \qquad (20.972)$$

which we can solve to get

$$A = \frac{\lambda \bar{L}\sinh(\alpha a)}{\alpha^2(1 + i\omega\tau)}, \qquad (20.973)$$

$$D = \frac{-\lambda \bar{L}}{\alpha^2(1 + i\omega\tau)}e^{-\alpha a}. \qquad (20.974)$$

Thus,

$$I_1 = \begin{cases} \frac{\lambda \bar{L}\sinh(\alpha a)}{\alpha^2(1+i\omega\tau)}e^{-\alpha|x|}, & |x| > a, \\ \frac{\lambda \bar{L}}{\alpha^2(1+i\omega\tau)}(1 - e^{-\alpha a}\cosh(\alpha x)), & |x| < a. \end{cases} \qquad (20.975)$$

1192

The gain, G, at $x = 0$ is given by

$$G(0, \omega) = \frac{R_1(0, \omega)}{\bar{L}} \tag{20.976}$$

$$= \frac{E_1(0, \omega) - I_1(0, \omega)}{\bar{L}} \tag{20.977}$$

$$= \frac{1}{1 + i\omega\tau} \left(1 - \frac{\lambda}{\alpha^2}(1 - e^{-\alpha a})\right). \tag{20.978}$$

To study the behaviour of $|G(0, \omega)|$ as a function of a we consider two extreme cases; $a = 0$ and $a = \infty$. When $a = 0$, $G(0, \omega) = 1/(1 + i\omega\tau)$, which implies that

$$|G(0, \omega)|\Big|_{a=0} = \frac{1}{\sqrt{1 + \omega^2\tau^2}}. \tag{20.979}$$

This is a monotonic decreasing function of ω.

However,

$$G(0, \omega)\Big|_{a=\infty} = \frac{1}{1 + i\omega\tau} \cdot \frac{1 + i\omega}{1 + \lambda + i\omega\tau} \tag{20.980}$$

and thus

$$|G(0, \omega)|^2\Big|_{a=\infty} = \frac{1 + \omega^2}{1 + \omega^2\tau} \cdot \frac{1}{(1 + \lambda)^2 + \omega^2\tau^2}. \tag{20.981}$$

When τ is small enough this function first increases as ω increases, and then decreases, i.e., it demonstrates band-pass characteristics, with greater amplitude at a band of intermediate frequencies. This is illustrated in Fig. 20.82 where we plot $|G(0, \omega)|^2\big|_{a=\infty}$ and $|G(0, \omega)|^2\big|_{a=0}$ as functions of ω.

9. Calculate the response of the lateral inhibition model (Section 19.4) to a moving step of light. Show that as the speed tends to zero, the response approaches the response to a steady step, while as the speed goes to infinity, the response behaves like the response to a step of light presented simultaneously to the entire retina. (This question is taken from Peskin (1976)).

Hint: to exhibit the space-like limit write R as a function of $x + ct$, where c is the speed of the moving step. To exhibit the time-like limit, write R as a function of $t + x/c$.

Solution

Consider first the space-like limit, i.e., the limit as the speed of the moving step tends to zero. Define a new travelling wave variable $\xi = x + ct$, where c is the speed of the moving step. In this new variable, $L(\xi) = H(\xi)$, where H is the Heaviside function. We look for solutions of the form $E(\xi)$, $I(\xi)$ and $R(\xi)$. Since

$$\frac{\partial E(x, t)}{\partial t} = c\frac{dE(\xi)}{dt}, \quad \text{and} \tag{20.982}$$

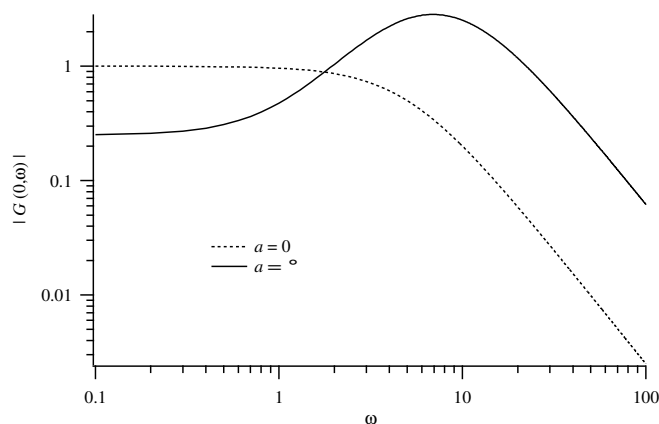$$\frac{\partial^2 I(x, t)}{\partial x^2} = \frac{d^2 I(\xi)}{dx^2}, \tag{20.983}$$

Figure 20.82: Plots of $\left.|G(0,\omega)|^2\right|_{a=\infty}$ and $\left.|G(0,\omega)|^2\right|_{a=0}$ using the arbitrary parameter values $\tau = 0.2$, $\lambda = 1$. We plot them as log-log plots as this is a common way of plotting gain against frequency (see Fig. 19.22).

it follows that the response is found by solving

$$c\tau E' + E \;\; = \;\; L, \tag{20.984}$$
$$I'' - cI' - I \;\; = \;\; -\lambda(E - I), \tag{20.985}$$

where a prime denotes differentiation with respect to ξ.

We now need to take the limit of these equations as $c \to 0$. However, this is not such a trivial matter as it might appear at first. Firstly, note that we must take the limit $c \to 0$ for a fixed t and thus the limit will hold only for any finite time. (In other words, we shall show that for any finite time, in the limit as $c \to 0$ the response to the moving step looks like the response to a fixed step).

Secondly, if we just let $c \to 0$ directly, we get $E = L$ and

$$I'' = (1 + \lambda)I - \lambda L, \tag{20.986}$$

which is just the same as (**??**), which gives, as we showed before, the response to a steady step. Although this gives the correct answer, one should be a little more careful about taking the limit as $c \to 0$ in (20.984) as in the limit the highest derivative of E is lost.

A better approach is to write the equation for E as

$$c\tau E' = -E + \begin{cases} 0, & \xi < 0, \\ 1, & \xi > 0. \end{cases} \tag{20.987}$$

On the region $\xi < 0$, boundedness of the solution requires that $E \equiv 0$ there, while on the region $\xi > 0$ we use the boundary condition $E(0) = 0$ to get

$$E(\xi) = \begin{cases} 0, & \xi < 0, \\ 1 - e^{\frac{-\xi}{c\tau}}, & \xi > 0. \end{cases} \tag{20.988}$$

Clearly, as $c \to 0$ (for fixed t) E just tends toward the Heaviside function, i.e., $E \to L$.

It is much easier to take the limit of (20.985) as $c \to 0$, as the highest derivative is not now lost in the limit; one can safely just set $c = 0$.

Next we consider the time-like limit. Define the traveling wave variable

$$\eta = t + \frac{x}{c}, \tag{20.989}$$

and let a prime now denote differentiation with respect to η. This gives

$$\tau E' + E = L, \tag{20.990}$$

$$\frac{1}{c^2} I'' - I' - (1 + \lambda)I = -\lambda E. \tag{20.991}$$

For any fixed x we can let $c \to \infty$ to get $\eta \to x$ and

$$\tau E' + E = L, \tag{20.992}$$

$$I' + (1 + \lambda)I = \lambda E, \tag{20.993}$$

which is the same as (??) and (??), i.e., we just get the space-independent behavior as required.

However, it is best to check that taking the limit as $c \to \infty$ in (20.991) gives no nasty surprises as the highest derivative is lost. What happens is the following. For any value of c we can solve (20.992) and (20.993) on the two regions $\xi < 0$ and $\xi > 0$. Since each region will give two unknown constants in the solution that gives a total of four unknown constants. These constants may then be determined from the two boundary conditions at $\pm\infty$ and the requirement that the solution and its derivative be continuous at $\xi = 0$. However, as $c \to \infty$ we find that we are no longer able to force the derivative to be continuous at $\xi = 0$, and thus, in the limit, we get a solution with a "kink" at $\xi = 0$ (i.e., at $t = 0$). This is, of course, precisely the solution plotted in Fig. 19.12A. Note that the loss of the highest derivative in the differential equation results merely in the loss of a continuous derivative at $\xi = 0$, but the solution itself remains continuous.